

HANDBOOK OF SHOCK WAVES

EDITORS

Gabi Ben-Dor

Ozer Igra

Tov Elperin

VOLUME

2

Shock Wave Interactions and
Propagation



Handbook of Shock Waves

Handbook of Shock Waves

VOLUME 1 Theoretical, Experimental, and Numerical Techniques

VOLUME 2 Shock Wave Interactions and Propagation

VOLUME 3 Chemical Reactions in Shock Waves and Detonations

Handbook of Shock Waves

VOLUME 2 Shock Wave Interactions and Propagation

EDITORS

GABI BEN-DOR

OZER IGRA

TOV ELPERIN

*Pearlstone Center for Aeronautical
Engineering Studies
Department of Mechanical
Engineering
Ben-Gurion University of the Negev
Beer Sheva
Israel*

ACADEMIC PRESS

A Harcourt Science and Technology Company

San Diego San Francisco New York Boston
London Sydney Tokyo

This book is printed on acid-free paper. (∞)

Copyright © 2001 by Academic Press

All rights reserved.

No part of this publication may be reproduced or transmitted in any form or by any means, electronic or mechanical, including photocopy, recording, or any information storage and retrieval system, without permission in writing from the publisher.

Requests for permission to make copies of any part of the work should be mailed to: Permissions Department, Harcourt, Inc., 6277 Sea Harbor Drive, Orlando, Florida, 32887-6777.

The appearance of code at the bottom of the first page of a chapter in this book indicates the Publisher's consent that copies of the chapter may be made for personal or internal use of specific clients. This consent is given on the condition, however, that the copier pay the stated per-copy fee through the Copyright Clearance Center, Inc. (222 Rosewood Drive, Danvers, Massachusetts 01923), for copying beyond that permitted by Sections 107 or 108 of the U.S. Copyright Law. This consent does not extend to other kinds of copying, such as copying for general distribution, for advertising or promotional purposes, for creating new collective works, or for resale. Copy fees for pre-1998 chapters are as shown on the title pages; if no fee code appears on the title page, the copy fee is the same as for current chapters, \$35.00.

ACADEMIC PRESS

A Harcourt Science and Technology Company

525 B Street, Suite 1900, San Diego, CA 92101-4495, USA

<http://www.academicpress.com>

Academic Press

Harcourt Place, 32 Jamestown Road, London, NW1 7BY, UK

Library of Congress Catalog Card Number: 00-106364

Set International Standard Book Number: 0-12-086430-4

International Standard Book Number, Volume 2: 0-12-086432-2

Printed in the United States of America

00 01 02 03 04 IP 9 8 7 6 5 4 3 2 1

CONTENTS

<i>Preface</i>	xvii
<i>Contributors</i>	xxi
<i>Volume Contents</i>	xxvii

7 One-Dimensional Interactions

by Ozer Igra

7.1 Background and Introduction	1
7.2 Head-on Collision between Two Shock Waves	3
7.3 Head-on Collision between a Shock Wave and a Rarefaction Wave	9
7.4 Head-on Collision of a Shock Wave with a Contact Discontinuity	15
7.5 Head-on Collision of a Rarefaction Wave with a Contact Discontinuity	19
7.6 Shock Wave Overtaking Another Shock Wave	20
7.7 Shock Wave Overtaken by a Rarefaction Wave	22
7.8 Shock Wave Overtaking a Rarefaction Wave	24
7.9 The General Riemann Problem Solver	26
7.9.1 Concluding Remarks	34
7.10 Head-on Collision of a Planar Shock Wave with a Nonrigid Wall	35

7.11 Summary and Conclusions	62
References	64

8 Two Dimensional Interactions

8.1 Oblique Shock Wave Reflections

by Gabi Ben-Dor

8.1.1 Introduction and Historical Background	68
8.1.2 Analytical Approaches for Describing Regular and Mach Reflections	69
8.1.2.1 Two-Shock Theory	70
8.1.2.2 Three-Shock Theory	71
8.1.2.3 Shock Polars	72
8.1.2.4 Suggested Transition Criteria	75
8.1.2.5 Dual-Solution Domain	81
8.1.2.6 Hysteresis Phenomenon in the $RR \leftrightarrow IR$ Transition	82
8.1.3 Steady Flows	83
8.1.3.1 Categories of Steady Shock Wave Reflections	83
8.1.3.2 Hysteresis Phenomena	88
8.1.3.3 Analytical Prediction of the Mach Reflection Wave Configuration	106
8.1.3.4 Modification of the Perfect Two- and Three-Shock Theories	113
8.1.4 Pseudo-Steady Flow	117
8.1.4.1 Shock Wave Diffraction Process	117
8.1.4.2 Shock Wave Reflection Phenomena	118
8.1.4.3 Regular Reflection RR	119
8.1.4.4 Single-Mach Reflection SMR	120
8.1.4.5 Transitional-Mach Reflection TMR	121
8.1.4.6 Double-Mach Reflection DMR	124
8.1.4.7 von Neumann Reflection, vNR	130
8.1.4.8 Triple Point Trajectory Angles	133
8.1.4.9 Transition Criteria	143
8.1.4.10 Domains of Different Types of Reflections	145
8.1.4.11 Modification of the Two- and Three-Shock Theories	146
8.1.5 Unsteady Flow	153
8.1.5.1 Reflection of Constant Velocity Shock Waves over Non-straight Surfaces	153
8.1.5.2 Non-Constant Velocity Shock Wave Reflections over Straight Surfaces	170

8.1.5.3	Spherical Shock Wave Reflections over Straight and Non-Straight Surfaces	171
	Acknowledgements	174
	References	174
8.2	<i>The Refraction of Shock Waves</i>	
	<i>by Leroy F. Henderson</i>	
8.2.1	Introduction	181
8.2.2	One-Dimensional Refraction	183
8.2.2.1	The Wave Systems	183
8.2.2.2	The Wave Impedance	184
8.2.2.3	The Reflection and Transmission Coefficients	184
8.2.2.4	The Continuity Conditions at the Interface	185
8.2.2.5	The Refraction Limits	186
8.2.2.6	Solution of One-Dimensional Refraction	187
8.2.3	Two-Dimensional Refraction	188
8.2.3.1	Two-Dimensional Wave Systems	188
8.2.3.2	The Wave Impedance of an Oblique Shock	190
8.2.3.3	The Refraction Law	191
8.2.3.4	The Relative Refractive Index	193
8.2.3.5	The Shock Polar	193
8.2.4	Solution of Fast–Slow Refraction $\eta_a > 1$	197
8.2.5	Solution of Slow–Fast Refraction $\eta_a < 1$	198
8.2.6	The Minimum Time Principle	201
	References	202
8.3	<i>Shock Wave/Boundary Layer Interactions</i>	
	<i>by Jean M. D�elery</i>	
8.3.1	Introduction	205
8.3.2	Properties of Shock-Induced Interactions	208
8.3.2.1	The Different Kinds of Interaction	208
8.3.2.2	Interaction without Boundary Layer Separation	211
8.3.2.3	Interaction with Boundary Layer Separation	216
8.3.2.4	Hypersonic Interaction	230
8.3.2.5	Other Aspects of Shock-Induced Interaction	235
8.3.3	Interaction Control Methods	245
8.3.3.1	Mechanisms for Control Action	245
8.3.3.2	Examination of Some Control Actions	247
8.3.4	Problems Raised by Interaction Modeling	252
8.3.4.1	Numerical Accuracy of the Codes	253

8.3.4.2 The Physical Modeling	256
8.3.5 Concluding Remarks	260
Acknowledgments	261
References	261

9 Axisymmetric Shock Wave Reflections

by Brian E. Milton

9.1 Introduction	266
9.2 External Reflections over Simple Upstream-Facing Cones	267
9.2.1 Simple Cones in Steady Supersonic Flows	267
9.2.2 Moving Shock Waves	271
9.3 Generalized Solution of Conical Moving Shock Waves	274
9.3.1 Formulation for Ray-Shock Calculations in Conical Mach Reflection	275
9.3.2 Equations for the Generalized Ray-Shock Solution	276
9.3.3 Curved Mach Stems	278
9.3.4 Solution Procedures for Cases without Self-Similarity	279
9.3.5 Postreflection Rays Parallel to the Centerline	279
9.4 Some Conical Mach Reflection Results from the Ray-Shock Theory	280
9.4.1 External (Expanding) Flows	280
9.4.2 Converging (Internal) Cases	285
9.5 Experimental Conical Mach Reflection Studies	289
9.5.1 Validation for External Cone Cases	289
9.5.2 Mach Reflection within Conical Contractions	293
9.6 Numerical Experiments (CFD)	298
9.6.1 CFD Scheme for Conical Mach Reflection	299
9.6.2 Comparison of the Ray-Shock Theory CFD Results	306
9.7 Some Theoretical Aspects of Conical Mach Reflection	310
9.7.1 Von Neumann Mach Reflection Effects in Conical Reflections	310
9.7.2 Self-Similar and Non-Self-Similar Axisymmetric Mach Reflection	311
9.7.3 Transition from Regular to Mach Reflection in Conical Problems	312
9.8 Some Applications of Axisymmetric Calculations	314

9.8.1	Mach Reflection over a Simple Cone	314
9.8.2	Axisymmetric Shock Wave Focusing	314
9.9	Final Discussion	315
	References	317

10 Shock Waves in Channels

by Werner Heilig and Ozer Igra

10.1	Introduction	320
10.2	Scenarios of Shock Wave Propagation in Channels	320
10.3	Phenomenology of Shock Wave Propagation in Channels	322
10.3.1	Brief Description of the Conventional Shock Tube	325
10.3.2	Visualization of Shock Wave Propagation in Various Channel Configurations	325
10.3.3	Comments on the Usefulness of Flow Visualization and Its Evaluation	348
10.4	Approximate Analytical Methods	350
10.4.1	The Unsteady Quasi-One-Dimensional Flow	350
10.4.2	Rudinger's Method	352
10.4.3	The Chester–Chisnell–Whitham Channel Formula	356
10.4.4	Whitham's Theory of Shock Dynamics	361
10.4.5	Analytical Treatment of Shock Propagation through a Class of Bifurcated Ducts using Whitham's Theory	367
10.5	Numerical Methods	375
10.5.1	Example Calculations using Wave Propagation Codes	377
10.5.2	The GRP (General Riemann Problem) Code	383
10.5.3	Solving a Quasi-One-Dimensional Flow using the Random Choice Method (RCM)	387
10.6	Data Bases	390
10.7	Final Remarks	391
	References	392

11 Shock Wave Focusing

by Fumio Higashino

11.1	Introduction	397
------	--------------	-----

11.2	Theoretical Analyses	403
11.2.1	Basic Equations	403
11.2.2	Characteristics Method and CCW Approximation	404
11.2.3	Similarity Method for Imploding Shock Wave	405
11.3	Results and Discussion	407
11.3.1	Shock Tube Experiment	407
11.3.2	Blast Waves	408
	References	412

12 Applications of Shock Waves in Medicine

by Achim M. Loske

12.1	Introduction	415
12.2	Brief Physical Background	417
12.2.1	Lithotripsy Pressure Pulses	417
12.2.2	Shock Wave Propagation and Interaction with Matter	418
12.3	Extracorporeal Shock Wave Lithotripsy	421
12.3.1	Electrohydraulic Shock Wave Lithotripters	421
12.3.2	Electromagnetic Shock Wave Lithotripters	426
12.3.3	Piezoelectric Shock Wave Lithotripters	428
12.3.4	Microexplosive Lithotripters	429
12.4	Shock Waves in Orthopedics	429
12.5	Shock Waves in Ophthalmology	431
12.6	Shock Waves in Oncology and Gene Therapy	432
12.7	Shock Waves as a Possible Method for Food Preservation	434
12.8	Shock Wave Thrombus Ablation	436
	Acknowledgments	437
	References	437

13 Spherical Shock Waves

13.1 Expanding Spherical Shocks (Blast Waves)

by John M. Dewey

13.1.1	Introduction	442
13.1.2	Physical Properties of Expanding Spherical Shock Waves	443
13.1.2.1	Physical Properties in the Radius-Time (r - t) Plane	443
13.1.2.2	Shock Front Properties	445
13.1.2.3	The Shape of the Shock Wave	447

13.1.2.4	A Compendium of Physical Properties	451
13.1.3	Scaling Laws	455
13.1.4	Analytical Solutions	460
13.1.5	Numerical Methods	462
13.1.5.1	Numerical Modeling	462
13.1.5.2	Numerical Reconstruction	465
13.1.6	Experimental Measurement Techniques	466
13.1.6.1	Introduction	466
13.1.6.2	Electronic Methods	466
13.1.6.3	Photogrammetric Methods	467
13.1.6.4	Passive Methods	470
13.1.7	Spherical Shock Reflections	471
13.1.7.1	Regular and Mach Reflections	471
13.1.7.2	Height-of-Burst Curves	473
	Acknowledgments	477
	References	478
13.2	<i>General Attenuation Law for Spherical Shock Wave Propagating in Pure Gases</i>	
	<i>by Felix Aizik, Gobi Ben-Dor, Tov Elperin, and Ozer Igra</i>	
13.2.1	Introduction	483
13.2.2	Background	484
13.2.2.1	The Assumptions	485
13.2.3	General Attenuation Law	485
	References	488
14	Shock-Induced Instability of Interfaces	
	<i>by Dov Shvarts, Oren Sadot, Dan Oron, Avi Rikanati, and Uri Alon</i>	
14.1	Introduction: Hydrodynamic Instability	490
14.2	The Rayleigh–Taylor Instability	491
14.2.1	Linear Analysis	491
14.2.2	Analysis of the Early Nonlinear Stages	494
14.2.3	The Late Nonlinear Stage (Layzer Model for $A = 1$)	497
14.2.4	Density Ratio Dependence	498
14.2.5	Spike Behavior	500
14.2.6	Dimensionality Dependence	501
14.3	The Richtmyer–Meshkov Instability	503
14.4	Experimental Studies	506

14.4.1	Experimental Studies of the Single-Mode Rayleigh–Taylor Instability	506
14.4.2	Experimental Studies of the Richtmyer–Meshkov Instability	508
14.5	Random Initial Conditions	523
14.5.1	Two-Dimensional Statistical Mechanics Model and Late Time Scaling Laws	525
14.5.2	Three-Dimensional Effects on the Late Time Scaling Laws	528
14.5.3	Shock Wave Experiments of the Bubble Competition Process	532
14.5.4	Re-Shock Experiments	534
14.6	Summary	539
	Acknowledgments	540
	References	540

15 Shock Wave Propagation in Multi-Phase Media

15.1 Shock Wave Propagation in Porous Media

by Beric W. Skews, Avi Levy and David Levi-Hevroni

15.1.1	Introduction	546
15.1.2	General Description of the Wave Propagation	546
15.1.3	The Nature of Porous Foams	548
15.1.4	Scientific Background	551
15.1.4.1	Systems with Flexible Skeletons	551
15.1.4.2	Systems with Rigid Skeletons	560
15.1.4.3	Blast Wave Loading	562
15.1.4.4	Multidimensional Studies	563
15.1.4.5	Theory and Modeling	569
15.1.5	Macroscopic Governing Equations	575
15.1.5.1	The Assumptions	575
15.1.5.2	The Balance Equations	576
15.1.6	Case Studies	579
15.1.6.1	One-dimensional Shock Wave Interaction with Rigid Porous Material	580
15.1.6.2	One-dimensional Shock Wave Interaction with Flexible Foam	584
15.1.6.3	Regular Reflection from a Rigid Porous Surface in Pseudo-Steady Flows	588
	References	592

15.2 Weak Shock Wave Interaction with Inert Granular Media

by Alexander Britan and Avi Levy

15.2.1	Introduction	598
15.2.2	Experimental Methods and Materials	600
15.2.3	Two-dimensional Packing of Cylinders and Disks	614
	15.2.3.1 Unsteady Flow Pattern	614
	15.2.3.2 Dynamics of the Contact Stress Transfer	617
	15.2.3.3 Role of the Sidewall Friction	619
15.2.4	Three-Dimensional Packing of Spherical Particles	623
	15.2.4.1 Behavior of the Unsteady End-Wall Peak	623
	15.2.4.2 Bridging effect and Size of the Pressure Transducer	632
	15.2.4.3 Packing Density and Gas Filtration	635
	15.2.4.4 Effective Stress Behavior	638
15.2.5	Dynamics of the Granular Layer Compression	643
	15.2.5.1 Wave Processes	643
	15.2.5.2 Dynamic Young Moduli	649
15.2.6	Shielding Characteristics of Granular Filters	653
	15.2.6.1 Problem Description	653
	15.2.6.2 Attenuation Performance of Granular Materials	656
15.2.7	Physical Models and Simulations	658
15.2.8	Conclusion	661
	References	663

15.3 Shock Waves in Inert and Reactive Bubbly Liquids

by Valery K. Kedrinskii

15.3.1	Shock Waves in Inert Bubbly Liquids	668
	15.3.1.1 Introduction	668
	15.3.1.2 Shock Wave and Spherical Bubble Interaction: Cumulative Jet Formation	673
	15.3.1.3 Plane Shock Waves and Gas Layers	680
	15.3.1.4 Shock Wave Transformation by Bubbly-Layers	683
	15.3.1.5 The Iordansky-Kogarko-van- Wijngaarden Nonequilibrium Two- Phase Model of a Bubbly Liquid	695
	15.3.1.6 Amplification, Collision, and Focusing of Shock Waves in Bubbly Liquids	702
15.3.2	Bubbly Detonation: Waves in Reactive Bubbly Liquids	711

15.3.2.1	Introduction	711
15.3.2.2	Single Bubble Dynamics with Chemical Reactions	712
15.3.2.3	Reactive Bubble Dynamics and the Interface Mass Transfer	718
15.3.2.4	Shock Waves in Reactive Bubbly Liquids	725
15.3.2.5	Initiation, Formation, and Collision of Bubbly Detonation Waves: "Hot spots" Mechanism	733
	References	741

15.4 Shock Wave Interaction with Liquid Gas Suspensions

by Marinus E. H. Van Dongen

15.4.1	Introduction	748
15.4.2	Thermodynamic Properties of a Liquid Gas Suspension	750
15.4.3	Speeds of Sound	752
15.4.3.1	Fully Frozen Sound Speed	753
15.4.3.2	Partly Frozen Sound Speed	753
15.4.3.3	Equilibrium Sound Speed	753
15.4.4	Jump Conditions Across a Normal Shock Wave in a Liquid Gas Suspension	756
15.4.4.1	Approximate Rankine-Hugoniot Relations for Weak Shocks	757
15.4.4.2	Guha's Exact Analytical Solution for Specified p_1 , T_1 , T_2 and f_g	757
15.4.5	Transfer of Momentum, Mass, and Energy from Gas to Droplets; Dilute Condensable Component	759
15.4.5.1	Continuum Regime	761
15.4.5.2	The Free Molecular Regime	762
15.4.5.3	The Transition Regime	762
15.4.6	Estimates of Characteristic Relaxation Times	763
15.4.6.1	Exchange of Momentum	763
15.4.6.2	Exchange of Heat	765
15.4.6.3	Exchange of Mass: Evaporation	766
15.4.6.4	Comparison of the Characteristic Relaxation Times	767
15.4.7	Shock-Induced Evaporation in the Wet-Bulb Regime	768
15.4.8	Experimental Observations	770
15.4.9	Shock Waves in Wet Steam	774

15.4.10 Fully Dispersed Shock Waves in Wet Steam	777
15.4.11 Conclusions	779
Acknowledgment	780
References	780

This Page Intentionally Left Blank

PREFACE

Shock waves have fascinated mankind from the dawn of history. Before the discovery of explosive materials the commonly encountered shock waves were thunders. Until the seventeenth century such violent phenomena were enshrouded in mystery and they were related to evil powers. As mentioned in Section 1.4.1, Earnshaw (1851) was probably the first who related the thunder propagation to supersonic velocity. Now we know that shock waves result from a very sudden release of chemical, electrical, nuclear, or mechanical energy in a limited space. In nature the most frequently encountered shock wave is the thunder that follows lightning. Shock waves are also associated with earthquakes and volcanic eruptions. A typical man-made shock wave results from the detonation of explosive materials. Also, complex shock wave structures appear in all supersonic flights. These all can range from weak shock waves associated with the use of any firearm up to shock waves resulting from nuclear explosions reaching enormous magnitudes. In descriptive terms, a shock wave is a very sharp, thin front through which there exists a sudden change in all flow properties, such as pressure, temperature, density, velocity and entropy. At standard atmospheric conditions the width of a shock wave front is about 2.5 Angstrom.

Shock waves appear in many forms and in various media. In the *Handbook of Shock Waves* we have tried to cover as many as possible of these forms. First, in Chapter 1, a brief historical description indicating milestones of shock wave research and activities starting in the sixteenth century and continuing up to the end of the Second World War is given. The historical survey ends at 1945 since many of the postwar investigations are presented in the various chapters of the Handbook.

General propagation laws governing shock wave transmission through matter are outlined in Chapter 2, in which the basic equations governing shock wave propagation are presented. These equations are used in subsequent chapters.

In Chapter 3.1 a detailed description of shock wave propagation in gases is given; shock wave propagation in liquids follows in Chapter 3.2 and shock wave propagation in solids in Chapter 3.3. The rest of Chapter 3 is dedicated to special aspects of shock waves in gases. In Chapter 3.4 the unique case of rarefaction shocks is discussed; this is followed, in Chapter 3.5, by a discussion on shock wave stability. Although most of the Handbook deals with shock waves on earth and in the earth's atmosphere, shock waves are not limited to our planet. One of the theories explaining the creation of the universe is via the "big-bang," which is the ultimate shock wave. Shock waves are daily events in the sun's corona and a frequent occurrence in the solar wind in space. Chapter 3.6 is devoted to shock waves in space.

For experimental studies of shock waves one needs facilities that can generate flows in which shock waves appear in a laboratory environment. Furthermore, special diagnostics systems are required in order to detect, observe and provide records enabling the analysis of a laboratory-generated shock. In Chapter 4 various facilities suitable for the generation of shock waves are presented. The classical shock tube facility and the flow field it produces are outlined in Chapter 4.1. The extension of the shock tube concept to shock tunnels and piston driven shock and expansion tunnels is described in Chapters 4.2 and 4.3, respectively. The various shock tube facilities described in Chapters 4.1 to 4.3 are primarily designed to produce step-like shock waves, i.e., shock waves associated with a sudden jump between two different, uniform states.

However, shocks generated in the atmosphere, i.e., blast waves, are usually different from those defined above. In such waves fast pressure decay follows the sudden jump in the pressure across the shock front. Chapter 4.4 describes blast tubes, which are facilities suitable for producing blast waves. A common feature to all facilities described in Chapters 4.1 to 4.4 is the fact that they all produce very short duration flows, significantly less than a second. When longer flow durations are needed, for example, if steady flow is studied, one resorts to supersonic and hypersonic wind tunnels. The flow duration in such facilities is measured in minutes. The construction and operation of supersonic and hypersonic wind tunnels is described in Chapter 4.5. Experimental investigation of shock wave phenomena requires, in addition to the facility for producing shock waves, appropriate measuring techniques. Such devices must have extremely short response times, should not disturb the investigated flow field and should produce unambiguous results. A survey of diagnostic techniques suitable for flow visualization is given in Chapter 5.1. A comple-

mentary diagnostic used for studying high temperature flows generated behind strong shock waves is spectroscopy. This technique is presented in Chapter 5.2.

Until the late 1960's most of the shock wave investigations were experimental. This was an unavoidable consequence of the fact that the equations of motion governing shock wave generated flows are non-linear. Only for special flow conditions do such equations have analytical solutions. Otherwise, a numerical solution is the only available option. This option became feasible only after the rapid development in computer software and hardware that started in the 1970's. Today, numerical analysis is replacing experimental investigation as a primary tool in studying shock wave phenomena. Many different codes have been developed especially for studying shock wave phenomena. The major ones are described in Chapter 6 where numerical methods suitable for investigating shock wave phenomena are discussed.

The rest of the Handbook deals with some specific types and aspects of shock wave phenomena. In Chapter 7 the simplest shock wave generated flow and wave interactions, the one-dimensional flow case, is discussed. The natural second step, described in Chapter 8, is the two-dimensional wave interaction. In Chapter 8.1 reflections of oblique shock waves from rigid surfaces are discussed. Shock wave refraction is presented in Chapter 8.2, followed, in Chapter 8.3, by a description of shock waves interactions with boundary layers. This complex process is of major importance because it appears in real supersonic flows over bodies. A special case of two-dimensional flow is that resulting from shock wave reflection from axisymmetric bodies; such cases are the topic of Chapter 9.

Propagation of shock waves in straight tunnels was described while discussing shock tube facilities (Chapter 4.1) and one-dimensional interactions (Chapter 7). In practice one encounters tunnels in which there are bends, curvatures, splittings and other obstacles. Obviously, such additions spoil the one-dimensional nature of the flow and thereby increase the complexity of the prevailing flow field. Chapter 10 treats, theoretically, experimentally and numerically shock wave propagation in channels of different geometry.

A special case of one-dimensional shock wave flow is the case in which the flow has a spherical symmetry. Spherical shock waves result from detonation of spherical explosives. These shocks decay as they expand until they reduce to sound waves. Their fast decay is a direct result of the fact that a given amount of energy is spread out over an ever-increasing volume of fluid. The opposite is true for spherical shock waves that propagate towards the center namely, imploding shocks. In such cases the shock strength increases as it approaches the center. The physical background of imploding shock waves is outlined in Chapter 11 where shock wave focusing is discussed. Shock wave focusing is the cornerstone of lithotripsy, a technique employed for shattering kidney stones. Recently it was extended for usage in ophthalmology, gene therapy,

thrombus ablation and food preservation. Details regarding these recent applications are given in Chapter 12 where the application of shock waves in medicine is discussed. A survey of expanding spherical shock waves (blast waves) is given in Chapter 13.1. The last chapter discussing spherical shocks, Chapter 13.2, provides a general attenuation law for spherical expanding shock waves.

An important topic that has drawn attention in recent years is shock-induced instabilities of interfaces separating different gases or phases. This is the topic of Chapter 14. Chapter 15 deals with various aspects of shock wave propagation in multi-phase media. In Chapter 15.1 shock wave propagation in porous media is presented. The considered media are composed of deformable or rigid skeletons whose voids are filled with gas. A special case of porous media is a granular medium. In such a case the skeleton is composed of small solid particles packed on together. Propagation of shock waves in granular media is the topic of Chapter 15.2. Cases of two-phase flow are discussed in Chapters 15.3 and 15.4. The former deals with shock wave in inert and reactive bubbly liquids and the latter with shock wave propagation in liquid-gas suspensions.

The last part of the Handbook, Volume 3, edited by Professor Assa Lifshitz of the Hebrew University in Jerusalem, is dedicated to chemical reactions taking place in the hot post-shock flow. These topics are considered in Chapter 16. A special case of chemical reactions induced by strong shock waves propagating in a combustible gas mixture is the case of combustion, detonation and deflagration. This topic is covered in Chapter 17.

The present Handbook is the result of a cooperative effort of 47 scientists from 15 countries, each knowledgeable in his own field. We hope it will serve as a useful source of information for scientists, engineers and students active in shock wave research. Although we have tried to cover as many aspects of shock wave phenomena as we could, we are fully aware that this is a target one may approach but not necessarily reach. It is hoped that in future editions additional topics will be added.

Many scientists, engineers and students around the world are engaged in shock wave studies. Each has his reason for being attracted to investigating these phenomena. For two of us (Gabi Ben-Dor and Ozer Igra) it was the late Professor Irvine I. Glass who opened the door to the world of shock waves and was our guide though this fascinating subject while we took our early steps in the field of shock wave phenomena. We are grateful to him for introducing us to the path along which we continue to walk with ever-increasing interest.

CONTRIBUTORS

URI ALON (Ch 14), Faculty of Physics, The Weizmann Institute of Science, Rhovot 76100, Israel

GABI BEN-DOR (Ch 8.1, 13.2), Pearlstone Center for Aeronautical Engineering Studies, Department of Mechanical Engineering, Ben-Gurion University of the Negev, Beer Sheva 84105, Israel, Tel: +972 7 647 7082; Fax: +972 7 647 2813; E-mail: bendorg@bgumail.bgu.ac.il

ALEX BRITAN (Ch 15.2), Pearlstone Center for Aeurnautical Engineering Studies, Department of Mechanical Engineering, Ben-Gurion University of the Negev, Beer-Sheva 84105, Israel, Tel: +972 7 647 7068; Fax: +972 7 647 2813; E-mail: britan@menix.bgu.ac.il

BRUNO CHANETZ (Ch 4.5), Head of Unit “Experimental Simulation,” Head of Hypersonic Hyperenthalpic Project, ONERA, 8 rue des Vertugadins 92190 Meudon, France, Tel: +33 1 46 23 51 60; Fax: +33 1 46 23 51 51; E-mail: Bruno.Chanetz@onera.fr

AMER CHPOUN (Ch. 4.5), Laboratoire d’Aérothermique du CNRS, 4 ter, Route Des Gardes 92190 Meudon, France, Tel: +33 2 38 25 77 00; Fax: +33 2 38 25 77 77; E-mail: chpoun@atlas.cnrs-bellevue.fr

DAVID F. DAVIDSON (Ch 5.2), Mechanical Engineering Department, Stanford University, Stanford, California, 94305, USA, Tel: 650 725 2072; Fax: 650 723 1748; E-mail: dfd@stanford.edu

JEAN DÉLERY (Ch 8.3), Fundamental/Experimental Aerodynamics Department, Onera 92190, Meudon, France, Tel: +33 1 46 23 51 61; Fax: +33 1 46 23 51 58; E-mail: Jean.Delery@onera.fr

JOHN DEWEY (Ch 13.1), Department of Physics and Astronomy, University of Victoria, Victoria, BC, Canada, Tel: +1 250 721 7707; Fax: +1 250 721 7715; E-mail: jdewey@uvic.ca

TOV ELPERIN (Ch 13.2), Pearlstone Center for Aeronautical Engineering Studies, Department of Mechanical Engineering, Ben-Gurion University of the Negev, Beer Sheva 84105, Israel, Tel: +972 7 647 7078; Fax: +972 7 647 2813; E-mail: elperin@menix.bgu.ac.il

GEORGE EMANUEL (Ch 3.1), School of Aerospace and Mechanical Engineering, University of Oklahoma, Norman, Oklahoma, 73019, USA, Tel: 388 5809 885; E-mail: emanuel@mae.uta.edu

MICHAEL GEDALIN (Ch 3.6), Department of Physics, Ben-Gurion University of the Negev, Beer Sheva 84105, Israel, Tel: +972 7 646 1645; Fax: +972 7 647 2904; E-mail: gedalin@bgumail.bgu.ac.il

ZHAO-YUAN HAN (Ch 3.7), Department of Modern Mechanics, University of Science and Technology of China, Hefei, Anhui 230026, PR China, Tel: +86 551 360 3704; Fax: +86 551 363 1760; E-mail: zyhan@ustc.edu.cn

RONALD K. HANSON, (Ch 5.2), Mechanical Engineering Department, Stanford University, Stanford, California, 94305, USA

WERNER HEILIG (Ch 10), Fraunhofer Gesellschaft für Angewandte Forschung-Ernst-Mach-Institut, Eckerstrasse 4, D-79104 Freiburg, Germany, Tel: +49 761 271 4334; Fax: +49 761 271 4316; E-mail: Heilig@emi.fhg.de

LE ROY F. HENDERSON (Ch 2, 8.2), Professor Emeritus, 8 Damour Avenue, East Lindfield, Sydney, New South Wales 2070, Australia, Tel: +61 2 9416 7041; Fax: +61 2 9416 1029; E-mail: lfh@s054.aone.net.au

FUMIO HIGASHINO (Ch 11), Department of Mechanical Systems Engineering, Faculty of Engineering, Tokyo-Noko University, Nakacho 2-24-16, Japan, Tel: +81 42 388 7074; Fax: +81 42 383 1431; E-mail: higasino@cc.tuat.ac.jp

OZER IGRA (Ch 7, Ch 13.2), Pearlstone Center for Aeronautical Engineering Studies, Department of Mechanical Engineering, Ben-Gurion University of the Negev, Beer Sheva 84105, Israel, Tel: +972 7 647 7081; Fax: +972 7 647 2813; E-mail: ozer@bgumail.bgu.ac.il

SHIGERU ITOH (Ch 3.2), Shock Wave and Condensed Matter Research Center, Kumamoto University, Kumamoto, Japan, Tel: +81 96 342 3299; Fax: +81 96 342 3299; E-mail: itoh@mech.kumamoto-u.ac.jp

VALERY KEDRINSKII (Ch 15.3), M.A. Lavrentjev Institute of Hydrodynamics, Novosibirsk, 630090, Russia, Tel: +7 3832 33 26 65; Fax: +7 3832 33 16 12; E-mail: kedr@hydro.nsc.ru

RALPH DONALD KERN, JR. (Ch 16.1), Department of Chemistry, University of New Orleans, New Orleans, Louisiana, 70148, USA, Tel: 504 280 6847; Fax: 504 280 6860; E-mail: rdkcm@jazz.ucc.uno.edu

JOHN H. KIEFER (Ch 16.2), Department of Chemical Engineering, University of Illinois at Chicago, Chicago, Illinois, 60607, USA, Tel: 312 996 5711; Fax: 312 996 0808; E-mail: kiefer@uic.edu

HARALD KLEINE (Ch 5.1), Department of Aeronautics and Space Engineering, Graduate School of Engineering, Tohoku University, Sendai, 980-8579 Japan, Tel: +81 22 217 7003; Fax: +81 22 217 7003; E-mail: hkleine@rainbow.ifs.tohoku.ac.jp

ALFRED KLUWICK (Ch 3.4), Institute of Fluid Mechanics and Heat Transfer, Vienna, University of Technology, Vienna, Austria, Tel: +43 1 58801 32220; Fax: +43 1 48801 32299; E-mail: A.Kluwick@tuwien.ac.at

PETER KREHL (Ch 1), Ernst-Mach-Institut, Fraunhofer-Institut für Kurzzeitdynamik, Eckerstr. 4, D-79104 Freiburg, Germany, Tel: +49 7561 2714 333; Fax: +49 7561 2714 316; E-mail: Krehl@emi.fhg.de

N.M. KUZNETSOV (Ch 3.5), N. Semenov Institute of Chemical Physics, Russian Academy of Sciences, Moscow, 117977, Russia, E-mail: kuznetzv@center.chph.ras.ru or nix@ns.unexim.ru

JOHN LEE (Ch 17), Professor of Mechanical Engineering, McGill University, Montreal, Quebec, Canada, Tel: +1 514398 6298; Fax: +1 514 398 7365; E-mail: jhslee@mecheng.mcgill.ca

DAVID LEVI-HEVRONI (Ch 15.1), Ben-Gurion University of the Negev, Beer-Sheva 84105, Israel, Tel: +972 7 656 7418; Fax: +972 656 7878; E-mail: davidlh@netvision.net.il

AVI LEVY (Ch 15.1, 15.2), Pearlstone Center for Aeronautical Engineering Studies, Department of Mechanical Engineering, Ben-Gurion University of the Negev, Beer-Sheva 84105, Israel, Tel: +972 7 647 7092; Fax: +972 7 647 2813; E-mail: avi@bgumail.bgu.ac.il

ASSA LIFSHITZ (Ch 16.3, 16.4, 16.5), Department of Physical Chemistry, The Hebrew University of Jerusalem, Jerusalem 91904, Israel, Tel: +972 2 658 5865; Fax: +972 2 561 7812; E-mail: assa@vms.huji.ac.il

ACHIM MAX LOSKE MEHLING (Ch 12), Instituto de Fisica, UNAM, Fisica Aplicada y tecnologia Avanzada, A.P. 1-1010, 76000 Queretaro, QRO, Mexico, Tel: +52 42 38 11 64; Fax: +52 42 38 11 65; E-mail: loske@fenix.ifisicacu.unam.mx

JOE VICTOR MICHAEL (Ch 16.3), Chemistry Division, Argonne National Laboratory, 9700 S. Cass Avenue, Argonne, Illinois, 60439, USA, Tel: 630 252 3171; Fax: 630 252 4470; E-mail: michael@anlchm.chm.anl.gov

BRIAN E. MILTON (Ch 9), School of Mechanical and Manufacturing Engineering, University of New South Wales, Sydney, N.S.W., 2052, Australia, Tel: +61 2 385 4088; Fax: +61 2 663 1222; E-mail: B.Milton@unsw.edu.au

RICHARD GARETH MORGAN (Ch 4.2, 4.3), Director, The Centre for Hypersonics, The University of Queensland, Brisbane, Australia 4067, Tel: +61 7 3365 3592; Fax: +61 7 3365 4799; E-mail: morgan@mech.uq.edu.au

KUNIHITO NAGAYAMA (Ch 3.3), Department of Aeronautics and Astronautics, Kyushu University, Fukuoka 812-8581, Japan, Tel: +81 92 642 3804; Fax: +81 92 642 4143; E-mail: nagayama@aero.kyushu-u.ac.jp

MICHIO NISHIDA (Ch 4.1), Department of Aeronautics and Astronautics, Kyushu University, Fukuoka 812-8581, Japan, Tel: +81 92 642 3722; Fax: +81 92 642 3752; E-mail: nishida@aero.kyushu-u.ac.jp

DAN ORON (Ch 14), Department of Physics, Nuclear Research Center Negev 84190, Israel, and Department of Physics, Ben-Gurion University of the Negev, Beer-Sheva 84105, Israel

AVI RIKANATI (Ch 14) Department of Physics, Nuclear Research Center Negev 84190, Israel, and Department of Physics, Ben-Gurion University of the Negev, Beer-Sheva 84105, Israel

ROBERT W. ROBEY (Ch 4.4), Los Alamos National Laboratory, Los Alamos, USA, Tel: 505 662 2018 or 505 255 8280; E-mail: robey@mesatop.com

PHILIP LAWRENCE ROE (Ch 6), W. M. Keck Foundation Laboratory for Computational Fluid Dynamics, Department of Aerospace Engineering, University of Michigan, Ann Arbor, Michigan, 48109-2118, USA, Tel: 734 764 3394; Fax: 734 763 0578; E-mail: philroe@engin.umich.edu

OREN SADOT (Ch 14) Department of Physics, Nuclear Research Center Negev 84190, Israel, and Department of Mechanical Engineering, Ben-Gurion University of the Negev, Beer-Sheva 84105, Israel

DOV SHVARTS (Ch 14) Department of Physics, Nuclear Research Center Negev 84190, Israel, and Department of Mechanical Engineering, Ben-Gurion University of the Negev, Beer-Sheva 84105, Israel, Tel: +972 7 656 7500; Fax: +972 7 656 7665; E-mail: shvarts@bgumail.bgu.ac.il

H.J. SINGH (Ch 16.1), Department of Chemistry, University of New Orleans, New Orleans, Louisiana, 70148, USA

BERIC WILLIAM SKEWS (Ch 15.1), School of Mechanical Engineering, University of the Witwatersrand, PO WITS, 2050, South Africa, Tel: +27 11 717 7324; Fax: +27 11 339 7997; E-mail: bskews@hertz.mech.wits.ac.za

WING TSANG (Ch 16.4), National Institute of Standards and Technology, Gaithersburg, MD 20899, USA, Tel: 301 975 2507; Fax: 301 975 3670; E-mail: wing.tsang@nist.gov

MARINUS E.H. VAN DONGEN (Ch 15.4), Burgers Centre for Fluid Dynamics, Department of Applied Physics, Eindhoven University of Technology, P.O. Box 513, 5600 MB, Eindhoven, The Netherlands, Tel: +31 40 2473194; Fax: +31 40 2464151; E-mail: M.E.H.v.Dongen@tue.nl

HAI WANG (Ch 16.6), Department of Mechanical Engineering, University of Delaware, Newark, Delaware, 19716, USA, Tel: 302 831 4464; Fax: 302 831 3619; E-mail: Lwang@me.udel.edu

XIE-ZHEN YIN (Ch 3.7), Department of Modern Mechanics, University of Science and Technology of China, Hefei, Anhui 230026, PR China, Tel: +86 551 360 3704; Fax: +86 551 363 1760

Q. ZHANG (Ch 16.1), Department of Chemistry, University of New Orleans, New Orleans, Louisiana, 70148, USA

This Page Intentionally Left Blank

Volume Contents

VOLUME 1 *Theoretical, Experimental, and Numerical Techniques*

1 History of Shock Waves

by P. Krehl

2 General Laws for Propagation of Shock Waves through Matter

by L.F. Henderson

3 Theory of Shock Waves

3.1 Shock Waves in Gases

by G. Emanuel

3.2 Shock Waves in Liquids

by S. Itoh

3.3 Shock Waves in Solids

by K. Nagayama

- 3.4 Rarefaction Shocks**
by A. Kluwick
 - 3.5 Stability of Shock Waves**
by N. M. Kuznetsov
 - 3.6 Shock Waves in Space**
by M. Gedalin
 - 3.7 Geometrical Shock Dynamics**
by Z-Y Han and X-Z Yin
- 4 Shock Tubes and Tunnels: Facilities, Instrumentation and Techniques**
 - 4.1 Shock Tubes**
by M. Nishida
 - 4.2 Free Piston-Driven Reflected Shock Tunnels**
by R. Morgan
 - 4.3 Free Piston-Driven Expansion Tubes**
by R. Morgan
 - 4.4 Blast Tubes**
by R. Robey
 - 4.5 Supersonic and Hypersonic Wind Tunnels**
by B. Chanetz and A. Chpoun
- 5 Measurement Techniques and Diagnostics**
 - 5.1 Flow Visualization**
by H. Kleine
 - 5.2 Spectroscopic Diagnostics**
by D.F. Davidson & R.K. Hanson
- 6 Numerical Methods**
by P. Roe

VOLUME 2

Shock Wave Interactions and Propagation

7 One-Dimensional Interactions

by O. Igra

8 Two-Dimensional Interactions

8.1 *Oblique Shock Wave Reflections*

by G. Ben-Dor

8.2 *The Refraction of Shock Waves*

by L.F. Henderson

8.3 *Shock Wave/Boundary Layer Interactions*

by J.M. Détery

9 Axisymmetric Shock Wave Reflections

by B.E. Milton

10 Shock Waves in Channels

by W. Heilig & O. Igra

11 Shock Wave Focusing

by F. Higashino

12 Applications of Shock Waves in Medicine

by A.M. Loske

13 Spherical Shock Waves

13.1 *Expanding Spherical Shocks (Blast Waves)*

by J.M. Dewey

13.2 *General Attenuation Law for Spherical Shock Wave Propagating in Pure Gases*

by F. Aizik, G. Ben-Dor, T. Elperin & O. Igra

14 Shock Induced Instability of Interfaces

by D. Shvarts, O. Sadot, D. Oron, A. Rikanati and U. Alon

15 Shock Wave Propagation in Multi-Phase Media

15.1 Shock Wave Propagation in Porous Media

by B. Skews, A. Levy & D. Levi-Hevroni

15.2 Weak Shock Wave Interaction with Inert Granular Media

by A. Britan & A. Levy

15.3 Shock Waves in Inert and Reactive Bubbly Liquids

by V. Kedrinskii

15.4 Shock Wave Interaction with Liquid-Gas Suspensions

by M.E.H. van Dongen

VOLUME **3**
***Chemical Reactions in Shock Waves
and Detonations***

16 Chemical and Combustion Kinetics

16.1 *Mass Spectrometric Methods for Chemical Kinetics in Shock Tubes*

by R.D. Kern, H.J. Singh & Q. Zhang

**16.2 *The Application of Densitometric Methods to the
Measurement of Rate Processes in Shock Tubes***

by J.H. Kiefer

**16.3 *Atomic Resonance Absorption Spectrometric with
Flash or Laser Photolysis in Shock Wave Experiments***

by J.V. Michael & A. Lifshitz

16.4 *Single Pulse Shock Tube*

by W. Tsang & A. Lifshitz

16.5 *Ignition Delay Times*

by A. Lifshitz

16.6 *Particulate Formation and Analysis*

by H. Wang

17 Combustion, Detonation and Deflagration

by J. Lee

One-Dimensional Interactions

OZER IGRA

Department of Mechanical Engineering, Ben-Gurion University of the Negev, Beer Sheva, 84105 Israel

-
- 7.1 Background and Introduction
 - 7.2 Head-on Collision between Two Shock Waves
 - 7.3 Head-on Collision between a Shock Wave and a Rarefaction Wave
 - 7.4 Head-on Collision of a Shock Wave with a Contact Discontinuity
 - 7.5 Head-on Collision of a Rarefaction Wave with a Contact Discontinuity
 - 7.6 Shock Wave Overtaking another Shock Wave
 - 7.7 Shock Wave Overtaken by a Rarefaction Wave
 - 7.8 Shock Wave Overtaking a Rarefaction Wave
 - 7.9 The General Riemann Problem Solver
 - 7.9.1 Concluding Remarks
 - 7.10 Head-on Collision of a Planar Shock Wave with a Non-Rigid Wall
 - 7.11 Summary and Conclusions
 - References

7.1 BACKGROUND AND INTRODUCTION

Wave interactions (shock and/or rarefaction waves) in a one-dimensional flow were the subject of many investigations during the precomputer era. Because of the lack of “numerical power,” the conservation equations of mass, momentum and energy (Eqs. (7.1) to (7.3)) were solved in simple situations (self similar flows) by reducing them to a set of algebraic equations in the (p, u) -plane. Alternatively, researchers restored to experiments in shock tubes. For example, von Neumann (1943) wrote one of the earliest papers in this topic. He

discussed the interaction of two plane shock waves in a one-dimensional flow. Courant and Friedrichs (1943) published a more general analysis of one-dimensional interactions of shock waves, rarefaction waves, and contact surfaces. They predicted the results of interaction of simple waves using graphical discussions in the (p, u) -plane. Similar arguments will be shown subsequently in descriptions of some specific wave interactions. Guderley (1942) obtained a graphical solution to the flow field resulting from collision between a shock and a rarefaction wave. Because of the lack of complete and accurate solutions to Eqs. (7.1) to (7.3), an extensive experimental investigation was launched, for example at the Institute of Aerophysics, University of Toronto (whose name was changed in the early 1960s to The Institute of Aerospace Studies). Nicholl (1951) studied the head-on collision of shock and rarefaction waves; Henshaw (1950) investigated the interaction between a shock wave and a contact surface; Gould (1952) studied the head-on collision of two shock waves and the collision between shock and rarefaction waves. Bull, Fowell, and Henshaw (1953) studied the interaction of two similarly facing shock waves; McKee (1954) conducted an experimental study of the interaction of a plane shock wave with a contact surface; and Ford and Glass (1954) published an experimental study of shock wave refractions. An experimental study of one-dimensional refraction of a rarefaction wave at a contact surface was published by Billington (1955), and Glass, Heuckroth, and Molder (1959) studied the one-dimensional overtaking of a shock wave by a rarefaction wave.

The flow field resulting from all these cases and, in principle, all cases of one-dimensional wave interactions can readily be obtained by solving Eqs. (7.1) to (7.3) for the appropriate boundary and initial conditions. Solving such flows is essentially solving the well-known Riemann problem, which models the one-dimensional interaction between a pair of uniform (but different) states of a compressible fluid that are initially separated by a plane of discontinuity. A scheme developed by Falcovitz and Ben-Artzi (1995), the GRP (generalized Riemann problem solver), is employed in Section 7.9 to study the head-on interaction between a shock wave and a rarefaction wave.

For a perfect fluid (inviscid and thermally nonconductive) the conservation equations of mass, momentum, and energy in a one-dimensional flow are as follows:

Conservation of mass

$$\frac{\partial \rho}{\partial t} + \frac{\partial}{\partial x}(\rho u) = 0 \quad (7.1)$$

Conservation of momentum

$$\frac{\partial}{\partial t}(\rho u) + \frac{\partial}{\partial x}(\rho u^2 + p) = 0 \quad (7.2)$$

Conservation of energy

$$\frac{\partial E}{\partial t} + \frac{\partial}{\partial x} \{E\rho u + pu\} = 0 \quad (7.3)$$

where ρ , u , p , E , and e are flow density, velocity, pressure, and specific total and specific internal energy, respectively. Assuming that a local thermodynamic equilibrium exist for every fluid state, the pressure is related to (ρ, e) through an equation of state, such as the perfect gas relation

$$e = p/[\rho(\gamma - 1)] \quad (7.4)$$

where γ is a constant polytropic index. The relation between the total and internal energies is given by $E = e + \frac{1}{2}u^2$.

At present many computer programs suitable for handling one-dimensional flows are available; see, for example, Chapter 6. In Section 7.9 information about a second-order, Godunov-based scheme, which is especially suitable for handling flow discontinuities, is given. This scheme is employed for producing some of the subsequent results.

Until the 1960s, gas-dynamic interactions were rarely computed by numerically integrating the governing equations (7.1) to (7.4). Rather, researchers resorted to simple analysis of idealized models. In the following some of these analytical models are presented. Their contemporary significance lies in bringing out the mathematical and physical aspects of wave interactions, and not merely replacing detailed numerical computations.

In the last section of the present chapter, in Section 7.10, the head-on collision of a planar shock wave with a nonrigid wall is discussed.

7.2 HEAD-ON COLLISION BETWEEN TWO SHOCK WAVES

In contemporary analysis the Rankine–Hugoniot shock relations (for a moving shock wave) are recast in the mathematical form of a “jump condition” (e.g., in Chorin and Marsden, 1990). These relations are

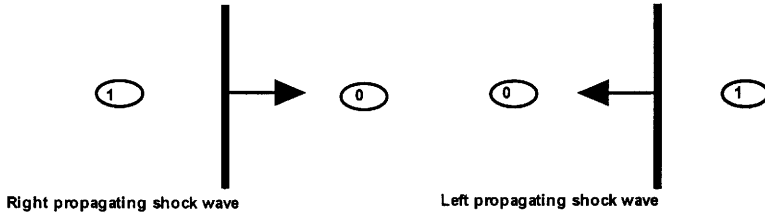
$$U_s(\rho_1 - \rho_0) = \rho_1 u_1 - \rho_0 u_0 \quad (7.5)$$

$$U_s(\rho_1 u_1 - \rho_0 u_0) = (p_1 + \rho_1 u_1^2) - (p_0 + \rho_0 u_0^2) \quad (7.6)$$

$$U_s(\rho_1 E_1 - \rho_0 E_0) = (p_1 + \rho_1 E_1)u_1 - (p_0 + \rho_0 E_0)u_0 \quad (7.7)$$

where U_s is the propagation velocity of the incident shock wave, and subscripts 0, 1 refer to constant states on each side of the shock wave. For the case when $U_s = 0$, the stationary jump conditions are obtained, which amounts to the continuity of all flux components across the shock wave. In one space dimension, shock-wave propagation with respect to the fluid can be either to

the right (right-propagating shock), or to the left (left-propagating shock), see the accompanying illustration.



The basic relation across a rarefaction wave is

$$u_1 \pm \frac{2}{\gamma - 1} a_1 = u_0 \pm \frac{2}{\gamma - 1} a_0, \quad (7.8)$$

and since the flow in a rarefaction wave is isentropic, we also have

$$\frac{\rho_1}{\rho_0} = \left(\frac{p_1}{p_0} \right)^{1/\gamma}; \quad \frac{a_1}{a_0} = \left(\frac{p_1}{p_0} \right)^{(\gamma-1)/2\gamma} = \left(\frac{\rho_1}{\rho_0} \right)^{(\gamma-1)/2} = \left(\frac{T_1}{T_0} \right)^{1/2}. \quad (7.9)$$

Combining Eqs. (7.4) to (7.7), after some algebra, yields

$$u_1 = u_0 + a_0 \left(\frac{p_1}{p_0} - 1 \right) \sqrt{\frac{2}{\gamma(\gamma - 1) \left[1 + \frac{\gamma + 1}{\gamma - 1} \frac{p_1}{p_0} \right]}}. \quad (7.10)$$

Following the convention specified in Chapter 3 (Section 3.1.2.3) the positive sign is to be taken for shock waves propagating along the positive x -direction (forward-facing) and the negative sign for a backward-facing shock wave. A forward-facing wave is a wave in which the flow particles enter it from right to left. The opposite is true for a backward-facing wave.

Combining Eqs. (7.8) and (7.9) yields

$$u_1 = u_0 \pm \frac{2a_0}{\gamma - 1} \left[1 - \left(\frac{p_1}{p_0} \right)^{(\gamma-1)/2\gamma} \right]. \quad (7.11)$$

Again, a positive sign is associated with a forward-facing rarefaction wave.

It is convenient to describe waves interaction in a (p, u) -plane. Using Eqs. (7.10) or (7.11), the locus of all states (1) that can be reached from a known state (0) through a shock wave (Fig. 7.1a) or a rarefaction wave (Fig. 7.1b) can be drawn; this is shown schematically in Fig. 7.1. Figure 7.2 shows the locus of all states (1) that may be reached from a known state (0) by either a shock or a rarefaction wave when the known state is on the left of the considered wave. Figure 7.3 presents a similar case, but when the known state (0) is located on the right of the considered wave. From such plots the problem of interaction could be solved as follows:

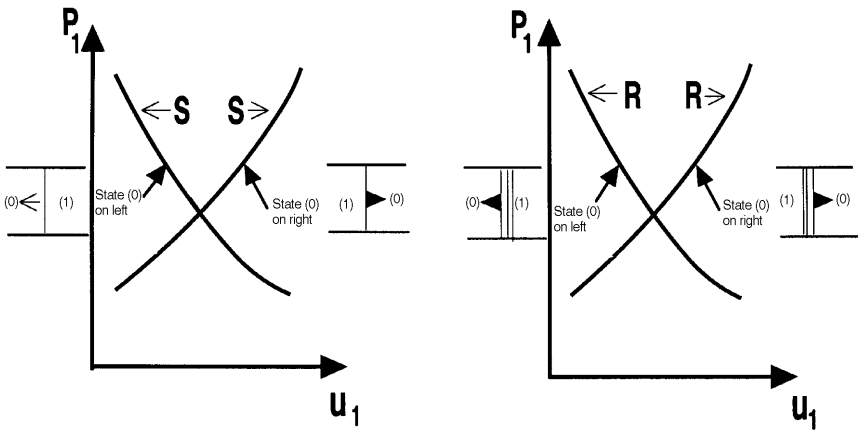


FIGURE 7.1 (a) Locus of all states (1) that may be connected through a shock wave to a known state (0). (b) Locus of all states (1) that may be connected through a rarefaction wave to a known state (0).

Suppose we have two known shock waves, which propagate toward each other through a known state (0). Call the state behind the shock wave propagating from left to right by (l) and the state behind the shock wave propagating from right to left by (r). Since the waves strength is known and the state into which they propagate is also known, states (l) and (r) are known and could be identified in the (p, u) -plane. Now curves connecting state (l) to state (0) and state (r) to state (0) can be drawn using Eq. (7.10). Once the

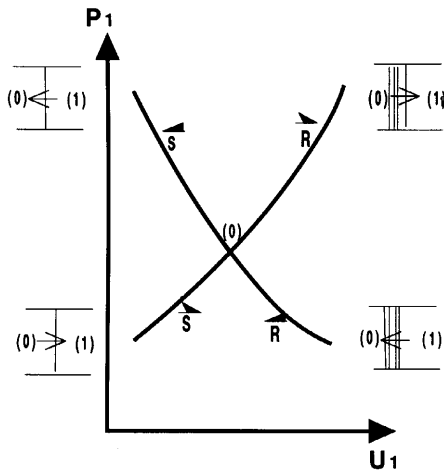


FIGURE 7.2 Locus of all states (1) that may be connected through a shock or a rarefaction wave to a known state (0) on the left.

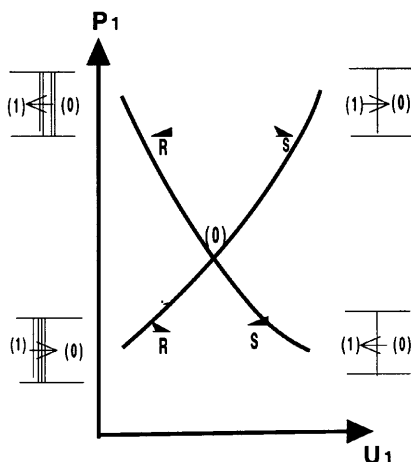


FIGURE 7.3 Locus of all states (1) that may be connected through a shock or a rarefaction wave to a known state (0) on the right.

interaction between the colliding shock waves begins, state (0) disappears, and either instantaneously or after a period of penetration, a forward-facing shock wave propagates into state (r) and a backward-facing shock wave propagates into state (l). These two reflected waves are separated by a new state. The new state can be found in the (p , u)-plane; it is located at the intersection of the two curves, drawn with the aid of Eq. (7.10), passing through states (l) and (r). Figure 7.4 illustrates the head-on collision of two shock waves in the (p , u)-plane. Initially these waves, of known strength, connect states (l) and (r) into the known, uniform state (0).

Thus, states (0), (l) and (r) can be plotted on the (p , u)-diagram as shown schematically in Fig. 7.4. Also, the appropriate curves connecting (0)–(l) and (0)–(r) could be drawn using Eq. (7.10). These curves provide the locus of all points that may be connected to (l) and (r) through forward- or backward-facing shock or rarefaction waves. Each intersection of these curves represents a possible new state formed after the head-on collision between the two known shock waves. Figure 7.4 suggests that three intersections are possible: states (3), (3^*), and (3^{**}). However, only one is physically possible. If the new state (3^*) could be formed after the head-on collision, it would be reached via a forward-facing shock wave proceeding to state (r) on its right and a forward-facing rarefaction wave moving from state (l) on its left. Since these two waves propagate in the same direction, an overtaking is inevitable and therefore, reaching a uniform state (3^*) is impossible since the overtaking process results in a continually changing state, whereas we are looking for a uniform state. Similar arguments hold for state (3^{**}), which is reached via backward-facing shock and rarefaction waves. Only state (3) results in a state having uniform

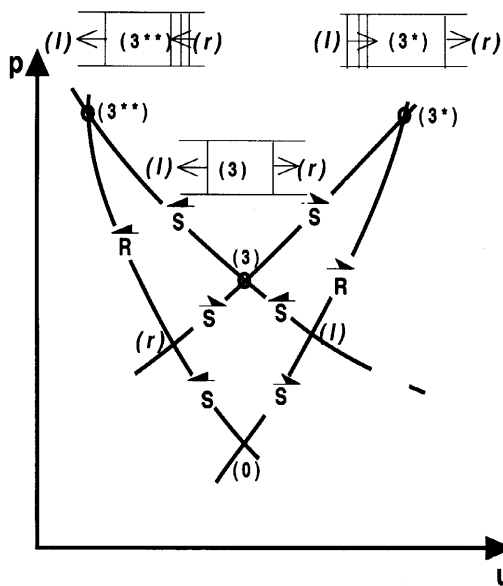
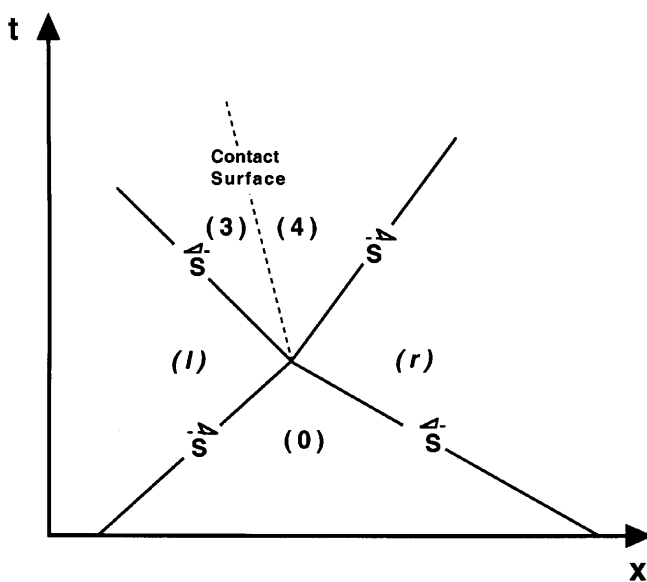
FIGURE 7.4 Head-on collision between two shock waves in the (p, u) -plane.

FIGURE 7.5 Head-on collision between two shock waves, in the (x, t) -plane.

pressure and velocity. In this case the head-on collision results in a forward-facing shock wave propagating into the uniform state (r) on its right and a backward-facing shock wave propagating into the uniform state (l) on its left; see Fig. 7.4. A region of uniform pressure and velocity separates these shock waves; state (3).

A schematic presentation of this head-on collision is shown in the (x, t) -plane in Fig. 7.5. State (3) in Fig. 7.5 is divided into two regions separated by a contact surface. The contact surface is invisible in Fig. 7.4 since equal pressures and equal velocities exist across it. However, other flow properties, such as density, entropy, and temperature, experience a discontinuous change across the contact surface.

Employing Eq. (7.10) across each of the four shock waves shown in Fig. 7.5 and noting that across the contact surface we have $u_3 = u_4$ and $p_3 = p_4$ results in the following equations:

$$u_3 = u_r - a_r \left(\frac{p_3}{p_r} - 1 \right) \sqrt{\frac{2}{\gamma(\gamma-1) \left[1 + \frac{\gamma+1}{\gamma-1} \frac{p_3}{p_r} \right]}} \quad (7.12)$$

$$u_3 = u_l - a_l \left(\frac{p_3}{p_l} - 1 \right) \sqrt{\frac{2}{\gamma(\gamma-1) \left[1 + \frac{\gamma+1}{\gamma-1} \frac{p_3}{p_l} \right]}} \quad (7.13)$$

$$u_r = u_0 - a_0 \left(\frac{p_r}{p_0} - 1 \right) \sqrt{\frac{2}{\gamma(\gamma-1) \left[1 + \frac{\gamma+1}{\gamma-1} \frac{p_r}{p_0} \right]}} \quad (7.14)$$

$$u_l = u_0 - a_0 \left(\frac{p_l}{p_0} - 1 \right) \sqrt{\frac{2}{\gamma(\gamma-1) \left[1 + \frac{\gamma+1}{\gamma-1} \frac{p_l}{p_0} \right]}}. \quad (7.15)$$

Combining Eqs. (7.12)–(7.15) in order to find a solution for p_3/p_r results in the following expression, from which p_3/p_r could be found by an iteration procedure:

$$\frac{p_3}{p_r} = 1 + \sqrt{1 + \frac{\gamma+1}{\gamma-1} \frac{p_3}{p_r}} \left\{ A - C \left[B + \frac{\frac{p_0 p_3}{p_l p_r} - \frac{p_0}{p_r}}{\sqrt{\frac{p_0}{p_r} \left(\frac{\gamma+1}{\gamma-1} \frac{p_0 p_3}{p_l p_r} + \frac{p_0}{p_r} \right)}} \right] \right\}. \quad (7.16)$$

Here,

$$A = \frac{1 - \frac{p_0}{p_r}}{\sqrt{1 + \frac{\gamma + 1}{\gamma - 1} \frac{p_0}{p_r}}}, \quad B = \frac{\frac{p_0}{p_l} - 1}{\sqrt{1 + \frac{\gamma + 1}{\gamma - 1} \frac{p_0}{p_l}}},$$

$$C = \sqrt{\frac{\frac{p_0}{p_r} \left(\frac{\gamma + 1}{\gamma - 1} + \frac{p_0}{p_r} \right) \left(1 + \frac{\gamma + 1}{\gamma - 1} \frac{p_0}{p_l} \right)}{\left(1 + \frac{\gamma + 1}{\gamma - 1} \frac{p_0}{p_r} \right) \frac{p_0}{p_l} \left(\frac{\gamma + 1}{\gamma - 1} + \frac{p_0}{p_l} \right)}}.$$

When the two incident shock waves are of equal strength, that is, $p_r/p_0 = p_l/p_0$, Eq. (7.16) reduces to

$$\frac{p_3}{p_r} = \frac{p_3}{p_l} = \frac{2 + \frac{\gamma + 1}{\gamma - 1} - \frac{p_0}{p_r}}{1 + \frac{\gamma + 1}{\gamma - 1} \frac{p_0}{p_r}} = \frac{2 + \frac{\gamma + 1}{\gamma - 1} - \frac{p_0}{p_l}}{1 + \frac{\gamma + 1}{\gamma - 1} \frac{p_0}{p_l}}. \quad (7.17)$$

As could be expected, the preceding expression is identical to what is obtained for a normal shock wave reflection from a rigid wall.

7.3 HEAD-ON COLLISION BETWEEN A SHOCK WAVE AND A RAREFACTION WAVE

In Fig. 7.6 the head-on collision between a planar shock wave and a rarefaction wave is shown schematically. A shock wave of known strength proceeds from a state (1) on its left into a known state (0) on its right. A rarefaction wave of a known strength proceeds in an opposite direction, from state (2) on its right into the known state (0) on its left. Since states (0), (1), and (2) are known, they can be drawn in the (p, u) -plane, as shown schematically in Fig. 7.6. Using Eqs. (7.10) and (7.11), the locus of all points in the (p, u) -plane that could be connected to the known states (1) and (2) through a forward- or backward-facing shock/rarefaction waves can be drawn. Each intersection of these curves represents a possible new state, to result from the head-on collision between the known shock and rarefaction waves. The curves forming this possible new state define the type of the postcollision waves. As in the previous case, Fig. 7.6 suggests that three new states are possible after the collision, marked as (3), (3*), and (3**) in Fig. 7.6. Again, only one of these three states is physically possible, since only one results in uniform states. If

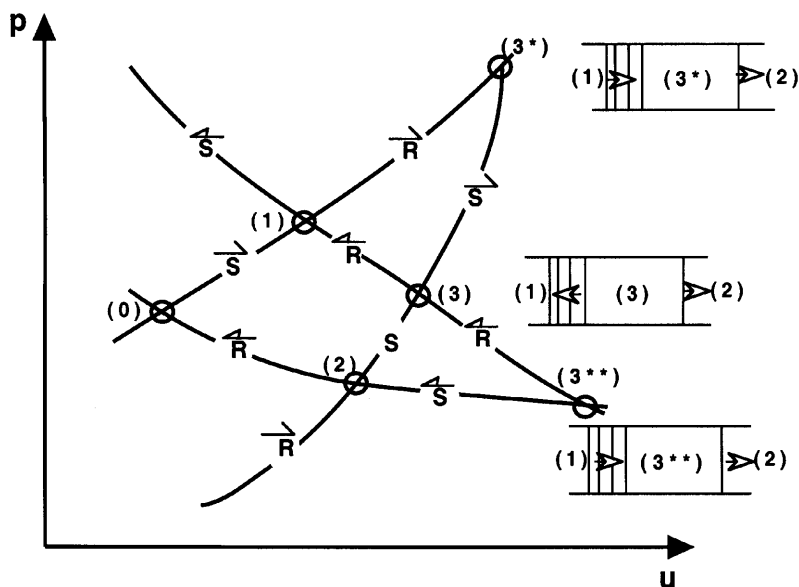


FIGURE 7.6 Head-on collision between a shock wave and a rarefaction wave, in the (p, u) -plane.

state (3^*) could result from the collision between the shock and the rarefaction waves, then it would be reached by a forward-facing rarefaction wave [progressing from state (1) on its left] and a forward-facing shock wave [propagating into state (2) on its right]. This means that a shock wave and a part of the rarefaction wave originate from some point x and at some time t , and they move in the same direction. As they will immediately overtake, this could not result in a uniform state (3^*) , and therefore this solution is physically impossible. The same arguments rule out the possibility of state (3^{**}) . On the other hand, state (3) represents a physically possible state resulting from the head-on collision between the initial shock and rarefaction waves. It suggests that the collision results in a rarefaction wave moving to the left, into state (1), and a shock wave moving to the right, into state (2). This is the only possible state in which we have a uniform pressure and a uniform velocity in the new state that separates between states (1) and (2).

Presentation of state (3) and the appropriate waves leading to this result in the (x, t) -plane are shown schematically in Fig. 7.7. The colliding shock and rarefaction waves [separating between states (0) and (1), and states (0) and (2), respectively] and the transmitted shock wave [separating between states

(2) and (4)] and the rarefaction wave [(separating between states (1) and (3)] are clearly visible in Fig. 7.7. States (3) and (4) have the same pressure and flow velocity (and therefore they appear as a point “3” in Fig. 7.6), but they differ in density, temperature, and entropy. Therefore, they appear as two different states in Fig. 7.7. This can be demonstrated as follows. When following the path of particle “a” in Fig. 7.7, we notice that it experiences a certain entropy jump while crossing the incident shock wave. Thereafter, it maintains this entropy level since its passage through the transmitted rarefaction wave is an isentropic process. All particles on the left of this particle path (particle “a” in Fig. 7.7) are experiencing the same entropy jump while crossing the original, incident shock wave. As the shock wave penetrates into the rarefaction wave it is continuously weakened and therefore, each consecutive particle that crosses the shock wave experiences a different (smaller) entropy jump. Once the shock wave emerges from the rarefaction wave it proceeds with a constant speed (a straight line in Fig. 7.7) into state (2). From the moment it emerges from the rarefaction wave, all consecutive particles that cross the transmitted shock wave experience the same entropy jump. Thus, particle paths labeled “a” and “b” (in Fig. 7.7) define the boundary of a contact region separating the two uniform states (3) and (4), such that $p_3 = p_4$, $u_3 = u_4$, but $T_3 \neq T_4$, $\rho_3 \neq \rho_4$, and $S_3 \neq S_4$. In this transition region density, temperature and entropy vary smoothly.

Applying Eqs. (7.10) and (7.11) across the four waves shown in Fig. 7.7 and making use of the fact that across the contact region $p_3 = p_4$ and

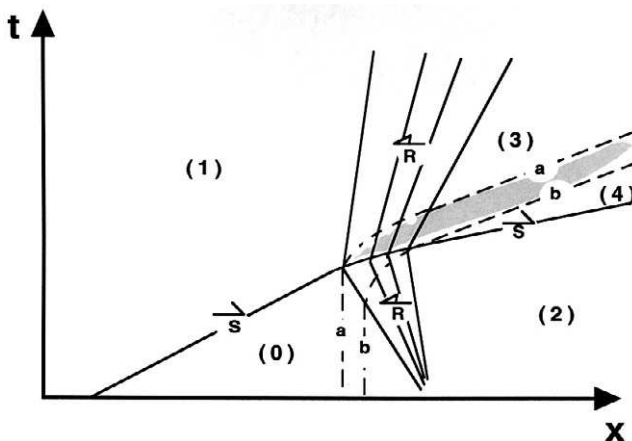


FIGURE 7.7 Head-on collision between a shock wave and a rarefaction wave, in the (x, t) -plane.

$u_3 = u_4$ results in

$$u_3 = u_1 - \frac{2a_1}{\gamma - 1} \left[\left(\frac{p_3}{p_1} \right)^{(\gamma-1)/2\gamma} - 1 \right] \quad (7.18)$$

$$u_3 = u_2 + a_2 \left(\frac{p_3}{p_2} - 1 \right) \sqrt{\frac{2}{\gamma(\gamma-1) \left[1 + \frac{\gamma+1}{\gamma-1} \frac{p_3}{p_2} \right]}} \quad (7.19)$$

$$u_1 = u_0 + a_0 \left(\frac{p_1}{p_0} - 1 \right) \sqrt{\frac{2}{\gamma(\gamma-1) \left[1 + \frac{\gamma+1}{\gamma-1} \frac{p_1}{p_0} \right]}} \quad (7.20)$$

$$u_2 = u_0 - \frac{2a_0}{\gamma - 1} \left[\left(\frac{p_2}{p_0} \right)^{(\gamma-1)/2\gamma} - 1 \right]. \quad (7.21)$$

The speeds of sounds a_1 and a_2 are given by

$$a_1 = a_0 \sqrt{\frac{\frac{\gamma+1}{\gamma-1} + \frac{p_1}{p_0}}{\frac{p_1}{p_0} \left(1 + \frac{\gamma+1}{\gamma-1} \frac{p_1}{p_0} \right)}},$$

$a_2 = a_0 \left(\frac{p_2}{p_0} \right)^{(\gamma-1)/2\gamma}$. Eliminating u_1, u_2 , and u_3 from Eqs. (7.18) to (7.21) results in the following equation for p_3/p_2 in term of the known values for p_1/p_0 and p_0/p_2 :

$$\frac{p_3}{p_2} = 1 + \sqrt{1 + \frac{\gamma+1}{\gamma-1} \frac{p_3}{p_2}} \left\{ D - E \left[\left(\frac{p_3 p_0}{p_2 p_1} \right)^{(\gamma-1)/2\gamma} - \left(\frac{p_0}{p_2} \right)^{(\gamma-1)/2\gamma} \right] \right\}. \quad (7.22)$$

Here,

$$D = \left(\frac{p_0}{p_2} \right)^{(\gamma-1)/2\gamma} \frac{\left(\frac{p_1}{p_0} - 1 \right)}{\sqrt{1 + \frac{\gamma+1}{\gamma-1} \frac{p_1}{p_0}}} + \sqrt{1 + \frac{\gamma+1}{\gamma-1}} \left[1 - \left(\frac{p_0}{p_2} \right)^{(\gamma-1)/2\gamma} \right]$$

and

$$E = \sqrt{\left(1 + \frac{\gamma+1}{\gamma-1} \right) \frac{\frac{\gamma+1}{\gamma-1} + \frac{p_1}{p_0}}{\frac{p_1}{p_0} \left(1 + \frac{\gamma+1}{\gamma-1} \frac{p_1}{p_0} \right)}}.$$

Equation (7.22) provides an algebraic equation for calculating, in an iterative way, the final states and waves strengths resulting from the head-on collision between a shock and a rarefaction wave. It could also be used for calculating the flow properties, and for plotting the shock wave path through the rarefaction wave. This can be achieved as shown subsequently.

The incident rarefaction wave is divided into a number of small sections. As the flow inside the rarefaction wave is isentropic, p, u, ρ , and a may be calculated along any C_- characteristic of the incident rarefaction wave using the following well-known relations:

$$\frac{x}{a_0 t} = \frac{u}{a_0} - \frac{a}{a_0} \quad \text{and} \quad \frac{u}{a_0} + \frac{2}{\gamma - 1} \frac{a}{a_0} = \frac{u_0}{a_0} + \frac{2}{\gamma - 1}.$$

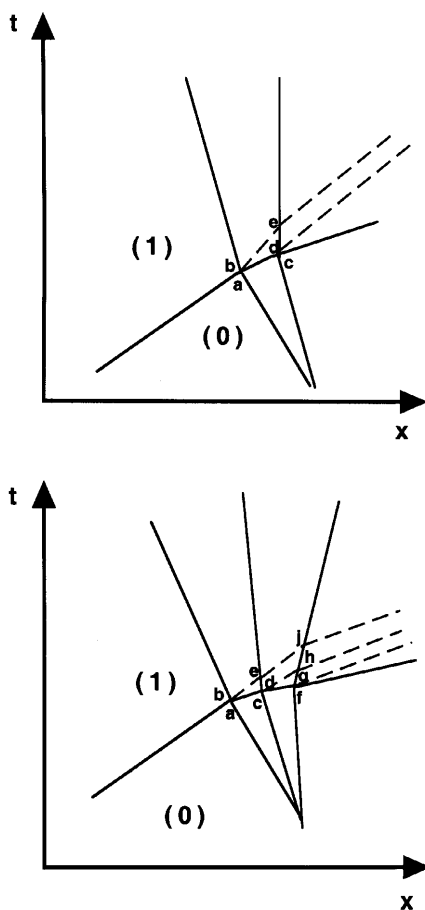


FIGURE 7.8 The penetration region developed during the head-on collision between a shock and a rarefaction wave.

Consider the small section, from a to c, of the rarefaction wave shown in Fig. 7.8. From the known strength (p_1/p_0) of the incident shock wave, its slope (dx/dt) in the (x, t)-plane can be evaluated using the normal jump relation across the shock, e.g.,

$$\frac{p_1}{p_0} = 1 + \frac{2\gamma}{\gamma + 1} \left[\left(\frac{U}{a_0} \right)^2 - 1 \right].$$

This yields

$$\left(\frac{1}{a_0} \frac{dx}{dt} \right)_{Shock} = \frac{U}{a_0} = \frac{u_0}{a_0} + \sqrt{\frac{\frac{\gamma + 1}{\gamma - 1} \frac{p_1}{p_0} + 1}{\frac{2\gamma}{\gamma - 1}}}, \quad (7.23)$$

where U is the velocity of the incident shock wave. The particle velocity in region (1), u_1 , can be obtained from Eq. (7.20). As the strength p_a/p_c of the small increment of the incident rarefaction wave is known, using Eq. (7.22) provides the strength p_d/p_c . [This is easily reached by substituting p_d/p_c for p_3/p_2 and p_a/p_c for p_0/p_2 in Eq. (7.22).] The slope of the shock wave at point c can be evaluated with the help of Eq. (7.23); the particle velocities at points d and e can be found using Eq. (7.20) with the appropriate pressure ratios. In drawing Fig. 7.8, the shock wave velocity between points a and c is taken as the average of the shock wave slopes at these points. Similarly, the particle path between points b and e is drawn having the average slope of that at b and e, and the characteristic line between d and e is drawn with a slope

$$\frac{1}{a_0} \frac{dx}{dt} = \frac{u_d}{a_0} - \frac{1}{2} \left(\frac{a_d}{a_0} + \frac{a_e}{a_0} \right).$$

Proceeding now to the time when the next segment of the incident rarefaction wave hits the shock wave at “f,” the shock strength p_g/p_f can be evaluated in the same manner as done earlier—that is, substituting in Eq. (7.22) p_a/p_f instead of p_0/p_2 and p_g/p_f instead of p_3/p_2 . p_a/p_f and p_1/p_0 are known values. The slope cf of the transmitted shock wave is drawn as the average of the values at points c and f. The segments of particle paths ej and dh are drawn with slopes equal to the average values at e and j, and d and h, respectively. Obviously, particle paths at j, h, and g have the same slope. This procedure is repeated until the rarefaction wave is completely crossed by the transmitted shock wave and final states (3) and (4) are reached. As mentioned earlier, this tedious process can now be avoided by solving numerically the governing differential equations (7.1) and (7.3) with the appropriate initial and boundary conditions. An example of a numerical scheme suitable for solving

Eqs. (7.1) to (7.3) is given in Section 7.9. Results obtained using this scheme for $p_0/p_2 = 5$ and $p_1/p_0 = 5$ are shown in Fig. 7.23.

7.4 HEAD-ON COLLISION OF A SHOCK WAVE WITH A CONTACT DISCONTINUITY

The interaction of a planar shock wave with a contact surface is shown schematically, in the (p, u) -plane, in Fig. 7.9 and in the (x, t) -plane in Figs. 7.10 (the shock tube case) and 7.11 (the case of stationary contact surface). Note that in Fig. 7.10 the considered interaction is between the reflected shock wave from the shock tube end wall and the contact surface.

Therefore, region 6 in Fig. 7.10 is equivalent to region 3 in Fig. 7.9 (final condition c), and region 7 in Fig. 7.10 is equivalent to region 2 in Fig. 7.9 (final condition b). Such an interaction is a frequent occurrence in many shock wave phenomena, e.g., in shock tube operation as shown schematically in Fig. 7.10. In this example, the contact surface separates the gases, which were initially separated by the diaphragm. In principle three different final states are possible for such an interaction. They are illustrated in Fig. 7.9 as a reflected and a transmitted shock waves; a reflected Mach wave and a transmitted shock wave and a reflected rarefaction wave and a transmitted shock wave. Which of these

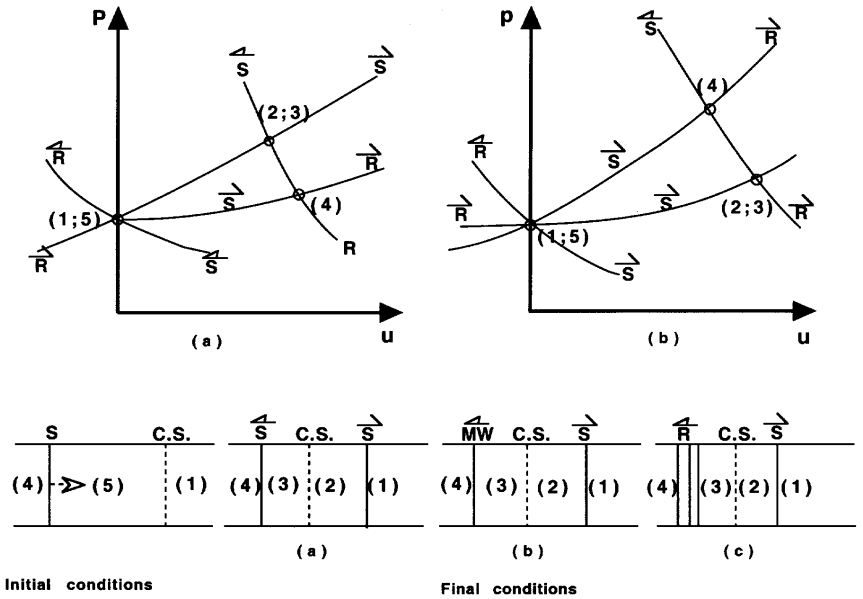


FIGURE 7.9 Head-on collision between a shock wave and a contact surface.

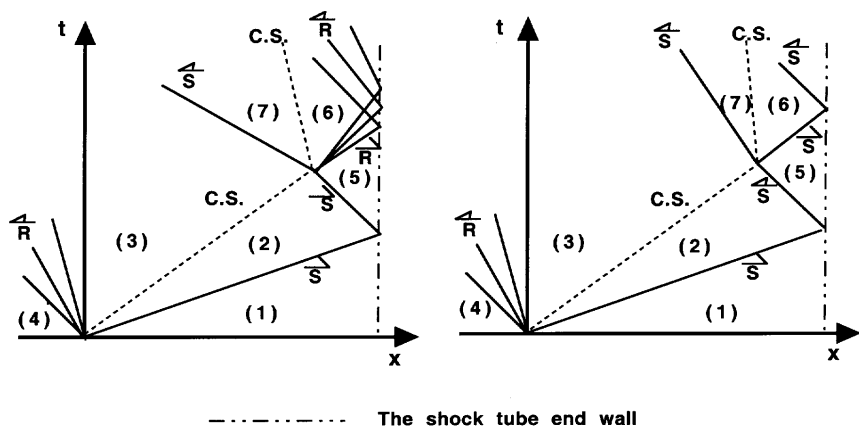


FIGURE 7.10 Head-on collision between a shock wave and a contact discontinuity; the shock tube case.

options takes place depends on the strength of the incident shock wave (p_4/p_5) and the ratio of internal energies across the contact surface (e_1/e_5). The interaction between an incident shock wave and a stationary contact surface is described in a closed form by the following equations (for details see Bitondo *et al.*, 1950).

For the case of a reflected shock wave,

$$\frac{e_1}{e_5} = \frac{\left(\alpha_1 + \frac{p_5 p_4}{p_4 p_3}\right) \left(\alpha_5 \frac{p_5}{p_4} + 1\right)}{\left(1 - \frac{p_5 p_4}{p_4 p_3}\right)^2 \left(\alpha_5 + \frac{p_5}{p_4}\right)} \left[\frac{\left(1 - \frac{p_5}{p_4}\right) \sqrt{\frac{p_4}{p_3}}}{\sqrt{\alpha_5 \frac{p_5}{p_4} + 1}} + \frac{\frac{p_4}{p_3} - 1}{\sqrt{\alpha_5 + \frac{p_4}{p_3}}} \right]^2, \quad (7.24)$$

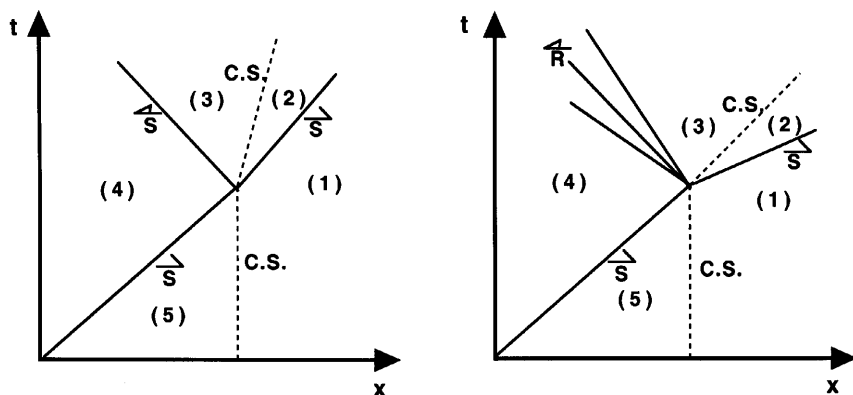


FIGURE 7.11 Head-on collision between a shock wave and a stationary contact surface. Region's numbers as in Fig. 7.9.

where $\alpha = (\gamma + 1)/(\gamma - 1)$; for indexes see Fig. 7.9. The reflected wave from the contact surface will be a shock wave when the following inequality holds (Glass and Hall, 1959):

$$\frac{e_1}{e_5} \leq \left(\alpha_1 + \frac{p_5}{p_4} \right) \left(\alpha_5 + \frac{p_5}{p_4} \right)^{-1}.$$

At the lower limit, when equality is reached, the reflected wave is a Mach wave. As could be expected, it is evident from the schematic illustration shown in Fig. 7.9 that for the case of a reflected shock wave both the absolute pressure and the pressure ratio across the transmitted shock wave (p_2 and p_2/p_1) are higher than those existing across the incident shock wave (p_4 and p_4/p_5).

A reflected rarefaction wave is present when

$$\begin{aligned} \left(\frac{p_3}{p_4} \right)^{\beta_5} + \left(\frac{\alpha_5 + \frac{p_5}{p_4}}{\alpha_5 \frac{p_5}{p_4} + 1} \right)^{1/2} \left(\frac{p_3}{p_4} - \frac{p_5}{p_4} \right) \sqrt{\frac{\beta_5 \frac{e_5}{e_4}}{\alpha_1 \frac{p_3}{p_4} + \frac{p_5}{p_4}}} \\ - \left(1 - \frac{p_5}{p_4} \right) \sqrt{\frac{\beta_5}{\alpha_5 \frac{p_5}{p_4} + 1}} - 1 = 0, \end{aligned} \quad (7.24a)$$

where $\beta = (\gamma - 1)/(2\gamma)$. In the present case the following inequality holds:

$$\frac{e_1}{e_5} \geq \left(\alpha_1 + \frac{p_5}{p_4} \right) \left(\alpha_5 + \frac{p_5}{p_4} \right)^{-1}.$$

As could be expected, it is apparent from Fig. 7.9 that the absolute pressure (p_2) and the pressure ratio (p_2/p_1) across the transmitted shock wave are lower than those experienced through the incident shock wave (p_4 and p_4/p_5). In the present case the transmitted shock wave is weakened while crossing the contact surface. By proper selection of gases across the contact surface (selection of e_1/e_5), the transmitted shock wave could either be amplified or attenuated. A reflected Mach wave is present when the last inequality changes into an equal sign.

The question whether a reflected shock wave or a reflected rarefaction wave results from the head-on collision between a shock wave and a contact discontinuity could be answered with reference to the (p, u) -diagram shown in Fig. 7.9A. Across the contact surface $p_1 = p_5$ and $u_1 = u_5$. However, it is possible that $\rho_1 \neq \rho_5$ and $\gamma_1 \neq \gamma_5$, and especially the acoustic impedance $(\rho a)_1 \neq (\rho a)_5$.

We designate $S_R(5)$, $R_R(5)$ the shock and the rarefaction branches, in the (p, u) -diagram shown in Fig. 7.9A, which propagate to the right, into zone 5. Similarly, the wave reflected from the contact surface, moving to the left into zone 4 is $S_L(4)$, $R_L(4)$. The wave transmitted into zone 1 is a right moving

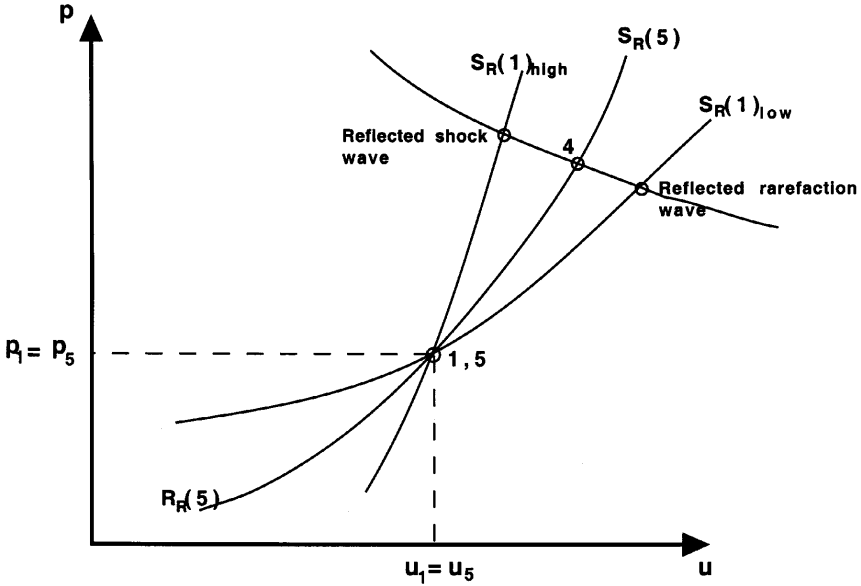


FIGURE 7.9A Schematic description in the (p, u) -plane of the head-on collision between a shock wave and a contact discontinuity.

wave, $S_R(1)$, $R_R(1)$. In Fig. 7.9A this branch is drawn twice, once with an index “high” and once with the index “low”. The difference between these two branches is in the magnitude of the derivative $(dp/du)_1$ at point 1. For the branch marked “high” we have $(dp/du)_1 > (dp/du)_5$ and for the branch marked “low” $(dp/du)_1 < (dp/du)_5$. However, at 1 and/or 5 we have $(dp/du) = \rho a$. Therefore, the Riemann solution to the interaction of a shock wave with a contact surface is a shock wave for the “high” case, $(\rho a)_1 > (\rho a)_5$ and a rarefaction wave for the “low” case, $(\rho a)_1 < (\rho a)_5$.

In the foregoing analysis, the acoustic impedance criterion for the type of the reflected wave is correct for weak to moderate waves. When the incident wave is of high intensity, the type of reflected wave may depend on the magnitude of the incident wave, as well as on the properties of the media separated by the contact surface. The detailed analysis in this case is more complex than the simple arguments leading to the acoustic impedance criterion. For the case of head-on collision of a shock wave with a contact surface, Bitondo *et al.* (1950) offered the criterion appearing in the inequality following Eq. (7.24). For the case of head-on collision of a rarefaction wave with a contact surface Billington and Glass (1955) suggested the criterion appearing in Section 7.5. One possible use of a detailed wave criterion analysis might be the design of “tailored conditions,” i.e., the combination of an

incident wave and two media separated by a contact surface, that results in a zero-intensity reflected wave. Such design may be useful, for example, in the smooth operation of piston-driven shock tunnels or similar installations.

7.5 HEAD-ON COLLISION OF A RAREFACTION WAVE WITH A CONTACT DISCONTINUITY

When a rarefaction wave collides and traverse through a contact surface, three different wave patterns are possible. These are shown schematically, in the (p, u) -plane, in Fig. 7.12. In all three cases the transmitted wave is a rarefaction wave.

The type of the reflected wave depends on the internal energy ratio (e_1/e_5) across the contact surface and the strength of the incident rarefaction wave. It could be either a reflected rarefaction wave, a reflected Mach wave or a reflected compression wave. The compression wave will quickly coalesce into a shock wave. The considered interaction is shown in the (x, t) -plane for a case of a stationary contact surface, in Fig. 7.13. It is shown in Billington

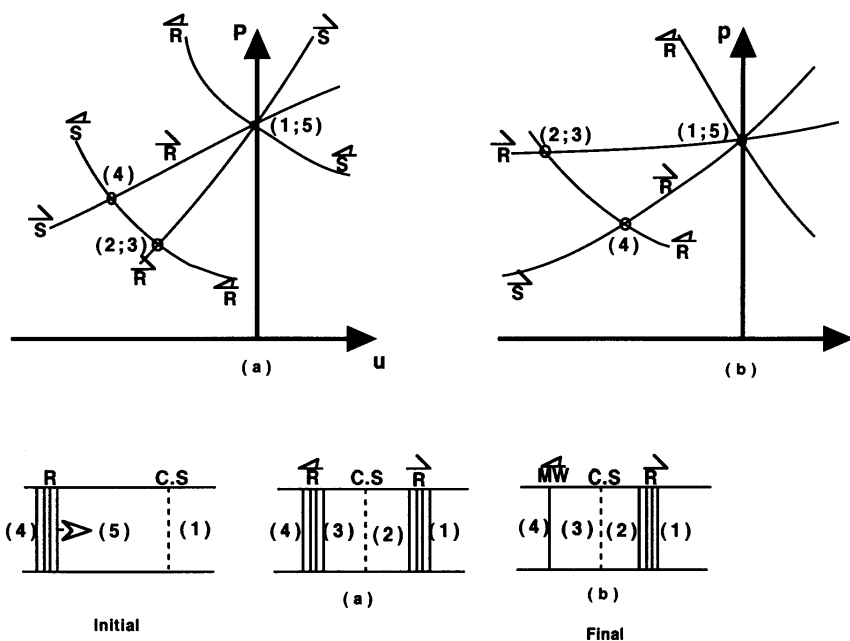


FIGURE 7.12 Head-on collision between a rarefaction wave and a contact discontinuity.

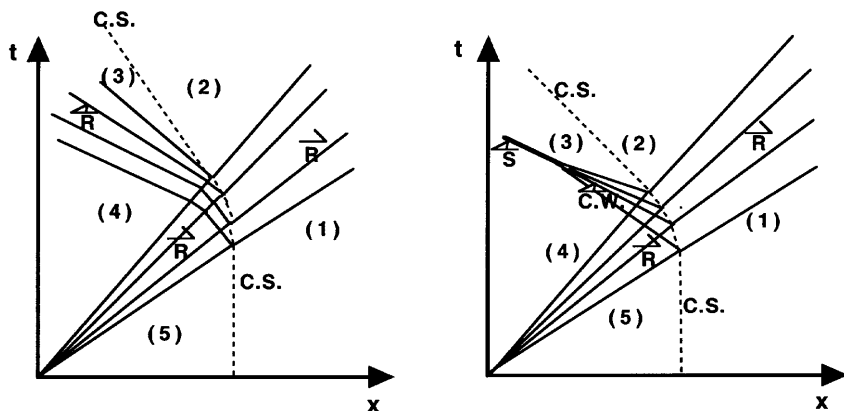


FIGURE 7.13 Head-on collision between a rarefaction wave and a contact discontinuity. Region numbers as in Fig. 7.12.

and Glass (1955) that a critical value $(e_1/e_5)_{\text{crit}}$ exists; when $(e_1/e_5) > (e_1/e_5)_{\text{crit}}$, the reflected wave is a rarefaction wave. The value of this critical energy ratio is

$$\left(\frac{e_1}{e_5}\right)_{\text{crit}} = \frac{\beta_1}{\beta_5} \left[\frac{1 - \left(\frac{p_4}{p_5}\right)^{\beta_5}}{1 - \left(\frac{p_4}{p_5}\right)^{\beta_1}} \right]^2.$$

When $(e_1/e_5) = (e_1/e_5)_{\text{crit}}$, the reflected wave is a Mach wave, and when $(e_1/e_5) < (e_1/e_5)_{\text{crit}}$, a compression wave is reflected. As mentioned, this compression wave will steepen quickly to a shock wave.

7.6 SHOCK WAVE OVERTAKING ANOTHER SHOCK WAVE

The case of a shock wave overtaking another shock wave is shown schematically, in the (p, u) -plane, in Fig. 7.14. As indicated in the figure, in principle, three different wave patterns could result from such an overtaking. In all three cases the transmitted wave is a shock wave while the reflected wave could be either a shock, a Mach, or a rarefaction wave. It is shown in Bull *et al.* (1953) that for all real gases ($\gamma \leq \frac{5}{3}$) the reflected wave is always a rarefaction wave. For gases having $\gamma > \frac{5}{3}$ a reflected shock wave is possible. The considered interaction for real gases ($\gamma \leq \frac{5}{3}$) is shown in the (x, t) -plane in Fig. 7.15. In such an interaction the strength of the two transmitted shock waves, p_4/p_5 and p_5/p_1 ,

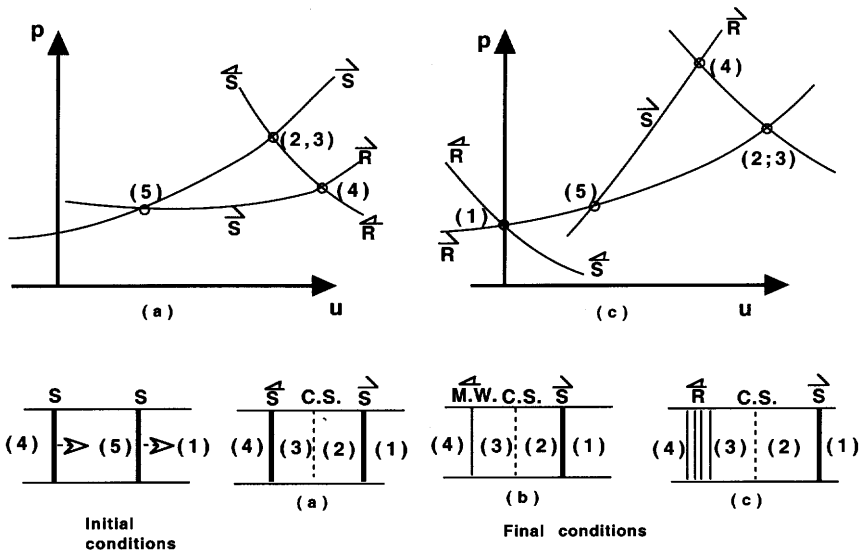


FIGURE 7.14 Overtaking of a shock wave by a faster shock wave.

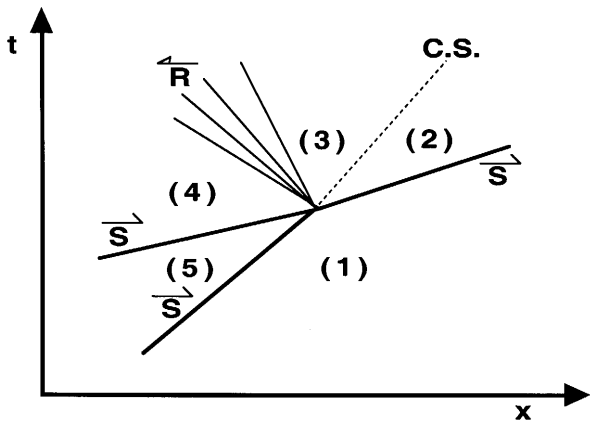


FIGURE 7.15 Overtaking of a shock wave by a faster shock wave, in the (x, t) -plane.

are known (and therefore, p_4/p_1 is also known). The interaction result, that is, the pressure ratio across the reflected rarefaction wave (p_3/p_4) and across the transmitted shock wave (p_2/p_1), can be evaluated from the following algebraic equations (Glass and Hall, 1959):

$$\sqrt{\frac{\beta_1 \left(1 + \alpha_1 \frac{p_4}{p_5}\right)}{\left(\alpha_1 + \frac{p_4}{p_5}\right) \left(1 + \alpha_1 \frac{p_1}{p_5}\right) \frac{p_4}{p_5}}} \left[\left(\frac{p_3}{p_4} - \frac{p_1}{p_4}\right) \sqrt{\frac{\left(\alpha_1 + \frac{p_1}{p_5}\right) \frac{p_4}{p_5}}{\frac{p_1}{p_4} + \alpha_1 \frac{p_3}{p_4}}} \right. \\ \left. - \left(\frac{p_4}{p_5} - 1\right) \sqrt{\frac{\left(\alpha_1 \frac{p_1}{p_5} + 1\right)}{1 + \alpha_1 \frac{p_4}{p_5}}} - \left(1 - \frac{p_1}{p_5}\right) \right] + \left(\frac{p_3}{p_4}\right)^{\beta_1} - 1 = 0. \quad (7.25)$$

Once p_3/p_4 is evaluated from Eq. (7.25), p_2/p_1 can easily found from the following relation:

$$\frac{p_3}{p_4} = \frac{p_1 p_2}{p_4 p_1}.$$

7.7 SHOCK WAVE OVERTAKEN BY A RAREFACTION WAVE

This interaction is shown schematically, in the (p, u) -plane, in Fig. 7.16. Again, this interaction can result, in principle, in any of the following three different wave patterns: a reflected rarefaction wave, a reflected Mach wave, or a reflected compression wave that may steepen into a shock wave. In all three options the transmitted wave is a shock wave, which is weaker than the original transmitted shock wave. As this transmitted shock wave is decaying during the overtaking process, its strength (the pressure jump across it) decreases and the entropy change across it diminishes. This will give rise to a region of entropy change, i.e., a contact region rather than the contact surface observed in some of the previously discussed cases. Algebraic equations relating the pressures ratios across the transmitted shock wave, (p_2/p_1) and across the reflected rarefaction wave (p_4/p_3) (or the reflected compression wave) to the known values of pressures ratios across the incident shock wave (p_5/p_1) and the overtaking rarefaction wave (p_5/p_4) are given in Glass *et al.* (1959). In the following, equations for only two of the possible options are given.

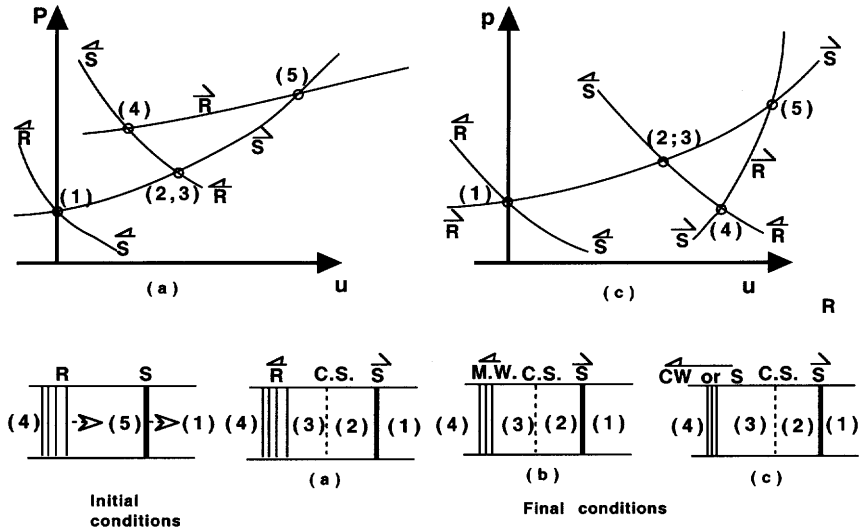


FIGURE 7.16 Shock wave overtaken by a rarefaction wave.

When the overtaking rarefaction wave is weak and the interaction results in a reflected rarefaction wave (case a in Fig. 7.16) the eventually reached, quasi-steady flow in regions (2) and (3) can be evaluated using the following algebraic equations:

$$\begin{aligned}
 & \sqrt{\frac{\beta_1 \frac{p_1}{p_5} \left(\alpha_1 + \frac{p_1}{p_5} \right)}{\left(1 + \alpha_1 \frac{p_1}{p_5} \right)}} \left[\frac{1 - \frac{p_1}{p_5}}{\sqrt{\frac{p_1}{p_5} \left(\alpha_1 + \frac{p_1}{p_5} \right)}} + \frac{1 - \frac{p_2}{p_1}}{\sqrt{\alpha_1 \frac{p_2}{p_1} + 1}} \right] \\
 & + 2 \left(\frac{p_4}{p_5} \right)^{\beta_1} - \left(\frac{p_2 p_1}{p_1 p_5} \right)^{\beta_1} - 1 = 0
 \end{aligned} \tag{7.26}$$

and

$$\left(\frac{p_3}{p_4} \right) = \frac{p_2 p_1 p_5}{p_1 p_5 p_4}.$$

If the overtaking rarefaction wave is strong enough, it will weaken the transmitted shock wave until it is attenuated to a Mach wave. This Mach wave will be one of the Mach lines of the rarefaction wave. Therefore, in such a case the wave pattern consists of a transmitted rarefaction wave, and a reflected rarefaction, a reflected Mach wave, or a reflected compression wave will be present. These wave patterns are shown schematically in Fig. 7.17.

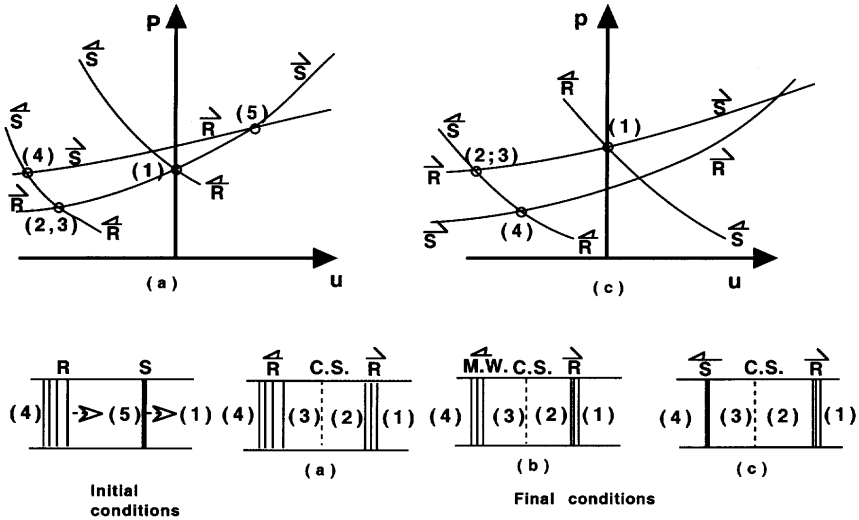


FIGURE 7.17 Shock wave overtaken by a strong rarefaction wave.

In the case of a strong overtaking rarefaction wave, when the reflected wave is a rarefaction wave the pressure across the transmitted wave p_2/p_1 , when a quasi-steady state is reached, can be calculated from

$$\sqrt{\frac{p_1}{p_5} \left(\alpha_1 + \frac{p_1}{p_5} \right)} \left[\frac{\left(1 - \frac{p_1}{p_5} \right) \sqrt{\beta_1}}{\sqrt{\frac{p_1}{p_5} \left(\alpha_1 + \frac{p_1}{p_5} \right)}} + \left(1 - \left(\frac{p_2}{p_1} \right)^{\beta_1} \right) \right] + 2 \left(\frac{p_4}{p_5} \right)^{\beta_1} - \left(\frac{p_2 p_1}{p_1 p_5} \right)^{\beta_1} - 1 = 0 \quad (7.27)$$

7.8 SHOCK WAVE OVERTAKING A RAREFACTION WAVE

As in the previously described case, here, too, the resulting wave pattern depends on the strength of the overtaking shock wave. For a relatively weak shock wave, the wave patterns shown in Fig. 7.18 are possible. In all three options the resulting transmitted wave is a rarefaction wave. The reflected wave could be either a shock wave or a Mach wave, or a rarefaction wave. In the limit of a very weak shock wave, the overtaking shock wave is weakened until it is attenuated to a Mach wave, which is one of the Mach lines in the rarefaction wave.

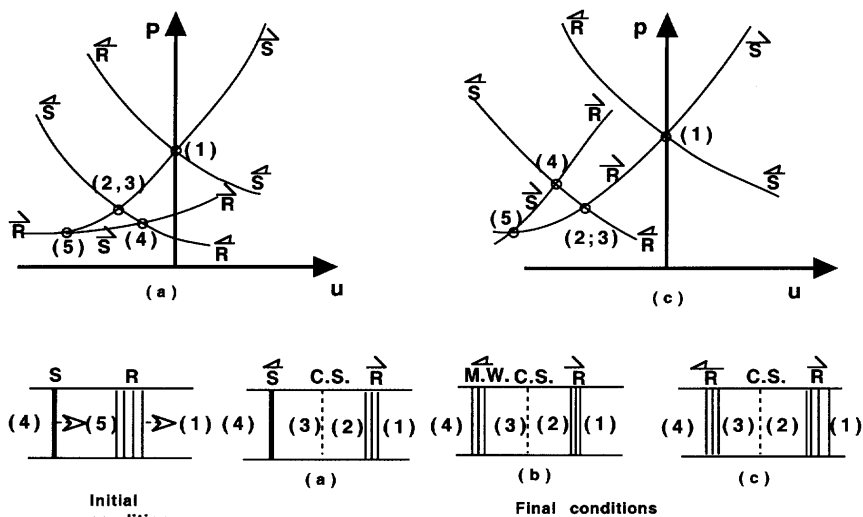


FIGURE 7.18 Shock wave overtaking a rarefaction wave.

For a weak incident shock wave (a case when it completely attenuated to a Mach wave), when the reflected wave is a shock wave (case a in Fig. 7.18), pressures in the eventually reached quasi-steady states (2) and (3) can be evaluated from

$$\frac{1 - \left(\frac{p_3}{p_4}\right)^\beta \left(\frac{p_4}{p_5}\right)^\beta}{\sqrt{\beta}} + \frac{\left(\frac{p_4}{p_5} - 1\right)}{\left[1 + \alpha \left(\frac{p_4}{p_5}\right)\right]^{1/2}} + \left[\frac{\frac{p_4}{p_5} \left(\alpha + \frac{p_4}{p_5}\right)}{1 + \alpha \frac{p_4}{p_5}}\right]^{1/2} \frac{\left(1 - \frac{p_3}{p_4}\right)}{\left[1 + \alpha \frac{p_3}{p_4}\right]^{1/2}} = 0. \quad (7.28)$$

Once p_3/p_4 is known, p_2/p_1 can easily be found from $p_2/p_1 = \frac{p_3}{p_4} \frac{p_4}{p_5} \frac{p_5}{p_1}$. When the overtaking shock is very strong it will penetrate through the rarefaction wave. The possible resulting wave configuration is shown schematically in Fig. 7.19. While in all three possible wave configurations the transmitted wave is a shock wave (which is weaker than the original, overtaking shock wave); the reflected wave can be, in principle, either a rarefaction wave or a Mach wave, or a compression wave that will steepen to a shock wave. It was shown in Bremner *et al.* (1960) that for all real gases ($1 < \gamma \leq \frac{5}{3}$) and a strong overtaking shock wave, the only possible configuration is a reflected compression wave, which steepens to a shock wave. In this case, the pressure

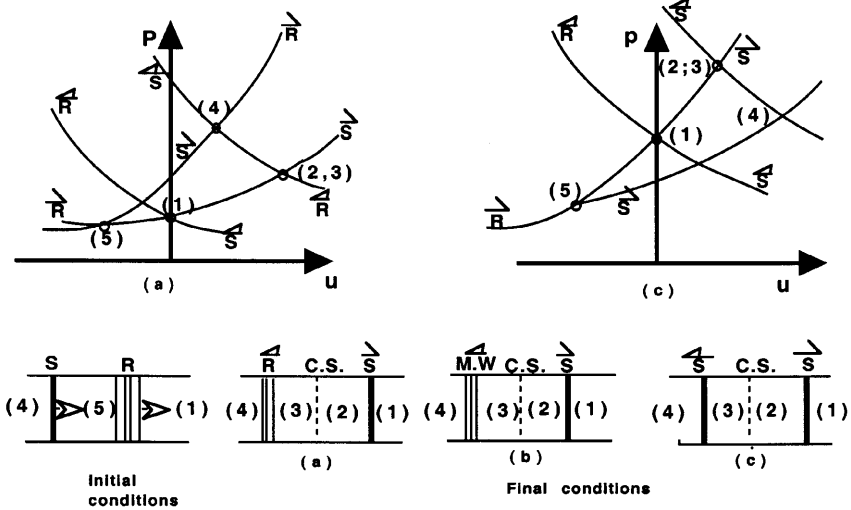


FIGURE 7.19 Strong shock wave overtaking a rarefaction wave.

ratio across the reflected shock wave, p_3/p_4 , when a quasi-steady state is reached, is given by

$$1 - \left(\frac{p_5}{p_1}\right)^{-\beta} - \frac{\sqrt{\beta} \left(\frac{p_5}{p_1}\right)^{-\beta} \left(\frac{p_3 p_4 p_5}{p_4 p_5 p_1} - 1\right)}{\left[1 + \alpha \frac{p_3 p_4 p_5}{p_4 p_5 p_1}\right]^{1/2}} + \left[\frac{\beta \frac{p_4}{p_5} \left(\alpha + \frac{p_4}{p_5}\right)}{1 + \alpha \frac{p_4}{p_5}} \right]^{1/2} \frac{1 - \frac{p_3}{p_4}}{\left[1 + \alpha \frac{p_3}{p_4}\right]^{1/2}} + \frac{\sqrt{\beta} \left(\frac{p_4}{p_5} - 1\right)}{\left[1 + \alpha \frac{p_4}{p_5}\right]^{1/2}} = 0.$$

7.9 THE GENERAL RIEMANN PROBLEM SOLVER

All examples shown so far are particular cases of the well-known Riemann problem, which models the one-dimensional interaction between a pair of uniform states of compressible fluids that are initially separated by a plane of discontinuity. The most commonplace interaction of this kind is the “shock

tube problem” consisting of two states of quiescent gas having different thermodynamic states, which are separated by a thin diaphragm that ideally vanishes abruptly. Other typical interactions of physical significance are those discussed in Sections 7.2 to 7.8.

In recent decades, following the advent of Godunov’s (1959) scheme for the fluid dynamic conservation laws, the Riemann problem became preeminent in computational fluid dynamics. When the GRP scheme (Ben-Artzi and Falco-vitz, 1986) was proposed as a second-order extension of the Godunov scheme, it was necessary to develop an algorithm for computing solutions to Riemann problems. This algorithm is presented here as the “GRP Solver”. It is subsequently given in the form of FORTRAN code for evaluating the solution to a single specified Riemann problem for ideal gases.

Mathematically speaking, the Riemann problem is an initial value problem in space-time (x, t) defined as follows. The equations governing the one-dimensional flow of an inviscid compressible fluid as function of the space coordinate x and the time t are given in Eqs. (7.1) to (7.3); written in a vector form these equations are

$$\frac{\partial}{\partial t} U + \frac{\partial}{\partial x} F(U) = 0 \quad (7.29)$$

$$U(x, t) = \begin{pmatrix} \rho \\ \rho u \\ \rho E \end{pmatrix}, \quad F(U) = \begin{pmatrix} \rho u \\ \rho u^2 \\ (\rho E + p)u \end{pmatrix}. \quad (7.30)$$

In general, the thermodynamic variables p, ρ, e are related by an “equation of state.” Here we refer to the most common case, that of a perfect “ γ -law” gas, where

$$p = (\gamma - 1)\rho e; \quad \gamma > 1. \quad (7.31)$$

A Riemann problem is the initial value problem for Eq. (7.29) with the data

$$U_L = [u_L; p_L; \rho_L], \quad \gamma = \gamma_L, \quad x < 0$$

$$U_R = [u_R; p_R; \rho_R], \quad \gamma = \gamma_R, \quad x > 0$$

where subscripts L and R denote the left and right states, respectively.

The solution to a Riemann problem is self-similar because of the absence of a characteristic time or length scale in either the equations or the initial conditions. This solution is shown schematically as an (x, t) -wave diagram in Fig. (7.20).

The flow represented by this wave diagram generally consists of a left-facing wave and a right-facing wave, separated by a contact discontinuity, which evolves from the interface that initially separated the left state from the right state. Since the velocity and the pressure are continuous at a contact

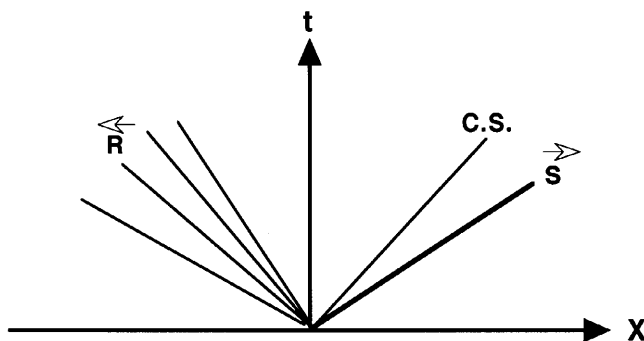


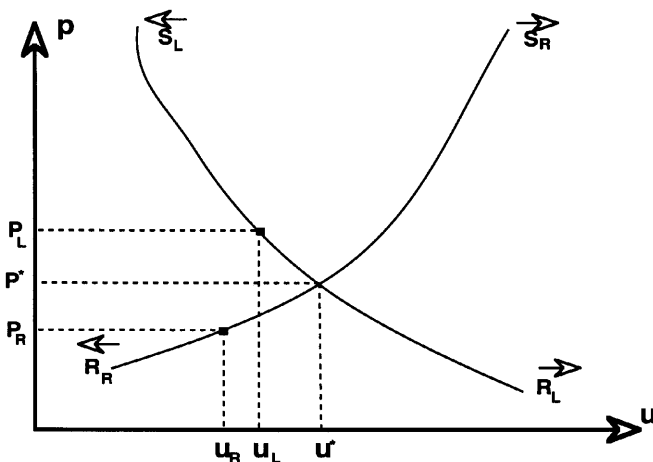
FIGURE 7.20 Self-similar solution of the Riemann problem.

discontinuity, the task of solving a Riemann problem consists in finding the contact velocity and pressure (u^*, p^*). The algorithms used to evaluate these unknowns are presented in the following.

The strategy for solving a Riemann problem is to seek the velocity and pressure (u^*, p^*) prevailing behind the left-facing wave, as well as behind the right-facing wave (see Fig. 7.20). Since the left-facing wave is propagating into the left state U_L , and the right-facing wave is propagating into the right state U_R , we seek the left and right “interaction curves,” which are the loci of all flow states reached by a single shock or rarefaction wave from the respective left or right state. Each interaction curve consists of two branches: a rarefaction branch (denoted R_L or R_R) and a shock branch (denoted S_L or S_R). On the (u, p) -plane, S_L and S_R are characterized by an increased pressure relative to the respective initial pressure, whereas on R_L and R_R the pressure is lower than the respective initial pressure. The velocity jump on S_R and R_R is of the same sign as the pressure jump, whereas for S_L and R_L the velocity sign is reversed. We thus seek (u^*, p^*) as the point of intersection between the left and the right interaction curves on the (u, p) -plane, as is shown schematically in Fig. 7.21.

The detailed algorithm used to perform the computation of (u^*, p^*) consists of three phases as follows. First, is an a priori determination of the kind of branch (i.e., shock or rarefaction) on which the intersection point (u^*, p^*) is located. For that, a simple sorting algorithm that relies solely on the monotonous property of interaction curves in (u, p) , as presented subsequently, is employed. Then, we proceed to present explicit shock or rarefaction relations in (u, p) for the left and right branches thus determined. Finally, an efficient Newton–Raphson scheme for evaluating the intersection point (u^*, p^*) by successive iterations is presented.

The solution to a Riemann problem is obtained from the intersection of the left and right interaction curves on the (u, p) -plane. Let these curves be

FIGURE 7.21 Solving Riemann problem by intersection of (u, p) interaction curves

denoted by

$p = G_L(u)$	left interaction curve
$p = G_R(u)$	right interaction curve, or
$u = H_L(p)$	left interaction curve
$u = H_R(p)$	right interaction curve.

Each interaction curve consists of a shock branch and a rarefaction branch that are smoothly joined at the (u, p) -point corresponding to the respective left or right state.

A simple algorithm is proposed for the a priori determination of the branch on which the intersection point (u^*, p^*) is located. It is based on the sole assumption of monotonicity of the interaction curves, and it is

$$\frac{dG_L(u)}{du} < 0 \quad \text{and} \quad \frac{dG_R(u)}{du} > 0, \quad (7.32)$$

with similar conditions on $H_L(p)$ and on $H_R(p)$.

The sorting algorithm consists in examining the velocity and pressure on one interaction curve, as a function of the initial state of the opposite side. To fix our ideas, let us consider the left interaction curve at points corresponding to the right state, as shown schematically in Fig. 7.22.

Thus, in this instance we consider the two points on the left interaction curve that are specified by $p_{LR} = G_L(u_R)$ and $u_{LR} = H_L(p_R)$; where it is obvious that since $u_R < u_L$ the point p_{LR} is located on the left shock branch, and since $p_R < p_L$ the point u_{LR} is located on the left rarefaction branch (see Fig. 7.22). Now, taking notice of the monotonicity of the right interaction curve, two

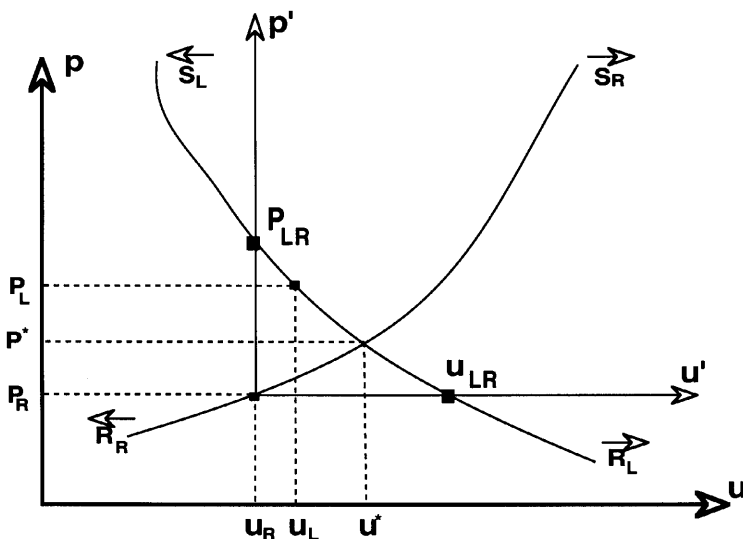


FIGURE 7.22 Determination of the right intersecting branch.

inequality relations are possible: either $p_{LR} > p_R$ and $u_{LR} > u_R$, or $p_{LR} < p_R$ and $u_{LR} < u_R$.

In the present example the first one of these alternate inequalities holds, which leads to the conclusion that the point of intersection (u^*, p^*) must be on the shock branch of the right state. These arguments can be rephrased geometrically as follows. With respect to a new set of (u', p') axes centered at point (u_R, p_R) , the monotonous assumption implies that the right shock branch is always located in the first quadrant of these axes, while the right rarefaction branch is always in the third quadrant. Considering specifically the case depicted in Fig. 7.22, the segment of the left interaction curve between points (u_R, p_{LR}) and (u_{LR}, p_R) must be wholly within the first quadrant, by virtue of the left curve monotonicity. This implies that the intersection point (u^*, p^*) in this case must also be in the first quadrant, and hence on the right shock branch. The kind of left state intersection branch is readily determined by an analogous procedure.

In conclusion, we reiterate that the sorting algorithm is based solely on the monotonicity assumption. In particular, it is independent of the specific equation of state obeyed by the fluid, as long as that equation of state is in compliance with the monotonicity assumption.

We introduce a new notation in which states $(.)_L$ or $(.)_R$ are denoted by $(.)_0$, with the postwave variables written with no index at all. The shock branch is most conveniently specified parametrically, with the parameter being the shock

Mach number M_S , which is defined as the ratio between the (positive) shock speed relative to the fluid ahead and the speed of sound a_0 . The velocity and pressure are thus given by

$$p - p_0 = \left(\frac{2\gamma}{\gamma + 1} \right) (M_S^2 - 1) p_0 \quad (7.33)$$

$$u - u_0 = \pm \frac{a_0}{\gamma M_S} \left(\frac{p - p_0}{p_0} \right), \quad (7.34)$$

where it is evident that when $M_S = 1$, i.e., a “sonic” shock of zero intensity, the pressure and velocity jumps vanish. Following the notation used in the previous sections, the sign for u is “+” for a right-facing wave, and “−” for a left-facing wave. The expression for $u(p)$ is readily derived by eliminating M_S from the last two equations, yielding

$$(u - u_0)_{\text{shock}} = \pm \frac{a_0}{\gamma} \left(\frac{p - p_0}{p_0} \right) \left[1 + \left(\frac{\gamma + 1}{2\gamma} \right) \left(\frac{p - p_0}{p_0} \right) \right]^{-1/2} \quad (7.35)$$

It should be noted that Eq. (7.35) is the same as Eq. (7.20), but written in a different form.

The relationship for a rarefaction wave is the Riemann invariant expression that for an ideal gas is given in Eq. (7.11). For the purpose of finding the intersection point (u^*, p^*) it is convenient to transform the relations $u(p)$ to $u(\zeta)$, where the transformation $\zeta = \zeta(p)$ is chosen to produce a linear function for the rarefaction branch $u = u(\zeta)$. This transformation is given by $\zeta = p^{(\gamma-1)/2\gamma}$, $p = \zeta^{2\gamma/(\gamma-1)}$.

Using this transformation, the (u, ζ) shock and rarefaction relations become

$$(u - u_0)_{\text{shock}} = \pm \frac{a_0}{\gamma} \left[\left(\frac{\zeta}{\zeta_0} \right)^{2\gamma/(\gamma-1)} - 1 \right] \left[1 + \left(\frac{\gamma + 1}{2\gamma} \right) \left\{ \left(\frac{\zeta}{\zeta_0} \right)^{2\gamma/(\gamma-1)} - 1 \right\} \right]^{-1/2};$$

$$(u - u_0)_{\text{rarefaction}} = \pm a_0 \left(\frac{2}{\gamma - 1} \right) \left[\frac{\zeta}{\zeta_0} - 1 \right]. \quad (7.36)$$

In order to perform a Newton–Raphson iteration we need the derivatives of $u(\zeta)$ for the two branches. Using expressions (7.36) we get, after some algebra,

$$\begin{aligned} \left(\frac{du}{d\zeta}\right)_{\text{shock}} &= \pm \left(\frac{2}{\gamma-1}\right) \frac{a_0}{\zeta} \left(\frac{\zeta}{\zeta_0}\right)^{2\gamma/(\gamma-1)} \left[1 + \left(\frac{\gamma+1}{4\gamma}\right) \left\{ \left(\frac{\zeta}{\zeta_0}\right)^{2\gamma/(\gamma-1)} - 1 \right\} \right] \\ &\quad \times \left\{ 1 + \left(\frac{\gamma+1}{2\gamma}\right) \left[\left(\frac{\zeta}{\zeta_0}\right)^{2\gamma/(\gamma-1)} - 1 \right] \right\}^{-3/2} \\ \left(\frac{du}{d\zeta}\right)_{\text{rarefaction}} &= \mp \frac{a_0}{\zeta_0} \left(\frac{2}{\gamma-1}\right). \end{aligned} \quad (7.37)$$

In the following a brief outline of the iteration scheme is given; the reader is referred to the source code itself for further details. Let the iteration index be $n = 0, 1, 2, \dots$, where the initial guess is obtained by a special procedure that we describe later, and iteration $n+1$ is obtained from iteration n as follows.

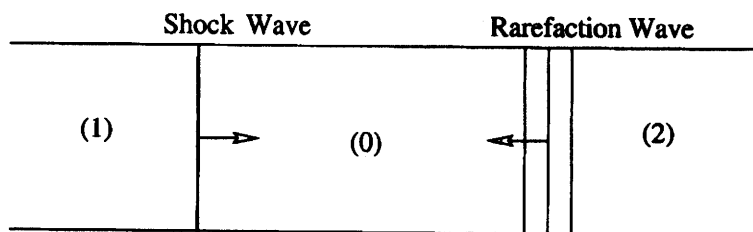
The result of iteration n is the approximate intersection point (u_n^*, p_n^*) . This approximation is deemed adequate if $|H_L(p_n^*) - H_R(p_n^*)| < \varepsilon_u$, where ε_u is some small acceptable error in the determination of u^* . If the n approximation is inadequate, then the $n+1$ iteration is computed by evaluating the point (u_{n+1}^*, p_{n+1}^*) as the intersection point of the left and right tangent lines in the (u, ζ) -plane, which are defined as follows. Let the left tangent point be the point $u = G_L(p_n^*)$, $p = p_n^*$ on the left interaction curve. Likewise, let the right tangent point be the point $u = G_R(p_n^*)$, $p = p_n^*$ on the right interaction curve. Then the tangent lines are the tangents in the (u, ζ) -plane, drawn at the left point for the left interaction curve, and at the right point for the right interaction curve. The formerly derived expressions for the derivatives of $u(\zeta)$ are used for this purpose. Once the new intersection point is determined, its adequacy is checked, and if found inadequate the iteration is repeated.

The zero iteration ($n = 0$) is performed by taking as intersecting tangent lines the tangents at points (u_L, ζ_L) and (u_R, ζ_R) on the respective interaction curves. In fact, these tangent lines are the rarefaction branch of the respective interaction curves on the (u, ζ) -plane. This initial guess is indeed identical to a linearized “acoustic” approximation to the solution of a Riemann problem, so that for states U_L and U_R that differ by a small amount, the zero approximation may already be adequate.

This iteration scheme converges quite rapidly. Experience has shown that in most cases the solution to a Riemann problem typically requires only three iterations.

For a solution of an arbitrary time-dependent flow in one space dimension, the generalized Riemann problem (GRP) scheme developed by Falcovitz and

Ben-Artzi (1995) is a very suitable code.¹ This scheme was employed for solving the previously discussed case of head-on collision between a shock wave and a rarefaction wave (see Section 7.3). The obtained results, shown in Fig. 7.23, contain the accurate version of the schematic description given earlier in Figs. 7.6 and 7.7.



Initial State

Initial Condition:

$T_0=300\text{K}$, $P_0=10^5\text{ Pa}$, $P_1/P_0=5$, $T_1=533\text{K}$, $P_2/P_0=0.2$, $T_2=189.6\text{K}$ and $U_0=0$.

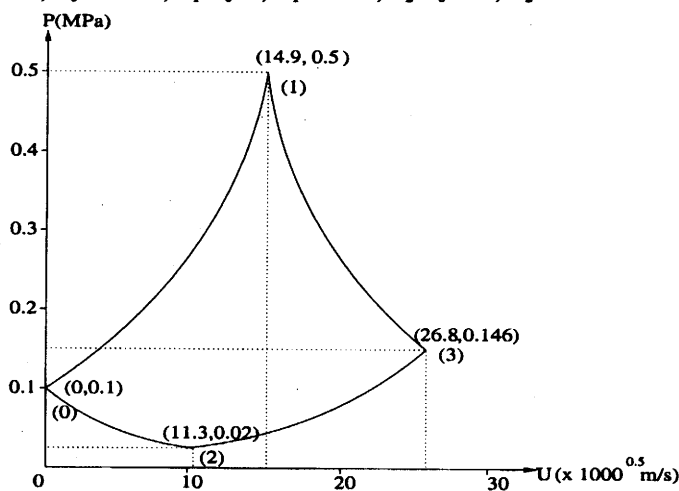


FIGURE 7.23 Head-on collision between a shock wave and a rarefaction wave.

¹The code can be obtained by ftp from 132.64.32.12, user name: ftp, password: e-mail address, in subdirectory ccjfi.

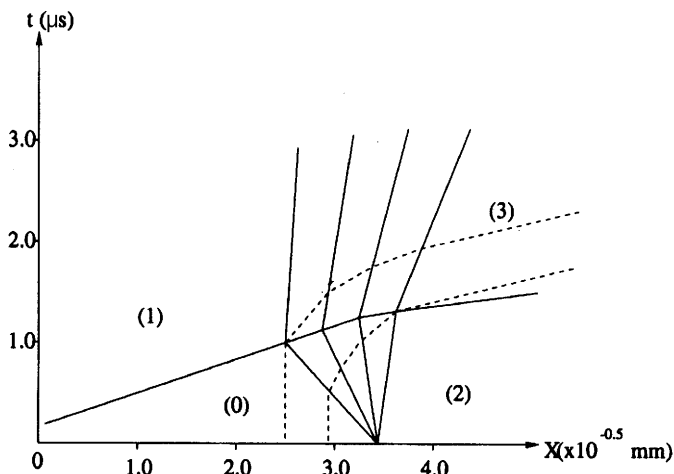


FIGURE 7.23 (continued).

7.9.1 CONCLUDING REMARKS

At present, employing a numerical solver to the appropriate Riemann problem, as shown in Section 7.9, can easily and accurately solve one-dimensional wave interactions. This was not the case before the computer era, when solutions were conducted manually, in an iterative process, using the algebraic equations presented in Sections 7.2 to 7.8.

It should be noted here that having a genuine one-dimensional flow is a rare event in engineering practice. However, many real flows are approximated as being quasi-one-dimensional. In many cases the approximation is valid, in others it does not. For example, Greatrix and Gottlieb (1982) studied shock wave interactions with area-change segments in ducts, treating the entire flow as being quasi-one-dimensional. Gottlieb and Igra (1983) and Igra and Gottlieb (1985) studied the interaction process between rarefaction waves and area enlargement or reduction segments in ducts, treating the flow as being quasi-one-dimensional throughout. Igra, Wang, and Falcovitz (1998) studied the interaction process between shock/rarefaction wave and area change segments in ducts treating it as being truly unsteady, two-dimensional flow. It was shown by Igra *et al.* (1998) that the interaction process between a shock wave and an area change segment in a duct approaches, at a late time when all wave interactions have subsided, the quasi-one-dimensional solution. However, in the case of a rarefaction wave impingement on an area reduction in a duct the observed flow field, upstream of the flow exit from the area change segment, is

genuinely a two-dimensional flow, even at very late times when all local wave interactions have subsided. In the considered case (Igra *et al.*, 1998), a steady Mach reflection is evident near the flow exit from the area change segment.

7.10 HEAD-ON COLLISION OF A PLANAR SHOCK WAVE WITH A NONRIGID WALL

The simple case of shock wave reflection from a planar, rigid wall placed perpendicular to the shock direction of propagation can easily be studied by using the equations provided in Section 7.2 when the colliding shocks are of equal strength. In such a case a simple boundary condition exists: The flow velocity at the rigid wall is equal to zero. This boundary condition does not hold when the incident shock wave collides, head-on, with a nonrigid wall placed perpendicular to the shock direction of propagation. An example of a practical case is when the wall from which the shock reflects is made of an elastic material. It could be a rubber (elastomer) or a highly porous material, such as a rubber foam. In both cases the wave pattern resulting from the collision between the shock wave and the nonrigid wall will be different from, and more complex than, that observed in a similar reflection from a rigid wall. Now, both the waves in the gaseous phase and in the solid phase have to be considered. Once the incident shock wave hits the wall, a reflected shock will propagate into the gas, ahead of the wall, and a shock (or compression) wave will be transmitted into the elastic wall material. Once the transmitted wave reaches the elastic material rear-end it will be reflected and will propagate back and forth inside the elastic material.

Subsequently, a brief description of head-on collision between a planar shock wave and a rubber supported plate (wall) is given. The head-on collision between a normal shock wave, propagating into a quiescent gas, and a rubber-supported plate was investigated theoretically and experimentally by Mazor *et al.* (1992) and Igra *et al.* (1992, 1997). In the theoretical part, a physical model was proposed for describing the collision process. In principle the rubber can be loaded in any of the following three different ways because of its collision with the incident shock wave. They are uniaxial stress loading, biaxial stress loading, and uniaxial strain loading; these options are shown schematically in Fig. 7.24. In the first two modes (Figs. 7.24a and 7.24b) the rubber can expand while carrying the shock loading, and therefore it can be treated as being incompressible. This is not the case when it experiences a uniaxial strain loading (Fig. 7.24c), as now it cannot expand and it should be treated as a compressible medium.

The model proposed by Mazor *et al.* (1992) was based on both the conservation equations and on an appropriate strain–stress relation describing

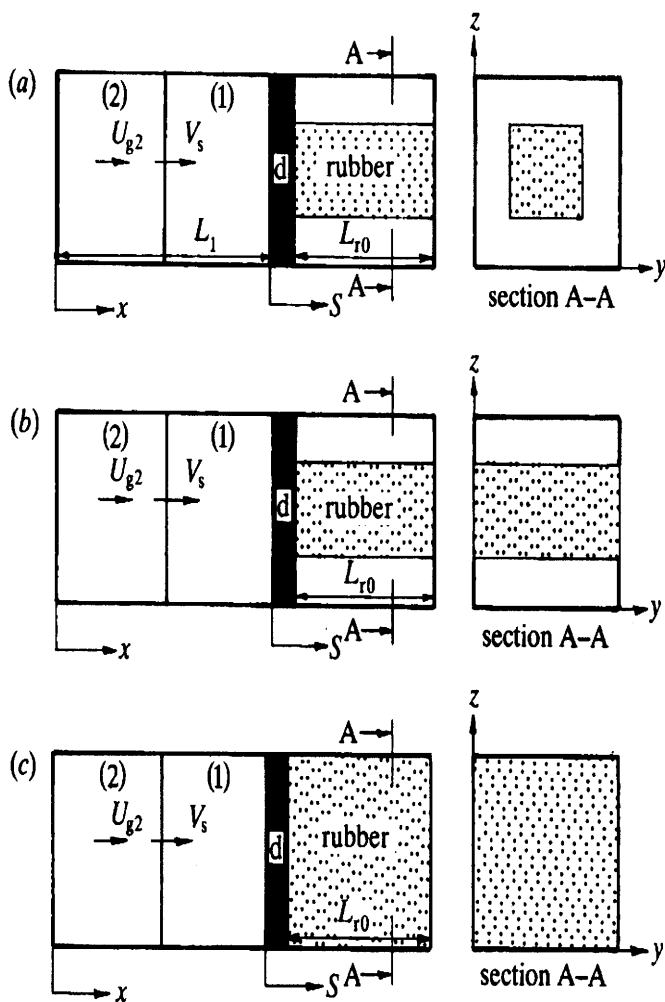


FIGURE 7.24 Schematic description of the three different loading modes. (a) uniaxial stress loading, (b) biaxial stress loading, and (c) uniaxial strain loading.

the rubber response to loading. The model was solved numerically for all the three different loading modes. In order to verify the validity of the proposed model and the accuracy of the used numerical scheme some of the obtained numerical results were compared with experimental findings.

Adopting a Lagrangian approach, the conservation equations for the gaseous and the solid phases, expressed in a nondimensional form (for a detailed derivation, see Mazor *et al.*, 1992), are as follows:

Conservation of mass in the gas:

$$\frac{\partial}{\partial t^*} \left[\rho_g^*(h_g^*, t_g^*) \frac{\partial x^*(h_g^*, t_g^*)}{\partial h_g^*} \right] = 0 \quad (7.38)$$

Definition of the gas velocity:

$$U_g^*(h_g^*, t^*) = \frac{\partial x^*(h_g^*, t^*)}{\partial t^*} \quad (7.39)$$

Conservation of momentum in the gas:

$$\frac{\partial U_g^*(h_g^*, t^*)}{\partial t^*} = - \frac{\partial P_g^*(h_g^*, t^*)}{\partial h_g^*} \quad (7.40)$$

Conservation of energy in the gas:

$$\frac{\partial T^*(h_g^*, t^*)}{\partial t^*} = -P^*(h_g^*, t^*) \frac{\partial V_g^*(h_g^*, t^*)}{\partial t^*} \quad (7.41)$$

Equation of state for the gas:

$$P^*(h_g^*, t^*) = (\gamma - 1)T^*(h_g^*, t^*)/V_g^*(h_g^*, t^*) \quad (7.42)$$

Conservation of mass for the rubber (incompressible for the case of uni- and biaxial stress loadings):

$$\frac{\partial}{\partial t^*} \left[\frac{\partial S^*(h_r^*, t^*)}{\partial h_r^*} A_r^*(h_r^*, t^*) \right] = 0 \quad (7.43)$$

Definition of velocity in the rubber:

$$U_r^*(h_r^*, t^*) = \frac{\partial S^*(h_r^*, t^*)}{\partial t^*} \quad (7.44)$$

Definition of the extension ratio in the rubber:

$$\lambda_x(h_r^*, t^*) = \frac{\partial S^*(h_r^*, t^*)}{\partial h_r^*} \quad (7.45)$$

Conservation of momentum in the rubber:

$$\frac{\partial U_r^*(h_r^*, t^*)}{\partial t^*} = - \frac{\partial |\sigma_x^*(h_r^*, t^*)|}{\partial h_r^*} \quad (7.46)$$

The additional needed constitutive equation, depending upon the loading mode, is as follows:

For a uniaxial stress loading:

$$\sigma_x^*(h_r^*, t^*) = \frac{G}{\rho_{r_0} c_0^2} [\lambda_x(h_r^*, t^*) - \lambda_x^{-2}(h_r^*, t^*)] \quad (7.47a)$$

For a biaxial stress loading:

$$\sigma_x^*(h_r^*, t^*) = \frac{G}{\rho_{r_0} c_0^2} [\lambda_x(h_r^*, t^*) - \lambda_x^{-3}(h_r^*, t^*)] \quad (7.47b)$$

For a uniaxial strain loading:

$$\sigma_x^*(h_r^*, t^*) = \frac{2G(1+v)}{\rho_{r_0} c_0^2 [1 - 2v^2/(1-v)]} [\lambda_x(h_r^*, t^*) - 1] \quad (7.47c)$$

The nondimensional parameters [indicated by asterisk in Eqs. (7.38) to (7.47)] are defined as follows:

$$t_g^* = \frac{ta_1}{L_1}, t_r^* = \frac{tc_0}{L_{r_0}}, P^* = \frac{P}{\rho_{g1} a_1^2}, \sigma^* = \frac{\sigma}{\rho_{r_0} c_0^2}, \rho_g^* = \frac{\rho_g}{\rho_{g1}}, \rho_r^* = \frac{\rho_r}{\rho_{r_0}}, x^* = \frac{x}{L_1},$$

$$S^* = \frac{S}{L_{r_0}}, U_g^* = \frac{U_g}{a_1}, U_r^* = \frac{U_r}{c_0}, T^* = \frac{C_V T}{a_1^2}, A_r^* = \frac{A_r}{A_{r_0}}, h_g^* = \frac{h_g}{\rho_{g1} L_1 A_g},$$

$$h_r^* = \frac{h_r}{\rho_{r_0} L_{r_0} A_{r_0}},$$

where indices 0 and 1 indicate preshock conditions in the rubber and the gas, respectively. L_1 is some reference length in the gas and L_{r_0} is the initial length of the rubber rod; a_1 and c_0 are the undisturbed speed of sound in the gas and in the rubber, respectively. ρ , U , p , T , and σ are density, velocity, pressure, temperature, and stress, respectively. Index g indicates gas and index r , rubber. h is the Lagrangian variable, defined as

$$h = \int_{x(0,t)}^{x(h,t)} \rho A \, dx,$$

where x is distance, t is time, and A is cross-sectional area. V , γ , S , and λ_x are volume, specific heat ratio, axial position of area A_r at time t , and extension ratio, respectively. G is the rubber's shear modulus, and v is its Poisson ratio.

Equations (7.38) to (7.47) contain eight partial differential equations and two algebraic equations for 10 dependent variables: ρ_g^* , P^* , T^* , U_g^* , x^* , σ_x^* , λ_x , S^* , A_r^* , and U_r^* . The independent variables are h_g^* and t^* for the gas and h_r^* and t^* for the rubber. This set of equations was solved numerically by Mazor *et al.* (1992) for the following boundary conditions: The gas velocity at the rubber-supported plate is equal to the plate velocity and to the rubber velocity where it

touches the plate. The rubber velocity at the rear end of the rubber rod, where it is attached to a rigid wall, is zero. In the following only some of the results presented in Mazor *et al.* (1992) and in Igra *et al.* (1997) are given.

The collision process between the incident shock wave and the rubber-supported wall is shown schematically in Fig. 7.25. Immediately after the collision, the incident shock wave is reflected backwards as a shock wave S_r and a transmitted shock wave S_t propagate into the rubber rod; see time t_1 in Fig. 7.25. (As shown later, the transmitted wave starts as a compression wave,

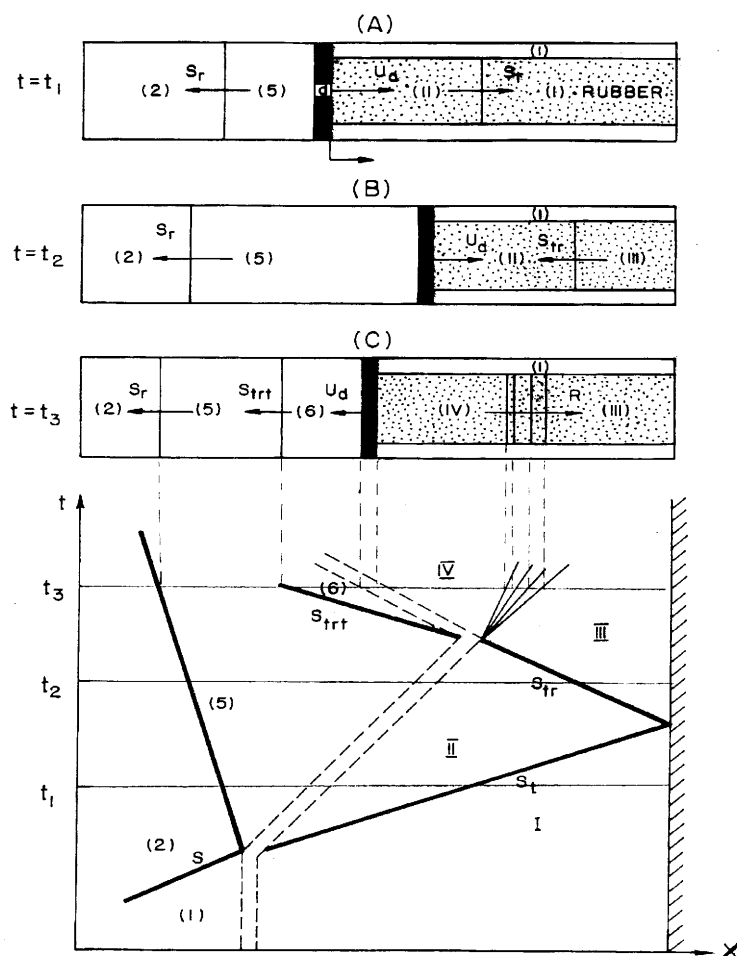


FIGURE 7.25 Wave patterns, in gas and in rubber, resulting from a head-on collision between the incident shock wave and the rubber-supported plate.

which might steepen into a shock wave.) The reflected shock wave S_r changes the gas properties from state (2) to state (5) and the transmitted shock wave S_t , changes the rubber properties from state (I) to state (II). Because of the high pressure behind the reflected shock wave P_5 , the plate d is accelerated. The plate assumes a velocity U_d . Once the transmitted shock wave reaches the rubber's rear end, it is reflected (shock wave S_{tr} in Fig. 7.25 at time t_2) into state (II) and changes it into a new state (III). Until the shock wave S_{tr} reaches the rubber's leading edge, the plate d continues to move from left to right and the rubber length is continually reduced. Once the shock wave S_{tr} reaches the rubber's leading edge, it is reflected backward as a rarefaction wave, R , and a shock wave S_{trt} is transmitted into the gas; see at time t_3 in Fig. 7.25. The transmitted shock wave S_{trt} separates between two flow states, (5) and (6). At this point the rubber reaches its maximum deformation (minimum length). When the rarefaction wave propagating inside the rubber reaches the rubber's rear end it reflects back and upon its reaching the rubber's leading edge, it will be reflected as a compression wave and a rarefaction wave will be transmitted into the gas; for details see Mazor *et al.* (1992).

Samples of the numerical results obtained by Mazor *et al.* (1992), who solved Eqs. (7.38)–(7.47) for the initial conditions $M_5 = 1.75$, $p_1 = 1$ bar, $U_{g1} = U_{r1} = 0$, $T_1 = 300$ K, $\sigma_{t1} = 1$ bar, $A_g/A_{r0} = 2$, $L_{r0} = 0.25$ cm, $m_r/m_d = 20$, $v = 0.495$, $\rho_{r0} = 930$ kg/m³, $c_0 = 46$ m/s, and $G = 4$ bar, are shown in Figs. 7.26 to 7.29. In Fig. 7.26 the pressure p_d/p_1 acting on the plate supported by the rubber rod is shown as function of the nondimensional time tc_0/Lr_0 , for the three different loading modes. For reference, the results obtained for a similar reflection from a rigid wall are also shown (5s). It is evident that the gas pressure acting on the plate goes through the following changes. Initially it is equal to the ambient pressure P_1 ; then the reflected shock wave changes it to P_5 . Thereafter, the transmitted shock wave (S_{tr}) changes it to P_6 , and finally the transmitted rarefaction wave changes it to P_7 . While P_5 and P_6 remain constant, P_7 decreases monotonically. For all three loading modes the obtained values for P_5 are smaller than that which is reached behind a similar reflection from a rigid wall (P_{5s}). The smallest value of P_5 is obtained for the uniaxial stress loading, the largest, in the case of uniaxial strain loading. On the other hand, in all three loading modes P_6 is larger than P_{5s} . The largest value of P_6 is obtained in the uniaxial stress loading, and the smallest in the case of uniaxial strain loading.

Variations in the rubber stress at its leading edge, where it is attached to the plate, are shown in Fig. 7.27. As could be expected, the largest stress is obtained for a uniaxial strain loading, while the smallest is obtained in a uniaxial stress loading. Since $A_g/A_{r0} = 2$, it is expected that σ_{td} will be higher than P_5 (shown in Fig. 7.26). The stress σ_{tw} and the strain λ_w experienced by the rubber at its rear end, where it is attached to a rigid wall, are shown in Figs.

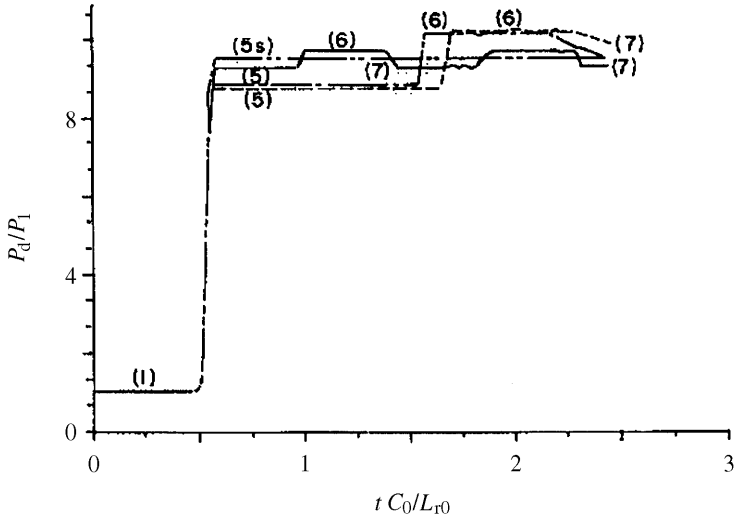


FIGURE 7.26 Gas pressure acting on the rubber supported plate as function of time. (---) Uniaxial stress; (-.-) biaxial stress; (—) uniaxial strain; and (.....) reflection from a rigid wall.

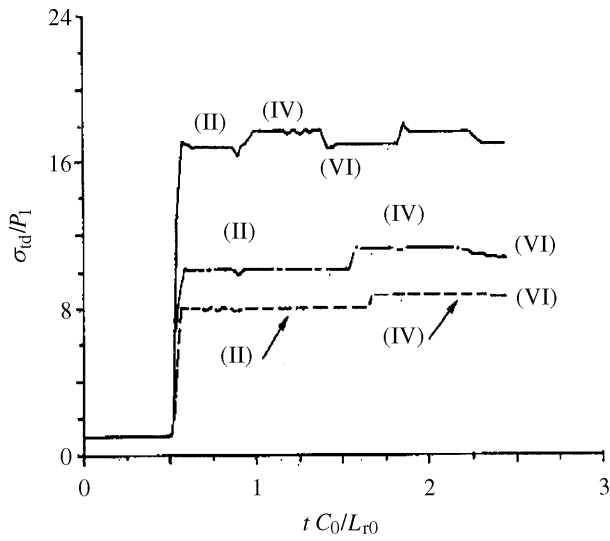


FIGURE 7.27 Stress at the rubber leading edge as function of time. (---) Uniaxial stress; (-.-) biaxial stress; (—) uniaxial strain.

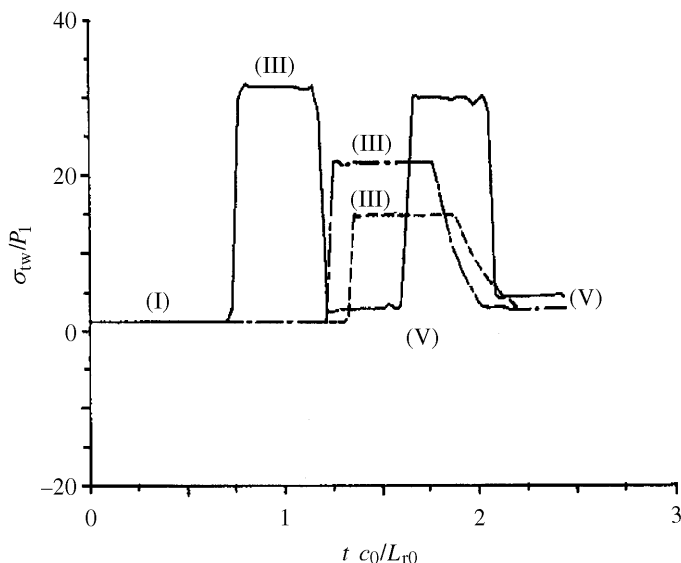


FIGURE 7.28 The rubber stress, at its rear end, as a function of time. (---) Uni-axial stress. (- · -) Biaxial stress; (—) uniaxial strain.

7.28 and 7.29, respectively. It is apparent from these figures that the largest stress and the smallest strain are obtained for the uniaxial strain loading, whereas the smallest stress and the largest strain, at the rubber rear end, are obtained for the uniaxial stress loading. It should be noted that the stress experienced by the rubber at its rear end is significantly larger than the gas pressure acting on the plate. It is also significantly larger than the pressure obtained behind a reflected shock wave from a rigid wall under similar initial conditions. Additional numerical results are available in Mazor *et al.* (1992).

In order to verify the validity of the proposed physical model, Eqs. (7.38) to (7.47), and its numerical solution, shock tube experiments were conducted. The experiments were made in the 110 mm by 40 mm (cross-section) test section of the Ernst Mach Institute in Freiburg, Germany. Details regarding the shock tube and the diagnostic used are given in Mazor *et al.* (1992). In the following, results are given for a biaxial stress loading under the following initial conditions in the shock tube: $M_5 = 1.55$, $m_d = 0.123$ kg, $T_1 = 294.7$ K, $P_1 = 0.99$ bar, and $A_g = 0.0044$ m². (Results obtained for the uniaxial strain loading are shown subsequently.) The rubber rod used in the experiments was 100 mm long and had a square cross section of 40 mm by 40 mm. Its

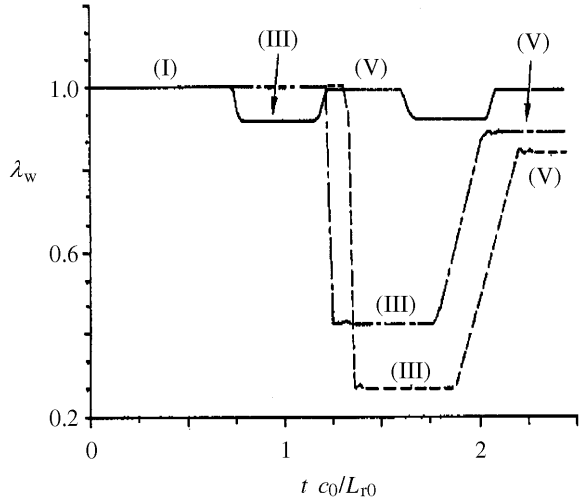


FIGURE 7.29 The rubber strain, at its rear end, as a function of time. (---) Uniaxial stress; (-.-) biaxial stress; (—) uniaxial strain.

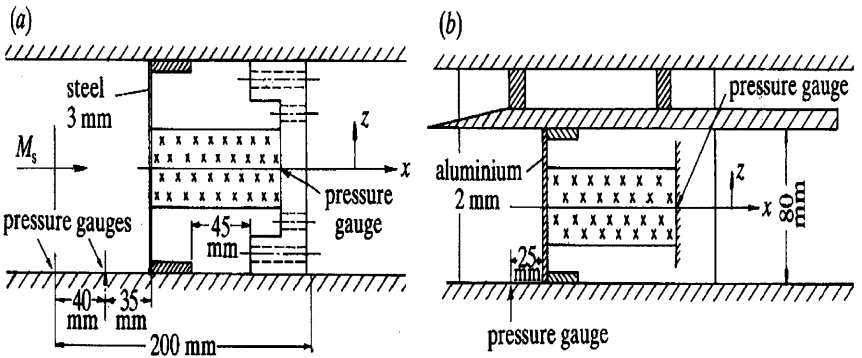


FIGURE 7.30 Illustration showing the two options for placing the tested model inside the shock tube test section.

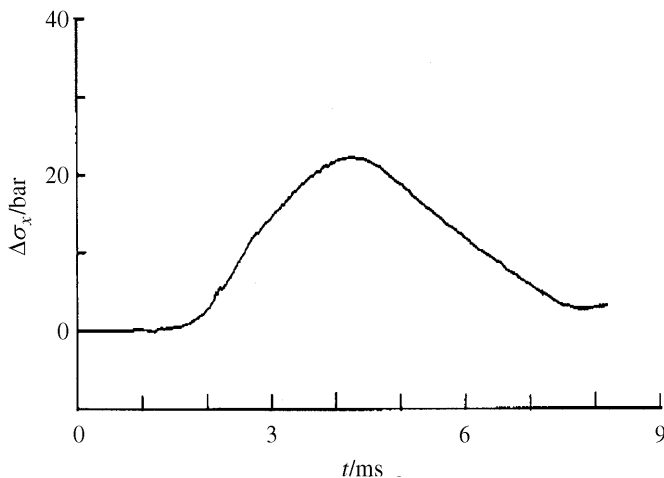


FIGURE 7.31 Recorded pressure history at the rear end of the rubber rod.

installation inside the test section is shown in Fig. 7.30a. The rubber chemical composition and its physical properties are listed in Mazor *et al.* (1992).

The stress recorded at the rubber rear end, where it is attached to a rigid wall, is given in Fig. 7.31. It is clear that the pressure there increases gradually through the transmitted compression waves to a maximum and, thereafter, gradually decreases through the reflected rarefaction wave. In the considered case the maximum value of the rubber stress is almost five times larger than the initial gas pressure behind the reflected shock wave, p_5 (see Fig. 17 in Mazor *et al.*, 1992). The entire interaction process between the incident shock wave and the rubber support plate was recorded in 24 shadowgraph photos (Fig. 19 in Mazor *et al.*, 1992). These photos, which were taken every 0.4 ms, show the rubber rod at different times during its loading by the impinging shock wave. Four photos, taken from the set of 24, are shown in Fig. 7.32. They show the rubber rod just before it is stuck by the incident shock wave and at three different times thereafter. The last, at $t = 6.8$ ms, shows the rubber rod at its maximum deformation, i.e., when its length is reduced to about 60% of its original length. Based on the observed geometry of the rubber rod during its loading, it is possible to verify some of the basic assumptions made in constructing the proposed physical model for the rubber behavior under its dynamic loading. For example, in the uni- and biaxial stress loadings it was assumed that the rubber is incompressible. Because of this assumption, in a biaxial stress loading, $\lambda_z = 1/\lambda_x$. In Fig. 7.32, where the rubber at about 4 ms after its collision with the incident shock wave is shown, the rubber rod

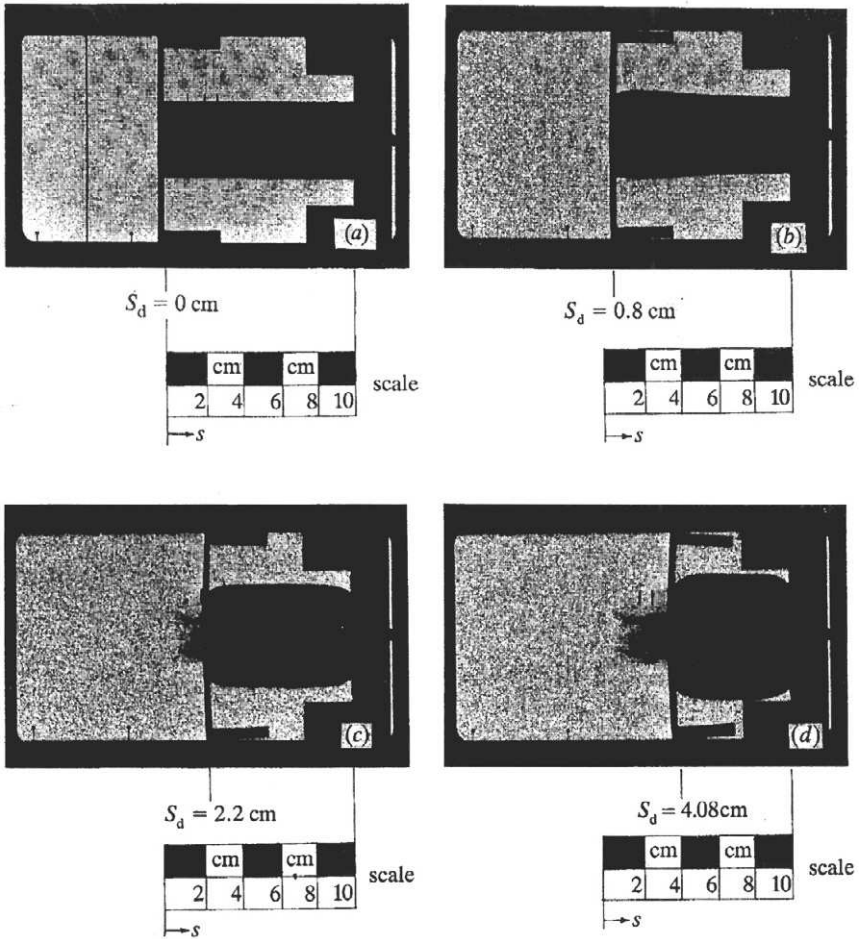


FIGURE 7.32 Shadowgraphs taken at different times during the shock collision with the rubber-supported plate. (a) At time $t = 2.78$ ms, (b) at $t = 4$ ms, (c) at $t = 5.2$ ms, and (d) at $t = 6.8$ ms.

reaches its maximum compression and its length is reduced by 4.08 cm. Therefore, $\lambda_x = (10 - 4.08)/10 = 0.592$. At this time the rubber experiences its maximum expansion in the z -direction, about 2.75 cm. Therefore, $\lambda_z = (4 + 2.75)/4 = 1.688$. These values of λ_x and λ_z perfectly agree with the incompressibility condition, i.e., $\lambda_x \lambda_z = 1$.

Numerical and experimental results obtained for the displacement of the rubber-rod leading edge S_d are shown in Fig. 7.33. Experimental findings appear as small circles. The short lines above and below the S_d circles indicate the

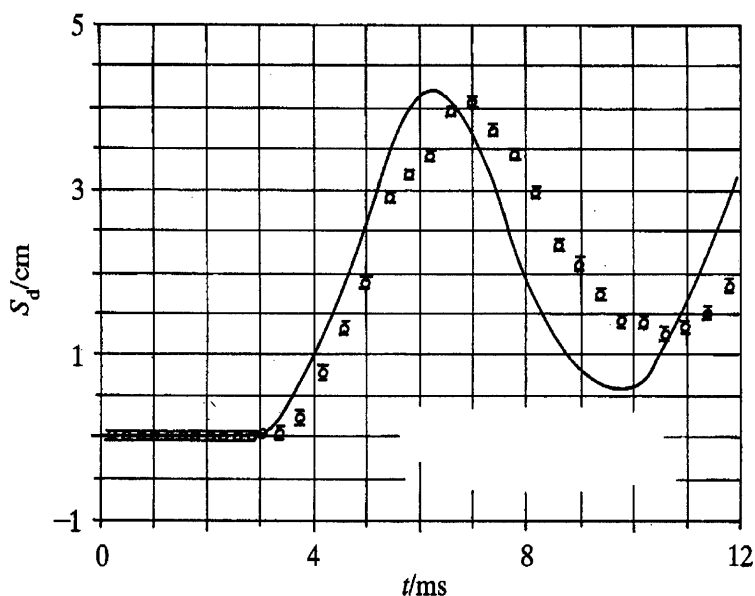


FIGURE 7.33 Displacement of the rubber-supported plate. (—) Numerical results; (○) experimental findings.

range of the experimental error. It is apparent from Fig. 7.33 that good agreement exists between experimental and numerical results for times $t < 5.5$ ms. The reason for the difference between the two results is mainly due to the fact that in the numerical solution friction between the rubber and the shock tube windows was neglected. (In addition, the interaction between the reflected shock wave S_r and the contact surface is not included in the present numerical solution.) Apparently, in spite of the lubrication used, at a high rubber compression the force pressing the rubber to the test-section windows is too large to be ignored. It should be noted that both the experimental and the numerical results exhibit the same trend, i.e., similar amplitude and time period. It is very clear from the experimental results that at the end of the pressure release the rubber does not return to its original length.

A comparison between experimental and numerical results obtained for the gas pressure on the rubber-supported plate p_d is shown in Fig. 7.34. Very good agreement between the two is evident. A comparison between experimental and numerical results obtained for the rubber stress, at its rear end where it is attached to a rigid wall, is given in Fig. 7.35. It is evident from this figure that the head of the compression wave reaches the rear end of the rubber earlier in the actual experiment than in the numerical simulation. This fact suggests that the actual value of G , which determines the wave propagation velocity in the rubber, is slightly larger than the value used in the numerical simulations. The

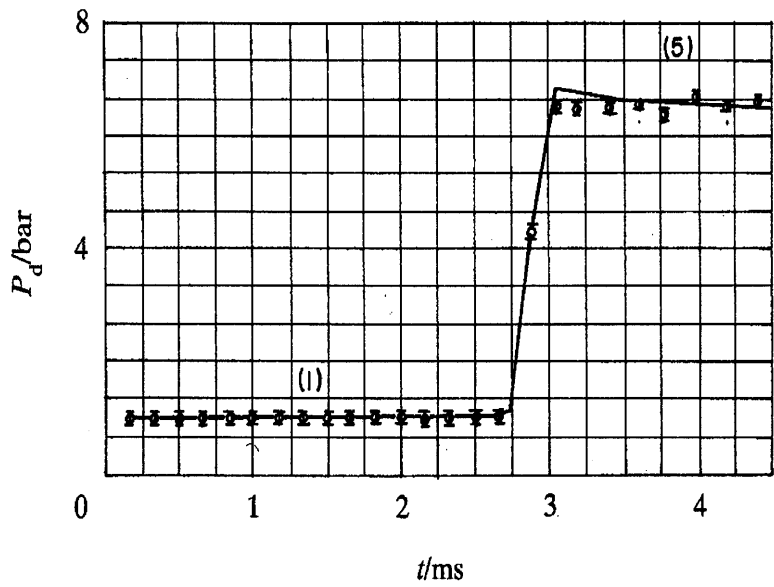


FIGURE 7.34 Gas pressure acting on the rubber-supported plate. (—) Numerical results; (O) experimental findings.

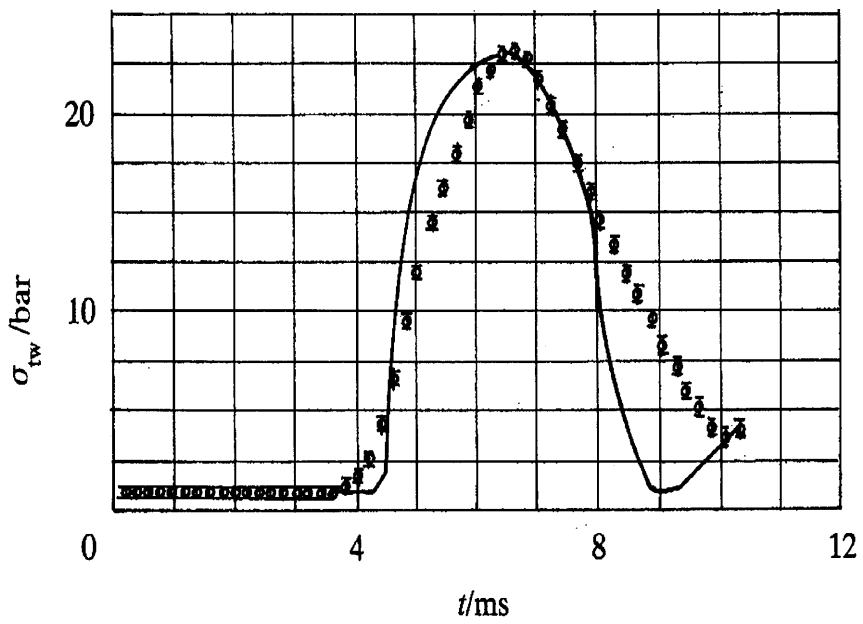


FIGURE 7.35 Stress at the rubber rear end where it is attached to rigid wall. (—) Numerical results; (O) experimental findings.

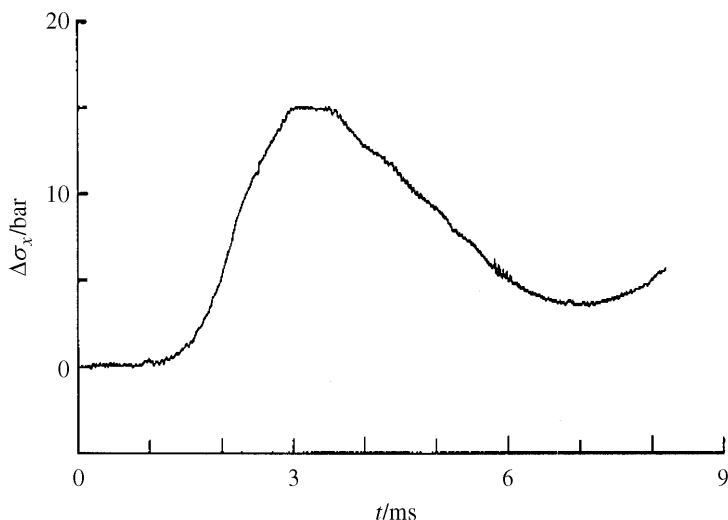


FIGURE 7.36 Pressure history recorded at the rear end of the rubber rod.

presently used value ($G = 9.317$ bar) was deduced from static loading of the used rubber-rod.

In the results shown so far, the transmitted wave in the rubber was a compression wave. In another experiment, where the compression waves coalesce to a shock wave, the installation of the rubber and the plate it supports inside the test section is shown in Fig. 7.30b. In this experiment the initial conditions were $T_1 = 294.8$ K, $P_1 = 0.996$ bar, $M_5 = 1.562$, $m_d = 0.032$ kg, and $A_g = 0.0032$ m². The pressure history (stress) recorded at the rubber rear end, where it is attached to a rigid wall, is shown in Fig. 7.36. The plateau seen in the figure for $3 \leq t \leq 3.75$ ms, which was not observed in Fig. 7.31, is a clear evidence that a shock wave is reflected from the rear end of the rubber rod. Comparing Fig. 7.36 with 7.31 indicates that the stress rise in the former is quicker and the stress variation with time is less symmetric than that shown in Fig. 7.31. This is a further indication that a shock wave has been formed in the case described in Fig. 7.36, whereas a compression wave existed in Fig. 7.31. In Fig. 7.37 numerical results obtained for the rubber stress, at four different times, $t = 2.93, 3.73, 4.13$, and 5.33 ms, are shown. It is apparent that at $t = 3.73$ ms the transmitted compression wave head is located at $S \cong 5.3$ cm. This is verified in Fig. 7.38b, where a change in the rubber's width is evident at $S \cong 5$ cm. The position along the x -axis where changes in the width of the rubber rod are first noticed is most likely the location of the

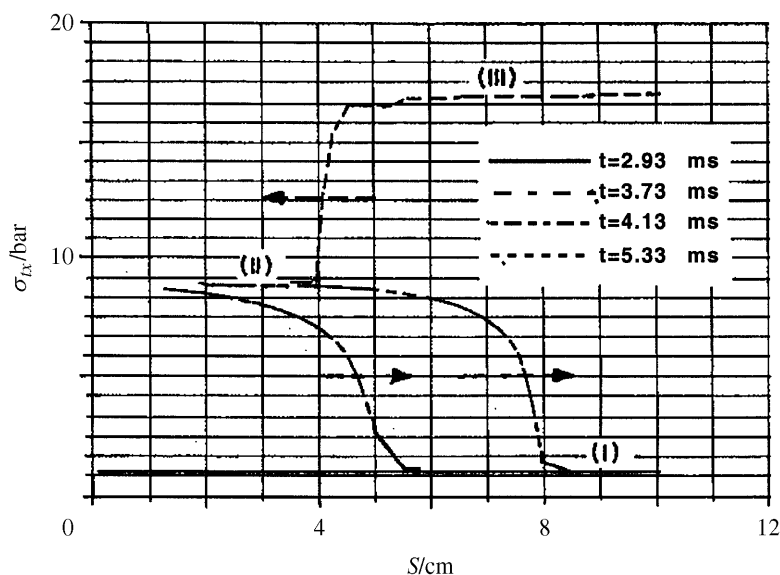


FIGURE 7.37 Stress in the rubber rod versus distance at different times during the rubber compression.

head of the transmitted compression wave. For $t = 4.13$ ms it is clear from Fig. 7.37 that the compression wave coalesces to a shock wave whose position is at $S \cong 7.5$ cm. (Now the changes in the rubber width are larger than those shown in Fig. 7.38b; this confirms the existence of a shock wave in Fig. 7.38c.) It is apparent from Fig. 7.38c that the shock wave position S is approximately at 7.5 cm. At $t = 5.33$ ms a reflected shock wave propagates inside the rubber (Fig. 7.37); for this time Fig. 7.38d indicates the existence of the reflected shock wave.

It is evident from Fig. 7.38b that there is a fairly good agreement between the numerically predicted position of the shock wave and the experimental findings.

A comparison between the numerical and experimental results for the pressure acting on the rubber-supported plate is given in Fig. 7.39. It is evident from Fig. 7.39 that good agreement exists between the two. Experimental and numerical results obtained for the rubber stress at its rear end, where it is attached to a rigid wall, are shown in Fig. 7.40. Fair agreement is witnessed for the early part of the rubber compression process.

The agreement deteriorates at a later time due to friction existing between the rubber rod and the shock tube windows; friction processes are not included

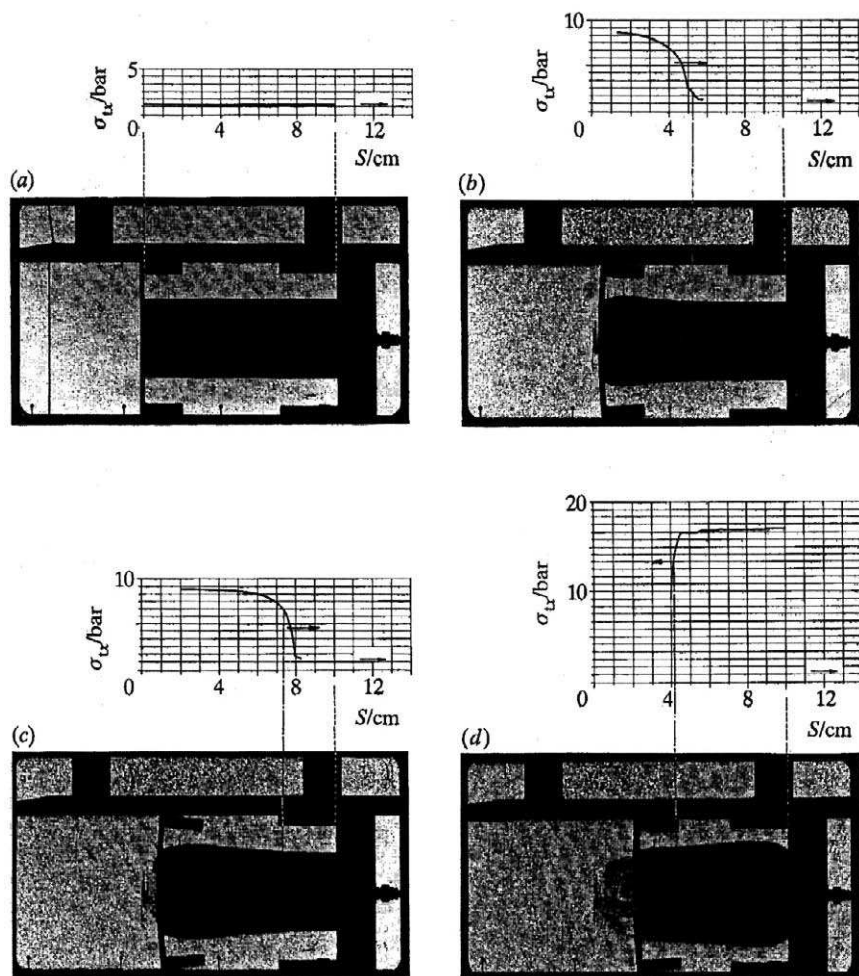


FIGURE 7.38 Shadowgraphs showing specific events from the collision process between an incident shock wave and a rubber-supported plate. Photos taken at (a) $t = 2.93$ ms, (b) $t = 3.73$ ms, (c) $t = 4.13$ ms, (d) $t = 5.33$ ms.

in the model used for the numerical investigation. Comparing the results shown in Fig. 7.40 with those of Fig. 7.35 indicates that the rise in the rubber stress is much quicker in Fig. 7.40 and that it reaches a constant value for a short time. This is a further indication that a shock wave is reflected from the rear end of the rubber rod.

In summary, the proposed physical model, Eqs. (7.38) to (7.46), (7.47b), provides a reliable description for the head-on collision between a planar shock

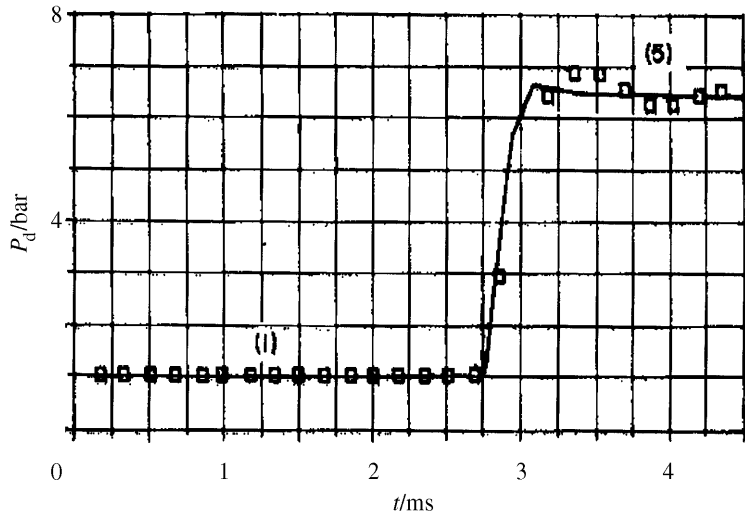


FIGURE 7.39 Pressure history on the rubber-supported plate. Solid line indicates numerical results and squares, experimental findings.

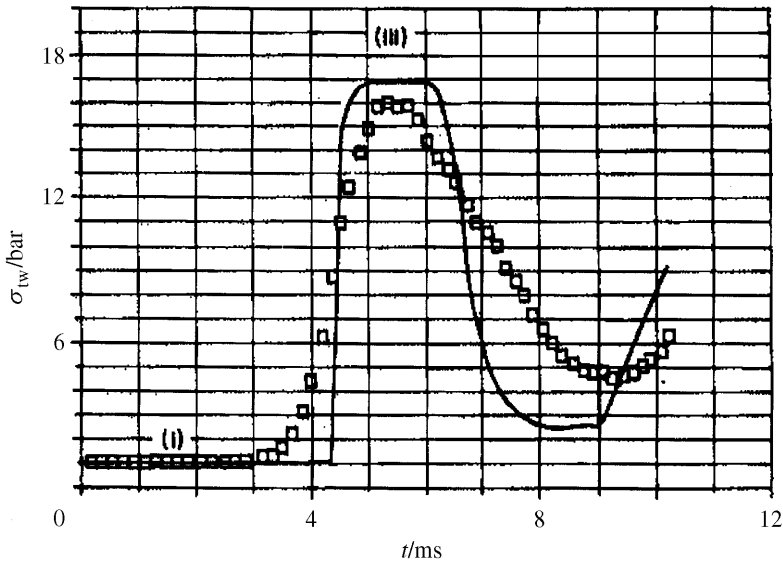


FIGURE 7.40 Stress at the rubber rear end where it is attached to a rigid wall. Solid line indicates numerical results and squares, experimental findings.

wave and a rubber-supported plate for the biaxial stress loading case. In order to confirm the validity of the proposed model for the other loading modes relevant experimental findings are needed. This is done in the following where the case of uniaxial strain loading is discussed.

In developing the conservation equations (7.38) to (7.47), the following assumptions were made:

- (a) The rubber is an isotropic elastic body and omit changes in its internal energy are negligibly small.
- (b) Body forces (gravity) and friction forces acting on the external surfaces of the rubber rod are negligibly small.
- (c) Stresses developed in the rubber rod are uniformly distributed along any cross-sectional area perpendicular to the x -axis. Therefore, the rubber's cross-sectional area remains planar throughout the deformation process.
- (d) The rubber is assumed to be incompressible.

In the case of a uniaxial strain loading (Fig. 7.24c), assumptions (b) and (d) are unacceptable. Therefore, one must include friction forces and the rubber compressibility in the conservation equations. The only two equations to be affected by relaxing these two, unrealistic assumptions are Eqs. (7.43) and (7.46). Accounting for the rubber compressibility alters equation (7.43) to

$$\frac{\partial}{\partial t} \left[\rho_r(h_r, t) \frac{\partial S(h_r, t)}{\partial h_r} A_r(h_r, t) \right] = 0. \quad (7.48)$$

Accounting for friction in the development of the conservation equations will be manifested in one modification only: consider a rubber rod element having a rectangular cross section of H by W (where H is its height and W is its width). The friction force exerted on its peripheral surfaces by the shock tube walls is given by

$$F_{\text{friction}} = 2(H + W)\Delta S\mu\sigma_n\text{sign}(U_r) = \left[\frac{\Gamma_r}{A_r}\mu\frac{v}{1-v}\sigma_x\text{sign}(U_r) \right] A_r\Delta S, \quad (7.49)$$

where ΔS , $\Gamma_r = 2(H + W)$, and $A_r = HW$ are elemental axial length, perimeter, and cross-sectional area of the element, respectively; μ and v are the friction coefficient and the Poisson ratio, respectively. σ_n is the normal stress acting on the element surfaces; in the present case, $\sigma_n = \sigma_y$, and Eq. (35) in Mazor *et al.* (1992) is used for its evaluation. If we define a frictional force per unit volume as

$$\sigma_f = \frac{\Gamma_r}{A_r}\mu\frac{v}{1-v}\sigma_x\text{sign}(U_r), \quad (7.50)$$

then the rubber's conservation of momentum, Eq. (7.46), is replaced by

$$\frac{\partial U_r}{\partial t} = -A_{r0} \frac{\partial \sigma_x}{\partial h_r} - \frac{\sigma_f}{\rho_r}. \quad (7.51)$$

In Eqs. (7.49) and (7.50) the function $\text{sign}(x)$ is the sign operator, which can take on values of $+1$ or -1 depending upon the sign of the argument x . It should be noted that unlike Eqs. (7.38)–(7.47), which are expressed in a nondimensional form, Eqs. (7.48)–(7.51) are expressed in a dimensional form.

As in the previously described biaxial stress loading experiments, the present set of experiments (uniaxial strain loading) was also conducted in the shock tube of the Ernst Mach Institute, Freiburg, Germany. In this shock tube the test section is equipped with windows having optical field of view of 200×110 mm, and its depth is 40 mm. It is designed for using “two-dimensional” models. During experiments the gas flow and the rubber behavior were monitored by pressure measurements. In contrast to the previous study, the rubber displacements, because of its uniaxial strain loading by the incident shock wave, are too small to be detected by high-speed shadowgraph photography. Therefore, other means for measuring the rubber's displacement were employed. In early experiments the uniaxial strain loading of a rubber specimen was achieved by placing it inside the shock tube test section, as is shown in Fig. 7.41. (The same rubber rod was used in the biaxial stress and in the uniaxial strain loading experiments.) Results obtained for this geometry were reported in Ben-Dor *et al.* (1993). Poor agreement was found between experimentally obtained pressures (stresses) in the rubber and the appropriate numerical simulations. For details, see Fig. 3 in Ben-Dor *et al.* (1993). The main reason for the discrepancy between experimental and numerical results was the use of pressure gauges made for pressure measurements in gases, to measure pressure (stress) in the rubber rod. In order to confirm the validity of this explanation regarding the discrepancy between experimental and numerical results obtained for pressures in the rubber rod, a different experimental approach was taken.

In the new experiments the same rubber specimen was used. It was rotated by 90° relative to its original position (see Fig. 7.42). Now the length of the rubber was significantly shorter while the walls bounding it were positioned further away relative to the case shown in Fig. 7.41. In the new setting a provision was made for an air gap between the rubber rear surface and the shock tube end wall. Using this provision results in using the Kistler gauges (MK 2, 3, 4 shown in Fig. 7.42) for pressure measurements in air. Such measurements should be accurate since they were within the specifications of the gauges. Experiments with a few different thicknesses of the air gap δ_1 were made and are reported in Igra *et al.* (1997). Results obtained for one of these cases ($\delta_1 = 5$ mm) are shown subsequently. In addition to pressure measure-

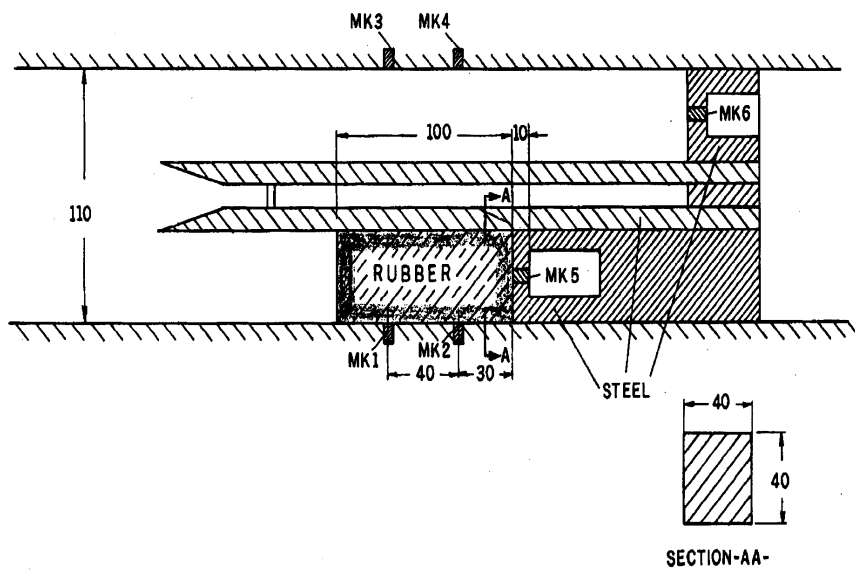


FIGURE 7.41 The rubber rod installment in the shock tube test-section. MK i ($i = 1, 2, \dots, 4$) indicate location of pressure gauges.

ments, the rubber displacement was also recorded using an electrooptical displacement-measuring device. Its positioning relative to the shock tube test section is shown in Fig. 7.42. A schematic description of the electrooptical unit is given in Fig. 7.43. This device measures the displacement of a black and white edge in normal direction. A lens focuses the light beam reflected from the black and white edge into the photocathode of an image converter. The electron image is reflected within the photocathode to a diaphragm having a small hole. At the beginning of each test an adjustment was made to ensure that the measuring beam passes exactly through the hole in the diaphragm. When the black and white lines are displaced, a control circuit displaces the electron image in such a way that a chosen point of the edge always falls on the diaphragm's hole.

The current in the control circuit is proportional to the edge displacement; it represents the measuring signal. The rise time of the signal (from 0 to 63%) is less than $1 \mu\text{s}$. This optical device can measure displacements to within $\pm 0.03 \text{ mm}$.

In Fig. 7.44 experimental (solid line) and numerical (dotted line) results obtained for the static pressure ahead of the rubber specimen (i.e., measured by gauge MK1 of Fig. 7.42) are shown. For obtaining results shown in Figs. 7.44 to 7.46 the following initial conditions were used: $M_5 = 1.54$, $\delta_1 = 5 \text{ mm}$, $\delta_2 = 15 \text{ mm}$, $P_0 = 0.99 \text{ bar}$, and $T_0 = 22.8^\circ\text{C}$. Good agreement exists between

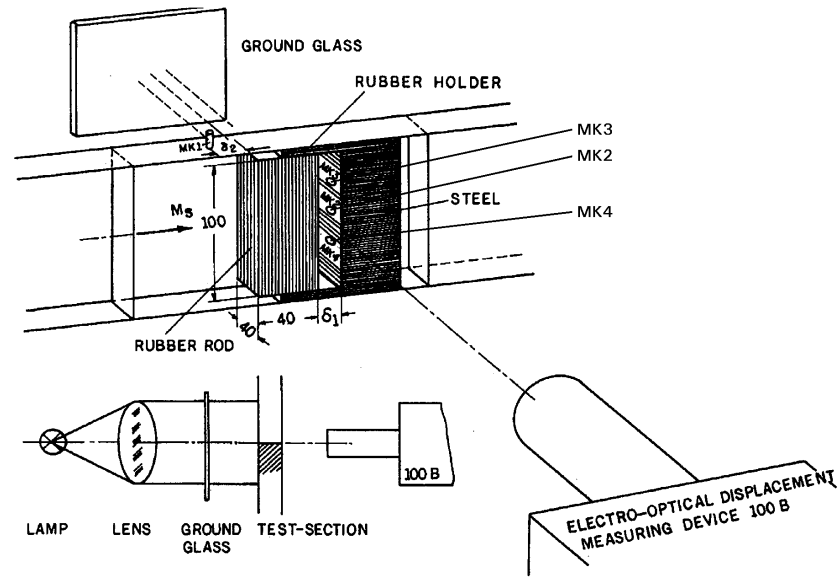


FIGURE 7.42 An alternative positioning of the rubber rod in the test section. Also shown is the electrooptical displacement measuring device alignment relative to the shock tube test section. MK1 indicate pressure gauges.

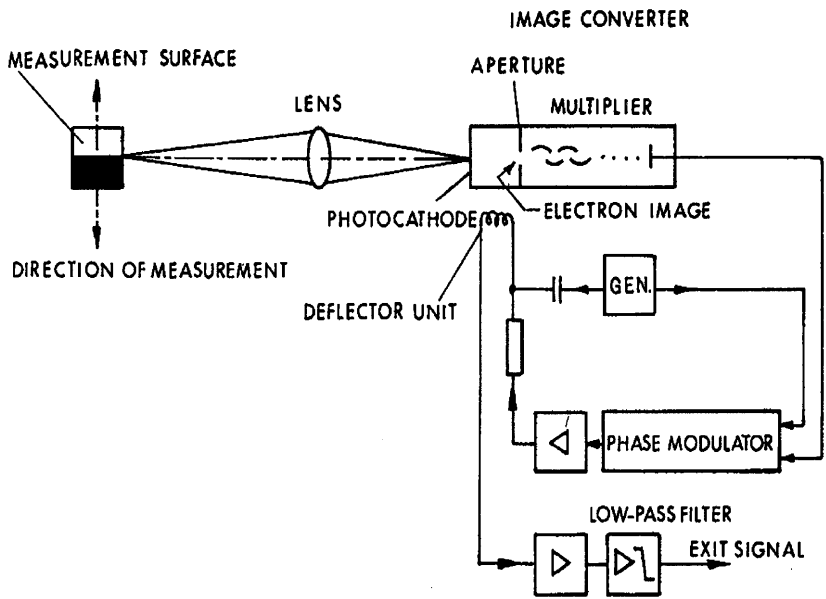


FIGURE 7.43 Schematic illustration of the electrooptical displacement device.

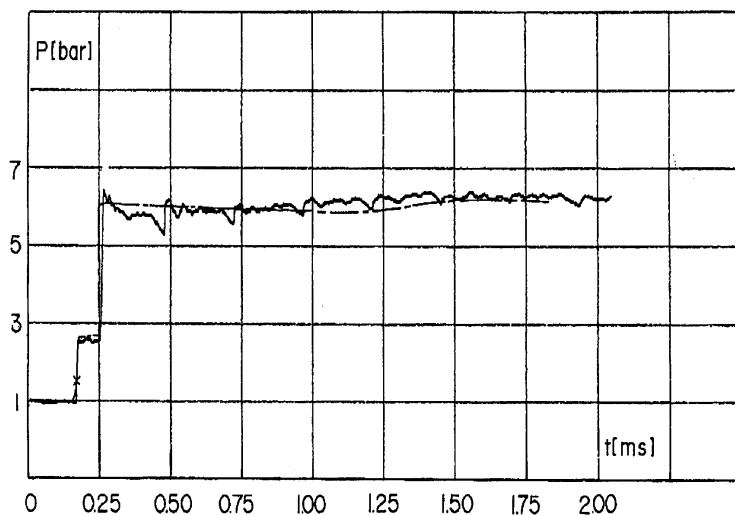


FIGURE 7.44 Pressure history recorded by gauge MK1 (shown in Fig. 7.42).

the two results regarding the pressure jump across the incident and the reflected shock waves. Experimental and numerical results for the displacement of the rubber rear surface are shown in Fig. 7.45. Again, very good agreement is found between the two results, up to the point where the recorder reading the experimental data saturated. A comparison between numerical and experimental results for the pressure in the air gap, at the shock tube end wall, where pressure gauge MK2 is placed, is shown in Fig. 7.46. Good agreement is found between the two results. In all of the numerical results shown a friction coefficient of $\mu = 0.04$ was used. Based upon the agreement between the two sets of results, it can be stated with confidence that the proposed physical model, and its numerical solution, describes the uniaxial strain loading case quite well.

In order to assess the role played by the friction developed between the rubber rod and the shock tube walls, the proposed physical model was solved numerically for three different friction coefficients, i.e., $\mu = 0, 0.04$, and 0.09 . All cases were solved for the geometry shown in Fig. 7.41 and for $M_S = 1.507$, $P_0 = 0.983$ bar, and $T_0 = 21.2^\circ\text{C}$. For the employed rubber, $G = 9.317$ bar, $\rho_{r_0} = 1.007 \text{ g/cm}^3$, and $\nu = 0.495$. The results obtained for pressures in the gas and in the rubber are shown in Fig. 7.47. At time $t = 0$, marked as line 1 in Fig. 7.47, the incident shock wave is shown prior to its head-on collision with the rubber rod. The gas ahead of the shock wave and the

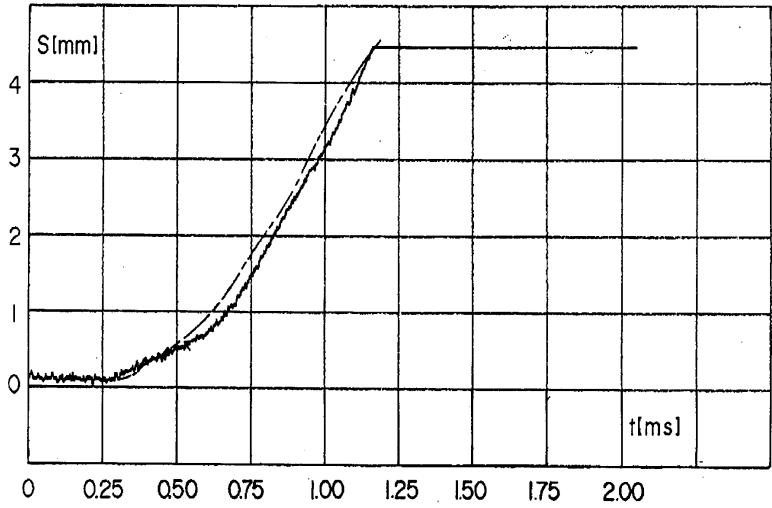


FIGURE 7.45 Displacement of the rubber-rod rear surface versus time.

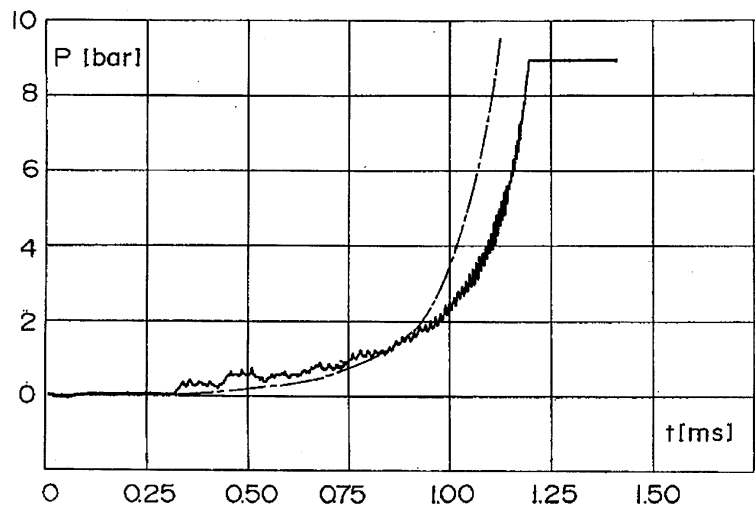


FIGURE 7.46 Pressure history recorded by gauge MK2 (shown in Fig. 7.42).

rubber specimen are still experiencing the initial pressure, i.e., $P_0 = 0.983$ bar; 76.1 μ s later, the lines marked as 2 in Fig. 7.47 shows the reflected and the transmitted waves. The one on the left is the shock wave reflected from the rubber frontal surface and the one on the right is the transmitted wave in the rubber. As time progresses both waves propagate further into the gas and into the rubber, respectively. It is apparent from Fig. 7.47 that the friction force has significant effect on strength of the transmitted wave, in the rubber, but not on its propagation velocity. As could be expected it has no effect on the reflected shock wave in the gas. In the case where no friction is included ($\mu = 0$) the strengths of both the reflected and the transmitted waves are unchanged. Introducing friction causes a clear weakening of the transmitted wave in the rubber. The larger μ is, the smaller is the pressure jump across the transmitted wave; see Fig. 7.47. How changes in μ affect the strength of the transmitted compression wave in the rubber, and its propagation velocity, is shown in Fig. 7.48. It is clear from this figure that while the velocity of the compression wave is independent of μ (the S versus t curve is a straight line for all μ), the postwave pressure depends strongly upon μ . The fact that the wave strength changes without any changes in its velocity is an indication that this is a linear wave (compression wave) rather than a shock wave.

As noted in Mazar *et al.* (1992), compression waves do not coalesce to a shock wave for the uniaxial strain loading case. Therefore, in such a loading only compression waves, exist and they propagate with the speed of sound (elastic longitudinal wave). It was also mentioned there that the highest speed of sound is encountered in the uniaxial strain loading case. The present numerical results indicate that waves propagating in the rubber move with a constant velocity, in the present case 305.2 m/s. The rubber particle velocity is significantly smaller; in the present case it is only 1.46 m/s. It is possible to calculate these two velocities analytically, directly from the conservation and constitutive equations. This computation is worth conducting since it may serve as a further verification of the numerical scheme used.

Consider an incident shock wave (I.S.W.) in the gas moving to the right (see Fig. 7.49a) toward a plane AB separating between gas and rubber. This shock wave is partly reflected back into the gas and partly transmitted into the rubber. First consider a rubber element $ABB'A'$, shown in Fig. 7.49b. The prevailing conditions at AB and $A'B'$ are shown in Fig. 7.49b, where σ_x is the stress generated in the rubber by the transmitted compression wave (T.C.W.), D is the speed of propagation of the compressive wave in the rubber. Ambient conditions exist ahead of the compression wave in the rubber. u_p is the particle velocity induced by the compression wave in the rubber. From conservation of mass one obtains:

$$\rho_{r0} D = \rho_r (D - u_p), \quad (7.52)$$

Number	1	2	3	4	5	6	7
Time (μs)	0	76.1	136.7	197.3	255.2	311.9	359.7

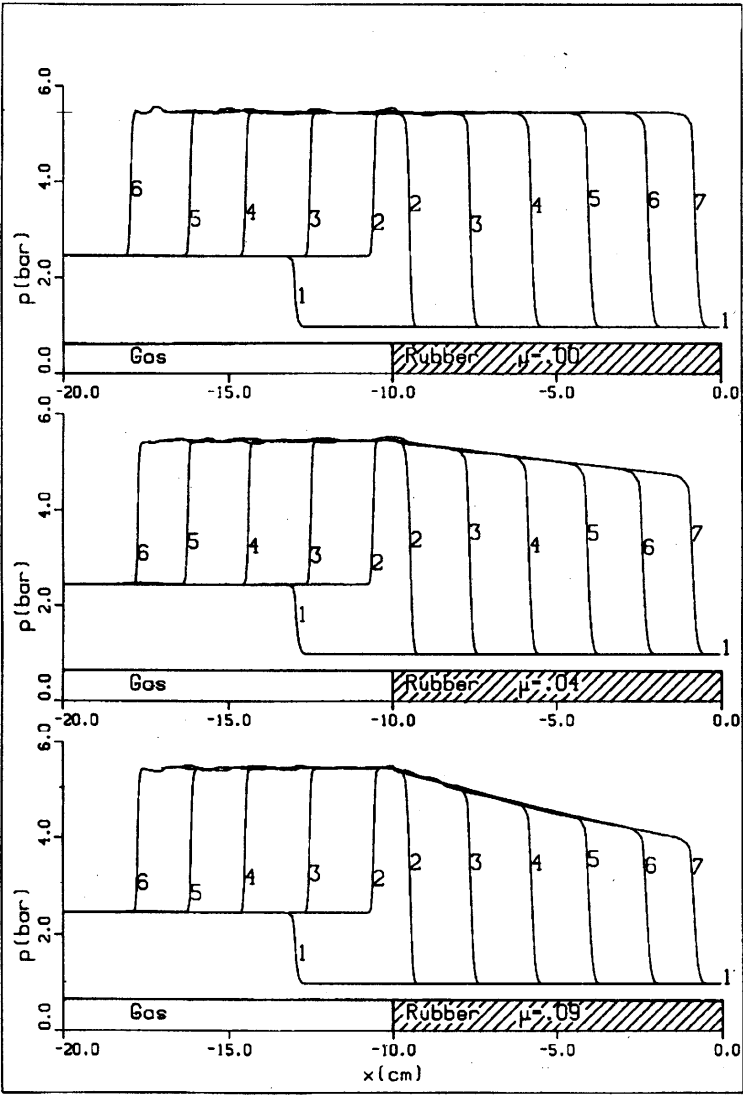


FIGURE 7.47 Numerical results showing shock waves in air and compression waves in the rubber at different times. The initial conditions are $P_0 = 0.893$ bar, $T_0 = 21.2^\circ\text{C}$, $M_5 = 1.507$, $G = 9.317$ bar, $v = 0.495$, and $\rho_{r_0} = 1.007$ g/cm³.

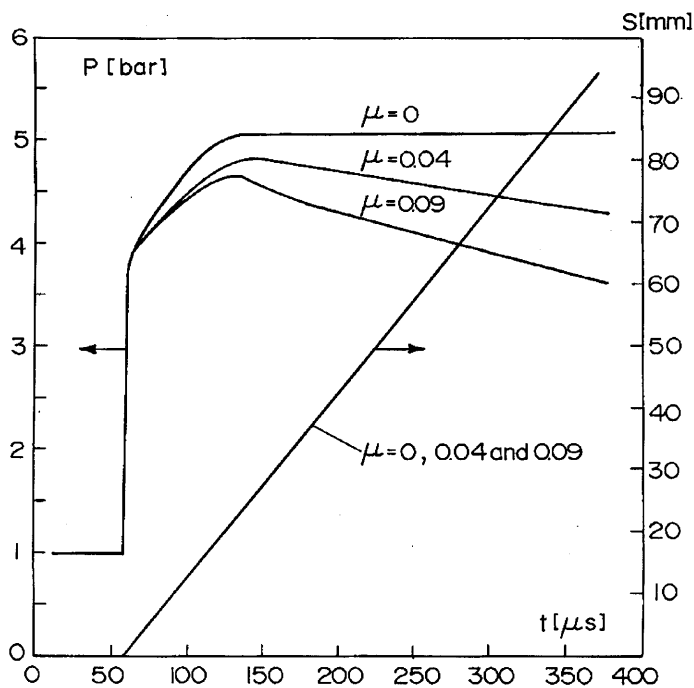


FIGURE 7.48 Numerical predictions of the pressure inside the rubber and the displacement of its frontal surface due to the propagation of a compression wave in it. (Initial conditions as in Fig. 7.47.)

and from conservation of momentum,

$$\rho_{r0} D u_p = \sigma_x - P_0. \quad (7.53)$$

Here σ_x is positive for compression.

Combining Eqs. (7.52) and (7.53) yields

$$\rho_r u_p (D - u_p) = \sigma_x - P_0 \quad (7.54)$$

or

$$D = u_p + \frac{\sigma_x - P_0}{\rho_r u_p} \quad (7.55)$$

Alternatively, from Eq. (7.52) one obtains

$$D = \frac{\rho_r u_p}{\rho_r - \rho_{r0}}. \quad (7.56)$$

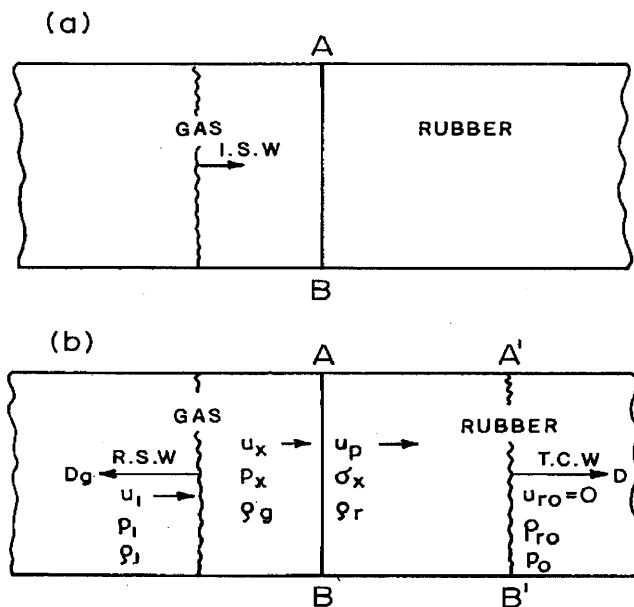


FIGURE 7.49 An illustration showing: (a) an incident shock wave in the gas prior to its head-on collision with a rubber rod, and (b) the reflected shock in the gas and the transmitted compression wave in the rubber shortly after the collision.

From Eqs. (7.55) and (7.56) we have

$$\frac{\rho_{r0}}{\rho_r} = 1 - \frac{\rho_{r0} u_p^2}{\sigma_x - P_0}. \quad (7.57)$$

Equation (7.57) relates the rubber densities and pressures (stresses) to its particle velocity. In order to assess the rubber particle velocity, an additional, constitutive equation is needed, i.e., the rubber's stress-strain relation. For a uniaxial strain loading case, we have

$$\sigma_x = \tilde{E}(1 - \lambda_x) + P_0; \quad (7.58)$$

where $\tilde{E} \equiv E(1 - \nu)/(1 - \nu - 2\nu^2)$. The rubber's nondimensional extension ratio λ_x , is

$$\lambda_x = \frac{\Delta S}{\Delta S_0} = \frac{\rho_{r0}}{\rho_r}$$

so that Eq. (7.58) can be rewritten as

$$\sigma_x = \tilde{E} \left(1 - \frac{\rho_{r_0}}{\rho_r} \right) + P_0. \quad (7.59)$$

Substituting ρ_{r_0}/ρ_r from Eq. (7.48) into Eq. (7.59) yields

$$u_p = \frac{\sigma_x - P_0}{\sqrt{\rho_{r_0} \tilde{E}}}. \quad (7.60)$$

Equation (7.60) relates the particle velocity induced by the incident elastic compression wave to the stress intensity, σ_x . For the reflected shock wave (R.S.W.) in the gas a similar (u_p, p)-relation can be obtained. It is known from gas dynamics (see Eq. 20 on page 67 in Glass and Hall, 1959) that

$$u_x = u_1 - \frac{P_x - P_1}{\sqrt{\frac{\gamma + 1}{2} \rho_1 \left(P_x + \frac{\gamma - 1}{\gamma + 1} P_1 \right)}}. \quad (7.61)$$

For the nomenclature used in Eq. (7.61), see Fig. 7.49b. The particle velocity induced by the compression wave, transmitted through the rubber, and the gas velocity behind the reflected shock wave in the gas could be found with the aid of Eqs. (7.60) and (7.61) using the following interface conditions:

1. The forces acting on plane AB (Fig. 7.49b) by the gas and by the rubber are equal.
2. At plane AB the particle velocity of the rubber is equal to that of the gas.

For the initial conditions used to obtain the results shown in Fig. 7.47 ($M_5 = 1.507$, $p_0 = 0.983$ bar, $T_0 = 22.2^\circ\text{C}$, $G = 9.317$ bar, $v = 0.495$, $\rho_{r_0} = 1.007$ g/cm³), u_p is 1.467 m/s, which is almost identical to the numerical result $u_{p,\text{num}} = 1.4575$ m/s. Once u_p is known, D can easily be calculated from Eq. (7.52) to yield $D = 305.69$ m/s. Again, we observe a very good agreement with the numerical result $D = 305.2$ m/s.

The case of a shock wave colliding head-on with a much softer material, e.g., polyurethane, is described in Chapter 15.1, section 15.1.6.2.

7.11 SUMMARY AND CONCLUSIONS

A physical model capable of describing the head-on collision of a planar shock wave with a rubber rod, which results in a uniaxial stress loading, a biaxial stress loading, or a uniaxial strain loading, was proposed. This model includes the rubber's compressibility and the friction force developed between the

rubber contact areas with its surrounding walls. The proposed physical model was solved numerically for all three loading modes. The good agreement obtained between numerical and experimental results, for the cases of biaxial stress loading and uniaxial strain loading, confirms the reliability of the proposed model and the accuracy of the numerical scheme used for its solution. Additional support to the accuracy of the present numerical solution is obtained from comparing the analytical and the numerical results obtained for the velocity of the compression wave, in the rubber, and the rubber's particle velocity. As was shown, for the case of a uniaxial strain loading, the analytically and numerically obtained values for these velocities are almost the same.

We may draw the following conclusions from the described numerical and experimental studies:

- The speed of wave propagation, in the rubber for the case of uniaxial strain loading is much larger than that obtained for the other two loading modes. At an early time after the head-on collision higher pressures behind the reflected shock wave were obtained in the case of a uniaxial strain loading, as compared with the other two loading cases. However, in all three cases the pressures obtained behind the reflected shock wave were lower than those obtained in a similar reflection from a rigid wall. At a later time after the collision, the pressure acting on the rubber-supported plate was higher than that obtained in a similar reflection from a rigid wall. The stress in the rubber-rod leading edge and at its rear end was significantly higher than the pressure acting on the rubber-supported plate and/or the pressure behind a reflected shock wave in a similar rigid wall case. It should be noted that both the stress in the rubber-rod leading edge and that at its rear end are strongly affected by the area ratio A_g/A_r . Therefore, the obtained results should be used only for the specified area ratios.

- When presenting the numerical results for the rubber variables as a function of distance, for different times, the existence of the wave patterns shown schematically in Fig. 7.25 was confirmed.

- By proper selection of the physical properties of the rubber and the plate supports, one could ensure that the transmitted compression wave in the rubber will either remain a compression wave or coalesce into a shock wave.

- In a case of uniaxial strain loading friction forces play an important role in the rubber loading due to its head-on collision with a planar shock wave.

- The higher the friction coefficient is, the stronger is the wave damping in the rubber.

- In a uniaxial strain loading only compression and/or rarefaction waves exists in the rubber rod, i.e., no shock waves. The waves propagate with a

constant velocity, independent of the friction coefficient and of the intensity of the colliding shock wave.

REFERENCES

- Ben-Artzi, M., and Falcovitz, J. (1986). An upwind second order scheme for compressible duct flows. *SIAM J. Stat. Comp.* 7, 744–768.
- Ben-Dor, G., Mazon, G., Mond, M., Igra, O., Heilig, W., and Reichenbach, H. (1993). Reflection of planar shock waves from rubber walls: uniaxial strain case. *AIAA J.* 31, 2184–2186.
- Billington, I. J. (1955). An experimental study of one-dimensional reflection of a rarefaction wave at a contact surface. Univ. Toronto Inst. Aerophysics, UTIA Rept. 32.
- Billington, I. J., and Glass, I. I. (1955). On the one-dimensional refraction of a rarefaction wave at a contact surface. Univ. Toronto Inst. Aerophysics, UTIA Rept. 31.
- Bitondo, D., Glass, I. I., and Patterson, G. N. (1950). One-dimensional theory of absorption and amplification of a plane shock wave by a gaseous layer. Univ. Toronto Inst. Aerophysics, UTIA Rept. 5.
- Bremner, G. E., Dukowitz, J. K., and Glass, I. I. (1960). On the one-dimensional overtaking of a rarefaction wave by a shock wave. Univ. Toronto Inst. Aerophysics, UTIA Tech. Note 33.
- Bull, G. V., Fowell, L. R., and Henshaw, D. H. (1953). The interaction of two similarly-facing shock waves. Univ. Toronto Inst. Aerophysics, UTIA Rept. 23.
- Chorin, A. J., and Marsden, J. E. (1990). *Mathematical Introduction to Fluid Mechanics*, Springer-Verlag, New York.
- Courant, R., and Friedrichs, K. O. (1943). Interaction of shock and rarefaction waves in one-dimensional motion. Appl. Mathematics Group, New York Univ. 1.
- Courant, R., and Friedrichs, K. O. (1976). *Supersonic Flow and Shock Waves*, Springer-Verlag, New York.
- Falcovitz, J., and Ben-Artzi, M. (1995). Recent developments of the GRP method. *JSME Intl. J. Ser. B* 38, 497–517.
- Ford, C. A., and Glass, I. I. (1954). An experimental study of shock-wave refraction. Univ. Toronto Inst. Aerophysics, UTIA Rept. No. 29.
- Glass, I. I., and Hall, J. (1959). Shock tubes. In *Handbook of Supersonic Aerodynamics*, Section 18 (ed. S. L. Penn), NAVORD Rept. 1488 (Vol. 6). Bureau of Naval Weapon Publ.
- Glass, I. I., Heuckroth, L. E., and Molder, S. (1959). On the one-dimensional overtaking of a shock wave by a rarefaction wave. Univ. Toronto Inst. Aerophysics, UTIA Tech. Note 30.
- Godunov, S. K. (1959). A finite difference method for the numerical computation of discontinuous solutions of the equations of fluid dynamics. *Mat. Sbornik* 47, 271–295.
- Gottlieb, J. J., and Igra, O. (1983). Interaction of rarefaction waves with area reductions in ducts. *J. Fluid Mech.* 137, 285.
- Gould, D. G. (1952). The head-on collision of two shock waves and a shock and rarefaction wave in one-dimensional flow. Univ. Toronto Inst. Aerophysics, UTIA Rept. 17.
- Greatrix, D. R., and Gottlieb, J. J. (1982). An analytical and numerical study of a shock wave interaction with an area change. Univ. Toronto. Inst. Aerospace Studies, UTIAS Rept. 268.
- Guderley, G. (1942). Non-steady gas flow in thin tubes of variable cross section. *Zentrale für Wissenschaftliches Berichwesen der luftfahrtforschung des generalluftzeugmeisters*. 1744, translated as N. R. C. (Canada) Translation TT-82.
- Henshaw, D. H. (1950). Refraction of a shock wave at a gaseous interface. Univ. Toronto Inst. Aerophysics, UTIA Rept. 11.

- Igra, O., and Gottlieb, J. J. (1985). Interaction of rarefaction waves with area enlargements in ducts. *AIAA J.* **23**, 1014.
- Igra, O., Ben-Dor, G., Mazon, G., and Mond, M. (1992). Head-on collision between normal shock waves and a rubber-supported plate, a parametric study. *Shock Waves* **2**, 189.
- Igra, O., Wang, L., Ben Dor, G., Reichenbach, H., and Heilig, W. (1997). Uni-axial strain loading of a rubber rod by planar shock waves. *Acta Mechanica* **120**, 91–107.
- Igra, O., Wang, L., and Falcovitz, J. (1998). Nonstationary compressible flow in ducts with varying cross-section. *J. Aerospace Eng., Proc. Inst. Mech. Eng.*, **212**, Part G, 225–243.
- Mazon, G., Igra, O., Ben-Dor, G., Mond, M., and Reichenbach, H. (1992). Head-on collision of normal shock waves with a rubber supported wall. *Phil. Trans. R. Soc. Lond. A* **338**, 237–269.
- McKee, R. M. (1954). An experimental study of the interaction of a plane shock wave with a contact region. Univ. Toronto. Inst. Aerophysics, UTIA Tech. Note 1.
- Nicholl, C. I. H. (1951). The head-on collision of shock and rarefaction waves. Univ. Toronto Inst. Aerophysics, UTIA Rept. 10.
- von Neumann, J. (1943). Progress report on the theory of shock waves. *Nat. Def. Comm.*, Div. 8, Off. Sci. R&D No. 1140.

This Page Intentionally Left Blank

Two Dimensional Interactions

8.1 Oblique Shock Wave Reflections

GABI BEN-DOR

Department of Mechanical Engineering, Ben-Gurion University of the Negev, Beer Sheva, Israel, 84105

-
- 8.1.1 Introduction and Historical Background
 - 8.1.2 Analytical Approaches for Describing Regular and Mach Reflections
 - 8.1.2.1 Two-Shock Theory
 - 8.1.2.2 Three-Shock Theory
 - 8.1.2.3 Shock Polars
 - 8.1.2.4 Suggested Transition Criteria
 - 8.1.2.5 Dual-Solution Domain
 - 8.1.2.6 Hysteresis Phenomenon in the Transition
 - 8.1.3 Steady Flows
 - 8.1.3.1 Categories of Steady Shock Wave Reflections
 - 8.1.3.2 Hysteresis Phenomena
 - 8.1.3.3 Analytical Prediction of the Mach Reflection Wave Configuration
 - 8.1.3.4 Modification of the Perfect Two- and Three Shock Theories
 - 8.1.4 Pseudo-Steady Flow
 - 8.1.4.1 Shock Wave Diffraction Process
 - 8.1.4.2 Shock Wave Reflection Phenomena
 - 8.1.4.3 Regular Reflection-RR
 - 8.1.4.4 Single-Mach Reflection-SMR
 - 8.1.4.5 Transitional-Mach Reflection-TMR
 - 8.1.4.6 Double-Mach Reflection-DMR
 - 8.1.4.7 von Neumann Reflection-vNR
 - 8.1.4.8 Triple Point Trajectory Angles
 - 8.1.4.9 Transition Criteria

8.1.5 Unsteady Flow

8.1.5.1 Reflection of Constant Velocity Shock

Waves over Non-straight Surfaces

8.1.5.2 Non-Constant Velocity Shock Wave

Reflections over Straight Surfaces

8.1.5.3 Spherical Shock Wave Reflections over

Straight and Non-Straight Surfaces

References

8.1.1 INTRODUCTION AND HISTORICAL BACKGROUND

When a shock wave propagating in a medium encounters another medium obliquely, it experiences a reflection that is known as oblique shock wave reflection. The first scientist to notice and record the reflection phenomenon of shock waves was Ernst Mach, who reported his experimental discovery as early as 1878.

In general, the reflection of shock waves can be divided into regular reflection (RR) or irregular reflections (IR). The RR consists of two shock waves (the incident, i , and the reflected, r). They meet on the reflecting surface at the reflection point. All the other wave configurations are termed irregular reflections (IR). The IR can be divided, in general, into Mach reflections (MR) and von Neumann reflections (vNR). The MR consists of three shock waves (the incident, i , the reflected, r , and the Mach stem, m) and one slipstream, s . These four discontinuities meet above the reflecting surface at the triple point (T). The point, where the Mach stem touches the reflecting surface is the reflection point. Colella and Henderson (1990) found that there are cases in which the reflected shock wave degenerates, near the triple point, to a compression wave. When this is the case, the reflection is not an MR but a vNR.

Courant and Friedrichs (1948) indicated that three different types of MR wave configurations are theoretically possible, depending on the direction of the deflection of the streamline that passes across the Mach stem near the triple point. If the streamline is deflected away from the reflected shock wave, the MR is a direct-Mach reflection (D_iMR); if it is not deflected, the MR is a stationary Mach reflection (S_iMR); and if the streamline is deflected toward the reflected shock wave, the MR is an inverse Mach reflection¹ (I_nMR).

Smith (1945) and White (1951) found that the D_iMR could be subdivided, in pseudo and unsteady flows, into a single Mach reflection² (SMR), a transitional Mach reflection³ (TMR), and a double Mach reflection (DMR).

¹Originally this wave configuration was termed inverted Mach reflection.

²Originally this wave configuration was termed simple Mach reflection (SMR).

³Originally this wave configuration was termed complex Mach reflection (CMR).

In addition, Ben-Dor (1981) showed that the trajectory angle of the second triple point (χ'), in a DMR, could be either larger or smaller than the trajectory angle of the first triple point (χ). Lee and Glass (1984) termed the DMR with $\chi' > \chi$ as DMR⁺ and the DMR with $\chi' < \chi$ as DMR⁻.

8.1.2 ANALYTICAL APPROACHES FOR DESCRIBING REGULAR AND MACH REFLECTIONS

The analytical approaches for describing the RR, i.e., the *two-shock theory*, and the MR, i.e., the *three-shock theory*, wave configurations were both initiated by von Neumann (1943a,b). Both theories make use of the conservation equations across an oblique shock wave, together with appropriate boundary conditions.

Let us consider an oblique shock wave. The flow states ahead and behind it are (i) and (j), respectively. The angle of incidence between the oncoming flow and the oblique shock wave is $-\beta_j$. While passing through the oblique shock wave the flow is deflected by an angle of $-\theta_j$. The conservation equations relating states (i) and (j) for a steady inviscid flow are as follows:

Conservation of mass:

$$\rho_i w_i \sin \beta_j = \rho_j w_j \sin(\beta_j - \theta_j) \quad (8.1.1)$$

Conservation of normal momentum:

$$p_i + \rho_i w_i^2 \sin^2 \beta_j = p_j + \rho_j w_j^2 \sin^2(\beta_j - \theta_j) \quad (8.1.2)$$

Conservation of tangential momentum:

$$\rho_i \operatorname{tg} \beta_j = \rho_j \operatorname{tg}(\beta_j - \theta_j) \quad (8.1.3)$$

Conservation of energy:

$$h_i + \frac{1}{2} w_i^2 \sin^2 \beta_j = h_j + \frac{1}{2} w_j^2 \sin^2(\beta_j - \theta_j) \quad (8.1.4)$$

where w is the flow velocity in a frame of reference attached to the oblique shock wave and ρ , p , and h are the flow density, static pressure, and enthalpy, respectively.

If thermodynamic equilibrium is assumed on both sides of the shock wave, then two thermodynamic properties are sufficient to define a thermodynamic state, e.g., $\rho = \rho(p, T)$ and $h = h(p, T)$, where T is the flow temperature. Consequently, the preceding set of four equations contains eight parameters, namely, p_i , p_j , T_i , T_j , w_i , w_j , β_j , and θ_j . If four of these parameters are known, the set is solvable in the principle.

8.1.2.1 TWO-SHOCK THEORY

The two-shock theory describes the flow field in the vicinity of the reflection point of an RR. The wave configuration of an RR (see Fig. 8.1.1) consists of two discontinuities, the incident i and the reflected r shock waves. They meet at the reflection point, R . The RR is, in general, not linear, i.e., $\omega_i \neq \omega_r$.

By replacing i with 0 and j with 1 in Eqs. (8.1.1)–(8.1.4), the four conservation equations across the incident shock wave i are obtained. Similarly by replacing i with 1 and j with 2 in Eqs. (8.1.1)–(8.1.4), the four conservation equations across the reflected shock wave r are obtained.

In addition to these eight conservation equations, there is also the condition that if the flow is assumed to be inviscid, then its deflection while passing through the reflected shock wave should be equal and opposite to its deflection while passing through the incident shock wave, i.e.,

$$\theta_1 - \theta_2 = 0. \quad (8.1.5)$$

The two-shock theory consists of a set of nine equations. If thermodynamic equilibrium is assumed, then this set of nine equations contains 13 parameters, $p_0, p_1, p_2, T_0, T_1, T_2, w_0, w_1, w_2, \beta_1, \beta_2, \theta_1$, and θ_2 . Consequently, four of these parameters must be known in order to have a solvable set.

Henderson (1982) showed that if the gas is assumed to obey the equation of state of a perfect gas, i.e., $p = \rho RT$, then the governing equations of an RR can be reduced to a single sixth-order polynomial. Although a sixth-order polynomial yields six roots, Henderson (1982) showed that four of them could be discarded. This implies that the governing equations do not result in a unique solution for a given set of initial conditions.

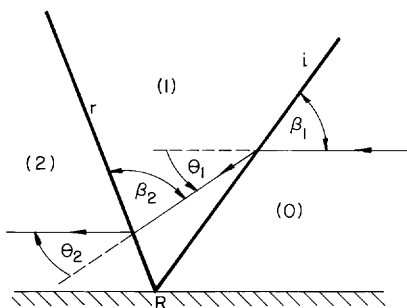


FIGURE 8.1.1 The wave configuration of a regular reflection, RR.

8.1.2.2 THREE-SHOCK THEORY

The three-shock theory describes the flow field in the vicinity of the triple point of an MR. The wave configuration of an MR (see Fig. 8.1.2) consists of four discontinuities, the incident i , the reflected r , and the Mach stem s shock waves, and one slipstream. They meet at the triple point, T , which is located above the reflecting surface. The Mach stem is usually curved (depending upon the initial conditions it can be either concave or convex). Its foot is perpendicular to the reflecting surface at the reflection point, R .

By replacing i with 0 and j with 1, in Eqs. (8.1.1)–(8.1.4), the four conservation equations across the incident shock wave i are obtained. By replacing i with 1 and j with 2 in Eqs. (8.1.1)–(8.1.4), the four conservation equations across the reflected shock wave r are obtained. By replacing i with 0 and j with 3 in Eqs. (8.1.1)–(8.1.4), the four conservation equations across the Mach stem m are obtained.

In addition to these 12 conservation equations, there are also two boundary conditions that arise from the fact that the flow states (2) and (3) are separated by a contact surface across which the pressure remains constant, i.e.,

$$p_2 = p_3. \quad (8.1.6)$$

Furthermore, if the flow is assumed to be inviscid and if the contact surface is assumed to be infinitely thin, i.e., a slipstream, then the flows on both sides of the slipstream are parallel, i.e.,

$$\theta_1 - \theta_2 = \theta_3. \quad (8.1.7)$$

The three-shock theory consists of fourteen equations. If thermodynamic equilibrium is assumed, then this set of 14 governing equations contains 18 parameters, namely; $p_0, p_1, p_2, p_3, T_0, T_1, T_2, T_3, w_0, w_1, w_2, w_3, \beta_1, \beta_2, \beta_3, \theta_1,$

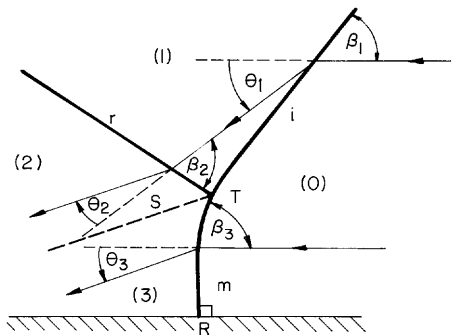


FIGURE 8.1.2 The wave configuration of a Mach reflection, MR.

θ_2 , and θ_3 . Consequently, four of these parameters must be known in order to have a solvable set.

Henderson (1982) showed that if the gas is assumed to behave as a perfect gas, then the governing equations of an MR can be reduced to a single tenth-order polynomial, with the pressure ratio p_3/p_0 as the variable. The polynomial coefficients were taken to be a function of the specific heat capacities ratio, γ , the flow Mach number in state (0), M_0 , and the pressure ratio across the incident shock wave, p_1/p_0 . Although a tenth-order polynomial yields 10 roots, Henderson (1982) showed that seven of them could be discarded. This implies that the governing equations of an MR do not yield a unique solution for a given set of initial conditions.

8.1.2.3 SHOCK POLARS

The graphical presentation of the relationship between the flow pressure, p , obtained behind an oblique shock wave and the angle, θ , by which the flow is deflected while passing through the oblique shock wave for a fixed value of the flow Mach number, M_0 , is called a *pressure-deflection shock polar*. A typical (p, θ) -shock polar for $M_0 = 5$ and $\gamma = 1.4$ is shown in Fig. 8.1.3. A detailed description of shock polars can be found in Section 1.4 of Ben-Dor (1991).

Owing to the fact that the boundary conditions of both the RR and the MR are expressed in terms of the flow deflection angles and the flow pressures

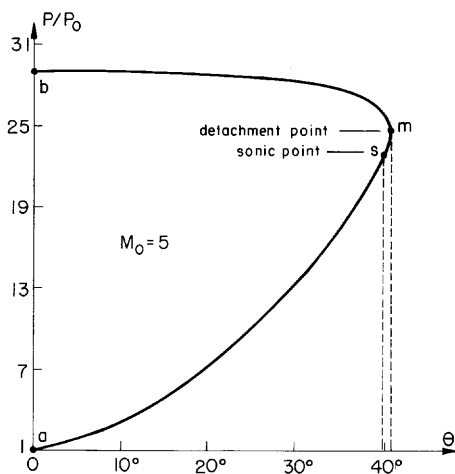


FIGURE 8.1.3 A typical (p, θ) -shock polar ($M_0 = 5$ and $\gamma = 1.4$).

[Eqs. (8.1.5)–(8.1.7)], Kawamura and Saito (1956) suggested using (p, θ) -shock polars in order to better understand the reflection phenomenon.

In addition, as mentioned earlier, in many phenomena involving shock wave interactions there is a possibility of more than one theoretical solution. In such cases shock polars can be useful in discarding unrealistic solutions and indicating the real solution.

8.1.2.3.1 Shock Polar Presentation of a Regular Reflection

The (p, θ) -polar solution of the flow field in the vicinity of the reflection point of an RR is shown in Fig. 8.1.4. The locus of all the flow states that can be obtained from state (0) by passing through any oblique shock wave is represented by the I-polar. Thus, state (0) is at the origin, and state (1), which is obtained from state (0) by passing through the incident shock wave, is on the I-polar. The locus of all the flow states that can be obtained from state (1) by passing through any oblique shock wave is represented by the R-polar. Since the flow deflection through the reflected shock wave is opposite to that through the incident shock wave, the R-polar is drawn in a direction opposite to the I-polar. Consequently, state (2), which is obtained from state (1) by passing through the reflected shock wave, is on the R-polar. The boundary condition for an RR, Eq. (8.1.5), implies that state (2) is obtained at the point where the R-polar intersects the p -axis.

Figure 8.1.4 indicates that there are two such points (2^w and 2^s). Point 2^w is known as the *weak shock solution* and point 2^s is known as the *strong shock solution*. The RR at the weak or strong shock solutions are known as weak or

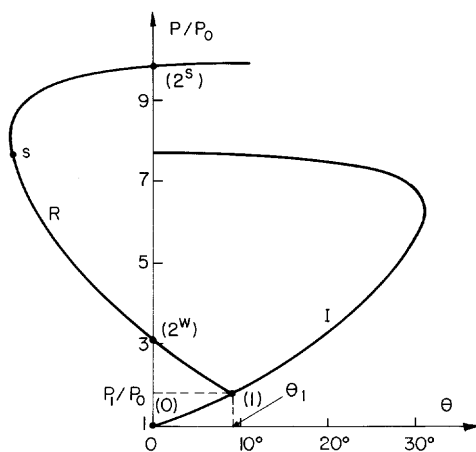


FIGURE 8.1.4 Shock polar solution of a regular reflection.

strong regular reflections. They are labelled in the following as wRR and sRR, respectively. None of these solutions can be discarded on theoretical grounds. However, it is an experimental fact that the weak shock solution is the one that usually occurs. Consequently, the flow state behind the reflected shock wave is represented by point 2^w . In the following this state will be referred to as (2) only.

8.1.2.3.2 Shock Polar Presentation of a Mach Reflection

The (p, θ) -polar solution of the flow field in the vicinity of the triple point of an MR is shown in Fig. 8.1.5. The locus of all the flow states that can be obtained from state (0) by passing through any oblique shock wave is represented by the I-polar. Thus, state (0) is at the origin, and state (1), behind the incident shock wave, and state (3), behind the Mach stem, lie on the I-polar. State (1) is the origin of the R-polar, which is drawn in a direction opposite to the I-polar. State (2), behind the reflected shock wave, lies on the R-polar. Since across the slipstream the pressures are equal [Eq. (8.1.6)] and the streamlines are parallel [Eq. (8.1.7)], states (2) and (3) coincide in the (p, θ) -plane, and hence states (2) and (3) are obtained at the point where the I- and R-polars intersect.

Three different possible solutions of the flow field in the vicinity of the triple point of an MR are shown in Fig. 8.1.6, in which, unlike Fig. 8.1.5, the left branch of the I-polar is also drawn. The three solutions are indicated by “a,” “b,” and “c.” In the MR at “a,” the net flow deflection is positive with respect to the original direction in state (0). In the MR at “b,” the net deflection is zero, and in the MR at “c,” the net deflection is negative. Courant and Friedrichs

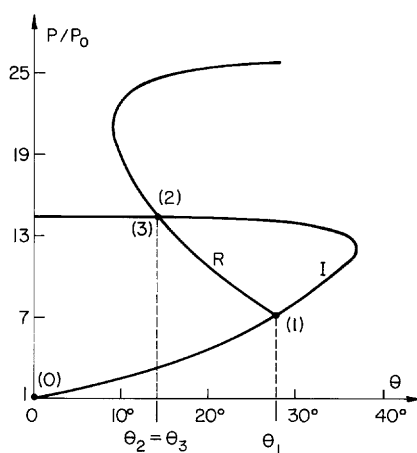


FIGURE 8.1.5 Shock polar solution of a Mach reflection.

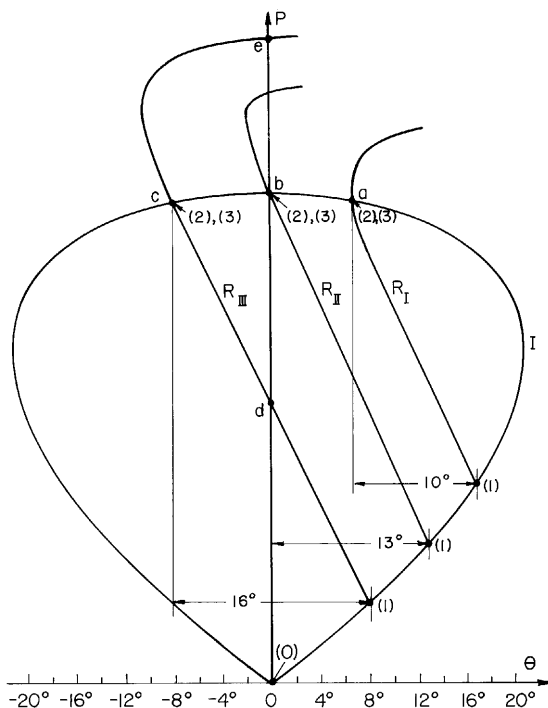


FIGURE 8.1.6 Different possible MR solutions: a direct-Mach reflection at “a,” a stationary-Mach reflection at “b,” and an inverse-Mach reflection at “c.”

(1948) termed these three different MRs as direct-Mach reflection (D_i MR), stationary-Mach reflection (S_t MR), and inverse-Mach reflection (I_n MR), respectively.

In addition to the S_t MR at “b,” the I - R_{II} shock-polar combination also suggests a possible RR solution since the R_{II} -polar intersects the p -axis at that point. Similarly, in addition to the I_n MR at “c,” the I - R_{III} shock-polar combination suggests a possible RR solution at “d,” where the R_{III} -polar intersects the p -axis. Thus, it is again evident that different reflection configurations are possible for the same initial conditions.

8.1.2.4 SUGGESTED $RR \leftrightarrow IR$ TRANSITION CRITERIA

The search for the $RR \leftrightarrow IR$ transition criterion has been the objective of numerous studies since von Neumann reinitiated the investigation of the

shock wave reflection phenomena in the early 1940s. The reason for the continuous search for the correct RR \leftrightarrow IR transition criterion was mainly due to the fact that the agreement between the various proposed criteria and the experimental results was never satisfactory. The various proposed RR \leftrightarrow IR transition criteria are discussed in the following, in detail, using shock polars for explanatory purposes.

8.1.2.4.1 Detachment Criterion

Whereas in the RR case shown in Fig. 8.1.4 the R-polar intersects the p -axis at two points; in the MR case shown in Fig. 8.1.5 the R-polar does not intersect the p -axis at all. The intermediate case, i.e., the case in which the R-polar is tangent to the p -axis, is known as the *detachment criterion*.

The point of tangency between the R-polar and the p -axis can be either outside or inside the I-polar, as shown in Figs. 8.1.7a and 8.1.7b, respectively. Henderson (1982) suggested referring to incident shock waves, which result in a situation such as those shown in Figs. 8.1.7a and 8.1.7b, as *strong* and *weak* shock waves, respectively.

Three interesting I-R shock polar combinations are possible for “weak” shock waves. They are shown in Figs. 8.1.8a to 8.1.8c. Figure 8.1.8a presents an MR for which the streamline deflection while passing through the reflected shock wave is in the opposite direction to the streamline deflection while passing through the incident shock wave. A different MR is represented by Fig. 8.1.8b. Now, the streamline deflections while passing through the incident and reflected shock waves are in the same direction. In the intermediate case, shown in Fig. 8.1.8c, the reflected shock wave is normal to the oncoming flow and hence the streamline does not deflect while passing through it. The three MR wave configurations just mentioned are schematically illustrated in Figs. 8.1.9a to 8.1.9c, respectively.

If one wishes to use the three-shock theory in order to calculate the flow properties in the vicinity of the triple points of the three different MR wave configurations shown in Figs. 8.1.9a to 8.1.9c, then Eq. (8.17) should be modified, since it is correct only for the MR shown in Fig. 8.1.9a. For calculating the MR shown in Fig. 8.1.9b, Eq. (8.17) should be replaced by $\theta_1 + \theta_2 = \theta_3$. For the intermediate MR shown in Fig. 8.1.9c, for which $\theta_2 = 0$, either $\theta_1 - \theta_2 = \theta_3$ or $\theta_1 + \theta_2 = \theta_3$ can be used, since they both degenerate to $\theta_1 = \theta_3$.

As is shown subsequently, the theoretical possible MR wave configuration shown in Fig. 8.1.9b does not materialize in reality. Instead, another type of reflection, the von Neumann reflection, vNR, is obtained. The major difference between an MR and a vNR is that the reflected shock wave of an MR is replaced

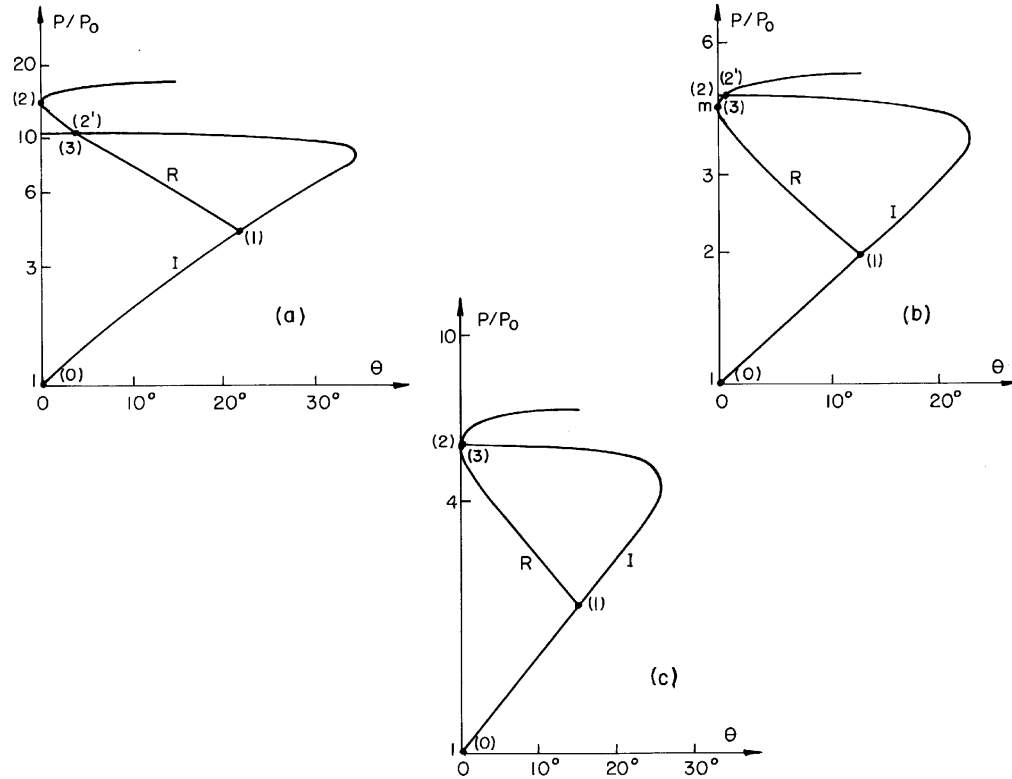


FIGURE 8.1.7 Different I-R polar combinations: (a) the R-polar is tangent to the p -axis outside the I-polar, (b) the R-polar is tangent to the p -axis inside the I-polar, and (c) the R-polar is tangent to the p -axis at the normal shock point of the I-polar.

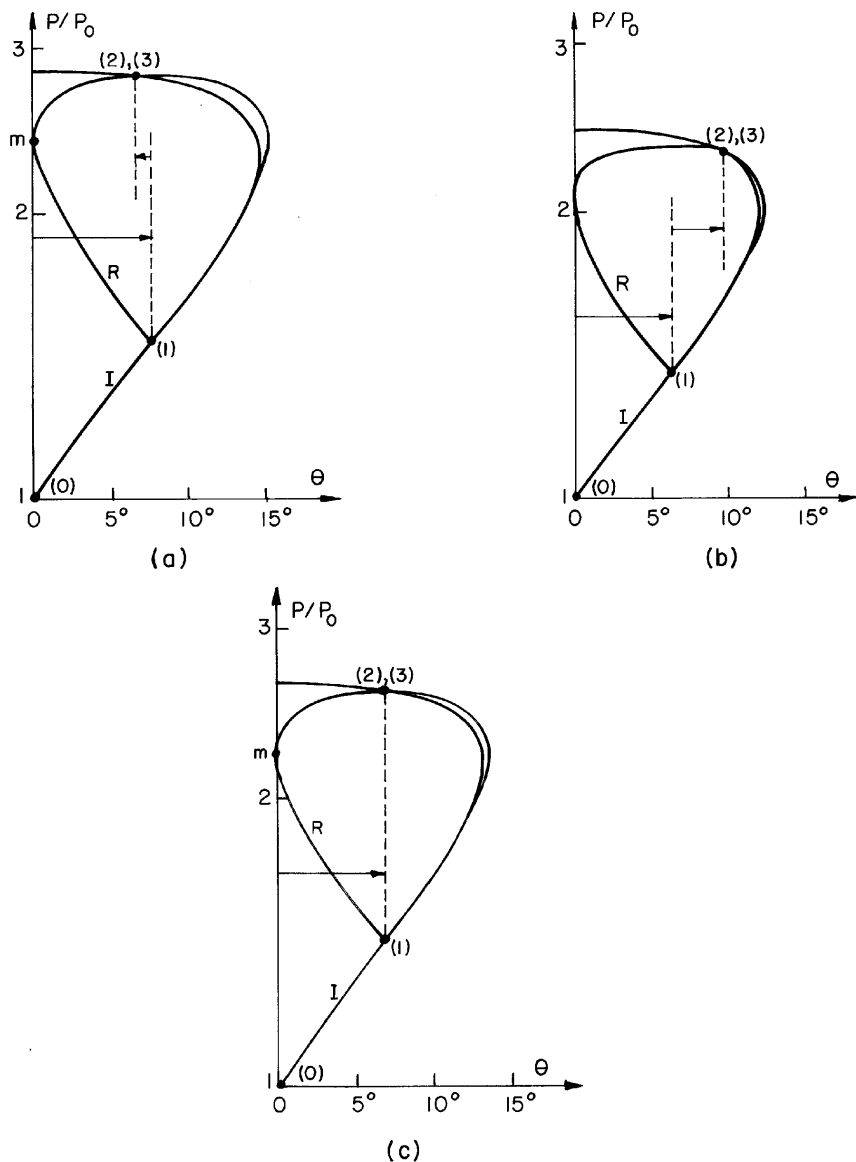


FIGURE 8.1.8 Shock polar combinations of three different Mach reflection wave configurations: (a) the streamline deflection while passing through the reflected shock wave is in an opposite direction to the streamline deflection while passing through the incident shock wave, (b) the streamline deflections while passing through the incident and reflected shock waves are in the same direction, and (c) the reflected shock wave is normal to the oncoming flow and hence the streamline does not deflect while passing through it.

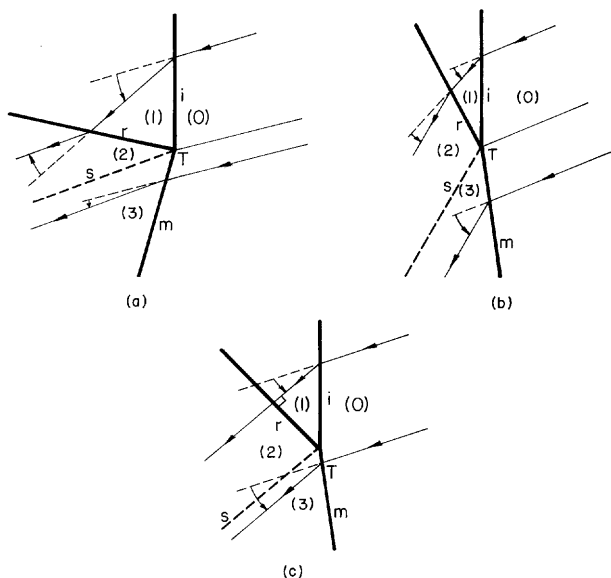


FIGURE 8.1.9 Schematic illustrations of the wave configurations appropriate to the three (p, θ) -shock polar combinations shown in Figs. 8.1.8a to 8.1.8c, respectively.

in the vNR by a compression wave. Colella and Henderson (1990) first hypothesized this fact.

8.1.2.4.2 von Neumann Criterion

This criterion, which was originally suggested by von Neumann (1943a, 1943b), was reinstituted as the *mechanical equilibrium criterions* by Henderson and Lozzi (1975). The shock polar combination corresponding to this criterion is shown in Fig. 8.1.10. The R-polar intersects the p -axis exactly at the normal shock point of the I-polar. Consequently, both an RR and an MR are theoretically possible for the same conditions. Hence, from the pressure point of view, the transition would be continuous and in mechanical equilibrium. In terms of flow deflection angles the von Neumann criterion is $\theta_1 - \theta_2 = \theta_3 = 0$.

8.1.2.4.3 Sonic Criterion

This transition criterion, which was also first introduced as a possible transition criterion, by von Neumann (1943a, 1943b), is based on the argument that the $RR \leftrightarrow IR$ transition cannot occur as long as the corner-

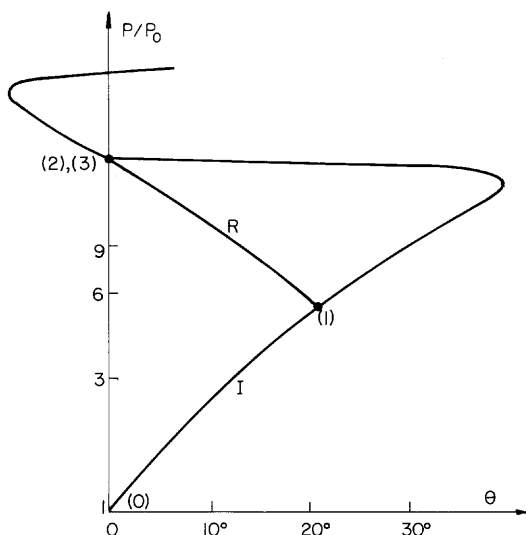


FIGURE 8.1.10 I-R polar combination illustrating the von Neumann (mechanical equilibrium) criterion.

generated signals cannot catch up with the reflection point of the RR. Hence, as long as the flow Mach number behind the reflected shock wave is supersonic, the reflection point is isolated from the corner-generated signals, and they cannot reach it. In terms of shock polars, the sonic criterion is represented by the combination in which the R-polar intersects the p -axis exactly as its sonic point. Owing to the proximity between the sonic and the detachment points on a shock polar, the sonic and the detachment criteria could be treated, from a practical point of view, as the same. Lock and Dewey (1989) developed an ingenious experimental setup, that enabled them to distinguish between the sonic and the detachment criteria. Their experimental investigation, in pseudo-steady flows, revealed that the $RR \leftrightarrow IR$ transition occurred at the sonic condition when the corner-generated signals caught up with the reflection point.

8.1.2.4.4 Length Scale Criterion

Hornung, Oertel and Sandeman (1979) argued that in order for an MR, i.e., a wave configuration that includes a finite length shock wave, to be established, a physical length scale must be available at the reflection point, i.e., pressure signals must be communicated to the reflection point of the RR. This argument eventually led them to conclude that there are two different termination criteria for the RR. In steady flows the length scale criterion predicts a

transition at the same point predicted by the von Neumann criterion, and in pseudo-steady flows it predicts transition at the same point predicted by the sonic criterion. (More details are given in Section 1.5.4 of Ben-Dor, 1991.)

8.1.2.4.5 Summary of Transition Criteria

The four transition criteria just proposed lead to three different RR \leftrightarrow IR transition conditions. The transition condition arising from the detachment criterion can be calculated using the two-shock theory while requiring that $\theta_2 = \theta_{2m}$. The transition condition arising from the sonic criterion can be calculated using the two-shock theory while requiring that $\theta_2 = \theta_{2s}$. Recall that, as mentioned earlier, the transition conditions arising from the detachment and the sonic criteria are practically identical. The transition condition arising from the von Neumann criterion can be calculated using the three-shock theory while requiring that $\theta_1 - \theta_2 = \theta_3 = 0$. The transition condition arising from the length scale criterion is identical to that arising from the sonic criterion in pseudo-steady flows and to that arising from the von Neumann criterion in steady flows.

Thus, the transition criteria just presented practically result in two possible transition conditions $\theta_2 = \theta_{2m} \cong \theta_{2s}$ and $\theta_1 - \theta_2 = \theta_3 = 0$.

Experimental results in both steady and unsteady (including pseudo-steady) flows suggest that in steady flows the RR \leftrightarrow IR transition generally agrees with the condition given by the von Neumann criterion, whereas in unsteady flows the RR \leftrightarrow IR transition agrees with the condition given by the detachment criterion.

As shown by Ben-Dor (1991) the agreement between this transition criterion and careful experimental investigations was never satisfactory in the vicinity of the transition lines. This fact motivated investigators to continue searching for the “correct” RR \leftrightarrow IR transition criterion. However, one must recall that the transition criterion are based on the two- and three-shock theories that were developed under the simplifying assumptions that all the discontinuities are straight in the vicinity of their intersection points, and hence that the flow states bounded by the discontinuities are uniform. In addition to this assumption, which introduces inherent errors into predictions based on the two- and three-shock theories, it was shown by Ben-Dor (1991) that the inclusion of viscous effects and real gas effects does improve the agreement between experiments and predictions based on these two fundamental theories.

8.1.2.5 DUAL-SOLUTION DOMAIN

Figure 8.1.11 illustrates three different I-R polar combinations. The I-R_I polar combination corresponds to the von Neumann condition and the I-R_{III} polar

and MR wave configurations are theoretically possible led Hornung, Oertel, and Sandeman (1979) to hypothesize that a hysteresis can exist in the $RR \leftrightarrow IR$ transition process. Based on their hypothesis one can start with a value of β in the range $\beta < \beta^N$ for which only an RR is theoretically possible, and then increase β until the condition $\beta = \beta^D$, above which an RR is theoretically impossible, is reached. At this point the $RR \rightarrow MR$ transition should take place. If β is now decreased, then the reversed transition, i.e., the $MR \rightarrow RR$ transition, should occur when the condition $\beta = \beta^N$, below which an MR is theoretically impossible, is reached. Hence, based on this hypothesis RR and MR wave configurations can be obtained for identical flow conditions for values of β inside the dual-solution domain, i.e., $\beta^N < \beta < \beta^D$. (A detailed presentation of the hysteresis process is given in Section 8.1.3.2.)

8.1.3 STEADY FLOWS

The analytical investigation of the reflection phenomenon of shock waves in steady flows is much simpler than that in pseudo-steady and unsteady flows. Unlike the reflection process in pseudo-steady flows, which is coupled with the flow deflection process (see Section 8.1.4.1), the reflection process in steady flows is independent. As a result out of the various shock reflection wave configurations which were presented in Section 8.1.1 only RR and MR are possible in steady flows. An explanation for not obtaining a TMR and a DMR in steady flows was given by Ben-Dor (1991, Section 3.1.4.1).

8.1.3.1 CATEGORIES OF STEADY SHOCK WAVE REFLECTIONS

The shock wave reflection phenomenon can be divided into four categories:

1. The reflection of a curved incident shock wave from a straight surface
2. The reflection of a straight incident shock wave from a curved surface
3. The reflection of a curved incident shock wave from a curved surface
4. The reflection of a straight incident shock wave from a straight surface

8.1.3.1.1 Reflection of Curved Incident Shock Waves from Straight Surfaces

If a supersonic flow, $M_0 > 1$, encounters a concave or a convex wedge, the generated shock wave is also concave or convex. The reflections of the incident shock wave for these two possibilities are shown schematically in Figs. 8.1.12a

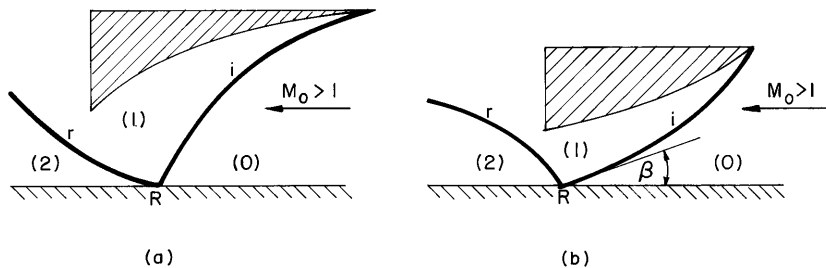


FIGURE 8.1.12 Schematic illustrations of the wave configurations that result from the reflection of a concave (a) and a convex (b) incident shock wave from a straight surface.

and 8.1.12b, respectively. The intermediate case of a straight reflecting wedge results in a straight attached shock wave, provided the reflecting wedge angle is smaller than the maximum flow deflection angle appropriate to the flow Mach number, M_0 . If, however, the reflecting wedge angle is greater than the maximum flow deflection angle, the straight reflecting wedge results in a detached bow shock wave. Although only RR wave configurations are shown in Figs. 8.1.12a and 8.1.12b, MR wave configurations are also possible in this steady flow reflection category.

Pant (1971) analytically studied the reflection of steady curved shock waves. He showed that for weak incident shock waves there is a wave angle, $\beta = \beta^*$, for which the reflected shock wave is straight. Based on his analysis β^* was independent of M_0 and equal to

$$\beta^* = \cos^{-1} \left[\frac{(\gamma + 1)^{1/2}}{2} \right]. \quad (8.1.8)$$

Thus, in the reflection of weak shock waves of all strengths for $\beta < \beta^*$ the incident and the reflected shock waves have curvatures of opposite sign. As the wave angle in the vicinity of the reflection point approaches β^* the reflected shock wave straightens until it becomes straight at $\beta = \beta^*$. For $\beta > \beta^*$ the curvatures of the incident and the reflected shock waves have the same sign.

Molder (1971) numerically investigated this type of steady flow reflection. For RR a zero downstream curvature on the streamline behind the reflected shock wave in the vicinity of the reflection point, R , was imposed, and for MR the pressure gradients and curvatures of the streamlines along the slipstream, in the vicinity of the triple point, T , were matched. The results showed many possible combinations of reflected shock curvatures, streamline curvatures, and pressure gradients.

8.1.3.1.2 Reflection of Straight Incident Shock Waves from Curved Surfaces

Two general cases, which belong to this category, are shown schematically in Figs. 8.1.13a and 8.1.13b. The incident shock waves are straight and the reflecting surfaces are straight up to the reflection point, R, after which they are either concave or convex. Depending upon the curvature of the reflecting surface a concave or a convex reflected shock wave could be obtained. The curvature of the reflected shock wave has the same sign as the curvature of the reflecting surface. Although only RR wave configurations are shown in Figs. 8.1.13a and 8.1.13b, MR wave configurations are also possible in this steady flow reflection category.

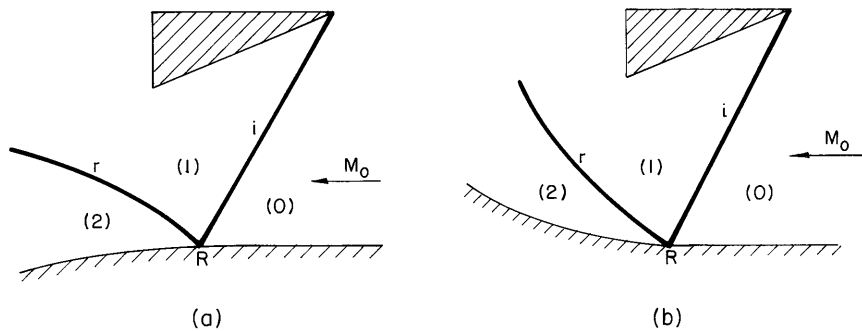


FIGURE 8.1.13 Schematic illustrations of the wave configurations that result from the reflection of a straight shock wave over a convex (a) and concave (b) surface.

8.1.3.1.3 Reflection of Curved Incident Shock Waves from Curved Surfaces

Four general cases, which belong to this category, are shown schematically in Figs. 8.1.14a through 8.1.14d. The incident shock waves in each of these cases is curved and the reflecting surface is straight up to the reflection point, R, beyond which it is either concave or convex. The reflected shock waves assume a curvature with the same sign as the curvature of the reflecting surface. Although only RR wave configurations are shown in Figs. 8.1.14a through 8.1.14d, MR wave configurations are also possible in this steady flow reflection category.

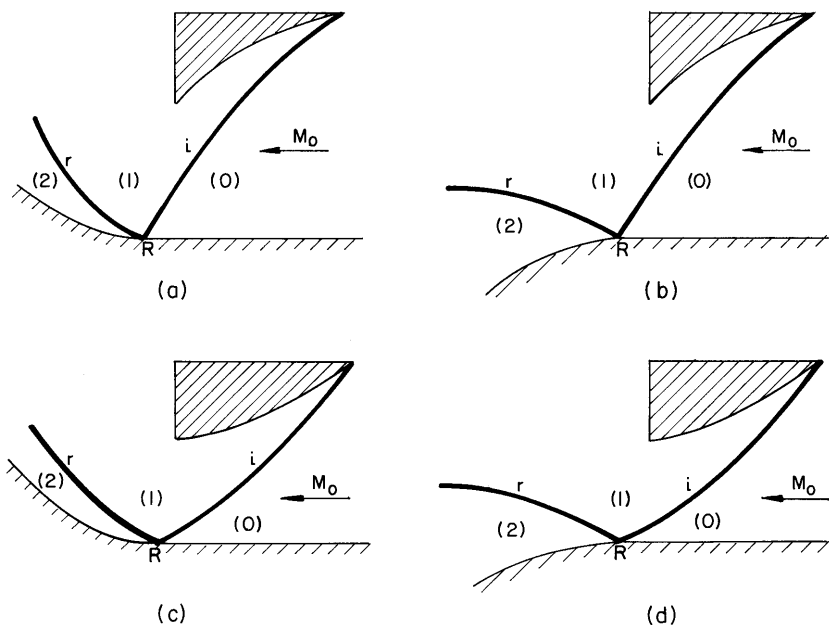


FIGURE 8.1.14 Schematic illustrations of the wave configurations that result from the reflection of curved shock waves over curved surfaces: (a) a concave shock wave reflection over a convex surface; (b) a concave shock wave reflection over a concave surface; (c) a convex shock wave reflection over a convex surfaces; (d) a convex shock wave reflection over a concave surface.

8.1.3.1.4 Reflection of Straight Incident Shock Waves from Straight Surfaces

This category of shock wave reflections in steady flows is the easiest one to treat analytically since the incident and the reflected shock waves and the reflecting surface are straight. Most of the reported analytical and experimental studies on the reflection of shock waves in steady flows are in this category.

8.1.3.1.4.1 Types of Reflections

Only two shock reflection wave configurations are possible in this category of steady flows: regular reflection (RR) and Mach reflection (MR).

Schematic illustrations of the wave configurations of the RR and the MR are shown in Figs. 8.1.15a and 8.1.15b, respectively. The interaction between the supersonic flow, M_0 , and the reflecting wedge generates the straight oblique incident shock wave. It is attached to the leading edge of the reflecting wedge. While passing through it the flow is deflected by an angle of $\theta_1 = \theta_w$ to become

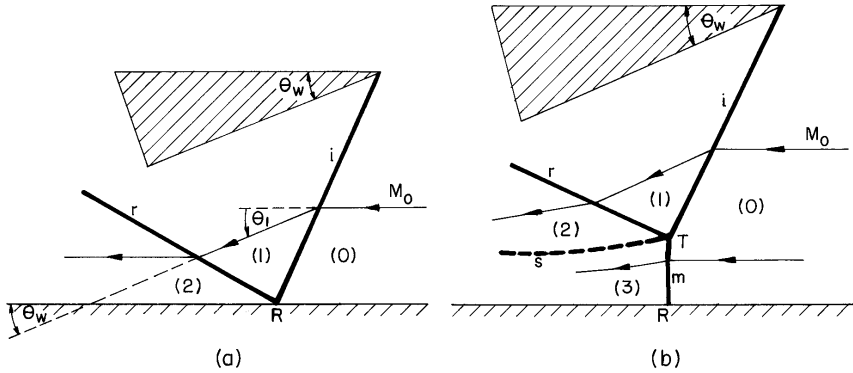


FIGURE 8.1.15 Schematic illustrations of the wave configurations of an RR and an MR in the reflection of straight shock waves from straight surfaces in steady flows: (a) regular reflection RR; (b) Mach reflection MR.

parallel to the reflecting surface. The flow behind the incident shock wave is supersonic. The deflected flow obliquely approaches the bottom surface with an angle equal to θ_w . The supersonic flow can negotiate this obstacle with the aids of either an RR or an MR as shown in Figs. 8.1.15a and 8.1.15b, respectively.

8.1.3.1.4.2 RR \leftrightarrow MR Transition Criterion

Hornung and Robinson (1982) showed that the RR \leftrightarrow MR transition line in steady flows is that arising from the length scale criterion (see Section 8.1.2.4.4). In the case of steady flows, the length scale criterion results in two different transition formulas depending upon whether the incident flow Mach number, M_0 , is smaller or larger than M_{0C} , which is the value appropriate to the point at which the transition lines arising from the von Neumann (see Section 8.1.2.4.2) and the detachment criteria (see Section 8.1.2.4.1) intersect (see Fig. 8.1.7c). The exact values of M_{0C} for a diatomic ($\gamma = \frac{7}{5}$) and a monatomic ($\gamma = \frac{5}{3}$) perfect gas were calculated by Molder (1979) to be 2.202 and 2.470, respectively.

For $M_0 \geq M_{0C}$ the length scale criterion results in a transition at the von Neumann criterion (see Section 8.1.2.4.2):

$$\theta_1 - \theta_2 = \theta_3 = 0. \quad (8.1.9)$$

For $M_0 \leq M_{0C}$, for which Eq. (8.1.9) cannot be satisfied, the length scale criterion predicts transition at the sonic criterion (see Section 8.1.2.4.3):

$$M_2^R = 1. \quad (8.1.10)$$

M_2^R is the flow Mach number behind the reflected shock wave with respect to the reflection point R. Equation (8.1.10) can be rewritten to read

$$\theta_1 - \theta_{2s} = 0. \quad (8.1.11)$$

The transition lines that result from Eqs. (8.1.9) and (8.1.10) or (8.1.11) join at $M_0 = M_{0C}$.

8.1.3.1.4.3 Domains of Regular and Mach Reflections in the (M_0, β_1) -Plane

The domains of different types of reflections in steady flows in the (M_0, β_1) -plane are shown in Figs. 8.1.16a and 8.1.16b for nitrogen and argon, respectively. The solid lines are for a perfect gas and the dashed boundary lines are for an imperfect gas (dissociational equilibrium for nitrogen and ionizational equilibrium for argon). The NR (no reflection) domains correspond to the unobtainable strong shock solution, i.e., $M_1^R < 1$. The $RR \leftrightarrow MR$ transition line is calculated differently depending upon whether M_0 is smaller or larger than M_{0C} (see Section 8.1.3.1.4.2). The strong influence of real gas effects on shifting the $RR \leftrightarrow MR$ and the $MR \leftrightarrow NR$ transition lines is clear.

8.1.3.1.4.4 Experimental Verification of the $RR \leftrightarrow MR$ Transition Criterion

Henderson and Lozzi (1975, 1979), Hornung, Oertel, and Sandeman (1979), and Hornung and Robinson (1982) experimentally verified the $RR \leftrightarrow MR$ transition lines as given by Eqs. (8.1.9) and (8.1.10).

The results of the experimental investigation of Hornung and Robinson (1982) are shown in Fig. 8.1.17, where the normalized height of the Mach stem, L_m/L_w , as a function of the angle of incidence, β_1 , for different flow Mach numbers, M_0 , is shown (L_w is the length of the reflecting surface). By extrapolating their experimental results to $L_m = 0$ they showed that the actual $RR \leftrightarrow MR$ transition occurs at a value of β appropriate to the von Neumann criterion, i.e., β_1^N . The analytical values of β_1^N for the four incident flow Mach numbers are shown in Fig. 8.1.17 by arrowheads.

8.1.3.2 HYSTERESIS PHENOMENA

As mentioned in Section 8.1.2.5 a dual-solution domain exists in the reflection phenomenon. The dual-solution domain, inside which both RR and MR are theoretically possible, in the (M_0, β) - and the (M_0, θ_w) -planes is shown in Figs. 8.1.18a and 8.1.18b, respectively. The transition lines arising from the

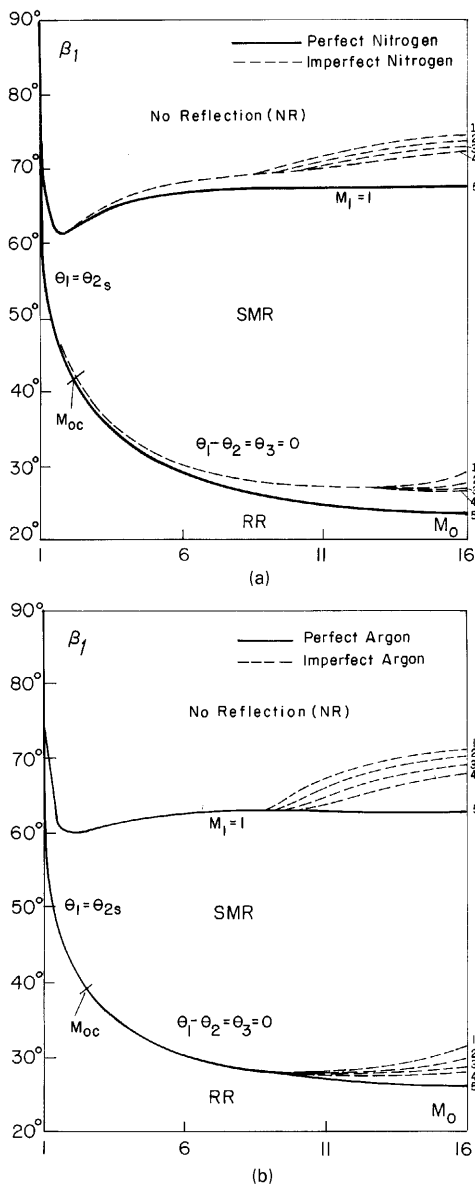


FIGURE 8.1.16 Domains and transition boundaries of various types of shock wave reflections in the (M_0, β_1) -plane. (a) Solid lines are for perfect nitrogen with $\gamma = \frac{7}{5}$. Dashed lines are for nitrogen in dissociational equilibrium. (b) Solid lines are for perfect argon with $\gamma = \frac{5}{3}$. Dashed lines are for argon in ionizational equilibrium. (For both cases $T_0 = 300$ K and $p_0 = 1, 10, 100$ and 1000 torr for lines 1 to 4, respectively.)

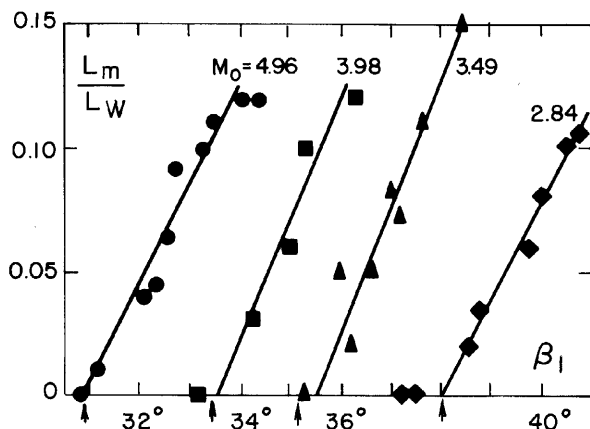


FIGURE 8.1.17 Experimental measurements of the height of the Mach stem as a function of the angle of incidence for various flow Mach numbers and the determination of the transition angle.

detachment and the von Neumann criteria divide the (M_0, β) - and the (M_0, θ_w) -planes into three domains:

- A domain inside which only an RR is theoretically possible
- A domain inside which only an MR is theoretically possible
- A domain inside which both RR and MR are theoretically possible

The existence of conditions beyond which RR or MR wave configurations are theoretically impossible and the existence of a domain inside which both RR and MR wave configurations are theoretically possible led Hornung, Oertel, and Sandeman (1979) to hypothesize that a hysteresis could exist in the

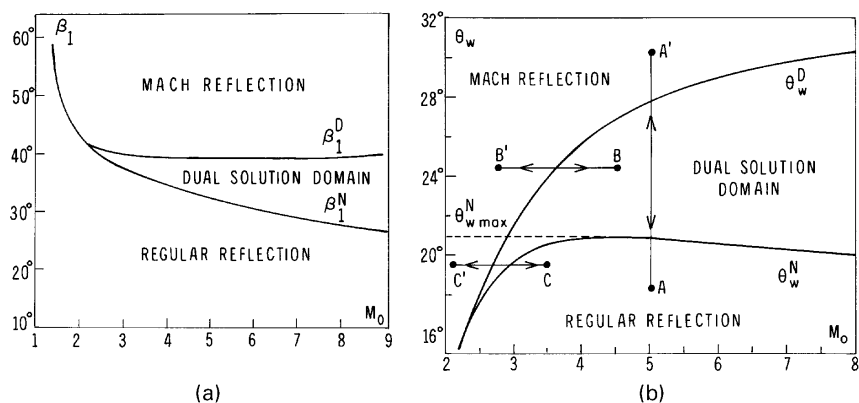


FIGURE 8.1.18 Domains of possible shock wave reflection wave configurations (a) in the (M_0, β) -plane and (b) in the (M_0, θ_w) -plane.

RR \leftrightarrow MR transition process. Based on their hypothesis, when the flow Mach number is kept constant and the wedge angle is changed from a value $\theta_w < \theta_w^N$ (or $\beta < \beta^N$), for which only an RR is theoretically possible, to a value $\theta_w > \theta_w^D$ (or $\beta > \beta^D$), for which only an MR is theoretically possible, and then back to the initial value (e.g., along the path AA'A in Fig. 8.1.18b), they expected that the RR \rightarrow MR transition would occur in accordance with the detachment criterion, whereas the MR \rightarrow RR transition would take place at the von Neumann criterion. This hysteresis is a *wedge-angle-variation-induced hysteresis* (or an *angle-of-incidence-variation-induced hysteresis*).

Inspection of the dual-solution domain, shown in Figs. 8.1.18a and 8.1.18b, indicates that, in fact two general hysteresis processes are theoretically possible:

- A *wedge-angle-variation-induced hysteresis*. In this hysteresis process the flow Mach number is kept constant and the wedge angle (i.e., the angle of incidence) is changed.
- A *flow-Mach-number-variation-induced hysteresis*. In this hysteresis process the wedge angle is kept constant and the flow Mach number is changed.

8.1.3.2.1 Stability of RR in the Dual-Solution Domain

Henderson and Lozzi (1975, 1979) who experimentally failed to record the wedge-angle-variation-induced hysteresis process concluded that the RR is unstable in the dual-solution domain and that as a consequence both the MR \rightarrow RR and RR \rightarrow MR transitions occur at the von Neumann condition.

In a following experimental attempt, Hornung and Robinson (1982) also failed to record the hypothesized hysteresis. As a result they adopted Henderson and Lozzi's (1979) conclusion that the RR is unstable in the dual-solution domain.

Teshukov (1989) analytically proved, by using a linear stability technique that RR is stable inside the dual-solution domain.

Li and Ben-Dor (1996) analytically proved, by applying the principle of minimum entropy production, that RR is stable in most of the dual-solution domain.

Chpoun *et al.* (1995) were the first to experimentally record stable RR wave configurations inside the dual-solution domain.

Vuillon *et al.* (1995) were the first to numerically obtain stable RR and MR wave configurations for the same flow Mach numbers and reflecting wedge angle.

8.1.3.2.2 Symmetric Wedges

8.1.3.2.2.1 Wedge-Angle-Variation-Induced Hysteresis

Chpoun *et al.* (1995) were also the first to experimentally record the wedge-angle-variation-induced hysteresis in the $RR \leftrightarrow MR$ transition; similar hysteresis was experimentally recorded, a few years later, by Ivanov *et al.* (1998c).

Ivanov, Gimelshein, and Beylich (1995) were the first to numerically verify, using the DSMC technique, the existence of a wedge-angle-variation-induced hysteresis in the $RR \leftrightarrow MR$ transition. Following their study the hysteresis phenomenon was verified by many investigators using a variety of numerical codes:

- *Direct Simulation Monte Carlo (DSMC)*
Ivanov *et al.* (1996)
Ben-Dor, Elperin and Golshtein (1997)
Ivanov *et al.* (1998d)
- *Second Order Upwind and High Resolution Schemes*
Ivanov *et al.* (1996)
- *Total Variation Diminishing (TVD)*
Shirozu and Nishida (1995)
- *Godunov and van Leer*
Chpoun and Ben-Dor (1995)
Ivanov *et al.* (1998d)
- *Steger and Warming Flux Splitting*
Ben-Dor *et al.* (1999a)

A numerical illustration of the angle-of-incidence-variation-induced hysteresis, for $M_0 = 5$, is shown in Fig. 8.1.19. The simulation starts with an angle of incidence equal to 29.8° for which, as can be seen in frame 1, an RR is obtained. Upon an increase in the angle of incidence the RR is maintained (follow frames 2, 3, and 4) until it suddenly changes to an MR between the calculations appropriate to 39° (frame 4) and 39.6° (frame 5). If at this point the direction of changing the angle of incidence is reversed the MR is seen to persist (follow frames 6 and 7) until it changes back to MR between the calculations appropriate to 34.5° (frame 7) and 32.3° (frame 8).

The fact that the numerically obtained transition angles in Fig. 8.1.19 do not agree with the respective von Neumann and the detachment angles of incidence (for $M_0 = 5$, $\beta^N = 30.9^\circ$, and $\beta^D = 39.3^\circ$) is owing to the fact that the mesh size in the calculations was not fine enough. Perfect agreement was obtained in similar calculations with sufficient mesh refinement.

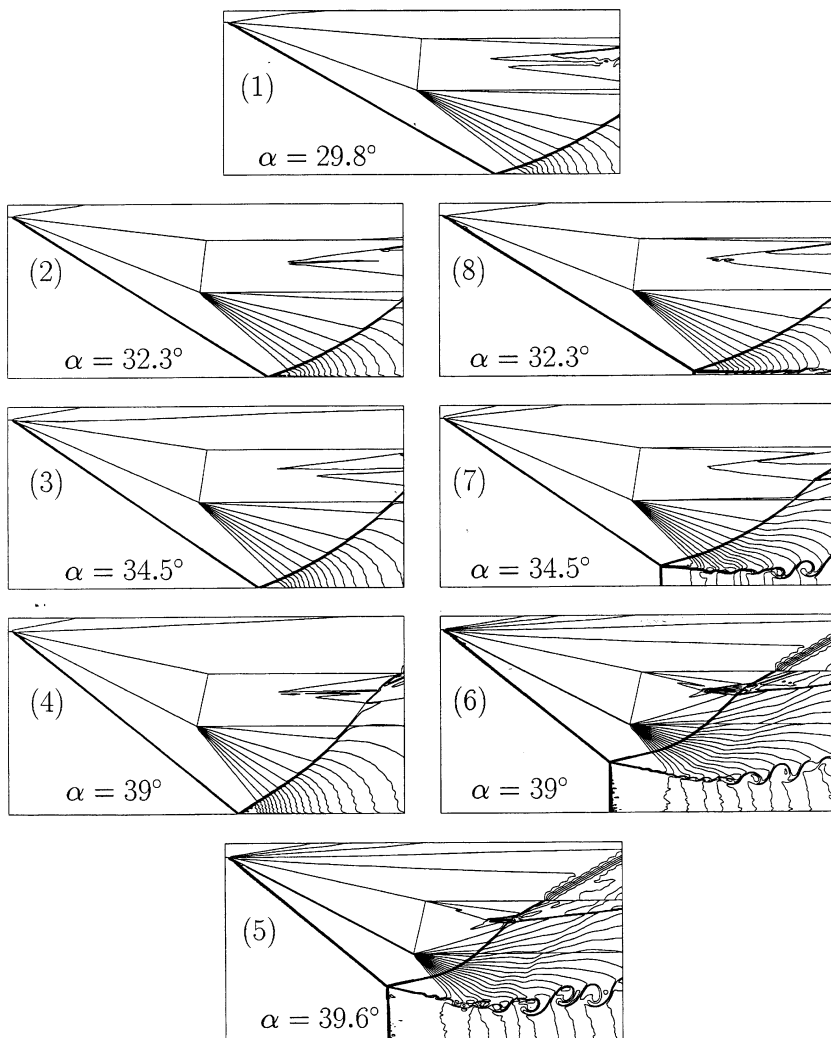


FIGURE 8.1.19 Angle-of-incidence-variation-induced hysteresis for $M_0 = 5$.

8.1.3.2.2.2 Flow-Mach-Number-Variation-Induced Hysteresis

As mentioned earlier, an inspection of Fig. 8.1.18b indicates that a hysteresis process can be also obtained in another way, keeping the wedge angle constant and changing the flow Mach number. This is a flow-Mach-number-variation-induced hysteresis. In this case there exist two possibilities:

- If $\theta_w > \theta_{w,\max}^N$, the Mach number is changed as for the path $BB'B$ from a value inside the dual-solution domain to a value for which only an MR is

theoretically possible and then back to the initial value. After transition to MR, the wave configuration never goes through a reverse transition to RR because the path does not cross the curve $\theta_w^N(M)$. Therefore, a full hysteresis loop does not exist in this case, though both RR and MR wave configurations can be observed for the same values of the wedge angle and the flow Mach number.

- If $\theta_w < \theta_{w,\max}^N$, the Mach number can be changed from a value for which only an RR is theoretically possible to a value for which only an MR is theoretically possible and then back to the initial value crossing both $\theta_w^N(M)$ and $\theta_w^D(M)$ curves (see the path $CC'C$ in fig. 8.1.18b).

Consequently, similar to the hysteresis process in the case of a wedge-angle-variation-induced hysteresis, this is also a full hysteresis loop, with a return to the initial shock wave configuration.

The preceding two cases were numerically investigated by Onofri and Nasuti (1999) and Ivanov *et al.* (2000a). Typical results for the former are shown in Fig. 8.1.20a. The wedge angle was kept constant at $\theta_w = 27^\circ$ ($>\theta_{w,\max}^N = 20.92^\circ$) while the flow Mach number, M_0 , was first decreased from 5 to 4.45 and then increased back to 5. The first frame, with $M_0 = 5$, shows an RR inside the dual-solution domain. As M_0 was decreased, the detachment transition line, below which an RR is theoretically impossible, was reached at $M_0 = 4.57$. The RR→MR transition took place between frames 3 and 4 when the flow Mach number changed from 4.5 to 4.45, i.e., at $M_0 = 4.475 \pm 0.025$. This numerical value is in reasonable agreement with the theoretical value of 4.57. The existence of an RR slightly beyond the theoretical limit has also been observed in many numerical simulations of the wedge-angle-variation-induced hysteresis and can be explained by the influence of numerical viscosity inherent in shock-capturing codes. Once an MR was established, the flow Mach number, M_0 , was increased back to its initial value $M_0 = 5$. Since theoretically an MR can exist for values of M_0 inside the dual-solution, the reversed MR→RR transition did not take place at the detachment line. As a result, two different wave configurations, an RR and an MR, were obtained for identical flow conditions (i.e., M_0 and β or θ_w). This can clearly be seen by comparing the pairs of the frames 1 and 7, 2 and 6, and 3 and 5 in which the first frame shows an RR and the second one shows an MR, respectively.

Typical results for the latter are shown in Fig. 8.1.20b. The wedge angle was kept constant at $\theta_w = 20.5^\circ$ ($<\theta_{w,\max}^N = 20.92^\circ$). For this value of θ_w , the Mach number values that correspond to the von Neumann criterion are 3.47 and 6.31, while that corresponding to the detachment criterion is 2.84. The Mach number was decreased from $M_0 = 3.5$ to $M_0 = 2.8$ and then increased back to the initial value. Some frames showing the sequence of events are given

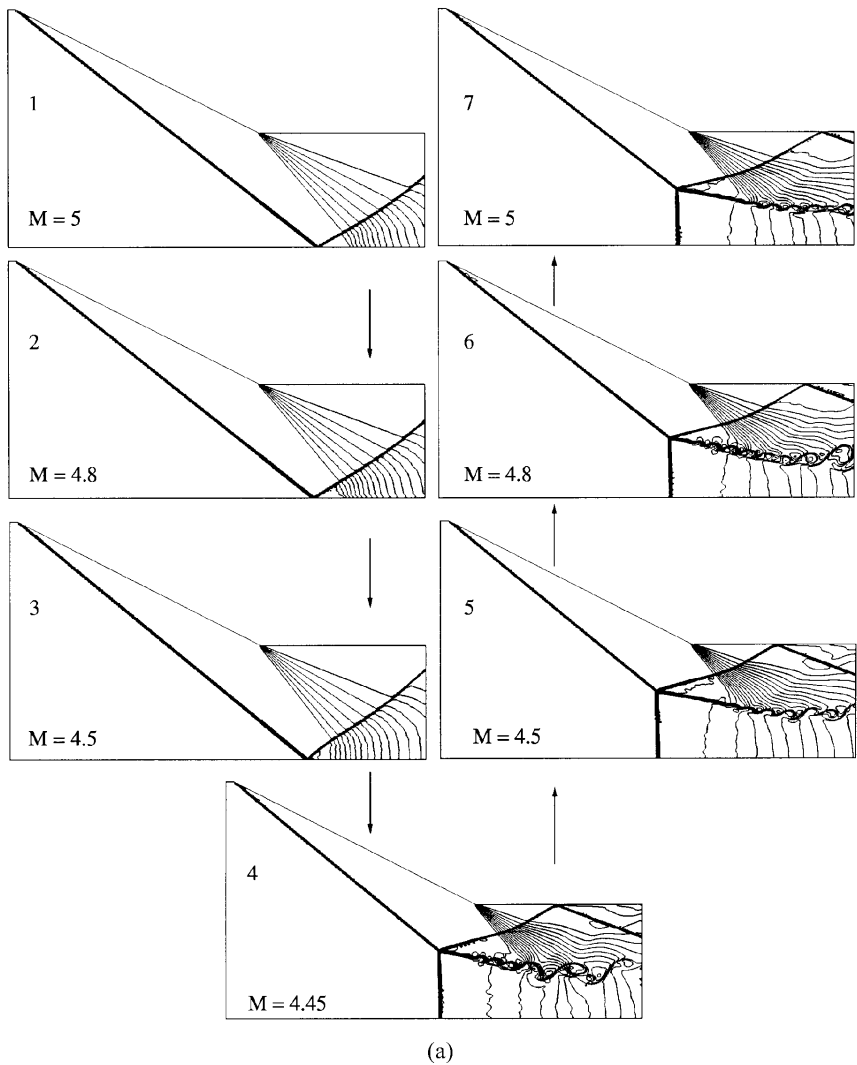


FIGURE 8.1.20 Flow-Mach-number-variation-induced hysteresis for (a) $\theta_w = 27^\circ$ and (b) $\theta_w = 20.5^\circ$. (Courtesy of M. Ivanov)

in Fig. 8.1.20b. The RR→MR transition occurs between the frames appropriate to $M_0 = 3.0$ and $M_0 = 2.8$ in close agreement with the theoretical value, whereas the reverse, MR→RR, transition is observed between the frames appropriate to $M_0 = 3.2$ and $M_0 = 3.5$, i.e., slightly earlier than the theoretical value. This disagreement can be attributed to the very small height of the Mach

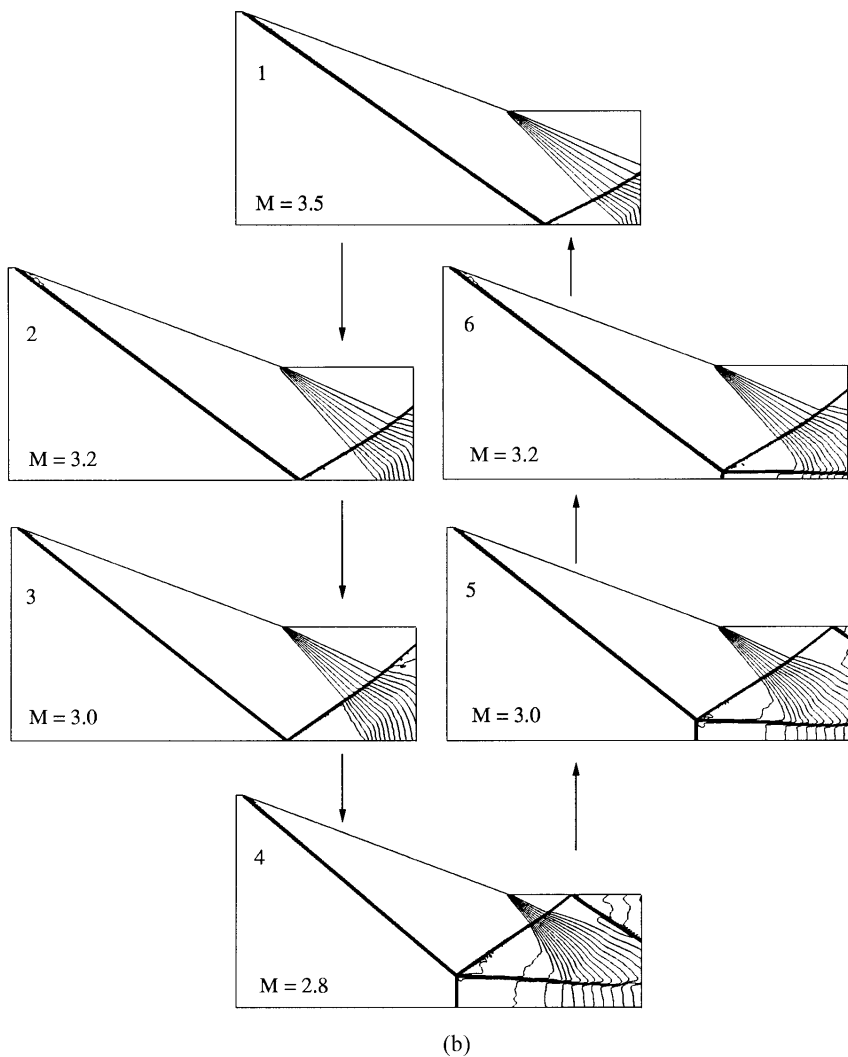


FIGURE 8.1.20 (continued)

stem near the von Neumann criterion, which makes its numerical resolution very difficult.

8.1.3.2.2.3 Aspect-Ratio-Variation-Induced Hysteresis

In addition to numerically illustrating that the RR wave configuration is stable in the dual-solution domain, Vuillon *et al.* (1995) also showed that

depending on geometric parameters stable MR or stable RR wave configurations could be established inside the dual-solution domain for the same flow Mach number and wedge angle (i.e., angle of incidence). This was proven by keeping both the flow Mach number and the wedge angle constant and varying the distance between the wedge and the line of symmetry.

Sudani *et al.* (1999) experimentally illustrated that Vuillon *et al.*'s (1995) numerical discovery led, in fact, to an aspect-ratio-variation-induced-hysteresis. (Here the aspect ratio is the ratio between the distance from the leading edge of the wedge to the line of symmetry to the width of the wedge.) In their experiment they started with a large aspect ratio for which an RR was obtained. When the aspect ratio was decreased a sudden transition from RR to MR took place. Increasing the aspect ratio did not result in a reversed transition, from MR to RR, at the same value of aspect ratio but much later.

8.1.3.2.2.4 Three-Dimensional Effects

The foregoing presentation led to the unavoidable question: why had the hysteresis phenomenon been recorded in the course of some experimental investigations and not in others? Although the answer to this question has not been fully understood yet, two possible reasons have been mentioned:

1. The extent of the hysteresis depends on the type of the wind tunnel which is used for conducting the experiment. Fomin *et al.* (1996) and Ivanov *et al.* (1998b, 1998c) showed that whereas in a closed test section wind tunnel the hysteresis is hardly detected, a clear hysteresis is obtained in an open test section wind tunnel. Not surprisingly a closed section wind tunnel was used by Henderson and Lozzi (1975, 1979) and Hornung *et al.* (1979) and Hornung and Robinson (1982), who did not detect the hysteresis, and an open jet type wind tunnel was used by Chpoun *et al.* (1995) and Fomin *et al.* (1996), who did detect it.
2. The hysteresis is promoted by three-dimensional effects. Skews (1997, 1998) and Ivanov *et al.* (1998a, 1998b, 1998c) claimed that the experimental results in which a hysteresis was recorded were all contaminated by three-dimensional effects and hence could not be considered as purely two-dimensional. Skews (2000) showed that three-dimensional edge effects are evident in actual wave configurations associated with the reflection of supposedly two-dimensional flows.

Kudryavtsev *et al.* (1999) demonstrated both numerically and experimentally that increasing the aspect ratio could reduce the influence of the three-dimensional edge effects. Consider Fig. 8.1.21 and note that by increasing the aspect ratio the actual Mach stem height approaches the numerically calculated height, which is appropriate to a purely two-dimensional reflection. Hence, an

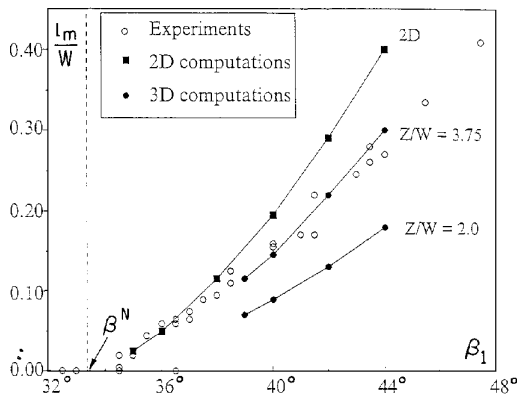


FIGURE 8.1.21 Dependence of the Mach stem height on the aspect ratio. Note that an equality between the Mach stem height of an actual reflection and the one numerically calculated, using a 2D code, is a necessary but not sufficient condition for the actual Mach reflection to be two-dimensional. (Courtesy of M. Ivanov)

actual Mach reflection cannot be considered as free of three-dimensional edge effects as long as its Mach stem height is smaller than that appropriate to a purely two-dimensional Mach reflection. This condition is necessary but not sufficient to ensure that the reflection is purely two-dimensional.

8.1.3.2.3 Asymmetric Wedges

The reflection process over asymmetric wedges was investigated experimentally by Chpoun and Lengrand (1997), both analytically and experimentally by Li, Chpoun, and Ben-Dor (1999), and numerically by Ivanov *et al.* (2000b). Two extreme transition criteria, one analogous to the detachment criterion and the other analogous to the von Neumann criterion were identified in the course of the analytical study of Li, Chpoun, and Ben-Dor (1999). Two extreme transition criteria resulted in a dual-solution domain.

8.1.3.2.3.1 The Overall Wave Configurations

Li, Chpoun, and Ben-Dor (1999) provided a detailed analysis of the two-dimensional reflection of asymmetric shock waves in steady flows. In similar to the interaction of symmetric shock waves in steady flows, the interaction of asymmetric shock waves leads to two types of overall wave configurations: an overall regular reflection (oRR) and an overall Mach reflection (oMR). These two overall wave configurations are shown, schematically, in Figs. 8.1.22a and 8.1.22b.

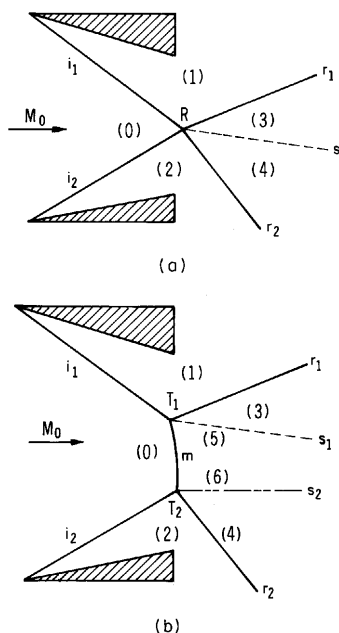


FIGURE 8.1.22 Schematic illustration of two general wave configurations that can be obtained from the reflection of asymmetric shock waves in steady flows: (a) an overall regular reflection (oRR), and (b) an overall Mach reflection (oMR).

1. An oRR wave configuration (Fig. 8.1.22a) consists of two incident shock waves (i_1 and i_2), two reflected shock waves (r_1 and r_2), and one slipstream (s). These five discontinuities meet at a single point (R). The boundary condition for an oRR is $\theta_1 - \theta_3 = \theta_2 - \theta_4 = \delta$, where θ_1 , θ_2 , θ_3 , and θ_4 are the flow deflection angles through i_1 , i_2 , r_1 , and r_2 . (For a symmetric reflection $\theta_1 = \theta_2$ and $\delta = 0$). The oRR wave configuration can consist of either two weak RRs or one weak RR and one strong RR. (For more details on weak and strong RRs see Section 8.1.2.3.1.) These two different oRR wave configurations are labeled as oRR[wRR + wRR] and oRR[wRR + sRR], respectively.

2. In addition to the incident and reflected shock waves (i_1 , i_2 , r_1 , r_2) a Mach stem (m) appears in an oMR wave configuration (Fig. 8.1.22b). The Mach stem bridges two triple points (T_1 and T_2) from which two slipstreams (s_1 and s_2) emanate. The boundary conditions for an oMR are $\theta_1 - \theta_3 = \delta_1$ and $\theta_2 - \theta_4 = \delta_2$. (For a symmetric reflection $\theta_1 = \theta_2$ and $\theta_3 = \theta_4$, i.e., $\delta_1 = \delta_2$.) The oMR wave configuration can consist of two D_i MRs, or one D_i MR and one S_i MR, or one D_i MR and one I_n MR (for details on D_i MR, S_i MR, and I_n MR, see Section 8.1.2.3.2). These three different oMR wave configurations are

labeled as $\text{oMR}[D_i\text{MR} + D_i\text{MR}]$, $\text{oMR}[D_i\text{MR} + S_t\text{MR}]$, and $\text{oMR}[D_i\text{MR} + I_n\text{MR}]$, respectively.

8.1.3.2.3.2 The Dual-Solution Domain

The dual-solution domain is shown in Fig. 8.1.23. The transition lines corresponding to the “detachment” and the “von Neumann” criteria, θ_2^E and θ_2^T , respectively, are drawn as solid lines in the (θ_1, θ_2) -plane for $M_0 = 4.96$ (note that the wedge angles θ_1 and θ_2 are symmetric). The dual-solution domain, in which the overall wave configuration can be either an oRR or an oMR, extends between these two transition lines. The two dashed lines, marked θ_1^N and θ_2^N , indicate the von Neumann condition for the reflection over a single wedge (i.e., a symmetric reflection). On one side of the dashed line the Mach reflection is direct, i.e., $D_i\text{MR}$; on its other side it is inverse, i.e., $I_n\text{MR}$; and on the line itself it is stationary, i.e., $S_t\text{MR}$. (For details on $D_i\text{MR}$, $S_t\text{MR}$, $I_n\text{MR}$, see Section 8.1.2.3.2.)

Based on Fig. 8.1.23 the dual-solution domain can be divided into two parts:

- In one part, the overall wave configuration can be either an oRR or an oMR, which consists of two $D_i\text{MR}$ s.
- In the other part, the overall wave configuration can be either an oRR or an oMR, which consists of one $D_i\text{MR}$ and one $I_n\text{MR}$.

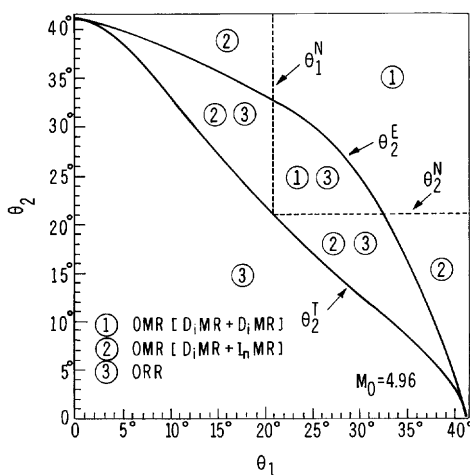


FIGURE 8.1.23 The dual-solution domain in the reflection of asymmetric shock waves.

8.1.3.2.3.3 Angle-of-Incidence-Variation-Induced Hysteresis

Figure 8.1.23 indicates that one can start with an oRR having a value of $\theta_2 < \theta_2^T$ and then increase θ_2 until the “detachment” transition line, θ_2^E , above which an oRR is theoretically impossible, will be reached. At this line the oRR must change to an oMR. If the direction of the change in θ_2 is now reversed and θ_2 is decreased, the oMR can continue to exist until the “von Neumann” transition line, θ_2^T , below which an oMR is theoretically impossible, will be reached. At this line the oMR must change to an oRR.

Based on Fig. 8.1.23, which is drawn for $M_0 = 4.96$, it is evident that, depending on whether θ_1 is smaller or larger than θ_1^N , two different sequences of transition of the overall reflection are possible during the process of first increasing θ_2 and then decreasing it back to its initial value:

1. For $\theta_1 < \theta_1^N$ the process starts with an oRR that is maintained until the line, θ_2^E , is reached. At this point a transition takes place and the oRR changes to an oMR[D_i MR + I_n MR]. On the reverse path the oMR[D_i MR + I_n MR] is maintained until the line, θ_2^T , is reached. At this point the reversed transition takes place and the oMR changes to an oRR.
2. For $\theta_1 > \theta_1^N$ the process starts with an oRR that is maintained until the line, θ_2^E , is reached. At this point a transition takes place and the oRR changes to an oMR[D_i MR + D_i MR]. On the reverse path the oMR[D_i MR + D_i MR] is maintained until the line θ_2^N is reached. Exactly on this line the reflection becomes an oMR[D_i MR + S_i MR]. Then it changes to an oMR[D_i MR + I_n MR] that is maintained until the line, θ_2^T , is reached. At this point the reversed transition takes place and the oMR changes to an oRR.

Chpoun and Lengrand (1997) and Li, Chpoun, and Ben-Dor (1999) experimentally verified both the existence of an oMR consisting of one D_i MR and one I_n MR, and the existence of an angle-of-incidence-variation-induced hysteresis in the oRR \leftrightarrow oMR transition. Owing to technical limitations of their experimental capabilities, the two just-described theoretically possible sequences of events in the oRR \leftrightarrow oMR transition were not recorded. The experimental results of Li *et al.* (1999) excellently agreed with the analytical transition lines, just presented.

Numerical simulations of the above mentioned two different sequences of events are shown in Figs. 8.1.24a and 8.1.24b for $M_0 = 4.96$ and $\theta_1 = 18^\circ$ and for $M_0 = 4.96$ and $\theta_1 = 28^\circ$, respectively. Each of these figures consists of frames displaying density isolines. Each simulation starts at the top frame and then goes around in a counterclockwise direction. Each one of the horizontal pairs of the frames has the same flow conditions. Hence, the previously discussed hysteresis is clearly seen in these figures.

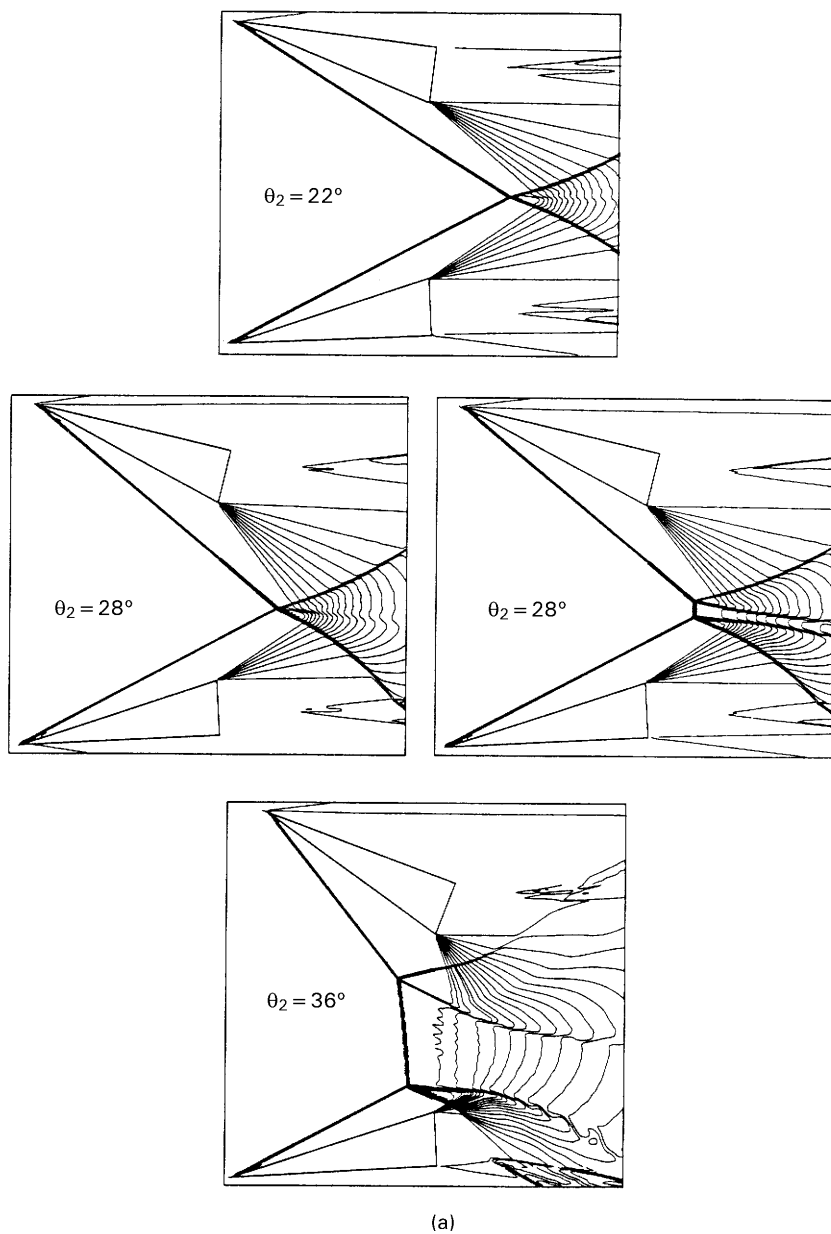


FIGURE 8.1.24 Numerical frames illustrating the hysteresis loop for (a) $M_0 = 4.96$ and $\theta_1 = 18^\circ$ and (b) $M_0 = 4.96$ and $\theta_1 = 28^\circ$. (The wave configurations are shown on the right and the appropriate shock polar solutions on the left.)

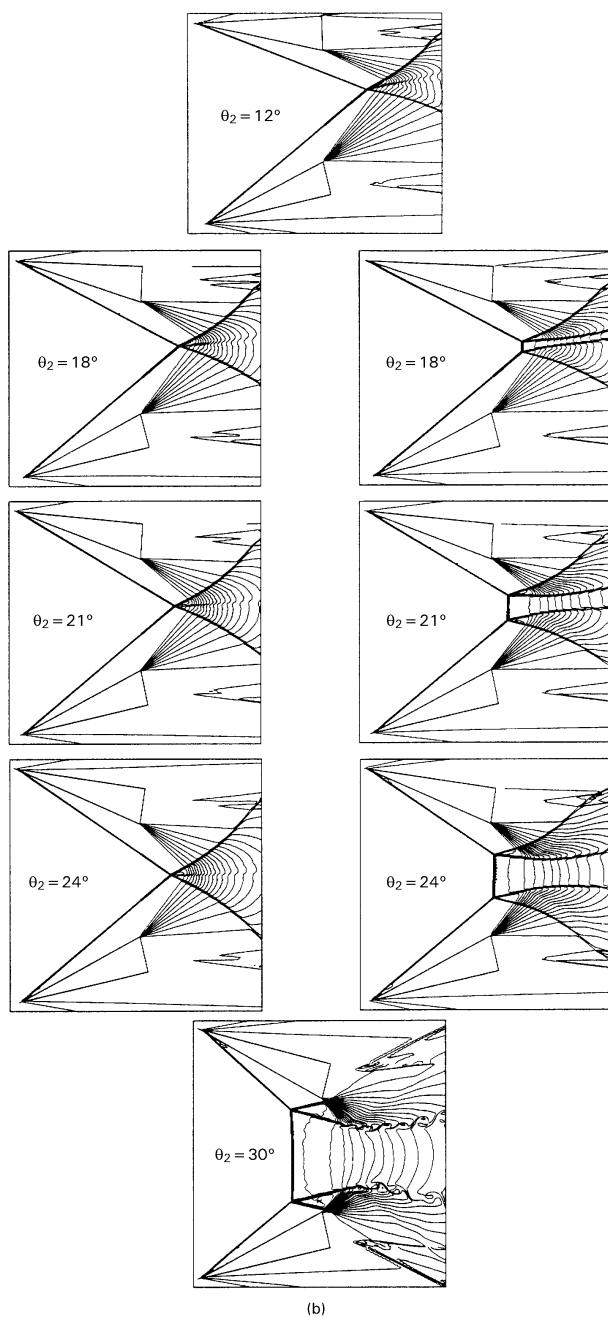


FIGURE 8.1.24 (continued)

The sequence that is shown in Fig. 8.1.24a starts with an oRR at $\theta_2 = 22^\circ$. When θ_2 is increased the oRR still exists at $\theta_2 = 28^\circ$. At $\theta_2 = 36^\circ$, that is, above θ_2^E , an oRR can no longer exist and the overall reflection is an oMR[D_iMR + I_nMR], i.e., the lower wave configuration is a D_iMR and the upper one is an I_nMR. When θ_2 is decreased from $\theta_2 = 36^\circ$ back to its initial value, i.e., $\theta_2 = 22^\circ$, the oMR[D_iMR + I_nMR] is maintained in the dual-solution domain. Thus, for example, at $\theta_2 = 28^\circ$ (see Fig. 8.1.24a), two different shock wave configurations are actually observed, in perfect agreement with shock polar analysis.

The sequence that is shown in Fig. 8.1.24b starts with an oRR at $\theta_2 = 12^\circ$. When θ_2 is increased the oRR still exists at $\theta_2 = 24^\circ$. At $\theta_2 = 30^\circ > \theta_2^E$ the overall reflection is an oMR[D_iMR + D_iMR], in which both the upper and the lower wave configurations are D_iMRs. When θ_2 is decreased from $\theta_2 = 30^\circ$ back to its initial value, i.e., $\theta_2 = 12^\circ$, the orientation of the slipstream of the lower MR changes continuously. As a result, at $\theta_2 = 21^\circ$, which is very close to the analytical value $\theta_2^N = 20.87^\circ$ that was previously mentioned, the upper wave configuration is close to being an S_tMR (i.e., its slipstream is almost parallel to the oncoming flow at the triple point). Upon a further decrease in θ_2 the lower wave configuration changes to an I_nMR, and the oMR consists now of a D_iMR and an I_nMR, i.e., it is an oMR[D_iMR + I_nMR], as shown for $\theta_2 = 18^\circ$.

8.1.3.2.3.4 Flow-Mach-Number-Variation-Induced Hysteresis

Similar to the flow-Mach-number-variation-induced hysteresis process, in the reflection of symmetric shock waves, which was numerically verified by Ivanov *et al.* (2000a; see Section 8.1.3.2.2.2 for details), it is hypothesized here that a similar flow-Mach-number-variation-induced hysteresis process should also exist in the reflection of asymmetric shock waves.

8.1.3.2.4 Axisymmetric (Conical) Wedge

Ben-Dor *et al.* (2000) investigated both experimentally and numerically the reflection process in an axisymmetric flow field, which, by definition, is free of three-dimensional effects. They investigated the interaction of two conical shock waves, one converging and straight and the other diverging and curvilinear. The incident converging straight conical shock wave was created using a conical ring with a sharp leading edge. This shock wave was then interacted with a diverging curvilinear conical shock wave, which was generated by a curvilinear cone. The strength of the diverging curvilinear conical shock wave engulfing the curvilinear cone varied along its front. The interaction of these two conical shock waves led to the formation of either an RR or an MR. Since

the strength of the diverging curvilinear conical shock wave changed along its front, different angles of interaction with the incident converging straight conical shock wave were encountered as the curvilinear cone was moved back and forth along the axis of symmetry. This change in the angles of interaction led to actual transitions between the RR and the MR wave configurations.

Unlike in the cases of the reflection of planar shock waves (see Sections 8.1.3.2.2 and 8.1.3.2.3), where there is only one hysteresis loop, in the case of conical shock waves there are a few hysteresis loops in the transition process.

In addition, unlike the experimental investigations of the hysteresis process using two-dimensional configurations, in which some researchers claimed that the recorded hysteresis processes were promoted by three-dimensional effects, the hysteresis process that was recorded in the case of an axisymmetric flow field was absolutely free of three-dimensional effects (see Section 8.1.3.2.2.4).

8.1.3.2.4.1 Angle-of-Incidence-Variation-Induced Hysteresis

Ben-Dor *et al.* (1996b) experimentally discovered a double-loop hysteresis process. In the course of their numerical investigation a multiloop hysteresis was found. The major hysteresis loop involved different overall shock wave reflection configurations, and the minor hysteresis loops involved different flow patterns for identical flow conditions.

8.1.3.2.4.2 Flow-Mach-Number-Variation-Induced Hysteresis

In similar to the flow-Mach-number-variation-induced hysteresis process, in the reflection of symmetric shock waves, which was numerically verified by Ivanov *et al.* (2000a); see Section 8.1.3.2.2.2 for details), it is hypothesized here that similar flow-Mach-number-variation-induced hysteresis process should also exist in the reflection axisymmetric shock waves.

8.1.3.2.5 Downstream-Pressure-Variation-Induced Hysteresis

In all the foregoing treated flow fields the shock wave reflection processes were free of downstream influences. Henderson and Lozzi (1979) hypothesized that the RR \leftrightarrow MR transition could be promoted or suppressed by suitable choice of the downstream boundary conditions.

Ben-Dor *et al.* (1999a) investigated the effect of the downstream pressure (defined as the wake pressure behind the tail of the reflecting wedge) on the shock wave reflection both numerically and analytically. They discovered a downstream-pressure-variation-induced hysteresis.

Thus, Ben-Dor *et al.*'s (1999a) study confirmed the hypothesis just mentioned and showed both numerically and analytically how the RR and the MR wave configurations depend on the downstream pressure.

The numerically obtained downstream-pressure-variation-induced hysteresis is shown in Fig. 8.1.25. The initial conditions for this simulation are $M_0 = 4.96$ and $\beta_1 = 29.5^\circ$. The results shown in Fig. 8.1.25 were obtained in the following way. First the case with $p_w/p_0 = 10$ was solved (p_w is the wake pressure behind the tail of the reflecting wedge). Then, the final results for $p_w/p_0 = 10$ were used as the initial conditions for $p_w/p_0 = 12$. This procedure was repeated until $p_w/p_0 = 22$ was reached. Then p_w/p_0 was decreased, again by using the final results of the previous case as the initial conditions for the next case until $p_w/p_0 = 10$ was reached again.

As can be seen from the results shown in Fig. 8.1.25, a hysteresis exists in the reflection phenomenon. Whereas the RR→MR transition took place between frames 5 and 6, the reversed MR→RR transition occurred between frames 12 and 13.

The downstream-pressure-variation-induced hysteresis loop is shown in Fig. 8.1.26 in the $(L_m/L, p_w/p_0)$ -plane (L_m is the Mach stem height and L is the length of the wedge surface). As can be seen the MR→RR transition occurs at $p_w/p_0 = 19.63$ and the reversed RR→MR transition occurs at $p_w/p_0 = 10$. Both the MR→RR and the RR→MR transitions are associated with a sudden disappearance and appearance of a finite size Mach stem.

8.1.3.3 ANALYTICAL PREDICTION OF THE MACH REFLECTION WAVE CONFIGURATION

As mentioned in Section 8.1.2.2, the three-shock theory describes the flow field in the vicinity of the triple point. Since the three-shock theory is inherently independent of any physical length scale, it is incapable of predicting the actual wave configuration of an MR, i.e., the height of the Mach stem.

Azevedo (1989) suggested the first analytical model for predicting the height of the Mach stem of an MR. In his model he made the following assumptions:

1. The Mach stem is straight and perpendicular to the bottom surface
2. The Mach stem, the slipstream, and the bottom surface form a one-dimensional converging nozzle
3. The throat of this converging nozzle is at the point where the leading characteristic of the expansion wave, generated by the rear edge of the reflecting wedge, intersects the slipstream, point F in Fig. 8.1.27

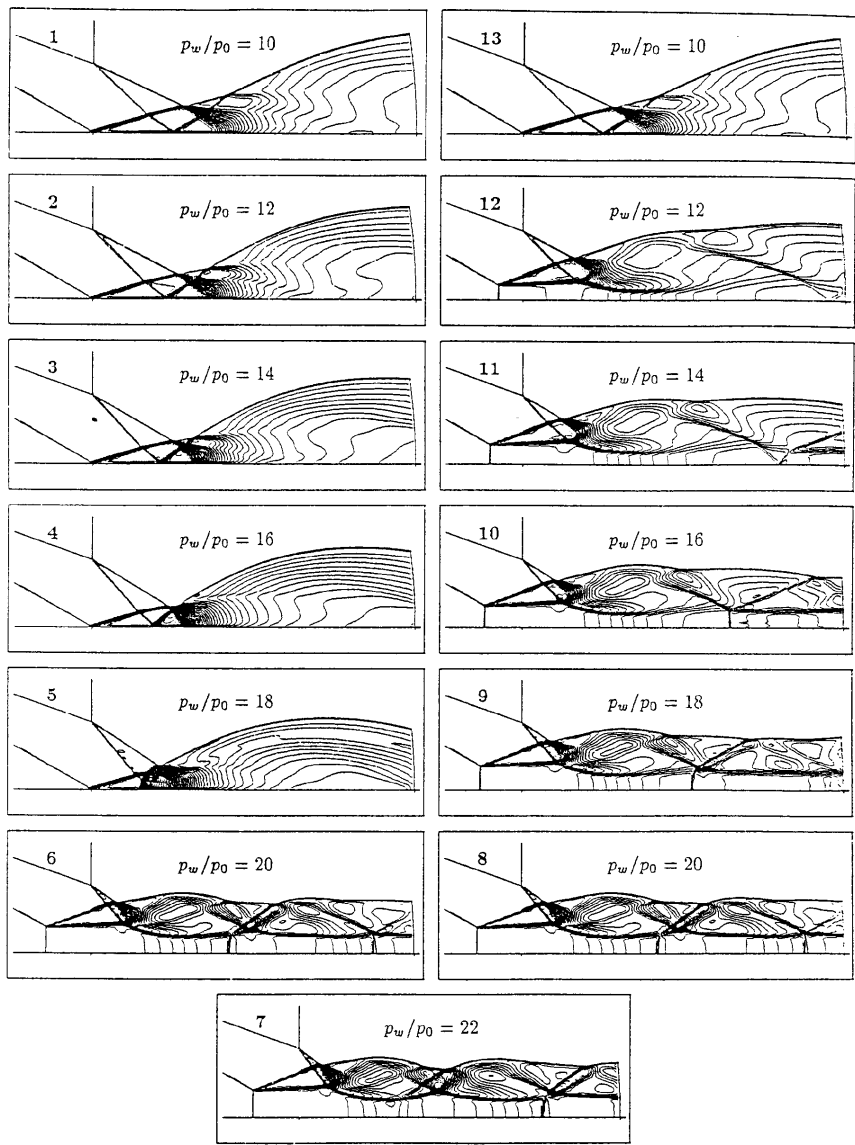


FIGURE 8.1.25 The downstream-pressure-variation-induced hysteresis.

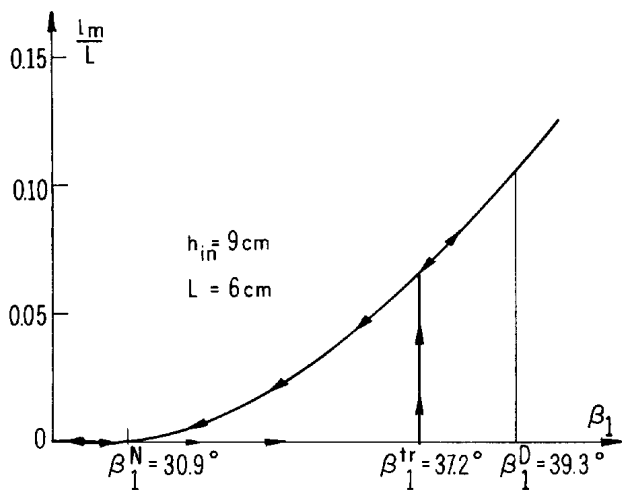


FIGURE 8.1.26 The downstream pressure variation induced hysteresis loop in the $(l_m/L, p_w/p_0)$ -plane.

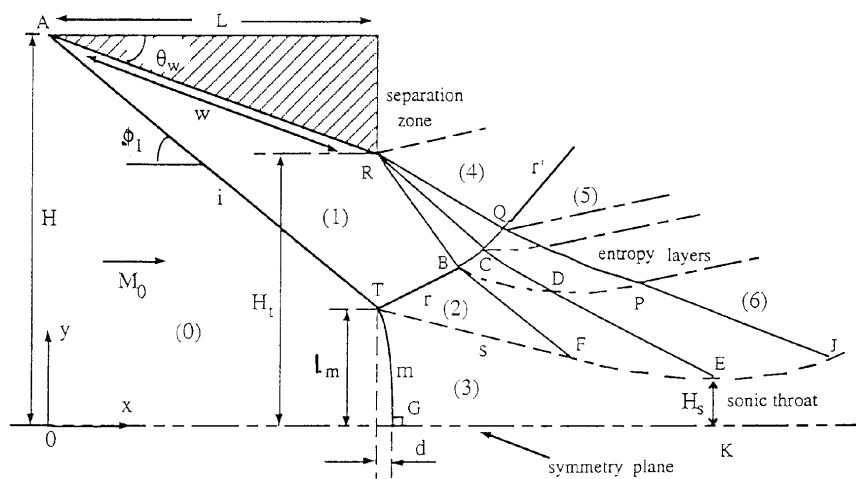


FIGURE 8.1.27 Detailed schematic illustration of an MR wave configuration.

4. The flow behind the Mach stem inside the converging nozzle is isentropic
5. The flow inside the converging nozzle reaches sonic conditions at the throat
6. The gas is an ideal fluid, i.e., $\mu = 0$ and $k = 0$

By applying the conservation laws of mass and linear momentum, Azevedo (1989) presented a closed set of governing equations by which the height of the Mach stem could be calculated.

The predicted values of the height of the Mach stem as obtained using Azevedo's model are shown in Figs. 8.1.28a and 8.1.28b, together with the experimental results of Hornung and Robinson (1982). The predicted results show a trend similar to that in the experimental results. In addition, the RR \leftrightarrow MR transition angles, as predicted by the analytical model, agree relatively well with those predicted by the von Neumann criterion [compare the analytical values obtained for $\beta_1(L_m = 0)$ and the corresponding arrow-heads along the β_1 -axis that indicate the measured transition angles].

Although the agreement between the predicted values for the Mach stem height and the experimental ones is far from satisfactory, one must admit that, in general, the analytical predictions are surprisingly good in view of the oversimplifying assumptions upon which the analytical model is based.

The foregoing discussion clearly indicates that a physical length associated with the reflecting wedge, which is communicated by the expansion wave to the triple point of the MR, determines the actual height of the Mach stem. More details regarding Azevedo's model can be found in Ben-Dor (1991, Section 3.3) and Azevedo and Liu (1993).

Li and Ben-Dor (1997) introduced a modification of Azevedo's model. Unlike in Azevedo's analysis, the interactions of the Prandtl–Meyer expansion fan with the reflected shock wave and the slipstream, s , were solved. In addition, the Mach stem, m , was assumed to be slightly curved. The minimal cross section of the one-dimensional converging nozzle was analytically calculated. As a result the throat of the one-dimensional converging nozzle was obtained downstream of the point assumed by Azevedo (compare points E and F in Fig. 8.1.27).

A comparison between the normalized Mach stem height L_m/L as predicted based on Li and Ben-Dor's (1997) model (solid line) and the experimental results of Hornung and Robinson (1982) (solid squares) is shown in Figs. 8.1.29a and 8.1.29b for $M_0 = 2.84$ and 3.98, respectively. Azevedo and Liu's (1993) calculated results (dashed line) and Vuillon, Zeitoun, and Ben-Dor's (1995) numerical results (open circles) are also added to Figs. 8.1.29a and 8.1.29b. The superiority of the prediction based on Li and Ben-Dor's model over those based on Azevedo and Liu's model is clearly seen. Furthermore, the

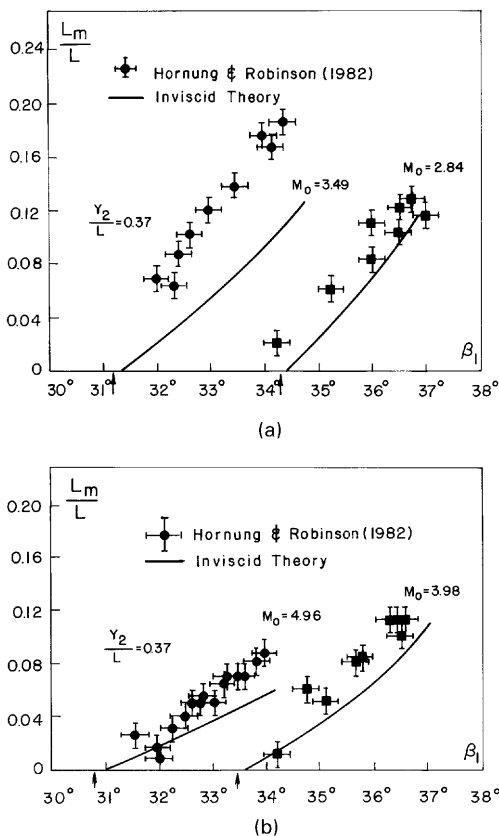


FIGURE 8.1.28 Comparison between the analytically predicted and experimentally measured values of the height of the Mach stem for (a) $M_0 = 2.84$ and 3.49 ; (b) $M_0 = 3.98$ and 4.96 .

heights of the Mach stem based on Li and Ben-Dor's model approach zero exactly at the von Neumann transition point, β_1^N . This is an additional indication that the MR→RR transition takes place at von Neumann criterion. Note that Azevedo and Liu's (1993) predicted transition angle is greater than the von Neumann transition angle (Figs. 8.1.29a and 8.1.29b).

The maximum shift of the Mach stem foot, normalized by the Mach stem height, d/L_m , as a function of the incident shock angle, β_1 , is shown in Fig. 8.1.30. The maximum value of d/L_m is about 0.02. This means that the curvatures of Mach stem are very small. This is consistent with experimental observations. This fact explains why the errors in models, which assumed a straight Mach stem, were not too big. (Based on Li and Ben-Dor's 1997 model, a straight Mach stem can be theoretically obtained only at $\beta_1 = \beta_1^N$, but at this condition the model yields $L_m = 0$.)

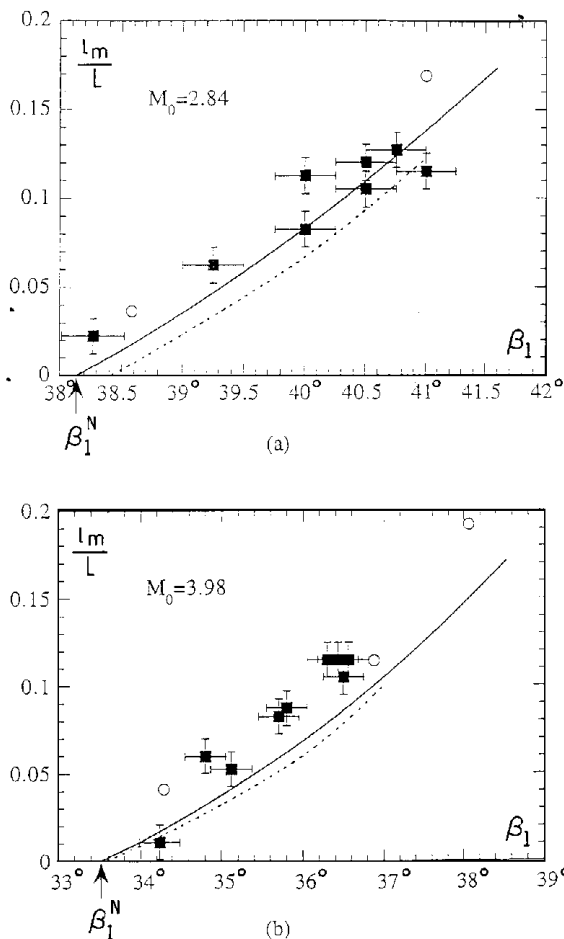


FIGURE 8.1.29 A comparison between the normalized Mach stem height L_m/L as predicted by Li and Ben-Dor's (1997) model (solid line) and the experimental results of Hornung and Robinson (1982) (solid squares). (a) $M_0 = 2.84$, (b) $M_0 = 3.98$.

An MR wave configuration, which was calculated using Li and Ben-Dor's (1997) analytical model, is shown in Fig. 8.1.31. It is evident that the interaction of the expansion fan generated at the trailing edge with the reflected shock wave, and the slipstream, results in a curved part of the shock wave (BC), a curved part of the characteristic (CD), and a curved part of the slipstream (FE). The sonic throat (point E) is located downstream of point F where the head of the expansion fan intersects the slipstream. Recall that Azevedo and Liu (1993) assumed that the sonic throat is located at point F. Obviously, this is not the case.

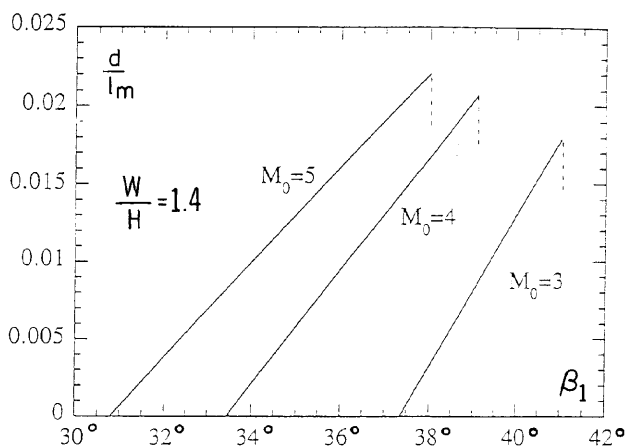


FIGURE 8.1.30 Dependence of the normalized horizontal shift of the foot of the Mach stem, d/L_m , on the angle of incidence, β_1 , for different flow Mach numbers.

As noted first by Sternberg (1959) and by Hornung, Oertel, and Sandeman (1979) and later verified by Li and Ben-Dor (1997), the height and radius of curvature of the Mach stem are determined by the physical length of the reflecting wedge, which is communicated to the triple point. The information regarding the physical length scale is communicated through the expansion fan

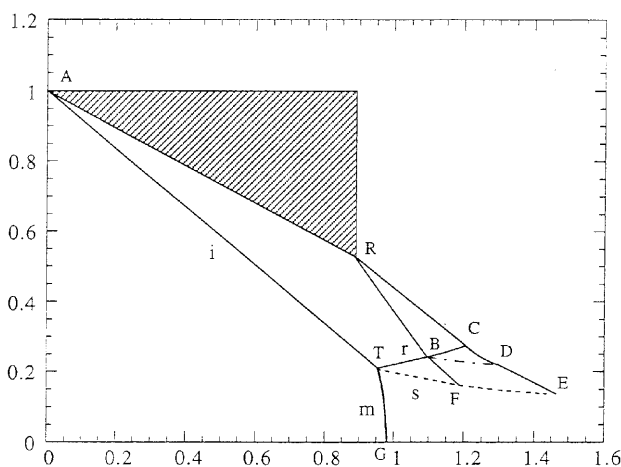


FIGURE 8.1.31 Analytical prediction of an MR wave configuration for $M_0 = 5$ and $\theta_w = 28^\circ$.

to the sonic throat, and then upstream along the subsonic pocket, which exists behind the Mach stem, to the triple point.

It should be mentioned here that all the results and discussion were based on the assumption that the MR wave configuration is isolated from downstream influences, which could exist under some circumstances. In the presence of such influences the Mach stem heights can either increase or decrease. Henderson and Lozzi (1979) and Hornung and Robinson (1982) experimentally observed the the Mach stem heights became greater by introducing higher downstream pressures. (More details regarding this issue can be found in Section 8.1.3.2.5.)

8.1.3.4 MODIFICATION OF THE PERFECT TWO- AND THREE-SHOCK THEORIES

Nonideal effects might influence the reflection phenomenon in steady flows. The possible influences of some of them are presented in the following.

8.1.3.4.1 Nonstraight Discontinuities

One of the main assumptions of the three-shock theory is that all the discontinuities at the triple point of an MR are straight. However, although the incident and the reflected shock waves are straight, the Mach stem and the slipstream are curved. This implies that predictions based on the three-shock theory include an inherent error.

8.1.3.4.2 Viscous Effects

The flow in state (0) develops a boundary layer along the bottom surface, and hence the incident shock wave interacts with this boundary layer to result in a relatively complex structure near the reflection point at the bottom surface. The interaction with the boundary layer depends on whether the boundary layer is laminar or turbulent as shown schematically in Fig. 8.1.32, where the structure of the incident shock wave interacting with the boundary layer in the vicinity of the reflection point of an RR is shown schematically. It is clear from this figure that if one is to accurately solve the flow field in the vicinity of the reflection point of an RR, then a very complicated flow field must be dealt with.

Henderson (1967) analytically investigated the reflection of a shock wave from a rigid wall in the presence of a boundary layer by treating the problem not as a reflection but as a refraction process. He found that a Mach stem was

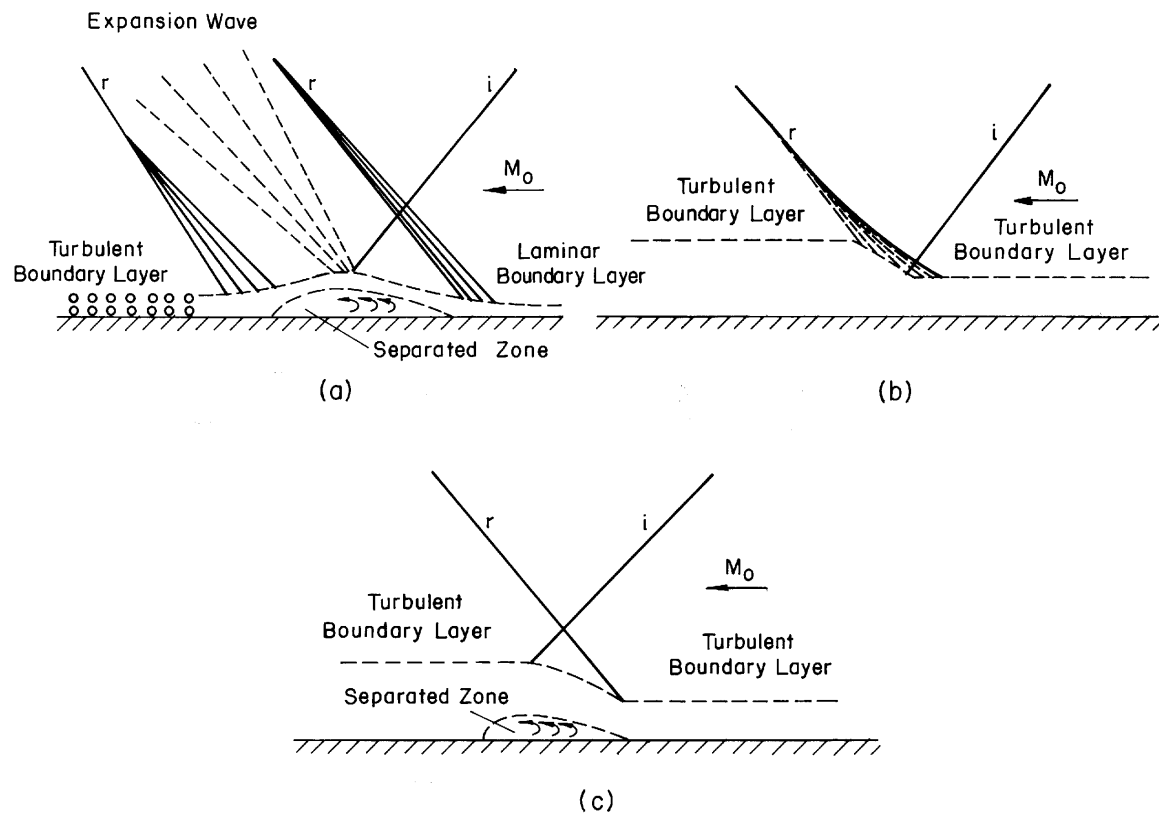


FIGURE 8.1.32 Schematic illustration of the way in which the boundary layer over the reflecting surface affects the wave structure of an RR near the reflection point.

always present and that the bottom of this wave was bifurcated (a lambda foot). The reflection was said to be regular (RR) if the Mach stem and the lambda foot were confined to the boundary layer and irregular (IR) if either extended into the main stream. Two types of regular reflection were found: one that had a reflected compression wave, and another that had both reflected compression waves and expansion waves. Henderson (1967) presented initial conditions that enable one to decide which type of reflection would appear. He reported, furthermore, that they were two types of IR: one that had a Mach stem present in the main stream, and another that was characterized by a four-wave configuration. There were also two processes by which the RR became an IR. One was due to the formation of a downstream shock wave that subsequently swept upstream to establish the irregular system, and the other was due to boundary layer separation, which forced the lambda foot into the main stream. (A detailed description of the shock wave boundary layer interaction is given in Chapter 8.3.)

By using a relatively simple experimental setup, the foregoing shock wave/boundary layer interaction along the bottom surface can be avoided. This is shown in Fig. 8.1.33, where two identical reflecting wedges are placed in such a way that they produce two symmetrical RRs (Fig. 8.1.33a) or MRs (Fig. 8.1.33b). In this experimental setup, the line of symmetry replaces the bottom wedge, thus completely eliminating viscous effects along it. Hence, it is possible to generate inviscid RR in steady flows. Viscous effects along the slipstream of an MR eliminate the possibility of having an inviscid MR. A method for modifying the three-shock theory is presented in Section 8.1.4.11.4. As shown in Fig. 8.1.33b, the use of the symmetrical setup also eliminates the interaction between the foot of the Mach stem and the boundary layer. Some excellent photographs illustrating the interactions of both the

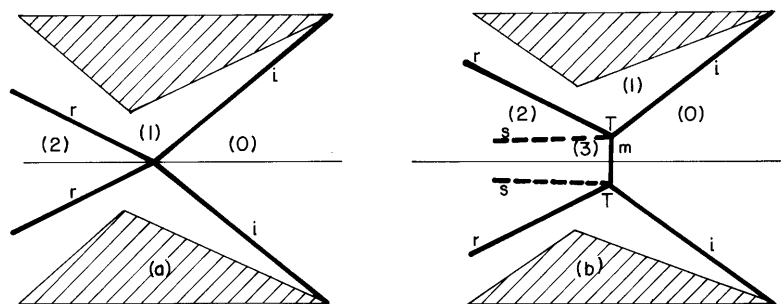


FIGURE 8.1.33 Schematic illustration of a symmetrical experimental setup for eliminating the boundary layer effect: (A) RR, (B) MR.

incident shock wave of an RR and the Mach stem of an MR with the boundary layer can be found in Shapiro (1953, Section 28.3).

8.1.3.4.3 Thermal Conduction Effects

Heat transfer might also affect the flow fields in the vicinity of the reflection point of an RR and the triple point of an MR. Not much can be added regarding this effect, since neither experimental nor analytical studies of it are available.

The foregoing remark on the elimination of viscous effects by using a symmetrical wedge setup is also valid for the heat transfer effects, which are also eliminated along the line of symmetry. Along the slipstream, however, heat transfer effects might still play an important role.

8.1.3.4.4 Real Gas Effects

The question whether real gas effects are important and therefore must be accounted for depends on the ratio between the relaxation length of a certain degree of freedom and the physical characteristic length of the reflection phenomenon.

When the flow fields in the vicinity of the reflection point of an RR or the triple point of an MR are concerned, it is quite appropriate to assume that the flow is frozen with its preshock thermodynamic state. However, as the flow moves away from the incident shock front, its internal degrees of freedom are excited, if the temperatures are sufficiently high, and the flow fields ahead of and behind the reflected shock wave are no longer uniform.

Consider Fig. 8.1.34, where two reflecting wedges having identical wedge angles, θ_w , are used to produce two RRs, which are different in their size. The two corresponding reflection points are labelled R_1 and R_2 , respectively. Although the flow fields associated with these two regular reflections seem to be identical (one is an enlargement of the other), this is not the case, because the relaxation length behind the incident shock wave is the same for both cases. Thus, although the reflected shock wave, r_1 , of the upper RR is completely inside the relaxation zone, and hence faces a nonequilibrium flow along its entire length, the reflected shock wave, r_2 , of the lower RR faces an equilibrium flow along its part, which is outside of the relaxation zone. This implies that the flow fields that develop behind the shock waves r_1 and r_2 are different, although they were generated using identical initial conditions. Thus, when the shock reflection phenomenon is investigated in steady flows, the influence of real gas effects should be carefully considered prior to their neglect or inclusion.

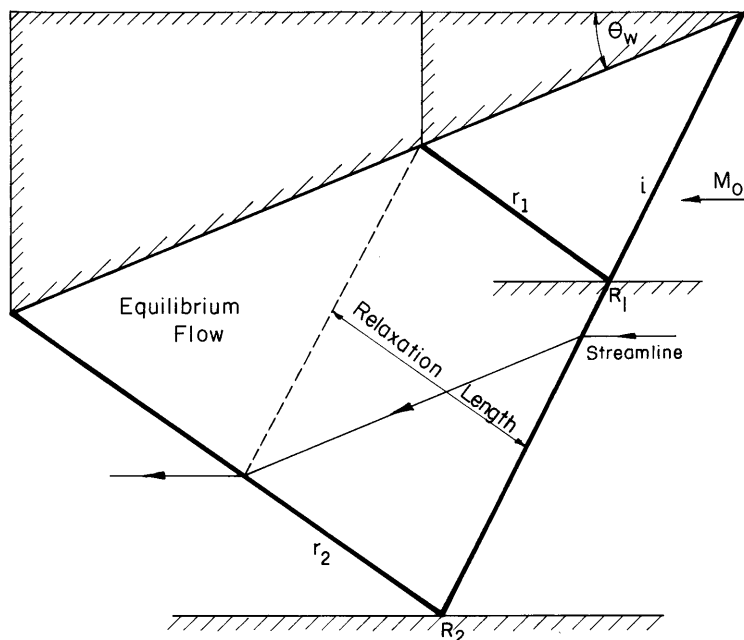


FIGURE 8.1.34 A schematic illustration of the way in which the reflection in steady flows is affected by the excitation of the internal degrees of freedom.

8.1.4 PSEUDO-STEADY FLOW

The flow field that results when a shock wave encounters a solid surface is unsteady, in general. However, if the shock wave has a constant velocity and if the solid surface is straight, the unsteady flow field can be transformed, by means of a Galilean transformation, and be made pseudo-steady. A pseudo-steady flow field can be investigated using steady flow concepts.

8.1.4.1 SHOCK WAVE DIFFRACTION PROCESS

Unlike the shock wave reflection process in steady flows (see Section 8.1.3), which is independent of any other process, in pseudo-steady flow the entire phenomenon is a result of an interaction of two processes, namely the *shock wave reflection process* and the *flow deflection process*. The former refer to the reflection of the planar shock wave over the reflecting surface, and the latter to

the deflection of the shock-induced flow around the leading edge of the reflecting wedge. The interaction of these two processes was referred to by Ben-Dor (1978a) as the *shock wave diffraction process*. Consequently, consideration of the reflection process must account for the possible influence of the flow deflection process.

As shown by Li and Ben-Dor (1995a), if one defines the pressures induced by the shock wave reflection and the flow deflection processes on both sides of the interaction plane of these two processes as p_2 and p_b , respectively, then two situations are possible:

- If $p_b > p_2$, then a band of compression disturbances propagates toward region (2) behind the reflected shock wave.
- If $p_b < p_2$, then a band of expansion disturbances propagates toward region (2) behind the reflected shock wave.

Based on Semenov and Syshchikova (1975), the boundary between these two situations, i.e., $p_b = p_2$, could be associated with the case in which the shock wave induced flow is sonic in the laboratory frame of reference, i.e., $M_1^L = 1$. As a consequence, $p_b > p_2$ when $M_1^L > 1$ and $p_b < p_2$ when $M_1^L < 1$.

8.1.4.2 SHOCK WAVE REFLECTION PHENOMENA

When a planar moving incident shock wave encounters a sharp compressive straight corner, it is reflected by the wedge surface. Depending upon the incident shock wave Mach number, M_s , and the reflecting wedge angle, θ_w , the three general types of reflection RR, vNR, and MR can be obtained. The MR, in pseudo-steady flows, is always a direct Mach reflection, D_i MR, i.e., an MR in which the triple point, T, moves away from the reflecting surface. The D_i MR in pseudo-steady flows can be further divided into a single-Mach reflection, SMR, a transitional-Mach reflection, TMR, and a double-Mach reflection, DMR. These three MR-wave configuration types were first observed and reported by Mach (1878), Smith (1945), and White (1951), respectively.

Ben-Dor (1981) proved analytically that two different DMR-wave configurations are possible. In one of them the trajectory angle of the second triple point is larger than that of the first triple point, i.e., $\chi' > \chi$, and in the other one, $\chi' < \chi$. Lee and Glass (1984) observed these wave configurations experimentally and termed them positive and negative double-Mach reflections (DMR^+ and DMR^- , respectively). They also reported cases in which the second triple point of the double-Mach reflection was located on the reflecting wedge surface, i.e., $\chi' = 0$. They termed this wave configuration a terminal double-Mach reflection, TDMR. Li and Ben-Dor (1995) proved analytically that a TMDR is not physical.

8.1.4.3 REGULAR REFLECTION RR

The wave configuration of a pseudo-steady RR is shown in Fig. 8.1.35. The incident shock wave, i , propagates up the reflecting surface toward the quiescent gas in state (0). It touches the reflecting surface at the reflection point, R . Unlike the incident shock wave, the reflected shock wave, r , which emanates from the reflection point and terminates perpendicularly on the shock tube bottom wall, is straight only near the reflection point. The entire wave configuration grows linearly with time.

In a frame of reference attached to the reflection point, the incident and the reflected shock waves are stationary, and the RR becomes pseudo-steady. The flow in state (0), which moves parallel to the reflecting surface, encounters the incident shock wave obliquely, with an angle of incidence $\beta_1 = 90^\circ - \theta_w$. Upon passing through the incident shock wave, the flow is deflected toward the wedge surface by an angle θ_1 and assumes a new thermodynamic state, state (1). The reflected shock wave, which has an angle of incidence β_2 with respect to the flow in state (1), deflects the flow in an opposite direction by an angle θ_2 to become again parallel to the reflecting surface. The flow behind the reflected shock wave assumes a new thermodynamic state, state (2). Thus, the boundary condition in the vicinity of the reflection point of an RR is $\theta_1 - \theta_2 = 0$.

Since, as mentioned in Section 8.1.2.4.3, the sonic criterion is most likely the correct $RR \leftrightarrow IR$ transition criterion in pseudo-steady flows, the flow behind the reflection point, R , is always supersonic with respect to R , i.e., $M_2^R > 1$. The RR terminates when the flow in state (2) becomes sonic with

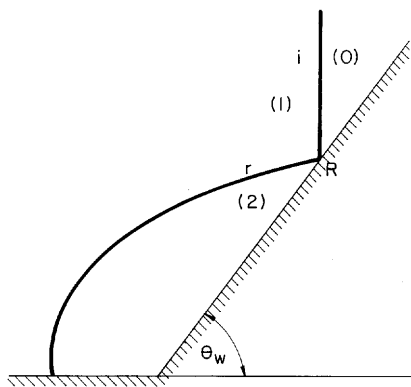


FIGURE 8.1.35 The wave configuration of a pseudo-steady RR.

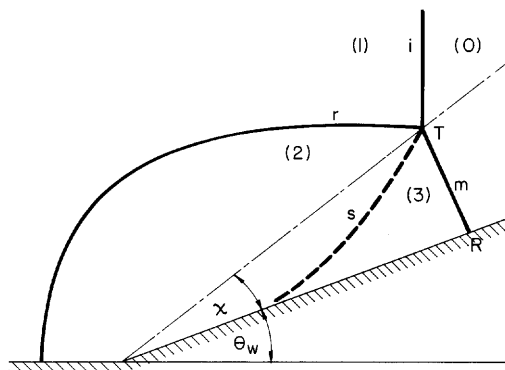


FIGURE 8.1.36 The wave configuration of a pseudo-steady SMR.

respect to R, i.e., $M_2^R = 1$. This fact implies that the reflected shock wave is always straight in the vicinity of the reflection point, R, and hence one of the basic assumptions upon which the two shock theory is based, namely, uniform flow regions in the vicinity of the reflection point, is satisfied.

It should be mentioned, however, that there are photographs showing RR-wave configurations with a curved reflected shock wave in the vicinity of the reflection point. This implies probably that the sonic criterion has been violated. Consequently, based on these results, it is possible that the transition criterion in pseudo-steady flows is the detachment rather than the sonic criterion.

8.1.4.4 SINGLE-MACH REFLECTION SMR

The wave configuration, in a pseudo-steady SMR is shown in Fig. 8.1.36. The four discontinuities typical of an MR meet at the triple point, T, which moves along a straight line originating at the leading edge of the reflecting wedge and forming an angle χ with the reflecting surface.⁴ Unlike the incident shock wave, i , which is straight, the reflected shock, r , the Mach stem, m , and the slipstream, s , are curved.

⁴Henderson and Gray (1981) were the first to raise some doubts on whether the first triple point originates at the leading edge of the reflecting wedge. Experimental support of their doubts was given by Reichenbach (1985) and by Schmidt (1989a). Schmidt (1989a) attributed his findings to viscous effects. He concluded that the reflection, which is unsteady in the vicinity of the leading edge, becomes pseudo-steady only after the incident shock wave has propagated some distance from the leading edge.

In a frame of reference attached to the triple point, T, the four discontinuities, i.e., i, r, m, and s, are stationary, and the SMR becomes pseudo-steady. The flow in state (0), which was originally above the triple point trajectory, encounters the incident shock wave with an angle of incidence $\beta_1 = 90^\circ - (\theta_w + \chi)$. Upon passing through the incident shock wave, the flow is deflected toward the reflecting surface by an angle θ_1 and assumes a new thermodynamic state, state (1). The reflected shock wave, which has an angle of incidence β_2 with respect to the flow in state (1), deflects the flow in an opposite direction by an angle θ_2 to become parallel to the slipstream, s. The flow in state (0), which was originally below the triple point trajectory, encounters the Mach stem with an angle of incidence β_3 . Upon passing through the Mach stem it is deflected by an angle θ_3 to also become parallel to the slipstream. Thus, the boundary condition in the vicinity of the triple point of an MR is $\theta_1 - \theta_2 = \theta_3$.

An SMR can exist as long as the flow behind the reflected shock wave is subsonic, in a frame of reference attached to the triple point, i.e., $M_2^T < 1$. For this reason the reflected shock wave is curved, and only the incident shock wave is straight in the vicinity of the triple point. Therefore, two of the basic assumptions of the three-shock theory, namely, straight discontinuities and uniform flow regions in the vicinity of the triple point, are inherently violated in the case of an SMR. This fact might account for disagreements, regarding the SMR, between experiments and predictions based on the three-shock theory. The condition $M_2^T < 1$ is met when the R-polar intersects the I-polar along its strong portion. This can occur only if the R-polar becomes tangent to the p -axis inside the I-polar. If, however, the R-polar intersects the I-polar along its weak portion, then $M_2^T > 1$ and an SMR is impossible. (For more details, see section 8.1.2.4.1.)

An inspection of SMR photographs (e.g., Ben-Dor, 1978b) indicates that when $M_1^T < 1$, the slipstream of the SMR merges smoothly into the reflecting surface, and when $M_1^T > 1$, the slipstream of the SMR rolls forward.

8.1.4.5 TRANSITIONAL-MACH REFLECTION TMR

When the flow Mach number behind the reflected shock wave becomes supersonic with respect to the triple point, i.e., $M_2^T > 1$, the reflected shock wave straightens near the triple point and the reflection ceases to be an SMR.

Based on the foregoing discussion regarding the role of the pressure p_b and p_2 (see Section 8.1.4.1), Li and Ben-Dor (1995a) argued that there are two types of TMR:

- When $p_b < p_2$, the reflection is a pseudo-TMR in which the leading disturbance propagating toward region (2) is an expansive wave, and hence, a reversal of curvature does not exist on the reflected shock wave, r.
- When $p_b > p_2$ the reflection is either a TMR or a DMR depending on whether the interaction between the shock reflection and the flow deflection processes is strong or weak. This, in turn, depends for a given gas on the incident shock wave Mach number, M_s , and the reflecting wedge surface, θ_w .

The wave configuration of a pseudo-steady TMR, in which $p_b > p_2$, is shown in Fig. 8.1.37. As mentioned earlier, this TMR is typified by a disturbed band of compression waves that propagates toward region (2) and does not converge to form a shock wave. The disturbed band of the compression waves, which interacts with the reflected shock wave, forces the reflected shock wave to curve and reverse its curvature. The point along the reflected shock wave where the reversal of curvature takes place is known as the kink, K. The kink indicates the farthest point, along the reflected shock wave, that has been reached by the compression waves. The band of compression waves, which extends from the kink to the slipstream, is probably responsible for the forward curling of the slipstream (see Fig. 8.1.37) as hypothesized by Henderson and Lozzi (1975) and later verified experimentally by Ben-Dor and Glass (1978).

Unlike the case of an SMR where the reflected shock wave is curved along its entire length, in a TMR, the reflected shock wave emanating from the triple point, T, has a straight part, which extends from the triple point, T, to the kink, K. Beyond the kink the reflected shock wave (m' in Fig. 8.1.37) is curved along its entire length until it terminates, perpendicularly, on the shock tube bottom wall.

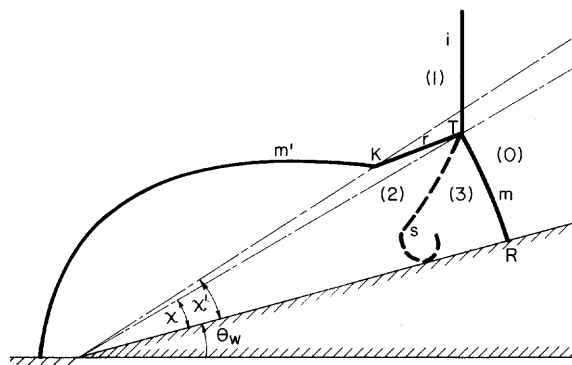


FIGURE 8.1.37 The wave configuration of a pseudo-steady TMR.

The kink moves along a straight line originating from the leading edge of the reflecting wedge and forming an angle χ_K with the reflecting surface. Since the entire wave configuration grows linearly with time, the distance between the triple point T and the kink K also increases linearly. Thus, in a frame of reference attached to the triple point the kink moves away from T and hence the flow Mach number in state (2) is smaller with respect to K than with respect to T. As mentioned earlier the condition for the existence of a TMR is $M_2^T > 1$.

8.1.4.5.1 Analytical Formulation of a TMR

The governing equations of the flow field in the vicinity of the triple point of a TMR are those given by the three-shock theory (see Section 8.1.2.2). Since the three-shock theory was developed under the assumption of straight shock waves in the vicinity of the triple point, it is expected that the flow field would be better predicted in a TMR (where the reflected shock wave is straight) than in an SMR (where the reflected shock wave is curved).

An analytical model for solving the wave configuration of a TMR was presented by Li and Ben-Dor (1995a). Based on the model, the trajectory angle of the kink is

$$\chi_K = \text{tg}^{-1} \frac{M_s a_0 \text{tg}(\theta_w + \chi) + \frac{\overline{KT}}{\Delta t} \cos \omega_{ir}}{M_s a_0 - \frac{\overline{KT}}{\Delta t} \sin \omega_{ir}} - \theta_w \quad (8.1.12)$$

where $\overline{KT}/\Delta t$ is at the rate at which the kink, K, moves away from the triple point, T, and $\omega_{ir} = \pi - (\beta_1 + \beta_2 - \theta_1)$ is the angle between the incident and the reflected shock waves. Li and Ben-Dor (1995a) showed that

$$\frac{\overline{KT}}{\Delta t} = a_2 \{M_2 \cos(\beta_2 - \theta_2) - [1 - M_2^2 \sin^2(\beta_2 - \theta_2)]^{1/2}\} \quad (8.1.13)$$

which together with Eq. (8.1.12) results in

$$\begin{aligned} \chi_K = & \text{tg}^{-1} \\ & \times \frac{M_s a_0 \text{tg}(\theta_w + \chi) + a_2 \{M_2 \cos(\beta_2 - \theta_2) - [1 - M_2^2 \sin^2(\beta_2 - \theta_2)]^{1/2}\} \cos \omega_{ir}}{M_s a_0 - a_2 \{M_2 \cos(\beta_2 - \theta_2) - [1 - M_2^2 \sin^2(\beta_2 - \theta_2)]^{1/2}\} \sin \omega_{ir}} \\ & - \theta_w. \end{aligned} \quad (8.1.14)$$

Predictions of the location of the kink of a TMR were found to agree very well with experimental results (for more details, see Li and Ben-Dor, 1995a). The predictions also indicated that, in accordance with theoretical considerations, $\overline{KT} \rightarrow 0$ as M_s or θ_w decrease toward the appropriate TMR→SMR transition point.

8.1.4.6 DOUBLE-MACH REFLECTION DMR

If the interaction between the shock wave reflection and the shock-induced flow deflection processes is strong, the compression waves converge to form a shock wave, r' . This shock wave forces the reflected shock wave, r , to develop a strong discontinuity (a sharp kink) that is known as the second triple point T' . Owing to gas dynamic considerations, a slipstream complements the second triple point.

8.1.4.6.1 Analytical Formulation of a DMR

Unlike the previous cases of an SMR and a TMR, an analytical model capable of accurately predicting the second triple point trajectory angle is unavailable as yet. According to Li and Ben-Dor (1995a) the only way to determine the exact location of the second triple point is by solving the full Navier–Stokes equations describing the flow field.

Fortunately, with the aid of some simplifying assumptions, Li and Ben-Dor (1995a) developed two analytical models, describing two different double-Mach reflection wave configurations. The two wave configurations, shown schematically in Figs. 8.1.38a and 8.1.38b, differ in the way the second reflected shock wave, r' , interacts with the primary slipstream, s . In the first wave configuration, shown in Fig. 8.1.38a, r' terminates somewhere along s . Gas-dynamic considerations require that r' be normal to s . In the second wave configuration, shown in Fig. 8.1.38b, r' terminates at (or near) the point where s reaches the reflecting surface. In this case gas-dynamic considerations do not require that r' be normal to s .

In both configurations, the reflected shock wave, r , is straight between the two triple points, T and T' . Beyond the second triple point it is curved along its entire length until it terminates perpendicularly on the shock tube bottom wall. The curved part of the reflected shock wave is labeled m' , for it serves in the second triple point as the Mach stem, m , does in the first triple point.

As shown by Li and Ben-Dor (1995a) the transition criterion between these two different DMR-wave configurations is

$$\frac{\sin(\chi' - \chi)}{\sin(\beta_2 + \chi' - \chi - \theta_1)} = \frac{\sin \chi}{\cos(\beta_3 - \theta_3)}.$$

The following general assumptions were incorporated in the two models just discussed:

1. The DMR wave configuration is self-similar.
2. The second reflected shock wave, r' , is straight.

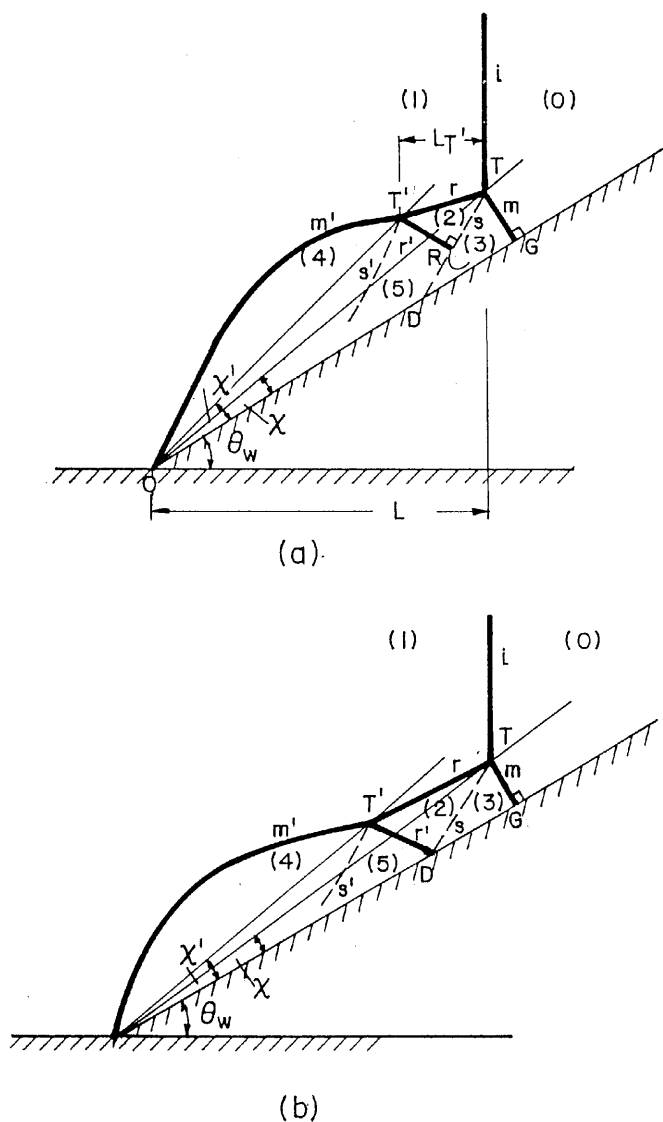


FIGURE 8.1.38 The wave configurations of two possible pseudo-steady DMRs: (a) the secondary reflected shock wave terminates, perpendicularly, on the primary slipstream; (b) the secondary reflected shock wave terminates on the reflecting surface at the point where the primary slipstream reaches it.

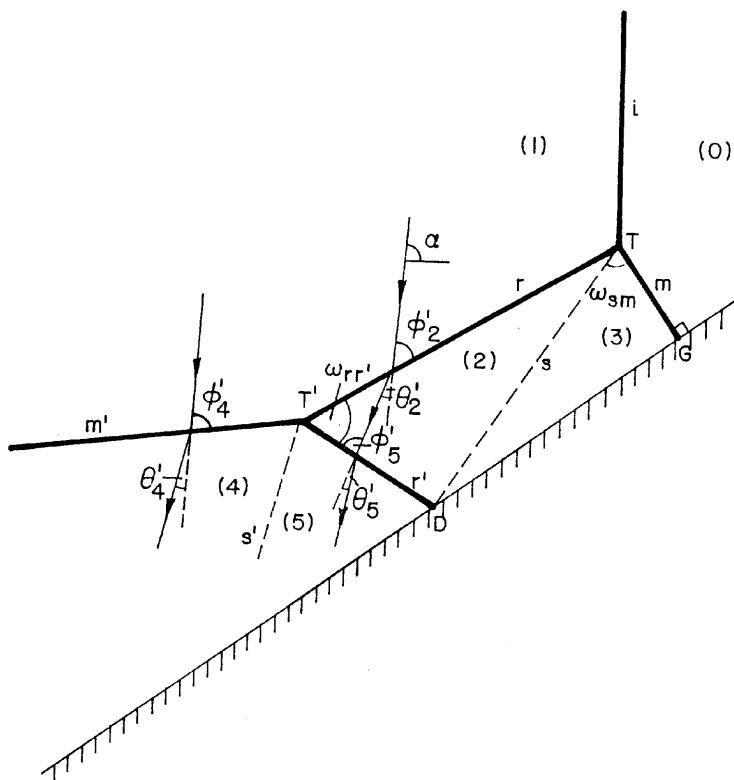


FIGURE 8.1.39(b) Enlargement of the wave configuration of that shown in Fig. 8.1.38b.

The flow deflection across the shock wave r is obtained by setting $i = 1$ and $j = 2$; the flow deflection across the shock wave m' is obtained by setting $i = 1$ and $j = 4$; and the flow deflection across the shock wave r' is obtained by setting $i = 2$ and $j = 5$.

The pressures in regions (4) and (5) can be obtained from

$$p_j = p_i \frac{2\gamma(M'_i \sin \phi'_j)^2 - (\gamma - 1)}{\gamma + 1}. \quad (8.1.18)-(8.1.19)$$

The pressure in state (4) is obtained by setting $i = 1$ and $j = 4$, and that in state (5) is obtained by setting $i = 2$ and $j = 5$.

The matching conditions across the second slipstream, s' , are

$$p_4 = p_5 \quad (8.1.20)$$

and

$$\theta'_2 - \theta'_5 = \theta'_4. \quad (8.1.21)$$

(Unlike the kinematic properties that are frame of reference dependent and hence are denoted with a prime, the thermodynamic properties do not carry a prime, since they are independent of the frame of reference.)

M'_1 in Eqs. (8.1.15), (8.1.16), and (8.1.18) is obtained from the following relations:

$$M'_1 = \left[(M_1^t)^2 + \left(\frac{V_{T'}}{a_1} \right)^2 - \frac{2M_1^t V_{T'} \cos(\theta_w + \chi')}{a_1} \right] \quad (8.1.22)$$

$$V_{T'} = \frac{M_s a_0 - V_T^T \sin \omega_{ir}}{\cos(\theta_w + \chi)} \quad (8.1.23)$$

$$V_T^T = \frac{V_T \sin(\chi' - \chi)}{\sin(\beta_2 + \chi' - \chi - \theta_1)} \quad (8.1.24)$$

$$V_T = \frac{M_s a_0}{\cos(\theta_w + \chi)}. \quad (8.1.25)$$

In these relations V_T and $V_{T'}$ are the velocities of the first T, and second, T', triple points in the laboratory frame of reference, respectively; V_T^T is the velocity of T' relative to T. The rest of the parameters are all obtained from the solution of the flow field in the vicinity of the first triple point. [Recall that ω_{ir} , the angle between the incident and reflected shock waves, is $\omega_{ir} = \pi - (\beta_1 + \beta_2 - \theta_1)$.]

In addition to the preceding expressions,

$$\alpha = \text{tg}^{-1} \left[\frac{V_{T'} \sin(\theta_w + \chi')}{V_{T'} \cos(\theta_w + \chi') - M_1^t a_1} \right] \quad (8.1.26)$$

where α is the orientation of the flow in state (1), with respect to a horizontal line, in a frame of reference attached to T'. The angle α is related to the angle of incidence β'_2 through

$$\beta'_2 = \alpha - \left(\omega_{ir} - \frac{\pi}{2} \right). \quad (8.1.27)$$

In addition,

$$\omega_{rr} = \frac{\pi}{2} - (\beta_2 - \theta_2) \quad (8.1.28)$$

$$\phi'_5 = \pi - (\omega_{rr'} + \beta'_2 - \theta'_2) \quad (8.1.29)$$

and

$$M'_2 = \frac{\left\{ 1 + (\gamma - 1)(M'_1 \sin \beta'_2)^2 + \left[\left(\frac{\gamma + 1}{2} \right)^2 - \gamma \sin^2 \beta'_2 \right] (M'_1 \sin \beta'_2)^2 \right\}^{1/2}}{\left[\gamma (M'_1 \sin \beta'_2)^2 - \frac{\gamma - 1}{2} \right]^{1/2} \left[\frac{\gamma - 1}{2} (M'_1 \sin \beta'_2)^2 + 1 \right]^{1/2}}. \quad (8.1.30)$$

Since M_s , M_1^L , a_0 , a_1 , β_2 , θ_1 , θ_2 , θ_w , χ , and ω_{1r} are known from the solution of the flow field in the vicinity of the first triple point, the preceding set of equations consists of 16 equations and 16 unknowns: β'_2 , β'_4 , β'_5 , θ'_2 , θ'_4 , θ'_5 , p_4 , p_5 , M'_1 , M'_2 , V_T , $V_{T'}$, $V_T^{T'}$, α , $\omega_{1T'}$, and χ' .

8.1.4.6.1.2 Case 2 of a DMR Wave Configuration (r' Intersects the Reflecting Surface at the Point Where s Reaches it)

A schematic illustration of the flow field of interest is shown in Fig. 8.1.39b. Owing to the separation zone that results from the interaction between the slipstream, s , and the wall boundary layer, the flow passing through the second reflected shock wave, r' , is not parallel to the reflecting surface. In fact, the second reflected shock wave, r' , never reaches the reflecting surface. Instead, as described by Landau and Lifshitz (1987, p. 425), r' is pushed under the separation zone. Therefore, requiring that the flow immediately behind r' in the vicinity of point D, where the slipstream, s , reaches the reflecting surface, should be parallel to the reflecting surface is wrong. However, in view of the fact that the size of the separation zone is small in comparison to the size of the entire wave configuration, it is reasonable to assume that the interaction point of r' and s is, practically, located on the reflecting surface. Based on this assumption, the following relations can be developed (for details, see Li and Ben-Dor, 1995a):

$$V_T^D = \frac{V_T \sin \chi}{\cos(\beta_3 - \theta_3)} \quad (8.1.31)$$

and

$$\omega_{rr'} = \text{tg}^{-1} \left[\frac{V_T^D \sin(\beta_2 - \theta_2)}{V_T^{T'} - V_T^D \cos(\beta_2 - \theta_2)} \right]. \quad (8.1.32)$$

In the preceding relations V_T^D is the velocity of T relative to D. Equations (8.1.15)–(8.1.25) and (8.1.29)–(8.1.32) form a set of 17 equations with the following 17 unknowns: β'_2 , β'_4 , β'_5 , θ'_2 , θ'_4 , θ'_5 , p_4 , p_5 , M'_1 , M'_2 , V_T , $V_{T'}$, $V_T^{T'}$, V_T^D , α , $\omega_{rr'}$, and χ' .

8.1.4.6.2 Subtypes of DMR

Ben-Dor (1981) showed that the analytical solution of a DMR results in situations in which the trajectory angle of the first triple point, χ , can be either larger or smaller than the trajectory angle of the second triple point, χ' . This prediction was verified by Lee and Glass (1984), whose experimental

investigation led to the recognition that the DMR wave configuration can be further divided into subtypes of DMR.

8.1.4.6.2.1 Positive Double-Mach Reflection DMR^+

A DMR in which $\chi < \chi'$ is shown in Fig. 8.1.40a. This DMR wave configuration was termed by Lee and Glass (1984) as a positive double-Mach reflection, DMR^+ .

8.1.4.6.2.2 Negative Double-Mach Reflection DMR^-

A DMR in which $\chi > \chi'$ is shown in Fig. 8.1.40b. This DMR wave configuration was termed by Lee and Glass (1984) as a negative double-Mach reflection, DMR^- .

The intermediate case between a DMR^+ and a DMR^- , i.e., a DMR wave configuration in which $\chi = \chi'$, is shown in Fig. 8.1.40c.

8.1.4.7 VON NEUMANN REFLECTION, vNR

The two- and three-shock theories, which were found to fairly well predict the shock wave reflection phenomena for moderate and strong incident shock waves, failed completely in the case of weak incident shock waves. A wave configuration that resembles a classical SMR was obtained in actual experiments at initial conditions for which based on the two- or three-shock theories, neither an RR nor an MR were theoretically possible. Birkhoff (1950) named this fact, which had puzzled many investigators in the past five decades, as the *von Neumann paradox*. Using a sophisticated numerical code Colella and Henderson (1990) were able to resolve the detailed structures of the discontinuities in the vicinity of the triple point. Their numerical study revealed that the reflected wave at the triple point was not a shock wave, but a smoothly distributed self-similar band of compression waves of finite thickness, which evidently was too small to be resolved experimentally, but clear enough to be resolved numerically. As the compression waves retreated from the triple point, they converged into a sharp shock wave. The distance over which this happened was too small to be resolved experimentally. Hence, the observed wave configurations were not SMRs at all. Thus, the fact that the three-shock theory failed to predict a wave configuration in which there were only two shock waves should not be surprising. For this reason the term “von Neumann paradox” is misleading. The just-mentioned wave configuration, which consists of an incident shock wave, a band of self-similar reflected compression waves, a Mach stem, and a slipstream, is shown schematically in Fig. 8.1.41.

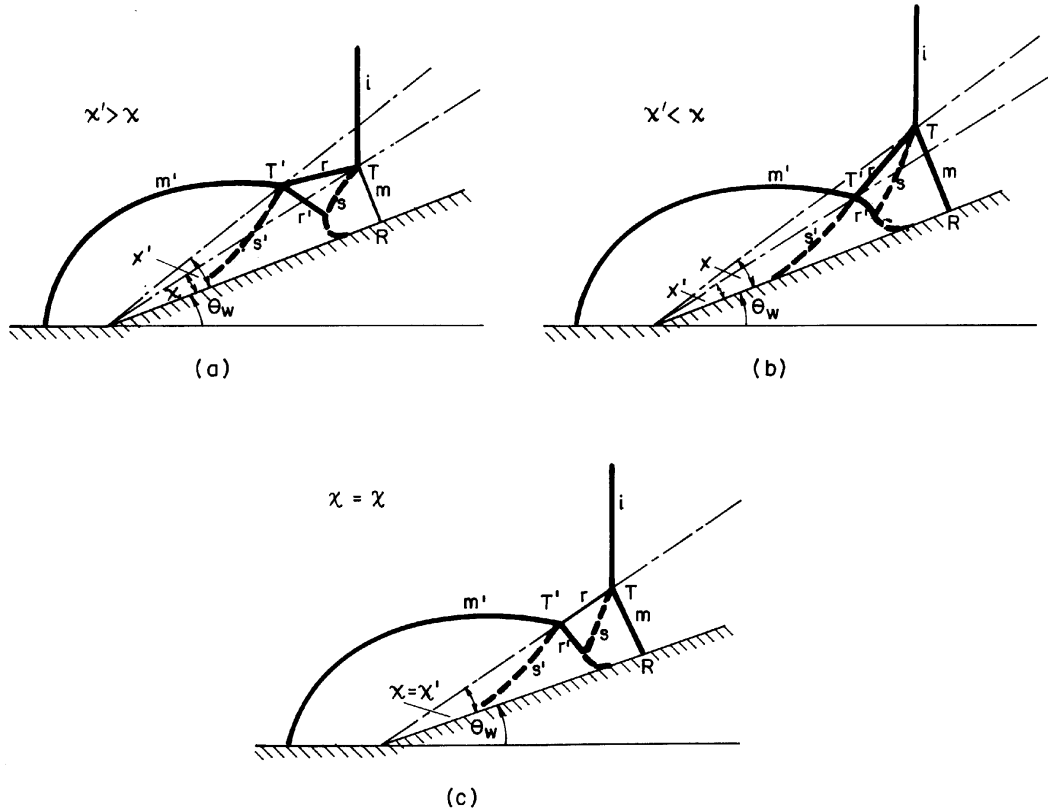


FIGURE 8.1.40 Three various wave configurations of possible pseudo-steady DMR: (a) $\chi < \chi'$, i.e., DMR⁺; (b) $\chi > \chi'$, i.e., DMR⁻; (c) $\chi = \chi'$.

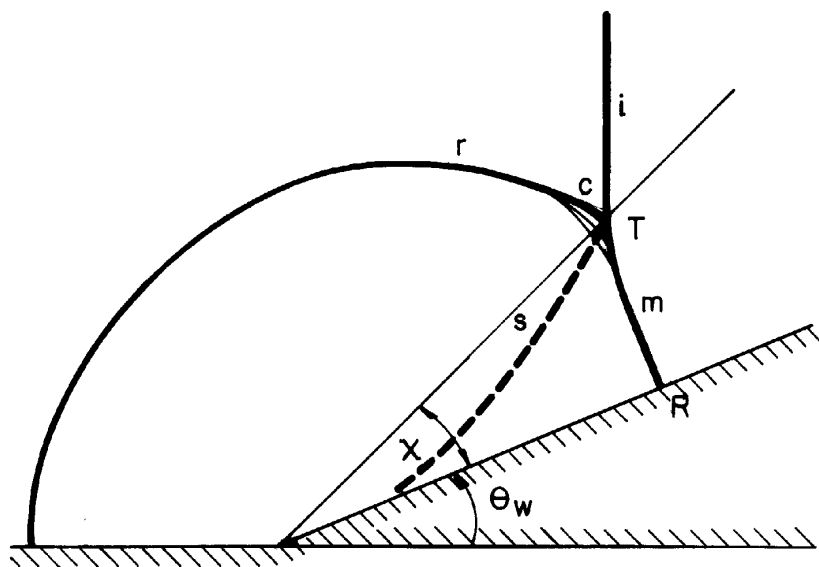


FIGURE 8.1.41 The wave configuration of a pseudo-steady vNR.

Colella and Henderson (1990) termed this wave configuration as a von Neumann reflection, vNR.

A comparison between the wave configurations of an SMR and a vNR reveals that, whereas in an SMR there is a slope discontinuity between the incident shock wave and the Mach stem at the triple point, in a vNR the incident shock wave and the Mach stem appear to be a single shock wave front with a smoothly turning tangent near the triple point. Furthermore, whereas the slipstream is quite sharp in SMR photographs, it is fuzzy in vNR photographs. In fact, the slipstream of a vNR resembles a distributed shear layer rather than a shear discontinuity. Finally, the so-called “triple point” of a vNR is not a well-defined single point, as in the case of an SMR.

8.1.4.7.1 Shock Polar Presentation of a vNR

As presented by Ben-Dor (1991), the shock polar solution of a vNR is similar to that of an SMR. The only difference is that the shock polar corresponding to the reflected shock wave should be replaced by the (p, θ) -relation of a compression wave, i.e.,

$$\ln \frac{p}{p_r} = \frac{\gamma M_r^2}{\sqrt{M_r^2 - 1}} (\theta - \theta_r). \quad (8.1.33)$$

8.1.4.8 TRIPLE POINT TRAJECTORY ANGLES

For many years the triple points T and T' were believed to move along straight lines originating at the leading edge of the reflecting wedge. The angles between these lines and the reflecting surface are the first and second triple point trajectory angles, χ and χ' , respectively. Henderson and Gray (1981) were the first to raise some doubts concerning the fact that the first triple point originates at the leading edge of the reflecting wedge. Experimental support of their hypothesis was given by Schmidt (1989a), who attributed his findings to viscous effects. He concluded that the reflection, which is unsteady in the vicinity of the leading edge of the reflecting wedge, becomes pseudo-steady only after the incident shock wave has propagated some distance from the leading edge.

It should be mentioned here that by using a shock tube with a 30-cm high test section Dewey and van Netten (1991, 1995) were able to record actual reflections, over 45- to 50-cm long straight wedges, that were RR at their early stages and turned into MR further up the wedge.

Since the analysis so far is limited to inviscid flows, the following results are based on the assumption that both the first and the second triple points are generated at the leading edge of the reflecting wedge at the instant the incident shock wave strikes it. Even though this assumption might not be correct, it is believed that the error introduced by using it is negligibly small.

8.1.4.8.1 First Triple Point Trajectory Angle χ

A fairly good method for predicting the value of χ was suggested by Law and Glass (1971). Their analytical model was based on the experimental observation that the curvature of the Mach stem is not too large in most MR wave configurations. Based on this observation, they assumed a straight Mach stem, which is normal to the reflecting surface at the point where it touches it, i.e., the reflection point. Using this assumption together with the assumption that the first triple point trajectory originates at the leading edge of the reflecting wedge, they proposed the following geometrical relation:

$$\chi = \frac{\pi}{2} - \beta_3. \quad (8.1.34)$$

Using this expression χ could be simply calculated following the solution of the governing equations of the three-shock theory.

Finally, χ could be related to the usual initial conditions of pseudo-steady flows M_s and θ_w using

$$\theta_w = \frac{\pi}{2} - \beta_1 - \chi$$

and

$$M_s = M_0 \sin \beta_1.$$

The dependence of the first triple point trajectory angle on the incident shock wave Mach number for nine different values of reflecting wedge angles is shown in Fig. 8.1.42. The solid lines are for perfect nitrogen and the dashed lines are for real nitrogen in dissociational equilibrium. The real gas effects result in an increase in χ . In reality, the flow behind the triple point is probably neither perfect nor in dissociational equilibrium, but in an intermediate nonequilibrium thermodynamic state. Consequently, the lines in Fig. 8.1.42 should most likely be regarded as the lower and upper bounds of the actual value of χ .

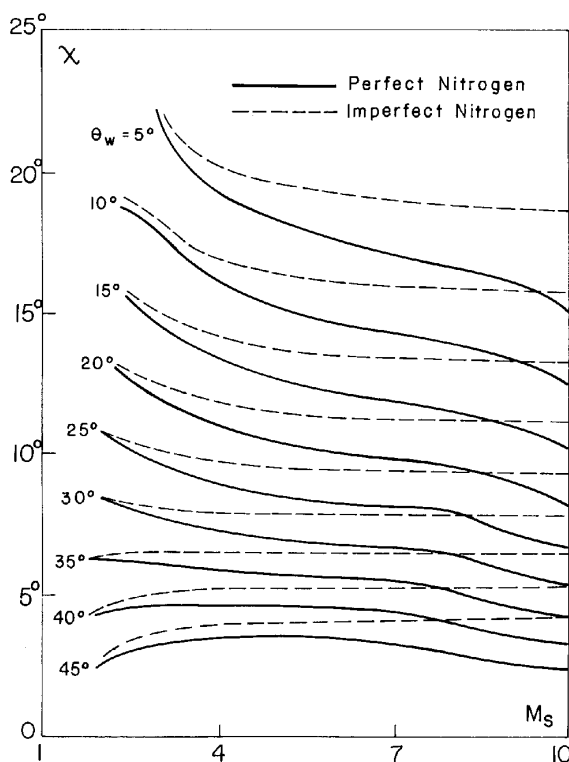


FIGURE 8.1.42 Variation of χ with M_s for given θ_w . Solid lines: perfect nitrogen ($\gamma = 1.4$). Dashed lines: nitrogen in dissociational equilibrium ($p_0 = 15$ torr and $T_0 = 300$ K).

The dependence of the first triple point trajectory angle on the reflecting wedge angle for three different values of incident shock wave Mach numbers, for perfect nitrogen, is shown in Fig. 8.1.43.

A comparison between experimental results and the analytical predictions of the first triple point trajectory angle can be found in Ben-Dor (1991, Section 2.2.1.1). The comparison indicated that the actual values of χ lay in general between the values predicted by the perfect- and real-gas models. As M_s decreased the experimental results approached the perfect-gas line. A clear disagreement was evident for $\theta_w = 40^\circ$. This was explained by Bazhenova, Fokeev, and Gvozdeva (1976), who showed that the assumption of a straight Mach stem becomes progressively worse as θ_w approaches 40° . Thus, to better predict χ , the Mach stem curvature should probably be accounted for.

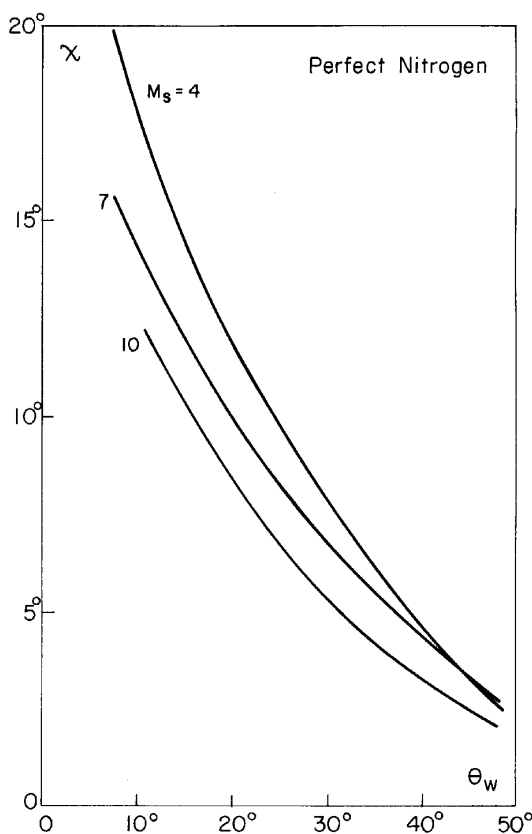


FIGURE 8.1.43 Variation of χ with θ_w for a given M_s for perfect nitrogen ($\gamma = 1.4$).

The analytical model just described also failed to predict χ , with sufficient accuracy, for $M_s < 2$ when $\theta_w < 5^\circ$. For this reason Ben-Dor (1978a) put forward a technical approach for better predicting χ , in the reflection of weak and moderate shock waves over small wedge angles. A detailed description of the approach is given subsequently and in Ben-Dor (1991, Section 2.2.1.2).

8.1.4.8.2 First Triple Point Trajectory Angle for Small Wedge Angles

Ben-Dor (1978a) made use of the fact that an MR or a vNR was obtained, in shock tube experiments, even for cases when the flow behind the incident shock wave was subsonic with respect to the reflection point, R, i.e., $M_1^R < 1$. The formation of the triple point, T, in this cases resulted in a situation in which $M_1^T > 1$. This observation implied that χ assumed a value large enough to force β_1 ($\beta_1 = \pi/2 - \chi - \theta_w$) to be sufficiently small so that M_1^T becomes supersonic. Consequently, assuming that in the case of small wedge angles, χ assumes a value so that β_1 reaches the value appropriate to $M_1^T = 1$, one obtains

$$\chi = \frac{\pi}{2} - \beta_{1(M_1^T=1)} - \theta_w. \quad (8.1.35)$$

Note that, unlike the analytical method presented in Section 8.1.4.8.1, the technical approach does not require the solution of the governing equations of the flow field in the vicinity of the first triple point.

The dependence of the first triple point trajectory angle on the incident shock wave Mach number for five different values of small reflecting wedge angles is shown in Fig. 8.1.44. The solid lines are for perfect nitrogen and the dashed lines are for real nitrogen in dissociational equilibrium. The value of χ is decreased as a result of real-gas effects.

A comparison between experimental results and the predictions, using the technical approach, of the first triple point trajectory angle can be found in Ben-Dor (1991, Section 2.2.1.2). Although the prediction of χ using this approach is far from being satisfactory, it is much better than that obtained using the analytical method of Law and Glass (1971), which was presented in Section 8.1.4.8.1. The agreement improves as θ_w decreases.

8.1.4.8.3 Triple Point Trajectory Angle at Glancing Incidence

Theoretically, the predictions of the technical approach should be excellent for the case of glancing incidence, i.e., $\theta_w \rightarrow 0$. Ben-Dor, Takayama and Dewey (1987c) showed that for this case

$$\chi_g = \tan^{-1} \left\{ \frac{1}{M_s} [A_{10}^2 - (V_{11} - V_{10})^2]^{1/2} \right\}, \quad (8.1.36)$$

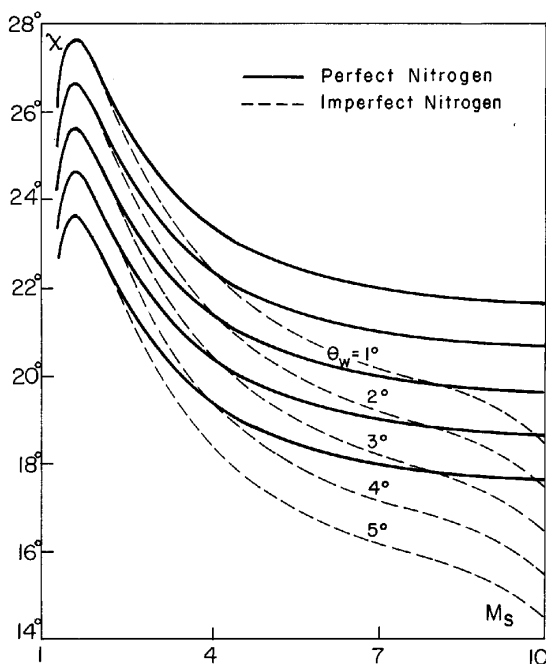


FIGURE 8.1.44 Variation of χ with M_s for given small θ_w . Solid lines: perfect nitrogen ($\gamma = 1.4$). Dashed lines: real nitrogen in dissociational equilibrium ($p_0 = 15$ torr and $T_0 = 300$ K).

$A_{10} = a_1/a_0$, $V_{10} = v_1/a_0$, and $V_{11} = v_1/a_1$. Here a_0 and a_1 are the local speeds of sound ahead of and behind the incident shock wave, respectively, and v_1 is the incident shock induced flow velocity. A_{10} , V_{10} , and V_{11} ($=V_{10}/A_{10}$) depend solely on the incident shock wave Mach number, M_s , through the following relations:

$$V_{10} = \frac{2(M_s^2 - 1)}{(\gamma + 1)M_s}$$

and

$$A_{10} = \frac{\gamma - 1}{\gamma + 1} \frac{1}{M_s} \left[\left(\frac{2\gamma}{\gamma - 1} M_s^2 - 1 \right) \left(M_s^2 + \frac{2}{\gamma - 1} \right) \right]^{1/2}.$$

Using the Galilean transformation, Eq. (8.1.36) becomes

$$\chi_g = \tan^{-1} \left\{ \left[\frac{A_{10}^2}{M_s} (1 - M_1^2) \right]^{1/2} \right\}, \quad (8.1.37)$$

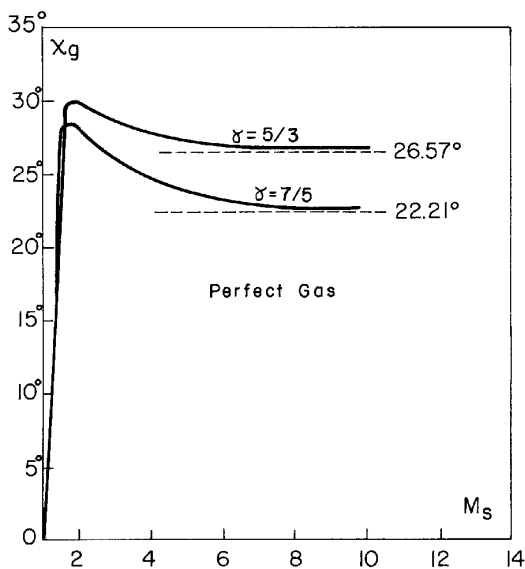


FIGURE 8.1.45 Dependence of the triple point trajectory angle on the incident shock wave Mach number at glancing incidence.

where $M_1 = w_1/a_1$ and w_1 is the flow velocity behind the incident shock wave in a frame of reference attached to the incident shock wave. M_1 depends solely on M_s through

$$M_1 = \frac{M_s - V_{10}}{A_{10}}.$$

The triple point trajectory angle at glancing incidence is shown in Fig. 8.1.45. Following a maximum, it reaches, as $M_s \rightarrow \infty$, an asymptotic value given by

$$\chi_g|_{M_s \rightarrow \infty} = \tan^{-1} \left(\frac{\gamma - 1}{\gamma + 1} \right)^{1/2}. \quad (8.1.38)$$

8.1.4.8.4 Second Triple Point Trajectory Angle χ'

The two analytical models of a DMR just presented (see Sections 8.1.4.6.1.1 and 8.1.4.6.1.2) do not provide an explicit expression for χ' .

Ben-Dor (1980) suggested a fairly good analytical method for predicting the χ' . In addition to the assumptions upon which the method for predicting χ is based (see Section 8.1.4.8.1), it was assumed that:

1. The second triple point trajectory also originates at the leading edge of the reflecting wedge. In view of the previously mentioned doubts regarding a similar assumption about the first triple point, this assumption could introduce an inherent error into the analytical predictions.
2. The horizontal velocity of the second triple point of a DMR in the laboratory frame of reference is equal to the incident shock induced flow velocity. This velocity was needed in order to perform the Galilean transformation from the first to the second triple point. Bazhenova, Fokeev, and Gvozdeva (1976) showed experimentally that this assumption, known as the Law–Glass assumption (see Law and Glass, 1971), is good only in the range $\theta_w < 40^\circ$.

The method for calculating the second triple point trajectory angle is based on the following geometrical relation (for details see Section 2.2.2 in Ben-Dor, 1991):

$$\chi' = \frac{\pi}{2} - \theta_w - \beta_1^{T'}$$

where $\beta_1^{T'}$ the angle of incidence of the flow in state (0), and the incident shock wave in a frame of reference attached to the second triple point is given by

$$\beta_1^{T'} = \text{tg}^{-1} \left[\frac{1 - \rho_0/\rho_1}{\text{ctg } \beta_1 - \rho_0/\rho_1 \text{ ctg } (\beta_1 + \beta_2 - \theta_1)} \right]. \quad (8.1.39)$$

The dependence of χ' on M_s for different reflecting wedge angles is shown in Fig. 8.1.46. The dashed lines are for real nitrogen in dissociational equilibrium and the solid lines are for perfect nitrogen. The excitation of the internal degrees of freedom causes an increase in the value of χ' compared to its value when the gas is assumed to behave as a perfect gas. However, since the flow is most likely neither perfect nor in dissociational equilibrium, the actual value of χ' is most likely between the predictions based on perfect and real gas behaviors.

The dependence of χ' on θ_w for different shock wave Mach numbers is shown in Fig. 8.1.47 for perfect nitrogen.

A comparison between experimental results and the analytical predictions of the second triple point trajectory angle can be found in Ben-Dor (1991, Section 2.2.2.1). The comparison indicated that the experimental results lay, as expected, between the lines appropriate to predictions based on the perfect- and real-gas models.

The dependence of χ' on M_s for $\theta_w = 30^\circ$ and $\theta_w = 40^\circ$ for $\gamma = 1.4$ as calculated using the models presented in Sections 8.1.4.6.1.1 and 8.1.4.6.1.2 and the model based on the Law–Glass assumption and experimental results are shown in Fig. 8.1.48. The superiority of the models presented in Sections 8.1.4.6.1.1 and 8.1.4.6.1.2 over the model based on the Law–Glass assumption

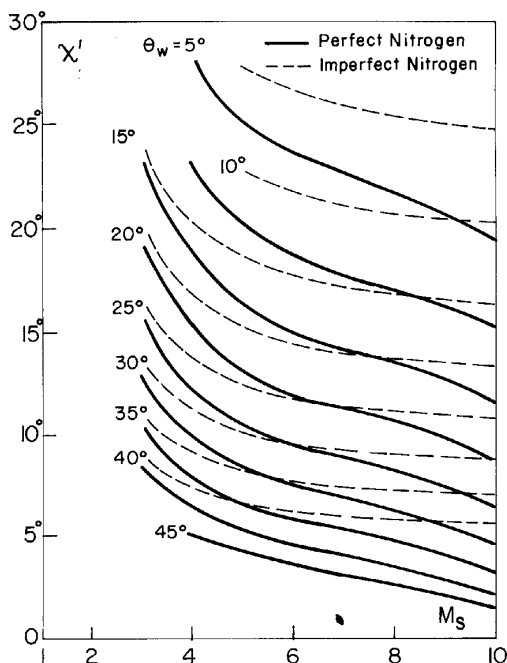


FIGURE 8.1.46 Variation of χ' with M_s for given θ_w . Solid lines: perfect nitrogen ($\gamma = 1.4$). Dashed lines: nitrogen in dissociational equilibrium ($p_0 = 15$ torr and $T_0 = 300$ K).

is clearly evident at $M_s < 6$. Note that at $M_s > 6$ the predictions of the various models approach each other.

8.1.4.8.5 Comparison between the First and Second Triple Point Trajectory Angles

The first and second triple point trajectory angles are plotted as a function of the incident shock wave Mach number for different reflecting wedge angles for perfect nitrogen in Fig. 8.1.49. The results are based on a model using the Law–Glass assumption. It is seen that, for a given value θ_w , there is a value of M_s , say M_s^* , at which $\chi = \chi'$. $\chi < \chi'$ for $M_s < M_s^*$ and $\chi > \chi'$ for $M_s > M_s^*$. The locus of M_s^* is shown in Fig. 8.1.49 by a dotted line. This locus is the transition boundary between a positive double-Mach reflection, DMR^+ , typified by $\chi < \chi'$, and a negative double-Mach reflection, DMR^- , typified by $\chi > \chi'$. (See Section 8.1.4.6.2.)

As shown in Ben-Dor (1991, Section 3.2.3) for real nitrogen (in dissociational equilibrium immediately behind the shock wave fronts), χ' approaches χ asymptotically as M_s increases, and a situation in which $\chi > \chi'$ is never reached. However, since experimental results indicate that there are DMR^-

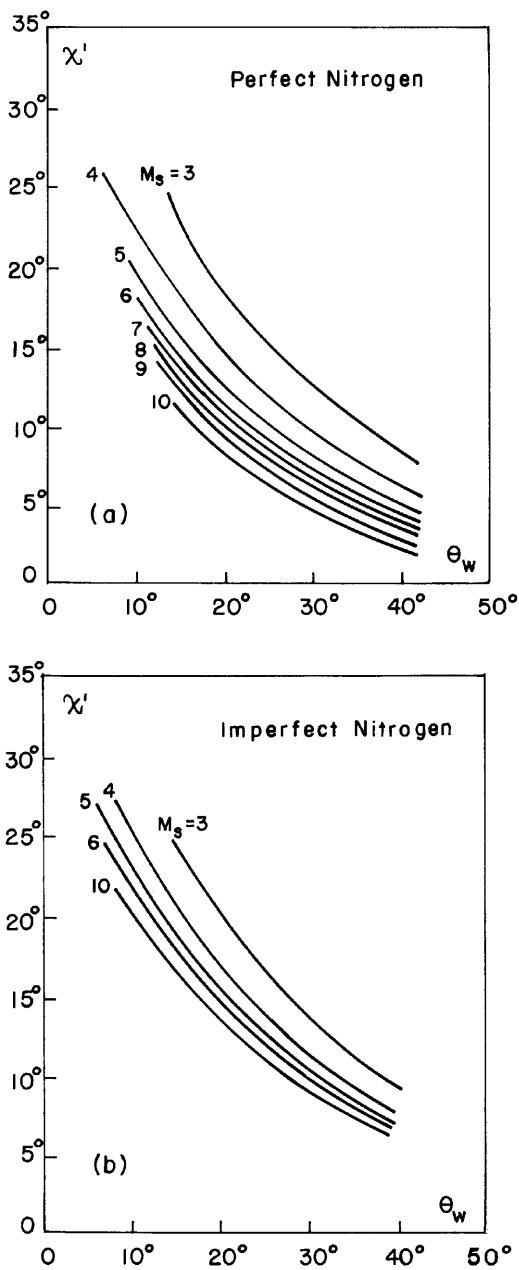


FIGURE 8.1.47 Variation of χ' with θ_w for given M_s for (a) perfect nitrogen ($\gamma = 1.4$), and (b) imperfect nitrogen in dissociated equilibrium ($\rho_o = 15$ torr and $T_o = 300$ K).

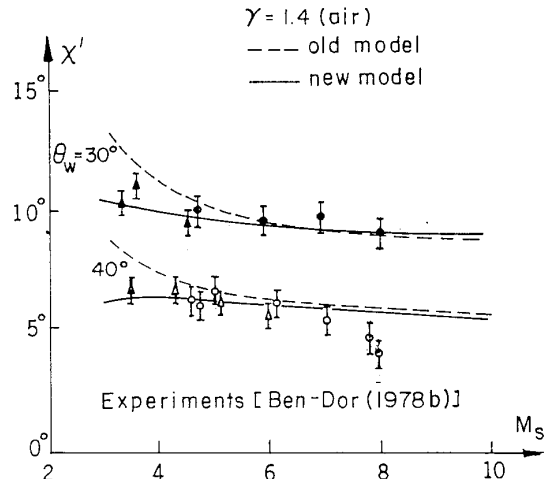


FIGURE 8.1.48 Comparison between the predictions of χ' by the various models with experimental results.

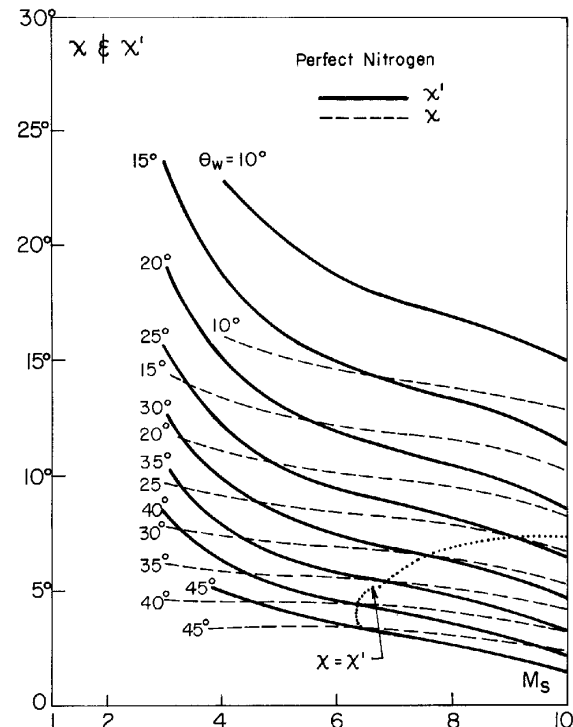


FIGURE 8.1.49 Comparison between χ and χ' for perfect nitrogen.

wave configurations in which $\chi > \chi'$, it can be concluded that using the assumption of dissociational equilibrium immediately behind the shock wave fronts is probably wrong. Alternatively, nonequilibrium relaxation zone should be considered.

Comparison between χ and χ' for a perfect argon (see Ben-Dor, 1991, Section 3.2.3) indicated not only that always $\chi' > \chi$, but also that the difference between χ' and χ approached a constant value as M_s was increased. Similar results were reported by Li and Ben-Dor (1995a), who showed, while using the models presented in Sections 8.1.4.6.1.1 and 8.1.4.6.1.2, that $\chi' > \chi$ in the range $2.8 < M_s < 7$ for perfect argon. Consequently, the specific heat capacities ratio, γ , plays a significant role in determining whether χ can exceed the value of χ' .

8.1.4.9 TRANSITION CRITERIA

Out of the various suggested criteria for the termination of RR, the one that best agrees with pseudo-steady shock tube experimental data is the one arising from the length scale concept, which suggests that in pseudo-steady flows the RR terminates when the flow behind the reflection point, R, of the RR becomes sonic in a frame of reference attached to R. This implies that the $RR \leftrightarrow MR$ transition criterion is

$$M_2^R = 1, \quad (8.1.40)$$

where M_2^R is the flow Mach number in state (2) behind the reflected shock wave of an RR with respect to the reflection point R. As long as $M_2^R > 1$, the corner-generated signals cannot catch up with the reflection point and an IR configuration is impossible.

Once the corner-generated signals catch up with the reflection point, a physical (geometrical) length scale becomes available at the reflection point and an IR-wave configuration, typified by a shock wave with a finite length (i.e., the Mach stem) is formed. The IR can be either an MR or a vNR depending on the angle of incidence between the flow in state (1) and the reflected wave. The reflection is an MR as long as $\beta_2 < 90^\circ$. Consequently, the $MR \leftrightarrow vNR$ transition criterion is

$$\beta_2 = 90^\circ. \quad (8.1.41a)$$

When $\beta_2 = 90^\circ$, the flow passing through the reflected wave, r, is not deflected. Since the flow behind r must be parallel to the slipstream, s, it is

obvious that the preceding $MR \leftrightarrow vNR$ transition criterion can also be expressed as

$$\omega_{rs} = 90^\circ, \quad (8.1.41b)$$

where ω_{rs} is the angle between the reflected wave and the slipstream.

Since S_tMR and I_nMR cannot occur in pseudo-steady flows, the MR in pseudo-steady flows is always a D_iMR . Once the condition for the existence of a D_iMR is met, the value of the flow Mach number, in state (2), behind the reflected shock wave of a D_iMR with respect to the triple point, T, becomes the significant parameter in determining the particular type of the D_iMR .

As long as $M_2^T < 1$ the reflection is an SMR, typified by a curved reflected shock wave along its entire length. The fact that the reflected shock wave is curved along its entire length implies that a physical length scale is communicated to the triple point (from which the reflected shock wave emanates) through state (2). This communication path is possible only as long as $M_2^T < 1$. When the flow in state (2) becomes supersonic, i.e., $M_2^T > 1$, the communication path is blocked by a supersonic flow zone, and the reflected shock wave develops a straight portion, terminated by a kink, which most likely indicates the point along the reflected shock wave that has been reached by the corner-generated signals. Thus, a necessary condition for the termination of an SMR is $M_2^T = 1$. However, as mentioned earlier, in order for a kink to be formed the interaction between the shock reflection and the flow deflection processes should be strong. This implies that the condition $M_1^L = 1$ should also be met (see Section 8.1.4.1). Consequently, the necessary and sufficient conditions for the termination of an SMR and the formation of a TMR are

$$M_2^T = 1 \quad (8.1.42a)$$

and

$$M_1^L = 1. \quad (8.1.42b)$$

Since a TMR is a primary stage of a DMR, the determination of a condition that sharply distinguishes between them is not simple. In general, the condition for the existence of a TMR is

$$M_2^K = 1. \quad (8.1.43)$$

Similarly, the condition for the existence of a DMR is

$$M_2^{T'} > 1. \quad (8.1.44)$$

8.1.4.10 DOMAINS OF DIFFERENT TYPES OF REFLECTIONS

The domains of RR, SMR, TMR, and DMR in the (M_s, θ_w) -plane are shown, for air, in Fig. 8.1.50. The SMR domain is A. The TMR domain is B. Inside this domain $M_2^K = 1$ everywhere. The line separating domains A and B is calculated from the condition $M_2^T = 1$. The DMR domain is C. The line separating domains B and C is calculated from the condition $M_2^{T'} = 1 + \varepsilon$, where $\varepsilon \rightarrow 0$. The reason for not calculating this line from the condition $M_2^{T'} = 1$ is that this requirement implies that the secondary reflected shock wave, r' , is not a shock wave, $M_2^{T'} = 1 + \varepsilon$ should be used. The exact location of the line separating the TMR and DMR domains depends on the value assigned to ε . In Fig. 8.1.50, $\varepsilon = 0.01$. Larger values of ε would shift the transition line further into the DMR domain. Since the existence of both TMR and DMR implies that the interaction between the shock reflection and flow deflection processes should be strong, i.e., $M_1^L > 1$, the transition lines $M_2^T = 1$ and $M_2^{T'} = 1 + \varepsilon$ are terminated at $M_s = 2.07$, which is the incident shock wave Mach number for which $M_1^L = 1$. The curve appropriate to $M_2^D = 1$ clearly indicates that Hornung's (1986) suggestion that $M_2^D > 1$ should be met in order for a DMR to exist is not necessary.

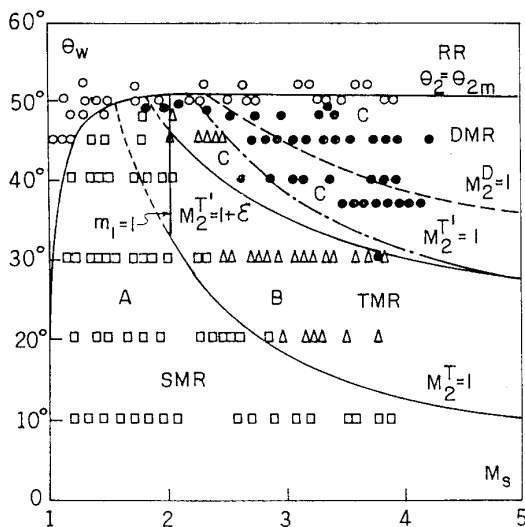


FIGURE 8.1.50 Domains of RR, SMR, TMR, and DMR in the (M_s, θ_w) -plane.

The experimental results, which were added to Fig. 8.1.50, imply that the various transition lines separate very well between the various shock wave reflection configurations.

8.1.4.11 MODIFICATION OF THE TWO- AND THREE-SHOCK THEORIES

The foregoing comparisons between analytical predictions based on the two- and three-shock theories and the experimental results, as well as many more comparisons that can be found in Ben-Dor (1991, Section 2.4.3) for a variety of gases, clearly indicate that there is room for modifying both the two- and three-shock theories.

The major assumptions of the two- and three-shock theories are as follows:

1. The flow field is steady.
2. The discontinuities at the reflection point of an RR and at the triple points of an MR are straight, i.e., the flow regions bounded by them are uniform.
3. The gas behaves as a perfect gas ($p = \rho RT$).
4. The flow is inviscid ($\mu = 0$).
5. The flow is thermally nonconductive ($k = 0$).
6. The contact discontinuity of the triple point is infinitely thin, i.e., a slipstream.

In the following, the validity of each of these assumptions is discussed.

8.1.4.11.1 Nonsteady Effects

The two- and three-shock theories assume that the flow fields in the vicinity of the reflection point of an RR, and in the vicinities of the triple points of an MR, are steady. Hence, strictly speaking, these theories are applicable only in steady flows, which is not the case in the present chapter.

The use of the two- and three-shock theories for investigating shock-wave reflection configurations in this case was justified by experimental observations, from the early 1940s that the wave configurations were self-similar, and hence, the flow field could be considered as pseudo-steady.

Unfortunately, however, as mentioned earlier, experimental investigations regarding the point of formation of the first triple point raised doubts about the validity of self-similarity in MR. Reichenbach (1985) and Schmidt (1989b) provided experimental evidence that the triple point does not form at the leading edge of the reflecting wedge, but at some distance up the reflecting surface. They showed that the triple point trajectory is not straight near the

point where it is formed. Consequently, an MR in its early stages cannot have a self-similar structure. It does approach, however, a self-similar structure after the triple point trajectory straightens out.

8.1.4.11.2 Nonstraight Discontinuities

The two- and three-shock theories assume that the discontinuities at the reflection point of an RR and at the triple points of an MR are straight. This assumption implies that the flow region bounded by any two neighboring discontinuities is uniform.

In the case of an RR, which exists as long as the flow behind the reflection point, R, is supersonic with respect to the reflection point, this assumption is justified since both the incident and the reflected shock waves are separating supersonic flow regions. Thus, the assumption of straight discontinuities in the vicinity of the reflection point of an RR should not introduce any error into predictions based on the two-shock theory when it is used to calculate the flow properties in the vicinity of R.

Unfortunately, however, this is not the case with the three-shock theory. While the incident shock wave, i , of the first triple point, T, of an MR is always straight, both the Mach stem, m , and the slipstream, s , are curved in the vicinity of T. Thus, the assumption of straight discontinuities in the vicinity of T introduces an inherent error into predictions based on the three-shock theory.

Furthermore, the reflected shock wave, r , of the first triple point is straight only for TMR and DMR. In the case of an SMR r is curved in the vicinity of T since the flow behind r in an SMR is subsonic. This fact introduces a further inherent error into predictions based on the three-shock theory when it is used to calculate the flow properties in the vicinity of T of an SMR.

Similarly, the discontinuities in the vicinity of the second triple point, T' , of a DMR are not all straight. Both the second Mach stem, m' , and the second slipstream, s' , are curved. Thus, the use of the assumption of straight discontinuities introduces an inherent error into predictions based on the three-shock theory when it is used to calculate the flow properties in the vicinity of T' of a DMR, or the kink, K, of a TMR.

8.1.4.11.3 Real Gas Effects

When a shock wave propagates through a gas, the translational and rotational degrees of freedom are excited to a new state of equilibrium. The distance along which this occurs is known as the relaxation length. The length is equal to a few mean free paths. The other internal degrees of freedom require a

longer distance (or time) to reach equilibrium. Thus, in the analysis of gas-dynamic shock wave phenomena the role of the relaxation length is very important. If the relaxation length of an internal degree of freedom is much longer than the characteristic length of the phenomenon, then it can be treated as frozen at its preshock state. If, however, the relaxation length of an internal degree of freedom is considerably shorter than the characteristic length of the phenomenon, it can be assumed to be in equilibrium immediately behind the shock wave front. Note that this is only a simplifying assumption, since equilibrium is approached only at distance on the order of the relaxation length. The gas is in nonequilibrium when the relaxation length is on the order of the characteristic length of the phenomenon. In such cases, the solutions based on the frozen and the equilibrium models might be considered as two extreme cases bounding the real nonequilibrium solution.

Although there are no straightforward rules for choosing the characteristic length of a given phenomenon, there are cases where the choice is quite simple. In the case of the TMR \leftrightarrow DMR transition, which is based on the flow Mach number behind the reflected shock wave with respect to the second triple point, the distance between the first, T, and the second, T', triple points can be considered as a characteristic length. This is because the flow state in the vicinity of the second triple point depends on the length of the relaxation zone behind the incident shock wave (for more details see Ben-Dor, 1991, Section 2.5.3).

Note, that unlike T', which moves backwards with respect to the incident shock wave, T is a part of the incident shock wave and hence all the internal degrees of freedom are frozen in its vicinity and retain their preshock states. Therefore, although real gas effects must be accounted for when the flow field in the vicinity of T' is solved, a frozen gas solution should be carried out for the flow in the vicinity of T. This implies that the SMR \leftrightarrow TMR transition line should be calculated using a frozen flow model, while the TMR \leftrightarrow DMR transition line should be calculated using either an equilibrium or a non-equilibrium flow model, depending how far is T' from T.

It is evident from the foregoing discussion that the choice of a characteristic length in the case of a DMR is quite obvious if the flow in the vicinity T' is to be solved. In other cases, such as RR or SMR, the choice of a characteristic length is much more difficult. However, as long as the flow fields in the vicinities of R of an RR, or T of an MR, are to be solved, it seems justified to assume that the internal degrees of freedom remain frozen and hence retain their preshock states. Thus, gases such as Ar, N₂, O₂, and air, which at room temperature can be assumed to behave as perfect gases, should be treated as perfect gases. Similarly, gases that are already excited at room temperature, such as Freon-12, SF₆, and CO₂, should be treated as frozen at their excited level in the vicinities of R and T.

The foregoing discussion also suggests that even in the case of a single reflection configuration, it is not possible to determine one single characteristic length. In the case of a DMR, for example, two different characteristic lengths should be considered for treating each of the two triple points. The two characteristic lengths might differ by orders of magnitude. In addition, the internal degrees of freedom do not relax in the simplified manner. The dissociational relaxation does not start after vibrational equilibrium is reached, but earlier. Therefore, there are positions in the flow field where both the vibrational and dissociational degrees of freedom are not fully excited. When the temperatures are high enough, electronic excitation and ionization further complicate the phenomenon.

Obtaining a real nonequilibrium solution might be too complicated. Therefore, it is a common practice to model real gas behavior by assuming equilibrium of the most likely activated degree of freedom. Such a model should therefore be regarded as an upper bound on the phenomenon, where the perfect gas model most likely results in the lower bound. Further discussions concerning the assumptions regarding the excitation of the internal degrees of freedom can be found in Shirouzu and Glass (1986) and Glaz *et al.* (1988). For more details, see Fig. 2.49 and 2.50 in Ben-Dor (1991).

8.1.4.11.4 Viscous Effects

One of the assumptions upon which the analyses of the regular and Mach reflections were based was that the fluid is inviscid. However, in reality all fluids are viscous. The viscosity will cause the flows, flowing over the reflected surface in both RR and MR and on both sides of the slipstream in an MR, to develop velocity profiles. Consequently, treating the flow fields as inviscid, i.e., uniform flow profiles, introduces an inherent error.

There is, however, a method known as the *boundary layer displacement technique*, to overcome this difficulty. This technique enables one to change the boundary conditions, in such a way that the flow can be treated as inviscid.

Hornung and Taylor (1982) presented the application of this technique in order to get a better agreement between the experiments and analytical predictions of the RR \leftrightarrow IR transition criterion. Shirouzu and Glass (1986) used this technique in order to get a better agreement between the experiments and analytical predictions of the angle between the incident and the reflected shock waves on an RR. Details of these studies can be found in Ben-Dor (1991, Section 2.5.4.1).

Wheeler (1986) showed experimentally that because of viscous effects, the deviation of the actual RR \leftrightarrow IR transition line from the one predicted using the inviscid two-shock theory increases with a drop in the initial pressure, p_0 , in a manner consistent with the boundary layer theory.

The viscous effects along the reflecting surface have little to do with the solution of the flow field in the vicinity of the triple point. They do, however, have some influence, for they affect the flow field in the vicinity of the reflection point, where the foot of the Mach stem touches the reflecting surface. Since the flow behind the Mach stem is subsonic, in a frame of reference attached to the triple point, the influence of the boundary layer, which develops along the reflecting surface, could be communicated to the triple point, and influence it as well. The fact that the boundary layer affects the foot of the Mach stem was reported by Dewey and McMillin (1985), who experimentally observed that the foot of the Mach stem is not perpendicular to the reflecting wedge surface, as it should be if the flow is assumed to be inviscid.

Viscous effects on both sides of the slipstream significantly influence the flow field in the vicinity of the triple point, upon which the predictions of the $SMR \leftrightarrow TMR$ transition criterion, as well as the angles between the four discontinuities, are based.

Ben-Dor (1987) showed that by applying the boundary layer displacement technique to the flow field along the slipstream, the agreement between experimental measurements of the angles between the various discontinuities at the triple point and predictions based on the inviscid three-shock theory were improved. A similar treatment should also be applied to the second triple point. For more details, see Ben-Dor (1991, Section 2.5.4.2).

8.1.4.11.5 Special Reflecting Surface Conditions

The recognition of the role of the kinematic boundary layer in influencing the $RR \leftrightarrow IR$ motivated various investigations to study the reflection of shock waves over wedges, where the surface conditions were such that they could either enhance or reduce the rate of growth of the boundary layers.

8.1.4.11.5.1 Rough Reflecting Surface

By imposing a roughness on the reflecting wedge surface, the rate of the boundary layer growth and its size could be strongly enhanced. A detailed experimental and analytical study on the influence of surface roughness on the $RR \leftrightarrow IR$ transition was carried out by Ben-Dor *et al.* (1987b). The experimental results indicate that for a given incident shock wave Mach number the surface roughness reduces the $RR \leftrightarrow IR$ transition wedge angle. The greater the roughness size, the larger the reduction in the transition wedge angle. It is important to note that whereas Ben-Dor *et al.* (1987b), in their experiments, used a saw-tooth-shaped roughness, Reichenbach (1985), who used in his experiments different shapes of roughness, reported the same shifts in the

transition wedge angle for identical heights of the roughness. For more details see Ben-Dor (1991, Section 2.5.4.3.1).

8.1.4.11.5.2 Perforated Reflecting Surface

Friend (1958) and Onodera (1986) investigated experimentally the reflection of shock waves over perforated plates. The effect of a perforated plate is similar to that of a rough surface, because the boundary layer displacement technique results in a situation in which fluid is being drawn away from the flow field since it is allowed to flow into the real reflecting surface. A similar effect occurs when the plate is perforated, since the fluid is now also drawn away from the flow field as it penetrates the perforated plate and flows through it. For more details see Ben-Dor (1991, Section 2.5.4.3.2).

8.1.4.11.5.3 Slitted Reflecting Surface

Onodera and Takayama (1990) investigated experimentally and analytically the reflection phenomenon over a slitted reflecting surface. Their experimental study was conducted using three different models. In some of their models the slits were open (as in perforated plates), whereas in others the slits were closed. Their experimental results indicated that the transition wedge angles do not depend on whether the slits are open or closed. For more details see Ben-Dor (1991, Section 2.5.4.3.3).

8.1.4.11.5.4 Porous Reflecting Surface

Clarke (1984a, 1984b) investigated the case of a weak regular reflection over a porous surface both experimentally and analytically. An impermeable solid substance backed the porous material. A central feature of Clarke's model was that the porous material swallowed or regurgitated air until such time as the pressure within the porous material was uniform and equal to the external air pressure. Clarke (1984a) did not use his analysis to predict the $RR \leftrightarrow IR$ transition over porous surfaces. More details can be found in Ben-Dor (1991, Section 2.5.4.3.4).

Li, Levy, and Ben-Dor (1995) developed an analytical model for solving the flow field associated with RRs of planar shock waves over porous layers. The governing equations of the gas inside the porous material were obtained by simplifying the general macroscopic balance equations. Excellent agreement between the analytical predictions and the experimental results of Skews (1992) and Kobayashi, Adachi, and Suzuki (1995) was evident.

8.1.4.11.5.5 *Nonsolid Reflecting Surface*

Takayama, Miyoshi, and Abe (1989), Takayama and Ben-Dor (1989a), and Henderson, Ma, Sakurai, and Takayama (1990) investigated experimentally the reflection of planar shock waves over water surfaces. More details on these studies can be found in Ben-Dor (1991, Section 2.5.4.3.5).

8.1.4.11.6 Thermal Conduction Effects

When the gas is assumed to be an ideal fluid, i.e., $\mu = 0$ and $k = 0$, the two- and three-shock theories inherently assume a discontinuity in the temperature field along the wedge, which is usually at room temperature and along the slipstream. In reality, however, because of thermal conductivity the temperature must be continuous.

Unfortunately, an analysis of the two- or the three-shock theories in which thermal conduction is accounted for has never been undertaken. Therefore, it is impossible to quantitatively assess the influence of thermal conductivity on the reflection phenomenon. For more details see Ben-Dor (1991, Section 2.5.5).

8.1.4.11.7 Non-Infinitely Thin Contact Discontinuity

Skews (1971/2) and Zaslavskii and Safarov (1973) suggested that the failure of the inviscid three-shock theory in correctly predicting the angles between the four discontinuities of a triple point might arise from an inadequate choice of the boundary conditions across the contact discontinuity. As discussed in Section 8.1.2.2, the contact discontinuity of the triple point was assumed, in the three-shock theory, to be infinitely thin, i.e., a slipstream. Hence, the flows on both sides of the slipstream were assumed to be parallel, i.e., $\theta_1 - \theta_2 = \theta_3$. Alternatively, Skews (1971/2) hypothesized that perhaps the contact discontinuity is an angular contact zone rather than an infinitely thin slipstream. Courant and Friedrichs (1948) originally suggested the possibility of such a wave configuration. If this is the case, then, according to Skews (1971/2), the preceding boundary condition of an MR should be replaced $\theta_1 - \theta_2 = \theta_3 - \zeta$, where ζ is the divergence angle of the angular contact zone. Ben-Dor (1990) followed Skews' (1971/2) hypothesis and analysed an actual photograph. No clear conclusion could be drawn. For more details see Ben-Dor (1991, Sections 2.5.6).

8.1.4.11.8 Non-Self-Similar Effects

Some comments suggesting that the flow field associated with shock wave reflections in pseudo-steady flows cannot be self-similar were given earlier in Section 8.1.4.11.1, where nonsteady effects were considered.

The assumption of self-similarity was checked and verified experimentally by many investigators. However, in light of the foregoing discussions on viscous, heat transfer, and real gas effects, one is left to wonder whether poor experimental resolution techniques mistakenly led to an incorrect conclusion of a self-similar behavior. The three flow zones arising from the above-mentioned three effects, namely, the kinematic boundary layer, the thermal boundary layer and the relaxation zone, are all non-self-similar. The kinematic boundary layer thickness depends solely on the Reynolds number, the thermal boundary layer thickness depends on both the Reynolds and the Prandtl numbers, and the relaxation lengths depend solely on the shock wave Mach number. Thus, whereas the wave configurations seem to grow linearly with time, these three lengths remain constant in a frame of reference attached to either the reflection point of an RR or the triple point of an MR. For these reasons it is unavoidable to conclude that actual shock wave reflections in pseudo-steady flows are not self-similar.

8.1.5 UNSTEADY FLOW

Unsteady shock wave reflections can be obtained in one of the following ways:

1. Reflecting a shock wave propagating with a constant velocity over a nonstraight surface
2. Reflecting a shock wave propagating with a nonconstant velocity over a straight surface
3. Reflecting a shock wave propagating with a nonconstant velocity over a nonstraight surface

8.1.5.1 REFLECTION OF CONSTANT VELOCITY SHOCK WAVES OVER NONSTRAIGHT SURFACES

If the reflecting surface is curved, either concave or convex, then point R, at which the foot of the incident shock wave touches the surface, has a constant velocity, equal to the incident shock wave velocity, in the direction of propagation of the incident shock wave. Unlike the case of a reflection over a straight reflecting surface, the velocity of R in the direction normal to the direction of propagation of the incident shock wave is not constant.

Thus, if a frame of reference is attached to R, then the angle of incidence of the oncoming flow, β_1 , changes continuously as the shock wave propagates. Since $M_0 = M_s / \sin \beta_1$, it is clear that the Mach number of the oncoming flow, M_0 , also changes continuously.

8.1.5.1.1 Shock Wave Reflections over Concave Cylinders

When a planar shock wave encounters a concave cylinder, it reflects over it either as an RR or as an MR, depending upon the initial wedge angle and the incident shock wave Mach number. The initial type of reflection can be determined using the pseudo-steady shock reflection theory presented in Section 8.1.4.

Consider, for example, Fig. 8.1.50 and note that if one draws a constant M_s line, then the number of transition boundaries intersected by this line depends on the value of M_s .

Let us consider the most general case of an incident shock wave having a Mach number M_s for which all the four types of reflection, i.e., SMR, TMR, DMR, and RR, are possible. Let us also define the corresponding three transition wedge angles as $\theta_w^{SMR \leftrightarrow TMR}$, $\theta_w^{TMR \leftrightarrow DMR}$, and $\theta_w^{DMR \leftrightarrow RR}$.

Consider Fig. 8.1.51, where four different concave cylinders are drawn. Although they all have the same radius of curvature, their initial wedge angles

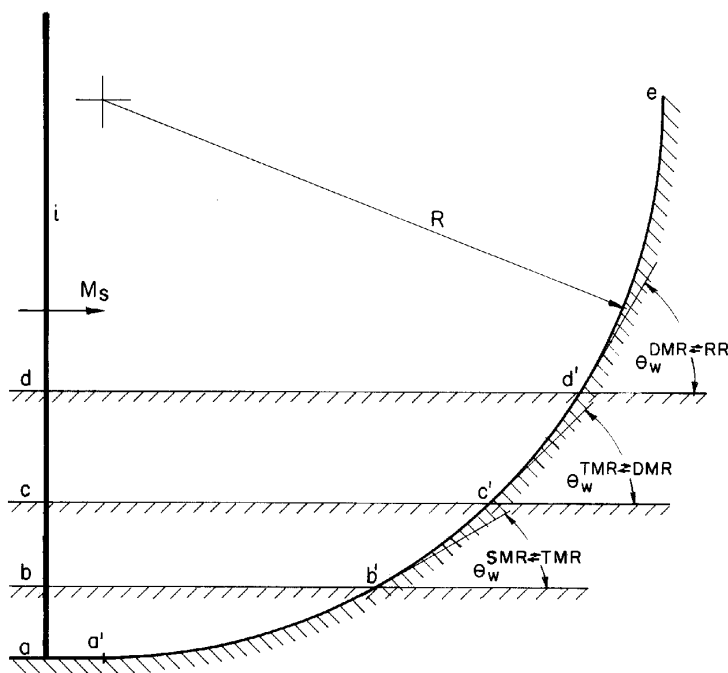


FIGURE 8.1.51 Schematic illustration of four different concave cylinders over which different reflection processes take place.

are different. The slopes are zero for the wedge $aa'e$, $\theta_w^{\text{SMR} \leftrightarrow \text{TMR}}$ for the wedge $bb'e$, $\theta_w^{\text{TMR} \leftrightarrow \text{DMR}}$ for the wedge $cc'e$, and $\theta_w^{\text{DMR} \leftrightarrow \text{RR}}$ for the wedge $dd'e$. Thus,

1. For all the concave cylinders with an initial angle in the range $\theta \leq \theta_w^{\text{initial}} \leq \theta_w^{\text{SMR} \leftrightarrow \text{TMR}}$, the initial reflection will be an SMR.
2. For all the concave cylinders with an initial angle in the range $\theta_w^{\text{SMR} \leftrightarrow \text{TMR}} \leq \theta_w^{\text{initial}} \leq \theta_w^{\text{TMR} \leftrightarrow \text{DMR}}$, the initial reflection will be a TMR.
3. For all the concave cylinders with an initial angle in the range $\theta_w^{\text{TMR} \leftrightarrow \text{DMR}} \leq \theta_w^{\text{initial}} \leq \theta_w^{\text{DMR} \leftrightarrow \text{RR}}$, the initial reflection will be a DMR.
4. For all the concave cylinders with an initial angle in the range $\theta_w^{\text{DMR} \leftrightarrow \text{RR}} \leq \theta_w^{\text{initial}} \leq 90^\circ$, the initial reflection will be an RR.

Consequently, the initial reflection over a concave cylinder can be an SMR, a TMR, a DMR, or an RR, depending upon the initial wedge angle.

An incident shock wave that propagates along the concave cylinder encounters an ever-increasing wedge angle. Consequently, if the initial reflection is an MR, then it will eventually change into an RR. If, however, the initial reflection is an RR, then it will persist.

The foregoing discussion implies that if the initial reflection is an SMR, it will follow the sequence $\text{SMR} \rightarrow \text{TMR} \rightarrow \text{DMR} \rightarrow \text{RR}$; if the initial reflection is a TMR, it will follow the sequence $\text{TMR} \rightarrow \text{DMR} \rightarrow \text{RR}$; if the initial reflection is a DMR it will follow the sequence $\text{DMR} \rightarrow \text{RR}$; and if the initial reflection is an RR it will remain an RR. Photographs of an SMR, a TMR, a DMR, and an RR over a cylindrical concave surface are shown in Figs. 4.2a to 4.2d, respectively, of Ben-Dor (1991).

8.1.5.1.1.1 MR \rightarrow RR Transition

As mentioned earlier, if a shock wave reflects initially over a concave cylinder as an MR, it will eventually change to an RR. In an extensive experimental study, Takayama and Sasaki (1983) showed that the $\text{MR} \rightarrow \text{RR}$ transition wedge angle θ_w^{tr} depends, in addition to the incident shock wave Mach number, M_s , on both radius of curvature of the cylindrical wedge, \mathfrak{R} , and the initial wedge angle $\theta_w^{\text{initial}}$. The results of their experimental study are shown in Fig. 8.1.52. Line AB, the von Neumann criterion, is, the $\text{RR} \leftrightarrow \text{MR}$ transition line, appropriate to steady flows. Line AC, the detachment criterion, is the $\text{RR} \leftrightarrow \text{MR}$ transition line appropriate to pseudo-steady flows. All the recorded transition wedge angles lie above the $\text{RR} \leftrightarrow \text{MR}$ transition line of steady flows. Furthermore, as the radius of curvature increases the transition wedge angles decrease and approach the steady flow $\text{MR} \leftrightarrow \text{RR}$ transition line. Similarly, the experimental results indicate that the transition wedge angle decreases with increasing wedge angles.

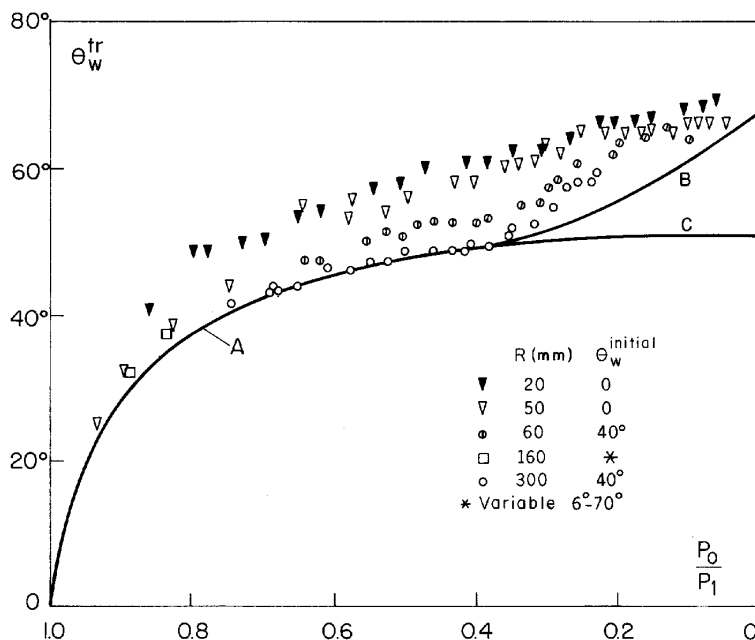


FIGURE 8.1.52 Experimental data with air illustrating the dependence of the transition wedge angle over a concave cylinder on the radius of curvature and the initial wedge angle.

The experimental results suggest that as the radius of curvature approaches infinity, $R \rightarrow \infty$, the actual transition wedge angles approach those appropriate to steady flows.

8.1.5.1.1.1 Effect of Surface Roughness Takayama, Ben-Dor, and Gotoh (1981) investigated experimentally the effect of surface roughness on the MR \rightarrow RR transition. Pasting different sandpapers on the reflecting wedge surface imposed the roughness. It was evident that θ_w^{tr} decreased as the roughness of the reflecting surface increased. In the case of an extremely rough surface, θ_w^{tr} was almost independent of M_s . Furthermore, whereas for smooth surfaces θ_w^{tr} was always greater than θ_w^{tr} that is appropriate to steady flows, i.e., the von Neumann criterion (see Fig. 8.1.52), for rough surfaces there were cases where θ_w^{tr} was smaller than θ_w^{tr} appropriate to steady flows. However, even with the extremely high roughness the recorded values of θ_w^{tr} were always greater than θ_w^{tr} appropriate to pseudo-steady flows (i.e., the detachment criterion). For more details regarding this issue see also Ben-Dor (1991, Section 4.1.1.1.1).

8.1.5.1.1.2 Dynamics of the MR \rightarrow RR Transition

Detailed experimental investigations of the MR \rightarrow RR transition over concave cylinders (see Ben-Dor and Takayama, 1986/7) indicated that during the reflection process over a concave cylinder with $\theta_w^{\text{initial}} = 0$ the length of the Mach stem increases from zero at the leading edge to a maximum, after which it decreases until it vanishes, at the point where the MR \rightarrow RR transition takes place. Consequently, three different types of MR wave configuration are encountered during the reflection process, depending on the direction of propagation of the triple point, T, of the MR. When the length of the Mach stem increases, T moves away from the reflecting surface and the MR is a D_i MR; when T moves parallel to the reflecting surface (even momentarily) the MR is an S_t MR; and when the length of the Mach stem decreases, T moves toward the reflecting surface, the MR is an I_n MR. Since a special wave structure is attached to the RR that is formed upon the termination of the I_n MR (see Section 8.1.5.1.1.2.3), it is called transitional regular reflection, TRR.

In summary, experimental investigations of the MR \rightarrow RR transition over concave cylinders revealed that the reflection process goes through the following sequence of wave configurations:

$$D_i\text{MR} \rightarrow S_t\text{MR} \rightarrow I_n\text{MR} \rightarrow \text{TRR}$$

The shock-polar presentation of this sequence of events is shown in Fig. 8.1.53. The dashed line $a \rightarrow b \rightarrow c$ shows the $D_i\text{MR} \rightarrow S_t\text{MR} \rightarrow I_n\text{MR}$ path.

8.1.5.1.1.2.1 Stationary-Mach Reflection S_t MR An S_t MR and its I-R shock polar presentation are shown in Fig. 8.1.53. The wave configuration of an S_t MR is very similar to that of a D_i MR. The only difference is that its slipstream is parallel to the reflecting surface.

8.1.5.1.1.2.2 Inverse-Mach Reflection I_n MR An I_n MR and its I-R shock polar presentation are shown in Fig. 8.1.53. The wave configuration of an I_n MR is very similar to that of a D_i MR. The only difference is in the orientation of the slipstream. Whereas in a D_i MR the slipstream extends from the triple point toward the reflecting surface, in an I_n MR the slipstream extends away from the reflecting surface. For this reason, the I_n MR is a temporary reflection. It will terminate as soon as its triple point collides with the reflecting surface. Upon the termination of an I_n MR, a TRR is formed.

8.1.5.1.1.2.3 Transitional Regular Reflection TRR Figure 8.1.54 is a schematic illustration showing the dynamics of the termination of an I_n MR and the formation of a TRR. An I_n MR moving toward the reflecting surface is

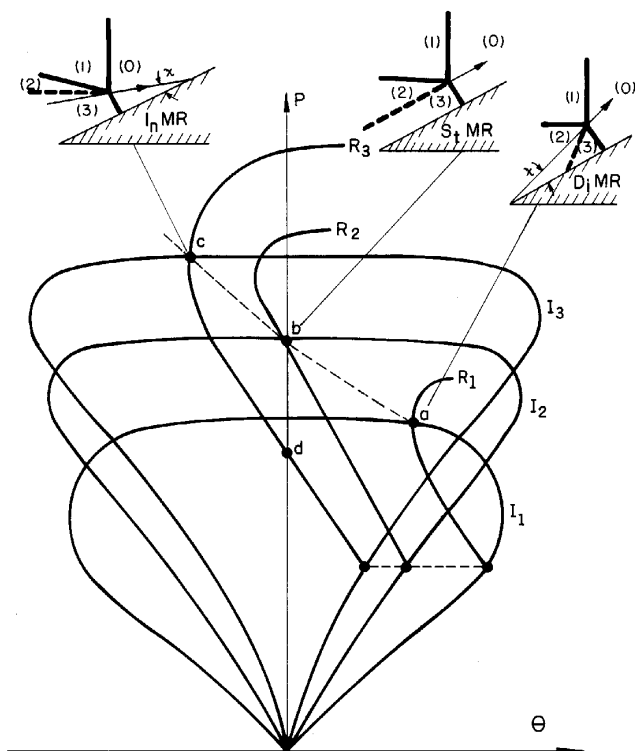


FIGURE 8.1.53 Schematic illustration in the (p, θ) -plane of the solutions of a D_1 MR, an S_1 MR, and I_1 MR, and the D_1 MR \rightarrow S_1 MR \rightarrow I_1 MR transition path.

seen in Fig. 8.1.54a. Figure 8.1.54b illustrates the wave configuration at the moment the triple point, T, collides with the reflecting surface. The Mach stem, m, vanishes and the incident shock wave, i, and reflected shock wave, r, meet on the reflecting surface. The wave configuration that is obtained immediately after the termination of an I_n MR is shown in Fig. 8.1.54c. The main part of the wave configuration is an RR, followed by a new triple point, T^* , which is formed on the reflected shock wave. It is also seen in Fig. 8.1.54c that an additional shock wave complements this new triple point. This additional shock wave, which is not necessarily straight, emanates from T^* and terminates perpendicularly on the reflecting surface.

The physical reason for the formation of the additional shock wave is the need, first hypothesized by Henderson and Lozzi (1975), to support the sudden pressure drop that is associated with the I_n MR \rightarrow TRR transition.

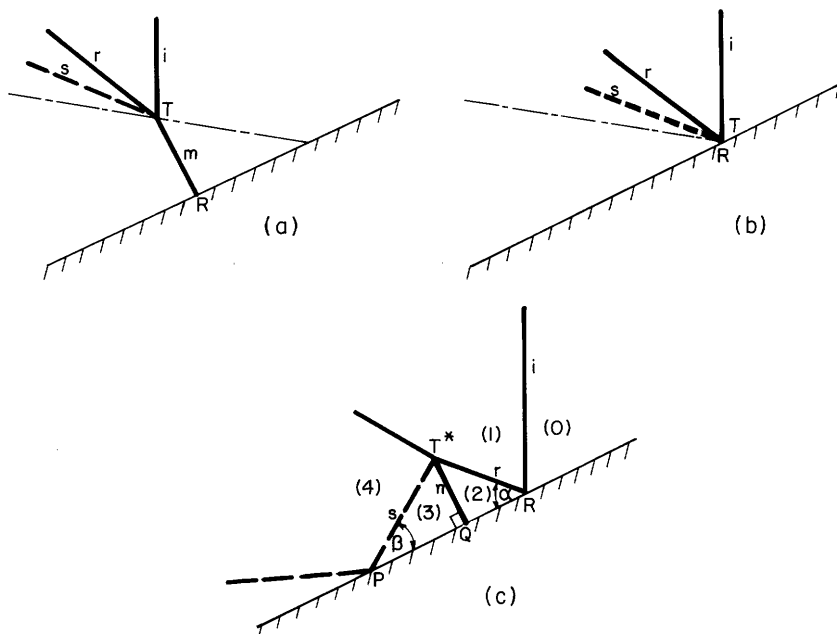


FIGURE 8.1.54 Schematic illustration showing the dynamics of the termination of an I_n MR and the formation of a TRR.

As can be seen in Fig. 8.1.53, the termination of the I_n MR at point “c” and the formation of a TRR at point “d” are associated with a sudden pressure drop.

An analytical model for solving a TRR was developed by Ben-Dor and Elperin (1991). It is also presented in Ben-Dor (1991, Section 4.1.1.2.3.1).

8.1.5.1.1.3 Analytical Considerations

Although the analytical consideration of the reflected phenomenon over concave cylinders is extremely difficult, some simplified analytical models, limited to relatively weak incident shock waves, for predicting the MR \rightarrow RR transition and some other aspects related to the reflection phenomenon are available in the literature.

8.1.5.1.1.3.1 Analytical Prediction of the I_n MR \rightarrow TRR Transition The various analytical models for predicting I_n MR \rightarrow TRR were based on the length scale transition criterion of Hornung, Oertel, and Sandeman (1979) that was found to correctly predict the MR \rightarrow RR transition in both steady and

pseudo-steady flows. The length scale criterion implies that an MR cannot exist unless a physical length scale is communicated to its triple point (see Section 8.1.2.4.4).

Ben-Dor and Takayama (1985) proposed an approach for predicting the $I_n\text{MR} \rightarrow \text{TRR}$ transition over concave cylinders. Their approach required the definition of the propagation path of the corner signals. They assumed two different communication paths, which eventually led to two different transition formulas, given by

$$\frac{\sin \theta_w^{\text{tr}}}{\theta_w^{\text{tr}}} = \frac{M_s}{V_{10} + A_{10}} \quad (8.1.45)$$

and

$$\cos \frac{\theta_w^{\text{tr}}}{2} = \frac{M_s}{V_{10} + A_{10}}, \quad (8.1.46)$$

where V_{10} and A_{10} are given by relations following Eq. (8.1.36). A detailed derivation of these expressions is also given in Ben-Dor (1991, Section 4.1.1.3.1).

The transition lines as obtained from the transition formulas given by Eqs. (8.1.1.45) and (8.1.1.46) and experimental results of the transition wedge angle for $\mathfrak{R} = 50$ mm and $\theta_w^{\text{initial}} = 0$ are presented in Fig. 8.1.55. Lines AB and AC are the $\text{RR} \rightarrow \text{MR}$ transition lines in steady and pseudo-steady flows, respectively. Lines D and E are the transition lines as predicted by Eq. (8.1.45) and (8.1.46), respectively. (Line F will be referred to subsequently.) The agreement between line D [Eq. (8.1.45)] and the experiments is quite good in the range $1.25 < M_s < 4$. (The upper limit arises from the lack of experimental results for $M_s > 4$.) At the smaller Mach number range, $1 < M_s < 1.25$, the agreement between line D and the experiments is very poor (see the three experiments marked with an arrow that lie 4.5° to 7.5° above line D). Transition line E [Eq. (8.1.46)] shows excellent agreement with these experiments only, i.e., it is good only in the range $1 < M_s < 1.25$.

In order to improve the analytical prediction of the $I_n\text{MR} \rightarrow \text{TRR}$ transition over concave cylinders, an additional analytical approach, also based on the length scale concept, was put forward by Takayama and Ben-Dor (1998b). Their approach resulted in

$$\theta = \frac{V_{10}}{M_s} \sin \theta_w^{\text{tr}} \quad (8.1.47a)$$

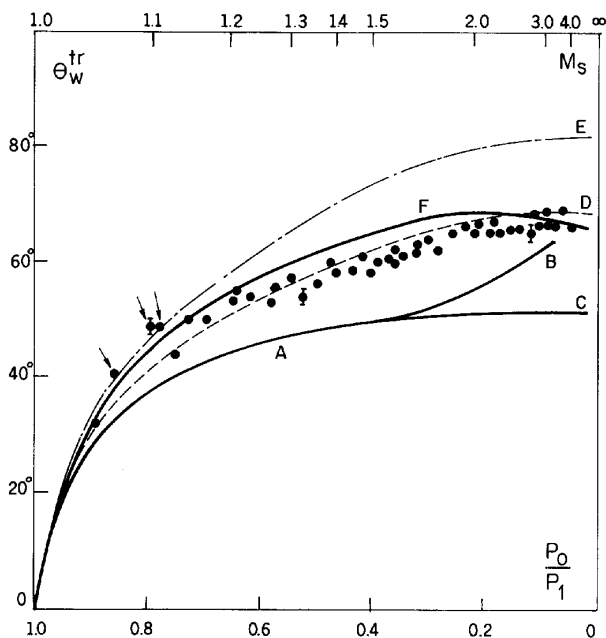


FIGURE 8.1.55 Comparison between the analytical transition lines arising from Eqs. (8.1.1.45) and (8.1.1.46) and experimental results of the transition wedge angle over a concave cylinder with $\mathfrak{R} = 50$ mm and $\theta_w^{\text{initial}} = 0$.

and

$$\frac{2 \sin \frac{\theta_w^{tr} - \theta}{2}}{\sin \theta_w^{tr}} = \frac{A_{10}}{M_s}. \quad (8.1.47b)$$

θ in the preceding transition formulas is the angular position reached by a gas particle that propagated along the cylindrical concave surface from the moment the incident shock wave reached the leading edge of the wedge.

The transition line as obtained from Eqs. (8.1.47a) and (8.1.47b) is shown, as curve F, in Fig. 8.1.55. Unlike the transition lines D and E, which were good only at $M_s > 1.25$ and $M_s < 1.25$, respectively, and very poor outside these ranges, line F shows a fairly good agreement with the experiments in the entire range of M_s .

Unfortunately, the foregoing three models for predicting the analytical $I_n \text{MR} \rightarrow \text{TRR}$ transition, which are all based on the length scale criterion, are independent of the radius of curvature of the concave cylinder, \mathfrak{R} , and its

initial angle, $\theta_w^{\text{initial}}$, which as shown in Fig. 8.1.52 do affect the actual $I_n\text{MR} \rightarrow \text{TRR}$ transition.

An approach partially overcoming these problems was suggested by Ben-Dor and Takayama (1985), who included $\theta_w^{\text{initial}}$ in the transition criterion given by Eq. (8.1.45) to obtain

$$\frac{\sin \theta_w^{\text{tr}} - \sin \theta_w^{\text{initial}}}{\theta_w^{\text{tr}} - \theta_w^{\text{initial}}} = \frac{M_s}{V_{10} + A_{10}}. \quad (8.1.48)$$

Similarly, Ben-Dor and Takayama (1985) showed that including $\theta_w^{\text{initial}}$ in the transition criterion given by Eq. (8.1.46) results in

$$\frac{\sin \theta_w^{\text{tr}} - \sin \theta_w^{\text{initial}}}{\sin \frac{1}{2}(\theta_w^{\text{tr}} - \theta_w^{\text{initial}})} = 2 \frac{M_s}{V_{10} + A_{10}}. \quad (8.1.49)$$

A comparison of predictions based on Eq. (8.1.48) and experimental results are shown in Fig. 4.17 of Ben-Dor (1991).

8.1.5.1.1.3.2 Triple Point Trajectory for Weak Incident Shock Waves

Using the assumptions of the model by which Eq. (8.1.47a) and (8.1.47b) were developed, Ben-Dor, Takayama, and Dewey (1987) developed an analytical model for predicting the triple point trajectory for relatively weak incident shock waves:

$$\chi = \text{tg}^{-1} \left\{ \frac{1}{M_s} [A_{10}^2 - (M_s - V_{10})^2]^{1/2} + \frac{V_{10}}{M_s} \theta \right\}. \quad (8.1.50)$$

By performing $\chi_g = \lim_{\theta \rightarrow 0} \chi$, the triple point trajectory angle at glancing incidence, χ_g , given by Eq. (8.1.36) is obtained. More details regarding this matter are given in Ben-Dor (1991, Section 4.1.1.3.2).

8.1.5.1.2 Shock Wave Reflections over Convex Cylinders

When a planar shock wave encounters a convex cylinder, it reflects over it either as an RR or as an MR, depending upon the initial wedge angle and the incident shock wave Mach number. The initial type of reflection can be determined using the pseudo-steady shock reflection theory presented in Section 8.1.4.

Consider, for example, Fig. 8.1.50 and note that if one draws a constant M_s line, then the number of transition boundaries intersected by this line depends on the value of M_s .

Let us consider the most general case of an incident shock wave having a Mach number M_s for which all the four types of reflection, i.e., SMR, TMR,

DMR, and RR, are possible. Let us also define the corresponding three transition wedge angles as $\theta_w^{\text{SMR} \leftrightarrow \text{TMR}}$, $\theta_w^{\text{TMR} \leftrightarrow \text{DMR}}$, and $\theta_w^{\text{DMR} \leftrightarrow \text{RR}}$.

Consider Fig. 8.1.56, where four different convex cylinders are drawn. Although they all have the same radius of curvature, their initial wedge angles are different. The slopes are 90° for the wedge $aa'e$, $\theta_w^{\text{RR} \leftrightarrow \text{DMR}}$ for the wedge $bb'e$, $\theta_w^{\text{DMR} \leftrightarrow \text{TMR}}$ for the wedge $cc'e$, and $\theta_w^{\text{TMR} \leftrightarrow \text{SMR}}$ for the wedge $dd'e$. Thus:

1. For all the convex cylinders with an initial angle in the range $\theta_w^{\text{RR} \leftrightarrow \text{DMR}} \leq \theta_w^{\text{initial}} \leq 90^\circ$, the initial reflection will be an RR.
2. For all the convex cylinders with an initial angle in the range $\theta_w^{\text{DMR} \leftrightarrow \text{TMR}} \leq \theta_w^{\text{initial}} \leq \theta_w^{\text{RR} \leftrightarrow \text{DMR}}$, the initial reflection will be a DMR.
3. For all the convex cylinders with an initial angle in the range $\theta_w^{\text{TMR} \leftrightarrow \text{SMR}} \leq \theta_w^{\text{initial}} \leq \theta_w^{\text{DMR} \leftrightarrow \text{TMR}}$, the initial reflection will be a TMR.

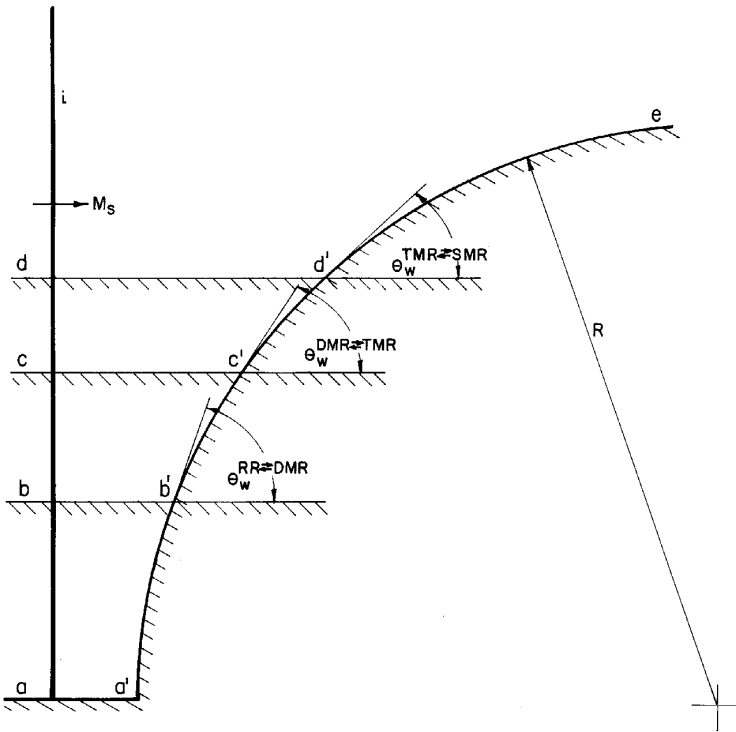


FIGURE 8.1.56 Schematic illustration of four different convex cylinders over which different reflection processes take place.

4. For all the convex cylinders with an initial angle in the range $0 \leq \theta_w^{\text{initial}} \leq \theta_w^{\text{TMR} \leftrightarrow \text{SMR}}$, the initial reflection will be an SMR.

Consequently, the initial reflection over a convex cylinder can be an RR, a DMR, a TMR, or an SMR, depending on the initial wedge angle.

An incident shock wave that propagates along the convex cylinder encounters an ever-decreasing wedge angle. Consequently, if the initial reflection is an RR, then it will eventually change into an MR. If, however, the initial reflection is an MR, then it will persist.

The foregoing discussion implies that if the initial reflection is an RR, it will follow the sequence $\text{RR} \rightarrow \text{DMR} \rightarrow \text{TMR} \rightarrow \text{SMR}$; if the initial reflection is a DMR, it will follow the sequence $\text{DMR} \rightarrow \text{TMR} \rightarrow \text{SMR}$; if the initial reflection is a TMR it will follow the sequence $\text{TMR} \rightarrow \text{SMR}$; and if the initial reflection is an SMR, it will remain an SMR. Photographs of an RR, a DMR, a TMR, and an SMR over a cylindrical convex surface are shown in Figs. 4.22a to 4.22d, respectively, of Ben-Dor (1991).

8.1.5.1.2.1 *RR→MR Transition*

As mentioned earlier, if a shock wave reflects initially over convex cylinder as an RR, it will eventually change to an MR. In an extensive experimental study Takayama and Sasaki (1983) showed that the $\text{RR} \rightarrow \text{MR}$ transition wedge angle θ_w^{tr} depends, in addition to the incident shock wave Mach number, M_s , on both the radius of curvature of the cylindrical wedge \mathfrak{R} and the initial wedge angle $\theta_w^{\text{initial}}$. The results of their experimental study are shown in Fig. 8.1.57. Line AB, the von Neumann criterion, is the $\text{RR} \leftrightarrow \text{MR}$ transition line appropriate to steady flows. Line AC, the detachment criterion, is the $\text{RR} \leftrightarrow \text{MR}$ transition line appropriate to pseudo-steady flows. All the recorded transition wedge angles lie below the $\text{MR} \leftrightarrow \text{RR}$ transition line of pseudo-steady flows. Furthermore, as the radius of curvature increases, the transition wedge angles increase and approach the pseudo-steady flow $\text{RR} \leftrightarrow \text{MR}$ transition line. Similarly, the experimental results indicate that the transition wedge angle decreases with decreasing initial wedge angles.

The experimental results suggest that as the radius of curvature approaches infinity, $\mathfrak{R} \rightarrow \infty$, the actual transition wedge angles approach those appropriate to pseudo-steady flows.

8.1.5.1.2.1 Effect of Surface Roughness Takayama, Ben-Dor, and Gotoh (1981) investigated, experimentally, the effect of surface roughness on the $\text{RR} \rightarrow \text{MR}$ transition. Pasting different sandpapers on the reflecting wedge surface imposed the roughness. It was evident from that θ_w^{tr} decreased as the roughness of the reflecting surface increased. In the case of an extremely rough

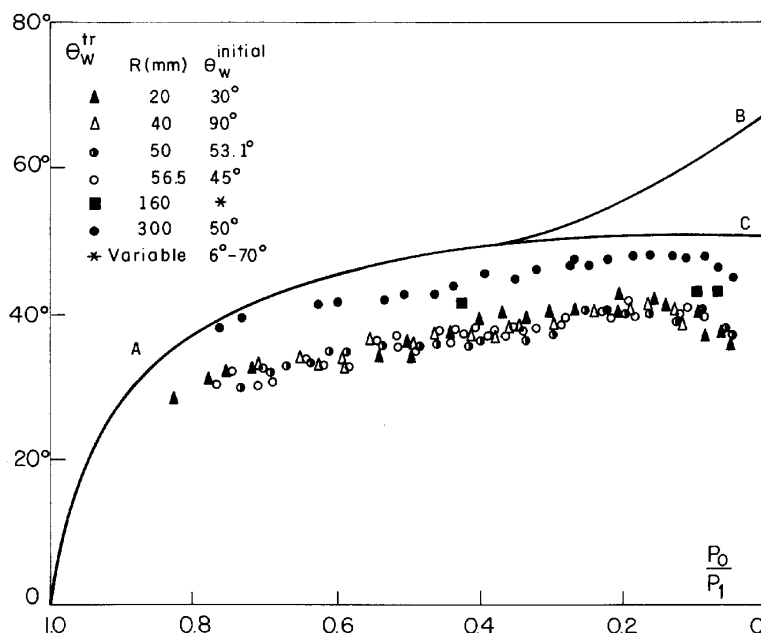


FIGURE 8.1.57 Experimental data with air illustrating the dependence of the transition wedge angle over a convex cylinder on the radius of curvature and the initial wedge angle.

surface, θ_w^{tr} was almost independent of M_s . This behavior of reduction in θ_w^{tr} with increasing roughness also occurs in the case of shock wave reflection over concave cylinders (see Section 8.1.5.1.1.1.1). For more details regarding this issue see also Ben-Dor (1991, Section 4.1.2.1.1).

Reichenbach (1985) investigated, experimentally, the RR \leftrightarrow MR transition over rough cylindrical surfaces, using cylindrical wedges whose surfaces were machined to obtain step and cubically shaped roughness. He showed that the roughness height ε , rather than its shape, is the dominant factor in determining the transition wedge angle.

8.1.5.1.2.2 Analytical Considerations

Similar to the reflection over concave cylinders (see Section 8.1.5.1.1.3) the RR \rightarrow MR transition occurs when the corner-generated signals catch up with the incident shock wave. Thus, the RR \rightarrow MR transition lines could be obtained, in principle, using models similar to those described in Section 8.1.5.1.1.3.1. Unfortunately, however, similar analytical considerations for convex surfaces are much more difficult because the reflected shock wave, at

the leading edge of the reflecting wedge, is much stronger when the incident shock wave reflects over a convex surface. Therefore, the simplifying assumptions used to analyze shock wave reflections over concave surfaces cannot be applied in the case of shock wave reflections over convex surfaces.

8.1.5.1.2.3 Numerical Predictions of the RR \rightarrow MR Transition

Although there are no analytical models for predicting the RR \rightarrow MR transition over convex cylinders, there are some relatively simple numerical codes capable of predicting this transition.

Recorded transition wedge angles, θ_w^{tr} , over a convex cylinder with $R = 50$ mm and $\theta_w^{initial} = 90^\circ$ are shown in Fig. 8.1.58 together with some analytical and numerical transition lines. Lines AB and AC are the RR \leftrightarrow MR transition lines in steady and in pseudo-steady flows, respectively. Line D was numerically calculated by Heilig (1969), who applied Whitham's (1957) classical ray-shock theory. Line E is a similar calculation by Itoh, Okazaki, and Itaya (1981), who used Milton's (1975) modification of Whitham's theory.

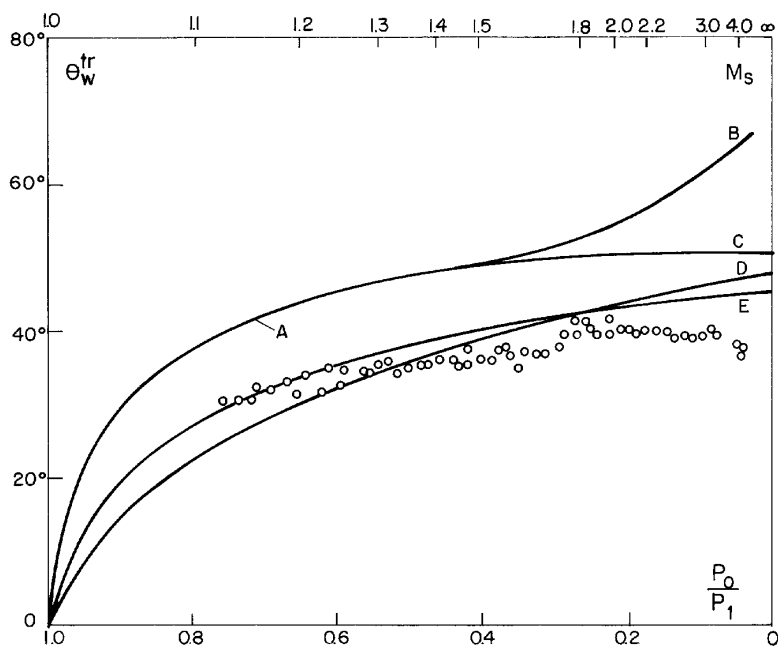


FIGURE 8.1.58 Comparison between the numerical predictions and experimental results of the transition wedge angle over a convex cylinder with $R = 50$ mm and $\theta_w^{initial} = 90^\circ$.

A comparison between curves D and E and the experimental results indicates that Milton's modification of Whitham's theory improves the agreement between the numerical predictions and the experimental results. The numerical predictions of Heilig (1969) and Itoh, Okazaki and Itaya (1981) become poorer as M_s increases beyond $M_s \approx 2$ because the transition lines gradually increase with increasing M_s , whereas the experimental results level out and even exhibit a slight decrease. This could be due to the fact that for $M_s > 2$ the shock induced flow becomes supersonic.

8.1.5.1.2.4 Additional Remark

The reflection of shock waves over elliptical convex surfaces was investigated experimentally by Heilig (1969). The results resembled, in general, features of those obtained over convex cylinders with the appropriate radius of curvature.

8.1.5.1.3 Shock Wave Reflections over Two-Facet Wedges

Ginzburg and Markov (1975) and Srivastava and Deschambault (1984) experimentally investigated the reflection of planar shock waves over two-facet concave and convex wedges, respectively. Schematic drawings of a concave and a convex two-facet wedge are shown in Figs. 8.1.59a and 8.1.59b, respectively. For both wedges, θ_{w1} and θ_{w2} are the angles of the first and second surfaces and $\Delta\theta_w$ is the inclination of the second surface with respect to the first surface, i.e., $\Delta\theta_w = \theta_{w2} - \theta_{w1}$. Based on these definitions,

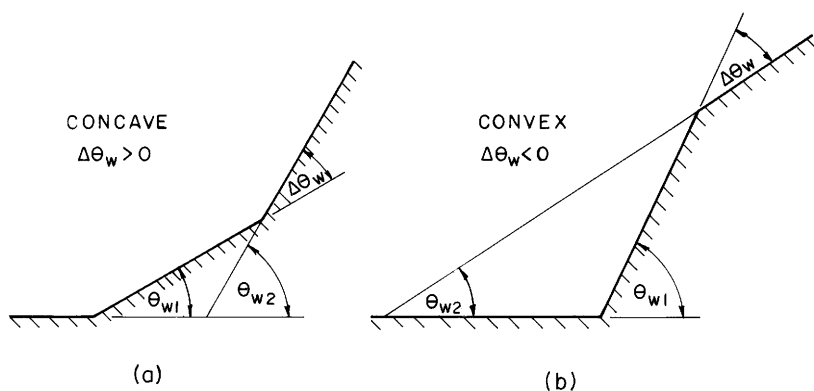


FIGURE 8.1.59 Schematic illustrations of (a) two-facet concave wedge; (b) two-facet convex wedge.

$\Delta\theta_w > 0$ for a concave two-facet wedge, $\Delta\theta_w < 0$ for a convex two-facet wedge, and $\Delta\theta_w = 0$ for a single-face straight wedge.

8.1.5.1.3.1 Domains of Different Types of Reflection Processes

Ben-Dor, Dewey, and Takayama (1987a) and Ben-Dor *et al.* (1988) studied the reflection of planar shock waves over two-facet wedges both analytically and experimentally. They showed that seven different reflection processes are possible. They are shown in Fig. 8.1.60 in the $(\theta_{w1}, \theta_{w2})$ -plane for a given M_s . The line $\Delta\theta_w = 0$ divides the $(\theta_{w1}, \theta_{w2})$ -plane into two domains: the convex and the concave two-facet wedge domains. The $RR \leftrightarrow MR$ transition condition in pseudo-steady flows, namely the detachment angle, is $\theta_w^D(M_s)$. Consequently, the line $\theta_{w1} = \theta_w^D(M_s)$ divides the $(\theta_{w1}, \theta_{w2})$ -plane into two domains: a domain in which the incident shock wave reflects over the first surface as an MR, i.e., $\theta_{w1} < \theta_w^D(M_s)$, and a domain in which the incident shock wave reflects over the first surface as an RR, i.e., $\theta_{w1} > \theta_w^D(M_s)$. Similarly, the line $\theta_{w2} = \theta_w^D(M_s)$ divides the $(\theta_{w1}, \theta_{w2})$ -plane into two domains: a domain in which the finally established reflection over the second surface is an MR, i.e., $\theta_{w2} < \theta_w^D(M_s)$, and

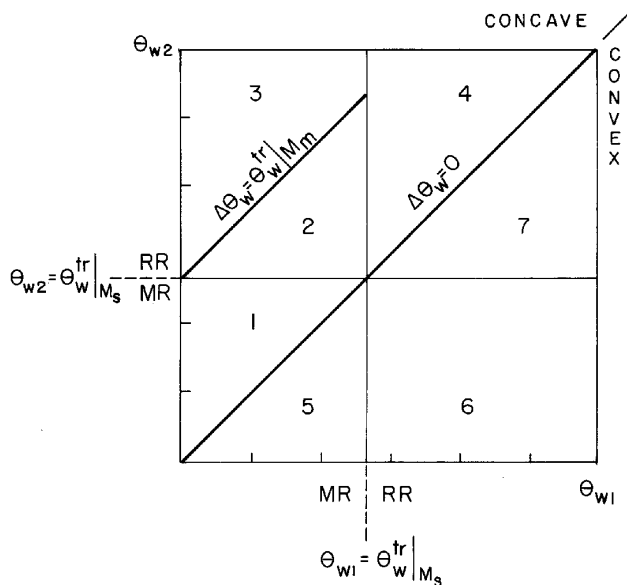


FIGURE 8.1.60 Domains of different reflection processes over two-facet wedges.

a domain in which the finally established reflection over the second surface is an RR, i.e., $\theta_{w2} > \theta_w^D(M_s)$.

Finally, if $\theta_{w1} < \theta_w^D(M_s)$ and if $\Delta\theta_w > 0$, the Mach stem of the MR that is formed over the first surface interacts with a compressive wedge having an angle of $\Delta\theta_w = \theta_{w2} - \theta_{w1}$. Consequently, the subdomain defined by $\theta_{w1} < \theta_w^D(M_s)$ and $\theta_{w2} > \theta_w^D(M_s)$ in which the reflection over the first surface is an MR and the final reflection over the second surface is an RR is further divided by the line $\Delta\theta_w = \theta_w^D(M_m)$, where $\theta_w^D(M_m)$ is the detachment angle appropriate to the Mach stem Mach number, M_m , into two parts: The Mach stem that propagates along the first surface reflects over the second surface as an MR for $\Delta\theta_w < \theta_w^D(M_m)$, and as an RR for $\Delta\theta_w > \theta_w^D(M_m)$. If the Mach stem is assumed to be straight and perpendicular to the surface, then

$$M_m = M_s \frac{\cos \chi}{\cos(\theta_{w1} + \chi)},$$

where χ is the triple point trajectory angle. This relation indicates that $M_m > M_s$. However, as shown in Fig. 8.1.50, for $M_s \geq 2$ the detachment angle does not depend strongly on M_s . Hence, $\theta_w^D(M_s) \cong \theta_w^D(M_m)$.

Ben-Dor *et al.* (1988) showed experimentally that if the second surface of a two-facet wedge is long enough, then the final wave configuration of the reflection that develops over it (an RR on an MR) asymptotically approaches the wave configuration that would have been obtained had the incident shock wave reflected over a straight wedge having an angle equal to θ_{w2} .

The seven domains of the different types of reflection processes are numbers 1 to 7 in Fig. 8.1.60 and are summarized in Table 8.1.1.

TABLE 8.1.1 The Seven Different Processes of Shock Wave Reflection over Convex and Concave Two-Facet Wedges

	θ_{w1}	θ_{w2}	$\Delta\theta_w$	First surface	Second surface	Domain in Fig. 8.1.60
Convex	$> \theta_w^D(M_s)$	$> \theta_w^D(M_s)$	—	RR	RR	7
Convex	$< \theta_w^D(M_s)$	$< \theta_w^D(M_s)$	—	MR	MR	5
Convex	$> \theta_w^D(M_s)$	$< \theta_w^D(M_s)$	—	RR	MR	6
Concave	$> \theta_w^D(M_s)$	$> \theta_w^D(M_s)$	—	RR	RR	4
Concave	$< \theta_w^D(M_s)$	$> \theta_w^D(M_s)$	$> \theta_w^D(M_m)$	MR	RR \rightarrow RR	3
Concave	$< \theta_w^D(M_s)$	$< \theta_w^D(M_s)$	$< \theta_w^D(M_m)$	MR	MR \rightarrow MR	1
Concave	$< \theta_w^D(M_s)$	$> \theta_w^D(M_s)$	$< \theta_w^D(M_m)$	MR	MR \rightarrow TRR	2

8.1.5.1.3.2 *RR \leftrightarrow MR Transition over Two-Facet Wedges*

The experimental study of Ben-Dor, Takayama, and Dewey (1987c) indicated that the actual RR \leftrightarrow MR transition wedge angle, θ_w^{tr} , over a two-facet wedge depends on $\Delta\theta_w$. Based on their study θ_w^{tr} is greater than that appropriate to the sonic criterion for concave two-facet wedges, and θ_w^{tr} is smaller than that appropriate to the sonic criterion for convex two-facet wedges. This behavior is similar to that shown earlier for concave and convex cylinders (see Sections 8.1.5.1.1.1 and 8.1.5.1.2.1, respectively). However, whereas in the case of shock wave reflections over concave cylinders the actual θ_w^{tr} is above the analytical steady-flow RR \leftrightarrow MR transition line (see line B in Fig. 8.1.52), for the reflection of shock waves over concave two-facet wedges it is possible to obtain actual transition wedge angles below this transition line. For more details see Ben-Dor (1991, Section 4.1.3.2).

8.1.5.1.3.3 *Additional Remarks*

The wave configurations associated with the reflection processes of some of the domains shown in Fig. 8.1.60 and described in Table 8.1.1 were solved analytically. Li and Ben-Dor (1995b) solved the reflection process associated with domain (4); Li, Ben-Dor, and Han (1994) solved the reflection process associated with domain (7); Li and Ben-Dor (1999) solved the reflection processes associated with domains (1) and (2).

8.1.5.2 NONCONSTANT VELOCITY SHOCK WAVE REFLECTIONS OVER STRAIGHT SURFACES

The reflection of a nonconstant velocity shock wave over straight surfaces is another example of a truly unsteady process. Although the analytical treatment of a reflection of this type might be important to better understand the more complex reflection of a spherical shock wave (nonconstant velocity shock wave) over the ground surface (straight surface), which is dealt with in the next section, unfortunately, to the best of the author's knowledge, no work has been done on this reflection process. This is in spite of the fact that experimental investigations of this type of shock wave reflection process can be performed in a relatively easy way in a shock tube. The only requirement is to generate an accelerating or a decelerating (decaying) planar shock wave and reflect it over a wedge with a straight surface. Techniques for generating decaying planar shock waves in shock tubes can be found in the literature related to shock tubes.

8.1.5.3 SPHERICAL SHOCK WAVE REFLECTIONS OVER STRAIGHT AND NONSTRAIGHT SURFACES

The reflection of spherical shock waves, e.g., blast waves over straight and nonstraight surfaces, has been experimentally investigated quite extensively in the past few decades, e.g., Dewey, McMillin, and Classen (1977), Dewey and McMillin (1981), and Hu and Glass (1986).

When an explosive is detonated above the ground, a spherical shock wave is formed. Such a spherical shock wave, at two different times, is shown in Fig. 8.1.61. As the spherical shock wave propagates outward, the point where it touches the surface encounters an ever-decreasing effective reflecting wedge angle, i.e., $\theta_{w,2} < \theta_{w,1}$. Thus, besides the continuous decrease in the instantaneous incident shock wave Mach number, $M_{s,2} < M_{s,1}$, the effective reflecting wedge angle also decreases with time. Consequently, the spherical shock wave reflects over the surface initially as an RR, then, depending upon its strength, the reflection changes as it propagates outwards to a DMR, a TMR and finally to an SMR. A regular and a Mach reflection of a spherical shock wave over a straight surface are shown in Figs. 8.1.62a and 8.1.62b, respectively.

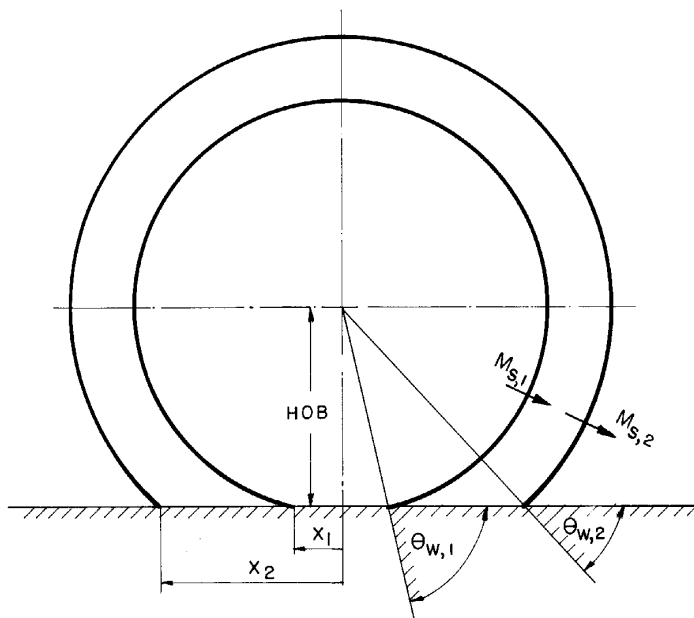


FIGURE 8.1.61 Schematic illustration of the instantaneous reflecting wedge angle of a spherical shock wave propagating over a straight surface. Recall that the instantaneous incident shock wave Mach number also decreases with time.

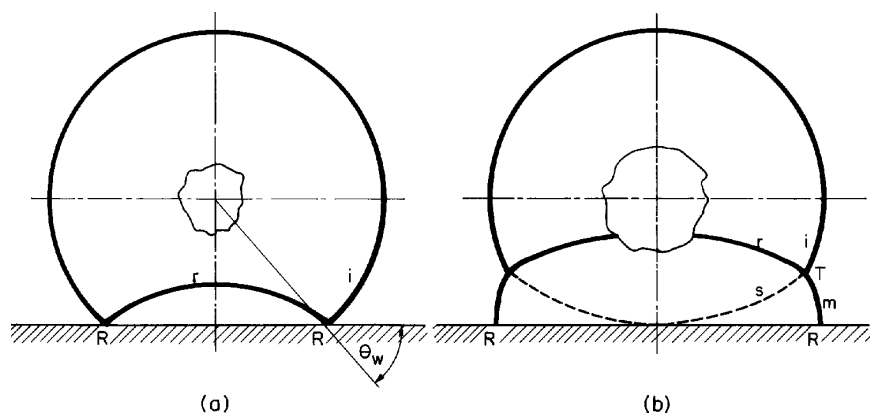


FIGURE 8.1.62 Schematic illustration of (a) regular reflection and (b) Mach reflection of a spherical shock wave over a straight surface.

The domains of different types of reflections (in pseudo-steady flows) in the (M_s, θ_w) -plane for air together with spherical shock wave trajectories, i.e., $M_s(\theta_w)$, are shown in Fig. 8.1.63, which was originally drawn by Hu and Glass (1986). The trajectories differ from each other by the nondimensional height of burst, HOB (see Fig. 8.1.61).

The nondimensional factor is $(Wp_0/W_0p)^{1/3}$, where W is the weight (equivalent to TNT) of the explosive charge used to generate the blast wave, and p is the atmospheric pressure ($W_0 = 1$ kg TNT and $p_0 = 1$ atm). The nondimensional distance X denotes the radial location (measured from the center of explosion on the ground; see Fig. 8.1.61). The $X = 0$ line coincides with the $\theta_w = 90^\circ$ line. It is seen that for an explosive charge of 1 kg TNT and a height of burst of 0.8 m, at 1 atm, the blast wave has a strength equivalent to $M_s \cong 3.7$ upon colliding with the reflecting surface. The initial reflection for this case is an RR that changes later to a DMR, then to a TMR, and finally to an SMR until the spherical shock wave degenerates to a sound wave, $M_s \rightarrow 1$. On the other hand, if the HOB for the same charge is 2 m, the instantaneous Mach number when the blast wave collides with the ground surface is $M_s \cong 2$ and the RR changes directly to an SMR before it degenerates to a sound wave. The trajectories shown in Fig. 8.1.63 are fits based on the best experimental data. Since the pseudo-steady transition lines shown in Fig. 8.1.63 are not applicable for unsteady flows, the foregoing description should be regarded as explanatory only.

An experimental test of the applicability of the transition lines between the various types of reflections in pseudo-steady flows for the case of blast wave reflections is shown in Fig. 8.1.64, where the actual $RR \rightarrow MR$ transition

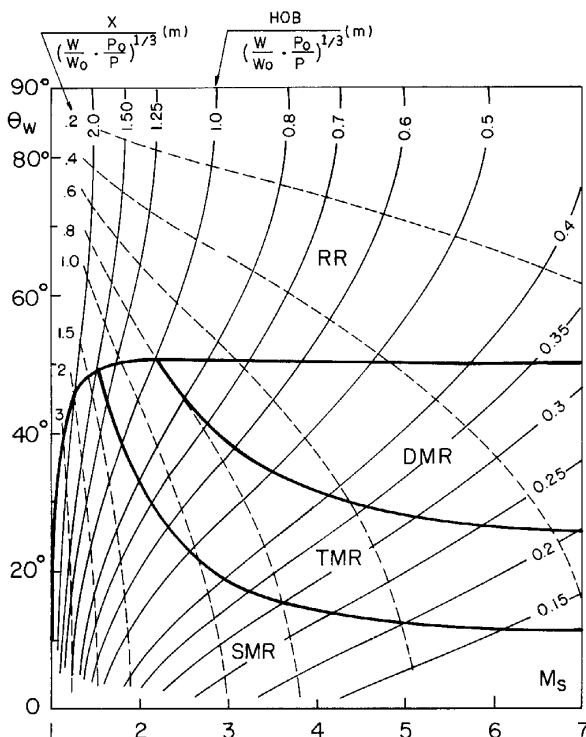


FIGURE 8.1.63 Domains of different types of reflections in pseudo-steady flows and spherical shock wave trajectories (courtesy of Professor I. I. Glass).

angles for seven different heights of burst experiments are connected by a dashed line. The experimental $RR \rightarrow MR$ transition wedge angles are up to 10° smaller or larger than the pseudo-steady $RR \leftrightarrow MR$ transition line. Furthermore, whereas the pseudo-steady $RR \leftrightarrow MR$ transition line slightly decreases as M_s increases, the unsteady experimental $RR \rightarrow MR$ transition line shows a gradual increase with increasing M_s . Thus, despite the fact that the (M_s, θ_w) plot is helpful in determining the sequence of events during the $RR \rightarrow MR$ transition, it is quite obvious that it cannot predict the actual transition angles accurately enough.

8.1.5.3.1 Additional Remarks

Spherical shock waves can be generated in shock tubes by producing a planar shock wave inside a tube and allowing the shock wave to emerge from it.

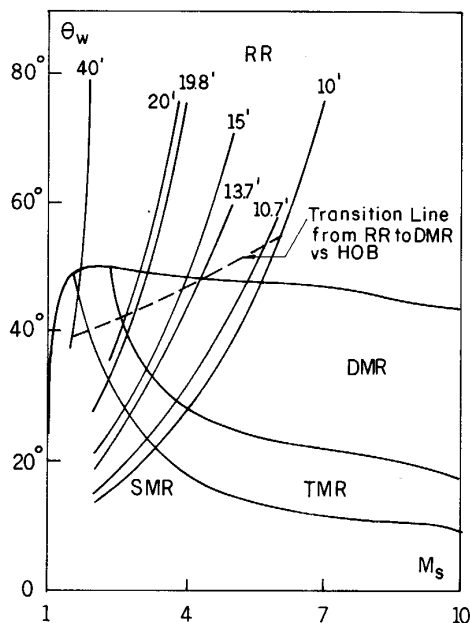


FIGURE 8.1.64 Comparison of average transition lines of actual blast wave experiments with the transition boundaries appropriate to pseudo-steady reflections in real nitrogen (courtesy of Mr. J. Wisotski, Denver Research Institute, Denver, Colorado).

Although at early stages the shape of the shock wave emerging from the end of the tube is not spherical, at later times it attains a perfectly spherical shape. Takayama and Sekiguchi (1981a, 1981b) used this technique of producing spherical shock waves in a shock tube to investigate the reflection of spherical shock waves from various surfaces.

ACKNOWLEDGMENTS

The author thanks his colleagues Profs. A. Chpoum, J. M. Dewey, M. Ivanov, K. Takayama and D. Zeitoun with whom he has been collaborating for over 20 years in order to better understand the shock wave reflection phenomena.

REFERENCES

- Azevedo, D.J. (1989). "Analytic prediction of shock patterns in a high-speed, wedge-bounded duct," Ph.D. Thesis, Dept. Mech. and Aero. Eng., State Univ. N.Y. Buffalo, New York.

- Azevedo, D.J. and Liu, C.S. (1993). "Engineering approach to the prediction of shock patterns in bounded high-speed flows," *AIAA J.* **31**(1): 83–90.
- Bazhenova, T.V., Fokeev, V.P., and Gvozdeva, L.G. (1976). "Regions of various forms of Mach reflection and its transition to regular reflection," *Acta Astro.* **3**: 131–150.
- Ben-Dor, G. (1978a). "Regions and transitions of nonstationary oblique shock wave diffractions in perfect and imperfect gases," UTIAS Rept. 232, Inst. Aerospace Studies, Univ. Toronto, Toronto, Canada.
- Ben-Dor, G. (1978b). "Nonstationary oblique shock wave reflections in nitrogen and argon: Experimental results," UTIAS Rept. 237, Inst. Aerospace Studies, Univ. Toronto, Canada.
- Ben-Dor, G. (1980). "Analytical solution of a double Mach reflection," *AIAA J.* **18**: 1036–1043.
- Ben-Dor, G. (1981). "Relations between first and second triple point trajectory angles in double Mach reflection," *AIAA J.* **19**: 531–533.
- Ben-Dor, G. (1987). "A reconsideration of the three-shock theory for a pseudo-steady Mach reflection," *J. Fluid Mech.* **181**: 467–484.
- Ben-Dor, G. (1990). "Structure of the contact discontinuity of nonstationary Mach reflections," *AIAA J.* **28**: 1314–1316.
- Ben-Dor, G. (1991). *Shock Wave Reflection Phenomena*. Springer Verlag, New York.
- Ben-Dor, G. and Elperin, T. (1991). "Analysis of the wave configuration resulting from the termination of an inverse Mach reflection," *Shock Waves* **1**(3): 237–241.
- Ben-Dor, G., and Glass, I.I. (1978). "Nonstationary oblique shock wave reflections: Actual isopycnics and numerical experiments," *AIAA J.* **16**: 1146–1153.
- Ben-Dor, G., and Takayama, K. (1985). "Analytical prediction of the transition from Mach to regular reflection over concave cylinders," *J. Fluid Mech.* **158**: 365–380.
- Ben-Dor, G., and Takayama, K. (1986/7). "The dynamics of the transition from Mach to regular reflection over concave cylinders," *Israel J. Tech.* **23**: 71–74.
- Ben-Dor, G., Dewey, J.M. and Takayama, K. (1987a). "The reflection of a planar shock wave over a double wedge," *J. Fluid Mech.* **176**: 483–520.
- Ben-Dor, G., Mazor, G., Takayama, K., and Igra, O. (1987b). "The influence of surface roughness on the transition from regular to Mach reflection in a pseudo-steady flow," *J. Fluid Mech.* **176**: 336–356.
- Ben-Dor, G., Takayama, K., and Dewey, J.M. (1987c). "Further analytical considerations of the reflection of weak shock waves over a concave wedge," *Fluid Dyn. Res.* **2**: 77–85.
- Ben-Dor, G., Dewey, J.M., McMillin, D.J., and Takayama, K. (1988). "Experimental investigation of the asymptotically approached Mach reflection over the second surface in the reflection over a double wedge," *Exp. Fluids* **6**: 429–434.
- Ben-Dor, G., Elperin, T., and Golshtein, E. (1997). "Monte Carlo analysis of the hysteresis phenomenon in steady shock wave reflections," *AIAA J.* **35**(11): 1777–1779.
- Ben-Dor, G., Elperin, T., Li, H., and Vasiliev, E. (1999a). "The influence of downstream-pressure on the shock wave reflection phenomenon in steady flows," *J. Fluid Mech.* **386**: 213–232.
- Ben-Dor, G., Vasiliev, E., Elperin, T., and Chpoun, A. (2000). "Hysteresis phenomena in the interaction process of conical shock waves. Experimental and numerical investigations," *J. Fluid Mech.*, to be published.
- Birkhoff, G. (1950). *Hydrodynamics, A Study in Logic, Fact and Similitude*, Princeton Univ. Press.
- Chpoun, A., and Ben-Dor, G. (1995). "Numerical conformation of the hysteresis phenomenon in the regular to the Mach reflection transition in steady flows," *Shock Waves* **5**(4): 199–204.
- Chpoun, A., and Lengrand, J.C. (1997). "Conformation experimentale d'un phenomene d'hysteresis lors de l'interaction de deux chocs obliques de familles differentes," *C.R. Acad. Sci. Paris*, **304**: 1.
- Chpoun, A., Passerel, D., Li, H., and Ben-Dor, G. (1995). "Reconsideration of the oblique shock wave reflection in steady flows. I. Experimental investigation," *J. Fluid Mech.* **301**: 19–35.

- Clarke, J.F. (1984a). "Regular reflection of a weak shock wave from a rigid porous wall," *Quar. J. Mech. and Math.* 37: 87–111.
- Clarke, J.F. (1984b). "The reflection of weak shock waves from absorbent surfaces," *Proc. Roy. Soc. Lond. A396*: 365–382.
- Colella, P. and Henderson, L.F. (1990). "The von Neumann paradox for the diffraction of weak shock waves," *J. Fluid Mech.* 213: 71–94.
- Courant, R., and Freidrichs, K.O. (1948). *Hypersonic Flow and Shock Waves*, Wiley Interscience, New York.
- Dewey, J.M., and McMillin, D.J. (1981). "An analysis of the particle trajectories in spherical blast waves reflected from real and ideal surfaces," *Canadian J. Phys.* 59: 1380–1390.
- Dewey, J.M., and McMillin, D.J. (1985). "Observation and analysis of the Mach reflection of weak uniform plane shock waves. Part 1. Observation," *J. Fluid Mech.* 152: 49–66.
- Dewey, J.M., and van Netten, A.A. (1991). "Observations of the initial stages of the Mach reflection process," in *Shock Waves*, Vol. 1, Ed. K. Takayama, Springer Verlag, Heidelberg, pp. 227–232.
- Dewey, J.M., and van Netten, A.A. (1995). "Non-self-similarity of the initial stages of Mach reflection," in *Shock Waves*, Ed. B. Sturtevant, J.E. Shepherd, and H.G. Hornung, World Scientific, Singapore, pp. 399–404.
- Dewey, J.M., McMillin, D.J., and Classen, D.F. (1977). "Photogrammetry of spherical shocks reflected from real and ideal surfaces," *J. Fluid Mech.* 81: 701–717.
- Fomin, V.M., Hornung, H.G., Ivanov, M.S., Kharitonov, A.M., Klemenov, G.P., Kudryavtsev, A.N., and Pavlov, A.A. (1996). "The study of transition between regular and Mach reflection of shock waves in different wind tunnels," *Proc. 12th Intl. Reflection Symp.*, Pilanesberg, South Africa, 137–151.
- Friend, W.H. (1958). "The interaction of plane shock wave with an inclined perforated plate," UTIAS TN 25, Inst. Aerospace Studies, Univ. Toronto, Toronto, Ont., Canada.
- Ginzburg, I.P. and Marakov, Y.S. (1975). "Experimental investigation of the reflection of a shock wave from a two-facet wedge," *Fluid Mech.—Soviet Res.* 4: 167–172.
- Glaz, H.M., Colella, P., Collins, J.P., and Ferguson, E. (1988). "Nonequilibrium effects in oblique shock-wave reflection," *AIAA J.* 26: 698–705.
- Heilig, W.H. (1969). "Diffraction of shock wave by a cylinder," *Phys. Fluids Suppl. I.* 12: 154–157.
- Henderson, L.F. (1967). "The reflection of a shock wave at a rigid wall in the presence of a boundary layer," *J. Fluid Mech.* 30: 699–722.
- Henderson, L.F. (1982). "Exact expressions for shock reflection transition criteria in a perfect gas," *ZAMM* 62: 258–261.
- Henderson, L.F., and Gray, P.M. (1981). "Experiments on the diffraction of strong blast waves," *Proc. Roy. Soc. Lond. A377*: 363–378.
- Henderson, L.F., and Lozzi, A. (1975). "Experiments on transition of Mach reflection," *J. Fluid Mech.* 68: 139–155.
- Henderson, L.F., and Lozzi, A. (1979). "Further experiments on transition to Mach reflection," *J. Fluid Mech.* 94: 541–559.
- Henderson, L.F., Ma, J.H., Sakurai, A., and Takayama, K. (1990). "Refraction of a shock wave at an air–water interface," *Fluid Dyn. Res.* 5: 337–350.
- Hornung, H.G. (1986). "Regular and Mach reflection of shock waves," *Ann. Rev. Fluid Mech.* 18: 33–58.
- Hornung, H.G., and Robinson, M.L. (1982). "Transition from regular to Mach reflection of shock waves. Part 2. The steady flow criterion," *J. Fluid Mech.* 123: 155–164.
- Hornung, H.G., and Taylor, J.R. (1982). "Transition from regular to Mach reflection of shock waves. Part 1. The effect of viscosity on the pseudo-steady case," *J. Fluid Mech.* 123: 143–153.

- Hornung, H.G., Oertel, H., Jr., and Sandeman, R.J. (1979). "Transition to Mach reflection of shock waves in steady and pseudo-steady flows with and without relaxation," *J. Fluid Mech.* **90**: 541–560.
- Hu, T.C.J., and Glass, I.I. (1986). "Blast wave reflection trajectories from a height of burst," *AIAA J.* **24**: 607–610.
- Itoh, S., Okazaki, N., and Itaya, M. (1981). "On the transition between regular and Mach reflection in truly non-stationary flows," *J. Fluid Mech.* **108**: 383–400.
- Ivanov, M.S., Gimelshein, S.F., and Beylich, A.E. (1995). "Hysteresis effect in stationary reflection of shock waves," *Phys. Fluids* **7**: 685–687.
- Ivanov, M.S., Zeitoun, D., Vuillon, J., Gimelshein, S.F., and Markelov, G.N. (1996). "Investigation of the hysteresis phenomena in steady shock wave reflection using kinetic and continuum methods," *Shock Waves* **5**(6): 341–346.
- Ivanov, M.S., Gimelshein, S.F., Kudryavtsev, A.N., and Markelov, G.N. (1998a). "Transition from regular to Mach reflection in two- and three-dimensional flows," *Proc. 21st Intl. Symp. Shock Waves*, Vol. 2, Panther Publishing, Fyshwick, pp. 813–818.
- Ivanov, M.S., Kharitonov, A.M., Klemenkov, G.P., Kudryavtsev, A.N., Nikiforov, S.B., and Fomin, V.M. (1998b). "Influence of test model aspect ratio in experiments on the MR \leftrightarrow RR transition," *Proc. 13th Intl. Mach Reflection Symp.*, Beer-Sheva, Israel, Vol. 3, Ed. G. Ben-Dor.
- Ivanov, M.S., Klemenkov, G.P., Kudryavtsev, A.N., Nikiforov, S.B., Pavlov, A.A., Fomin, V.M., Kharitonov, A.M., Khotyanovsky, D.V., and Hornung, H.G. (1998c). "Experimental and numerical study of the transition between regular and Mach reflections of shock waves in steady flows," *Proc. 21st Intl. Symp. Shock Waves*, Vol. 2, Panther Publishing, Fyshwick, pp. 819–824.
- Ivanov, M.S., Markelov, G.N., Kudryavtsev, A.N., and Gimelshein, S.F. (1998d). "Numerical analysis of shock wave reflection transition in steady flows," *AIAA J.* **36**(11): 2079–2086.
- Ivanov, M.S., Ben-Dor, G., Elperin, T., Kudryavtsev, A.N., and Khotyanovsky, D.V. (2000a). "Flow-Mach-number-variation-induced hysteresis in steady shock wave reflections," *AIAA J.* to be published.
- Ivanov, M.S., Ben-Dor, G., Elperin, T., Kudryavtsev, A.N., and Khotyanovsky, D.V. (2000b). "The reflection of asymmetric shock waves in steady flows: A numerical investigation," *J. Fluid Mech.*, to be published.
- Kawamura, R., and Saito, H. (1956). "Reflection of shock waves—1. Pseudo-stationary case," *J. Phys. Soc. Japan* **11**: 584–592.
- Kobayashi, S., Adachi, T., and Suzuki, T. (1995). "Regular reflection of a shock wave over a porous layer: Theory and experiment," in *Shock Waves @ Marseille IV*, Eds. R. Brun and L.Z. Dumitrescu, Springer-Verlag, Heidelberg, Germany, pp. 175–180.
- Kudryavtsev, A.N., Khotyanovsky, D.V., Markelov, G.N., and Ivanov, M.S. (1999). "Numerical simulation of reflection of shock waves by finite-width wedge," *22nd Intl. Symp. Shock Waves*, London.
- Landau, L.D., and Lifshitz, E.M. (1987). *Fluid Mechanics*, 2nd Ed., Pergamon Press, Oxford.
- Law, C.K., and Glass, I.I. (1971). "Diffraction of strong shock waves by a sharp compressive corner," *CASI Trans.* **4**: 2–12.
- Lee, J.-H., and Glass, I.I. (1984). "Pseudo-stationary oblique-shock wave reflections in frozen and equilibrium air," *Prog. Aerospace Sci.* **21**: 33–80.
- Li, H., and Ben-Dor, G. (1995a). "Reconsideration of pseudo-steady shock wave reflections and transition criteria between them," *Shock Waves* **5**: 59–73.
- Li, H., and Ben-Dor, G. (1995b). "Interaction of regular reflection with a compressive wedge: Analytical solution," *AIAA J.* **33**(5): 955–958.
- Li, H., and Ben-Dor, G. (1996). "Application of the principle of minimum entropy production to shock wave reflections. I. Steady flows," *J. Appl. Phys.* **80**: 2027–2037.

- Li, H., and Ben-Dor, G. (1997). "A parametric study of Mach reflection in steady flows," *J. Fluid Mech.* 341: 101–125.
- Li, H., and Ben-Dor, G. (1999). "Interaction of two Mach reflections over concave double wedges—Analytical model," *Shock Waves* 9(4): 259–268.
- Li, H., Ben-Dor, G., and Han, Z.Y. (1994). "Analytical prediction of the reflected–diffracted shock wave shape in the interaction of a regular reflection with an expansive corner," *Fluid Dyn. Res.* 14: 229–239.
- Li, H., Levy, A., and Ben-Dor, G. (1995). "Analytical prediction of regular reflection over porous surfaces in pseudo-steady flows," *J. Fluid Mech.* 282: 219–232.
- Li, H., Chpoun, A., and Ben-Dor, G. (1999). "Analytical and experimental investigations of the reflection of asymmetric shock waves in steady flow," *J. Fluid Mech.* 390: 25–43.
- Lock, G., and Dewey, J.M. (1989). "An experimental investigation of the sonic criterion for transition from regular to Mach reflection of weak shock waves," *Exp. Fluids* 7: 289–292.
- Mach, E. (1878). "Über den Verlauf von Funkenwellen in der Ebene und im Raume," *Sitzungsber. Akad. Wiss. Wien* 78: 819–838.
- Milton, B.E. (1975). "Mach reflection using ray-shock theory," *AIAA J.* 13: 1531–1533.
- Molder, S. (1971). "Reflection of curved shock waves in steady supersonic flow," *CASI Trans.* 4: 73–80.
- Molder, S. (1979). "Particular conditions for the termination of regular reflection of shock waves," *CASI Trans.* 25: 44–49.
- Onodera, H. (1986). "Shock propagation over perforated wedges," M.Sc. Thesis, Inst. High Speed Mech., Tohoku Univ., Sendai, Japan.
- Onodera, H., and Takayama, K. (1990). "Shock wave propagation over slitted wedges," *Inst. Fluid Sci. Rept.*, 1, 45–66, Tohoku Univ., Sendai, Japan.
- Onofri, M., and Nasuti, F. (1999). "Theoretical considerations on shock reflections and their implications on the evaluations of air intake performance," *Proc. 22nd Int. Symp. Shock Waves*, London. Vol. 2, pp. 1285–1290.
- Pant, J.C. (1971). "Reflection of a curved shock from a straight rigid boundary," *Phys. Fluids* 14: 534–538.
- Reichenbach, H. (1985). "Roughness and heated layer effects on shock-wave propagation and reflection—Experimental results," *Ernst Mach Inst.*, Rept. E24/85, Freiburg, West Germany.
- Schmidt, B. (1989a). "Shock wave transition from regular to Mach reflection on a wedge-shaped edge," *Z. Ang. Math. and Mech.* 65: 234–236.
- Schmidt, B. (1989b). "Structure of incipient triple point at the transition from regular reflection to Mach reflection," in *Refined Gas Dynamics: Theoretical and Computational Techniques*, Eds. E.P. Muntz, D.P. Weaver, D.H. Campbell, Progress in Astronautics and Aeronautics, Vol. 118, pp. 597–607.
- Semenov, A.N., and Syshchikova, M.P. (1975). "Properties of Mach reflection in the interaction of shock waves with a stationary wedge," *Comb. Expl. Shock Waves* 11: 506–515.
- Shapiro, A.H. (1953). *The Dynamics and Thermodynamics of Compressible Fluid Flow*, Vol. II, The Ronald Press Co., New York.
- Shirouzu, M., and Glass, I.I. (1986). "Evaluation of assumptions and criteria in pseudo-stationary oblique shock-wave reflections," *Proc. Roy. Soc. Lond., Ser. A* 406: 75–92.
- Shiroyu, T., and Nishida, M. (1995). "Numerical studies of oblique shock reflection in steady two dimensional flows," *Memoirs Faculty Eng., Kyushu Univ.* 55: 193–204.
- Skews, B.W. (1971/2). "The effect of an angular slipstream on Mach reflection," Dept. Note, McMaster Univ., Hamilton, Ont., Canada.
- Skews, B.W. (1992). "Oblique reflection of shock waves from rigid porous materials," 10th Mach Reflection Symp., Univ. of Denver, Colorado.

- Skews, B.W. (1997). "Aspect ratio effects in wind tunnel studies of shock wave reflection transition," *Shock Waves* 7: 373–383.
- Skews, B.W. (1998). "Oblique shadowgraph study of shock wave reflection between two wedges in supersonic flow," Proc. 13th Intl. Mach. Reflection Symp., Vol. 3, Ed. G. Gen-Dor, Beer Sheva, Israel.
- Skews, B.W. (2000). "Three-dimensional effects in wind tunnel studies of shock wave reflection," *J. Fluid Mech.* 407: 85–104.
- Smith, L.G. (1945). "Photographi investigation of the reflection of plane shocks in air," OSRD Rept. 6271, Off. Sci. Res. Dev., Washington, D.C., or NDRC Rept. A-350.
- Srivastava, R.S., and Deschambault, R.L. (1984). "Pressure distribution behind a nonstationary reflected-diffracted oblique shock wave," *AIAA J.* 22: 305–306.
- Sternberg, J. (1959). "Triple shock wave interactions," *Phys. Fluids* 2: 179–206.
- Sudani, N., Sato, M., Watanabe, M., Node, J., Tate, A., and Karasawa, T. (1999). "Three-dimensional effects on shock wave reflections in steady flows," AIAA Paper 99-0148.
- Takayama, K., and Ben-Dor, G. (1989a). "Pseudo-steady oblique shock-wave reflections over water wedges," *Exp. Fluids* 8: 129–136.
- Takayama, K., and Ben-Dor, G. (1989b). "A reconsideration of the transioin criterion from Mach to regular reflection over cylindrical concave surfaces," *KSME J.* 3: 6–9.
- Takayama, K., and Sasaki, M. (1983). "Effects of radius of curvature and initial angle on the shock transition over concave and convex walls," *Rept. Inst. High Speed Mech., Tohoku Univ., Sendai, Japan* 46: 1–30.
- Takayama, K., and Sekiguchi, H. (1981a). "Triple-point trajectory of strong spherical shock wave," *AIAA J.* 19: 815–817.
- Takayama, K., and Sekiguchi, H. (1981b). "Formation and diffraction of spherical shock waves in shock tube," *Rept. Inst. High Speed Mech., Tohoku Univ., Sendai, Japan* 43: 89–119.
- Tayakayam, K., Ben-Dor, G., and Gotoh, J. (1981). "Regular to Mach reflection transition in truly nonstationary flows—Influence of surface roughness," *AIAA J.* 19: 1238–1240.
- Takayama, K., Miyoshi, H., and Abe, A. (1989). "Shock wave reflection over gas/liquid interface," *Inst. High Speed Mech. Rept., Tohoku Univ., Sendai, Japan* 57: 1–25.
- Teshukov, V.M. (1989). "On stability of regular reflection of shock waves," *Prilki Mekhanika i Techn. Fizika* (translated into English in *Appl. Mech. and Tech. Phys.*) 2: 26–33 (in Russian).
- von Neumann, J. (1943a). "Oblique reflection of shocks," Explos. Res. Rept. 12, Navy Dept., Bureau of Ordinance, Washington, D.C.
- von Neumann, J. (1943b). "Refraction, intersection and reflection of shock waves," NAVORD Rept. 203–45, Navy Dept., Bureau of Ordinance, Washington, D.C.
- Vuillon, J., Zeitoun, D., and Ben-Dor, G. (1995). "Reconstruction of oblique shock wave reflection in steady flows. Part 2. Numerical investigation," *J. Fluid Mech.* 301: 37–50.
- Wheeler, J. (1986). "An interferometric investigation of the regular to Mach reflection transition boundary in pseudo-stationary flow in air," UTIAS TN 256, Inst. Aerospace Studies, Univ. Toronto, Toronto, Ont., Canada.
- White, D.R. (1951). "An experimental survey of the Mach reflection of shock waves," Princeton Univ., Dept. Phys., Tech. Rept. II-10, Princeton, NJ.
- Whitham, G.B. (1957). "A new approach to problems of shock dynamics. Part I. Two dimensional problems," *J. Fluid Mech.* 2: 145–171.
- Zaslavskii, B.I., and Safarov, R.A. (1973). "Mach reflection of weak shock waves from a rigid wall," *Zh. Prikl. Mek. Tek. Fiz.* 5: 26–33.

This Page Intentionally Left Blank

Two-Dimensional Interactions

8.2 The Refraction of Shock Waves

LE ROY F. HENDERSON

8 Damour Avenue, East Lindfield, Sydney, New South Wales, Australia

-
- 8.2.1 Introduction
 - 8.2.2 One-Dimensional Refraction
 - 8.2.2.1 The Wave Systems
 - 8.2.2.2 The Wave Impedance
 - 8.2.2.3 The Reflection and Transmission Coefficients
 - 8.2.2.4 The Continuity Conditions at the Interface
 - 8.2.2.5 The Refraction Limits
 - 8.2.2.6 Solution of One-Dimensional Refraction
 - 8.2.3 Two-Dimensional Refraction
 - 8.2.3.1 Two-Dimensional Wave Systems
 - 8.2.3.2 The Wave Impedance of an Oblique Shock
 - 8.2.3.3 The Refraction Law
 - 8.2.3.4 The Relative Refractive Index
 - 8.2.3.5 The Shock Polar
 - 8.2.4 Solution of Fast–Slow Refraction $\eta_a > 1$
 - 8.2.5 Solution of Fast–Slow Refraction $\eta_1 < 1$
 - 8.2.6 The Minimum Time Principle
 - References

8.2.1 INTRODUCTION

Consider a material (I) in a given thermodynamic state. Consider the impulsive motion of a boundary, say a piston, which drives (I) causing an initial shock wave (i) to propagate through it at a wave velocity \tilde{U}_i . Suppose that subse-

quently i enters a region where the material is either in a different state, or where it is a *different* material (II). Generally the shock wave velocity will change to, say, \tilde{U}_t . By definition the shock wave is refracted whenever $\tilde{U}_i \neq \tilde{U}_t$. The refracted shock is called the *transmitted* shock (t), and the second state, or material, is the *receiving* state, or material.

The problem is simplified by considering only a two-material (I-II) system (a two-state refraction in the same material is entirely analogous). The i -shock is assumed to be a plane surface and so is the boundary between the two materials in their undisturbed state. It is also assumed that the equations of state (EOS) of the materials obey two mild constraints. These are the convexity condition, $G > 0$, and the medium condition, $\Gamma \leq \gamma$ (see Chapter 2). They are satisfied, for example, by every single-phase material for practically every state. However, the materials need not be in the same phase; for example, one may be air and the other water. Several important results follow from this assumption; for example, entropy-increasing compression shock waves are permitted, but expansion shock waves are excluded (see Chapter 2). Finally, it is assumed that the wave vector \tilde{U}_i is constant in its magnitude and direction so that the discussion is restricted to steady-state flows and self-similar systems.

Experiments with shock waves refracting at gas interfaces were conducted by Jahn (1956, 1957), Abdel-Fattah *et al.* (1976), Abdel-Fattah and Henderson (1978a, 1978b), Haas and Sturtevant (1987), Bonazza and Sturtevant (1991), and Haas (1993). Analytical studies were done by Polachek and Seeger (1951), Henderson (1966, 1989), and Catherasoo and Sturtevant (1983), and at air/water interfaces by Flores and Holt (1982) and Henderson (1990). Numerical studies of the phenomena were made by Henderson *et al.* (1991), Samtaney and Meiron (1997), Puckett *et al.* (1997), Samtaney *et al.* (1998). The Richtmyer–Meshkov and Rayleigh–Taylor instabilities at an accelerated interface were extensively studied both numerically and in experiments (see the review by Rupert, 1991; also see Haas, 1993; Jourdan *et al.*, 1997; and Sadot *et al.*, 1998). Many materials have been studied in experiments using one-dimensional (1-D) shock wave refractions; see the books by Meyers (1994), and Graham (1992), and the references therein and in the *Proceedings of the International Symposia on Shock Waves* (ISSW). Two-dimensional (2-D) refractions, that is, refraction of an oblique shocks, have also been studied in condensed materials by Nagayama (1993); see also the *Proceedings of the International Symposia on Shock Waves* (ISSW).

8.2.2 ONE-DIMENSIONAL REFRACTION

8.2.2.1 THE WAVE SYSTEMS

Refraction is one-dimensional (1-D) if the initial shock wave, i , is always parallel to the material interface as it approaches it (see Fig. 8.2.1a). As soon as i enters the receiving material the moving boundary begins to drive it and i becomes the transmitted shock wave, t ; the interface is thus impulsively accelerated. Additionally, a reflected wave is propagated back into the initial material; it can be either a shock wave, r , or an expansion wave, e (see Fig. 8.2.1b and 8.2.1c). By symmetry all the waves are parallel to the interface. It is usually assumed that the pressure, p , and the particle velocity, \tilde{u} , are the same on both sides of the interface (von Neumann, 1943),

$$p_2 = p_t \quad (8.2.1)$$

$$\tilde{u}_2 = \tilde{u}_t. \quad (8.2.2)$$

These are the continuity conditions for the interface. Solid materials do not always remain in contact during refraction; it is possible for a void to open at the interface (see, e.g., Thompson, 1972).

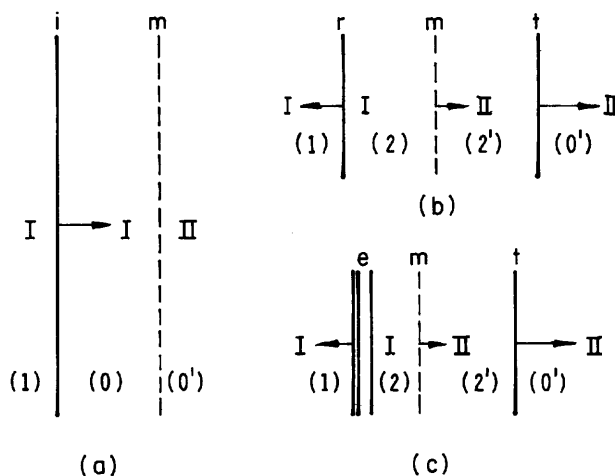


FIGURE 8.2.1 One-dimensional refraction of an incident shock, i . I, initial material; II, receiving material.

8.2.2.2 THE WAVE IMPEDANCE

The nature of the reflected wave can be found by considering the wave impedance (Z) of each wave; for the i-shock,

$$Z_i \equiv \frac{p_1 - p_0}{u_1 - u_0} = \frac{p_1 - p_0}{U_{pi}}, \quad (8.2.3)$$

where u_0 and u_1 are the particle *speeds* upstream and downstream of the i-shock, and

$$U_{pi} = u_1 - u_0 \quad (8.2.4)$$

is its piston speed. It is useful to give Z_i a sign. If the shock wave moves to the right ($x > 0$ direction) so that $U_i > U_{pi} > 0$, and because $(p_1 - p_0) > 0$, then $Z_i > 0$; similarly, $Z_i < 0$, for a left-moving shock wave. The definitions for Z_r and Z_t are analogous. The definition remains valid for the impedance Z_e of a reflected isentropic expansion; in this case the piston withdraws from the wave. The definition of Z is the same for both laboratory and wave fixed coordinates. In the former frame the momentum Eq. (2.2) is

$$p_1 - p_0 = \rho_0 U_i U_{pi}, \quad (8.2.5)$$

where ρ_0 is the initial density. By comparing Eqs. (2.2) with (8.2.3), it follows that Z_i can also be defined as the *mass flux* (see Eq. (2.1)) through the shock,

$$Z_i \equiv \rho_0 U_i. \quad (8.2.6)$$

By comparing the last result with the Rayleigh Eq. (2.11), it is found that Z_i is also an average adiabatic bulk modulus,

$$Z_i \equiv \sqrt{-\frac{\Delta p}{\Delta v}}, \quad (8.2.7)$$

where $v = 1/\rho$ is the specific volume.

8.2.2.3 THE REFLECTION AND TRANSMISSION COEFFICIENTS

The *pressure* coefficients are defined as

$$R \equiv \frac{p_2 - p_1}{p_1 - p_0} \quad (8.2.8)$$

$$T \equiv \frac{p_2 - p_0}{p_1 - p_0}. \quad (8.2.9)$$

The *shock intensity* I is defined as the average power flux per unit area normal to the direction of propagation; for the i-shock,

$$I_i \equiv (p_1 - p_0)(u_1 - u_0) = (p_1 - p_0)U_{pi}, \quad (8.2.10)$$

with similar definitions for I_t and I_r . Combining Eqs. (8.2.3) and (8.2.10),

$$I_i = \frac{(p_1 - p_0)^2}{Z_i}, \quad (8.2.11)$$

again with similar expressions for I_t and I_r . The intensity reflection and transmission coefficients are defined as

$$R_i \equiv \frac{I_r}{I_i} = \frac{(p_2 - p_1)^2 Z_i}{(p_1 - p_0)^2 Z_r} = R^2 \left| \frac{Z_i}{Z_r} \right| \quad (8.2.12)$$

$$T_i \equiv \frac{I_t}{I_i} = \frac{(p_{2'} - p_0)^2 Z_i}{(p_1 - p_0)^2 Z_t} = T^2 \left| \frac{Z_i}{Z_t} \right|. \quad (8.2.13)$$

The power transmitted along a stream-tube of cross-sectional area A is A_i , so the so the *power reflection and transmission* coefficients are

$$R_\pi \equiv \frac{A_r I_r}{A_i I_i} = \left[\frac{A_r (p_2 - p_1)^2}{A_i (p_1 - p_0)^2} \right]^2 \left| \frac{Z_i}{Z_r} \right| = R^2 \frac{A_t}{A_i} \left| \frac{Z_i}{Z_r} \right| \quad (8.2.14)$$

$$T_\pi \equiv \frac{A_t I_t}{A_i I_i} = \left[\frac{A_t (p_{2'} - p_0)^2}{A_i (p_1 - p_0)^2} \right]^2 \left| \frac{Z_i}{Z_t} \right| = T^2 \frac{A_t}{A_i} \left| \frac{Z_i}{Z_t} \right|. \quad (8.2.15)$$

8.2.2.4 THE CONTINUITY CONDITIONS AT THE INTERFACE

The conditions (8.2.1) and (8.2.2) can be written

$$(p_2 - p_1) + (p_1 - p_0) = (p_{2'} - p_0) \quad (8.2.16)$$

$$(u_2 - u_1) + (u_1 - u_0) = (u_{2'} - u_0) \quad (8.2.17a)$$

or

$$U_{pi} + U_{pr} = U_{p2'}. \quad (8.2.17b)$$

Dividing Eq. (8.2.16) by Eq. (8.2.17) results in

$$\frac{(p_2 - p_1) + (p_1 - p_0)}{U_{pi} + U_{pr}} = \frac{p_{2'} - p_0}{U_{p2'}} = Z_t. \quad (8.2.18)$$

Now eliminating U_{pi} etc. with Z_i , etc., yields

$$R = \frac{Z_r(Z_t - Z_i)}{Z_t(Z_r - Z_t)}. \quad (8.2.19)$$

But if one divides Eq. (8.2.16) by $(p_1 - p_0)$, one gets

$$T = 1 + R \quad (8.2.20)$$

and so

$$T = \frac{Z_t(Z_i - Z_t)}{Z_i(Z_t - Z_r)}. \quad (8.2.21)$$

Whenever $G > 0$ and $\Gamma \leq \gamma$, by (8.2.9) $T > 0$, *independently of the nature of the reflected wave*. Suppose that i and t are right-moving shock waves; then Z_i and Z_t are positive. The reflected wave must move to the left; $U_{pi} < 0$ if it is a shock wave, and also $(p_1 - p_0) > 0$ so $Z_r < 0$; but if it is an expansion wave $U_{pi} > 0$ (the piston withdraws to the right), $(p_2 - p_1) < 0$, and again $Z_r < 0$. So a left-moving reflected wave has a negative impedance irrespective of whether it is a shock or an expansion. Inspection of Eq. (8.2.21) shows that it is consistent with Eq. (8.2.9), as it should be. Furthermore, from Eq. (8.2.19) we obtain the important results that if the impedance increases ($Z_t > Z_i$), $R > 0$ and by Eq. (8.2.8) the reflected wave is a shock; similarly, it is a Mach line if $Z_t = Z_i$ because $R = 0$; but if $Z_t < Z_i$, then $R < 0$ and it is an expansion. Consequently, the reflected wave is determined by the way in which the wave impedance changes during refraction. The equality of impedance condition follows from Eq. (8.2.6),

$$Z_i \equiv \rho_0 U_i = \rho_0 U_t \equiv Z_t, \quad (8.2.22)$$

which is the condition for the reflection to reduce to a Mach line.

8.2.2.5 THE REFRACTION LIMITS

The *acoustic limit*: A shock or an expansion degenerates to a Mach line at this limit, and wave impedance becomes an *acoustic impedance*, $Z \rightarrow r \equiv \rho a$. Thus,

$Z_t \rightarrow r_t \equiv \rho_0 a_t$ and $Z_r \rightarrow Z_i \rightarrow Z_i \equiv \rho_0 a_i$ while Eqs. (8.2.19) and (8.2.21) reduce to well-known acoustic formulas (Kinsler *et al.*, 1982),

$$R = \frac{r_t - r_i}{r_t + r_i} \quad (8.2.23a)$$

and

$$T = \frac{2r_t}{r_t + r_i}. \quad (8.2.23b)$$

These equations are symmetric in r_i and r_t , so R and T are the same irrespective of whether i passes from the first material into the second or vice versa. This is known as the *principle of acoustic reciprocity*.

The rigid limit: If the impedance of the receiving material increases without limit, $Z_t \rightarrow \infty$, it will become infinitely rigid. If it is assumed that Z_i and Z_r remain finite and nonzero as this happens, then

$$R \rightarrow \frac{Z_r}{Z_i} > 0, \quad T \rightarrow 1 + \frac{Z_r}{Z_i} > 0, \quad R_i \rightarrow \frac{Z_r}{Z_i}; \quad \text{and} \quad T_i \rightarrow 0. \quad (8.2.24)$$

During one-dimensional refraction there is no change in A , R_π and T_π are the same as R_i and T_i . So although a shock can penetrate a rigid body, no energy is transmitted. The reflection is always a shock in this case because $R > 0$. The effect is called *total reflection*.

The compliant limit: Here $Z_t \rightarrow 0$, and again we assume that Z_i and Z_r remain finite and nonzero; from Eqs. (8.2.19) and (8.2.21) $R \rightarrow -1$, and $T \rightarrow 0$. The reflection is now an expansion and the t-shock is reduced to a Mach line $p_{\text{t}} = p_0$. This is called the *pressure release condition* in acoustics, but we call it the *compliant limit*. Since $T_\pi \rightarrow T_i = 0$, no energy is transmitted and the condition is also called *total internal reflection*.

Furthermore, if $Z_i \rightarrow \infty$ and $Z_r \rightarrow \infty$ while Z_t stays finite, then $R \rightarrow -1$ and $T \rightarrow 0$. So a shock propagating in a material of infinite impedance is also totally internally reflected if it encounters a second material where the impedance is finite. Thus, extreme impedance mismatch greatly attenuates the transmission of energy and power.

8.2.2.6 SOLUTION OF ONE-DIMENSIONAL REFRACTION

The refraction of the i -shock may produce a reflected expansion. The solution of any 1-D problem is obtained by using wave curves (see Fig. 8.2.2), these are the union of the Hugoniot locus for $p_1 - p_0 > 0$ and the isentropic locus for

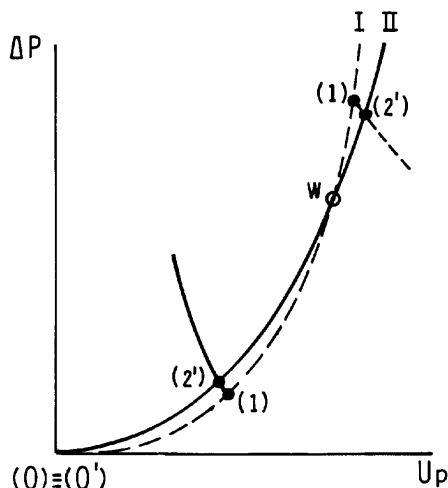


FIGURE 8.2.2 Solution of one-dimensional shock refraction using wave curves in the $(u_p, \Delta p)$ -plane. 0–1, wave curve for the i-shock in material I; 1–2', wave curve for the r-shock in material I; 1'–2', wave curve for the e-expansion in material I; 0'–2' wave curve for the t-shock in material II. (Adapted from Henderson and Menikoff, *Journal of Fluid Mechanics*, 366: 179–210, 1998, Cambridge University Press, with permission).

$p < p_0$ (Menikoff and Plohr, 1989). The continuity conditions (8.2.1) and (8.2.2) suggest that it is convenient to solve the problem in the $(U_p, \Delta p)$ -plane because these conditions are satisfied at every point where the wave curves of the i and t shocks intersect. If $G > 0$ and $\Gamma \leq \gamma$, the wave curves are convex (i.e., the curve is above all of its tangents) and the intersection (solution) is unique (Menikoff and Plohr, 1989). Figure 8.2.2 shows examples where the reflection is either a shock wave or an expansion wave. The separating condition is at the point W, which also defines the equality of wave impedance.

8.2.3 TWO-DIMENSIONAL REFRACTION

8.2.3.1 TWO-DIMENSIONAL WAVE SYSTEMS

The refraction is 2-D whenever the i-shock is not parallel to the interface during its approach to it. The inclined shock makes an angle of incidence ω_0 with the interface (mm). There is also a t-shock and either a reflected shock wave, r, or an expansion wave, e. In the examples shown in Fig. 8.2.3, all the waves meet at a point called a *node*, and all are locally plane at the node. Consequently, the flow is uniform between any two adjacent waves; such wave systems are called *regular refraction* (RR) (von Neumann, 1943).

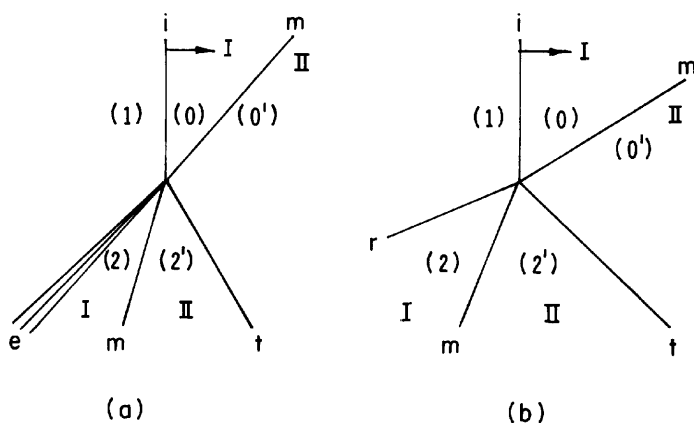


FIGURE 8.2.3 Regular refraction wave systems: (a) with a reflected expansion wave, *e*; (b) with a reflected shock wave, *r*. (With permission from Cambridge University Press).

By contrast, the flows between the adjacent waves in Fig. 8.2.4 are not everywhere uniform and they are *irregular refractions* (IR).

The continuity equation (8.2.1) remains valid, but Eq. (8.2.2) must be replaced by

$$\delta_0 + \delta_1 = \delta_{2'}, \quad (8.2.25)$$

where δ is the streamline deflection across an oblique shock or across a centered expansion (see Fig. 8.2.5). This equation follows from the assumption

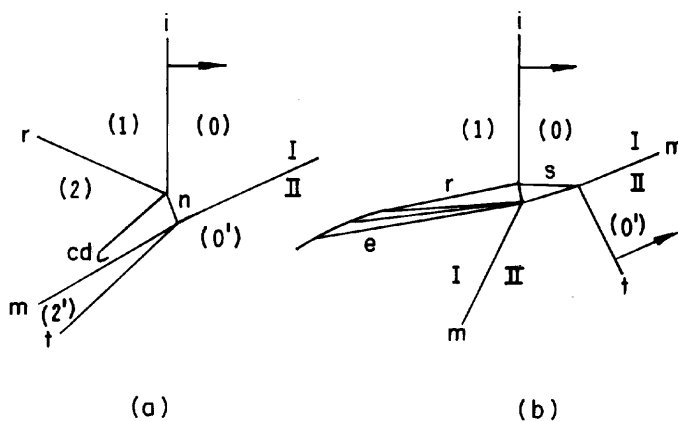


FIGURE 8.2.4 Some irregular shock refraction systems. *N*, Mach shock; *cd*, contact discontinuity; *s*, side shock. (With permission from Cambridge University Press).

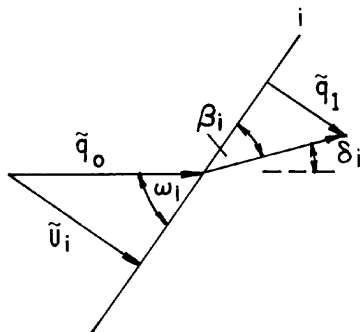


FIGURE 8.2.5 Definitions of angles, wave and particle vectors, and components for the *i*-shock wave in shock fixed coordinates. (With permission from Cambridge University Press).

that the materials always remain in contact along their interface. Note that the interface lies in a new plane after refraction (see Fig. 8.2.3).

The components of the particle velocities normal to the interface must be equal if the materials are to remain in contact; therefore,

$$U_{pi} \cos \beta_i + U_{pr} \cos \beta_r = U_{pt} \cos \beta_2, \quad (8.2.26)$$

where β is the angle between a wave and the *deflected* interface (see Fig. 8.2.6). An RR problem is solved without serious difficulty by constructing a shock polar for each of *i*, *t* and *r*, and an isentropic curve for *e*, in the (δ, p) -plane (von Neumann, 1943). The polar/isentropic intersections satisfy the continuity equations and define the solutions. Multiple solutions are often present even when $\Gamma \leq \gamma$. The multiplicity is resolved by considering the boundary conditions for each solution. An IR is implied when there are no physically realistic RR solutions.

8.2.3.2 THE WAVE IMPEDANCE OF AN OBLIQUE SHOCK

If Eq. (8.2.1) is divided by Eq. (8.2.26), after some algebra one again obtains Eqs. (8.2.19) and (8.2.21), provided that the *oblique shock impedance* is defined to be

$$Z_i \equiv \frac{p_1 - p_0}{U_{pi} \cos \beta_i}. \quad (8.2.27)$$

8.2.3.4 THE RELATIVE REFRACTIVE INDEX

The *relative refractive index* is defined by

$$\eta = \frac{U_i}{U_t}. \quad (8.2.31)$$

The refraction is said to be *slow-fast* when $\eta < 1$ and *fast-slow* when $\eta > 1$, but there is no refraction when $\eta = 1$ even if the two materials are different. Suppose that i weakens to an acoustic (Mach line) wave so that $U_i \rightarrow a_0$ and $U_t \rightarrow a_0$. Since these quantities are material properties, we may also consider the relative *acoustic* index to be a property of the two-material system, where

$$\eta_a \equiv \frac{\omega_i}{\omega_t}. \quad (8.2.32)$$

By contrast, η is not a material property because it depends on the wave speeds of the shocks; instead it will be regarded as a property of the refraction system.

Using Eq. (8.2.29) to eliminate U_i and U_t from Eq. (8.2.31), we get

$$\eta \equiv \frac{U_i}{U_t} = \frac{\sin \alpha_i}{\sin \alpha_t}. \quad (8.2.33)$$

Notice that slow-fast refraction implies that $\omega_i < \omega_t$, so the shock becomes steeper when it is refracted (bent). Conversely, it becomes less steep for a fast-slow system, $\omega_i > \omega_t$, but when $\eta = 1$, $\omega_i = \omega_t$, and the shock wave is not refracted at all.

8.2.3.5 THE SHOCK POLAR

The shock polar is equivalent to the Rankine-Hugoniot equations (Eqs. (2.6)–(2.8)). Grove (1988) obtained its general equation,

$$\tan^2 \delta = \left(\frac{\Delta p}{\rho_0 q_0^2 - \Delta p} \right)^2 \left(\frac{q_0^2}{U_i^2} - 1 \right), \quad (8.2.34)$$

where $\Delta p \equiv p - p_0$, \tilde{q}_0 is the velocity of the upstream flow that approaches the shock wave, and U_i is the component of \tilde{q}_0 normal to the shock wave (see Fig. 8.2.5),

$$U_i = q_0 \cos \omega_i. \quad (8.2.35)$$

The only material properties are ρ_0 , so the equation applies to any material. However, the EOSs for a material, or equivalently tables of properties, must be

known before a polar can be plotted. The plot is done in the $(\delta, \Delta p)$ -plane with q_0 held constant for a particular polar.

Geometrical polar properties are easily obtained from Eq. (8.2.34) and are illustrated in Fig. 8.2.8. A polar is symmetrical about the Δp axis; $\delta = 0$ when $\Delta p = 0$, corresponding to a Mach line at (O); also $\delta = 0$ when $U_i = q_0$, corresponding to a normal shock (N). By Eq. (8.2.5), Δp is bounded when ρ_0 , U_{pi} , and U_i are bounded. Furthermore, $d\Delta p/d\delta = 0$ at N, $d\Delta p/d\delta \rightarrow \infty$ at E; that is, there are vertical tangents at E, so δ has lateral extremities there. These extremities are called the shock *detachment* points because they correspond to a shock detaching from a wedge. Thus, a polar is everywhere bounded in the $(\delta, \Delta p)$ -plane. Further important properties follow if the material EOSs satisfy the mild constraints $G > 0$ and $\Gamma \leq \gamma$. It can be shown that a *sufficient* condition for E to be unique in the $\delta > 0$ half-plane is that $\Gamma \leq \gamma$, and similarly in the $\delta < 0$ half-plane (Henderson and Menikoff, 1998). Furthermore, there is a unique sonic point (S) in each half-plane *if and only if* $h + \frac{1}{2}a^2$ is monotonic increasing along the Hugoniot (Teshukov, 1986; Henderson and Menikoff, 1998). Here h is the specific enthalpy. Although the latter constraint has not been studied, Henderson and Menikoff (1998) argued that “typically” the condition will be satisfied whenever $G > 0$ and $\Gamma \leq \gamma$. If the i-shock is plane and oblique and maps into a point below S, the particle flow downstream of it and relative to it will be supersonic. It will be subsonic if it maps above .

Kontorovich (1959) studied the stability of a plane shock wave against 2-D and 3-D disturbances and found a somewhat more restrictive constraint than $\Gamma \leq \gamma$. Ripple instabilities develop on a shock if *his* limit is violated. Experiments with dissociating and ionizing gases by Griffith *et al.* (1975) and Glass and Liu (1978) confirmed the instability. Menikoff and Plohr (1989) proposed

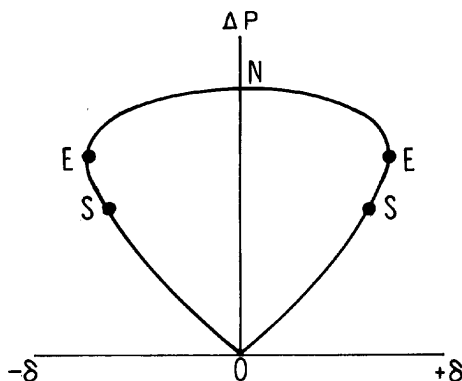


FIGURE 8.2.8 Typical shock polar when the material equation of state satisfies $G > 0$ and $\Gamma \leq \gamma$.

the stability constraint $\Gamma \leq \gamma - 1$ as *sufficient* for stability, but because it is only sufficient it is probably too restrictive. Fowles (1981) showed that the Kontorovich (1959) constraint is geometrically equivalent to the sonic point S coinciding with the detachment point E on the polar. The shock is only stable when S lies below E, and this occurs *if and only if*

$$(\Gamma + 1) \frac{\Delta p}{p} \leq \gamma. \quad (8.2.36)$$

See also the discussion in Chapter 2 and in Henderson and Menikoff (1998). Conversely, the shock is unstable if S is above E, as may occur with dissociating and ionizing gases. In what follows it will be assumed that every polar has the foregoing properties and that every shock is stable.

The two-material refraction problem is further simplified by assuming that initially the materials are everywhere at the same pressure p_0 . Since they are also in contact, the i- and t-polars have the same origin (see Fig. 8.2.9). By Eq. (8.2.29), the polars have the same q_0 but in general the materials do not have the same ρ_0 ; therefore, by Eq. (8.2.34) the polars do not coincide (see Fig. 8.2.9). The polars are usually nested for weak shock waves when the difference in the density of the materials is small, as for gases (see Fig. 8.2.9a). Otherwise they may intersect at the equality of the impedance point (W) (see Figs. 8.2.9b and 8.2.9c).

It is sometimes convenient to plot the polars by expressing q_0 in terms of the upstream flow Mach numbers for shock fixed coordinates. For example, M_i is defined as

$$M_i \equiv \frac{U_i}{a_i \sin \omega_i}. \quad (8.2.37)$$

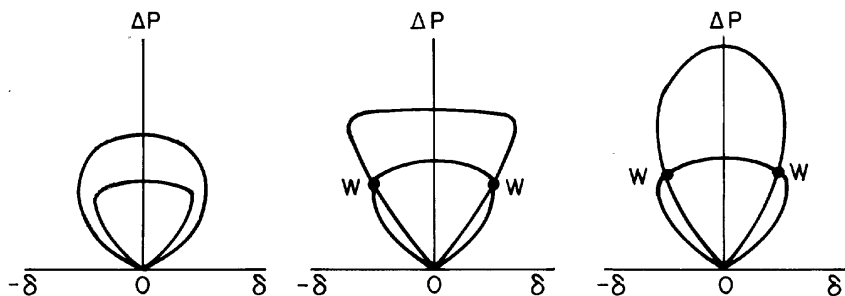


FIGURE 8.2.9 Polars for the i and t shock waves. (a) Nested polars; (b) intersecting polars at W on the supersonic parts of both polars; (c) intersecting polars at W on the subsonic part of the smaller polar and the supersonic part of the larger. (With permission from Cambridge University Press)

Extracting the i and t terms from Eq. (8.2.29) results in

$$M_i a_i = M_t a_t. \quad (8.2.38)$$

This provides the relation between the constant polar Mach numbers. Now $M_i \propto a_i^{-1}$ and $M_t \propto a_t^{-1}$, and because q_0 is the same by Eq. (8.2.29) *fast-slow* is equivalent to $M_i > M_t$ or $\eta_a > 1$, and conversely for *slow-fast* we have $\eta_a < 1$ and $M_i < M_t$.

8.2.4 SOLUTION OF FAST-SLOW REFRACTION $\eta_a > 1$

The method of solution is described by an example, namely, an He/CO₂ interface (see Fig. 8.2.10). The polars corresponding to the i - and t -shock waves are (I) and (II), respectively. The polar corresponding to the r -shock wave is (III). It is superimposed on (I) and (II). Noting that r occurs in the moving flow behind i , III is found by calculating q_1 (see Fig. 8.2.5) and a_1 from the i -shock equations. The Mach number for III is $M_r \equiv q_1/a_1$; its coordinates follow from Eq. (8.2.34) and are plotted by placing the origin of III at (δ, p_1) and multiplying p_2 by p_1/p_0 . The continuity conditions (8.2.1) and (8.2.25) are satisfied at every point (α_1, α_2) where III intersects II (see Fig. 8.2.10a); these are solutions to regular refraction with a reflected shock (RRR). Because the α_1 -point determines the r -shock on III and the t -shock on II, we write $\alpha_1 \equiv r \equiv t$; similarly, α_2 determines an alternative solution $\alpha_2 \equiv r \equiv t$. The boundary conditions decide which solution actually appears. This problem has been studied in the experiments of Abdel-Fattah and Henderson (1978a), and they found that the smaller pressure (weaker) α_1 solution appeared.

If p_1 is continuously increased, III shrinks because q_1 becomes smaller and a_1 larger. The α_1 and α_2 points approach each other and eventually coincide $\alpha_1 \equiv \alpha_2$ (see Fig. 8.2.10b). If p_1 increases any more then there are no solutions for RRR (see Fig. 8.2.10c). This means that the continuity conditions cannot be satisfied for the regular refraction. Experiment shows there is now an irregular system, a Mach reflection-refraction (MRR). At present such a problem can only be solved by numerical methods. There are other fast-slow systems that have been detected during experiments (Jahn, 1956, Abdel-Fattah and Henderson, 1978a).

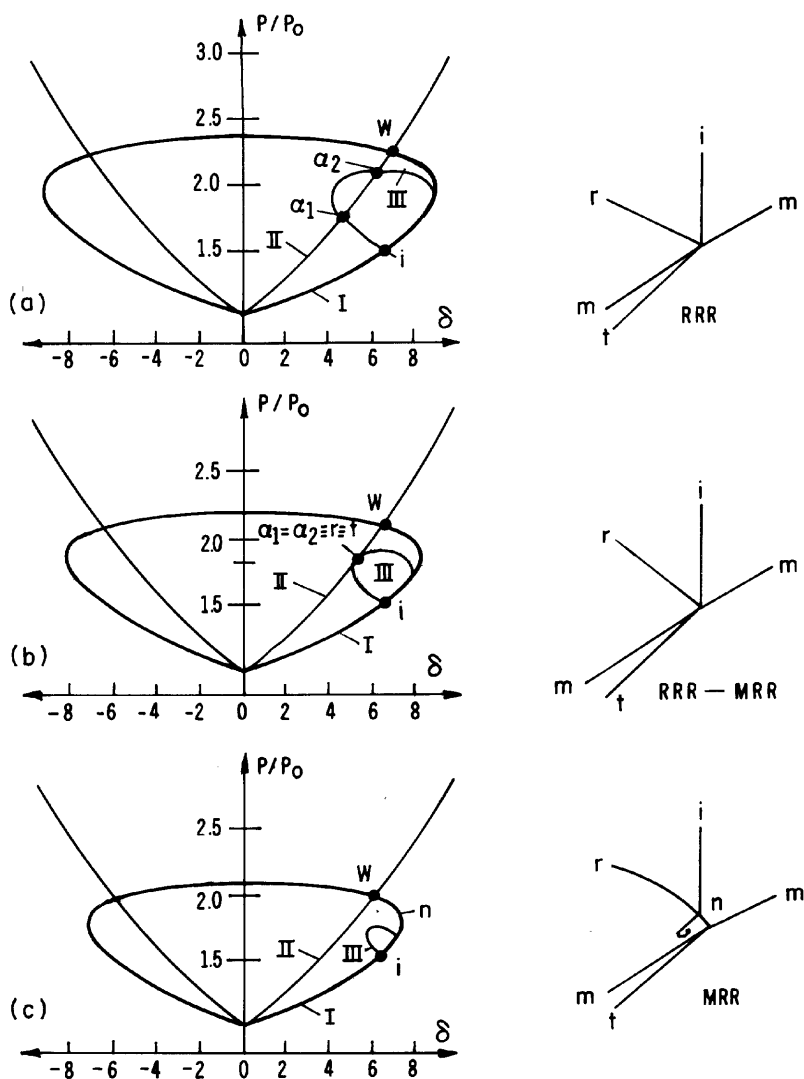


FIGURE 8.2.10 Refraction of a plane shock wave at the He/CO₂ ($\eta_a > 1$) interface. (a) Regular refraction with a reflected shock wave (RRR); (b) The RRR \leftrightarrow MRR transition; (c) Mach reflection refraction (MRR); α_1 and α_2 are polar solutions for RRR; W marks the equality of impedance. (With permission from Cambridge University Press)

8.2.5 SOLUTION OF SLOW-FAST REFRACTION $\eta_a < 1$

The solution method is the same as in the previous section, although a different irregular system is obtained. In this case the example is of a CO_2/CH_4 interface (see Fig. 8.2.11). Initially two RRR solutions (α_1, α_2) are attained (see Fig. 8.2.11a), and with increasing p_1 the $\alpha_1 \equiv \alpha_2$ point is again attained (see Fig. 8.2.11b). If p_1 increases any more, the t-shock detaches from the RRR node and propagates ahead of it (see Fig. 8.2.11c); this IR system is a free-precursor system (FPR) and it has been observed in the experiments of Jahn (1956), Abdel-Fattah *et al.* (1978), and Henderson *et al.* (1991). Numerical results for the sequence shown in Fig. 8.2.11 are also presented in the last paper cited. The t-shock now refracts back into the CO_2 , generating the s-shock (side shock); this in turn interacts with the i-shock and modifies it into the k-shock. The interaction also produces an r-shock. The four-shock node is called a cross node (Glimm *et al.*, 1985). The k-shock propagates to the gas interface and undergoes a *total internal reflection* $R = -1$, $T = 0$. The pressure gradient is locally zero and k is reflected back into the CO_2 as the

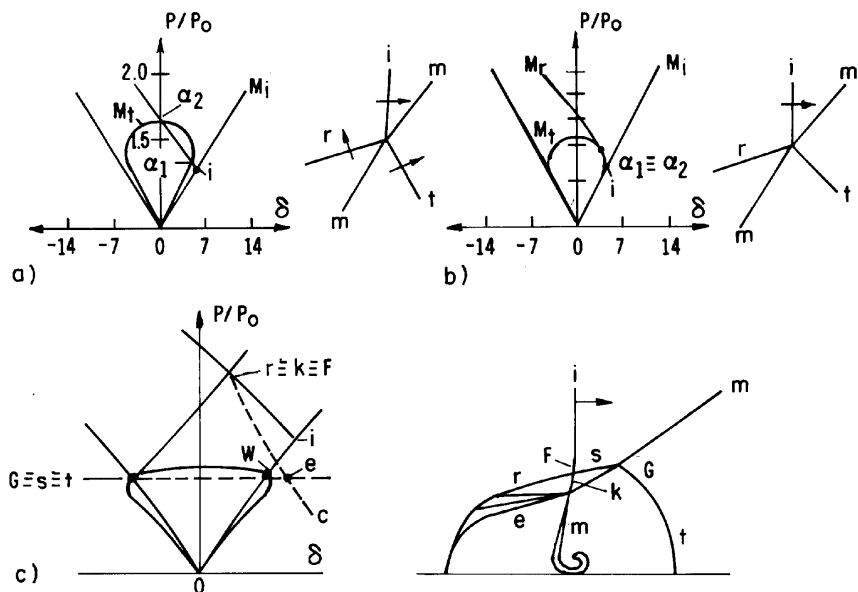


FIGURE 8.2.11 Refraction of a plane shock wave at the CO_2/CH_4 ($\eta_a < 1$) interface. (a) Regular refraction with a reflected shock wave (RRR); (b) the RRR \leftrightarrow FPR transition; (c) Free-precursor-shock (t-s) irregular refraction (FPR). (With permission from Cambridge University Press).

expansion, e; the situation is found also when an oblique shock refracts at the edge of a supersonic jet. Since the RRR system has broken up, it is plain that the refraction law has been violated; in fact, Eq. (8.2.29) can now be written in part using the vector magnitudes

$$q_0 = \frac{U_i}{\sin \alpha_i} < \frac{U_t}{\sin \alpha_t}. \quad (8.2.39)$$

The RRR → FPR transition: Rearranging Eq. (8.2.39)

$$\sin \omega_i \geq \frac{U_i}{U_t} \sin \omega_t \equiv \eta \sin \omega_t. \quad (8.2.40)$$

For α_t one may write

$$\cos \omega_t = \sqrt{1 - \sin^2 \omega_t} = \sqrt{1 - \eta^{-2} \sin^2 \omega_i} \quad (8.2.41)$$

Evidently, ω_t is real for fast-slow refraction, since $\eta^2 \geq 1 \geq \sin^2 \omega_i$. It may also be real for slow-fast refraction, provided that $\sin^2 \omega_i \leq \eta^2$. The critical condition (ω_c) is where $\sin^2 \omega_c \equiv \sin^2 \omega_i = \eta^2$, where also $\omega_t = 90^\circ = \beta_t$, and the t-shock is perpendicular to the interface; thus,

$$\sin^2 \omega_c \equiv \sin^2 \omega_i = \eta^2 = \frac{U_i^2}{U_t^2} \leq 1. \quad (8.2.42)$$

By Eq. (8.2.27), $Z_t \rightarrow \infty$, because $\beta_1 = 90^\circ$. If $\omega_i > \omega_c$, then ω_t and β_t are undefined, so ω_c is a criterion for the t-shock to become a free precursor. Numerical studies (Henderson *et al.*, 1991) showed that through the RRR → FPR transition the t-shock changed from a backward-leaning shock $\omega_t < 90^\circ$, to $\omega_t = 90^\circ$ at or near transition, to $\omega_t > 90^\circ$ when it is a free precursor. A similar argument can be developed to show a limit on ω_t when it is perpendicular to the interface. In this case the flow is subsonic behind i and there is no reflection. Only the i- and t-shocks exist and the refraction is reduced to a two-shock regular system.

Evanesence of the t-shock: Sometimes the t-shock is replaced by a continuous band of isentropic waves called an *evanescent* wave. Evidence for it is found in the experiments of Jahn (see, for example, the interferogram, Fig. 8.2.14d, of his paper for the Air/CH₄), also see the schlieren photograph in Fig. 8.2.4 of the Abdel-Fattah and Henderson (1978b) paper. Henderson *et al.* (1991) numerically studied the phenomenon and obtained insight into its structure. Since it is a precursor, Eq. (8.2.39) must be satisfied. Furthermore, since it is isentropic each wavelet is a Mach line; Eq. (8.2.39) can be written

$$a_t \geq U_i \frac{\sin v_t}{\sin \omega_i} = q_0 \sin v_t \quad (8.2.43)$$

for each Mach line. We see that evanescence requires that the speed ($a_t / \sin v_t$) of a Mach line along the interface in material II be greater than the shock in material I. The separating condition between a precursor t-shock and an evanescent wave occurs when both are perpendicular to the interface, $v_t = \omega_t = 90^\circ$ and $U_t = a_t$.

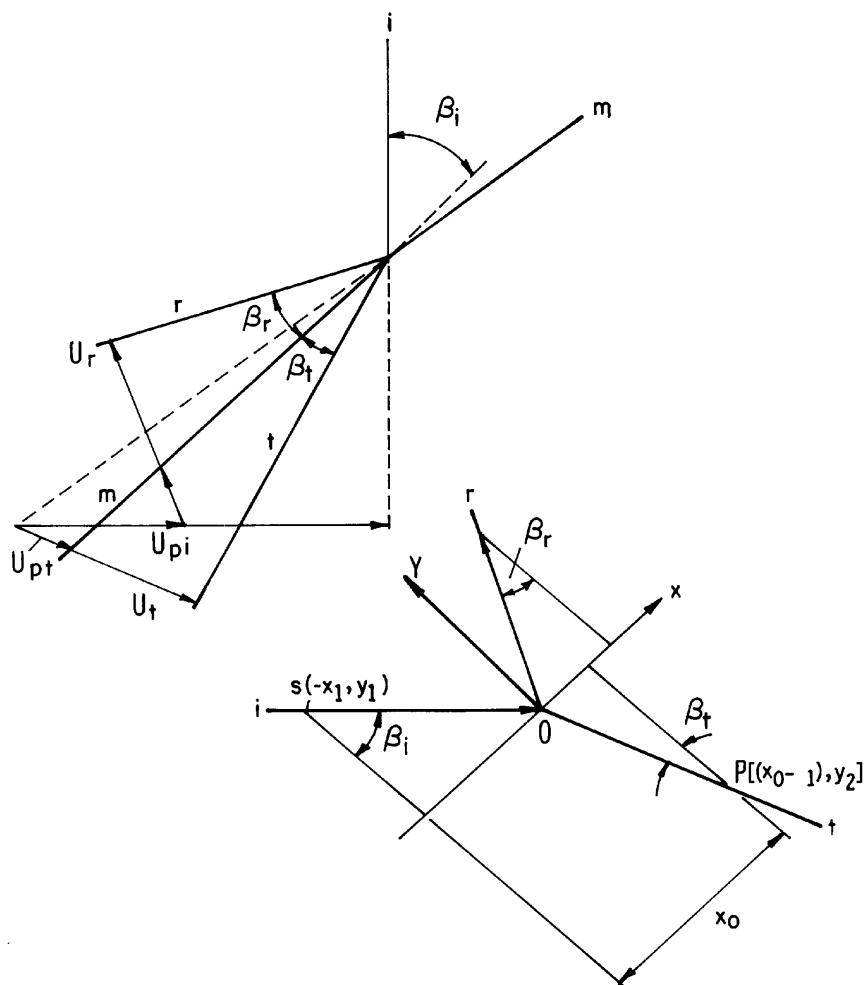


FIGURE 8.2.12 Wave diagram and ray path diagram for a regular refraction with a reflected shock wave. (a) Wave diagram; (b) path diagram. (With permission from Cambridge University Press).

8.2.6 THE MINIMUM TIME PRINCIPLE

An arbitrary point on a propagating wave traces a ray path out. It will be shown that for stationary and self-similar systems, the path is one of minimum time. This extends Fermat's principle from acoustics to shock and expansion waves. The derivation differs from acoustics in that the deflection of the interface by the wave must be taken into account. The derivation is obtained for an arbitrary point S on the i-shock as it travels along its path to the point P on the t-shock (see Fig. 8.2.12). The time τ for the point to pass from S to P is

$$\tau = \sqrt{\frac{x_1^2 + y_1^2}{U_i}} + \sqrt{\frac{(x_0^2 - x_1^2) + y_2^2}{U_t}}. \quad (8.2.44)$$

Now U_i and U_t are constants for the path, so the variations that have to be considered are merely those of the path direction. Therefore, x_1 is the only variable on the right side of the equation. Thus, if τ is to have a stationary value for the path, then

$$\frac{d\tau}{dx_1} = 0 = \frac{x_1}{U_i \sqrt{x_1^2 + y_1^2}} - \frac{x_0 - x_1}{U_t \sqrt{(x_0 - x_1)^2 + y_2^2}}$$

and so

$$0 = \frac{\sin \beta_i}{U_i} - \frac{\sin_t}{U_t}.$$

So we have recovered the refraction law! A second differentiation confirms that τ is a minimum. The derivation for the reflected wave, be it a shock or an expansion, follows without difficulty; the details are omitted. Similarly, the principle can be extended to free precursor waves (Henderson, 1989).

REFERENCES

- Abdel-Fattah, A.M. and Henderson, L.F. (1978a). Shock waves at a fast-slow gas interface, *J. Fluid Mech.* 86: 15.
- Abdel-Fattah, A.M., and Henderson, L.F. (1978b). Shock waves at a slow-fast gas interface. *J. Fluid Mech.* 89: 79.
- Abdel-Fattah, A.M., Henderson, L.F., and Lozzi, A. (1976). Precursor shock waves at a slow-fast gas interface. *J. Fluid Mech.* 76: 157.
- Bonazza, R. and Sturtevant, B. (1991). X-ray densitometry of shock-excited Richtmyer-Meshkov instability at an air-xenon interface. *Proc. 18th Int. Symp. Shock Waves*, p. 331 (Ed. K. Takayama). Springer, Berlin.
- Catherasoo, C.J. and Sturtevant, B. (1983). Shock dynamics in non-uniform media. *J. Fluid Mech.* 127: 539.

- Flores, J. and Holt, M. (1982). Shock wave interactions with the ocean surface. *Phys. Fluids* 25: 238.
- Fowles, G. (1981). *Phys. Fluids*. 24: 220.
- Glass, I.I., and Liu, W.S. (1978) "Effects of hydrogen impurities on shock structure and stability in ionizing monatomic gases" *J. Fluid Mech.* 84: 55–77.
- Glimm, J., Klingenberg, C., McBryan, O., Plohr, B., Sharp, D., and Yaniv, S. (1985). Front tracking and two dimensional Riemann problems. *Adv. Appl. Math.* 6: 259.
- Graham, R.A. (1992). *Solids Under High-Pressure Shock Compression*, Springer, New York.
- Griffith, R.W. Sandeman, R.J., and Hornung, H.G. (1975) "The stability of shock waves in ionizing and dissociating gases" *J. Phys. D: Appl. Phys.* 8, 1681–1691. "Henderson (1978)"
- Grove, J. (1988). Front tracking and shock-contact interactions. In *Advances in Computer Methods for Partial Differential Equations* (Eds. R. Vichnevetsky, and R. Stepleman). Rutgers Univ. Press, New Brunswick, NJ.
- Haas, J.F. (1993). *Experiments and Simulations on Shock Waves in Non-Homogeneous Gases. Shock Waves @ Marseille IV*, (Eds. R. Brun, and L. Dumitrescu), p. 27. Springer, Berlin.
- Haas, J.F. and Sturtevant, B. (1987). Interaction of weak shock waves with cylindrical and spherical gas inhomogeneities. *J. Fluid Mech.* 181: 41.
- Henderson, L.F. (1966). The refraction of a plane shock wave at a gas interface. *J. Fluid Mech.* 26: 607.
- Henderson, L.F. (1989). On the refraction of shock waves. *J. Fluid Mech.* 198: 365.
- Henderson, L.F. (1990). Refraction of a shock wave at an air–water interface. *Fluid Dyn. Res.* 5: 337–350.
- Henderson, L.F. and Menikoff, R. (1998). Triple shock entropy theorem and its consequences. *J. Fluid Mech.* 366: 179.
- Henderson, L.F., Colella, P., and Puckett, E.G. (1991). On the refraction of shock waves at a slow–fast gas interface. *J. Fluid Mech.* 224: 1.
- Jahn, R.G. (1956). The refraction of shock waves at a gaseous interface. *J. Fluid Mech.* 1: 457.
- Jahn, R.G. (1957). Transition processes in shock wave interactions. *J. Fluid Mech.* 2: 33–48.
- Jourdan, G., Houas, L., Haas, J. F., and Ben-Dor, G. (1997). Thickness and volume measurements of a Richtmyer–Meshkov instability induced mixing zone in a square shock tube. *J. Fluid Mech.* 349: 67–94.
- Kinseler *et al.* (1982).
- Kontorovich, V.M. (1959). Reflection and refraction of sound by shock waves. *Sov. Phys. Acoust.* 5: 320. (Translation from *Akusticheskii Zl.*)
- Rotelnikov and Montgomery (1997).
- Menikoff, R. and Plohr, B.J. (1989). The Riemann problem for fluid flow of real materials. *Rev. Modern Phys.* 61: 75.
- Meyers, M.A. (1994). *Dynamic Behavior of Materials*, John Wiley & Sons, New York.
- Nagayama, K. (1993). Shock wave interaction in solid materials. In *Shock Waves in Material Science* (Ed. A.B. Sawaoka), p. 195. Springer, Tokyo.
- Polachek, H. and Seeger, R.J. (1951). On shock-wave phenomena; refraction of shock waves at a gaseous interface. *Phys. Rev.* 84: 922.
- Puckett, E.G., Almgren, A.S., Bell, J.B., Marcus, D.L., and Rider, W.J. (1997). CFD for tracking gas interfaces, Euler and Navier–Stokes Rayleigh–Taylor problems. *J. Comp. Phys.* 130: 269.
- Rupert, V. (1991). Shock interface interaction: Current research on the Richtmyer–Meshkov problem. In *Proc. 18th Int. Symp. Shock Waves* (Ed. K. Takayama), p. 331. Springer.
- Sadot, O., Erez, L., Alon, U., Oron, D., Levin, L. A., Erez, G., Ben-Dor, G., and Shvarts, D. (1998). Study of nonlinear evolution of single-mode and two-bubble interaction under Richtmyer–Meshkov instability. *Phys. Rev. Lett.* 80(8): 1654–1657.
- Samtaney, R. and Meiron, D.I. (1997). Hypervelocity Richtmyer–Meshkov instability numerics. *Phys. Fluids* 9: 1783.

- Samtaney, R. Jaideep, R., and Zabusky, N.J. (1998). Vorticity at a slow-fast interface. *Phys. Fluids* **10**: 1217.
- Teshukov, V.M. (1986). On a shock polar in a gas with general equation of state. *PMM USSR* **50**, 71. (Translation from *Prikl. Matem. Mech.* **50**(1): 98.)
- Thompson, P.A. (1972). *Compressible-Fluid Dynamics*. McGraw-Hill, New York.
- von Neumann, J. (1943). Oblique reflection of shock waves. In *Collected Works*, Vol. VI (Ed. A.H. Taub), p. 238. Pergamon Press, Oxford.

This Page Intentionally Left Blank

Two-Dimensional Interactions

8.3 Shock Wave/Boundary Layer Interactions

JEAN M. DÉLERY

Fundamental/Experimental Aerodynamics Department, Onera 92190 Meudon, France

-
- 8.3.1 Introduction
 - 8.3.2 Properties of Shock-Induced Interactions
 - 8.3.2.1 The Different Kinds of Interaction
 - 8.3.2.2 Interaction without Boundary Layer Separation
 - 8.3.2.3 Interaction with Boundary Layer Separation
 - 8.3.2.4. Hypersonic Interaction
 - 8.3.2.5 Other Aspects of Shock-Induced Interaction
 - 8.3.3 Interaction Control Methods
 - 8.3.3.1 Mechanisms for Control Action
 - 8.3.3.2 Examination of Some Control Actions
 - 8.3.4 Problems Raised by Interaction Modeling
 - 8.3.4.1 Numerical Accuracy of the Codes
 - 8.3.4.2 The Physical Modeling
 - 8.3.5 Concluding Remarks
 - References

8.3.1 INTRODUCTION

When the flow past a vehicle flying at a high velocity becomes supersonic, shock waves inevitably form, caused either by a change in the slope of a surface or by a back pressure that constrains the flow, causing it to become subsonic again. In modern aerodynamics, one can cite a large number of circumstances

where shock waves are present. On subsonic transport aircraft, a nearly normal shock terminates the supersonic pocket present on the wing in certain flight conditions. This transonic situation is also encountered on a helicopter rotor blade or in a turbomachine. Supersonic aircraft are evidently much affected by shock phenomena, which are of prime importance in air intakes, whose purpose is to decelerate a supersonic incoming flow down to low subsonic flow in the engine entrance section. The thrust efficiency of a supersonic transport aircraft depends crucially on its air intakes. Shock phenomena also occur in overexpanded propulsive nozzles where strong shocks form in the exit plane if the exit pressure is much lower than the outside pressure. At hypersonic speeds, shock waves have vital importance due to their effect on the thermodynamic behavior of air (the so-called “real gas effects”) and their multiple repercussions on the vehicle aerodynamics. Shocks also affect missiles and aircraft afterbodies as well as projectiles of all kinds.

Of special importance are the phenomena resulting from the encounter of a shock wave with the boundary layer developing on the external and/or internal surfaces of the vehicle. Then complex processes take place due to the rapid retardation of the boundary layer flow and the propagation of the shock into a multilayered structure. The consequences of the so-called shock wave/boundary layer interaction are multiple and often critical for the vehicle or machine performance. The shock submits the boundary layer to an adverse pressure gradient, distorting its velocity distribution, which becomes less filled (its shape parameter increases). As the same time, in turbulent flows turbulence production is enhanced, which amplifies the viscous dissipation, leading to increased efficiency losses in internal flow machines or substantial drag rise for profiles or wings. The distortion of the boundary layer results also in an increase of its displacement effect, that is, of its influence on the contiguous inviscid flow. This interaction effect—felt through a viscous–inviscid coupling—can greatly affect the flow past a transonic profile or inside an airintake. The foregoing consequences are exarcebated when the shock is strong enough to separate the boundary layer: The consequence can be a dramatic change of the whole flow field with the formation of intense vortices and complex shock patterns replacing the simple purely inviscid flow structure. In addition, shock-induced separation may trigger large-scale unsteadiness, damaging the vehicle structure and limiting its performance (buffeting for wings, buzz for air-intakes, unsteady side loads in separated nozzles. . .).

In some respects, shock-induced separation can be viewed as the compressible facet of the ubiquitous separation phenomenon, the shock being simply an epiphenomenon of the process. Indeed, the behavior of the separating boundary layer is largely the same as in an incompressible separation and the separated flow topology is identical. The most distinct and salient feature of shock separated flows is the accompanying shock patterns, whose existence has major consequences for the entire flow field.

Shock wave/boundary layer interactions—and more generally shock wave/shear layer interactions—do not have only negative effects. The increase in fluctuation level resulting from the interaction can be used to enhance fuel–air mixing in scramjet combustion chambers or to accelerate the disorganization of hazardous flows, such as vortices. Also, since interaction with separation leads to some smearing or splitting of the shock system, the phenomenon can be used to decrease the wave drag produced by the shocks. This last point illustrates the subtle physical features involved in shock wave/boundary layer interactions.

Because of their most often negative effects, shock wave/boundary layer interactions have been actively investigated since the beginning of high-speed aerodynamics in the 1940s. The subject has given rise to a huge number of publications, which would be impossible to cite here. We have retained either “historical” papers or recent publications (reviews on the subject can be found in Green, 1970; Détery and Marvin, 1986; Détery and Panaras, 1996).

The following developments will be restricted to the physical description of the phenomena resulting from shock wave/boundary layer interactions by placing emphasis on the boundary layer response and its repercussion on the associated outer flow organization (see Section 8.3.2). It is not intended to go deeply into the problems raised by interaction prediction, the question involving both numerical difficulties (capture of the discontinuities) and basic questions about turbulence modeling. This last aspect is too vast and still too uncertain to be considered here in detail. We will simply point out the features that still render difficult accurate prediction of shock wave/boundary layer interactions (see Section 8.3.4).

Most of the forthcoming developments deal with two-dimensional flows (planar or axisymmetric) for several reasons:

- It is far easier to analyze the physics and to understand the properties of two-dimensional flows than to grasp the structure of a three-dimensional flow field.
- For a very long time, predictive methods were limited to two-dimensional flows. It is rather recently that three-dimensional calculations have become feasible. However, even now such calculations remain costly and systematic basic studies are still performed with two-dimensional codes.
- There exist practical configurations (control surfaces, air-intake compression ramps, propulsive nozzles) that are not too far from a two-dimensional geometry, so that information obtained on two-dimensional flows can be helpful.

Nevertheless, it should be realized that the world having three dimensions, the two-dimensional assumption is an approximation that is never encountered. Even on a perfectly two-dimensional geometry, the real flow adopts a three-dimensional structure at either a macroscopic or a microscopic scale. The

question is to define how far the two-dimensional flow is from the reality; otherwise, validation of two-dimensional theoretical models on nominally two-dimensional experiments affected by important three-dimensional effects can be made meaningless. Lastly, the vast majority of practical situations being three-dimensional, three-dimensional shock wave/boundary layer interactions should not be completely ignored. These aspects are considered in Section 8.3.2.5.3.

Since shock wave/boundary layer interactions cannot be avoided in many circumstances, techniques have been devised to control the phenomenon in order to limit its damaging consequences (occurrence of large separation and large-scale unsteadiness) or to reduce the drag or the efficiency losses resulting from the presence of strong shocks in the flow. The subject is considered in Section 8.3.3, since control techniques are presently the subject of an active research effort.

8.3.2 PROPERTIES OF SHOCK-INDUCED INTERACTIONS

8.3.2.1 THE DIFFERENT KINDS OF INTERACTION

A shock wave/boundary layer interaction can be viewed as a competition between a variable property flow, the boundary layer in which viscous forces are at work, and an abrupt pressure rise. The result of this conflict depends of the amplitude of the pressure rise and of the properties of the boundary layer flow.

It is usual to distinguish between laminar and turbulent interactions according to the nature of the boundary layer meeting the shock wave. If one considers an averaged turbulent flow—in the sense of the Reynolds or Favre averaging, which filters out all the fluctuating components—there are no basic differences between the two kinds of flows, regarding the overall physics and the topology of the interaction. Thus, any description of the interaction of one nature can be applied—*mutatis mutandis*—to the interaction of the other nature. For this reason, in the forthcoming sections laminar and turbulent interactions are examined in a global manner with the choice of the most frequent turbulent interactions to illustrate the descriptions. However, as far as quantitative properties are concerned, there are dramatic differences between laminar and turbulent flows that make the nature of the incoming boundary layer an essential parameter. Basically, the streamwise length scales involved in a laminar interaction are considerably longer than in a turbulent one.

A major cause of the observed differences lies in the difference in the velocity distribution of the incoming boundary layer. If one considers that during an interaction the flow behavior is dictated by the resistance of the boundary layer to the pressure jump imparted by the shock, it is clear that a turbulent boundary layer, having a well-filled velocity distribution—thus carrying more momentum—will react less than a laminar boundary layer whose velocity profile is far less filled. The more or less filled nature of the boundary layer may be characterized by the incompressible shape parameter H_{inc} . For a flat plate boundary layer, H_{inc} is close to 2.5 in laminar flow and in the range 1.2–1.4 for a turbulent flow. A low value of H_{inc} indicates a well-filled velocity profile. When a boundary layer is submitted to an adverse pressure gradient, its shape parameter increases, the velocity profile becoming less filled due to the retardation action. Also, since the interaction is quite dependent of the thickness of the subsonic part of the boundary layer, a laminar boundary layer, whose subsonic layer is thicker, will respond differently from a turbulent one whose subsonic layer is much thinner, the outer Mach number being the same (see Section 8.3.2.2.1).

The boundary layer velocity profile is only one of the factors—perhaps the most important—influencing an interaction. The shear forces play also a key role, since they represent a force counteracting the retardation imposed by the shock, that is, by the outer inviscid stream. This role is obvious in the case of a laminar boundary layer, which is a viscosity-dominated flow. As the relative magnitude of the viscous forces decreases when the Reynolds number increases, the resistance of a laminar boundary layer will be less at high than at low Reynolds number (see the free interaction theory in Section 8.3.2.3.1). In turbulent flows, the influence of the shear forces is less obvious, the interaction depending weakly of the Reynolds number. This means that for a well-established turbulent regime, there is practically no influence of the Reynolds number, in contrast to a laminar interaction.

On the other hand it must be clear that turbulence plays a central role in the interaction, since the turbulent eddies operate a transfer of momentum from the outer high-speed flow to the inner low-speed part of the boundary layer—hence the greater resistance to the shock and the shorter extent of the separated region when it forms. This aspect also explains the behavior of transitional interactions where the laminar–turbulent transition occurs within the interaction domain (see Section 8.3.2.5.1).

Although the boundary layer response is determined by the intensity of the pressure jump (or more precisely of the pressure gradient)—whatever its origin or cause—the overall flow field structure greatly depends on the way the shock is generated and on the Mach number range. In addition, hypersonic interactions lead to specific phenomena resulting from the intensity of the shocks, their small inclination with respect to the velocity and the high enthalpy level of the outer flow (see Section 8.3.2.4).

What can be considered as the three basic interactions between a shock wave and a boundary layer are the impinging-reflecting shock, the ramp flow, and the normal shock (see Fig. 8.3.1).

1. In the oblique shock reflection, the incoming supersonic flow of Mach number M_0 undergoes a deflection $\Delta\varphi_1$ through the incident shock (C_1) and the necessity for the downstream flow to be again parallel to the wall entails the formation of a reflected shock (C_2), the deflection across (C_2) being $\Delta\varphi_2 = -\Delta\varphi_1$.

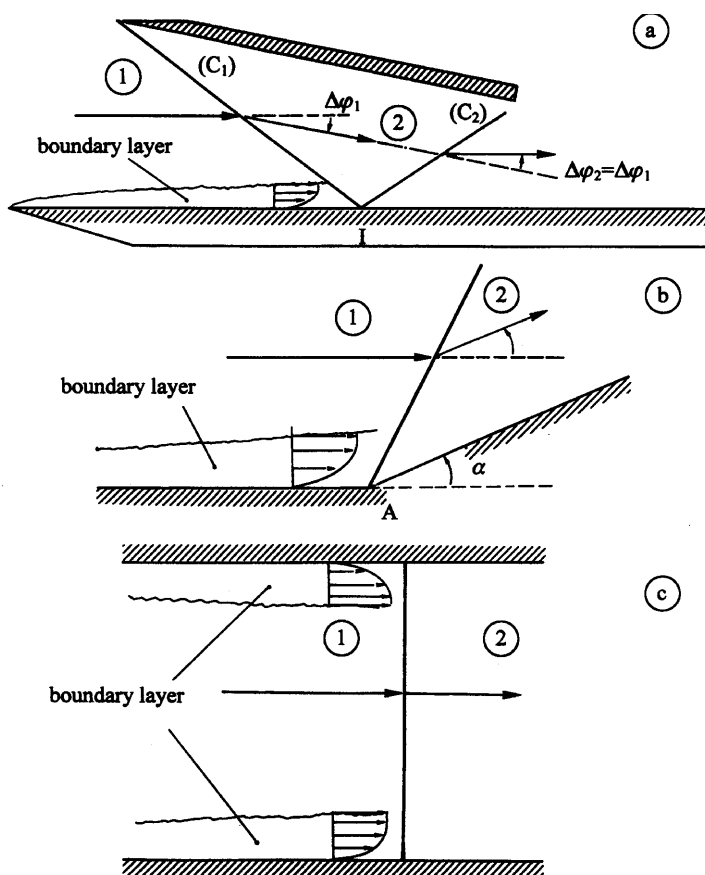


FIGURE 8.3.1 The different kinds of shock wave/boundary layer interactions. (a) Oblique shock reflections; (b) ramp-induced shock; (c) normal shock.

2. In the ramp flow, a discontinuous change in the wall inclination is the origin of a shock through which the incoming flow undergoes a deflection $\Delta\phi_1$ equal to the wedge angle α .
3. A normal shock wave is produced in a supersonic flow by a back-pressure forcing the flow to become subsonic. The distinctive feature of a normal shock is to decelerate the flow without imparting a deflection to the velocity vector, the Mach number behind the shock being subsonic. Normal shocks are frequently met in channel flows, in shock tubes, and over transonic profiles where they terminate the supersonic pocket.

As far as the boundary layer response to the shock is concerned, there are no basic differences between these three situations, so we do not distinguish these different cases when discussing the viscous flow behavior in the forthcoming sections. The distinction is made between interactions without and with separation, since these flows may display dramatic differences.

8.3.2.2 INTERACTION WITHOUT BOUNDARY LAYER SEPARATION

8.3.2.2.1. The Boundary Layer Multilayered Structure

When a boundary layer is submitted to the strong retardation imparted by a shock wave, complex phenomena occur within its structure, which is basically a parallel rotational flow with the Mach number varying from the outer supersonic value to zero at the wall. The process has been analyzed by Lighthill in the framework of its famous triple-deck theory (Lighthill, 1953, see also Stewartson and Williams, 1969).

During the first part of the interaction, most of the flow, including the greatest part of the boundary layer, behaves like an inviscid flow, the pressure and inertia terms of the Navier–Stokes equations being predominant compared to the viscous terms. Thus, many aspects of the boundary layer response can be interpreted by calling upon perfect fluid arguments.

The interaction resulting from the reflection of an oblique shock (C_1) is sketched in Fig. 8.3.2. The incident shock—assumed plane in the outer uniform flow to simplify—penetrates into the rotational inviscid part of the boundary layer, in which it progressively curves because of the decrease in the local Mach number. Correlatively, its intensity weakens, the shock vanishing when it reaches the boundary layer sonic line. At the same time, the pressure rise through (C_1) is felt upstream of the impact point of the incident shock in the inviscid fluid model. This upstream influence phenomenon is in great part an inviscid mechanism, the pressure rise caused by the shock being trans-

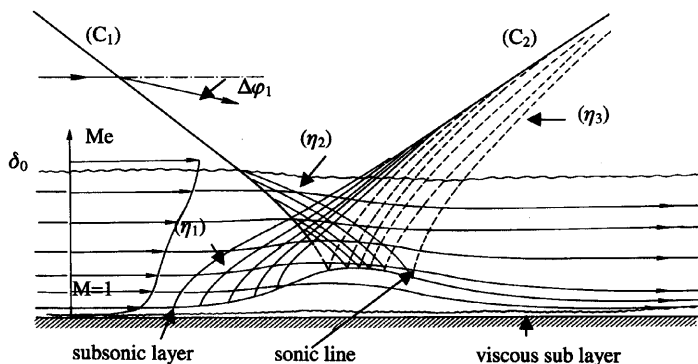


FIGURE 8.3.2 Physical features of an oblique shock reflection without boundary layer separation. The upstream propagation mechanism.

mitted upstream through the subsonic part of the boundary layer. There results a spreading of the wall pressure distribution compared to the purely inviscid flow solution (see Fig. 8.3.3). The dilatation of the boundary layer subsonic region is felt by the outer supersonic flow — which includes the major part of the boundary layer — as a ramp effect inducing compression waves (η_1) whose coalescence forms the reflected shock (C_2). The refraction of these waves — like that of the incident shock — as they propagate through the rotational supersonic layer induces the secondary wave system (η_2). The sonic line reflects these last waves as expansion waves (η_3) present behind the reflected shock (C_2). The thickness of the subsonic layer depending on the velocity distribution; a fuller profile involves a thinner subsonic channel, and hence a

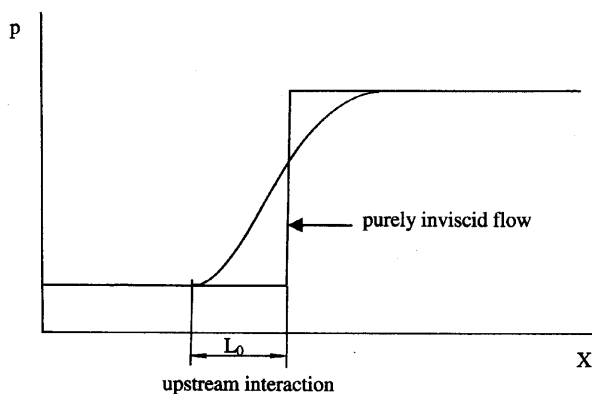


FIGURE 8.3.3 Wall pressure distribution in an oblique shock reflection without boundary layer separation. Example of a weak viscid-inviscid interaction.

shorter upstream influence length. At the same time, a boundary layer profile with a small velocity deficit has a higher momentum, and hence a greater resistance to the retardation imparted by an adverse pressure gradient.

Because of the no-slip condition to be satisfied at the wall, a viscous part must be considered in the near-wall region; otherwise, the model leads to inconsistencies. Thus, the flow resulting from the interaction can be seen as the piling of three layers, or decks:

1. An outer deck, outside of the boundary layer where the fluid is nonviscous and in general irrotational
2. A middle deck—or main deck—incorporating the major part of the boundary layer where the viscosity can be temporarily neglected and where the flow is rotational
3. An inner deck where viscosity again plays a predominant role

For weak incident shocks, the upstream influence is short at the boundary layer scale, so that the above flow pattern is embedded within the boundary layer (in the turbulent case). Thus, at the outer flow scale the only reflected wave is a shock (C_2) with a deflection equal—but with opposite sign—to that of the incident shock (C_1). In this case the shock reflection is said to be a weak viscid-inviscid interaction process in the sense that the (real) viscous flow closely resembles the inviscid flow solution.

8.3.2.2.2 The Upstream Influence Length

An upstream influence length L_0 can be defined as the distance separating the interaction onset (i.e., the location where the wall pressure starts to rise) from the impact point of the incident shock in the inviscid flow model (see Fig. 8.3.3). It is a measure of the interaction spreading caused by the boundary layer. The main parameters likely to influence L_0 ; that is, the extent of the shock wave/boundary layer interactions is as follows (Green, 1970):

1. The upstream Mach number M_0
2. The Reynolds number R_{δ_0}
3. The incident shock intensity, defined by the deflection through the incident shock $\Delta\varphi_1$ (for example)
4. The thickness of the incoming boundary layer δ_0 .

If one considers that any typical streamwise length L_0 scaled to the incoming boundary-layer physical thickness, or displacement thickness, there remain the three following parameters: M_0 , R_{δ_0} , and $\Delta\varphi_1$. If we now focus our attention on the dimensionless length L/δ_0 , it is found that for a fixed value of R_{δ_0} ,

1. L/δ_0 increases with $\Delta\varphi_1$ for a fixed Mach number M_0
2. L/δ_0 decreases when M_0 increases for a fixed $\Delta\varphi_1$
3. For a laminar boundary layer, L/δ_0 increases when R_{δ_0} increases

For a turbulent boundary layer, the influence of the Reynolds number on L/δ_0 is less clear, but it is agreed that L/δ_0 increases when R_{δ_0} increases at moderate Reynolds number and decreases when R_{δ_0} increases at high Reynolds number, the frontier between the two tendencies being around $R_{\delta_0} \approx 10^5$. In fact, the Reynolds number can be a misleading parameter in the sense that it traduces two effects. Considering a flat plate turbulent boundary layer, a high Reynolds number means a reduced importance of the viscous forces, hence a lesser resistance of the boundary layer to an adverse pressure gradient: The interaction length tends to increase. On the other hand, a high Reynolds number means a fuller velocity profile, hence a higher momentum of the boundary layer flow and a decrease of the subsonic channel thickness, so that the interaction length tends to decrease (Settles, 1975). In the first case, the Reynolds number has a local signification, whereas in the second case it characterizes a history effect. This point is further discussed in Section 8.3.2.3.1.

8.3.2.2.3 Other Interacting Flow Organizations

In the case of a shock induced by a change in the direction of the wall—or a ramp—the structure of the flow is different as shown in Fig. 8.3.4. As in the previous case, the pressure rise associated with the shock (C_1) is transmitted upstream of the point A origin of the ramp through the boundary layer subsonic channel. There results a dilatation of the subsonic channel inducing

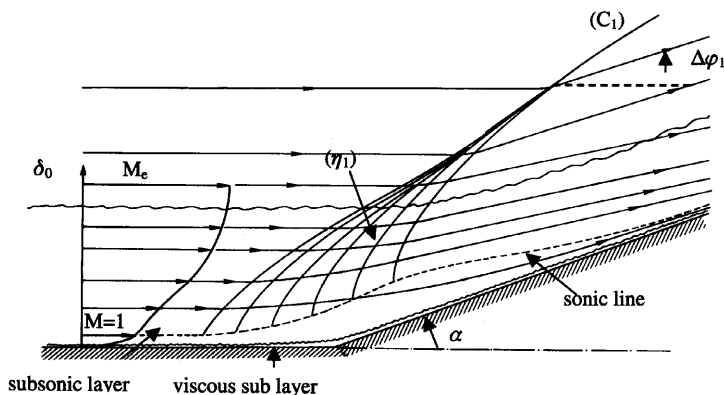
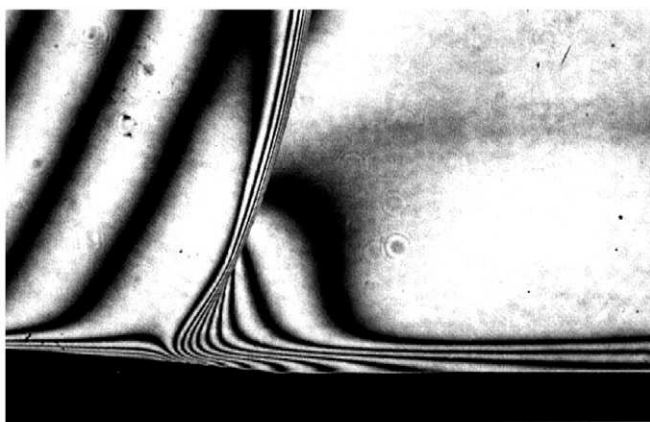


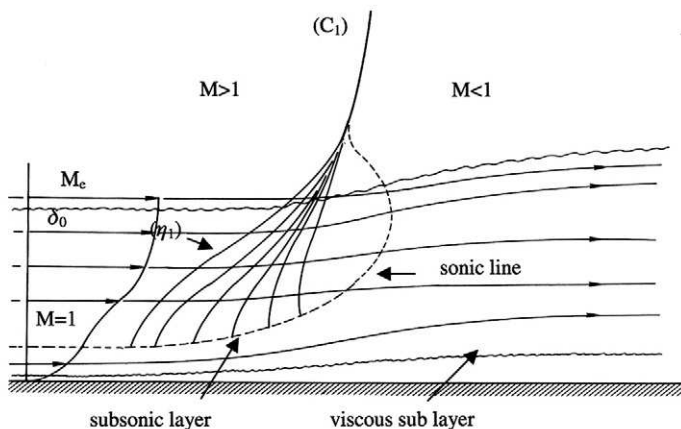
FIGURE 8.3.4 Physical features of a ramp flow without boundary layer separation.

compression waves (η_1) in the contiguous supersonic part. In fact, the shock (C_1) emanating from the ramp origin results from the coalescence of these waves. Thus, the intensity of (C_1) increases steadily until it reaches the value corresponding to the entirely inviscid solution.

In transonic flow, the shock is produced by a rise of the back pressure and most often belongs to the strong oblique shock solution of the Rankine–Hugoniot equations (even though the shock intensity can be very small, as on a transonic profile). For the perfect fluid case, this shock is normal at a wall. As



(a) - Interferogram of a transonic interaction



(b) - Sketch of the flowfield

FIGURE 8.3.5 Physical features of a normal shock interaction without boundary layer separation.

shown by the interferogram in Fig. 8.3.5a and the sketch in Fig 8.3.5b, in the presence of a boundary layer, the same upstream transmission mechanism as in the previous cases takes place. The compression waves induced by the subsonic layer thickening coalesce into the nearly normal shock (C_1). Since the compression in the lower part of the interaction is almost isentropic (except in the viscous layer in contact with the wall), the entropy level on each streamline is less than behind the shock forming at some distance from the wall. Consequently, the Mach number is higher near the wall where a more or less extended pocket of still supersonic flow subsists.

8.3.2.3 INTERACTION WITH BOUNDARY LAYER SEPARATION

8.3.2.3.1 The Boundary Layer Response

Since the retardation effect is larger in the boundary layer inner part, a situation can be reached where the flow is pushed in the upstream direction by the adverse pressure gradient so that a separated region forms. Then, the flow adopts the structure sketched in Fig. 8.3.6. Downstream of the separation point S there exists a bubble made of a recirculating flow bounded by a discriminating streamline (S) that separates the recirculating flow from the flow streaming from upstream to downstream “infinity.” The streamline (S) originates at the separation point S and ends at the reattachment point R . Because of the action of the strong mixing taking place in the detached shear layer that emanates from S , an energy transfer is operated from the outer high

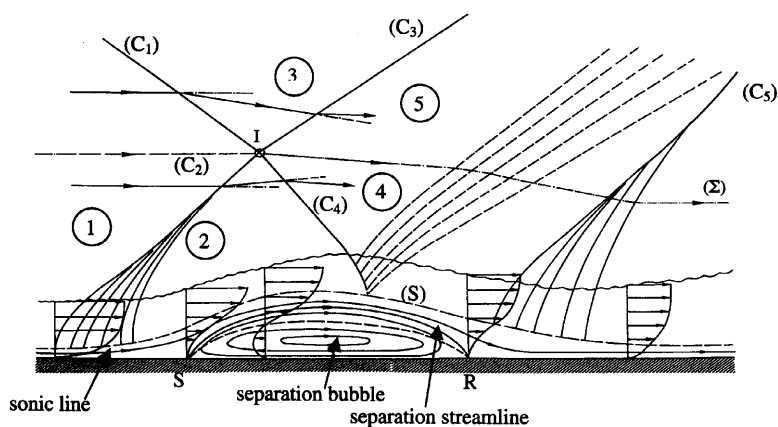


FIGURE 8.3.6 Physical features of an oblique shock reflection with boundary layer separation.

speed flow toward the separated region. As a consequence, the velocity U_s on the discriminating streamline (S) steadily increases, until the reattachment process begins.

The transmitted shock (C_4) penetrates in the separated viscous flow where it is reflected as an expansion wave. There results a deflection of the shear layer toward the wall on which it reattaches. At reattachment, the separated bubble vanishes, the flow on (S) being decelerated until it stagnates at R. This process is accompanied by a compression wave ending into a reattachment shock in the outer stream. As shown in Fig. 8.3.7, the wall pressure distribution exhibits a first step rise, associated with separation, followed by a plateau typical of separated flows. A second more progressive pressure rise takes place during reattachment. Now, the flow field structure is markedly different from what it would be for the purely inviscid case: The shock reflection is said to be a strong viscous-inviscid interaction.

The separation process itself is basically a free interaction process resulting from a local self-induced interaction between the boundary layer and the outer

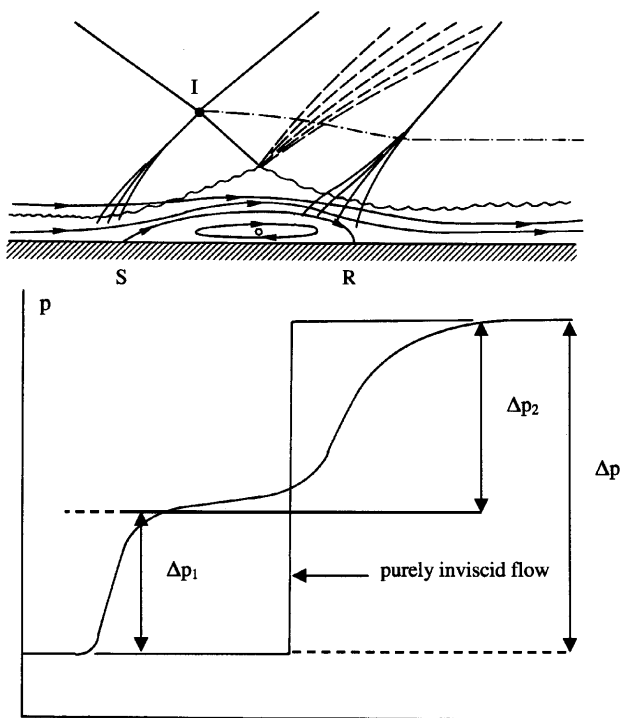


FIGURE 8.3.7 Wall pressure distribution in an oblique shock reflection with boundary layer separation. Example of a strong viscous-inviscid interaction.

inviscid stream. Chapman demonstrated this fact in the 1950s by a simplified analysis, which led to the following expression for the pressure rise during the interaction (Chapman *et al.*, 1957):

$$\frac{p - p_0}{q_0} = F(X) \sqrt{\frac{2C_{f_0}}{\sqrt{M_0^2 - 1}}}.$$

Here p is the pressure, q the dynamic pressure, M the Mach number, and C_f the skin friction coefficient; 0 designates the conditions at the interaction origin; and $F(X)$ is a dimensionless correlation function depending on the streamwise scaled distance X .

It is seen that the pressure rise undergone by the boundary layer is of the form

$$\frac{p - p_0}{q_0} \propto (C_{f_0})^{1/2} (M_0^2 - 1)^{-1/4}.$$

In hypersonic flows $(M_0^2 - 1)^{-1/4} \approx M_0^{-1/2}$, and knowing that $q_0 = (\gamma/2)p_0 M_0^2$, we have

$$\frac{p - p_0}{p_0} \propto (C_{f_0})^{-1/2} M_0^{3/2}.$$

In a similar way the free interaction theory shows that the streamwise extent L of the interaction first part obeys a law of the form

$$L \propto \delta_0^* (C_{f_0})^{-1/2} (M_0^2 - 1)^{-1/4},$$

where δ_0^* is the incoming boundary layer displacement thickness.

The preceding relations show that the pressure rise Δp_1 at separation and the extent of the interaction first part depend only on the flow properties at the interaction onset and not on the downstream conditions, in particular the intensity of the incident shock. The separation pressure rise Δp_1 is entirely determined by the upstream flow conditions. During the interaction first part, the flow results of a reciprocal and mutual influence—or coupling—involving the local boundary layer and the inviscid contiguous stream, and not the further development of the interaction: hence the denomination free interaction or free separation. This important result, well verified by experiment, explains many features of an interaction with shock-induced separation.

A major consequence of the interaction is to divide the pressure jump Δp imparted by the shock reflection into a first compression Δp_1 at separation—with the associated shock (C_2)—and a second compression Δp_2 at reattachment, the overall pressure rise being such that $\Delta p_1 + \Delta p_2 = \Delta p$ (see Fig. 8.3.7). The extent of the separated region is dictated by the ability of the shear layer issuing from the separation point S to overcome the pressure rise at

reattachment. This ability is function of the momentum available on (S) at the starting of the reattachment process. Since the pressure rise to separation does not depend on downstream conditions, an increase of the overall pressure rise imparted to the boundary layer — or incident shock strength — entails a higher pressure rise at reattachment. This can only be achieved by an increase of the maximum velocity $(U_s)_{max}$ reached on the discriminating streamline, hence an increase of the shear layer length allowing a greater transfer of momentum from the outer flow. Thus, the length of the separated region will grow in proportion to the pressure rise at reattachment and the separation point will move in the upstream direction.

Since the relative importance of the viscous forces decreases when the Reynolds number increases, the free interaction theory predicts an augmentation of the interaction extent and a decrease of the overall pressure rise when the Reynolds number is raised. A consequence is that — for given laminar or turbulent regimes — separation of the boundary layer requires a stronger shock at low Reynolds numbers than at high Reynolds numbers. This behavior is well confirmed by experiment in laminar flows and in turbulent flows as long as the local Reynolds number R_δ is less than 10^5 . Beyond this value, the tendency is reversed, the interaction domain contracting when the Reynolds number increases and the turbulent boundary layer becomes more resistant to separation. The conflict is in fact resolved if one considers that the behavior of the boundary layer during the interaction is commended both by inertia and viscous forces. The free interaction theory privileges viscous forces, since it involves only the skin friction coefficient. The predominance of viscosity is manifest in laminar flows or low Reynolds number turbulent flows. At high Reynolds number, the momentum transported by the boundary layer becomes the predominant factor in the interaction with the shock. Since the boundary layer profile is fuller when the Reynolds number increases, the resistance of the boundary layer is greater.

Incipient shock-induced separation. The definition of a limit for shock-induced separation is also a question of major concern since for applications it is important to know the maximum shock intensity that a boundary layer can withstand without separating. This limit is most often defined in the plane of two variables: the ramp angle (or equivalent angle leading to the same total pressure rise for shock reflection) and the Reynolds number, a different curve corresponding to each value of the Mach number M_0 (Délery and Marvin, 1986). As a consequence of the above comments, for a given upstream Mach number, the shock strength required to separate a turbulent boundary layer first decreases when the Reynolds number increases. Above $R_\delta \approx 10^5$ a trend reversal occurs, the limit shock strength increasing with the Reynolds number. At fixed Reynolds number, the shock intensity entailing separation increases with the Mach number.

8.3.2.3.2 The Outer Inviscid Flow Structure

8.3.2.3.2.1 The Incident-Reflecting Shock

When there is separation, the interaction of the shock wave with the boundary layer has deep repercussions on the contiguous inviscid flow. As shown in Fig. 8.3.6, the simple purely inviscid shock system made of an incident plus reflected shock is now replaced by a pattern involving five shock waves:

- The incident shock (C_1)
- The separation shock (C_2)
- The transmitted shock (C_3) emanating from the intersection point I of (C_1) and (C_2)
- The second transmitted shock (C_4)
- The reattachment shock (C_5).

The structure or pattern made of shocks (C_1), (C_2), (C_3), and (C_4) is a type I shock/shock interference according to Edney's classification (Edney, 1968).

The interference at point I can be represented in the shock polar diagram shown in Fig. 8.3.8 where the polar (Γ_1) is associated to the upstream uniform state 1 and represents any shock forming in 1, in particular the incident shock

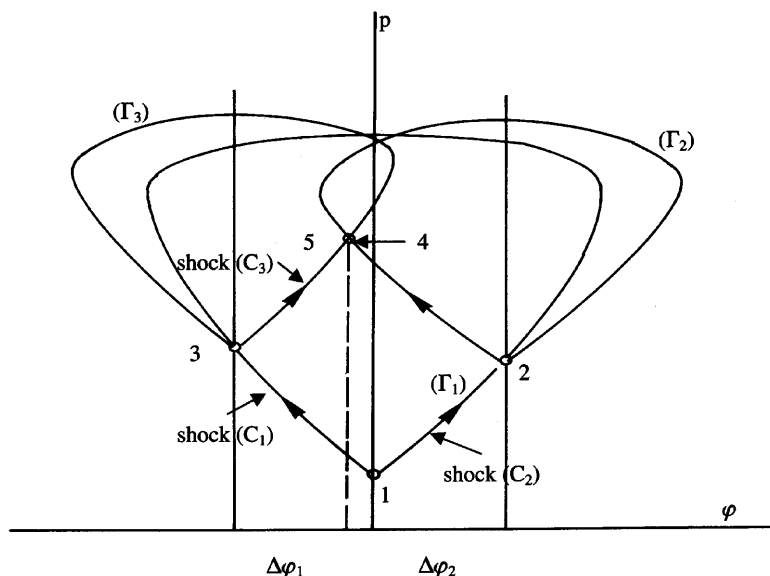


FIGURE 8.3.8 Shock polar diagram of the shock system in an oblique shock reflection with boundary layer separation. Regular intersection of the incident and separation shocks.

(C_1). The image of the downstream flow 3 is the point 3 on (Γ_1), the deflection imparted by (C_1) being negative (the velocity is deflected towards the wall). The separation shock (C_2) is also represented by (Γ_1) since the upstream state is 1. The image of the downstream flow 2 is at point 2 on (Γ_1), the deflection $\Delta\varphi_2$ being upward. The situation downstream of I is at the intersection of the polars (Γ_3) and (Γ_2) respectively attached to the states 3 and 2. Their intersection is the image of two states 4 and 5 having the same pressure ($p_4 = p_5$) and the same direction ($\varphi_4 = \varphi_5$), hence compatible with the Rankine-Hugoniot equations. The set of successive shocks (C_1) + (C_3), being different from the set (C_2) + (C_4), the flows having traversed (C_1) + (C_3), on the one hand, and (C_2) + (C_4), on the other hand, have undergone different entropy rises. Hence, a slip line (Σ) separates flows 4 and 5, which have different velocities, densities, temperatures, and Mach numbers (but identical pressures). In real flow a shear layer develops along (Σ) ensuring a continuous variation of the flow properties between states 4 and 5.

The fluid, having streamed along a streamline passing under the point I and belonging to the inviscid part of the field, crosses three shock waves: (C_2) + (C_4) plus the reattachment shock (C_5). Hence, its final entropy level is lower than for the entirely inviscid case where the fluid traverses the incident + reflected shocks. This is also true for the interaction without separation, which is close to the inviscid model at some distance from the wall (see Fig. 8.3.2). The conclusion is that entropy production through the shock system may be smaller in a shock-induced interaction than in an interaction without separation or in the limiting case of the inviscid model. This result is exploited by control techniques designed to reduce wing drag or efficiency losses in internal flows (see Section 8.3.3.2).

If the strength of the incident shock is increased, a situation can be reached where the two polars (Γ_2) and (Γ_3) do not intersect. Then a type II interference occurs at the crossing of shocks (C_1) and (C_2), a nearly normal shock, or Mach stem, forming between the triple points I_1 and I_2 (see Figs. 8.3.9 and 8.3.10). The downstream states 4 and 6 located at the intersection of the polars (Γ_1) and (Γ_2) are separated in the physical plane by the slip line (Σ_1), whereas the downstream states 5 and 7 at the intersection of (Γ_1) and (Γ_3) are separated by the slip line (Σ_2). The subsonic channel downstream of the Mach stem (C_5) is accelerated under the influence of the contiguous supersonic flows, so that a sonic throat appears after which the flow is supersonic. In the present case, the interaction produces a completely different outer flow structure with the formation of a complex shock pattern replacing the simple purely inviscid flow solution.

Transonic and ramp-induced interactions lead to similar separated flow organization, the boundary layer reacting to a given pressure rise, no matter the

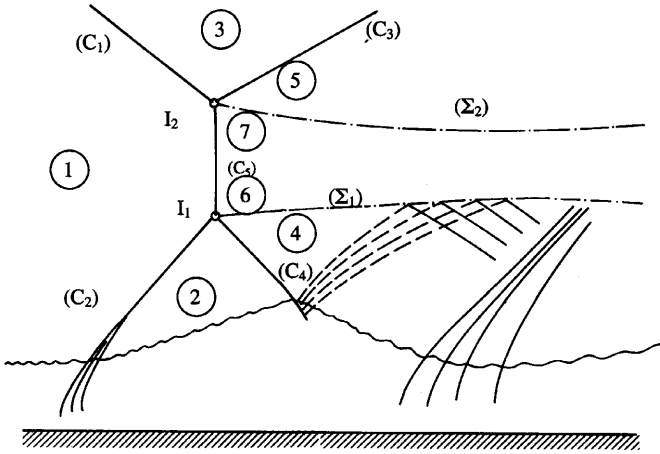


FIGURE 8.3.9 Physical features of an oblique shock reflection with boundary layer separation. Singular intersection of the incident and separation shocks.

cause of this pressure rise. Thus, the wall pressure distribution in a separated ramp flow is nearly coincident with the distribution produced by a shock reflection giving the same overall pressure rise as the ramp (see Fig. 8.3.11). By comparison with the oblique shock reflection, what changes is the shock pattern associated with the interaction.

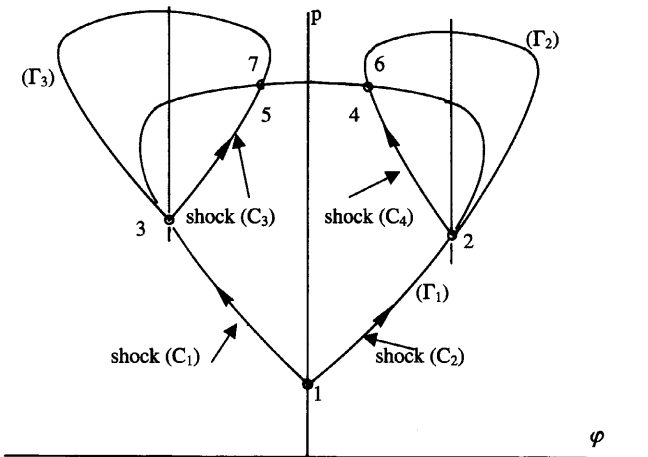


FIGURE 8.3.10 Shock polar diagram of the shock system in an oblique shock reflection with boundary layer separation. Singular intersection of the incident and separation shocks.

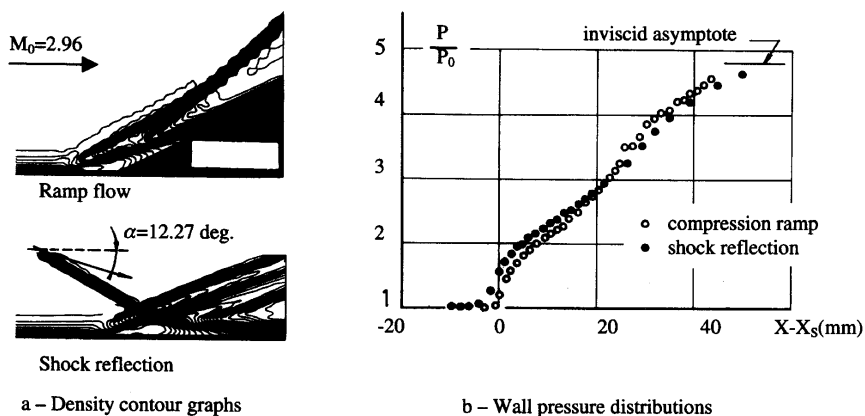


FIGURE 8.3.11 Comparison of wall pressure distributions in a ramp flow and a shock reflection at $M_0 = 2.96$ (Shang *et al.*, 1976).

8.3.2.3.2 Ramp-Induced Interaction

In the case of the interaction at a ramp, the shock system is a type VI interference produced by the intersection of the separation shock (C_1) and the reattachment shock (C_2), both running upward, as shown in Fig. 8.3.12. The situation at point I where the two shocks (C_1) and (C_2) meet is represented in the shock polar diagram of Fig. 8.3.13. The solution is made of the shock (C_3), which is seen as the shock induced by the ramp at large distance from the wall, and of the states 3 and 6, at the same pressure, and separated in the physical plane by the slip line (Σ). An intermediate state 4 has to be introduced between 2 and 6. In the case sketched in Fig. 8.3.12, state 6—compatible with 3—is obtained at the intersection of the polar (Γ_4) attached to state 4 and of the polar (Γ_1) attached to 1. Thus, in this case a fourth shock (C_4)—in general very weak—emanates from I and propagates toward the wall. This situation is met in low Mach number supersonic flows. At higher Mach number, the respective position of the polars changes, (Γ_2) being entirely inside (Γ_1). Then, the state 6, compatible with 3, is obtained at the crossing of the shock polar (Γ_1) and of the polar (Δ) representing an isentropic expansion from state 4. Now, a centered expansion emanates from the triple point I and propagates in the direction of the wall on which it is reflected as a new expansion wave.

In hypersonic flows, the shocks are weakly inclined with respect to the velocity and the boundary layer subsonic channel is excessively thin. In these conditions, as shown in Fig. 8.3.14, the separation shock starts from a point very close to the wall and the shock pattern may be embedded in the boundary layer flow. The type IV interference at the intersection of the separation and

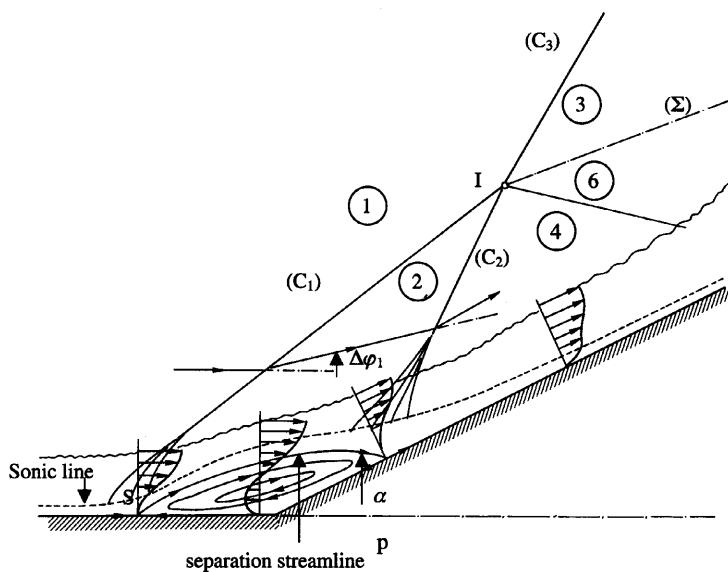


FIGURE 8.3.12 Physical features of a ramp flow with boundary layer separation.

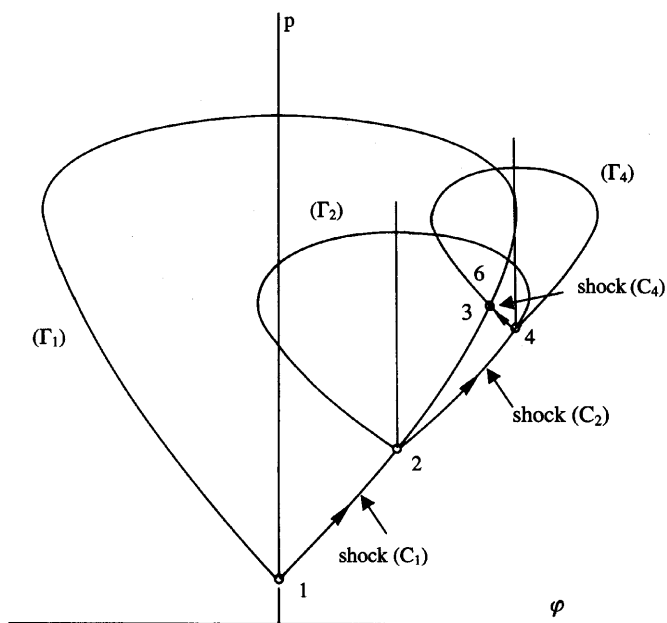


FIGURE 8.3.13 Shock polar diagram of the shock system in a ramp flow with boundary layer separation.

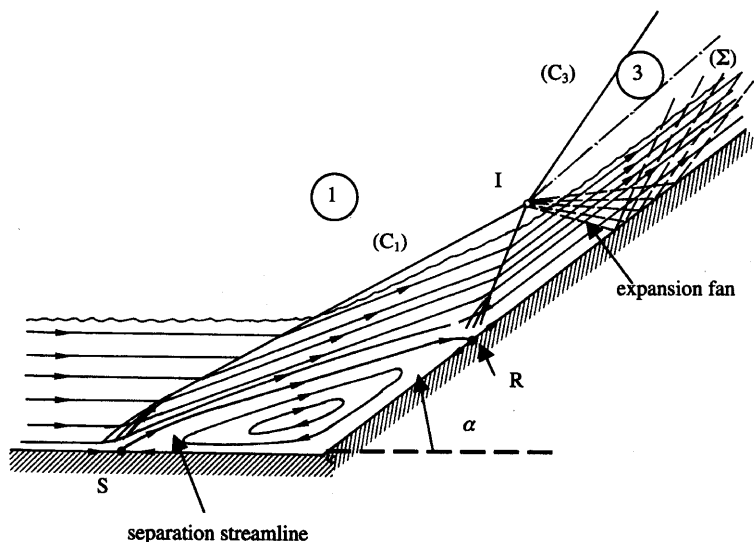


FIGURE 8.3.14 Physical features of a ramp flow at hypersonic Mach number.

attachment shocks produces an expansion whose signature on the nearby wall is denoted by a sharp pressure decrease following the rise at reattachment, as illustrated in Fig. 8.3.15.

To illustrate this type of flow, Fig. 8.3.16 shows a shadowgraph picture of a ramp-induced interaction in a Mach 9.2 hypersonic flow. One clearly sees the shear layer emanating from the separation region, and the crossing of the separation and reattachment shocks that occurs very close to the ramp.

8.3.2.3.3 Normal Shock Interaction

The interferogram in Fig. 8.3.17a shows a transonic interaction with shock-induced separation taking place in a channel, Fig. 8.3.17b giving an interpretative sketch of the flow field. Boundary layer separation induces an oblique shock (C_1) after which the flow is still supersonic. The shock (C_1) meets the normal shock (C_3), cause of separation, at the point I, giving an interference similar to the Edney type VI. The situation at the point I in the shock polar diagram is shown in Fig. 8.3.18. Compatibility conditions downstream of I entail the formation of a “trailing” shock (C_2) represented on the shock polar (Γ_2). The two compatible downstream states 3 and 4 are separated by the slip line (Σ). At transonic velocity (upstream Mach number $M_0 \approx 1.4$ – 1.5) the flow 2 is weakly supersonic ($M_2 \approx 1.20$ – 1.10). The shock (C_2) is a strong oblique shock (in the sense of the strong solution to the oblique shock

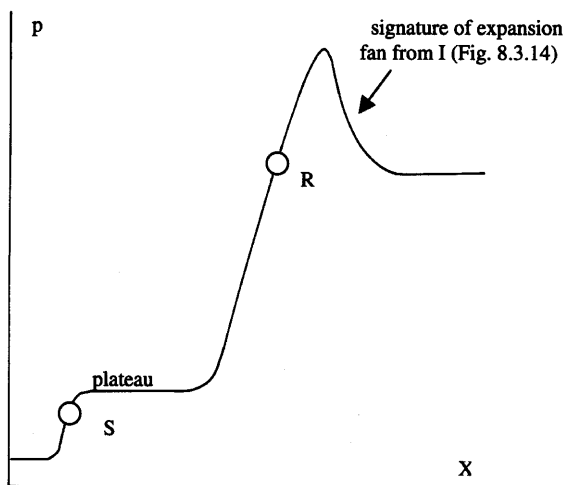


FIGURE 8.3.15 Wall pressure distribution in a separated ramp flow at hypersonic Mach number.

equations) whose intensity is in fact very weak. Downstream of (C_2), the flow may be subsonic or still supersonic with a Mach number close to 1. The rest of the compression is nearly isentropic with a continuous transition to subsonic velocities. The supersonic domain behind (C_2)—the so-called supersonic tongue—is more or less extended, depending on the local and downstream boundary conditions. This structure, typical of shock induced separation in transonic flow, is termed a lambda shock pattern.

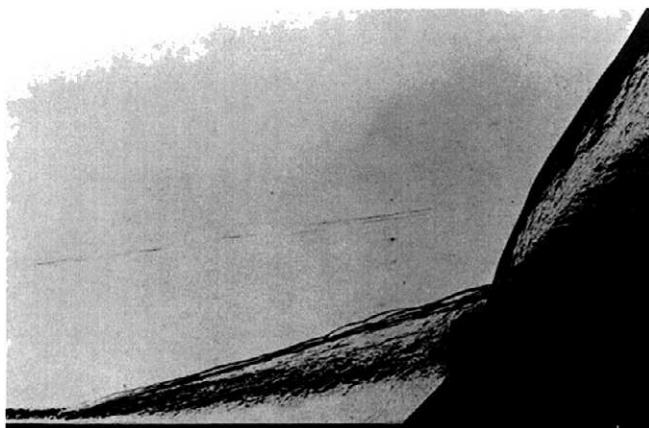
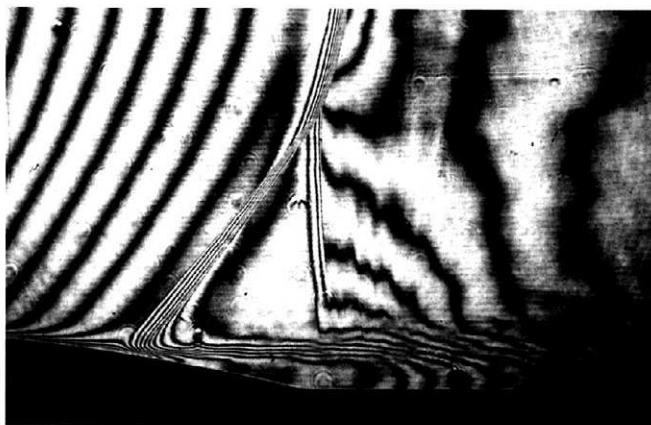
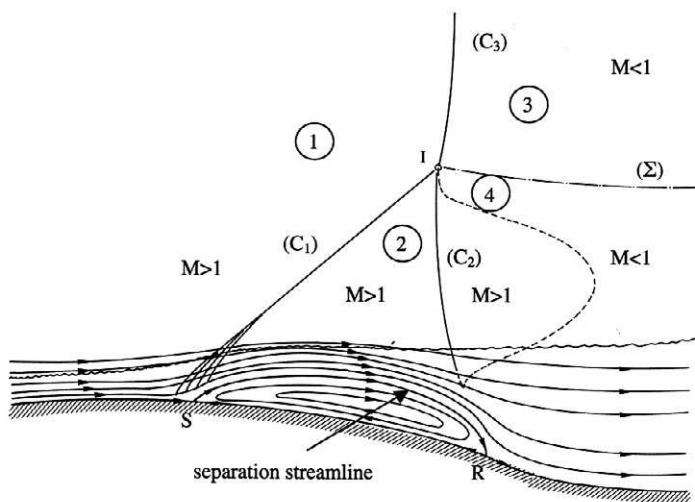


FIGURE 8.3.16 Shadowgraph of a turbulent ramp flow at Mach 9.2 (Elfstrom, 1971).



Onera document

a - Interferogram of a transonic interaction



b - Sketch of flow field

FIGURE 8.3.17 Physical features of a normal shock interaction with boundary layer separation. The lambda shock pattern.

The evolutions of the boundary layer characteristics during the present interaction are plotted in Fig. 8.3.19. The displacement thickness δ^* starts to increase sharply at the interaction onset, provoking a "viscous ramp" effect which is at the origin of the separation shock (C_1). Thereafter, δ^* undergoes a

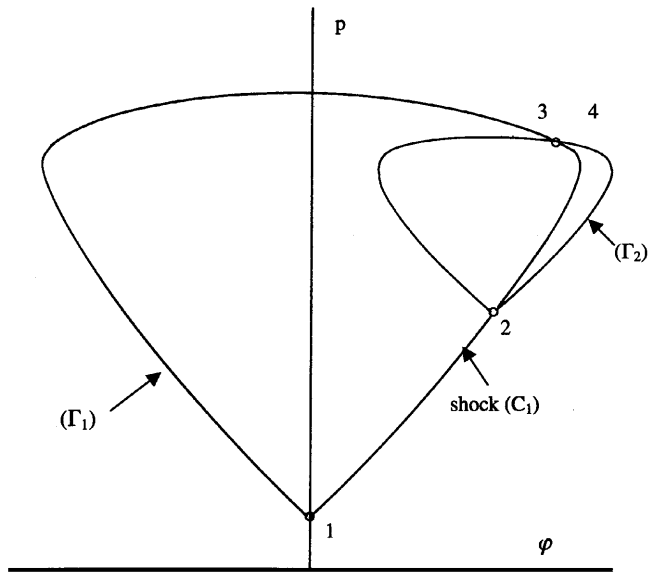


FIGURE 8.3.18 Shock polar diagram of the shock system in a normal shock interaction with boundary layer separation.

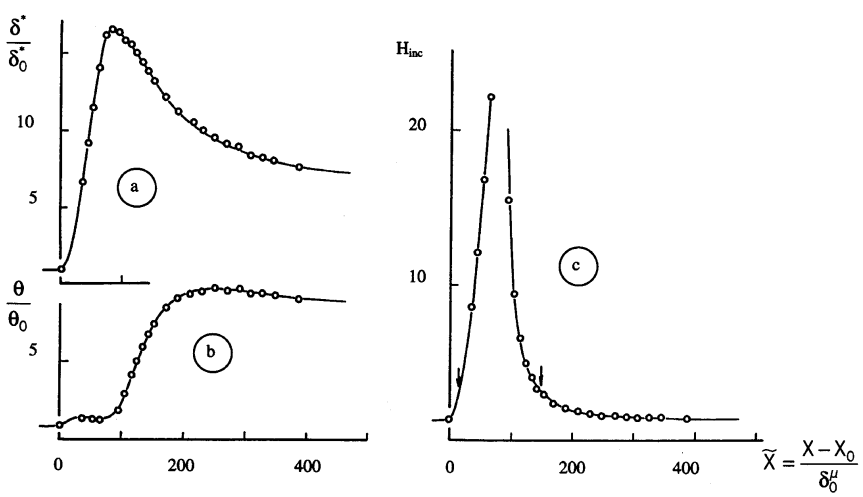
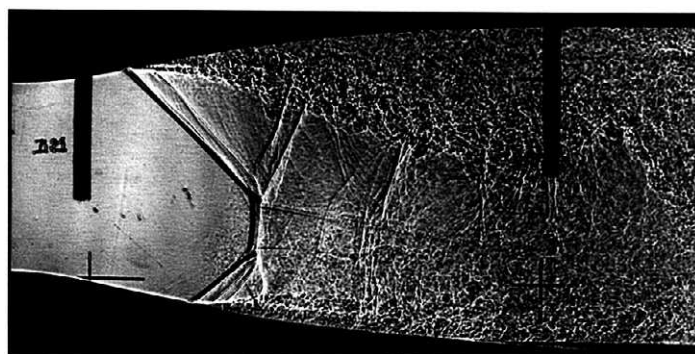


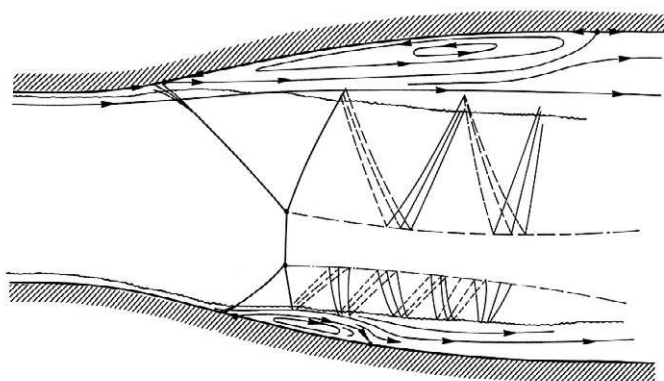
FIGURE 8.3.19 Evolution of the boundary layer characteristics during a transonic interaction with separation. (a) Displacement thickness, (b) momentum thickness, (c) incompressible shape parameter.

considerable rise during the development of the separated bubble, until it starts to decrease when reattachment begins. The momentum thickness θ rises continuously during the interaction representing the momentum loss of the flow, which will be felt by a drag increase, or an efficiency loss. At the same time the incompressible shape parameter H_{inc} reaches very high values in the separated region, denoting the extreme emptying of the velocity profiles that contain a back-flow region. When reattachment begins, H_{inc} decreases rapidly down to values typical of a flat plate boundary layer, this tendency corresponding to the so-called rehabilitation process.

The sketch in Fig. 8.3.20b, established from the short exposure time shadowgraph of Fig. 8.3.20a, gives an example of strong interactions occurring



a - Short exposure time shadowgraph



b - Sketch of the flow field

FIGURE 8.3.20 Nonsymmetrical shock-induced separation in a supersonic nozzle (Reijasse *et al.*, 1999).

in a planar supersonic nozzle whose flow is choked by a second throat (Reijasse *et al.*, 1999). For reasons not yet fully understood, the separated flow adopts an asymmetric structure, separation on the upper wall taking place earlier than on the lower wall, although the geometry is symmetric (this point will not be discussed here). The very large separation on the upper wall gives rise to a lambda shock pattern, the flow behind the trailing shock (C_2) being still well supersonic. Separation on the lower wall causes a smaller lambda pattern associated with a reduced separated region. Intersection of the separation shocks (C_1) and (C_3) is here a type II interference with the existence of a Mach phenomenon made of the nearly normal shock (C_5) with the two triple points I_1 and I_2 . The slip lines (Σ_1) and (Σ_2) emanating from I_1 and I_2 form a fluidic subsonic channel between two supersonic streams. Because of the conditions imposed by the adjacent supersonic flows, the flow in this channel accelerates until it reaches the sonic speed at a throat. Thereafter, the channel section increasing, the expansion continues in supersonic. The penetration of (C_2) in the separated shear layer generates a reflected expansion wave, which is reflected by the slip line (Σ_1) into a wave made of converging compression waves. These waves are in turn reflected by the nearly isobaric separated region into expansion waves, the pattern being repeated over a certain distance. A similar pattern can be observed near the lower wall. The present configuration is a striking example of the coupling between the separated regions and the inviscid part of the flow. This coupling here generates complex structures because of the confinement of the flow, as is the case in channel-type flows, such as supersonic diffusers, compressor cascades, or propulsive nozzles.

8.3.2.4. HYPERSONIC INTERACTION

The high specific enthalpy level typical of hypersonic conditions has three direct consequences on shock-wave/boundary layer interactions:

1. When the wall temperature is well below the outer stream stagnation temperature, a cold wall situation arises that may significantly affect the interaction properties.
2. Heat transfer processes take dramatic importance, especially in separated flows where the shear layer emanating from the separation region impacts on the reattachment surface.
3. Real-gas effects resulting from the intense heating produced by the bow shocks modify the thermodynamic and transport properties of the fluid (most often air) in a way that may influence the interaction.

8.3.2.4.1 Wall Temperature Effect on the Interaction Properties

The thermal condition at the wall is characterized by the ratio of the wall temperature T_w to the recovery temperature T_r corresponding to adiabatic conditions at the wall, that is, without heat transfer. Experiments performed at high Mach number on a laminar ramp-induced interaction showed that wall cooling ($T_w/T_r < 1$) provokes a contraction of the interaction domain as compared to the adiabatic case (Lewis *et al.*, 1968). The same tendency has been observed in turbulent interactions, energetic wall cooling reducing substantially the separation distance or the upstream interaction length (Spaid and Frishett, 1972). Results on shock wave/boundary layer interaction on a heated wall ($T_w/T_r > 1$) are more scarce, since this situation is less frequent (it could be encountered on a hypersonic vehicle releasing at low altitude the heat stored during the high-speed part of the reentry trajectory). They show that wall heating entails an extension of the interaction domain, which in fact confirms—a contrario—observations made on a cooled wall (Délery, 1992).

There is not a unique explanation of the decrease in L_s/δ_0 with the wall temperature (or its increase when T_w is raised). This tendency is in agreement with the free interaction theory (see Section 8.3.2.3.1) since a lowering of the wall temperature provokes an increase of the skin friction coefficient and a reduction of the boundary layer displacement thickness (the density level in the boundary layer being raised): hence a contraction of L_s . However, the observed dependence on wall temperature is much beyond that predicted by the free interaction theory. Contraction of the interaction domain results also in the thinning of the boundary layer subsonic part. Indeed, as experiment shows, the velocity distribution across a boundary layer is almost unaffected by the wall temperature (this is true for both cooled and heated wall). Since lower temperatures entail smaller sound velocity, the Mach number in the inner part of the boundary layer is higher: hence a thinner subsonic channel. The same argument is valid for a heated wall, since then the sound velocity, being higher the Mach number, is reduced.

The wall temperature level may have a more subtle influence through its effect on the state of the incoming boundary layer. In ramp flow experiments it was found that, compared to the adiabatic case, surface pressure distributions displayed a greater extent of the separated region when the model was cooled, the pressure plateau forming well ahead of the ramp origin, (Délery and Coët, 1990). At the same time compression on the ramp was more spread out. At first sight these tendencies are in contradiction with the preceding conclusions, wall cooling generally tending to contract the interaction domain. In fact the observed behavior had to be attributed to the fact that the laminar-to-turbulent transition occurred in the interaction domain itself. Since wall cooling tends to delay transition, the boundary layer developing on the cooled model is “more

laminar” than on an adiabatic model. This fact explained that in the present case the separated zone was more extended for the cooled boundary layer.

8.3.2.4.2 Heat Transfer in Hypersonic Interactions

The salient feature of hypersonic interactions is the existence of high transfer rates in the interaction region, especially when there is separation. This problem, which is crucial for the sizing of the thermal protection in parts of the vehicle where such interactions are likely to occur, has been studied by many investigators, in laminar as well as in turbulent flows (Holden, 1977). Heat transfer rates are particularly intense in the vicinity of the point, R where the separated flow reattaches. This rise in heat transfer is associated with the stagnation at R of the shear layer developing from the separation point. In some respects, the situation at R is similar to a nose stagnation point, with the difference that the flow impinging on the ramp (or control surface) has been compressed through a succession of oblique shocks at separation and reattachment (see Section 8.3.2.3.2) instead of a unique normal shock. Consequently its (average) stagnation pressure being higher, transfer processes are much more efficient, hence higher heat transfer levels.

The surface heat transfer is most often represented in a nondimensional form by the Stanton number, defined by

$$S_t = \frac{q_w}{\rho_\infty U_\infty (h_{t_\infty} - h_w)},$$

where q_w is the wall heat transfer (in W/m^2), ρ_∞ , U_∞ the density and velocity of the upstream flow, h_{t_∞} the upstream flow specific stagnation enthalpy, and h_w the flow specific enthalpy at the wall. It should be noted that the true Stanton number is

$$S_t = \frac{q_w}{\rho_e U_e (h_r - h_w)},$$

where ρ_e and U_e are relative to the local flow conditions at the boundary layer edge. Because these quantities, like the recovery enthalpy h_r , are difficult to determine in hypersonic interactions, the first definition of the Stanton number is more often used. Another way to circumvent the difficulty is to plot the ratio q_w/q_{ref} , where q_{ref} is the heat transfer that would be measured at the wall in the absence of interaction.

The laminar heat transfer distribution shown in Fig. 8.3.21 has been measured at $M_\infty = 10$ in a ramp-induced separation (Délerly and Coët, 1990). A semilogarithmic scale has been used to emphasize the phenomena in the interaction first part. The heat transfer decreases slowly in the upstream part of the cylinder, in agreement with the hypersonic strong/weak viscous interaction theory (Hayes and Probstein, 1959). A more rapid decrease starts at

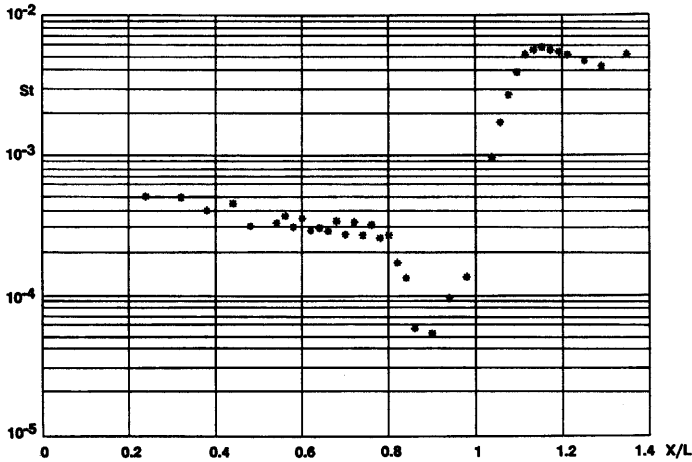


FIGURE 8.3.21 Heat transfer distribution in a laminar ramp induced interaction (Délery and Coët, 1990).

a location coincident with the separation onset. This decrease is typical of shock-induced separation in laminar flows. Heat transfer goes through a minimum in the separated region, then rises sharply during reattachment, the peak value being reached downstream of the reattachment point, as determined from a surface flow visualization.

Results relative to a turbulent interaction produced by a 35° ramp are presented in Fig. 8.3.22. Although the upstream Mach number is modest

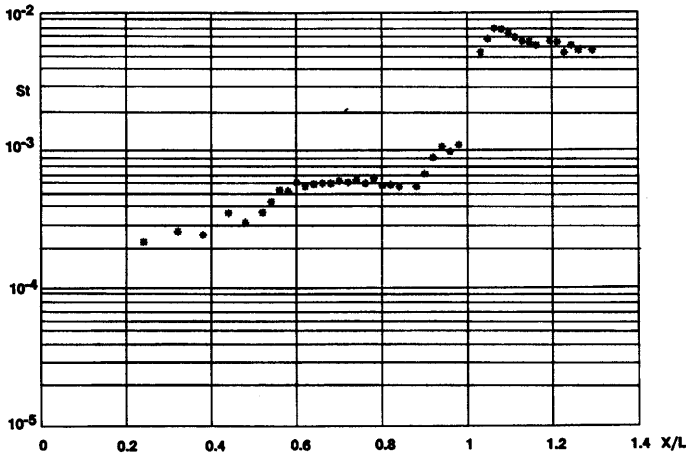


FIGURE 8.3.22 Heat transfer distribution in a turbulent ramp induced interaction (Délery and Coët, 1990).

($M_\infty = 5$), these results are similar to those obtained at high Mach numbers (Détery and Coët, 1990). In this case heat transfer first decreases slowly in the most upstream part of the model. The first rise, followed by a slow decrease, is due to laminar–turbulent transition. A second rise takes place at the separation location, this behavior opposite to that observed in laminar flow being typical of turbulent shock-induced separation. Further downstream, the heat transfer increases sharply during reattachment to reach a peak value downstream of the reattachment point. The heat transfer rise at separation may be explained by amplification of turbulence in the vicinity of the separation point and further downstream. Since the flow then “leaves” the surface, large eddies can develop that promote exchanges between the wall region and the outer high-enthalpy flow, leading to a rise in heat transfer.

8.3.2.4.3 Real-Gas Effects on Shock Wave/Boundary Layer Interaction

At hypersonic speeds the flow over the vehicle exhibits real-gas effects due to dissociation and ionization provoked by the passage of the air through the strong bow shock. Such effects are also present after intense shock waves produced by explosions or in shock tubes. Hence, a further interaction will involve a gas whose composition and physical properties are modified compared to an equilibrium nondissociated gas. In this situation real-gas effects are coupled with complex viscous/inviscid interactions. If the calorically perfect gas (i.e., a gas with constant ratio of specific heats γ throughout the flow field) is taken as benchmark, the real gas or chemical effects will be felt at two stages:

1. Since the thermodynamic properties are not the same, the structure of the inviscid part of the flow is modified compared to the constant γ case.
2. Dissociation and chemical phenomena affect the transport properties (viscosity, heat conduction, and diffusion coefficients), which has repercussions on the viscous part of the flow.

Thus, at high enthalpy, nonequilibrium vibrational excitation and chemical reactions may affect the scaling of a separated region through a change in shock angle and in the incoming boundary layer thickness. As compared to the perfect gas case, there are few experimental results about the incidence of real gas effects on shock wave/boundary layer interaction, basic experiments on this influence being difficult to make. They have to be executed in high enthalpy facilities, which are very scarce in the world and costly to operate. In addition, it is difficult to make parametric investigations in these facilities, since running at different high enthalpy levels entails changes in the other flow parameters (upstream composition and thermodynamic properties, Mach and Reynolds numbers). As a consequence, it is almost impossible to establish a

clear identification of the influence of only the real-gas effects. Information must be obtained in great part from computations considering fully laminar interactions. Thus, in ramp-type flow it was found, under the assumption of chemical equilibrium, that in dissociated air a smaller separated region forms because of weaker shock waves. Moreover, the heat transfer rates are lower because of lower temperatures (Grasso and Leone, 1992).

In the case of an impinging-reflecting shock, and with consideration of nonequilibrium chemistry for air, it was found that real gas effects at low Reynolds numbers weakly affect the interaction (Ballaro and Anderson, 1991). Then the flow can be computed with a fair degree of accuracy by assuming a constant local value of γ . This assumption may be invalid if the reflection becomes singular (occurrence of a Mach phenomenon; see Section 8.3.2.3.2). Then an accurate calculation of the adjacent inviscid flow is necessary. On the other hand, at high Reynolds number, chemistry effects lead to substantial differences in the wall pressure and heat transfer distributions, with an increase of the heat transfer levels.

Major differences between the noncatalytic and catalytic wall conditions have to be anticipated. In the latter case, the interaction is much affected by the high-energy release taking place in the separated region. This provokes a dilatation of the separation bubble (similar to the dilatation of the separated region on a heated wall; see Section 8.3.2.4.1) and a spectacular increase of the wall heat transfer (Grummet *et al.*, 1991).

8.3.2.5 OTHER ASPECTS OF SHOCK-INDUCED INTERACTION

8.3.2.5.1 Transitional Interaction

In most aeronautical applications, the boundary layer becomes turbulent shortly after attachment at the nose or the leading edge, since the Reynolds numbers are very high. However, circumstances exist where a laminar regime is met. This is the case of hypersonic vehicles or reentry bodies in the upper part of the atmosphere where density is very low. Also, laminar conditions can be encountered in turbomachines because of the small size of the blades. On transonic laminar profiles designed to reduce aircraft drag, the boundary layer can be laminar at the level of the shock. In fact, the situation is less simple than the existence of two distinct states, one laminar, the other turbulent, with clearly identified physical properties. The perturbation caused by the shock is a very efficient means of triggering transition, and in nearly all cases the interaction has a transitional nature that renders its prediction still more difficult.

The effect of laminar–turbulent transition on shock wave/boundary layer interaction is a complex question, which has been scarcely investigated. Starting from a fully laminar interaction, it is established that a rise in the Reynolds number R_L provokes a move of the transition in the upstream direction until it reaches the interaction region. Then the peak heat transfer becomes much higher than that in the fully laminar case. At the same time, a reversal in the Reynolds number dependence occurs, with the extent of the separated region decreasing with an increase of R_L (Heffner, 1993). When R_L is raised, the transition first stays in the reattachment region until a limit value of R_L is reached, beyond which it suddenly moves to the separation region. With a further increase of the Reynolds number, transition takes place upstream of the interaction, strongly affecting the flow structure. For example, the separated zone may disappear, the ramp angle (or impinging shock strength) becoming no longer sufficient to separate the boundary layer.

In fact, most of the so-called “laminar” hypersonic interactions are transitional since maintaining a laminar regime throughout the interaction domain is difficult because of the extreme sensitivity of the separated shear layer to disturbances. At usual Reynolds numbers, this shear layer tends to transition after separation, its state at reattachment being intermediate between laminar and fully turbulent. This transition produces a “mixed” interaction in which separation has the feature of a laminar flow (decrease of the wall heat transfer), whereas reattachment has a turbulent behavior (high pressure and heat transfer peaks). This point is a major issue in providing laminar cases for the validation of computer codes (Grasso *et al.*, 1994).

8.3.2.5.2 Unsteady Phenomena

The unsteady aspects of shock wave/boundary layer interaction have been up to now ignored in this article, although this question has been a subject of major concern (for a review of the question, see Dolling, 1993). A distinction must be made between large-scale unsteadiness affecting the entire flow field and small-scale fluctuations interesting only the interaction region and the nearby flow (Muck *et al.*, 1988). There is a close correlation between the second type of fluctuations and the fluctuating nature of a turbulent boundary layer, which makes that the interacting shock “feels” a variable incoming flow and reacts accordingly. Then several questions are raised: What is the nature of the interaction between turbulence and the induced shock oscillations? Is it possible that such a mechanism operates a transfer of energy from the outer flow to the turbulent field, thus enhancing the turbulence level? If this is true, what is the validity of the classical turbulence models, which do not incorporate such a mechanism? Answering to these questions is an arduous task,

requiring sophisticated experimental techniques and advanced theoretical approaches.

When the flow separates, the fluctuation level in general increases, two behaviors being observed.

- As the separated bubble is a region of low mechanical energy, it reacts more strongly to the fluctuations produced by the interaction of the separation shock with the turbulent field. The contraction and stretching of the separated bubble result in an amplification of the flow unsteadiness, which is transmitted upstream through the mechanism explained in Section 8.3.2.2.1. This feedback process entails a general rise of the fluctuation level. This behavior is observed in shock-induced separation, the amplitude of the shock motion being of the order of the incoming boundary layer thickness.

- In some circumstances, the foregoing mechanism is dramatically amplified, the entire flow field being affected by large-scale fluctuations which can be periodic or not, depending of the conditions. This phenomenon is at work in transonic airfoil buffeting where the normal shock can move over a significant portion of the chord length, the separated bubble disappearing and reappearing in a periodic manner. Overexpanded propulsive nozzles are affected by unsteady and asymmetric shock-induced separation at the origin of variable side loads, which can be very high during the startup transient. Similar phenomena take place in supersonic air intakes, leading to unsteadiness which can cause engine unstart. Here, there is not enough room to discuss these phenomena, which are not fully understood.

8.3.2.5.3 Three-Dimensional Effects

The consideration of three-dimensional interactions requires a reexamination of the separation phenomenon, the two-dimensional definition becoming inadequate in three dimensions. The separated bubble made of closed streamlines circling around a common point D and bounded by a separation streamline (S) issuing from the separation point S and ending at the reattachment point R does not exist in three-dimensional flows. In three dimensions, the flow supposed initially two-dimensional (like the boundary layer developing on a flat plate) has the capability to escape along the spanwise dimension when it is confronted with an adverse pressure gradient. The closed organization of Fig. 8.3.23a has to be replaced by the open bubble of Fig. 8.3.23b in which the streamlines are no longer closed curves but spiral around a common point or focus F into which they disappear, the flow escaping laterally from F . The mass conservation principle (in steady flows) then requires that the streamline (S) issuing from the separation point be distinct from the streamline (A) stagnating at the reattachment point R .

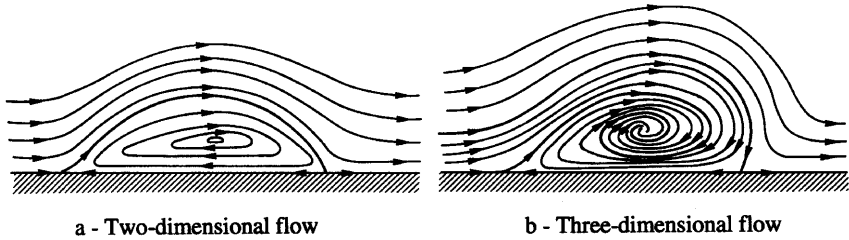


FIGURE 8.3.23 Simple conceptions of separation and separated bubble.

This possibility leads us to reconsider the definition of separation on a three-dimensional obstacle, which is made by calling upon the critical point theory (Legendre, 1956). This theory focuses on the skin friction lines on an obstacle, which are the lines tangent to the local skin friction vector at each of their points. Such lines constitute the skin friction line pattern. More precisely, one examines the behavior of the skin friction lines in the vicinity of a point where the skin friction vanishes. Such a point, which is termed a critical point, can be of the node, saddle-point, or focus type according to the skin friction line behavior in its vicinity (see Fig. 8.3.24). All the skin friction lines, except

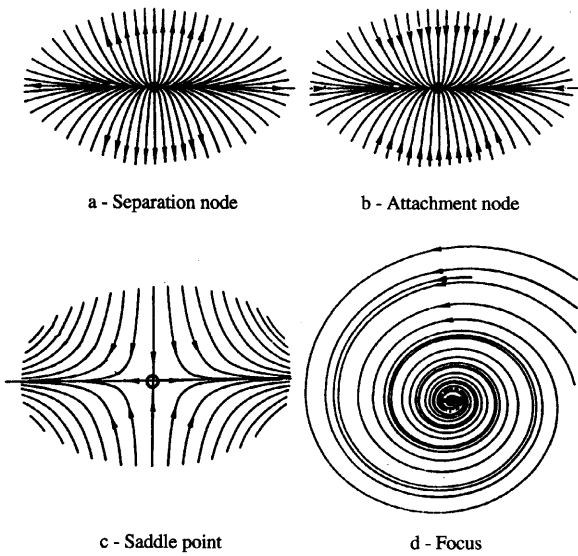


FIGURE 8.3.24 The different critical points of the skin friction line pattern.

one, go through a node that can be of the separation or attachment type. Only two skin friction lines go through a saddle point S , all the other lines avoiding S by taking a hyperbolic shape, as shown in Fig. 8.3.24c. These special skin friction lines, which are called separators, are of the separation or attachment type according to the flow behavior in their vicinity (see Fig. 8.3.25). A flow is separated if its skin friction line pattern contains at least one saddle point through which passes a separation line. This line is the trace on the surface of a streamsurface, called a separation surface, the rolling up of which forms a vortical structure typical of three-dimensional separated flows.

In this restricted space we consider a very limited application of the critical point theory to the analysis of the topology of separated three-dimensional flows, in particular those produced by a shock wave (for more complete information, see Déléry, 1999).

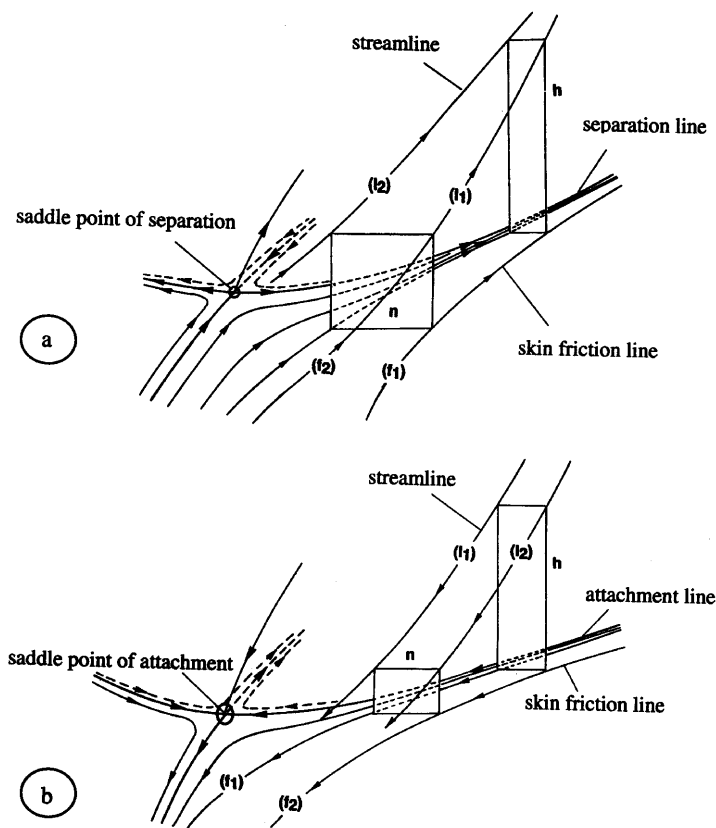


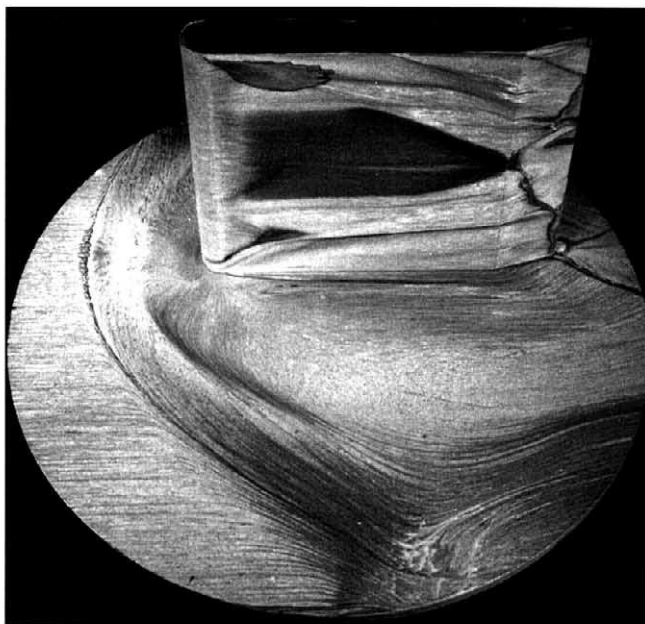
FIGURE 8.3.25 Separation line (a) and attachment line (b).

Basic three-dimensional shock wave/boundary layer interactions are produced by a swept wedge, a sharp fin at incidence, a blunt fin, or a three-dimensional transonic channel. Each of these flows has been thoroughly studied and is described in detail elsewhere (Settles, 1993; Délery, 1993). We only consider here the flow produced by a blunt fin placed normally to a flat plate, this flow containing most of the physics of three-dimensional shock-induced separation. In the case chosen to illustrate this interaction, the upstream Mach number is equal to 2, the flat plate boundary layer being turbulent (Barberis and Molton, 1995). Basic information on the interaction is provided by the surface flow visualization showing the skin friction line pattern (see Fig. 8.3.26). A first separation saddle point S_1 is present well in front of the obstacle. Through S_1 passes the primary separation line (S_1) that separates the skin friction lines coming from upstream “infinity” from those originating at the attachment node N_1 placed behind S_1 . A second saddle point S_2 exists downstream of S_1 with a secondary separation line (S_2). For topological reasons, an attachment line (A_1) originates at the node N_1 and separates the skin friction lines flowing toward (S_1) from those flowing toward (S_2). A third separation line (S_3) is present very close to the fin.

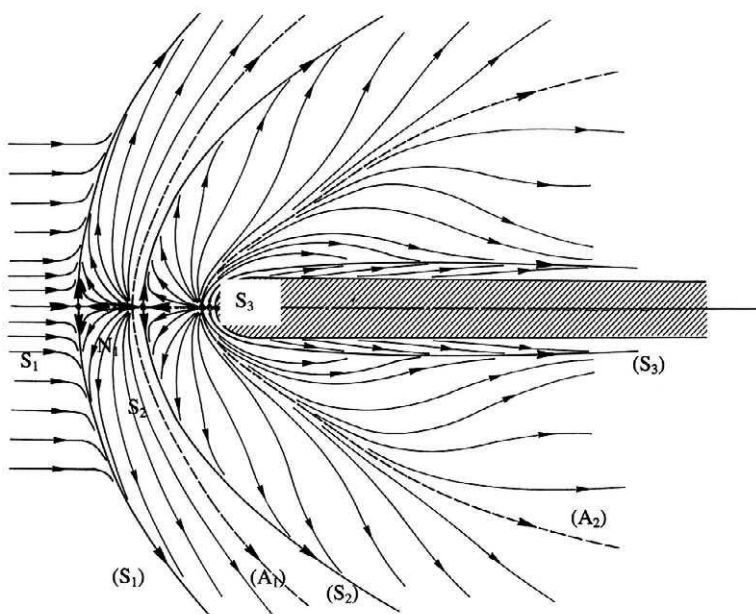
The schlieren picture and the sketch in Fig. 8.3.27 show the structure of the flow in a vertical plane containing the fin plane of symmetry. The blunt leading edge provokes the separation of the boundary layer well ahead of the fin, a lambda shock pattern forming in the inviscid part of the flow field. The separation shock (C_1), the trailing shock (C_2), and the shock (C_3) produced by the fin meet at the triple point I, from which emanates a shear layer striking the fin leading edge. This structure can also be seen in side planes, sensibly normal to the primary separation line (S_1).

The flow topology in the plane of symmetry is sketched in Fig. 8.3.28a (the vertical scale is greatly increased in this picture). The main outer flow separation line (S_1) springs out from the separation point S_1 and spirals around the focus F_1 . The attachment line (A_1) ends at the half saddle point coincident with the node N_1 in the surface. The streamlines flowing between (S_1) and (A_1) disappear into the focus F_1 . Two other similar structures exist associated to the separation lines (S_2) and (S_3). The three foci F_1 , F_2 , and F_3 are the traces in the symmetry plane of three horseshoe vortices surrounding the obstacle as sketched in Fig. 8.3.28b. These vortices result from the rolling up of the separation surfaces (Σ_1), (Σ_2), and (Σ_3) withstood by the three separation lines. The topology of the flow in planes sensibly normal to (S_1) is similar, the difference being that the lines in question are projected streamlines and not actual streamlines.

In the framework of the foregoing general definition, two-dimensional separation appears as a very particular case in which the separation line is made of an infinite number of saddle points (Délery, 1999). The separation

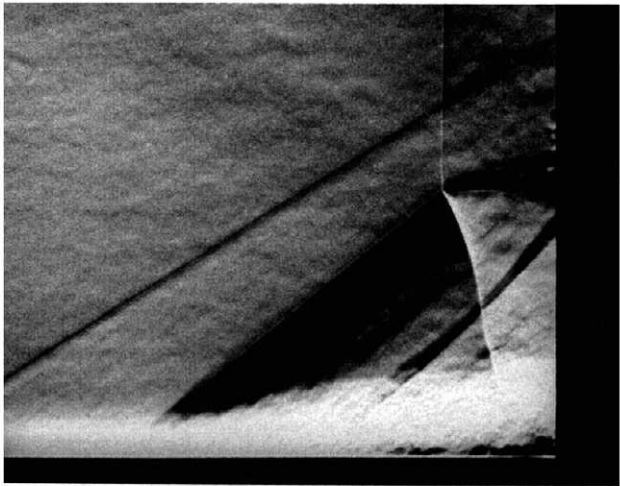


a - Surface flow visualisation

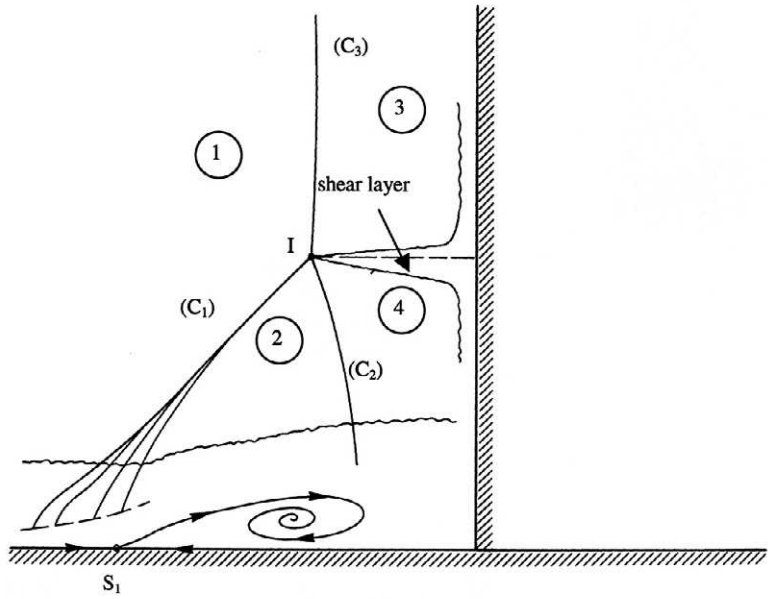


b - Topological interpretation

FIGURE 8.3.26 Turbulent separation induced by a blunt fin in supersonic flow at $M_0 = 1.97$ (Barberis and Molton, 1995).

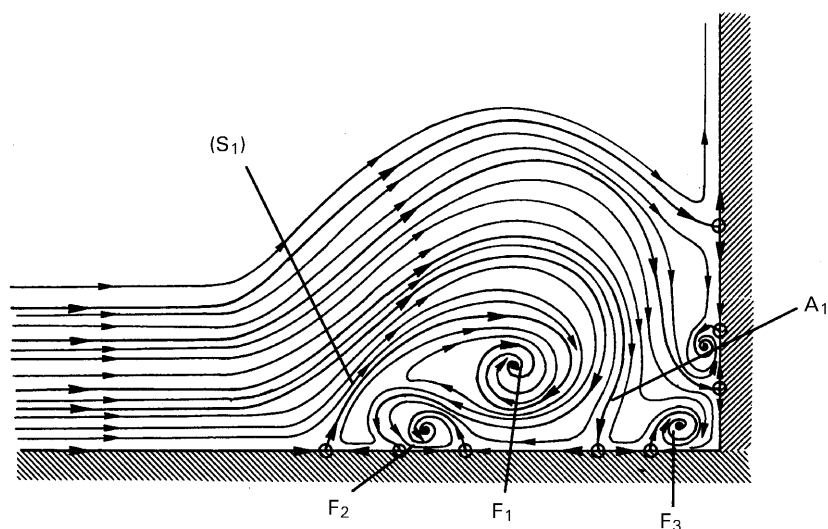


a - Schlieren photograph

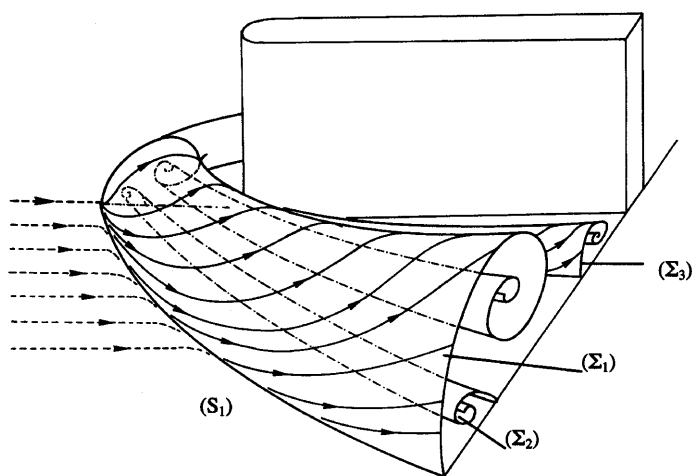


b - Interpretative sketch

FIGURE 8.3.27 Blunt fin-induced separation. Flow organization in the plane of symmetry (Barberis and Molton, 1995).



a - Streamlines in the symmetry plane



b - Separation surfaces

FIGURE 8.3.28 Blunt fin-induced separation. Schematic flow field organization.

point is at the crossing by this line of the plane containing the two-dimensional flow. This situation being unlikely in the real three-dimensional world, even with two-dimensional geometries and upstream boundary conditions, separated flows adopt a three-dimensional organization. In experiments performed in a two-dimensional test section, the skin friction line pattern has a macro-

scopic three-dimensional organization, like the one sketched in Fig. 8.3.29a. A saddle point S_1 exists in the test section symmetry plane through which goes the separation line (S) spiraling into the foci F_1 and F_2 . Reattachment takes place along the attachment line (A) going through the reattachment saddle point S_2 . This surface flow pattern can be highly three-dimensional if the ratio of the test section width to the incoming boundary layer thickness is not sufficient. In the case of an axisymmetric configuration, the periodicity condition imposes a three-dimensional organization in which a finite number of critical points, of the node and saddle types, are distributed in succession on the reattachment line as sketched in Fig. 8.3.29b. This pattern can be interpreted as the trace on the surface or Görtler-type vortices whose origin is unclear and that are intensified by the concave curvature effect resulting from the reattachment of the shear layer. It is probable that these

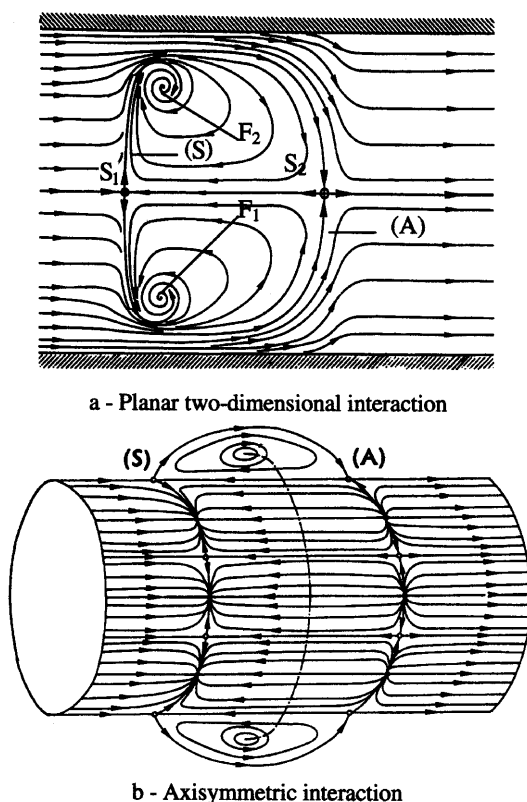


FIGURE 8.3.29 Three-dimensional effects on the skin friction line pattern in nominally two-dimensional interactions.

“microstructures,” which are scaled by the incoming boundary layer thickness, have a weak influence on the overall flow organization, so that the reality is not far from the axisymmetric idealization.

8.3.3 INTERACTION CONTROL METHODS

8.3.3.1 MECHANISMS FOR CONTROL ACTION

Since it is often difficult to avoid damaging shock wave/boundary layer interactions, the idea soon arose to control the phenomenon by an appropriate “manipulation” of the flow either before or during the interaction process (Regenscheit, 1941; Fage and Sargent, 1943; Délery, 1985, for a review of the subject). The target of the control techniques was mainly to prevent shock-induced separation and/or to stabilize the shock in naturally unsteady configurations. The upstream influence of the shock and the resistance of a turbulent boundary layer depending mainly on its momentum, as seen in Section 8.3.2.3.1, a way to limit the shock effect is to increase the boundary layer momentum prior to its interaction with the shock. This can be done by proper boundary layer manipulation:

1. One can perform an injection through one or several slots located upstream of the shock origin, this technique being called boundary layer blowing.
2. A distributed suction applied over a certain boundary layer run before the interaction reduces its shape parameter, thus producing a fuller velocity profile.
3. It is also possible to eliminate the low-speed part of the boundary layer by making a strong suction through a slot located at a well-chosen location in the interaction region or slightly upstream of it.
4. By placing vortex generators upstream of the shock, a transfer of momentum is operated from the outer high-speed stream to the benefit of the boundary layer low velocity part. This transfer enhances its resistance to an adverse pressure gradient.

A local action can also be performed in the immediate vicinity of the interaction or within it. As a key role is played by the velocity level that must be reached on the separating streamline (S) to allow shear layer reattachment (see Section 8.3.2.3.1), any action modifying this level will influence the interaction. If some fluid is sucked off through the wall, topological considerations lead to the flow structure sketched in Fig. 8.3.30b. The streamline (S_2), which stagnates at the reattachment point R being located at a greater distance

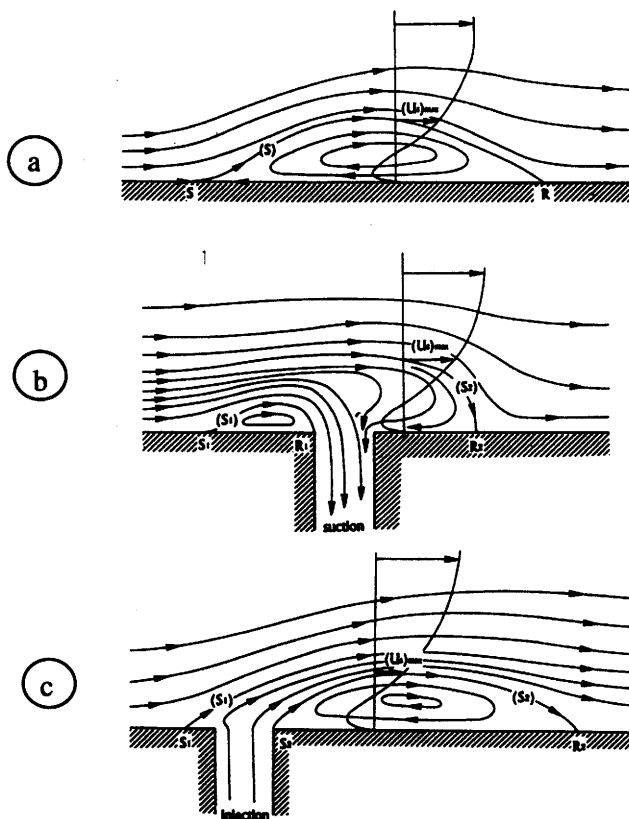


FIGURE 8.3.30 Schematic representation of the flow in a separated bubble. (a) Basic case; (b) with mass suction; (c) with mass injection.

from the wall, the velocity $(U_s)_{max}$ on (S_2) is greater than in the basic case of Fig. 8.3.30a: hence an increase of the ability of the flow to withstand a more important compression, and a subsequent contraction of the interaction domain. The case of fluid injection at low velocity is sketched in Fig. 8.3.30c. Now, the velocity on (S_2) is smaller, (S_2) being at a lower altitude on the velocity profile. The effect is a lengthening of the separated bubble. However, if the injected mass flow is increased, there will be a reversal of the effect, since the velocity on the bottom part of the profile—and in particular $(U_s)_{max}$ —will increase if the mass flow fed into the separated region goes beyond a certain limit.

One can also contract the interaction domain by cooling the wall on which the interaction takes place since on a cold wall the boundary layer has a more

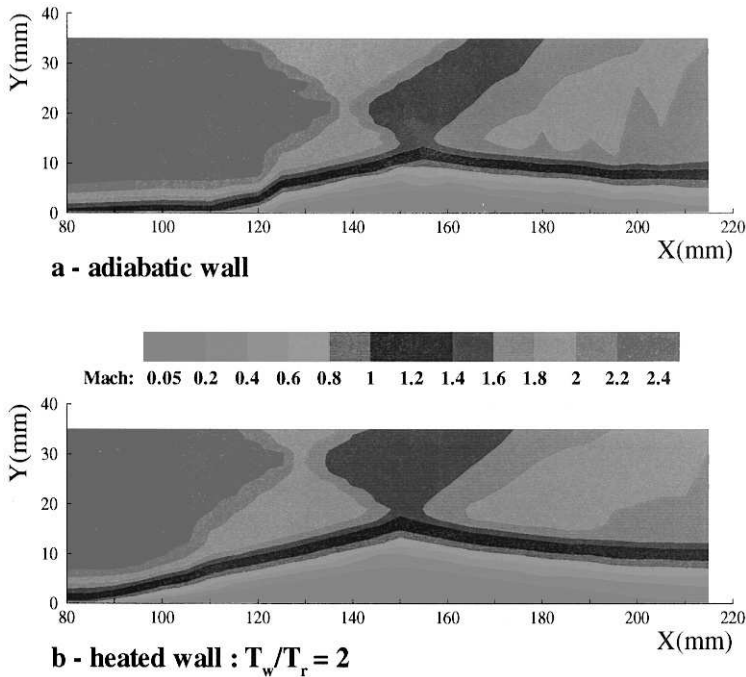


FIGURE 8.3.31 Wall temperature effect on an oblique shock reflection at $M_\infty = 2.4$ (Délery, 1992). (See Color Plate 1).

filled profile than on a wall at recovery temperature, as seen in Section 8.3.2.4.2. This control technique can be envisaged on vehicles using cryogenic fuels, as hypersonic planes or space launchers. As an example, Fig. 8.3.31 shows the effect of wall heating on an oblique shock reflection. In this case of temperature control, spreading of the interaction domain occurs.

8.3.3.2 EXAMINATION OF SOME CONTROL ACTIONS

When considering shock wave/boundary layer interaction control, it is essential to state the objectives:

- As seen earlier, a control action can be used to prevent separation and/or stabilize the shock in a duct or a nozzle. Boundary layer blowing, suction, and wall cooling can be very effective for this purpose.

- If the aim is to decrease the drag of a profile or limit the loss of efficiency in an air intake, the situation is more subtle since the drag has its origin both in the shock—the wave drag—and in the boundary layer—the friction drag.

Application of control techniques will be illustrated by results obtained in a thorough investigation of interaction control in transonic flow (Stanewsky *et al.*, 1997).

8.3.3.2.1 Active Control

By removing the low-energy part of the boundary layer the upstream propagation mechanism is inhibited and the thickening of the boundary layer reduced. So, the flow behavior tends to the perfect fluid solution with a shock propagating practically to the surface. Any action strengthening the boundary layer tends also to strengthen the shock, since the spreading caused by the interaction is reduced. This effect is illustrated in Figs. 8.3.32a and b, which show a comparison between a transonic interaction without control and the flow resulting from boundary layer suction. The plotted Mach number contours have been computed from LDV velocity measurements (Bur *et al.*, 1998). In the second case, entropy production through the shock is more important and the wave drag higher. On the other hand, since the downstream boundary layer profile is more filled, the momentum loss in the boundary layer is reduced.

8.3.3.2.2 Passive Control

As seen in Section 8.3.2.3.2, when separation occurs, the smearing of the shock system and splitting of the compression achieved by the interaction reduce the wave drag, or the efficiency loss, due to the shock. On the other hand, the momentum loss in a separated boundary layer is far more important than that through an attached boundary layer, so that separation results in an increase of drag or efficiency loss. However, since separation has a favorable effect on the wave drag, one can envisage replacing strong but not separated interaction by a separated or separated-like flow organization. The passive control concept combines the two effects by spreading the shock system while reducing the boundary layer thickening (Savu *et al.*, 1983). The principle of passive control consists of replacing a part of the surface by a perforated plate installed over a closed cavity. The plate being implemented in the shock region, a natural circulation occurs—via the cavity—from the downstream high-pressure part of the interaction to the upstream low-pressure part. The resulting effect on the flow is sketched in Fig. 8.3.33a. The upstream transpiration provokes a rapid

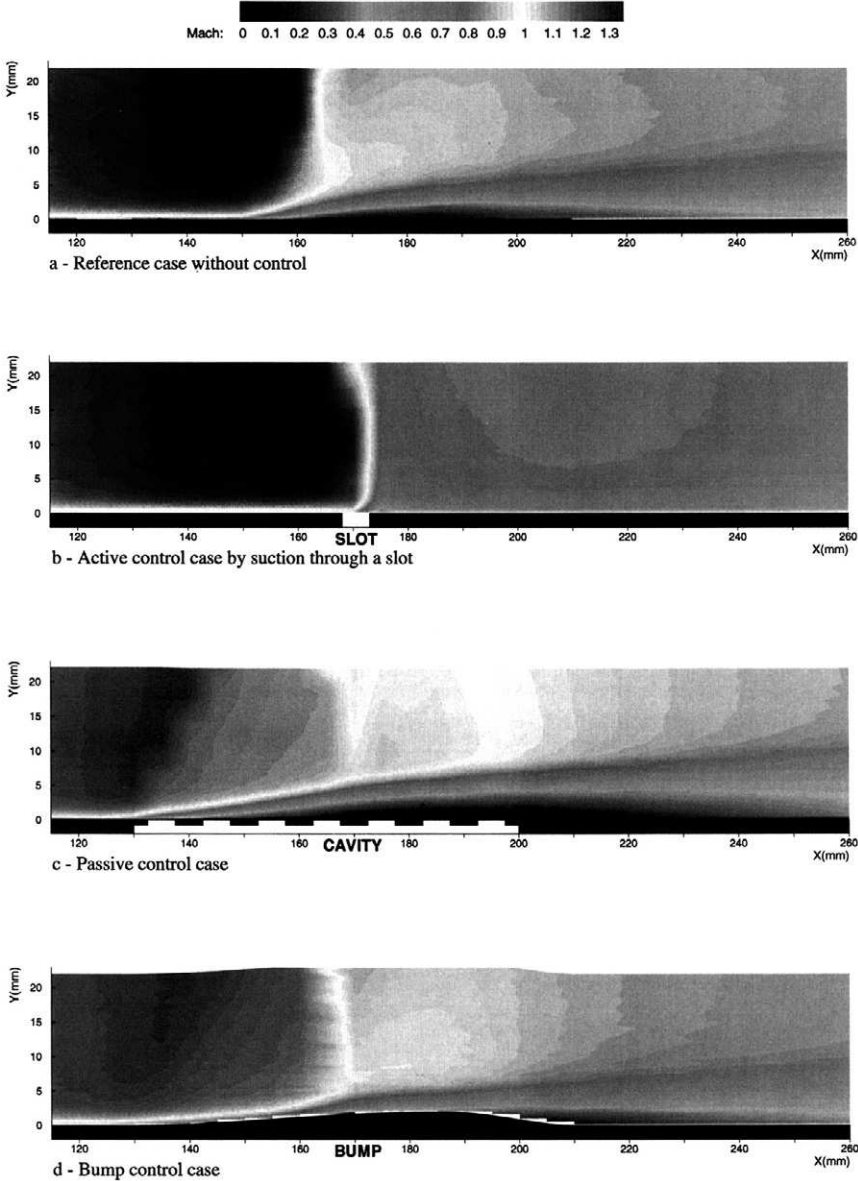


FIGURE 8.3.32 Shock wave/boundary layer interaction control in transonic flow. Measured Mach number contours (Bur *et al.*, 1998).

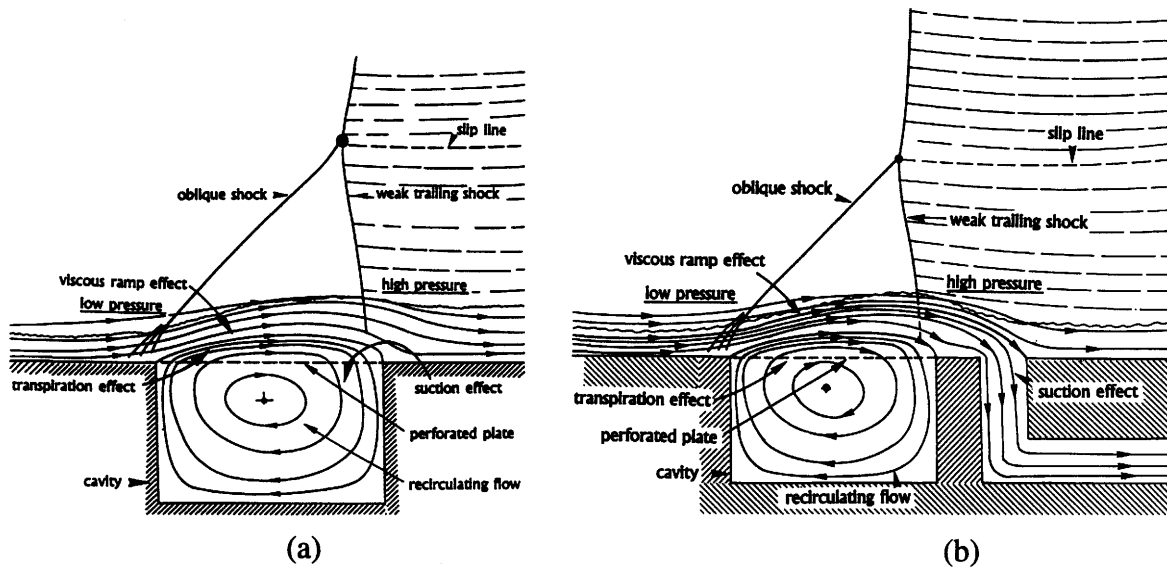


FIGURE 8.3.33 Principle of passive control (a) and hybrid control (b) of transonic interaction.

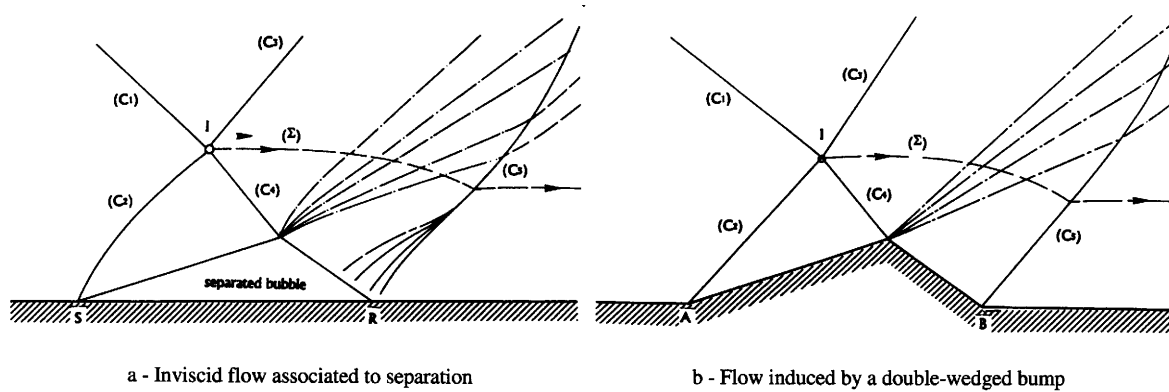


FIGURE 8.3.34 Interaction control by a local deformation of the wall or the bump concept.

growth of the boundary layer displacement thickness inducing an oblique shock (C_1). The situation is similar to the case of the natural shock-induced separation represented in Fig. 8.3.17, the strong normal shock (C_2) being replaced by a two-shock system in the vicinity of the surface: hence a reduction of the wave drag. The negative effect on the boundary layer is limited by the suction operated in the downstream part of the perforated plate. The effect of passive control is illustrated in Fig. 8.3.32c, where the smearing of the transonic shock and the thickening of the boundary layer are visible. Passive control can be very effective to stabilize a shock, even if its interest for drag reduction is questionable.

8.3.3.2.3 Hybrid Control

The foregoing concept can be improved by placing a suction slot downstream of the passive control cavity as shown in Fig. 8.3.33b. This hybrid control device combines the advantage of passive control to reduce the wave drag and the effectiveness of suction to reduce friction losses.

8.3.3.2.4 Wall Contouring

Since friction drag production in passive control is in general unacceptable and since fluid suction requires an energy supply that can compromise the economical benefit of control, one may consider the possibility of mimicking the separated flow structure by a local deformation of the surface. For example, a bump having a double wedge shape would materialize the viscous separated fluid induced by a shock reflection (see Fig. 8.3.6). As sketched in Fig. 8.3.34b, such a bump induces a first shock at its origin and a second shock at its trailing edge. In transonic flow, the bump has a more progressive contour, with an upstream concave part achieving a nearly isentropic compression, which weakens the normal shock forming at the bump location, as shown in Fig. 8.3.32d. This system slightly affects the boundary layer while substantially reducing the wave drag.

8.3.4 PROBLEMS RAISED BY INTERACTION MODELING

In spite of the spectacular progress made over the past 30 years by numerical methods and computer technology, accurate prediction of shock wave/boundary layer interaction remains a challenging problem for theoreticians. Here we shall only consider solutions obtained by solving the Navier–Stokes equations

valid in the continuum flow regime. In transitional and rarefied flow regimes, other equations or models must be applied, such as the direct simulation by Monte Carlo (DSMC) method. For turbulent interactions we will only envisage predictive methods using the classical Reynolds averaged Navier–Stokes (RANS) equations. Even in these limits, we do not intend to thoroughly discuss the question of interacting flow computation (for an overview of these calculations, see Détery and Panaras, 1996). We restrict ourselves to comments about “hard” points encountered when computing flows with shock wave/boundary layer interactions.

8.3.4.1 NUMERICAL ACCURACY OF THE CODES

Interacting flows contain regions of steep gradients, either of the wave type (shocks, expansion–compression waves) or of the slip line and boundary layer types (which includes shear layers), through which the flow properties vary over a very short distance. This problem is acute in shock separated flows where, as seen earlier, shocks interfere to produce complex wave patterns containing thin viscous layers. The numerical schemes must be robust enough to withstand these rapid flow variations while preserving high accuracy. In addition, these discontinuities or regions of high gradients have locations not known in advance, which makes their correct capture delicate because of the difficulty of adequately defining the computational mesh. The advent of a new class of schemes, based on upwind techniques, has in large part solved the problem of the capture of strong discontinuities. Also, adaptive meshing offers the possibility of tracking the regions of strong gradients by properly adjusting the refinement of the grid. Nevertheless, application of the most modern codes to strong interactions containing extended separated regions may lead to a large discrepancy with experiment. Moreover, the correct prediction of quantities such as the skin friction and wall heat transfer necessitates a very accurate calculation of the spatial derivatives, which imposes a strong demand on computational precision.

There is still a need for experimental data obtained on basic geometries, in completely laminar flow, in the continuum regime (no rarefaction effects) and in conditions such that the gas may be assumed calorically perfect. Then attention can be focused on the numerical accuracy of the codes. There exist a limited number of experiments performed on two-dimensional laminar ramp flows. Unfortunately, the side effects resulting from the finite span of the models render comparison with two-dimensional codes questionable, the flow being in reality three-dimensional (see Section 8.3.2.5.3). For the incipient and small separation conditions, there is in general good agreement between ramp flow experiment and two-dimensional laminar calculations. For well-separated

flow, three-dimensional calculations taking into consideration the finite span of the model are required to obtain good agreement with experiment (Rudy *et al.*, 1991).

The solution keeping the mathematical simplicity of two-dimensional flows while avoiding side effects is an axisymmetric geometry such as a hollow cylinder-plus-flare model. Figure 8.3.35 shows an electron beam visualization of the flow produced by such a model placed in a low Reynolds number facility. To produce a large separation at low Reynolds number the flare has an angle equal to 30° ; it is followed by a cylindrical part in order to displace the base far downstream of the investigated area. Then the base flow, difficult to compute, has no effect on the interaction domain. The experiment was made at $M_\infty = 9.91$ and a Reynolds number low enough to ensure a laminar regime throughout the interaction domain; no appreciable real gas effects were present. Great care was taken to align the model with the upstream velocity to achieve an axisymmetric configuration. In the framework of a cooperative validation action, this flow has been computed by three Navier–Stokes codes (Chanetz *et al.*, 1998). Great attention was paid to mesh construction to ensure excellent spatial convergence of the three calculations. In addition, the codes were run on the same mesh to allow meaningful confrontations. The comparisons with experiment in Fig. 8.3.36a show that there is a good agreement between the measured and computed surface pressure distributions, although differences may be noticed on the flare in the reattachment region. Also, some

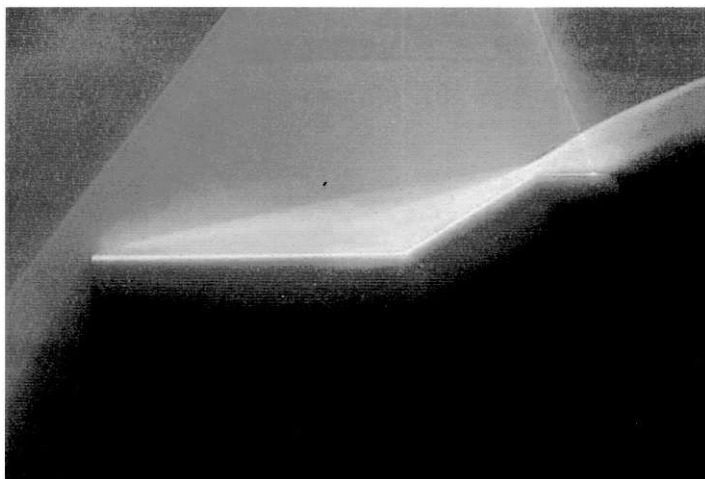
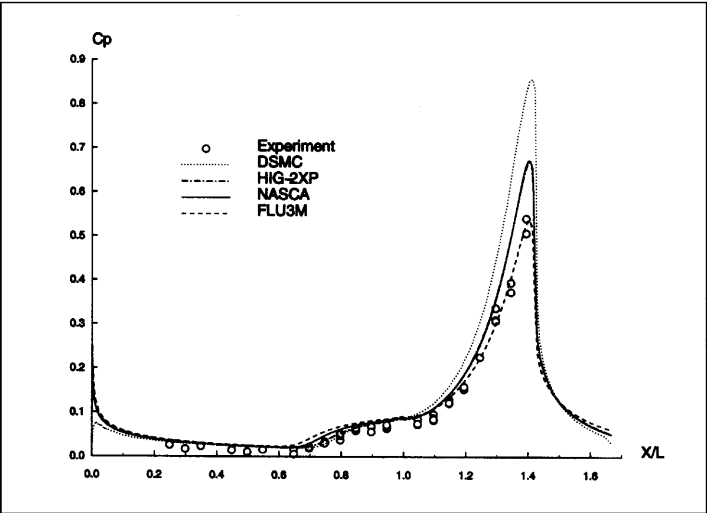


FIGURE 8.3.35 The hollow cylinder-flare model for assessment of code accuracy on a laminar high Mach number interaction (Chanetz *et al.*, 1998). (See Color Plate 2).

a



b

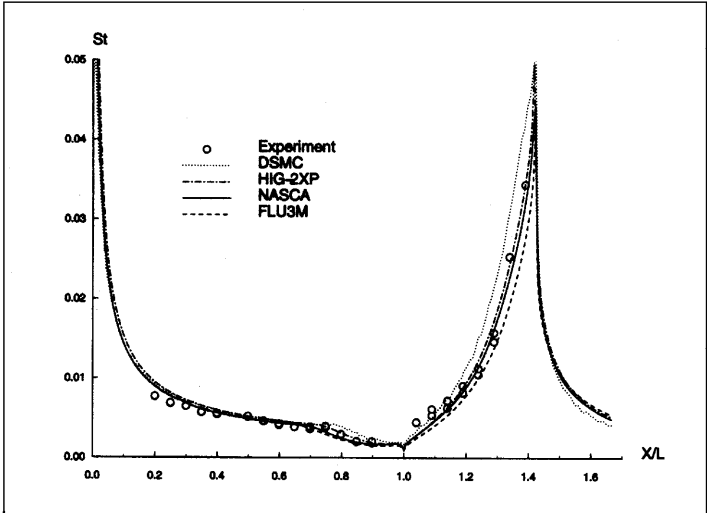


FIGURE 8.3.36 Comparison of computed and measured wall pressure and heat transfer distributions for the hollow cylinder-flare model (Chanetz *et al.*, 1998), (a) wall pressure (b) wall heat transfer

codes predict a too early separation, as compared to the experimental separation revealed by the first pressure rise and confirmed by surface flow visualizations. The same discrepancy is observed on the surface heat transfer distribution (see Fig. 8.3.36b). The flow has also been computed by a DSMC

code, the experiments achieving conditions for which both the DSMC and the Navier–Stokes approaches could be used.

8.3.4.2 THE PHYSICAL MODELING

Apart from the purely numerical aspects, shock wave/boundary layer interactions raise many other difficulties pertaining to the physical modeling itself, especially in the turbulent case, which is the most important for practical applications.

In the computation of shock-separated flows, the most challenging problem remains the modeling of turbulence. Shock wave boundary/layer interactions are characterized by the existence of very rapid changes to which the turbulent field reacts in a way difficult to model. The difficulties are present in several regions:

- Firstly, in the separation region where the retardation effect is at its maximum and anisotropy effects important
- Secondly, in the separated shear layer along which turbulent structures undergo rapid growth and where compressibility plays a key role as soon as the Mach number is above 2
- Thirdly, in the “rehabilitation” region downstream of reattachment where the flow recovers a boundary layer structure but have the memory of the previous events.

In addition, at high Mach numbers the shock penetrates inside the boundary layer, which leads to specific shock–turbulence interactions. Lastly, shock wave/boundary layer interactions are the seat of unsteadiness whose origin is not clear and that may interfere with the turbulent fluctuations (see Section 8.3.2.5.2). What follows is a brief discussion of problems raised by turbulence modeling in shock separated flows. More information can be found in the cited references, which are among the most recent publications on the subject.

Much attention has been devoted to the prediction of shock separated flows, with a success that can be considered as mitigated. The maximum effort is presently concentrated on transonic flows because of their crucial and strategic importance for the design of transport aircraft and turbomachines. The great majority of the present calculation methods use the so-called Reynolds–Favre averaged Navier–Stokes equations involving turbulent correlations at one point (one point closure). The main target of turbulence modeling is to express the Reynolds tensor components $\overline{\rho u'_i u'_j}$ present in the averaged

momentum equation. This tensor is most often expressed through the Boussinesq assumption in the form

$$-\bar{\rho}\overline{u'_i u'_j} = \mu_T \left[\bar{\bar{D}} - \frac{1}{3} \text{div} \bar{\vec{V}} \bar{\vec{I}} \right]$$

where μ_T is the eddy viscosity, $\bar{\bar{D}}$ being the strain tensor, $\bar{\vec{V}}$ the velocity vector, and $\bar{\vec{I}}$ the identity tensor.

At the simplest level of approximation, μ_T is given by an algebraic relation involving only the mean flow properties. Most often these purely algebraic turbulence models, like the popular Baldwin–Lomax model, give poor results because they do not include any history effects on the turbulence, which is assumed to adjust instantly to a change in the mean field. Models in which a turbulent quantity is computed by means of a separate differential equation achieve some improvement. This allows partial disconnection of turbulence from the mean field, turbulence having its proper response to changes in the flow conditions. Such one-transport equation models, like the one proposed by Spalart and Allmaras, give fair results for transonic airfoils but are less satisfactory for internal flows with extended separation (Spalart and Allmaras, 1992). Turbulence models using two transport equations give a more realistic representation of the turbulence behavior. Frequently the transported quantities are the specific turbulence kinetic energy k and its rate of dissipation ε , the eddy viscosity being computed by the relation:

$$\mu_T = \bar{\rho} C_\mu \frac{k^2}{\varepsilon}$$

where in principle C_μ is a constant close to 0.09. Some variability of C_μ is introduced to adjust the eddy viscosity behavior in the near-wall region. Other two-equation models exist that give in general similar results.

Even with these models the quantitative agreement with experiment is not always good in strongly interacting flows. The source of the discrepancies could be in the use of the Boussinesq law, which is unable to represent the nonisotropic behavior of the turbulent shear stress in the circumstances met during shock wave/boundary layer interaction (Délery, 1983). Another limitation of the preceding turbulence models is that they ignore, or underrepresent, the contribution of the normal Reynolds stress components.

Several directions, with many variants, are presently explored to improve the situation. The most advanced models—within the classical RANS approach—use second-order closure, which consists of solving transport equations for all the Reynolds tensor components (Reynolds stress equations, or RSE models; see Zha and Knight, 1996; Gerolymos and Vallet, 1997). In addition, relations more elaborate than the simple linear—or isotropic—Boussinesq law are derived to express the Reynolds stress tensor. Such relations

for the eddy viscosity are obtained from a nonlinear explicit expansion of the Reynolds stress tensor $\bar{\rho} \overline{u_i' u_j'}$ in terms of the strain and vorticity tensors, the Boussinesq law being the first term of this expansion (Loyau *et al.*, 1998).

One way to keep the simplicity of two-equation models, but with a more physical eddy viscosity law, is to derive algebraic expressions for the Reynolds stress components from simplified RSE. The Reynolds stress tensor components are then computed by solving an algebraic system involving k , ε , and the mean-field strain and vorticity tensors. This leads to the algebraic stress model (ASM), and more recently to the explicit algebraic stress model (EASM, Gatski and Speziale, 1993). Another basic difficulty encountered by turbulence modeling is the near-wall region where the transport equations are no longer valid because of the smallness of the local — or turbulent — Reynolds number. There a more or less empirical treatment must be adopted by using either wall functions or low Reynolds number extension of the transport equations (Gerolymos and Vallet, 1996). Many variants of the published models differ in the treatment of the wall region.

Modeling of turbulent shock wave/boundary layer interactions involves many other aspects whose consideration would require too long a development on a subject still in continuous evolution. For instance, the cost and ease of a calculation are important factors that may favor the choice of a less physical but more robust model in place of an accurate model leading to numerical difficulties or lengthy convergence; hence the frequent use of two-transport equation models whose weakness is well known in shock-separated flows.

Before drawing any conclusion about the accuracy of a turbulence model, one must be sure that the calculation represents as faithfully as possible the experimental case used to validate the code. Thus, a model tested with a two-dimensional code may be invalidated simply because the side effects affecting planar two-dimensional experiments have been ignored. Running a three-dimensional code, taking into account the interactions on the wind tunnel side walls, may lead to a completely different conclusion about the same model (Gerolymos and Vallet, 1996).

8.3.4.2.1 Hypersonic Interactions

The modeling of hypersonic interactions raises other difficulties because of the extreme conditions met at high temperature.

The correct representation of the flow thermodynamics requires adequate descriptions of the gas physical and chemical behaviors, which is not always possible, the kinetics of certain nonequilibrium reactions not being well known. The transfer properties of the gas (molecular viscosity, heat conduction) have to be well known to correctly predict the skin friction and the wall heat transfer.

In reacting gas, heat transfer depends on the chemical state at the wall. For nonequilibrium flows, catalytic effects have dramatic repercussions, heat transfer being minimized on a noncatalytic wall, or amplified on a fully catalytic wall. As seen in Section 8.3.2.4.3, the energy release occurring when the wall is catalytic can greatly affect the size of a separated region, acting like a strong heating of the surface. In many applications, the catalytic properties of the material constituting the vehicle surface are not known accurately.

Turbulence modeling in hypersonic flows is confronted with specific problems. At Mach numbers above 6, terms involving density fluctuations in the time-averaged equations, the so-called compressibility terms, become significant and can no longer be ignored (Grasso and Falconi, 1993). As mentioned earlier, at high Mach number the shock waves penetrate the boundary layer, leading to shock wave/turbulence interaction that affects the further development of turbulence (Jacquin *et al.*, 1993). In extreme conditions, there is a coupling between turbulence and the chemical activity of the flow through complex mechanisms (Leclère and Aupoix, 1994).

The greatest discrepancies between experiment and theory are observed in the prediction of the peak heat transfer at reattachment. Several thorough examinations of this question showed that the cause of the poor performance of the calculation could be attributed to a bad modeling of the compressibility terms, which are supposed to be essential in high Mach number interactions. Their consideration led to rather disappointing results in the prediction of heat transfer at reattachment (Horstman, 1987; Knight, 1993; Douay, 1994). It is also possible that poor prediction is due to insufficient numerical accuracy.

8.3.2.4.2 Transitional Interactions

Low Reynolds number interactions remain rarely entirely laminar, the shock being a very effective way to trigger transition. In most practical situations, such as control surfaces of a hypersonic vehicle or turbomachine blades, one has to predict a transitional interaction that is laminar during separation and turbulent at reattachment. The calculation of such a flow is still out of reach of our present modeling capabilities. In practice one must rely on rather rough theoretical models using a good dose of empiricism. For example, the calculation can be performed in the laminar regime until the start of the reattachment process where the turbulence model is switched. The rest of the calculation is made in the turbulent regime (Grasso *et al.*, 1994).

8.3.5 CONCLUDING REMARKS

Shock wave/boundary layer interaction is intrinsically linked to the occurrence of shocks in high-speed flows or in shock tubes. The phenomenon is the consequence of the response of the boundary layer to the sudden local compression imparted by the shock. Because of its structure the boundary layer reacts as a nonuniform flow in which viscous and inertia terms combine in an intricate manner. The most significant result of the interaction is to spread the pressure discontinuity caused by the shock, whose influence may be felt well upstream of its location in the perfect fluid model. When the shock is strong enough to separate the boundary layer, the interaction has dramatic consequences on both the boundary layer development and the contiguous inviscid flow field. Then, complex shock patterns form involving shock/shock interferences whose nature depends on the way the primary shock is produced (ramp, shock reflection, normal shock) and on the Mach number. On the other hand, the boundary layer behavior obeys specific laws mainly dictated by the intensity of the overall pressure rise imparted by the shock, no matter how the shock is generated. Although the basic flow topology is the same, laminar and turbulent interactions have very distinct properties, the difference stemming from the far greater resistance of a turbulent boundary layer to flow retardation. Also, interactions in hypersonic flows have specific features coming from the high enthalpy level of the outer flow.

The most salient feature of shock-induced separation is probably not the boundary layer, which behaves mostly as in an ordinary separation, the shock being an epiphenomenon of a process whose essence is the same as in subsonic flows. The most striking feature of the interaction is the overwhelming repercussion on the contiguous inviscid and supersonic stream, which can be dramatic in internal flows.

The physics of shock wave/boundary layer interaction can be considered well understood, at least in two-dimensional flows, which cannot be considered satisfactory since nearly all the practical situations are three-dimensional. The obstacle, then, is the difficulty of grasping the structure of three-dimensional flows and arriving at a consistent topological description of the flow field organization. At the same time, the definition of separation in three-dimensional flow is far more subtle than in two-dimensional flows, where it is associated with the zeroing of the skin friction coefficient. The description and study of three-dimensional shock wave/boundary layer interactions must first consider this basic question, which necessitates calling upon the critical point theory, the consideration of which here would have required too lengthy a development. A side effect of three-dimensional analysis is to demonstrate that two-dimensional flows do not exist in the real world, which may lead to a

complete reconsideration of the description of separated flows and, in consequence, of the modeling activity.

The predictive capabilities are still limited in turbulent flows where theoreticians are confronted with the frustrating problem of turbulence modeling. The usual two-transport equation models perform poorly as soon as a noticeable separated region forms. Turbulence in interacting flows involves many aspects: compressibility terms in the time-averaged equations, shock/turbulence interaction, memory effects, flow unsteadiness, strong anisotropy, turbulence/chemistry coupling in hypersonic flows, and transfer processes, to name the most important. Substantial improvements are brought by RSE models transporting the full Reynolds stress tensor or models using nonlinear explicit expansion of the Reynolds stress tensor in terms of the strain and vorticity tensors (the Boussinesq law being the first term of this expansion). However, one should be cautious when drawing pessimistic conclusions from a poor agreement between theory and experiment. Many of the existing results, although instructive for the physical understanding of interactions, are without utility for theoretical models and code validation because of poorly identified flow conditions, undesirable side effects, or unwanted transition in the course of the interaction. There is still a need for well-executed and well-documented experiments providing test cases to validate codes aiming at the prediction of shock wave/boundary layer interaction. On the other hand, it becomes clear that the two-dimensional assumption has to be given up, since it corresponds to unrealistic and only apparently simple configurations.

ACKNOWLEDGMENTS

The investigation of shock wave/boundary layer interaction control in transonic flow has been performed within the projects EUROSHOCK 1 and 2 funded by the European Community. Experiments on asymmetrical separation in a supersonic nozzle are part of a research program on unsteady side loads financed by the Centre National d'Etudes Spatiales. The author is grateful to Florence Marie for the preparation of the manuscript.

REFERENCES

- Ballaro, C.A. and Anderson, J.D. Jr. (1991). Shock strength effects on separated flows in non-equilibrium chemically reacting air shock wave/boundary layer interaction. AIAA Paper 91-0250.
- Barberis, D. and Molton, P. (1995). Shock wave/turbulent boundary layer interaction in a three-dimensional flow. AIAA Paper 95-0227.

- Bur, R., Corbel, B., and Délery, J. (1998). Study of passive control in a transonic shock wave/boundary layer interaction. *AIAA J.* 36: 740–752.
- Chanetz, B., Benay, R., Bousquet, J.-M., Bur, R., Pot, T., Grasso, F., and Moss, J. (1998). Experimental and numerical study of the laminar separation in hypersonic flow. *Aerospace Sci. Technol.* 3: 205–218.
- Chapman, D.R., Kuehn, D.M., and Larson, H.K. (1957). Investigation of separated flows in supersonic and subsonic streams with emphasis on the effect of transition. NACA TN-3869.
- Délery, J. (1983). Investigation of strong shock wave/turbulent boundary layer interactions in 2D transonic flows with emphasis on turbulence phenomena. *AIAA J.* 21: 180–185.
- Délery, J. (1985). Shock wave/turbulent boundary layer interaction and its control. *Prog. Aerospace Sci.* 22: 209–280.
- Délery, J. (1992). Etude expérimentale de la réflexion d'une onde de choc sur une paroi chauffée en présence d'une couche limite turbulente (Experimental study of the reflection of a shock wave on a heated surface in presence of a turbulent boundary layer). *La Recherche Aérospatiale*, No. 1992-1, pp. 1–23 (French and English editions).
- Délery, J. (1993). Contribution of laser doppler velocimetry to the physical description of shock wave/turbulent boundary layer interaction with incidence on turbulence modeling. AGARD/FDP-VKI Special Course on *Shock Wave/Boundary Layer Interactions in Supersonic and Hypersonic Flows*, AGARD Report No. 792.
- Délery, J. (1999). Topologie des écoulements tridimensionnels décollés stationnaires: points singuliers, séparatrices et structures tourbillonnaires (Topology of steady three-dimensional separated flows: critical points, separators and vortical structures). Onera RT 121/7078DAFE/N (Jan. 1999).
- Délery, J. and Coët, M.-C. (1990). Experiments on shock wave/boundary layer interactions produced by two-dimensional ramps and three-dimensional obstacles. *Workshop on Hypersonic Flows for Re-entry Problems*, Antibes, France.
- Délery, J. and Marvin, J.G. (1986). *Shock wave/boundary layer interactions*. AGARDograph No. 280.
- Délery, J. and Panaras, A. (1996). Shock wave/boundary layer interactions in high Mach number flows. AGARD/FDP Working Group 18 on *Hypersonic Experimental and Computational Capability, Improvement and Validation*, AGARD AR-319, Vol. 1.
- Dolling, D.S. (1993). Unsteady phenomena in shock wave/boundary layer interaction. AGARD/FDP-VKI Special Course on *Shock Wave/Boundary Layer Interactions in Supersonic and Hypersonic Flows*, AGARD Report No. 792.
- Douay, G. (1994). Modélisation et étude numérique de la turbulence compressible en écoulement supersonique (Modeling and numerical study of compressible turbulence in supersonic flow). Ph.D. Thesis, University of Rouen, France.
- Edney, B. (1968). Anomalous heat transfer and pressure distributions on blunt bodies at hypersonic speeds in the presence of an impinging shock. Aeronautical Research Institute of Sweden, FFA Report No. 115.
- Elfstrom, G.M. (1971). Turbulent hypersonic flow. *J. Fluid Mech.* 53(1): 113–129.
- Fage, A., and Sargent, R.F. (1943). Effect on airfoil drag of boundary layer suction behind a shock wave. ARC R&M No. 1913.
- Gatski, T.B., and Speziale, C.G. (1993). On explicit algebraic stress models for complex turbulent flows. *J. Fluid Mech.* 254: 59–78.
- Gerolymos, G.A., and Vallet, I. (1996). Implicit computation of three-dimensional compressible Navier–Stokes equations using $k-\epsilon$ closure. *AIAA J.* 34: 1321–1330.
- Gerolymos, G.A., and Vallet, I. (1997). Near-wall Reynolds-stress three-dimensional transonic flow computation. *AIAA J.* 35: 228–236.

- Grasso, F. and Falconi, D. (1993). High speed turbulence modeling of shock wave/boundary layer interaction. *AIAA J.* 31: 1199–1206.
- Grasso, F. and Leone, G. (1992). Chemistry effects in shock wave/boundary layer interaction problems. *IUTAM Symposium on Aerothermochemistry of Spacecraft and Associated Hypersonic Flows*, Marseille, France.
- Grasso, F., Leone, D., and Déleré, J. (1994). Validation procedure for the analysis of shock wave/boundary layer interaction problems. *AIAA J.* 32: 1820–1827.
- Green, J.E. (1970). Interaction between shock waves and turbulent boundary layers. *Prog. Aerospace Sci.* 11: 235–340.
- Grummet, A.A., Anderson, J.D., and Lewis, M.J. (1991). A numerical study of shock wave/boundary layer interaction in non-equilibrium chemically reacting air. The effects of catalytic walls. *AIAA Paper* 91-0245.
- Hayes, W.D. and Probstein, R.F. (1959). *Hypersonic Flow Theory*. Academic Press, London.
- Heffner, K. (1993). Contribution à l'étude d'une rampe de compression en écoulement hypersonique. Partie I : Régime de transition laminaire-turbulent de couche limite. Partie II : Régime de transition écoulement continu-écoulement moléculaire libre (Contribution to the study of a compression ramp in hypersonic flow. Part I: Laminar to turbulent transition regime of the boundary layer. Part II: Transition from free molecular to continuum regime). Ph.D. Thesis, University Pierre-et-Marie Curie, Paris.
- Holden, M. (1977). Shock wave/turbulent boundary layer interaction in hypersonic flow. *AIAA Paper* 77-0045.
- Horstman, C.C. (1987). Prediction of hypersonic shock wave/turbulent boundary layer interaction flow. *AIAA Paper* 87-1367.
- Jacquín, L., Cambon, C., and Blin, E. (1993). Turbulence amplification by a shock wave and rapid distortion theory. *Phys. Fluids* A5–10: 2539–2550.
- Knight, D.D. (1993). Numerical simulation of 3-D shock wave/turbulent boundary layer interactions. AGARD/FDP-VKI Special Course on *Shock Wave/Boundary layer Interactions in Supersonic and Hypersonic Flows*, AGARD Report No. 792.
- Leclère, F. and Aupoix, B. (1994). Hypersonic nonequilibrium reactive nozzle flow calculations. *ICAS 94, 19th Congress of the International Council of the Aeronautical Sciences*, Anaheim, CA, 18–23 Sept. 1994.
- Legendre, R. (1956). Séparation de l'écoulement laminaire tridimensionnel (Separation of the three-dimensional laminar boundary layer). *La Recherche Aéronautique*, No. 54, Nov.–Dec. 1956.
- Lewis, J.E., Kubota, T., and Lees, L. (1968). Experimental investigation of supersonic laminar two-dimensional boundary layer separation in a compression corner with and without cooling. *AIAA J.* 6: 7–14.
- Lighthill, M.J. (1953). On boundary-layer upstream influence. II Supersonic flows without separation. *Proc. R. Soc. A* 217: 478–507.
- Loyau, H., Batten, P., and Leschziner, M.A. (1998). Modeling shock/boundary layer interaction with nonlinear eddy viscosity closures. *J. Flow, Turbulence Combust.* 60: 257–282.
- Muck, K.-C., Andreopoulos, J., and Dussauge J.-P. (1988). Unsteady nature of shock wave/turbulent boundary layer interaction, *AIAA J.* 26: 179–187.
- Regenscheit, B. (1941) Versuche zur Widerstandsverringierung eines Flügels bei hoher Machscher-Zahl durch Absaugung der hinter dem Gebiet un stetiger Verdichtung abgelösten Grenzschicht. ZWB, Forschungsbericht No. 1424; English translation: NACA TM No. 1168.
- Reijasse, P., Corbel, B., and Soulevant, D. (1999). Unsteadiness and asymmetry of shock-induced separation in a planar two-dimensional nozzle: A flow description. *AIAA Paper* 99-3694.
- Rudy, D.H., Thomas, J.L., Kumar, A., Gnoffo, P.A., and Chakravarthy, S.R. (1991). Computation of laminar hypersonic compression-corner flow. *AIAA J.* 29: 1108–1113.

- Savu, G., Trifu, O., and Dumitrescu, L. Z. (1983). Suppression of shocks on transonic airfoil. *14th Int. Symp. on Shock Tubes and Waves*, Sydney, Australia.
- Settles, G.S. (1975). An experimental study of compressible boundary layer separation at high Mach number. Ph.D. Thesis, Princeton University.
- Settles, G.S. (1993). Swept shock/boundary layer interaction scaling laws, flow field structure and experimental methods. AGARD/FDP-VKI Special Course on *Shock Wave/Boundary Layer Interactions in Supersonic and Hypersonic Flows*, AGARD Report No. 792.
- Shang, J.S., Hankey, W.L., Jr., and Law, C.H. (1976). Numerical simulation of shock wave/turbulent boundary layer interaction. *AIAA J.* **14**: 1451–1457.
- Spaid, F.W. and Frishett, J.C. (1972). Incipient separation of a supersonic, turbulent boundary layer, including effects of heat transfer. *AIAA J.* **10**: 915–922.
- Spalart, P.-R. and Allmaras, S.R. (1992) A one equation turbulence model for aerodynamic flows. AIAA Paper 92-439.
- Stanewsky, E., Délery, J., Fulker, J., and Geissler, W. (1997) *EUROSHOCK—Drag Reduction by Passive Shock Control*. Notes on Numerical Fluid Mechanics, Vol. 56, Vieweg.
- Stewartson, K. and Williams, P.G. (1969). Self-induced separation. *Proc. R. Soc. A* **312**: 181–206.
- Zha, G.-C. and Knight, D. (1996) Three-dimensional shock/boundary layer interaction using Reynolds stress equation turbulence model. *AIAA J.* **34**: 1313–1321.

Axisymmetric Shock Wave Reflections

BRIAN E. MILTON

School of Mechanical and Manufacturing Engineering, University of New South Wales, Sydney, N.S.W., 2052, Australia

-
- 9.1 Introduction
 - 9.2 External Reflections over Simple Upstream-Facing Cones
 - 9.2.1 Simple Cones in Steady Supersonic Flows
 - 9.2.2 Moving Shock Waves
 - 9.3 Generalized Solution of Conical Moving Shock Waves
 - 9.3.1 Formulation for Ray-Shock Calculations in Conical Mach Reflection
 - 9.3.2 Equations for the Generalized Ray-Shock Solution
 - 9.3.3 Curved Mach Stems
 - 9.3.4 Solution Procedures for Cases without Self-Similarity
 - 9.3.5 Postreflection Rays Parallel to the Centerline
 - 9.4 Some Conical Mach Reflection Results from the Ray-Shock Theory
 - 9.4.1 External (Expanding) Flows
 - 9.4.2 Converging (Internal) Cases
 - 9.5 Experimental Conical Mach Reflection Studies
 - 9.5.1 Validation for External Cone Cases
 - 9.5.2 Mach Reflection within Conical Contractions
 - 9.6 Numerical Experiments (CFD)
 - 9.6.1 CFD Scheme for Conical Mach Reflection
 - 9.6.2 Comparison of the Ray-Shock Theory CFD Results
 - 9.7 Some Theoretical Aspects of Conical Mach Reflection
 - 9.7.1 Von Neumann Mach Reflection Effects in Conical Reflections

- 9.7.2 Self-Similar and Non-Self-Similar Axisymmetric Mach Reflection
- 9.7.3 Transition from Regular to Mach Reflection in Conical Problems
- 9.8 Some Applications of Axisymmetric Calculations
 - 9.8.1 Mach Reflection over a Simple Cone
 - 9.8.2 Axisymmetric Shock Wave Focusing
- 9.9 Final Discussion
- References

9.1 INTRODUCTION

The axisymmetric reflection of moving shock waves is an important phenomenon in engineering practice. All real situations in nature are three-dimensional, and the axisymmetric case (mathematically a pseudo two-dimensional case) appears frequently because a great many flow configurations occur in pipes and ducts of circular cross-section. For a reflection pattern to occur, the shocks may impinge on a cone with apex facing the flow or be transmitted in a converging duct tapered toward a reduced cross-sectional area in the flow direction. The former includes center bodies within ducts as well as isolated cones. Some practical examples among many are the internal flows in pipes, jet or rocket engine nozzles, external flows over aircraft or projectiles, and internal/external flows in engine intakes. Note that curved surfaces may be considered as a series of limiting successive wedge or conical reflections in plane or axisymmetric cases, respectively. Thus, there are many practical reasons for studying axisymmetric shock wave reflection. In addition, the theoretical approach used is intrinsically important because it illustrates the general trends that occur in fully three-dimensional flows while having a much reduced complexity and combination of configurations. This makes axisymmetric cases easier to examine experimentally and more tractable theoretically.

The reflections most commonly considered in experimental, analytical, and numerical work are those of a plane shock wave approaching a wedge. This is often termed two-dimensional. However, given that the axisymmetric case, as mentioned earlier, also falls within that classification, the term used here will be a wedge reflection, and that for the axisymmetric cases a conical reflection. The detailed phenomena associated with plane wedge Mach reflection of moving shock waves have been extensively studied and are described thoroughly by Ben-Dor (1992). Much less material is available on conical reflections. The purpose here is to highlight the similarities and differences in conical reflections from those over wedges from theory and to validate these from experiment and CFD calculation results for the conical phenomena.

Theoretically, axisymmetric reflection has detailed features that are likely to be the same as those in wedge reflections, but also has others that are different. The former are basically those that occur at a microscopic level immediately at the reflection point. As a larger view of the phenomenon is taken and the full reflection pattern considered, differences start to become apparent. This can be illustrated by considering a conical reflection at some finite radius from the centerline of the cone. The ray-tube concept of Whitham (1957, 1959) provides the simplest basis for obtaining an understanding. For a tube Δr thick at a finite radius r , it can be seen from Fig. 9.1 that, as Δr approaches zero, the ratio of the reflection depth to arc length becomes so small that the effect of the arc curvature can be neglected. Hence, in the limit, the conical reflection becomes identical to that of the wedge. However, for Δr large, the effect of the radius is pronounced. That is, the reflection pattern changes from initially a wedge type at the triple point to a fully axisymmetric one across the region from the triple point to the reflecting wall.

Two fundamental cases have most commonly been studied. These are when a plane shock wave moving normal to the axis of the conical section reflects as follows:

- (i) Over the surface of an upstream-facing cone (apex upstream) and
- (ii) Into a downstream-facing conical contraction (base upstream)

However, many other cases exist. Some examples are the self-reflection of a converging shock wave at its axis of symmetry, the interaction of two conical shocks of different angular direction at a finite distance from their common centerline, and the reflection of shocks moving from one conical surface to another either internally or externally. A range of possibilities is depicted in Fig. 9.2.

9.2 EXTERNAL REFLECTION OVER SIMPLE UPSTREAM-FACING CONES

9.2.1 SIMPLE CONES IN STEADY SUPERSONIC FLOWS

It is not the purpose of this chapter to examine shocks in steady flows. Nevertheless, they highlight the fact that differences between axisymmetric and plane wedge type flows exist and that similar possibilities need to be sought in unsteady flow. Stationary attached shocks in conical supersonic flows have been studied for many years. These are well described in Shapiro (1954) and are summarized very briefly here using his nomenclature. Although a range of

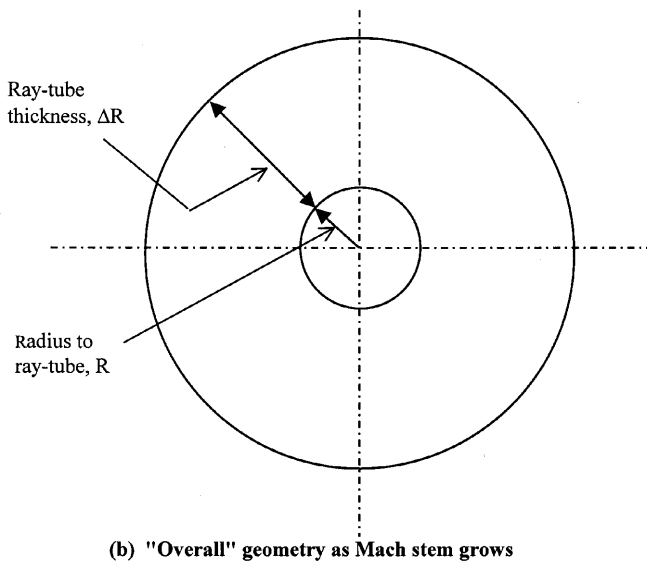
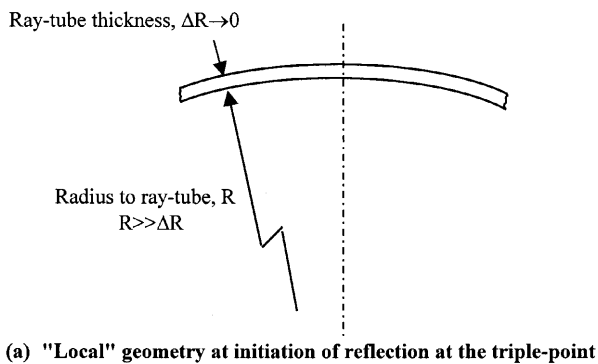
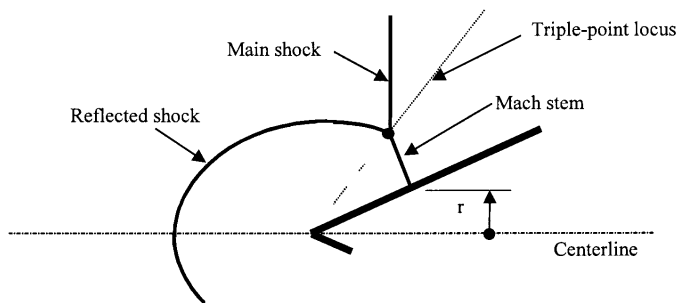
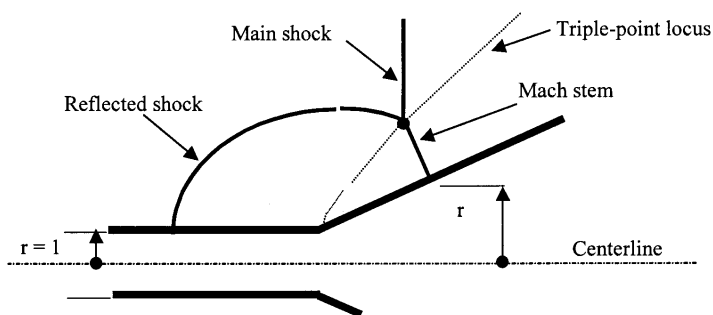


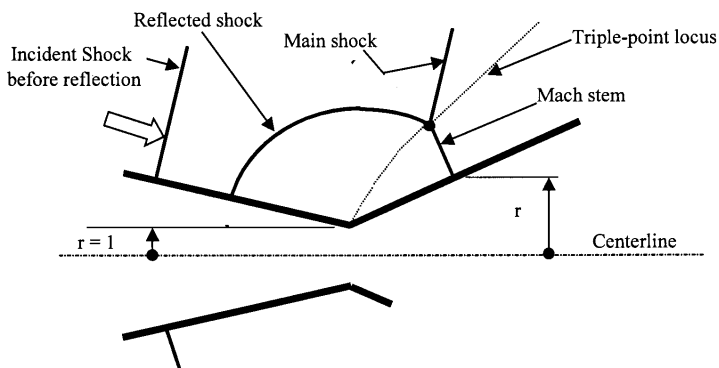
FIGURE 9.1 Geometrical schematic of ray-tube thickness relative to radius. (a) As $R \rightarrow \infty$, reflection approaches wedge type. (b) Reflection has axisymmetric effects.



(a) Simple external conical Mach reflection



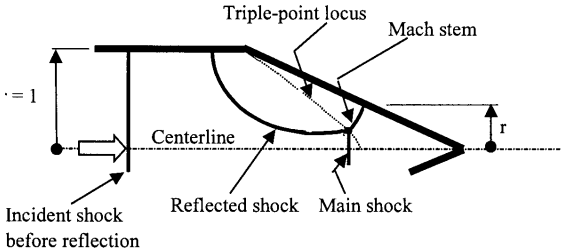
(b) Cylinder-to-cone external Mach reflection



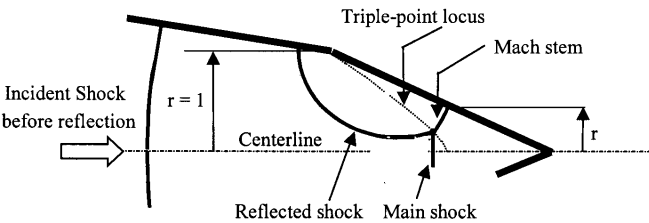
(c) Cone-to-cone external Mach reflection

i. External conical Mach reflection configurations

FIGURE 9.2 Some possible conical Mach reflection configurations. (i) External cases: (a) simple cone, (b) cylinder–cone (c) double cone. (ii) Internal cases: (d) cylinder–cone, (e) cone–cone. (iii) Other cases: (f) self-reflection from centerline, (g) from outer wall.

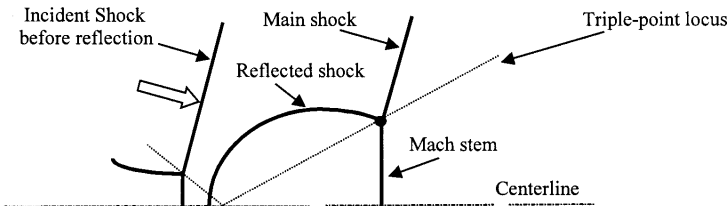


(d) Simple internal conical Mach reflection

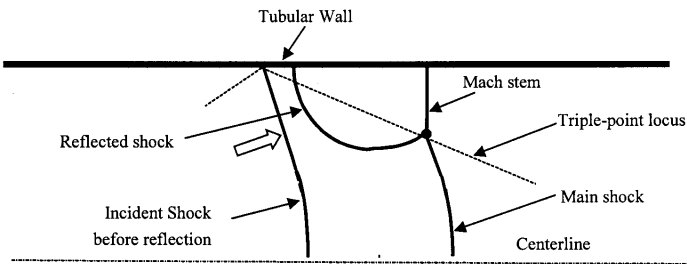


(e) Cone-to-cone internal conical Mach reflection

ii. Internal conical Mach reflection configurations



(f) Contracting shock reflecting at the centerline



(g) Expanding shock reflecting at external circular wall

iii. Other conical Mach reflection configurations

FIGURE 9.2 (continued)

problems have been addressed, the most common is that of a flow approaching a cone of half-apex angle δ . A toroidal element is selected in the flow field downstream of the shock and is located somewhere between the shock and the cone surface. The flow components are considered along (direction r) and normal to (direction ω) the vector from the cone apex to the element. The governing equations of continuity, irrotationality, momentum (Euler), sound speed, and energy are then combined to describe the flow, forming an ordinary, nonlinear differential equation for V_r (in direction r) in terms of the angle ω from the centerline to the element. This derivation is well described in Shapiro (1954) and need not be repeated here. Shapiro notes that the equation was first integrated graphically by Busemann (1929) and numerically by Taylor and Maccoll (1933) using cut and try methods for the shock angle σ and the flow angle θ . Note that θ is not necessarily parallel to the cone wall. Again, the method is thoroughly described by Shapiro (1954). Macoll (1937) obtained experimental verification of the theory using shadowgraph photographs for a range of flow Mach numbers from 1.090 to 1.794. Agreement was very good.

The results of this theory for cones is compared with the plane wedge oblique shock solution in Table 9.1. It can be seen that there is substantial difference between the two cases, with the wedge forming a shock that is at a substantially higher angle than that of the cone for the same angular deflection of the surface.

9.2.2 MOVING SHOCK WAVES

In nature, processes are commonly unsteady. Thus, moving shock waves are the general case and stationary ones are special cases where the wave is fixed

TABLE 9.1 Comparison of Wedge and Cone Attached Shock Angles
(Data from Shapiro, 1954)

Incoming flow Mach number, M_i	Wedge or cone (half) angle to flow, δ	Wedge shock angle, σ_w	Cone shock angle, σ_c
2.0	0°	30°	30°
	10°	39.5°	31.5°
	20°	53.5°	39°
3.0	0°	19.5°	19.5°
	10°	27.5°	22°
	20°	37.5°	30°
	30°	52°	37.5°
	40°		52°

by a flow of equal velocity opposed to its motion. The study of moving shock waves is quite difficult experimentally because of the short times available for observations and theoretically because of the time-dependent terms in the equations.

Unlike wedge configurations, only limited experimental work is available for axisymmetric cases. The most commonly studied configuration, as in steady flow, is that of a moving shock wave impinging on a center-body cone with its apex facing upstream. Here, the external flow allows good visualization of the shock wave pattern as it progresses. However, there has been work on internal converging configurations, although their shock wave structures are very difficult to visualize experimentally. In addition, CFD techniques have been used. These may also be regarded as a type of experimentation, as many runs are required with the outputs delineating the trends. Again, in the axisymmetric cases, the CFD formulation is more difficult and the computational time longer than in wedge cases.

9.2.2.1 A Theoretical Approach: The Ray-Shock Theory

The ray-shock theory was originally devised by Whitham (1957, 1959) for two- and three-dimensional shock wave diffraction and is based on the division of the flow field into an orthogonal grid as shown in Fig. 9.3. The theory and applications are fully described by Han and Yin (1993). It is based on a grid of progressive shock front positions and rays that are normal to the shocks. Ray tubes are formed by adjacent rays. It is assumed that locally the particles follow the ray tube direction. The geometry allows a pair of kinematic equations to be developed relating the Mach number, M , the area of the ray tubes which is assumed to be a function of Mach number [i.e., $A = f(M)$], and the ray direction, θ . These can be used to form a “characteristic” invariant equation such that

$$\theta \pm \omega = \text{const.} \quad (9.1)$$

where

$$\omega = \int \frac{dM}{AC}; \quad C^{\pm} = \pm \sqrt{\frac{-MdM}{AdA}}.$$

The characteristic angle (i.e., angle to the incident ray) is given by

$$m = \tan^{-1} \frac{AC}{M}. \quad (9.2)$$

Intersection of these “characteristics” form the shocks. For Mach reflection, the triple point is regarded as a disturbance propagated along the shock wave front (forming the triple-point locus at angle χ relative to the local, incident ray

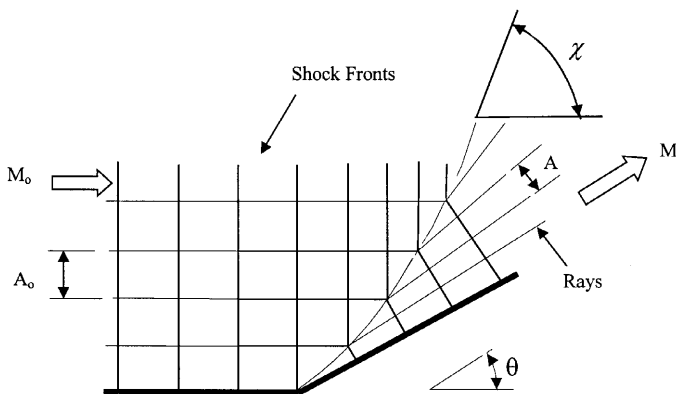


FIGURE 9.3 Ray-shock grid for development of basic Mach reflection equations.

direction in Mach reflection, which Whitham designated as the shock-shock). Equations for both the area ratio A/A_0 of the ray tubes and the shock wave Mach number ratio M/M_0 within them that is required to maintain the shock front contiguity at the triple point can be established. These are

$$\frac{A}{A_0} = \frac{\sin(\chi - \theta)}{\sin(\chi)}, \quad \frac{M}{M_0} = \frac{\cos(\chi - \theta)}{\cos(\chi)}. \quad (9.3)$$

For a given θ , there are three unknowns, A , M , and χ . To find the third equation [i.e., the $A = f(M)$ function], the shock is assumed to propagate in the ray tubes as in a bounded duct. The function usually used was first obtained by Chester (1954), integrated by Chisnell (1957), and later rederived in a simpler but identical form by Whitham (1958). It has been modified with second-order terms to improve its accuracy for shock wave Mach reflection by Yousaf (1974) and Milton (1975). Note that even then the theory continues to predict Mach reflection at values of wall angle higher than those where regular reflection appears. As Whitham points out, this is largely due to the fact that the reflected shock must be chosen so that it matches both the pressure and stream deflection behind the Mach stem, which is one condition too many. Nevertheless, at smaller angles, the theory should work well. For incident shock waves of $M > 3$ approximately (i.e., for “strong” shocks), the complex term in the area/Mach number function tends toward a constant value as shown by Whitham (1957). The area Mach number dependency becomes simply $A_0 M_0^n = A M^n$, where n is a constant. The Mach reflection solution for χ is then independent of incident shock Mach number and only varies with θ . For incident shock waves of lesser strength, χ varies with both M and θ .

In his original papers, Whitham examined the self-similar Mach reflection cases for such strong shocks interacting with both a wedge and an (external) cone. If the Mach stem is taken as straight and normal to the wall, the solution in the wedge case is direct and can be obtained for a given wall angle, θ_{wall} . In the conical case, both M and θ were written as functions of a single variable η [where $\eta = \tan^{-1}(r/x)$]. The solution procedure was obtained by selecting a value for the ratio of the Mach number at the triple point just after reflection to that just before. A solution for χ and θ the local triple-point locus and ray angles, respectively, was then found at the triple point. Integrating from the triple-point locus to the wall gave the wall angle when $\eta = \theta$. That is, the solution is obtained indirectly by estimating the Mach number of the stem at the triple-point boundary and integrating across the stem to check if the ray direction at the other boundary, that is, the wall, is satisfied. This requires repetition until the correct wall value is obtained. In Whitham's example, the Mach number ratio at the triple point was taken as 1.2, giving χ , θ values at that location of 35.8° and 22.4° , respectively. The corresponding wall angle θ_{wall} was found to be 28.8° . Note that this solution applies to strong shocks only and that it is indirect. In engineering practice, it is more convenient to work from a known cone wall angle to the unknown triple-point values.

9.3 GENERALIZED SOLUTION OF CONICAL MOVING SHOCK WAVES

The ray-shock theory has proven to be quite effective in assessing conical Mach reflection patterns even though it only gives details of the main shock wave front, neglecting the reflected wave. In summary, the ray-shock solution techniques are as follows:

- (i) Indirect, requiring repetitive solutions to determine shock pattern details for a given conical shape. It has been used for external flow over simple cones and flow from circular ducts into a conical convergence (Whitham, 1959; Setchell *et al.*, 1972). Solutions are obtained by numerical integration giving continuous shock wave and triple-point locus shapes. Although a solution covering all Mach number ranges is possible using this method, only the strong shock wave approximation for the $A = f(M)$ function is usually applied.
- (ii) Direct, using an *a priori* approximation for the ray direction and hence shock wave shape in the Mach stem region. This assumption is usually that the rays are parallel to the wall with the stem straight and normal to it. The solution integrates numerically along the triple-point locus, which is again a continuous curve. Any $A = f(M)$ function can be

readily incorporated. The method has been used for shock movement within complex cones (Milton and Archer, 1969) and, with a modified formulation, external progression over simple cones (Han *et al.*, 1992). In spite of the straight stem approximation, it is reasonably accurate.

- (iii) An incremental approach working from the wall ray by ray with each new ray having its direction reevaluated (Duong and Milton, 1985; Milton *et al.*, 1986). The solution proceeds incrementally with both the shock Mach stem and triple-point locus being assumed straight between neighboring rays. Hence, as long as the ray spacing is kept small, both the Mach stem and triple-point locus exhibit curvature. Again, it is easy to use complex $A = f(M)$ functions. This method has only been used in internal cases, but could be readily adapted for external ones.

Alternatively, a simple, generalized formulation applicable to all configurations can be used (Milton and Archer, 1996). This method and its results are now discussed.

9.3.1 FORMULATION FOR RAY-SHOCK CALCULATIONS IN CONICAL MACH REFLECTION

First, a suitable sign convention is required so that all cases use identical formulas. Also, instead of integrating fully from centerline to wall or stepping incrementally across every ray tube, the integration proceeds from the wall until the ray direction at the triple point differs by a predetermined angular increment from that of the initial wall ray. The reflection at this point is likely to have progressed only partway across the field being examined. Across this section, the triple-point locus is curved but the Mach stem is straight. Once this ray angle limit is exceeded, the ray at the triple point is taken as a new boundary (i.e., an artificial “wall”) and the process is repeated. Except for this ray deflection angle, the calculation is identical to that of the previous section. The initial radius is different, but as the formulas are normalized on radius, it has no effect. All that is required is direct scaling of the output to fit the end point of the first calculation to the commencement of the second. This process is continuously repeated until the centerline is reached in internal cases or the flow field has been fully covered in external ones. The accuracy can be set to any required value by selecting the allowable triple-point ray deviation. Computations are extremely quick.

9.3.2 EQUATIONS FOR THE GENERALIZED RAY-SHOCK SOLUTION

The basic equations are then of the general form

$$A/A_0 = f_1(\chi, \theta, r) \quad (9.4)$$

$$d\chi/dr = f_2(M/M_0, \chi, \theta, r) \quad (9.5)$$

$$A/A_0 = f_3(M/M_0) \quad (9.6)$$

Equation (9.6) does not depend on the ray-shock configuration, but it has a noticeable effect on the solution as discussed by Milton and Archer (1996). For the wedge case, which has well known results, they compared for accuracy

- (i) The original CCW relationship (Whitham, 1958)
- (ii) Its modified version, Eq. (9.7) (Milton, 1975)
- (iii) Itoh *et al.* (1981) further revision

They found a significant difference in the solution between (i) and (ii). No noticeable further improvement was found using (iii), although it is much more complex, and therefore (ii) has been used in the conical studies here:

$$\frac{dA}{A} = - \left\{ \frac{2M}{K(M)(M^2 - 1)} + \frac{\eta}{M} \right\} dM \quad (9.7)$$

where

$$K(M) = 2 \left\{ 1 + \frac{2}{\gamma + 1} \left(\frac{1 - \mu^2}{\mu} \right) \right\}^{-1} \left(2\mu + 1 + \frac{1}{M^2} \right); \quad \mu^2 = \frac{(\gamma - 1)M^2 + 2}{2\gamma M^2 - (\gamma - 1)}$$

$$\eta = \frac{1}{2\gamma} \left\{ \left[\frac{\gamma(\gamma - 1)}{2} \right]^{0.5} + 1 \right\} \left[1 - \left(\frac{M_0}{M} \right)^2 \right] + \frac{1}{2} \ln \frac{A_0}{A}.$$

Equation (9.7) with $\eta = 0$ applies to situations where the ray discontinuity angle $\theta \rightarrow 0$, and it is then identical to the CCW relationship. However, in the general Mach number case, even using numerical techniques, Eq. (9.7) is awkward to use in computations and an approximate integration, Eq. (9.8) (Duong and Milton, 1985), gives good accuracy over most of the shock Mach number range:

$$A(M - 1)^\alpha (M + 1)^\beta (M - \delta)^\epsilon M^\eta = \text{const.} \quad (9.8)$$

For $\gamma = 1.4$ and 1.667, the values of α , β , δ , ϵ are as in Table 9.2, while η is obtained from Eq. (9.7). Summation of α , β , δ (with $\eta = 0$) gives a value very close (within 0.03%) to that of $n = 5.0743$ with $\gamma = 1.4$ as derived directly by Whitham (1958) from the full formulation for the strong shock case.

TABLE 9.2 Constants for Eq. (9.8)

	α	β	δ	ϵ	n	$\Sigma(\alpha + \beta + \delta)$
$\gamma = 1.4$	2.000	2.719	0.493	0.354	5.0743	5.073
$\gamma = 1.667$	2.000	2.234	0.867	0.203	4.4360	4.437

Equations (9.4) and (9.5) are developed using the configuration and sign convention shown in Fig. 9.4. The shock wave motion is assumed to be to the right. Angular directions are measured relative to the horizontal (3 o'clock) position and, in external (diverging) cases are positive anticlockwise, whereas in the internal (converging) case, they are positive clockwise. The angular change $\Delta\theta = \theta - \theta_0$, where θ_0 is the incident ray direction. Here, a normalized radius r is used such that $r = R/R_0$, where R is the radius at any position on the conical wall surface at the Mach stem intersection point and R_0 is the initial value at the cylindrical entrance. For diverging and contracting cases, $r > 1$ and $r < 1$ respectively.

The area ratio equation is obtained by rotation of both the stem length and its incident shock section about the axis and is given in Eq. (9.9). The $\cos\theta_0$ term in the denominator allows for the incoming rays to be aligned at an angle to the axis. The common case is $\theta_0 = 0^\circ$ where the incident shock is normal to and moving along the centerline.

$$\frac{A}{A_0} = \frac{\sin(\chi - \Delta\theta)}{\sin\chi} \left[\frac{r - \frac{(1-r)\tan(\chi - \Delta\theta)}{2\tan\theta}}{1 - \frac{(1-r)\sin\chi\cos\theta_0}{2\sin\theta\cos(\chi - \Delta\theta)}} \right] \quad (9.9)$$

Here, $\Delta\theta$ is the angle change at the cone wall, χ the local triple-point locus angle relative to the incident shock rays, and r the dimensionless radius to the Mach stem position on the wall. (Note that the initial radius, that of the duct, is assumed to have a value of 1 unit.) Subscripts $_0$ refer to the incident values of A , M , R , and θ . When unsubscripted, these describe each new stem position after reflection. Also, from the shock kinematics,

$$\alpha = \frac{x}{M_0} = \frac{(1-r)\cos\chi}{M_0\sin\chi\cos\chi}, \quad (9.10)$$

from which

$$\frac{d\chi}{dr} = \left[\frac{M_0}{M} - \frac{\cos\chi}{\cos(\chi - \Delta\theta)} \right] \left[\frac{\cos^2(\chi - \Delta\theta)}{(1-r)\sin\Delta\theta} \right]. \quad (9.11)$$

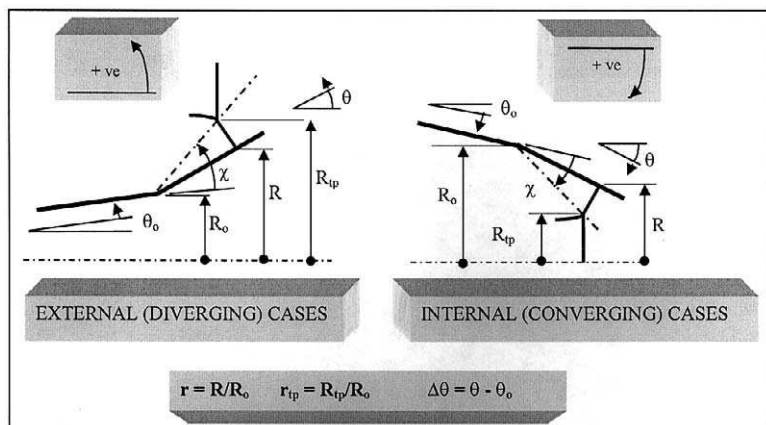


FIGURE 9.4 Sign convention for generalized ray-shock theory equations in conical Mach reflection.

Note that with $r > 1$ in the external reflection case, $d\chi/dr$ is negative, whereas for $r < 1$ in the internal case, $d\chi/dr$ is positive. That is, χ should decrease in the external (diverging) and increase in the internal (contracting) case. Equations (9.9) and (9.11) apply generally with one exception, this being when the rays following the corner are parallel to the centerline, as discussed later.

9.3.3 CURVED MACH STEMS

If the Mach reflection is not self-similar, both the triple-point locus and the Mach stem are curved, a typical known configuration being shown in Fig. 9.2d for the simple internal conical case. Even in self-similar cases, while the triple-point locus is straight, the Mach stem is again curved. Whitham estimated that a variation of about 6.4° exists from the wall ray to that at the triple-point locus for the 28.8° half-angle cone, strong incident shock wave case that he considered. This is because the disturbances generated initially at the triple point distribute over a changing area as the flow proceeds and are then either reinforced in converging or attenuated in diverging flows. For the triple point at any finite radius, the initial scale of the disturbance is infinitesimal relative to the local radius. The local reflection is then given by Eqs. (9.9) and (9.11) by using $r = 1$ [or obtained independently from the wedge equations (9.3), which are then identical]. However, in conical cases, disturbances from the triple point are distributed across a different area ratio calculated by Eq. (9.9) with $r \neq 1$. When the triple point is at its initial reflection point at the wall, its

downstream ray direction is that of the wall, θ_{wall} , but elsewhere it is different and is designated simply as θ . This direction must be found. The ray discontinuity angle may be called $\Delta\theta_R = \theta - \theta_0$. Away from the wall, the value of χ relative to the incoming rays, which are at θ_0 , is known from the end-point calculation of the previous reflection section. As $\Delta\theta_R$ can be found from Eqs. (9.3) if χ is known, the local ray direction at the triple point after reflection, θ , follows. That is, the wedge kinematic equations at the triple-point locus (more precisely termed the triple-point jump conditions) enable Eq. (9.12) for the ray direction change at the triple-point to be found by elimination of χ :

$$\Delta\theta_R = \cos^{-1} \left(\frac{\frac{AM}{A_0 M_0} + 1}{\frac{A}{A_0} + \frac{M}{M_0}} \right). \quad (9.12)$$

The direction θ of the new boundary for the next computational section is given by $\theta = \theta_0 + \theta_R$. This procedure is repeated until the desired geometrical range has been covered. Because the Mach stem is normal to the boundary of each computed section, its shape is curved incrementally.

9.3.4 SOLUTION PROCEDURES FOR CASES WITHOUT SELF-SIMILARITY

For self-similar cases, χ is constant and once found, it applies everywhere on the triple point, as does the downstream ray direction, θ . The conical equations (9.9) and (9.11) become independent of r , and an algebraic solution follows. For reflections without self-similarity, the initial reflection commences at a finite radius from the centerline. As noted, this has been taken as $r = 1$. Equations (9.9) and (9.11) are now not independent of r and must be integrated to develop the triple-point locus. Starting values of χ are required. When the triple-point locus is on the wall, $\theta = \theta_{\text{wall}}$. Hence, the triple-point jump (wedge) formulation of Eq. (9.3) applies at this point for a known $\Delta\theta$ allowing $\chi = \chi_{\text{wedge}}$ to be found. The integration gives the local χ values for $r \neq 1$ and the coordinates along the triple-point locus. The local ray direction change $\Delta\theta_R$ follows from Eq. (9.12).

9.3.5 POSTREFLECTION RAYS PARALLEL TO THE CENTERLINE

As noted earlier, the conical solution applies generally except when the rays following the reflection are parallel to the centerline as in Figs. 9.2f and 9.2g. In

this case, the dimension r in Fig. 9.4 at the foot of the Mach stem on the reflecting surface cannot, being constant, uniquely locate the configuration. However, the triple-point locus cannot now be parallel to the centerline and can be used instead. If the dimensionless radius to the triple point, designated as r_{tp} , is used, the area ratio and change of χ are given by

$$\frac{A}{A_0} = \frac{\sin(\chi - \Delta\theta)[1 - (1 - r_{tp})/2]}{\sin \chi \left[1 - \frac{(1 - r_{tp})}{2} \frac{\sin \chi \cos \theta_0}{\sin(\chi - \Delta\theta)} \right]} \quad (9.13)$$

$$\frac{d\chi}{dr_{tp}} = \frac{\sin \chi \cos(\chi - \Delta\theta) \left[\frac{\cos \chi}{\cos(\chi - \Delta\theta)} - \frac{M_0}{M} \right]}{r_{tp} \left[1 - \frac{M_0}{M} \cos \Delta\theta \right]}. \quad (9.14)$$

When θ equals zero, θ_0 must be equal to $\Delta\theta$. Then, for a shock wave self-reflecting from its own centerline, r_{tp} (which is R_{tp}/R_0) approaches infinity and the equations (9.13) and (9.14) reduce to (9.15) and (9.16), from which $\chi = \text{constant}$ giving a straight triple-point locus. For finite values of r_{tp} , both A/A_0 and $d\chi/dr_{tp}$ vary with the location and the locus is curved.

$$\frac{A}{A_0} = \frac{\sin(\chi - \Delta\theta)}{\sin \chi} \left[\frac{\sin(\chi - \Delta\theta)}{\sin \chi \cos \Delta\theta} \right] \quad (9.15)$$

$$\frac{d\chi}{dr_{tp}} \rightarrow 0 \quad (9.16)$$

9.4 SOME CONICAL MACH REFLECTION RESULTS FROM THE RAY-SHOCK THEORY

9.4.1 EXTERNAL (EXPANDING) FLOWS

Regular reflection is possible as in wedge reflections. The transition from regular to Mach reflection is discussed later. It will be assumed that Mach reflection, always predicted by the ray-shock theory, occurs. Two cones of different cone angles intersecting at a finite radius as depicted in Fig. 9.2c provide the most general configuration. Following the convention defined earlier for angular direction, as long as $\theta > \theta_0$, the compression corner for a Mach reflection will exist. To simplify the calculations, it is assumed here that the incident shock wave is straight and of uniform strength, although it may be inclined to the centerline. In practice, this is only possible when θ_0 equals zero (Figs. 9.2a, 9.2b, and 9.2d). This is because an initially straight shock moving

with a radial direction component will be transmitted through a continuously changing ray tube area, each ray tube varying at a different rate along its length. Hence, it must develop curvature and shock strength variation during its motion even prior to reflection. Although this can be coped with without too much difficulty by the ray-shock theory, it would obscure the trends to be studied here and so has been ignored. Also, for experimental verification, straight, uniform incident shocks at other than $\theta_0 = 0^\circ$ are hard to produce and cannot be maintained constant over the time period of the reflection. Hence, the best configurations for experimental comparison, are when $\theta_0 = 0^\circ$, which is, in external reflections, a plane shock moving along the surface of a cylinder onto a diverging conical surface (Fig. 9.2b). When the radius of the cylinder R_0 equals zero, the configuration becomes a plane shock, simple cone interaction as shown in Fig. 9.2a. A converging conical shock self-reflecting from its own centerline (Fig. 9.2f) is another case where the radius R_0 is also zero. Here, θ_0 is negative and the incident shock near the centerline may be assumed to be straight to obtain an understanding of the process. However, experimentally the problem of incident shock curvature during the reflection process as discussed earlier will exist because of the radial component of its motion.

9.4.1.1 Simple Upstream-Facing Cones

The calculation gives a single value of χ for each reflecting angle. In this case, the calculations show that the triple-point locus angle (expressed as $\chi - \Delta\theta$ for greater clarity) reduces as $\Delta\theta$ increases. It also increases as M_0 increases, with the values converging as higher Mach numbers are reached. These results parallel those of wedge reflections, although the actual values are different, being lower in the conical case. Results are shown in Fig. 9.5.

9.4.1.2 Cylinder-to-Cone Interactions

The general configuration sufficient to explain the process is that of a normal shock wave moving along the surface of a cylinder and reflecting at its intersection with a diverging cone (Fig. 9.2b). This case does not have self-similarity, and hence the equations require integration from the starting values (see Section 9.3.4). The resulting triple-point locus curves toward the cone surface from its initial starting χ value, which is equal to that of the equivalent angle wedge. In the limit, as r becomes very large, χ approaches the lower simple cone value and the subsequent reflection eventually tends toward self-similarity. From a position where the surface radius is about five times that of the cylinder, there is little difference in the value of χ from that of the simple cone, although the triple-point locus is displaced further into the flow by the

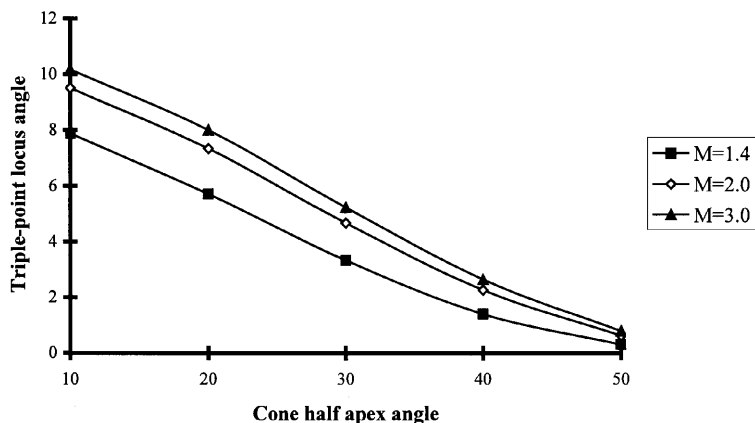


FIGURE 9.5 Triple-point locus angle, plotted as $\chi - \Delta\theta$ versus $\Delta\theta$ for a simple cone.

initially higher χ value. Figure 9.6 shows an example of the results of this type of calculation for an incident shock wave Mach number of 2.0 and a cone half-apex angle of 20° . Three results are depicted, these being the two straight triple-point loci for the wedge and simple cone calculations, respectively, and the curved locus for the general case. The curved triple-point locus changes progressively from the wedge χ angle to the simple cone value as the shock wave system moves downstream and is displaced into the flow field. Figure 9.7, also for $M_0 = 2.0$, shows the variation in χ (i.e., $\Delta\chi^0$) through different radial locations from its initial (wedge) value at the reflecting corner ($r = 1$) to its final (simple cone) value, the greatest change occurring with the smaller $\Delta\theta$ values. Initially, the wall and ray through the triple point are at the same angle and there is no deviation. Further into the flow, the wall is at a greater angle than the triple-point ray and so the Mach stem is curved forward from the wall toward the triple point. That is, the deviation values between wall and triple-point rays increase downstream from the reflection point as r increases but are asymptotic, approaching the values for the equivalent, simple cones as r becomes large, from about 5 or 6 onward. The angular deviation of the rays between their wall and the triple-point locus values for a range of cylinder/cones at an incident shock $M_0 = 2.0$ varies from about 2° to 4° . The maximum deviation at $M_0 = 2.0$ occurs for the 20° half-apex-angle cone.

Values of χ and for the $M_0 = 3$ case are plotted against cone half-angle $\Delta\theta$ for several values of r on Fig. 9.8(a) while their difference as a percentage of the limiting values of χ at $r = 1$ and $r = 1000$ (essentially at infinity) are plotted against r on Fig. 9.8b. At $r = 2$, the locus angle χ is about halfway between these limits and approaches the minimum value asymptotically. At lower $\Delta\theta$

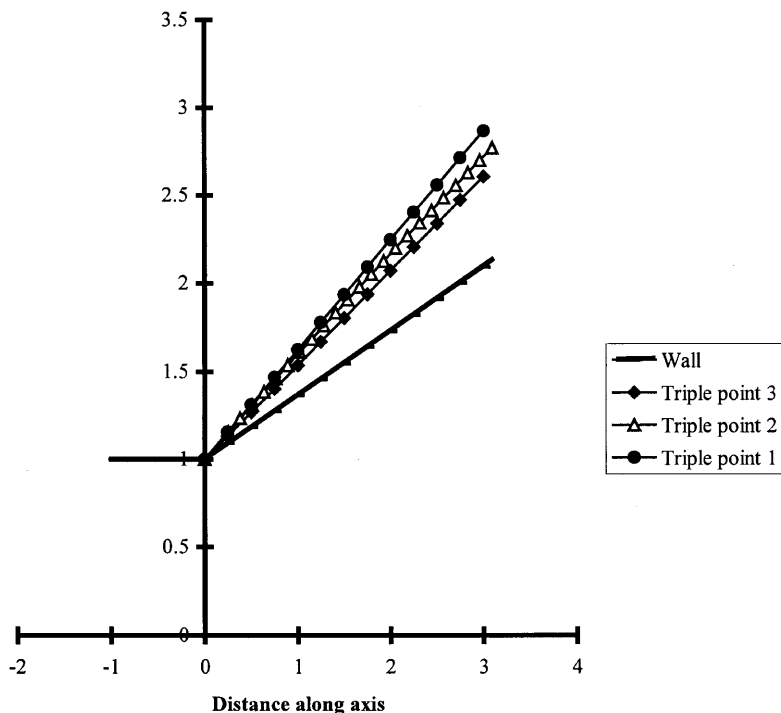


FIGURE 9.6 The general cylinder-cone solution for the triple-point locus in external Mach reflection over a 20° cone with incident shock wave of $M_0 = 2.0$. Triple point 1: wedge solution; triple point 2: conical solution using finite cylinder entry radius; triple point 3: solution for a simple cone with entry radius of zero. Note that the vertical (radial) scale is double the horizontal.

angles, the initial percentage reduction in χ with increase in radius is greater. For $r \rightarrow \infty$ (in these calculations, $r = 1000$), the configuration is identical with that of a simple cone, which is therefore a special case of the cylinder-cone configuration.

9.4.1.3 External Cone-to-Cone Cases

These more general cases have still to be validated experimentally. However, the calculations are of interest. The effect of a nonzero value of θ_0 on the triple-point locus angle χ is illustrated in Fig. 9.9, the particular cases being considered having $R_0 = 0$ and θ_0 equal to $+10^\circ$ (initially expanding), 0° (axial), and -10° (initially contracting), all with $M_0 = 2.0$. At any one value of angular deviation, $\Delta\theta$ at the corner, the contracting case produces the largest

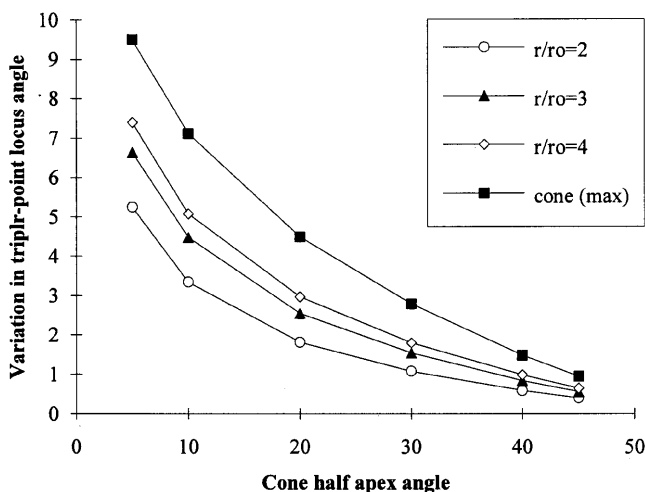
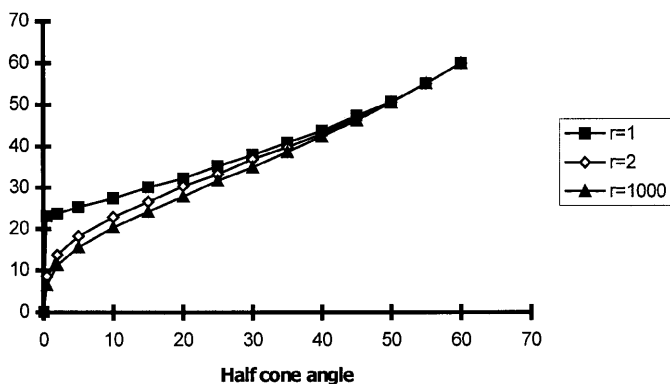
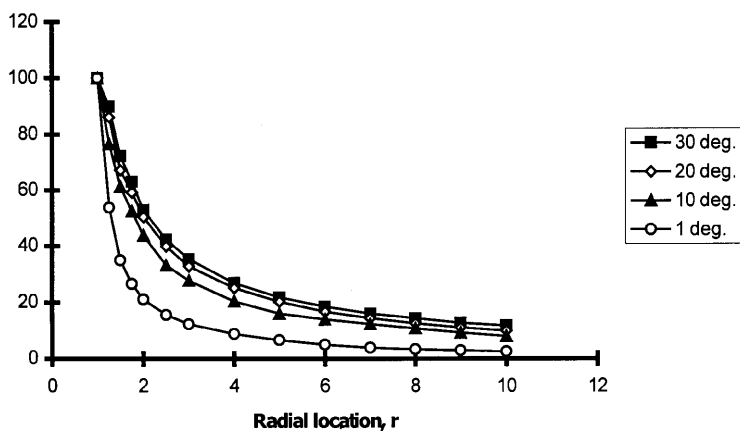


FIGURE 9.7 External conical Mach reflections, $M_0 = 2.0$. Variation in the triple point trajectory angle $\Delta\chi$ with radial position and $\Delta\theta$. Note: Variation (vertical scale) is $\Delta\chi = \chi_{[\text{wedge}(r=1)]} - \chi_{[\text{conical}, (r>1)]}$.

value of χ relative to the θ_0 direction while the expanding case gives the smallest. This is due to the accumulating disturbances as the rays converge in the former and their dispersal with the latter. The results for an incident shock wave normal to the axis lies in between, as would be expected.

9.4.1.4 Conically Converging Shocks Self-Reflecting at the Axis of Symmetry

In converging ducts, the converging conical shock moves inward, self-reflecting when the triple point reaches the centerline. As the angle change is anticlockwise, this is an expanding case even though it is within a contraction. Here, from symmetry, the initial direction of the reflected stem is normal to the axis. As $r = 0$, Eqs. 9.15 and 9.16 apply and the configuration is again self-similar with the triple-point locus being straight. Its direction, at $\chi - \Delta\theta$ to the axis, varies only with the Mach number and the direction of the incident shock wave. Values are plotted against $\Delta\theta$ in Fig. 9.10 where they are compared with the wedge (2D) and simple cone cases. It can be seen that $\chi > \chi_{\text{wedge}}$, unlike the simple cone where $\chi < \chi_{\text{wedge}}$ by about the same margin. As in Section 9.4.1.3, this is due to the converging incident shock wave.

(a) TP locus angle χ plotted as a function of cone half apex angle $\Delta\theta$ for $M_0 = 3$ (b) percentage of the maximum change in χ from $r = 1$ (initial, wedge value) to $r = \infty$ (final, simple cone) for $M_0 = 3$ FIGURE 9.8 External conical Mach reflections: effect at wall radii greater than that of the cylinder on χ and M for $M_0 = 3$.

9.4.2 CONVERGING (INTERNAL) CASES

All internal cases must have $R_0 > 0$. For finite R_0 , the value of θ_0 (measured positive clockwise) must be less than θ for a compression corner to occur and the possible configurations are a circular duct to cone case where θ_0 equals zero (Fig. 9.2d) and the cone-to-cone cases (Fig. 9.2e) discussed by Milton *et al.* (1986). The latter exist when a shock converging in an existing cone reflects

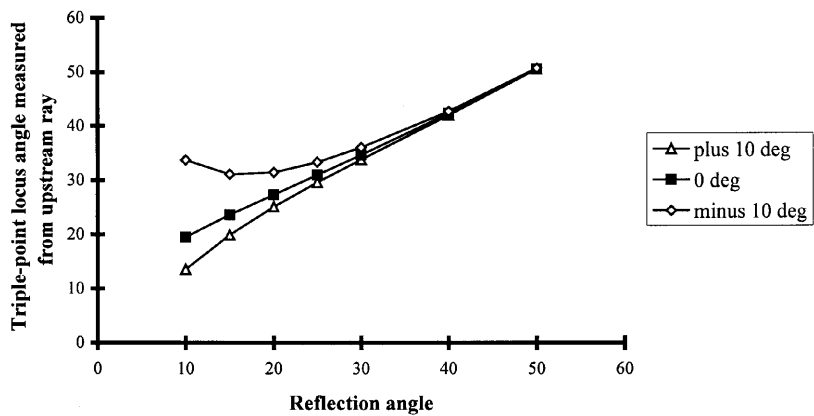


FIGURE 9.9 External conical Mach reflection over simple cones for $M_0 = 2.0$ showing the effect of the incident ray direction.

at a larger-angle, concentric cone and are of particular significance when studying curved, axisymmetric surfaces of monotonically decreasing area.

9.4.2.1 Cylinder-to-Cone Problem

No converging cases can show self-similarity because $R < R_0$ and hence R_0 must be non-zero. That is, equations (9.13) and (9.14) must be integrated from

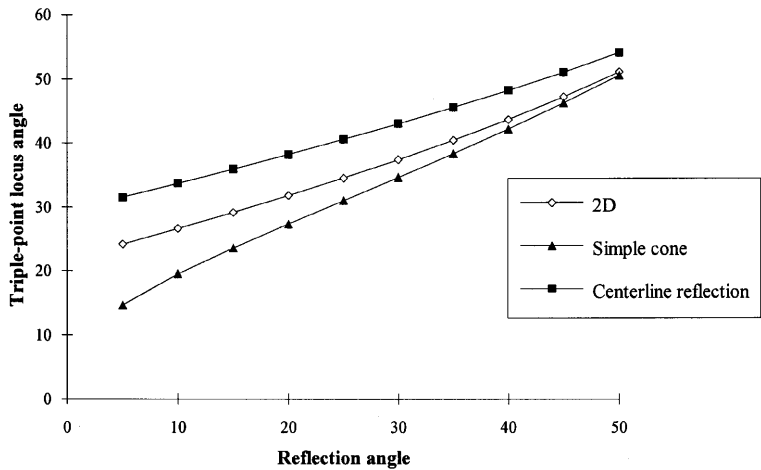


FIGURE 9.10 A comparison of different self-similar cases in external conical Mach reflections for $M_0 = 2.0$.

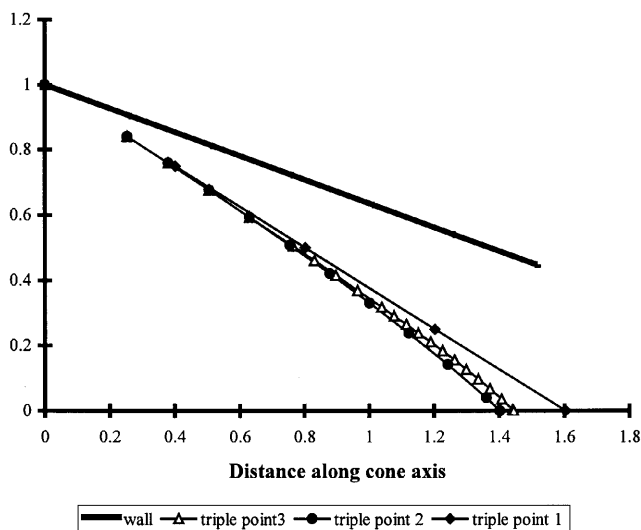


FIGURE 9.11 Internal conical Mach reflection in a 20° cone at $M_0 = 2.0$. Effect of Mach stem curvature on triple point locus shape. Triple point 1, wedge calculation; triple point 2, straight stem, conical calculation; triple point 3, stem curved in three stages, each 2° , conical calculation.

their starting values. The basic case is that of a shock wave moving inside a cylindrical duct entering a converging cone. Figure 9.11 shows, for a 20° half-apex angle cone with an incident shock wave of $M_0 = 2.0$, the calculated triple-point locus up to its intersection with the centerline for three cases:

- (i) Wedge
- (ii) Conical assuming a straight, normal stem throughout
- (iii) Conical with the stem curvature obtained as described in Section 9.3.3 with the allowable ray deviation being set at 2° from the previous value.

The conical calculations indicate noticeably shorter intersection distances. The curved stem assumption of case (iii) provides a very small increase over the straight stem value of case (ii) fundamentally because of the larger surface area available to the curved stem. Figure 9.12 provides a comparison at different reflecting angles of the variation in triple-point-centerline location using wedge, straight stem conical, and curved stem conical (with different allowable ray deviations of 1° and 2°) assumptions. As the radius of the cone section decreases, the ray angle increases from its initial, cone wall direction, initially very slowly. Very close to the centerline (within a few percent of the radius), this value becomes very high. Once some curvature in the stem is established

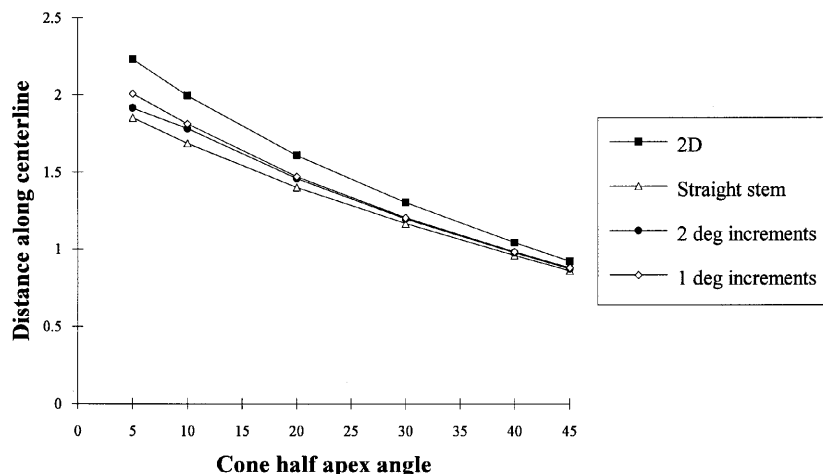


FIGURE 9.12 Effect of Mach stem curvature on the centerline-triple-point locus intersection. Internal conical Mach reflections, 20° cone, $M_0 = 2.0$. Triple point 1, wedge (2D) calculation; triple point 2, straight stem, conical calculation; triple point 3, Stem curved in three stages, each 2° , conical calculation.

(e.g., a 2° calculation tolerance), a more precise adjustment to smaller incremental allowances (e.g., 1°) makes little difference, particularly at the higher $\Delta\theta$ reflecting angles. That is, the large angular Mach stem ray deviation that appears near to the centerline has little effect on the overall Mach reflection pattern.

9.4.2.2 Internal Cone-to-Cone Cases

The initial cone may be converging, which is the most likely case; parallel, as in Section 9.4.2.1; or expanding. In internal cases, all can provide compression corners if the second cone is of greater positive angle than the first. The intersection of the triple-point locus with the centerline is different in each case, even when the wall angle change is the same. This is illustrated in Fig. 9.13, where $\theta_0 = \pm 10^\circ$ (contracting), 0° (axial) and -10° (expanding) are compared for different reflection angles, $\Delta\theta$ with $M_0 = 2.0$. This is equivalent to Fig. 9.9 for the external case. An initially contracting cone results in the shortest intersection length while an initially expanding one has the greatest. The parallel duct case lies in between.

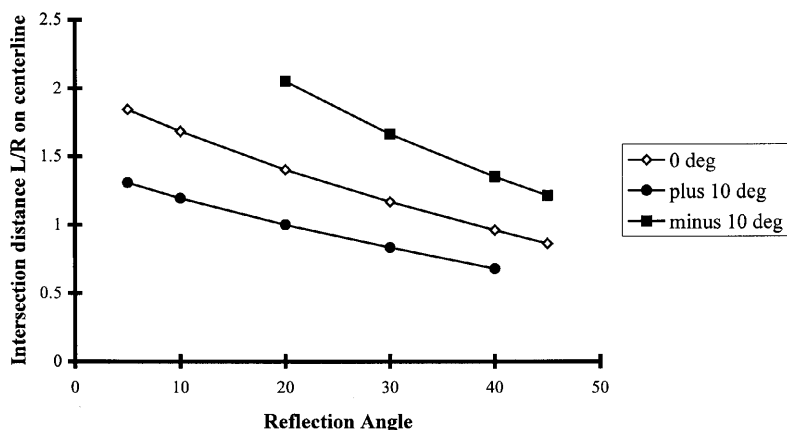


FIGURE 9.13 Internal conical Mach reflection over simple cones for $M_0 = 2.0$ showing the effect of the incident ray direction, θ_0 .

9.5 EXPERIMENTAL CONICAL MACH REFLECTION STUDIES

The ray-shock theory and calculations based on it provide substantial information regarding the behavior of shock waves in conical Mach reflection. The generalized method and results discussed in Sections 9.3 and 9.4 allows easy calculation of many configurations. However, other work exists and comparison with shock tube experiments and CFD studies is necessary.

9.5.1 VALIDATION FOR EXTERNAL CONE CASES

Early experimental work on external flows over cones and spheres was carried out by Bryson and Gross (1961), with the particular intention of evaluating Whitham's ray-shock theory. Experiments used a schlieren system and calculations followed the indirect procedure suggested by Whitham (1959). The Bryson and Gross experimental results at an incident shock Mach number of 3.68 and cones of half-apex angles ranging from 9.7° to 44.7° show a Mach reflection pattern similar to the conventional wedge reflection with a Mach stem, triple-point, reflected shock, and contact discontinuity (slipstream). The reflection exhibited a straight triple-point locus and is therefore self-similar, as is the wedge reflection. The triple-point locus angles, however, differed from

the wedge values and, unlike the wedge case, a slightly curved Mach stem is implied from the calculated results, although this is difficult to measure in the photographic material supplied from the experiments. Their analysis followed Whitham's method and included additional calculations for shocks of Mach numbers less than those in the strong shock regime, that is, for $M_0 < 3$ (down to $M_0 = 1.01$). For strong incident shock waves, their calculations cover a full range of reflecting angles (which include Whitham's specific case), showing a ray angle throughout that is noticeably greater at the wall than at the triple-point trajectory, the difference decreasing with increasing wall angle. Note that the shock wave is normal to the wall only at the cone surface.

Takayama and Sekiguchi (1976) examined plane shock wave reflection at the external surface of simple, upstream-facing cones. They used 50 cones with cone half-apex angles $\Delta\theta$ ranging from 3.75° to 75° , predominantly at 1° increments. Shock wave Mach numbers were 1.04, 1.08, 1.21, 1.53, 1.81, and 3.09. That is, except for the last, they were in the region where the triple-point locus angle χ would be expected to vary with the change in Mach number at any given $\Delta\theta$. The principal focus of their work was to determine the critical angles for the onset of Mach reflection from regular reflection. In their analysis, they used a simplified version of the ray-shock theory that assumed that the Mach stem remains straight and normal to the surface. They concluded that shock diffraction over cones is different from that on wedges, that this approximate analysis gave reasonable agreement with experiment, and that, within experimental error, there is no difference in critical (transition) angle between wedge and cone. Their agreement with theory was slightly inferior to that of Bryson and Gross at small cone angles but, given the straight stem assumption, was still quite reasonable.

Experimental and ray-shock theory calculations for wedge and simple external conical Mach reflections are shown in Fig. 9.14. Both wedge and cone reflections have straight triple-point locus directions and these can therefore each be categorized by a single angle χ . The ray-shock theory results are for an incident shock Mach number of 3, which just falls into the strong shock classification. Typical experimental results for cones from Takayama and Sekiguchi (1976) are included in this figure, and the agreement between experiment and calculation is good. It can be seen that the conical triple-point locus angle is always less than that of the wedge, although the computational values converge at high reflection angles, approaching each other closely at $\Delta\theta = 55^\circ$.

Over a large range of reflection angles, the conical approach described by the ray-shock theory agrees well with experiment. The calculations highlight an important trend, which is that the difference between the wedge and cone cases becomes much larger at small θ_{wall} (i.e., $\Delta\theta$) values. The lower cone values are because the angular difference, $\chi - \Delta\theta$, that categorizes the stem

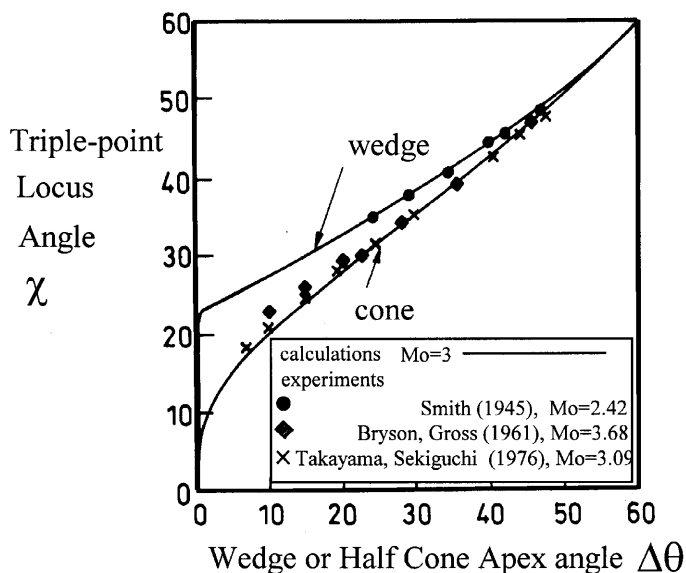
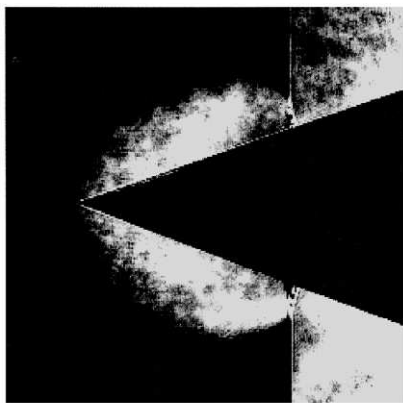


FIGURE 9.14 Comparison of ray-shock theory with experiment for wedge and simple external cone cases.

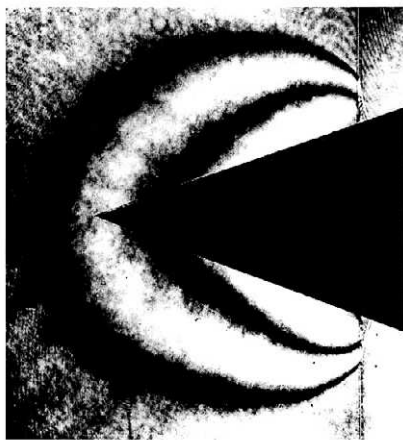
length (and hence the relative area ratios) has more influence in the conical case on the final value of χ . In other words, with the cone, the effect of the disturbance creating the Mach stem is spread over a much larger area than with the wedge because of the rotational symmetry for the same progression of the reflection pattern. It therefore has proportionally less effect in displacing the triple point out into the flow field. Below an angle of about $\Delta\theta = 10^\circ$, the conical χ value departs rapidly from that of the wedge and, as $\Delta\theta \rightarrow 0^\circ$, the conical χ approaches 0° very rapidly while the wedge χ does not. Because of numerical singularities, conical calculations using $\Delta\theta = 0^\circ$ cannot be undertaken. Instead, for comparison using an incident shock of Mach number 3 at the very small angle of $\Delta\theta = 0.01^\circ$, a solution for χ_{wedge} is 21.8° and χ_{conical} is 1.82° .

Milton and Takayama (1998) carried out generalized experiments using both simple cones and ones with reflection from a cylindrical entry section. Cones of either 10° or 20° half-apex angle were used. The cylinders had an internal cylindrical “cookie cutter” so that the incident shock wave passed along their surface without disturbance as a plane shock to be reflected at the intersection with the cone. All tests had an incident shock wave Mach number $M_0 = 1.42$.

Interferograms for the simple cones are shown for two positions in each part of Fig. 9.15 for a simple cone of half-apex angles 20° . The photographs are at two different positions, 20 mm and 50 mm from the apex of the cone, respectively, but have been scaled to nearly the same size at the shock. They show identical Mach stem patterns and triple-point locations, demonstrating self-similarity. For the cylinder–cone combination, similar interferograms of the reflection are shown for the progressive development of the reflection



(a) Shock at 20 mm from cone apex



(b) Shock at 50 mm from cone apex

FIGURE 9.15 Self-similar reflection over the surface of a simple cone, $M_0 = 1.42$, cone half-apex angle $\Delta\theta = 20^\circ$.

pattern in Fig. 9.16 for a cone half-angle of 20° . The shock progression can be seen as the cylinders have been scaled to an identical radius. The χ value in each picture and the detailed pattern show some variation as the reflection progresses. For example, the Mach stem gradually curves forward towards the triple-point. That is, the reflection is not self- similar.

9.5.2 MACH REFLECTION WITHIN CONICAL CONTRACTIONS

Shock tube experiments on Mach reflection (and to a lesser extent, regular reflection) within contractions are more difficult than in external flows for many reasons. For example, for visualization, the conical test section walls must be machined directly into transparent material. This needs to be of sufficient strength to withstand the shock wave pressures and, as the time available for the event is limited to microseconds, flow visualization is inhibited by poor-quality light transmission and wall distortion effects. Also, internal axisymmetric reflections are never self-similar, thereby presenting further problems both analytically and experimentally.



FIGURE 9.16 External reflection from a conical surface to a cone, $M_s = 1.42$, cone half-apex angle $\Delta\theta = 20^\circ$.

Early studies concentrated on the outcomes of the reflection process, which is the shock wave reinforcement by area convergence. Belokon *et al.* (1965), in an attempt to retain shock wave stability during implosion, used an octagonal pyramidal converging cavity of 10° half-angle instead of a cone and measured the magnification of the intensity of the plasma glow spectra as the strong incident shock waves converged to a point. They found this to be intensified some 1000 times. They noted the repeated jumps in intensity during the process due to the Mach reflection, which they analyzed by assuming χ constant for each of the multiple Mach reflections. Russell (1967) used a 10° half-angle cone to study the shock strengthening over a convergence with area ratio of 292 : 1, measuring shock velocity via heat transfer gauges in a parallel output tube. Results were extrapolated back to the cone exit. Reasonable agreement was found with the one-dimensional application of the CCW relationship.

To obtain an analytical solution for a shock wave moving from a parallel, circular duct into a cone, Milton and Archer (1969), using an early version of the direct ray-shock solution, assuming a ray-direction distribution that provided an implosion converging toward the cone apex. Note that this assumption was later changed to rays parallel to the wall. Designating the downstream ray direction allowed a simplified ray-shock approach. From this, they determined that the triple-point locus curved toward the centerline of the cone, and hence the locus–centerline intersection point could be found. As their aim was to create a well-focused implosion (i.e., where all triple points intersect the centerline at a single point), the calculations were repeated for a range of configurations where a shock moved from one cone to another of greater apex angle. This allowed the implosion-generating profile to be designed. That is, their approach was very general, covering a wide range of possibilities. The selection of Mach stem ray direction with a direct solution for a given cone angle $\Delta\theta$ was a precursor to the general method described in Section 9.3. However, no experiments were available at that time to confirm their calculations.

A thorough study of a single conical contraction was undertaken by Setchell *et al.* (1975) using argon in a 10° half-angle cone with shock waves from a circular shock tube of Mach numbers 6.0 and 10.2 in the “strong” incident shock range. They measured shock wave velocity on the centerline of the contraction using two sets of twin piezoelectric crystals on a thin tube inserted from the cone apex. Calibration measurements indicated an accuracy of 1 to 4%. The results showed that centerline velocity jumped at intervals as reflected and rereflected shocks arrived at that location. Between jumps, the velocity decayed by some 30 to 50% at about the midpoint because of expansion from the centerline, before rising slightly immediately prior to the next jump. The analysis used the ray-shock theory, written in terms of radial coordinates and

expressed as r/R , the range of the local radius to the cone entry radius. The solution procedure followed the initial Whitham approach by selecting the M/M_0 ratio and integrating to find the corresponding r/R . Then χ from the triple-point jump equations was obtained with the triple-point locus coordinates, and finally, the intersection with the centerline, x/R , followed. In the region downstream of centerline rereflection, rays were assumed to be straight with constant Mach numbers in each ray tube. Theoretical results followed the one-dimensional (CCW theory) trend, the conical Mach reflection approach giving velocities that oscillated around the linear CCW values as the repeated reflected shock waves arrived at the centerline. This is expected because of the use of the same CCW formulation as their $A = f(M)$ function in the ray-shock solution. The experimental results showed that the shock jump occurred on the centerline some 10% downstream of that calculated, indicating that the basic ray-shock theory here, as in other applications, slightly overpredicts the triple-point locus angle, χ .

An extended range of several cones (10° , 20° , 30° half-angle) was examined by Duong and Milton (1985) for incident shock wave Mach numbers of 1.47 and 2.40 (less than the strong shock regime) in air. They used an upstream-facing pressure transducer on a centerline probe that could be relocated to an infinite number of axial positions to locate and evaluate the pressure increase at the centerline reflection shock jump positions. Figure 9.17 shows typical results. They reformulated the ray-shock theory to give a direct, ray-by-ray incremental solution from the cone angle and used a modified $A = f(M)$ function (Milton, 1975) to improve the accuracy of the solution. Also, this approach allowed the more complex area change function for low and medium strength shocks to be applied as easily as the simple strong shock relationship. Experimental and calculated values were in very good agreement, both with their own measurements in air and with those of Setchell *et al.* in argon. By comparing their calculations with those of a wedge of similar angle, they noted that the shock reinforcement in the cone as it converges to the apex is greater because of both the higher shock strength gain at each reflection and the increased number of reflections in a given axial length.

Although centerline velocity or pressure measurements are valuable, flow visualization can give much more information. In the external cases, schlieren or interferometric methods are appropriate for direct visualization of the phenomena, making it easy to trace the growth in the reflection pattern. However, for the internal type, flow visualization is quite difficult. Using both the centerline pressure probe technique in an aluminum test section and either a diffuse holographic or an aspheric lens photographic technique (see Takayama and Onodera, 1983) to examine shock motion inside acrylic test sections, Milton *et al.* (1986) investigated cylinder-to-cone and cone-to-cone (double cone) Mach reflections. In double-cone geometries, a number of

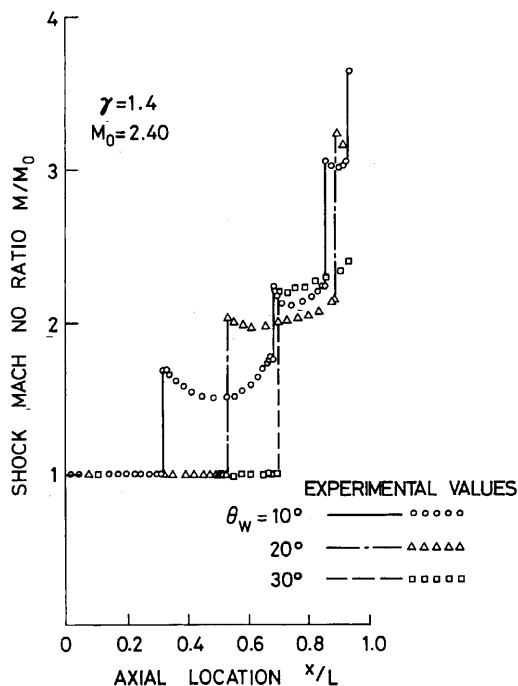


FIGURE 9.17 Mach reflection in cones of $\Delta\theta = 10^\circ$, 20° , and 30° at $M_0 = 2.42$. Pressure transducer measurements on the contraction centerline.

possible reflected shock configurations are possible depending on the length of the primary cone, as shown in Fig. 9.18. If it is of zero length (called type 0), the pattern is simply a duct-to-cone type. As the primary cone length increases, the triple-point trajectories from the successive compressive corners can intersect before (type 1), exactly on (type 2), or after (type 3) the first reflects from the centerline. A further type (type 4) is possible where the centerline rereflection from the first cone arrives back at the duct wall exactly at the second corner. Only types 1 and 3 (in addition to the previous basic type 0) were considered experimentally because of the precision required for the other two. At $M = 1.47$ and 2.40 , there was good agreement with the theoretical centerline intersection position even for these complex cases. Also, the visualization confirmed that both the triple-point locus and the Mach stem were curved. Figure 9.19 shows the results from the flow visualization measurements. Shock wave visualization examples using the aspheric lens technique are shown here with two methods, a single pulse result in Fig. 9.20a and a double pulse, infinite fringe hologram in Fig. 9.20b. Both were taken at

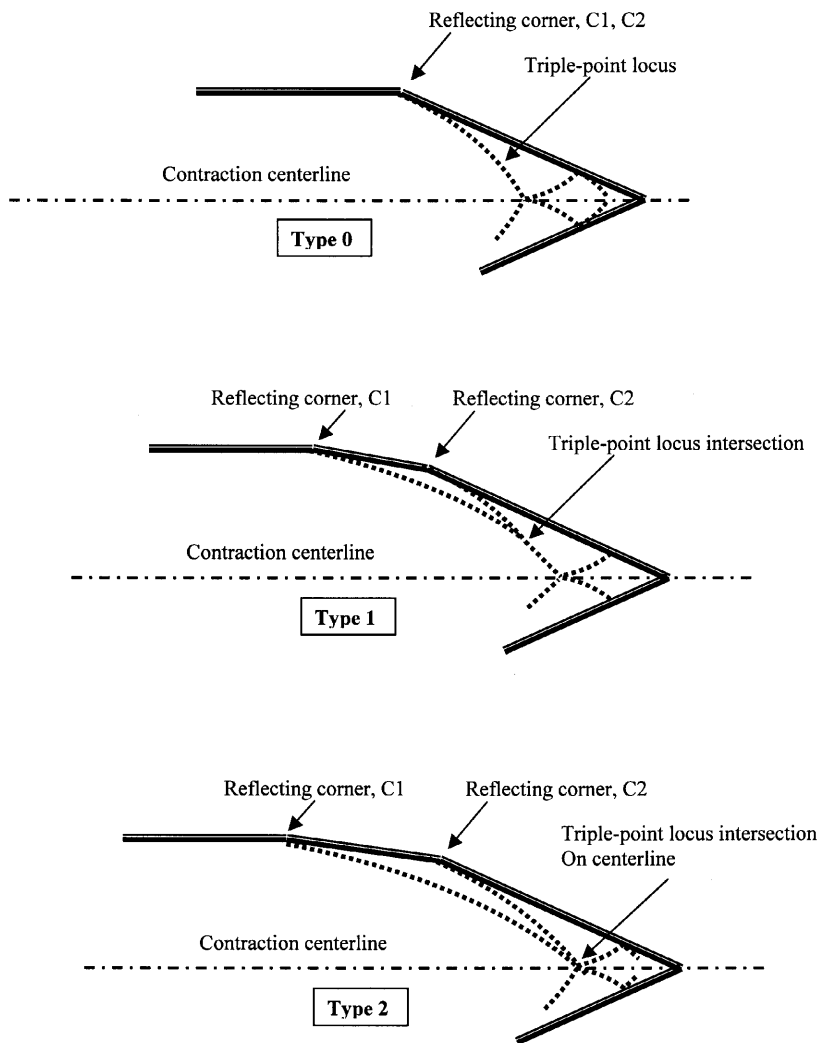


FIGURE 9.18 Cone-to cone (double corner) Mach reflections showing the different possibilities for triple-point intersection.

the Institute of Fluid Science, Tohoku University. The main shock front is clearly visible and the desired features of the flow can be distinguished. The reflected wave for the case of a 10° corner is very weak, but nevertheless, from careful viewing of the original photograph, it can be discerned in the image shown in Fig. 9.20a. A noticeable feature is that the side wall is not clearly

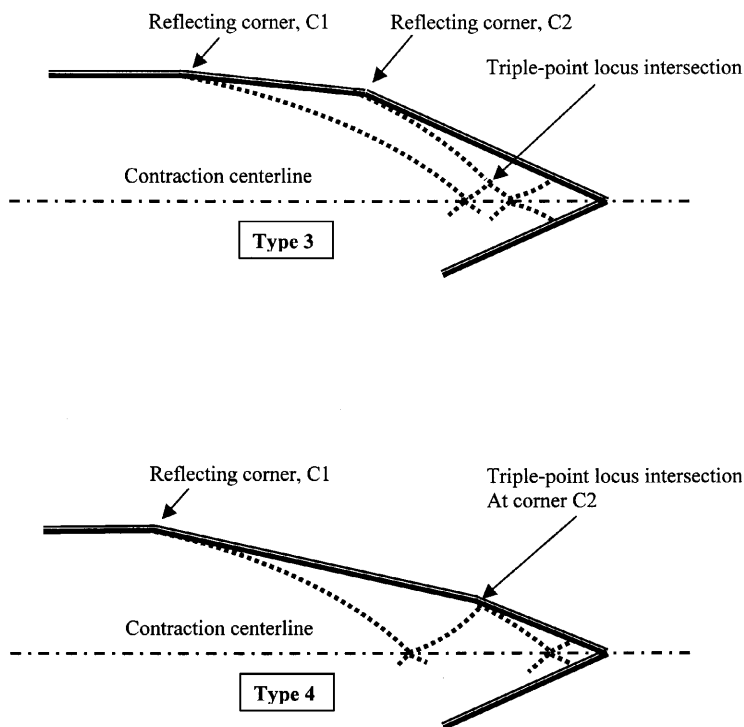


FIGURE 9.18 (continued)

defined. This is most probably because of the total internal reflection within the lens that appears right at the top and bottom surface. At this position, the light beam direction is particularly sensitive to slight internal surface irregularities. The direct ray-shock solution described in Section 9.3 was used for comparison, giving good agreement with experiment (Fig. 9.19). The calculations show that the curvature becomes very marked as the triple point approaches the centerline of the contraction, particularly for large corner angles, as Mach reflection is then maintained to a very high angle to the incident flow by the double cone. For example, if the cone angle is 40° , a Mach stem converging inward at well over 80° is possible near the centerline.

9.6 NUMERICAL EXPERIMENTS (CFD)

Although CFD cannot provide the validation that physical experiments achieve, it can, when used in conjunction with the shock tube results, give

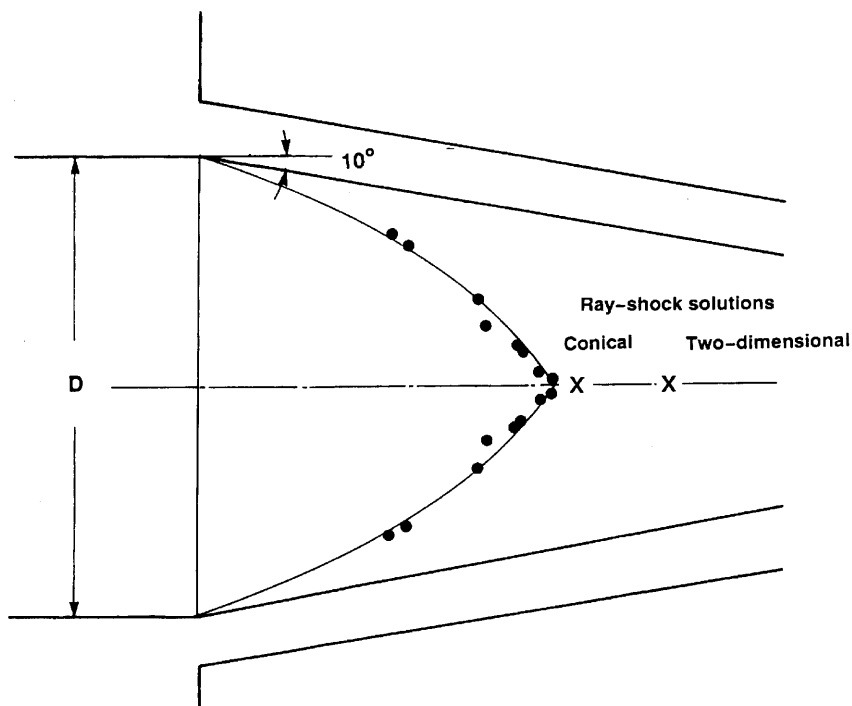
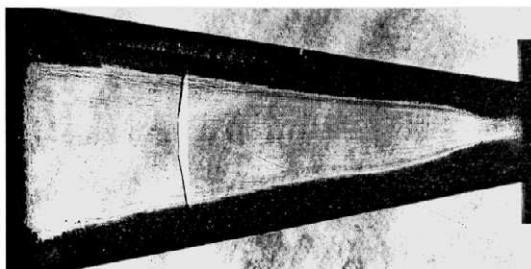


FIGURE 9.19 Internal conical Mach reflections for $M_0 = 1.76$ and $\Delta\theta = 10^\circ$. Experimental results from visualization technique and centerline pressure transducer measurements compared with ray-shock theory.

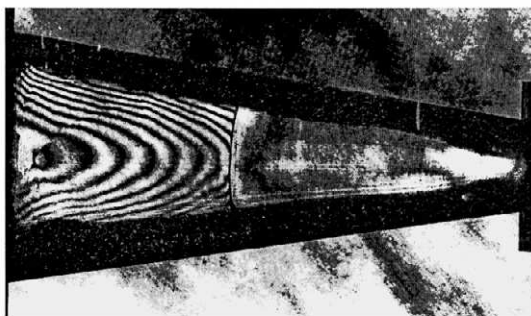
valuable insights into the flow details. Essentially, CFD is an experimental technique itself rather than a theoretical approach, as it relies on interpretation of outputs to help evaluate and support theory.

9.6.1 CFD SCHEME FOR CONICAL MACH REFLECTION

An appropriate CFD code for study of both internal and external cases of Mach reflection is the TVD approach. Such a scheme is described in Babinsky *et al.* (1995). It is a WAF (weighted average flux) scheme (see Toro, 1989) using an exact Riemann solver and a Superbee flux limiter. Using this scheme, Milton and Takayama (1998) examined some conical Mach reflection configurations.



(a) Single pulsed system



(b) Double pulsed system

FIGURE 9.20 Results of internal conical Mach reflection using the aspheric lens system, $M_0 = 1.76$, cone half-apex angle $\Delta\theta = 10^\circ$.

The results were compared with both shock tube experiments and ray-shock theory solutions. The following flows were examined:

- (i) External flows, both simple cone and cylinder-to-cone cases
- (ii) Internal flows, cylinder-to-cone reflections

The reflection angles used for calculation purposes were 10° , 20° , and 30° , while the incident shock wave Mach numbers were a basic case of $M_0 = 2.0$ applied at all reflecting angles, with additional runs at $M_0 = 1.5$ and $M_0 = 2.2$ for the angle of 20° only.

9.6.1.1 External Cases

The CFD results are illustrated here using only density contours. For the simple cones, these are shown for three incident shock wave Mach numbers,

$M_0 = 1.5, 2.0$, and 2.2 at $\theta = 20^\circ$ in Fig. 9.21, and in Fig. 9.22 for three cone angles of $\theta = 10^\circ, 20^\circ$, and 30° with an incident shock wave of $M_0 = 2.0$. All cases except the $M_0 = 2.0, 30^\circ$ case have a Mach stem that curves forward from the wall to the triple point, but this is more marked as the incident shock becomes weaker and the corner angle smaller. Generally, the Mach stem has greater curvature near the triple point and is substantially straight near the wall. For a given cone angle, the stronger Mach number displaces the triple point fractionally further out into the flow field, while strengthening and flattening the reflected shock wave. At $\Delta\theta = 10^\circ$ and $M_0 = 2.0$ (Fig. 9.22), the Mach stem is curved throughout in a typical (NMR) reflection pattern. At this Mach number at the higher angles, such as $\Delta\theta = 30^\circ$, it is shorter and straight with the reflected shock wave and slipstream becoming strongly delineated. In all cases, the pattern does not vary as it progresses downstream. That is, the phenomenon is self-similar.

For cylinder–cone cases, the effect of the entry cylinder ahead of a half-cone angle of 30° is shown in Fig. 9.23 where the shocks of $M_0 = 2.0$ are progressively at different positions. Each position is designated by the dimensionless radius $r = R/R_0$ (the local radius R at the foot of the Mach stem over the initial cylinder radius R_0) with values of $1.8375, 2.675$, and ∞ . As the reflection proceeds, the triple-point position moves closer to the surface of the cylinder as r increases. From $r = 1.8375$ to 2.675 the change is smaller than from $r = 2.675$ to ∞ . The Mach stem is approximately straight and normal to the wall, indicating that the ray direction variation is closely packed near the triple point. Similar results are available for different corner angles and Mach numbers, except that a slight forward curvature of the stem is noted at small values of both.

9.6.1.2 Internal Cases

Figure 9.24 shows the CFD results for a shock wave progressively moving from a cylindrical duct down a 20° conical contraction. The series of six density contours cover the reflection range from near the reflecting corner to the centerline. Near to the corner, the Mach stem is straight and the pattern is indistinguishable from wedge types. However, a progressive increase in Mach stem curvature from straight near the corner to backward leaning toward the triple-point appears as the system approaches the centerline. This is most noticeable in the third and fourth frames. In the fifth, the curvature does not seem to have increased further, which may be due to the Mach stem no longer growing into new ray tubes (see Section 9.7.3). In the sixth, the reflected shock has self-reflected at the centerline and is starting to modify the flow by strengthening the Mach stem in the central region.

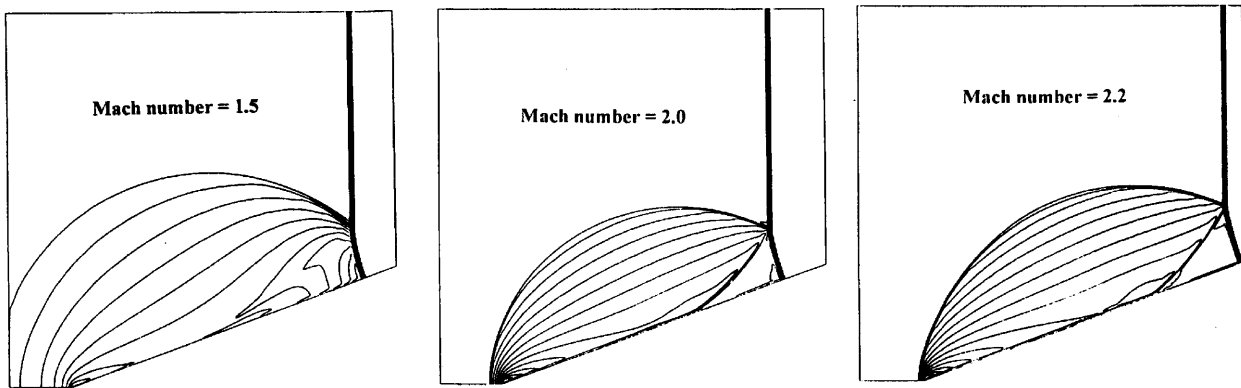


FIGURE 9.21 CFD results for external conical Mach reflection over a 20° simple cone for incident shocks at different Mach numbers.

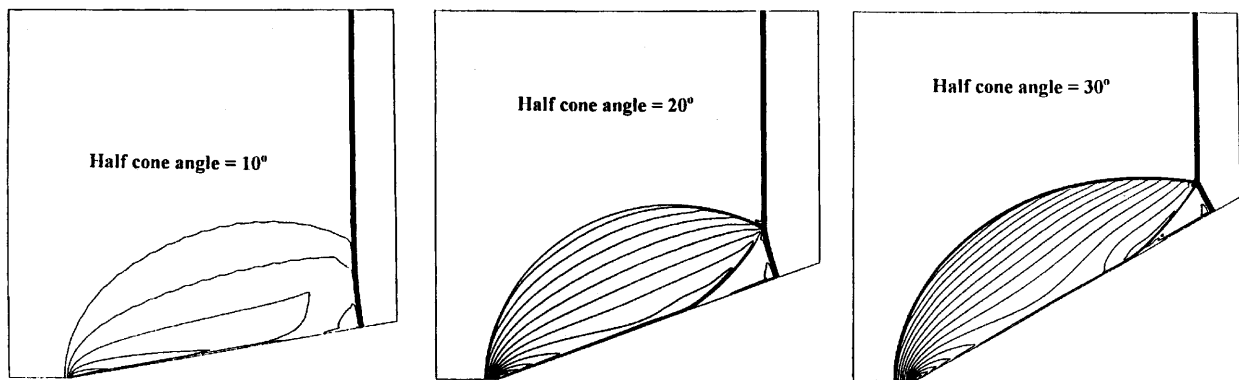


FIGURE 9.22 CFD results for external conical Mach reflection over simple cones at Mach number 2.0 for different cone angles.

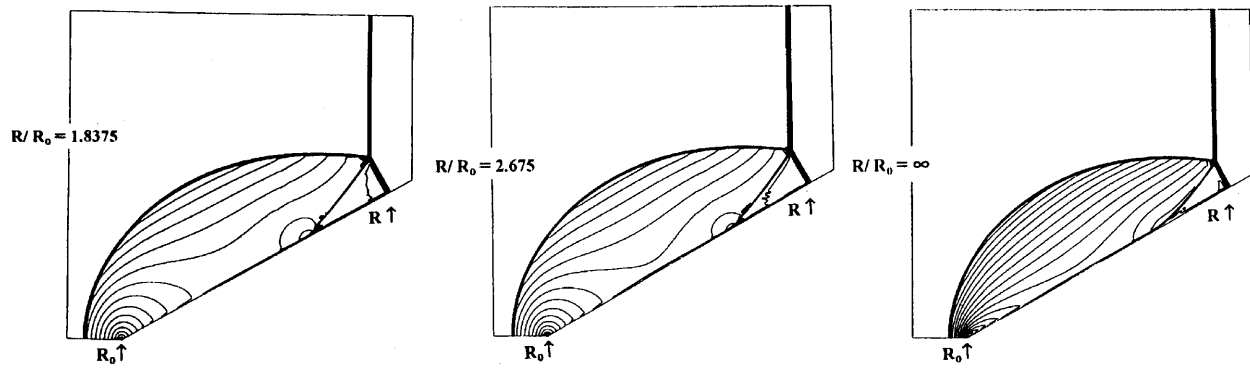


FIGURE 9.23 CFD results for progressive external conical Mach reflection over a cylinder-cone configuration (20° cone) for Mach number 2.0.

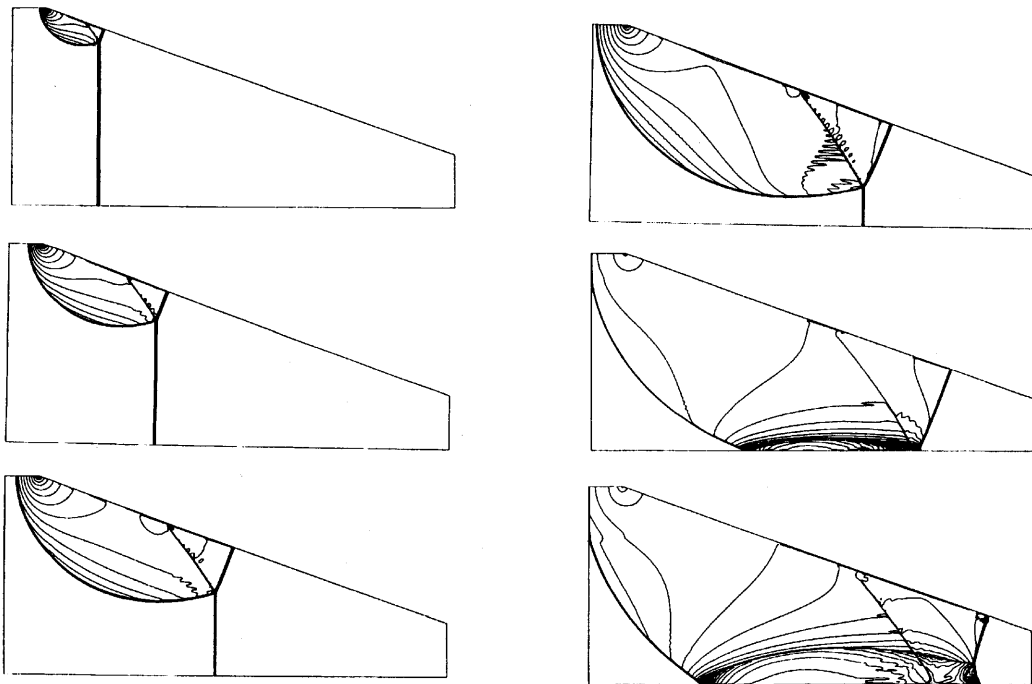


FIGURE 9.24 CFD results for progressive internal conical Mach reflection into a 20° contraction for Mach number 2.0.

As in the external case, the effects of a variation in Mach number and reflection angle are independently illustrated in Figs. 9.25 and 9.26. At a corner of 20° , at the lowest Mach number, $M_0 = 1.5$, the stem is curved very slightly forward to the triple-point and is noticeably shorter than at the higher values of $M_0 = 2.0$ and 2.2 . Its slipstream and reflected shock wave extend farther back into the flow. At the two higher Mach numbers, a slight backward curvature has appeared. In both these latter cases, similar Mach stem shapes exist although, in the $M_0 = 2.2$ case, the backward curvature is very slightly more. For the three different angles at $M_0 = 2.0$, the stem length decreases with increase of corner angle, the backward Mach stem curvature being more noticeable at 30° .

9.6.2 COMPARISON OF THE RAY-SHOCK THEORY CFD RESULTS

For external cases at $M_0 = 2.0$, the triple-point locus angle at different corner angles is compared with both the wedge and conical ray-shock theory calculations in Fig. 9.27. The conical ray-shock theory results compare more closely to the conical CFD solutions at the larger corner angles. At the 10° angle, the CFD results tend toward the wedge values, but this does not indicate a superiority in the wedge ray-shock calculations here. It is more probable that the NMR reflection is very dominant for these conditions (see Section 9.7.1). The curve through the CFD points and the conical ray-shock results are converging at higher corner angles. However, further CFD results for these conditions are required to fully decide whether the curves converge, diverge again, or cross each other.

For cylinder cones, CFD and ray-shock results are shown for the $M_0 = 2.0$, corner angle, and 30° case in Fig. 9.28. The plots show the local triple-point locus angle $\chi - \Delta\theta$ as it varies with the Mach stem position, $r = R/R_0$. From the ray-shock calculations, both the wedge and simple cone values, being self-similar, naturally show no variation and are substantially different from the fully conical solution values. These reduce from the wedge to the simple cone values as the value of r increases from 1 to infinity. The CFD cylinder-cone results show similar trends, reducing as r increases, but are slightly larger than the conical ray-shock values throughout.

For contractions, the conical ray-shock solution described in Section 9.3 is used to compare the shape of the triple-point locus with the CFD results from the corner to its intersection with the centerline. This is shown in Fig. 9.29 for the case where $M_0 = 2.0$, $\Delta\theta = 20^\circ$. The agreement both in shape and location is very good, the CFD showing values only very slightly extended from those of

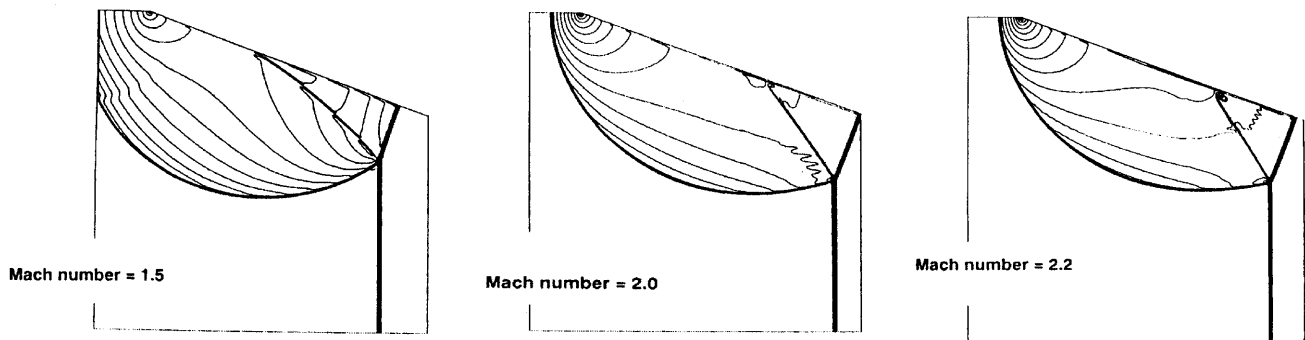


FIGURE 9.25 CFD results for internal conical Mach reflection into a 20° convergence for incident shocks at different Mach numbers.

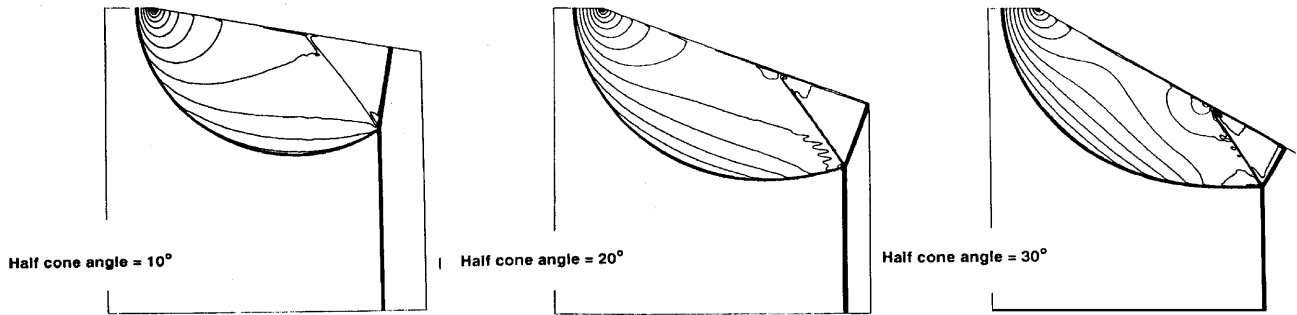


FIGURE 9.26 CFD results for internal conical Mach reflection at Mach number 2.0 for different convergence angles.

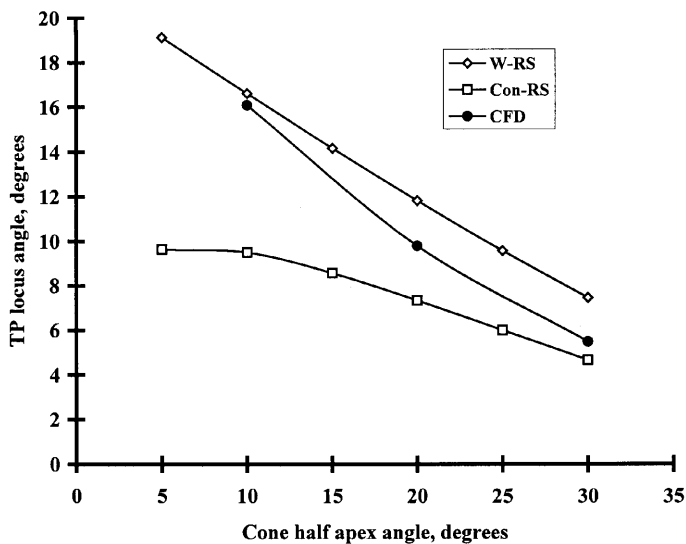


FIGURE 9.27 Comparison of CFD with wedge (W-RS) and conical (Con-RS) ray-shock theory results. $M_0 = 2.0$; TP locus angle is plotted as $\chi - \Delta\theta$.

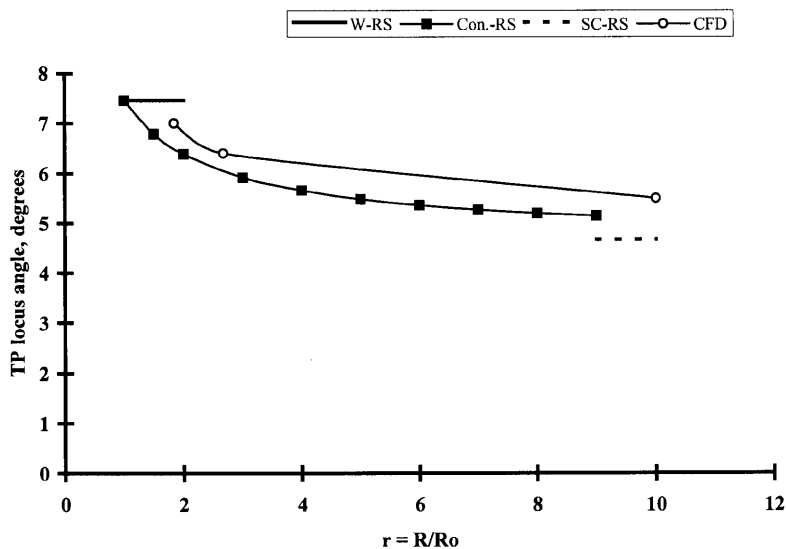


FIGURE 9.28 Comparison of CFD with conical ray-shock (RS) theory using wedge (W-RS), simple cone (SC-RS), cylinder-cone (Con-RS) solutions. $M_0 = 2.0$, $\Delta\theta = 30^\circ$. Note: TP locus angle is $\chi - \Delta\theta$.

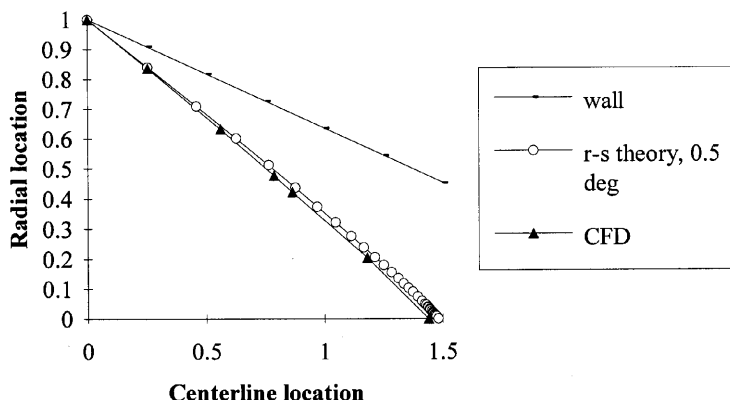


FIGURE 9.29 Comparison of the triple-point locus from CFD and ray-shock theory results for a conical contraction, $M_0 = 2.0$, $\Delta\theta = 20^\circ$.

the theory. Given the approximations in the theory, this is exceptionally good. Here, the theoretical calculations used an incremental value of 0.5° for Mach stem curvature, as this has been shown to designate the convergence of the method.

These comparisons, in both external and internal configurations, demonstrate that the generalized conical ray-shock approach predicts trends very well. Good quantitative values are also obtained, particularly in internal (converging) cases.

9.7 SOME THEORETICAL ASPECTS OF CONICAL MACH REFLECTION

9.7.1 VON NEUMANN MACH REFLECTION EFFECTS IN CONICAL REFLECTIONS

With Mach reflection over wedges, there has been for many years considerable debate about the curvature that occurs in the Mach stem at low corner angles and/or incident shock strengths. A straight Mach stem normal to the wall exists at corners above a value of approximately 10° to 20° , this being less for strong and more for weak shock strengths. Below these values, the Mach stem is curved forward from the wall to the triple point. The former is termed single Mach reflection (SMR), the latter von Neumann Mach reflection (NMR). For details, see Ben Dor (1992). The debate is whether the stem is curved more or

less uniformly right from the wall or from a position nearer to the triple point. If the second, it is presumed that the stem is straight near the wall because of the accumulated disturbances propagated at about the angle given by the ray-shock theory (Whitham's shock-shock) with the curvature beyond that due to the initial sound wave from the corner. The reflected shock is then partially or fully replaced by a series of isentropic waves distributed across the curved region. It would be expected that some NMR reflection also exists in conical cases, as the theory assumes that there is no difference right at the triple-point, but how the Mach stem is affected between the triple-point and the wall needs to be examined.

If the experimental and CFD results are viewed, the following can be seen. If the simple cone, the external cylinder-cone and the internal conical contraction results for any fixed wall angle (say 20°) and Mach number (say $M_0 = 2.0$) are compared (see Figs. 9.22, 9.23, 9.26), it is evident that any forward curvature in the Mach stem toward the triple point is more pronounced in the first, least pronounced in the last. In the simple external cone case, the accumulated disturbances are immediately weakened by the outward radial expansion because the conical value of χ applies right from the corner. In the external cylinder-cone case, χ initially has wedge values and a weakening to the cone solution takes place as the pattern grows. In the converging case, accumulated signals strengthen the shock. The likely effect is then that the curved stem NMR range for M_0 , $\Delta\theta$ will be extended to higher Mach numbers and corner angles for external reflection over cones, but reduced to lower Mach numbers and corner angles in the internal cases when compared to wedge reflection. All the results found here are consistent with this explanation. Note that Yang *et al.* (1995), using a large number of simple cones, also found experimentally that the NMR reflection range was extended.

9.7.2 SELF-SIMILAR AND NON-SELF-SIMILAR AXISYMMETRIC MACH REFLECTION

Consistent experimental and calculated features of conical Mach reflection show that in external reflection over simple upstream-facing cones the triple-point locus is straight, whereas within conical contractions it is curved. That is, the external cases are self-similar while the internal ones are not. The ray-shock theory can be used to explain these differences, as discussed by Han *et al.* (1992). For clarity, only parallel duct-to-cone cases are considered here, although the arguments apply generally. Also, the moderately small effect of including Mach stem curvature is neglected.

Consider the external case first. For a simple cone with an impinging shock wave normal to its axis, $\theta_0 = 0$, $\Delta\theta = \theta$, R_0 is zero and $r \rightarrow \infty$. Hence Eq. (9.9) reduces to Eq. (9.17), and it can be seen that A/A_0 is independent of r . Also, from Eq. (9.11), $d\chi/dr = 0$ and χ is constant everywhere. This is self-similarity. For $\chi = \text{constant}$, the shock contiguity condition is given by Eq. (9.18).

$$\frac{A}{A_0} = \frac{\sin(\chi - \theta)[2 \sin \chi - \sin(\chi - \Delta\theta) \cos \theta]}{\sin^2 \chi} \quad (9.17)$$

$$\frac{M}{M_0} = \frac{\cos \chi}{\cos(\chi - \Delta\theta)} \quad (9.18)$$

If the equations for either internal reflection in a contraction or external reflection starting away from the centerline are considered, $r \neq \infty$ and Eqs. (9.9) and (9.11) apply in full. Then, A/A_0 depends on r and $d\chi/dr$ must always be a function of r . Hence, χ cannot be constant and M/M_0 also varies with r . The flow is therefore never self-similar. The triple-point trajectory curves inward toward the centerline. In the converging case, this is at first gradual but the rate increases as the axis is approached. In the external case, the rate of triple-point locus curvature decreases as the pattern grows, approaching the self-similar simple cone solution as the radius to the triple-point becomes very large relative to that of the initial cylinder.

Self-similarity is therefore fundamentally a function of the initial radius R_0 . In any configuration where the initial reflection point is at zero radius, the value of R_0 is zero and hence r is always infinity, even when the triple point has moved away but is still very close to the reflecting corner. These are all self-similar reflection patterns. When $R_0 \neq 0$, r is finite, $d\chi/dr$ cannot be equal to zero, and the triple-point locus must curve. That is, only when the reflection point is on the centerline is self-similarity possible in axisymmetry.

9.7.3 TRANSITION FROM REGULAR TO MACH REFLECTION IN CONICAL PROBLEMS

The transition from regular to Mach reflection in wedge configurations has long been a topic of considerable interest. The work reported has included precise measurements of the transition angles, discussion of the differences with steady flow, boundary layer interactions, and hysteresis. The reader is referred to Ben-Dor (1992) for discussion of this problem. The important question here is not the details of the transition process, but whether there are likely to be any differences in conical cases when compared with wedges.

As discussed in Section 9.3, if a circular cross-section of a ray tube is of infinitesimally small radial width compared to the radius to the triple point, the local flow “sees” the reflection in exactly the same way as in a wedge. Only when the value of $R_0 \rightarrow 0$ are differences likely to appear. As this is an extremely small region close to the apex of a simple cone, it is essentially impossible to determine any difference experimentally. As the regular reflection moves along the surface away from the reflecting corner, no difference should occur at the reflected shock intersection with the main shock front while regular reflection is maintained. Therefore, transition from regular to Mach reflection should have identical values for cones or wedges. The experiments of Takayama and Sekiguchi (1976) show that, within the limits of experimental error, there is in fact no difference. More recently, Yang *et al.* (1995) redetermined these transition angles. They found that, in conical cases, they were close to but slightly smaller than the wedge values. This could be associated with the initial reflection at the apex and may not exist for reflections starting at finite radii. For all practical purposes, it can be assumed that the transition angles on the conical surface are identical to those for wedges.

However, during a Mach reflection, when the triple point has moved away from the surface, there are some interesting possibilities. Take, for example, a reflection pattern from a circular duct to a converging cone. As the reflection progresses, the rays after the reflection become steeper and the change from the upstream ray direction can substantially exceed the transition angle to regular reflection. What happens when the transition angle is reached? To examine this, designate the downstream ray direction as θ_T . Obviously, there is still a Mach stem, as this has already formed. However, in the subsequent reflection, does the intersection of the incident and reflected shocks now follow the ray with direction θ_T , which locally would be a type of regular reflection, or does it continue to move away from it, which would be a Mach reflection? Such differences would be difficult to observe in practice. However, if the former, it may explain why the triple-point curvature late in the process in the converging cone is slightly less than predicted by the ray-shock theory. In the external cases, the rays away from the surface are at a lesser angle than those on the surface, and no such similar problem would be expected. That is, if regular reflection exists on the surface of a cone, it should not move off the surface to experience a smaller angle change giving an onset of Mach reflection. However, if some slight surface irregularities exist, a very small Mach stem may form close to the surface at some local position. At the triple point, the ray angle is then reduced, and it is possible that the Mach reflection configuration may be sustained very close to the wall. This may explain the slight differences found between conical and wedge cases by Yang *et al.* (1995).

9.8 SOME APPLICATIONS OF AXISYMMETRIC CALCULATIONS

9.8.1 MACH REFLECTION OVER A SIMPLE CONE

In the general case, the initial value of R_0 is nonzero and the integration procedure described in Section 9.3.4 must be followed. All cases may be simplified by assuming that the Mach stem is straight and normal to the wall across its full length throughout the motion and the error introduced to the positioning of the triple-point locus is fairly small. For the very common application of external reflection over a simple cone, the calculation can be further reduced as the situation is self-similar. A very easy solution is possible using Eqs. (9.17), (9.18), and (9.6). The question is, what accuracy can be achieved? With this approach, an example has been considered that is compared with the example previously calculated by Whitham (1959) for a deflection $\Delta\theta$ of 28.8° and a strong incident shock wave. Results are given in Table 9.3.

There is a noticeable variation in the reduced cone solution both in the value of χ and the M/M_0 ratio from the values for the wedge, but much less from the accurate solution for the cone. That is, in spite of the totally straight stem assumption, this reduced method is reasonably accurate while being very simple to use.

9.8.2 AXISYMMETRIC SHOCK WAVE FOCUSING

A properly shaped contracting duct can provide a progressive series of Mach reflections that effectively concentrate the shock wave, giving very high pressures at the focus. This can have either destructive potential or many useful applications such as in metal forming, powder compaction, and biomedical work. A particular case of note in the last is the noninvasive

TABLE 9.3 Reduced Solution for a Simple Cone

	Reduced method (cone)	Whitham's solution (cone)	Wedge solution
χ°	35.5	35.8	39.7
M/M_0 (at TP)	1.220	1.200	1.280
M/M_0 (average)	1.220	1.208	1.280
M/M_0 (wall)	1.220	1.216	1.280

crushing and removal of kidney stones (i.e., shock wave lithotripsy; see, for example, Kandel, 1991). Whether the result is destructive or constructive, an axisymmetric convergence provides much greater reinforcement and pressure rise than does the equivalent plane case because of the greater area ratio. As previously discussed, the reinforcement in excess of wedge-type focusing during the repeated Mach reflection processes is due both to higher average Mach stem strengths for a given angular deflection and the greater reflection repetitions due to the inward curvature of the triple-point locus.

In wedge-type flows, it has been shown that a progressively curved surface increases the transmitted shock strength (Bird, 1959). This is because the Mach stem length is increased. A similar strengthening could be expected in conical flows. The best focusing, either wedge-type or axisymmetric, is achieved from a curved surface where the reflections may be regarded as taking place from a series of successive corners, each approaching glancing incidence, with the triple points converging to a single point (Milton *et al.*, 1988). Whereas there is sufficient information to design such a wedge-type focusing contraction (a logarithmic spiral), a good knowledge of conical Mach reflection is necessary for the equivalent axisymmetric profile.

Glancing incidence conically converging reflection processes have not been studied. However, if the ray-shock theory can be assumed to have reasonable validity for these cases, it can be applied. Reflections can be calculated only for finite angular deflections $\Delta\theta$, but these can be extrapolated to glancing incidence values. In the limit toward glancing incidence, they provide a basis for designing a reinforcing contraction for a shock wave as it enters a progressively more steeply curved axisymmetric contraction. A suggested shape has been given by Milton and Archer (1969). Note that, once designed, the focusing can be checked by a CFD approach, but the inverse, designing directly by use of CFD, is impractical. Experiments have been carried out on the axisymmetric focusing profile (Milton *et al.*, 1988) that indicate that the focusing obtained this way is very good.

9.9 FINAL DISCUSSION

Conical reflection of shock waves is either the same or very similar to plane wedge reflection under some circumstances. This is most likely to be in the details of the flow in the immediate vicinity of the point where the reflected shock wave intersects the incident wave (the reflection point in regular reflection, the triple point in Mach reflection). Hence, for regular reflection and the transition from regular to Mach reflection, the similarities observed in conical flows are consistent with those for wedge flows. For Mach reflection, along the triple-point locus the reflection when viewed microscopically at the

triple-point should again be the same as in the wedge case. However, the total reflection pattern between the triple point and the reflecting wall can be quite different. This is due to the spread of the disturbance over the either larger or smaller Mach stem front areas (compared with the wedge case) in external or internal conical flows, respectively. This causes significant differences in external and internal conical patterns. In the general case where it commences at a finite radius, the former has a triple-point locus that curves toward the surface with the curvature becoming more gradual as the pattern enlarges. With the latter, the opposite occurs, the triple-point locus curving toward the centerline of the cone, curvature becoming more pronounced as the structure grows. Also, conical Mach reflections are not inherently self-similar. Self-similarity only occurs when the reflecting corner is on the centerline (radius of zero). The particular case of the upstream-facing cone is one of the most common both in practice and experiment, and it is self-similar. However, unlike wedge reflection patterns, self-similarity is the exception rather than the rule. In all conical cases, self-similar or not, the Mach stem is curved. This is quite independent of any weak shock wave (NMR) effects, which can modify the curvature.

To examine conical Mach reflection theoretically, the ray-shock theory is used. Various formulations and solution techniques are possible, either indirect (the conical surface angle not being explicit) or direct (from the known surface angle). Some formulations are difficult to use for other than the strong ($M > 3$ approximately) incident shock wave case where the area/Mach number function used in the theory can be simplified. Other methods are more tractable. The formulation used here is a generalized version that is direct, tractable, and fast to compute. It is based on the *a priori* assumption that the Mach stem is normal to the surface ray. This is not limiting as it first appears because continuous reevaluation of the “reflecting surface” is undertaken, allowing curvature to develop in the Mach stem. All investigations to date have shown that this approach is very effective in predicting both the triple-point locus and the shape of the Mach stem.

A number of reflecting configurations have been studied and are discussed here. They consist of both wall configurations used in experiments and some unusual cases, such as cone-to-cone reflections, which are of importance in developing axisymmetric focusing profiles. Self-reflection of shocks at the centerline of a convergence has been included. Other cases can be easily evaluated with this method. The ease and rapidity of the ray-shock procedure is a major asset in all conical cases.

Extensive comparisons with shock tube and CFD results show that this theory correctly predicts the major trends, although some inaccuracies exist. Non-self-similar external cases (the cylinder-cones) become self-similar patterns as predicted by the theory when the radius to the triple-point is

very much greater than that of the reflecting corner. In these cases, the initial triple-point locus angle χ changes from an initial value equal to that of a wedge of the same angle at the onset of reflection to the fully conical self-similar value after the reflection has fully developed. Specific values determined by the theory for the triple-point locus location show reasonable accuracy, but some deviation from measurement as in wedge reflection exists, particularly at small corner angles. Values for internal cases agree better than those for external cases. This is most likely to be due to the disturbances from the wall that move across the shock (i.e., the shock-shock) being reinforced in the internal case as the post-shock rays converge, but weakened by ray divergence in the external cases. The likely effect when compared to wedge cases is that a weak shock, NMR reflection pattern prevails over the SMR type pattern to higher Mach numbers and/or corner angles for external conical Mach reflections when compared to wedges of the same wall angle. For internal cases, the reverse is the case.

An important outcome, internal axisymmetric focusing of shock waves, can now be fully investigated. Investigations to date show that the focusing profiles designed using the axisymmetric version of the ray-shock theory provide an excellent starting point for this process.

REFERENCES

- Babinsky, H., Saito, T., and Takayama, K. (1995) Computation of a Shock Wave Through an Expanding Tube with Different TVD Schemes, *Proc. Jap. Shock Wave Symp.*, Yokohama, 337–340.
- Belokon, V. A., Petrukhnin, A. I., and Proskuryakov, V. A. (1965) Entrance of a Strong Shock Wave into a Wedge-like Cavity, *Soviet Physics, J. Expt. and Theor. Phys.* 21: 33–40.
- Ben-Dor, G. (1992) *Phenomena of Shock Reflections*, Springer-Verlag, Heidelberg, NY.
- Bird, G. A. (1959) The Effect of Wall Shape on the Degree of Reinforcement of a Shock Wave Moving into a Converging Channel, *J. Fluid Mech.* 5: 60–66.
- Bryson, A. E., and Gross, R. W. F. (1961) Diffraction of Strong Shocks by Cones, Cylinders and Spheres, *J. Fluid Mech.* 10: 1–16.
- Busemann, A. (1929) Drucke auf kegelförmige Spitzen bei Bewegung mit Überschallgeschwindigkeit, *A.a.M.M.* 9: 496.
- Chester, W. (1954) The Quasi-Cylindrical Shock Tube, *Phil. Mag.* 45: 1293–1301.
- Chisnell, R. F. (1957) The Motion of a Shock Wave in a Channel, with Applications to Cylindrical and Spherical Waves, *J. Fluid Mech.* 2: 286–298.
- Duong, D. Q., and Milton, B. E. (1985) The Mach Reflection of Shock Waves in Converging Cylindrical Channels, *Expts. Fluids* 3: 161–168.
- Han, Z. Y., and Yin, X. (1993) *Shock Dynamics*, Kluwer Academic Publishers Group, Netherlands.
- Han, Z. Y., Milton, B. E., and Takayama, K. (1992) The Mach Reflection Triple-point Locus for Internal and External Conical Diffraction of a Moving Shock Wave, *Shock Waves* 2: 5–12.
- Itoh, S., Okazaki, N., and Itaya, M. (1981) On the Transition between Regular and Mach Reflection in Truly Non-stationary Flows, *J. Fluid Mech.* 108: 384–400.

- Kandel, L. B. (1991) Research Issues of Concern: Scientific and Medical, in *Shock Waves*, ed. K. Takayama, Springer-Verlag, Berlin, Proc. 18th Int. Symp. on Shock Waves, Sendai, Japan, 17–18.
- Maccoll, J. W. (1937) The Conical Shock Wave Formed by a Cone Moving at High Speed, *Proc. Royal Soc. A* **159**: 459.
- Milton, B. E. (1975) Mach Reflection using Ray-shock Theory, *AIAA J.* **13**: 1531–1533.
- Milton, B. E., and Archer, R. D. (1969) Generation of Implosions by Area Change in a Shock Tube, *AIAA J.* **4**: 779–780.
- Milton, B. E., and Archer, R. D. (1996) Conical Mach Reflection of Moving Shock Waves, Part 1: Analytical Considerations, *Shock Waves* **6**: 29–39.
- Milton, B. E., and Takayama, K. (1998) Conical Mach Reflection of Moving Shock Waves, Part 2: Physical and CFD Experimentation, *Shock Waves* **8**: 93–103.
- Milton, B. E., Duong, D. Q., and Takayama, K. (1986) Multiple Internal Conical Mach Reflections. In *Recent Developments in Shock Tube Research*, ed. D. Bershader and W. Griffiths, Stanford Univ. Press, Proc. 15th Int. Symp. on Shock Waves and Shock Tubes, 113–119.
- Milton, B. E., Takayama, K., and Archer, R. D. (1988) An Evaluation of Two-Dimensional and Axisymmetric Focusing of a Plane Shock Wave, In *Shock Tubes and Waves*, ed. H. Gronig, VCH Verlagsgesellschaft, Weinheim, Germany, Proc. 16th Int. Symp. on Shock Tubes and Waves, 567–573.
- Milton, B. E., Takayama, K., and Onodera, O. (1997) Visualization of Shock Wave Convergence in Internal Duct Flows, *J. Flow Vis. Image Processing* **4** 81–93.
- Russell, D. A. (1967) Shock-wave Strengthening by Area Convergence, *J. Fluid Mech.* **27**: 305–314.
- Setchell, R. E., Storm, E., and Sturtevant, B. (1972) An Investigation of Shock Strengthening in a Conical Convergent Channel, *J. Fluid Mech.* **56**: 505–522.
- Shapiro, A. H. (1954) *The Dynamics and Thermodynamics of Compressible Fluid Flow*, Vol. II, Chapter 17, The Ronald Press Company.
- Takayama, K., and Onodera, O. (1983) Shock Wave Propagation Past Circular Cross-sectional 90° Bends, *Shock Tubes and Waves*, ed Archer and Milton, Sydney Shock Tube Publishers, UNSW, Kensington, Australia, Proc. 14th Int. Symp. on Shock Tubes and Waves, 205–212.
- Takayama, K., and Sekiguchi, H. (1976) Shock Wave Reflection by Cones, Rept. Inst. High Speed Mech., Tohoku Univ., Japan.
- Taylor, G. I., and Maccoll, J. W. (1933) The Air Pressure on a Cone Moving at High Speed, *Proc. Royal Soc. (London)* **A 139**: 278.
- Toro, E. F. (1989) A Weighted Average Flux Method for Hyperbolic Conservation Laws, *Proc. Royal Soc. (London)* **A 423**: 401–418.
- Whitham, G. B. (1957) A New Approach to Problems of Shock Dynamics, Part 1: Two Dimensional Problems, *J. Fluid Mech* **2**: 145–171.
- Whitham, G. B. (1958) On the Propagation of Shock Waves through Regions of Non-uniform Area or Flow, *J. Fluid Mech.* **4**: 337–360.
- Whitham, G. B. (1959) A New Approach to Problems of Shock Dynamics, Part 2: Three Dimensional Problems, *J. Fluid Mech.* **5**: 369–386.
- Yang, J., Suzuki, M., and Takayama, K. (1995) An Investigation of Shock Wave Reflection over Cones, Proc. Jap. Shock Wave Symp., Yokohama, 625–628.
- Yousaf, M. (1974) The Effect of Overtaking Disturbances on the Motion of Converging Shock Waves, *J. Fluid Mech.* **66**: 577–591.

Shock Waves in Channels

WERNER HEILIG* AND OZER IGRA†

**Fraunhofer-Institut für Kurzzeiddynamik, Forschung–Ernst–Mach–Institut, Eckerstrasse 4, D-79104 Freiburg, Germany*

†*Pearlstone Center for Aeronautical Engineering Studies, Department of Mechanical Engineering, Ben-Gurion University of the Negev, Beer Sheva, 84015, Israel*

-
- 10.1 Introduction
 - 10.2 Scenarios of Shock Wave Propagation in Channels
 - 10.3 Phenomenology of Shock Wave Propagation in Channels
 - 10.3.1 Brief Description of the Conventional Shock Tube
 - 10.3.2 Visualization of Shock Wave Propagation in Various Channel Configurations
 - 10.3.3 Comments on the Usefulness of Flow Visualization and Its Evaluation
 - 10.4 Approximate Analytical Methods
 - 10.4.1 The Unsteady Quasi-One-Dimensional Flow
 - 10.4.2 Rudinger's Method
 - 10.4.3 The Chester–Chisnell–Whitham Channel Formula
 - 10.4.4 Whitham's Theory of Shock Dynamics
 - 10.4.5 Analytical Treatment of Shock Propagation through a Class of Bifurcated Ducts using Whitham's Theory
 - 10.5 Numerical Methods
 - 10.5.1 Example Calculations using Wave Propagation Codes
 - 10.5.2 The GRP (General Riemann Problem) Code
 - 10.5.3 Solving a Quasi-One-Dimensional Flow using the Random Choice Method (RCM)
 - 10.6 Data Bases
 - 10.7 Final Remarks
 - References

10.1 INTRODUCTION

Shock waves are a widespread phenomenon in the field of continuum mechanics; their frequent occurrence is based on the fact that matter is more or less compressible. Large disturbances in a compressible medium propagate supersonically as abrupt changes in the state of the medium. Shock waves surround humans' everyday life. In nature they are generated by lightning, earthquakes, volcanic eruptions, and meteorite impact. Even the Earth, shielded by its own magnetic field, pushes a shock wave to a distance of about 20 Earth radii as a head wave in the solar wind. In several ways shocks come into existence by artificial generation, such as with nuclear or chemical explosions, with the sonic boom of supersonic aircraft and any supersonic flying projectile, by a bullet pushing the air in the barrel of a rifle, as bow waves around an obstacle in a supersonic wind tunnel, or as shock waves around a reentry vehicle. These shock waves are either steady waves, that is, attached at the body, or unsteady ones, which change their place with passing time. All types of the mentioned shock waves can have destructive effects and steps must be undertaken to minimize them. An excellent survey of shock wave phenomena is given by I. I. Glass (1991). From the theoretical point of view shock waves are a good example of a nonlinear wave propagation.

The present chapter deals with unsteady shock waves propagating inside channels. As will be shown, the channel geometry has a pronounced effect on the transmitted shock wave. Unsteady shock waves arise according to the classical definition of shock wave production: "A shock wave is generated when energy is suddenly released or deposited in a material (gas, liquid, solid) thereby causing an explosion" (Glass, 1974; Glass and Sislian, 1994). In the case of a free air explosion, the expanding sphere consisting of hot gases and detonation products under high pressure drives a shock wave into the surrounding material. Propagating, it engulfs a continually increasing volume, thus getting weaker and weaker, and finally decays into a sound wave. In the following discussions—if not otherwise stated—the medium through which waves propagate is air. It will be considered as an ideal gas.

10.2 SCENARIOS OF SHOCK WAVE PROPAGATION IN CHANNELS

Knowledge of shock wave propagation in channels of arbitrary geometry is important since such phenomena appear in many engineering applications: among others, in mines when dangerous shocks, caused by exploding coal dust, propagate along the mine shafts causing irreparable damage, or in long

pipes transmitting natural gas (or explosive gases) in which accidental explosions occur. It is also found in the exhaust pipes of multicylindrical reciprocating engines and in channels leading to underground shelters made for protecting either humans or facilities from explosion generated by shock or blast waves. Ducts leading to underground shelters must be especially designed in order to ensure decaying of the transmitted shock/blast waves before entering the protected zone. Several countries undertook considerable effort in providing safe underground shelters. Figure 10.1 provides an imaginary illustration of such a construction; it involves channels, expansion chambers, and blind tunnels in order to reduce the strength of transmitted shocks. The interaction of shock/blast waves with structures above ground level is a separate issue.

In most of the cases mentioned, the main demands are to reduce the strength of the propagating shock and to reduce the fast pressure–time rise across the shock front in order to minimize its damaging effects. Efficient methods for reaching this goal are ensuring rough duct walls or, even better, introducing baffles inside the duct that cause energy and momentum dissipation from the flow. Other used techniques are enlarging the duct's cross-

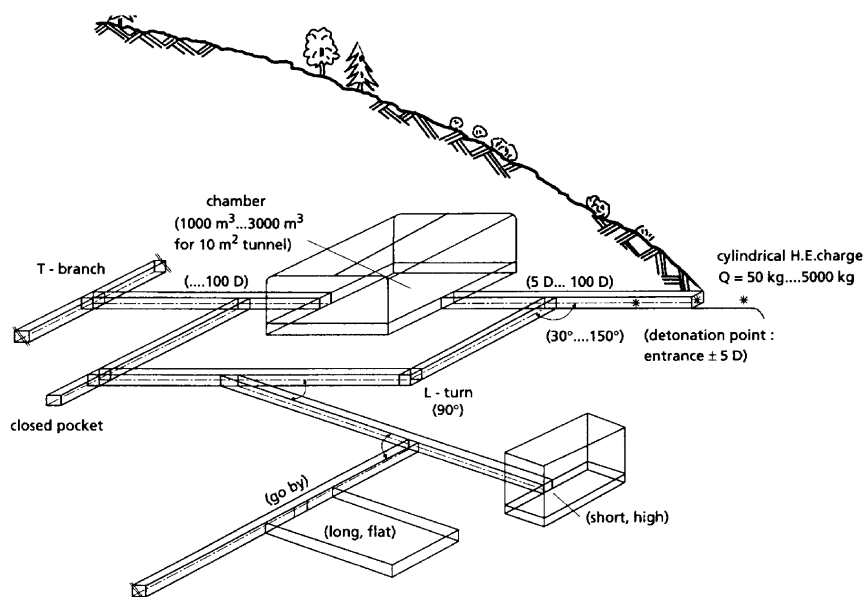


FIGURE 10.1 Sketch of an underground channel system for storage of various goods in a shelter. The effect expected from such installations (duct, expansion chamber, blind tunnel) is to reduce the strength of a shock wave either entering the system from above ground or leaving it in the case of an interior explosion.

section by inserting expansion chambers, or introducing branches and deflections into the duct system.

In contrast, for some applications intensification of the transmitted shock wave is of interest: for example, in connection with compaction processes, such as the production of diamonds starting from graphite, or in the general field of shock wave focusing. It was also thought that nuclear fusion could be started when working with very strong shock waves. Here the channel's contraction is an effective method for obtaining a significant shock amplification. Figures 10.2a and 10.2b provide examples of such a case (Milton, 1990; Milton and Archer, 1971; Inoue *et al.*, 1993).

10.3 PHENOMENOLOGY OF SHOCK WAVE PROPAGATION IN CHANNELS

Experimental work was conducted in tunnels and corridors of natural provenance and original size (e.g., underground tunnels and/or railway tunnels) in Sweden, Norway, France, Switzerland, in the United States called "Magdalena tests," and in Germany (see Section 10.6). Such tests include natural parameters such as the air humidity, the condition of the tunnel's walls (roughness), variations in the tunnel cross-section, and the influence of loose stones, particles, and dust with grains of varying sizes. The expenditures for preparation and instrumentation of such tests are enormous. Normally only pressure measurements, using pressure gauges, can be performed in such large-scale experiments. The incoming shock is driven by an explosion and its strength is deduced from pressure–time records. Generally speaking, such tests are not repeatable and the obtained results are closely related to the specific tunnel system because the influences of the specific physical parameters are appreciable.

Experiments in medium scales (in the range of meters) are mostly performed on test sites. Propulsion of the incident shock is made with the so-called membrane operation of a shock tube, but it can be driven by explosives as well. Such experiments allow a more precise choice of boundary conditions (i.e., angles of channel bifurcations, controlled roughness of the inner walls).

Laboratory experiments using a shock tube provide the highest precision. Though the sizes of the tested models are rather small, and only 2D models can be used, the optical methods (shadow-method, shadow-schlieren method, interferometry, Reichenbach, 1992; and holographic methods, Takayama, 1987) yield an abundance of accurate information regarding the flow evaluation and an insight into the investigated processes. In comparison with the

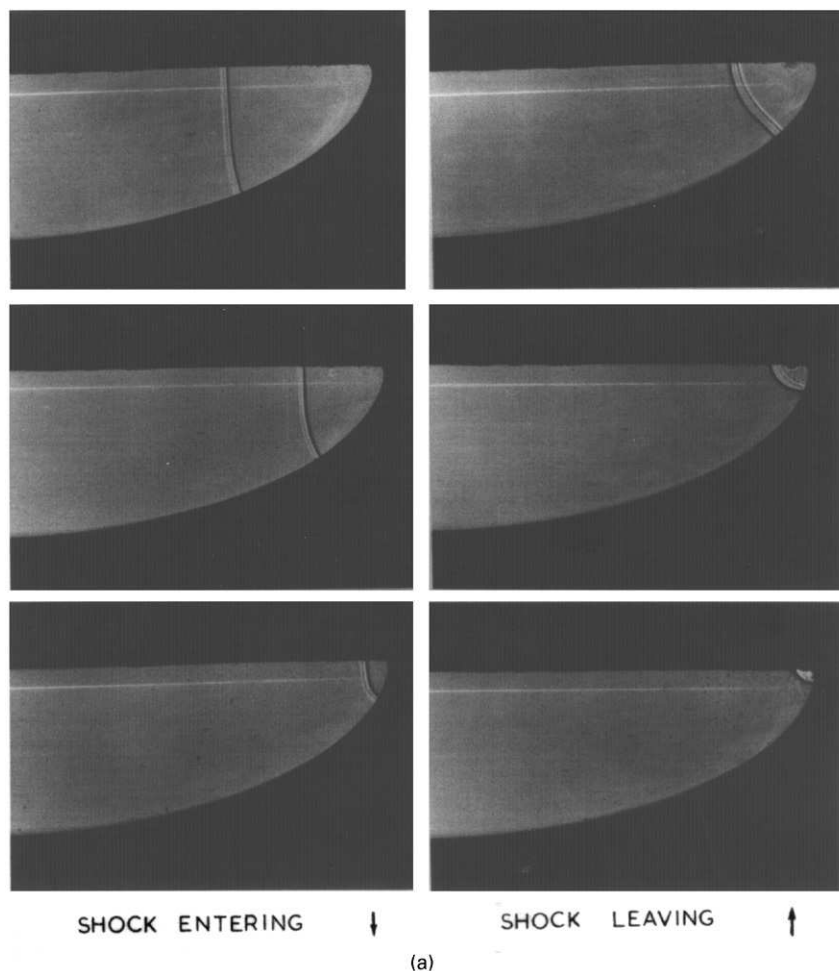


FIGURE 10.2 (a) Shock wave passage through a converging channel (shadowgraphs in time sequence) whereby the shock wave is strengthened. By forming the bottom wall as a logarithmic spiral, the rise of the reflected shock is suppressed, thus optimizing the strengthening effect.

mentioned methods, a shock tube experiment can be run under a variety of well-defined conditions. The optical analogy of the shock tube's flow visualization (i.e., interferograms) can be reproduced as outputs of numerical simulations using appropriate computer codes. Shock tube experiments and numerical simulations are two independent sources for gathering useful data. The combination of these two sources leads to new insights in the study of shock wave propagation in channels.

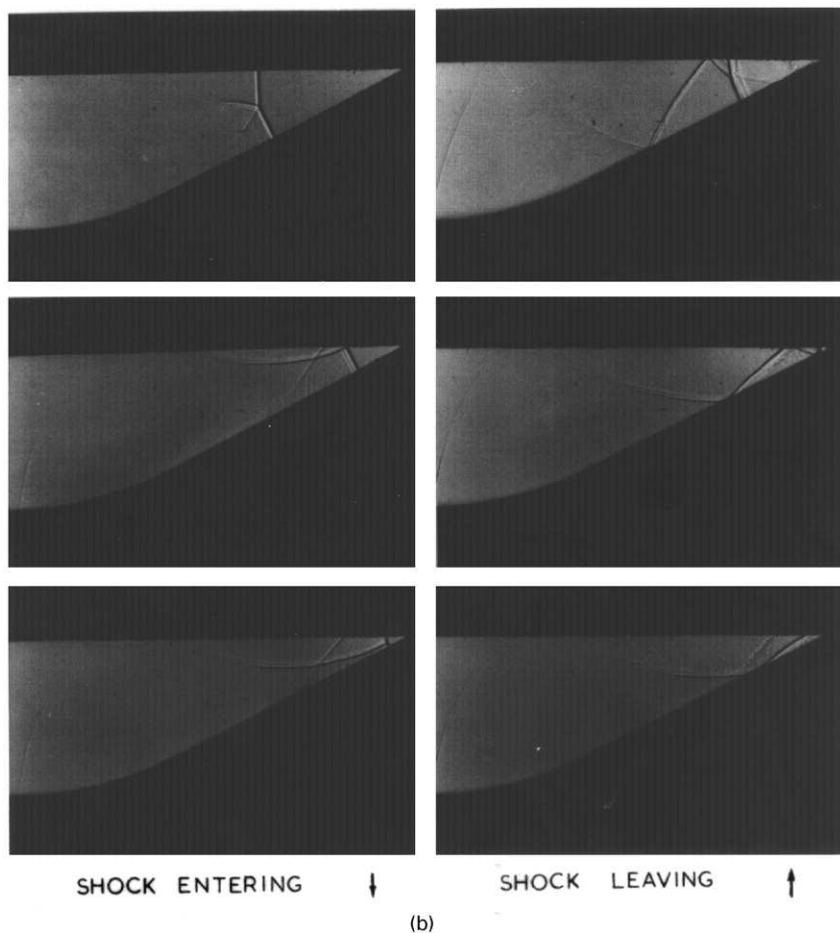


FIGURE 10.2 (b) Shock wave passage through a converging channel (shadowgraphs in time sequence) whereby the transmitted shock wave is strengthened. Unlike in (a), the lower boundary consists of a rounded inlet joined by a plane wall. Therefore, no “loss-free” reflection of the incident shock occurs. Instead, regular and Mach reflections appear in the postshock region. Both figures are by courtesy of Professor B. Milton, The University of New South Wales, Sydney, NSW, Australia.

In the present section visualizations of shock wave propagation in channels are presented. The recorded work was obtained in shock tube experiments, and therefore it is necessary to briefly describe the shock tube concept. A detailed description of shock tubes is given in Chapter 4.1.

10.3.1 BRIEF DESCRIPTION OF THE CONVENTIONAL SHOCK TUBE

An illustration of the shock tube used for obtaining most of the results shown subsequently is given in Fig. 10.3, which shows the shock tube of the Ernst-Mach-Institut in Freiburg, Germany. It consists of two parts. The shorter part is the high-pressure section (chamber) and the longer part is the low-pressure section (channel); the two parts are separated by a diaphragm (membrane). After the diaphragm's rupture a flow is developed in the shock tube having the wave pattern shown schematically in Fig. 10.4. The front \vec{S} of the generated shock wave travels with speed U ; its Mach number M_0 is given by $M_0 = U/a_0$ (a_0 being the ambient sound speed). Across the shock front a sudden pressure jump from the ambient value p_0 to the postshock value p_1 occurs. The pressure ratio $P_{10} = p_1/p_0$ is called the strength of the shock front and it depends on U , for air, as

$$P_{10} = \frac{7M_0^2 - 1}{6}. \quad (10.1)$$

This is one of the well-known Rankine–Hugoniot relations. In order to produce shock waves with a step profile, the channel and the chamber lengths must be in a certain proportion. If the chamber is too short relative to the channel, a blast wave will be produced. Such a wave is characterized by a rapid pressure decrease behind the steep front.

The width of the shock front in atmospheric conditions is of the order of a few micrometers (Morduchow and Libby, 1962; Zucrow and Hoffmann, 1976, 1977). For engineering purposes the shock front width is assumed to be equal to zero. Spatial distributions of pressure, density, and flow velocity are shown schematically in Fig. 10.4.

10.3.2 VISUALIZATION OF SHOCK WAVE PROPAGATION IN VARIOUS CHANNEL CONFIGURATIONS

An effective visualization of shock wave propagation and interaction processes can only be performed in a laboratory using high-quality instrumentation. An optical imaging system (shadowgraph, schlieren-system, or Mach–Zehnder interferometer) must be carefully installed, and an appropriate high-speed camera (e.g., a Cranz–Schardin multiple spark camera) is required. Such

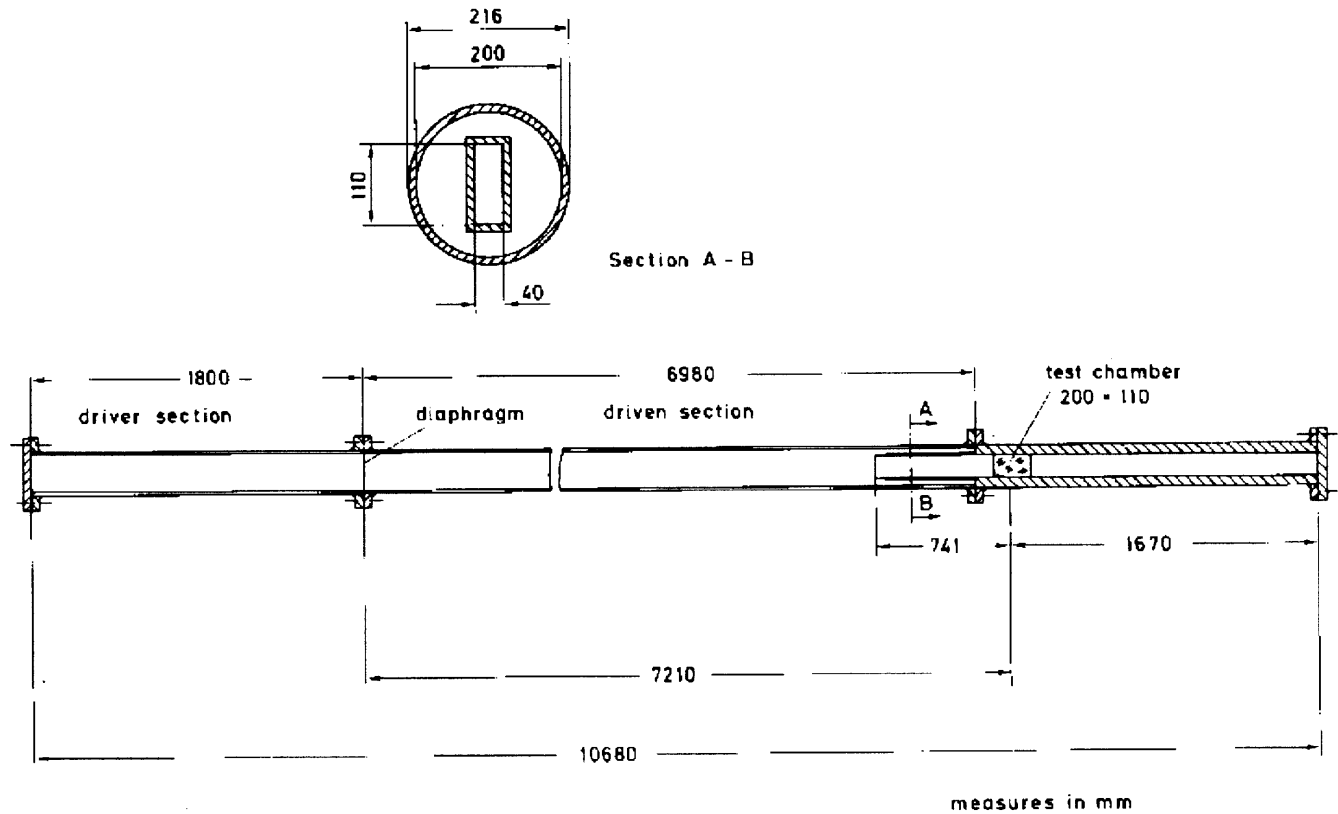


FIGURE 10.3 Sketch of the EMI shock tube in which most of the following visualizations were made. Note the cookie-cutter system (section A-B) and the test chamber (200 mm long, 110 mm high, 40 mm deep).

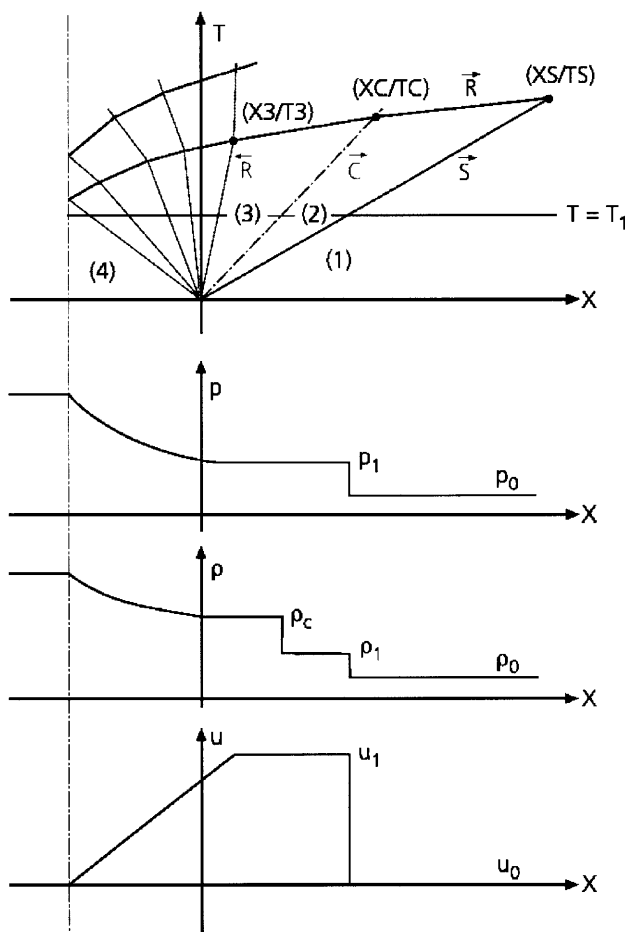


FIGURE 10.4 Wave diagram of a “scaled” shock tube. The diaphragm is placed at the origin. The vertical dash-dotted line indicates the left endwall of the driver. Imagine that the right endwall of the channel is situated either between the points (XC/TC) and (XS/TS) or on the right side of (XS/TS) . In the first case we obtain a shock wave with a step profile (see profiles for pressure, density, and particle velocity below at the time $T = T_1$). In the latter case a blast wave is generated in which the flow parameters behind the front decay in an exponential way.

equipment is available at several institutes around the globe. Flow visualization is a powerful diagnostic for assessing the wave interaction process. It does not disturb the investigated flow field and the obtained results are very accurate. Some examples of wave interaction and propagation in various ducts are shown subsequently.

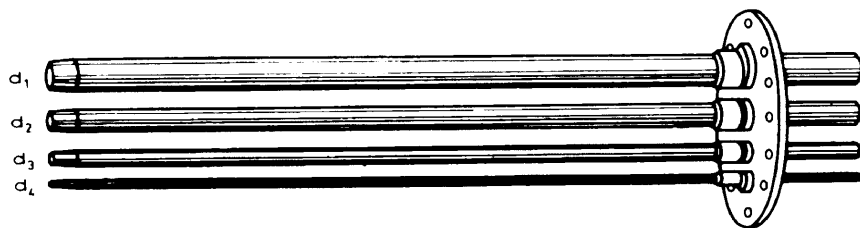


FIGURE 10.5 Illustration showing the mounting of four tubes inside the shock tube being parallel to the flow direction. They have the same length (100 cm) but different diameters (44, 28, 20, and 10 mm) and are equipped with sharp leading edges.

10.3.2.1 Straight Ducts

In a shock tube one can readily study wave propagation in straight ducts. For a given duct length and an entering shock wave Mach number, the parameters that influence the wave propagation inside the duct are the duct's effective diameter and the magnitude of its wall roughness. A simple way for studying wave propagation in straight ducts is shown in Fig. 10.5. Four tubes of equal length and with different cross-sectional areas and sharp mouths are mounted on a circular plate that is clamped between the flanges of the shock tube. The tubes outlets extend into the shock tube's test section. From the flow visualization shown in Fig. 10.6 it is apparent that the shock front in the tube having the largest diameter propagates faster than the shocks in the smaller diameter tubes. The slowest propagation velocity is associated with the smallest diameter tube. Apparently shock wave attenuation depends on the tube's length L and on its diameter d , that is, on the ratio L/d . This is so since in every tube a boundary layer is generated; it grows with time and for a small diameter tube it will significantly reduce the free flow cross-sectional area. In a large diameter tube the boundary layer influence will be much smaller, if not negligible. Therefore, in the smallest tube shown in Fig. 10.6 it alters the flow in the tube very soon from an initially inviscid to a fully developed viscous flow. This results in attenuating the transmitted shock wave (Schardin and Reichenbach, 1965).

For demonstrating wall friction effects on the attenuation of a transmitted shock wave, a similar experiment was conducted. In the present case identical shock waves are transmitted via three two-dimensional ducts shown in Fig. 10.7. All three ducts have the same cross-sectional area; however, whereas the walls of the upper and lower ducts are smooth, the walls of the middle duct are coated with sandpaper of various grain sizes. As can be expected, it is clearly visible in Fig. 10.7 that the shock wave propagating in the middle duct experiences larger attenuation. Increasing the wall roughness will result in further attenuation of the transmitted shock wave (Schardin and Reichenbach, 1965).

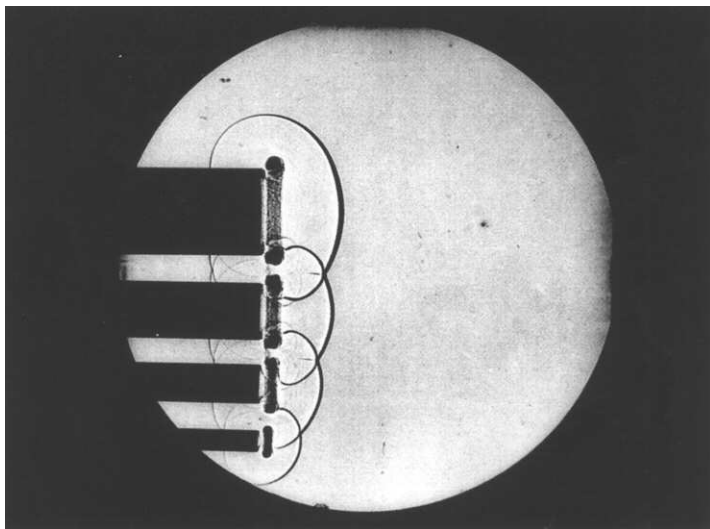


FIGURE 10.6 Shadowgraph showing the trailing edges (exits) of the four tubes (Fig. 10.5) which extend into the test section. Assuming that the shocks cut out from the incoming shock by the leading edges are of approx. the same strength, it is clearly seen that the shock passing through the largest diameter tube experiences the smallest attenuation, while that one passing through the smallest diameter tube is the most attenuated.

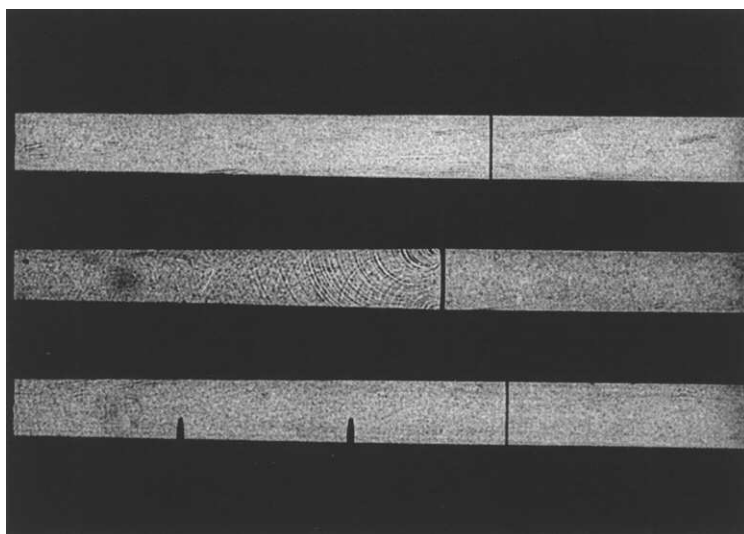


FIGURE 10.7 Two-dimensional “channels” mounted in the test chamber of the shock tube. The walls of the upper and the lower channel are smooth, whereas the channel in the middle is coated with sandpaper with a grain size G . The ratio $G/D = 0.5\%$ holds for the real channel height of 1.5 cm. The rougher walls causes greater attenuation of the running shock wave. Note the constriction of the second (middle) channel due to a thicker boundary layer.

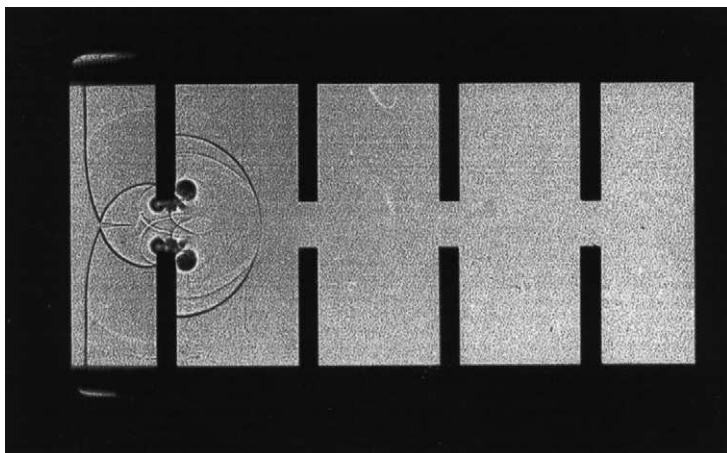


FIGURE 10.8 A plane shock wave enters a channel with built-in baffles. Depending on the height of the opening, the part of the shock that penetrates is weakened by diffraction and by vortices generated at the edges. This process is repeated at the next inlet, and the attenuation effect is enhanced with increasing number of inlets.

A way to achieve quick shock wave attenuation is by installing baffles inside the channel, for example as shown in Figs. 10.8 and 10.9. The attenuation mechanism in such a case consists mainly of vortex generation at the baffle edges. Significant amounts of energy and momentum are consumed in the



FIGURE 10.9 The process shown in Fig. 10.8 at a later time instant; now it is shown as an interferogram. (See Color Plate 3).

produced vortex flows. It can be shown that the attenuation obtained while using a baffle system with dislocated teeth is greater than that obtained in a regular arrangement, like that shown in Figs. 10.8 and 10.9. The visualization becomes more impressive if an interference method is applied. From interferograms like the one shown in Fig. 10.9 a density mapping of the considered flow field can be evaluated. One may consider the baffles as an extreme wall roughness (Reichenbach and Kuhl, 1993).

Another example of the straight propagation of a transmitted shock wave over a unique wall is shown in Fig. 10.10. In the considered case the transmitted shock wave propagates over a comblike structure. The wall consists of sharp and deep teeth tied at the bottom of the model. Such a

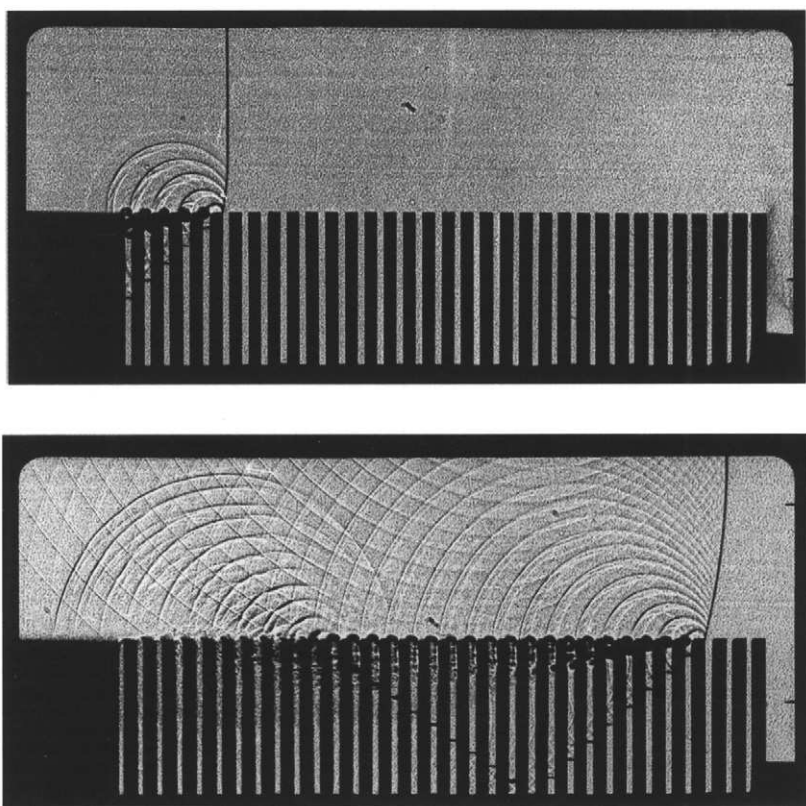


FIGURE 10.10 Shock propagation over a comblike structure. Note the diffracted shock front entering the gaps and the set of curved reflected shocks behind the transmitted shock wave. The attenuation experienced by the traveling shock wave can be estimated from the amount of curvature that the incident shock undergoes.

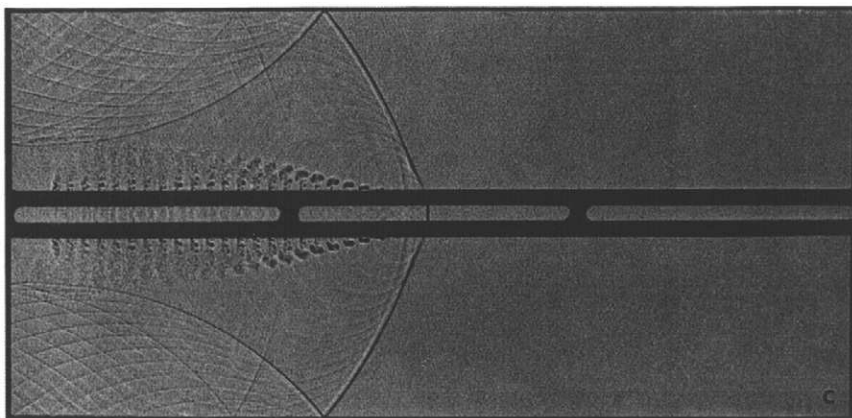


FIGURE 10.11 Shock wave propagation along a perforated tube. Parts of the shock leave the perforations; these are followed by emitted flow. This concept can be used for shock wave attenuation.

geometry yields a considerable attenuation of the shock sweeping over it. A further similar example for a geometry suitable for shock wave attenuation in straight ducts is the use of ducts with perforated walls, as in the case shown in Fig. 10.11. The mass loss through perforations is the dominant mechanism leading to the obtained shock attenuation (Reichenbach, 1970).

A completely different way to affect shock wave propagation in ducts is by temperature control of the duct's walls. The schlieren photo in Fig. 10.12 shows this effect when a shock wave propagates over a heated plate. In this photo density variations, due to the emitted heat, are seen. The part of the transmitted shock wave traveling over the heated region moves faster than the part traveling in the relatively cold region. This lower part of the shock wave is stronger than its upper part due to the energy contributed by the heated region. A similar result could be obtained by implementing a helium layer, at ambient temperature, over the wall instead of heating. This is so because of the relatively high sound speed of helium. Therefore, one can simulate a high temperature by replacing the heated air layer with a helium layer at ambient temperature as is shown in Fig. 10.13 (Reichenbach, 1995; Reichenbach and Kuhl, 1987).

Opposite results can be obtained by cooling the wall over which the shock wave propagates. Results obtained when the bottom of the shock tube test section was covered by a Freon layer are shown in Fig. 10.14. In this case the wall temperature is significantly below ambient and as a result a slowing of the lower part of the transmitted shock wave traveling in the cold layer is clearly evident (Kuhl and Reichenbach, 1989).

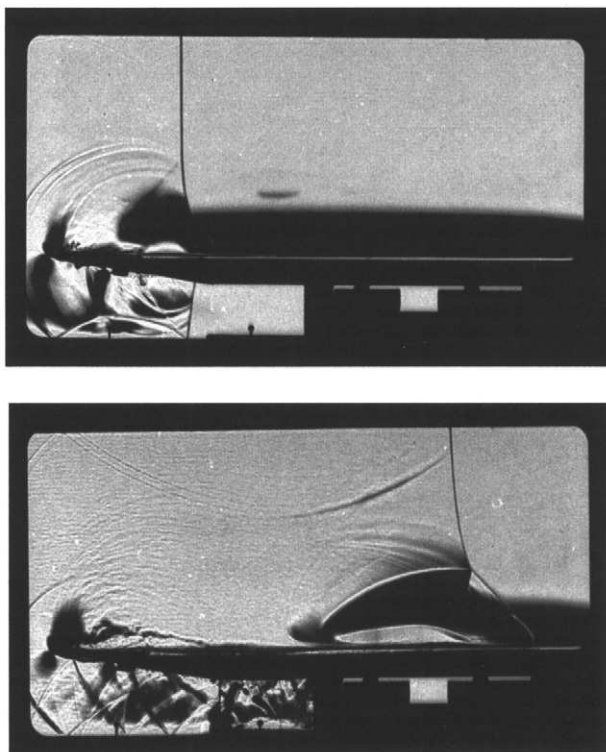


FIGURE 10.12 Shock propagation over a heated plate. The region of heated air is shown by the schlieren layer. The incident shock is influenced by the heated layer. It is accelerated there.

In the following, straight channels having nonuniform cross-sectional areas are discussed.

10.3.2.2 Straight Channels with Varying Cross-Sections

Another method to influence the strength of a transmitted shock wave is by varying the channel's cross-sectional area. It is plausible that an area reduction increases the strength of the transmitted shock and an area enlargement reduces its strength. The physical reason is that the energy per unit volume is changed and consequently the pressure jump across the transmitted shock wave also changes.

A duct having a change in its cross-sectional area is shown in Fig. 10.15. Expansion waves are generated at the corners where the area change starts. These waves weaken the transmitted shock wave. In the case of an area

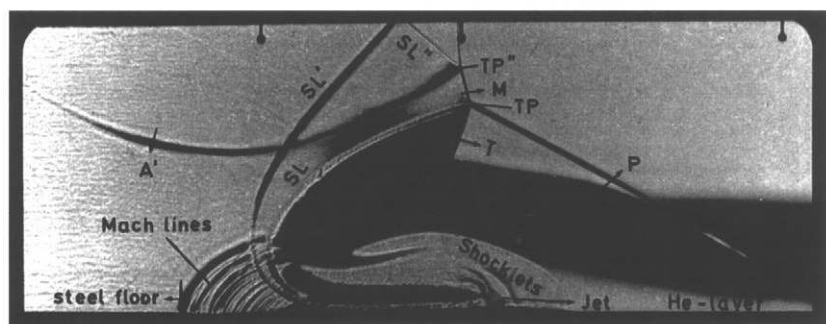
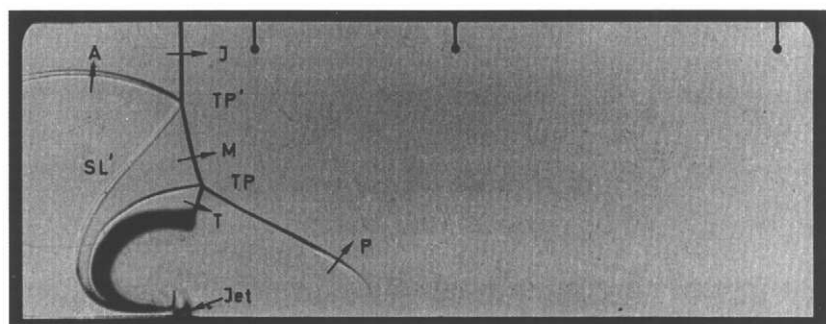
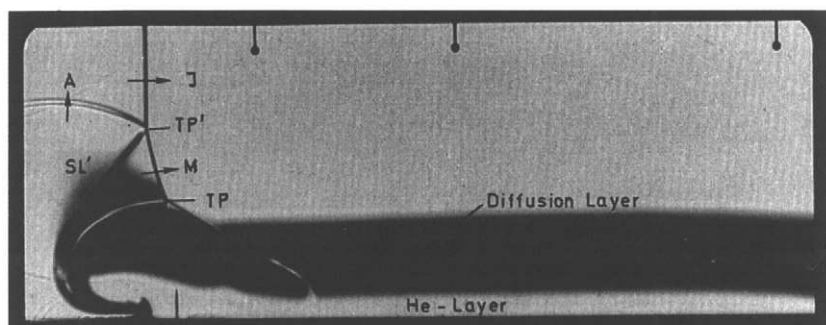


FIGURE 10.13 Instead of heating the plate, it can be covered by a helium layer at ambient temperature.

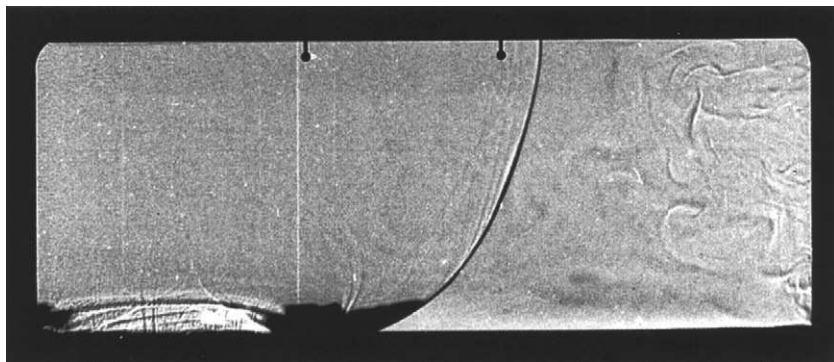
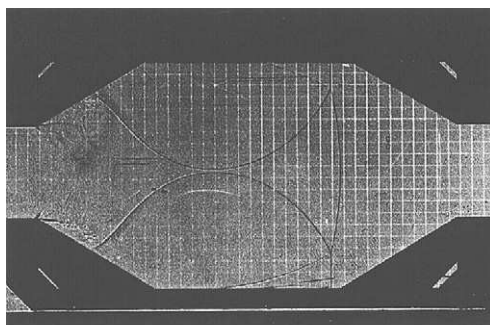
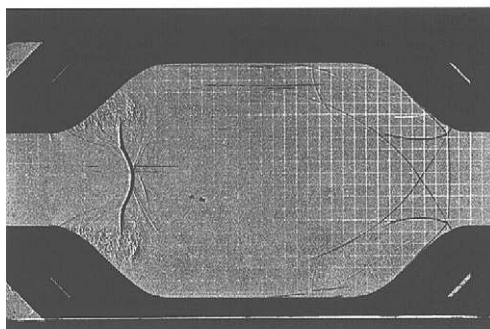


FIGURE 10.14 A Freon layer (CCl_6F) simulates a cold wall; the cold medium slows down the incident shock wave.



(a)



(b)

FIGURE 10.15 Shock propagation through a channel enlargement and a channel constriction. The incident shock, when entering the enlargement, is affected by expansion waves that curve its front. Along the horizontal wall this curved shock undergoes Mach reflections, recognizable by the straight vertical Mach stems (a). On the walls of the constriction new Mach stems are created. At late times (b) a shock wave focusing can be observed in the diverging section of the duct. By courtesy of the French-German Research Institute, St. Louis, France. The figures come from the slide archive of the Institute.

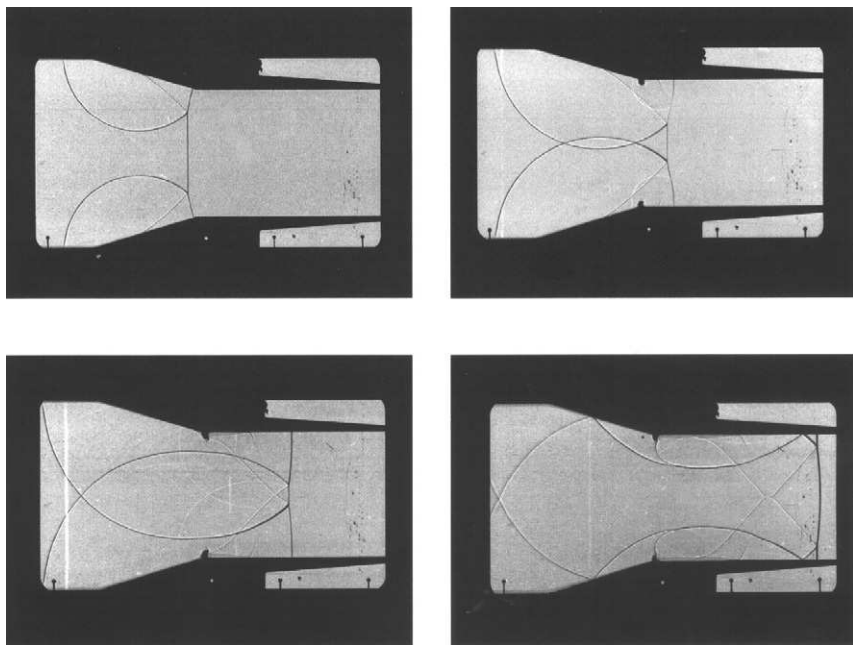


FIGURE 10.16 Shock propagation along a channel having an area constriction segment. Mach reflections occur at the converging walls, the reflected shocks interact and are further reflected from the walls, thereby steepening the transmitted shock wave.

reduction, shown in Fig. 10.16, Mach reflections from the duct's walls interact with each other and generate a new Mach stem. The new transmitted Mach stem is stronger than the original transmitted shock wave. A different area reduction geometry was shown in Fig. 10.2. Because of the specific geometry employed in Fig. 10.2, a loss-free enhancement of the transmitted shock is realized, that is, no expansion or reflected waves are created (Sommerfeld *et al.*, 1985).

Wave evolution in a case of flow through a duct having an abrupt area change is demonstrated in the sequence of shadowgraph photos shown in Fig. 10.17. An area change ratio of 1 : 10 is used in the considered case. A very intense expansion takes place at the corners where vortices appear. Also visible is the diffracted shock front, which starts as a cylindrical wave. Once it hits the duct's walls, it reflects toward the duct's plane of symmetry. Subsequent multiple reflections from the duct's walls eventually turn this curved shock wave into a planar shock wave. For an incident shock, in air, whose Mach number is greater than 2.08 the flow expansion over the 90° corner will be via a centered rarefaction wave. In such a case, a secondary shock wave is generated (see Fig. 10.17) in order to match between the high-pressure zone existing behind the transmitted shock wave and the low-pressure zone behind

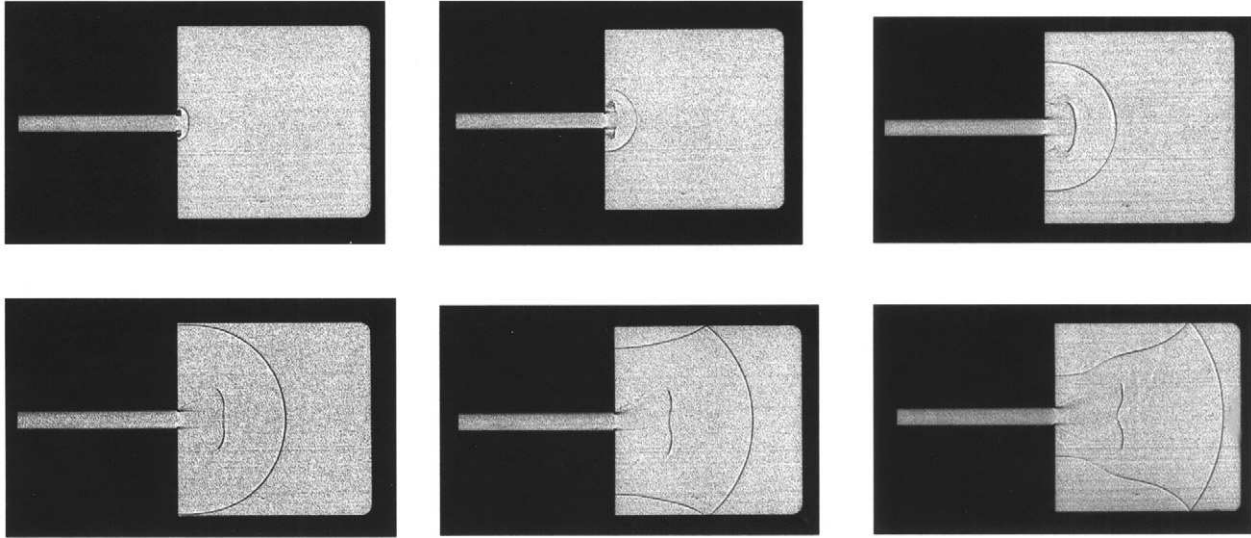


FIGURE 10.17 A shock travels from a narrow duct into an abruptly joined large duct (area ratio 1:10). Note the diffraction of the cylindrically expanding shock front at the edges and its reflection from the walls. A secondary shock matching the supersonic and the subsonic flow fields is generated.

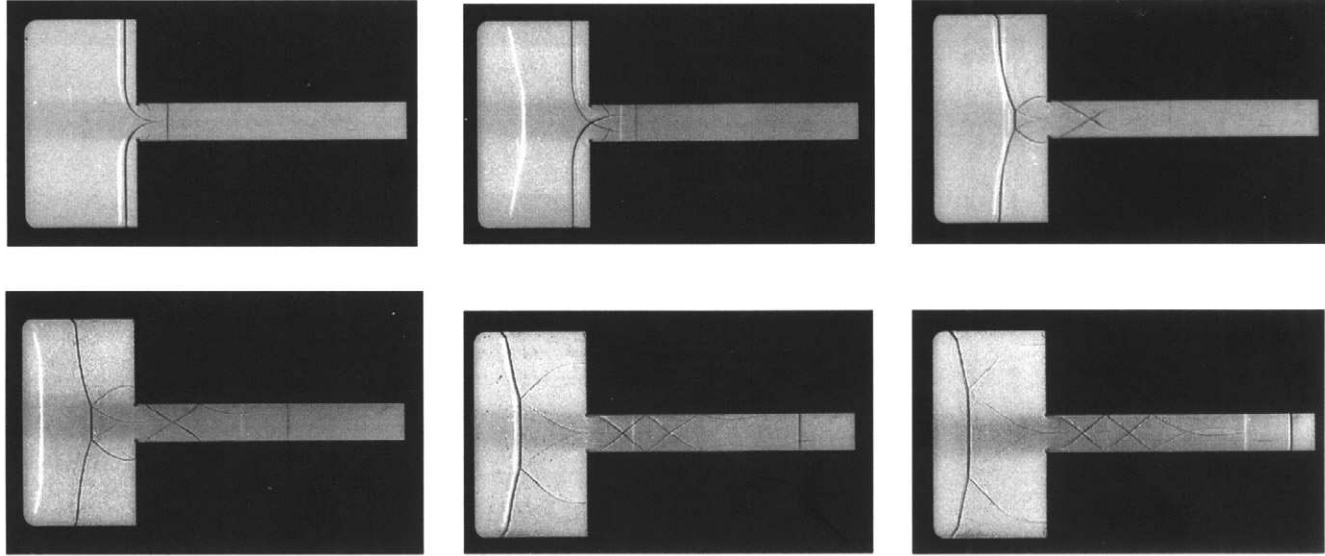


FIGURE 10.18 Penetration of a shock wave into a narrow channel via an abrupt area change. A major part of the incoming shock wave is reflected. Secondary, oblique shocks appear in the small cross-section channel before the flow becomes uniform again. The process can serve as an illustration of a shock entering a subterranean duct from open space.

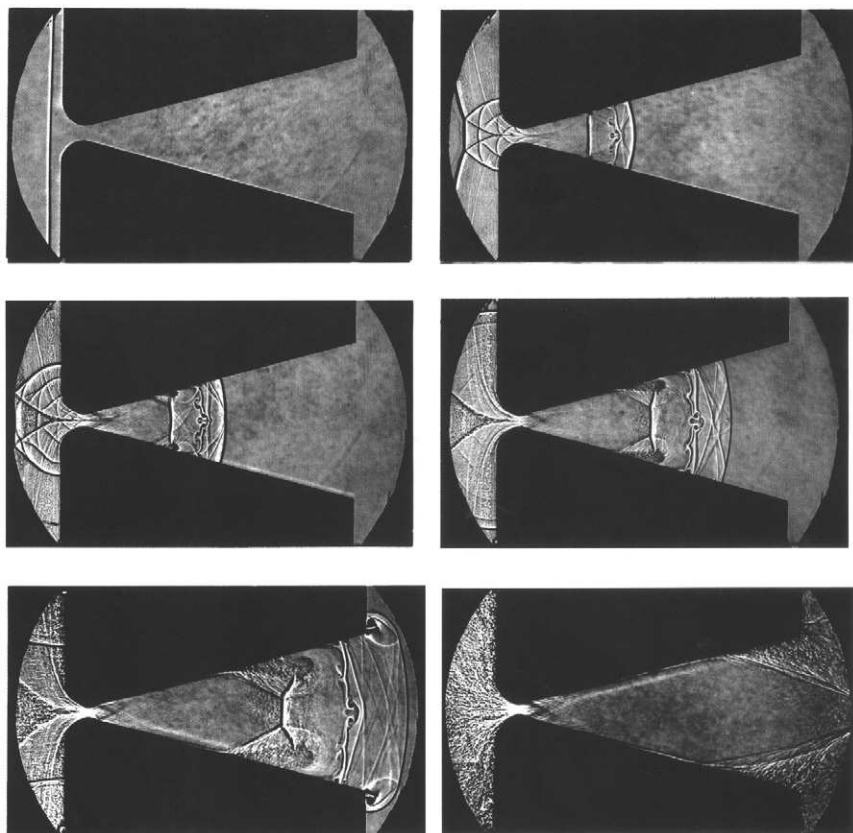


FIGURE 10.19 A process similar to the one shown in Fig. 10.18. Now the area change is not abrupt. This demonstrates the starting phase of a so-called reflection nozzle.

the centered expansion wave. When the flow behind the transmitted shock wave is subsonic ($M_0 < 2.08$ in air) the flow expansion over the duct's corners will be via vortices shed from the corners. In an opposite case, that of a sudden area reduction (like that shown in Fig. 10.18 and having the same area ratio as in Fig. 10.17), most of the incident shock wave is reflected and only a small part of it enters into the narrow channel.

If the transition between the two sections of the duct is not via a sudden area change, as in Fig. 10.18, but via a smooth area change, for example via a nozzle as shown in Fig. 10.19, then the obtained flow field is a typical shock tunnel starting flow (Amann, 1971; Amann and Reichenbach, 1973).

Detailed description of shock wave interaction with area changes in a duct can be found in Greatrix and Gottlieb (1982). Gottlieb and Igra (1983) and Igra and Gottlieb (1985) treated flows resulting from the interaction of a rarefaction wave with area enlargement and area reduction segments in a duct,

respectively. The flow in these references was assumed to be a quasi-one-dimensional flow. It was shown in Igra, Wang, and Falcovitz (1998a) that while the interaction between a shock wave and area change segment in a duct results in a flow approaching the quasi-steady one-dimensional flow approximation (after all wave reflections have subsided), the flow resulting from the interaction between a rarefaction wave and an area reduction in a duct is inherently two-dimensional. It cannot be approximated as a quasi-one-dimensional flow. Details regarding the starting flow in nozzles can be found in Igra *et al.* (1998b).

10.3.2.3 Channels Including Abrupt Deviations and Expansion Chambers

A practical engineering channel system, for example a channel leading to an underground storage site, must be designed according to given limitations. These limitations dictate changes in direction, cross-sectional area, and/or geometry. In many cases such systems consist of several abrupt turns in the ducts. Examples showing a 90° turn and a 135° turn in channels are shown in Figs. 10.20 and 10.21. Sudden changes in the channel direction cause attenuation of the transmitted shock wave. The attenuation effect observed in the 135° turn is greater than that associated with the 90° turn. A rule of thumb for 90° turns says that the overpressure behind the shock front is reduced by a factor of $0.94n$, where n is the number of turns. Such a rule of thumb is based on experimental results obtained in shock tube generated flow through models like the one shown in Fig. 10.22. If many turns exist in a channel, the energy dissipation occurs mainly through vortices.

In some practical cases it may also be necessary to install expansion chambers in the channel system. The shock wave attenuation associated with chamber inclusion can be deduced from shock tube results like those shown in Fig. 10.23 (Igra *et al.*, 1999; Heilig, 1993).

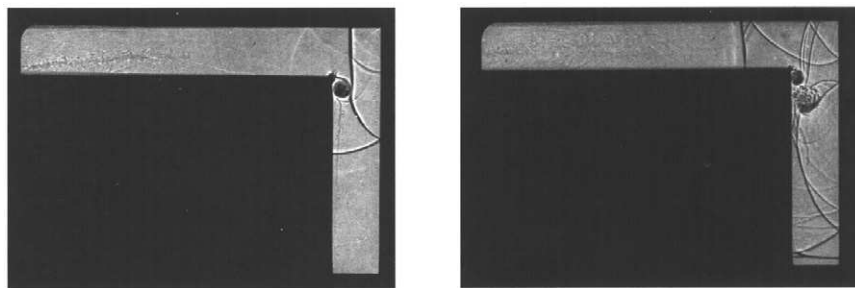


FIGURE 10.20 Shock propagation in a channel with an abrupt 90° bend. The reflected shock interacts with the vortex (typical of subsonic flow prevailing behind the transmitted shock wave) and thereafter travels upstream. The transmitted shock front tends to smooth out.

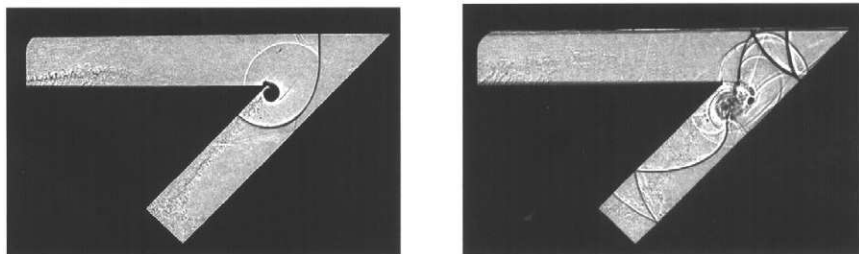


FIGURE 10.21 Shock propagation into a 135° junction. The incident shock is diffracted at the sharp corner where a vortex is generated (due to the subsonic postshock flow). The curved diffracted shock is reflected at the plane side branch wall; a part of it joins the shock in the main branch. In both straight branches the shocks finally steepen up.

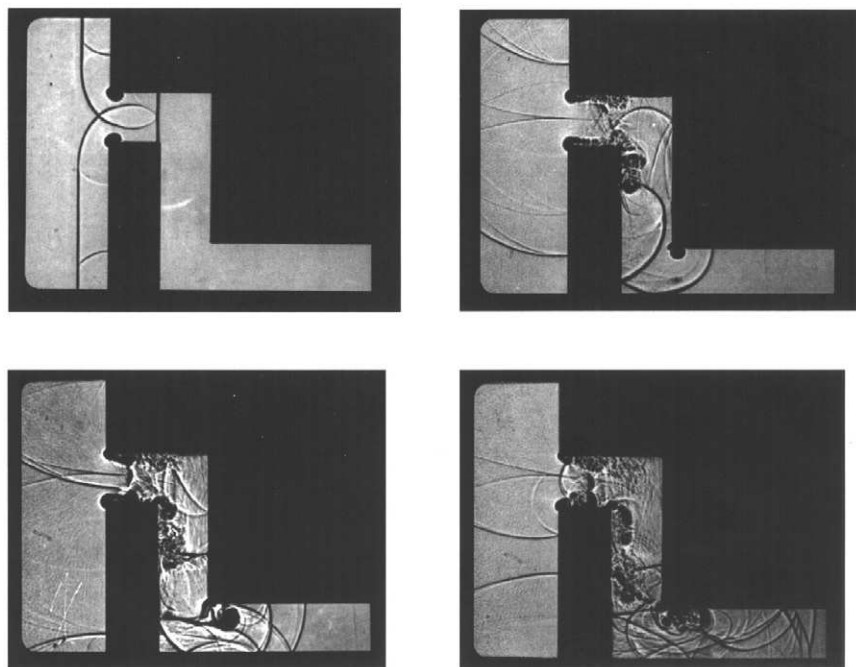


FIGURE 10.22 Four shadowgraphs made with the Cranz-Schardin 24 multiple spark camera in time sequence showing the penetration of a shock wave into a double bent channel after its interaction with the entrance wall.

10.3.2.4 Curved Ducts

The influence that the channel curvature exerts on the shock wave transmitted through it is demonstrated in the example shown in Fig. 10.24. This figure shows, via six shadow-schlieren photos taken during one shock tube experi-

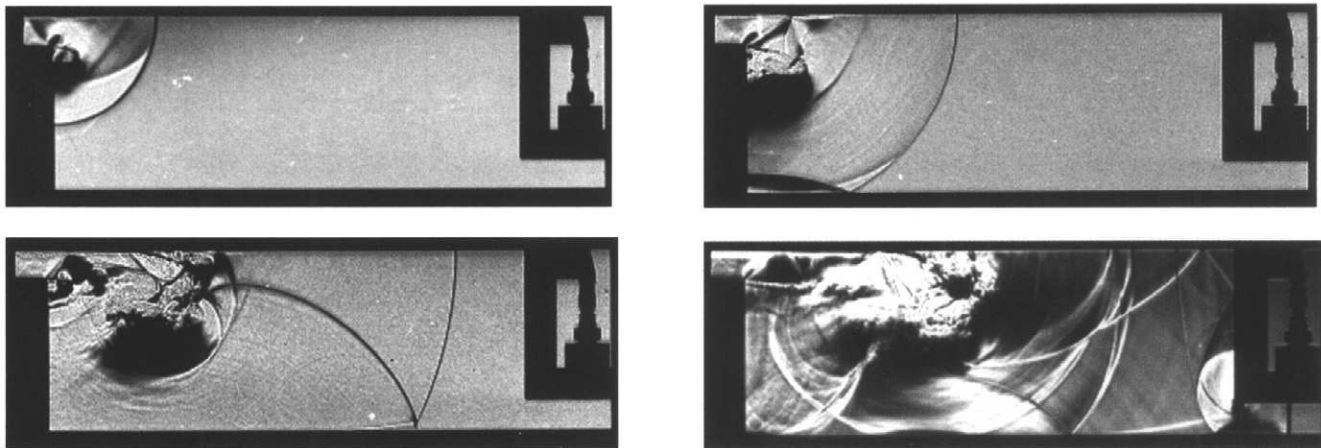


FIGURE 10.23 A sequence of shadow schlieren pictures of a shock running through an expansion chamber. The incoming shock (from left) is diffracted into the chamber and weakened. Only a part of it enters the small exit channel.

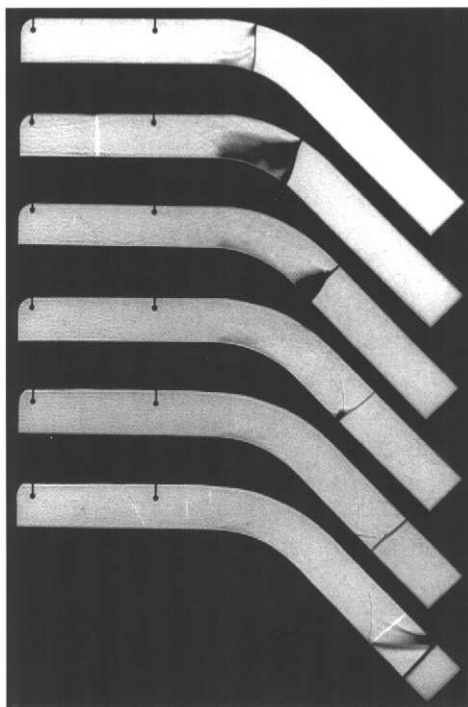


FIGURE 10.24 Six shadow-schlieren photos taken from a series made with the Craanz-Schardin 24-spark camera showing the propagation of a shock wave down a channel bent by 45° with rounded edges. Apparently the shock front is weakly attenuated while propagating through such a channel bend.

ment, the propagation of a transmitted shock wave through a duct that turns the incoming flow by 45° . The flow turning is achieved via a smooth circular curving of the duct. It is apparent from Fig. 10.24 that the transmitted shock wave experiences only a few reflections from the duct's walls. Furthermore, there are no upstream-facing shock waves; one could therefore safely conclude that the transmitted shock wave experiences only a mild attenuation.

If a faster attenuation is desirable for the considered shock wave and duct, then the 45° turning should be made via abrupt changes as is shown in Figs. 10.25 and 10.26. Disturbances caused by the sharp flow deflections produce shock waves that travel in the upstream direction, in the present subsonic flow prevailing behind the transmitted shock wave. Therefore the obtained attenuation in the cases shown in Figs. 10.25 and 10.26 is much stronger than that achieved using the geometry shown in Fig. 10.24.

Conclusions from the examples just shown hold for the considered incident shock wave strength and duct of uniform cross-section. The situation might

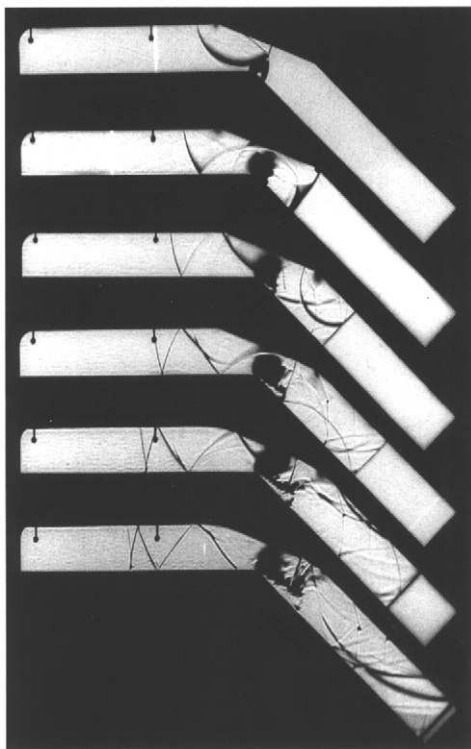


FIGURE 10.25 A corresponding process to that shown in Fig. 10.24. Now the bend contains sharp corners, two at the upper wall and one at the lower. This causes stronger wave perturbations in the bending area. Because of the subsonic flow in the channel's inlet, the reflected shock travels upstream, causing greater energy losses for the transmitted shock.

change when these parameters are altered, for example, the duct's cross-section or wall roughness. Quantitative data about the flow processes in such ducts can be obtained by pressure measurements, using appropriate gauges, or by evaluation of shadow-schlieren photos. A detailed and comprehensive evaluation of the flow processes in curved ducts is only feasible by numerical simulations.

10.3.2.5 Channel Branching

An effective way to attenuate a transmitted shock wave is by branching the channel through which the shock wave travels. Channel branching is also applied as duct bypassing in connection with underground ammunition storage. In case of detonation, the main duct and the bypass are locked by a "klotz" triggered by the wave-generated pressure. Such bypasses can be achieved using branched ducts.

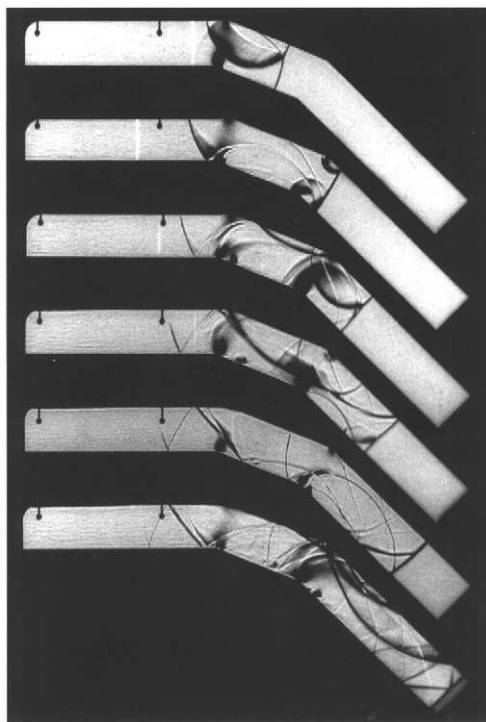


FIGURE 10.26 A corresponding process to that shown in Fig. 10.25. Now the bend contains more sharp corners, two at the upper wall and two at the lower wall (otherwise see legends of Fig. 10.24 and 10.25).

Shock wave propagation in branch ducts is demonstrated in the shadowgraphs shown in Figs. 10.27 (for a 90° branching) and 10.28 (for a 45° branching). Other usable branching options are those shown in Fig. 10.29 (a perpendicular cross-junction) and in Fig. 10.30 (a Y cross-junction). A common feature in the processes shown in the shadowgraphs of these figures is that the incident shock wave diffracts at the inlet corner of the branching segment of the duct. The diffracted shock wave propagates into the branching space until it meets the opposite corner. There it is split up into two parts; one continues traveling along the main branch while the other penetrates into the side branch. It is apparent from the considered shadowgraphs that after propagating a distance of a few duct's widths downstream of the branching segment, shock wave reflections from the duct's wall subside and the transmitted shock waves regain a planar shape. During the process leading to a planar transmitted shock wave, followed by a quasi-uniform flow, the transmitted wave experiences multiple reflections from the duct's walls. These reflections include regular and Mach reflections depending on the temporal Mach wave of the transmitted shock wave. Other observed phenomena during

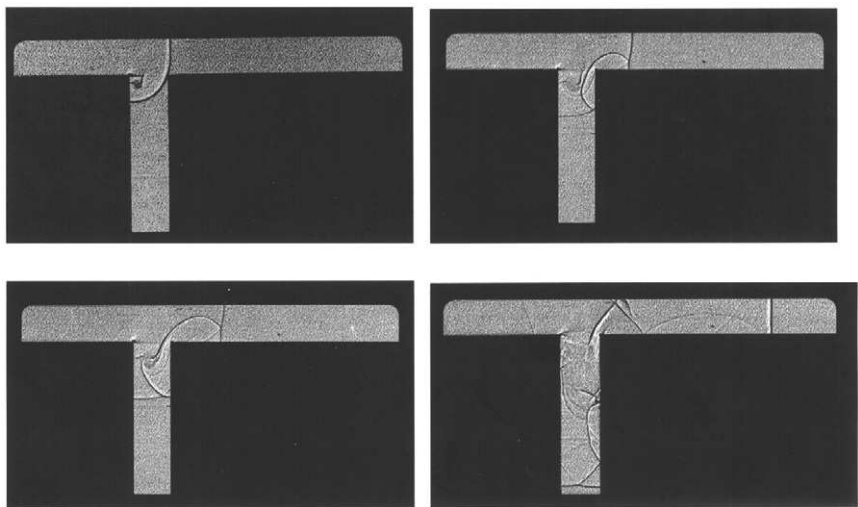


FIGURE 10.27 Shock propagation through a 90° junction. Four shadowgraphs out of 24 made using a Cranz–Schardin multiple spark camera showing the flow in the considered channel. The channel depth in view direction is 40 mm and its height is 20 mm. Time intervals between photos are 12.5, 25, and 87.5 μsec .

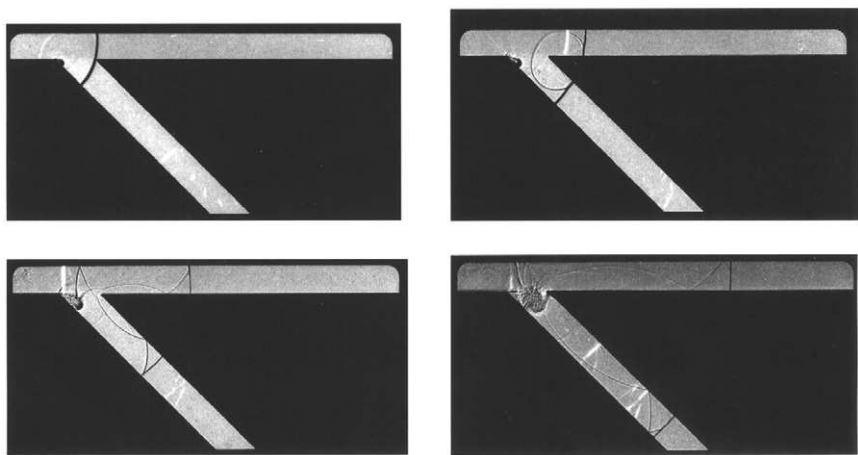


FIGURE 10.28 Shock propagation through a 45° junction (see legend of Fig. 10.27). Otherwise: Channel height: 15 mm. Time intervals between photos: 60, 60, and 100 μsec .

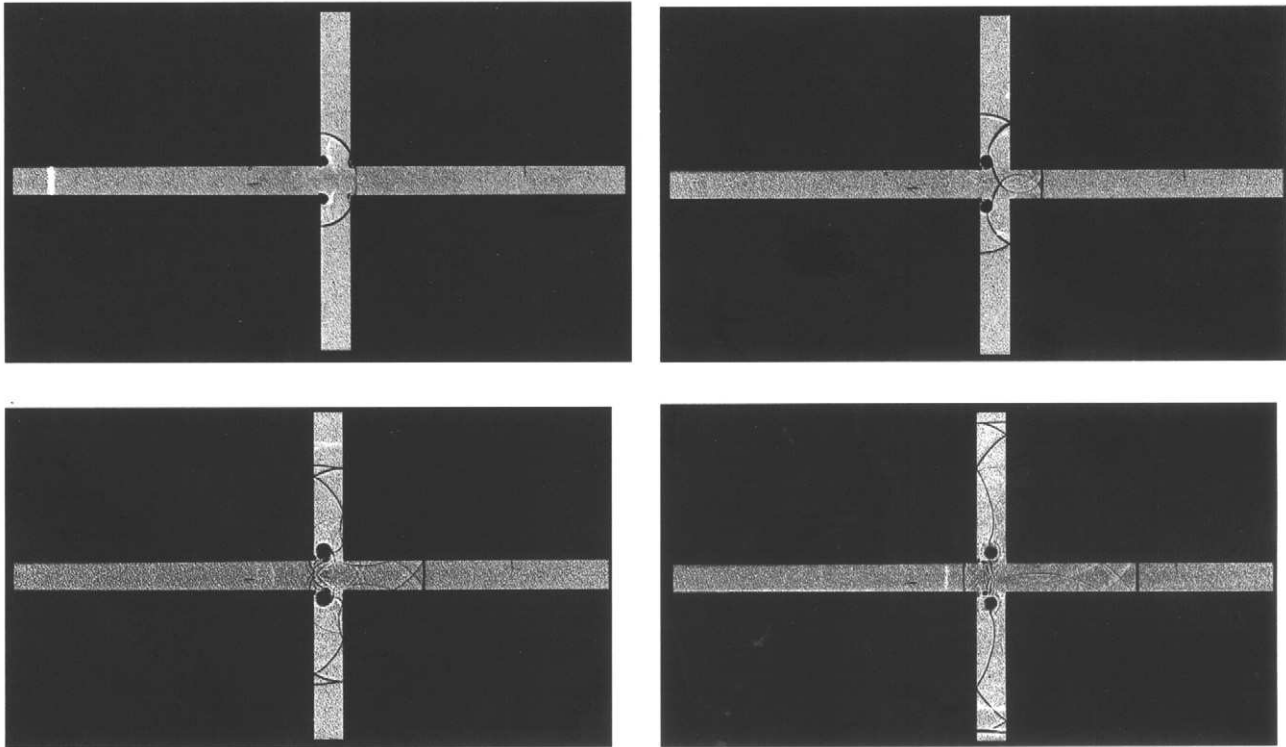


FIGURE 10.29 Shock propagation through a cross-junction (see legend of Fig. 10.27). Otherwise: Channel height: 10 mm. Time intervals between photos: 20, 20 and 80 μsec .

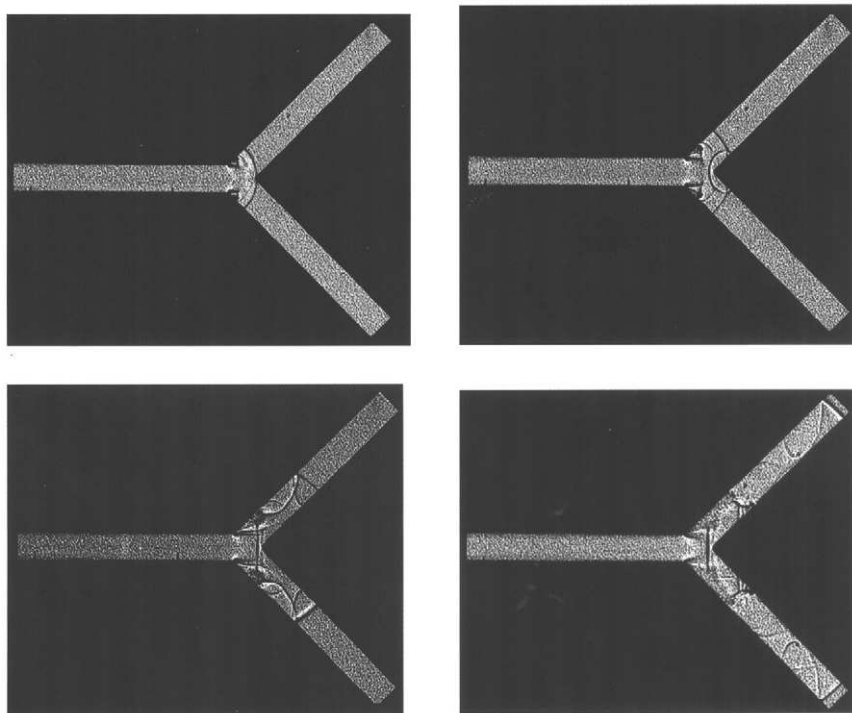


FIGURE 10.30 Shock propagation through a double 45° junction, or Y cross-junction (see legend of Fig. 10.27). Otherwise: Channel height: 15 mm. Time intervals between photos: 10, 10, and $70\mu\text{sec}$.

the transition period, until a planar shock wave is reached, are secondary shocks and slip lines. A secondary shock is witnessed when the flow behind the incident shock wave is supersonic, and therefore the flow expansion over the branching corner is via a centred rarefaction wave. In the subsonic case no secondary shock wave is needed for pressure matching since the flow expansion is via a vortex shed from the expansive branching corner (Heilig, 1975; Heilig, 1978a).

The salient feature of these four branching processes is the fact that the diffracted shock wave is split up by a sharp corner. Apparently that is not the case for other branched ducts (see Fig. 10.21).

10.3.3 COMMENTS ON THE USEFULNESS OF FLOW VISUALIZATION AND ITS EVALUATION

Figures 10.6 to 10.30 contain shadowgraphs or schlieren photos of various flows. These flow fields are well defined and two-dimensional, and they have

clear boundaries. Obviously, in regular tubes with circular cross-sections flow processes are more complex, especially in the branching segments of the duct. However, the main features and basic mechanisms are captured in the pictures shown. Therefore, visualization certainly helps in understanding what happens in channel flows and enables assessing how effective various geometries are in enhancing or attenuating the transmitted shock wave. Additionally, quantitative data can also be obtained. This can be achieved by distance–time measurement of the propagating shock fronts from picture to picture as provided by the Cranz–Schardin camera knowing the recording frequency. In this way the shock's velocity is measured, which with the aid of the Rankine–Hugoniot relations yields all parameters (pressure, density, velocity, etc.) behind the shock front. Experience confirms that this is a very reliable method that can be checked independently against direct pressure measurements. Careful instrumentation of a shock tube allows recording shadow-schlieren pictures simultaneously with pressure measurements using piezoelectric gauges.

A very important fact is that while analyzing visualized processes, ideas can be gained for development of analytical gasdynamic theories even though these photos do not provide all details. Examples for this are the developments of the so-called “two-shock theory” and the “three-shock theory” (von Neumann, 1963; Ben-Dor, 1992; Bleakney and Taub, 1949) describing the regular reflection and the Mach reflection of shock waves. Starting from the visualized process of the reflection of a planar shock wave from a steep wall, a reflected shock is produced that is connected with the incident shock at the so-called reflection point on the wall. The Rankine–Hugoniot theory applied to the two oblique shocks yields a set of two equations for the strength of the reflected shock and for the reflection angle, knowing the strength of the incident shock and incident wave angle (wall steepness). Similarly, a single Mach reflection with three shocks is theoretically obtained. Both theories assume straight shocks throughout and are based on the assumption that the flows in regions bounded by the shocks are uniform. Furthermore, they are steady theories; the time variable is not included explicitly. Solutions of the regular reflection describe the physical phenomenon accurately, except for the situation when one comes very close to the wall angle where the transition to Mach reflection takes place. For stronger incident shocks, excellent agreement with measurements prevails for the case of the Mach reflection theory; for weak shocks the theory deviates slightly from measurements (von Neumann Paradox; Collela and Henderson, 1990). These examples give rise to the development of similar theories to be reported in the following sections.

Being semitheoretical or empirical theories, they are not capable of covering all phenomena detected in experiments. Detailed coverage can be reached by employing numerical methods, which are becoming more and more efficient.

In the following section shock wave propagation in channels is discussed based on theoretical/numerical findings.

10.4 APPROXIMATE ANALYTICAL METHODS

In order to be able to calculate the processes demonstrated in the previous sections theories are needed which after specifying the appropriate initial and boundary conditions yield the flow parameters independently from the experiment. However, the basic gasdynamic equations, that is, the laws of conservation of mass, momentum, and energy, are nonlinear partial differential equations of second order and are in general not solvable in a closed analytical form, except for a one-dimensional unsteady flow. Fortunately, it is now possible to resort to numerical methods. The field of computational fluid dynamics has experienced very rapid development during the past two decades. It can now handle even the most complex flows. This was not the case in the past, not even in the recent past, and therefore one had to resort to approximate solutions. In an approximate solution care should be given, on one hand, to ensure that the approximation does not alter the nature of the considered problem, and on the other hand, that it allows an analytical solution. Searching for and using approximate solutions was an active venue during the 1960s and 1970s when the state of the art of computational capabilities was still in its infancy. In order to pay tribute to this important branch of theoretical research the most ingenious activities are briefly outlined in the following subsections. These deal with approximate analytical methods and the needed skill to find out those parameters that have lesser influence on the considered problem, whose omission will allow analytical solutions without altering the problem at hand.

10.4.1 THE UNSTEADY QUASI-ONE-DIMENSIONAL FLOW

Computations for shock wave propagation in ducts can be performed on the basis of the conservation laws for ideal and perfect gases. For purposes of the present section solutions can only be obtained from the equations of unsteady quasi-one-dimensional flow. By this we mean flows with cylindrical and spherical symmetry and flows in ducts with a slowly varying cross-sectional area. The flow velocity and thermodynamic properties of the gas are assumed to be constant on a surface perpendicular to streamlines. It follows that the

streamlines' radius of curvature is large in comparison with the linear dimensions of the duct in the direction of the radius of curvature.

The continuity equation for an arbitrary fluid element in an inviscid, one-dimensional flow is

$$\frac{\partial \rho}{\partial t} + \frac{1}{A} \frac{\partial}{\partial x} (\rho \cdot u \cdot A) = 0, \quad (10.2)$$

where ρ , u , and A are density, velocity, and flow cross-sectional area, respectively.

If we rewrite this and define the parameter λ as

$$\lambda = \frac{x}{A} \cdot \frac{dA}{dx},$$

then Eq. (10.2) holds for a constant-area duct flow if $\lambda = 0$, for a flow with cylindrical symmetry if $\lambda = 1$, and for a flow with spherical symmetry if $\lambda = 2$. The cross-sectional area A is a known function of distance x .

The conservation of momentum and energy in the considered flows can be expressed as

$$\frac{\partial u}{\partial t} + u \frac{\partial u}{\partial x} + \frac{1}{\rho} \frac{\partial p}{\partial x} = 0 \quad (10.3)$$

$$\frac{\partial}{\partial t} (p \rho^{-\gamma}) + u \frac{\partial}{\partial x} (p \rho^{-\gamma}) = 0 \quad (10.4)$$

where p is the pressure.

Whereas Eq. (10.3) is self-explanatory, the energy equation (10.4) requires some comments. It is based on the first law of thermodynamics for a fluid element undergoing a reversible adiabatic process. For such a process the entropy of each fluid element remains constant during its motion. This follows directly from the definition of entropy, $ds = (dQ/T)_{\text{rev}}$, where Q is the heat per unit mass of the flow; T is temperature in kelvins; and s denotes the entropy of the gas. From the combination of the first and the second laws of thermodynamics one obtains $T \cdot ds = de + p \cdot d(1/\rho)$ where e is the specific internal energy. For one-dimensional, or quasi-one-dimensional, isentropic flows one has

$$\frac{\partial s}{\partial t} + u \cdot \frac{\partial s}{\partial x} = 0.$$

Employing the equation of state for an ideal gas, that is, $p = \rho \cdot R \cdot T$, one finds

$$\frac{ds}{c_v} = \frac{dp}{p} - \gamma \frac{d\rho}{\rho}.$$

These relations are used for deriving the form of the energy conservation equation appearing in Eq. (10.4).

In several articles the equations of the unsteady quasi-one-dimensional flow are written in the alternative form

$$\frac{\partial \rho}{\partial t} + \frac{\partial}{\partial x}(\rho \cdot u) + \frac{1}{A} \cdot \frac{dA}{dx} \cdot (\rho \cdot u) = 0 \quad (10.5a)$$

$$\frac{\partial}{\partial t}(\rho \cdot u) + \frac{\partial}{\partial x}(\rho \cdot u^2 + p) + \frac{1}{A} \cdot \frac{dA}{dx} \cdot (\rho \cdot u^2) = 0 \quad (10.5b)$$

$$\frac{\partial E}{\partial t} + \frac{\partial}{\partial x} \cdot \{(E + p) \cdot u\} + \frac{1}{A} \cdot \frac{dA}{dx} \cdot \{(E + p) \cdot u\} = 0, \quad (10.5c)$$

where $E = p/(\gamma - 1) + \rho \cdot u^2/2$ denotes the total energy per unit volume. Equations (10.3) and (10.4) follow by elimination of dA/dx with the aid of Eq. (10.5a).

10.4.2 RUDINGER'S METHOD

In the literature (Rudinger, 1960, 1955) a comprehensive procedure is given for treating the propagation of shock waves in ducts having either a gradually changing cross-section or a discontinuous one. The real flow patterns increase in complexity as demonstrated in the previously shown flow visualizations, and in spite of simplifying assumptions no analytical solution can be obtained. The procedure applicable in practice is the method of wave diagrams in which one neglects all unsteady wave phenomena, that is, assuming the flow to be quasi-steady. This would be meaningful when all unsteady disturbances have disappeared.

Consider two straight tubes of constant but different cross-sections, which are connected by a tube segment of varying cross-section (enlargement or reduction). Upon passage of a shock wave through the transition segment, unsteady flow patterns will occur in the transition region. Transmitted disturbances move downstream, overtake the shock, and alter its shape and strength. Reflected disturbances travel upstream relative to the moving gas. If their speeds exceed the oncoming local flow speed, they move upstream, forming either an upstream-facing shock or a rarefaction wave. If the local flow speed exceeds the wave speeds, the disturbances are swept downstream. They may coalesce to a shock wave standing in the area transition segment or swept downstream, or result in a rarefaction wave. After a sufficiently long time, the transient interaction phenomena subside and all flow regions and wave patterns asymptotically reach steady flow conditions. Some general qualitative trends for the transition time are known. A larger change in the cross-sectional areas requires a longer transition time for reaching the quasi-steady flow pattern. This is also true for a long transition section. This is the solution “in

the large," which disregards the unsteady details in the interaction region. In the following only such flows are considered, that is, when the conditions behind the shock are independent of time and when the shock moves downstream with uniform speed and strength. This method is called "steady-state theory" (Napolitano, 1961; Kahane *et al.*, 1954). However, if the solution "in the small" is wanted, the methods of characteristics should be employed.

In Fig. 10.31 four cases are shown describing shock wave interaction with a sudden area enlargement in a duct. Although the same geometry prevails in all four cases, the incident shock wave strength differs from case to case. The interface C is always formed since particles passing through the transmitted shock undergo an entropy rise, which is different from the sum of entropy rises when these particles pass through the remaining discontinuities.

In diagram (a) of Fig. 10.31 the incident shock wave is relatively weak and therefore the flow it produces, in all regions, is subsonic. Increasing the strength of the incident shock wave increases the strength of the reflected rarefaction waves; this process will continue until the flow leaving the narrow duct becomes sonic and region (5) disappears (Fig. 10.31b). An additional increase in the incident shock strength leads to a stationary shock at the plane of area change in the duct. This is so since the flow can no longer become subsonic isentropically in region (6) (Fig. 10.31c). A further increase in the strength of the incident shock wave turns the flow in region (3) to supersonic; no reflected waves can occur and the rarefaction waves disappear. An extreme situation is when the incident shock wave has such a strength that the secondary shock is swept toward the larger section and travels downstream as a backward-facing shock (Fig. 10.31d).

The previously described wave patterns depend on the incident shock strength and on the magnitude of the area change. They come out automatically when the procedure is applied on gradual changes in the cross-sectional area. However, they cannot be predicted when one deals with discontinuous area changes. Therefore, in practice one has to find out which of the patterns satisfies the pertinent equations together with the assigned initial conditions. In a corresponding way the interaction of simple waves with cross-section discontinuities can be treated (Ferri, 1961).

The extreme case in which the shock is swept downstream, which is demonstrated in Fig. 10.31d, corresponds to the flow visualization shown in Fig. 10.17. There the incident shock Mach number is about 3.0; it propagates into a channel having an abrupt area enlargement with a ratio of 1:10. The wave diagram (d) indicates that the transmitted shock is separated from the secondary shock by a contact surface (not visible in the shadowgraph of Fig. 10.17). The secondary shock wave is necessary for adjusting between the supersonic inflow and the subsonic expansion into the enlarged section of the duct.

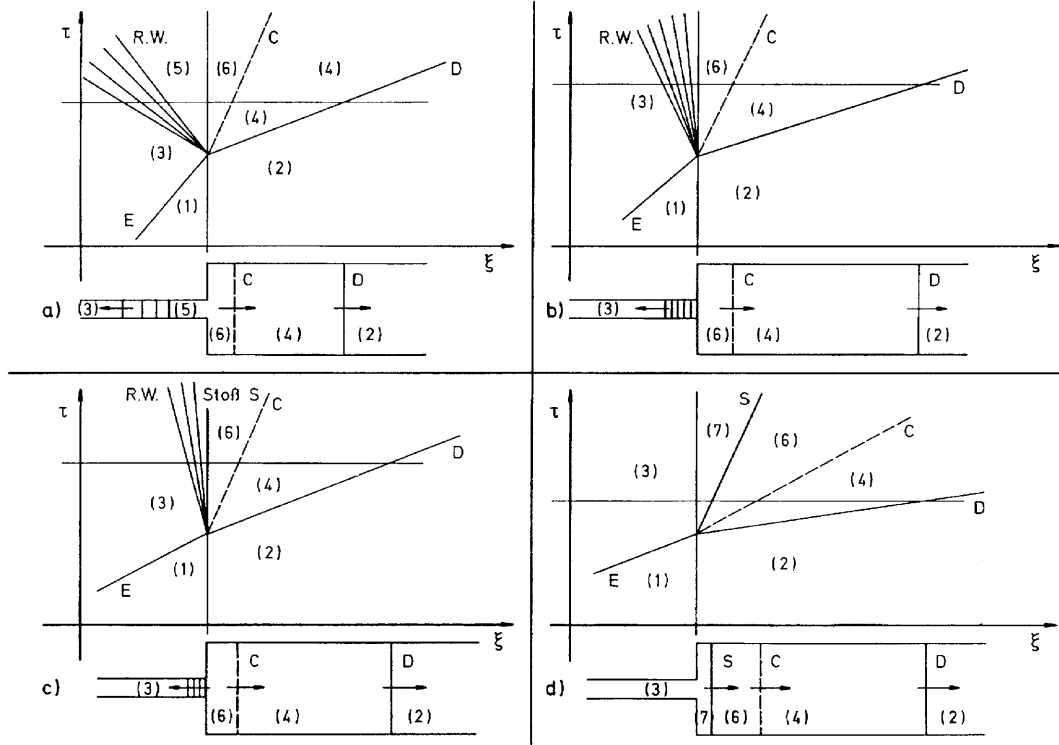


FIGURE 10.31 Four possible cases for the interaction of shocks with a discontinuous area change in ducts. E , incident shock; $R.W.$, rarefaction wave; S , secondary shock; C , contact surface; D , transmitted shock.

It is of interest to learn how the method works in the case mentioned. The analysis uses the Rankine–Hugoniot (RH) equations and assumes a quasi-one-dimensional, steady flow field. Under these assumptions and for two arbitrary flow regions with the indices 1 and 2 one has the continuity equation $A_1 \cdot \rho_1 \cdot u_1 = A_2 \cdot \rho_2 \cdot u_2$, which leads to $A_1 \cdot D_1 = A_2 \cdot D_2$, whereas

$$D = \frac{M}{(M^2 + f)^{(1+f)/2}}$$

with $f = 2/(\gamma - 1)$ (5 for air) and with M_1 and M_2 as the steady flow Mach numbers. Using the equation of state for a perfect gas leads to $(a_2/a_1)^2 = (p_2/p_1)/(\rho_2/\rho_1)$. The adiabatic condition is expressed as $p_2/p_1 = (\rho_2/\rho_1)^\gamma$ and the energy balance equation as $u^2 + fa^2 = fa_0^2$ (a_0 : reference sound speed), yielding $(a_n/a_2)^2 = (f + M_2^2)/(f + M_1^2)$.

Across the incident shock [(1) \rightarrow (3) in Fig. 10.31] the Rankine–Hugoniot equations yield

$$a_3/a_1 = 1.637; \quad u_3/a_1 = 2.222; \quad s_3 = 0.795; \quad p_3/p_1 = 10.33$$

(s_3 is the entropy jump). The equations for the nozzle flow yield (subscripts refer to flow regions as indicated in Fig. 10.31)

$$M_7 = 4.021; \quad a_7/a_1 = 0.931; \quad u_7/a_1 = 3.744; \quad p_7/p_1 = 0.2; \\ T_7/T_1 = 0.866,$$

with $T_1 = 293.16$ K and $T_7 = 253.75$ K, that is, a temperature decrease of roughly 40°C prevails.

A trial-and-error procedure is needed for determining the shock Mach numbers M_d and M_s of the transmitted and the secondary shock. States (2) and (1) are identical. Assuming $p_4/p_1 = 5$; then across C we have $p_6/p_1 = 5$ and using the RH one obtains $u_4/a_1 = u_6/a_1 = 1.359$. Using u_6/a_1 we are able to calculate the afterflow of the secondary shock: $|u_6 - u_7|/a_7 = 2.562$, which using the RH yields $p_6/p_7 = 13.09$. On the other hand, $p_6/p_7 = (p_6/p_1)/(p_7/p_1) = 5/0.2 = 25.0$. This is not consistent with 13.09. The appropriate value is $p_4/p_1 = 3.38$ which leads to a shock Mach number of $M_d = 1.74$ for the transmitted shock. From this $p_6/p_7 = 16.9$ follows, or $M_s = 3.83$ as the shock Mach number for the secondary shock. Because of $M_s < M_7$ the secondary shock is swept downstream as shown in the experiment.

This detailed treatment of a flow process according to the “steady state method” is an instructive example for understanding the behavior of shocks facing upstream but being swept downstream. For a detailed comprehension of a transient flow phenomenon, one has to resort to a numerical simulation. In Section 10.5 a numerical solution for this specific process is presented.

Several articles treat this subject (for example, Oppenheim *et al.*, 1964; Oertel, 1966; Laporte, 1954; Reichenbach and Dreizler, 1960).

10.4.3 THE CHESTER–CHISNELL–WHITHAM CHANNEL FORMULA

In many engineering problems considering compressible flow in ducts, a frequently encountered case is the interaction and propagation of shock waves via area change segments placed in the duct. In the following a brief review of approximate solutions to such a problem, as proposed by Chester (1953, 1960), Chisnell (1957), and Whitham (1958), is given. These approximate solutions were extensively used before the CFD era. As mentioned, detailed numerical solution to such interaction can be found in Greatrix and Gottlieb (1982), Gottlieb and Igra (1983), and Igra and Gottlieb (1985), in which the flow is treated as being unsteady but it is still assumed to be *quasi-one-dimensional*. Igra *et al.* (1998a) have treated the flow in ducts having area changed segments as truly two-dimensional flow.

The following Chester, Chisnell, and Whitham approximate solutions could be applied for a shock wave of finite strength traveling in a channel with continuously varying cross-section.

10.4.3.1 Whitham's Derivation

This procedure is rather short and illustrative. Equations (10.2) to (10.4) can be written in characteristic forms as

$$dp + \rho \cdot a \cdot du + \frac{\rho \cdot a^2 \cdot u}{u + a} \cdot \frac{dA}{A} = 0 \quad \text{along the } C_+ \text{ characteristic:} \quad \frac{dx}{dt} = u + a \quad (10.6a)$$

$$dp - \rho \cdot a \cdot du + \frac{\rho \cdot a^2 \cdot u}{u - a} \cdot \frac{dA}{A} = 0 \quad \text{along the } C_- \text{ characteristic:} \quad \frac{dx}{dt} = u - a \quad (10.6b)$$

$$dp - a^2 \cdot d\rho = 0 \quad \text{along the } P \text{ characteristic:} \quad \frac{dx}{dt} = u, \quad (10.6c)$$

where a is the speed of sound.

These equations can now be linearized assuming that the initial cross-section area (A_1) is uniform and the flow behind the incident shock is

described by index 1. Flow perturbations produced by the small area change dA , which allows a first-order approximation, can be expressed as

$$dp + \rho_1 \cdot a_1 \cdot du + \frac{\rho_1 \cdot a_1^2 \cdot u_1}{u_1 + a_1} \frac{dA}{A_1} = 0$$

along the C_+ characteristic: $\frac{dx}{dt} = u_1 + a_1$ (10.7a)

$$dp - \rho_1 \cdot a_1 \cdot du + \frac{\rho_1 \cdot a_1^2 \cdot u_1}{u_1 - a_1} \frac{dA}{A_1} = 0$$

along the C_- characteristic: $\frac{dx}{dt} = u_1 - a_1$ (10.7b)

$$dp - a_1^2 \cdot d\rho = 0 \quad \text{along the } P \text{ characteristic: } \frac{dx}{dt} = u_1. \quad (10.7c)$$

Furthermore, from the RH relations across a planar shock front, one obtains

$$\frac{p}{p_1} = z = \frac{1}{\gamma + 1} (2\gamma \cdot M^2 - (\gamma - 1)) \quad (10.8)$$

$$\frac{u}{a_1} = \frac{2}{\gamma + 1} \left(M - \frac{1}{M} \right) = (z - 1) \left[\frac{2}{\gamma \cdot [(\gamma + 1) \cdot z + (\gamma - 1)]} \right]^{1/2} \quad (10.9)$$

$$\frac{\rho}{\rho_1} = \frac{(\gamma + 1) \cdot M^2}{2 + (\gamma - 1) \cdot M^2} = \frac{(\gamma + 1) \cdot z + (\gamma - 1)}{(\gamma + 1) + (\gamma - 1) \cdot z} \quad (10.10)$$

$$\frac{a}{a_1} = \sqrt{\frac{p/p_1}{\rho/\rho_1}}, \quad (10.11)$$

where z is the pressure ratio across the shock wave moving through the area change dA and M is the shock Mach number. The pressure p , the velocity u , the density ρ , and the sound speed a are functions of z .

Substituting the shock transition relations (10.8) to (10.11) into (10.6) yields

$$\frac{M}{M^2 - 1} \cdot \lambda(M) \cdot \frac{dM}{dx} + \frac{1}{A} \cdot \frac{dA}{dx} = 0 \quad (10.12)$$

where

$$\lambda(M) = \left(1 + \frac{2}{\gamma + 1} \cdot \frac{1 - \mu^2}{\mu} \right) \cdot \left(1 + 2 \cdot \mu + \frac{1}{M^2} \right)$$

and

$$\mu^2 = \frac{(\gamma - 1)M^2 + 2}{2\gamma M^2 - (\gamma - 1)}.$$

This relation provides the small change dM , which results from the interaction of the shock wave (having shock Mach number M) with the small area change dA . The integration can be written as

$$\frac{A}{A_0} = \frac{f(M)}{f(M_0)} \quad \text{where} \quad f(M) = \exp\left(-\int_{M_0}^M \frac{m \cdot \lambda(m)}{m^2 - 1} \cdot dm\right). \quad (10.13)$$

In the literature this elegant procedure is called “Whitham’s Rule.” It is based on the idea that the C_+ characteristics in the (x, t) plane reach the shock front when it moves into the duct segment of changing cross-section. They carry the values of the Riemann invariant R_+ consisting of the postshock initial conditions and communicate these to the shock front. Thus, the shock strength z is changed. For more detailed information see Whitham (1974) and Igra *et al.* (1994).

10.4.3.2 Chester’s Derivation

Equation (10.12) was first derived by Chester (1953, 1960), who solved the linearized equations of motion for the flow behind a transmitted shock wave. Chester’s analysis also indicates that the obtained results are valid when the flow variables are averaged over the flow cross-sectional area during the actual motion through the area change segment. There is no need to wait until the shock wave, progressing through the segment, retains its planar shape.

10.4.3.3 Chisnell’s Derivation

Chisnell (1957) reached Eq. (10.12) using the steady-state theory. The channel considered is depicted in Fig. 10.32. Only the final flow (to be reached after all disturbances have subsided) is considered. In such a case the conditions behind the transmitted shock wave are independent of time, and the shock itself is moving along the downstream section with uniform strength. For a channel with a contraction as well as for an expansion, experimental evidence supports the assumption that the resulting wave pattern includes a transmitted shock wave, a reflected shock wave, or a rarefaction wave for the geometry in Fig. 10.32. Furthermore, it is necessary to include a contact discontinuity in the downstream section for matching between the different parts of the flow.

Using the nomenclature presented earlier, the incident shock wave strength is denoted by (see (10.8) also)

$$z = p_2/p_1. \quad (10.14)$$

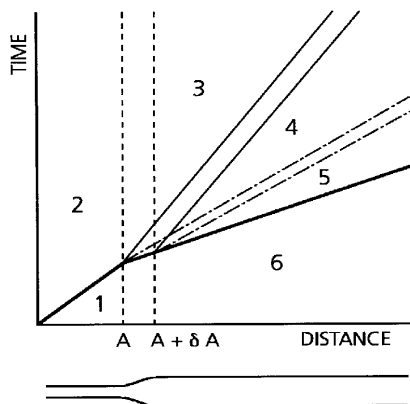


FIGURE 10.32 x - t diagram showing the interaction of a planar shock wave with an area enlargement in a duct. The interaction between a planar incident shock wave and a small area change segment extending from area A to area $A + \delta A$ is shown. The transmitted shock wave separates between regions 5 and 6. The fluid in the area change is set in motion and separates regions 4 and 5 by a contact discontinuity. A weak reflected disturbance is separating regions 3 and 4.

The transition from region 2 to region 3 is studied using mass and momentum conservation equations together with the relations for a steady isoennergetic flow, that is,

$$\frac{d\rho}{\rho} + \frac{du}{u} + \frac{dA}{A} = 0, \quad u \cdot du + \frac{dp}{\rho} = 0, \quad dp = a^2 \cdot d\rho. \quad (10.15)$$

From these relations one obtains

$$\frac{p_3}{p_2} = 1 - \frac{\gamma \cdot M_2^2}{(M_2^2 - 1)} \cdot \frac{\delta A}{A} \quad (10.16a)$$

$$\frac{\rho_3}{\rho_2} = 1 - \frac{M_2^2}{(M_2^2 - 1)} \cdot \frac{\delta A}{A} \quad (10.16b)$$

$$\frac{u_3}{u_2} = 1 + \frac{1}{(M_2^2 - 1)} \cdot \frac{\delta A}{A}. \quad (10.16c)$$

The double dotted-dashed line (Fig. 10.32) separates the fluid into parts that initially were on either side of the area change. After disturbances generated by the shock wave interaction with the area change segment have subsided, there will be no pressure and velocity disturbances in these regions; however, density, temperature, and entropy changes are still left. Therefore, one has

$$p_4 = p_5, \quad u_4 = u_5. \quad (10.17)$$

Once the shock has passed the area change its strength changes to $z + dz$. The flow in region 5 is described by a set of equations corresponding to Eqs. (10.8) to (10.11) with z replaced by $z + dz$ (conditions in region 1 and region 6 are identical). Combining all pressure and velocity equations for regions 3 and 4 one obtains

$$\frac{p_4}{p_3} = 1 + \frac{\delta z}{z} + \frac{\gamma \cdot M_2^2}{M_2^2 - 1} \cdot \frac{\delta A}{A} \quad (10.18)$$

$$\frac{u_4}{u_3} = 1 + \frac{\delta z}{z - 1} - \frac{(\gamma + 1)}{2 \cdot [(\gamma + 1) \cdot z + (\gamma - 1)]} \cdot \delta z - \frac{1}{(M_2^2 - 1)} \cdot \frac{\delta A}{A}. \quad (10.19)$$

The boundary between regions 3 and 4 must be interpreted as a sound wave, across which the pressure and the velocity jump can be derived by the expansion of $p_4 - p_3$ in powers of $u_4 - u_3$, (Courant and Friedrichs, 1948). The 1. Order expansion $p_4 - p_3 = -\rho_3 \cdot a_3 \cdot (u_4 - u_3)$ leads directly to

$$\frac{p_4}{p_3} = 1 - \gamma \cdot M_3 \cdot \left(\frac{u_4}{u_3} - 1 \right). \quad (10.20)$$

When we substitute Eqs. (10.18) and (10.19) into (10.20), a relation between the first order quantities of δA and δz results. It still contains M_2 and M_3 , which differ by a term of $\delta A/A$, thus, letting $\delta A \rightarrow 0$, both values may be replaced by $u_2/a_2 = M_2$, which could be evaluated from (10.9). After some algebra the following is reached:

$$\begin{aligned} -\frac{1}{A} \frac{dA}{dz} &= \frac{1}{\gamma \cdot z} + \frac{1}{z - 1} - \frac{(\gamma + 1)}{2 \cdot [(\gamma + 1) \cdot z + (\gamma - 1)]} \\ &+ \left[\frac{2}{\gamma \cdot z \cdot [(\gamma - 1) \cdot z + (\gamma + 1)]} \right]^{1/2} \\ &\times \left[1 - \frac{(\gamma + 1) \cdot (z - 1)}{2 \cdot [(\gamma + 1) \cdot z + (\gamma - 1)]} + \frac{(\gamma - 1) \cdot z + (\gamma + 1)}{2 \cdot (z - 1)} \right]. \end{aligned} \quad (10.21)$$

An equivalent formula was given in Chester (1960).

According to the derivation of (10.21) by matching steady-state flows in region 2 and 6—only time-independent relations are used—one obtains a solution valid only for long times after the interaction of the incident shock wave with the area change segment in the duct. Chester, however, solved only the linearized problem. He was able to show that the averaged shock strength depends only on the cross-sectional area of the channel. Thus, after the shock has passed the area change segment, the averaged shock strength $z + dz$ is constant and is given by the foregoing analysis.

Integration of (10.21) leads to the shock-strength/area relation

$$A \cdot f(z) = \text{const.}, \quad (10.22)$$

where

$$f(z) = z^{1/\gamma} \cdot (z - 1) \cdot \left(z + \frac{\gamma - 1}{\gamma + 1} \right)^{-1/2} \cdot \left[\frac{1 + R}{1 - R} \right]^{\sqrt{(\gamma/2)(\gamma-1)}} \cdot \left[\frac{R - \left(\frac{\gamma - 1}{2\gamma} \right)^{1/2}}{R + \left(\frac{\gamma - 1}{2\gamma} \right)^{1/2}} \right] \\ \times \exp \left[\left(\frac{2}{\gamma - 1} \right)^{1/2} \cdot \tan^{-1} \left\{ \frac{2\gamma^{1/2} R}{\gamma - 1} \right\} \right]$$

$$R = \left\{ 1 + \frac{(\gamma + 1)}{(\gamma - 1) \cdot z} \right\}^{-1/2} \\ z = \frac{2\gamma}{\gamma + 1} \cdot M^2 - \frac{\gamma - 1}{\gamma + 1}.$$

The preceding equation is valid for continuously varying cross-sectional area in a duct and for finite total changes. For large area changes, this equation provides only a rough approximation to the average shock strength because disturbances caused by reflected shock waves are no longer negligible. By neglecting these disturbances Eq. (10.22) becomes an approximate one for the average shock strength. Chisnell (1957) suggested that it is a relation between the shock Mach number and the cross-sectional area when the latter represents an arbitrary and continuous change, but with no restriction to small perturbations, which are not always insignificant. For the problem of converging cylindrical and spherical shocks, Chisnell's function is very accurate, because the perturbations that overtake the shock front cancel out. Chisnell (1957) also obtained Eq. (10.22) by integration of Eq. (10.12).

In the following subsections some applications of the Chester–Chisnell–Whitham channel formula are presented.

10.4.4 WHITHAM'S THEORY OF SHOCK DYNAMICS

Based on the foregoing discussion about shock wave propagation in channels, Whitham developed an approximate theory suitable for describing propagation of curved shocks. This theory was used in a wide range of applications, since it is founded on a solid basis of shock dynamics, using analytical methods. It predicts the shape of a moving shock wave as well as its strength. The predictions were favorably compared with experimental findings such as shadow-schlieren photos, direct pressure measurements, and interferometry

(Bryson and Gross, 1961; Heilig, 1969). For a detailed derivation of Whitham's theory the reader is advised to go to the source (Whitham, 1957, 1959). The aim of this subsection is to outline the theory for the shock wave diffraction in a two-dimensional flow field. This can easily be extended for studying shock wave diffraction in branched channels.

10.4.4.1 Whitham's Solution for Two-Dimensional Shock Wave Diffraction

A set of curves with coordinates $\alpha = \text{constant}$ is considered (Fig. 10.33) as it is formed by the positions in time sequence of a curved shock moving into a uniform medium. Additionally, "rays" are introduced with coordinates $\beta = \text{constant}$ forming an orthogonal set to the shocks.

As the quantity α is proportional to time, the term

$$\alpha = a_0 \cdot t \quad (10.23)$$

can be written, where a_0 stands for the preshock sound speed. When the shock wave at time t and at some ray coordinate β has a velocity U , the line element ds_1 along this ray between the shock positions α and $\alpha + d\alpha$ is given by

$$ds_1 = U \cdot dt = \frac{U}{a_0} \cdot a_0 \cdot dt = M(\alpha, \beta) \cdot d\alpha, \quad (10.24)$$

where M is the shock Mach number. The line element ds_2 along a shock $\alpha = \text{constant}$ between the ray positions β and $\beta + d\beta$ is built in an analogous way:

$$ds_2 = A(\alpha, \beta) \cdot d\beta. \quad (10.25)$$

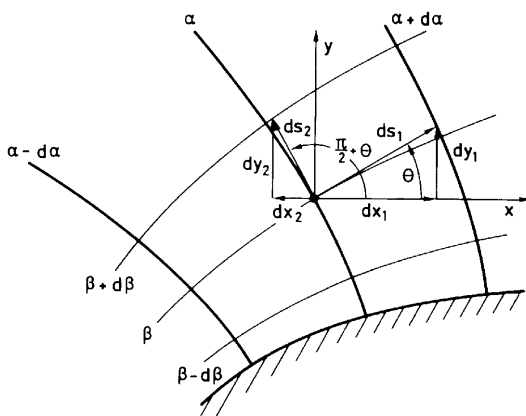


FIGURE 10.33 $(\alpha-\beta)$ and $(x-y)$ system of coordinates in Whitham's theory.

It can be shown that between the dependent variables M and A the following relation holds:

$$\frac{\partial}{\partial \alpha} \left(\frac{1}{M} \cdot \frac{\partial A}{\partial \alpha} \right) + \frac{\partial}{\partial \beta} \left(\frac{1}{A} \cdot \frac{\partial M}{\partial \beta} \right) = 0. \quad (10.26)$$

A second equation between M and A is required. To this end Whitham considered the shock propagation between two neighboring rays as a propagation in a channel having solid walls. The function $A(\alpha, \beta)$ represents the cross-sectional area of the channel produced by neighboring rays. The channel formula $A = A(M)$ (see Eq. (10.13)) is applied, which is the integrated form of

$$\frac{dA}{A} = -\frac{M \cdot dM}{W^2(M)} \quad \text{with} \quad W(M) = \sqrt{\frac{(M^2 - 1)}{\lambda(M)}}. \quad (10.27)$$

It is found that

$$\frac{dA}{dM} = A'(M) < 0,$$

and therefore, (10.26) is a second-order hyperbolic equation for M expressed with the independent variables α and β . Introducing the angle $\Theta = \Theta(\alpha, \beta)$ between a ray and the x -axis, which, as function of α and β , has continuous higher derivatives, the following system of two first-order quasi-linear hyperbolic equations is obtained:

$$\frac{\partial \Theta}{\partial \beta} - \frac{A'(M)}{M} \cdot \frac{\partial M}{\partial \alpha} = 0 \quad (10.28a)$$

$$\frac{\partial \Theta}{\partial \alpha} + \frac{1}{A(M)} \cdot \frac{\partial M}{\partial \beta} = 0. \quad (10.28b)$$

The characteristic forms are

$$\Theta + \int \frac{dM}{A \cdot c} = C_1 = \text{constant} \quad \text{on} \quad \frac{d\beta}{d\alpha} = +c(M) \quad (10.29a)$$

$$\Theta - \int \frac{dM}{A \cdot c} = C_2 = \text{constant} \quad \text{on} \quad \frac{d\beta}{d\alpha} = -c(M). \quad (10.29b)$$

Here, $c(M)$ represents the speed of a wave moving in the β direction with respect to α ; it holds that

$$c(M) = \frac{W(M)}{A(M)}. \quad (10.30)$$

10.4.4.2 Application of Whitham's Theory for Treating Shock Wave Diffraction around a Convex Corner

The theory results in a simple form when it is applied to a case of shock wave diffraction over a deflected wall (causing a flow expansion as in Fig. 10.34). In this case the solution of the system (10.29a) and (10.29b) is the so-called simple wave; it is analogous to ordinary gasdynamic solutions of Riemann's invariants. When a flow region is adjacent to a region of constant state the solution is always a simple wave with a characteristic serving as the separation line (see LP_0 in Fig. 10.34). Instead of (10.29a) and (10.29b), we now have

$$\Theta + \int \frac{dM}{A \cdot c} = \text{constant} = C_1 \quad \text{on} \quad \frac{d\beta}{d\alpha} = +c(M) \quad (10.31a)$$

$$\Theta - \int \frac{dM}{A \cdot c} = \text{constant} = C_2 \quad \text{everywhere else} \quad (10.31b)$$

It follows from the foregoing, first, that on each left-running characteristic the dependent variables M and Θ are individually constant, and secondly, that (from (10.31a)) the left-running characteristics are straight lines having a slope of

$$\beta = c(M) \cdot \alpha. \quad (10.32)$$

The theory becomes applicable when it is formulated in the $(x-y)$ coordinate system (see Fig. 10.33). Introducing the new independent variables,

$$x = x(\alpha, \beta) \quad y = y(\alpha, \beta), \quad (10.33)$$

the relations

$$x_\alpha = M \cdot \cos \Theta; \quad x_\beta = -A \cdot \sin \Theta \quad \text{and} \quad y_\alpha = M \cdot \sin \Theta; \quad y_\beta = A \cdot \cos \Theta \quad (10.34)$$

hold, with $x_\alpha = (\partial x / \partial \alpha)$, etc. The last expressions are easily derivable from Fig. 10.33 with the aid of the line elements. The general form for the characteristic slopes, given in Eqs. (10.29a) and (10.29b), is now reduced to

$$\frac{dy}{dx} = \tan(\Theta \pm m) \quad \text{with} \quad \tan m = \frac{A(M) \cdot c(M)}{M} = \frac{W(M)}{M} \quad (10.35)$$

(the upper sign corresponds to (10.29a), the lower to (10.29b)).

The relations (10.34) along a shock ($\alpha = \text{constant}$) and separately, along a ray ($\beta = \text{constant}$) can be integrated (Skews, 1967; Heilig, 1978b). The integration starts from $dx = -A \cdot \sin \Theta \cdot d\beta$ (Eq. (10.34)) and uses $\beta = c(M) \cdot \alpha$ (Eq. (10.32)). This yields, with Eq. (10.30), $d\beta = c'(M) \cdot dM = 1/A \cdot (W' + M/W) \cdot \alpha \cdot dM$. The equation to be integrated is $dx = -\sin \Theta \cdot (W' + M/W) \cdot \alpha \cdot dM$ with

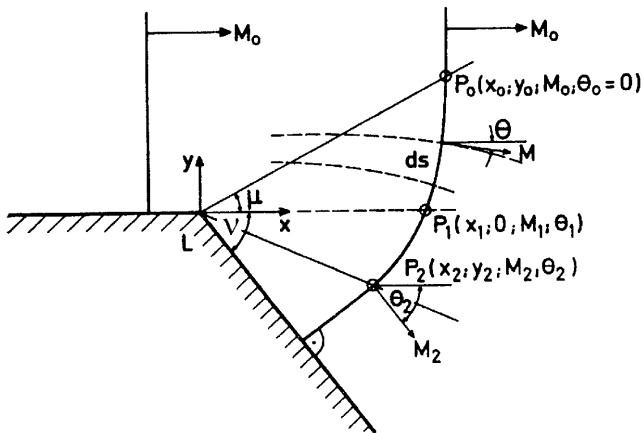


FIGURE 10.34 Diffraction of a planar shock wave, having a shock Mach number M_0 , around a convex corner of angle ν according to Whitham's theory.

$\Theta = \Theta(M)$. One finds

$$x = \alpha \cdot M \cdot \frac{\cos(\Theta + m)}{\cos m} + C_3. \quad (10.36)$$

The integration constant C_3 is determined by the flow initial conditions. The "point" P_0 (Fig. 10.34) has the coordinates

$$x_0 = \alpha \cdot M_0 \quad \text{and} \quad y_0 = \tan[\Theta(M_0) + m(M_0)] \cdot x_0 \quad \text{with} \quad \Theta(M_0) = 0. \quad (10.37)$$

It follows that $C_3 = 0$.

In a similar way the integration of $dy = A \cdot \cos \Theta \cdot d\beta$ is performed to result in

$$y = \alpha \cdot M \cdot \frac{\sin(\Theta + m)}{\cos m} + C_4. \quad (10.38)$$

Inserting the initial flow conditions $C_4 = 0$ follows.

The equations for the rays are

$$x = \beta \cdot A \cdot \frac{\cos(\Theta + m)}{\sin m} + C_5 \quad (10.39)$$

$$y = \beta \cdot A \cdot \frac{\sin(\Theta + m)}{\sin m} + C_6. \quad (10.40)$$

Again, from (10.37), $C_5 = C_6 = 0$ follows.

The constant α appearing in (10.36) and (10.38) indicates that the locations of the diffracted shock wave front at successive times t are geometrically similar with respect to the corner L , which is the center of expansion (Fig. 10.34). After Whitham, the diffraction process at a convex corner is pseudo-steady. In order to numerically evaluate (10.36) and (10.38) and likewise (10.39) and (10.40) for a given M_0 and a given deflection angle v , one proceeds as follows: The constant in (10.31b) is chosen so that the relation

$$\Theta = \int_{M_0}^M \frac{d\xi}{W(\xi)} \quad \text{with} \quad M \leq M_0 \quad (10.41)$$

is satisfied. With this the shock wave Mach number M_2 , at the tail of the expansion fan (LP_2 in Fig. 10.34) is calculated according to

$$v = -\Theta_2 = \int_{M_0}^{M_2} \frac{d\xi}{W(\xi)}. \quad (10.42)$$

The integral has to be evaluated numerically together with a root finder to determine M_2 . Choosing a value for M , within the interval $M_2 \leq M < M_0$, yields a value for Θ , and finally one obtains the space variables x and y of the shock contour ((10.36) and (10.38)) and of the rays ((10.39) and (10.40)). A sample calculation is given with the results shown in Fig. 10.35, where the incident shock ($M_0 = 3.08$) diffracts around a right-angle corner. Points in Fig. 10.35 represent contours of the diffracting shock wave as evaluated from shadowgraph series. The agreement between the experimental and calculated shock fronts is striking. Discrepancies increase for weaker incident shocks. For all M_0 the expansion fan (LP_0P_2 in Fig. 10.34) ends in the free flow field. The part of the diffracted shock leaving the fan at P_2 is planar again and of constant strength. For additional information on this topic, see Bazhenova and Gvozdeva (1987).

Following Whitham's theory the space variables of a diffracted shock and its intensity can be calculated. But the theory is not able to treat the flow region behind the moving shock. That is due to the assumption that the shock between two neighboring rays propagates as in a channel composed of solid walls. This would be true if the rays were particle paths, but in reality only behind the shock front the particles move along the ray direction.

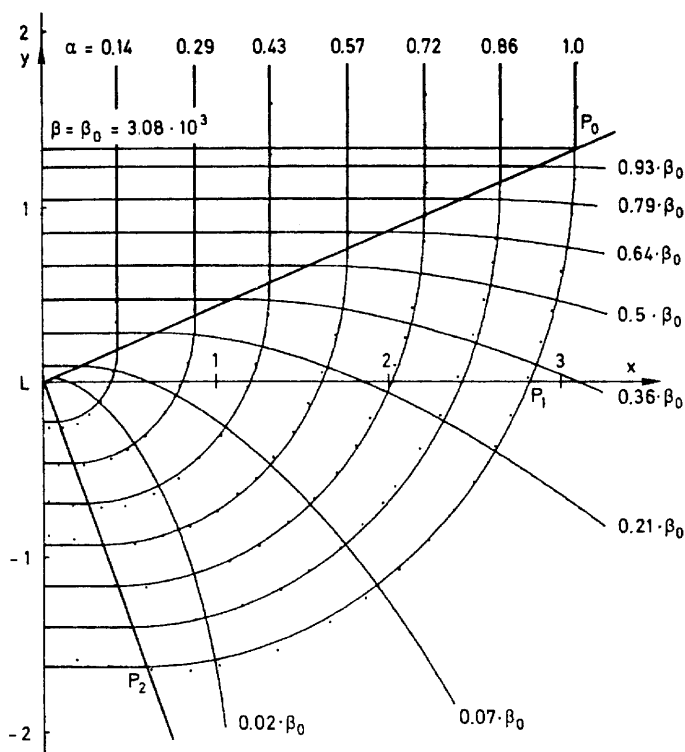


FIGURE 10.35 Data points indicate contours of diffracted shocks deduced from a shadowgraph obtained for $M_0 = 3.08$. The solid lines are the shocks α and the rays β after Whitham's theory.

10.4.5 ANALYTICAL TREATMENT OF SHOCK PROPAGATION THROUGH A CLASS OF BIFURCATED DUCTS USING WHITHAM'S THEORY

In the framework of the approximate analytical treatment of shock wave propagation in channels, a few examples are described.

Consider the propagation of a shock wave through the geometry shown in Fig. 10.36, where the main duct contains a 45° side branch. The problem is to determine the strength M_T of the wave transmitted into the main branch and the strength of the shock M_D in the 45° branch. In the subsequent, approximate analytical solution, the shock waves strengths are evaluated after all disturbances (due to multiple shock reflections) subsided and both transmitted waves obtain planar fronts.

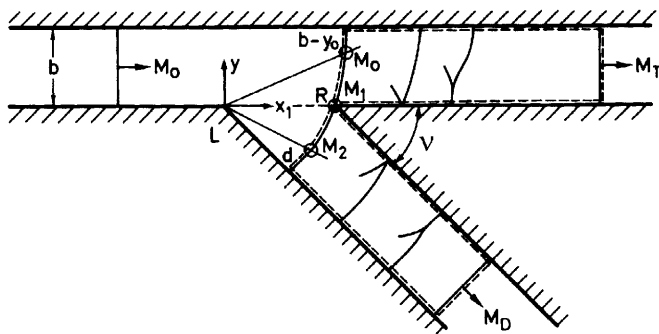


FIGURE 10.36 Schematic description of shock wave propagation through a 45° branched duct.

10.4.5.1 Description of the Analytical Model

The incident shock, after its diffraction at the corner L, is shown in Fig. 10.36 at the moment when it reaches the sharp edge R of the junction. There it is split up into two curved shocks, each traveling into one of the ducts. As shown in previous shadowgraphs (see Fig. 10.28) the waves enter as curved shocks, and upon traveling downstream through the ducts, their fronts become planar. This occurs via a sequence of alternating regular and Mach reflections at the opposite channel walls, during which the reflected shock overtakes the first shock, thus bringing back some of the energy consumed during interactions with the duct's walls. In this way the postshock flow approaches a uniform flow state. It is postulated that the energy of the incident shock wave is divided according to the way that it is split up at point R, that is, the energy associated with the curved shock upon its entrance into the main duct is conserved during its steepening. The same is true for the curved shock entering the branched duct. Certainly this is a rough assumption, since it neglects viscous and heat losses. It also ignores dissipated energy through the head shock possibly arising at R (Fig. 10.36), via vortices (Fig. 10.28), by the upstream propagating weak reflected shock (in the case of subsonic flow, Fig. 10.28), and through secondary shocks in the branches (Fig. 10.27). Therefore, it can be expected that the proposed model predicts shock strengths larger than the measured values (for details see: Heilig, 1975; Heilig 1978a).

If we observe the control volume ABCD, shown in Fig. 10.37, the energy balance across the shock wave obviously is given by

$$\epsilon(t) = x_0 \cdot Q \cdot \rho_0 \cdot c_v \cdot T_0 + x_1 \cdot Q \cdot \rho_1 \cdot \left(c_v \cdot T_1 + \frac{1}{2} \cdot u_1^2 \right) \quad (10.43)$$

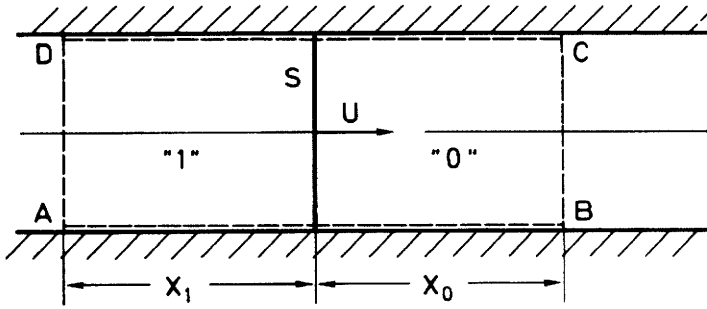


FIGURE 10.37 Schematic description showing a control volume used for deriving the energy balance across a shock wave.

where Q is the duct's cross-sectional area, u_1 is the postshock flow velocity, and U is the propagation velocity of the incident shock wave into the quiescent gas ahead of it. At the time $t + \Delta t$ one has

$$\begin{aligned} \epsilon(t + \Delta t) = & (x_0 - U \cdot \Delta t) \cdot Q \cdot \rho_0 \cdot c_v \cdot T_0 \\ & + (x_1 + U \cdot \Delta t) \cdot Q \cdot \rho_1 \cdot \left(c_v \cdot T_1 + \frac{1}{2} \cdot u_1^2 \right). \end{aligned} \quad (10.44)$$

With the aid of the sound speed a_0 and of the preshock pressure p_0 , the term

$$E = \frac{\epsilon(t + \Delta t) - \epsilon(t)}{Q \cdot a_0 \cdot p_0 \cdot \Delta t} \quad (10.45)$$

can be expressed as

$$E = \left(\rho_1 \cdot c_v \cdot T_1 + \frac{1}{2} \cdot \rho_1 \cdot u_1^2 - \rho_0 \cdot c_v \cdot T_0 \right) \cdot \frac{U}{p_0 \cdot a_0}. \quad (10.46)$$

E represents the nondimensional increase, per unit time, in energy that a shock traveling with speed U brings into the control volume.

Equation (10.46) can also be written in terms of the shock wave Mach number as

$$E = \left(z + \frac{(z-1)^2}{r+z} - 1 \right) \cdot \sqrt{\frac{r \cdot z + 1}{2 \cdot \gamma \cdot (\gamma - 1)}} \quad (10.47)$$

where

$$z = \frac{1}{r} \cdot \left(\frac{2 \cdot \gamma}{\gamma - 1} \cdot M^2 - 1 \right); \quad r = \frac{\gamma + 1}{\gamma - 1}. \quad (10.48)$$

Applying this idea to the channel having a 45° branch (Fig. 10.36) results in the following for the main channel:

$$\int_{M_1}^{M_0} E(M) \cdot \tau \cdot ds + E(M_0) \cdot \tau \cdot (b - y_0) = E(M_T) \cdot \tau \cdot b \quad \text{with} \quad b = x_1 \cdot \sin v \quad (10.49)$$

And, for the side branch

$$\int_{M_2}^{M_1} E(M) \cdot \tau \cdot ds + E(M_2) \cdot \tau \cdot d = E(M_D) \cdot \tau \cdot b. \quad (10.50)$$

M_0 is the Mach number of the incident shock wave; M is the Mach number along the curved shock wave. M_1 is the Mach number of the diffracted shock wave when it touches point R. The value of M_1 follows from Eqs. (10.38), (10.35), and (10.42); that is,

$$y(M_1) = 0 = \Theta(M_1) + m(M_1) = \int_{M_0}^{M_1} \frac{d\xi}{W(\xi)} + \arctan\left(\frac{W(M_1)}{M_1}\right),$$

which is an implicit equation for M_1 . M_2 is the Mach number of the shock at the end of the expansion fan shown in Fig. 10.36. M_2 can be evaluated from Eqs. (10.42). M_T is the Mach number of the eventually reached plane shock in the horizontal channel. M_D is the Mach number of the eventually reached plane shock wave in the branched channel. The line element along the curved shock (i.e., $\alpha = \text{const.}$) is $ds = ds_2 = A \cdot d\beta$ (Eq. (10.25)), and from Eqs. (10.32) and (10.27) follows

$$\frac{d\beta}{\alpha} = c'(M) \cdot dM \quad \text{yielding} \quad ds = \alpha \cdot \left(W' + \frac{M}{W} \right) \cdot dM.$$

The channel depth is τ (a dummy parameter). The height of the channel (2D flow) is b , with $b \geq y_0 \sin v$. This is the case for all incident shock strengths if $30^\circ \leq v \leq 90^\circ$ (v : angle of the side branch). The length of the straight portion of the diffracted shock when leaving the expansion fan at P_2 is $d = |y_2 \cdot \cos v - x_2 \cdot \sin v|$.

The values of M_T and M_D can be determined from solving Eqs. (10.49) and (10.50). Results are presented in Fig. 10.38.

The described procedure works for geometries like those shown in Fig. 10.36: that is, for geometries in which the transmitted shock wave is split up by an acute corner. Results obtained for a few different geometries are shown in Fig. 10.38. For channel geometries that do not have sharp corners, a different model, which is also based on the energy concept, was proposed (Peters and Merzkirch, 1975; Grönig, 1978; Imhof, 1976).

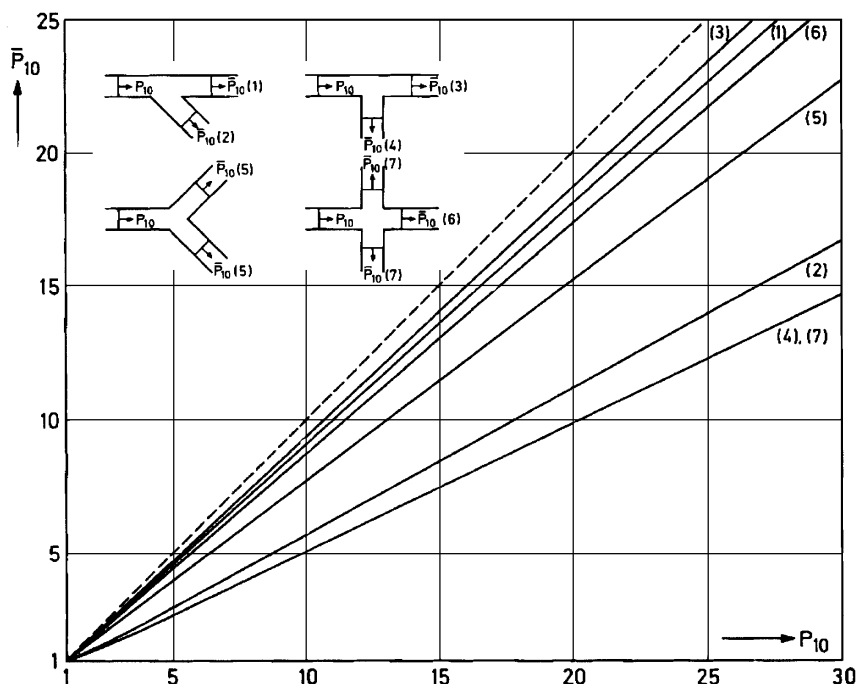


FIGURE 10.38 Graphical presentation of analytical results obtained for four different channel branchings.

In Fig. 10.38, P_{10} is the pressure ratio, p_1/p_0 , across the incident shock wave; p_1 is the postshock pressure; p_0 is the ambient pressure. \bar{P}_{10} stands for pressure ratios across the transmitted and deflected shock fronts in the various branches. The broken line represents a straight duct. It turns out that the shock strengths in the side branches of the 90° junction (4) and of the cross junction (7) are identical. Such a branching causes the strongest attenuation: More than 50% of the incident shock wave strength is lost. It is apparent that the curves in Fig. 10.38 are straight with the exception of a small region near the origin. As mentioned, the results provide strengths of the transmitted shocks after they have left the bifurcation region and regained a planar form.

10.4.5.2 Comparison between Calculated and Measured Transmitted Shock Strengths

For the branched duct geometries shown in Fig. 10.39, experimental data are available that were obtained in two different ways (Heilig, 1978a). The first

method was flow visualization in a shock tube having a test section of rectangular cross-section whose area is $Q_t = 4000 \text{ mm}^2$. From a series of 24 shadowgraphs, made during each experiment, with the help of a Cranz-Schardin multiple spark camera, the distance passed by the transmitted shocks could be measured. In addition, the time elapsed during this motion (given by the recording frequency of the camera) is also known. Based on this information the shock wave velocity is easily deduced. Using this velocity, the shock wave Mach number is evaluated, and based on this and the RH shock relations, the strength of the considered shock is easily determined. The second method is by direct pressure measurements using pressure gages. When employing this

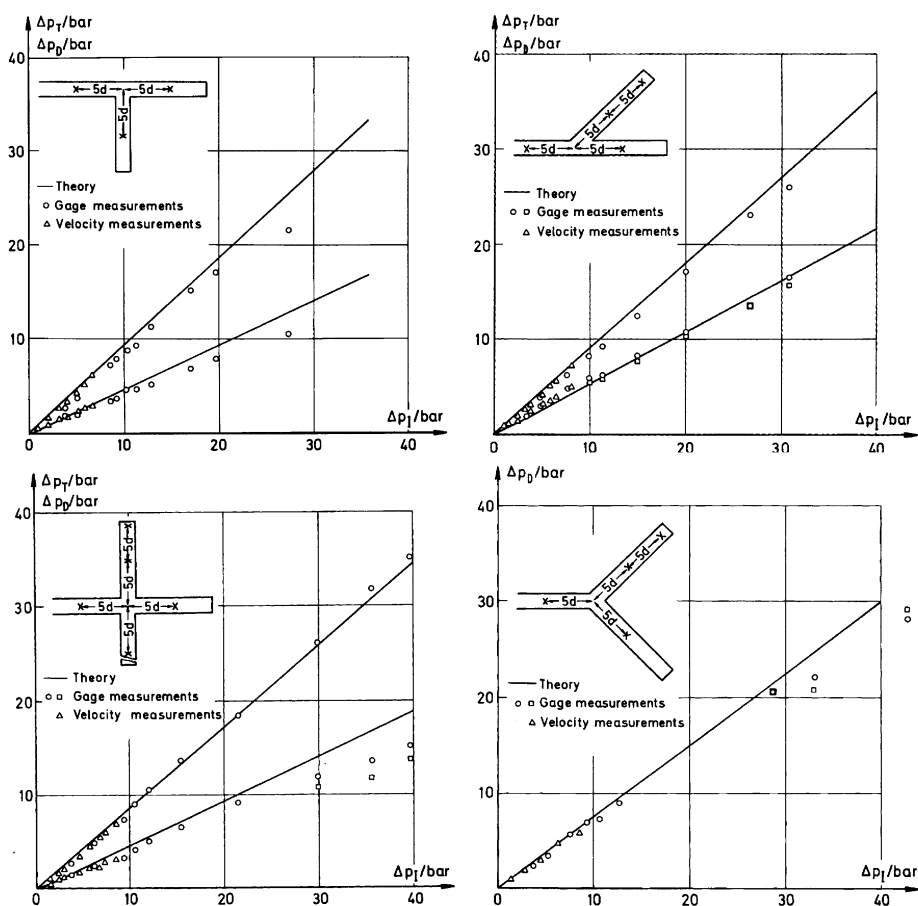


FIGURE 10.39 Comparison between analytical and experimental results.

method a tube with junctions having a circular cross-section area $Q_c = 1590 \text{ mm}^2$ was used. The pressure data are obtained by taking the first peaks in the pressure–time records.

In Fig. 10.39 $(\Delta p)_I$ stands for the overpressure (bar) behind the incident shock wave entering from left. $(\Delta p)_T$ and $(\Delta p)_D$ indicate the overpressures (bar) behind the shock wave transmitted or deflected through the branched channel. All overpressures are measured above the ambient pressure (1 bar). Symbols Δ are the pressure values obtained indirectly; from flow visualization. Symbols \circ and \square represent direct pressure measurements at ports placed 5 and 10 channel diameters away from the branching region, as shown in Fig. 10.39. The solid lines represent analytical solutions.

The results shown in Fig. 10.39 indicate that good agreement exists between experimental findings obtained for rectangular cross-section and for circular cross-section ducts, and those deduced from the analytical solution. Furthermore, there is no indication of the transition from subsonic to supersonic flow behind the incident shock wave, which occurs at $(\Delta p)_I = 3.9$ bar. Pressures change smoothly through the transition region. Discrepancies between pressure measurements conducted at 5 and 10 channel diameters d ($d = 45 \text{ mm}$) behind the branching section increase with increasing strength of the incident shock wave. The reasons that the theory predicts higher values than the measured ones, especially for stronger incident shocks, are that it ignores energy losses and assumes a quasi-one-dimensional flow in the analytical model. In summary, it can be stated that the observed agreement between experimental results and analytical predictions is striking, especially because of the simple approach made in constructing the analytical model.

It is of interest to compare the analytical predictions with results available in the literature. Diagrams shown in Fig. 10.40, for a 90° junction, are taken from Hammitt and Carpenter (1964). Their results contain both experimental and calculated data. It is apparent from Fig. 10.40 that analytical predictions are in good agreement with the measured values.

Measured and calculated pressures in the subsonic flow developed behind the transmitted shock wave in a 45° branched duct are shown in Fig. 10.41. The experimental results and the theoretical predictions (marked as (1)) are those of Dekker and Male (1968). Results marked as (2) are derived from the analytical model presented in the present subsection. It is apparent that the results derived from the present model are closer to measured values than Dekker and Male's predictions.

In summary, a branched duct geometry is effective in obtaining a meaningful attenuation of an incident shock wave. In the past most of the studies made with branched ducts were experimental and only approximate analytical models were suggested. These models assumed the flow to be a quasi-one-dimensional and free of losses. In many of these studies an attenuation

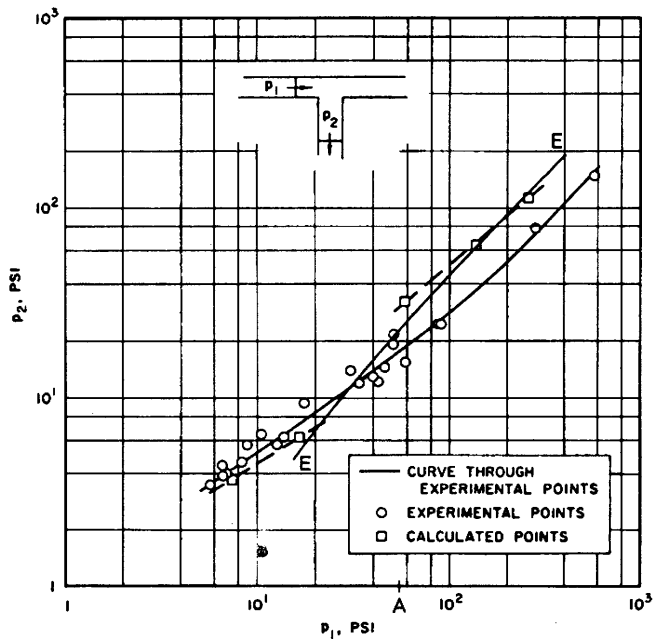
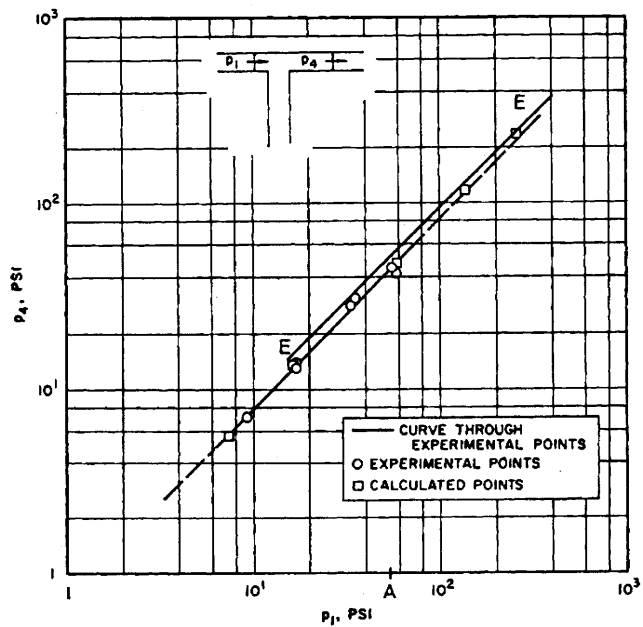


FIGURE 10.40 Comparison between Hammitt and Carpenter's experimental and calculated data obtained for a 90° junction with results derived from the proposed analytical model. The present analytical prediction is shown as solid line labeled E.

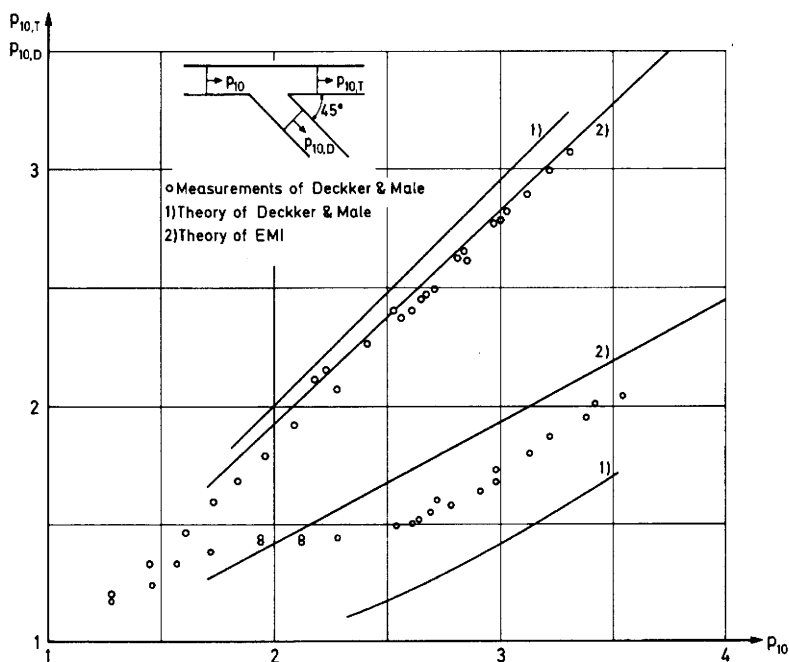


FIGURE 10.41 Comparison between calculated (curves (1)) and the measured (O-symbols) data of Dekker and Male obtained for a 45° junction and present results derived from the analytical model presented in the present subsection. p_{10} is the pressure ratio across the incident shock front; $p_{10,T}$ and $p_{10,D}$ are the pressure ratios across the transmitted shock fronts in the main and in the side branch, respectively.

parameter, F , was introduced. It is the overpressure produced by the transmitted shock wave divided by the overpressure produced by the incident shock wave.

10.5 NUMERICAL METHODS

The approximate methods presented in the previous sections contain limitations; they are not able to cover the entire flow field. It was shown that they predict the transmitted shock fronts in the branches of a channel system in good agreement with available experimental findings. However, they cannot predict the postshock flow parameters. Using these methods may lead to errors, such as when the loading on obstacles placed in a duct is under consideration. Relying only on the value of the shock front amplitude without

knowing the entire wave profile prohibits determination of the impulse acting on the hit structure. Assuming that the transmitted shock wave has a step profile may lead to an overestimation of the shock impulse. Furthermore, from the planarity of the transmitted shock front, no precise conclusions can be drawn on how much the shock wave has steepened up, that is, on the state of the postshock flow concerning its uniformity.

In order to overcome these limitations one resorts to numerical evaluations. These have to be time-dependent when dealing with traveling shock waves. Recent major developments of computer hardware and software meet these needs. Solving the conservation laws by appropriate numerical schemes enables the analyst to set up programs that are implemented into a code. It is adapted for repeatable runs on a high-performance computer and can be equipped with more or less comfortable pre- and postprocessors. The individually prepared codes mostly treat specific problems, whereas commercially available ones tend to cover wider ranges of application.

Two code types, among others, are commonly known and used.

The finite difference codes (FD) approximate the PDEs (partial differential equations of the conservation laws of mass, momentum, and energy) by difference equations and use an explicit integration method in the time domain. Mostly they are accurate to the second order in terms of the Taylor expansion. An additional equation is needed in order to fulfill the algebraic requirements. Treating air, this can be the ideal gas equation of state, which has a simple algebraic form. For solids a material law must be specified and the stress tensor is related to the strain, or to displacements. This can simply be Hooke's law. Unwanted oscillations, such as at shock fronts, are partially prevented by introducing the "artificial viscosity," which leads to a smearing of the shock across two or three grid points. Therefore, rise times are less realistic except when using very fine grids.

The finite element codes (FE) treat the PDEs in a completely different way. The one for the conservation of momentum is transformed into an equivalent variational integral according to the principle of minimizing the potential energy. The "shape functions" as polynomials of the first to third degree assign the displacement of every locus in the element to the displacement of the nodes. The local properties (mass, attenuation, stiffness) are collected in matrices. The solution in the time domain takes place either by the modal analysis or by direct time integration implicitly or explicitly. The FE codes enable treatment of complex geometries because they provide an extended stock of elements (rods, beams, plates, etc.), whereas the FD codes are restricted to corner fitted grids fixed in space (Euler coordinates). Common to all codes is that with finer grid and time resolution they converge to a stable solution, which, in principle, is the same one resulting either from an FD or from an FE code.

Great effort has been undertaken in developing new numerical schemes. For details, see Chapter 6.

For treating processes of shock wave propagation in channels and similar processes such as the loading of rigid obstacles, the FD codes are obviously suitable; they are therefore called wave propagation codes. But such processes can also be treated using FE codes. Compared with the approximate analytical methods and with experiments, code computations yield more information about the investigated process. They provide information on all flow variables, more than can normally be measured in experiments. Boundary conditions can be specified more realistically, such as by inclusion of physical wall properties (roughness, heat, etc.). Various gaseous media, such as dust and particle loaded air, can be set up. The time resolution of an unsteady process is higher than what is normally possible in experiments.

In order to be able to consciously rely on numerical results, a longer testing period must be conceded, during which comparison with experimental findings is crucial.

10.5.1 EXAMPLE CALCULATIONS USING WAVE PROPAGATION CODES

In the following a few examples of calculations regarding wave propagation in ducts employing frequently used codes are considered.

10.5.1.1 Application of SHAMRC: Shock Wave Propagation through a Channel having an Area Enlargement Ratio of 1 : 10

This computation is specifically conducted for comparison with visualization results and with the statements of the “steady-state method.” In Fig. 10.17 the incident shock wave ($M_0 = 3$) abruptly expands as a “cylindrical shock” from a narrow duct into a wider duct, whereas the area ratio of the cross-sections amounts to 1 : 10. The transmitted shock steepens, tends to become planar, and is attenuated. The wider channel in Fig. 10.17 is too short for this process to be completely observed. A secondary shock appears in the postshock flow region.

The process is simulated by applying SHAMRC (Second-order Hydrodynamic Automatic Mesh Refinement Code), frequently used for treating shock wave propagation. This code is a descendant of the HULL code (Matuska, 1984; Naz and Vermorel, 1988), which is an FD code and solves problems in the domain of detonations and impacts of large velocity. HULL was developed in the Air Force Weapons Laboratory starting in 1971 and originally applied to treat nuclear explosions. It was updated along the years and nowadays represents a hydrodynamic and elastic–plastic Eulerian code treating interac-

tions between different materials. For studying propagation of shock waves in gases, HULL was specifically prepared and called SHAMRC; it is now maintained by Applied Research (ARA), Albuquerque, NM (Needham and Crepeau, 1998). Extensive experience has accumulated with its application, especially in 2D computations. These are collected at several institutions. The grids in 2D are rectangular and an automatic mesh refinement option is included.

The input files of SHAMRC for the considered example are prepared in such a way that a shock wave ($M_0 = 3$) with step profile is generated in the narrow part of the duct. This is achieved by specifying the left boundary as an inflow boundary, which causes the postshock region to be uniform with flow parameters according to Rankine–Hugoniot relations. The boundaries for the narrow channel are chosen as $0.0 \leq x \leq 3.0$ and $5.5 \leq y \leq 6.5$, and for the wider channel $3.0 \leq x \leq 30.0$ and $1.0 \leq y \leq 11.0$ (cm). The walls are formulated as absolutely impermeable for any physical quantity. The computation is performed in 2D corresponding to the visualized process.

In Figs. 10.42a, 10.42b, and 10.42c isobars as well as the pressure histograms, evaluated along the duct's plane of symmetry, are shown for three time instants: 100, 200, and 400 μsec . The isobars can easily be compared with the shadow photos shown in Fig. 10.17.

The computed results shown in these figures are suitable for being compared with those of the “steady-state method” (Subsection 10.4.2), although the steady state is not reached as yet.

In Fig. 10.42a the pressure histogram along $y = 6$ cm, at the time instant 100 μsec , clearly exhibits the transmitted shock and the secondary upstream-facing shock wave. The pressure behind the incident shock wave is 10.33 bar (ambient pressure $p_1 = 1$ bar). When leaving the narrow channel the pressure decays rapidly to a low value p_λ comparable to $p_7 = 0.2$ bar (Subsection 10.4.2). Across the secondary shock the pressure increases from p_λ to about 3 bar. This is analogous to the steady-state value $p_6/p_7 = 16.9$, which, with $p_7 = 0.2$ bar, yields a value of $p_6 = 3.38$ bar. Thereafter, the pressure curve increases and reaches the transmitted shock wave. Its amplitude is $p_\tau = 3.8$ bar, which corresponds to the value of 3.38 bar (resulting from $M_d = 1.74$ in Subsection 10.4.2). Because of the strongly unsteady flow state prevailing at the considered time instant the comparison is only an approximate one.

In Fig. 10.42b the cylindrical transmitted shock of the previous figure is reflected from the duct's walls and Mach reflections occur. The reflected shocks interact at the plane of symmetry, producing a new shock, which appears just in front of the secondary shock. Both shocks will merge later. The secondary shock is stronger now and is swept downstream (compare with Fig. 10.42a).

In Fig. 10.42c the transmitted shock front approaches a planar shape. However, the postshock flow field is still nonuniform (oblique shocks, vortices). This indicates that a steady state is not reached at the considered

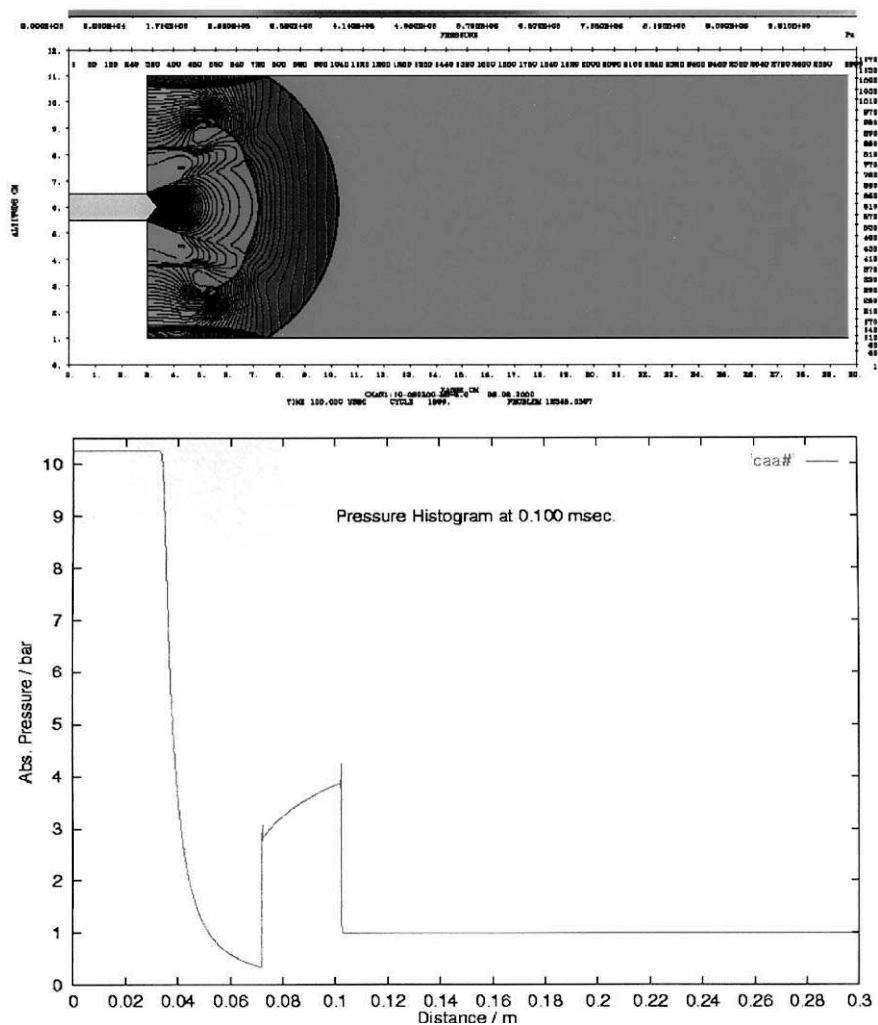


FIGURE 10.42 SHAMRC's isobars and pressure histograms (along the plane of symmetry: $y = 6$ cm) for the propagation of the transmitted shock wave ($M_0 = 3.0$) through an abrupt channel enlargement. The area ratio is 1:10. The figure shows the state of the flow (a) 100 μ sec, (b) 200 μ sec, and (c) 400 μ sec after flow initiation. The shock position at initiation time ($t = 0$ μ sec) is $x = 2.5$ cm. (See Color Plate 4).

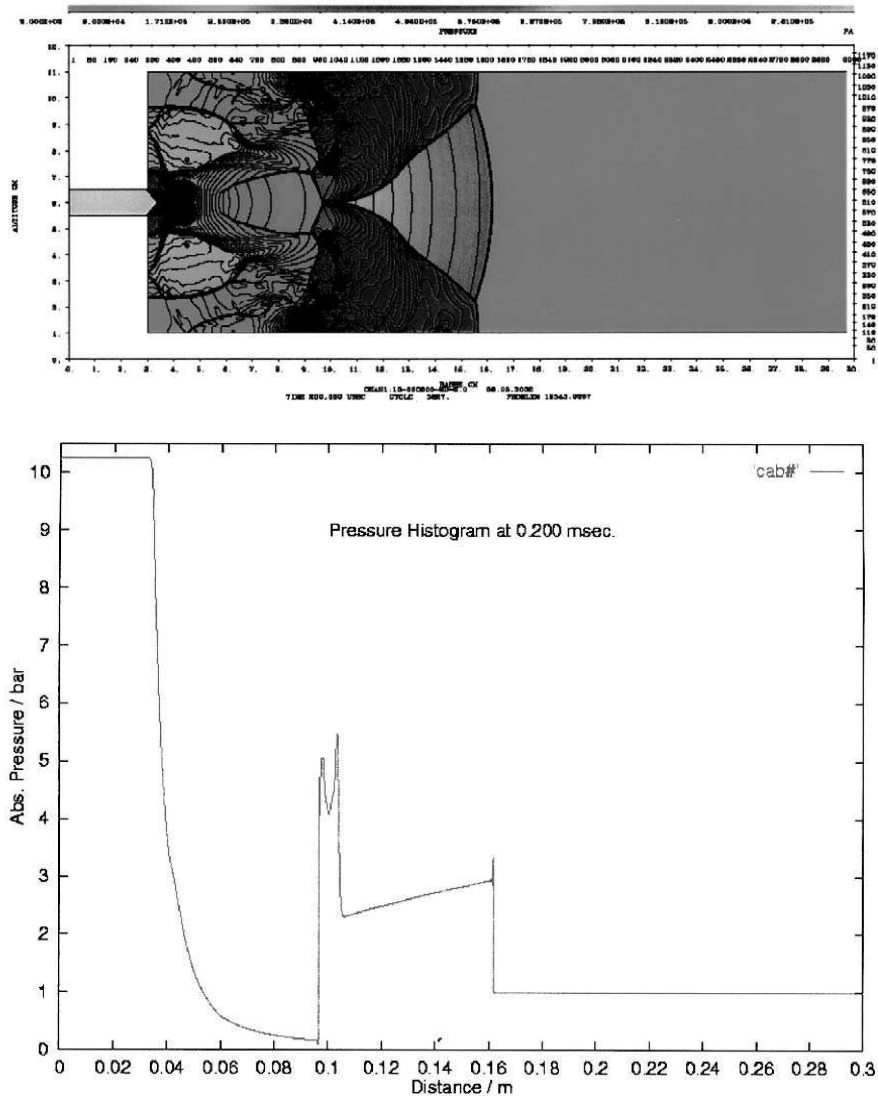


FIGURE 10.42 (continued)

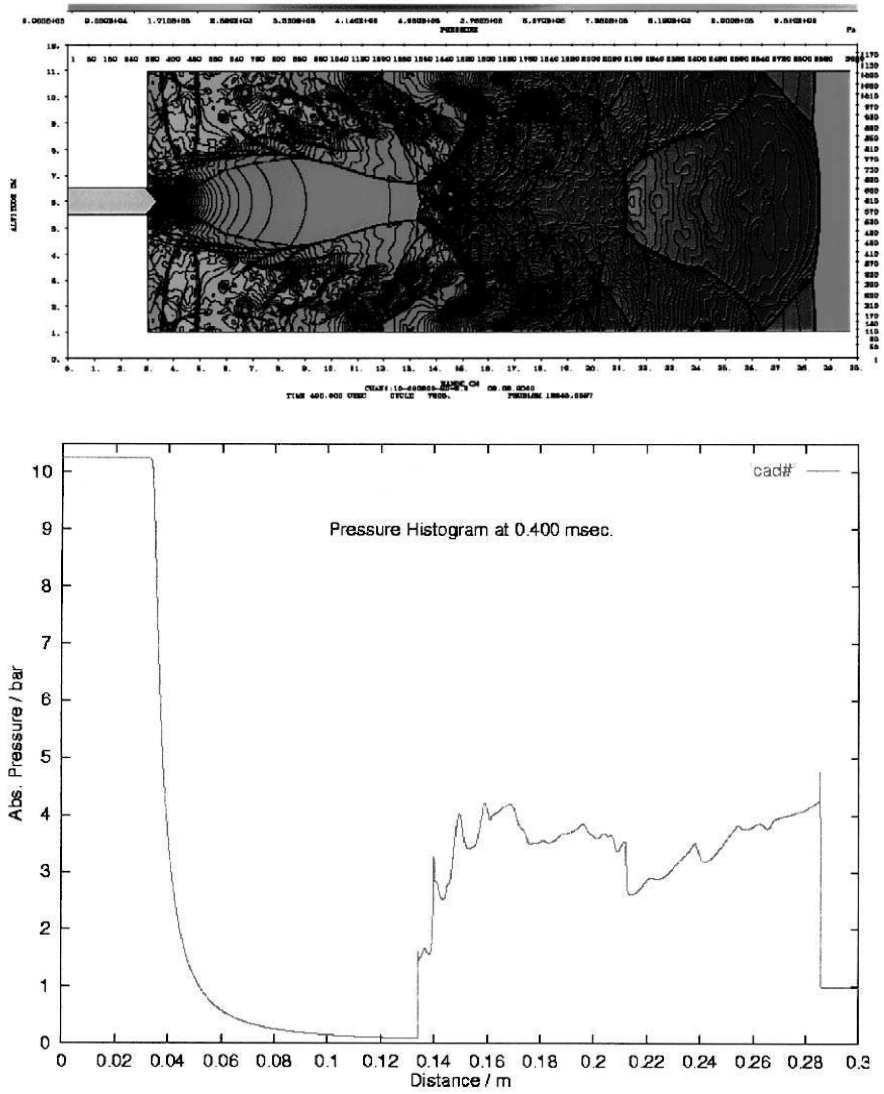


FIGURE 10.42 (continued)

time (400 μ sec). The pressure histogram along the duct's plane of symmetry identifies the strength of 4.2 bar for the transmitted shock. The pressure trend behind it demonstrates the still nonuniform flow; pressure oscillations of about 1.5 bar might indicate that the steady state could be reached. Two secondary shocks are present at this moment and are very close together.

The confrontation confirms the statement that the steady-state method presumably predicts the flow state at an unknown time instant after which all unsteady flow phenomena have subsided.

10.5.1.2 Comparison of SHAMRC Results with Predictions Obtained Previously for Bifurcated Ducts

In this subsection another application of SHAMRC is given. The shock wave propagation in bifurcated channels discussed in Subsection 10.4.5.2 is numerically simulated and the obtained results are compared with those obtained using the energy concept in connection with Whitham's theory and shown in Fig. 10.43 (Heilig and Klein, 1992). The time instants at which the code's data are evaluated correspond to those at which the transmitted shocks just reached the end of the branches visible in the shadowgraphs of Figs. 10.27 to 10.30.

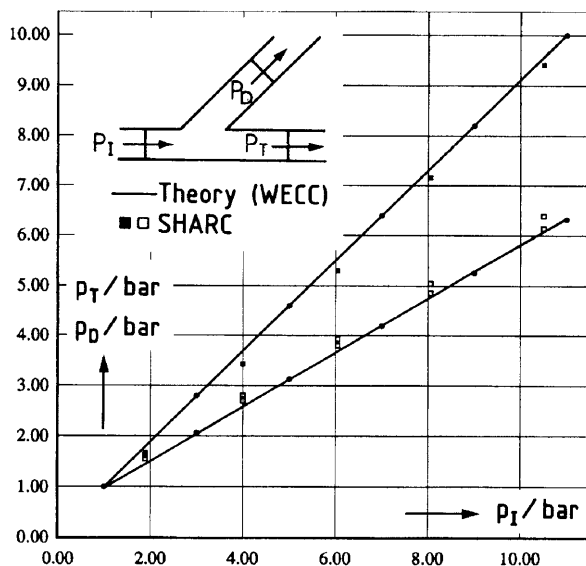


FIGURE 10.43 Comparison of results derived from the energy concept, in connection with Whitham's theory (WECC) (Subsection 10.4.5.2) with those obtained by numerical simulation using the SHAMRC. The solid lines represent the analytical findings and the points stand for numerical results.

The agreement is remarkable and holds for the other bifurcated channel types as well.

10.5.1.3 Treating Detonation Processes Applying the SHAMRC

The SHAMRC code is a second-order (in space and in time), three-dimensional scheme suitable for simulating nonequilibrium chemistry, turbulence ($k - \epsilon$ model), dust/debris sweep-up, and suspensions. The code contains a variety of options, such as to numerically initiate detonation of high explosives of various chemicals; a library of several materials with their equations of state; the capability of modelling nonresponding structures by “island” and “shore” zones; and a comfortable output system. Figure 10.44 shows results obtained for a two-dimensional propagation of a detonation wave in a multichamber system. For computations of blast waves propagation in multichamber shelters, see Baum *et al.* (1993).

10.5.2 THE GRP (GENERAL RIEMANN PROBLEM) CODE

As an alternative to the code just discussed, the GRP code stands as a further example of a wave propagation code suitable for treating wave phenomena. Its principles are given in Falcovitz and Ben Artzi (1995). It makes use of an operator-splitting method (Ben-Artzi and Falcovitz, 1984) and can be employed with grids of different geometry, to match different flow obstacles.

Igra *et al.* (1998a) applied the GRP code for comparing quasi-one-dimensional (1D) computations with fully two-dimensional (2D) computations and finds that in some cases the 2D results approach the corresponding 1D results for large times, whereas in other cases the 2D computed flow is genuinely 2D and cannot be reduced to a 1D equivalent.

The accuracy and validity of the GRP scheme can be proved in various ways. When the code is rerun after grid refinement, numerical convergence is found. Comparisons with experimental findings—see the benchmark test dealing with the Mach reflections from wedges (Takayama and Jiang, 1997), the regularly reflected shock pair at the end wall of a shock tube (Falcovitz *et al.*, 1993), or the study of shock wave interaction with a square cavity (Igra *et al.*, 1996)—all showed very good agreement with experimental findings.

The GPR scheme can be used for solving accurately several of the approximate theories mentioned in Section 10.4. Having an accurate solution could shed light on the range of validity of the proposed approximate solutions. This is demonstrated for the case of shock wave interaction with a

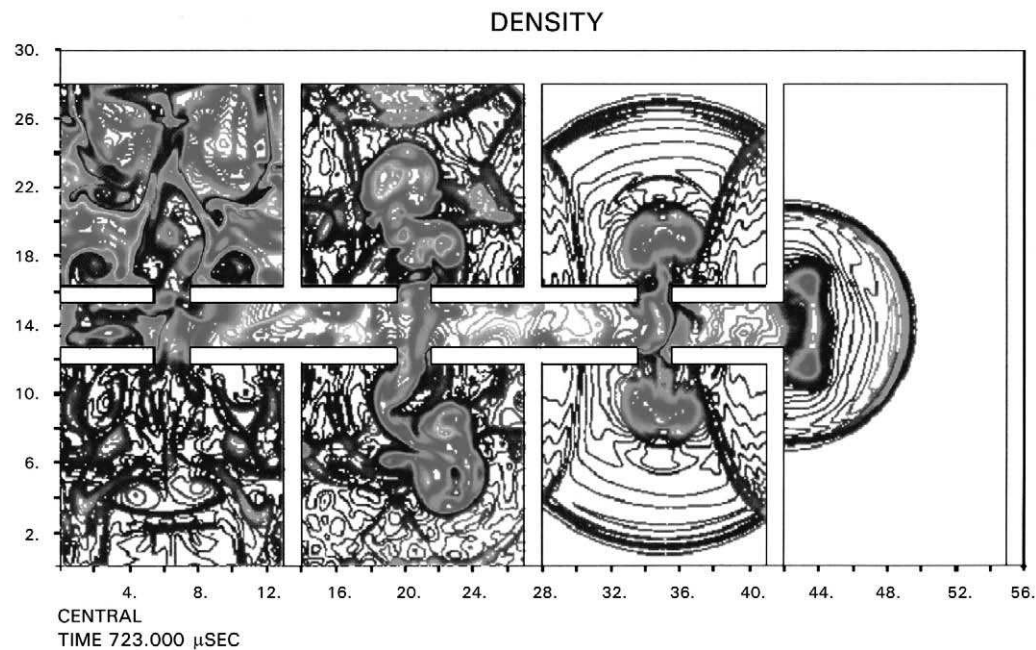


FIGURE 10.44 Isopycnics resulting from the propagation of a detonation wave (blast wave) in a multichamber system (2D). Rooms with a door are connected through a corridor. The wave is “numerically” initiated using a built-in option of SHAMRC by specifying a certain amount of a selectable explosive. (See Color Plate 5).

smooth area change segment joining two long ducts of constant cross-section. Such flow was treated previously using the Chester–Chisnell and Whitham approach in which the flow is considered to be quasi-1D. It is found (Igra *et al.*, 1994) that the interaction of moderately strong shock waves ($M_0 < 1.5$) with relatively small area changes (ratio < 2) can be studied using this approach. For strong shock waves and/or large area-change ratios, errors must be taken into account relative to the quasi-1D numerical solution. In these cases the flow through the area change segment turns out to be truly 2D. Summarizing, one can establish that a three-level hierarchy of approximate modeling prevails. The first is Whitham's approximation; the second is the quasi-1D duct approximation, and the third is the full 2D analysis of the duct flow.

In Fig. 10.45, taken from Igra *et al.* (1998a), results obtained from studying shock wave interaction with an area change segment in a duct is given. The solution was obtained applying the GRP scheme, first for a quasi-1D flow and thereafter as a full 2D flow field. In these computations the incident shock wave Mach number was set at $M_0 = 2.4$ (pressure ratio $p_2/p_1 = 6.55$). It interacts with the linear area-reduction contour described in

$$A(x) = A_u + (A_d - A_u) \cdot \frac{(x - x_u)}{L} \quad (10.51)$$

with $A_u/A_d = 2$ and $L/H_u = 0.5$. A_u and A_d denote the upstream and the downstream constant cross-section areas; L is the length of the transition section between the two ducts; and H_u is the height of the upstream channel section. The diagrams are displayed in the form of histograms for the density ratio ρ/ρ_0 ; the pressure ratio p/p_0 and for the flow Mach number M .

The following conclusions can be drawn from Fig. 10.45: 45 μsec after the entrance of incident shock into the area reduction segment four shocks are discernible in the isobar diagram, as well as a rarefaction wave at the expansive corner. Such a complex flow system means that the 1D data in each histogram strongly differ from the 2D ones. At a time of 90 μsec a large difference between the 2D and 1D predictions exists. The shock being reflected from the segment is curved, but not in the 1D case, where it can be only planar. The flow state at 135 μsec shows that the predictions of the 1D and 2D computation approach more and more except for the rarefaction wave at the duct's wall. Several curved shocks appear in the narrower part of the duct, which cause the parameter oscillations in the histograms of the 2D computations. Finally, at 225 μsec the difference between 1D and 2D data has further decreased, and probably with increasing time the 1D flow situation will result. That confirms the assumption that the quasi-1D flow prediction holds when a sufficient long time period has elapsed during which disturbances arising in the area change segment can decrease and the transmitted shock is sufficiently far away from the segment.

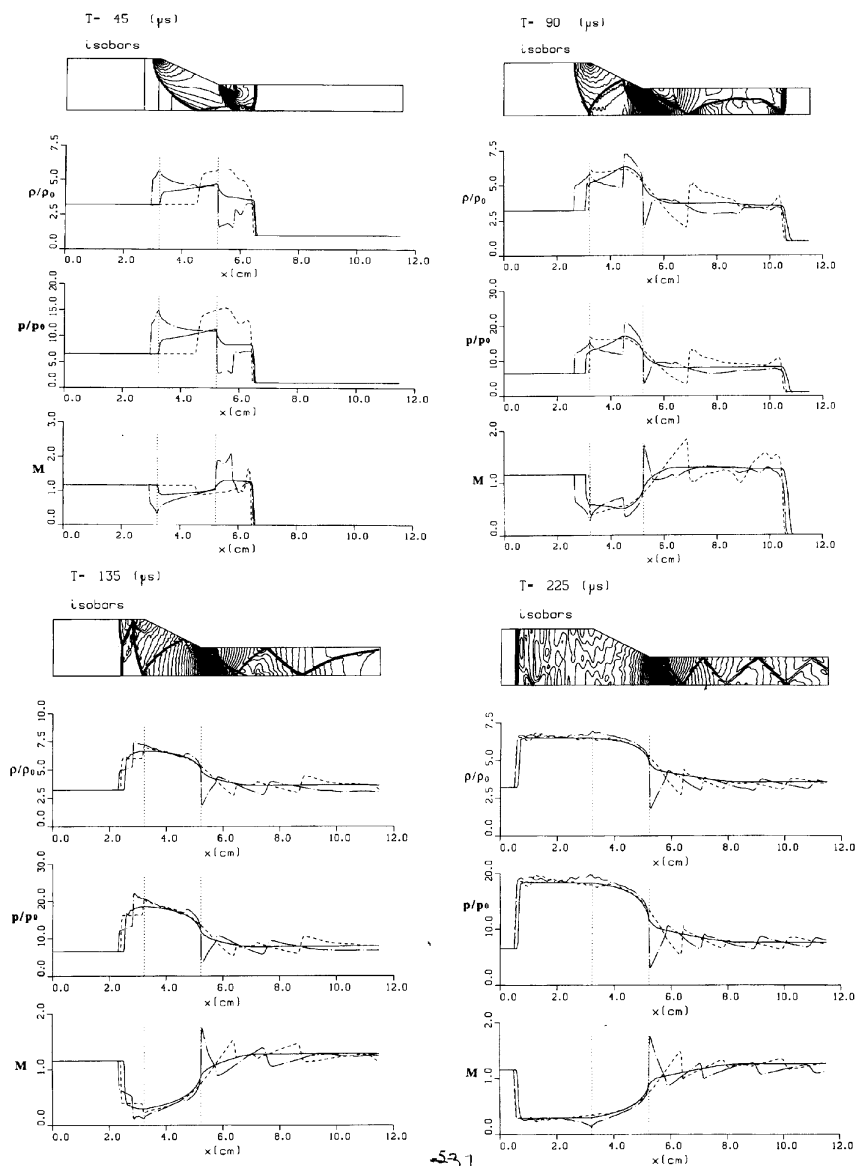


FIGURE 10.45 The flow field in a duct having a linear area-change segment at a few different times. The solid line (—) denotes the quasi-1D GRP results; the other lines represent results obtained for the full 2D GRP computation (---) along the plane of symmetry and (- · - · -) along the duct wall.

In the literature several contributions have been published that demonstrate applications of the GRP code. Amongst those are Igra *et al.* (1998b,c; 1999).

10.5.3 SOLVING A QUASI-ONE-DIMENSIONAL FLOW USING THE RANDOM CHOICE METHOD (RCM)

A noteworthy and useful numerical scheme in connection with shock wave propagation is the RCM. Developed by Glimm (1965), Chorin (1976), and Sod (1977), it enables solving one-dimensional time-dependent Euler equations by using splitting techniques and treating algebraic source terms (see Eqs. (10.5a) to (10.5c)). The method supplying the complete flow field resolves flow discontinuities as true discontinuities, whereas other numerical methods smear them out over several cells. Although the positions of the discontinuities are inaccurate to some extent and the flow variables as well, the predicted solutions on average are correct as proven by Glimm (1965). A concise description of the RCM is given in Toro (1997).

Greatrux and Gottlieb (1982) performed an extensive study regarding the interaction and propagation of a planar shock wave through area enlargements and area reductions in ducts using the RCM. They specified an area transition function between two ducts of constant area (upstream area A_u and downstream area A_d) as

$$A(x) = A_u \cdot \exp \left\{ \frac{1}{2} \cdot \ln \left(\frac{A_d}{A_u} \right) \cdot \left(1 - \cos \left\{ \frac{\pi \cdot x}{l} \right\} \right) \right\} \quad (10.52)$$

where the distance x is measured from the transition inlet ($x = 0$) to the outlet ($x = l$). This special area function is monotonic and smooth and holds both for enlargement and reduction. Furthermore, the transition section joins both constant-area ducts smoothly, thus accounting for less numerical noise in fixed grids. Finally, the flow solution depends only on the normalized distance x/l such that it is independent of the transition length.

For several channel induced flows initiated by shocks of various intensities and for several area ratios A_u/A_d , the authors compared the RCM results with Chisnell's analysis and the quasi-steady flow analysis. Some of the comparisons are shown in Figs. 10.46 and 10.47.

Figure 10.46 indicates that the shock wave Mach number, according to Chisnell's theory (Eq. (10.22)), decreases through the area enlargement and thereafter reaches a constant value. Downstream of the area-change segment it is always higher than the quasi-steady flow predictions. The RCM predictions for the flow properties inside the area-change segment are slightly smaller than

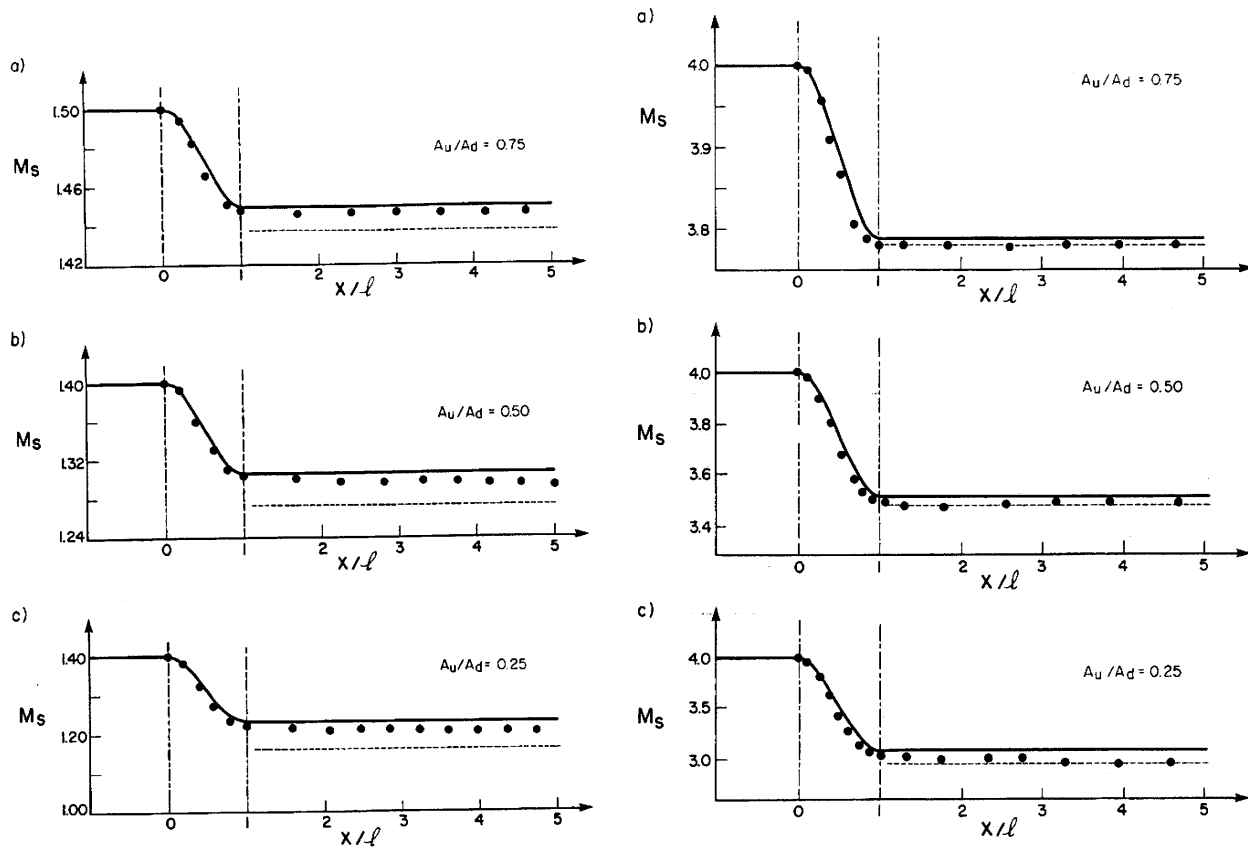


FIGURE 10.46 Comparison between results based on Chisnell's analysis (solid line), the quasi-steady analysis (dashed line), and the RCM (dots) for an incident shock Mach number of $M_0 = 1.4$ (left figure) and $M_0 = 4.0$ (right figure) moving through and beyond an area enlargement of $x/l = 1$.

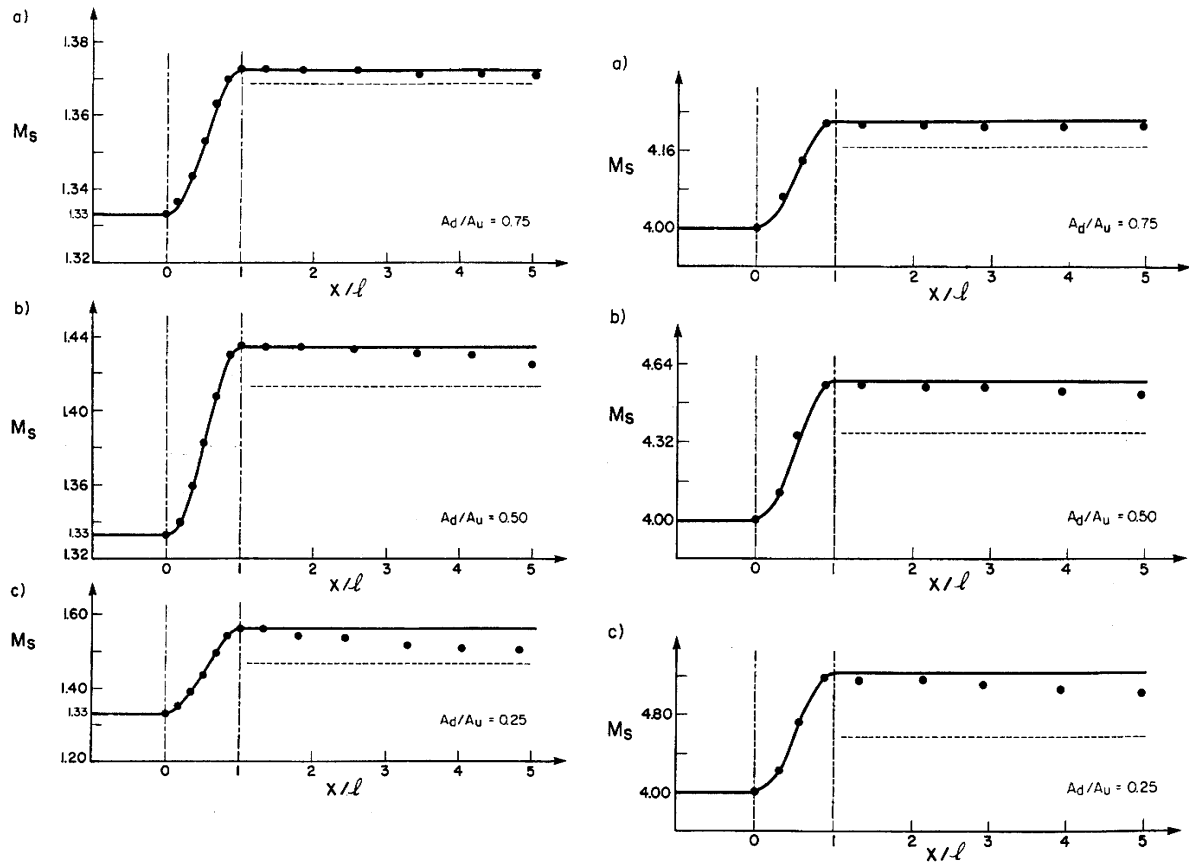


FIGURE 10.47 Comparison between results based on Chisnell's analysis (solid line), the quasi-steady analysis (dashed line), and the RCM (dots) for an incident shock Mach number of $M_0 = 1.33$ (left figure) and $M_0 = 4.0$ (right figure) moving through and beyond an area enlargement of $x/l = 1$.

the results obtained using Chisnell's analysis. Downstream of the area-change segment they approach the quasi-steady data. This behavior is evident for the two different incident shock wave Mach numbers.

Figure 10.47 shows that Chisnell's predictions agree well with those of the RCM in the area reduction segment. Because of disturbances arising in the area-change segment, the RCM predicts decreasing values downstream, but these are significantly higher than the quasi-steady data. The latter are always lower than Chisnell's predictions.

Olivier and Grönig (1986) extended RCM to treat shock focusing and diffraction in two dimensions.

The aim of the present section was to demonstrate some example calculations for shock wave propagation in channels using frequently employed codes. For details regarding numerical solutions suitable for handling flows with shock waves, the reader is directed to Chapter 6.

10.6 DATA BASES

Apart from the more fundamental studies reported previously, the aim of the present section is to briefly discuss large-scale experiments, that is, those performed in excavated tunnel systems of large dimensions (for example, see Fig. 10.1).

Apparently there is a need for such activity in order to obtain enough data for assessing risks of ammunition storage or to provide safe underground storage shelters for humans and/or goods against incoming pressure waves. The "Klotz Club" community is concerned with explosive safety problems in underground storage (Gürke, 1990). On the one hand, one has to bear in mind that with such experiments the primary shock is initiated by a detonation, which produces a nonstep wave profile often called blast wave. The physics of propagation of such waves, in small-scale experiments, has not been thoroughly studied so far (Heilig, 1999). In any case, blast waves experience different attenuation than shock waves. This is impressively demonstrated by Clark and Coulter (1960), who proposed an empirical formula for the attenuation of a blast wave moving in a cylindrical duct. In the considered case the blast attenuation is caused by the rarefaction wave, which overtakes the shock front. Therefore, it is questionable whether pressure data measured in shock tube experiments, where a step wave of long duration is produced, can be scaled up with the aid of a scaling law. The literature, on the other hand, does not precisely inform one about a scaling law for pressure waves moving in multibranched channels of geometrical similarity comparable to the well-known similarity law of Hopkinson Sachs ("cube-root scaling"), which deals with the propagation of spherical waves in open space.

If, however, in a small-scale device the initiation of the primary shock is made by a method similar to that used in a large-scale device, gauge readings from homologous places in geometrically similar tunnels and also at the surfaces of blocks installed agree surprisingly well. That was proved for the large blast simulator at Reiteralpe, in which the shock is generated by quick, simultaneous discharge of several highly pressurized gas bottles. In the corresponding EMI model simulator (scale 1:41.7) the primary shock is initiated by releasing a certain number of small-scale pressure bottles that are opened by exploding wires (Amann, 1985). Care must, however, be taken if vortices strongly influence the small-scale tests. It is known that they play a minor role in the large scale test because they do not scale and so the data scaling can disagree. Using these findings the concepts for the construction of large blast simulators could be supported, as in the case of the large blast simulator in Gramat, France (Amann, 1997).

Data coming from the evaluation of this kind of experiment are usually collected in handbooks and presented as fit functions. In this way they are readily accessible by computer programs. Activity in providing data bases, mostly supported by governments, is in progress or has been done in several countries. Some literature references are quoted here:

Bingelli and Anet (1999); Schläpfer and Bingelli (1997); Bingelli and Bingelli (1985); Hess and Bingelli (1994); Blumer and Itschner (1977)
Rinnan, Skeltorp and Jenssen (1973)
Hveding (1972)
Joachim and Armstrong (1993); Davies and Song (1997); Welch, Joachim, and Frankel (1997)
Gratias (1997); Naz and Parmentier (1988)
Scheklinski-Glück (1998; 1999); Gürke, Scheklinski-Glück, and Mehlin (1986); Mehlin and Froböse (1974)
Dewey and McMillin (1990)

Related work is predominantly presented in the proceedings of international conferences, such as "Interaction of the Effects of Munitions with Structures" and "Military Aspects of Blast and Shocks."

10.7 FINAL REMARKS

This chapter deals with processes occurring when shock waves propagate in channels. The main emphasis is put on the basic aspects of the subject. Tribute is paid to early works, which were performed on a high theoretical level and which led to approximate analytical methods. With help of such approximations, intensities of the transmitted and the reflected shock fronts arising in the

segments of varying cross-sections can be predicted rather accurately. However, such approximations cannot provide an accurate prediction for the postshock flow field. Parallel to this endeavor, the art of conducting experiments, mostly shock tube work, in connection with flow visualization and gauge measurements was cultivated. With the aid of such techniques shock waves propagation in various ducts can be studied using small-scale channel models of simple geometries. From analyzing the visualized flow patterns and the gauge readings, a fundamental understanding of the sequences of events can be obtained. This not only is of benefit for theoreticians, but also helps in planning and performing large-scale experiments.

The rapid advances in computer hard- and software make it possible to overcome the unavoidable limitations of approximate procedures. CFD methods enable computation of time-dependent processes of shock propagation in channels in all dimensions. Many successful applications are known for the 2D case. Because of a worldwide endeavor to develop numerical schemes, a high degree of reliability concerning uniqueness and convergence can be attributed to the numerical solutions. To ensure their suitability, especially in gas dynamics, they should be compared with available experimental findings. In any case, the CFD is a tool for flow simulations; not only for analysing events arising in engineering fields (e.g., “in the large”), but also a tool for doing numerical research toward exploiting still unresolved problems.

REFERENCES

- Amann, H. O. (1971) Vorgänge beim Start einer ebenen Reflexionsdüse. *Zeitschrift für Flugwissenschaften*, 19, 393–406.
- Amann, H. O. (1985) First results with the Model-Blastsimulator of Reiteralpe. Proc. the 9th Intern'l Symposium on Military Applications of Blast Simulation, Oxford, UK.
- Amann, H. O. (1997) Propagation and attenuation of blast waves in a long Model-Blastsimulator: Proc. of the 14th Int. Symposium on Military Aspects of Blast and Shock, Las Cruces, NM.
- Amann, H. O., and Reichenbach, H. (1973) Unsteady flow phenomena in shock-tube nozzles. Proc. of the 9th Int. Shock Tube Symposium, Stanford, CA.
- Baum, J. D., Luo, H., and Löhner, R. (1993) Numerical simulation of a blast within a multi-chamber shelter. Proc. of the 13th Int. Symposium on the Military Application of Blast Simulation, The Hague, The Netherlands.
- Bazhenova, T. V., and Gvozdeva, L. G. (1987) Unsteady interaction of shock waves. Proc. of the 16th Int. Symposium on Shock Tubes and Waves, Aachen, Germany.
- Ben-Artzi, M., and Falcovitz, J. (1984) A second-order Godunov-type scheme for compressible fluid dynamics. *J. Comp. Phys.*, 55, 1–32.
- Ben-Dor, G. (1992) *Shock Wave Reflection Phenomena*. Springer-Verlag.
- Bingelli, E., and Anet, B. (1999) The use of the LS2000-Design Chart for predictions of air blast loading in tunnels due to HE-detonations at the tunnel entrance. Proc. of the 9th Int. Symposium on Interaction of the Effects of Munitions with Structures, Berlin-Strausberg, Germany.

- Bingelli, E., and Bingelli, F. (1985) Luftstoßausbreitung in Stollen mit Querschnittserweiterungen und -verengungen. Rep. ACSL 8522, AC-Laboratorium, Spiez, Switzerland.
- Bleakney, W., and Taub, A. H. (1949) Interaction of shock waves. *Rev. Mod. Phys.*, **21**, 584–605.
- Blumer, W., and Itschner, D. (1977) Dokumentation des Computerprogramms “Tunnel.” FMB Report No. 77-14, Zürich, Switzerland.
- Bryson, A. E., and Gross, R. W. F. (1961) Diffraction of strong shock waves by cones, cylinders, and spheres. *J. Fluid Mech.*, **10**, 1–16.
- Chester, W. (1953) The propagation of shock waves in a channel of non-uniform width. *Quart. J. Mech. Appl. Math.*, **6**, 440–452.
- Chester, W. (1960) The propagation of shock waves along ducts of varying cross section. *Adv. Appl. Mech.*, **6**, 119–152.
- Chisnell, R. F. (1957) The motion of a shock wave in a channel, with applications to cylindrical and spherical shock waves. *J. Fluid Mech.*, **2**, 286–298.
- Chorin, A. J. (1976) Random choice solution of hyperbolic systems. *J. Comp. Phys.*, **22**, 517–533.
- Clark, R. O., and Coulter, G. A. (1960) Attenuation of Air Shock Waves in Tunnels. BRL Memorandum No. 1278; Dasa Rep. No. 1176.
- Collela, P., and Henderson, L. F. (1990) The von Neumann paradox for the diffraction of weak shock waves. *J. Fluid Mech.*, **213**, 71–94.
- Courant, R., and Friedrichs, K. O. (1948) *Supersonic Flow and Shock Waves*. Interscience Publishers, Inc., New York.
- Davis, L. K., and Song, S. (1997) Joint U.S./ROK R&D Program for new underground ammunition storage technologies. Rep. No. UAST-TR-96-001, US Army Engineer Waterways Experiment Station, Vicksburg, MS.
- Dekker, B. E. L., and Male, D. H. (1968) Fluid dynamic aspects of unsteady flow in branched ducts. *Proc. Instrn. Mech. Engrs.*, **182**, 167.
- Dewey, J. M., and McMillin, D. J. (1990) Älvdalen Tunnel Test, Smoke Puff Photogrammetry (September 1989). Rep. No. 3/90, Dewey McMillin & Associates Ltd., Victoria, B.C., Canada.
- Falcovitz, J., and Ben-Artzi, M. (1995) Recent developments of the GRP method. *JSME*, **38**, 497.
- Falcovitz, J., Alfandary, G., and Ben-Dor, G. (1993) Numerical simulation of the head-on reflection of a regular reflection. *Int. J. Num. Meth. Fluids*, **17**, 1055–1077.
- Ferri, A. (Ed.) (1961) *Fundamental Data Obtained from Shock-Tube Experiments*. Pergamon Press, New York.
- Glass, I. I. (1974) *Shock Waves and Man*. The University of Toronto Press.
- Glass, I. I. (1991) Over forty years of continuous research at UTIAS on non-stationary flows and shock waves. *Shock Waves*, **1**, 75–86.
- Glass, I. I., and Sislian, J. P. (1994) *Nonstationary Flows and Shock Waves*. Clarendon Press, Oxford.
- Glimm, J. (1965) Solution in the large for non-linear hyperbolic systems of equations. *Comm. Pure Appl. Math.*, **18**, 697–715.
- Gottlieb, J. J., and Igra, O. (1983) Interaction of rarefaction waves with area reductions in ducts. *J. Fluid Mech.*, **137**, 285.
- Gratias, S. (1997) The simulation of mechanical effects of nuclear explosions through the French contribution within the international community. Julius Meszaros Lecture. Military Aspects of Blast and Shock, 15th Int. Conference, Banff, Canada.
- Greatrix, D. R., and Gottlieb, J. J. (1982) An analytical and numerical study of a shock wave interaction with an area change. University of Toronto Institute for Aerospace Studies, UTIAS Rep. No. 268.
- Grönig, H. (1978) Dämpfung von Stoßwellen in verzweigten Rohrsystemen. Forschungsbericht des Landes Nordrhein-Westfalen, Westdeutscher Verlag, 2793.

- Gürke, G. (1990) Explosive Safety in Underground Storage—Blast in Tunnels and Chambers—a Bibliography. Report of the Fraunhofer-Institut für Kurzzeitdynamik Ernst-Mach-Institut E9/90.
- Gürke, G., Scheklinski-Glück, G., and Mehlin, H. P. (1986) Ein Rechenverfahren zur Ermittlung von Luftstoßparametern in geraden und rechtwinklig verzweigten Stollen bei der Detonation von Explosivstoffstangen im Eingangsquerschnitt. Report No. E6/68 of the Ernst-Mach-Institut der Fraunhofer Gesellschaft, Germany.
- Hammitt, A. G., and Carpenter, H. J. (1964) Unsteady flow past junctures in ducts. *AIAA J.*, 2, 2224.
- Heilig, W. (1969) Theoretische und experimentelle Untersuchungen zur Beugung von Stoßwellen an Kugeln und Zylindern. PhD-Thesis, Universität (TH) Karlsruhe.
- Heilig, W. (1975) Propagation of shock waves in various branched ducts. Proc. of the 10th Int. Shock Tube Symposium, Kyoto, Japan.
- Heilig, W. (1978a) Stoßwellenausbreitung in Kanälen mit Verzweigungen. Report No. 1/78 des Ernst-Mach-Instituts der Fraunhofer-Gesellschaft.
- Heilig, W. (1978b) An Integration in Whitham's Theory. Applied Fluid Mechanics, Festschrift zum 60. Geburtstag von Professor Dr. H. Oertel, Universität (TH), Karlsruhe.
- Heilig, W. (1993) About the attenuation effect of expansion chambers in channels. Proc. of the 13th Int. Symposium on Military Application of Blast Simulation, The Hague, The Netherlands.
- Heilig, W. (1999) Shock wave loading of rigid obstacles dependent on the pressure profile of the incident wave. Proc. of the 22nd Int. Symposium of Shock Waves, Imperial College, London.
- Heilig, W., and Klein, H. (1992) Numerically simulated blast propagation in simple tunnel systems. Proc. of the 12th Int. Symposium on the Military Application of Blast Simulation, Gramat, France.
- Hess, K., and Bingelli, E. (1994) Druckmessungen an einem oberirdischen Modellschutzbau im Maßstab 1 : 100 bzw. 1 : 400. Vergleich der Resultate mit 1 : 1 und 1 : 4 Untersuchungen. Report ACLS 9439, AC-Laboratorium, Spiez, Switzerland.
- Hveding, D. (1972) Shock wave transmission through an angled tunnel section. Proc. of the 3rd Intern'l Symposium on Military Application of Blast Simulation, Stockholm, Sweden.
- Igra, O., and Gottlieb, J. J. (1985) Interaction of rarefaction waves with area enlargements in ducts. *AIAA J.*, 23, 1014.
- Igra, O., Elperin, T., Falcovitz, J., and Zmiri, B. (1994) Shock wave interaction with area changes in ducts. *Shock Waves*, 3, 233–238.
- Igra, O., Falcovitz, J., Reichenbach, H., and Heilig, W. (1996) Experimental and numerical study of the interaction between a planar shock wave and a square cavity. *J. Fluid Mech.*, 313, 105–130.
- Igra, O., Wang, L., and Falcovitz, J. (1998a) Nonstationary compressible flow in ducts with varying cross-section. *Proc. Instn. Mech. Engrs.*, 212, 225–243.
- Igra, O., Wang, L., Falcovitz, J., and Amann, H. O. (1998b) Simulation of the starting flow in a wedge-like nozzle. *Shock Waves*, 8, 235–242.
- Igra, O., Wang, L., Falcovitz, J., and Heilig, W. (1998c) Shock wave propagation in a branched duct. *Shock Waves*, 8, 375–381.
- Igra, O., Falcovitz, J., Meguro, T., Takayama, K., and Heilig, W. (1999) Shock wave propagation through a double bent duct. Proc. of the 22nd Int. Symposium of Shock Waves, Imperial College, London.
- Imhof, H.-G. (1976) Ausbreitung von Stoßwellen in verzweigten Rohren. PhD-Thesis, Rheinisch-Westfälische Technische Hochschule, Aachen, Germany.
- Inoue, O., Takahashi, N., and Takayama, K. (1993) Shock wave focusing in a log-spiral duct. *AIAA J.*, 6, 1150–1152.

- Joachim, C. E., and Armstrong, B. J. (1993) Simulation of airblast propagation in an underground magazine, comparison of 3D hydrocode and a small-scale model results. Proc. of the 13th Int. Symposium on the Military Application of Blast Simulation, The Hague, The Netherlands.
- Kahane, A., Warren, W. R., Griffith, W. C., and Marino, A. A. (1954) A theoretical and experimental study of finite amplitude wave interactions with channels of varying area. *J. Aeronaut. Sci.*, **21**, 505–525.
- Kuhl, A. L., and Reichenbach, H. (1989) Organized structures in a turbulent boundary layer behind a shock. Proc. of the 17th Int. Symposium on Shock Waves and Shock Tubes, Bethlehem, PA.
- Laporte, O. (1954) On the interaction of a shock with a constriction. Report Los Alamos Scientific Laboratory of the University of California, LA- 1740.
- Matuska, D. A. (1984) HULL Final User's Manual. Report Air Force Armament Laboratory, Eglin (FL), AFATL-TR-84-59.
- Mehlin, H. P., and Froböse, M. (1974) Ausbreitung von Luftstoßwellen detonierender Sprengstoffstangen in einem Rohr mit rechtwinkliger Abzweigung. Report No. E6/68 of the Ernst-Mach-Institut der Fraunhofer Gesellschaft, Germany.
- Milton, B. E. (1990) The focussing of shock waves in two-dimensional and axisymmetrical ducts. *Proc. Int. Workshop on Shock Wave Focussing, Sendai, Japan*, Ed. K. Takayama, Pub. Shock Wave Research Center, Institute of Fluid Science, Tohoku University, 155–192.
- Milton, B. E., and Archer, R. D. (1971) Pressure and temperature rise in a logarithmic spiral contraction. Proc. of the 8th International Shock Tube Symposium, London, **55**, 1–11.
- Morduchow, M., and Libby, P. A. (1962) On the distribution of entropy within the structure of a normal shock wave. Polytechnic Institute of Brooklyn, Pibal Rep. 759.
- Napolitano, L. G. (1961) Flows with discontinuities. *Fundamental Data Obtained from Shock-Tube Experiments*, Ed. A. Ferri. Pergamon Press.
- Naz, P., and Parmentier, G. (1991) Blast waves: Scale models and numerical simulations. Proc. of the 12th Int. Symposium on Military Applications of Blast Simulation, Gramat, France.
- Naz, P., and Vermorel, J. (1988) Simulations numerique d'ondes de choc aeriennes a l'aide du code HULL. Rapport Institut Franco-Allemand de Recherche de Saint Louis, RT 516/88.
- Needham, C. E., and Crepeau, J. E. (1998) SHAMRC, Second-Order Hydrodynamic Automatic Mesh Refinement Code. Rep. Applied Research Associates (ARA), Inc., Albuquerque, NM, Vol. 2, User's Manual.
- Oertel, H. (1966) *Stossrohre*. Springer-Verlag.
- Olivier, H., and Grönig, H. (1986) The Random Choice Method applied to two-dimensional shock focussing and diffraction. *J. Comp. Phys.*, **65**, 85–106.
- Oppenheim, A. K., Urtiew, P. A., and Laderman, A. J. (1964) Vector polar method for the evaluation of wave interaction processes. *Archiwum Budowy Maszyn*, **11**, 441–495.
- Peters, F., and Merzkirch, W. (1975) *ZAMM*, **55T**, 1467.
- Reichenbach, H. (1970) Shock wave attenuation by perforated walls. Proc. of the 9th Int. Congress on High-Speed Photography and Cinematography, Denver, CO.
- Reichenbach, H. (1992) On the footsteps of Ernst Mach—A historical review of shock wave research at the Ernst-Mach-Institut. *Shock Waves*, **2**, 65–79.
- Reichenbach, H. (1995) 120 years of shock wave visualization—a fascinating activity. Proc. of the 20th Int. Symposium of Shock Waves, Pasadena, CA, **1**, 17–29.
- Reichenbach, H., and Dreizler, H. (1960) Über den Einfluß von Querschnittsänderungen und Gittern in Kanälen auf Stoßwellen. *Zeitschrift für Angewandte Physik*, **12**, 62–71.
- Reichenbach, H., and Kuhl, A. L. (1987) Techniques for creating precursors in shock tubes. Proc. of 16th Int. Symposium on Shock Tubes and Waves, Aachen, 847–853.
- Reichenbach, H., and Kuhl, A. L. (1993) Shock-induced turbulent flow in baffle systems. Proc. of the 19th Int. Symposium on Shock Waves, Marseille, France.

- Rinnan, A., Skjeltorp, A. T., and Jenssen, A. (1973) Underground ammunition storage: Model test to investigate the strength and effectiveness of a self-closing concrete block. Technical Note No. 98/73, Norwegian Defence Construction Service.
- Rudinger, G. (1955) *Wave Diagrams for Nonsteady Flows in Ducts*. D. van Nostrand Company, Inc.
- Rudinger, G. (1960) Passage of shock waves through ducts of variable cross section. *Phys. Fluids*, **3**, 449–455.
- Schardin, H., and Reichenbach, H. (1965) The behaviour of shock waves in ducts and when entering entrance structures. Proc. of the Symposium on Protective Structures for Civilian Populations, Nat. Acad. of Science, Washington, D.C.
- Scheklinski-Glück, G. (1998) The EMI Blast Program, Version 3 for combinations of tunnels and rooms. Report No. E14/98 of the Ernst-Mach-Institut der Fraunhofer Gesellschaft, Germany.
- Scheklinski-Glück, G. (1999) Development of an engineering model for inside detonations in 3-chamber systems. Proc of the 9th Int. Symposium on Interaction of the Effects of Munitions with Structures, Berlin-Strausberg, Germany.
- Schläpfer, D. B., and Bingelli, E. (1997) Airblast propagation in tunnel entrance configurations. A simple method to predict the blast parameters for different configurations of practical interest. Military Aspects of Blast and Shock, 15th Int. Conference, Banff, Canada.
- Skews, B. W. (1967) The shape of a diffracting shock wave. *J. Fluid Mech.*, **29**, 297–304.
- Sod, G. A. (1977) A numerical study of a converging cylindrical shock. *J. Fluid Mech.*, **83**, 785–794.
- Sommerfeld, M., Nishida, M., and Takayama, K. (1985) Shock propagation in a curved duct. Reports of the Institute of High Speed Mechanics, Tohoku University, Sendai, Japan.
- Takayama, K. (1987) Holographic interferometric study of shock wave propagation in two phase flow. Proc. of the 16th Int. Symposium on Shock Tubes and Waves, Aachen, Germany.
- Takayama, K., and Jiang, Z. (1997) Shock wave reflection over wedges: a benchmark test for CFD and experiments. *Shock Waves*, **7**, 191.
- Toro, E. F. (1997) *Riemann Solvers and Numerical Methods for Fluid Dynamics: A Practical Introduction*. Springer-Verlag.
- von Neumann, J. (1963) *Collected Works*, Vol. 6. Pergamon Press.
- Welch, C. R., Joachim, C. E., and Frankel, M. (1997) In-tunnel airblast engineering model for internal and external detonations. Proc. of the 8th Int. Symposium on Interaction of the Effects of Munitions with Structures. McLean, VA.
- Whitham, G. B. (1957) A new approach to problems of shock dynamics. Part I. Two-dimensional problems. *J. Fluid. Mech.*, **2**, 146–171.
- Whitham, G. B. (1958) On the propagation of shock waves through regions of non-uniform area or flow. *J. Fluid. Mech.*, **4**, 337–360.
- Whitham, G. B. (1959) A new approach to problems of shock dynamics. Part II. Three-dimensional problems. *J. Fluid. Mech.*, **5**, 369–386.
- Whitham, G. B. (1974) *Linear and Nonlinear Waves*. John Wiley and Sons, Inc.
- Zucrow, M. J., and Hoffman, J. D. (1976) *Gas Dynamics*, Vol. 1, John Wiley and Sons.
- Zucrow, M. J., and Hoffman, J. D. (1977) *Gas Dynamics, Multidimensional Flow*, Vol. 2. John Wiley and Sons.

Shock Wave Focusing

FUMIO HIGASHINO

Department of Mechanical Systems Engineering, Tokyo Noko University, Koganeishi, Tokyo 184-8588, Japan

-
- 11.1 Introduction
 - 11.2 Theoretical Analyses
 - 11.2.1 Basic Equations
 - 11.2.2 Characteristics Method and CCW Approximation
 - 11.2.3 Similarity Method for Impeding Shock Wave
 - 11.3 Results and Discussion
 - 11.3.1 Shock Tube Experiment
 - 11.3.2 Blast Waves
 - References

11.1 INTRODUCTION

Imploding cylindrical shock waves can be thought of as induced by a cylindrical piston converging onto the central axis. When strong shock waves collapse toward an implosion center, very high pressures, temperatures, and densities can be realized at the central region. Final collapse of the implosion occurs in a small region where mostly subsequent vortices are generated and remain nearly stationary. A perfect focus occurs when a finite portion of the wave front converges to a single point. Extremely high pressures and temperatures may be generated at the focusing spot in a gas by using uniformly converging shock waves or detonation waves. The peak overpressures and temperatures achieved at the implosion center are limited by the degree of symmetry maintained by the imploding shock wave front and characterized by a nonlinear interaction between the shock wave and the flow behind it. These properties of focusing shock wave can be applied to initiate and control thermonuclear fusion in gas, Lau (1971), and Wang (1982) and medical applications such as lithotripsy for kidney stone treatment in water Kitayama *et al.* (1988), Groenig (1989), and Eisenberger *et al.*, (1991).

One widely used method of producing a cylindrical imploding shock wave is to utilize a tear drop section in a tubular shock tube or a detonation chamber. Perry and Kantrowits (1951) were the first to produce converging cylindrical shock waves by inserting an inverted teardrop model along the axis of an annular shock tube as shown in Fig. 11.1. A cylindrically collapsing shock wave front can be observed between the end plate of the shock tube and the model plate. Thereby the shock wave front is split and turned around it to implode. Lee and Lee (1965), Knystautas *et al.* (1969), and Lee *et al.* (1969) applied the teardrop technique to cylindrically converging detonation waves as shown in Fig. 11.2. Terao (1984) applied the teardrop method to generate spherical imploding detonation waves by setting an inverted teardrop model at the end of a detonation tube as shown in Fig. 11.3. An alternative method for generating a line focus is the use of a logarithmic spiral-shaped contraction in a rectangular shock tube. Milton and Archer (1969, 1971) obtained converging shock waves by using a spiral geometry of a shock tube as shown in Fig. 11.4. Higashino and Oshima (1970) investigated real-gas effects of high-temperature oxygen and nitrogen gases on converging shock waves propagating in the two dimensional test section of a shock tube. For the purpose of medical applications, reflected shock waves from a solid wall are utilized, in general, to get very high pressures in the focusing region, Russel (1986), Mueller (1987), and

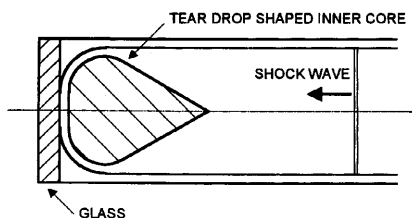


FIGURE 11.1 A typical inverted teardrop model inserted in a cylindrical shock tube.

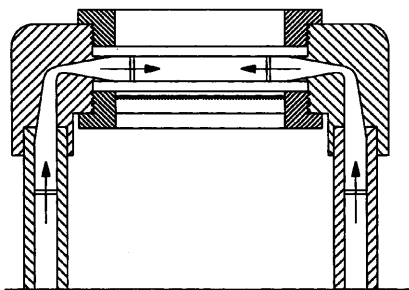


FIGURE 11.2 Axisymmetric setup for converging detonation waves.

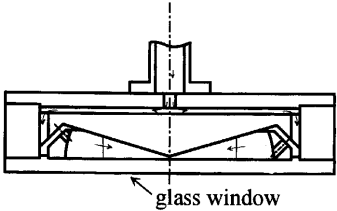


FIGURE 11.3 Spherically symmetric setup for converging detonation waves.

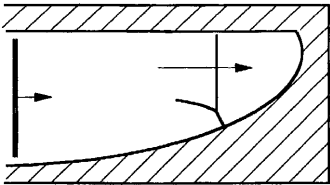


FIGURE 11.4 A logarithmic spiral-shaped construction in a rectangular shock tube.

Sommerfeld *et al.* (1988). Holl *et al.* (1983) used ellipsoidal reflectors together with electric discharges as a point energy source as shown in Fig. 11.5. The shock wave process is essentially a free-field focusing with the inherent limitation that only a small portion of the shock wave emerging from the reflector is finally directed toward the focus. Such shock waves to focus are referred to as converging shock waves for contrast and comparison with

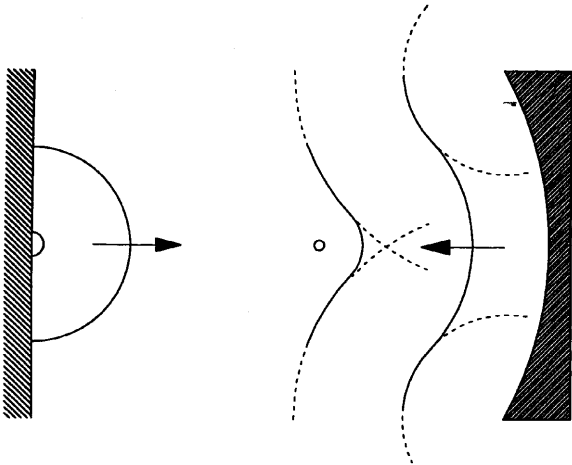


FIGURE 11.5 Spherically converging blast waves reflected from a concave wall.

imploding shock waves. However, focusing a shock wave to a point rather than to a line offers the potential for considerably increased gas pressures to be achieved. The final overpressure achieved at the focusing spot of the reflected shock wave is strongly influenced by the geometry of the reflector, because the reflected wave front is reinforced during focusing processes by the expansion waves spreading progressively from the cut corner of the reflector. The shape of the converging shock front is also deformed through the reflection from the curved surfaces of a solid wall. Transition from regular (RR) to Mach reflection (MR), Duong and Milton (1985), is also an important factor to get the high pressure at the focusing region. Curved shock fronts, being concave in the direction of propagation, exhibit different kinds of behavior depending on both the strength of the shock wave and the rate of focusing, since the speed of the shock front increases as the radius decreases, so that the retarded section, on the basis of curvature, will acquire a large velocity and hence catch up to the rest of the shock front. The curvature of shock fronts breaks down into a kink form close to the focusing area. Such an increase of shock velocity with a decrease in radius is even stronger in spherical waves than in the cylindrical case. When the strength of the wave front is sufficiently weak, the wave front will focus along a caustic surface and may behave like a cusp, called an arete by Sturtevant and Kullkarny (1974, 1976) as shown in Fig. 11.6. Cramer and Seebass (1978), and Cramer (1981) analyzed the focusing of weak shock waves at an axisymmetric arete by applying the CCW approximation.

Only a few exact solutions are known to the flow behind converging shock waves. One exact solution is derived from the method of characteristics. In this case, the solutions to the basic nonlinear partial differential equations can be expressed analytically by the characteristic forms, Stanyukovich (1960), and Caerant and Friedrichs (1967). Although the method to analyze a flow behind imploding shock waves is well established and gives an exact solution for a perfect gas, construction of the grids of the characteristics, which are composed of three characteristic curves, are fairly tiresome and the result is much affected by its grid sizes. In the general case, when the characteristics are curved, the points of intersection of the two families do not occur at equal

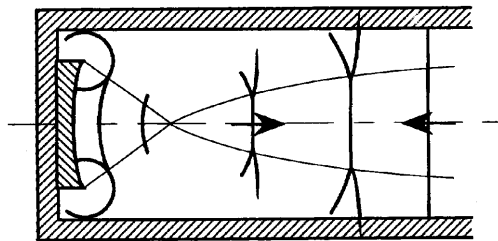


FIGURE 11.6 Weak converging shock waves reflected from a concave reflector in a shock tube.

intervals. Hartree (1958) proposed a new method to avoid this difficulty by interpolating during the process of computation on a rectangular grid. It is noticed that the motion of contact discontinuities cannot be analyzed by the method of characteristics as stated by Oswatitsch (1952), Sauer (1966), and Zucrow and Hoffman (1976). de Neef and Hechtman (1978) calculated cylindrically imploding shock waves by using the characteristics method. Glimm (1965) developed Hartree's method to solve a Riemann problem. Sod (1977) extended his method and simulated the flow of imploding shock waves by applying the Random Choice method originally developed by Chorin (1976).

The motion of shock waves can be analyzed simply by applying the CCW approximation without solving the characteristic equations for the flow behind the shock wave front in detail. The approximate values of the pressure, the density, and the temperature immediately behind the shock wave front can be easily estimated by this method. However, the results are much influenced by the numerical mesh sizes taken along the shock wave front. Moreover, computational instability is observed when the radius of curvature of the shock wave front becomes small, where a small shock wave front with large curvature may be bifurcated into two shock wave segments with entropy discontinuities.

Chester (1954) considered the motion of a shock wave through a channel consisting of a section of slowly varying area separating two uniform ducts. Chisnell (1955) integrated Chester's linearized formula with respect to the area difference between the uniform sections. Whitham (1957, 1973) showed that the motion of a shock wave can be analyzed without solving the whole flow-field behind the shock wave and obtained the differential relation to be satisfied by the flow quantities along a positive characteristic line pertinent to the flow quantities behind the shock wave. Final formulation of Whitham's rule was very consistent with the results obtained by Chester and Chisnell. Approximate treatment proposed for estimating the change in shock wave strength owing to area change experienced by the shock wave front is referred to as the CCW model after the names of the scientists. This approximate treatment for shock wave motion is generally extended to geometrical shock wave dynamics or ray shock wave theory and is often applied to analyses of shock focusing on reflected shock waves from the reflectors. Henshaw *et al.* (1986) investigated the motion of a shock wave with complex geometry by applying the CCW model to analyze the focusing phenomena of the plane shock front in a shock tube. Sakamoto *et al.* (1993) extended their analysis to a curved shock front with arbitrary radius of curvature to explain the shock wave focusing process of reflected blast waves. In general, the results were strongly influenced by the mesh size constructing grid system consisting of rays and shock front segments.

Other exact solutions on imploding shock waves were obtained by applying the similarity method. Taylor (1950) and Sedov (1959) obtained self-similar solutions for infinitely strong blast waves. Sakurai (1953) and Oshima (1960) applied the similarity method to analyze decay of blast waves with finite shock wave strength. The process of shock implosion is the inverse phenomenon of explosion, Mishkin and Fujimoto (1978). When a shock wave front collapses in a cylindrically or spherically symmetric manner, such shock waves are referred to as imploding shock waves, contrasted with explosion. The self-similar motion for imploding shock waves in a uniform perfect gas was first studied by Guderley (1942) and Butler (1954) separately. Zel'dovich (1959), Lee and Lee (1965), and Lee *et al.* (1969) applied their methods to the analysis of imploding shock waves to explain the focusing process of detonation waves with finite strength. Higashino (1971) obtained a similarity solution for the motion of imploding shock waves in high-temperature air that includes the effects of vibrational excitation and dissociation of diatomic molecules. Although in the case of similarity analyses, the shape of the imploding shock waves is limited to either axisymmetric or spherically symmetric, an analytical solution is obtained. In addition, the final numerical results are independent of the mesh widths for integration as pointed out by Guderley (1942). So the similarity method is a most useful one to analyze the singular property of imploding shock waves appearing in the vicinity of the center of implosion, although the effect of viscosity is not taken into account.

Numerical simulations are another important approach to the study of converging shock waves. The complicated flow field behind converging shock waves was analyzed during shock wave focusing by using various computer codes. Although numerical simulations computed by either finite differences or finite volume schemes revealed physically interesting features during the focusing process of shock waves with viscous effect, the results were also much affected by the mesh sizes adopted in the computation. The finite volume computation is superior to the finite difference scheme, since the singular property can be weakened in the immediate vicinity of the implosion center where the physical values are averaged in a cell. Numerical computations for contracting shock waves were performed by Payne (1957) and Welsh (1966). Saito and Glass (1979) extended his method to the problem of imploding spherical shock waves and compared experimental results with experiments. The effect of initial grid geometry for simulations had always appeared near to the focusing point as shown by Aki and Higashino (1989) and Book and Loehner (1989). When a polygonal column composed of many high-pressure and -temperature or -density columns is given as initial conditions instead of a whole circular cylinder, the shock wave front caused by the column may not be axisymmetric from the beginning. Consequently, a complete simulation of imploding shock waves with a circular shock wave front

cannot be simulated. Such initial conditions have inherently nonuniform character owing to disturbances originated from each node of the polygons. Such flow nonuniformity generates flow instability close to the focusing point.

11.2 THEORETICAL ANALYSES

11.2.1 BASIC EQUATIONS

The basic equations for the unsteady flow field, which is developed behind converging or imploding shock waves, are as follows:

Conservation of mass:

$$\frac{\partial \rho}{\partial t} + u \frac{\partial \rho}{\partial r} + \rho \frac{\partial u}{\partial r} + j \frac{\rho u}{r} = 0. \quad (11.1)$$

Conservation of momentum:

$$\frac{\partial u}{\partial t} + u \frac{\partial u}{\partial r} + \frac{1}{\rho} \frac{\partial p}{\partial r} = 0. \quad (11.2)$$

Conservation of energy:

$$\frac{\partial e}{\partial t} + u \frac{\partial e}{\partial r} - \frac{p}{\rho^2} \left(\frac{\partial \rho}{\partial t} + u \frac{\partial \rho}{\partial r} \right) = 0. \quad (11.3)$$

Here p , ρ , and u are the pressure, density, and flow velocity of the gas, respectively; r is the distance from the center of symmetry; and t is the time. e is the specific internal energy, defined by

$$e = \frac{1}{\gamma - 1} \frac{p}{\rho}, \quad (11.4)$$

where γ is the ratio of specific heats, and j in Eq. (11.1) takes the value of 0, 1, 2 for planar, cylindrically, and spherically symmetric flow, respectively.

The thermal equation of state for a perfect gas is given by

$$p = \rho RT. \quad (11.5)$$

These basic equations are integrated by applying one of the methods of characteristics, the finite differences, the finite volume schemes, or the similarity methods. To analyze the motion of shock wave fronts, the CCW approximation is a very useful method for investigating the focusing phenomena of shock waves. Although the CCW model gives a useful formulation to predict the unsteady motion of shock waves, one cannot distinguish the difference between the flows generated in a shock tube and the flows resulted from explosions.

11.2.2 CHARACTERISTICS METHOD AND CCW APPROXIMATION

The basic equations (11.1)–(11.5) are rewritten in the characteristic forms along the characteristic lines as

$$\Delta u + \frac{1}{\rho a} \Delta p = -j \frac{au}{r} \Delta t, \quad \Delta r = (u + a) \Delta t \quad (11.6)$$

$$\Delta u - \frac{1}{\rho a} \Delta p = j \frac{au}{r} \Delta t, \quad \Delta r = (u - a) \Delta t \quad (11.7)$$

$$p\rho^{-\gamma} = \text{const.}, \quad \Delta r = u \Delta t. \quad (11.8)$$

Although these equations, for cylindrically or spherically symmetric flows, can be easily integrated along the characteristic curves, the center of implosion at $r = 0$ is a mathematically singular point at which the speed of sound becomes infinity, so the grid system close to the implosion center ($r = 0$) should be constructed with care. According to Whitham's rule, the change in shock wave Mach number M is related to that in a cross-sectional area A of shock wave front as

$$\frac{2M}{(M^2 - 1)} \frac{dM}{K(M)} + \frac{dA}{A} = 0, \quad (11.9)$$

where M is the shock wave Mach number. $K(M)$ and μ are

$$K(M) = 2 \left\{ \left(1 + \frac{2}{\gamma + 1} \frac{1 - \mu^2}{\mu} \right) \left(2\mu + 1 + \frac{1}{M^2} \right) \right\}^{-1} \quad (11.10)$$

$$\mu^2 = \frac{(\gamma - 1)M^2 + 2}{2\gamma M^2 - (\gamma - 1)}. \quad (11.11)$$

For the two-dimensional case, the original set of equations are modified slightly by using the local radius of curvature r so as to be $dA/A = dr/r$ and $a_0 M/dr = dM/dt$ with time step dt . It is also convenient to use a ray n_i that is a coordinate segment perpendicular to a shock wave front. In practice, the local contour of shock wave fronts was approximated by a quadratic equation of the form $x(y) = \alpha_1 + \alpha_2 y + \alpha_3 y^2$ in a (x, y) plane. After some algebra, Eq. (11.9) is reduced to the following form with sound speed a by using r_i and n_i as:

$$\frac{dM}{dt} = \frac{n_{i-1} - n_{i+1}}{|n_{i-1} - n_{i+1}|} \frac{a}{2|r_i|} (M^2 - 1) \cdot K(M). \quad (11.12)$$

Here r_i and n_i are given with numerical constants α_1 , α_2 , and α_3 as follows:

$$r_i = \frac{1}{\alpha_3} (1 + n_i^2)^{3/2} \quad (11.13)$$

$$n_i = (\alpha_2 + 2\alpha_3 y_i). \quad (11.14)$$

These ordinary equations are numerically integrated using the Runge–Kutta method with normal shock wave relations across a shock wave front.

11.2.3 SIMILARITY METHOD FOR IMPLODING SHOCK WAVE

Following dimensional analysis, the independent variables (r, t) for the basic equations were transformed into non-dimensional variables as

$$\xi = \frac{r}{R}, \quad M = \frac{\dot{R}}{a_0}, \quad (11.15)$$

where R is the position of the shock wave front and a_0 is the speed of sound in front of the shock wave. Dot means the derivative with respect to time. In addition, p , ρ , and u are also transformed into nondimensional pressure f , density ψ , and velocity ϕ as follows:

$$\begin{aligned} p(r, t) &= \rho_0 \dot{R} f(\xi, M) \\ \rho(r, t) &= \rho_0 \psi(\xi, M) \\ u(r, t) &= \dot{R} \phi(\xi, M). \end{aligned} \quad (11.16)$$

Also, the derivatives with respect to dependent variables (r, t) are transformed into the equations

$$\begin{aligned} \frac{\partial}{\partial r} &= \frac{1}{R} \frac{\partial}{\partial \xi} \\ \frac{\partial}{\partial t} &= \frac{\dot{R}}{R} \left[-\xi \frac{\partial}{\partial \xi} + \theta M \frac{\partial}{\partial M} \right], \end{aligned}$$

where θ is a function of the shock wave Mach number M only and is defined by

$$\theta = \frac{R}{M} \frac{dM}{dR}. \quad (11.17)$$

By introducing the foregoing similarity parameters, the basic equations (11.1), (11.2), and (11.3) are reduced to

$$(\phi - \xi) \frac{\partial \psi}{\partial \xi} + \psi \frac{\partial \phi}{\partial \xi} = \lambda_1 \theta \psi \quad (11.18)$$

$$(\phi - \xi) \frac{\partial \phi}{\partial \xi} + \frac{1}{\psi} \frac{\partial f}{\partial \xi} = \lambda_2 \theta \phi \quad (11.19)$$

$$(\phi - \xi) \left(\frac{\partial f}{\partial \xi} - \frac{\gamma f}{\psi} \frac{\partial \psi}{\partial \xi} \right) = \lambda_3 \theta f, \quad (11.20)$$

where

$$\lambda_1 = - \left(\frac{M}{\psi} \frac{\partial \psi}{\partial M} + j \frac{\phi}{\theta \xi} \right) \quad (11.21)$$

$$\lambda_2 = - \left(1 + \frac{M}{\phi} \frac{\partial \phi}{\partial M} \right) \quad (11.22)$$

$$\lambda_3 = -2 - \frac{M}{f} \left(\frac{\partial f}{\partial M} - \frac{\gamma f}{\psi} \frac{\partial \psi}{\partial M} \right). \quad (11.23)$$

The derivatives f , ϕ , and ψ , with respect to Mach number M , appearing in Eqs. (11.21)–(11.23), can be given in explicit forms under the appropriate assumptions such as quasi-similarity flows. Thus, the basic equations (11.18)–(11.20) are reduced to a set of ordinary differential equations as follows:

$$\frac{df}{d\xi} = \frac{\theta[(\phi - \xi)(\lambda_3 f + \gamma f \lambda_1) - \gamma f \lambda_2 \phi]}{(\phi - \xi)^2 - \gamma f / \psi} \quad (11.24)$$

$$\frac{d\phi}{d\xi} = \frac{\theta[\lambda_2 \phi(\phi - \xi) - f(\gamma \lambda_1 + \lambda_3) / \psi]}{(\phi - \xi)^2 - \gamma f / \psi} \quad (11.25)$$

$$\frac{d\psi}{d\xi} = \frac{\theta[\lambda_3 + \psi(\phi - \xi)\{\lambda_1(\phi - \xi) - \lambda_2 \phi\}]}{(\phi - \xi)\{(\phi - \xi)^2 - \gamma f / \psi\}}. \quad (11.26)$$

This set of ordinary differential equations can be integrated by using the Runge–Kutta method together with the following initial conditions across the shock wave front as

$$1 = \psi(1 - \phi) \quad (11.27)$$

$$\frac{1}{\gamma M} + 1 = f + \frac{1}{\psi} \quad (11.28)$$

$$\frac{1}{(\gamma - 1)M} + \frac{1}{2} = \frac{\gamma}{\gamma - 1} \frac{f}{\psi} + \frac{1}{2\psi^2}. \quad (11.29)$$

In the case of imploding shock waves, the basic equations are always integrated by taking the time increment with a negative sign, because the

TABLE 11.1 Similarity Exponent α for Imploding Shocks ($p \sim R^{-\alpha}$)

Similarity exponent		
Guderley	0.834	Spherical
Butler	0.835217	Spherical
Stanykovich	0.834	Spherical
Mishkin and Fujimoto	0.828	Spherical
Takayama	0.828–0.832	Spherical
Glass	0.834	Detonation
Terao	0.8 ± 0.1	Detonation
Witham	0.3944	Cylindrical
Higashino	0.299–0.3922	Cylindrical

computation is carried out from the shock wave front to the center of implosion. When strong shock waves collapse toward an implosion center, very high pressures, temperatures, and densities can be realized at the central region. Under such circumstances, real gas effects such as dissociation and ionization should take place. Higashino (1971) obtained a similarity solution for an imploding shock wave that includes the real-gas effects in an initially pure diatomic gas.

For the case of explosions, the similarity parameter θ is determined from the requirement that the energy involved in the region surrounded by a blast wave be constant or under a point source explosion. In case of imploding shock waves, θ can be determined by satisfying the regularity condition in the vicinity of the implosion center where the basic equations have the singularity property. To start computations so as to satisfy the regularity condition at the implosion center, it is convenient to apply the CCW analysis to estimate the first approximate value of θ . The similarity indices θ as an eigenvalue is determined through iterative computations. A typical value of θ of Eq. (11.17) was -0.1966 for strong shock waves, whereas the value of θ for the dissociating oxygen was -0.1495 (Higashino, 1971). Typical self-similar exponents corresponding to the similarity index obtained by many investigators are listed in Table 11.1.

11.3 RESULTS AND DISCUSSION

11.3.1 SHOCK TUBE EXPERIMENT

The shape of converging shock waves propagating toward their implosion center is always deformed from a cylindrical shape, Groenig (1986). This is due

to the presence of struts needed to support the inner obstructions to the stability of converging shock waves. To overcome this problem, Milton and Archer (1969) proposed a different method for shock wave focusing by using spiral geometry of a shock tube. A schematic illustration of his facility is shown in Fig. 11.4. However, another flow instability was observed behind the Mach stem over the wall surface during the shock wave propagation in the vicinity of the focusing point, Fong and Ahlborn (1979), Gardner *et al.* (1982), Higashino and Suzuki (1986), Demming and Hehmsoth (1989), and Wu *et al.* (1979). Further details are available in another section of this handbook by Milton.

Setchell *et al.* (1972) observed focusing processes of weak converging reflected shock waves in a shock tube and compared their experimental findings with results of the CCW analysis. In their experiments a concave reflector was placed at the end of the driven section in the shock tube as shown in Fig. 11.6. In their method the reflected shock wave from the reflector always interacted with the flow induced by the incident shock wave during its focusing process. However, such an effect of counterflow interacting with the converging shock waves on the focusing process cannot be analyzed by using the CCW model. Higashino *et al.* (1986, 1987) carried out similar experiments and compared their findings to numerical computations that included the effect of the counterflow during shock focusing. In their experiments a two-dimensional concave reflector was mounted at the end of the shock tube. A plane shock wave propagated initially toward a parabolic reflector, and then the deformed shock wave front after the reflection of the reflector propagated in the opposite direction to the incident shock wave to focus. The detailed process of the shock wave collapsing corresponding to the experiments, the two-dimensional Euler equations were integrated by means of the operator-splitting method, and the PLM scheme was employed in each sweep. The locus of the gas-dynamic focus, defined as a spot in which maximum overpressure was reached, was found to deviate from the geometrical focus, Nishida *et al.* (1986).

11.3.2 BLAST WAVES

Holl and Groenig (1983) investigated convergence of reflected spherical blast waves generated by electric discharges and compared the findings with the results obtained from the CCW model. Sakamoto *et al.* (1993) used cylindrical blast waves generated by exploding wires to study the converging process of reflected blast waves. Two kinds of the experimental setup were used as shown in Figs. 11.7a and 11.7b, and experimental results were compared with the CCW model and numerical simulations. In these experiments, the effect of the expansion waves originating from the corner of the reflector on the shock wave convergence process was significant. Shock wave interaction of either normal

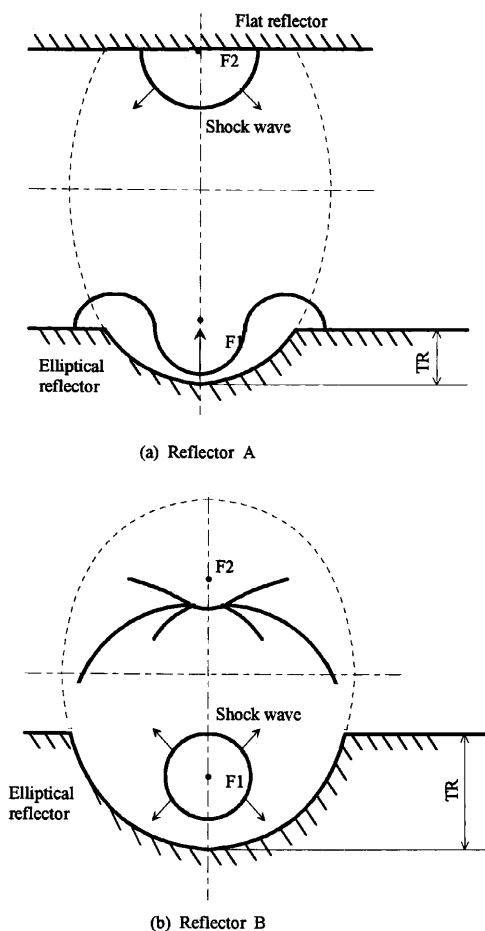


FIGURE 11.7 Cylindrically converging blast waves reflected from a concave wall.

or Mach reflection close to the focusing point was observed in all the experiments. The shape of the reflected shock wave may be strongly influenced by the geometry of the reflectors as well as the nonlinear interaction of the shock wave. Even if a confined ellipsoidal cavity was used as a reflector as shown in Fig. 11.8 (Takayama, 1989), the shape of the converging shock wave fronts deviated from that of ideally imploding shock waves, because the explosion process was not coherent, that is, the size of the explosives is always finite, Hooker *et al.* (1969).

Glass (1967) constructed a hemispherical implosion chamber to drive a piston in the barrel of a ballistic range. The front plate consisted of a segmented

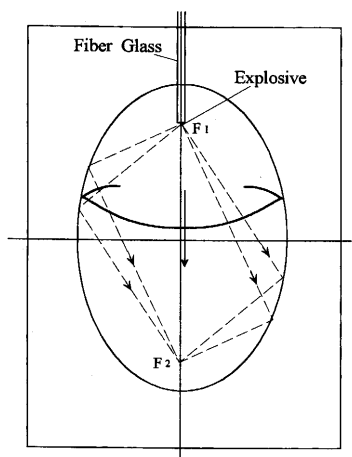


FIGURE 11.8 Blast wave focusing in a confined ellipsoidal cavity.

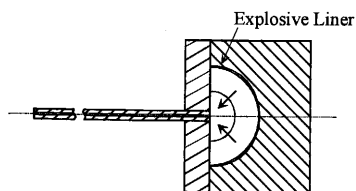


FIGURE 11.9 Shock wave focusing of spherical imploding detonation waves.

cone that supported the barrel, the gas inlet, and the ignition feed-through for an exploding wire, Glass and Sagie (1982). The chamber consisted of two halves, a front plate and a rear plate. They effectively used imploding shock waves to produce extremely high-pressure states for the driver gas. Imploding shock waves were generated by using explosive liners attached on a hemispherical surface that was uniformly ignited by a reflected detonation wave propagating in stoichiometric hydrogen and oxygen gas mixtures. A schematic picture of their experimental setup is shown in Fig. 11.9. Saito and Glass (1979) performed numerical simulations corresponding to these experiments.

The locus of the gas-dynamic focus is defined as the spot in which a maximum overpressure is reached. This locus is, in general, different from the geometrical focus. Two physical models have been investigated as shown in Figs. 11.7a and 11.7b for the blast wave focusing. F_1 and F_2 are two geometrical foci of an ellipsoid. An exploding wire, to generate cylindrical blast waves, is initially placed at one of the geometrical focus F_1 or F_2 of the

ellipsoid. Figure 11.7a shows the case in which the blast wave is generated at a focus located on a flat reflector F2 and propagates toward a concave reflector. Upon reaching the reflector, a cylindrical blast wave is reflected from a segment of the elliptic reflector to be converged close to the second focus F1. Another model is that a blast wave is generated by initiating exploding wires close to a focus F1 as shown in Fig. 11.7b and propagates toward the concave reflector at first. Then a part of the reflected blast wave from the reflector is converged nearly at another focus F2. Results based on the CCW computations showed good agreement with exploding wire experiments both qualitatively and quantitatively, and also with numerical simulations carried out by the PLM scheme, when the initial shock wave conditions were given appropriately. The maximum value of the peak over pressure ratios was influenced by the strength of the reflected compression waves. The location of the shock wave focusing spot was strongly influenced by the strength of diffracted shock waves around corners. The pressure changes close to the focusing spot are shown in Fig. 11.10. Good agreement of the motion of converging shock waves was obtained between experiments and the numerical simulation together with the ray shock wave theory. The effect of supporting struts on the flow stability during the shock wave focusing process is significant, especially in the vicinity of the converging center. To diminish the effect of the diffracted shock wave around the corner, Hosseini *et al.* (1997) constructed an annular strut-free diaphragmless shock tube. Hosseini *et al.* (1999) reconstructed a vertical coaxial diaphragmless shock tube having a self-sustained structure of converging

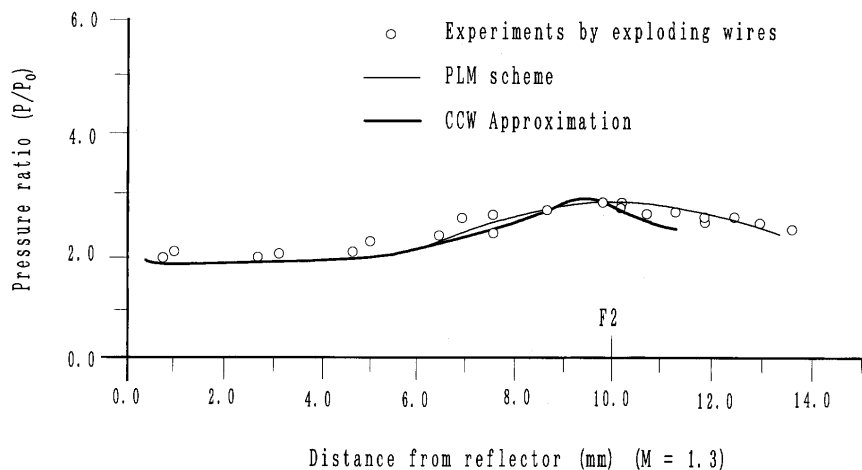


FIGURE 11.10 Comparisons between experimental data and CCW approximation and numerical computations (Sakamoto, Higashino, and Holl).

shock waves. The result shows that the shock wave produced by these shock tubes was very stable. In case of converging detonation waves, such flow instability is rather small in comparison with the case of converging shock waves. This tendency in the shock wave front instability was experimentally confirmed by both Knystautas *et al.* (1969) and Terao (1984).

REFERENCES

- Aki, T., and Higashino, F. (1989) A numerical study on implosion of polygonally interaction shocks and consecutive explosion in a box. *Proc. 17th Int. Symp. Shock Waves & Shock Tubes*, Bethlehem, 167–172.
- Book, D. L., and Loehner, R. (1989) *Proc. Int. Workshop Shock Wave Focusing*, Sendai, 193–206.
- Butler, D. S. (1954) Converging spherical and cylindrical shocks, 54/54 Armament Res. & Development Establishment, Ministry of Supply.
- Chester, W. (1954) The quasi-cylindrical shock tube. *Phil. Mag.*, 45, 1293–1301.
- Chisnell, R. F. (1955) The formation of a shock wave in a channel. *J. Fluid Mech.*, 2, 286–298.
- Chorin, A. J. (1976) Random choice solution of hyperbolic systems of equation. *J. Comput. Phys.*, 22, 517–533.
- Courant, R., and Friedrichs, K. O. (1967) *Supersonic Flow and Shock Waves*, Interscience Publ., Inc., New York.
- Cramer, M. S. (1981) The focusing of weak shock waves at an axisymmetric arete. *J. Fluid Mech.*, 110, 249–253.
- Cramer, M. S., and Seebass, A. R. (1978) Focusing of weak shock waves at an arete. *J. Fluid Mech.*, 88, 209–222.
- de Neef, T., and Hechtman, C. (1978) Numerical study of the flow due to a cylindrical implosion. *Computer and Fluid*, 6, 185–202.
- Demming, F., and Hehmsoth, H. (1989) Model computation of converging cylindrical shock waves. *Proc. 17th Int. Symp. Shock Waves & Shock Tubes*, Bethlehem, 155–160.
- Duong, D. Q. and Milton, B. E. (1985) The Mach-reflection of shock waves in converging cylindrical channels, *Exp. Fluids*, 3, 161–168.
- Eisenberger, F., Miller, K., and Rassweiler, J. (1991) *Stone therapy in urology*, Thieme Medical Publ. Inc. New York.
- Fong, K., and Ahlborn, B. (1979) Stability of converging shock waves. *Phys. Fluids*, 22(3), 416–421.
- Gardner, J. H., Book, D. L., and Bernstein, I. B. (1982) Stability of imploding shocks. *J. Fluid Mech.*, 114, 41–58.
- Glass, I. I. (1967) Research frontiers at hypervelocities. *Canadian Aeronautics & Space J.*, 13, 401–426.
- Glass, I. I., and Sagie, D. (1982) Application of explosive driven implosions to fusion. *Phys. Fluids*, 25, 269–270.
- Glimm, J. (1965) Solution in the large for nonlinear hyperbolic systems of equations. *Comm. Pure Appl. Math.*, 18, 697–715.
- Groenig, H. (1986) Shock wave focusing phenomena, *Proc. 15th Int. Symp. Shock Tubes and Waves*, Stanford Univ. Press, 43–56.
- Groenig, H. (1989) Past, Present and future of shock focusing research, *Int. Workshop on Shock Wave Focusing*, Tohoku Univ., Sendai.
- Guderley, G. (1942) Luftfahrtforschung, starke kugelige und zylindrische Verdichtungsstoesse in der Nahe des Kugelmittelpunktes bzw. der Zylinderachse, 19, 302–312.

- Hartree, D. R. (1958) Numerical analysis, Second edition, Oxford University Press, London/New York, 209–216.
- Henshaw, W. D., Smyth, N.F., and Schwendeman, D. W. (1986) Numerical shock propagation using geometrical shock dynamics. *J. Fluid Mech.*, **171**, 519–545.
- Higashino, F. (1971) Imploding shock waves with chemical reactions. *Trans. Japan Soc. Aero. Space Sci.*, **14**, 25–46.
- Higashino, F., and Oshima, N. (1970) Real gas effects on converging shock waves. *Astron. Acta*, **15**, 523–529.
- Higashino, F., and Suzuki, Y. (1986) An application of PLM to the shock focusing on 2-dimensional blast waves. *Proc. Japan Conf. Fluid Mech.*, **14**, 565–571.
- Higashino, F., Suzuki, Y., Nishida, M., and Aki, T. (1987) Focusing of cylindrical shock waves. *Proc. 16th Int. Symp. Shock Tubes & Waves*, Aachen, VCH, 559–566.
- Hooker, W. J., Watson, R., and Morsell, A. L. (1969) Measurements with powered solids in shock tubes. *Phys. of Fluids, Suppl. I*, 165–167.
- Holl, R., Groenig, H., and Olivier, H. (1983) Focusing of weak blast waves. *Proc. 14th Int. Symp. Shock Tubes & Waves*, Sydney, 563–569.
- Hosseini, S. H. R., Onodera, O., Falcovits, J., and Takayama, K. (1997) Converging cylindrical shock wave in an annular diaphragmless shock tube. *Proc. 21st Int. Symp. Shock Waves*, Great Keppel Island, 1511–1516.
- Hosseini, S. H. R., Onodera, O., and Takayama, K. (1999) Stability of converging cylindrical shock waves in a vertical annular co-axial diaphragmless shock tube. *Trans. Japan Soc. Aero. Space Sci.*, **135**, 19–26.
- Kitayama, O., Ise, H., Sato, T., and Takayama, K. (1988) Non-invasive gallstone disintegration by underwater shock focusing. *Proc. 16th Int. Symp. Shock Tubes and Waves*, Aachen, 897–903.
- Knystautas, R., Lee, B. H. K., and Lee, J.H. (1969) Diagnostic experiments on converging detonations. *Phys. Fluids Supplement I*, 1-165–168.
- Lau, J.H. (1971) Spherically converging shock waves in dense plasma research, CASI, Trans. 4, 13–22.
- Lee, J. H., and Lee, B. H. K. (1965) Cylindrical imploding shock waves. *Phys. Fluids*, **8**, 2148–2152.
- Lee, J. H., Knystautas R., and Bach G. G. (1969) Theory of explosions. MERL Report 69-10, McGill Univ. Montreal.
- Milton, B. E., and Archer, R. D. (1969) Generation of implosions by area change in a shock tube. *AIAA J.*, **7**, 779–780.
- Milton, B. E., and Archer, R. D. (1971) *Proc. 8th Int. Shock Tube Symp.* London, 55/1–55/11.
- Mishkin, E.A. and Fujimoto, Y. (1978) Analysis of a cylindrical imploding shock wave. *J. Fluid Mech.*, **89**, Part 1, 61–78.
- Mueller, M. (1987) Stosswellenfokussierung in Wasser, Dissertation, RWTH Aachen.
- Nishida, M., Nakagawa, T., and Kikuyama, Y. (1986) Focusing of reflected shock waves. *Trans. Japan Soc. Space Sci.*, **28**, 209–217.
- Oshima, K. (1960) Blast wave produced by exploding wire, Univ. of Tokyo, Aeronautical Research Institute, Rept. No. 358.
- Oswatitsch, K. (1952) *Gasdinamik*. Springer, Wien.
- Payne, R. B. (1957) A numerical method for a converging cylindrical shock. *J. Fluid Mech.*, **2**, 185–200.
- Perry, R. W., and Kantrowits, A. (1951) The production and stability of converging shock waves. *J. Appl. Phys.*, **22**, 878–886.
- Russel, D. A. (1986) Shock dynamics of noninvasive fracturing of kidney stones. *Proc. 15th Int. Symp. Shock Tubes and Waves*, Berkeley, 57–64.

- Saito, T., and Glass, I. I. (1979) An application of random-choice method to problems in shock detonation wave dynamics, UTIAS Rept. 240, Univ. Toronto, and also (1989), Proc. Int. Workshop on Shock Wave Focusing, Sendai, 91–121.
- Sakamoto, I., Higashino, F., and Holl R. (1993). Focusing of reflected shock waves analyzed by means of geometrical shock dynamics. *JSME Int. Journal*, **36**, 560–566.
- Sakurai, A. (1953) On the propagation and structure of a blast wave, *I. J. Phys. Soc. Japan*, **8**, 662–668.
- Sauer, R. (1966) *Nichtstationaere Probleme der Gasdynamik*. Springer, Berlin.
- Sedov, L. I. (1959) *Similarity and Dimensional Methods in Mechanics* (transl. ed. by M. Holt), Academic Press, New York.
- Setchell, R. E., Storm, E., and Sturtevant, B. (1972) An investigation of shock strengthening in a conical convergent channel. *J. Fluid Mech.*, **56**(3), 505–522.
- Sod, G. A. (1977) A numerical study of a converging cylindrical shock. *J. Fluid Mech.*, **83**, 795–814.
- Sommerfeld, M., and Muellor, H. M. (1988) Experimental and numerical studies of shock waves focusing in water. *Experiments in Fluids*, **6**, 209–215.
- Stanyukovich, K. P. (1960) *Unsteady Motion of Continuous Media* (Trans. Holt, M. and Adashko, J.), Pergamon Press, Oxford, 417–489.
- Sturtevant, B. and Kulkarny, V. A. (1974) Dynamics of weak shock waves at a focus, Proc. 2nd Inter-Agency Symp. Univ. Res. Transportation Noise, North Carolina State Univ., Raleigh, 402–415.
- Sturtevant, B., and Kulkarny, V. A. (1976) The focusing of weak shock waves. *J. Fluid Mech.*, **73**, 651–671.
- Takayama, K. (1989) Intl. Workshop on Shock Waves Focusing, Tohoku Univ. Shock Wave Research Center, Sendai, 217–226.
- Taylor, G. I. (1950) The formation of a blast wave by a very intense explosion I. *Proc. Roy. Soc. Lond.*, **A201**, 159–167.
- Terao, K. (1984) Experimental study on spherically imploding detonation waves. *Japan J. Appl. Phys.*, **23**, 27–33.
- Wang, J. C. T. (1982), On the theory of imploding shocks, *ZAMP*, **33**, 53–62.
- Welsh, R. L. (1966) Imploding shocks and detonations. Univ. California Rept. No. AS-66-1.
- Whitham, G.B. (1957), A new approach to the problems of shock dynamics, Part 1. Two-dimensional problems. *J. Fluid Mech.* **2**, 146–171.
- Whitham, G. B. (1973) *Linear and Nonlinear Waves*. John Wiley & Sons, New York.
- Wo, J. H. T., Yu, T. S. H., Neemeh, R. A., and Ostrowski, P. P. (1979) Stability of cylindrical converging shock perturbed by a bleed aperture, shock tubes and waves. Proc. 12th Int. Symp. Shock Tubes and Waves, Jerusalem, 324–333.
- Zel'dovich, Ya. B. (1959) Converging cylindrical detonation waves. *Soviet Phys. JETP*, **36**(9), 550–556.
- Zucrow, M. J., and Hoffman, J. D. (1976) *Gas Dynamics*. John Wiley & Sons, New York.

Applications of Shock Waves in Medicine

ACHIM M. LOSKE

Instituto de Física, UNAM, A.P. 1-1010, Querétaro, 76000 Qro., México

-
- 12.1 Introduction
 - 12.2 Brief Physical Background
 - 12.2.1 Lithotripsy Pressure Pulses
 - 12.2.2 Shock Wave Propagation and Interaction with Matter
 - 12.3 Extracorporeal Shock Wave Lithotripsy
 - 12.3.1 Electrohydraulic Shock Wave Lithotripters
 - 12.3.2 Electromagnetic Shock Wave Lithotripters
 - 12.3.3 Piezoelectric Shock Wave Lithotripters
 - 12.3.4 Microexplosive Lithotripters
 - 12.4 Shock Waves in Orthopedics
 - 12.5 Shock Waves in Ophthalmology
 - 12.6 Shock Waves in Oncology and Gene Therapy
 - 12.7 Shock Waves as a Possible Method for Food Preservation
 - 12.8 Shock Wave Thrombus Ablation
 - References

12.1 INTRODUCTION

Underwater shock waves have been the subject of many theoretical and experimental studies in the past 25 years. This increased interest has been motivated by the success of the techniques developed to use shock waves for the noninvasive treatment of nephrolithiasis, known as *extracorporeal shock wave lithotripsy* (ESWL¹). For the same reason, the effects of shock waves on

¹ Dornier Medizintechnik GmbH, Germering, Germany

living cells have also been the subject of many investigations (Delius, 1994; Loske and Prieto, 1995). Nowadays there are more research groups working on the application of shock waves to medicine and chemistry than during the development of ESWL, indicating that this is still a promising research field. Information on the historical development of lithotripsy can be found in the literature (Häusler, 1985; Delius and Brendel, 1990; Jocham, 1987; Lingeman *et al.*, 1989; Loske and Prieto, 1999).

Since the first treatment in 1980, ESWL has become the standard treatment for the majority of patients with renal and ureteral calculi (Chaussy *et al.*, 1980; Loske and Prieto, 1999) and an alternative in the treatment of gallbladder stones (Nahrwold, 1993), pancreatic concrements (van der Hul *et al.*, 1993), and stones of the salivary gland (Iro *et al.*, 1989; Hessling *et al.*, 1993). ESWL is believed to be a safe and reliable procedure and tends to be used on an outpatient basis. Considering that an ESWL patient can be back at work in about 48 hours, and that, for instance, in the United States about 700,000 patients per year are ESWL candidates, the benefit to the health care services is not doubtful. Today more than 2000 ESWL devices (*lithotripters*) are in use in about 30 countries and more than 5 million ESWL treatments have been performed successfully. Nevertheless, intrarenal and subcapsular hematoma have been found after ESWL in a high percentage of cases examined (Evan *et al.*, 1991; Rubin *et al.*, 1987).

New clinical applications of shock waves are the rupture of cataractous material in the eye (Dodick, 1991) and the treatment of nonunion fractures (Haupt *et al.*, 1992), as well as the management of pseudarthrosis (Schleberger and Senge, 1992), tendinopathy, and other orthopedic diseases (Haupt, 1997). The treatment of tumors with shock waves is another experimental approach (Oosterhof *et al.*, 1990).

Despite the fact that ESWL has been used successfully for two decades, continuous modifications are being made to improve the technique. For research purposes, some universities and hospitals have decided to build their own shock wave generating devices (Prieto *et al.*, 1991); nevertheless, more research is still needed about the mode of action of shock waves on tissues and about the chemical effects of shock waves *in vivo*. Contraindications for shock wave therapy are pregnancy, bleeding disorders, lung tissue in the shock wave path, life-threatening cardiac problems, and the presence of some types of cardiac pacemakers.

It is the purpose of this chapter to describe the physical principles of the various applications of weak shock waves in medicine and in new research areas such as food preservation.

12.2 BRIEF PHYSICAL BACKGROUND

12.2.1 LITHOTRIPSY PRESSURE PULSES

Whether they are technically shocked or not, in general ESWL pulses are called shock waves to denote the high-amplitude pulse generated. Furthermore, most articles dealing with the suppression of tumor growth by pressure pulses refer to these shock waves as high-energy shock waves, even if their amplitude is not larger. Because of the finite aperture size of the shock wave sources, diffraction takes place and has to be included in addition to nonlinear propagation. Existing theoretical models require long computing times, and few of them are relevant to lithotripsy focusing fields (Choi *et al.*, 1991). Nevertheless, nonlinear effects are only prominent at a distance of a few millimeters in the focal area, since shock waves in water, with high-pressure amplitudes compared to gaseous media, are rather weak in the gas-dynamic sense. The pressure generated during ESWL is about one order of magnitude higher than that generated by ultrasound imaging devices.

The focal region of a lithotripter is defined as the volume in which, at any point, the pressure has more than 50% of the maximum amplitude. It is also called *dynamic focus* or *−6 dB zone*. The pressure variation at the dynamic focus has a compressive (positive) pressure component with a steep shock front (10–600 ns rise time) reaching up to about 150 MPa, with a phase duration of 0.5 to 3 μ s, followed by a rarefaction (“negative”) phase of about 2 to 30 MPa, with a phase duration of about 2 to 20 μ s (Coleman and Saunders, 1989). Pulse energies are in the range of 10–100 mJ (Folberth *et al.*, 1992). For the distances R (several inches) and the energies E (several hundred joules) characteristic of ESWL, the pressure P can be approximated by (Marshall *et al.*, 1988) $P = P_0 e^{-t/\theta}$, where $P_0 = 72(E^{1/3}/R)^{1.18}$ in pounds per square inch, and $\theta = 1.09 \times 10^{-3}(E^{1/3}/R)^{-0.185}$ in milliseconds.

Many problems arise when measuring the pressure generated by a lithotripter. Reflections created in the transducer due to the entrance and exit of the wave produce interference, small alignment errors affect the measurements, and manufacturers normally do not calibrate their gauges in the same environment. In general, the nonconstant pressure profile over the diaphragm of the transducer is not considered. An accurate pressure measurement of a shock wave lasting 1 μ s or less and having a 10-ns rise time requires a transducer with a rise time on the order of nanoseconds. In the early days of ESWL the fastest commercial piezoelectric pressure transducers were too slow. Nowadays higher sensitivities are obtained by thin piezoelectric elements in which the voltage is measured instead of the polarization current. Well suited for shock wave measurements are bilaminar shielded *polivinyllidene difluoride*

(PVDF) membrane hydrophones (GEC, Marconi Research Centre, Chelmsford, Essex, U.K.) or needle PVDF hydrophones (Imotec GmbH, Würselen, Germany); however, there is a limited possibility of measuring negative pressures, since both hydrophones have metal surfaces that suffer damage due to cavitation induced by the negative pressure waves. Nowadays, probably the most convenient instrument for ultrasonic and shock wave measurement in water is the fiber optical hydrophone (Staudenraus and Eisenmenger, 1993). This device measures the pressure-dependent change of the density and the index of optical refraction in water. Laser light is coupled into a glass fiber and reflected off the end of the fiber, which is immersed in water in the region where the shock wave passes. A photodetector connected to an oscilloscope registers the reflected light. Pressure changes at the tip of the fiber result in changes in the optical signal giving information on the shock wave profile. The rise time (at the present about 5 ns) of this hydrophone is limited only by the electronic amplifier. Another advantage of this system is the fact that the fiber has a high resistance against shock wave damage. The signal-to-noise ratio of the glass fiber system is sufficient to resolve a single shock wave within an accuracy of a few bars.

12.2.2 SHOCK WAVE PROPAGATION AND INTERACTION WITH MATTER

As the wave propagates through a medium, energy is lost to friction, causing energy absorption and a pressure and intensity reduction. The pressure reduction can be estimated by $P = P_0 e^{-\alpha x}$, where x stands for depth in centimeters, P_0 is the initial pressure, and α is the absorption coefficient. Since in a biological medium the absorption coefficient $\alpha = bf^m$ (b and m are constants, f is the frequency), high-frequency waves will be absorbed more than low-frequency waves. Because of the physical characteristics of these waves, sonic absorption in biological tissue is quite low. Most biological tissues have a value of $1 < m < 2$. The intensity $I = I_0 e^{-2\alpha x}$, where I_0 is the incident intensity and I the intensity of the wave at a depth x , decreases rapidly as the frequency f increases. Since shock waves have lower frequencies compared with ultrasound, they have a higher penetration power. High frequencies composing the sharp portion of the wave front are attenuated more than the low components associated with the tensile phase, leading to a higher reduction in the positive peak. Traumatic effects of low-frequency components are due to the large displacement amplitudes (some orders higher) compared to the high-frequency domain. Therapeutic effective components for ESWL are considered to be above 200 kHz. Components with no effect are between 20

and 200 kHz, and low-frequency components are below 20 kHz. To simulate the pressure field near the focal region of a lithotripter, a model must consider shifts in the relative phase of harmonics generated during propagation due to nonlinear effects.

Kidney stones, which develop from crystals that separate from urine and build up on the inner surfaces of the kidney, are brittle composite materials, having weak spots and flaws, generally composed of crystals joined together by organic deposits. These organic deposits are weak. Compression and tension of the stone results in a loss of cohesiveness due to growth of microscopic flaws. Most common types of stones contain calcium in combination with either phosphate or oxalate. So-called *struvite* or infection stones are caused by infection in the urinary tract. Uric acid and *cystine* stones are less common.

The application of shock waves for ESWL is based on the fact that the tensile strength of kidney stones is one order of magnitude lower than their compressive strength. Destruction occurs by conversion of positive pressure pulses into tensile stress inside the stone. As the shock wave enters the stone, the sign of the wave is not changed because the acoustic impedance of the stone is greater than that of tissue or urine. However, on the back surface, when the shock wave exits the stone, a portion of the wave is reflected and becomes tensile. Incident and reflected waves add and a fracture plane will develop at the point where the net effect of the two waves is sufficiently tensile to induce a cleavage plane.

It is difficult to make precise correlations between shock wave parameters and calculus disintegration mechanisms, but it is known that the peak pressure produces a compressional force on the stone and that the rarefactional part of the wave is associated with tensile forces and cavitation bubbles around the focal point (Church, 1989). The rarefaction components of the shock waves converging toward the focal region exceed the threshold for cavitation in water (urine) and induce cavitation bubbles in the neighborhood of the stone. When these cavitation bubbles collapse, they produce high-speed (100–400 m/s) liquid microjets, damaging the stone surface. Although the total energy of a cavitation event is small, its concentration into a very small volume may cause an enormous energy density, with a large potential for damage. Temperatures and pressures within a collapsing cavity are about 10,000 K and 100 MPa, respectively. Cavitation is known to be one of the most important mechanisms for stone fragmentation and tissue damage during ESWL. It is also known that higher amplitudes generate stronger spalling effects and that the rise time is related to shear forces produced in the concretions. Cavitation may also explain reports of decreases in both persistent urinary tract infection and bacteriuria after ESWL of infection stones (Michaels *et al.*, 1988; Pode *et al.*, 1988). The disintegration process of renal calculi depends on the surrounding

media. Calculi confined in a small cavity are more difficult to destroy, since less cavitation occurs.

When a sound wave hits an interface between two media of impedance Z_a and Z_b , part of it is reflected and part of the wave is transmitted. The reflection and transmission coefficient at the boundary between the two media are (Cameron and Skofronick, 1979)

$$P_r/P_i = (Z_b - Z_a)/(Z_a + Z_b) \quad \text{and} \quad P_t/P_i = 2Z_b/(Z_a + Z_b), \quad (12.1)$$

respectively, where P_i , P_r , and P_t are the pressure amplitudes of the incident, reflected, and transmitted waves. In order to maintain the energy balance at the boundary, the sum of the absolute value of the intensity of the transmitted and reflected waves must be equal to the intensity of the incident wave. The reflectivity and the transmissivity are

$$I_r/I_i = (Z_b - Z_a)^2/(Z_a + Z_b)^2 \quad \text{and} \quad I_t/I_i = 4Z_aZ_b/(Z_a + Z_b)^2, \quad (12.2)$$

respectively, and the intensity I is defined as the energy crossing a unit area per unit time (Cameron and Skofronick, 1979),

$$I = \frac{1}{2} \rho v A^2 (2\pi f)^2 = \frac{1}{2} Z (A\omega)^2 = P_0^2 / 2Z, \quad (12.3)$$

where f , ω , A , and P_0 represent the frequency, the angular frequency, the maximum displacement amplitude of atoms or molecules (particles), and the maximum change in pressure. The acoustic impedance Z is defined as the product of the density ρ and the wave velocity v , or, in terms of the bulk modulus of elasticity B , $Z = (B\rho)^{1/2}$.

This explains why, when a wave propagates from a low-impedance to a high-impedance medium ($Z_a < Z_b$), such as from soft tissue ($Z \approx 1.6 \times 10^6 \text{ kg/m}^2/\text{s}$) to cortical bone ($Z \approx 5.9 \times 10^6 \text{ kg/m}^2/\text{s}$), the pressure amplitude of the transmitted wave is greater than that of the incident wave (Eq. (12.1)); however, the transmitted energy is smaller than that of the incident wave (Eq. (12.2)). On the other hand, when the wave travels from kidney stone (Z between 2×10^6 and $5 \times 10^6 \text{ kg/m}^2/\text{s}$) to soft tissue or urine ($Z \approx 1.4 \times 10^6 \text{ kg/m}^2/\text{s}$), the pressure amplitude of the transmitted wave is smaller than that of the incident wave. Reflection at an interface presenting a decrease in impedance to the incoming wave leads to a phase change in the reflected wave (Eq. (12.2)). In order to maintain balance at the boundary, the acoustic pressure of the transmitted wave always is in phase with the incident wave. Because of the impedance mismatch between kidney stones and the surrounding urine, the compressive component of the incident shock wave, propagating through the stone, will produce strong reflected dilating stresses at the wave exit site or at stone layer boundaries between crystalline and matrix materials. Theoretically, the fracture depth is about one-half the wavelength of the stress. The amplitude of the transmitted waves is an important factor in the

fragmentation speed; however, recent studies have demonstrated that acoustic energy correlates with fragmentation much better than the positive pressure or the rise time of the shock wave. Initially it was thought that the shock wave pressure is the most important shock wave parameter for stone disintegration. As measuring techniques improved, the acoustic energy hitting the stone was identified as the mechanism with the greatest effect.

Even if in renal tissue or water only longitudinal waves can exist, in general, a longitudinal and a transversal wave will be generated in the stone. Obviously, the chemical composition and stone geometry influence the disintegration rate. Inner reflections of the two shock fronts create alternative compressions and rarefactions, producing small fissures. As these fissures become filled with liquid (urine), cavitation is formed by subsequent shock waves, contributing to a fast disintegration of the stone. Short pulses are desirable in ESWL because the fragments of the stones become smaller and the tissue damage decreases with shorter pulses.

Spallation damage (Hopkinson effect) will be produced if the tensile stress exceeds the tensile failure strength of the calculus. The location of the spall planes depends on the shape of the calculus, the material properties and the pulse width. In addition to tensile stress created inside the stone, cavitation will act on it from the outside.

12.3 EXTRACORPOREAL SHOCK WAVE LITHOTRIPSY

The goal of ESWL is to provide efficient fragmentation of calculi with the least amount of tissue damage. Since its introduction, more than 40 different variations of lithotripters have become available, but only four basic methods of shock wave generation are used: electrohydraulic, piezoelectric, electromagnetic, and, to a much lesser extent, microexplosive (Kuwahara *et al.*, 1986; Coptcoat *et al.*, 1987; Loske and Prieto, 1999).

12.3.1 ELECTROHYDRAULIC SHOCK WAVE LITHOTRIPTERS

Electrohydraulic shock wave lithotripters induce low-intensity shock waves by electrical breakdown (15–30 kV) of water between two electrodes, located at the focus (normally referred to as F_1) closest to a paraellipsoidal reflector (Fig. 12.1). The peak current at discharge is in the range 10–20 kA, depending on the inductance of the circuit. Energy is stored in a set of capacitors by a high-

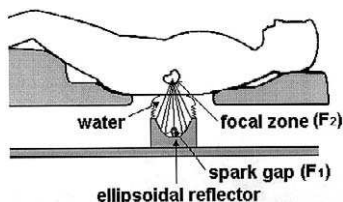


FIGURE 12.1 Schematic drawing of an electrohydraulic lithotripter.

voltage source. Two electrodes are connected to the capacitor terminals and submerged underwater. When the spark plug fires, dielectric breakdown occurs and a bubble filled with steam and other gases is generated at temperatures of about 20,000 K. The initial pressure wave, which is an intense sinusoidal half-wave, is created by the bubble expansion. As it propagates through the water, the pressure peak increases its speed enough to overtake the front end of the wave, changing its shape. An analysis of the relationship between the arrival time of the shock wave and its amplitude appears to indicate that when the plasma formation is faster, more of the stored energy is converted into mechanical energy (Loske, 1990). Waves are created at F_1 , partially reflected off the reflector, and concentrated at the second focus, F_2 . If the patient is properly positioned with the calculus located at F_2 , the shock wave enters the body with little attenuation, becomes focused on the calculus, and fractures it. It is only a small percentage of the discharge energy (less than 5%) that reaches the calculi (Coleman and Saunders, 1989). A warm water bath or water-filled cushion couples the energy generated at F_1 with the patient's body. Pressure attenuation through the membrane of the water cushion (about 20%) is compensated for by increasing the voltage. Several hundred shock waves are needed to completely disintegrate the stone. In order to control the repetition rate of the shock waves, a spark gap driver and a trigger switch driven by a pulse generator are used. Basically, the circuit consists of two parts: the capacitor charging system and the discharge control system. In order to get a fast discharge, the inductance should be as low as possible. The relation between the discharge energy E , the capacitance C , and the applied voltage U is $E = \frac{1}{2}CU^2$, which is proportional to the square of the maximum pressure amplitude.

Disintegration efficiency and also patient pain and trauma depend, to a certain extent, on the design of the reflector. Depending on the type and model of the lithotripter, the pressure in the vicinity of F_2 ranges from 300 to 1500 bar, and the major axis a , the minor axis b , and the depth P of the reflector range from about $a = 270$ mm, $b = 150$ mm, and $P = 120$ mm to approximately $a = 340$ mm, $b = 220$ mm, and $P = 160$ mm. From the beginning of ESWL, the tendency has been to increase these three parameters in

order to obtain a smaller focal region, a larger aperture, and consequently less pain and damage to the surrounding tissue. Because the path from F_1 to the reflector and to F_2 is the same for all parts of the shock front, shock waves are in phase at F_2 . The fundamental law of geometrical acoustics, which predicts that the angle of incidence α_1 of an incoming spherical wave equals its angle of reflection α_2 , is valid only for low pressures. The design of a reflector for a lithotripter must take into account, however, that the angle of reflection is bigger than the angle of incidence (Müller, 1987). This difference increases as α_1 becomes larger and also as the pressure rises. As shown in Fig. 12.2, this phenomenon shifts the focal region a few millimeters away from the reflector and from F_2 . In Fig. 12.2, all rays are perpendicular to the shock front. At the deepest section of the mirror, the angle of incidence is similar to the angle of reflection. For those rays arriving at larger angles α_1 , the angle of reflection α_2 increases considerably, preventing them from reaching F_2 . It is also important to notice that the energy density of the incoming spherical shock wave is constant, whereas the energy density of the reflected wave in the vicinity of F_2 is much higher near the axis of symmetry y . If the pressure in the central region of the reflected shock front is higher, its velocity will also increase, producing a flattening (Fig. 12.2) of the shock front near the y -axis. Because of this effect, sometimes the focal region is shifted toward the reflector. Depending on the energy of the shock wave and the geometry of the mirror, either of the two above-mentioned phenomena will predominate. Because of diffraction at the edge of the reflector, the shock front changes its curvature as shown in Fig. 12.2. The dynamic focus varies in shape and position with the voltage applied on the capacitor of the shock wave generator. Furthermore, an increase in voltage will produce an increase in the rise time of the shock wave. These

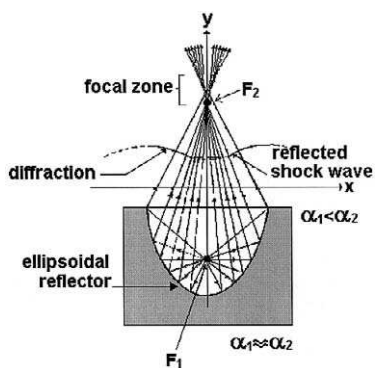


FIGURE 12.2 Two-dimensional diagram of the reflector used in electrohydraulic lithotrippers, showing a few rays perpendicular to the shock front and the reflected shock front traveling toward the focal region.

changes affect stone fragmentation. In general, the reflectors are made of brass or stainless steel. Since the acoustic impedance of the material is related to the reflected energy, high acoustic impedances are desired. Brass is nearly acoustically rigid in water (normal pressure amplitude reflection coefficient $R = 0.94$) and is often used for the reflectors of electrohydraulic lithotripters; nevertheless, with stainless steel, the reflected energy is about 7% higher than that obtained with brass. So called *pressure-release* ellipsoidal reflectors, made out of polyurethane foam (normal pressure amplitude reflection coefficient R is -0.88) have also been proposed and compared to standard rigid reflectors (Bailey *et al.*, 1998). Although the pulses produced by the two reflectors are similar in amplitude, duration, and rise time, they are different in waveform and produce different cavitation. The pulse from a pressure-release reflector is a negative pressure trough, followed by a positive spike. So far, no pressure-release reflectors have been used clinically; nevertheless, experimentally they have provided a tool for comparing effects in cavitating fields.

Electrohydraulic lithotripters generate not just one, but three shock waves. The first, as already mentioned, is due to the water breakdown by the spark into a gas bubble. Part of it will travel directly from F_1 to F_2 ; however, most of the energy is reflected off the reflector, reaching F_2 about $50\text{ }\mu\text{s}$ later. This is followed by the shock wave generated by the cavitation bubbles at F_2 and the shock wave originated when the large plasma bubble at F_1 collapses (Loske, 1990). Figure 12.3 shows a typical pressure record obtained by placing a needle hydrophone (Imotec GmbH, Würselen, Germany) with a 20-ns rise time at F_2 . The electromagnetic signal of the high-voltage discharge can be seen at the beginning of the trace. It is followed about $170\text{ }\mu\text{s}$ later by the pressure pulse coming directly from the spark gap. The pulse reflected off the ellipsoidal reflector can be distinguished by its large amplitude. This is the only pulse having sufficient energy to be useful in ESWL. The front of the waveform is shocked and the measured rise time of about 30 ns is limited by the

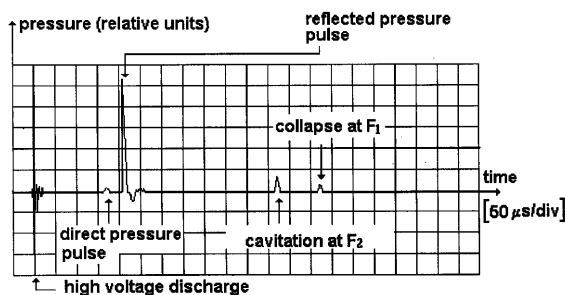


FIGURE 12.3 Typical pressure record obtained at the focal region of an electrohydraulic lithotripter.

hydrophone. Theoretically it should be much less. A tensile tail follows the positive pulse.

Disadvantages of this shock wave generation method are the high variance in pressure (up to 40%), the change in shock wave energy as the electrodes burn off, and the fact that, in general, electrodes have to be replaced after each treatment. In order to reduce time between voltage application and spark gap generation, the electrode gap should not exceed 3 mm (Loske and Prieto, 1993). In general, the spark does not link the two electrodes by the shortest path, so that the plasma formation is rarely located exactly at F_1 , leading to dispersed pressure peaks around F_2 . Axial positioning of the electrodes in the ellipsoid provides a smaller focal zone. Nevertheless, the spark gap method has advantages such as the high plasma expansion velocity produced by the discharge, the relative simplicity, and the low cost of the generator, compared to other systems. It was the first shock wave generation principle in use for ESWL.

In order to improve the effectiveness of electrohydraulic extracorporeal lithotripters, composite reflectors have been proposed (Loske, 1994; Prieto and Loske, 1994, 1995, 1999; Loske and Prieto, 1996) and are presently being tested clinically. In contrast to the standard design, composite reflectors are obtained by combining two sectors of two rotationally symmetric ellipsoidal reflectors with different geometry. Each sector is part of an ellipsoid with different separations between their foci (F_1, F_2) and (F'_1, F'_2). As shown in Fig. 12.4, the foci F_1 and F'_1 coincide, creating a separation between F_2 and F'_2 . The purpose of the bifocal reflector is to temporally and spatially phase out the shock wave generated at $F_1(F'_1)$. The reflected shock wave is divided in one shock front that converges toward F_2 and another front that is focused to F'_2 .

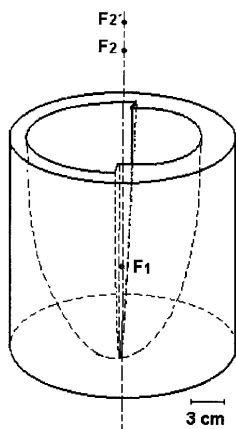


FIGURE 12.4 Schematic drawing of a bifocal reflector for electrohydraulic lithotripters.

Theoretical acoustics predicts that the energy density has its maximum value somewhere between F_2 and F'_2 . Because of the nonsymmetric geometry of the reflector it has a discontinuity at the focal axis. As in a conventional reflector, the pressure in the central region is higher, flattening the shock front. On the other hand, because α_1 is not equal to α_2 , the rays reflected from each component of the reflector do not arrive at their respective foci F_2 and F'_2 but form a focal region between them. Experiments showed that composite reflectors are more efficient than conventional reflectors in breaking up kidney-stone models and revealed that enhanced stone fragmentation did not occur at the regions of maximum pressure, indicating that spatial and temporal phasing out of the shock front plays a significant role in stone fragmentation and should be considered in designing reflectors for ESWL and other medical applications (Prieto and Loske, 1999). Similar designs were also suggested by Zhong *et al.* (1997), using longer time delays between the two shock waves, in order to produce controlled, forced collapse of the cavitation bubbles near the stone.

Spark gaps in water generate broadband pressure pulses with very short duration and pressures, which depend on several parameters, some of which can be controlled and some of which cannot. The radiant output of the underwater spark has a continuum in the ultraviolet. Short rise times and high pressures are considered convenient for ESWL; nevertheless, as already mentioned, stone fragmentation does not depend only on the pressure amplitude, but also on the pressure profile of the shock wave.

12.3.2 ELECTROMAGNETIC SHOCK WAVE LITHOTRIPTERS

Similar to the system used in a loudspeaker, electromagnetic shock wave lithotripters generate shock waves by moving a metal diaphragm, about 12 cm in diameter, located in the base of a water-filled shock tube. When a very short electrical pulse (16–22 kV) is sent through a coil, it produces an increasing magnetic field, which induces eddy currents in the metallic membrane. These eddy currents also produce a magnetic field, which is opposed to that of the coil. Because of this, the membrane is repelled, transmitting the energy to the water. The sudden movement of the membrane produces a pressure wave propagating through the water. During its path through water, the pulse steepens and forms a shock wave, after passing through a lens. A foil insulates the membrane from the water. Shock waves are focused by an acoustical polystyrene lens (Fig. 12.5). The distance from the center of the lens to the focus is approximately 12 cm and its aperture angle about 60° . Coupling of the shock wave to the patient is facilitated by a water-filled silicone cushion.

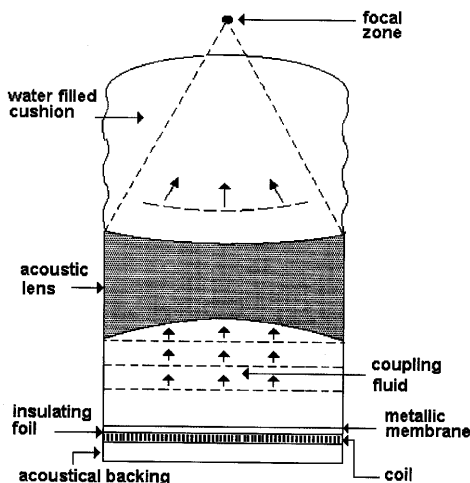


FIGURE 12.5 Schematic drawing of an electromagnetic shock wave generator for ESWL.

Electromagnetic lithotripters were developed at the beginning of the 1980s. Some of them are configured with bilateral shock wave generators (Loske and Prieto, 1999). Compared to electrohydraulic systems, their pressure varies much less (about 1%) between two discharges with the same initial energy. The electric discharge circuit is in principle similar to the one mentioned in Section 12.3.1.

The main disadvantage of the system is its relatively large negative pulse. On the other hand, the rise time of the pressure pulse is longer, compared to electrohydraulic lithotripters (Coptcoat *et al.*, 1987; Loske and Prieto, 1999).

An alternative design has been developed, in which a cylindrically diverging wave is generated by an electromagnetically driven cylindrical membrane, as shown in Fig. 12.6 (Köhrmann *et al.*, 1995; Loske and Prieto, 1999). It consists of a hollow acoustical backing supporting a coil system, insulated from the copper membrane by a foil. The working principle is similar to the electromagnetic generator discussed earlier; however, in this case, the acoustic pulses are radially radiated perpendicular to the cylinder axis, after application of short electrical pulses to the coil. Focusing of the cylindrical wave is done by reflection off a rotational symmetric reflector (about 30 cm in diameter) with a parabolic surface given by $y = 2px$, as shown in Fig. 12.6. Main advantages are the possibility of incorporating a coaxial location system (ultrasound scanner) into the hollow cylinder and the fact that no lenses are needed. With this design, shock wave generation is also possible using the piezoelectric effect. Normally the aperture angle of the reflector is about 80° , and the focal distance approximately 150 mm, providing a large penetration depth.

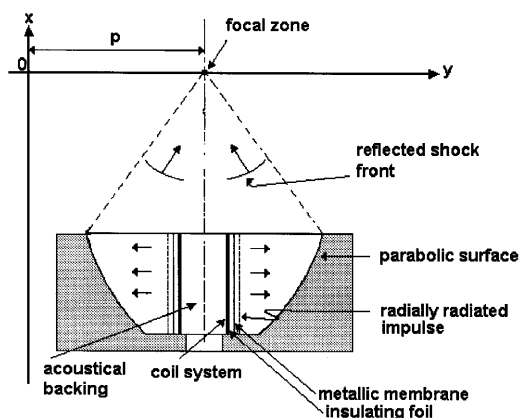


FIGURE 12.6 Schematic drawing of a cylindrical electromagnetic shock wave generator for ESWL.

12.3.3 PIEZOELECTRIC SHOCK WAVE LITHOTRIPTERS

Piezoelectric shock wave lithotripters use between about 30 and 3000 oscillating piezoceramic crystals, arranged on the concave surface of a spherical metallic dish, stimulated by an electric discharge, which is generated with a pulse generator, allowing different levels of pulse intensity (Fig. 12.7). Applying the electric field across the piezoelectric crystals changes their dimensions. Movement of the crystals produces a pressure wave. When the crystals return to their original shape, tensile pressure results. An interference phenomenon, produced by these piezoelectric radiators because of excitation, is present during propagation of the pressure pulse. Because of the shape of the dish, the energy is focused to the center of the sphere (40–50 cm in diameter), where the stone should be placed. The hemispherical arrangement of the piezoelements produces a focal zone in the shape of a cigar measuring about 17×3 mm. The

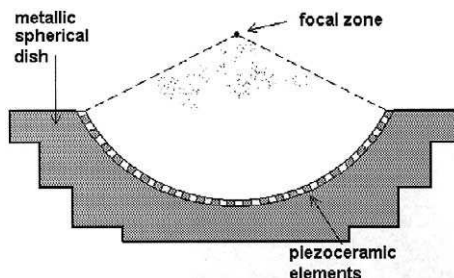


FIGURE 12.7 Schematic drawing of a piezoelectric shock wave generator for ESWL.

rear side of the dish has an irregular contour to prevent the formation of a strong tensile wave. In many designs, a 4-MHz ultrasonic scanner is fixed to the center of the shock wave generator, making possible real-time imaging during treatment. The dish with the ceramic elements mounted on it is placed inside a cavity filled with degassed water, warmed to body temperature, and closed with a rubber membrane that comes into contact with the skin of the patient through a coupling gel. In some devices the patient skin is in direct contact with the water (Loske and Prieto, 1999). For focusing purposes, the generator can be moved in three directions. In general, the shock wave pulse sequence (1–2.5 Hz) and the energy can be varied. Some piezoelectric lithotripters have more than one pulse discharge circuit. Their main advantages are the low maintenance costs and the fact that the generated electromagnetic radiation is low. Its relatively large negative pressure pulse is considered as a disadvantage.

Recently, much smaller piezoelectric generators, with crystals mounted on the inner and outer sides of a spherical dish, have been developed. Crystals mounted on the concave surface are fired after those on the convex side. Superposition of the pressure pulses compensates for the pressure loss due to the smaller size of the dish. Some of these new designs use solid media instead of water for coupling. Specially designed piezoelectric shock wave generators have also been used for veterinary applications, especially for orthopedic diseases in racing horses.

12.3.4 MICROEXPLOSIVE LITHOTRIPTERS

Microexplosion shock wave generation for ESWL was developed in Japan (Kuwahara *et al.*, 1986) and is not common. Similar to electrohydraulic lithotripters, these shock wave generators use ellipsoidal reflectors to concentrate the energy on the calculi, located at F_2 ; however, in this case, shock waves are produced by the explosion of a small 10-mg lead or silver azide pellet placed at F_1 . The microexplosive has to be replaced after each explosion. The need to replace the microexplosive, the fact that the system is noisy, and the storage of explosives are considered as the main disadvantages. The pressure profile produced with explosive pellets is similar to that generated using electric discharges. Advantages of the microexplosive design are low construction and operation costs and the absence of a high-voltage discharge circuit. The first patient was treated in 1985, sitting in a water tub (Loske and Prieto, 1999).

12.4 SHOCK WAVES IN ORTHOPEDICS

Because of the crystalline composition and high percentage of the collagen matrix, bones are not damaged by shock waves as are kidney stones.

Furthermore, bones cannot be considered as brittle structures compared with kidney stones because their tensile and compression strength do not differ much from each other. Nevertheless, the acoustic impedance of bone is about four times higher than that of soft tissue, opening up the possibility for an action of the pressure pulse. At the soft tissue/bone interface, shock wave reflection and refraction generate tensile waves within the bone, which might exceed its strength and induce fracturing. Trabecular fractures and displacement of marrow contents from within the bone to the space below the periosteum were found. Experiments also showed that the lesions were produced by cavitation. Shock waves are not expected to affect cartilage because of its lack of vascularization, since fluid is needed for cavitation to occur.

Extracorporeal shock wave therapy (ESWT), also called *extracorporeal shock wave application* (ESWA), introduced in Germany in 1989, refers to the clinical use of shock waves for orthopedic applications. So far more than 50,000 ESWT procedures have been performed in Germany; however, the mechanics of ESWT are not yet fully understood. Patients are treated on an outpatient basis using local anesthesia. The average treatment time is about 30 minutes. ESWT usually consists of one to three sessions of about 2000 shock waves and has become important in sports medicine.

So far, mainly three uses have been proposed for shock waves in clinical orthopedics: (a) to cause microfractures of cortical bone used to perform closed *osteotomies* or to stimulate local hematoma formation and bone healing at the site of nonunion; (b) to fragment polymethylmethacrylate (PMMA) cement and separate it from bone; and (c) to bring relief to patients suffering from pain due to chronic *chalk shoulder*, *heel spur*, or *tennis elbow*. Nevertheless, more research is still needed about the morphological changes induced in bone *in vivo* by shock waves. For the first two applications, energies as in ESWL are used. The treatment of pain requires less energy.

Fracture healing that does not appear within 6 months is called *pseudarthrosis* and can be improved by physical influences such as ultrasound, electromagnetic fields, electrical stimulation, intermittent tension, and micro-movement. The *osteogenetic potential* of shock waves, that is, fracture healing, was discovered in 1986 (Haupt *et al.*, 1992).

The possibility to produce microfissures and fracture hematoma enables one to reactivate bone growth by osteogenetic response. Shock waves break up the sclerotic bone ends, producing microfissures, which enhance blood supply. In contrast to ultrasound, heating of the bone is not to be expected, since shock waves do not transfer energy as heat.

First treatments of patients with delayed union or nonunion of fractures were reported by Valchanou and Michailov (1991). Schleberger and Senge (1992) obtained similar results. The application of 1000 to 4000 shock waves induced bony union in about 85% of the patients. Modified lithotripters and

specially designed shock wave generators for orthopedics have been developed by several companies (Loske and Prieto, 1999).

Shock waves have also been used for the loosening of bone cement, which constitutes a problem during *revision arthroplasty* (Braun *et al.*, 1992). About 100,000 hip arthroplasty surgeries using PMMA have been performed each year in the United States annually. Up to 41% of patients require revision arthroplasty. A problem during revision arthroplasty is the removal of the adherent bone cement from the intramedullary canal. In general this canal is difficult to reach with instruments. Fortunately, there is no chemical bonding between bone and cement. Furthermore, the acoustic impedance of bone is about twice as large as the impedance of bone cement. When the shock wave passes the bone/cement interface, conversion of pressure waves into tensile waves results in the release of mechanical energy, which leads to disintegration of the cement when its strength has been exceeded. In 1986 Weinstein and co-workers proposed a preoperative shock wave application to loosened cemented arthroplasties (Weinstein *et al.*, 1986). The main problem of this technique is the fact that shock waves may liberate bone marrow particles, which could cause fat embolism (Braun *et al.*, 1992).

As already mentioned, shock waves have also been applied in cases of *epicondylitis humeri radialis*, known as tennis elbow. Three treatments consisting of approximately 1000 shock waves having an energy density of about 0.06 mJ/mm^2 were successful in about 90% of patients (Rompe *et al.*, 1995). The tendons in the shoulder can also be freed from calcareous inclusions using shock wave therapy (Loew *et al.*, 1995). Painful plantar heel spur, or plantar clinical syndrome, characterized by pain and tenderness beneath the heel, has also been treated with shock waves. In general, a circumscribed pain of no more than about 7 mm in diameter is considered as a prerequisite for successful shock wave treatment.

It is believed that shock waves stimulate the metabolic reaction of tissue, changing the membrane permeability and causing the development of stress fibers. They also create cavitation bubbles, which break calcific deposits and induce an analgesic effect by stimulating the *axons*. Because of this, the patient's pain threshold is increased.

ESWT has also been used to treat racehorses suffering *podotrochilitis* in the hoof, *insertion desmopathies* in the leg, *sesamoidosis* in the region of the sesamoid bone, and *tendopathies*.

12.5 SHOCK WAVES IN OPHTHALMOLOGY

Phacoemulsification and aspiration was introduced more than 30 years ago by Kelman (1967) as a new technique of cataract removal, laying the basis for

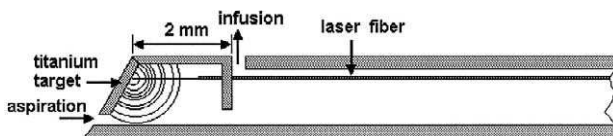


FIGURE 12.8 Schematic drawing of an irrigating and aspirating probe to perform laser phacolysis using shock waves.

small-incision cataract surgery. During ultrasound phacoemulsification, energy is released at a probe tip to the cataract. Problems are associated with its effects on nontarget tissues such as the corneal endothelium, iris, and posterior capsule. Since the probe houses a motor to drive the needle to emulsify the lens, it is not easy to handle.

Shock waves were used in ophthalmology for the first time by Dodick (1991). The device consists of a pulsed 1064 Nd:YAG laser that transmits light through a 300 μm quartz fiber optic that enters into an irrigating and aspirating probe (Fig. 12.8). Less than 2 mm in front of the fiber end, a titanium target acts as a transducer to convert laser energy into shock waves. When the laser strikes the target, plasma formation occurs. The shock waves spread out inside the aspiration chamber to the mouth of the aspirating port, while the probe is held close to the cataractous tissue. Shock waves cause the cataractous material to be broken off and be aspirated down the aspiration line. A *capsulotomy* is followed by laser lysis of the nucleus.

Advantages of laser phacolysis over ultrasound phacoemulsification are that the Nd:YAG laser generates considerably less heat, and that the laser probe does not contain a motor, being much smaller than ultrasound probes. Furthermore, the laser probe does not require vibrating needles, which are subject to wear and breakdown, and the probe can be fabricated with curved or flexible cannulas.

12.6 SHOCK WAVES IN ONCOLOGY AND GENE THERAPY

Since Russo *et al.* showed that underwater shock waves can be cytotoxic to tumor cells, several research centers have performed similar experiments (Russo *et al.*, 1985; Oosterhof *et al.*, 1989; Randazzo *et al.*, 1988). Shock waves delivered by extracorporeal lithotrippers showed to be cytotoxic to several tumor cell lines, both *in vitro* and *in vivo* (Russo *et al.*, 1986; Chaussy *et al.*, 1986). However, the tumor growth suppression observed *in vivo* is temporary, indicating that shock waves are not likely to be useful as mono-

therapy. Oosterhof *et al.* (1990) demonstrated that the effect is dependent on the number of shock waves, on the tumor line, and on the tumor volume. Tumor necrosis and hemorrhage were the main microscopic findings. Damage to the vascularization of the tumor may explain the temporal growth delay after shock wave exposure. *In vivo* proliferation studies on human renal cell carcinoma xenografts showed a decrease in tumor size after shock wave treatment, but without complete regression; however, by combined application of shock waves and biological response modifiers, a complete regression of the tumor could be obtained. Free radical production, high pressures, and acoustic cavitation may be responsible for the just-mentioned *in vitro* tumor cytotoxicity and *in vivo* tumor growth suppression. Cavitation produces shear forces from fluid movement around moving cavities. These shear forces may cause perturbation and open pores in the cell membrane.

The increase in human renal cell carcinoma xenografts loss in vials containing air was reported to be 40% higher than in vials without air (Steinbach *et al.*, 1992). This might be explained by an increased occurrence of transient cavitation, caused by reflection of the pressure wave at the liquid–air interface. The main problem of *in vivo* shock wave treatment of malignant tumors is the development of metastases (Oosterhof *et al.*, 1996).

Disruption of cells has long been known to be an effect of ultrasound *in vitro*. Shock waves having energies as used in ESWL are capable of causing cell lysis *in vitro* (Delijs, 1994), resulting from irreversible cell membrane damage, which in the case of erythrocytes releases the hemoglobin into the surrounding medium. If the cells survive shock wave application, it is possible that external molecules leak into injured cells and remain trapped inside. Using this method of cell permeabilization (*sonoporation*), it is possible to load molecules such as DNA into cultured cells by shock wave exposure. Permeabilization of the plasma membrane is a very promising tool for gaining access to the cytosol. Sonoporation opens the possibility of gene transfer into cells and utilization of this phenomenon for gene therapy. However, it is possible that the destructive cell lysis effect of shock wave exposure tends to limit the range of targets to consider. Cancer is one target for which tissue destruction can be acceptable. Because of increased membrane permeability, shock wave treatment can be used to enhance cell uptake of cytotoxic agents and thus be used in cancer chemotherapy. Other authors (Gambihler *et al.*, 1994; Lauer *et al.*, 1997) showed that at low dosage, lithotripter shock waves can cause a transient increase in cell membrane permeability without killing the cells. Gene transfer therefore can be induced *in vivo*, particularly using enhanced cavitation. Composite reflectors (see Section 12.3.1) may be useful to control shock wave bubble interaction in order to obtain an optimal gene transfer or drug delivery to the target cells with minimal damage to surrounding tissues.

Gambihler *et al.* (1994) demonstrated that cell permeabilization of L1210 mouse leukemia cells with lithotripter shock waves results in the intracellular internalization of fluorescein-labeled dextrans. They observed that the effects of 100–2000 shock waves generated with an electrohydraulic shock wave generator at 15–25 kV on suspended L1210 cells were cell disruption, decreased ability to exclude trypan blue, and a transitory decrease in proliferation (Gambihler *et al.*, 1990). Cell disruption was absent when cells were exposed to shock waves at an elevated hydrostatic pressure, indicating that cavitation is responsible for producing cell disruption. Cells that were not disrupted after shock wave exposure were only partly trypan-blue negative, suggesting that a second effect of shock waves was an alteration of the integrity of cellular membranes. Subsequent studies performed by Delius and co-workers revealed that this mechanism also holds true for nucleic acids (Delius, 1994). Conventional methods for loading macromolecules into cells, such as by creating electropores, are restricted to *in vitro* studies; however, shock waves can be applied *in vivo* and can be focused through the skin, deep into the body. A combination of shock waves with certain drugs might be of interest for local drug targeting. The pores or defects created at the cell membrane due to shock wave application have a diameter of at least 50 nm. This enables accurate targeting of organs and tumors with either transcutaneous local DNA application or delivery via the circulation.

12.7 SHOCK WAVES AS A POSSIBLE METHOD FOR FOOD PRESERVATION

The destructive effects of ultrasonic waves on bacterial cells, known for many years, and the damage to living cells observed during ESWL (Delius *et al.*, 1988) lead to the idea of using shock waves as a possible method for food preservation. In the food industry, heat treatments are commonly used to inactivate pathogenic microorganisms. Nevertheless, because heat may affect the organoleptic and nutritional characteristics of foods, there is great interest in nonthermal processes. The possibility of using underwater shock waves in order to cause death in undesired microorganisms found in certain foods has been evaluated (Loske *et al.*, 1999) on *Escherichia coli*. *E. coli* was chosen as the first microorganism for a study of the effect of shock waves because it is a well-known and easy-to-handle bacterium.

An experimental underwater shock wave generator was used (Prieto *et al.*, 1991; Loske *et al.*, 1998). The device is similar to electrohydraulic shock wave lithotripters used in ESWL (Fig. 12.9). Either parabolic or ellipsoidal reflectors may be installed. Vials containing an *E. coli* suspension, were placed on a

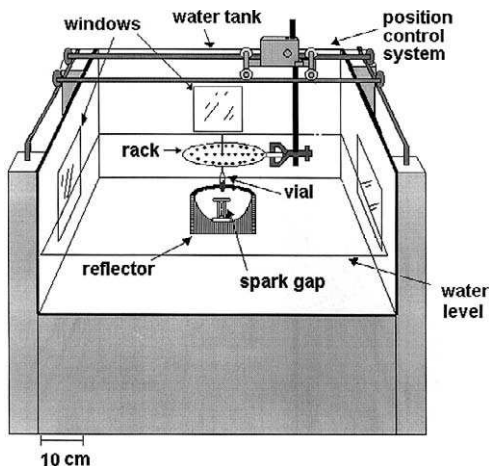


FIGURE 12.9 Drawing of an experimental electrohydraulic shock wave generator, during shock wave exposure to a vial containing a suspension of *Escherichia coli*.

specially designed rack fastened to the position control system. Samples were serial-diluted, and the amount of surviving bacteria determined by plate counting. The number of colony-forming units per milliliter (CFU/mL) obtained to fill the vials before treatment was used as a sample for zero discharges. Results indicate that an increase in the applied shock wave number between 500 and 2000 shock waves, generated using an 80-nF capacitor, a voltage of 20 kV, and a parabolic reflector, produces a nearly exponential reduction in the *E. coli* population. In order to determine the mortality index of the exposed *E. coli* bacteria, an initial count between 10^5 and 10^7 CFU/mL was used. The average dose needed to reduce the initial amount of microorganisms by 90% was about 570 shock waves.

The radiant output of the underwater spark has a continuum in the ultraviolet (UV), having a peak at approximately 55 to 150 nm. This ultraviolet radiation contributes to microorganism death, even if the intensity of this radiation is reduced significantly during its path through the water and the polypropylene vial. Recent results obtained at about 80 MPa using an ellipsoidal reflector, have shown that the influence of UV radiation on the reduction of microorganism population is important (Hernández, 1999). On the other hand, experiments on human tumor cells, exposed to electrohydraulically generated shock waves using opaque polypropylene pipettes, have shown no evidence of cell death due to UV light (Berens *et al.*, 1989). The fact that Ohshima *et al.* (1991) found that cells of *E. coli* are hard to destroy with shock waves using a shock tube that does not generate UV light support the results obtained by Hernández (1999). Even if it is known that *E. coli* can grow at

static pressures up to 55 MPa, the response to dynamic pressures is expected to be different, since in this case there is not an even distribution of pressure in the cell suspension. Furthermore, static pressures do not produce cavitation in the suspension. The bactericidal effect of ultrasound has also been attributed to cavitation. Microorganisms can be killed by static pressure of about 100 MPa, but complete sterilization is often difficult because of so-called persisters. There are many reasons why simple compression and decompression does not harm microorganisms in the same way as the repeated administration of shock waves.

Kerfoot *et al.* (1992) did experiments designed to isolate the effects of shock waves on *Pseudomonas aeruginosa*, *Streptococcus faecalis*, *Staphylococcus aureus*, and *Escherichia coli* and determine whether bactericidal activity exists. In this study, the suspension received up to 4000 shock waves at 20 kV and a rate of 100 shocks per minute on a HM3 Dornier electrohydraulic lithotripter (Dornier Medizintechnik GmbH, Germering, Germany). Aliquots of bacterial suspensions of each of the four bacterial strains were also exposed to 4000 shock waves generated by a Wolf Piezolith 2200 piezoelectric lithotripter (Richard Wolf GmbH, Knittlingen, Germany), which does not generate UV radiation, at energy level 4 and a rate of 120 shock waves per minute. The authors concluded that shock waves do not possess significant bactericidal activity. Since Kerfoot and co-workers filled each test tube completely in order to exclude air bubbles, it is possible that the bactericidal effect observed in other studies is due to shock wave reflection and cavitation at the air-liquid interface. Ohshima *et al.* (1991) found that cells of *E. coli* were killed predominantly when small bubbles were introduced into the cell solution. Experiments using aerated fluids in order to enhance cavitation in the cell suspensions could show a strong bactericidal effect of shock waves.

The exact mechanism of the induced microorganism death is still unknown. Cavitation, microjets, acceleration, shearing forces, and formation of free radicals may cause the observed effect. Other possible mechanisms of cell death are resonance effects and collisions between microorganisms.

A detailed knowledge of microorganism shock wave killing could have many practical applications in the food and pharmaceutical industries and in medicine.

12.8 SHOCK WAVE THROMBUS ABLATION

More efficient thrombolytic therapies for acute myocardial infarction are still needed. Despite the similarities in acoustical impedance between thrombus and the surrounding tissue, interesting results have been obtained using shock waves for thrombus ablation *in vitro* (Rosenshein *et al.*, 1992). Thrombi were

prepared *in vitro* and inserted in excised human femoral artery segments. The arterial segments were ligated, placed at the focal region of a HM3 Dornier lithotripter (Dornier Medizintechnik GmbH, Germering, Germany), and exposed to 1000 shock waves at 24 kV. After shock wave application, the arterial content was flushed and the residual solid thrombus was separated from the fluid portion and reweighed. A significant ablation of thrombus mass was achieved. No perforations or other damage to the arterial segments was found. It is believed that cavitation is the principal mechanism underlying shock wave thrombus ablation.

ACKNOWLEDGMENTS

The author thanks Frederick L. Yarger for helpful discussions and revision of the manuscript. The assistance of Claudia Hernández, Eduardo Armenta, Arturo Méndez, Alfredo Sánchez, Marco Veytia, Francisco Fernández, Ulises Mora, and Francisco Mercado is acknowledged with thanks. Special thanks are due to Fernando E. Prieto for constant encouragement and assistance for more than 10 years, and to Víctor M. Castaño and the *Instituto de Física (FATA)* for support.

REFERENCES

- Bailey, M. R., Blackstock, D. T., Cleveland, R. O., and Crum, L. A. (1998) Comparison of electrohydraulic lithotripters with rigid and pressure-release ellipsoidal reflectors. I. Acoustic fields. *J. Acoust. Soc. Am.* **104**(4), 2517–2524.
- Berens, M. E., Welander, C. E., Griffin, A. S., and McCullough, D. L. (1989) Effect of acoustic shock waves on clonogenic growth and drug sensitivity of human tumor cells *in vitro*. *J. Urol.* **142**, 1090–1094.
- Braun, W., Claes, L., Rüter, A., and Paschke, D. (1992) Effects of extracorporeal shock waves on the stability of interface between bone and polymethylmethacrylate: an *in vitro* study on human femoral segments. *Clinical Biomechanics* **7**, 47–54.
- Cameron, J., and Skofronick, J. (1979) *Sound in Medicine in Medical Physics*. Wiley, New York.
- Chaussy, Ch., Brendel, W., and Schmidt, E. (1980) Extracorporeally induced destruction of kidney stones by shock waves. *Lancet* **2**, 1265–1268.
- Chaussy, Ch., Randazzo, R. F., and Fuchs, G. J. (1986) The effects of extracorporeal shock waves on Fanft bladder tumors in C3H/He mice. *J. Urol.* **135**, 289A.
- Choi, M. J., Coleman, A. J., and Saunders, J. E. (1991) Theoretical predictions of the acoustic pressure generated by a shock wave lithotripter. *Ultrasound in Med. & Biol.* **17**(3).
- Church, Ch. (1989) Theoretical study of cavitation generated by an extracorporeal shock wave lithotripter. *J. Acoust. Soc. Am.* **86**, 215–227.
- Coleman, A. J., and Saunders, J. E. (1989) A survey of the acoustic output of commercial extracorporeal shock wave lithotripters. *Ultrasound in Med. & Biol.* **15**, 213–227.
- Coptcoat, M. J., Miller, R. A., and Wickham, J. E. A. (1987) *The End of the Stone Age*. BDI Publishing, London, p. 199.
- Delius, M. (1994) Medical application and bioeffects of extracorporeal shock waves. *Shock Waves* **4**, 55–72.

- Delius, M., and Brendel, W. (1990) Historical roots of lithotripsy. *J. Lithotripsy & St. Disease* 2(3), 161–163.
- Delius, M., Jordan, M., Eizenhoefer, H., Marlinghaus, E., Heine, G., Liebich, H. G., and Brendel, W. (1988) Biological effects of shock waves: Kidney hemorrhage by shock waves in dogs—administration rate dependence. *Ultrasound in Med. & Biol.* 14, 689–694.
- Dodick, J. M. (1991) Laser phacolysis of the human cataractous lens. *Developments in Ophthalmology* 22, 56–64.
- Evan, A. P., Willis, L. R., Connors, B. A., McAteer, J. A., and Lingeman, J. E. (1991) Renal injury after ESWL. *J. Endourol.* 5, 25–35.
- Folberth, W., Köhler, G., Rohwedder, A., and Matura, E. (1992) Pressure distribution and energy flow in the focal region of two different electromagnetic shock wave sources. *J. Stone Disease* 4, 1–7.
- Gambihler, S., Delius, M., and Brendel, W. (1990) Biological effects of shock waves: cell disruption, viability, and proliferation of L1210 cells exposed to shock waves *in vitro*. *Ultrasound in Med. & Biol.* 16(6), 587–594.
- Gambihler, S., Delius, M., and Ellwart, J. W. (1994) Permeabilization of the plasma membrane of L1210 mouse leukemia cells using lithotripter shock waves. *J. Membr. Biol.* 141, 267–275.
- Haupt, G. (1997) Use of extracorporeal shock waves in the treatment of pseudarthrosis, tendinopathy and other orthopedic diseases. *J. Urol.* 158, 4–11.
- Haupt, G., Haupt, A., Ekkernkamp, A., Gerety, B., and Chvapil, M. (1992) Influence of shock waves on fracture healing. *Urology* 39, 529–532.
- Häusler, E. (1985) Physical principles of kidney stone destruction. *Proc. Third Congress of the International Society of Urology and Endoscopy, Karlsruhe, Germany*. BUA Verlag Werner Steinbruck, pp. 433–435.
- Hernández, C. (1999) *Aplicación de ondas de choque a Escherichia coli como alternativa a la conservación de alimentos*. BSc Thesis, Mexico, Facultad de Química, Universidad Nacional Autónoma de México, p. 69.
- Hessling, K. H., Schlick, R. W., Luckey, R., Gratz, K., Qaiumi, S. A., Allhoff, E. P. (1993) Die therapeutische Wertigkeit der ambulanten extrakorporalen Stosswellenlithotripsie von Speichelsteinen. *Laryngorhinootologie* 72, 109.
- Iro, H., Nitsche, N., Schneider, H. T., and Ell, Ch. (1989) Extracorporeal shock wave lithotripsy of salivary gland stones. *Lancet* II(5), 115.
- Jocham, D. (1987) Historical development of ESWL. In *Principles of Extracorporeal Shock Wave Lithotripsy* (eds. R.A. Riehle, R.C. Newman), pp. 1–11. Churchill Livingstone, New York.
- Kelman, C. D. (1967) Phaco-emulsification and aspiration: A new technique of cataract removal, a preliminary report. *Am. J. Ophthalmol.* 64, 23–35.
- Kerfoot, W. W., Beshai, A. Z., and Carson, C. C. (1992) The effect of isolated high-energy shock wave treatments on subsequent bacterial growth. *Urol. Res.* 20, 183–186.
- Köhrmann, K. U., Rassweiler, J. J., Manning, M., Mohr, G., Henkel, T. O., Jünemann, K. P., and Alken, P. (1995) The clinical introduction of a third generation lithotripter: Modulith SL20. *J. Urol.* 9, 1379–1383.
- Kuwahara, M., Kambe, K., Kurosu, S., Orikasa, S., and Takayama, K. (1986) Extracorporeal stone disintegration using chemical explosive pellets as an energy source of underwater shock waves. *J. Urol.* 135, 814–817.
- Lauer, U., Burgelt, E., Squire, Z., Messmer, K., Hofschneider, P. H., Gregor, M., and Delius, M. (1997) Shock wave permeabilization as a new gene transfer method. *Gene Ther.* 4, 710–715.
- Lingeman, J. E., Smith, L. H., Woods, J. R., and Newman, D. M. (1989) *Urinary Calculi: ESWL, Endourology and Medical Therapy*. Lea and Febiger, Philadelphia.
- Loew, M., Jurgowski, W., and Thomsen, M. (1995) Calcareous tendinitis of the shoulder—first experiences with a treatment by extracorporeal shock wave application (ESWA). *Urol. (A)* 34, 49–53.

- Loske, A. M. (1990) *Generación de ondas de choque débiles en agua por rompimiento eléctrico*. M.Sc. Thesis, Mexico, Facultad de Ciencias, Universidad Nacional Autónoma de México, p. 273.
- Loske, A. M. (1994) *Interacción de ondas de choque débiles en agua con la materia: diseño de electrodos y reflectores novedosos para litotriptores electrohidráulicos*. Ph.D. Thesis, Mexico, Centro de Investigación Científica y de Educación Superior de Ensenada, B.C., p. 168.
- Loske, A. M., and Prieto, F. E. (1993) The influence of electrode shape on the performance of electrohydraulic lithotripters. *J. Lith. Stone Disease* 5(4), 228–239.
- Loske, A. M., and Prieto, F. E. (1995) *Shock Waves in Medicine: Commented Bibliographical Data Base*. Mexico, Coordinación de la Investigación Científica, UNAM, ISBN 968-36-4466-X.
- Loske, A. M., and Prieto, F. E. (1996) Improving underwater shock wave focusing efficiency. In *Urolithiasis* (eds. C. Y. C. Pak, M. I. Resnick, and G. M. Preminger), pp. 401–402. Millet Printers, Dallas.
- Loske, A. M., and Prieto, F. E. (1999) *Fundamentos Técnicos de Litotripsia Extracorporal*. Mexico, Ciencia y Cultura Latinoamérica S.A. de C.V.
- Loske, A. M., Prieto, F. E., and Méndez, A. (1998) Generador de ondas de choque experimental. *Proc. 1st Latin-American Biomedical Engineering Conference* (eds. E. Sacristí, V. Medina, and O. Yañez S.), Revista Mexicana de Ingeniería Biomédica, Mexico, pp. 54–57.
- Loske, A. M., Prieto, F. E., Zavala, M. L., Santana, A. D., and Armenta, E. (1999) Repeated application of shock waves as a possible method for food preservation. *Shock Waves* 9, 49–55.
- Marshall, F. F., Weiskopf, F., Singh, A., Mark, F., Leo, F., Sanders, R., Makofski, R., Walsh, P. C., and Smith, N. (1988) A prototype device for nonimmersion shock wave lithotripsy using ultrasonography for calculus localization. *J. Urol.* 140, 249–253.
- Michaels, E., Fowler, J. E., and Mariano, M. (1988) Bacteriuria following extracorporeal shock wave lithotripsy of infection stones. *J. Urol.* 140, 254–256.
- Müller, M. (1987) *Stosswellenfokussierung in Wasser*. Ph.D. Thesis, Aachen, Germany, Rheinisch-Westfälische Technische Hochschule.
- Nahrwold D. L. (1993) Gallstone lithotripsy. *Am. J. Surgery* 165, 43.
- Ohshima, T., Tanaka, S., and Teshima, K. (1991) Effects of shock wave on micro-organisms: An evaluation method of the effects. In *Shock Waves* (ed. K. Takayama), pp. 1215–1219. Springer, Berlin.
- Oosterhof, G. O. N., Smits, G. A. H. J., de Ruyter, A. E., van Moorselaar, R. J. A., Schalken, J. A., and Debruyne, F. M. J. (1989) The *in vitro* effect of electromagnetically generated shock waves on the Dunning R 3327 PAT-2 rat prostatic cancer cell-line. *Urol. Res.* 17, 13–19.
- Oosterhof, G. O. N., Smits, G. A. H. J., de Ruyter, A. E., Schalken, J. A., and Debruyne, F. M. J. (1990) Effects of high energy shock waves combined with biological response modifiers in different human kidney cancer xenografts. *Urol. Res.* 18, 419–424.
- Oosterhof, G. O. N., Cornel, E. B., Smits, G. A. H. J., Debruyne, F. M. J., and Schalken, J. A. (1996) The influence of high-energy shock waves on the development of metastases. *Ultrasound in Med. & Biol.* 22(3), 339–344.
- Pode, D., Lenkovsky, Z., Shapiro, A., and Pfau, A. (1988) Can extracorporeal shock wave lithotripsy eradicate persistent urinary infections associated with infection stones? *J. Urol.* 140, 257.
- Prieto, F. E., and Loske, A. M. (1994) Mexican patent SECOFI number 945421.
- Prieto, F. E., and Loske, A. M. (1995) International patent P.C.T./MX 95/00008.
- Prieto, F. E., and Loske, A. M. (1999) Bifocal reflector for electrohydraulic lithotripters. *J. Endourol.* 13(2), 65–75.
- Prieto, F. E., Loske, A. M., and Yarger, F. L. (1991) An underwater shock wave research device. *Rev. Scientific Instrum.* 62(7), 1849–1854.
- Randazzo, R. F., Chaussy, Ch., Fuchs, G. J., Bhuta, S. M., Lovrekovich, H., and Kernion, J. B. (1988) The *in vitro* and *in vivo* effects of extracorporeal shock waves on malignant cells. *Urol. Res.* 16, 419–426.

- Rompe, J. D., Hopf, C., Eysel, P., Heine, J., Witzsch, U., and Nafe, B. (1995) Extrakorporale Stosswellentherapie des therapieresistenten Tennisellenbogens—erste Ergebnisse von 150 Patienten. In *Die Stosswelle* (eds. Ch. Chaussy, F. Eisenberger, D. Jocham, and D. Wilbert), Attempto Verlag, Tübingen.
- Rosenschein, U., Yakubov, S. J., Guberinich, D., Bach, D. S., Sonda, P. L., Abrams, G. D., and Topol, E. J. (1992) Shock wave thrombus ablation, a new method for noninvasive mechanical thrombolysis. *Am. J. Cardiol.* 70, 1358–1361.
- Rubin, J. I., Arger, P. H., Pollack, H. M., Banner, M. P., Coleman, B. G., Mintz, M. C., and Arsdalen, K. N. (1987) Kidney changes after ESWL: CT evaluation. *Radiology* 162, 21–24.
- Russo, P., Heston, W. D. W., and Fair, R. (1985) Suppression of *in vitro* and *in vivo* tumor growth by high energy shock waves. *Surg. Forum* 36, 64–65.
- Russo, P., Stephenson, R. A., Mies, C., Huryk, R., Heston, W. D., Melamed, M. R., and Fair, W. R. (1986) High energy shock waves suppress tumor growth *in vitro* and *in vivo*. *J. Urol.* 135, 626–628.
- Schleberger, R., and Senge, T. (1992) Non-invasive treatment of long bone pseudarthrosis by shock waves (ESWL). *Arch. Orthop. Trauma Surg.* 111, 224.
- Staudenraus, J., and Eisenmenger, W. (1993) Fiber-optic hydrophone for ultrasonic and shock wave measurements in water. *Ultrasonics* 31(4), 267–273.
- Steinbach, P., Hofstädter, F., Nicolai, H., Rössler, W., and Wieland, W. (1992) *In vitro* investigation on cellular damage, induced by high energy shock waves. *Ultrasound in Med. & Biol.* 18, 691–699.
- Valchanou, V. D., and Michailov, P. (1991) High energy shock waves in the treatment of delayed and nonunion of fractures. *Internat Orthopaedics (SICOT)* 15, 181–184.
- van der Hul, R. L., Plaisier, P. W., den Room, R., van Blankenstein, M., Terpstra, O. T., and Jeekel, J. (1993) Schokgolffvergruizing van steenen in het pancreas; de eerste 16 in Rotterdam-Dijkzigt behandelde patienten. *Ned. Tijdschr. Geneesk.* 137, 763.
- Weinstein, J. N., Wroble, R. R., and Loening, S. (1986) Revision total joint arthroplasty facilitated by extracorporeal shock wave lithotripsy: a case report. *Iowa Orthop J.* 6, 121–124.
- Zhong, P., Cocks, F. H., Cioanta, I., Preminger, G. M. (1997) Controlled, forced collapse of cavitation bubbles for improved stone fragmentation during shock wave lithotripsy. *J. Urol.* 158, 2323–2328.

Spherical Shock Waves

13.1 Expanding Spherical Shocks (Blast Waves)

JOHN M. DEWEY

*Professor Emeritus, Department of Physics and Astronomy, University of Victoria,
Victoria, BC, Canada*

-
- 13.1.1 Introduction
 - 13.1.2 Physical Properties of Expanding Spherical Shock Waves
 - 13.1.2.1 Physical Properties in Radius-Time (r - t) Plane
 - 13.1.2.2 Shock front Properties
 - 13.1.2.3 The Shape of the Shock Wave
 - 13.1.2.4 A Compendium of Physical Properties
 - 13.1.3 Scaling Laws
 - 13.1.4 Analytical Solutions
 - 13.1.5 Numerical Methods
 - 13.1.5.1 Numerical Modeling
 - 13.1.5.2 Numerical Reconstruction
 - 13.1.6 Experimental Measurement Techniques
 - 13.1.6.1 Introduction
 - 13.1.6.2 Electronic Methods
 - 13.1.6.3 Photogrammetric Methods
 - 13.1.6.4 Passive Methods
 - 13.1.7 Spherical Shock Reflections
 - 13.1.7.1 Regular and Mach Reflections
 - 13.1.7.2 Height-Of-Burst Curves
 - References

13.1.1 INTRODUCTION

An expanding spherical shock wave is normally produced by the rapid release of energy from a centered source. The simplest configuration would be the instantaneous release of energy at a point in a uniform medium, but this is impossible in practice, and not amenable to analytical or numerical solution. The closest configuration to a point release of energy is a nuclear explosion, but even this involves the introduction of some mass of material at the center. Other sources of spherical shocks are the centered detonation of a high explosive chemical, the rupture of a spherical pressurized vessel, an electric spark and a focused laser beam. The complete shock wave produced by such sources, including the shock front and the subsequent gas flow, is called a blast wave.

A uniform chemical detonation rapidly produces a high-pressure, high-temperature sphere of gas, which expands in the ambient medium to produce a spherical shock wave. The contact surface between the detonation products and the ambient gas soon becomes irregular and there is considerable mixing of the two gases (Zhang and Sohn, 1999), but only in extreme cases, such as when there has been a nonsymmetrical detonation, does this affect the uniformity of the expanding spherical shock. The release of energy from a detonation is rapid, but not instantaneous, and if the explosive is deficient in oxygen, as is the case with TNT, for example, the mixing of the detonation products with ambient air produces after-burning, which continues to release energy for a period after the detonation. After-burning has little effect on the spherical shock front, but changes the flow properties in the region behind the shock.

The rupture of a pressurized vessel also produces a spherical blast wave similar to that from a chemical detonation, but the initial shock speed is normally less for the same amount of released energy. The gas from the pressurized vessel may be more uniform than that produced by a detonation, but in this case there are effects from the fragments of the vessel, which have a much higher momentum than the expanding gases. They are therefore less affected by the rarefaction wave that follows the expanding spherical shock, and retain a high velocity that may eventually exceed that of the decelerating shock front. Occasionally, some of these solid particles may pass through and move ahead of the shock front. A similar phenomenon may occur in a blast wave produced by the detonation of an explosive charge contained in a solid casing. Initially, the fragments from the containing vessel absorb energy from the expanding gases. Later, some of this energy may be restored to the gases within the blast wave. Casing fragments redistribute the energy of the original source, temporally and spatially.

A spark produces an expanding shock, but this may not be a well-centered wave. A spark between two electrodes produces a cylindrical plasma that expands to produce a cylindrical blast wave. The electrodes affect the initial expansion at

the ends of the cylinder. An exploding wire, fused by a large electrical current, produces a similar blast wave. A spark formed within a vented cavity produces a plasma jet with initial cylindrical rather than spherical symmetry.

A focused laser beam also tends to produce an initial nonsymmetrical energy source. The ambient gas is ionized at the focus, and this heating and ionization extends back along the incident laser beam to produce a non-uniform source. The symmetry can be improved by using a very short laser pulse, or multidirectional laser beams with the same focus (Steiner, Gretler, and Hirsdhler, 1998; Jiang *et al.*, 1998).

Independent of the nature of the source, the shock front produced by a rapid release of energy quickly achieves a high order of sphericity. This is a characteristic of all shock waves that have moved sufficiently far from their driving source. Any part of a shock front traveling more rapidly than an adjacent shock will be followed by a region of higher pressure, which will cause a transverse flow of energy, thus eventually producing a spherical shock. Nevertheless, in spite of this tendency to a spherical shock front, the physical properties of an expanding blast wave, including the rate of deceleration of the shock front, have unique characteristics related to the nature, shape, and rate of energy release of the source.

13.1.2 PHYSICAL PROPERTIES OF EXPANDING SPHERICAL SHOCK WAVES

13.1.2.1 PHYSICAL PROPERTIES IN THE RADIUS–TIME (r - t) PLANE

The loci of the primary shock front and several other features of an expanding spherical shock or blast wave are shown in Fig. 13.1.1. It is assumed that the detonation of a spherical chemical explosive, or the rupture of a pressurized spherical container, with an initial radius R_c , generates the shock wave. The contact surface between the detonation products or high-pressure gas and the ambient air, CS, expands at high velocity and almost immediately produces the primary shock front, S. At the early stage of its expansion, the shock may be strong enough that it is luminous, and this will conceal the visibility of the detonation products. Both CS and S decelerate monotonically as they expand in three dimensions. CS is a very unstable interface (Anisimov *et al.*, 1983; Zhang and Sohn, 1999). The instability produces considerable turbulent mixing of the driver and ambient gases, and chemical interactions may occur, producing after-burning of the detonation products, which continues to introduce energy at the back of the shock wave.

The deceleration of CS produces an outward-moving rarefaction wave and an inward-facing second shock, S' , which may initially be swept outward by

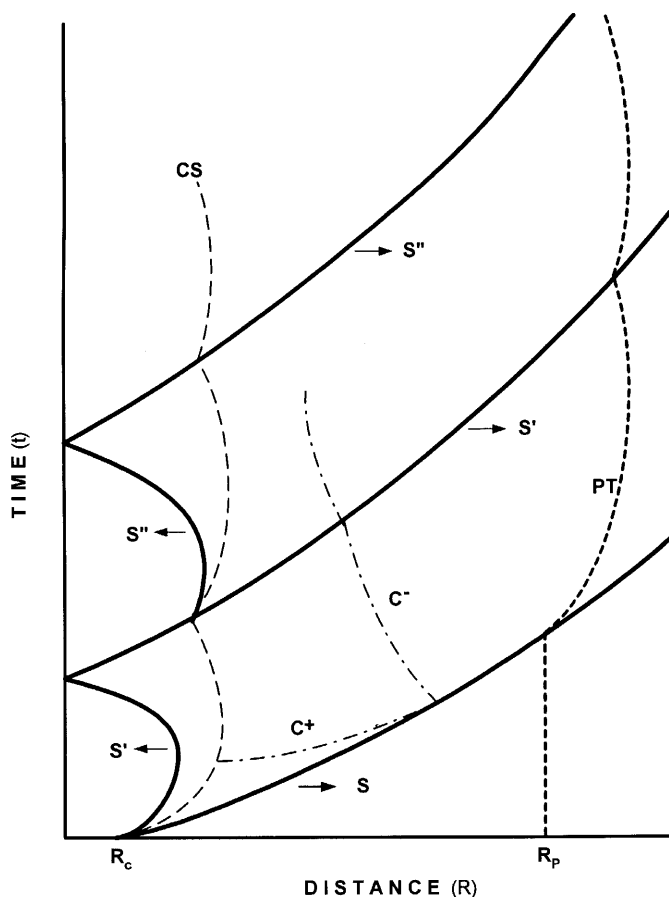


FIGURE 13.1.1 The principal features of a spherically expanding shock or blast wave plotted in the radius-time (R, t) plane. S , S' and S'' are the loci of the primary, secondary and tertiary shocks, respectively; PT , the trajectory of a gas particle initially at rest at a distance R_p from the centre of the wave; R_c , the initial radius of the explosive source, and CS , the contact surface between the driving and driven gases. C^+ is the characteristic path of a forward facing small disturbance that moves with speed of $u + a$, and C^- , the characteristic path of a backward facing small disturbance that moves with a speed of $u - a$, where u is the particle velocity, and a the local sound speed.

the expanding driver gas. S' implodes to the center and is reflected as an outward-moving shock. S' subsequently interacts with CS , causing it to move outward again, and is partially transmitted and partially reflected as the third shock, S'' . In theory this process continues indefinitely, but in practice only the second shock and rarely the third shock are observable.

An element of the ambient gas, originally at a distance R_p from the center, is struck by the primary shock and accelerated to its Rankine-Hugoniot speed. It

is then slowed by the rarefaction before being accelerated again by S' . The element will experience an entropy change as S passes through it, but its subsequent movement will be isentropic until struck by S' .

Any outward-moving signal within the wave, such as one produced on CS , will move along the positive $u + a$ characteristic, C^+ , where u and a are the particle and sound speeds, respectively. C^+ may eventually overtake the primary shock, and if the signal is strong enough it will accelerate or decelerate S , depending on whether it is a compression or rarefaction. Moving along CS in the r - t plane, a point will be reached from which an originating C^+ can no longer reach S . This is the limiting characteristic, and any signal produced above this locus in the r - t plane cannot affect the properties of the primary shock (Thornhill, 1957a). Any inward-facing signal, such as one produced by the primary shock interacting with a small object, will move along a $u - a$ negative characteristic, C^- . In order to trace the locus of any disturbance within an expanding spherical shock, a knowledge of the u and a fields in the r - t plane is therefore necessary.

13.1.2.2 SHOCK FRONT PROPERTIES

The strength of a spherical shock produced by a centered energy source monotonically decreases as it expands in three dimensions. The Rankine–Hugoniot relationships (Chapter 3.1, Table 3.1.3) across a curved shock are the same as those for a plane shock, even for a very small radius of curvature. As a result, if the ratio of the values of any single physical property across the shock is known, then the values of the ratios of all the other physical properties can be calculated. These ratios are most easily calculated in terms of the shock Mach number, $M_S = V_S/a_0$, where V_S is the shock speed and a_0 is the speed of sound of the ambient gas into which the shock is moving. Some of the more commonly used of these relationships are given below, where P is the hydrostatic pressure, ρ the gas density, T the absolute gas temperature, u the gas particle velocity, S the entropy, γ the ratio of specific heats, and C_p the specific heat at constant pressure. The subscripts s and 0 , respectively, indicate the properties immediately behind the primary shock front and in the ambient gas ahead of the shock. The far right-hand expressions in the first four equations assume that the shock is moving into an ideal gas with a ratio of specific heats of 1.4.

$$\frac{P_S}{P_0} = 1 + \left(\frac{2\gamma}{\gamma + 1} \right) (M_S^2 - 1) = 1 + \frac{7}{6} (M_S^2 - 1) \quad (13.1.1)$$

The preceding equation gives $(P_S/P_0) - 1$, the hydrostatic overpressure in atmospheres.

$$\frac{\rho_S}{\rho_0} = \frac{(\gamma + 1)M_S^2}{(\gamma - 1)M_S^2 + 2} = \frac{6M_S^2}{M_S^2 + 5} \quad (13.1.2)$$

$$\frac{T_S}{T_0} = \frac{(2\gamma M_S^2 - \gamma + 1)[(\gamma - 1)M_S^2 + 2]}{(\gamma + 1)^2 M_S^2} = \frac{(7M_S^2 - 1)(M_S^2 + 5)}{36M_S^2} \quad (13.1.3)$$

$$\frac{u_S}{a_0} = \frac{2}{\gamma + 1} \left(\frac{M_S^2 - 1}{M_S} \right) = \frac{5}{6} \left(\frac{M_S^2 - 1}{M_S} \right) \quad (13.1.4)$$

$$\Delta S = C_P \ln \left\{ \frac{T_S/T_0}{(P_S/P_0)^{(\gamma-1)/\gamma}} \right\} = C_P \ln \left\{ \frac{(P_S/P_0)^{1/\gamma}}{\rho_S/\rho_0} \right\} \quad (13.1.5)$$

The theoretical locus in the r - t plane of the spherical shock produced by a centered release of energy is of the form $R = f(t^{2/5})$ (Taylor, 1950a; Zel'dovich and Raiser, 1966), but this is approximately true only close to the energy source when the shock Mach number is greater than 2.8, which corresponds to a hydrostatic pressure of 10 atm immediately behind the shock. An empirical relationship of the form

$$R = A + Ba_0 t + C \ln(1 + a_0 t) + D\sqrt{\ln(1 + a_0 t)} \quad (13.1.6)$$

has been used successfully to describe experimental observations of shock front trajectories of spherical shocks from centered chemical explosions. A , B , C , and D , are fitted coefficients, and a_0 is the ambient speed of sound (Dewey, 1971). For small ranges of data close to the energy source, the final term in the preceding expression may not be required. Other workers e.g. Sadek and Gottlieb (1983), have used similar empirical relationships to describe portions of the spherical shock front trajectory.

Experimentally obtained values of the coefficients in Eq. (13.1.6) for the spherical shock produced by the detonation of a 1 kg charge of TNT in air at NTP ($a_0 = 340.292 \text{ m s}^{-1}$) are $A = -0.55963$, $B = 1.01751$, $C = -0.45403$, and $D = 2.05527$, and for the hemispherical shock produced by a 1 kg charge of TNT detonated on a rigid surface are $A = -0.60257$, $B = 1.02709$, $C = -0.53264$, and $D = 2.45101$. Theoretically, the value of the coefficient B should be unity, but the values just given better describe the observed trajectories of spherical shocks produced by TNT explosions. The preceding coefficients and other experimental results presented in this chapter have been obtained from the *AirBlast* expert system (Dewey and McMillin, 1989), which uses databases of experimental results from a large number of experiments using TNT and other explosive sources.

The time derivative of Eq. (13.1.6) is

$$\frac{dR}{dt} = a_0 \left(B + \frac{C}{1 + a_0 t} + \frac{D}{2(1 + a_0 t)\sqrt{\ln(1 + a_0 t)}} \right), \quad (13.1.7)$$

and so the Mach number of the shock,

$$M_s = \frac{1}{a_0} \frac{dR}{dt}, \quad (13.1.8)$$

can be calculated for any value of R and used in Eq. (13.1.1) to (13.1.4) to determine the approximate value of any of the physical properties immediately behind the shock. Use of these empirical relationships is not recommended for shock Mach numbers below about 1.04. This is because the accuracy of the shock speed obtained from Eq. (13.1.7) decreases for larger radii, and the inaccuracy increases when the square of the Mach number is used in Equations (13.1.1) to (13.1.4).

13.1.2.3 THE SHAPE OF THE SHOCK WAVE

Hydrostatic overpressure profiles of a spherical, centered shock wave are shown in Fig. 13.1.2. The contact surface, CS in Fig. 13.1.1, is decelerating, and this generates a rarefaction wave immediately behind the primary shock.

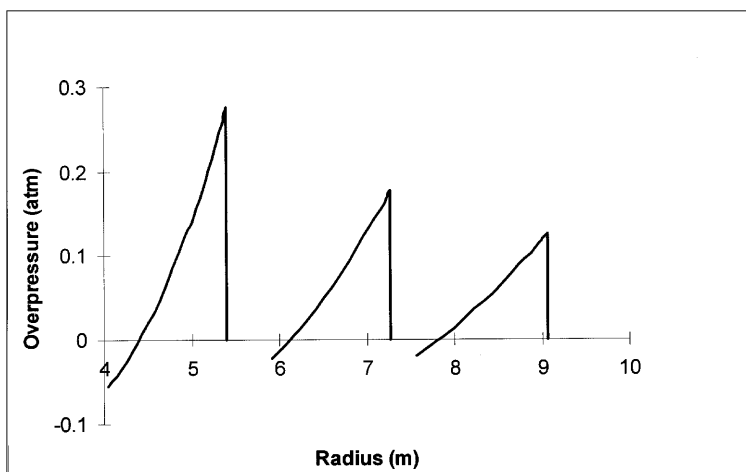


FIGURE 13.1.2 Hydrostatic overpressure profiles of the blast wave produced by the detonation of 1 kg of TNT in air, at times of 10, 15 and 20 ms after detonation, respectively from left to right. The profiles end approximately at the position of the second shock. (Data obtained from the *AirBlast* expert system)

The profiles of all the physical properties, except entropy, have a similar, but not identical shape. These profiles are not self-similar, although self-similarity is sometimes assumed in order to attempt analytical solutions of spherical shock waves. The form of the wave profile of entropy is shown in Fig. 13.1.3. As the primary shock front moves through the ambient gas it produces an increase of entropy related to the shock strength, in accordance with Eq. (13.1.5). The gas then remains at constant entropy until there is another small increase caused by the second shock. The monotonically decaying shock front therefore leaves the gas in a state of radially decreasing entropy, as shown in Fig. 13.1.3.

The shape of an expanding spherical shock is more usually described in the form of time histories of the physical properties at specified radii, because these are the properties, which can be recorded by spatially fixed measuring devices. A typical hydrostatic overpressure time history is shown as Fig. 13.1.4. Such a time history is not self-similar at different radii. The decay rates or shapes of the time histories of the different physical properties are not the same, as is illustrated in Fig. 13.1.5, which shows the time histories of several physical properties, normalized to their peak values, in the shock wave produced by the detonation of a 1-kg charge of TNT in air at NTP. The time for a physical property to return to its ambient value is called the positive duration, and the positive durations of the different physical properties are slightly different, as illustrated in Fig. 13.1.4.

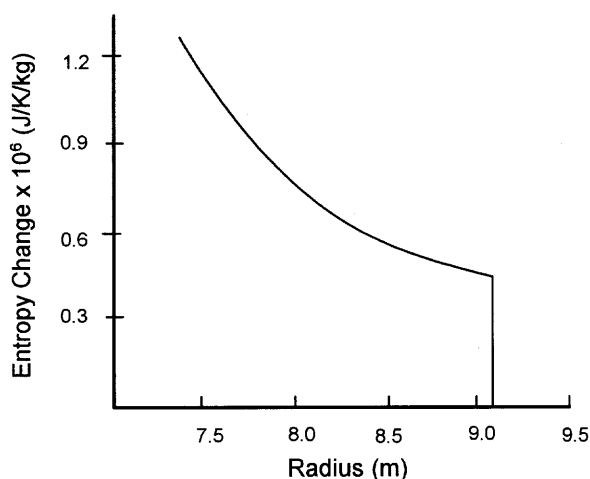


FIGURE 13.1.3 Profile of the entropy increase of the gas in the shock wave produced by the detonation of 1 kg of TNT in air. The expanding shock wave leaves the gas in a state of radially decreasing entropy. After the passage of the primary shock each gas element moves isentropically until the arrival of the second shock. (Data obtained from the *AirBlast* expert system)

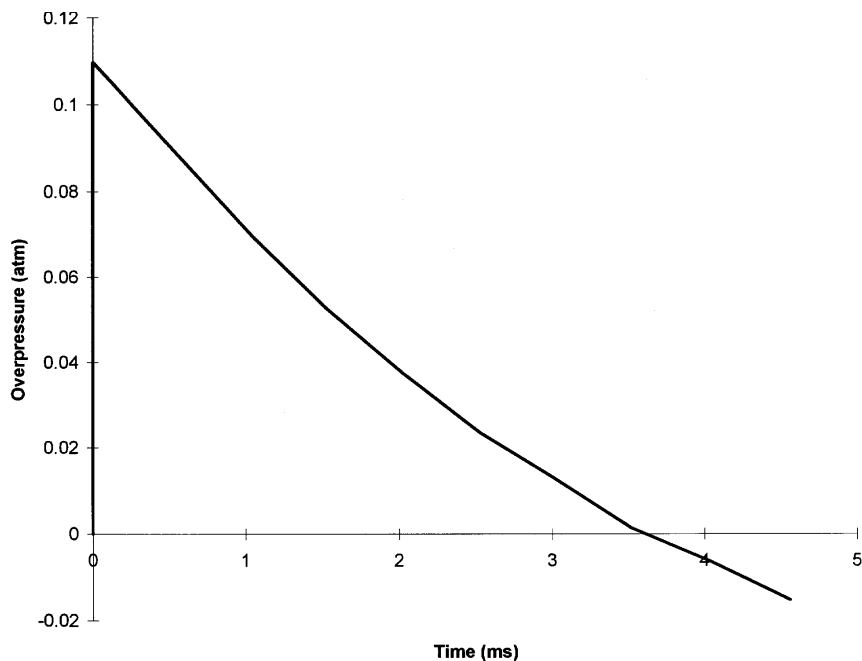


FIGURE 13.1.4 Time history of hydrostatic overpressure at a distance of 10 m from the detonation of 1 kg of TNT in air. The history ends approximately at the time of arrival of the second shock. (Data obtained from the *AirBlast* expert system)

The shape of the time history of a physical property of a spherical shock wave as it passes a fixed location may be described by the Friedlander (1946) equation,

$$P = P_S e^{-\alpha t} \left(1 - \frac{t}{t^+}\right), \quad (13.1.9)$$

where P is the value of a physical property at a time t measured from the arrival of the shock at the chosen location, P_S is the value of that property immediately behind the shock front, α is a decay constant, and t^+ is the positive duration or time for the property to return to its ambient value. Note that the values for α and t^+ are different for each physical property. If the time history of a physical property has been measured, an approximate value for α can be found by making a least squares fit of the initial one-third of the data to

$$\ln \frac{P}{P_S} = -\alpha t, \quad (13.1.10)$$

or by plotting P/P_S versus t on semilog paper and measuring the slope in the region close to $t = 0$. Also, the intercept of this line with the $t = 0$ axis is a good way of determining P_S from a noisy experimental record.

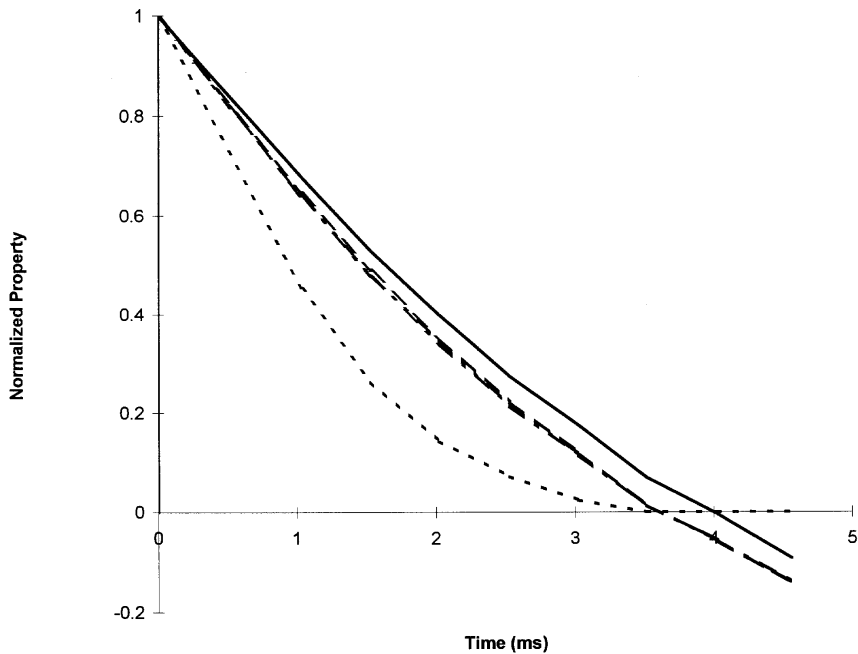


FIGURE 13.1.5 Time histories of hydrostatic overpressure, density, temperature, dynamic pressure and particle velocity at 10 m from the detonation of 1 kg of TNT. Each curve has been normalized to the peak value immediately behind the primary shock. The solid line is particle velocity, the dashed line dynamic pressure, and the curves for the other three properties are virtually indistinguishable. (Data obtained from the *AirBlast* expert system)

Determination of t^+ from a measured time history may not be easy if the signal is noisy and the slope almost parallel to the time axis. Also, some properties for some explosives may not return to their ambient value before the arrival of the second shock. For this reason, Thornhill (1959) suggests that the shape of a time history be described by a relaxation time, t^* , defined as the time for the property, P , to decay to $1/e$ of its peak value, P_S . t^* is usually easy to determine from an experimental record. Writing $P = P_S/e$ in (9) gives

$$t^+ = t^*(e^{\alpha t^{*-1}} - 1)^{-1}. \quad (13.1.11)$$

Applying α determined from Eq. (13.1.10), and the measured value of t^* yields an approximate value for t^+ .

The form given by Eq. (13.1.9) does not apply for the time history of entropy. The entropy of the gas flowing past a fixed location increases in time because the gas from closer to the energy source was traversed by a stronger shock and therefore experienced a larger entropy increase. Similarly, the gas traversed by

the strong shock close to the energy source may remain at a temperature higher than the ambient value, even after the passage of the rarefaction wave that follows the primary shock front. In this case there is no value for t^+ . Depending on the rate of energy release from the source, the time history of particle velocity, and therefore of the dynamic pressure, $P_D \equiv \frac{1}{2}\rho u^2$, may not be reduced to zero in the rarefaction wave. This is the case for TNT at some distances from the center because of the after-burning described previously. The burning produces a long slow energy release that causes a continuing outward flow which may not be brought to rest by the rarefaction wave. The time history of particle flow for this region of a blast wave may be described by a modified form of the Friedlander equation (13.1.9) (Dewey, 1964), viz.,

$$u = u_s e^{-\alpha t} (1 - \beta t) + A \ln(1 + \beta t), \quad (13.1.12)$$

where A and β are fitted coefficients. In this case β should not be considered as $1/t^+$, but as a normalizing factor for time. Work flux, or the flux of available energy, which will be defined later, is another property of a shocked gas that may not return to the ambient value before the arrival of the second shock.

The integral of the time history of a physical property, P , from the time of arrival of the primary shock to the positive duration,

$$I = \int_{t=0}^{t^+} P dt, \quad (13.1.13)$$

may be of physical significance. For example, the time integrals, or impulses, of hydrostatic and dynamic pressure and of available energy flux may be related to the damage or deformation of a slowly responding structure exposed to the passage of a blast wave. If the physical property does not return to the ambient value before the arrival of the second shock, as may be the case for dynamic pressure and available energy flux at some locations, the integral is usually terminated at the time the property falls to its minimum value.

13.1.2.4 A COMPENDIUM OF PHYSICAL PROPERTIES

The physical properties of an expanding spherical shock or blast wave may be displayed as functions of distance from the center of the energy source. The properties are usually presented as a log-log plot, which provides a convenient format for showing values ranging over several orders of magnitude, and lends itself to easy scaling for different amounts of energy release from the centered source, as described later. Compendia of such results are presented as Fig. 13.1.6 for the spherical shock wave produced by the detonation of 1 kg of TNT in free air, and in Fig. 13.1.7 for the hemispherical wave produced by the

AirBlast : 1 kg TNT Free Air

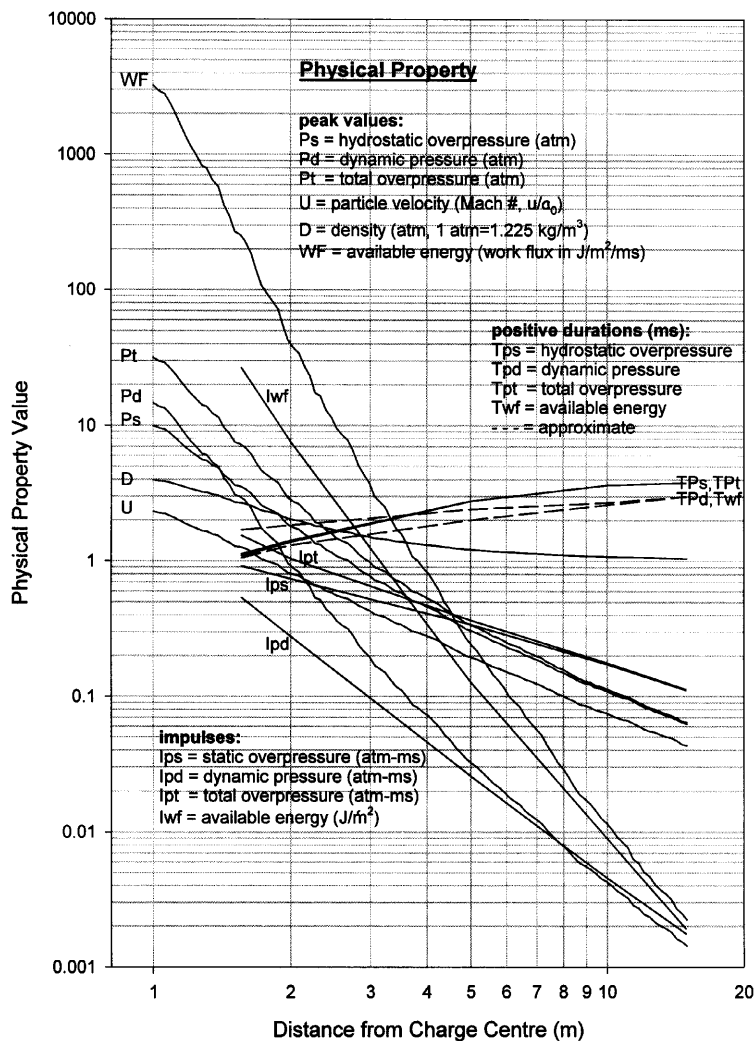


FIGURE 13.1.6 Some of the physical properties of the spherical shock or blast wave produced by the detonation of 1 kg of TNT in free-air at NTP. Some curves show slight irregularities because they are derived from a database (*AirBlast*) of a large number of experimental measurements.

AirBlast : 1 kg TNT Surface Burst

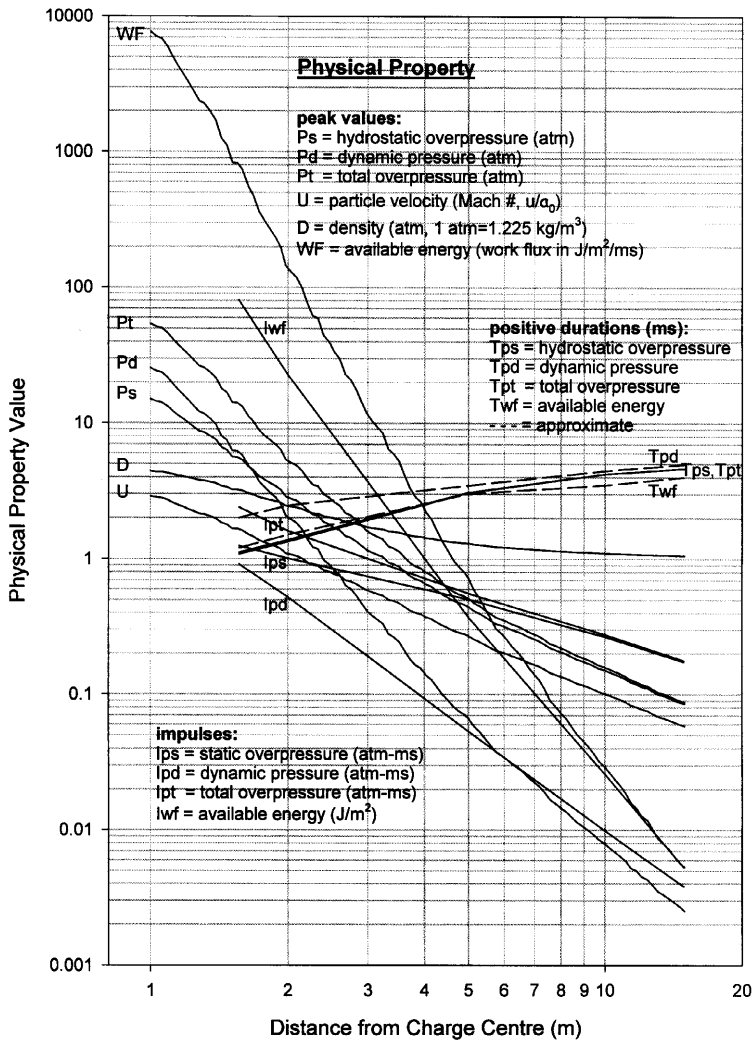


FIGURE 13.1.7 Some of the physical properties of the hemispherical shock or blast wave produced by the detonation of 1 kg of TNT on a rigid surface in an atmosphere at NTP. Some curves show slight irregularities because they are derived from a database (*AirBlast*) of a large number of experimental measurements.

detonation of 1 kg of TNT on a rigid plane surface. Both sets of values are presented because the blast wave produced by a 1-kg surface burst charge is not the same as that produced by a 2-kg free-air charge, except at large distances from the center. The values shown in Figs. 13.1.6 and 13.1.7 were obtained from the *AirBlast* expert system described previously.

The physical properties shown in these figures are defined as follows. P_s is the hydrostatic overpressure, in atmospheres, immediately behind the primary shock, as would be measured by a sensor placed side-on to the flow so that it did not detect any component of the dynamic pressure. P_D is the dynamic pressure, defined as $\frac{1}{2}\rho u^2$, where ρ is the gas density and u the particle velocity. P_t is the total or stagnation overpressure that will be recorded by a sensor placed face-on to the blast wave so that the flow is brought to rest. P_t is a function of the hydrostatic pressure and the particle flow velocity or the dynamic pressure, the functional relationship depending on whether the flow speed is locally sub- or super-sonic, that is, whether $M_u \leq 1$ or > 1 , where $M_u \equiv u/a$, u is the particle flow speed, and a the local sound speed. Since $a^2 = \gamma P/\rho$,

$$M_u^2 = \frac{\rho u^2}{\gamma P} = \frac{2 P_D}{\gamma P}, \quad (13.1.14)$$

where γ is the ratio of specific heats. For $\gamma = 1.4$ and $M_u \leq 1$,

$$P_t = P(0.2M_u^2 + 1)^{3.5}, \quad (13.1.15)$$

and for $M_u > 1$,

$$P_t = \frac{PM_u^2(3.58 \times 10^{-3})}{\left[1.167 - \left(\frac{0.167}{M_u^2}\right)\right]^{2.5}}. \quad (13.1.16)$$

In Figs. 13.1.6 and 13.1.7, U is the particle flow speed immediately behind the primary shock, expressed as a Mach number relative to the ambient sound speed, that is, $U = u_s/a_0$. $D = \rho_s/\rho_0$, is the gas density behind the shock relative to the ambient density. WF is the available energy or work flux immediately behind the shock and is a function of the internal energy at the stagnation pressure P_t . The passage of the shock front produces an increase of the internal energy density and the kinetic energy of the gas, but only a fraction of that energy can be extracted to do work. That fraction is the work flux, which has units of $\text{J m}^{-2} \text{ms}^{-1}$ and is a measure of the available energy passing through a unit area perpendicular to the flow direction in unit time. This is the energy available to cause damage to a structure in the path of the blast wave.

T_{ps} , T_{pd} , T_{pt} , and T_{wf} are the positive durations of the hydrostatic overpressure, dynamic pressure, total overpressure, and available energy, respec-

tively. For a TNT explosion the dynamic pressure and available energy do not return to their ambient values before the arrival of the second shock at all distances, and in these cases the times plotted in the figures are those at which these properties reach their minimum values.

The time integrals, or impulses of hydrostatic overpressure, dynamic pressure, and total overpressure, I_{ps} , I_{pd} , I_{pt} , respectively, and of available energy flux, I_{wf} , are also plotted as functions of distance in Figs. 13.1.6 and 13.1.7. These integrals or impulses are frequently used with the peak values behind the shock to formulate damage/injury criteria curves (P-I diagrams) for the estimation of damage to structures or injury to persons, arising from exposure to blast waves (Thornhill, 1957b; Baker *et al.*, 1983; van Netten and Dewey, 1997).

The variations with distance of the physical properties shown in Figs. 13.1.6 and 13.1.7 are not linear when plotted on log-log scales and cannot therefore be described by simple power law functions. In these figures, if the curve for any specific property, such as P_5 , were to be extended closer to the energy source, it would asymptotically approach a maximum value related to the energy density of the driver gas or detonation products. This would be a very high value for an intense explosion, such as a nuclear detonation, and a much lower value for a pressurized sphere or the deflagration of a combustible gas mixture. For this reason the curves in Figs. 13.1.6 and 13.1.7 have not been shown in the region close to the energy source.

Several authors have suggested analytical forms to describe the far field relationship between P_5 and R . Examples are $P \propto 1/R(\ln R)^{1/2}$ by Bethe (1947), Thornhill (1960), and Goodman (1960); and $P \propto 1/R$ by Baker (1983). In practice, all these forms give results that are so similar they cannot be distinguished by experimental measurements.

It will be shown below how the data presented in Figs. 13.1.6 and 13.1.7 can be scaled to provide the physical properties of the blast wave produced by an explosion of a charge of any size or in any type of atmosphere.

13.1.3 SCALING LAWS

The physical properties of a spherically expanding shock wave, expressed either as wave profiles at specific times or as time histories at specific distances, are not self-similar as is often the case with one-dimensional waves and their reflections. On the other hand, they are subject to precise scaling laws related to the amount of energy, E , released at the center and the properties of the ambient gas into which the shock wave is expanding.

Hopkinson (1915) and Cranz (1926) originally defined the scaling laws for blast waves. They showed that the distance from the center of an explosive

charge of a specific-property peak value immediately behind the primary shock, P_S , and the duration, t^+ or t^* , are proportional to the linear dimension of the spherical charge. The linear dimension of the charge is also proportional to the cube root of the charge mass, $W^{1/3}$, and thus the cube root of the amount of energy released by the explosion, $E^{1/3}$. If a peak property value, P_S , occurs at a distance R_1 from a charge of mass W_1 or energy release E_1 , and at a distance R_2 from a charge of the same material with a mass W_2 or energy E_2 , then

$$\frac{R_1}{R_2} = \left(\frac{W_1}{W_2}\right)^{1/3} = \left(\frac{E_1}{E_2}\right)^{1/3}. \quad (13.1.17)$$

Sachs (1944) added to this scaling law to account for differences in the ambient pressure, P_0 , and temperature, T_0 , of the gas into which the shock wave is moving. Sachs stated that (a) the peak values of hydrostatic pressure, P_S , density, ρ_S , and absolute temperature, T_S , scale in proportion to their values in the ambient gas, P_0 , ρ_0 and T_0 , respectively; (b) distances and durations will scale in inverse proportion to the cube root of the ambient pressure; and (c) durations and times of arrival will be proportional to the sound speed in the ambient gas, a_0 , and thus to the square root of the ambient absolute temperature. Equation (13.1.17) may therefore be expanded to

$$\frac{R_1}{R_2} = \left(\frac{W_1}{W_2}\right)^{1/3} \left(\frac{P_{02}}{P_{01}}\right)^{1/3} = \left(\frac{E_1}{E_2}\right)^{1/3} \left(\frac{P_{02}}{P_{01}}\right)^{1/3}. \quad (13.1.18)$$

Times of arrival of the primary shock at specific distances and times of duration will scale as

$$\frac{t_1}{t_2} = \left(\frac{W_1}{W_2}\right)^{1/3} \left(\frac{P_{02}}{P_{01}}\right)^{1/3} \left(\frac{T_1}{T_2}\right)^{1/2} = \left(\frac{E_1}{E_2}\right)^{1/3} \left(\frac{P_{02}}{P_{01}}\right)^{1/3} \left(\frac{T_1}{T_2}\right)^{1/2}. \quad (13.1.19)$$

The preceding scaling laws can be used with great accuracy to predict the physical properties of the blast wave from a given size of explosive charge or energy release, if the physical properties are known for the same explosive or rate of energy release, for a different size of charge or energy release. Dewey (1964) demonstrated the validity of the scaling laws applied to the peak values immediately behind the primary shock, and for wave durations and shapes, for explosive charges ranging from 25 to 10^5 kg. Subsequent experiments have extended that range from 10^{-3} to 5×10^6 kg, that is, over six orders of magnitude. For reasons discussed later, the scaling laws are only approximately valid when comparing blast waves produced by two different types of explosives, or for different rates of energy release.

For some explosives, such as ammonium nitrate fuel oil (ANFO), which is usually in the form of ammonium nitrate pellets mixed with a small amount of

fuel oil, the density of the explosive may change with the charge size because of the weight of the material involved. This may affect the detonation properties, so that the relative energy yield may increase with the charge mass. In addition, some explosives such as TNT and ANFO cannot be reproducibly detonated in small quantities as uncased charges. Casing the charge in a rigid material affects the equivalent energy yield unless the casing mass to charge mass ratio is small. For very large explosions, on the order of megatonnes of TNT, it may no longer be valid to consider the atmosphere as a uniform medium, and temperature gradients may affect the magnitude of the shock wave at long distances.

Figure 13.1.8 shows the variation of peak hydrostatic overpressure with distance for two charge masses, W_1 and W_2 , of the same explosive. A particular hydrostatic overpressure, P_S/P_0 , normalized to the ambient pressure, occurs at distances R_1 and R_2 , respectively from the two explosions. If W_1 is known, then W_2 , the mass of the second charge can be calculated from (13.1.18). Figure 13.1.9 shows schematically the types of hydrostatic overpressure variation with distance that might be expected with several different types of explosive with the same energy release. The scaling relationship just described is valid when comparing properties from two different explosives, only for the range of distances when the curves overlap, and this range may not be known. Comparisons of charge mass or energy yield of two different explosives should therefore be for a stated overpressure level. In the absence of other criteria, it is suggested that 1 atm overpressure be used for this purpose.

In the method just described above to determine the equivalent energy yield of an explosive, the yield is usually related to that of TNT, which is about 4.8 MJ kg^{-1} . TNT was chosen as the standard because it was a relatively well-behaved and widely available explosive. However, it was not an ideal choice. TNT, trinitrotoluene, is an oxygen-deficient explosive, and its detonation products continue to burn and release additional energy in the presence of atmospheric oxygen for a long period after detonation is complete. The “after-burning” has little effect on the properties of the primary shock front, but does change the characteristics of the wave profile when compared to that of other explosives. Also, TNT cannot be reproducibly detonated as an uncased charge in amounts less than about 5 kg. Nevertheless, a large amount of experimental information about the properties of TNT is in existence, for free-air, surface-burst, and height-of-burst (HOB) detonations.

The relative energy yields per kilogram of the detonation of a large number of explosives are given in several sources, such as Kinney and Graham (1985), but the values may have been derived by several different methods, for example, a theoretical chemical analysis; measurements using a bomb calorimeter; or by comparing the blast wave properties using Eqs. (13.1.17) or (13.1.18). For a variety of reasons, these may not all give the same result. Not

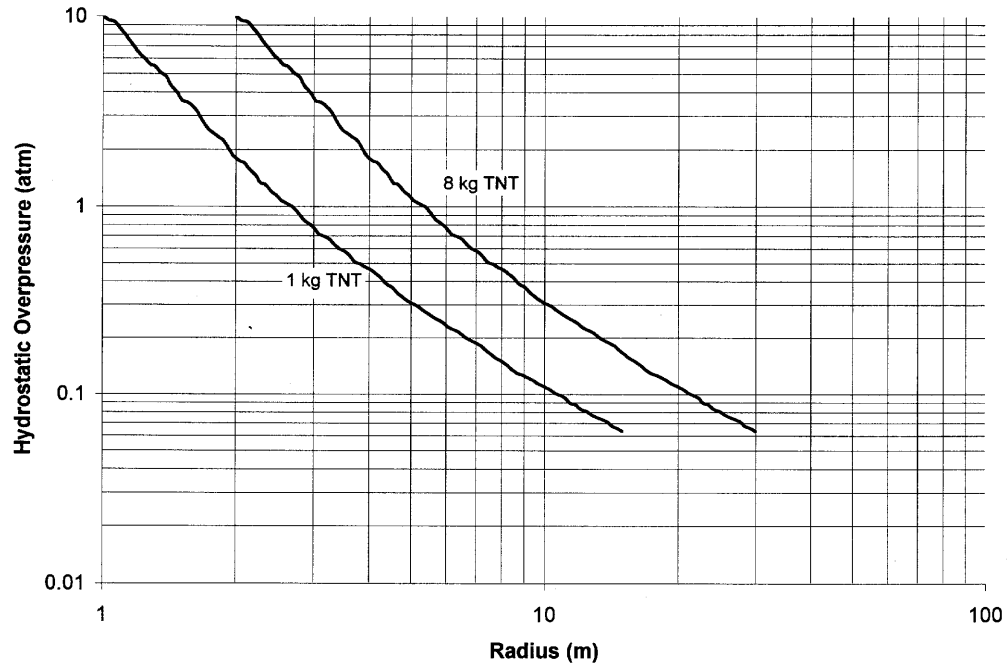


FIGURE 13.1.8 Peak hydrostatic overpressure versus radius in the blast waves produced by the detonation of 1 kg and 8 kg charges of TNT detonated in free air at NTP to show the effect of cube-root scaling. The radius at which a specific overpressure is produced by an 8 kg charge is exactly twice that for a 1 kg charge. (Data obtained from the *AirBlast* expert system)

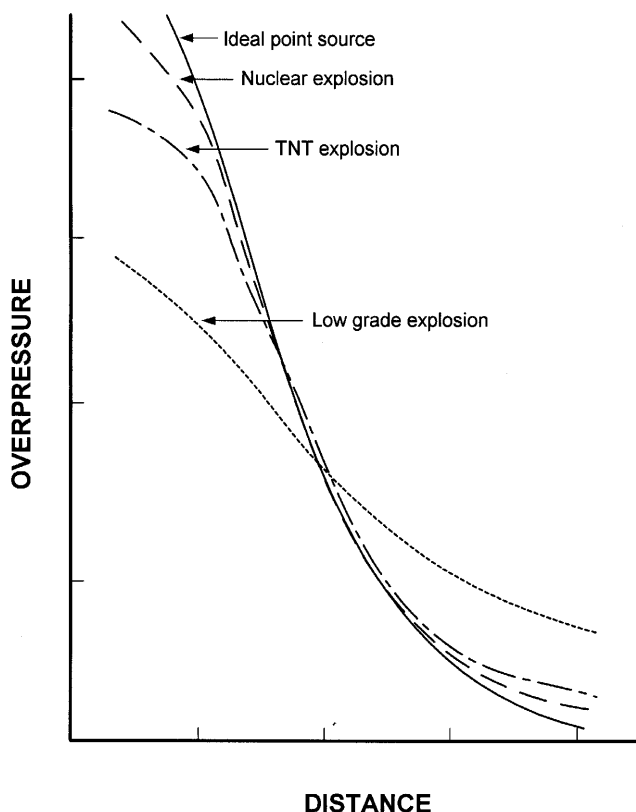


FIGURE 13.1.9 Conceptualized variation of hydrostatic overpressure versus distance, plotted on logarithmic scales, for the detonation of several different explosives with the same total energy yield. Explosives that produce high initial pressures, cause relatively lower pressures at larger distances.

all of the available chemical energy may be released in the detonation; a bomb calorimeter provides a strong casing for the chemical reaction, which may affect the detonation properties and allows no after-burning; and the equivalence obtained by comparing shock wave properties may depend on the shock strength at which the comparison was made. Fortunately, properties calculated using Eqs. (13.1.17) or (13.1.18) depend on the cube root of the energy ratio so that small errors in the energy equivalence may not have a significant affect on the calculated properties.

Figure 13.1.9 shows the way in which a shock wave property may vary with distance from several types of explosive source, each with the same energy release. The main differences occur at small distances where the initial pressure

of the release has a strong effect. At intermediate distances the rates of decay for many explosive sources are similar. At greater distances the curves may again separate because those sources, which produced weaker initial shocks, caused smaller entropy changes and dissipated less energy. There is therefore more energy remaining in the shock wave at greater distances. For this reason also, a deflagrating chemical may produce a stronger shock wave at greater distances than if it had detonated.

13.1.4 ANALYTICAL SOLUTIONS

The spherically expanding shock wave, produced by the instantaneous release of energy at a point in a uniform medium, is probably one of the simplest configurations in fluid dynamics, and yet it defies analytical solution. Taylor (1946, 1950a, b) made the first attempts at such a solution in 1939 and 1941. The first of these references deals with the wave produced by an expanding sphere, which requires a constant supply of energy, and Taylor derived an analytical solution by assuming a similarity such that the linear dimensions of the disturbance increased linearly with time. The energy associated with such a motion increases proportionally to the cube of the radius, and the pressure and velocity at corresponding points are independent of time. This type of similarity assumption is not valid in the case of a blast wave for which the total energy remains constant and the intensity of the disturbance decreases with increasing distance.

The similarity assumptions for an expanding shock wave of constant total energy are

$$\begin{aligned}\frac{P}{P_0} &= R^{-3}f \\ \frac{\rho}{\rho_0} &= \phi\end{aligned}\tag{13.1.20}$$

and

$$u = R^{3/2}\phi,$$

where P , P_0 , ρ , ρ_0 , and u are as defined previously, R is the radius of the shock, f , ϕ , and ϕ are functions of r/R , and r is the radial distance of any part of the wave. At the shock front the Rankine–Hugoniot equations must be satisfied, viz.,

$$\frac{\rho_S}{\rho_0} = \frac{\gamma - 1 + (\gamma + 1)\frac{P_S}{P_0}}{\gamma + 1 + (\gamma - 1)\frac{P_S}{P_0}},\tag{13.1.21}$$

$$M_S^2 = \frac{1}{2\gamma} \left[\gamma - 1 + (\gamma + 1)\frac{P_S}{P_0} \right]$$

and

$$\frac{u_s}{a_0 M_S} = \frac{2 \left(\frac{P_S}{P_0} - 1 \right)}{\gamma - 1 + (\gamma + 1) \frac{P_S}{P_0}}.$$

In general, these are inconsistent with the self-similarity equations, (13.1.20). However, Taylor pointed out that if the hydrostatic pressure, P_0 , is much greater than the ambient atmospheric pressure, P_0 , the Rankine–Hugoniot equations (13.1.21) reduce to

$$\frac{\rho}{\rho_0} = \frac{\gamma + 1}{\gamma - 1}; M_S^2 = \frac{\gamma + 1}{2\gamma} \frac{P_S}{P_0}, \text{ and } \frac{u_s}{a_0 M_S} = \frac{2}{\gamma + 1}, \quad (13.1.22)$$

which are consistent with the similarity assumption and yield

$$\varphi = \frac{\gamma + 1}{\gamma - 1}, f = \frac{2\gamma}{\gamma + 1} \text{ and } \phi = \frac{2}{\gamma + 1} \quad (13.1.23)$$

at the shock front where $r/R = 1$. With these initial values Taylor made step-by-step calculations to determine the variation of φ , f and ϕ with r/R for $1 \geq r/R \geq 0.5$.

These calculations provided predictions subsequently found to be in excellent agreement with measurements of the initial phases of the first nuclear explosion (Taylor, 1950b). They also permitted Taylor to predict that approximately 50% of the energy released from such an intense explosion would be in the form of electromagnetic and nuclear radiation, with the remainder of the energy contained in the expanding shock wave.

Although Sir G. I. Taylor's paper (1950a) is a classic example of a theoretical description of a spherical shock wave, its use for detailed analyses is restricted to waves originating from a point source and with peak pressures greater than approximately 10 atm. A qualitative description of the spherical shock wave in intermediate and low pressure regions was obtained by Bethe and von Neumann (1958) by assuming in the first case that $\gamma - 1$ was small, and for the low pressure region that an approximate acoustical theory could be applied.

Sakurai (1953, 1954) extended the technique used by Taylor, including the plane and cylindrical wave cases, by expressing the physical properties of the shock wave in the form of power series in $1/M_S^2$. For example, the distance of the shock from the center is given by

$$\frac{1}{M_S^2} \left(\frac{R_0}{R} \right)^{\alpha+1} = J_0 \left[1 + \lambda_1 \left(\frac{1}{M_S^2} \right) + \frac{1}{2} \lambda_2 \left(\frac{1}{M_S^2} \right)^2 + \dots \right], \quad (13.1.24)$$

where $\alpha = 0, 1$ or 2 for plane, cylindrical, or spherical shocks, respectively; R_0 is a characteristic length related to the energy of the source; and J_0 and λ_i are

constants that may be determined by successive approximations, using Taylor's solutions as a first approximation, and the Rankine–Hugoniot relationships across the shock as a set of boundary conditions. Oshima (1960) applied Sakurai's results to data, principally in the form of interferometric density measurements, obtained with exploding wires. He found that the Taylor–Sakurai theory described the blast wave well in the initial period of high peak pressure, but did not predict the flow at greater distances from the explosion. To describe the flow in this region he developed a quasi-similarity technique in which the similarity assumption was made for the normalized velocity, pressure, and density over a narrow range of shock strengths and close to the shock front. This method gave good predictions for the blast characteristics close to the shock in the region of intermediate shock strengths ($10 \geq M_s \geq 1.5$). At smaller shock strengths Oshima found that the flow characteristics could be best predicted by Whitham's (1957, 1959) analysis.

Similar approaches in the search for an analytical solution to describe the physical properties of a centered spherical shock are discussed by Stanyukovich (1960), Zel'dovich and Raizer (1966) and Oppenheim *et al.* (1972). However, searches for analytical solutions ceased to be a priority with the advent of high-speed computers, which made possible highly successful numerical solutions of this problem.

13.1.5 NUMERICAL METHODS

13.1.5.1 NUMERICAL MODELLING

The advent of high-speed digital computers made it possible to carry out complete numerical solutions of the shock waves produced by spherically symmetrical explosions. Brode (1955) made an early analysis for a point source release of energy, using the solutions of Taylor and Bethe, described earlier, as the initial conditions. Brode subsequently made similar calculations for the shocks produced by a pressurized sphere (Brode, 1956) and the detonation of a spherical charge of TNT (Brode 1956, 1957, 1959). These results were compared with experimental measurements, for example, Boyer *et al.* (1958) and Boyer (1959, 1960) for the pressurized sphere, and Dewey (1964, 1971) for TNT. In the case of the pressurized sphere, there were significant differences between the observed and calculated loci of the shock and contact surface, but this was because the calculations did not take into account the significant mass of the glass used to hold the pressurized gas. In the case of the TNT detonation, there was excellent agreement between the calculated and observed properties of the primary shock front, but a less good agreement for

the decay of some of the properties behind the shock because the calculation had not taken into account the effect of after-burning of TNT in atmospheric oxygen. Had a less oxygen-deficient explosive been used, with a correct assessment of the total energy release, Brode's calculations would undoubtedly have given excellent descriptions of the properties of a centered shock wave.

Taylor (1950a) pointed out that a spherically expanding shock leaves the air in a state of radially decreasing entropy so that the density is not a single-valued function of the pressure. However, each element of gas traversed by the primary shock moves isentropically until traversed by the second shock. This suggests that an analytical or numerical solution of a spherically expanding shock wave might best be made in Lagrangian coordinates, following the individual gas elements. Brode used this coordinate system, and the following equations for his calculations:

$$\frac{\rho}{\rho_0} = \frac{r_0^2}{r^2} \frac{1}{(\partial r / \partial r_0)}, \text{ conservation of mass} \quad (13.1.25)$$

$$\rho_0 \frac{\partial u}{\partial t} = - \frac{r^2}{r_0^2} \frac{\partial P}{\partial r_0}, \text{ conservation of momentum} \quad (13.1.26)$$

$$\frac{\partial E}{\partial t} = \frac{P}{\rho^2} \frac{\partial \rho}{\partial t}, \text{ conservation of energy} \quad (13.1.27)$$

$$P(E, \rho), \text{ caloric equation of state} \quad (13.1.28)$$

$$T(E, \rho), \text{ thermal equation of state} \quad (13.1.29)$$

and

$$u = \frac{\partial r}{\partial t}, \text{ definition of particle velocity} \quad (13.1.30)$$

where ρ , ρ_0 , u , P , and t are as previously defined, r is the radial position of a gas element, r_0 is the original position of the element before the arrival of the primary shock, and E is the internal energy.

Brode's work demonstrated the wealth of detailed information about the physical properties of spherical shocks that could be provided by numerical methods, and these methods have been continuously developed to take advantage of bigger and faster computers. Several hydrocodes are now available commercially that can be used to calculate the properties of spherically expanding shocks and their reflections and interactions. Well-tested examples are SHARC (Hikida *et al.*, 1988 and Crepeau, 1998) by Applied Research Associates Ltd, Albuquerque, NM, and AUTODYNE (Fairlie, 1998, and Robertson, Hayhurst, and Fairlie, 1994) by Century Dynamics, Horsham, West Sussex, UK. These are large and powerful codes that allow the user to define the characteristics of an explosive source and its casing materials, and to

allow for a variety of equations of state. If a high-resolution computing grid is to be used to permit a detailed definition of the shock front properties, a large and fast computer is required.

Simpler codes running on smaller computers can also be used to calculate the physical properties of a spherical shock if it is not required to calculate the detonation phenomena of an explosive source. The complexities of the detonation process may be bypassed by replacing the detonation source with a high-pressure, high-temperature sphere of gas, the properties of which can be further modified by changing the rate of energy release. The initial conditions can be chosen to represent different types of detonation phenomena.

The one-dimensional conservation equations that need to be solved are

$$\frac{\partial \rho}{\partial t} + \frac{\partial(\rho u)}{\partial r} = -\frac{(\eta - 1)}{r} \rho u \quad (13.1.31)$$

$$\frac{\partial(\rho u)}{\partial t} + \frac{\partial(\rho u^2 + P)}{\partial r} = -\frac{(\eta - 1)}{r} \rho u^2 \quad (13.1.32)$$

and

$$\frac{\partial E}{\partial t} + \frac{\partial[u(E + P)]}{\partial r} = -\frac{(\eta - 1)}{r} u(E + P), \quad (13.1.33)$$

where E is the total energy per unit volume, η is a geometric parameter equal to 1 for planar, 2 for cylindrical, and 3 for spherical symmetry, respectively, and the other symbols are as previously defined. These equations can be solved using a variety of the numerical techniques described in Chapter 6.

One problem associated with the numerical calculation of spherical shocks is the accumulation of small numerical errors. This arises, even if round-off is ignored as a source error, because in most numerical techniques the physical properties calculated for an elementary cell are assigned to the center of the cell. Since the equations being solved are not linear, this introduces a small error, and in an extensive calculation of a spherical shock these errors all have the same bias and eventually accumulate to an error that may be significant at large distances from the center. An interesting solution to this problem is the random choice method (Saito and Glass, 1979; Lau and Gottlieb, 1984; Glimm, 1965; Chorin, 1976; and Sod, 1977). In this method, an exact local solution is sampled randomly, the exact local solution being that of a shock tube defined using adjacent cells as driver and driven sections, also known as the Riemann problem. The random sample is assigned to a point half way between the cells, and the process is repeated for all pairs of adjacent cells. At the next time step the process is repeated and the second set of random samples assigned back to the cell centers. This general approach, using exact local solutions, is due to Gudonov (1959, 1976). The random choice technique provides calculation of the properties of a spherical shock over large ranges, which agree well with

experimental measurements at all distances. The random choice method does not provide an entirely smooth solution if, for example, the peak pressure is plotted against distance, but the variations are related to the cell size used in the calculation. The random choice method has not been successfully applied to the solution of truly two- or three-dimensional flows.

13.1.5.2 NUMERICAL RECONSTRUCTION

Another application of numerical modelling is the numerical reconstruction of a specific spherical shock for which some physical properties have been measured (Lau and Gottlieb, 1984). In this procedure, the input parameters to a numerical simulation are varied until particular experimental measurements are reproduced as nearly as possible. It is then assumed that the numerical results reconstruct the event in which the experimental measurements were made, over some range of distances and times.

The piston-path method has been used extensively to reconstruct the shock waves from a large number of air- and surface-burst explosions. In this method, a numerical modeling technique is used to calculate the flow ahead of a piston that is put into motion with some instantaneous speed. The motion of the piston is varied systematically until experimentally measured data in the flow ahead of the piston, such as electronically measured pressure-time histories, are reproduced. The starting time, initial speed, and distance-time locus of the piston are varied until an optimal match between the calculated and measured physical properties is achieved.

The motions of smoke tracers measured photographically have been used successfully for this purpose (Dewey and McMillin, 1987, 1990; Dewey *et al.*, 1995; McMillin and Dewey, 1995). The trajectory of the numerical piston is made identical to the measured trajectory of a tracer placed as close as practicable to the center of the explosion. The measured motions of other smoke tracers, placed far from the explosion, are compared to the calculated motions of the gas elements at the same distances. If necessary, the original piston path is adjusted to achieve an optimum match. Little adjustment to the original piston path is normally required. The random choice method is a stable and accurate numerical technique to use with the piston-path method and is excellent for reconstructing the pseudo-one-dimensional radial flows produced by air-, surface- and height-of-burst explosions. The data shown in Figs. 13.1.6 and 13.1.7, and the other results presented in this chapter derived from the *AirBlast* expert system, were generated using the piston-path and random-choice methods.

13.1.6 EXPERIMENTAL MEASUREMENT TECHNIQUES

13.1.6.1 INTRODUCTION

Many methods have been developed to measure the physical properties of spherically expanding shocks because of the military, industrial, and civilian applications of blast waves from explosive sources. Three types of measurement technique are commonly used: electronic, photogrammetric, and passive. Electronic and passive methods are described in detail by Reisler *et al.* (1995), and photogrammetric methods by Dewey (1997a, b).

The measurement of spherical shock waves is complicated by the fact that the expanding and decaying shock leaves the air in a state of radially decreasing entropy. As a result, the flow past a stationary measurement point is nonisentropic, and there is no single valued functional relationship between the thermodynamic properties measured at that point. In order to fully describe those thermodynamic properties it is necessary to independently measure three of them, for example, hydrostatic pressure, dynamic pressure, and density. Hydrostatic pressure is the easiest property to measure, and therefore the one most commonly used for blast wave diagnostics. However, hydrostatic pressure provides the least information about the flow field. For example, it provides no information about the changes of the physical properties in a boundary layer where there may be very large gradients of the dynamic pressure. In contrast, measurement of the time-resolved particle trajectories permits a determination of all the thermodynamic properties in the flow field (Dewey, 1964, 1971).

13.1.6.2 ELECTRONIC METHODS

Electronic measurement techniques involve some form of transducer to transform the magnitude of a thermodynamic property of the gas, such as hydrostatic or dynamic pressure, density, temperature, or velocity, into a time-resolved electrical signal that can be amplified and stored by a magnetic or solid state recorder.

Frequently used hydrostatic pressure transducers are piezoelectric, capacitance, or strain measuring devices. The transducer must be mounted in such a way as to cause minimum disturbance of the flow being measured. This can be done most simply to monitor the hemispherical shock wave from a surface burst explosion because the sensitive surface of the transducer can be flush mounted in the ground surface. In order to measure the hydrostatic pressure in the spherical shock from an air-burst explosion, the transducer must be mounted in

a streamlined holder causing as little disturbance as possible to the shock wave flow. These devices, sometimes called lollipop or pancake gauges, must be carefully aligned to the center of the explosion so that the transducer does not detect any component of the flow normal to the surface of the transducer.

The design of a pressure gauge must incorporate a number of features. The pressure increase in a shock wave is accompanied by temperature changes, and the pressure transducer must be shielded so that the thermal effects do not influence it. It must not be sensitive to the radiant heat or light from the explosive source, to acceleration effects due to the motion or vibration of the mount, or to strains caused by the shock wave loading on the casing containing the sensitive element of the transducer.

Ideally, there should be a linear relationship between the pressure on the transducer and the magnitude of the electrical signal it produces. In practice the piezoelectric relationship may be nonlinear and may change with ambient temperature and with time. Wherever possible the gauge should be calibrated as soon as possible before and after each measurement. This is done most easily by exposing the transducer to a series of shocks produced in a shock-tube-like device, with a range of strengths that bracket the expected strength of the shock that is to be measured. The speed of the calibrating shocks can be measured by noting the time interval as the shock passes over two pressure-sensitive time-of-arrival detectors. Knowing the ambient temperature and thus the ambient sound speed, the Mach number of the calibrating shock can be calculated and used in the Rankine–Hugoniot relationship (13.1.1) to determine the peak pressure.

To measure the dynamic pressure in a shock wave the transducer must be mounted face-on to the flow, in a mount that will stagnate the flow but cause a minimum of disturbance to the shock wave. In order to determine the dynamic pressure, $P_D \equiv \frac{1}{2}\rho u^2$, from the measured total or stagnation pressure, P_t , the hydrostatic pressure, P , must be simultaneously measured at the same location. The relationship between P_t and P is a function of the Mach number of the flow, M_u , and the function depends on whether $M_u \leq 1$ or > 1 . Thus, P_D can be calculated from the measured values of P_t and P , using (13.1.14), and (13.1.15) or (13.1.16). Large errors will arise in the measurement of P_t if there is any dust entrained in the flow. Reisler *et al.* (1995) described gauges that are designed to eliminate this effect.

A face-on pressure gauge used to measure P_t will initially sense the peak normal reflected shock pressure, P_R , given by

$$\begin{aligned} \frac{P_R}{P_0} &= \left[\frac{2\gamma M_S^2 - (\gamma - 1)}{\gamma + 1} \right] \left[\frac{(3\gamma - 1)M_S^2 - 2(\gamma - 1)}{(\gamma - 1)M_S^2 + 2} \right] \\ &= \frac{(7M_S^2 - 1)(4M_S^2 - 1)}{3(M_S^2 + 5)} \end{aligned} \quad (13.1.34)$$

(for $\gamma = 1.4$) see Chapter 3, Table 3.1.4, Gaydon and Hurle (1963), and Bradley (1962). This high pressure may exist for only a short time before it is relieved by the rarefaction wave formed as the shock moves past the front surface of the gauge mount. If the frontal cross-section of the gauge is small, and unless the response time of the transducer is very fast, it may never detect the peak value of the reflected pressure given by (13.1.34).

The time variation of gas density in a spherical expanding shock has been measured by recording the absorption of soft β radiation (Dewey and Anson, 1963). A similar device has been incorporated into a blast measurement station (Ritzel, 1985), which simultaneously measures the time histories of hydrostatic and dynamic pressure, and density.

There have been few successful methods developed for the direct measurement of the temperature of the gas in a shock wave, unless the shock is so strong that radiation methods can be used, such as the spectrum line reversal method (Gaydon and Hurle, 1963). Attempts have been made to use thermistors, but even very small devices have a large enough thermal capacity that correction procedures must be used to compensate for the slow response time (Muller *et al.* 1995). In addition, the device must be protected from solar heating and direct radiation from the explosive source.

13.1.6.3 PHOTOGRAMMETRIC METHODS

Several of the high-speed photographic techniques for the measurement of shock wave properties described in Chapter 5, have been applied to the measurement of spherical shocks (Dewey, 1997a,b). Two extensively used methods have been a modification of shadow photography, known as refractive image analysis, and flow visualization of particle tracers, known as particle trajectory analysis.

The increase of the density at the front of a spherical shock causes an intense gradient of the refractive index of the ambient air, which produces a distortion of the observed background behind the shock, as shown in Fig. 13.1.10. This distortion can be photographed with a high-speed camera to produce a sequence of images from which the radius of the spherical shock can be calculated as a function of time. Because the shock front is spherical, the radius of the shock image measured in the film plane translates to an apparent radius, R , in the object plane parallel to the film plane and containing the center of the shock. The actual shock radius, R , may then be derived from the trigonometrical relationship

$$R = D \sin \left[\tan^{-1} \frac{\cos \kappa}{\left(\frac{D}{R'} - \sin \kappa \right)} \right], \quad (13.1.35)$$

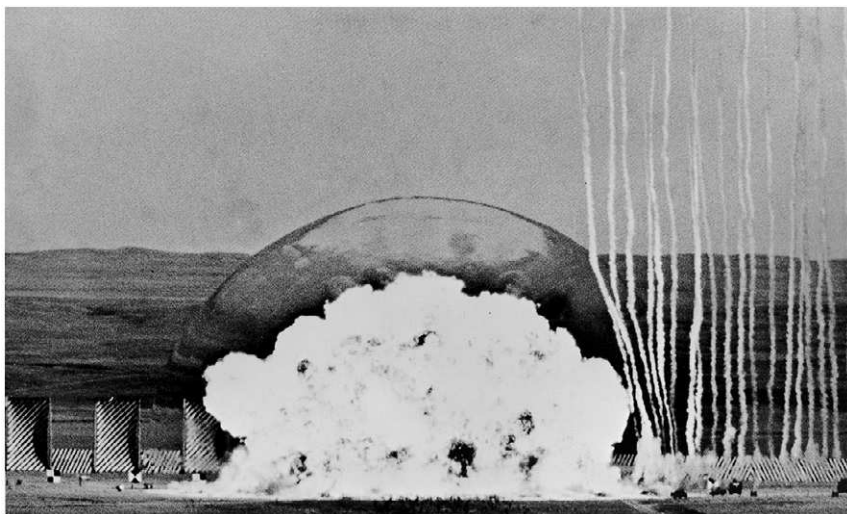


FIGURE 13.1.10 Surface detonation of 200 tonnes of TNT. The refractive image of the primary shock can be seen as it distorts the view of the hill and sky background. From a sequence of such images, the radius of the shock can be determined as a function of time to yield the shock Mach number as a function of distance. To the right, the displacement of an array of white smoke trails was used to determine the flow speed and density within the blast wave. The black and white striped panels to the left, used to better visualize the shock, were approximately 15 m high. A number of military vehicles can be seen to the right of the explosion. (Photograph courtesy of the Defence Research Establishment Suffield, Canada)

where D is the distance from the camera to the center of the shock and κ is the offset angle of the optical axis of the camera from the shock center. (N.B. This simple relationship is for the special case when the shock center, the center of the image plane, the shock image, and the camera are coplanar. In other situations a more complicated three-dimensional photogrammetric correction must be used.) From a sequence of frames from the high-speed film the variation of the shock radius with time can be measured and used in Eq. (13.1.7) to determine the shock speed and thus the shock Mach number. This, in turn, can be used in Eqs. (13.1.1) to (13.1.4) to calculate the peak values of the thermodynamic properties behind the shock at any position within the range of the measured shock radii.

The passage of a spherical shock leaves the ambient gas in a state of radially decreasing entropy. However, each gas element traversed by the primary shock moves with an initial velocity given by Eq. (13.1.4) and remains isentropic until the arrival of the second shock. As a result of this Lagrangian isentropy, Dewey (1964, 1971) showed that knowledge of the time-resolved particle trajectories in a spherical shock is sufficient information to define all the

physical properties of the shock, as functions of time and distance. The particle trajectories can be measured by high-speed photography of tracers in the form of smoke trails, introduced into the ambient gas immediately before the arrival of the shock, as shown in Fig. 13.1.10.

The time-resolved particle trajectories can be analysed using the piston-path random-choice technique first proposed by Lau and Gottlieb (1984) and described in Section 13.1.5.2. The measured trajectory in the distance–time plane of a particle tracer close to the centered source is used as the trajectory of a spherical piston. The shock wave generated by this piston is calculated using the random choice method. The results of the numerical simulation are used to calculate the trajectories of particles with initial positions the same as those of the smoke tracers used in the experiment. The calculated and observed trajectories are compared; if there is not good agreement, slight changes are made to the piston path trajectory, and the calculation is rerun until an optimum match is achieved. In practice, it has been found that very little, if any, iteration is required to obtain an excellent match between the calculated and observed trajectories. The resulting numerical simulation can then be used to reconstruct all the physical properties of the shock wave as functions of distance and time. This method has been used to analyse the blast waves from a large number of explosions (Dewey and McMillin, 1987; McMillin and Dewey, 1995) and has been the primary source of data incorporated in the *AirBlast* expert system (Dewey and McMillin, 1989), which is a compendium of properties of blast waves from free-air, surface-burst, and near-surface-burst explosions.

The method described earlier, in which the physical properties of a spherical shock are “reconstructed” from the observed particle trajectories, is one that can easily be applied using other numerical simulation algorithms and other experimental measurements. The reconstruction techniques require that the energy source be described by a limited number of parameters such as a time-resolved piston path or a pressurized high-temperature sphere, possibly with a controlled rate of energy release. Several of the numerical methods presented in Chapter 5 can then be used to calculate the spherical flow field. The results of the calculations are matched to experimental measurements, such as shock-front time-of-arrival or pressure–time histories, and the initial boundary conditions are varied until an optimal match is achieved.

13.1.6.4 PASSIVE METHODS

Passive methods of monitoring the properties of spherical shocks are those that do not involve active systems such as electronic recorders or cameras. A variety of such methods are described by Reisler *et al.* (1995) and include measures of

the displacement of free-standing cubes (Ethridge and Flory, 1993), the rupture and displacement of foil membranes (Manweiler, 1973), and the bending or brittle fracture of cantilevers (van Netten and Dewey, 1997). Although lacking some of the precision of methods described previously, passive techniques have the advantages that they are usually cheap and can be left in place for long periods without attention. Their response then can be evaluated if an explosion should occur. They are suitable for monitoring environments such as a chemical factory or the vicinity of a volcano. Most passive gauges were first conceived when damage to structures occurred as a result of an unexpected explosion, and the damage was subsequently analyzed to determine the properties of the resulting blast wave (e.g., Penney *et al.*, 1970).

13.1.7 SPHERICAL SHOCK REFLECTIONS

13.1.7.1 REGULAR AND MACH REFLECTIONS

The phenomena of regular and Mach reflection of shock waves in two dimensions have been discussed extensively in Chapter 8 and by Ben-Dor (1991). The same shock configurations arise when a spherical shock expanding in three dimensions interacts with a plane rigid surface. The theories describing plane shock reflections, initiated by von Neumann (1943), normally assume that regions of uniform flow follow the incident and reflected shocks. In practice, this assumption is valid only for the reflection of a plane shock with a speed of approximately Mach 2. In the case of a spherical shock reflection the assumption is clearly not valid and the strength of the incident shock decreases as the reflection proceeds. Nevertheless, it has not been demonstrated that the criteria for transition from regular to Mach reflection of spherical shocks are significantly different from those of plane shocks, that is, the detachment criterion is a reasonable approximation for the point of transition for spherical shocks reflecting from a plane surface.

The Mach stem produced by a spherical shock reflection is approximately hemispherical and centered on the point on the reflecting surface closest to the center of the shock; “ground zero” in the case of an explosion above the ground. The properties of this Mach stem shock, including its rate of decay, are different from those of shocks from a free-air or surface burst explosion, and depend on the height of burst (HOB) (Dewey, McMillin and Classen, 1977; Dewey and McMillin, 1981).

Double Mach reflection (Chapter 8) also occurs for spherical shocks of sufficient strength, and in the case of air burst explosions, the flow toward the

reflecting surface produced by such a reflection and the subsequent boundary jet flow may entrain a considerable amount of dust, which will have a large effect on the physical properties of the flow close to the ground.

In the case of a very intense explosion, such as that from a nuclear weapon, the high temperature close to the source may produce radiant heating of the ground, which will cause a layer of heated air immediately above the ground surface ahead of the incident or Mach stem shock. The shock close to the ground will move more rapidly into this heated layer and produce what is known as a thermal precursor shock (Glasstone and Dolan, 1977). The radiant heating may also be sufficient to ignite surface vegetation and vaporize surface material ahead of the approaching shock. These phenomena clearly have a major influence on the properties of the shock wave close to the ground, and in particular, may greatly increase the dynamic pressure (Kuhl *et al.*, 1995).

The configurations of the Mach stem and precursor shocks produced by spherical shock reflections, obtained by numerical modeling, are shown in Figs. 13.1.11a and 13.1.11b.

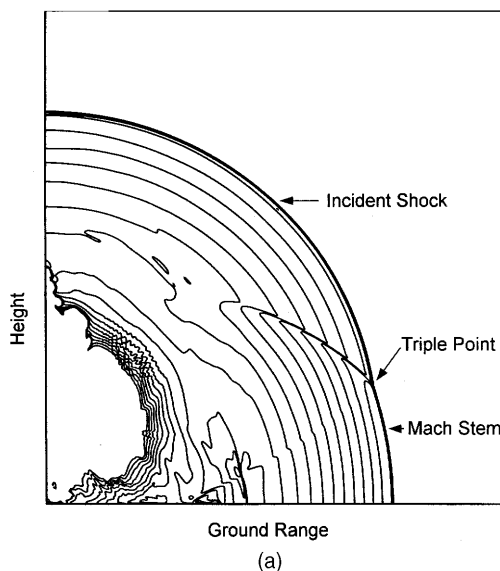


FIGURE 13.1.11a Numerical simulation of a Mach reflection produced by an above-ground explosion. The lines are isopycnics. (The simulation was made with the AWAFF code.)

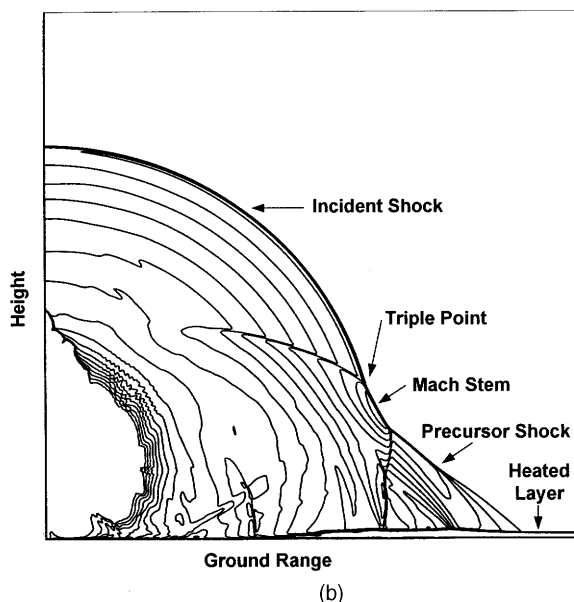


FIGURE 13.1.11b The same numerical simulation as shown in figure 11a, but with a thin layer of high temperature gas above the ground surface. Such a layer is produced by the thermal radiation from a nuclear explosion, and causes a significant change to the Mach stem, known as a thermal precursor. All of the physical properties of the blast wave close to the ground are significantly changed by the precursor. (The simulation was made with the AWAFF code.)

13.1.7.2 HEIGHT-OF-BURST CURVES

The two- and three-shock theories developed by von Neumann (1943) predict that there will be a large increase of hydrostatic pressure close to the reflection point in the region of transition from regular to Mach reflection. Experiments in which uniform plane shocks were reflected from plane wedges with a range of different angles of inclination have confirmed an increase of pressure at transition, although the measured increase was never as large as that predicted by the two- and three-shock theories (Heilig and van Netten, 1991).

The two- and three-shock theories were used to calculate the peak hydrostatic pressure that might be expected on the ground surface as the result of a nuclear explosion at a specified height of burst above the ground. The results of these calculations were plotted as isobars of maximum overpressure along the ground in the plane of height-of-burst versus ground-range, where the ground range is measured from ground zero, the point on the ground immediately beneath the explosion. A height-of-burst curve from one of these calculations is shown in Fig. 13.1.12. The height-of-burst curves

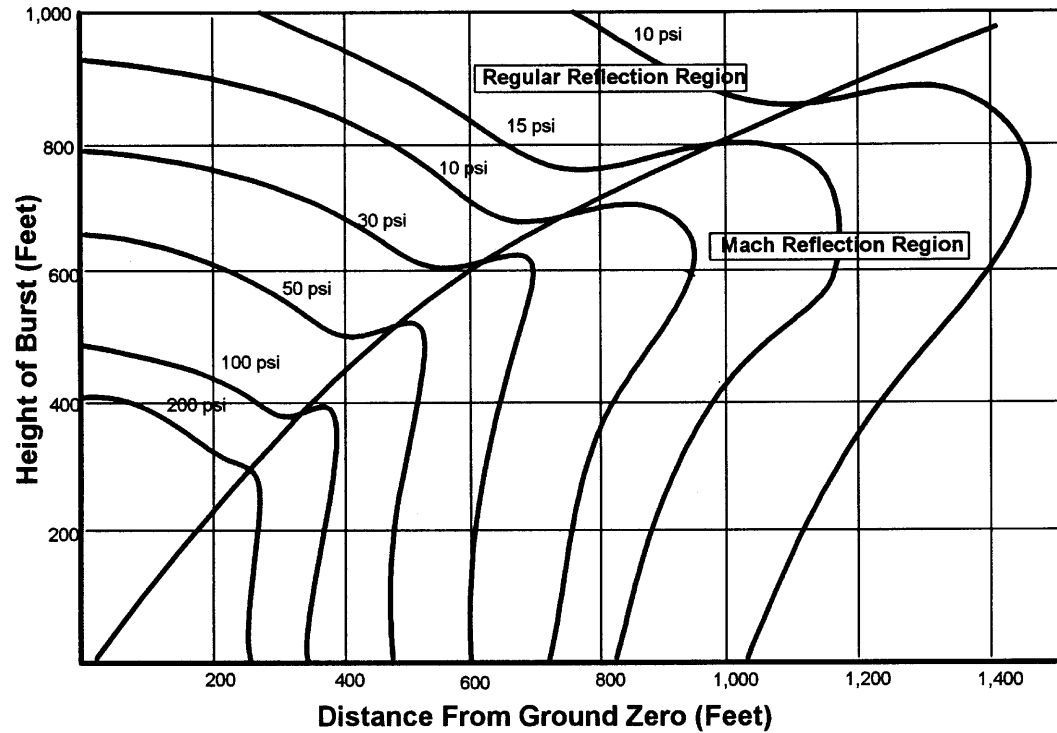


FIGURE 13.1.12 Theoretical height-of-burst curves of peak hydrostatic overpressure for a 1 kt nuclear explosion, showing extended high pressures in the regions of transition from regular to Mach reflection (von Neumann, 1943).

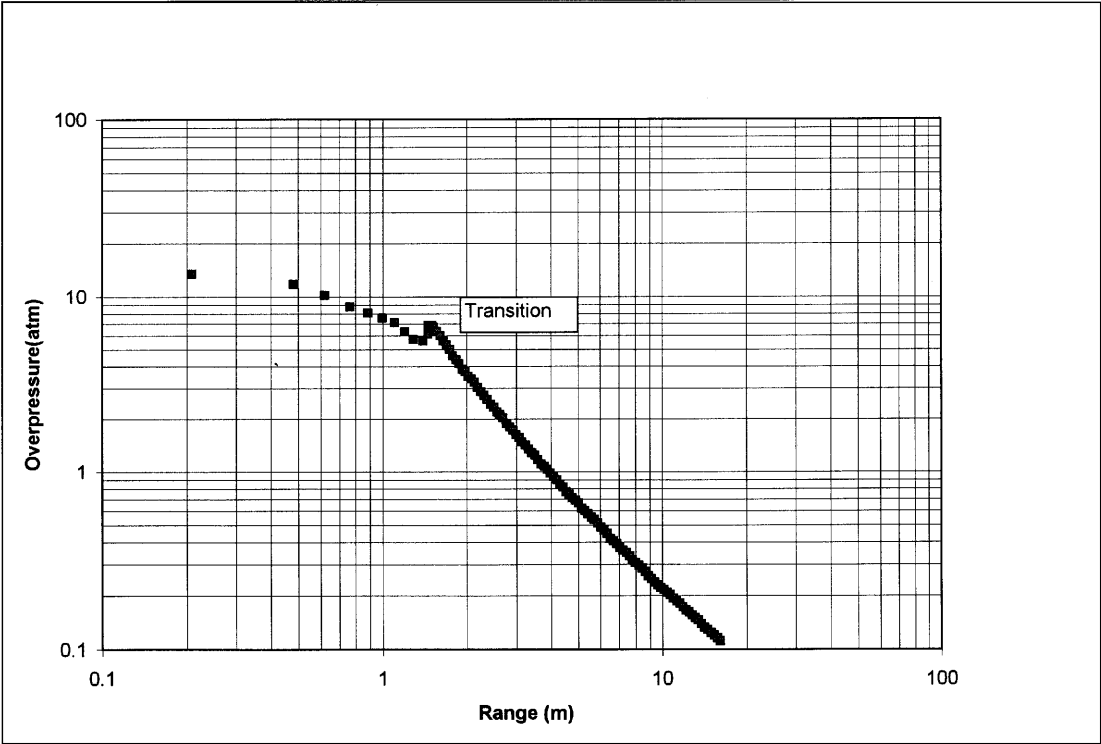


FIGURE 13.1.13 Peak hydrostatic overpressure versus distance for a 1.25 kg charge of TNT at a height of burst of 1.7 m, derived from the *AirBlast* database of experimental measurements. The increase of pressure in the transition region is clearly seen.

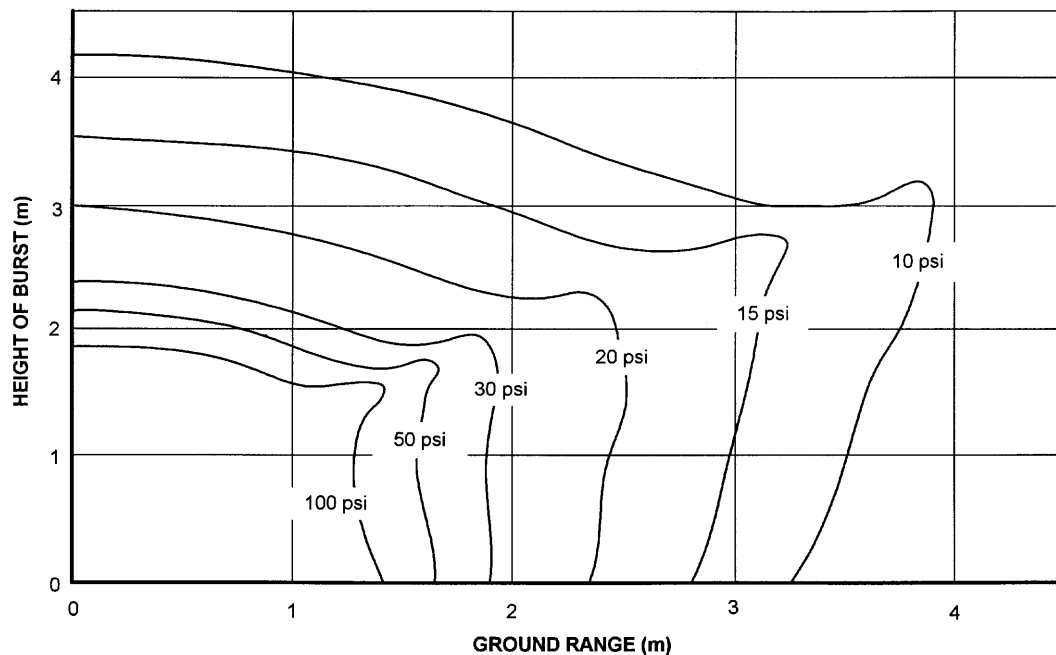


FIGURE 13.1.14 Height-of-burst curves of peak hydrostatic overpressure for a 1 kg charge of TNT, derived from the AirBlast database of experimental measurements. The extended high pressures in the regions of transition can be seen, but are not as extensive as those predicted in Figure 13.1.12.

calculated in this way show a considerable extension of the isobars in the region of transition from regular to Mach reflection, indicating that there may be an extended region in which the overpressure will increase with increasing distance from ground zero, for example the 100 psi to 10 psi isobars in Fig. 13.1.12. These regions of the isobars have been called the “knees.”

When nuclear tests were carried out under controlled conditions, pressure gauge arrays failed to identify the expected pressure increase at transition from regular to Mach reflection, and the height-of-burst curves were redrawn without the knees. No pressure increase was observed by Heilig (1969, 1977) for plane shocks moving from regular to Mach reflection on cylindrical surfaces, or more recently by Reichenbach and Kuhl (1989, 1993) using 0.5-g charges detonated above a smooth, rigid reflection surface. However, Dewey and van Netten (1998) reported a pressure increase in the transition region for spherical shocks from 500-kg charges detonated above the ground, measured using refractive image and particle trajectory photogrammetry, as shown in Fig. 13.1.13. Similar pressure increases at transition have been observed using electronic pressure transducers in experiments with 500-kg and 200-t air-burst chemical charges. Dewey and van Netten (1998) also detected the pressure rise for plane shocks reflection from a cylindrical surface with a large radius of curvature, using very small pressure transducers, and showed that the pressure signature was similar to that predicted using numerical simulation. Height-of-burst curves derived using the *AirBlast* database are shown in Fig. 13.1.14.

It is therefore suggested that an increase of pressure does occur close to the region of transition for spherical shocks reflection from a rigid surface. The pressure increase appears to be localized and may only be significant for very large-scale explosions, or when the pressure detector is small and with a fast response time. The pressure increase may not have been detected on the large-scale nuclear tests because the height-of-burst isobars were drawn by interpolation between widely spaced pressure measurements. In the Reichenbach and Kuhl (1989, 1993) experiments, the pressure gauges may have been too large to detect the short duration pressure increase in the shock reflection produced by 0.5-g explosive charges.

ACKNOWLEDGMENTS

J. M. Dewey gratefully acknowledges the assistance of his colleagues D. J. McMillin, K. Jessee and A. A. van Netten in the preparation of this chapter on expanding spherical shock waves. The measured physical properties of blast waves presented in the chapter are derived from the *AirBlast* expert system. The numerical simulations were made using the AWAFF code. *AirBlast* and AWAFF are proprietary software of Dewey McMillin & Associates Ltd, of Victoria, BC, Canada.

REFERENCES

- Anisimov, S. I., Zel'dovich, Y. B., Inogamov, N. A. & Ivanov, M. F. 1983 The Taylor instability of contact boundary between expanding detonation products and a surrounding gas, *Shock Waves, Explosions and Detonations*, Ed. J. R. Bowen, N. Manson, A. K. Oppenheim and R.I. Soloukin, *Prog. Astro. Aero.*, 87, 218–227.
- Baker, W. E. (1983) *Explosions in air*, Wilfred Baker Engineering, San Antonio, TX.
- Baker, W. E., Cox, P. A., Westine, P. S., Kulesz, J. J. & Strehlow, R. A. (1983) *Explosive Hazards and Evaluation*, Elsevier, Amsterdam, Netherlands.
- Ben-Dor, G. (1991) *Shock Wave Reflection Phenomena*, Springer-Verlag, New York.
- Bethe, H. A. (1947) Blast Wave, 7(II) Los Alamos Sci. Lab. Tech. Series.
- Bethe, H.A. and von Neumann, J. (1958) Blast Wave: The Point Source Solution, Los Alamos Rept., LA-2000.
- Boyer, D. W. (1959) Spherical Explosions and Implosions, UTIA Rept. 58, Univ. Toronto Inst. Aero. Space Studies, Toronto, Ont. Canada.
- Boyer, D. W. (1960) An experimental study of the explosion generated by a pressurized sphere, *J. Fluid Mech.*, 9, 401–429.
- Boyer, D. W., Brode, H. L., Glass, I. I. & Hall, J. G. (1958) Blast from a Pressurized Sphere, UTIA Rept. 48, Univ. Toronto Inst. Aero. Space Studies Toronto, Ont. Canada.
- Bradley, J. N. (1962) *Shock Waves in Chemistry and Physics*, Methuen, London, England.
- Brode, H. L. (1955) Numerical solutions of spherical blast waves, *J. Appl. Phys.*, 26, 766–775.
- Brode, H. L. (1956) The Blast Wave in Air Resulting from a High Temperature, High Pressure Sphere of Air, Res. Memo. RM-1825-AEC, Rand Corp., Santa Monica, CA.
- Brode, H. L. (1957) A Calculation of the Blast Wave from a Spherical Charge of TNT, Res. Memo. RM-1965, Rand Corp., Santa Monica, CA.
- Brode, H.L. (1959) Blast Wave from a Spherical Charge, *Phys. Fluids*, 2, 217–229.
- Chorin, J. A., (1976) Random Choice Solution of Hyperbolic System, *J. Comp. Phys.*, 22, 517–533.
- Cranz, C. (1926) *Lehrbuch der Ballistik*, Springer-Verlag, Berlin.
- Crepeau, J. (1998), SHAMRC, *Second-order Hydrodynamic Automatic Mesh Refinement Code, 2: User's Manual*, Appl. Res. Ass., Inc., Albuquerque, NM.
- Dewey, J.M. (1964) The air velocity in blast waves from TNT explosions, *Proc. Roy. Soc. Lond., A*, 279, 366–385.
- Dewey, J.M. (1971) The properties of a blast wave obtained from an analysis of the particle trajectories, *Proc. Roy. Soc. Lond., A*, 324, 275–299.
- Dewey, J. M. (1997a) Shock waves from explosions, Chapter 16 in *High Speed Photography and Photonics*, Ed. S.F. Ray, Vol. 16, pp. 245–253, Focal Press, Oxford.
- Dewey, J. M. (1997b) Explosive flows: Shock tubes and blast waves, Chapter 29 in *Handbook of Flow Visualization*, 2nd ed., Ed. W-J. Yang, Hemisphere, New York.
- Dewey, J. M., and Anson, W. A. (1963) A blast wave density gauge using beta-radiation, *J. Sci. Instr.*, 40, 568–572.
- Dewey, J. M., and McMillin, D. J. (1981) An analysis of the particle trajectories in spherical blast waves reflected from real and ideal surfaces, *Can. J. Phys.*, 59(10), 1380–1390.
- Dewey, J. M., and McMillin, D. J. (1987) Numerical reconstruction of the flow field in experimentally observed Mach stem blast waves. *Proc. 10th Intl. Symp. Military Appl. Blast Simulation (MABS10)*, Ernst Mach Inst., Freiburg, Germany, 1, 287–299.
- Dewey, J. M., and McMillin, D. J. (1989) A computer system for presenting the physical properties of blast waves, *Proc. 11th Int. Symp. Mil. Appl. Blast Simulation (MABS11)*, Defense Nuclear Agency, Washington, D.C. 554–561.

- Dewey, J. M., and McMillin, D. J. (1990) Analysis of the results from high-speed photography of flow tracers in blast waves. *Proc. Intl. Cong. High-Speed Photo. & Photonics*, Ed. B. Garfield and J. Rendell, Soc. Photo-Optical Instr. Eng., SPIE 1358, 1, 246–253.
- Dewey, J. M., and van Netten, A. A. (1998) Do height-of-burst curves really have knees?, *Proc. 13th Int. Mach Reflection Symp., Ben Gurion Univ. Negev, Beer Sheva, Israel*, 2, 30.
- Dewey, J. M., McMillin, D. J., and Classen, D. F. (1977) Photogrammetry of spherical shocks reflected from real and ideal surfaces, *J. Fluid Mech.*, 81, 701–717.
- Dewey, J. M., McMillin, D. J., van Netten, A. A., Ethridge, N. H., Keefer, J. H., and Needham, C. E. (1995) A study of the boundary layer in a large scale blast wave over a natural surface, *Proc. 14th Int. Symp. Military Aspects Blast and Shock (MABS14)*, Defense Nuclear Agency, Washington, D.C., 1, 1–28.
- Etheridge, N. H., and Flory, R. A. (1993) Use of cube displacements as a measure of air blast, *Proc. 13th Int. Symp. Military Applications of Blast Simulation*, Roy. Inst. Eng. (Klvl), The Hague, Netherlands, 1, 57–78.
- Fairlie, G.E. (1998) The numerical simulation of high explosives using AUTODYN-2D & 3D, *Proc. Expo. '98*, Inst. Explosive Engineers.
- Friedlander, F. G. (1946) The diffraction of sound pulses, *Proc. Roy. Soc. Lond.*, 186, 322–367.
- Gaydon, A. G., and Hurlle, I. R. (1963) *The Shock Tube in High Temperature Chemical Physics*, Chapman & Hall.
- Glasstone, S., and Dolan, P. J. (1977) *The Effects of Nuclear Weapons*, U.S. Atomic Energy Comm., USA.
- Glimm, J. (1965) Solution in the large for nonlinear hyperbolic systems of equations, *Comm. Pure Appl. Math.*, 18, 697–715.
- Goodman, H. J. (1960) Compiled Free-Air Blast Data on Bare Spherical Pentolite, Aberdeen Proving Ground, U.S., BRL Rep. 1092.
- Gudonov, S. K. (1959) A finite difference method for the computation of discontinuous solutions of the equations of fluid dynamics, *Mat. Sbornik.*, 47, 357–393.
- Gudonov, S. K. (1976) *Numerical Solution of Multidimensional Problems in Gas Dynamics*, NAUKA, Moscow (in Russian).
- Heilig, W. H. (1969) Defraction of a shock wave by a cylinder, *Phys. Fluids, Suppl. I*, 12, 154–157.
- Heilig, W. H. (1977) A result concerning the transition from regular to Mach reflection of strong shock waves, in *Shock Tube and Shock Wave Research*, Ed. Ahlborn, B., Hertzberg, A., and Russell, D., Univ. Washington, Seattle.
- Heilig, W. A., and van Netten, A. A. (1991) A code based study of the pseudo-steady shock reflection process, *Shock Waves, Proc. 18th Int. Symp. Shock Waves*, Vol. 1, pp. 213–218, Springer-Verlag.
- Hikida, S., Bell, R. L., and Needham, C. E. (1988) The SHARC Codes: Documentation and Sample Problems, 1: Inviscid Fluid Dynamics, S-CUBED Tech. Rept. SSS-R-89-9878, Maxwell Indust., Albuquerque, NM.
- Hopkinson, B. (1915) British Ordnance Board Minutes, 13565.
- Jiang, Z., Takayama, K., Moosad, K. P. B., Onodera, O., and Sun, M. (1998) Numerical and experimental study of a micro-blast wave generated by pulsed-laser beam focusing, *Shock Waves*, 8, 6, 337–349.
- Kinney, G. F., and Graham, K. J. (1985) *Explosive Shocks in Air*, Springer-Verlag, New York.
- Kuhl, A. L., Bell, J. B., Ferguson, R. E., Chien, K.-Y., and Collins, J. P. (1995) Turbulent boundary layers in airblast precursors, *Proc. 14th Int. Symp. Military Aspects Blast Shock (MABS14)*, Defense Nuclear Agency, Alexandria, VA, pp. 535–564.
- Lau, S. C. M., and Gottlieb, J. J. (1984) Numerical Reconstruction of Part of an Actual Blast-Wave Flow Field to Agree with Available Experimental Data, UTIAS Tech. Note 251, Univ. Toronto Inst. Aerospace Studies, Toronto, Ont., Canada.

- Manweiler, R. W. (1973) Measurement of shock overpressure in air by a yielding foil membrane blast gage, Oak Ridge National Lab., ORNL-4868.
- McMillin, D. J., and Dewey, J. M. (1995) The characterization of a new explosive using smoke-trail photo-diagnostics, *Proc. 14th Intl. Symp. Military Aspects Blast and Shock*, (MABS14), Defense Nuclear Agency, Washington, D.C., 345–369.
- Muller, P. C., Schraml, S. J., and Mihalcin, A.F. (1995) Development of a transducer for the measurement of temperature of airblast flow fields, *Proc. 14th Int. Symp. Military Appl. Blast Simulation* (MABS14), Defense Nuclear Agency, Washington, D.C., 305–314.
- Oppenheim, A. K., Kuhl, A. L., Lundstrom, E. A., and Kamel, M. M. (1972) A parametric study of self-similar blast waves, *J. Fluid Mech.*, **55**, 257–270.
- Oshima, K. (1960) Blast waves produced by exploding wire, Aero. Res. Inst., Univ. Tokyo, Japan, Rept. 358.
- Penney, Lord; Samuels, D. E. J., and Scorgie, G. C. (1970) The nuclear explosive yields at Hiroshima and Nagasaki, *Roy. Soc. Phil. Trans.*, **266**, A, 357–424.
- Reichenbach, H., and Kuhl, A. (1989) HOB experiments with 0.5-g charges, *Proc. 11th Int. Symp. Military Appl. Blast Simulation* (MABS11), 597–611.
- Reichenbach, H., and Kuhl, A. L. (1993) Weak-shock reflection factors, *Proc. 13th Int. Symp. Military Aspects Blast & Shock* (MABS13), *Roy. Inst. Eng. Netherlands* (Klvi), *The Hague, Netherlands*, **1**, 117–127.
- Reisler, R. E., Keefer, J. H., and Ethridge, N. H. (1995) *Air Blast Instrumentation*, Vol. 1, *The Nuclear Era, 1945–1963*; Vol. 2, *The High Explosive Era, 1959–1993*; and Vol. 3, *Air Blast Structural Target and Gage Calibration*, MABS Monograph, Defense Nuclear Agency, Alexandria, VA.
- Ritzel, D.V. (1985) The DRES blast-gauge station, *Proc. Military Appl. Blast Simulation* (MABS9), *AWRE, Foulness, U.K.*, **1**(2), 1–13.
- Robertson, N. J., Hayhurst, C. J., and Fairlie, G. E. (1994) Numerical simulation of explosion phenomena, *Int. J. Comp. Appl. Tech., Nucl. Eng. Design*, **150**, 235–241.
- Sachs, R. G. (1944) The Dependence of Blast on Ambient Pressure and Temperature, BRL Rept., Aberdeen Proving Ground, MA.
- Sadek, H. S. and Gottlieb, J. J., (1983) Initial decay of flow properties of planar cylindrical and spherical blast waves, UTIAS Tech. Note No. 244, Univ. Toronto Inst. Aerospace Studies, Toronto.
- Saito, T., and Glass, I. I. (1979) Applications of Random-Choice Method to Problems in Shock and Detonation-Wave Dynamics, UTIAS Rept. 240, Univ. Toronto, Inst. Aerospace Studies, Toronto.
- Sakurai, A. (1953) On the propagation and structure of the blast wave, I, *J. Phys. Soc. Japan*, **8**, 662–669.
- Sakurai, A. (1954) On the propagation and structure of a blast wave, II, *J. Phys. Soc. Japan*, **9**, 256–266.
- Sod, G. A. (1977) A numerical study of converging cylindrical shock, *J. Fluid Mech.*, **83**, 785–794.
- Stanyukovich, K. P. (1960) *Unsteady Motion of Continuous Media*, Pergamon, New York.
- Steiner, H., Gretler, W., and Hirsdlher, T. (1998) Numerical solution for spherical laser-driven shock waves, *Shock Waves*, **8**, 139–147.
- Taylor, Sir G. (1946) The air wave surrounding an expanding sphere, *Proc. Roy. Soc. Lond.*, **186**, 273–292.
- Taylor, Sir Geoffrey (1950a) Formation of a blast wave by a very intense explosion, I. Theoretical discussion, *Proc. Roy. Soc. Lond.*, **A**, **201**, 159–174.
- Taylor, Sir Geoffrey (1950b), Formation of a blast wave by a very intense explosion, II. The atomic explosion of 1945, *Proc. Roy. Soc. Lond.*, **A**, **201**, 175–186.
- Thornhill, C. K. (1957a) The ultimate distribution of energy in a spherical explosion, ARDE Rep. (B) 27/57, HMSO, London, England.

- Thornhill, C. K., (1957b) A Unified Theory Of Damage From Minor External Blast, Armament Research and Development Establishment, A.R.D.E. Rep. (B) 24/57.
- Thornhill, C. K. (1959) The shape of a spherical blast wave, ARDE Memo. (B) 41/59, HMSO, London.
- Thornhill, C. K. (1960) Explosions in Air, Armament Research and Development Establishment, U.K., A.R.D.E. Memo (B) 57–60.
- van Netten, A. A., and Dewey, J. M. (1997) A study of blast wave loading on cantilevers, *Shock Waves*, 7, 175–190.
- Whitham, G. B. (1957) A new approach to problems of shock dynamics, Part 1—Two dimensional problems, *J. Fluid Mech.*, 2, 145–171.
- Whitham, G. B. (1959) A new approach to problems of shock dynamics, Part 2—Three-dimensional problems, *J. Fluid Mech.*, 5, 369–386.
- von Neumann, J. (1943) Oblique Reflection of Shocks, Explo. Res. Rep. 12, Navy Dept., Bureau of Ordnance, Washington, D.C.
- Zel'dovich, Ya. B., and Raizer, Yu. P. (1966) *Physics of Shock Waves and High-Temperature Hydrodynamic Phenomena*, Vol. 1, Academic Press, New York.
- Zhang, Q., and Sohn, S. I. (1999) Quantitative theory of Richtmyer–Meshkov instability in three dimensions, *Zeit. Angewandte Math. Phys.*, 50, 1–46

This Page Intentionally Left Blank

Spherical Shock Waves

13.2 General Attenuation Law for Spherical Shock Wave Propagating in Pure Gases

FELIX AIZIK, GOBI BEN-DOR, TOV ELPERIN, and OZER IGRA

Pearlstone Center for Aeronautical Engineering Studies, Department of Mechanical Engineering, Ben-Gurion University of the Negev, Beer Sheva, Israel, 84105

13.2.1	Introduction
13.2.2	Background
13.2.2.1	The Assumptions
13.2.3	General Attenuation Law
	References

13.2.1 INTRODUCTION

The most common shock wave in nature is a spherical one. Every shock wave, which is generated by a sudden release of a large amount of energy, even if its initial shape is not spherical, will turn into a spherical shock wave as it propagates into the surrounding atmosphere. This fact is the reason for the importance of knowing the flow field that is developed behind a spherical shock wave.

The governing equations of the flow field that is developed behind a spherical shock wave consist of partial differential and nonlinear equations. Since they must be solved simultaneously, they can be solved only numerically. Such solutions require significant resources (time, computers, etc.). The complexity of solving these equations on one hand and the importance, in many applications, of knowing the flow field properties in real time on the other hand is a motivation to develop an alternative way of obtaining the flow field properties immediately behind the shock wave front.

Such a way has been presented by Aizik *et al.* (2000), who developed a general attenuation law of spherical shock wave propagating in a pure gas. Their study is summarized in the following.

13.2.2 BACKGROUND

The spherical shock wave was generated by rupturing a spherical diaphragm (see Fig. 13.2.1) inside which the pressure was higher than the ambient pressure and the temperature was higher than or equal to the ambient temperature.

The governing equations describing the propagation of a spherical shock wave through a pure gas were formulated and solved numerically using the random choice method (RCM) with operator splitting technique.

The computer code was validated by comparing its predictions to all the experimental results of Boyer (1959, 1960). Very good agreement was evident. Full details of the comparison can be found in Aizik (1999), where a detailed derivation of the governing equations and their final form are also given. In the following only the assumptions upon which the governing equations were based are presented.

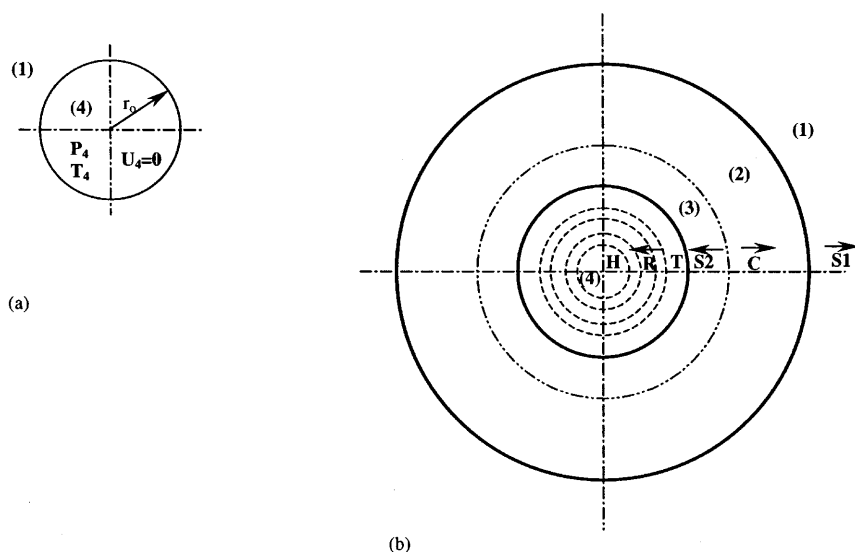


FIGURE 13.2.1 Schematic description of the considered flow field. (a) Before the diaphragm rupture, $t = 0$. (b) After the diaphragm rupture, $t > 0$. (R, rarefaction wave; H, head of the rarefaction wave; T, tail of the rarefaction wave; S_2 , secondary shock wave; C, contact surface; S_1 , primary shock wave.)

13.2.2.1 THE ASSUMPTIONS

1. The flow field is one-dimensional (radial) and unsteady.
2. The gaseous phase behaves as a perfect gas.
3. The dynamic viscosity, the thermal conductivity, and the specific heat capacity at constant pressure of the gaseous phase depend solely on its temperature.

13.2.3 GENERAL ATTENUATION LAW

In order to identify the parameters affecting the attenuation of a spherical shock wave and developing the expression to describe it, the governing equations were solved numerically for a variety of initial conditions. As expected, the results revealed that the most dominant parameter affecting the shock wave attenuation, in the case of a pure gas, is its initial strength, which can be derived from the energy confined in the spherical diaphragm prior to its rupture.

The initial strength of the shock wave can be calculated from the shock tube equation (see e.g., Glass and Sislian, 1994):

$$P_{41} = \frac{1}{\alpha_1} \left(\frac{M_{S,0}^2}{\beta_1} - 1 \right) \left[1 - \frac{1}{\alpha_1} \left(\frac{\beta_1}{\beta_1} E_{14} \right)^{1/2} \left(M_{S,0} - \frac{1}{M_{S,0}} \right) \right]^{-1/\beta_4}, \quad (13.2.1)$$

where

$$\alpha = \frac{\gamma + 1}{\gamma - 1}; \quad \beta = \frac{\gamma - 1}{2\gamma}; \quad E_{14} = \frac{(C_v T)_1}{(C_v T)_4}. \quad (13.2.2)$$

It can be seen that the initial Mach number of the shock wave depends on the pressure and the temperature ratios, P_{41} and T_{41} , respectively, across the diaphragm.

Not surprisingly, the numerical results indicated that the primary spherical shock wave attenuated exponentially. In addition, it is well known that spherical shock waves degenerate to sound waves far away from their origin. Under the preceding constraints it was decided to describe the attenuation of a spherical shock wave by the expression

$$M_S = (M_{S,0} - 1) \exp\left(-\frac{r - r_0}{R}\right) + 1, \quad (13.2.3)$$

where M_S is the instantaneous shock wave Mach number at the radius r , $M_{S,0}$ is the initial shock wave Mach number, R is the decay coefficient, and r_0 is the radius of the diaphragm. Correlation (13.2.3) describes appropriately the

exponential nature of the shock wave attenuation, and it fulfills the following boundary conditions:

$$M_S = \begin{cases} M_{S,0} & \text{for } r = r_0 \\ 1 & \text{for } r = \infty \end{cases}. \quad (13.2.4)$$

The rate with which the shock wave attenuates, that is, the decay coefficient R , depends on the initial strength of the shock wave $M_{S,0}$ and the temperature of the confined gas inside the diaphragm T_4 , prior to its rupture.

The governing equations were solved for the following range of parameters: $1.1 < M_{S,0} < 5$ and $1 < T_{41} < 6$. The upper value of the initial shock wave Mach number was limited by assumption 2, namely, that the gas behaved as a perfect gas. The decay coefficient R was obtained by a curve fitting analysis of the numerical results to Eq. (13.2.3), for 90 combinations of initial conditions, in the following form:

$$R(M_{S,0}, T_{41}) = (C_1 + C_2 \cdot T_{41}) \cdot M_{S,0}. \quad (13.2.5)$$

Substituting Eq. (13.2.5) into Eq. (13.2.3) results in the following expression, which describe the attenuation of spherical shock waves, generated from finite sources, in a pure gas:

$$M_S = (M_{S,0} - 1) \exp \left[- \frac{r - r_0}{(C_1 + C_2 T_{41}) M_{S,0}} \right] + 1. \quad (13.2.6)$$

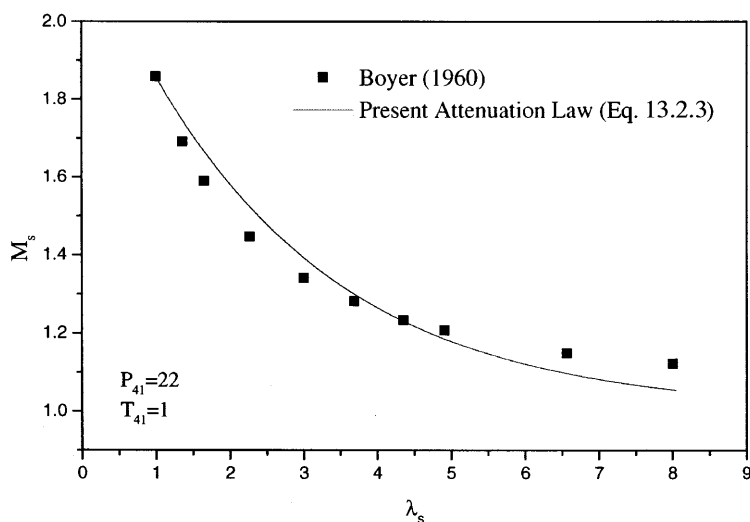


FIGURE 13.2.2 Comparison between the attenuation of the primary spherical shock wave as predicted by the Aizik *et al.*'s (2000) general attenuation law (solid line) and the experimental results of Boyer (1960) for an explosion of a 2-inch diameter sphere of pressurized air initially at 22 atm and room temperature.

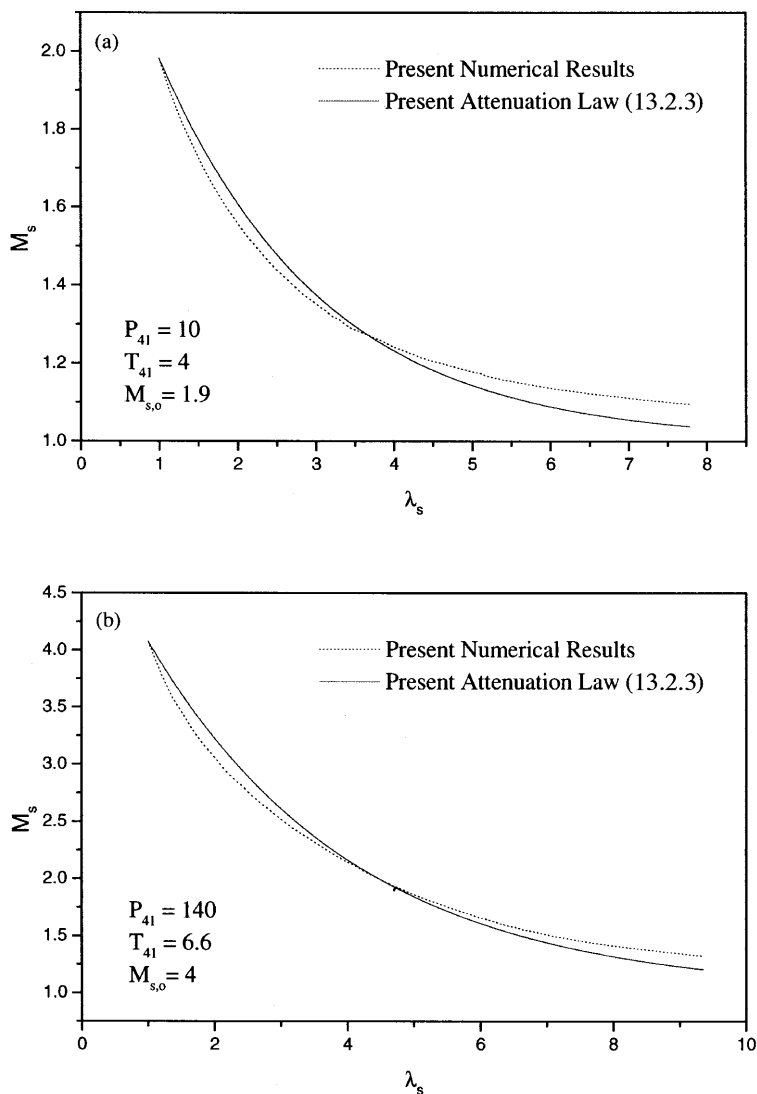


FIGURE 13.2.3 Comparisons between the attenuation of the primary spherical shock wave as predicted by Aizik *et al.*'s (2000) general attenuation law (solid lines) and the results obtained by full numerical solutions of the governing equations (dashed lines), for two cases: (a) a moderate initial shock wave, (b) a relatively strong initial shock wave.

The values of C_1 as obtained in the course of Aizik *et al.*'s (2000) study were $C_1 = 1.48044$ and $C_2 = -0.10839$.

The general attenuation law (13.2.6) enables one to calculate the instantaneous spherical shock wave Mach number, as it propagate in a pure gas, within 97% accuracy, without the need to conduct any complicated numerical calculations.

The just-proposed general attenuation law (13.2.6) was validated by comparing its predictions to the experimental results of Boyer (1960). A typical comparison is shown in Fig. 13.2.2. As can be seen, the agreement between the attenuation that is predicted by the general attenuation law (13.2.6) and the actual (experimental) attenuation is very good.

Additional comparisons were made between the attenuation predicted by the general attenuation law (13.2.6) and the results obtained by full numerical solutions of the governing equations for the same initial conditions. Two typical comparisons are shown in Figs. 13.2.3a and 13.2.3b. As can be seen, here too, the agreement is very good. It should be noted that the agreement is better for stronger initial shock waves.

REFERENCES

- Aizik, F. (1999) "Investigation of Spherical Shock Waves Propagation in Inert and Reactive Gas-Particle Suspensions," Ph.D. Thesis, Dept. Mech. Eng., Ben-Gurion Univ. Negev, Beer Sheva, Israel (in Hebrew).
- Aizik, F., Ben-Dor, G., Elperin, T., and Igra, O. (2000) "Universal Attenuation Laws for Spherical Shock Waves Propagating in Pure Gases and in Gas-Particle Suspensions," *AIAA J.*, to be published.
- Boyer, D. W. (1959) "Spherical Explosions and Implosions," UTIA Rep. 58.
- Boyer, D. W. (1960) "An Experimental Study of the Explosion Generated by a Pressurized Sphere," *Journal of Fluid Mechanics*, 9(3), 401-429.
- Glass, I. I., and Sislian, J. P. (1994) *Nonstationary Flows and Shock Waves*, Oxford Sci. Publ., Oxford.

Shock-Induced Instability of Interfaces

DOV SHVARTS^{*,†,**}, OREN SADOT^{*,†}, DAN ORON^{*,**},
 AVI RIKANATI^{*,**}, AND URI ALON^{††}

^{*} *Dept. of Physics, Nuclear Research Center Negev 84190, Israel*

[†] *Dept. of Mechanical Engineering, Ben Gurion University, Beer-Sheva 84015, Israel*

^{**} *Dept. of Physics, Ben Gurion University, Beer-Sheva 84015, Israel*

^{††} *Faculty of Physics, The Weizmann Institute of Science, Rehovot 76100, Israel*

14.1 Introduction: Hydrodynamic Instability

14.2 The Rayleigh–Taylor Instability

14.2.1 Linear Analysis

14.2.2 Analysis of the Early Nonlinear Stages

14.2.3 The Late Nonlinear Stage (Layzer Model for $A = 1$)

14.2.4 Density Ratio Dependence

14.2.5 Spike Behavior

14.2.6 Dimensionality Dependence

14.3 The Richtmyer–Meshkov Instability

14.4 Experimental Studies

14.4.1 Experimental Studies of the Single-Mode Rayleigh–Taylor Instability

14.4.2 Experimental Studies of the Richtmyer–Meshkov Instability

14.5 Random Initial Conditions

14.5.1 Two-Dimensional Statistical Mechanics Model and Late Time Scaling Laws

14.5.2 Three-Dimensional Effects on the Late Time Scaling Laws

14.5.3 Shock Wave Experiments of the Bubble Competition Process

14.5.4 Re-Shock Experiments

14.6 Summary

References

14.1 INTRODUCTION: HYDRODYNAMIC INSTABILITY

This chapter includes a comprehensive description of shock wave–induced hydrodynamic instability. This hydrodynamic instability called the Richtmyer–Meshkov (RM) instability (Richtmyer 1960; Meshkov 1969), is closely related to the well-known Rayleigh–Taylor (RT) (Rayleigh 1900; Taylor 1950) instability. We shall therefore begin by describing the more general instability, the Rayleigh–Taylor instability, and only then derive the details of the Richtmyer–Meshkov case.

When two fluids of different densities are subjected to an accelerating field, under certain circumstances an instability is created at the contact surface between them. If the acceleration is slowly varied and directed from the heavy fluid to the light one, the Rayleigh–Taylor instability occurs. In general unstable condition appear when the pressure gradient is in the opposite direction to the density gradient ($\nabla p \cdot \nabla \rho < 0$). The related Richtmyer–Meshkov instability occurs when a shock wave (impulsive acceleration) passes a perturbed interface between two fluids. The perturbation along the contact surface curves the shock wave, creating pressure fluctuations on both sides of the contact surfaces, increasing the initial perturbations.

It has been shown (Alon *et al.* 1995a) that the late time asymptotic evolution of a perturbation can be related to either the RT or to the RM case, depending on the acceleration field to which the interface is introduced. Assuming that the acceleration is a power law in time, $g(t) \sim t^\beta$, then when $\beta < -2$ the “RM-like” behavior is obtained, and when $\beta > -2$ the “RT-like” behavior is obtained.

An unstable mixing layer between two fluids can also occur when there is a tangential velocity different between the two fluids, leading to the creation of vortices along the interface and eventually to the formation of a mixing layer between the fluids. This instability is called the Kelvin–Helmholtz (KH) instability.

The RM, RT, and KH instabilities play a major role in Inertial Confinement Fusion (ICF), in astrophysics, and in engineering applications (see Lindl, 1998). For example, in the attempt to ignite fusion fuel in ICF, hydrodynamic instabilities such as RT and RM may break up the imploding shell and prevent the formation of a hot spot. Large deformation of the inner gas bubble due to instability growth may also inhibit ignition because of increased energy losses through thermal conduction. Stabilizing effects due to the ablative flow, which reduce the instability growth rate as compared with “classical” instability growth, may enable the design of fusion pellets with higher aspect ratio, requiring less driver energy to achieve energy gain. Convergence effects can also be of great importance in the final stages of the implosion.

Supernovae represent one of nature's most dramatic and spectacular exhibitions, with peak luminosities exceeding those of entire galaxies. Supernovae occur when the core of a star ignites and explodes due to gravitational pressure from the star's outer surface. A shock wave is created and expands from the center of the star toward outer space. When the shock passes between different layers in the star structure, hydrodynamic instabilities occur and initiate mixing processes. Until recently, most efforts have been focused on one-dimensional stellar evolution models. This changed with supernova SN1987 (Remington *et al.* 1997) when new observations were made, some of which can only be explained by two-dimensional hydrodynamic models.

In this chapter the evolution of the RT and RM instabilities in the linear and nonlinear stages is presented. We describe theoretical and experimental studies performed over the past 30 years in this area, concentrating mainly on work done in our group in the past 15 years regarding the late nonlinear stages of the instability evolution. Most of the chapter is devoted to single-mode evolution, but to complete the whole picture, a generalization of the single mode to the multimode case is presented.

In Section 14.2 the linear, nonlinear, and late time evolution of the Rayleigh–Taylor instability is derived; in Section 14.3 the derivation of the Rayleigh–Taylor is used to derive the Richtmeyer–Meshkov instability evolution. Some main experimental results of the Rayleigh–Taylor and Richtmeyer–Meshkov instabilities are presented in Section 14.4 to support those theories. Finally, a theoretical description of the evolution of a multimode RT and RM instability is presented and supported by shock tube experiments.

14.2 THE RAYLEIGH–TAYLOR INSTABILITY

14.2.1 LINEAR ANALYSIS

Consider the case of two fluids with different densities in a uniform acceleration field directed in the z direction, assuming that the fluids are in contact at a surface perpendicular to the z axis. If the heavy fluid (ρ_H) is on top of the light one (ρ_L), the surface is unstable and small perturbations on it grow (Fig. 14.1).

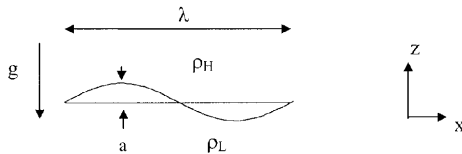


FIGURE 14.1 Initial conditions of the perturbed interface $z(x) = a \cdot \cos(kx)$ between two fluids in an acceleration field g . λ , wavelength; a , amplitude.

Let us first consider the simpler two-dimensional case (Rayleigh–Taylor instability in planar geometry). The effects of dimensionality on the instability evolution are discussed in Section 14.2.6.

In this section we derive the growth rate of those instabilities for the case of small amplitudes ($a \ll \lambda$) where linear analysis is valid. The complete solution to the first order is presented next, and highlights of higher-order solutions are presented in the next section.

In the limit of incompressible and irrotational flow, the velocity can be derived from a potential ϕ ; $\vec{U} = \vec{\nabla}\phi$. The flow dynamics of the two fluids is governed by the Laplace and Bernoulli equations for each fluid:

$$\begin{aligned}\nabla^2\phi &= 0 \\ \frac{\partial\phi}{\partial t} + \frac{1}{2}U^2 + gz + \frac{p}{\rho} &= \text{const.}\end{aligned}\tag{14.1}$$

The requirement that the interface move with the fluid,

$$\frac{\partial\phi}{\partial z} - \frac{\partial\phi}{\partial x} \frac{\partial Z(x, t)}{\partial x} = \frac{\partial Z(x, t)}{\partial t},\tag{14.2}$$

must be maintained on the contact surface. The first-order solution to Eq. (14.1) can be found by neglecting the U^2 term. This assumption is valid when $a \ll \lambda$. The eigenfunctions of Eq. (14.1) (excluding the U^2 term) are sine and cosine. So the potentials that satisfy Eq. (14.1) for the two fluids are

$$\begin{aligned}\phi_H(x, z, t) &= B_H(t) \exp(-kz) \cdot \cos(kx), & z > 0 \\ \phi_L(x, z, t) &= B_L(t) \exp(kz) \cdot \cos(kx), & z < 0 \\ Z(x, t) &= a(t) \cdot \cos(kx),\end{aligned}\tag{14.3}$$

where z and x are the vertical and horizontal coordinates, respectively. $B_H(t)$, $B_L(t)$, $a(t)$ are time-dependent parameters that will be determined later.

An analytical solution to (14.1) with (14.3) can be found using perturbation theory in the case of $a \ll \lambda$. The vertical velocity of the contact surface is equal to the flow velocity:

$$\begin{aligned}U_z &= \frac{\partial\phi}{\partial z} = \frac{\partial Z}{\partial t} \\ kB(t) \cdot \cos(kx) &= \frac{\partial a(t)}{\partial t} \cdot \cos(kx).\end{aligned}\tag{14.4}$$

Hence,

$$\frac{\partial a}{\partial t} = kB(t).\tag{14.5}$$

Equating the z component of the velocity from both sides of the contact surface (at $z = 0$), we write

$$U_{zH} = \frac{\partial \phi_H}{\partial z} = U_{zL} = \frac{\partial \phi_L}{\partial z} = k B_H \cdot \cos(kx) = k B_L \cdot \cos(kx). \quad (14.6)$$

After neglecting the U^2 term, the Bernoulli equation for both fluids has the form

$$\begin{aligned} \frac{\partial \phi_H}{\partial t} + gz + \frac{p_H}{\rho_H} &= \text{const}_H \\ \frac{\partial \phi_L}{\partial t} + gz + \frac{p_L}{\rho_L} &= \text{const}_L. \end{aligned} \quad (14.7)$$

Multiplying these equations by ρ_H and ρ_L , respectively, and selecting the constants so that: $\rho_H \text{const}_H = \rho_L \text{const}_L$, we get

$$\rho_H \left(\frac{\partial \phi_H}{\partial t} + zg \right) = \rho_L \left(\frac{\partial \phi_L}{\partial t} + zg \right). \quad (14.8)$$

By inserting the potential into Eq. (14.8) and taking the time derivative, we write

$$\begin{aligned} \rho_H \left(\frac{\partial B_H}{\partial t} \cdot \exp(-kz) \cdot \cos(kx) + g \cdot a \cdot \cos(kx) \right) \\ = \rho_L \left(\frac{\partial B_L}{\partial t} \cdot \exp(+kz) \cdot \cos(kx) + g \cdot a \cdot \cos(kx) \right). \end{aligned} \quad (14.9)$$

Using Eq. (14.4), a first-order differential equation for B is derived:

$$\frac{\partial B}{\partial t} = \frac{\rho_H - \rho_L}{\rho_H + \rho_L} \cdot g \cdot a(t). \quad (14.10)$$

We define the constant

$$A \equiv \frac{\rho_H - \rho_L}{\rho_H + \rho_L},$$

later to be referred to as the Atwood number.

From Eqs. (14.10) and (14.4) a second-order differential equation for $a(t)$ can be derived:

$$\frac{\partial^2 a(t)}{\partial t^2} = k \cdot A \cdot g \cdot a(t) = \gamma^2 \cdot z z a(t). \quad (14.11)$$

The solution of this equation when g is constant is

$$a(t) = a_0 \exp(\gamma t) \quad \text{where } \gamma = \sqrt{A \cdot g \cdot k}. \quad (14.12)$$

a_0 is the initial perturbation, k is the wave number, g is the constant acceleration, and A is the Atwood number. This solution diverges with time when A is positive (heavy fluid on top of a light one) and oscillates with time when A is negative ($-\gamma$ is a decaying solution to (14.11), which can be neglected with respect to the $+\gamma$ solution).

14.2.2 ANALYSIS OF THE EARLY NONLINEAR STAGES

The early nonlinear evolution can be derived by taking the second-order perturbation expansion presented in the previous section. The Bernoulli equation remains the same, and another term must be added to the kinematic condition:

$$\frac{\partial \phi}{\partial z} - \frac{\partial \phi}{\partial x} \frac{\partial Z(x, t)}{\partial x} = \frac{\partial Z(x, t)}{\partial t}. \quad (14.13)$$

Introducing the potential

$$\begin{aligned} \phi_H &= B_H^1(t) \cdot \exp(-kz) \cdot \cos(kx) + B_H^2(t) \cdot \exp(-2kz) \cdot \cos(2kx), & z > 0 \\ \phi_L &= B_L^1(t) \cdot \exp(kz) \cdot \cos(kx) + B_L^2(t) \cdot \exp(2kz) \cdot \cos(2kx), & z < 0 \end{aligned} \quad (14.14)$$

to the Bernoulli equation and repeating the same steps as in the previous section yields

$$\begin{aligned} Z(x) &= a_1 \cos(kx) & (1\text{st order}) \\ &- \left(\frac{1}{2} A k a_1\right) \cdot a_1 \cos(2kx), & (2\text{nd order}), \end{aligned} \quad (14.15)$$

where $a_1 = a_0 \exp(\gamma t)$. In second order a new mode (the second harmonic, $\cos(2kx)$) is generated while the amplitude of the principal mode is unaffected. The second harmonic introduces an asymmetry in the interface between the two fluid regions. The light fluid structures rising into the heavy fluid begin both to slow down and to broaden, because of the opposite phases of the two modes in that region. As a result of this behavior, these structures are known as *bubbles*. In contrast, for the structures of heavy fluid penetrating the light fluid, the two modes are in phase, resulting in an increased penetration velocity and a narrowing of the structure, known as a *spike*.

The derivation of third-order perturbation theory for the periodic case is

$$\begin{aligned}
 Z(x, t) &= a_1 \cos(kx) && (1\text{st order}) \\
 &- A \frac{k}{2} \cdot a_1^2 \cos(2kx) && (2\text{nd order}) \\
 &+ A^2 k^2 a_1^3 \left[\frac{1}{8} (4A^2 - 1) \cos(3kx) - \frac{1}{16} (1 + 3A^2) \cos(kx) \right] && (3\text{rd order}),
 \end{aligned} \tag{14.16}$$

where $a_1 = a_0 \exp(\gamma t)$. Notice that the third-order term contains a correction to the first-harmonic term, $\cos(kx)$.

Figure 14.2a shows the evolution of the unstable interface in units of ak at different times according to Eq. (14.16). At late time the tip of the bubble sharpens because of the third-order term. This effect is physically incorrect, and higher order terms must be introduced to compensate for it.

The tip of the bubble is at $kx = 0$. Inserting that into Eq. (14.16) yields the evolution of the bubble. The tip height is given by

$$Z(x, t) = a_1 - A \frac{k}{2} \cdot a_1^2 + A^2 k^2 a_1^3 \left[\frac{1}{8} (4A^2 - 1) - \frac{1}{16} (1 + 3A^2) \right]. \tag{14.17}$$

The temporal evolution of the bubble tip is shown in Fig. 14.2b as derived from the expansion to the first, second, and third orders. Notice the following:

1. The onset of nonlinearity can be defined as the amplitude at which nonlinearities begin to appreciably alter the primary mode amplitude (when the last term in Eq. (14.16) is, for example, 10% of the first term). This occurs when $a_1 \approx 0.1\lambda$ ($a_1 k \lesssim 1$).

2. Shortly after $Z > 0.1\lambda$, all orders become very similar in magnitude and more terms are needed to reasonably approximate the interface $Z(x)$. This limits the range of applicability of perturbation theory, and some kind of closure is needed. Kull (1986) conducted a detailed analysis of the generation of additional modes from an initial single-mode perturbation. His approach allows expansion of the flow potential in any number of harmonics and determines their amplitudes by minimizing the mean square error of the governing equations (Bernoulli's equation and a boundary equation stating that the interface moves with the fluid). It differs from perturbation theory in that it finds the overall optimal expansion of the solution with a given finite set of base functions. It was found that the number of necessary harmonics grows very quickly after the bubble amplitude reaches 0.1λ . Around 0.1λ , 3–4 harmonics give an accurate reconstruction of the fluid interface; at 0.2λ one needs more than 10 harmonics, and at 0.3λ the method completely breaks down. It therefore seems inappropriate to describe the evolution of the

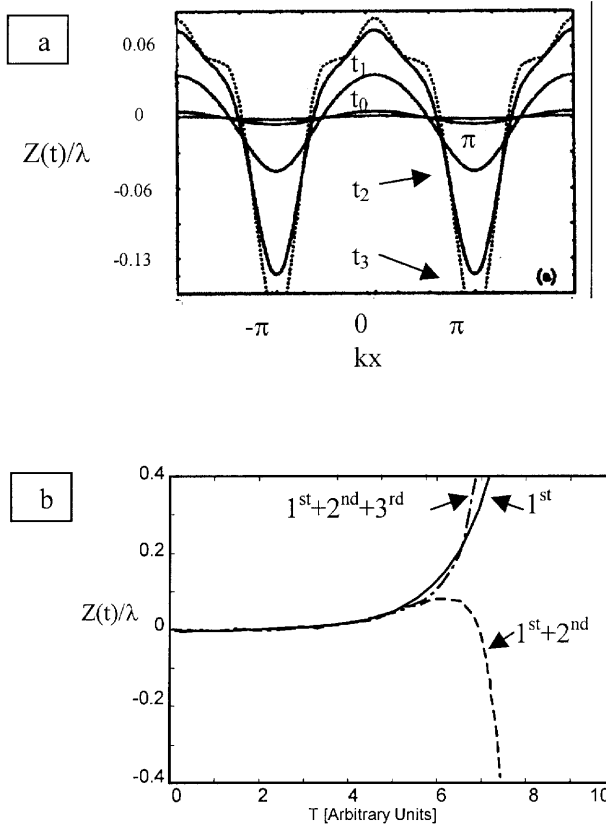


FIGURE 14.2 (a) Temporal evolution of a single mode perturbation ($A = 1$). The interface is plotted at different times. The nonlinearity increases and the difference between the bubble and spike becomes clearer. The interface is plotted at time steps [$t_1 = 2/\gamma$, $t_2 = 4/\gamma$, $t_3 = 4.9/\gamma$, dotted] (Bering and Rubenchik 1998). (b) Various approximations to the bubble height. Shown are the first, second, and third order solutions of the bubble height: first order (full line), second order (dashed line), and third order (dash-dot line).

instability this way. At late times, where $a/\lambda > 1$, the number of terms is enormous, so new techniques must be considered.

3. In the spike region all modes add up in phase to create a long thin spike, whereas in the bubble region the amplitude signs alternate to create a broad, slowly moving bubble, bringing about the bubble–spike asymmetry. These phase correlations are significant in attempting to construct a model that reasonably recreates the interface $Z(x)$ and not only the mode amplitudes.

14.2.3 THE LATE NONLINEAR STAGE (LAYZER MODEL FOR $A = 1$)

When the density ratio between the two fluids is very large ($A = 1$), the bubble form, at late times, columns of light fluid interleaved by falling spikes of heavy fluid. Eventually, in this case, the bubbles reach a constant velocity and the spikes fall with a constant acceleration. As shown, the perturbation expansion fails to describe the perturbation evolution for $a/\lambda > 0.1$. Layzer (1955) was the first to successfully describe the bubble evolution using a simple potential flow model. His model is based on an approximate description of the flow near the bubble tip and describes correctly both the linear growth and the asymptotic bubble velocity.

Following Layzer (1955) and Hecht *et al.* (1994) let us choose a flow potential $\phi(x, z, t)$ so that the fluid velocity is $\vec{v} = \vec{\nabla}\phi$. Assume that the flow is governed by the behavior in the vicinity of the bubble tips. Near the bubble tip (at $x = 0$) the interface is, to second order,

$$z(x, t) = z_0 + z_1 x^2. \quad (14.18)$$

The radius of curvature of the bubble is $R = -1/(2z_1)$. The interface moves with the fluid. This requirement is expressed by the kinematic equation

$$u_z - \frac{dz_0}{dt} - \frac{dz_1}{dt}(x)^2 - 2z_1(x)\left(v_x - \frac{dx}{dt}\right) = 0, \quad (14.19)$$

where the velocities are calculated at the interface using Eq. (14.2). The flow dynamics given by the Bernoulli equation for a constant supporting pressure:

$$\frac{\partial\phi}{\partial t} + \frac{1}{2}(v_x^2 + v_z^2) + gz = \text{const}. \quad (14.20)$$

The constant in this equation is the same for all bubbles on the same interface. For the periodic 2D RT case, assuming a container of width L , or equivalently a periodic array of wave length $\lambda = L$, the chosen potential that satisfies the Laplace equation is

$$\phi = a_p(t) \cos(kx) \exp(-kz), \quad (14.21)$$

where $k = 2\pi/\lambda$. Using this potential in Eqs. (14.1) and (14.2) yields

$$\begin{aligned} a_p k e^{-kz_0} + \frac{dz}{dt} &= 0 \\ a_p k^2 \left(z_1 + \frac{k}{2}\right) e^{-kz_0} - \frac{dz_1}{dt} + 2z_1 a_p k^2 e^{-kz_0} &= 0 \\ k e^{-kz_0} \left(z_1 + \frac{k}{2}\right) \frac{dp}{dt} + a_p^2 k^3 z_1 e^{-2kz_0} - g z_1 &= 0. \end{aligned} \quad (14.22)$$

These three equations correspond to the kinematic equation to order 0 and 2 and the second-order Bernoulli equation, respectively. Linearizing Eq. (14.14) for small perturbations leads to the correct linear growth rate (Eq. (14.11)) $\ddot{a} = \gamma^2 a$ with $\gamma = \sqrt{g \cdot k}$.

The resulting equation for the bubble velocity is

$$\begin{aligned} \frac{dU_B}{dt} &= \left(\frac{1-E}{2+E} \right) g - \left(\frac{6\pi}{2+E} \right) \frac{U_B^2}{\lambda} \\ E &= \exp\left(-6\pi \frac{a}{\lambda}\right). \end{aligned} \quad (14.23)$$

At late times a/λ increases so E approaches zero and Eq. (14.22) becomes

$$\frac{dU_B}{dt} = \left(\frac{1}{2} \right) g - \left(\frac{6\pi}{2} \right) \frac{U_B^2}{\lambda}. \quad (14.24)$$

Multiplying by 2ρ gives

$$\begin{array}{ccc} 2\rho \frac{dU_B}{dt} = & \rho g & -6\pi\rho \frac{U_B^2}{\lambda} \\ \downarrow & \downarrow & \downarrow \\ \text{(Added mass)} & \text{(Buoyancy)} & \text{(Drag)} \end{array} \quad (14.25a)$$

Each term in this equation has a physical meaning: The 2ρ factor on the left-hand side can be interpreted as the added mass, which is the mass of the heavy fluid that the bubble pushes against the acceleration field; the first term on the right is the buoyancy; and the last term is the drag, where the $1/\lambda$ factor comes from the surface-to-volume ratio of the bubble ($S/V \propto 1/\lambda$). Equation (14.24a) can be written as (Shvarts *et al.* 2000)

$$C_a \rho \frac{dU_B}{dt} = C_b \rho g - C_d \rho \frac{U_B^2}{\lambda}, \quad (14.25b)$$

with $C_a = 2$ (added mass coefficient), $C_b = 1$ (buoyancy coefficient,) and $C_d = 6\pi$ (drag coefficient). The Layzer model successfully predicts the evolution of the RT instability. It is accurate up to the third order and in the asymptotic stage. In Fig. 14.3 a comparison between the expansion to third order and the Layzer model is shown.

14.2.4 DENSITY RATIO DEPENDENCE

When $A < 1$, both the bubble and spike reach an asymptotic velocity at late time. Two forces govern the late nonlinear behavior of a single bubble or spike: the buoyancy, which forces the bubble up and the spike down, and the drag,

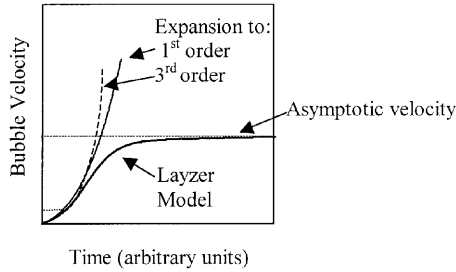


FIGURE 14.3 Comparison between the prediction of the bubble velocity from the Layzer Model and the expansion of the solution to the first and third orders.

which depresses the motion. Asymptotically the buoyancy and drag are balanced and constant velocity is achieved.

A vortex model (see Jacobs and Sheeley, 1996, and Rikanati *et al.*, 1998) shows explicitly the bubble and spike behavior at low A in the RM case. The model predicts the symmetry between the bubble and the spike and the values of the constants $C_a = 2$ and $C_d = 6\pi$ at $A = 0$ as in the $A = 1$ case.

When $A < 1$ additional terms, taking the density of the bubble into account, must be added to Eq. (14.25). These modifications are incorporated in the following equation, (Shvarts *et al.* 2000):

$$\begin{array}{ccccccc}
 (\rho_L + 2 \cdot \rho_H) \cdot \frac{dU}{dt} & = & (\rho_H - \rho_L) \cdot g & - & \frac{6\pi}{\lambda} \cdot \rho_H \cdot U^2 & & \\
 \downarrow & & \downarrow & & \downarrow & & \downarrow \\
 \text{Inertia} & & \text{Added mass} & & \text{Buoyancy} & & \text{Drag}
 \end{array} \quad (14.26)$$

The inertia of the bubble is taken into account along with the added mass term on the left-hand side of Eq. (14.26). On the right-hand side are the modified buoyancy term and the drag term.

In the asymptotic stage, the bubble reaches a constant velocity, $dU/dt = 0$, leading to

$$U = \sqrt{\left(\frac{2A}{1+A}\right) \cdot \frac{g \cdot \lambda}{6\pi}}. \quad (14.27)$$

This expression describes the asymptotic velocity of the bubble in the RT instability for any Atwood number. Equation (14.27) has been compared to

several experiments and numerical simulations and predicts correctly the late time evolution of the bubble (see Ofer *et al.* 1992).

14.2.5 SPIKE BEHAVIOR

The spike behavior can be derived from the perturbation expansion. In Section 14.2.2 the shape of the contact surface was derived to third order. By inserting $kx = \pi$ into Eq. (14.16), the function that describes the tip of the spike is obtained:

$$\begin{aligned}
 a_5(t) &= -a_1 & (1\text{st order}) \\
 -A \frac{k}{2} \cdot a_1^2 & & (2\text{nd order}) \\
 -A^2 k^2 a_1^3 \left[\frac{1}{8}(4A^2 - 1) - \frac{1}{16}(1 + 3A^2) \right] & & (3\text{rd order}).
 \end{aligned} \tag{14.28}$$

Since the first three orders are in phase for the spike, the nonlinear growth of the spike is higher than that of the bubble.

Simple kinematic considerations can be applied to obtain the late time spike evolution as well. Bubbles reach a constant velocity because of drag. Similarly, if $A < 1$, kinematic drag ultimately slows down the spike, and asymptotically the spike achieves a constant velocity. At that late stage, shear instability (the Kelvin–Helmholtz instability) on the side of the spikes creates mushroom-shaped tips (Figure 14.4), enabling the application of a similar buoyancy-drag equation for the spike. By replacing ρ_L by ρ_H and ρ_H by ρ_L in Eq. (14.26), the asymptotic velocity of the spike is derived.

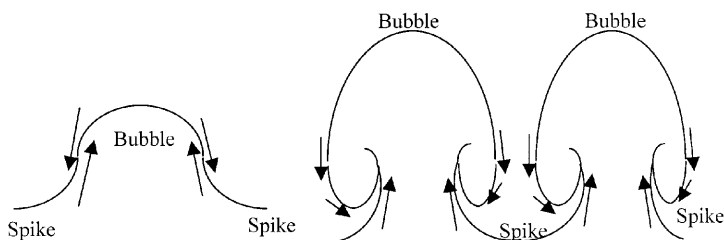


FIGURE 14.4 Schematic description of the creation of mushroom shapes due to the Kelvin–Helmholtz instability.

The equation of motion for the spike is:

$$(\rho_H + 2 \cdot \rho_L) \cdot \frac{dU_S}{dt} = (\rho_L - \rho_H) \cdot g - \frac{6\pi}{\lambda} \cdot \rho_L \cdot U_S^2 \quad (14.29)$$

and asymptotically:

$$U = \sqrt{\left(\frac{2A}{1-A}\right) \cdot \frac{g \cdot \lambda}{6\pi}} \quad (\text{for } A < 1). \quad (14.30)$$

When A is close to 1, no drag is present to oppose gravity, and the spikes fall freely. From Eq. (14.29) in the case of $A = 1$ ($\rho_L = 0$), the spike height evolves with time as $1/2 \cdot g \cdot t^2$.

The asymmetry between the bubble and the spike velocities is emphasized in the ratio between the velocities: $U_S^{\text{asy}}/U_B^{\text{asy}} = \sqrt{(1+A)/(1-A)}$. When A is close to 0 the ratio is close to 1 ($\approx 1 + A + O(A^2)$); when A is close to 1, the asymmetry increases and the relation diverges.

14.2.6 DIMENSIONALITY DEPENDENCE

The solution to the equation of motion in three dimensions in the RT case is derived by repeating the same steps as in the 2D case. Only the final results of expansion of the solution to the equation of motion to the first and second orders are presented here (see Berning and Rubenchik, 1998):

$$\begin{aligned} Z(x, y, t) = & a_1 \cos(k_x x) \cos(k_y y) \quad (1\text{st order}) \\ & + A a_1^2 \left(-\frac{k}{4} \cos(2k_x x) \cos(2k_y y) \right. \\ & + \frac{k_x(k_x^2 + 2k_y^2 - 2k_x k)}{4 \cdot k \cdot (2 \cdot k - k_x)} \cos(2k_x x) \quad (2\text{nd order}) \\ & \left. + \frac{k_y(k_x^2 + 2k_y^2 - 2k_y k)}{4 \cdot k \cdot (2 \cdot k - k_y)} \cos(2k_y y) \right) \end{aligned} \quad (14.31)$$

where $a_1 = \exp(\sqrt{k \cdot g \cdot A} \cdot t)$ and $k = \sqrt{k_x^2 + k_y^2}$. The asymptotic 3D behavior of the bubbles and spikes can be described by the Layzer model in the $k_x = k_y$, $A = 1$ case. At late time Hecht *et al.* (1994) showed that the bubble tip tends to become round even when initially $k_x \neq k_y$. The 3D model is solved most easily considering the case of a cylindrical container filled with a fluid for $z > 0$. This

fluid is supported by a constant-pressure, low density fluid at $z < 0$. For cylindrical symmetry the Bernoulli equation has the form

$$\frac{\partial \phi}{\partial t} - \frac{1}{2} \left[\left(\frac{\partial \phi}{\partial z} \right)^2 + \left(\frac{\partial \phi}{\partial r} \right)^2 \right] - gz = \text{const.} \quad (14.32)$$

The same kinematic condition as in the 2D case must be maintained on the contact surface.

The potential that satisfies the boundary condition and the Laplace equation is

$$\phi(r, z, t) = F(t)e^{-kz}J_0(rk), \quad (14.33)$$

where $J_0(rk)$ is the Bessel function of order zero. ($k = \beta_1/R$; β_1 is the first zero of the Bessel function.) Introducing the potential to the Bernoulli equation and to the kinematic conditions leads to three coupled differential equations. Linearizing the equation and expanding the flow near the tip, we obtain the nonlinear behavior of the flow (see section 14.2.3).

The resulting equation for the bubble velocity approaches, at late times, the form

$$\frac{dU_B}{dt} = g - \frac{2\pi U_B^2}{\lambda}, \quad (14.34)$$

where λ is the diameter of the cylinder. This result suggest that in 3D $C_a = 1$ and $C_d = 2\pi$, as opposed to $C_a = 2$ and $C_d = 6\pi$ in the 2D case.

Following the same assumptions as in the 2D case, the solution to (14.34) is

$$U_{\text{asy}}^{3D,B} = \sqrt{g \frac{\lambda}{2\pi}}. \quad (14.35)$$

The time dependence of the bubble velocity in the RT case is plotted in Fig. 14.5 for 2D and 3D.

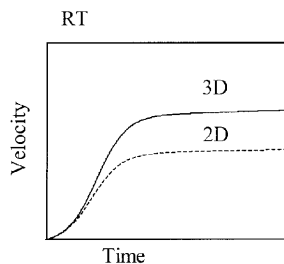


FIGURE 14.5 Bubble velocity in 2D and 3D in the Rayleigh–Taylor instability case with the same k (in the 3D case $k_x = k_y = k/\sqrt{2}$).

14.3 THE RICHTMYER–MESHKOV INSTABILITY

The RM instability occurs when a shock wave crosses an interface between two fluids with different densities. In this case small perturbations on the interface curve the transmitted and reflected waves. This local curvature of the waves causes pressure fluctuations on both sides of the interface. Local pressure differences between the two fluids create forces that increase the magnitude of the initial perturbation in the case of a shock traveling from a light fluid to a heavy fluid. In the case of a shock wave traveling from a heavy fluid to light fluid, a refraction wave reflects from the interface perturbation first decreases, then inverts phase and increases.

Richtmeyer (1960) modelled the instability in the linear stage by introducing an impulsive acceleration to Eq. (14.11) in the form of a delta function $g = \delta(t)U_{1D}$, where U_{1D} is the velocity induced by the shock wave.

Introducing the acceleration into Eq. (14.11) results in:

$$\frac{d^2 a(t)}{dt^2} = a(t) \cdot A \cdot \delta(t) \cdot U_{1D} \cdot k. \quad (14.36)$$

Integrating once over time yields

$$\frac{da(t)}{dt} = U_{RM} = a'_0 \cdot A' \cdot U_{1D} \cdot k. \quad (14.37)$$

The primed terms denote the postshock values. In the linear region the amplitude grows at a constant velocity. If the Atwood number is negative, a correction that was introduced by Meyer and Blewett (1972) must be made: a'_0 should be replaced by the average of the preshock amplitude and the postshock amplitude $(a'_0 + a_0)/2$ (for more details on the reasons for this correction see Yang *et al.*, 1994, and Vandenboomgaerde *et al.*, 1998).

By repeating the same derivation as in the case of the Rayleigh–Taylor instability (taking $g = 0$), higher harmonics of the perturbations are introduced. Equation (14.38) presents the expansion to third order:

$$\begin{aligned} Z(t) &= (1 - U_0 k A \cdot t) a_0 \cos(kx) && \text{(1st order)} \\ &- \frac{1}{2} A k a_0^2 (U_0 k A)^2 t^2 \cos(2kx) && \text{(2nd order)} \\ &- \frac{1}{24} k^2 a_0^3 (U_0 k A)^2 [3t^2 - (4A^2 + 1)U_0 k A t^3] \cos(kx) && \text{(3rd order)} \\ &- \frac{1}{8} k^2 a_0^3 (U_0 k A)^2 [(4A^2 + 1)U_0 k A t^3 + 3t^2] \cos(3kx). \end{aligned} \quad (14.38)$$

The extended Layzer model can be applied to the RM case at late time by assuming that the shock wave has no influence on the contact surface. In this case, setting $g = 0$ in Eq. (14.26) yields

$$(\rho_L + 2 \cdot \rho_H) \cdot \frac{dU}{dt} = -\frac{6\pi}{\lambda} \cdot \rho_H \cdot U^2, \quad (14.39)$$

where the first term on the left is the bubble inertia.

Solving this equation yields

$$U_{\text{asy}}^B = \frac{1}{6\pi} \left(\frac{3+A}{1+A} \right) \frac{\lambda}{t}. \quad (14.40)$$

A vortex model (Jacobs and Sheeley, 1996; Rikanati *et al.*, 1998) predicts at $A \rightarrow 0$ a bubble velocity to be $(1/2\pi) \cdot (\lambda/t)$ as opposed to $(\lambda/3\pi) \cdot (\lambda/t)$ at $A = 1$, confirming that also at low A 's with; $C_a = 2$ and $C_d = 6\pi$.

Since the RM bubble velocity approaches zero as $1/t$ at late time, a Padé approximation can be used to describe the interface evolution in a single formula. This type of expansion was introduced both by Velikovich and Dimonte (1996) and by Zhang and Sohn (1997). The bubble velocity is written as a fraction of two polynomials; the order of the denominator is higher than the order of the numerator. The polynomial coefficients are calculated in such a way that the Taylor expansion gives the same results as Eq. (14.38) for the RM instability. In this way the correct behavior of the bubble is extended to $a/\lambda \approx 0.4$ instead of $a/\lambda \approx 0.1$ in the expansion to third order. Equation (14.41) presents the bubble velocity resulting from the Padé approximation:

$$\begin{aligned} U_B &= -\dot{\eta}_a(0, t) + \dot{\eta}_b(0, t) \\ \dot{\eta}_a(0, t) &= \frac{U_0}{1 + U_0 a_0 k^2 t + \max(0, a_0^2 k^2 - A^2 + 0.5) U_0^2 k^2 t^2} \\ \dot{\eta}_b(0, t) &= \frac{AkU_0 t}{1 + 2k^2 a_0 U_0 t + 4k^2 U_0^2 (a_0^2 k^2 + 1/3(1 - A^2)) t^2}. \end{aligned} \quad (14.41)$$

However, at late times the Padé approximation does not predict the asymptotic velocity correctly. The asymptotic velocity from the Padé approximation is $1/4k^2 U_0^2 (a_0^2 k^2 + 1/3(1 - A^2))t$, which depends on the initial amplitude and does not fit the Layzer model prediction. Velikovich and Dimonte (1996) extended the Padé approximation to higher orders, but still obtained an incorrect asymptotic behavior.

The spike velocity can be found by using the same assumption as in the case of the RT spikes. By replacing ρ_H by ρ_L and ρ_L by ρ_H in Eq. (14.39), the

asymptotic velocity of the spike is derived. This equation of motion yields for the spikes

$$(\rho_H + 2 \cdot \rho_L) \cdot \frac{dU_S}{dt} = -\frac{6\pi}{\lambda} \cdot \rho_L \cdot U_S^2, \quad (14.42)$$

leading to the asymptotic velocity

$$U_{asy}^S = \frac{1}{6\pi} \left(\frac{3-A}{1-A} \right) \frac{\lambda}{t}. \quad (14.43)$$

This results has been confirmed both by numerical simulation and by experiments.

The expansion to the second order in 3D is presented in Eq. (14.44) when $k_y = k_x = k$:

$$\begin{aligned} Z(\vec{x}, t) = & a_0[(AkU_0t + 1)] \cos\left(\frac{k}{\sqrt{2}} \cdot x\right) \cdot \cos\left(\frac{k}{\sqrt{2}} \cdot y\right) \quad (1st \text{ order}) \\ & - a_0^2 A^3 k^3 U_0^2 t^2 \left(\frac{1}{4} \cos\left(2 \cdot \frac{k}{\sqrt{2}} \cdot x\right) \cdot \cos\left(2 \cdot \frac{k}{\sqrt{2}} \cdot y\right) \right) \quad (2nd \text{ order}) \\ & + \frac{1}{4} \cdot \frac{\sqrt{2}-1}{2\sqrt{2}} \cdot \left(\cos\left(2 \cdot \frac{k}{\sqrt{2}} \cdot x\right) + \cos\left(2 \cdot \frac{k}{\sqrt{2}} \cdot y\right) \right). \end{aligned} \quad (14.44)$$

This describes the evolution of the instability at early times. Again, for the late nonlinear stage a different treatment should be used.

By following the same steps as in the RT case to derive the RM evolution at the asymptotic stage the $A = 1$ 3D Layzer model can be used.

The resulting equation for the bubble velocity approaches, at late times, the form

$$\frac{dU_B}{dt} = -\frac{2\pi U_B^2}{\lambda}, \quad (14.45)$$

where λ is the cylinder diameter.

The solution to Eq. (14.45) is

$$U_{asy}^{3D,B} = \left(\frac{1}{\pi} \right) \left(\frac{1}{1+A} \right) \frac{\lambda}{t}. \quad (14.46)$$

The dependence of the bubble velocity on the dimensionality is plotted in Fig. 14.6.

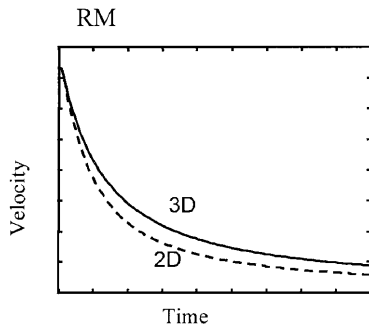


FIGURE 14.6 The dependence of the bubble velocity in the Richtmyer–Meshkov instability case on the dimensionality.

Finally, we found that the whole evolution of the single-mode bubble and spike in the Richtmyer–Meshkov case can be captured by a simple formula that fits the linear, early nonlinear, and asymptotic behavior:

$$U(t)_B = U_0 \cdot \frac{1 + Bt}{1 + Dt + Et^2}. \quad (14.47)$$

At early times this expression can be written as $U(t) = U_0(1 + t(B - D))$, and at late times as $U(t) = U_0 B/Et$, with $B = U_0 k$ and $D = (1 \pm A)U_0 k$, and $E = 3U_0^2 k^2(1 \pm A)/(3 \pm A)$ in the 2D case, with the plus sign for the bubble and the minus sign for the spike. An expansion of the flow equations to second order yields $U(t) = U_0(1 \mp AkU_0 t)$ (the minus sign is for the bubble, the plus for the spike), which determines the constant D . A is the postshock Atwood number, $k = 2\pi/\lambda$, and $U_0 = Ak\Delta U a_0$ is the Richtmyer initial velocity, with ΔU the velocity jump after the incident shock passage and a_0 the postshock amplitude. One can write a similar equation for the 3D case.

Equation (14.47) captures the linear and early nonlinear stages, up to second order, and converges to the correct asymptotic limit with the correct dependence on A .

14.4 EXPERIMENTAL STUDIES

14.4.1 EXPERIMENTAL STUDIES OF THE SINGLE-MODE RAYLEIGH–TAYLOR INSTABILITY

The evolution of single-mode perturbations (wavelength $\lambda = 2\pi/k$ and amplitude a) is well described by theory, simulation, and experiment. For $ka \ll 1$,

an RT unstable mode grows as $a = a_0 \exp(\gamma t)$, where $\gamma = \sqrt{Ak g}$ and $A = (\rho_H - \rho_L)/(\rho_H + \rho_L)$ is the Atwood number. When $ka > 1$, nonlinearities reduce the growth rate in an asymmetric manner. Much experimental work has been performed in the past three decades to study the single mode evolution. Previous experimental work (Lewis, 1960; Emmons *et al.* 1960; Duff *et al.* 1962; Ratafia, 1973) in this field has concentrated on the study of the growth of a single-mode perturbation. A novel single-mode experiment by Cole and Tankin was published in 1973. The study focused on the instability at a water/air contact surface. The glass-windowed test chamber was machined to a vertical cylinder, which permitted only one-dimensional motion. To create the initial single-mode perturbation, a vibrating paddle was inserted at one end of the test chamber. The paddle was attached to a loudspeaker to create an approximate sine wave of the desired wavelength and amplitude. The propulsion system, shown in Fig. 14.7, consisted of a double-ended air cylinder, an air compressor, and a storage tank. When the signal to accelerate the test chamber is given, the air pressure in the cylinder accelerates the piston and the test section downward. (More detail can be found in Cole and Tankin, 1973).

A series of evenly spaced images of the test chamber were taken. The contact surface was recognized in every image and the equation $a_i \cos(kx + \phi)$ was numerically fitted to it. The amplitude and wave number were used to calculate the growth rate of the waves. In Fig. 14.8 the growth rate is plotted in a semiexponential graph.

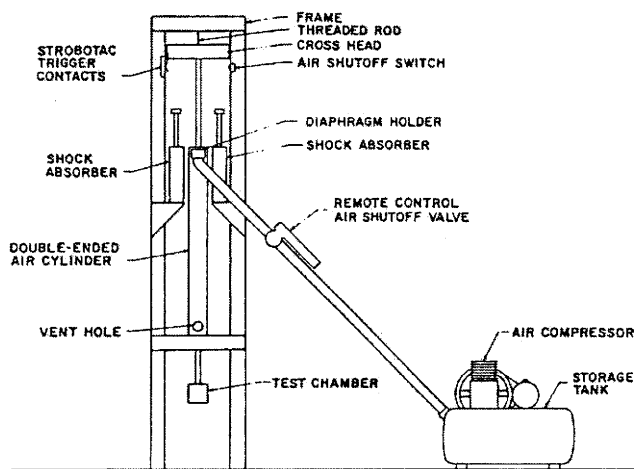


FIGURE 14.7 Schematic drawing of a propulsion system (Cole and Tankin, 1973).

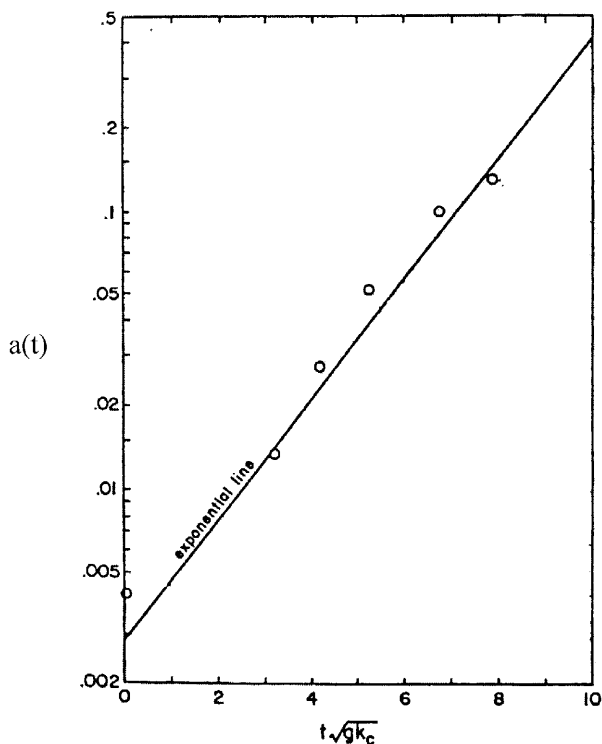


FIGURE 14.8 Typical plot of the Rayleigh–Taylor experimental growth rate from Cole and Tankin (1973).

The open circles present the experimental measurements; they are fitted to a straight line representing the exponential growth. The result clearly shows that the perturbation is in the linear stage, resulting in the exponential growth rate predicted by Eq. (14.12).

14.4.2 EXPERIMENTAL STUDIES OF THE RICHTMYER–MESHKOV INSTABILITY

A common method for experimental studies of the Richtmyer–Meshkov instability is to use a double-diaphragm shock tube apparatus (see Meshkov 1969, Sadot *et al.* 1998, Andronov *et al.*, 1976; Houas and Chemouni 1996; Jacobs and Catton 1988; Aleshin *et al.* 1991; Nikiforov *et al.* 1995; Smith *et al.* 1997; Brouillette and Sturtevant 1989; and Poggi *et al.* 1998). The apparatus is built from three chambers: driver, driven, and test section. A thick membrane

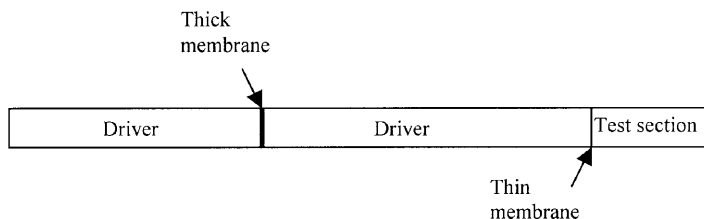


FIGURE 14.9 Schematic shock tube apparatus for Richtmyer–Meshkov instability investigation.

separates the driver from the driven (Fig. 14.9) and a very thin membrane separates the driven from the test section. Other techniques may be used to separate the driven gas from the test gas, such as parallel gases flow technique (see for example Jones and Jacobs, (1997) or Jacobs and Niederhaus (1997)).

A compressed gas is inserted into the driver and low-pressure gases are inserted into the other chambers. A shock wave is built in the driven section after the rupture of the thick membrane, traveling toward the test section. When the shock wave ruptures the thin membrane, a mixing process between the gas in the driven section and the gas in the test section is initiated. The waves propagating in the shock tube are shown in Figure 14.10.

Because of temperature differences between the gas in the driver section and the gas in the driven section, a contact surface ($C.S_1$) is created and travels toward the test section. A refraction fan (R.Fan) decreases the driving pressure

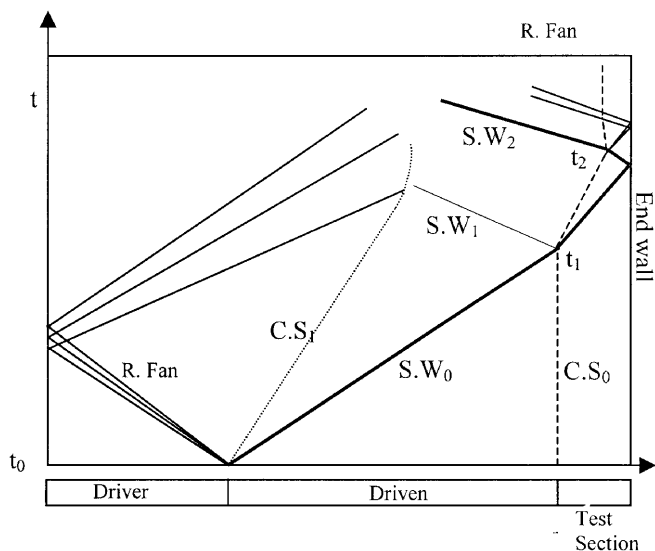


FIGURE 14.10 One-dimensional x - t diagram of the waves in a shock tube.

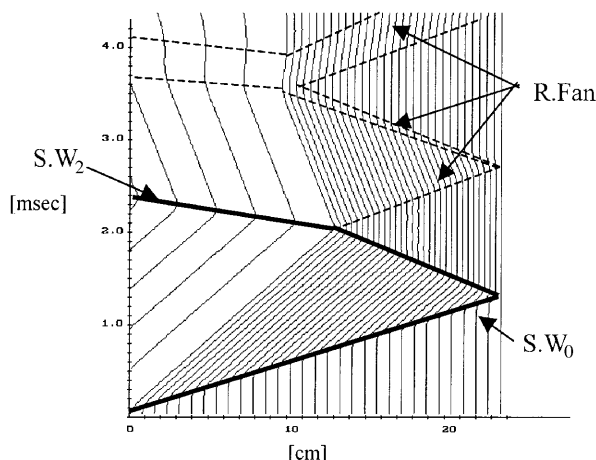


FIGURE 14.11 $x-t$ plot from a 1D simulation of the test section. The full thin lines follow the fluid motion track. The bold lines represent the shock waves. The dotted lines mark the rarefaction waves.

and is reflected from the back wall of the driver section toward the test section as well. A detailed $x-t$ plot, created using a 1D hydrodynamic simulation, describes the $x-t$ zone in which the experiment is carried out (Fig. 14.11).

The main shock ($S.W_0$) initiates the mixing by crossing the contact surface $C.S_0$. The reflected shock from the end wall hits the contact surface again. A set of weak shock and rarefaction waves bounces between the end wall (full reflection) and the contact surface (partial reflection)–($S.W_2$, $S.W_2$ R.Fan . . .). The Richtmyer–Meshkov instability can be studied using this apparatus in two cases: single shock and multishock. In the single-shock case, the experiment should be terminated before the reflected shock from the end wall reaches the contact surface. The multishock experiments should be terminated before the arrival of the refraction fan from the driver section to the contact surface. The dimensions of the shock tube must enable conducting experiments in a test section unaffected by the contact surface $C.S_1$ and the rarefaction fan from the driver section. Various gases are used for filling the different chambers in order to vary the shock Mach number and the test gas density ratio.

The results of the Richtmyer–Meshkov instability experiments are usually two-dimensional photographs. To produce the 2D photos, windows must be inserted in the test section and a schlieren or shadowgraph diagnostic technique used to visualize the contact surface. Other diagnostic systems based on velocity measurements (Souffland, *et al.* 1997) or IR absorption (Jourdan *et al.*, 1997) can also be used. In some cases it is useful to mark one of the gases with a fluorescent fluid and use a laser sheet to view the contact surface (Smith *et al.* 1997; Jacobs and Niederhans 1997).

The separation of the driven section from the test section can be done by other means than a thin membrane. Jones and Jacobs (1997) and Vorobieff *et al.* (1998) used continuous contact surface to avoid the disturbances introduced by the membrane.

Other techniques such as the Linear Electric Motor (LEM), used by Dimonte (1999) and Dimonte and Schneider (2000), allow studying the Rayleigh–Taylor instability and the Richtmyer–Meshkov instability using the same experimental apparatus. The LEM system is based on a test cell moving along a linear conducting rail. A controllable magnetic force can be exerted on the test cell by applying a pulsed electric current using a capacitor bank. Thus, the acceleration profile can be controlled.

14.4.2.1 Single-Mode Richtmyer–Meshkov Instability

The first reported experimental investigation of the Richtmyer–Meshkov instability was performed by Meshkov in 1969. The shock tube had a 120×40 mm rectangular test section. A thin film with a 2D sinusoidal shape separated the two gases. A camera with a schlieren optical system captured the interface evolution.

A shock wave with Mach number $M = 1.6$ was the initiator of the mixing process. Single-mode experiments were performed using different gas combinations and the perturbation growth was compared to the linear equation of Richtmyer (Eq. (14.31)). In Fig. 14.12a, photochronogram frames of the experiments with the following gas combinations are plotted: left, air/CO₂; center, He/Freon; right, Freon/He.

The comparison between the Richtmyer model (Eq. 14.37) and the experimental results is plotted in Fig. 14.12b. Good agreement was found in the linear stage of the experiment.

14.4.2.2 Richtmyer–Meshkov Bubble/Spike Experiments at Low Mach Numbers

In the work of Sadot *et al.* (1998) $M \approx 1.3$ air-to-SF₆ shock-tube experiments were performed. The experiments utilize a shock tube to study the Richtmyer–Meshkov instability of a system of two gases separated by a sawtooth perturbed interface. The test section has an $8 \text{ cm} \times 8 \text{ cm}$ square cross section and has transparent walls to facilitate flow visualization. An Air/SF₆ combination was used as working gases ($A = 0.67$). The diagnostic system is based on the schlieren technique. A fast camera captured about 20 pictures for each experiment. The initial perturbation shape was imposed on a thin ($0.1 \mu\text{m}$) membrane that separated the driven section and the test section. In Fig. 14.13 two sets of pictures are presented. The experiments were done with

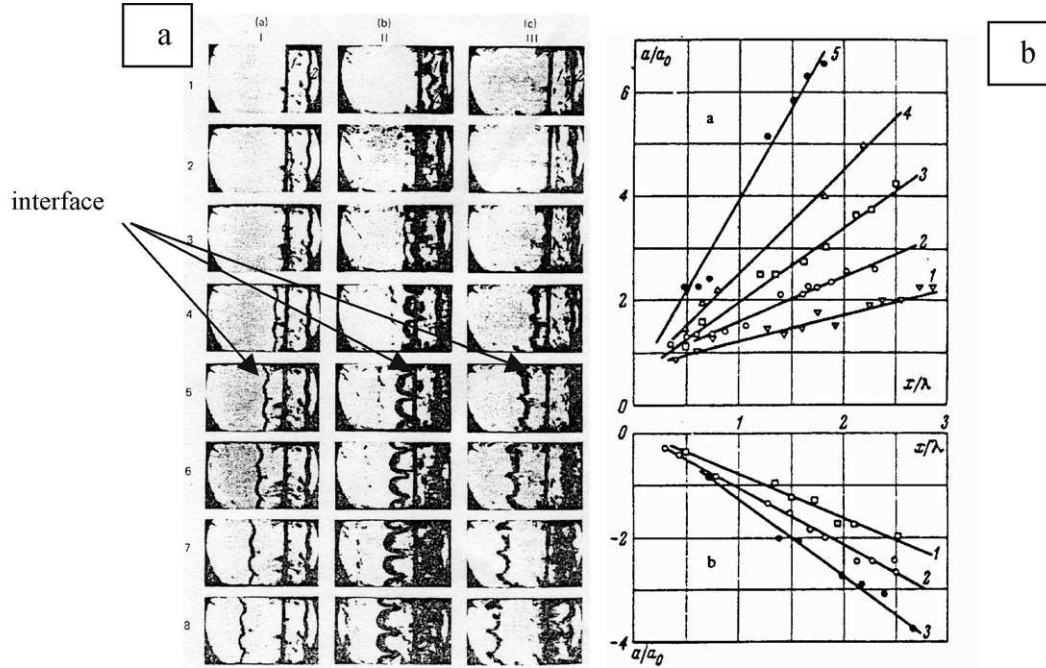


FIGURE 14.12 (a) Experimental results of the single mode Richtmyer–Meshkov instability (Meshkov, 1969). (b) Comparison of the experimental results with the linear theory of Richtmyer (the negative value is due to phase inversion).

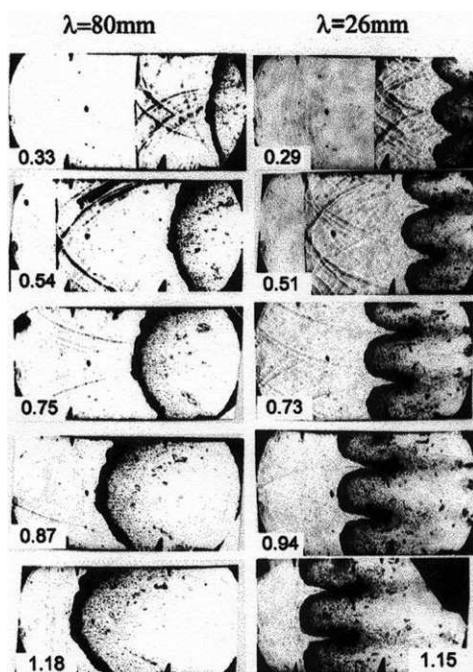


FIGURE 14.13 A set of single-mode experiments by Sadot *et al.* (1998).

$\lambda = 80$ mm, $a_0 = 3$ mm to study the linear growth and with $\lambda = 26$ mm, $a_0 = 3$ mm to study the nonlinear and asymptotic stages.

In the first two pictures the shock wave is shown traveling from right to left, followed by weak shocks that were created by the membrane holder. The contact surface follows the shock wave. Random perturbations on the interface caused by the surface roughness of the membrane thickens the contact surface between the two gases.

The bubble and spike heights were measured with respect to the unperturbed interface, as calculated analytically using the Rankine–Hugoniot relation and the measured shock velocity. In Fig. 14.14 a single picture from the experiment is shown. The picture shows the bubble and spike tip positions with respect to the unperturbed interface position.

The results from a set of single mode experiments are shown in Fig. 14.15a. Different stages of the instability evolution were captured in each experiment. To do so the perturbation wavelength was varied (80, 40, 26, and 16 mm), retaining the initial amplitude at all the experiments (3 mm), leading to different values of a_0/λ . The bubble and spike heights from these experiments are plotted in Fig. 14.15b using normalized coordinate, capturing the entire

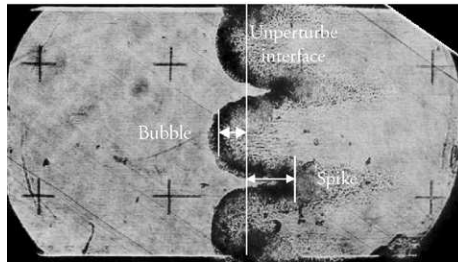


FIGURE 14.14 Bubble and spike height measurements with respect to the unperturbed interface in the air/SF₆ case.

instability evolution in a single graph. The linear stage is represented by the $\lambda = 80$ mm experiment, the early nonlinear stage by $\lambda = 40$ mm, and the late time evolution by the $\lambda = 26$ mm and $\lambda = 16$ mm experiments. Also plotted in Fig. 14.15b are the predictions of Eq. (14.47) in two cases: the full line is the high Atwood number case when the asymptotic velocity decreases as $(1/3\pi) \cdot \lambda/t$; the dotted line is the case of low Atwood number when the velocity decreases as $(1/2\pi) \cdot \lambda/t$. Clearly, the high Atwood prediction fits the results better.

14.4.2.3 Richtmyer–Meshkov Experiments with Various Atwood Numbers

The model prediction for the instability evolution Atwood dependence was also tested against experimental results. The various Atwood numbers were achieved by selecting different gas combinations as the mixing fluids. A 2D initial perturbation was used. The results were compared to the prediction of Eq. (14.47). The experimental setup was the same as that described in Section 14.4.2.2. An air/SF₆ combination was used for high Atwood number ($A = 0.67$) experiments and an air/Ar combination for low Atwood number ($A = 0.2$) experiments. Since the schlieren diagnostic technique requires a difference in the index of refraction larger than that between air and argon, it was necessary to use a smoke marker in the air to distinguish between the two gases. Figure 14.16 shows a set of photographs capturing the single mode evolution in (a) a high Atwood number air/SF₆ experiment and (b) a low Atwood number air + smoke/Ar experiment.

Figure 14.17 shows a comparison of the $A = 0.2$ experiment to the predictions of Eq. (14.47), where the dashed lines represent the $A = 1$ asymptotic behavior and the full lines represent the $A = 0$ asymptotic behavior.

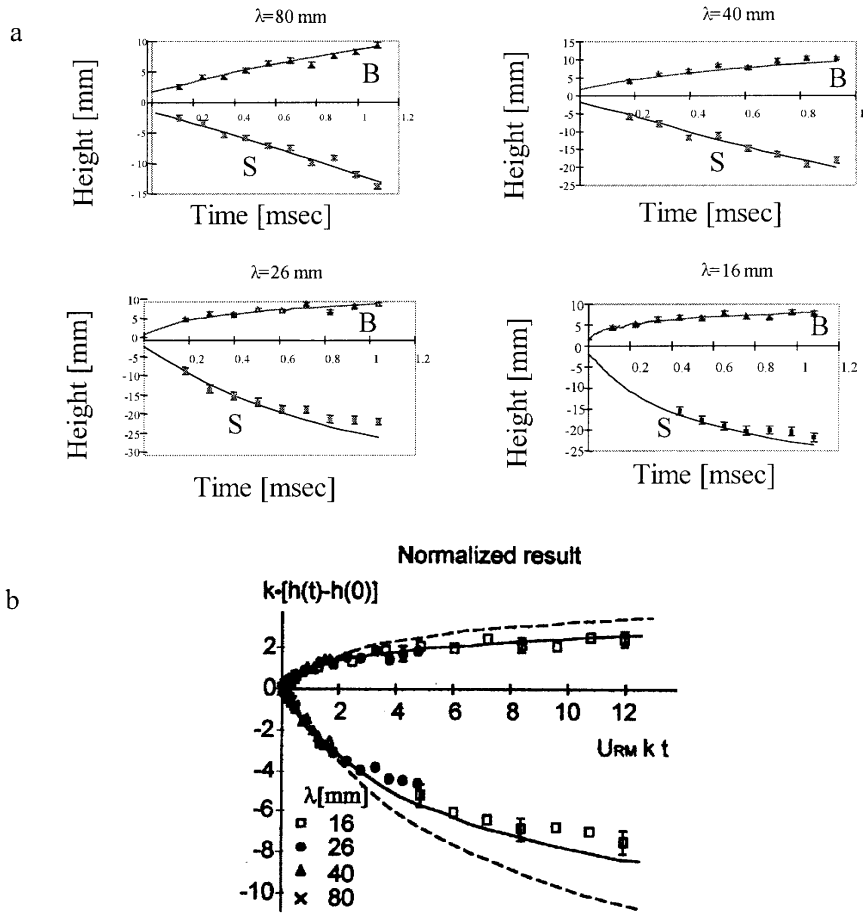


FIGURE 14.15 Results of a set of $A = 0.67$ single-mode experiments. (a) Bubble and spike height evolution in each experiment; (b) the whole set at a single graph using normalized coordinates. The lines are the predictions of Eq. (14.47) using the experimental initial velocity and Atwood number. The dotted line is the theoretical prediction using the $A = 0$ asymptotic behavior. The solid line, using the $A = 1$ asymptotic behavior, fits the experimental results better.

By comparing Figs. 14.15 and 14.17 it can be seen that as the Atwood number increases toward unity, the asymmetry between the bubble and spike increases as well. In the low Atwood case zero there is almost no difference between the bubble and the spike height (as seen in Fig. 14.17). Figure 14.18, showing both set of experiments together using normalized coordinates, demonstrates that behavior explicitly.

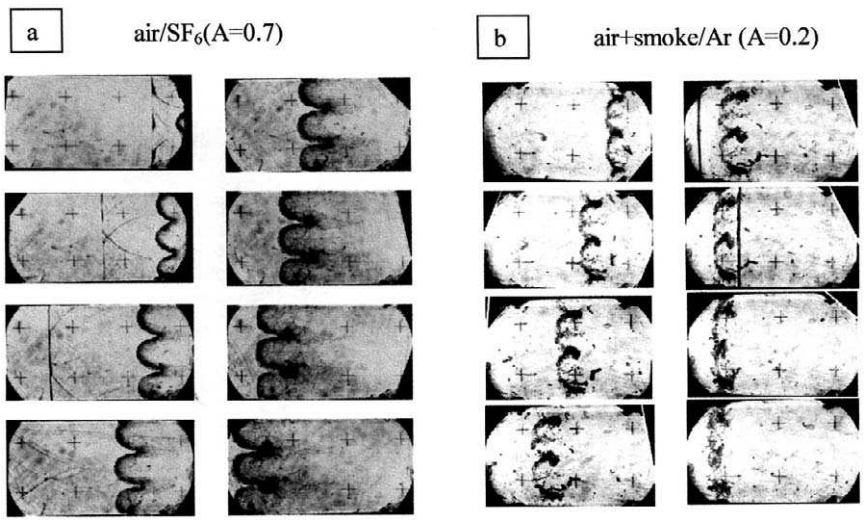


FIGURE 14.16 A set of schlieren photographs of a shock tube experiment. (a) High Atwood number, air/SF₆; (b) Low Atwood number, air+smoke/Ar.

14.4.2.4 Initial Three-Dimensional Richtmyer–Meshkov Experiments

Recent studies by Sadot *et al.* 1999 investigated the dependence of the Richtmyer–Meshkov instability on the dimensionality. In a shock tube apparatus, which was described in Section 14.4.2.2, a 3D initial perturbation was created. The membrane that separated the gases initially was shaped like a

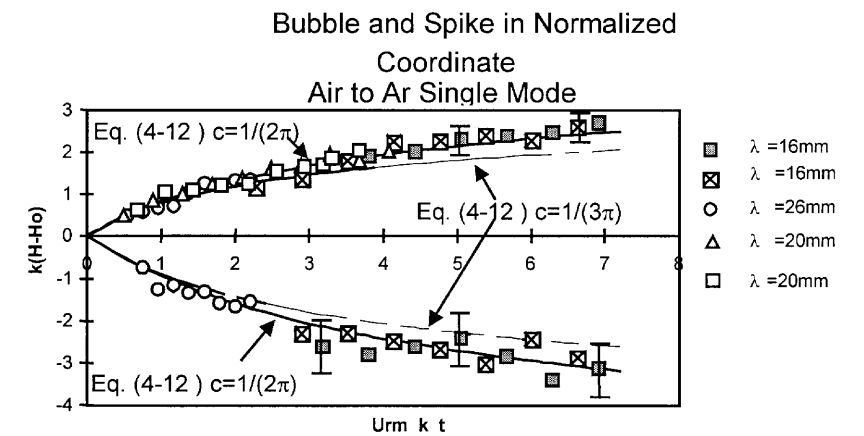


FIGURE 14.17 Bubble and spike heights vs the prediction from Eq. (14.38) in the low Atwood number case.

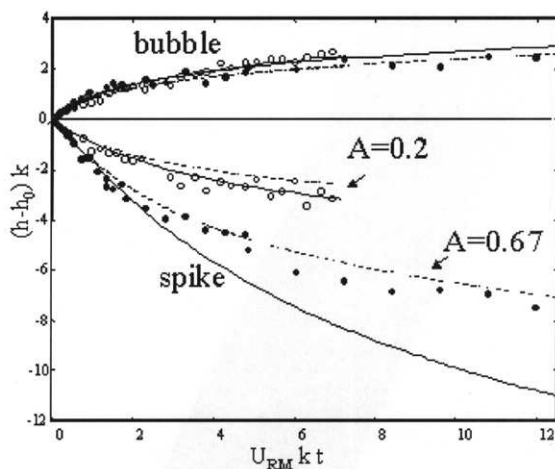


FIGURE 14.18 Bubble and spike height in two sets of experiments, one with $A = 0.67$, which fit better to $(1/3\pi)(\lambda/t)$, and the other with $A = 0.2$, which fit to $(1/2\pi)(\lambda/t)$.

pyramid with various base areas. This initial perturbation had a 3D symmetric shape near the bubble tip and a 2D shape near the base. Figure 14.19 is a schematic illustration of the membrane.

The experimental results were compared to a full ALE simulation (the description of the simulation is beyond the scope of this book and can be found in Hecht *et al.* 1995 and Ofer, 1995).

3D and 2D experiments having the same magnitude of the wave number k are presented in Figs. 14.20a and 14.20b. In Fig. 14.20c the bubble heights of these two experiments are plotted along with the calculation predictions. In the 2D case, the experimental bubble height is compared to the prediction of Eq.

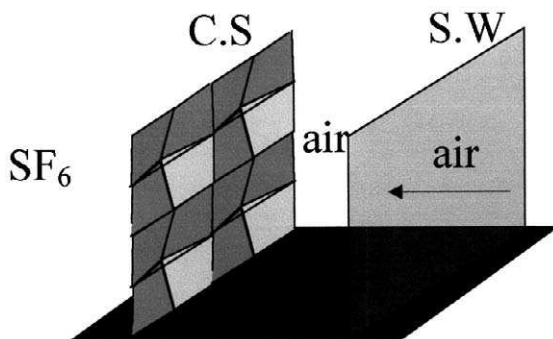


FIGURE 14.19 Initial perturbations in the experimental study of the dependence of the Richtmyer–Meshkov instability on the dimensionality.

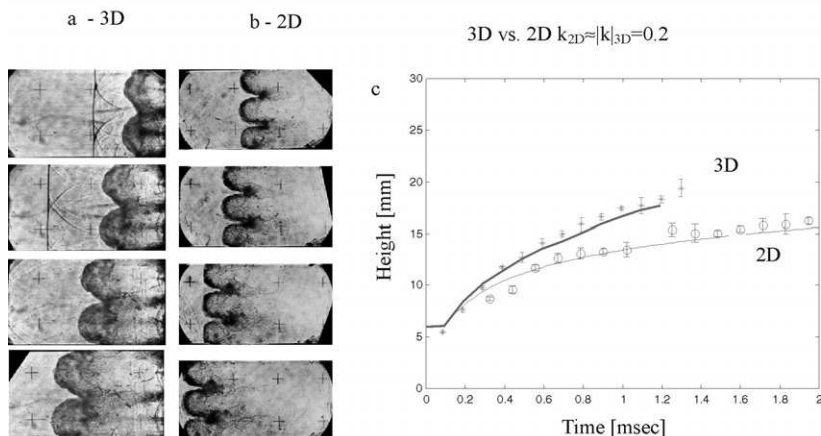


FIGURE 14.20 Experimental results of 3D Richtmyer–Meshkov instability. The initial perturbation was four pyramids with $400 \text{ mm} \times 40 \text{ mm}$ base $|k| = (k_x^2 + k_y^2)^{0.5} = 0.2$. (a) 3D results; (b) 2D results; (c) comparison of the experimental results with the simulation and the model.

(14.47). The 3D result is compared to a full numerical simulation. Since the value of $|k|$ and the initial perturbation amplitude are similar in 2D and 3D, the initial bubble velocities are equal. However, at the nonlinear regime the height difference between the 3D case and the 2D case increases, as expected from Eq. (14.46) and (14.41), respectively.

14.4.2.5 Richtmyer–Meshkov Experiments with Moderate Mach Numbers

Studies of the Richtmyer–Meshkov instability induced by a higher Mach number ($M = 3.5$) were performed by Zaytsev's group (Zaytsev *et al.* 1985 and Aleshin *et al.*, 1991). A single-mode perturbation was imposed on a thin ($2 \mu\text{m}$) polyester film. The working gases were argon and xenon ($A = 0.5$). The diagnostic system was based on the shlieren technique. A single photograph was taken for each run. To investigate the instability at different evolution stages a set of experiments were performed with different wavelengths. Figure 14.21 presents a set of pictures in which different wavelengths are used as initial perturbations. On the right, the time (within $\pm 10 \mu\text{s}$) elapsed from the entry of the shock wave into the xenon.

The authors report that the shape of the perturbation changes with time; the heavy fluid penetrates into the light one as a jet (spikes), while the light fluid penetrates into the heavy one as bubbles, and the radius of curvature of the bubble increases with time. In the experiment with $\lambda = 72 \text{ mm}$ only the linear

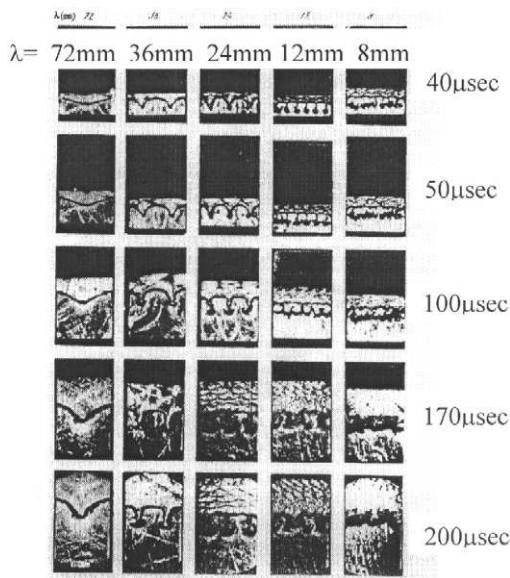


FIGURE 14.21 Five sets of experiments done by Aleshin *et al.* (1991) to capture the evolution at different stages. Different wavelengths were used.

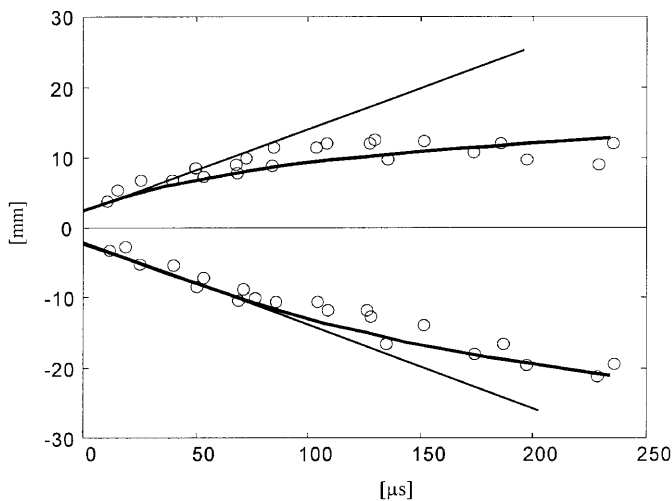


FIGURE 14.22 Bubble and spike height vs time for the $\lambda = 36$ mm experiments. Experimental results (\circ), Richtmyer linear velocity (thin line), and the prediction of Eq. (14.47) (thick line).

stage and the transition to the nonlinear stage were observed. In the $\lambda = 36$ mm experiment, linear, nonlinear, and late time stages were observed. In that experiment, the Kelvin–Helmholtz instability developed, and the jet took a mushroomlike shape. The bubble and jet (spike) heights were measured with respect to the unperturbed interface, whose position was calculated analytically. In Fig. 14.22 the experimental results are plotted in comparison with the linear stage Richtmyer velocity and the prediction of Eq. (14.47).

The agreement between the moderate Mach number experimental results and the prediction of the incompressible model suggests that no compressible effects arise in moderate Mach numbers.

14.4.2.6 Richtmyer–Meshkov Experiments with High Mach Numbers

RM experiments at high Mach numbers were conducted using the Nova laser facility at Lawrence Livermore National Laboratory (Dimonte and Remington 1993, Remington *et al.* 1993 and Dimonte *et al.* 1996). In the experiments very strong shocks are generated using an indirect drive configuration by focusing the laser beams into a radiation enclosure (hohlraum). This creates a uniform quasi-Planckian X-ray spectrum, whose equivalent radiation temperature is about 140 eV. The drive X-ray heats a target through a hole in the hohlraum wall, producing expanding ablation plasma at the surface and a 15.3 Mach shock wave moving into the target, as described in Dimonte *et al.* (1996). The target consists of a beryllium ablator and low-density foam tamper set in planar geometry. A two-dimensional perturbation is imposed at the interface between the beryllium and the tamper. The evolution is diagnosed with face-on and side-on radiography. A schematic description of the experimental setup is shown in Fig. 14.23.

In experiments with small initial perturbation amplitudes ($a_0 k < 0.1$), both the initial linear Richtmyer velocity and its nonlinear late time $1/t$ decay are clearly seen. The results are in good agreement with the previously described incompressible theory (Eqs. (14.39) and (14.47)) and with simulations, as can be seen in Fig. 14.24 (see Holmes *et al.*, 1999).

This result demonstrates that for low initial amplitudes, compressibility effects are evident only through the compression of the initial amplitude, despite the very strong incident shock wave. The compression factor is simply given by

$$a'_0 = a_0(U_{\text{sw}} - U_{\text{1D}})/U_{\text{sw}}. \quad (14.48)$$

Similar experiments but with high initial amplitudes ($a_0 k = 1-2$) result in a large deviation from the linear Richtmyer velocity. Holmes *et al.* (1999) suggested that this deviation from the linear theory is due to compressibility

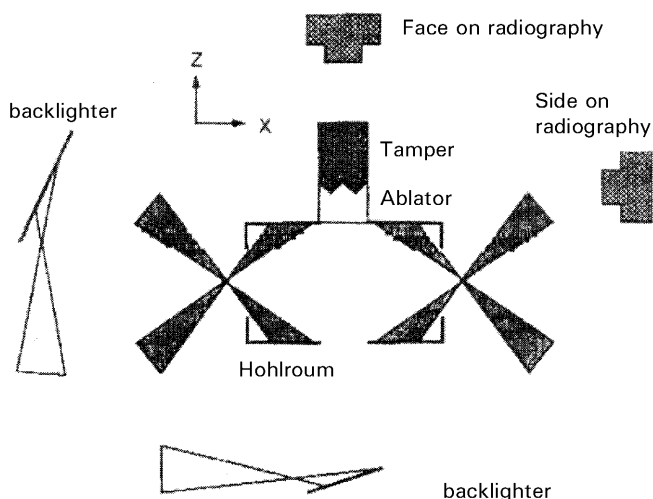


FIGURE 14.23 Experimental configuration showing the target mounted on the hohlraum for side-on and face-on radiography (from Dimonte *et al.* 1996).

effects, which are related to the high Mach number of the transmitted shock wave. A suggested compressible reduction factor, accounting for the ratio between the linear Richtmyer velocity and the difference between the 1D velocities of the interface and the transmitted shock, results in qualitative agreements with the experiments (see Fig. 14.24).

However, since all the experiments that did show a reduction in the linear velocity were done with high initial amplitudes, where the linear theory does not apply, it is not clear whether the reduction is due to compressibility or to the high initial perturbation amplitude.

In a publication analysing the initial velocity through an incompressible vorticity deposition model based on the geometry of the shocked interface, the linear velocity reduction factor due to the large initial perturbation amplitude is derived (Rikanati *et al.* 2000). The new reduction factor is derived by calculating the velocity of the bubble tip generated by the vorticity distribution on the shocked interface, assuming that the transmitted shock does not affect the interface evolution. Since the geometry of the shocked interface strongly depends on the initial amplitude and its compression, the velocity reduction predicted by the model is due only to the large initial amplitude rather than to compressibility effects after the initial compression. The model reduction factor is in good agreement with both the experiments and the simulations, as can be seen in Fig. 14.25.

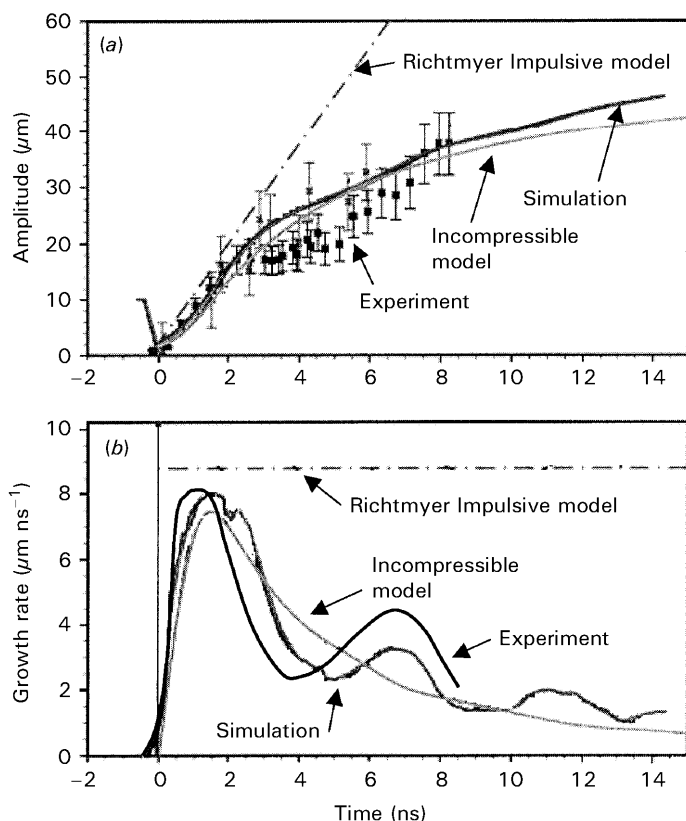


FIGURE 14.24 Experimental, simulation, and theoretical incompressible model (Eqs. (14.39) and (14.47)) predictions for perturbation growth for the Mach 15.3, $a_0 = 10 \mu\text{m}$ case; amplitude vs time (Holmes *et al.* 1999).

In order to distinguish between the effect of high initial amplitudes and the effect of compressibility, shock tube experiments were conducted at Ben-Gurion University at low Mach numbers (1.2) and large initial amplitudes (k^*a_0 up to 3: Sadot *et al.* 1999; Rikanati *et al.* 2000). Figures 14.26a–14.26c describe a set of schlieren pictures of the shock tube experiments, and Fig. 14.26d shows the experimental reduction factor of the linear velocity with respect to the Richtmyer prediction and a comparison to the vorticity deposition model prediction. As can be seen, very good agreement is achieved. The results obtained are similar to those derived for the 15.3 Mach number experiments.

We can conclude that the main reduction of the linear velocity should be attributed to the large initial amplitude rather than to the high Mach number of the incident shock. A true effect of compressibility on the Richtmyer–Meshkov

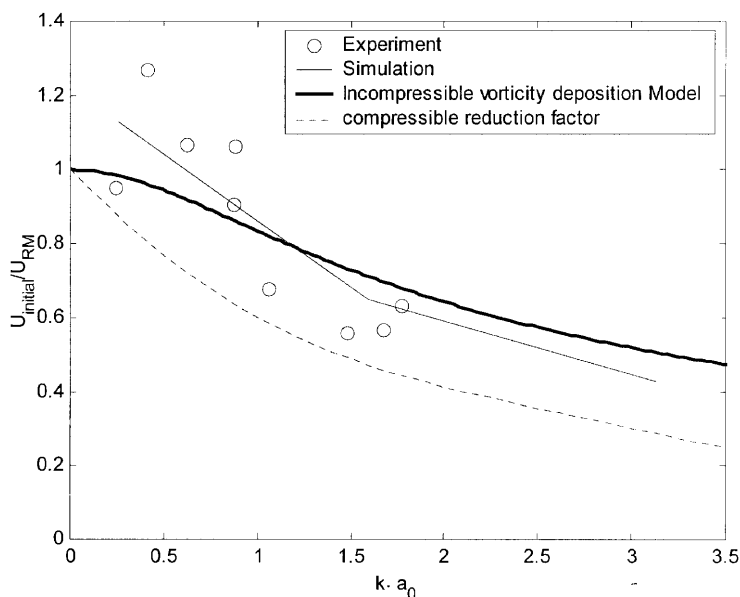


FIGURE 14.25 Comparison between experiments, simulation, the incompressible vorticity deposition model (Rikanati *et al.* 2000), and the compressible reduction factor (Holmes *et al.* 1999) for the $M = 15.3$ experiments. a_0 is the preshock amplitude, k the wave number \circ -LEM Results by Dimonte *et al.* (1996).

instability evolution in the linear regime can appear only when a strong shock impinges on a compressible material, so that the velocity jump of the material interface is only slightly lower than the shock velocity (which is not the case of the preceding experiments). In this case, the shock wave remains in the vicinity of the material interface for a long time, which inevitably causes modifications to the incompressible prediction. This is clearly demonstrated in cases when the tip velocity predicted by the incompressible model is higher than the shock velocity.

14.5 RANDOM INITIAL CONDITIONS

In the systems of a single-mode periodicity described to this point, the flow is governed, even at late times, by identical bubbles evolving in proximity with each other. In the RT case, bubbles growing with a constant velocity are formed, while for the RM case, bubbles growing with a velocity proportional to $1/t$ are formed.

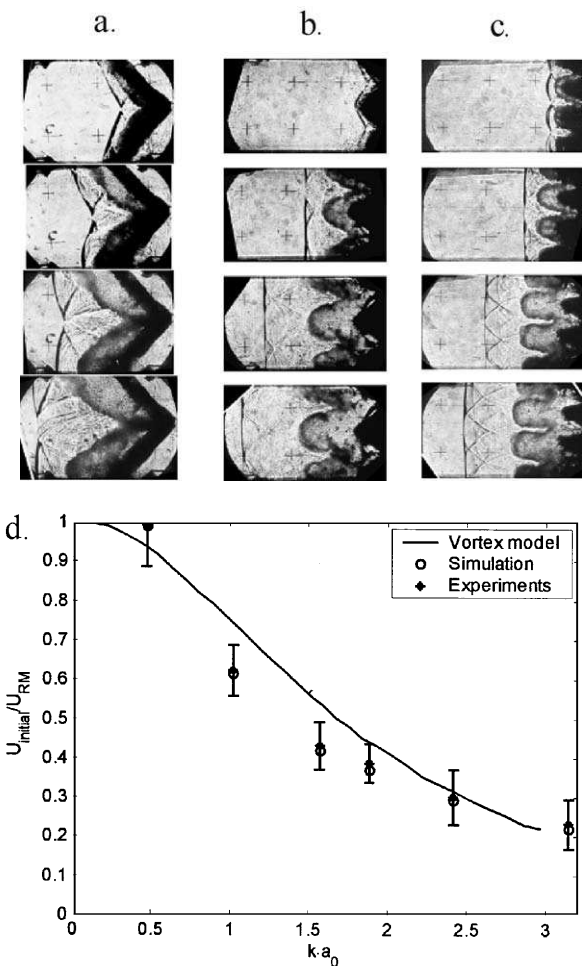


FIGURE 14.26 Reesults from a $M = 1.2$ experiment with large initial amplitude. Schlieren pictures for (a) $ak = 1.5$, (b) $ak = 0.9$, (c) $ak = 2.4$. (d) Comparison between the prediction of the vorticity deposition model and the experimental results (the experimental error is derived from simulations).

When a multimode initial perturbation is introduced, which is the case in most realistic systems, the instabilities develop from noisy initial perturbations that contain many short-wavelength modes. In this case the single-mode periodicity is broken, and the flow evolves differently. In inverse cascade process arises, in which larger and larger structures are continually generated. The fundamental cause of this process is competition between large coherent structures caused by the reduced drag per unit volume of large structures. A

bubble adjacent to smaller bubbles expands and accelerates while its neighbors shrink and are swept downstream. This process leads to a constant growth of the surviving bubbles and to an acceleration of the front in the RT case. This description of the mixing front was pioneered by Sharp and Wheeler (Sharp, 1984), who proposed a model for bubble rise and competition.

In this section we present briefly a bubble-merger model for the collective behavior of bubble ensembles at both RT and RM mixing fronts, from which the late time scaling laws can be derived (Alon *et al.* 1993; Alon *et al.* 1994; Shvarts *et al.* 1995; Oron *et al.* 1998; Rikanati *et al.* 1998).

14.5.1 TWO-DIMENSIONAL STATISTICAL MECHANICS MODEL AND LATE TIME SCALING LAWS

In the model the bubbles are arranged along a line, and are characterized by their diameters (wavelengths) λ_i . The bubble competition is introduced by a merger rule: two adjacent bubbles of diameters λ_i and λ_{i+1} merge at a rate $\omega(\lambda_i + \lambda_{i+1})$, forming a new bubble of size $\lambda_i + \lambda_{i+1}$. This represents the surviving bubble expanding to fill the space vacated by the smaller bubble that was washed away from the front. Each bubble rises with a velocity $U(\lambda_i)$ equal to the asymptotic velocity of a periodic array of bubbles with diameter λ_i . The mean interface height is found by integrating the average bubble velocity $dh(t)/dt = \langle U \rangle$.

To analyze the model, we define the size distribution function $g(\lambda, t)d\lambda$ as the number of bubbles in the front with wavelengths within $d\lambda$ of λ . In the mean field approximation, neglecting correlations between neighboring bubbles, we can write an evolution equation for the size distribution,

$$\begin{aligned} N(t)\partial g(\lambda, t)/\partial t = & -2g(\lambda, t) \int_0^\infty g(\lambda', t)\omega(\lambda, \lambda')d\lambda' \\ & + \int_0^\infty g(\lambda - \lambda', t)g(\lambda', t)\omega(\lambda - \lambda', \lambda')d\lambda' \end{aligned} \quad (14.49)$$

where $N(t) = \int_0^\infty g(\lambda, t)d\lambda$ is the total number of bubbles at time t . The first term on the right-hand side of Eq. (14.49) is the rate of elimination of bubbles of wavelength λ by mergers with other bubbles, and the second term is the rate of creation of bubbles of wavelength λ by the merger of two smaller bubbles. The merger rate $\omega(\lambda, \lambda')$ can be obtained either from full numerical simulations or simpler models for two-bubble interaction (such as the $A = 1$ extended potential flow model described by Hecht *et al.* 1994, and Alon *et al.* 1994). Figure 14.27A shows the $A = 1$ 2D merger rate for the RT and RM cases as a

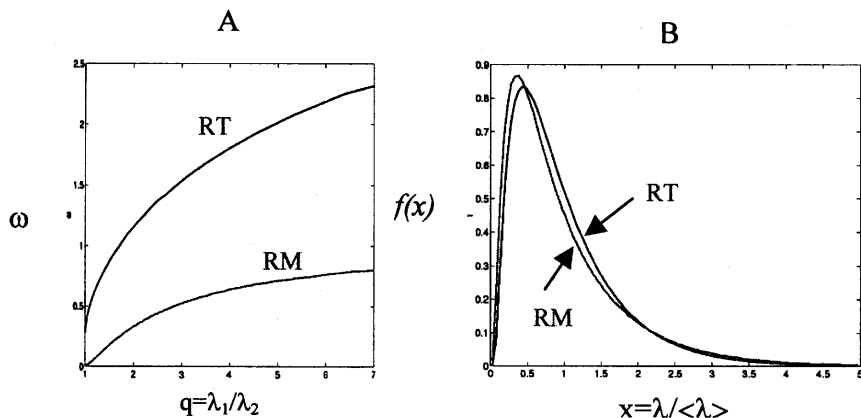


FIGURE 14.27 Results from the bubble merger model. (a) Merger rate in the RT and RM cases as a function of the bubble size ratio. (b) Self-similar bubble distribution as a function of $\lambda/\langle\lambda\rangle$ (Alon *et al.* 1994).

function of wavelength ratio, as derived from the aforementioned model (Hecht *et al.* 1994; Alon *et al.* 1995b and Oron *et al.* 1999).

The bubble merger model just described predicts that both the RT and RM front dynamics flow to a scale invariant regime, where the bubble size distribution scales with the average wavelength,

$$g(\lambda, t) = N(t)\langle\lambda(t)\rangle^{-1}f(\lambda/\langle\lambda\rangle), \quad (14.50)$$

where $\langle\lambda(t)\rangle$ is the mean bubble diameter at time t . The scaled distribution f is selected out of a family of fixed points. These distributions are shown in Fig. 14.27B for both the RT and RM cases.

The growth rate of the bubble front penetration h_b in this regime was derived from the model (for $A = 1$) and simulation (for all A 's). In the RT case, the model result is

$$h_b = \alpha_B \cdot A \cdot g \cdot t^2. \quad (14.51)$$

Using the scale-invariant fixed point distribution from the merger model, we find $\alpha_B = 0.05$. This result is in good agreement with experiments (Read, 1984) and simulations (Gardner *et al.* 1988; Youngs, 1984; Freed *et al.* 1991). The approach to a scale-invariant form independent of the detailed initial bubble distribution in the model explains the observed independence of the mixing rate on the initial perturbation (Alon *et al.* 1993; Glimm *et al.* 1990).

The results for the RM bubble front exhibit a new scaling behavior. The bubble front penetration is

$$h_B \approx \lambda_0 (U_0 t / \lambda)^{\theta_B}, \quad (14.52)$$

where $\theta_B = 0.4$ at all density ratios, and λ_0 and U_0 are the mean initial wavelength and velocity. This is an important difference from the RT case: in the RM case, the penetration depends on information from the initial perturbation at all times. These predictions are in good agreement with full numerical simulations (see Freed *et al.* 1991).

The spike front, where jets of heavy fluids penetrate the light fluid region, exhibits a different behavior. At a very large density ratio between the fluids ($A = 1$), the spikes behave as freely falling drops. In the RT case this leads to a spike front penetration that scales as $\frac{1}{2}gt^2$, a similar scaling to the bubble front. Nevertheless, in the RM case, at $A = 1$ the spikes fall at a constant velocity, that is, as $h_s = a_s t^{\theta_s}$, with $\theta_s = 1$ (compared to $\theta_B = 0.4$ for the bubbles). Thus, in the RM case, the bubble and spike fronts display different power laws.

To help understand the spike front behavior, we applied the following method to it: We note that the dominant spikes visible in the flow have roughly the same periodicity as the dominant bubble structures, and the coarsening of their size can therefore be described by the same merger rate ω . The spike velocity used in the merger model is not its terminal velocity, but rather the velocity of a single-mode spike when the amplitude of the corresponding bubble is $h_B / \lambda \sim 0.25$. In the RT case, this yields for the spike front penetration $h_s = \alpha_s(A) A \cdot g \cdot t^2$ with as $\alpha_s(A)$ an increasing function of the density ratio, which agrees well with simulation and experimental results. In RM, we find $h_s \sim \lambda_0 (u_0 / \lambda_0)^{\theta_s}$, with θ_s going from $\theta_s = 1$ at $A = 1$ to $\theta_s = \theta_B \sim 0.4$ at low A , where the bubble and spike fronts are almost symmetric. These results, shown in Fig. 14.28, are in good agreement with full numerical simulations.

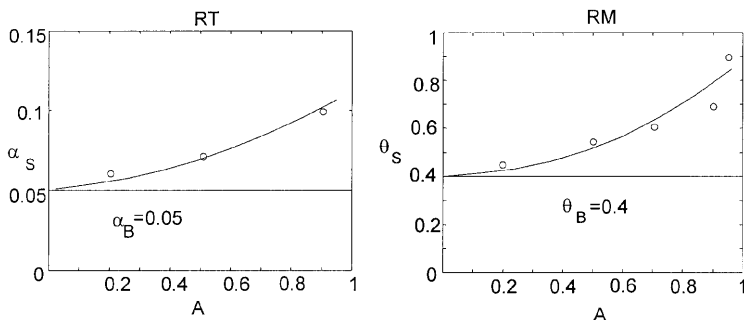


FIGURE 14.28 Main statistical model results in 2D. \circ -2D numerical simulation.

14.5.2 THREE-DIMENSIONALITY EFFECTS ON THE LATE TIME SCALING LAWS

Following the predictions of the foregoing model, Dimonte (1999) has performed a Linear Electric Motor (LEM) experiment measuring both the Rayleigh–Taylor (constant acceleration) and RM (impulsive acceleration) scaling laws. Their main results are as follows: (a) The RT scaling parameters α_B and $\alpha_5(A)$ were found to be in good agreement with the model predictions. (b) Although RM experiments have verified for the first time the two distinct scale behaviors, θ_B and $\theta_5(A)$ were found to be lower by almost a factor of 2 than the model and 2D numerical simulation predictions for all Atwood numbers. For example, θ_B of the order of 0.25 was obtained rather than the model prediction of 0.4. (c) The self-similarity parameter $h_B/\langle\lambda\rangle \approx 1.0\text{--}1.5$, a factor of 3–4 higher than the model prediction of 0.25–0.5.

These discrepancies between the model predictions and the experimental results can be explained by the difference between 3D experiments and the 2D model.

In order to check these assumptions, we first compare the results of 2D and 3D incompressible RT instability evolution using full numerical simulations. The initial conditions are of a multimode initial perturbation with an initial number of ~ 300 bubbles. The Atwood number is $A = 0.5$. Two typical consecutive frames from the 3D calculation, showing the interface between the heavy and the light fluid, are plotted in Fig. 14.29. The bubble front height scales, at late times, in both 2D and 3D as $h_B \approx 0.05 Agt^2$, and the spike front scales as $h_S \approx 0.7 Agt^2$. However, similar simulations of the RM instability case yield in 2D $\theta_B \approx 0.35$ and a significantly lower value of $\theta_B \approx 0.22$ in the 3D case. These values are in agreement with the experimental results (Dimonte and Schneider 2000).

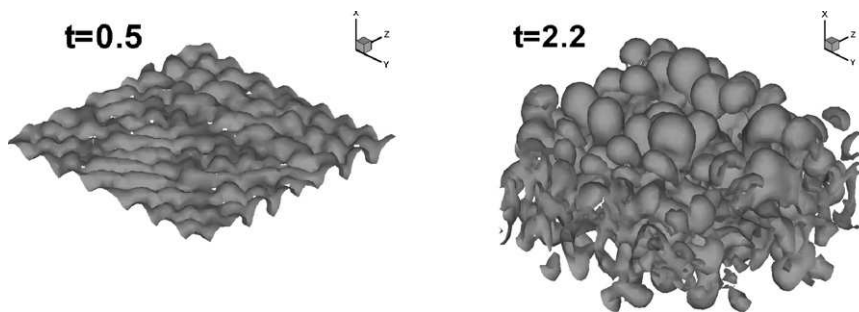


FIGURE 14.29 The interface between the heavy and the light fluid in two typical consecutive frames from the $A = 0.5$ 3D RT calculation (Shvarts *et al.* 2000).

In order to explain the difference in the dynamics of the 2D and 3D instability front, a simple drag-buoyancy Layzer type equation can be used (see Section 14.2.3) to describe the dominant mode evolution (Shvarts *et al.* 2000):

$$(\rho_L + C_a \cdot \rho_H) \cdot \frac{dU}{dt} = (\rho_H - \rho_L) \cdot g - \frac{C_d}{\lambda} \cdot \rho_H \cdot U^2. \quad (14.53)$$

Here C_a is an added mass coefficient and C_d a drag coefficient. From Sections 14.2.3 and 14.2.6 we get in 2D $C_a = 2$, $C_d = 6\pi$, and in 3D, $C_a = 1$, $C_d = 2\pi$. The A dependence of the asymptotic bubble velocities obtained from the model is

$$U_{RT} = \sqrt{\frac{2A}{(1+A)}} \cdot \frac{g\lambda}{C_d} \quad (14.54)$$

and

$$U_{RM} = \left(\frac{1-A}{1+A} + C_a \right) \cdot \frac{\lambda}{C_a t}. \quad (14.55)$$

For the multimode case we assume self-similarity, so that $\langle \lambda(t) \rangle = b(A)h_B(t)$, and solve Eq. (14.53) for both the RT ($g > 0$) and RM ($g = 0$) cases.

Asymptotically we get that the RT bubble front evolves as

$$h_B = \alpha_B A \cdot g \cdot t^2 \quad (14.56)$$

with

$$\alpha_B = \frac{1}{2(1+A)C_d b(A)}, \quad (14.57)$$

and the RM bubble front evolves as

$$h_B \approx t^{\theta_B} \quad (14.58)$$

with

$$\theta_B = \left(\frac{1-A}{1+A} + C_a \right) \cdot \frac{1}{C_d b(A)}. \quad (14.59)$$

We thus obtain for each value of the Atwood number two relations among the three parameters α_B , θ_B , and b , leaving one free parameter. The spike front height is derived similarly to Eq. (14.53) by calculating the spike velocity of a single mode when the bubble amplitude h_B reaches the similarity value of $b\lambda$.

Plotted in Figs. 14.30a–14.30e are the values of α_B , θ_B , α_S , θ_S , and $b = h_B/\langle \lambda \rangle$, respectively, as a function of A as obtained from Eqs. (14.56)–(14.59). The free parameter, chosen either as a constant α or as a constant θ , is obtained from models and simulations in the 2D case, and from the

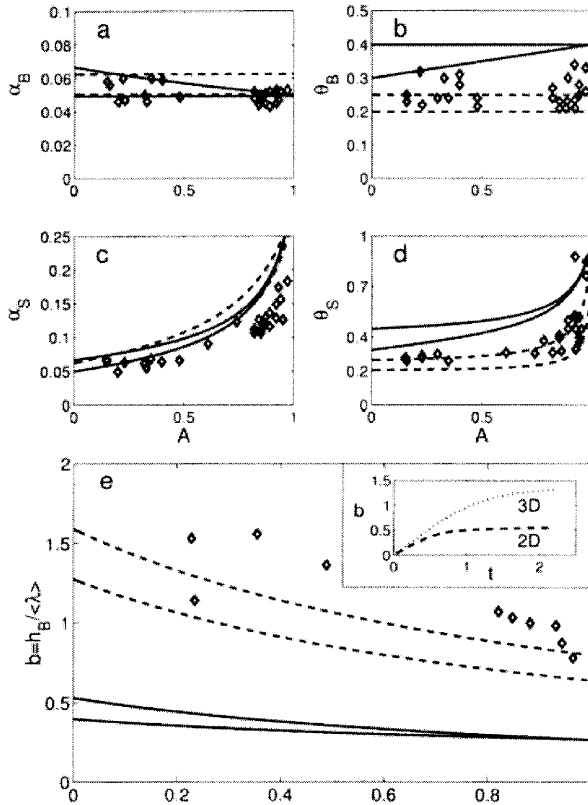


FIGURE 14.30 Parameter values as a function of A as obtained from the 2D drag-buoyancy equation assuming $\alpha_B = 0.05$ and $\theta_B = 0.4$ (full lines), from the 3D equation assuming $\alpha_B = 0.05$ and $\theta = 0.25$ (dashed lines), and Dimonte *et al* experimental results (diamonds): (a) α_B , (b) θ_B , (c) α_S , (d) θ_S , (e) $b = h_B / \langle \lambda \rangle$. The inset in (e) shows the temporal evolution of the self-similarity parameter $h_B / \langle \lambda \rangle$ in the 2D and 3D simulations.

experimental data in the 3D case. In the 2D case we plot the values assuming either $\alpha_B = 0.05$ or $\theta_B = 0.4$ (full lines), whereas in the 3D case we plot the values assuming either $\alpha_B = 0.05$ or $\theta = 0.25$ (dashed lines). Also plotted are Dimonte *et al.* LEM experimental results (Dimonte, 1999; Dimonte and Schneider 2000). As can be seen, the 3D model results are in much better agreement with the experimental results.

Note in particular the lower value of θ_B and θ_S , and the much higher value of $b = h_B / \langle \lambda \rangle$, very close to the experimental values. Here we assume that the wavelength λ is twice the measured bubble size width d_2 (rather than $\lambda = d_2$ as in Dimonte, 2000), since only half of the bubbles at the front are indeed rising (Haan, 1991, Alon *et al.* 1995a). In the inset of Fig. 14.30e are plotted the time

dependences of the 2D and 3D simulation values of b . As can be seen, while the 2D simulation value saturates at $b \sim 0.5$, the 3D value only saturates at $b \sim 1.5$, indicating growth of much more elongated bubbles in the 3D case.

This can be observed in Fig. 14.31, which compares a part of the 2D calculation domain (Fig. 14.31a) at a late time, after reaching the scale-invariant regime, when the bubble front height is 0.1, with a typical cut from the 3D simulation (Fig. 14.31b) at a similar bubble front height. As can be seen, the bubbles in the 2D case are less tightly packed, with wide areas of high-density fluid between them, resulting in a much lower aspect ratio than the 3D bubbles.

We have also modified the statistical mechanics model to include the following:

1. In 3D the conserved quantity when two bubbles merge is area rather than length. As a result, a 3D bubble has to overcome more of its neighbors in order to expand sideways.
2. The average number of neighbors in competition with a single bubble is ~ 6 in 3D. This can cause either a widening or a narrowing of the bubble size distribution, depending on the details of the merger process modeling, as compared to 2 in 2D.
3. The asymptotic single bubble velocity increases in 3D by a factor ~ 1.5 –2 due to the reduced drag per unit volume in 3D. This also results in an increased merger rate.

Incorporating these modifications into the 2D statistical mechanics model (i.e., using a modified bubble merger value due to (a) and (b), and modifying the asymptotic velocity and merger rate due to (c)), we can obtain appropriate 3D scaling parameters α , θ and $b = h/\langle\lambda\rangle$. The bubble size distribution changes mainly because of (a), resulting in a much narrower distribution. This tends to reduce the average merger rate. In the RT case this effect is compensated by the

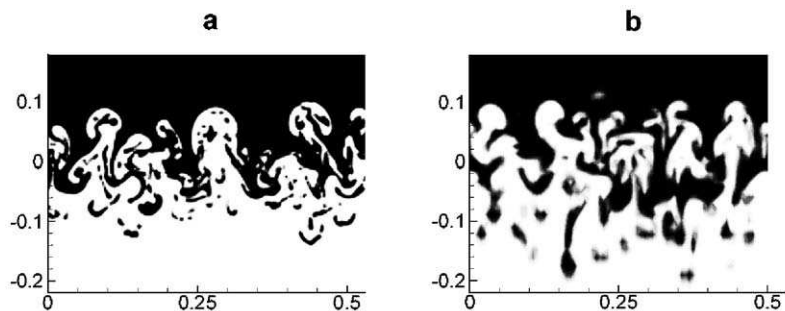


FIGURE 14.31 A cut through the calculation domain at a late time, after reaching the scale-invariant regime, when the bubble front height is 0.1, in the (a) 2D simulation, (b) 3D simulation.

higher asymptotic velocity resulting in a similar value of α in 2D and 3D. In the RM case, however, this results in a lower value of $\theta \sim 0.17\text{--}0.22$ in 3D. The lower merger rate and the slower expansion sideways result in a similarity parameter b three times higher than in the 2D case (Shvarts *et al.* 2000). These results are in good agreement with Dimonte's experiments (Dimonte and Schneider, 2000).

14.5.3 SHOCK WAVE EXPERIMENTS OF THE BUBBLE COMPETITION PROCESS

In the previous section we introduced a multimode model based on two basic physical elements: the single-mode bubble evolution, and the two-bubble interaction rate. A detailed experimental study of the first basic element—the single-mode evolution—was described in Section 14.4.2.2. In this section we describe the two-bubble interaction experiments. We choose an initial condition of an array of alternating large (about 25 mm) and small (10–15 mm) bubbles. The central part of the membrane consisted of a small bubble flanked by two large bubbles, and the two sides were completed by partial small bubbles. The initial amplitudes of the large and small bubbles were chosen so that their initial velocities according to Richtmyer formula were similar (i.e., $a_l/a_s = \lambda_s/\lambda_l$, where “s” and “l” are the small and large bubble, respectively). Figure 14.32a shows the temporal evolution of the interface in the 27 mm/17 mm experiment. Superimposed on the experimental pictures is the interface structure from a numerical simulation. The agreement between the experimental results and the numerical simulation is very good, including the change in the small bubble location and size relative to the two large neighboring bubbles. The bubble merger process can be seen from the shape of the small and large bubbles, and especially from the orientation of the spikes between the larger and smaller bubbles, which skew toward the large bubbles as the small bubble disappears.

The competition process is most dramatically demonstrated by plotting the bubble tip locations relative to those measured and calculated for the single-mode case. In Fig. 14.32b are plotted the two bubble heights, relative to the unperturbed interface. The figure shows the experimental results, the full numerical simulation, and the potential flow model of Hecht *et al.* (1994). For the model we use the $A = 1$ description but with the correct initial bubble velocity, which includes the A dependence. As shown by Alon *et al.* (1995c), this is the main A dependence of the process. Also plotted are the two individual non-interacting bubble evolution lines, derived from Eq. (14.47), which was shown earlier to fit the single-mode bubble evolution very well. As

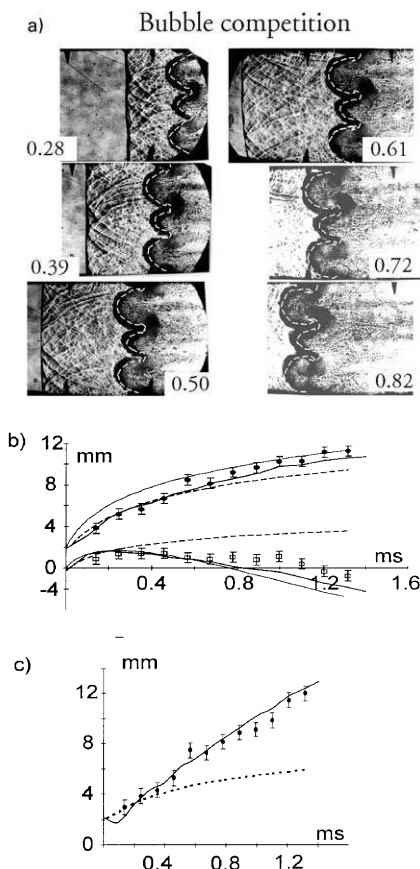


FIGURE 14.32 (a) Experimental results of the evolution of the interface for $M = 1.25$, $\lambda_1 = 27$ mm, $\lambda_2 = 17$ mm. Simulation results, dashed line. (b) Bubble height in the bubble-competition experiment: experiment, dots; potential flow model, light line; full-scale simulation, full line; and independent bubble from growth, dashed line. (c) Bubble height difference (Sadot *et al.* 1998).

can be seen, the bubble competition process is very evident and pronounced. Initially the two bubbles evolve according to the noninteracting lines, but in the nonlinear stage a strong interaction takes place, the result of which is the faster growth of the larger bubble and the shrinking of the smaller bubble downstream. The agreement between the numerical simulation and the experimental results is very good. Similar agreement is also found when comparing the experimental results with the simple potential flow model, especially in the prediction of the merger time. The bubble competition is even

more pronounced when one looks at the height difference between the tips of the two bubbles. This provides an accurate experimental measurement since it is independent of the interface location. Figure 14.32c shows the temporal evolution of the difference in the heights of the two bubbles. The rapid increase in the height difference compared to that of the two noninteracting bubbles is clearly seen, demonstrating the bubble-merger process, in which the larger bubble overtakes the smaller one.

14.5.4 RE-SHOCK EXPERIMENTS

In previous sections, we described shock tube experiments of single-mode evolution and two-bubble interaction driven by a single shock wave. However, a much more dramatic perturbation growth occurs after a re-shock passes the interface (Shvarts *et al.* 1997; Chebotareva *et al.* 1999). In the present section we extend this experiment to describe the effect of a re-shock, reflected from the end wall of the tube, on single-mode and two-bubble evolution. Finally we describe an experiment to study the evolution of a mixing zone generated from an initial random perturbation.

The shock tube apparatus used is described in Section 14.4.2. In order to create a re-shock, an end wall was placed at different distances from the interface. The results in this work are from an end wall at distances of 18 and 24 cm. The 24-cm configuration was designed to study single-mode and two-bubble interaction, where the wavelength is of the order of 20 mm. This distance allows sufficient time for the perturbation to enter well into the nonlinear stage before the re-shock. The 18-cm configuration was used for the random initial perturbation study, since the typical wavelength is much shorter (of the order of a few millimetres) and therefore less time is needed in order to reach a well-developed mixing stage before the re-shock. The experiments are compared to full numerical simulations using an ALE code with interface tracking and to theoretical models (for more details see Shvarts *et al.* (1997)).

14.5.4.1 Re-Shock Single-Model Experiments

In Fig. 14.33a the interface evolution for $\lambda = 26$ mm is shown at various times. The initial amplitude is $a_0 = 2$ mm. The re-shock reaches the perturbed interface at about $t = 2.1$ msec.

The perturbation is seen to develop an asymmetric bubble-spike shape before the re-shock, similar to that described in Sadot *et al.* (1998). The phase inversion caused by the re-shock is clearly seen immediately after the re-shock arrives at the perturbation. Later, a very nonlinear reversed bubble-spike structure is formed.

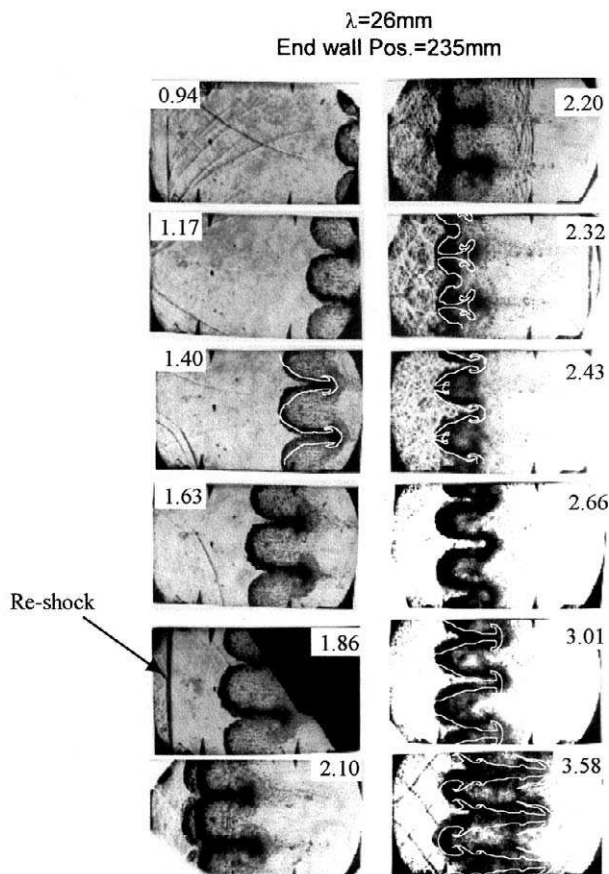


FIGURE 14.33 (a) Experimental results of the single-mode evolution for an $M = 1.2$ Air/SF₆ case, $\lambda = 26$ mm, $a_0 = 2$ mm, and end wall located at 235 mm. On some of the pictures a simulation was superimposed (white line).

The bubble and spike evolution, relative to the unperturbed interface, are compared in Fig. 14.33b and c to a theoretical model (Sadot *et al.* 1998), which accounts for the linear, early nonlinear, and asymptotic stages of the growth. In Fig. 14.33a the growth before the re-shock is shown, and in Fig. 14.33b the growth after the re-shock is shown, until $t = 3.2$ msec, when a rarefaction wave from this end wall reaches the interface. The model was initiated in Fig. 14.33b using the experimentally measured perturbation velocity immediately after the re-shock. Very good agreement is found between the experimental and theoretical results. The interface shape and growth are also in very good agreement with full-scale simulations (see Fig. 14.33a). Thus, even

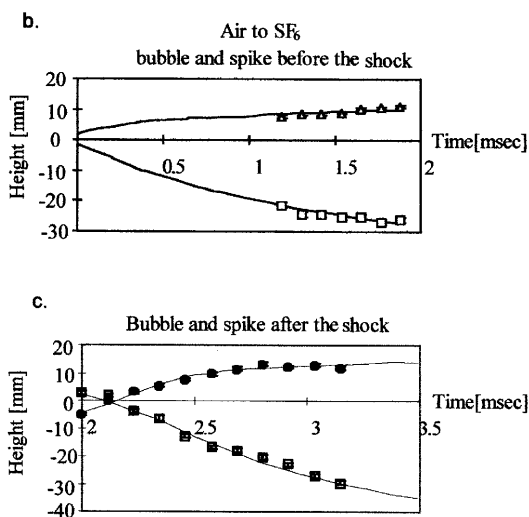


FIGURE 14.33 (b) and (c) Experimental and potential flow model results for bubble and spike evolution in the single-mode case (b) before the re-shock, (c) after the re-shock.

though the re-shock interacts with a perturbation, which is highly evolved both in space and velocity, a simple incompressible model describes the evolution after re-shock well.

14.5.4.2 Re-Shock Two-Bubble Experiments

In order to investigate whether the bubble competition phenomenon, which is a dominant mechanism in multimode evolution, is present after re-shock, we performed two-bubble interaction experiments with a re-shock. An array of alternating large (27 mm) and small (17 mm) bubbles was used, with the central part of the membrane consisting of a small bubble flanked by two large bubbles. However, as opposed to the structure used in Sadot *et al.* (1998), the initial perturbation was the inverse of that used in Sadot *et al.* (1998) with the bubble tip pointing toward the initial shock.

The interface evolution is shown in Fig. 14.34a, comparing the experimental results with full numerical simulations. Immediately after the shock passage, a small spike is generated flanked by two large spikes. Since the two centered bubbles, on either side of the small spike, are identical, no bubble competition is expected at this stage. After the passage of the re-shock, at time $t = 2.1$ msec, the perturbation inverts phase—the spikes become bubbles. The perturbation is thus inverted, creating a small bubble flanked by two large bubbles. As is clearly seen in both experiments and simulation, the bubble

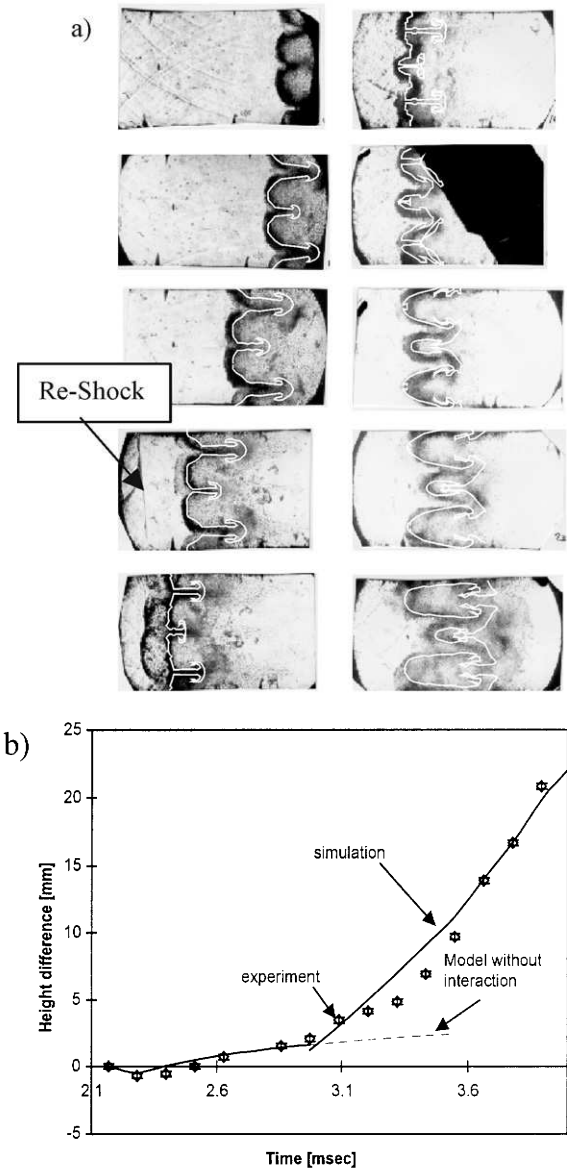


FIGURE 14.34 (a) Experimental and numerical (white line) results for the instability evolution in the two-bubble case. $M = 1.2$ air/SF₆, $\lambda_1 = 17$ mm, $\lambda_2 = 27$ mm, $a_1 = 2$ mm, $a_2 = 1$ mm, end wall located at 235 mm. (b) Bubble height difference in the two-bubble case of (a) after re-shock. Shown are the experimental and numerical results. Also shown is the predicted difference in bubble heights when no bubble interaction takes place.

competition process begins after the re-shock passage. Very good agreement can be seen between simulation and experiment at all stages—the initial (before the re-shock) stage, during phase inversion, and well after phase inversion, where bubble competition takes place. In Fig. 14.34b, the difference between the two bubble heights after the reshock is shown, comparing the experimental and the numerical simulation results with the height difference predicted for two independent bubbles.

This demonstrates the bubble competition, similar to the single-shock experiment. At early times after the re-shock the bubbles grow independently. After about 1 msec after re-shock, the height difference is seen to grow faster than that expected after the growth of independent bubbles as a result of the bubble competition process. Later on, 1.4 msec after re-shock, the height difference begins to grow much faster. This is attributed to a rarefaction wave that reaches the interface from the end wall. The agreement with the full simulation is very good at all stages.

14.5.4.3 Random Initial Perturbation Experiments

In order to study the evolution of the turbulent mixing zone (TMZ) from a random initial perturbation, a flat membrane with no imposed initial perturbation was used. The end wall was placed at 18 cm, and thus the re-shock arrives at an earlier time than in the previous cases—at $t = 1.6$ msec. Before the re-shock passage the TMZ thickness is small and only after the re-shock hits the interface is the growth pronounced.

In Fig. 14.35a, three representative frames show the TMZ at three times after the re-shock passage. In Fig. 14.35b the TMZ thickness is compared with simulation results. The simulation was initiated from an initial short-wavelength multimode perturbation with an initial rms amplitude of 1 mm. Shown in Fig. 14.35b are the numerical simulation predictions for the 10–90% and 1–99% TMZ.

The mixing zone grows slowly before the re-shock, with a best-fit power law of roughly $t^{0.5}$. After the re-shock, the mixing zone thickness initially decreases due to shock compression, and then starts to grow at a much-increased rate. This growth follows a power law of roughly $t^{0.7}$. At time $t = 2.6$ msec, the rarefaction wave from the end wall arrives at the interface, causing a further increase in the growth rate, due to the density decrease and the interface deceleration. The comparison between the experimental TMZ growth rate and the simulation is good.

It is at present difficult to accurately deduce the bubble and spike front growth separately in the random front experiment. In Fig. 14.35c, the numerical results for the bubble and spike fronts, defined as 1–99% (dotted line) and 10–90% (full line), respectively, are shown and compared with the

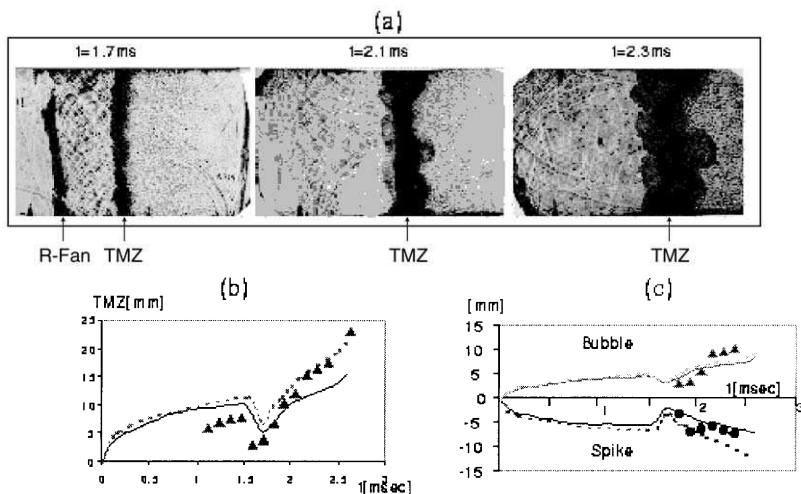


FIGURE 14.35 Evolution of a random initial perturbation. (a) Schlieren photographs after re-shock at $t = 1.7, 2.1, 2.3$ msec. (b) Turbulent mixing zone evolution, experiment vs simulation. (c) bubble and spike eight evolution (relative to the unperturbed interface), experiment vs simulation. $M = 1.2$ air/ SF_6 , end wall located at 180 mm. Simulation lines are 1–99% (dotted) and 10–90% (full)

estimated bubble and spike front locations deduced from the experimental data. The asymmetry between the bubble and spike front power laws is clearly seen in both the numerical and experimental results. The agreement between the experimental and the numerical results is fair, considering the relatively large error in defining the fronts and the unperturbed interface in the experiment.

14.6 SUMMARY

In this chapter we have presented a systematic treatment of shock-wave-induced hydrodynamic mixing instabilities, based on models, simulations, and experiments. The description, based on penetration of the light fluid in the heavy one (bubbles) and the heavy into the light (spikes), provides a comprehensive and understanding of the evolution of the instability for both single-mode and multimode cases.

However, a number of phenomena require further attention and even fundamental treatment. Among them are the following:

1. The case in which the compressibility of the material plays an important role throughout the whole evolution; see Section 14.4.2.6.

2. The evolution of the instability in nonplanar geometries, such as those of interest in ICF and in astrophysical phenomena. An initial step toward such a research can be found in Yedvab *et al.* (1997). A model has been developed and experiments are being carried out in high-power laser laboratories (see Glendinning, 1999).
3. Experimental investigation of 3D effects remains to be extended systematically in both shock tube and high-power laser facilities (see Edwards, 1999).

We anticipate that in the next few years these studies will provide a more comprehensive description of shock-wave-induced hydrodynamic instabilities.

ACKNOWLEDGMENTS

The author thanks their group members, L. Arazi, G. Ben-Dor, Y. Elbaz, G. Erez, L. Erez, J. Hecht, D. Kartoon, L. A. Levin, D. Ofer, E. Sarid, Y. Srebro, Y. Yedvab and A. Yosef-Hai, for many contributions during the past 10 years, during which our research was carried out.

REFERENCES

- Aleshin, A.N., Lazareva, E.V., Zaytsev, S.G., Rozanov, V.B., Gamalii, E.G., and Lebo, I.G. (1991). "Linear nonlinear and transient stage in the development of the Richtmyer–Meshkov instability," *Sov. Physics Dokl.* 35: 159.
- Alon U., Hecht J., Mukamel D. and Shvart D, (1994) "Scaling Invariant Mixing Rates of Hydrodynamically Unstable Interface", *Phys. Rev. Lett.* 72 (18) 2867.
- Alon, U., Shvarts, D., and Mukamel, D. (1993). "Scale invariant regime in Rayleigh–Taylor bubble front dynamics," *Phys. Rev. E* 48: 1008.
- Alon, U., Hecht, J., Ofer, D., and Shvarts, D. (1995a). "Power laws and similarity of Rayleigh–Taylor and Richtmyer–Meshkov mixing fronts at all density ratios," *Phys. Rev. Lett.* 74: 534.
- Alon, U., Ofer, D., and Shvarts, D. (1995b). "Rayleigh–Taylor instability under a time dependent acceleration" in Proceedings of the Fifth International Workshop on the Physics of Compressible Turbulent Mixing, edited by R. Young, J. Glimm, and B. Boston, p. 1.
- Alon, U., Ofer, D., and Shvarts, D. (1995c). "Scaling laws on nonlinear Rayleigh–Taylor and Richtmyer–Meshkov mixing," in Proceedings of the Fifth International Workshop on the Physics of Compressible Turbulent Mixing, edited by R. Young, J. Glimm and B. Boston, p. 8.
- Andronov, V.A., Bakhrakh, S.M., Meshkov, E.E., Mokhov, V.N., Nikiforov, V.V., Pevnitskii, A.V., and Tolshmyakov, A.I. (1976). "Turbulent mixing at contact surface accelerated by shock waves," *Sov. Phys. JETP* 44: 424.
- Berning, M. and Rubenchik, A.M. (1998). "A weakly nonlinear theory for the dynamical Rayleigh–Taylor instability," *Phys. Fluids* 10: 1564.
- Brouillette, M. and Sturtevant, B. (1989). "Growth induced by multiple shock waves normally incident on plan gaseous interface," *Physica D* 37: 248.
- Chebotaeva, E.I., Aleshin, A.N., Zaytsev, S.G., and Sergeev, S.V. (1999). "Investigation of interaction between reflected shocks and growing perturbation on an interface," *Shock Wave* 9: 81.

- Cole, R.L., and Tankin, R.S. (1973). "Experimental study of Taylor instability," *Phys. Fluids* 16: 1810.
- Dimonte, G. (1999). "Spanwise homogeneous buoyancy-drag model for Rayleigh–Taylor mixing and experimental verification," accepted for publication in *Phys. Plasmas*.
- Dimonte, G. and Remington, B. (1993). "Richtmyer–Meshkov experiments on the nova laser at high compression," *Phys. Rev. Lett.* 70: 1806.
- Dimonte, G. and Schneider, M. (2000). "Density ratio dependence of Rayleigh–Taylor mixing for sustained and impulsive acceleration histories," *Phys. Plasmas* 12: 304.
- Dimonte, G., Frerking, C.E., Schneider, M., and Remington, B. (1996). "Richtmyer–Meshkov instability with strong radioactively driven shock," *Phys. Plasmas* 3: 614.
- Duff R. E., Harlow F.H. and Hirt C. W. (1962) "Effects of Diffusion on Interface Instability between Gases" *Phys. of Fluids* 5, (4) 417.
- Edwards, M.J. (1999). "Turbulent hydrodynamics experiments using new plasma piston," *Bull. Am. Phys. Soc. Div. Plasma*, 17.
- Emmons, H.W., Chang, C.T., and Watson, B.C. (1960). "Taylor instability of finite surface waves," *J. Fluid Mech.* 7: 177.
- Freed N., Ofer D., Shvarts D., and Orszag S. O., (1991) "Two-phase flow analysis of self-similar turbulent mixing by Rayleigh–Taylor instability," *Phys. Fluids A* 3, 912.
- Gardner C. L., Glimm J., McBryan O., Menikoff R., Sharp D. H., and Zhang Q., (1988) "The Dynamics of Bubble Growth for Rayleigh–Taylor unstable Interfaces" *Phys. Fluids* 31 (3), 447.
- Glendinning, S. (1999). "Ablation front Rayleigh–Taylor growth experiments in spherically convergent geometry," in *Bull. Am. Phys. Soc. Plasma*, 155.
- Glimm J., Li X. L., Menikoff R., Sharp D. H., and Zhang Q., (1990) "A numerical study of bubble interactions in Rayleigh–Taylor instability for compressible fluids," *Phys. Fluids A* 2, 2046.
- Haan, S.W. (1991). "Weakly nonlinear hydrodynamic instabilities in inertial fusion," *Phys. Fluids B* 3: 2349.
- Hecht, H., Alon, U., and Shvarts, D. (1994). "Potential flow models of Rayleigh–Taylor and Richtmyer–Meshkov bubble fronts," *Phys. Fluids* 6: 4019.
- Hecht, J., Ofer, D., Alon, U., Shvarts D., Orszag, S.A., and McCrory, R.L. (1995). "Three dimensional simulation and analysis of the nonlinear stage of the Rayleigh–Taylor instability," *Laser Particle Beams* 13: 423.
- Holmes, R.L., Dimonte, G., Fryxell, B., Gitting, M.L., Grove, J.W., Schneider, M., Sharp, D.H., Velikovitch, A.L., Weaver, R.P., and Zhang, Q. (1999). "Richtmyer–Meshkov instability growth: experiments simulation and theory," *J. Fluid Mech.* 389: 55.
- Houas, L. and Chemouni, I. (1996). "Experimental investigation of Richtmyer–Meshkov instability in shock tube," *Phys. Fluids* 8: 614.
- Jacobs, J.W. and Catton, I.L. (1988). *J. Fluid Mech.* 187: 329.
- Jacobs, L.W. and Niederhaus, C.E. (1997). "PLIF flow visualization of single and multi mode incompressible Richtmyer–Meshkov instability," in *Proceedings of the Sixth International Workshop on the Physics of Compressible Turbulent Mixing*, edited by G. Jourdan and L. Houas, p. 214.
- Jacobs, J.W. and Sheeley, J.M. (1996). "Experimental study of incompressible Richtmyer–Meshkov instability," *Phys. Fluids* 8: 405.
- Jones, M. and Jacobs, J.W. (1997). "A membraneless experiments for the study of Richtmyer–Meshkov instability of a shock accelerated gas interface," *Phys.*
- Jourdan, J., Houas, L., and Billiotte, M. (1997). "Density evolution within a shock accelerated gaseous interface," *Phys. Rev. Lett.* 78: 452.
- Kull, H.J. (1986). "Nonlinear free-surface Rayleigh–Taylor instability," *Phys. Rev. A* 33: 1957.
- Layzer, D. (1955). "On the instability of superposed fluids in a gravitational field," *Astrophys. J.* 122, 1.

- Lindl, J.D. (1998). *Inertial Confinement Fusion*. Springer, New York.
- Lewis, D.J. (1960). "The instability of liquid surfaces when accelerated in direction perpendicular to their planes," *Proc. R. Soc. London, Ser. A*. **202**: 81.
- Meshkov, E.E. (1969). "Instability of the interface of two gases by a shock wave," *Izv. Acad. Sci. USSR Fluid Dynamics* **4**: 101.
- Meyer, K.M. and Blewett, P.J. (1972). "Numerical investigation of the stability of a shock-accelerated interface between two fluids," *Phys. Fluids* **15**: 753.
- Nikiforov, V.V., Andronov, V.A., and Razin, A.N. (1995). "Development of a turbulent mixing zone driven by a shock wave," *Phys. Dokl.* **40**(7): 333.
- Ofer, D. (1995). "Nonlinear evolution of the multi-mode Rayleigh–Taylor hydrodynamics instability," Ph.D. thesis, Weizmann Institute of Science.
- Ofer D., Shvarts D., Zinamon Z., and Orsag S. A. (1992)., "Mode coupling in nonlinear Rayleigh–Taylor instability" *Phys. Fluids B* **4**, 3549.
- Oron, D., Alon, U., and Shvarts, D. (1998). Scaling laws of the Rayleigh–Taylor ablation front mixing zone evolution in inertial confinement fusion," *Phys. Plasmas* **5**: 1467.
- Oron, D., Sadot, O., Srebro, Y., Rikanati, A., Yedvab, Y., Alon, U., Erez, L., Erez, G., Ben-Dor, G., Levin, L.A., Ofer, D., and Shvarts, D. (1999). "Studies in the nonlinear evolution of the Rayleigh–Taylor and Richtmyer–Meshkov instabilities and their role in inertial confinement fusion," *Laser and Particle Beams* **17**(3): 465.
- Poggi, F., Thorembey, M.H., and Rodriguz, G. (1998). "Velocity measurements in turbulent gaseous mixtures induced by Richtmyer–Meshkov instability," *Phys. Fluids* **10**: 2698.
- Ratafia M. (1973) Experimental investigation of RayleighTaylor instability. *Physics-of-Fluids*. **16**,8 1207.
- Lord Rayleigh (1900). "Investigation of the character of the equilibrium of an incompressible heavy fluid of variable density," In *Scientific Papers*, Vol. 2, p. 200.
- Read K. I., (1984) "Experimental investigation of turbulent mixing by RayleighTaylor instability," *Physica D* **12**, 45
- Remington, B.A., Weber, S.V., Haan, S.W., Kilkenny, J.D., Glendinning, S.G., Wallace, R.J., Goldstein, W.H., Wilson, B.G., and Nash, K.J. (1993). "Laser drive hydrodynamics instability experiments," *Phys. Fluids B* **5**: 2589.
- Remington B. A., Kane J., Drak R. P., Glendinning S. G., Estarook K., London R., Castor J., Wallace R. J., Arnett D., Liang E., McCray R., Rubenchik A., Fryxell B. (1997) "Supernova Hydrodynamics Experiments on the Nova Laser", *Phys. Plasmas* **4** (5), 1994.
- Ribe, F.L. (1975). "Fusion reactor system," *Rev. Mod. Phys.* **47**: 7.
- Richtmyer, R.D. (1960). "Taylor instability in shock acceleration of compressible fluids," *Commun. Pure Appl. Math.* **13**: 297.
- Rikanati A., Oron D., Sadot O., Shvart D., (2000) "Effect of High Machs Number and High Initial Amplitude on the Richtmyer–Meshkov Instability" to be published
- Rikanati, A., Alon, U., and Shvarts, D. (1998). "Vortex model for the nonlinear evolution of the multimode Richtmyer–Meshkov instability at low Atwood numbers," *Phys. Rev. E* **58**: 7410.
- Sadot, O., Erez, L., Alon, U., Oron, D., Levin, L.A., Erez, G., Ben-Dor, G., and Shvarts, D. (1998). "Study of nonlinear evolution of single-mode and two-bubble interaction under Richtmyer–Meshkov instability," *Phys. Rev. Lett.* **80**: 1654.
- Sadot, O., Yosef-Hai, A., Rikanati, A., Kartoon, D., Oron, D., Arazi, L., Levin, A.L., Sarid, E., Ben-Dor, G., and Shvarts, D. (1999). "Experimental studies of the dependence of the Richtmyer–Meshkov instability on the Atwood number and dimensionality", in the Bulletin of the American physics society of the division of plasma. 57.
- Sharp D. H., (1984) "An overview of Rayleigh–Taylor instability," *Physica D* **12**, 3.
- Shvarts D., Alon U., Ofer D., McCrory R.L., and Verdon C.P., (1995), "Nonlinear evolution of multimode RayleighTaylor instability in two and three dimensions" *Phys. Plasmas* **2**, 2465.

- Vorobieff P., Rightley P. M. and Benjamin R.F. (1997), "Power-Law Spectra of Incipient Gas-Curtain Turbulence", *Phys. Rev. Lett.* **81**, 2240.
- Shvarts, D., Sadot, O., Erez, L., Oron, D., Alon, U., Hanoch, G., Erez, G., and Ben-Dor, G. (1997). "Effects of re-shock on Richtmyer–Meshkov mixing; an experimental, numerical and theoretical study," in Proceedings of the Sixth International Workshop on the Physics of Compressible Turbulent Mixing, edited by G. Jourdan and L. Houas, p. 464.
- Shvarts, D., Oron, D., Kartoon, D. Sadot, O., Srebro, Y., Yedvab, Y., Ofer, D., Levin, A. L., Sarid, E., Ben-Dor, G., Erez, L., Erez, G., Yosef-Hai, A., Alon, U., and Erez, L. (2000). "Scaling laws of nonlinear Rayleigh–Taylor and Richtmyer–Meshkov instabilities in two and three dimensions," in *Inertial Fusion Sciences and Applications 99*, edited by C. Labaune, W.J. Hogan and K.A. Tanaka, Elsevier.
- Smith, A.V., Philpott, M.K., Miller, D.B., Holder, D.A., Cowperthwaite, N.W., and Youngs, D.L. (1997). "Shock tube investigation of the Richtmyer–Meshkov instability due to a single discrete perturbation on a plane gas discontinuity," in Proceedings of the Sixth International Workshop on the Physics of Compressible Turbulent Mixing, edited by G. Jourdan and L. Houas, p. 480.
- Souffland, D., Gregorio, G., Gauthier, S., Poggi, F., and Koenig, J.M. (1997). "Measurements and simulation of the turbulent energy levels in mixing zones generated in shock tube," in Proceedings of the Sixth International Workshop on the Physics of Compressible Mixing, edited by G. Jourdan and L. Houas, p. 486.
- Taylor, G.I. (1950). "The instability of liquid surfaces when accelerated in a direction perpendicular to their planes, I." *Proc. R. Soc. Lond. A* **201**: 192.
- Vandenboomgaerde, M., Mugler, C., and Gauthier, S. (1998). "Impulsive model for the Richtmyer–Meshkov instability," *Phys. Rev. E* **58**: 1874.
- Velikovich, A.L. and Dimonte, G. (1996). "Nonlinear perturbation theory of incompressible Richtmyer–Meshkov instability," *Phys. Rev. Lett.* **76**: 3112.
- Yedvab, Y., Alon, U., Oron, D., and Shvarts, D. (????). "Single and multi-mode Rayleigh–Taylor instability in cylindrical system," in Proceedings of the Sixth International Workshop on the Physics of Compressible Turbulent Mixing, edited by G. Jourdan and L. Houas, p. 528.
- Yang, Y., Zhang, Q., and Sharp, D. (1994). "Small amplitude theory of Richtmyer–Meshkov instability," *Phys. Fluids* **6**: 1856.
- Youngs D. L., (1984) "Numerical simulation of turbulent mixing by Rayleigh–Taylor instability," *Physica D* **12**, 32.
- Zaytsev, S.G., Lazareva, E.V., Chernukha, V.V., and Belyaev, V.M. (1985). "Intensification of mixing at the interface between media of different densities upon the passage of a shock wave through it," *Sov. Phys. Dokl.* **30**(7): 579.
- Zhang, Q. and Sohn, S.I. (1997). "Nonlinear theory of unstable fluid mixing driven by shock wave," *Phys. Fluids* **9**: 1106.

This Page Intentionally Left Blank

Shock Wave Propagation in Multi-Phase Media

15.1 Shock Wave Propagation in Porous Media

BERIC W. SKEWS

School of Mechanical Engineering, University of the Witwatersrand, PO WITS, 2050, South Africa

AVI LEVY AND DAVID LEVI-HEVRONI

Pearlstone Center for Aeronautical Engineering, Department of Mechanical Engineering, Ben-Gurion University of the Negev, Beer-Sheva 84105, Israel

-
- 15.1.1 Introduction
 - 15.1.2 General Description of the Wave Propagation
 - 15.1.3 The Nature of Porous Foams
 - 15.1.4 Scientific Background
 - 15.1.4.1 Systems with Flexible Skeletons
 - 15.1.4.2 Systems with Rigid Skeletons
 - 15.1.4.3 Blast Wave Loading
 - 15.1.4.4 Multidimensional Studies
 - 15.1.4.5 Theory and Modeling
 - 15.1.5 Macroscopic Governing Equations
 - 15.1.5.1 The Assumptions
 - 15.1.5.2 The Balance Equations
 - 15.1.6 Case Studies
 - 15.1.6.1 One-Dimensional Shock Wave Interaction with Rigid Porous Material
 - 15.1.6.2 One-Dimensional Shock Wave Interaction with Flexible Foam
 - 15.1.6.3 Regular Reflection from a Rigid Porous Surface in Pseudo-Steady Flows

References

15.1.1 INTRODUCTION

Early studies of the interaction of shock waves with porous materials were largely motivated by the need to explore methods to attenuate the effects of a wave. This could be simply to reduce noise levels as is encountered in acoustic treatment of surfaces, or for reducing loads such as in ducts such as may result from an accidental explosion in an industrial plant, and in free space as the result of an external explosion interacting with structures. The need to attenuate peak pressure and amplitude is important in cases such as in the design of protective apparel and where structural damage or response needs to be minimized. These studies form part of the broader field of shock wave propagation in two-phase media, as contained in other sections of this chapter. These include areas such as propagation in dusty gases, bubbly liquids, and liquid foams. They are of particular interest because of the nonlinear nature of the phenomena and the strong coupling between the phases.

Most investigations have concentrated on porous media where the pores are interconnected within a solid matrix and there is thus percolation of the gas through the skeleton material, although the case for closed cellular foams will be briefly dealt with. Two main cases for the permeable material can be identified: one where the matrix can be treated as being rigid since its stiffness is very much higher than that of the gas, and one where the matrix may itself deform under load as well as allowing flow through it. A particularly interesting case is where the matrix stiffness is somewhat lower than that of the fluid, since such materials, when placed adjacent to a rigid wall, exhibit the interesting property of amplifying the wall pressure above that which would have been achieved with no covering present. It is this feature that has driven much of the research. Research has progressed to a considerable extent over the past 30 years and now extends to studies of both rigid and compressible porous materials, with both liquid and gaseous pore fluid, and in more than one dimension.

15.1.2 GENERAL DESCRIPTION OF THE WAVE PROPAGATION

One of the most commonly conducted experiments is for the case of a block of compressible porous material placed against the rigid rear wall in a shock tube. On the assumption that this interaction may be represented by the one-dimensional refraction of a wave at the interface between two homogeneous materials, the resulting wave diagram is that shown in Fig. 15.1.1a. When the incident wave (1–2) strikes the material, a reflected wave (2–3) propagates

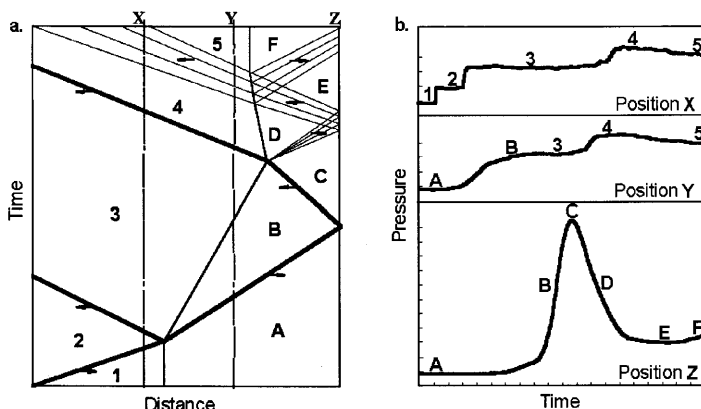


FIGURE 15.1.1 General description of wave propagation. (a) Waves diagram, and (b) typical pressure measurements obtained from tests in a shock tube using polyurethane foam with transducers positioned as indicated in (a).

back into the gas, and a transmitted wave (A–B) propagates into the foam, resulting in compression of the foam material in region B, and the movement of its front face toward the rigid wall. The transmitted wave is then reflected off the end wall compressing the foam still further (region C), and when reaching the gas/foam interface gives rise to a transmitted shock wave propagating out into the gas, and an expansion wave reflected back into the foam material. This latter wave will in turn reflect off the back wall, relieving the pressure there. On reaching the interface this expansion wave will be transmitted into the gas, and a compression wave back into the foam material. Typical pressure measurements obtained from tests in a shock tube using polyurethane foam with transducers positioned as indicated in Fig. 15.1.1a, are given in Fig. 15.1.1b. (Skews *et al.*, 1993). The pressure traces are marked with symbols corresponding to the regions of flow indicated on the wave diagram. These generally follow the expected pattern, although they differ in a number of respects from what would have been obtained if the simple refraction wave diagram were an accurate description of the phenomena with the foam behaving as a gas. These differences have been the focus of much of the recent research, and the reasons for the deviations from the expected waveform are discussed later. The most noticeable effect evident in the pressure traces is the lack of the very steep gradients characteristic of shock waves. Even the compression waves spread out in time as a consequence of the interaction between the flow and the solid matrix.

The earliest experimental and theoretical study that has been located, using porous foam, is that of Monti (1970). He was concerned with the general

behavior of a shock wave impacting on an arbitrary, deformable, solid material, without really being concerned with issues relating to porosity. The basic approach adopted was the simple refraction model illustrated in Fig. 15.1.1a. He found a closed-form solution for the case where the solid is perfectly elastic. Interestingly, for this case he established that under certain conditions, if the deformable solid is mounted onto a rigid wall, the overpressure could be higher than that obtained with reflection off the rigid wall alone, that is, in region C of Fig. 15.1.1a. In order to assess the theory against experiment, Monti sought a material that was sufficiently soft to give a measurable difference in reflected wave pressure. He settled for expanded foam material, the general properties of which are discussed in the next section. He established the stress-strain behavior of his material, fitted a polynomial to this characteristic, and then solved the resulting equations numerically. No account was taken of the behavior of the interstitial gas.

The instrumentation that Monti used consisted of a single transducer situated ahead of the foam. Thus, only the strength of the reflected waves in the gas in front of the foam face was measured, and no comparisons could be made with the strength, or nature, of the transmitted wave, or of the predicted pressure amplification on the back wall. He obtained pressure traces similar to that of the top trace in Fig. 15.1.1b. The rounding of the pressure trace of the second reflected wave was not commented on, and the significance of this was only appreciated some 20 years later. The approach adopted by Monti contained two main assumptions, which were to become main characteristics of investigations of the process for some considerable time after his paper: first, the assumption of simple refraction, with its associated implication of no gas flow across the interface; and second, the treatment of the foam as a single phase material, with its implication of a single sharp-fronted transmitted wave into the foam material.

15.1.3 THE NATURE OF POROUS FOAMS

The vast majority of tests done on highly flexible foam slabs have used porous polyurethane or rubber foams, although polyurethane tests have been predominant. Densities normally range from 15 to 40 kg/m³, although some tests have been done well outside this range. These materials come in two types: open cell types such as used for pillows and mattresses, and closed cell, which is generally used for thermal insulation. These materials are highly nonlinear and display the stress-strain behavior indicated in Fig. 15.1.2. The elongation characteristic is generally divided into three main regions (Gibson and Ashby, 1988): a small linearly elastic region, followed by a plateau in which the stress level hardly changes, followed by a densification region where the stress

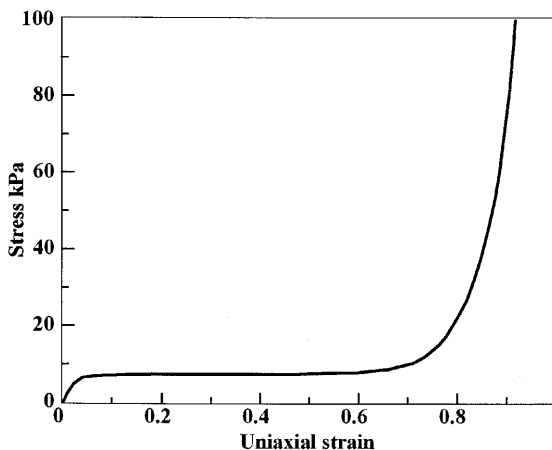


FIGURE 15.1.2 Typical stress-strain behavior of highly flexible foam slabs.

increases very rapidly. The plateau region results when the walls of the cells buckle under the applied load, and the densification or compaction region when the cell walls come into contact with each other, resulting in the material stiffening up very rapidly.

A number of workers have also established that the stress-strain relation is strain-rate dependent (e.g., Onodera and Takayama, 1994; Gvozdeva *et al.*, 1996; Gvozdeva *et al.*, 1997), although the conventional testing machines used have not been able to test at strain rates typical of shock tube experiments (80 m/s). Gvozdeva *et al.* (1996) inferred the position of the shock wave tests in the stress-strain plane and found them to be very much higher than in quasi-static tests. The inference drawn is that this is because of the increasing difficulty of the interstitial gas to escape as the strain rate increases. However, it does indicate that there are some questions still to be answered regarding work which models the material as not being sensitive to strain rate. The nature and study of this dynamic permeability still requires significant attention (Smeulders *et al.*, 1992; Johnson, 1989). Nernberg *et al.* (1997) have suggested means of developing models for use in simulations that will take account of strain rate effects.

Some tests with very high density foams (290 kg/m^3) having low porosity ($\phi = 0.76$) have shown significant hysteresis effects but limited strain rate effects (Yasahura *et al.*, 1995). Furthermore, this material also showed significant differences between uniaxial stress loading and uniaxial strain loading. For these foams there is no linear elastic component to the stress-strain characteristic, since the cell walls buckle at very low loads.

Furthermore, some materials exhibit an additional effect — that when the specimen is laterally constrained, as it is in a shock tube, the stress–strain curve is modified and an inflection point is evident in the plateau region, that is, there is a small region where stress reduces as the strain increases. Onodera and Takayama (1995) found some evidence of this affecting the nature of the phenomena depending on whether the shock wave pressure is above or below this inflection pressure. As far as is known, this has not been explored further.

It is also evident that the nature of the foam response will be sensitive to the nature of the confinement, as well as the method of loading. Some attempts have been made to model the behavior under conditions of uni-, bi-, and tri-axial loading conditions (Ben-Dor *et al.*, 1996a). There are very few data available where the differences between these loading conditions have been specifically investigated.

In order to obtain pressure-drop data, most workers requiring it have used simple steady flow rigs where the flow rate can be measured and the pressure drop monitored (e.g., Olim *et al.*, 1994, and Levy *et al.*, 1995). These experiments are generally conducted at comparatively low values of the superficial velocity. In general the data is found to satisfy the Forchheimer equation, and this is then assumed to be valid over the full range of test conditions. This led to poor comparison between shock tube experimental data and predictions of numerical simulations. As a consequence, Olim *et al.* (1994) multiply the values of the Forchheimer coefficients by 5–8, for flexible foam, and Levy (1995) by 2 for rigid porous material. This difference is presumably due to the unsteady effect on the momentum transfer between the gas and the porous materials. Hence, it was concluded that the values of the pressure drop, which were obtained for low superficial velocities in steady-state experiments, cannot be used for numerical predictions of abrupt loading. Recall that the stress–strain relation was also found to be much higher in dynamic loading than in a steady-state test. The derivation of the Forchheimer terms for the macroscopic balance equations in the case of multiphase porous media and their application to wave propagation in porous media was presented by Levy *et al.* (1999). It was shown that these terms represent the exchange between the phases at their common interface. Using these terms, a very good agreement was evident with experimental data. Ideally, tests should be conducted under appropriate conditions of uniaxial strain. Such tests give a strong indication of the effects of foam structure. Kitagawa and Yasahura (1997) for example, has tested two foams with very similar densities and porosities, but with different structure, and have found significantly different drag curves.

Experimental measurement of tortuosity has not yet reached a satisfactory state and it is frequently inferred indirectly from other measurements. A new technique using the increase in time of flight of an ultrasonic pulse between

two transducers when a layer of material is inserted has been suggested (Allard *et al.*, 1994). This could replace the more traditional technique using resistivity measurements by saturating the skeleton with a conducting fluid. This technique will, of course, only work for materials with a non-conducting skeleton. Levy *et al.* (1996a, 1996b) presented an analytical model for estimating the tortuosity by estimating the ratio of the speed of sound of the air inside the porous medium to that of pure air:

$$T^{*2} + \frac{1}{\gamma - 1} T^* - \frac{\gamma}{\gamma - 1} \left(\frac{a}{a_{\text{pure}}} \right)^2 = 0. \quad (15.1.1)$$

A further issue that has so far not been addressed at all is that stress strain information has always been obtained from cold tests. It is known from a number of numerical studies that heat transfer between the gas and the skeleton is important. What is not known is the degree to which the stiffness of the foam material is affected by temperature, particularly the high temperatures that will result from the significant degree of gas compression that occurs. Levy *et al.* (1998) conducted a parametric study on shock wave interaction with thermoelastic porous material. They concluded that the influence of the thermal expansion is negligible under the range of the tested conditions.

15.1.4 SCIENTIFIC BACKGROUND

Although the vast majority of tests have been done on highly flexible foam slabs, some work has been done on rigid porous samples. Both types of material come in two forms: open cell and closed cell. Although the basic physical wave configuration is similar, different behaviors are apparent due to the flexibility of the material.

15.1.4.1 SYSTEMS WITH FLEXIBLE SKELETONS

Over the decade from 1975 to 1985 two groups in Russia did the major investigations into shock wave loading of permeable foams, characterizing a number of interesting features of their behavior, and laying the groundwork for further study. The main physical model employed was the simple refraction model described earlier. The first measurements of pressure alongside and behind compressible porous material mounted on the back wall of a shock tube were conducted by Gelfand *et al.* (1975). Polyurethane foam blocks with lengths of 150 to 600 mm were used. These were the first experimental measurements to show that the peak pressure on the back wall is considerably

higher than what would be obtained with no foam present. The authors interpreted this result as being due to the momentum associated with the solid phase being set in motion, being transferred to the back wall. Furthermore they noted the longer rise time of the transmitted wave and interpreted this as being due to the large difference in acoustic resistance between air and foam ($\rho_a = 4.2 \times 10^2 \text{ kg/m}^2\text{s}$ for air and 4×10^3 for the foam material).

In 1983 Gelfand *et al.* published additional results on shock interaction with polyurethane foams and established a number of the features that have since become well known to workers in the field. Two different polyurethane foams were tested with densities of 20 and 35 kg/m^3 , and lengths between 300 and 800 mm, and with no backing to the foam, so that waves transmitted through the foam plug could be studied. The significant spreading out of the transmitted wave propagating through the foam was noted. A simple refraction model was assumed at both interfaces, that is, the flow was assumed to be that of a shock wave striking a finite length slug of a different homogeneous material situated within the tube. Specimens both with a side wall gap (1 mm) and with an interference fit were tested and clearly illustrated the effect of a wave moving through the small gap at a velocity faster than that in the foam. It was noted that the plug was set into motion down the tube, but no quantitative information was given as to its velocity. It was also shown that at the gas/foam interface the incident shock was reflected with an increase of pressure, whereas at the foam/gas interface the wave is attenuated to a value lower than that of the incident wave. An interesting theoretical analysis was presented, which was the first attempt to take into account the two-phase nature of the material. This was based on the concept of a pseudo-gas, as previously suggested by Rudinger (1965). In this model the foam/gas combination is treated as a single-phase medium with thermodynamic properties reflecting that of the mixture, the so-called "heavy gas" or "pseudo-gas" model. Results of the theoretical calculations using this model give reasonable predictions for the wave strengths. Some interesting studies were included for the case where there is a small gap between the downstream face of the specimen and a rigid wall. It was shown that the effect of the gap is to dramatically reduce the pressure on the back wall.

In 1985 an equally interesting paper by Gvozdeva and Faresov appeared. This presented an analytical model based on the assumption that the elasticity of the combined medium was largely determined by the elasticity of the gas and that the elasticity of the solid phase contributed little to the material response. This argument was based on the fact that the compressive strength of the skeleton at strains of 40% was of the order of 10 kPa, whereas that of the gas was at least an order of magnitude larger. The material was modeled as a collection of noninteracting solid particles suspended in a gas. Calculations of the simple refraction of the wave at the interface followed by reflection off a

rigid wall were conducted. Two sets of calculations were done, the one assuming isothermal and the other adiabatic conditions. The adiabatic calculation predicts the pressure on the back wall satisfactorily over a Mach number range of 1.3 to 1.8. The authors proposed that the discrepancy at higher Mach numbers is due to percolation of gas remote from the shock wave through the permeable skeleton, which would facilitate additional compression of the foam when the shock wave was reflected. Considerable later testing and numerical modeling have shown that the neglect of the stiffness of the foam skeleton in comparison to that of the interstitial gas is indeed a good assumption for conventional polyurethane foams, and to a large extent explains the success of the pseudo-gas treatment.

A companion paper (Gvozdeva *et al.*, 1985) notes, in particular, that the value of the maximum pressure on the back wall increases as the thickness of the foam increases up to a thickness of about 80 mm, whereafter it remains essentially constant. The final maximum value of pressure was found to be a function of both the material type and initial conditions. Complete reasons for this behavior have not yet been satisfactorily given. It is also noted that the duration of the high-pressure pulse increases as the thickness increases. These tests at high Mach numbers were also the first to show that the front face of the foam moves at constant velocity during the major part of the compression phase, following a very short initial acceleration phase.

This work was extended by Gvozdeva *et al.* (1986) with an experimental study of the impact of shock waves on porous slabs situated against a rigid wall, using specimens of polyurethane and polystyrene, the latter being semirigid. These tests were conducted with a 1-mm gap between the specimen and the side wall, which resulted in the precursor wave noted by Gelfand, but which was interpreted as being due to a wave through the solid phase. This precursor was followed by the main transmitted wave. The authors suggested that the wave transmitted into the polyurethane was a shock wave, whereas in the polystyrene the compression wave is nonlinear and of finite amplitude. For the highly compressible material it was assumed that it would behave in a similar fashion to a liquid containing gaseous bubbles, or a dusty gas. It was argued that during rapid compression of the material air does not have time to filter through the pores, that the elasticity is predominantly determined by the gaseous phase, and that the elasticity of the skeleton may be ignored. However, the rounding of the pressure trace on the back wall was ascribed to this filtration. It was also noted that the peak pressure on the back wall was followed by a number of oscillations that were found to be proportional to the length of the material. This would be consistent with the wave diagram of Fig. 15.1.1, if it were to be extended to longer times. The results confirmed the previous finding, for polyurethane, that the pressure amplification on the back wall over that for normal reflection with no foam lay midway between the

pseudo-gas model using isothermal and adiabatic assumptions. No firm conclusions could be drawn for the closed-cell polystyrene foam. A further interesting set of tests was undertaken to determine the effects of a longitudinal density gradient. This was achieved by placing two samples of different densities adjacent to each other in the shock tube. It was established that a negative gradient (with the higher density foam at the front) resulted in a reduction of the peak pressure behind the foam as well as increasing the duration of the pressure signal. This idea of utilizing longitudinal density gradients to either enhance or reduce the pressure amplification has not been taken up in later work.

Gvozdeva *et al.* (1987) applied a one-dimensional numerical model based on their previous pseudo-gas model, using the McCormick finite difference scheme with 100 elements, 50 of which were originally within the foam. Satisfactory agreement was obtained during the loading phase of the foam, but agreement deteriorated during the recovery phase. It is noted that a fairly sharp-fronted wave is found experimentally compared to later work, indicating that there may again have been a small gap between the sample and the walls of the shock tube. The experimental and calculated results for the nondimensionalized back wall and side wall pressure, as a function of Mach number and foam density (porosity 0.975), gave good agreement up to a Mach number of 1.75, whereafter there is a significant deviation in the back wall pressures. The authors ascribe this difference to the neglect of interphase motion inherent in the pseudo-gas model, and the assumptions made regarding heat transfer.

The preceding numerical model was extended by Rayevsky *et al.* (1989). They assumed a one-fluid two-temperature model with the skeleton being treated as an aggregate of absolutely hard particles, and included both the elasticity of the skeleton as well as heat flux from the gas phase to the skeleton material. However, the assumption that interphase momentum is negligible was retained. Good agreement was obtained between the experimental and theoretical results up to the point where the rarefaction wave reaches the back wall and the peak pressure is terminated. It is noted that the agreement with the previous numerical model is much improved by taking account of the heat transfer, compared to the adiabatic and thermal equilibrium models used earlier. Calculations also showed that the contribution of the elasticity of the skeleton was negligible, as assumed earlier by Gvozdeva *et al.* (1987).

An interesting aspect of this work was the extension to the case of blast wave reflection, which was simulated experimentally by allowing a shock wave to expand out of the open end of the shock tube before impinging on the foam. Of particular significance here is that on the axis of symmetry amplification at the rigid back wall occurs for Mach numbers greater than about 1.25, whereas below this value peak pressures are below that for reflection without the presence of the foam. The porous layer was 50 mm of polyurethane foam with

a density of 25 kg/m^3 . This effect was interpreted as being due to the reflection of the expansion phase of the blast, and filtration effects.

A comprehensive summary of the main findings of the Russian researchers can be found in the book by Korobeinikov (1989).

An interesting paper was presented by Henderson *et al.* (1989) at the 17th Shock Wave Symposium. Their tests used specimens very much longer than those used previously, some 1600 mm, in a circular tube, using polyurethane that was initially a snug fit in the tube. It was also noted that the front of the transmitted wave became less steep as the wave propagated down the tube. Of particular interest was the finding that the speed of the wave front, as measured by pressure transducers, decreases with increase in incident wave strength up to a Mach number of about 2.4, and then increases again. As far as is known no other workers have tested this behavior, and the reasons would be of significant interest. Very little other work exists under strong shock wave loading conditions. Sonic velocity in the material used was estimated by extrapolating the data to a pressure ratio of unity. This gives a value of some 240 m/s, a similar value to that quoted by Korobeinikov, but different from the results of some later workers. Calculations based on the elastic moduli of the material indicate a velocity very much lower than this. There can be considerable uncertainty associated with measuring the velocity of the leading edge of the wave, and thus determining the sound speed, because of the slow initial pressure increase making the location of the head of the wave uncertain. Henderson also indicated that the internal damping results in the strength of the wave reducing to below the strength of the incident wave after having propagated about 1 m into the foam. The nature of this attenuation curve has yet to be established, as all other workers have used very much shorter specimens. It is unfortunate that experiments have not been devised where very long specimens, such as used by Henderson, can be employed but that avoid the significant effects of wall friction. In his tests this resulted in the specimen remaining crumpled and compressed at the end of the tube.

A detailed study of the reflected wave field following impact of a weak shock wave on a range of foams was conducted by Skews (1991). It was shown that the pseudo-gas model of Gelfand *et al.* (1983) accurately predicts the strength of the first reflected shock wave. This agreement is somewhat surprising because there is evidence of gas entering the foam during the early stages of the process. The wave processes within the foam are clearly much more complex than allowed by the simple refraction model; the transmitted wave spreads out in time, and the head of the wave moves faster than that predicted from the theory. Specifically, it is shown that the average velocity of the head of the gas wave within the foam moves more slowly after reflection than it does before, notwithstanding the gas having been compressed. The net result is that the second reflected wave emerges from the foam face, back into the gaseous

region, very much earlier than the pseudo-gas model predicts. It should be noted that the skeletal material through which the reflected wave moves is also more dense, probably with higher tortuosity and higher pressure drops. Nevertheless, the reasons for this agreement in first reflected wave strength require further clarification, as the physics would tend to suggest otherwise.

Comprehensive tests done by Skews *et al.* (1991, 1993) extended the experimental study of the phenomena, by including photographs of the skeleton motion, as well as the more usual pressure measurement, by photographing the movement of oblique lines drawn on the surface of the test specimen. In particular it was shown that a compaction wave moves through the skeletal material at a velocity less than that of the gas wave, as measured by the pressure transducers, but faster than the front face of the foam. This showed very clearly that correct modeling would have to include the separate behavior of the two phases, but taking account of the strong coupling between them, and in particular the relative velocity with its associated pressure drop. This latter factor was seen to be the major reason for the spreading out of the transmitted wave. In addition, both these photographs and schlieren photographs confirmed the findings of Gvozdeva *et al.* (1985b), albeit for a much lower Mach number, that the front face of the foam moves at constant velocity during the compression phase except for a small acceleration period. The schlieren photographs also showed the emergence of a contact surface from the surface of the foam shortly before the position of maximum foam compaction. The actual time at which it emerged could not be established because of the slight concave curvature of the face of the foam. This feature was interpreted as being the front of the gas that had been compressively heated within the foam, being driven out through the compacted material by the very strong pressure gradients developed because of the high pressure on the back wall and the short compacted length of foam. The presence of this feature also shows that the face of the foam should not be treated as a contact interface as assumed in the simple refraction model. This new information was combined into the single consistent wave diagram (Skews *et al.*, 1993), which highlighted the essential differences between the actual process and that resulting from the assumption of a simple refraction at an interface between two media. The resolution of the measurements was not sufficient to establish whether gas was moving into the foam during the compression phase, the calculated gas velocity behind the first reflected shock wave being very similar to the velocity at which the foam face recedes. However, the evidence from the foam motion photographs, of some relaxation of a layer of material at the face of the foam, indicated that there must be some inflow. The growth of this uncompressed front layer was commented on further by Seitz and Skews (1991).

Persuasive experimental evidence of the existence of this inflow was given by Gvozdeva *et al.* (1993), who showed how the structure of the compaction

wave changed when a thin film of Mylar film was placed on the foam surface, thereby preventing ingress of gas. The compressed zone starts at the instant of shock impact and grows linearly as the compaction wave propagates through the material. The result is that the elastic recovery of the thin layer at the surface is prevented and the foam remains compressed over the full length of the compaction wave, from the head of the wave all the way back to the face of the foam. Back wall pressures are also found to be higher for the specimen with the protected surface. These tests indicate that the extent of the layer at the front face that recovers is from 5 to 11 mm depending on the test gas. The spacing of the lines on the specimen did not allow more accurate determination of the development of this layer to be determined; however, it would be expected to grow in time as indicated by Seitz and Skews (1996). The nature of the relaxation of this part of the compacted region is easy to explain. As the front face of the foam moves down the tube the flow into the face is reduced by the strongly compacted material ahead of it and the flow drag force essentially reduces to zero and is no longer able to overcome the elastic stress in the foam, which then rebounds locally.

In an attempt to explore internal flow effects, experiments were also conducted by Gvozdeva *et al.* (1993) with layers of Mylar film sandwiched between successive narrow layers of foam so that interstitial gas flow was also prevented. The result is that the reflected wave pressure becomes higher.

Van Dongen *et al.* (1993) have also commented on entrance effects. They infer that the reflected wave is not generated at the moment of shock impact, but that as the wave enters the foam it is slowed down by friction and that this results in reflected signals being propagated back out of the foam. These signals then coalesce into the reflected shock. There is certainly evidence of the strengthening of the reflected shock from careful pressure measurements taken on the side wall and also in accurate wave diagram analysis. On the other hand, many of the theoretical treatments of the phenomena assume instantaneous reflection of a fully formed shock wave at the surface. These studies were also among the first to draw attention to the fact that the stress measured by a pressure transducer on the back wall has contributions both from the interstitial gas and from the mechanical force applied by the skeleton material over the surface of the transducer. These conclusions derived from their earlier studies on wave propagation in liquid saturated particle beds. Various techniques have been used to measure these stresses separately. The usual technique, first highlighted by van der Grinten *et al.* (1985), is to have one pressure transducer flush with the wall and a second transducer slightly recessed so that it is not in contact with the foam. In the experiments by van Dongen *et al.* (1993) the differences between the traces are clearly distinguishable. For more dense foams (e.g., those used by Yasuhara *et al.*, 1996), the gas pressure and stress waves are significantly separated, and the gas pressure trace is very

similar in shape to tests with a rigid skeleton. This method of separating gas and matrix contributions to the total stress has not yet been fully validated, since researchers sometimes report gas-alone stresses higher than the total stress. This technique thus still needs further development.

A simple physical description of the phenomena has been given (Seitz and Skews, 1996) using a "leaky" piston analogy. This piston is taken to be that portion of the foam plug that collapses during the progressive compression of the foam, that is, all the material in the compaction wave. The piston increases in mass as it is driven toward the back wall by the pressure difference, being finally brought to rest by the pressure rise ahead of it, resulting from the gas in front of it being driven into the ever-reducing volume ahead of the piston. The compressed foam region of the piston can have a density many (~ 5) times that of the uncompressed foam as the gas in the pores is forced ahead of the advancing collapsed foam front. The permeability of the collapsed foam is very low, and it has been observed both experimentally and numerically that little gas passes through the piston. Van Dongen *et al.* (1996) have highlighted the strong dependence of permeability on the amount of matrix compression. It is shown from experimental measurement that both the permeability and the second Forchheimer coefficient depend strongly on the strain; thus, for example, this latter coefficient for the material tested by them varied by two decades for a strain variation between 0.3 and unity.

It is well established that the front face of foam moves at constant velocity. This was initially shown by Gvozdeva *et al.* (1985) and has been confirmed by a number of workers since then. This fact was used by Ben-Dor and Zaretsky (1994) to infer what the velocity of the compaction wave through the foam would be. This work assumes a linear relationship between the compaction velocity and the sound speed in the medium, which in turn is taken as a simple function of the void fraction. It should be noted that the equation they use gives the correct value for sound speed in the limit for zero void fraction, but gives an incorrect limit of zero speed for a void fraction of unity (i.e., pure gas). Since in most foams the void fraction is very close to unity, the effect of this assumption would need to be checked. They also assumed that the pressure acting on the face of the foam is dependent only on the incident shock wave strength and is not dependent on the face velocity.

The existence and nature of the compaction wave were first identified by Skews *et al.* (1991, 1993). This work showed that it was different from the gas wave sensed by side-wall pressure transducers and moved at a slower velocity. The technique used was to paint markings on the side surface of the specimen, photography of which would then show the associated deformation. The essential two-phase nature of the process thus became evident, showing that single-phase models such as the pseudo-gas model used earlier could not correctly represent the behavior. The mixture model of Baer (1992) confirmed

the gas motion inferred from pressure measurement in the preceding experimental studies, as well as predicting the motion of the foam skeleton.

The streak photography technique implemented by Gvozdeva's group (Gvozdeva *et al.*, 1996, Lagutov *et al.*, 1996) have enabled valuable studies to be made of the foam motion. Vertical lines painted on the side face of the foam, when viewed in streak mode, allow the easy identification of compression and expansion waves through the foam material. Although the results are affected to some extent by wall drag, as is evident from the streak images during the rebound phase where the center of the specimen is visible past that in contact with the wall, these studies still give the best information available of this important part of the process. This technique enables the motion of both the head and tail of the compaction wave to be established from a single test. Situations for weak waves and soft foams are generally more complex than the preceding tests have shown, primarily because the plateau stress is of similar order to the pressure and the contribution of the foam elasticity can no longer be neglected.

Since the pioneering work of Gelfand, there have been some tests where the rear face of the foam does not abut against a rigid wall. It would be necessary to test relatively long samples because of the transverse buckling effects; probably lengths of at least the major transverse dimension of the shock tube will be necessary for the process to reasonably approximate one-dimensional flow. Resultant flows will depend very much on whether the foam is constrained in any way because of the friction at the walls. If there is bulk motion of the sample, as distinct from motion due to compaction wave action alone, waves generated from the gross piston motion may swamp those due to the wave motion.

Unsupported foam tests were also conducted by Onodera and Takayama (1995). Twenty-five-millimeter long specimens were placed in a 60×150 mm shock tube and the motion determined from streak photography. Although some inferences were drawn from the pressure results, it would have been interesting to establish the foam shape. It would appear from limited studies of three-dimensional effects that there could have been significant transverse motion, even substantial bending. Some interesting results using closed cell foams have been given by Lagutov *et al.* (1995) using streak photography of both the gas and foam motion. There is clear evidence of the wave emerging from the back face of the foam followed by slight movement of the foam face itself, due to the drag of the precursor gas wave, and later by the very much stronger motion due to the compaction wave arriving at the back face, after which the whole compressed foam plug moves rapidly down the tube. A numerical simulation of this geometry would be of interest. A puzzling aspect in the photograph is the apparent vanishing of the gas between the back face of the foam and the back wall of the tube. The reason may be significant leakage past the sides of the specimen, since, it being closed cell, there cannot be flow through it.

Special tests to explore the effects of an air gap between the back of the foam plug and the back wall of the shock tube were conducted by Seitz and Skews (1996). In this case, however, the gap was kept at constant width by the foam being supported on a honeycomb matrix. This was done so that by monitoring the pressure in the constant volume gap, inferences can be drawn about the gas flows through the plug. Two foams were tested with about a two-to-one ratio in densities, with the lighter being much more permeable even though the cell structures were similar. The main result is that although the more dense foam gave significantly higher amplification when it abutted against the back wall, the reverse was true when there was a gap. The reason for this is that the denser material is less permeable, so that there is much less flow into the gap behind the foam and foam relaxation and rebound occurs before the cavity can be pressurized. Similar tests would enable useful data to be obtained on the flow through compacted foams as these tests indicate that in situations where there is a space behind the protective barrier the pressure achieved may well be influenced more by permeability than by density. A further interesting result from these tests is that for larger gaps the peak pressure, as measured by side wall transducers at positions covered by the foam, indicates that the compacted material traps high-pressure gas, which then tends to bleed away in both directions.

From the investigations just summarized, there now appears to be a fairly general understanding of the physical processes occurring when a plane shock wave strikes a slab of compressible porous material, although detailed effects for any particular fluid and foam type are not easy to predict. It is thus necessary to develop analytical and numerical models based on the controlling physical effects, so that the field may be more fully understood. As indicated later, there are fundamental difficulties in the measurement of some of the parameters and numerical and theoretical modeling offers the facility to explore individual effects in detail. Furthermore, studies need to go beyond one-dimensional situations.

15.1.4.2 SYSTEMS WITH RIGID SKELETONS

One of the earliest studies of shock impact on materials with a stiff skeleton is that of Beavers and Matta (1972). They investigated the strength of the reflected wave from three different porous materials, classified as foametal, feltmetal, and granular. The theoretical model assumes that there is no shock wave transmitted into the material and that the flow through the material is steady. Interestingly, an allowance is made for a thin inlet and outlet region, a few pore diameters in extent, where the flow adjusts to the effects of area change. The flow through the bulk of the material is assumed to be according to the extended Darcy equation, with the porosity, permeability, and inertial coefficient obtained from measurement. Considering the fairly dramatic

assumption of the neglect of transient effects, the predictions were found to be remarkably good except in the case of the foametal. This discrepancy was ascribed to the possibility of a transmitted shock wave occurring and to the distortion of the material.

A potentially very interesting area of investigation is the use of shock tubes for the study of wave propagation in liquids saturating a solid skeleton. Limited experimental work is available in this field. This is somewhat surprising since it is nearly 40 years since the existence of extra wave-mode solutions were discovered by Biot (1956). Foda (1987) has shown that such waves are of significance in important areas such as soil liquefaction, which occurs when saturated soils lose their rigidity when subjected to repeated seismic shocks, resulting in the sinking of heavy objects such as buildings. Although the second wave has been shown to exist, the first study to do so using shock waves generated in a shock tube was by van der Grinten *et al.* (1985, 1987). Their porous material consisted of a 1.875-m long, 75-mm diameter cylinder made up of 250–500 μm sand particles connected by glue. The sample was placed in a vertical shock tube and both air and water were used as the interstitial fluid. With air, the compressibility of the skeleton is very small compared to that of the gas, and the solid phase may be considered to be rigid. The single transmitted wave is strongly damped. Agreement with theory was found to be good if the Forchheimer equation is used to describe the pressure gradient, with the nonlinear term making a significant contribution. Experimentally determined steady-state values of the coefficients in this equation were found to be adequate. The existence of the second wave is clearly evident in the pressure traces and is strongly damped compared to the first wave. The effect of added mass was found to be important, and the permeability had to be adjusted to about one-third of the steady-state value in order to get agreement with the theory. Interestingly, the authors also attempted to measure the strains in the solid skeleton using strain gauges, and confirmed the interesting theoretical prediction that the first wave causes both the pore fluid and the skeleton to be compressed, whereas the second wave results in further compression of the pore fluid but expansion of the matrix.

The head-on collision of a planar shock wave with rigid porous materials having a large permeability has been investigated experimentally by Levy *et al.* (1993a). The experimental study has revealed the following:

1. Unlike flexible porous materials (e.g., polyurethane and/or polyethylene foams), where the available experimental data indicated that the transmitted compression waves did not converge to a sharp discontinuity, here there was clear evidence that sharp-front transmitted waves were formed in all the investigated rigid porous models.
2. The transmitted wave velocity was found to be nearly constant and about 3–5% smaller than the speed of sound of the air filling the pores.

3. The sharp jump across the transmitted waves was found to decay as the compaction wave propagates.
4. The pressure at the end-wall of the shock tube behind the reflected wave did not remain uniform, as expected, but slightly increased. The pressure rise increased as the air porosity increased. In addition, this phenomenon became more pronounced as the length of the model increased.
5. The last three observations suggests that the compaction wave broke down and developed a dispersed wave structure.
6. A comparison between test specimens with different large pore size indicated that the strengths of the transmitted compaction waves were almost identical when identical incident shock waves were used. This was not the case when the results of specimens with different small pore sizes were compared.
7. The pressure jump across the reflected shock wave was found to increase as it propagated backwards.

All the listed observations led Levy *et al.* (1993a) to modify the generally accepted phenomenological model of this reflection/interaction process. The proposed modified model implies that the entire interaction phenomenon is probably governed at its early stages by multiple interactions of the transmitted wave with the internal walls of the pores of the porous material. Only at a later time does the friction become the dominant process.

15.1.4.3 BLAST WAVE LOADING

Although much of the initial interest in the study of the effect of foam protective layers was for blast wave loading applications, very little experimental work has been conducted using explosives or simulated blast wave pressure profiles. The first of these was by Rayevsky *et al.* (1989), who allowed the approximately spherical shock wave emerging from the end of a shock tube to impinge on a foam layer. They found that below an incident shock Mach number of about 1.2 there is no pressure amplification, and the slab of foam acts to attenuate the wave. They ascribe this to the effects of the expansion wave behind the shock front reflecting off the foam surface. These tests thus indicate that situations with blast wave incident profiles are somewhat different than for shock wave profiles. Similar effects were noted by Lee *et al.* (1993), who showed that the nature (attenuation or amplification) of the back wall pressure relative to a wall with no covering is dependent on blast strength, whether the foam was open or closed cell, and on the particular stress-strain relation of the material.

A set of tests showing conclusively that closed cell cellular material can be used to attenuate a blast wave has been conducted by Makris *et al.* (1996). The

explosive was detonated outside of the foam slab and then penetrated into it—thus representing the typical geometry of a protective barrier exposed to external blast. These tests give significant insight into the coupling between the wave and the material. Single and multiple layers of 19-mm thick foam were exposed to blast waves generated from C4 explosives of charge mass of 18 and 770 g positioned at a distance giving shock Mach numbers at the instant of impact on the surface of the foam of 1.2 to 2.7. It was found that for a weak blast the pressure profile on the back wall steepened and the impulse increased as the number of foam layers was increased. An important result found is that for a given foam, back wall pressure amplification occurs for low charge mass, followed by a region of pressure attenuation as charge mass is increased, followed in turn by amplification once more for even higher charge mass. The authors interpret these effects in terms of the plateau stress of the foam and the conditions under which foam densification occurs. These issues are clearly of importance in designing protective barriers and, when compared with those of Rayevsky *et al.* (1989), indicate that significantly more work is required for the understanding of this interaction.

An interesting and practically significant study is that of Kleine *et al.* (1996). This examined the propagation of a spherical blast wave within a foam slab. This work highlights the importance of conducting tests that remove the side wall frictional effects, which many workers ignore in testing in shock tubes but which are known to be significant. A small (8 mg) charge of explosive was placed at the center of a rectangular foam block. The propagation of the wave was monitored by a series of contact gauges embedded inside the block as well as a single embedded pressure transducer. It was recognized that the transducer itself could disturb the flow. Measurements show that in the early part of the process the wave decays at the same rate as the equivalent blast wave in air, but then at a certain position starts decaying in a stronger fashion. The implication is that there are two effects in action with the one taking over from the other. The reasons for this rapid onset of attenuation have not been established. Numerical modeling of this geometry would be of considerable interest as the interplay between compaction and percolation could then be assessed. The pressure traces also exhibit the spreading out of the wave that had previously been noted in shock tube experiments. Over the range of densities tested (24 to 31 kg/m³) no effect of density on wave decay was found.

15.1.4.4 MULTIDIMENSIONAL STUDIES

During the early 1970s a number of two-dimensional studies were undertaken that have not received much attention, although they are rather interesting from the point of view of the dramatic attenuation in shock wave strength that they illustrate. The first of these was undertaken by Cloutier *et al.* (1971).

What was needed was a method to attenuate the shock wave from a hypersonic model in a free-flight ballistic range in order to study the turbulent wake. In the laboratory tests a rifle bullet was used to generate the shock wave. The attenuation material was attached to a solid table and a .303 bullet fired 100 mm above the surface. Measurements were made with schlieren and shadow-graph photography and a pressure transducer. Incident shock angle was about 28 degrees. A variety of materials were tested and it was found that by correctly choosing the thickness and density of the material the reflected wave could be virtually eliminated. Urethane foams gave between 25 and 55% reductions in reflected wave strength for foam densities of 18 to 51 kg/m³, and fiberglass blankets (12 kg/m³) resulted in reductions down to 4%. In general it was found that for any given material the reflections are weaker the lower the density.

In 1973 Guy investigated shock wave attenuation in a sudden enlargement in a duct with an absorbent lining. Transverse waves generated in ballistic range enclosures are undesirable, and the use of lining was investigated to dissipate these waves. A 40-mm diameter shock tube was used in conjunction with two test sections: a two-dimensional abrupt expansion with an area ratio of 2, and an axisymmetric expansion with an area ratio of 4 with a pressure transducer mounted on the axis. Twenty-five-millimeter thick polyurethane foam was used to line the cavity. The schlieren photographs showed that the transverse waves were almost totally eliminated. Pressure measurements on the axis of the tube showed elimination of the high frequencies associated with the removal of these multiple transverse waves. However, the traces also show a spreading out of the primary wave, an effect that is not evident in the schlieren photographs. The reason for this effect is not commented on and deserves future consideration.

The first comprehensive theoretical analysis of oblique reflection of a shock wave from a porous slab was conducted by Clarke (1984a). The interaction was assumed to comprise a reflected expansion wave terminated by a shock. The expansion wave was assumed to be necessary in order to account for the inflow into the porous material, although this does imply that the inflow velocity is greater than the vertical velocity component induced behind the incident wave. Darcy's law was used to define the pressure changes within the material. Distortions in the skeleton were taken to be small and the process was taken to be controlled by inflow and outflow from the porous material until the pressure was uniform within the layer and equal to the external pressure. It was concluded that substantial reductions in reflected wave strength could take place over distances of centimeters from the interface. Some limited experimental results are presented in Clarke (1982), and tolerable comparisons with the theory were obtained.

In order to examine inflow conditions in more detail, Clarke (1984b) considered the normal reflection of a shock from a matrix made of a slender

hollow tubes aligned in the direction of flow. The first part of the analysis considered the flow in a single tube to be an unsteady polytropic process with friction accounted for by a linearized momentum equation. Of particular interest is the introduction of the geometric “openness ratio” at the tube inlet, and it is shown that inertial effects are significant at early times if this ratio is small. One of the important outcomes of the analysis is that the reflected wave some time after the initiation of reflection will exceed that of reflection off a rigid wall. This has indeed been found to be the case for reflection off urethane plugs, if the strength of the reflected wave is taken to be that over the first and second reflected waves.

This work was then extended to the case of reflection off a polyurethane plug (Clarke, 1984c). In this case the material was theoretically modeled as an aggregate of thin tubes of different lengths. This extended the previous work with the inclusion of inertial effects. The need to do this was prompted by some experimental evidence, which indicated that the precursor expansion wave did not exist. The results were compared to experiments conducted in a shock tube (Bray and Clarke, 1984). These are possibly the first experimental results of wedge reflections using polyurethane foam. The reflected field domain consisted of a weak reflected shock followed by a steady increase in pressure to an asymptotic value corresponding to the pressure that would be reached for reflection from a rigid wall. By using suitable scaling of the results it is shown that the mathematical treatment gives satisfactory pressure histories when compared to the experiments. Specifically, it is predicted that relative reflected wave strengths are more than halved at distances of 80 to 220 cm from layers of foam between 2.5 and 10 cm deep. Unfortunately, the properties of the foam are not specified. Some schlieren measurements were conducted to determine reflected wave angles for a wedge covered with a layer of foam. Weak incident Mach numbers of 1.08 to 1.12 were used, and it was concluded that the reflected waves were weaker than would be obtained from reflection off a solid wedge; in fact, the angles of reflection were closer to what would be obtained if the reflected wave were a Mach wave. However, the differences were not large because of the very weak incident waves used.

At the time that these papers were written there was a sparsity of experimental results, and this is still largely true, although pertinent experiments are beginning to appear. There appears to be little doubt that there is a substantial amount of further work to be done to establish the range of applicability of Clarke’s model, and more generally the behavior relating to regular reflection. Conditions involving Mach reflection have not yet been explored.

The last paper in this series (Clarke, 1984c) dealt with a shock wave propagating over a porous layer embedded in the wall of a shock tube with the surface of the layer in line with the tube walls. The author regarded the theory

as largely explanatory rather than predictive and concluded that more extensive tests would need to be undertaken.

One of the serious concerns with the shock tube studies, which have been the primary device for investigations of these phenomena with compressible foams, is the influence of friction between the specimen and the tube walls. Some of the earlier works left a small gap between the side face of the specimen and the tube walls with the assumption that the specimen would only collapse in the direction of shock motion. It has been shown (Skews *et al.*, 1993), however, that the shock penetrates into the gap, resulting in a significant transverse pressure gradient, which results in substantial lateral collapse of the specimen. This would make sidewall pressure measurements for such tests suspect, and could even affect back-wall measurements. Thus, tests need to have a snug-fitting specimen but with the associated drag. Most foams have a very low Poisson ratio (0.001 according to Henderson *et al.*, 1989), but nevertheless there will be friction drag on the walls. A number of tests have shown that the effect of this is not insignificant. Unfortunately, many studies still ignore this fact, as do most correlations between experimental and numerical/theoretical results. Some indication of the extent of this effect has been given by Seitz and Skews (1991), with oblique photographs showing the extent of the dishing of the face of the foam. During the initial loading phase the front surface of the foam becomes concave and all conventional imaging systems thus record the edge of the foam being dragged back on the window surface, which can result in significant errors in measurement of foam length, particularly at positions near maximum compaction. Beyond this point, as the specimen relaxes the drag on the specimen is in the opposite direction and the face of the specimen becomes convex, with the central portion of the specimen moving back up the shock tube faster than the edges. This effect is more apparent in photography during this phase of the motion than for the loading phase. For example, clear evidence of it can be seen in the streak images of Gvozdeva *et al.* (1996), where both the edge of the specimen in contact with the wall and the shadow of that at the center of the tube are evident. A marked example of the frictional effect is recorded in a paper by Henderson *et al.* (1989), where unusually long specimens were used. In this case the friction forces over the large area between the specimen and the tube, coupled with Poisson ratio effects and elastic recovery forces, result in the specimen not recovering in length but remaining compacted at the end of the tube.

Few attempts have been made to overcome this problem. One preliminary study (Skews *et al.*, 1996) placed conical foam specimens with the base of the cone attached to the back wall of a shock tube. The problem is then two-dimensional axisymmetric with oblique reflection of the shock wave on the surface of the cone. It is shown that for similar base diameters the preamplification on the back wall at the axis of symmetry increases as the apex angle

decreases. This is to be expected because of the increasing height of the cone and the associated larger mass of foam material. Furthermore, the magnitude of the amplification reduces at increasing radius from the axis of symmetry, also as is to be expected. A surprising result, however, was that whereas the peak amplification for foams of densities of 16 and 32 kg/m³ were similar (1.3), that for 28 kg/m³ was very much larger (2.1), even though all specimens had similar porosity. The reason for this is not known but is thought to relate to the foam structure enabling much higher gas flows. This is inferred from the fact that these specimens collapsed to a much larger extent than the others.

Experimental studies on two-dimensional shock/foam interactions are almost nonexistent. However, significant insights into the mechanisms of oblique reflection off porous materials of a shock wave may be obtained from the studies of Onodera and Takayama (1994) and Skews and Takayama (1996) of shock reflection off a perforated surface. As far as is known, no thorough experimental results have been published using foam wedges, although edge effects would be of concern.

There are two obvious limits to reflection regimes. These are for a totally open surface, in which case the reflected wave is a sound wave, and for a totally impervious surface. Skews (1991) applied these in the one-dimensional case and Kobayashi *et al.* (1993) in the two-dimensional case, where they proposed two different analytical models for describing the phenomenon of regular reflection over rigid porous surfaces in pseudo-steady flows. Subsequently, they presented and solved an analytical model for only the simpler case, where the coupling between the pure gas phase and the porous phase is ignored. Unfortunately, however, this is a less realistic model. The two physical models proposed by Kobayashi *et al.* (1993) are shown schematically in Figs. 15.1.3a and 15.1.3b. Their first physical model, shown in Fig. 15.1.3a, was termed by them the *simple sink model*. The incoming flow [state (0)] parallel to the surface of the porous layer is deflected clockwise by an angle θ_1 as it passes across the incident shock wave, i. Then, as it passes across the reflected shock wave, r, it is deflected counterclockwise by an angle θ_2 . Since the flow in state (2) can penetrate into the porous layer, the boundary condition there is $\theta_1 - \theta_2 = \delta$, where δ is the overall deflection angle induced by the “sink” effect that is introduced by the porous layer. In the case of a reflection over a non-porous solid surface, $\delta = 0$. A similar model was proposed by Onodera and Takayama (1990), who investigated the propagation of planar shock waves over slit surfaces. Kobayashi *et al.* (1993) first physical model accounts only for the flow of the gas behind the reflected shock wave into the porous surface and completely ignores the fact that a shock wave should be transmitted into the porous layer as shown schematically in Fig. 15.1.3b, in which their second physical model is shown. This physical model was correctly called by them the *realistic model*. Following the schematic

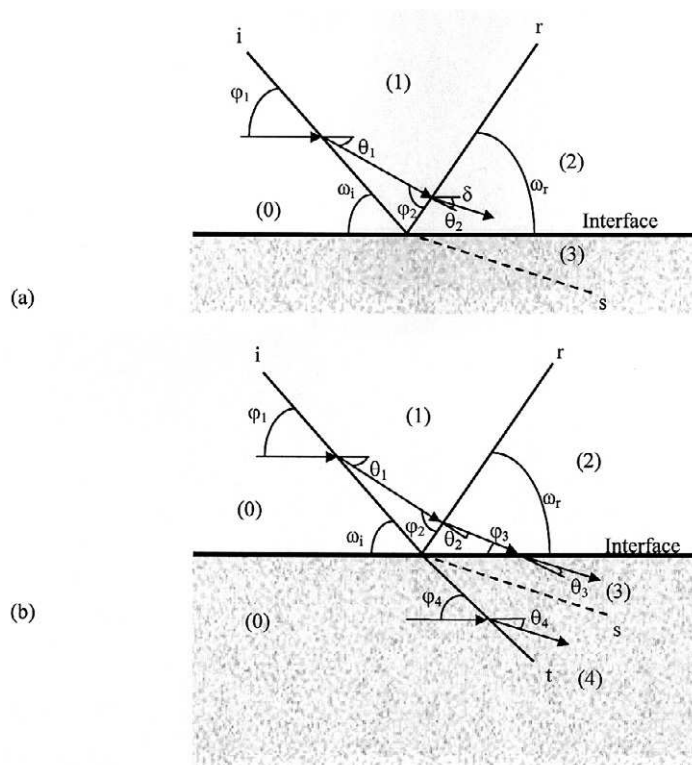


FIGURE 15.1.3 Schematic illustration of the two physical models proposed by Kobayashi *et al.* (1993). (a) The simple sink model; (b) the realistic model.

presentation of their realistic model, Kobayashi *et al.* (1993) claimed that “realistic as it is, it is not easy to solve the whole flow field since one must deal with the coupled problem between the pure gas phase and the porous phase.” Their solution of their first physical model was only empirical as they were not able to analytically relate the overall deflection angle, δ , to the initial conditions, namely, the incident flow Mach number, M_0 , the angle of incidence of the incident shock wave, ϕ_1 , and the porous layer properties. Instead, for each experiment they fitted an appropriate value of δ by which the angle between the incident and reflected shock waves, ω_i and ω_r , respectively, as obtained by solving the well-known two-shock theory with the boundary condition, agreed with that obtained experimentally.

In a following paper Li *et al.* (1995) presented an analytical solution of Kobayashi *et al.* (1993) realistic model, which deals with the coupled problem between the pure gaseous phase and the porous phase. This model and a

comparison of its prediction with experimental data are presented in Section 15.1.6.3.

15.1.4.5 THEORY AND MODELING

In general, two types of approaches have been employed by researchers for modeling, and for theoretical and numerical investigation of the shock wave interactions with porous media. They are classified as the single phase or multiphase approaches.

15.1.4.5.1 The Single Phase Approach

The basic idea in the single phase approach is to replace the two phases of which the porous material is composed, that is, the material of which the skeleton is made and the fluid occupying the pores, by a single fictitious phase. This approach has been applied in two different ways. The first one is known as the bulk approach and is appropriate for both flexible and rigid porous materials. The second one is known as the “pseudo-gas” approach and is appropriate to gas saturated weak flexible porous materials.

15.1.4.5.1.1 The Bulk Approach

In this approach, the porous material is assumed to be a single phase whose properties are derived from the properties of the individual phases comprising it, for example, the bulk density, ρ_b , which is given by

$$\rho_b = \sum_i \phi_i \rho_i, \quad (15.1.2)$$

where ρ_i is the density of the i th component and ϕ_i is its volume fraction. By definition,

$$\sum_i \phi_i = 1. \quad (15.1.3)$$

If the pores of the porous material are saturated with only one fluid, then Eqs. (15.1.2) and (15.1.3) can be rewritten as

$$\rho_b = \phi_f \rho_f + \phi_s \rho_s \quad (15.1.4)$$

and

$$\phi_f + \phi_s = 1, \quad (15.1.5)$$

where the subscripts f and s stand for the fluid occupying the pores and the solid material of which the skeleton of the porous material is made, respec-

tively. If, in addition, the fluid saturating the pores is a gas, then $\rho_f \ll \rho_s$, and Eq. (15.1.4) can be simplified to read

$$\rho_b \cong \phi_s \rho_s = (1 - \phi_f) \rho_s. \quad (15.1.6a)$$

Alternatively, this equation can be rewritten as

$$\frac{\rho_b}{\rho_s} \cong 1 - \phi_f. \quad (15.1.6b)$$

As pointed out by Gibson and Ashby (1988), the relative density, ρ_b/ρ_s , is the most important property of porous materials, because it determines the mechanical properties of the bulk material. For example, the modulus of elasticity, E_b , of an open-cell elastometric foam is obtained from

$$E_b = E_s \left(\frac{\rho_b}{\rho_s} \right)^2, \quad (15.1.7)$$

where E_s is the modulus of elasticity of the solid material of which the skeleton is made.

Ben-Dor *et al.* (1991) have reported on a computer code for the simulation of the phenomena. The foam was treated as a uniform solid phase, somewhat in the same manner as Monti (1970), but extending it to include various deformation models and loading types. Very high foam densities were assumed, from 100 to 500 kg/m³. The maximum pressures predicted for increasing foam length show the same trend as found experimentally, that is, that the pressure increases with length up to some critical length, after which it remains constant. This critical length is taken as the length required for the compression waves to coalesce into a shock wave. To date there has not been any experimental evidence to confirm this behavior.

The Lagrangian governing equations describing the head-on collision of planar shock waves with flexible foams were developed by Mazar *et al.* (1994). Numerical simulations based on this model were conducted by Ben-Dor *et al.* (1994). Relatively good agreement was evident when the numerical predictions were compared to experimental results. The lack of a perfect agreement was attributed to the lack of accurate stress–strain relations. Better stress–strain relations were proposed later by Ben-Dor (1996b) and Zaretsky and Ben-Dor (1995). Unfortunately, the numerical simulations were not repeated with these newly proposed better stress–strain relations.

15.1.4.5.1.2 The Pseudo-Gas Approach

Gelfand *et al.* (1983) proposed a pseudo-gas approach, in which the two-phase medium, that is, the gaseous phase and the skeleton of which the foam is

made, are treated as a homogeneous pseudo-gas with specific heat capacity ratio, $\bar{\gamma}$, and speed of sound, \bar{a} , given by

$$\bar{\gamma} = \frac{\gamma(1 + \eta^*\delta)}{1 + \gamma\eta^*\delta} \quad (15.1.7a)$$

and

$$\bar{a} = \left[\frac{\bar{\gamma}}{\gamma(1 + \eta^*)\phi_p^2} \right]^{1/2} a, \quad (15.1.7b)$$

where δ is the ratio of the specific heat capacity of the material of which the skeleton is made to the specific heat capacity of the gas (i.e., $\delta = C_m/C_p$), η^* is the ratio of the mass of the foam material to the mass of the gas occupying the pores (i.e., $\eta^* = \rho_s/\rho_p$), and γ and a are the specific heat capacity ratio and the local speed of sound of the gaseous phase, respectively.

As a result of this approach, the interaction problem is reduced to the refraction of a shock wave at a gaseous interface (i.e., the interface separating the pure gas and the pseudo-gas). Consequently, the flow field can be calculated using gas dynamic relations with the boundary condition that the pressures and the velocities in the flow states in either side of the gas/foam interface are equal.

Gvozdeva and Faresov (1986) adopted Gelfand *et al.* (1983) pseudo-gas model and presented an analytical model for calculating various parameters in the flow field (e.g., the compaction wave velocity, and the compaction induced flow velocity).

A similar approach has been adopted by Li and Ben-Dor (1995). However, their model was limited to analytical prediction of the flow field in the vicinity of the gas/foam interface immediately after the front edge of the foam was struck head-on by the planar shock wave. In addition, based on simple gas dynamic considerations, they also suggested a simple formula for calculating the peak pressure at the shock-tube end wall.

15.1.4.5.2 The Multiphase Approach

In this approach, the porous medium is considered as multiphase in which the various phases interact with each other. A detailed description of this approach was given by Baer and Nunziato (1986). A one dimensional two-phase analysis with air as the fluid phase was presented by Baer (1988), Powers *et al.* (1989), and Bear *et al.* (1992). In addition to numerical solutions, Baer (1988) and Powers *et al.* (1989) also presented simplified analytical models for calculating the jump conditions across compaction waves in rigid porous materials.

Biot's (1956) analysis was probably the first one to employ the notion of wave propagation in porous media. This was basically referred to microscopic representations of the phase balance equations within the framework of the theory of mixtures. A large number of papers have appeared in the literature following Biot's pioneering work. Among them are those by Smeulders *et al.* (1992), Degrande and de Roeck (1992), and Nigmatulin and Gubaidullin (1992). Most refer to linear acoustic waves that take place when momentum dissipation terms dominate. As an example, Attenborough (1982) presents a theory dealing with the motion of sound waves through an ideal saturated porous matrix with parallel cylindrical pores. Using microscopic physical parameters, he extended this to account for randomly distributed pores. An extensive literature survey of similar approaches is given by Corapcioglu (1991). The developed model is different in its approach and hence yields different terms in the governing equations. It is novel in establishing the macroscopic theoretical basis for nonlinear wave motion in multiphase deformable porous media. The modeling is based on conceptualizing the porous medium as a continuum composed of interacting compressible solid and multiple fluid phases. Macroscopic physical laws expressing mass and momentum balances for fluids and the solid matrix are formulated on the basis of representative elementary volume (REV) concepts, presented by Bear and Bachmat (1990).

Macroscopic momentum and energy balance equations, for a saturated porous medium, were developed by Levy *et al.* (1995) by conducting a dimensional analysis on the macroscopic balance equations of Bear *et al.* (1992) and Sorek *et al.* (1992). Based on the findings of Powers *et al.* (1989), these equations were simplified by Levy *et al.* (1993b), who proposed analytical expressions for calculating the jump conditions across compaction waves in rigid porous materials. The predictions of the model developed were found to be better than those of Powers *et al.* (1989) when they were compared to the experimental results of Sandusky and Liddiard (1985).

Skews (1991) reported on a series of shock tube experiments in which the interaction of weak planar shock waves with low density flexible foams was investigated. Detailed pressure measurements along the shock-tube side walls and at the shock-tube end wall were presented by him. Baer (1992) presented an analytical model, based on the continuum mixture theory for describing the shock-foam (porous material) interaction phenomena. His numerical simulations were found to agree quite well with Skews' experiments.

Bear *et al.* (1992) have developed a complete set of general macroscopic equations for the instantaneous exposure of a porous medium to a step change in pressure and temperature. They have illustrated that for a simple case the equations reduce to two coupled wave equations for the two phases. The fluid is assumed to be compressible Newtonian and the solid matrix, thermoelastic.

This model was based on the model that was developed for studies in granular explosives (Baer and Nunziato, 1986). The longitudinal pressure gradient is assumed to be dependent on the relative velocity as given by an extension of Darcy's equation, referred to as the Forchheimer equation. The constants of the Forchheimer equation were determined empirically from steady-state tests on samples of the material. The heat transfer is accounted for by using a correlation derived from fluidized-bed studies, and the material behavior from measurements of the variation of the pressure drop with uniaxial strain. This establishes the yield stress corresponding to the plateau region of the stress/strain curve, and this value is assumed to hold throughout the process. Of particular note is that the compaction wave in the material of the skeleton is correctly modeled and good agreement is obtained with experimental pressure traces. This model now enables more detailed studies of the flow to be made, particularly in areas that are not readily accessible to measurement. As an example, this code has been run to ascertain the gas particle paths in the vicinity of the front face of the foam (Baer, 1993b). The simulation shows a number of interesting features. Firstly, not only is there flow into the foam whilst it is accelerating, as inferred by Skews (1991), but there is a small percolation of gas into the material, and then out again, during the compression phase, followed by reentry of gas into the foam during the recovery phase. This result is consistent with findings using a powder tracer (Seitz and Skews, 1991) in that powder, initially spread on the surface, was found to have penetrated the foam by some 5 mm. A further interesting feature is the initial rapid acceleration of the compaction wave to a velocity initially much higher than the constant value it exhibits through most of the compression phase.

Olim *et al.* (1994), who also simulated the same experiments of Skews (1991), used a completely different approach. In their approach the skeleton was assumed to be infinitely weak and could be considered to be made up of a cloud of particles. As a result the problem was replaced by the well-known problem of calculating the relaxation zone in dusty shock waves (for details, see Igra and Ben-Dor, 1988). Furthermore, it is assumed that the heat transfer coefficient is infinite. Excellent agreement is obtained with the experimental pressure traces, and good predictions of foam face velocity (62 m/s) and the skeletal compaction wave velocity (105 m/s) are obtained compared to the experimental values of 55 and 90 m/s (70 mm foam, $\rho = 35 \text{ kg/m}^3$, $M = 1.4$). These values are similar to those found by Baer (60 and 100 m/s), and the differences from the experimental results are probably due to the effects of wall drag on the experimental measurements. Thus, very good predictions are now available over the ranges for which these models have been validated ($M = 1.25$ to 1.4 , and foam densities from 15 to 40 kg/m^3), and there is thus the opportunity to explore in more detail the effects of the foam properties

as contained in the Forchheimer equation, as these are still largely empirically determined.

Kitagawa and Yasuhara (1997, 1999) set up a numerical model based on Baer's (1992) equations to investigate the effect of pressure of shock wave diffusion by porous foam. The coefficients in the Forchheimer equation were then adjusted to give approximate equivalence to experimentation (as done by Olim *et al.*, 1994, and Levy *et al.*, 1996a). Very good fits of the pressure history are obtained. It should be pointed out that a factor of a 1000 was used on the values of the Forchheimer coefficients, which were obtained in steady-flow tests, in order to obtain numerical agreement with experimental data. Recall that Olim *et al.* (1994) multiply the values of the Forchheimer coefficients by 5–8, for flexible foam, and Levy (1995) by 2 for rigid porous material. They showed that their numerical prediction is more sensitive to the inertial component of the Forchheimer coefficients. It should be noted that this was also obtained from the dimensional analysis of Levy *et al.* (1995) and also shown by Levy (1995) and Levy *et al.* (1996a, 1999).

In a paper by Bear and Sorek (1990), a mathematical model was developed of an abrupt pressure impact applied to a compressible fluid flowing through saturated porous materials under isothermal conditions. It was shown that during a certain time period, following the onset of the pressure change, the macroscopic fluid momentum balance equation conforms to a wave form. Krylov *et al.* (1996) presented a 1D simple analytical solution of this wave equation. The wave equation was transformed to Euler's equation describing the motion of a "new" fluid with properties related to the fluid which actually occupies the pores of the porous material. A similar analytical solution was presented by Sorek *et al.* (1996) for the nonisothermal case. In that study they presented a method leading to a generalized fluid density, pressure and temperature. Using their generalized properties they wrote Euler's equation as a one-dimensional expression for the analytical solution of the fluid's equation of motion. To obtain this, the porosity, the matrix strain, and temperature of the solid were developed as explicit functions of the pressure.

Levy *et al.* (1996a) developed a model for describing wave propagation in a saturated rigid porous media. Unlike Krylov *et al.* (1996) and Sorek *et al.* (1996), who neglected the momentum and energy exchanges between the two phases and assumed that the coupling between them was only due to the effective stress, in this study the momentum and energy exchanges between the two phases is also accounted for. Based on the dimensional analysis of Levy *et al.* (1995), who showed that the linear Darcy term is much smaller than the nonlinear Forchheimer term, only the Forchheimer term appears in the momentum and energy exchanges between the two phases. The one-dimensional version of the governing equations of the flow field, which is obtained when a thermoelastic porous medium is struck head-on by a shock

wave, was solved numerically using a TVD-based numerical code. The numerical predictions are compared to experimental results, and good to excellent agreement was obtained for different porous materials and a wide range of initial conditions. The results of this study are presented in Section 15.1.6.1.

Levy *et al.* (1999) have developed the macroscopic mass, momentum, and energy equations for multiphase unsaturated porous media. It was shown that the Forchheimer terms represent the exchange between the interaction phases at their common interface. Using Forchheimer terms, a very good agreement was evident when the 1D numerical simulation of the propagation of compaction waves in a saturated thermoelastic porous medium was compared with shock-tube experimental data (Levy *et al.*, 1993a).

15.1.5 MACROSCOPIC GOVERNING EQUATIONS

A detailed derivation of the three-dimensional macroscopic governing equations describing the flow field in saturated and in unsaturated porous media was presented by Levy *et al.* (1995) and Levi-Hevroni (1999). In the following only the assumptions used in the derivation of the governing equations for the saturated porous media and the final form of the equations are given.

15.1.5.1 THE ASSUMPTIONS

1. The fluid is ideal (i.e., $\mu_f = 0$ and $\lambda_f = 0$, where μ_f is the dynamic viscosity and λ_f is the thermal conductivity).
2. The fluid is a perfect gas.
3. The dispersive and diffusive mass fluxes of the fluid, and the dispersive flux of the solid, are much smaller than the corresponding advective ones and may, therefore, be neglected.
4. The dispersive momentum flux is much smaller than its advective one and may, therefore, be neglected.
5. The conductive and dispersive heat fluxes of the phases are negligibly small when compared to their advective ones.
6. The microscopic solid/fluid interface is a material surface with respect to the mass of both phases.
7. The stress-strain relationships for the solid, at the microscopic level, and for the solid matrix, at the macroscopic level, have the same form.
8. The material of which the skeleton of the porous material is made is incompressible.

9. The specific heats at constant volume, C_f , and that at constant strain, C_s , for the solid are constant.
10. The energy processes for the fluid and for the solid are reversible.
11. There are no external energy sources.
12. The energy associated with the viscous dissipation is negligibly small.
13. The rate of heat transfer between the fluid and the solid phases is negligibly small.

15.1.5.2 THE BALANCE EQUATIONS

The macroscopic mass balance equation for the fluid phase is

$$\frac{\partial}{\partial t}(\phi_f \rho_f) = -\nabla \cdot (\phi_f \rho_f \mathbf{V}_f) \quad (15.1.8)$$

where ϕ_f , ρ_f , and \mathbf{V}_f are the porosity, the fluid density, and the velocity vector, respectively.

The macroscopic mass balance equation for the solid phase is

$$\frac{\partial}{\partial t}((1 - \phi_f) \rho_s) = -\nabla \cdot ((1 - \phi_f) \rho_s \mathbf{V}_s) \quad (15.1.9)$$

where ρ_s is the density of the solid and \mathbf{V}_s denotes its velocity vector.

The macroscopic momentum balance equation for the fluid phase is

$$\begin{aligned} \frac{\partial}{\partial t}(\phi_f \rho_f \mathbf{V}_f) = & -\nabla \cdot (\phi_f \rho_f \mathbf{V}_f \mathbf{V}_f) - \phi_f \mathbf{T}^* \nabla P \\ & - \phi_f \rho_f \mathbf{g} \mathbf{T}^* \nabla Z - \tilde{\mathbf{F}} \phi_f \rho_f |\mathbf{V}_f - \mathbf{V}_s| (\mathbf{V}_f - \mathbf{V}_s) \end{aligned} \quad (15.1.10)$$

where P , which denotes the pressure of the fluid, is prescribed by the equation of state (see Eq. (15.1.14)), \mathbf{g} denotes the acceleration of gravity in the z direction, and $\tilde{\mathbf{F}}$ and \mathbf{T}^* denote the Forchheimer tensor for an isotropic solid matrix and the tortuosity tensor associated with the directional cosines at the solid/fluid interface, respectively.

The macroscopic momentum balance equation for the solid phase is

$$\begin{aligned} \frac{\partial}{\partial t}((1 - \phi_f) \rho_s \mathbf{V}_s) = & -\nabla \cdot ((1 - \phi_f) \rho_s \mathbf{V}_s \mathbf{V}_s) - (1 - \phi_f) \mathbf{T}^* \nabla P \\ & + \nabla \sigma'_s - (1 - \phi_f) \rho_s \mathbf{g} \mathbf{T}^* \nabla Z \\ & + \tilde{\mathbf{F}} \phi_f \rho_f |\mathbf{V}_f - \mathbf{V}_s| (\mathbf{V}_f - \mathbf{V}_s) \end{aligned} \quad (15.1.11)$$

where σ'_s denotes the macroscopic constitutive relation for the effective stress of the solid matrix.

The macroscopic energy balance equation for the fluid phase is

$$\begin{aligned} \frac{\partial}{\partial t} \left(\phi_f \rho_f \left(C_f T_f + \frac{V_f^2}{2} \right) \right) = & -\nabla \cdot \left(\phi_f \rho_f \mathbf{V}_f \left(C_f T_f + \frac{V_f^2}{2} \right) \right) \\ & - \mathbf{T}^* \nabla (\phi_f P \mathbf{V}_f) + \mathbf{T}^* P \mathbf{V}_f \cdot \nabla \phi_f \\ & - \tilde{\mathbf{F}} \phi_f \rho_f |\mathbf{V}_f - \mathbf{V}_s| (\mathbf{V}_f - \mathbf{V}_s) \mathbf{V}_s \end{aligned} \quad (15.1.12)$$

where T_f and C_f are the temperature and the specific heat at constant volume of the fluid phase, respectively.

The macroscopic energy balance equation for the solid phase is

$$\begin{aligned} \frac{\partial}{\partial t} \left((1 - \phi_f) \rho_s \left(C_s T_s + \frac{V_s^2}{2} \right) \right) = & -\nabla \cdot \left((1 - \phi_f) \rho_s \mathbf{V}_s \left(C_s T_s + \frac{V_s^2}{2} \right) \right) \\ & + \nabla (\phi'_s \mathbf{V}_s) - \mathbf{T}^* \nabla ((1 - \phi_f) P \mathbf{V}_s) - \mathbf{T}^* P \mathbf{V}_s \cdot \nabla \phi_f \\ & + \tilde{\mathbf{F}} \phi_f \rho_f |\mathbf{V}_f - \mathbf{V}_s| (\mathbf{V}_f - \mathbf{V}_s) \mathbf{V}_s \end{aligned} \quad (15.1.13)$$

where T_s and C_s are the temperature and the specific heat at constant strain of the solid phase, respectively.

The equation of state for the fluid phase is

$$P = \rho_f \mathcal{R} T_f \quad (15.1.14)$$

where \mathcal{R} is the specific gas constant.

15.1.5.2.1 The Equations of State for the Solid Phase

A relation for the macroscopic effective stress of the solid matrix, σ'_s , is to be chosen according to the nature of the problem. In the following, two examples are presented. The first is a thermoelastic model, which was used by Levy *et al.* (1996a) for rigid porous samples, and the second is an elastoplastic mode, which was used by Levi-Hevroni (1999) to describe the behavior of flexible porous materials.

The constitutive relation for the effective stress of a thermoelastic porous material as used by Levy *et al.* (1996a) is

$$\sigma'_s = \lambda''_s e_s \mathbf{I} + \mu'_s \varepsilon - \eta (T_s - T_{s0}) \mathbf{I}. \quad (15.1.15)$$

Here λ''_s , μ'_s , and η are the Lamé constants of a thermoelastic solid matrix, \mathbf{I} is a unit tensor, e_s is the volumetric strain (dilatation), and ε is the macroscopic strain tensor.

In general, the effective stress tensor $\sigma'_s(\mathbf{x}, t)$ can be written as a sum of a deviator and a normal stresses, τ and P_s , respectively:

$$\sigma'_{sij} = -P_s \delta_{ij} + \tau_{ij}. \quad (15.1.16)$$

The deviator stress, τ , describes stress that is working on the solid in a constant volume, and it is also known as the shear stress. The normal stress, the solid's pressure, is defined positive for tension and negative in compression. Thus, the normal stress is an invariant of the stress tensor:

$$P_s = -\frac{1}{3} \sigma'_{s_{kk}} = -\frac{1}{3} (\sigma'_{s_{11}} + \sigma'_{s_{22}} + \sigma'_{s_{33}}). \quad (15.1.17)$$

Similarly to fluid dynamics, the solid's pressure can be described by a suitable constitutive equation. Such an equation describes the Hugoniot curve of the material, which can be obtained experimentally by loading the sample with various pressure and measuring the response of volumetric change. This curve describes the final states of the material and can be expressed by

$$P_s \equiv P_s(\eta_s), \quad \eta_s = \frac{V}{V_0} = \frac{\rho_{s_0}}{\rho_s}. \quad (15.1.18)$$

The description of the stress field is much more complex, since nine or six constitutive equations are needed for the unisotropic or isotropic case. Levi-Hevroni (1999) used such equations to calculate the normal stress (solid's pressure) and described the shear stress as for elastoplastic deformations. Equations (15.1.16) and (15.1.17) can be used to obtain shear stress as

$$\tau_{ij} = \sigma'_{s_{ij}} + P_s \delta_{ij} = \sigma'_{s_{ij}} - \frac{1}{3} \sigma'_{s_{kk}} \delta_{ij}. \quad (15.1.19)$$

The summation of the three diagonal components of the shear stress must be equal to zero as a constraint to each model that may be used to describe the shear stress:

$$\tau_{11} + \tau_{22} + \tau_{33} = 0. \quad (15.1.20)$$

The shear stress in the elastic zone can be written as

$$\tau_{ij} = 2G \left(\varepsilon_{ij} - \frac{1}{3} e_s \delta_{ij} \right) \quad (15.1.21)$$

where the shear modulus, G , is

$$G = \frac{E}{2(1 + \nu)}. \quad (15.1.22)$$

E is the Young's modulus and ν is the Poisson's ratio.

The elastic limit can be obtained by using the Von Mises theory. In general, this criterion can be used for most solid materials, including porous ones.

Based on the Von Mises theory, elastic deformation occurs when the three principal effective stresses satisfy the inequality

$$(\sigma'_{s_1} - \sigma'_{s_2})^2 + (\sigma'_{s_2} - \sigma'_{s_3})^2 + (\sigma'_{s_3} - \sigma'_{s_1})^2 \leq 2(Y^0)^2, \quad (15.1.23)$$

where Y^0 is the yield point stress, which may be obtained from a tension test. The left side of this inequality is proportional to the elastic energy per unit volume that can be stored in the material and may cause the material to return to its original volume upon release. Above this value, plastic deformation occurs and the maximum elastic energy, which was stored during the elastic deformation, remains constant. The criterion for the deviator stresses, that is, shear stresses, can be written as

$$(\tau_1 - \tau_2)^2 + (\tau_2 - \tau_3)^2 + (\tau_3 - \tau_1)^2 \leq 2(Y^0)^2. \quad (15.1.24)$$

The shear stress may be calculated from Eq. (15.1.21) for the elastic deformation. The obtained values can be substituted in the Von Mises criterion. When the criterion is satisfied the shear stress values remain as is; otherwise, the maximum values of the shear stresses are calculated by

$$\tau_i = \frac{\tau_i}{\sqrt{\tau_1^2 + \tau_2^2 + \tau_3^2}} \sqrt{\frac{2}{3}} Y^0. \quad (15.1.25)$$

When large deformation occurs (i.e., plastic deformation), the strain tensor cannot be well defined. Hence, the shear stresses cannot be calculated. Instead, the shear stress rate is calculated as a function of the strain rate. The strain rate is defined as

$$\dot{\epsilon}_{ij} = \frac{1}{2} \left(\frac{\partial u_i}{\partial x_j} + \frac{\partial u_j}{\partial x_i} \right) \quad (15.1.26)$$

and the shear stress rates defined by

$$\dot{\tau}_{ij} = 2G \left(\dot{\epsilon}_{ij} - \frac{1}{3} \dot{\epsilon}_s \delta_{ij} \right). \quad (15.1.27)$$

Thus, the shear stresses are calculated by integrating the shear stress rates with time.

15.1.6 CASE STUDIES

If a detailed analysis of the flow field that develops inside a porous medium that is interacting with a shock wave is required, then the process should be analyzed using the multiphase approach. In this approach, the porous medium is considered as multiphase, in which the various phases interact with each

other. In the following sections, using the macroscopic multiphase approach two 1D and one 2D cases will be presented.

15.1.6.1 ONE-DIMENSIONAL SHOCK WAVE INTERACTION WITH RIGID POROUS MATERIAL

The one-dimensional version of the governing equations, which was presented in Section 15.1.5, was solved numerically. An upwind TVD shock-capturing scheme, originally developed by Harten (1983), was extended by Levy *et al.* (1996a) to solve the problem of two-phase flow, which described wave propagation and interaction in a saturated rigid porous media.

In order to validate the physical model and the numerical code, the governing equations were solved numerically for different samples and a variety of initial conditions and compared to experimental results. The head-on collision of planar shock waves with rigid porous materials was investigated experimentally in order to validate the predictions of the physical model and the numerical code. The experiments were conducted in the 75 mm \times 75 mm shock tube of the School of Mechanical Engineering of the University of Witwatersrand in Johannesburg, South Africa. The incident shock wave Mach number range was $1.2 \leq M_i \leq 1.7$; the initial pressures and temperatures throughout the experimental study were about 830 mbar and 288 K, respectively. The rigid porous samples were made of silicon carbide (SiC) and alumina (Al₂O₃). The SiC porous material had either 10 or 20 pores per inch and the Al₂O₃ porous material had either 30 or 40 pores per inch. Twelve experiments were conducted with each sample. The samples were mounted at the end of the driven section of the shock tube in such a way that their back edges were supported by the shock-tube end-wall (for more details see Levy *et al.*, 1993a).

In order to solve the governing equations and compare the solution to the experimental results, the various parameters that appear in the physical model were estimated for each sample (for more details see Levy *et al.*, 1996a). The solution of the governing equations required the knowledge of the following parameters: the macroscopic Lamé coefficients for a thermoelastic solid, the Forchheimer factor, the tortuosity, the initial porosity, and the density of the solid matrix. Out of these six parameters only one, namely the density of the solid matrix, was available from the manufacturer. The other five parameters had to be estimated. Levy *et al.* (1993a) calculated the porosity using Eq. (15.1.6b). The bulk density value was obtained by dividing the mass of a given sample by its volume, and ρ_s , as mentioned earlier, was provided by the manufacturer. The porosity value as obtained and reported by Levy *et al.*

(1993) was 0.728 ± 0.016 . Based on the properties of the materials of which the samples were made, and the fact that the upper limit of the elastic stress reduces when the porosity increases, in a $(1 - \phi)^2$ manner (see Eq. (15.1.7)), the orders of magnitude of the macroscopic Lamé coefficients that appear in the macroscopic constitutive equation for thermoelastic porous materials, $E_e (\equiv \lambda_s'' + \mu_s')$ and $E_T (\equiv \eta/C_s)$, were estimated to be identical for all the samples used in the course of the experimental study: 380×10^7 Pa and 26.207 kg/m^3 . The tortuosity factors, T^* , were found, for the various samples, by estimating the ratio between the speed of sound of the air inside the porous medium and that in a pure air with the aid of Eq. (15.1.1). The Forchheimer factors, \tilde{F} , for the various samples were found experimentally. In these experiments, each sample was mounted in a pipe and the pressure drop across it was measured as a function of the airflow rate through it. The pressure drop was found to be a parabolic function of the air velocity. This was done by assuming that the pressure drop depended linearly on the length of the sample. The values of the tortuosity and the Forchheimer factors, as obtained experimentally for the various samples made of SiC, used in the study, are 0.7 and 300 m^{-1} .

Figures 15.1.4a, 15.1.4b, and 15.1.4c represent typical experimental results and their numerical simulations. The pressure history of the pure gas just ahead of the front edge of the porous material is shown in Figure 15.1.4a. The pressure histories of the gas occupying the pores of the porous material along the shock-tube side wall and at its end wall are shown in Figs. 15.1.4b and 15.1.4c, respectively. P_1 is the pressure ahead of the incident and the transmitted shock waves, P_2 is the theoretical pressure reached behind the incident shock wave, and P_5 is the theoretical pressure that would have been reached had the incident shock wave collided head-on with a solid end wall. The symbols represent the experimental results, and the solid lines are the numerically predicted values. In general, the agreement between the experimental and the numerical results is seen to be very good. Although Figs. 15.1.4a to 15.1.4c describe the results of only one experiment, similar agreements were obtained in the comparisons with all the experiments that were conducted in the course of the study. Details of all these comparisons are given in Levy (1995).

As mentioned earlier, numerical predictions based on a TVD-based computer code that was developed by Levy *et al.* (1996a) agreed very well to excellently with the experimental results of Levy *et al.* (1993a). Consequently, it might be assumed that the physical model and the numerical code are reliable enough to investigate the behavior of the flow field characteristics. The predication of the numerical simulation for the gas phase pressure, density, and velocity can be seen in Fig. 15.1.5. The incident shock wave Mach number was 1.38, and the porous sample was made of SiC with 10 ppi. As can be seen the

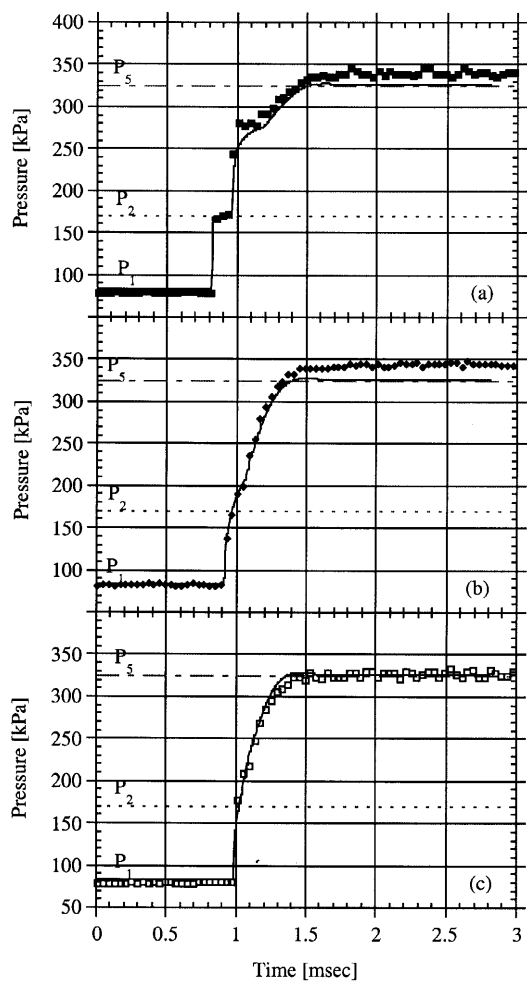


FIGURE 15.1.4 Comparison between the numerical predictions (solid lines) and the experimental results (squares and diamonds) of the pressure histories of the gas at various locations: (a) just ahead of the front edge of the porous material, (b) along the side wall, and (c) at the end wall.

time distance diagram, which was obtained by the numerical simulations, is similar to that reported by Skews *et al.* (1993) for shock wave interaction with flexible foam. In Fig. 15.1.5, both the reflected and the transmitted waves are clearly seen while additional compression waves exit from the porous sample and merge with the reflected shock wave and strengthen it. As a result, the reflected wave is slowly accelerating. During the interaction, air is penetrating

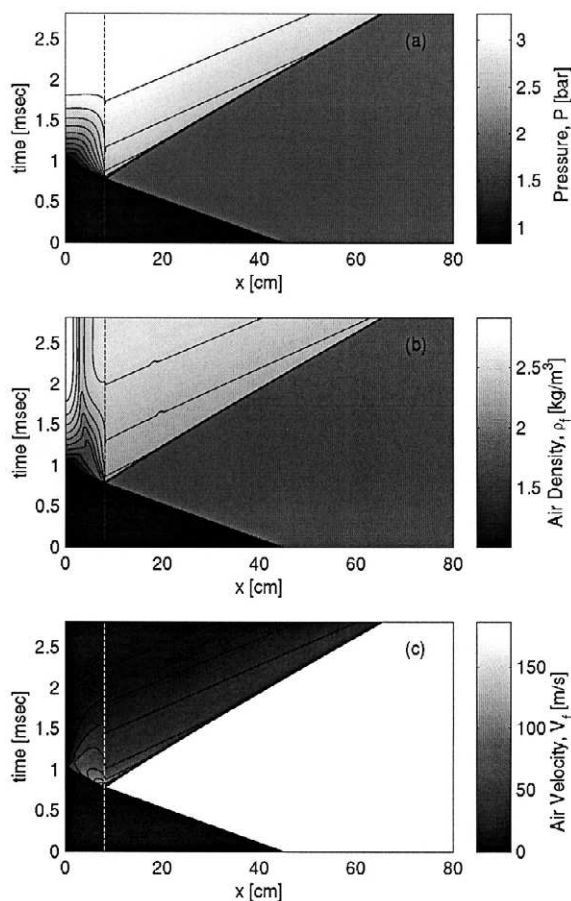


FIGURE 15.1.5 Time–distance diagram for shock wave ($M_i = 1.38$) interaction with a 81-mm thermoelastic porous sample made of SiC with 10ppi, as was predicted by the numerical simulations. (a) Pressure, (b) air density, and (c) air velocity.

into the porous sample and the highest value of the velocity of the air behind the transmitted wave is about 170 m/s (Fig. 15.1.5c). This velocity is attenuated down rapidly because of the solid–fluid interaction (Forchheimer term). Inside the porous sample, a contact surface can also be seen (Fig. 15.1.5b). As will be shown in the flowing case study, this contact surface is pushed out when the porous sample undergoes large deformation.

Using the constitutive relation for the effective stress of a thermoelastic porous material, Eq. (15.1.15), the prediction for the effective stress of the

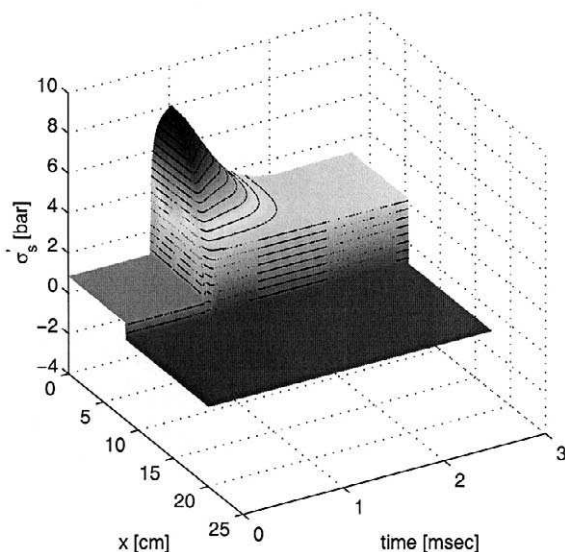


FIGURE 15.1.6 The predicted effective stress of the solid phase as a result of the interaction of a shock wave ($M_i = 1.38$) with an 81-mm thermoelastic porous sample made of SiC with 10ppi.

solid phase was obtained (Fig. 15.1.6). The effective stress of the porous media reached its maximum value very fast and then decayed slowly, while an expansion wave traversed from the front edge of the porous sample to the end wall. The maximum value of the solid stress was 2.5 times larger than the maximum value that could be obtained should the incident shock reflect from a solid wall. In addition, it was found that the compaction wave that was transmitted to the solid matrix was much faster than the wave transmitted into the gas phase.

15.1.6.2 ONE-DIMENSIONAL SHOCK WAVE INTERACTION WITH FLEXIBLE FOAM

As noted in Section 15.4.1, the experimental work of Skews *et al.* (1991, 1993) showed the separate existence of the compaction wave moving at a different velocity from the gas pressure wave, and also inferred that there must be gas motion across the air/foam interface. This demonstrated the essential two-phase nature of the interaction, and the need to account for it in modeling. Hence it was decided to solve the one-dimensional version of the governing equations for flexible foam, which was presented in Section 15.1.5, numerically. Thus, the shear stress model for elastoplastic deformations was used. An

upwind TVD shock-capturing scheme, originally developed by Harten (1983), was extended to solve the gas flow field only because it was difficult to keep track of the porous medium interface as it moved through the Eulerian mesh. As a consequence, a mixed Lagrangian and Eulerian method was adopted in order to solve and keep track of the front of the solid matrix. Details of the numerical scheme and its setup can be found in Levi-Hevroni (1999). As a validation test of the developed analytical model and computer code the problem treated by Levy (1995), where the solid matrix underwent only small deformations, was simulated. The comparisons between the numerical predictions and the experimental data of the gas pressure histories upstream of the porous material, on the side wall inside the porous material, and at the end wall clearly indicate that the developed numerical code reproduced the test problem very well. As a consequence, it was decided to use the numerical simulations to predict the flow field obtained when a flexible porous material is struck head-on by a planar shock wave. Since there were not enough experimental data to fully validate the theoretical model and the numerical simulations, only qualitative comparison and physical behavior were examined.

The trajectory of the front edge of the flexible porous material and its density field can be seen in Fig. 15.1.7. From this figure it is evident that the

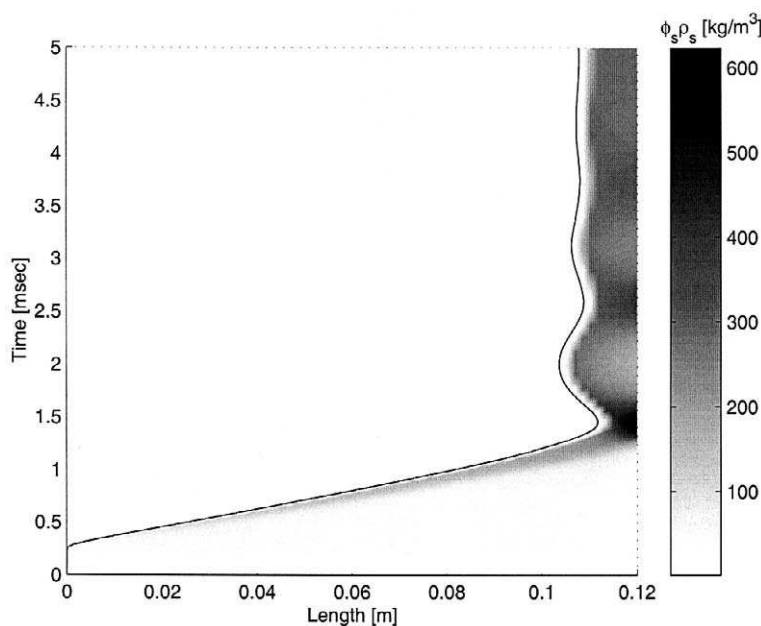


FIGURE 15.1.7 The calculated foam density field and the trajectory of its front edge as a result of the interaction of a shock wave with a flexible porous sample.

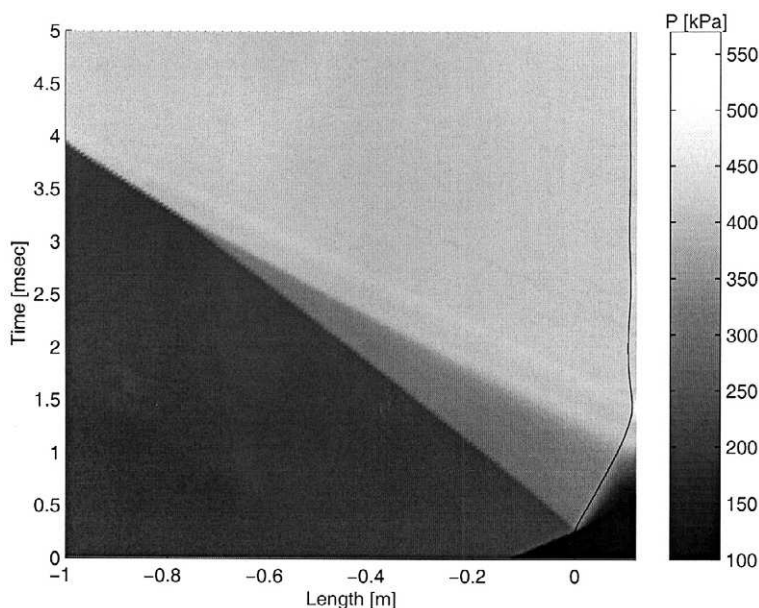


FIGURE 15.1.8 The calculated pressure and the trajectory of its front edge as a result of the interaction of a shock wave with a flexible porous sample.

front surface of the foam first undergoes about 80% deformation before it starts to retreat backwards. In addition, the foam wave head, as reported by Skews *et al.* (1993), can clearly be seen in the foam domain. The predictions of the numerical simulations for the gas pressure field are given in Fig. 15.1.8. The distance–time diagram obtained by the numerical simulations is similar to the distance–time diagram presented by Skews *et al.* (1993). In both wave diagrams, the reflected and the transmitted waves can be seen and additional compression waves are seen to be joining the reflected wave, strengthening and causing the wave to move faster. The calculated gas density field and the foam front edge are presented in Fig. 15.1.9. The contact surface of the gas, which originally filled the pores and was pushed out, as found experimentally by Skews *et al.* (1993), was reproduced numerically during this study. It should be noted here that the results shown in Figs. 15.1.7 to 15.1.9 could have been obtained only by performing a two-phase investigation of the phenomenon. Had one used the mixing approach of Biot (1956), the just-discussed details would have been missed altogether.

Gvozdeva *et al.* (1985) reported that, to some extent, the peak in the effective stress depends on the lengths of the foam slab. The longer the foam slab, the higher the peak of the effective stress (total pressure). This phenom-

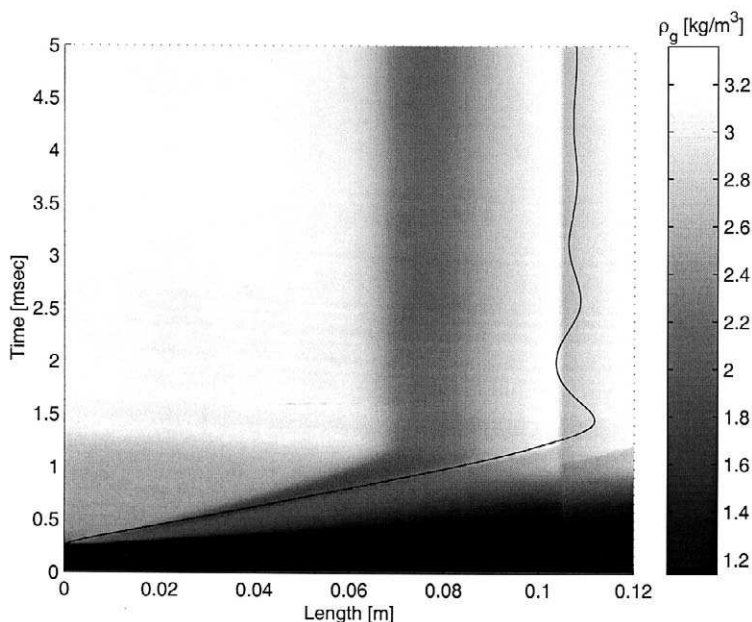


FIGURE 15.1.9 The calculated gas density field and the trajectory of its front edge as a result of the interaction of a shock wave with a flexible porous sample.

enon was reproduced by the present simulation, as shown in Fig. 15.1.10, where the pressure histories at the end wall for three foam slabs having the lengths 60, 90, and 120 mm are shown. As can be seen, the pressure amplifications appropriate to these three cases are about 6, 8.25, and 10.5, respectively. It is also interesting to note that regardless of the length of the foam slabs, the pressures at the end wall approach the same pressure after a few milliseconds. It should also be noted that total pressure amplifications obtained from the numerical simulations have similar behavior to those reported by Skews *et al.* (1993) and others.

In summary, the general macroscopic balance equations for a saturated flexible porous medium have been solved numerically. Special effort was put into simulating various factors that have been identified in the course of various experimental investigations as being of importance. The numerical predictions were compared, qualitatively, to experimental results, and good to excellent agreement was evident for different parameters. In particular, the following features were verified:

1. Two waves propagate inside the saturated porous foam: one in the gas filling the pores and one in the solid matrix.

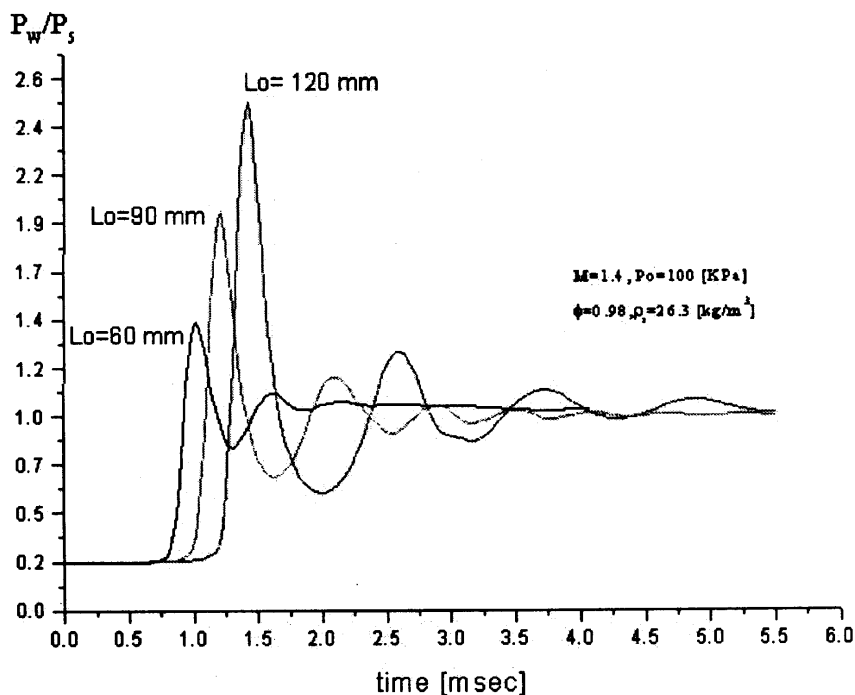


FIGURE 15.1.10 Calculated pressure histories at the end wall for different lengths of foam slabs.

2. The wave propagating in the gaseous phase is faster than that propagating in the solid matrix.
3. The gas originally filling the pores is pushed out of the pores in the course of the compression of the foam slab.
4. The flexible foam results in a strong pressure amplification at the end wall.
5. The longer the foam slab is, the larger is the pressure amplification.

15.1.6.3 REGULAR REFLECTION FROM A RIGID POROUS SURFACE IN PSEUDO-STEADY FLOWS

In this section, the governing equations for the wave configuration of regular reflection over a rigid porous surface, shown in Fig. 15.1.3b, and the model assumptions are presented. Although describing the gaseous phase flow through the various shock waves outside the porous layer in states (0), (1)

and (2) is relatively simple and well known, the description of the flow inside the porous material is much more complicated. The macroscopic mass, momentum, and energy balance equations for a two-phase saturated porous medium that were presented in Section 15.1.5 were adopted for the present study. Similarly to the modeling of the head-on reflection of a planar shock wave from the shock-tube end wall where both the momentum and energy exchanges between the gaseous phase and the rigid end wall are neglected, it can be assumed that the gaseous phase does not exchange momentum and energy with the rigid skeleton of the porous medium as it flows through the pores. Although this assumption cannot be justified at present, it is expected that it will be validated when the predictions of the developed analytical model are compared with available experimental results. Note that the use of this assumption is limited to the porous region near the interface only. Careful and refined measurements such as those of Adachi *et al.* (1992), Kobayashi *et al.* (1993), and Skews (1994) are needed to resolve the issue of how important momentum and energy exchanges are. It should be expected that as the gas propagates deeper into the porous material, the momentum and energy exchanges between the gas and the pores become significant. This was shown experimentally by Levy *et al.* (1993a), where the shock wave transmitted into the porous material became more and more dispersed as it propagated further and further into the porous material. It should also be noted that this assumption cannot be applied to flexible porous materials even in the region near the interface.

In addition to the assumption mentioned earlier, the classical assumptions of the well-known two-shock theory (see Ben-Dor *et al.*, 1991), that the flow field is pseudo-steady and all the discontinuities are straight, was adopted. The last assumption implies that all the flow regions bounded by the straight discontinuities are uniform in all their dynamic and thermodynamic properties.

15.1.6.3.1 The Governing Equations

Consider the wave configuration shown in Fig. 15.1.3b. This consists of three shock waves, namely, the incident shock wave *i*, the reflected shock wave *r*, the transmitted shock wave *t*, and a contact discontinuity *s*, which separates the flow which has been shocked by a single shock wave, the transmitted shock wave, and the flow shocked by both the incident and reflected shock waves.

State (0) is ahead of the incident and transmitted shock waves; state (1) is behind the incident shock wave; state (2) is behind the reflected shock wave and state (4) is behind the transmitted shock wave. State (3) is obtained from

state (2) when the flow penetrates the porous material. States (3) and (4) are separated by the contact discontinuity.

Applying the conservation equations of mass, normal momentum, tangential momentum, and energy across the oblique shock waves that compose the wave configuration shown in Fig. 15.1.3b results in the following equations:

Across the incident shock wave i:

$$\rho_0 u_0 \sin(\varphi_1) = \rho_1 u_1 \sin(\varphi_1 - \theta_1) \quad (15.1.28)$$

$$P_0 + \rho_0 u_0^2 \sin^2(\varphi_1) = P_1 + \rho_1 u_1^2 \sin^2(\varphi_1 - \theta_1) \quad (15.1.29)$$

$$\rho_0 \tan(\varphi_1) = \rho_1 \tan(\varphi_1 - \theta_1) \quad (15.1.30)$$

$$h_0 + \frac{1}{2} u_0^2 \sin(\varphi_1) = h_1 + \frac{1}{2} u_1^2 (\varphi_1 - \theta_1). \quad (15.1.31)$$

Across the reflected shock wave, r;

$$\rho_1 u_1 \sin(\varphi_2) = \rho_2 u_2 \sin(\varphi_2 - \theta_2) \quad (15.1.32)$$

$$P_1 + \rho_1 u_1^2 \sin^2(\varphi_2) = P_2 + \rho_2 u_2^2 \sin^2(\varphi_2 - \theta_2) \quad (15.1.33)$$

$$\rho_1 \tan(\varphi_2) = \rho_2 \tan(\varphi_2 - \theta_2) \quad (15.1.34)$$

$$h_1 + \frac{1}{2} u_1^2 \sin^2(\varphi_2) = h_2 + \frac{1}{2} u_2^2 \sin^2(\varphi_2 - \theta_2) \quad (15.1.35)$$

The properties of the gaseous phase, which flows inside the porous layer, can be redefined (transformed) to obtain properties that result in governing equations similar to those of a pure gas:

$$\begin{aligned} \bar{\rho} &= \rho, & \bar{P} &= T^* P, & \bar{T} &= T, & \bar{\gamma} &= 1 + (\gamma - 1) T^*, & \bar{\mathfrak{R}} &= T^* \mathfrak{R}, \\ \bar{h} &= \frac{\bar{\gamma}}{\gamma} h, & \bar{e} &= e, & \bar{C}_v &= C_v, & \bar{C}_p &= \frac{\bar{\gamma}}{\gamma} C_p. \end{aligned} \quad (15.1.36)$$

Using this novel approach, the overall treatment of the phenomena turns out to be much more convenient than the treatment of the original equations.

The governing equations across the transmitted shock wave t are:

$$\bar{\rho}_0 u_0 \sin(\varphi_4) = \bar{\rho}_4 u_4 \sin(\varphi_4 - \theta_4) \quad (15.1.37)$$

$$\bar{P}_0 + \bar{\rho}_0 u_0^2 \sin^2(\varphi_4) = \bar{P}_4 + \bar{\rho}_4 u_4^2 \sin^2(\varphi_4 - \theta_4) \quad (15.1.38)$$

$$\bar{\rho}_0 \tan(\varphi_4) = \bar{\rho}_4 \tan(\varphi_4 - \theta_4) \quad (15.1.39)$$

$$\bar{h}_0 + \frac{1}{2} u_0^2 \sin^2(\varphi_4) = \bar{h}_4 + \frac{1}{2} u_4^2 \sin^2(\varphi_4 - \theta_4). \quad (15.1.40)$$

In addition to the foregoing equations across the various oblique shock waves, the governing equations across the interface C (which separates the flow inside and outside the porous layer) should be added. Based on Skews (1992), who reported that the wave configurations over porous surfaces were similar to those obtained over slit surfaces, we assume that the porous surface (near the

interface) can be treated as a slit surface. Thus the governing equations across the interface C are as follows:

Conservation of mass:

$$\rho_2 u_2 \sin(\varphi_3) = \phi \bar{\rho}_3 u_3 \sin(\varphi_3 + \theta_3) \quad (15.1.41)$$

Conservation of normal momentum:

$$\phi P_2 + \rho_2 u_2^2 \sin^2(\varphi_3) = \frac{\phi}{T^*} \bar{P}_3 + \phi \bar{\rho}_3 u_3^2 \sin^2(\varphi_3 + \theta_3) \quad (15.1.42)$$

Conservation of tangential momentum:

$$u_2 \cos(\varphi_3) = u_3 \cos(\varphi_3 + \theta_3) \quad (15.1.43)$$

Conservation of energy:

$$h_2 + \frac{1}{2} u_2^2 \sin^2(\varphi_3) = \frac{\gamma}{\bar{\gamma}} \bar{h}_3 + \frac{1}{2} u_3^2 \sin^2(\varphi_3 + \theta_3) \quad (15.1.44)$$

From geometry:

$$\varphi_3 = \theta_1 - \theta_2. \quad (15.1.45)$$

Since the pressures across the contact discontinuity are equal, one can simply write

$$\bar{P}_3 = \bar{P}_4. \quad (15.1.46)$$

In addition, if the contact discontinuity, s , is assumed to be infinitely thin, that is, a slipstream, then

$$\theta_1 - \theta_2 + \theta_3 = \theta_4. \quad (15.1.47)$$

In the preceding equations, ϕ is the porosity of the porous layer, and h_i is the enthalpy, which can be expressed as

$$h_i = \frac{\gamma}{\gamma - 1} \frac{P_i}{\rho_i}. \quad (15.1.48a)$$

Similarly,

$$\bar{h}_i = \frac{\bar{\gamma}}{\bar{\gamma} - 1} \frac{\bar{P}_i}{\bar{\rho}_i}. \quad (15.1.48b)$$

In summary, the preceding set of governing equations consists of 19 algebraic equations with 25 unknowns, namely $\rho_0, \bar{\rho}_0, \rho_1, \rho_2, \bar{\rho}_3, \bar{\rho}_4, P_0, \bar{P}_0, P_1, P_2, \bar{P}_3, \bar{P}_4, u_0, u_1, u_2, u_3, u_4, \varphi_1, \varphi_2, \varphi_3, \varphi_4, \theta_1, \theta_2, \theta_3$, and θ_4 . Thus, in order to have a solvable set, six of the 25 unknowns should be supplied as initial conditions. The six that are usually the known initial conditions are $\rho_0, \bar{\rho}_0, P_0, \bar{P}_0, u_0$, and φ_1 .

Note that the physical properties of both the gaseous and the solid phases, that is, the specific heat capacities ratio γ , the specific gas constant \mathfrak{R} , the porosity ϕ , and the tortuosity T^* , are assumed to be known.

Li *et al.* (1995) solved the foregoing equation set numerically using the preceding analytical model and compared its predictions to the experimental results of Skews (1992) and Kobayashi *et al.* (1993). The very good to excellent agreement that was evident when the analytical predictions were compared with the experimental results validates the various assumptions used in the course of developing the analytical model and confirms the validity of the entire physical model.

REFERENCES

- Adachi, T., Kobayashi, S., and Suzuki, T. (1992). An experimental analysis of oblique shock reflection over a two-dimensional multi-guttered wedge. *Fluid Dynam. Res.* 9: 19–132.
- Allard J.F., Castagnede B., and Henry M. (1994). Evaluation of tortuosity in acoustic porous materials saturated by air. *Rev. Sci. Inst.* 65: 754–755.
- Attenborough, K. (1982). Acoustical characteristics of porous materials. *Phys. Rep.* 82: 179–227.
- Baer, M.R. (1988). Numerical studies of dynamic compaction of inert and energetic granular materials. *ASME J. Appl. Mech.* 55: 36–43.
- Baer M.R. (1992). A numerical study of shock wave reflections on low density foam. *Shock Waves* 2: 121–124.
- Baer M.R. (1993). A multiphase model for shock-induced flow in low density foam. (19th) *International Symposium on Shock Waves, Shock Waves @ Marseille*, Brun R. and Dumitrescu L.Z. (eds.). Springer (1995), pp. 169–174.
- Baer M.R., and Nunziato J.W. (1986). A two-phase mixture theory for the deflagration-to-detonation transition in reactive granular materials. *Int. J. Multiphase Flow* 12: 861–889.
- Bear, J. and Bachmat, Y., (1990). *Introduction to Modeling of Transport Phenomena in Porous Media*, Kluwer Academic Publishers, Dordrecht, Germany.
- Bear, J. and Sorek, S. (1990). Evolution of governing mass and momentum balances following an abrupt pressure impact in porous medium. *Transport in Porous Media* 5: 169–185.
- Bear J., Sorek S., Ben-Dor G., and Mazor G. (1992). Displacement waves in saturated thermoelastic porous media. I. Basic equations. *Fluid Dynam. Res.* 9: 155–164.
- Beavers, G.S., and Matta R.K. (1972). Reflection of Weak Shock Waves from Permeable Materials. *AIAA J.* 10: 959–961.
- Ben-Dor G., and Zaretsky E. (1994). Head-on interaction of planar shock waves with polyurethane foams—a semi-empirical model. *Arch. Appl. Mech.* 64: 365–372.
- Ben-Dor G., Mazor G., Cederbaum G., Igra O., and Sorek S. (1991). The enhancement of shock wave loads by means of porous media. In *Proceedings of the 18th International Symposium on Shock Waves*, Takayama K. (ed.), Springer Verlag.
- Ben-Dor, G., Mazor, G., Igra, O., Sorek, S., and Onodera, H. (1994). Shock wave interaction with cellular materials. II: Open cell foams; experimental and numerical results. *Shock Waves* 3: 167–179.
- Ben-Dor, G., Mazor, G., Cederbaum, G., and Igra, O. (1996). Stress-strain relations for elastomeric foams in uni- bi- and tri-axial compression modes. *Arch. Appl. Mech.* 66: 409–418.

- Ben-Dor, G., Mazor, G., Cederbaum, G., and Igra, O. (1996)b. Well tailored compressive stress-strain relations for elastomeric forms. *J. Mater. Sci.* 31: 1107–1113.
- Biot, M.A. (1956). Theory of propagation of elastic waves in fluid-saturated porous solid. *J. Acoust. Soc. Am.* 28: 168–191.
- Bray, R., and Clarke, J.F. (1984). Reflection of weak shock waves from acoustically absorbent materials. Cranfield Inst. of Tech., CoA Rep. No. 8405.
- Clarke, J.F. (1982). Regular reflection of a weak shock wave from a rigid porous wall; some additional results. Cranfield Inst. of Tech., CoA Memo. No. 8225.
- Clarke, J.F. (1984)a. Regular reflection of a weak shock wave from a rigid porous wall. *Q. Jl. Mech. Appl. Math.* 37: 87–111.
- Clarke, J.F. (1984)b. Reflection of a weak shock wave from a perforated plug. *J. Engng. Math.* 18: 335–349.
- Clarke, J.F. (1984)c. The reflection of weak shock waves from absorbent surfaces. *Proc. R. Soc. Lond. A* 396: 365–382.
- Cloutier, M., Devereux, F., Doyon, P., Fitchett, A., Heckman, D., Moir L., and Tardif, L. (1971). Reflections of weak shock waves from acoustic materials. *J. Acoust. Soc. Am.* 50: 1393–1396.
- Corapcioglu, M.Y. (1991). Wave propagation in porous media—a review. In *Transport Processes in Porous Media*, J. Bear and M.Y. Corapcioglu (eds.). Kluwer Academic Publishers, Dordrecht, Germany, pp. 373–469.
- Degrande, G., and de Roeck, G. (1992). FFT-based spectral analysis methodology for one-dimensional wave propagation in poroelastic media. *Transp. Porous Media* 9: 85–97.
- Foda, M.A. (1987). Internal dissipative waves in poroelastic media. *Proc. R. Soc. Lond. A* 413: 383–405.
- Gelfand, B.E., Gubin, S.A., Kogarko, S.M., and Popov, O.E. (1975). Investigation of the special characteristics of propagation and reflection of pressure waves in a porous medium. *Fiz. Prikl. Mekh. Tekh. Fiz.* 6: 74–77.
- Gelfand, B.E., Gubanov A.V., and Timofeev E.I. (1983). Interaction of shock waves in air with a porous barrier. *Izv. Akad. Nauk SSSR, Mekh. Zhidk. Gaza* 4: 79–84.
- Gibson, B.E., and Ashby, M.F. (1988). *Cellular Solids: Structure and Properties*. Pergamon Press.
- Guy, T.B. (1973). Attenuation of reflecting shock waves in a duct with absorbent lining. *J. Sound Vib.* 29: 501–503.
- Gvozdeva, L.G., and Faresov, Y.M. (1985). Calculating the parameters of steady shock waves in porous compressible media. *Zh. Tekh. Fiz.* 55: 773–775.
- Gvozdeva, L.G., and Faresov, Y.M. (1986). Approximate calculation of steady state shock wave parameters in porous compressible materials, *J. Appl. Mech. Techn. Phys.* (English translation of *PMTE Zh. Prikl. Mekh. Tekh. Fiz.*), 27: 107–111.
- Gvozdeva, L.G., Faresov, Y.M., and Fokeev, V.P. (1985). Interaction of air shock waves with porous compressible materials. *J. Appl. Mech. Tech. Phys.* 3: 401–405.
- Gvozdeva, L.G., Faresov, Y.M., Brossard, J., and Charpentier N. (1986). Normal shock wave reflection on porous compressible material. In *10th International Colloquium on the Dynamics of Explosions and Reactive Systems. Dynamics of Explosions*. Bowen, J.R., Leyer, J.C., and Solakin R.I. (eds.), Progress in Astronautics and Aeronautics, vol. 106, 155–165.
- Gvozdeva, L.G., Lyakhov, V.N., Raevskii, D.K., and Faresov, Y.M. (1987). Shock-wave propagation in a gas and a porous medium. *Fizika Goreniya i Vzryva* 23: 125–129.
- Gvozdeva, L.G., Faresov, Yu.M., and Sharov, Yu. L. (1993). Experimental studies of the structure of deformation wave in porous compressible materials under the influence of shock waves. In *(19th) International Symposium on Shock Waves. Shock Waves @ Marseille*, Brun R., Dumitrescu L.Z. (eds.), Springer (1995) .
- Gvozdeva, L.G., Lagutov, Y.P., Sharov, Y.L., and Sherbak, N.B. (1996). Structure of deformation waves in porous compressible materials – influence of percolation. In *Proceedings of the 20th*

- International Symposium on Shock Waves*, Sturtevant, B., Shepherd, J.E., and Hornung, H.G. (eds.). World Scientific, pp. 1393–1398.
- Gvozdeva, L.G., Lagutov, Y.P., Sharov, Y.L., Sherbak, N.B., and Baklanov, D.I. (1997). Some peculiarities of interaction of shock waves with porous materials. In *Proceedings of the 21st International Symposium on Shock Waves*. Houwing A.F P and Paull A. (eds.). Panther Publishing, pp. 1211–1214.
- Harten, A. (1983). High resolution schemes for hyperbolic conservation laws. *J. Comput. Phys.* **49**: 357–393.
- Henderson, L.F., Virona, R.J., Di J., and Gvozdeva, L.G. (1989). Refraction of a normal shock wave from nitrogen into polyurethane foam. In *17th International Symposium on Shock Waves. Current Topics in Shock Waves*, Kim Y.W. (ed.). American Institute of Physics Conference Proceedings **208**: 814–818.
- Igra, O. and Ben-Dor, G. (1988). Dusty shock waves. *ASME Appl. Mech. Rev.* **41**: 379–437.
- Johnson, D.L. (1989). Scaling function for dynamic permeability in porous media. *Phys. Rev. Lett.* **63**: 580.
- Kitagawa, K., and Yasuhara, M. (1997). On flow resistance of porous elastic body interacting with shock wave. In *21st International Symposium on Shock Waves*, Houwing A.F P and Paull A. (eds.). Panther Publishing, pp. 959–963.
- Kitagawa, K., and Yasuhara, M. (1999). Effect of pressure diffusion of shock wave by porous foam. In *23rd International Symposium on Shock Waves*, London, UK.
- Kleine, H., Diăconescu, G., and Lee, J.H.S. (1996). Blast-wave propagation in foam. In *Proceedings of the 20th International Symposium on Shockwaves*, Sturtevant, B., Shepherd, J.E., and Hornung, H.G. (eds.) World Scientific, pp. 1351–1356.
- Kobayashi, S., Adachi, T., and Suzuku, T. (1993). Regular reflection of a shock wave over a porous layer: Theory and experiment. *Shock Waves @ Marseille IV*, Brun, R., and Dumitrescu, L.Z. (eds.). Springer (1995), pp. 175–180.
- Korobeinikov V.P. (1989). *Unsteady Interaction of Shock and Detonation Waves in Gases*, Urtiew, P.A. (English-edition editor), Hemisphere Publ. Corp.
- Krylov, A., Sorek, S., Levy, A., and Ben-Dor, G. (1996). Simple waves in saturated porous media. I. The isothermal case. *Japan Soc. Mech. Engineers Int. J., Ser. B* **39**: 294–298.
- Lagutov Y.P., Sharov Y.L., and Gvozdeva L.G. (1995). Experimental investigation of the interaction of shock waves with closed cellular compressible foam. In *Proceedings of the 20th International Symposium on Shock Waves*, Sturtevant, B., Shepherd, J.E., Hornung, H.G. (eds.). World Scientific, pp. 1345–1350.
- Lee, J.J., Frost, D.L., and Lee J.H.S. (1993). Transmission of a blast wave through a deformable layer. In *19th International Symposium on Shock Waves, Shock Waves @ Marseille*, Brun R., and Dumitrescu, L.Z. (eds.). Springer (1995), pp. 181–186.
- Levi-Hevroni, D. (1999). Wave propagation in a multiphase porous medium. Ph.D Thesis, Department of Mechanical Engineering, Ben-Gurion University of the Negev, Beer Sheva, Israel (in Hebrew).
- Levy, A. (1995). Wave propagation in a saturated porous medium. Ph.D Thesis, Department of Mechanical Engineering, Ben-Gurion University of the Negev, Beer Sheva, Israel (in Hebrew).
- Levy, A., Skews, B.W., Ben-Dor, G., and Sorek, S. (1993). Head-on collision of normal shock waves with rigid porous materials. In *(19th) International Symposium on Shock Waves. Shock Waves @ Marseille*, Brun, R., and Dumitrescu, L.Z. (eds.). Springer (1995).
- Levy, A., Ben-Dor, G., Skews, B.W., and Sorek, S. (1993)a. Head-on collision of normal shock waves with rigid porous materials. *Exp. Fluids* **15**: 183–(190.)
- Levy, A., Ben-Dor, G., Sorek, S., and Bear, J., (1993)b. Jump conditions across strong compaction waves in gas saturated rigid porous media, *Shock Waves* **3**: 105–111.

- Levy, A., Sorek S., Ben-Dor, G., and Bear, J. (1995). Evolution of the balance equations in saturated thermoelastic porous media following abrupt simultaneous changes in pressure and temperature. *Transport in Porous Media* 21: 241–268.
- Levy, A., Ben-Dor, G., and Sorek, S. (1996)a. Numerical investigation of the propagation of shock waves in rigid porous materials: development of the computer code and comparison with experimental results. *J. Fluid Mech.* 324: 163–179.
- Levy, A., Sorek S., and Ben-Dor, G. (1996)b. Experimental and numerical investigation of the head-on collision of planar shock waves with rigid porous materials. In *Proceedings of the 20th International Symposium on Shock Waves*, Sturtevant, B., Shepherd, J.E., and Hornung, H.G. (eds.). World Scientific, pp. 1357–1362.
- Levy, A., Ben-Dor G., and Sorek, S. (1998). Numerical investigation of the propagation of shock waves in rigid porous materials: flow field behavior and parametric study. *Shock Waves* 8: 127–137.
- Levy, A., Levi-Hevroni, D., Sorek, S., and Ben-Dor G., (1999) Derivation of Forchheimer terms and their verification by application to waves propagation in porous media. *Int. J. Multiphase Flow* 25: 683–7.
- Li, H., and Ben-Dor G. (1995). Head-on interaction of weak planar shock waves with flexible porous materials—analytical model. *Int. J. Multiphase Flow* 21: 941–947.
- Li, H., Levy, A., and Ben-Dor, G. (1995). Analytical prediction of regular reflection over rigid porous surfaces in pseudo-steady flow. *J. Fluid Mech.* 282: 219–232.
- Makris, A., Frost, D.L., Nerenberg, J., and Lee J.H.S. (1996). Attenuation of a blast wave with a cellular material. In *Proceedings of the 20th International Symposium on Shock Waves*, Sturtevant, B., Shepherd, J.E., and Hornung, H.G. (eds.). World Scientific, pp. 1387–1392.
- Mazor, G., Ben-Dor, G., Igra, O., and Sorek, S. (1994). Shock wave interaction with cellular materials. Part I: Analytical investigation and governing equations. *Shock Waves* 3: 159–165.
- Monti, R. (1970). Normal shock wave reflection on deformable solid walls. *Meccanica* 5: 285–296.
- Nerenberg, J., Frost, D.L., and Makris, A. (1997). Blast wave loading of polymeric foams. In *21st International Symposium on Shock Waves*. Houwing, A.F.P., and Paull, A. (eds.). Panther Publishing, pp. 91–96.
- Nigmatulin, R.I., and Gubaidullin, A.A., (1992). Linear waves in saturated porous media, *Transport in Porous Media* 9: 135–142.
- Olim, M., van Dongen, M.E.H., Kitamura, T., and Takayama, K. (1994). Numerical simulation of the propagation of shock waves in compressible open-cell porous foams. *Int. J. Multiphase Flow* 20: 557–568.
- Onodera, H., and Takayama, K., (1990). Interaction of a plane shock wave with slitted wedges. *Exp. Fluids* 10: 109–115.
- Onodera, H., and Takayama, K. (1994). Analysis of shock wave propagation over perforated wall and its discharge coefficient. *JSME Int. J.* 37: 497–502.
- Onodera H., and Takayama, K. (1995). Shock wave structure in polyurethane foam. *JSME Int. J. B* 37: 268–274 .
- Powers, J.M., Stewart, D.S., and Krier, H., (1989). Analysis of steady compaction waves in pourous materials. *ASME J. of Appl. Mech.* 56: 15–24.
- Rayevsky, D.K., Gvozdeva, L.G., Faresov, Y., Brossard, J., and Bailly, P. (1989). Reflection of shock and explosion waves from surfaces covered with layers of polyurethane foam. *12th International Colloquium on Dynamics of Explosions and Reactive Systems*, University of Michigan.
- Rudinger G. (1965). Some effects of finite particle volume on the dynamics of gas-particle mixtures. *AIAA J.* 3: 1217–1222.
- Sandursky, H.W., and Lidiar, T.P. (1985). Dynamic compaction of porous beds, NSWC TR 83-256, Naval Surface Weapons Center, White Oak, Md., USA.

- Seitz, M.W., and Skews, B.W. (1991). Three-dimensional effects in the study of shock wave loading of compressible porous foams. In *Proceedings of the 18th International Symposium on Shock Waves*. Takayama K. (ed.). Springer Verlag.
- Seitz, M.W., and Skews, B.W. (1996). Shock impact on porous plugs with a fixed gap between the plug and the wall. In *Proceedings of the 20th International Symposium on Shock Waves*, Sturtevant, B., Shepherd, J.E., and Hornung, H.G. (eds.). World Scientific, pp. 1381–1386.
- Skews, B.W. (1991). The reflected pressure field in the interaction of weak shock waves with a compressible foam. *Shock Waves* 1: 205–211.
- Skews, B.W. (1992). Oblique reflection of shock waves from rigid porous materials. In 10th Mach Reflection Symposium, Univ. Denver, Denver, Colorado, USA.
- Skews, B.W. (1994). Oblique shock wave reflection from porous materials, *Shock Waves* 4: 145–154.
- Skews, B. W, and Takayama, K. (1996). Flow through a perforated surface due to shock-wave impact, *J. Fluid Mech.* 314: 27–52.
- Skews, B.W., Atkins, M.A., and Seitz, M.W. (1991). Gas dynamic and physical behavior of compressible porous foams struck by a weak shock wave. In *Shock Waves, Proceedings of the 18th International Symposium on Shock Waves*, Takayama K. (ed.). Springer Verlag.
- Skews, B.W., Atkins, M.D., and Seitz, M.W., (1993). Shock wave interactions with porous compressible materials. *J. Fluid Mech.* 253: 245–265.
- Skews, B.W., Sellschop, R.M., and Legoete, T. (1996). Axisymmetric tests of shock-wave impact on PUR foam. In *Proceedings of the 20th International Symposium on Shock Waves*. Sturtevant, B., Shepherd, J.E., and Hornung, H.G. (eds.) World Scientific, pp. 1375–1380.
- Smeulders, D.M.J., Eggels, R.L.G.M., and van Dongen, M.E.H. (1992). Dynamic permeability: Reformulation of theory and new experimental and numerical data. *J. Fluid Mech.* 245: 211–227.
- Sorek, S., Bear, J., Ben-Dor, G., and Mazor, G. (1992). Shock waves in saturated thermoelastic porous media, *Transport in Porous Media* 9: 3–13.
- Sorek, S., Krylov, A., Levy, A., and Ben-Dor, G. (1996). Simple waves in saturated porous media (II. The nonisothermal case). *JSME Int. J.* 39: 299–304.
- van der Grinten, J.G.M., van Dongen, M.E.H., and van der Kogel, H. (1985). A shock-tube technique for studying pore-pressure propagation in a dry and water-saturated porous medium. *J. Appl. Phys.* 58: 2937–2942.
- van der Grinten, J.G.M., van Dongen, M.E.H., and van der Kogel, H. (1987). Strain and pore pressure propagation in a water-saturated porous medium. *J. Appl. Phys.* 62: 4682–4687.
- van Dongen, M.E.H., Smeulders, D.M.J., Kitamura, T., and Takayama, K. (1993). On the modelling of wave phenomena in permeable foam. In *19th International Symposium on Shock Waves. Shock Waves @ Marseille*, Brun, R., Dumitrescu, L.Z. (eds) Springer (1995), pp. 163–168.
- van Dongen, M.E.H., Smeets, G.V.R., Hoeijmakers, H.W.M. (1996). Shock-induced wave phenomena in open-cell permeable and flexible foams. In *Proceedings of the 20th International Symposium on Shock Waves*, Sturtevant, B., Shepherd, J.E., and Hornung H.G. (eds.). World Scientific, pp. 1363–1368.
- Yasuhara, M., Watanabe, S., Kitagawa, K., Yasue, T., and Mizutani, M. (1996). Experiment on effects of porosity in the interaction of shock wave and foam. *JSME Int. J.* 39: 287–293.
- Zaretsky, E.B. and Ben-Dor, G. (1995). Compressive stress-strain relations and shock Hugoniot curves of flexible foams. *J. Eng. Mat. Technol.* 117: 278–284.

Shock Wave Propagation in Multi-Phase Media

15.2 Weak Shock Wave Interaction with Inert Granular Media

ALEXANDER BRITAN AND AVI LEVY

*Pearlstone Center for Aeronautical Engineering Studies, Department of Mechanical Engineering,
Ben-Gurion University of the Negev, Beer-Sheva, Israel, 84105*

-
- 15.2.1 Introduction
 - 15.2.2 Experimental Methods and Materials
 - 15.2.3 Two-Dimensional Packing of Cylinders and Disks
 - 15.2.3.1 Unsteady Flow Pattern
 - 15.2.3.2 Dynamics of the Contact Stress Transfer
 - 15.2.3.3 Role of the Sidewall Friction
 - 15.2.4 Three-Dimensional Packing of Spherical Particles
 - 15.2.4.1 Behavior of the Unsteady End-Wall Peak
 - 15.2.4.2 Bridging effect and Size of the Pressure Transducer
 - 15.2.4.3 Packing Density and Gas Filtration
 - 15.2.4.4 Effective Stress Behavior
 - 15.2.5 Dynamics of the Granular Layer Compression
 - 15.2.5.1 Wave Processes
 - 15.2.5.2 Dynamic Young Moduli
 - 15.2.6 Shielding Characteristics of Granular Filters
 - 15.2.6.1 Problem Description
 - 15.2.6.2 Attenuation Performance of the Granular Materials
 - 15.2.7 Physical Models and Simulations
 - 15.2.8 Conclusion
 - References

15.2.1 INTRODUCTION

Large conglomerations of discrete macroscopic particles known as granular materials behave differently from other familiar forms of matter such as solids, liquids, or gases, and therefore they might be considered as being an additional state of matter (Jaeger *et al.*, 1996). Owing to their quantities in nature and the large stocks of artificial products, granular materials are applicable in all scientific and engineering fields. Some examples of applications and research possibilities using granular materials are listed below.

In *material science*, they are used as an initial step in the preparation of composites, ceramics, and sintered materials whose qualities depend critically on the initial setting condition. More generally, they are the state in which most geological materials are first exploited in highly divided form.

Many processes in *chemical engineering* make use of finely pulverized matter, from combustion of solids to heat exchangers and catalysts. Filtration and chromatographic column performances depend upon the nature and quality of grain packing.

Agriculture and food industry processes use natural granular substances and powder of different grades in dry or wet phases, and the rheology of pastes in particular depends on the heterogeneous structure.

In *pharmacology*, grains of variable scale are usually mixed with a bonding agent to obtain a tablet, which is a convenient form in which a stated dosage of a drug might be used. A tablet must be stable in storage and be sufficiently strong to withstand handling. In addition, the variation between tablets, as far as dose and weight are concerned, must be negligible. The quantity of particulate material that goes to form the tablet is measured on a volumetric basis and, consequently, a uniform bulk density in the die is obtained if variations in weight are to be minimized. Variations of bulk density can arise from the segregation of particles according to size. Although this undesired phenomenon is largely eliminated by granulating prior to tableting, the production of tablets of constant weight and dosage depends on the production of constant density tablet of uniform composition, and both attributes are a function of the flow properties of the powder or granule system.

Natural geological structures provide the opportunity to observe many effects of flow of grains such as spatial distribution of density and granulometry of particles in sediments of preserved land strata, landslides, submarine slope failures, and formation and motion of dunes. The structure, porosity, and permeability of a soil and its natural as well as man-made evolution (shaping, underground pollution, etc.) are of prime importance on the living Earth.

In *civil and military engineering* low-added-value consolidated granular materials are widely used for structures and building, as well as sound and shock wave absorbents. The last have received increasing interest primarily

because of their implications for protection of people and plants, as well as for the understanding of the response of granular structures and materials to blast and dynamic loads. The grain properties and orientation, as well as the properties of the gas phase that fills the voids between the grains, control the mechanical properties of the granular material. The gas flow takes place in these large pores connected by narrower tubelike structures. This results in high-level friction losses and causes dispersion and dumping of the shock wave energy. This is probably the area in which the most research work has been done in recent years. The interaction between the pressure impulse and the granular material skeleton and the behavior of the gas flowing through the pores of reactive granular materials were extensively studied to gain insight into the problem of the onset of deflagration-to-detonation transition (e.g. Baer, 1988). The behavior of inert granular media compaction by means of strong blast waves is of importance to explosive welding (e.g., Nesterenko, 1992) and to compaction technology of powders by means of or explosion (e.g., Carstensen *et al.*, 1990).

The general subject of weak shock wave interaction with inert granular media has also advanced considerably over the past two decades. It should be noted that by using the term “inert” we mean to exclude a great number of interesting phenomena observed in experiments by using explosive granular materials, and these are beyond the scope of the following discussion. In addition, when using the term “weak” shock we refer to a shock wave that causes small local and elastic deformations at the contact points between two grains. In practice, its speed would be much less than the sound velocity in the particles composing the bulk material. Such conditions might be obtained when the distance between the origin of a blast wave and the impacted structure is great enough. Encouraging progress in understanding this problem has been made on several fronts, including theoretical modeling, numerical simulation, and the acquirement of experimental results. This review outlines recent developments and focuses on the main experimental methods, materials used during various investigations, and results that have been obtained with respect to the following points:

1. Mechanics of stress propagation through granular media and the role of the sidewall friction
2. Effect of the shock wave induced gas filtration
3. Unsteady waves and contact stress performances inside a granular medium
4. Shock wave damping caused by granular filters
5. Recent physical models and methods used for computer simulation to predict experimental findings

15.2.2 EXPERIMENTAL METHODS AND MATERIALS

The experimental techniques used to study granular media are quite broad and span a considerable range of sophistication. They range from counting spots left by particle contact on carbon paper that covers the container walls (Mueth *et al.*, 1998) to magnetic resonance imaging and X-ray tomography of the bulk material. However, the most remarkable applications of these techniques were demonstrated for the static behavior of granular materials; dynamic experiments have not yet received enough attention, because of their complex nature. For a variety of reasons the majority of the dynamic studies have been done in the area of free field experiments with real earth materials such as soils (Liakhov and Poliakova, 1972). In laboratory tests, different natural or man-made granular samples composed of spherical grains, disks or cylinders are widely used (Rossmannith and Shukla, 1982; van der Grinten *et al.*, 1985; Rogg *et al.*, 1985; Gelfand *et al.*, 1989; Britan *et al.*, 1995). As shown subsequently, the main point of interest was the rigorous analysis of the granular sample response to the shock wave impact.

Several kinds of pressure transducers, strain gauges, and, more rarely, optical observations are used for registration of total compressive stress, σ_t , acting in a cross section of a granular bulk:

$$\sigma_t = P + \sigma/(1 - \varepsilon). \quad (15.2.1)$$

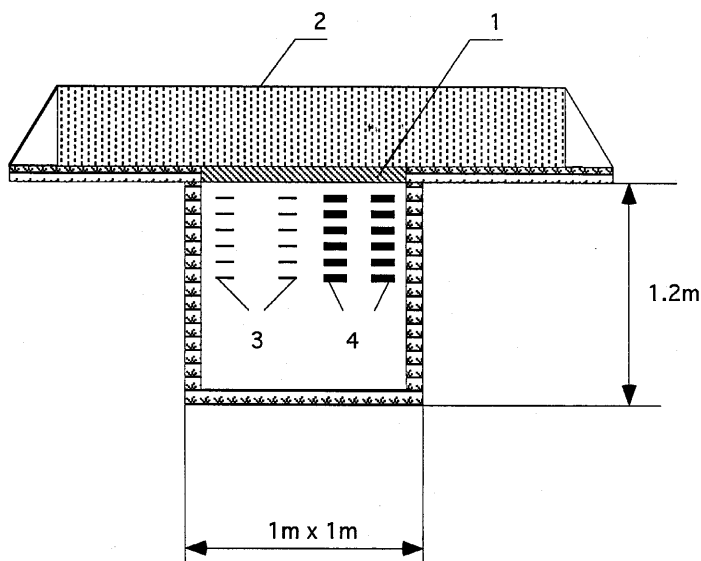
In this equation, P is the gas pressure inside the pores, $\sigma/(1 - \varepsilon)$ is the effective stress of the granular material, and σ is the stress acting between particles, which can be related to the porosity $\varepsilon = \varepsilon(\sigma)$. Other important characteristics of the granular material are its relative density, v , which is usually defined as the bulk density, ρ_b , over the particle density, ρ_p , i.e., $v = \rho_b/\rho_p$. When the density of the fluid filling the pores of the granular material is much less than that of the particle, the bulk material porosity can be then expressed by $\varepsilon = 1 - v$.

When the bulk material is loaded by a weak shock wave, the net result is that changes in the relative density, v , cause stress variations, which are usually rather small. Nevertheless, a properly designed experiment allows one to observe these variations in full scenarios, or even only isolated details such as gas flow filtration through the lattice (Rogg *et al.*, 1985; Levy *et al.*, 1993a; Britan *et al.*, 1997b), stress concentration and its propagation through the contact points between the grains (Rossmannith and Shukla, 1982), and shielding performances of the granular material (Ben-Dor *et al.*, 1997; Britan *et al.*, 1997a, 2000, etc.).

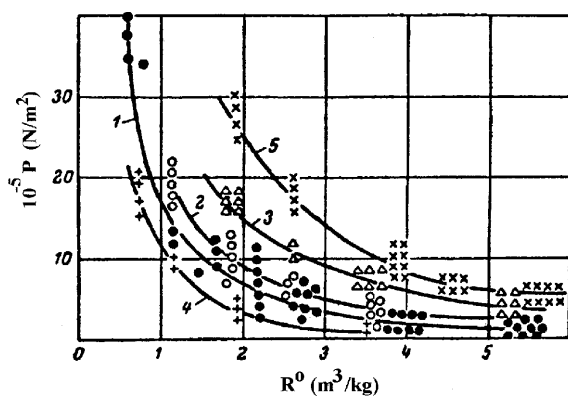
Early studies on the interaction between a shock wave (or shock waves) and a granular material were largely motivated by the need for deeper insight into

the problem of destructive effects caused by blast waves on constructions. To date the results, which were mostly obtained in free field tests, form the basic knowledge on blast wave amplitude and speed in air and underground at different distances from the explosive center (Liakhov and Poliakova, 1972). High-frequency strain gauges and/or piezoelectric pickups and portable data recorders are typical equipment used for free-field experiments on granular samples of natural composition. As an indicator of residual displacement of the granules after the blast, thin pieces of Al foil are usually placed inside the granular material before the experiment. To record normal and lateral pressures, the pickups' orientation can be adjusted either parallel or perpendicular to the direction of the wave propagation. Different arrangement of detonation charges and sensors placed on the ground or at the same depth under the ground allows utilizing plane or spherical detonation as well as camouflet explosion. Since granulometric composition of the samples depends on the testing region, most of the results, which are available in the literature, were obtained for sandy soil of fluvial, quarry sands, clayed soil, or loess with different water content. Typical arrangement of a free field experiment with a sample of water-saturated soil and flat explosives is shown in Fig. 15.2.1a. The sand is poured into a pit that was excavated on the bank of a river and filled with water. Before a flat charge (1 in Fig. 15.2.1a) was placed under the soil covering, 2, pressure sensors, 3, and pieces of thin foil, 4, were placed inside the pit while the pit was gradually filled with soil. Once all the sensors have been placed, the soil in the pit was trampled in layers until the required density of the sample was achieved. For the experiments with natural composition of unsaturated soils, sensors were usually placed inside special holes bored in parallel to the horizontal plane, so that the undisturbed structure of the soil remains between the sensors and the charge. After the experiment the soil was carefully removed from the pit, and the foil shift showed the grain displacement during the impact. Typical results of free field experiments of Liakhov and Poliakova (1972) are presented in Fig. 15.2.1b. The peak pressure at the shock wave front was measured as a function of the relative distance R^0 passed by the shock wave front through the soils with different moisture content (2–4, 5–7, 10–12, and 16–20%). From the experimental curves it follows that the peak pressure decreases with distance R^0 . This feature was strongly dependent on the soil moisture content. Hence, such pressure measurements can be safely used for moisture control in soils and other earth materials.

In contrast to free field experiments, when the main scaling parameter is the relative distance R^0 , the loading scenarios and the granular sample type and characteristics can be easily and widely varied in laboratory tests. Hveding (1985) reported on shock tube experiments in which the conditions thought to be similar to those determined by an air-blast wave with Mach number $M_s \approx 1.5$ sweeping over horizontal surface of a uniform or inhomogeneous



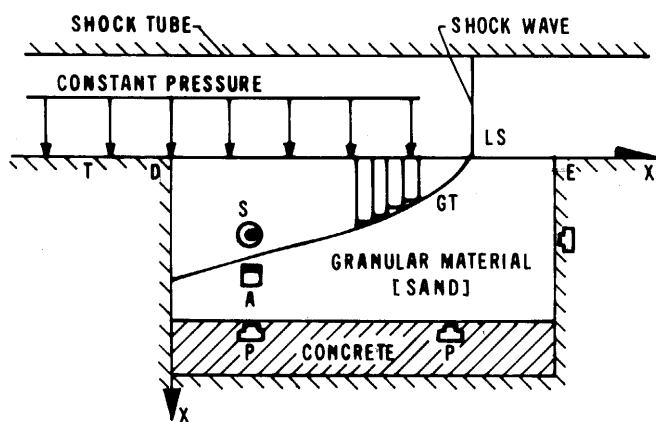
(a)



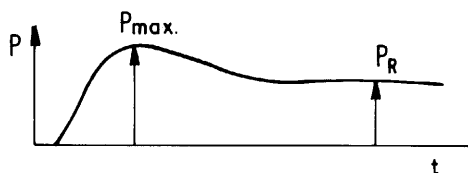
(b)

FIGURE 15.2.1 (a) Typical schematic of free field experiment of Liakhov and Poliakova (1972), and (b) maximum pressure behind the shock wave front as a function of distance R^0 : 1–4; unsaturated sandy soils (moisture content $\alpha_2 = 2$ –4, 10–12, and 16–20%); 5, water-saturated sandy soils, gas content $\alpha_1 = 0.2$ –0.4. Solid lines represent least square approximation for the experimental points.

semi-infinite free field ground. In this study, a large-scale container $1.3 \times 0.2 \times 0.5$ m was filled with a well-defined type of sand. The container was connected to a 400 mm-diameter shock tube. The schematic illustration of this experiment, shown in Fig. 15.2.2a, is similar to a one-dimensional (uniaxial) piston type loading on the surface by an incident shock wave (IS) that generates separate uniaxial transmitted pressure wave into the sand (GT) with assumably no interference by means of an impulse transfer mechanism. The front positions of these waves and a schematic illustration of the pressure forces and the positions of specially designed pressure transducers of types S, P, and A placed inside the sand are presented in Fig. 15.2.2a. Transducer types S and P were made from 3-mm thick round disks. These transducers were placed inside the bulk and mounted at the container walls as shown in Fig. 15.2.2a to measure the average side-oriented grain stress. Very small (1 cm) and light (2 g) A-transducers allowed measurement of the real changes in the average grain motion induced by the uniaxial pressure wave. Up to 100 transducers



LOCATION OF THE VARIOUS TRANSDUCERS
(a)



(b)

FIGURE 15.2.2 (a) Loading situations for shock tube experiments and (b) typical pressure signals as measured at the bottom of the container (Hveding, 1985).

placed in pairs in the center of the measuring point grid inside the granular bed allowed grain acceleration–time and velocity–time history to be obtained for each studied condition. The pressure profile, as measured at the bottom surface (see Fig. 15.2.2b), increased gradually to maximum pressure, P_{\max} , and after the unsteady part, a normal reflection pressure, P_R , was observed. The resultant pressure was typically 4 to 6 times the undisturbed pressure behind the incident shock (IS) above the sand surface, P_2 . The reflected pressure, P_R , remained high and near-steady over a long time period and was further used by the authors for comparison with the results of theoretical investigation. Since the incident shock (IS) passes over the sand surface, the wave reflected from the bottom can be considered as superimposed on the transmitted wave (GT). Thus, closer to the container bottom the loading situation becomes increasingly complex.

Based on gas-dynamic theory, the description of the gas phase behavior when an incident shock wave collides head-on with granular material looks much simpler. In the experiments of Rogg *et al.* (1985), special geometry was used to observe the net effects caused by shock induced gas filtration inside a solid array of cylinders and a packed bed of spherical pellets. The porous models were placed inside a shock tube normal to the propagation direction of the incident shock wave with Mach number $M_s = 2.05$. High-speed shadow-graphs provided quantitative information on the flow pattern inside the rigid array of cylinders, while the pressure field in the front of and within the porous models was measured using standard Kistler pressure transducers.

Propagation of pressure wave through water-saturated granular media was firstly investigated experimentally by van der Grinten *et al.* (1985). In these experiments the incident Mach number was $M_s \approx 1.5$ and the granular sample was fabricated from sand particles ($d_p = 340 \mu\text{m}$) using special technology, which allowed fixing the granules at their contact points with an epoxy resin. This prevented movement of the sand particles and their rearrangement as a result of the wave interactions. A granular column was placed inside the shock tube in such a way that the back edge of the sample was supported by the test section end-wall. A set of miniature gauges measured pore pressure, and both axial and circumferential strains at different distances from the sample top were used. Experimental results showed the existence of a two-wave system with the second wave strongly damped compared to the first one.

Similar rigid models fabricated from natural porous materials, silicon carbide (SiC) and alumina, were used by Levy *et al.* (1993a). Kistler pressure transducers registered gas pressure histories at different cross sections of the model. The incident shock wave Mach number was in the range $1.2 \leq M_s \leq 1.7$. A typical gas pressure history as was recorded by Levy *et al.* (1993a) inside the pore of the porous material in the experiment with a 81-mm long model made of SiC having 10 pores per inch is shown in Fig. 15.2.3.

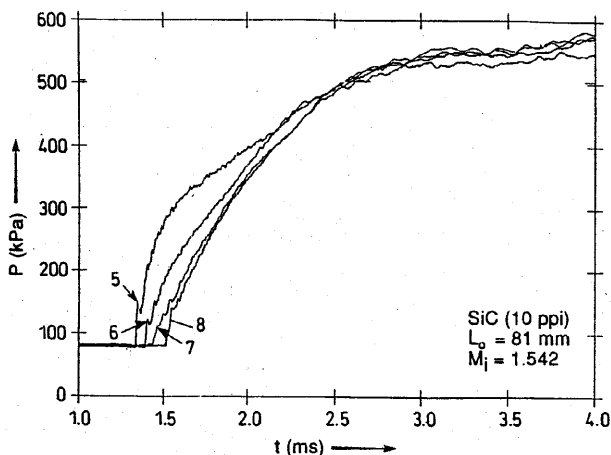


FIGURE 15.2.3 The gas pressure history in the pores of an 81-mm porous sample made of SiC as recorded at its side wall (5, 6, 7) and at the shock tube end wall (8) (Levy *et al.*, 1993a).

Pressure traces 5, 6 and 7 were recorded 63, 43 and 23 mm from the rear end of the model, respectively and pressure trace 8 was recorded at the shock tube end wall. From this figure, the following was clearly evident:

- All pressure traces resemble sharp fronts, which is typical for pressure jump across a shock wave
- The sharp front jumps are followed by continuous pressure increase
- As the compaction wave propagates, the pressure jump across it decreases, but the final pressure remains almost unchanged

Similar observations were obtained by the numerical simulations of Levy (1999) when a shock wave collided head-on with granular material made of alumina particles. It is noted that the deformations of the rigid porous models in experiments of Levy *et al.* (1993a) and van der Grinten *et al.* (1985) and the numerical study of Levy (1999) were negligibly small. Therefore it was concluded that the dominant effect for the pressure performance were due to shock wave penetration, which strongly depends upon the pore size, and gas filtration. It should be noted that gas filtration is often coupled with granular compression and may therefore influence stress-wave propagation in the bulk material. The investigation of Gelfand *et al.* (1989) was probably the first where two of these complex phenomena were observed simultaneously. Experiments were conducted in vertical shock tube for a single value of Mach number $M_s \approx 1.5$. The granular material was poured directly on the test section end wall and during the study the granular layer depth, diameter, and density of the granules were varied in a wide range. In order to read the history

of the gas pressure P , one of the two pressure transducers that were mounted at the end-wall of the test section was protected from having a direct contact with the particles by a screen permeable for gas. The second pressure transducer was installed without a protective screen to record the total stress, σ_t . To control the impulse transferred through the granular sample to the end wall, the stress signals were processed via a special electronic integrator. The end-wall pressure signatures displayed in Fig. 15.2.4 were obtained for a 20-mm depth of bulk material composed of 0.2-mm polystyrene particles. The upper trace in this figure represents the total stress, σ_t ; the bottom trace is the gas pressure, P , recorded by the protected transducer. From this figure it can be seen that the signals from the two transducers are quite different. The total stress signature demonstrates strong peak at the front and then rapid oscillatory decay to the pressure P_5 , while the gas pressure rises very slowly. Notably, the magnitude of the peak in the total stress signal can be significantly changed depending on the experimental conditions. Recall that this observation was not reported in free field experiments or in large-scale tests in the laboratory (see Fig. 15.2.2b). The narrow overshoot in the total stress signal is typical for shock tube experiments with a small aspect ratio of the granular sample (height/width). The highest peak, of about 62 bar, was reported by Sakakita and Hayashi (1992) for conditions when an incident shock wave with Mach number $M_s = 1.7$ strikes head-on a 10-mm granular layer composed of small-particle nylon powder ($d_p = 5 \mu\text{m}$). The powder was poured directly on the end wall of the shock tube with $50 \times 50 \text{ mm}$ cross section, and the aspect ratio of the

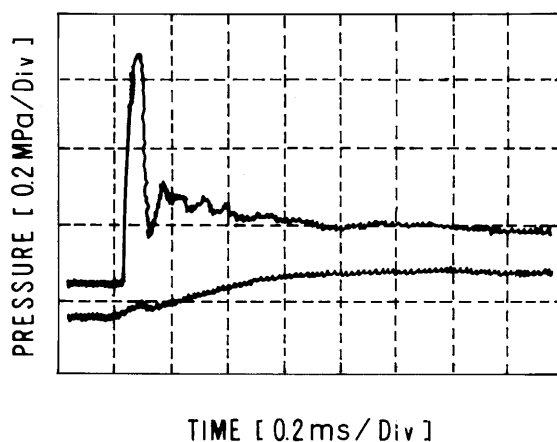


FIGURE 15.2.4 Typical pressure records for stepwise incident shock wave on a 20-mm granular layer composed of 0.2-mm polystyrene particles. The time and pressure scales are 0.2 ms and 0.2 MPa per division (Gelfand *et al.*, 1989).

sample (0.2) was rather small. As shown subsequently, the value of the aspect ratio is of paramount importance for this phenomenon.

A potentially very interesting area for investigation is the use of shock tube for studying the attenuation characteristics of shock waves in granular materials. In practice, every underground shelter must have a ventilation duct, which might be a route for blast wave penetration into the shelter (such a problem setup can be seen in Fig. 15.2.5a). It is a common practice to use filters composed of some kinds of granular material placed inside the air intake system to attenuate and to prevent wave penetration and/or to protect expensive chemical filters that are located downstream in the ventilation duct. Engebretsen *et al.* (1996) investigated experimentally a similar problem in a shock tube. Different granular materials were placed inside a special section installed in the channel, 5.0 m downstream of the diaphragm. The shock propagation was monitored by means of Kistler 603B and Kistler 412 pressure transducers. Comparison between pressure profiles, as measured upstream and downstream of a 220-mm long filter of 15-mm glass spheres and as obtained by RCM numerical simulation are shown in Fig. 15.2.5b. The pressure signal upstream of the filter consists of the first abrupt pressure jump with an overpressure of $\Delta P_2 = 0.7$ bar (marked by arrow) that corresponds to the arrival of the incident shock wave, and then pressure rises gradually because of unsteady effects behind the reflected shock wave. The overpressure ΔP_2 serves as an input parameter to estimate attenuation performances of the filter, while the output parameter is the overpressure as measured behind the transmitted shock wave downstream of the filter. Note that the output pressure shown in this figure can be assumed constant for a very short time period and is quickly followed by a gradual pressure rise. The difficulty of interpretation of such a signal can provide the reason for the poor correlation of the experiment with theory, which is evident from this figure. A brief analysis of the various results available in the literature for similar setups is presented in Section 15.2.6.

Extensive experimental investigations of weak shock wave interaction with granular media were conducted in a 31×31 mm square vertical shock tube at the Department of Mechanical Engineering, Ben-Gurion University of the Negev (Ben-Dor *et al.*, 1997; Britan *et al.*, 1995, 1997a,b, 1999, 2000). The schematic setup of the vertical shock tube is shown in Fig. 15.2.6a. The driver section was filled with air at an initial pressure up to 2.0 ± 0.001 MPa and the air in the channel was at atmospheric conditions. A detailed depiction of the test section can be seen in Fig. 15.2.6b. Suntzov 5136 pressure transducers were mounted at ports T1 to T4. A screen permeable to gas protected these transducers and prevented a direct contact with the particles. (Note that transducer protection was also used previously for similar purpose by Gelfand *et al.*, 1989, van Dongen *et al.*, 1996, and Yasuhara *et al.*, 1996). Two Kistler 601H transducers have been mounted at ports T5 and T6 without a protected

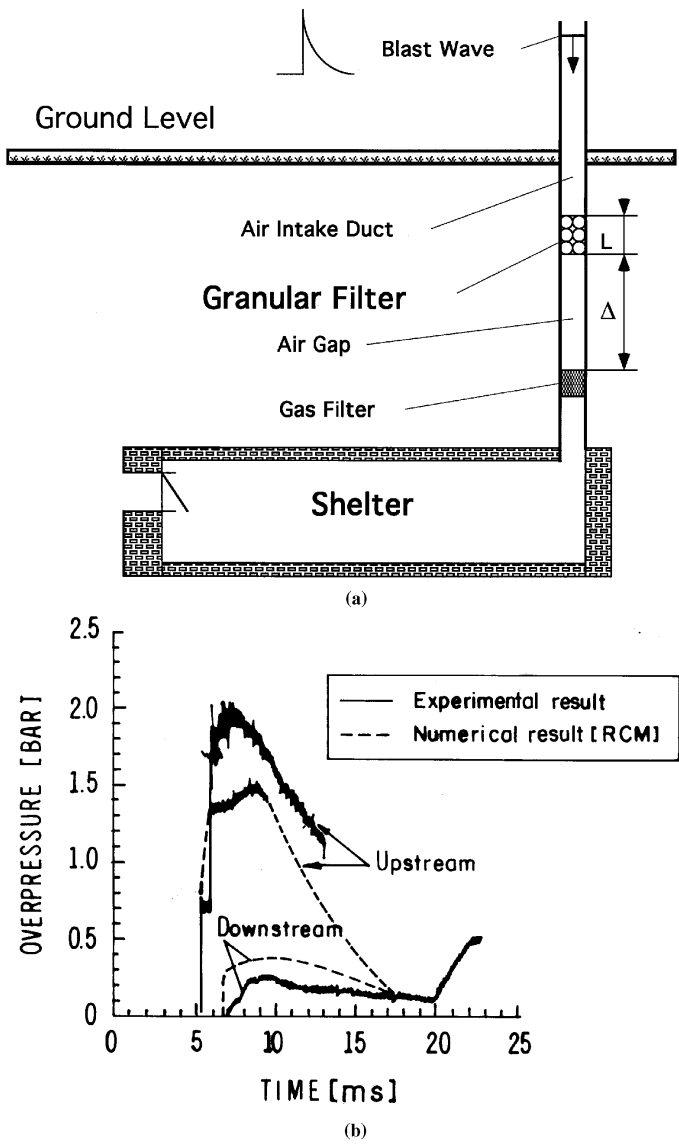
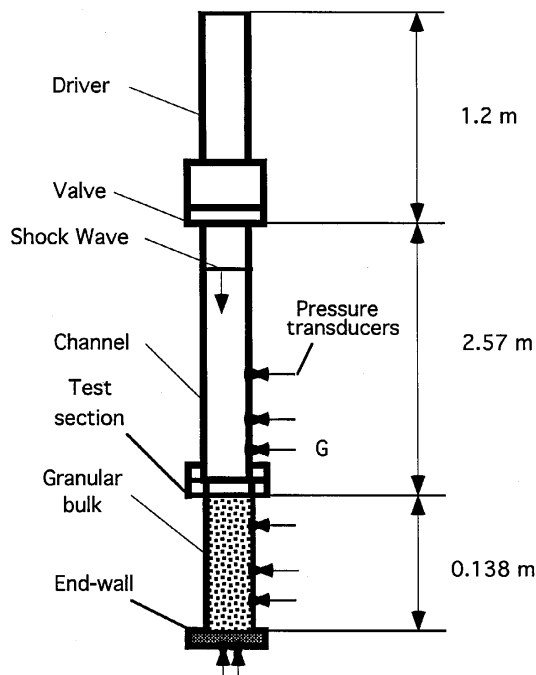
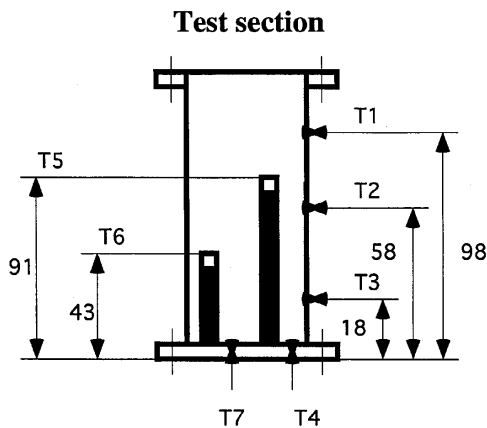


FIGURE 15.2.5 Schematic description of the interaction between blast wave and granular filter (a) and (b) typical pressure signals as obtained by Engebretsen *et al.* (1996) upstream and downstream of a granular filter.



Schematic of the shock tube

(a)



(b)

FIGURE 15.2.6 Schematic description of the Ben-Gurion University vertical shock tube (a) and test section (b).

TABLE 15.2.1 Properties of the Different Granular Materials used in the Experiments (Ben-Dor *et al.*, 1997; Britan *et al.*, 1995, 1997a,b, 1999)

N	Material	ρ_p (g/cm ³)	ρ_s (g/cm ³)	ρ_b (g/cm ³)	ν	ε	d_p (mm)	$f \times 10^5$ (mm ²)
1	PVC	1.400	1.400	0.856	0.611	0.389	3.33	954
2	Al ₂ O ₃	0.940	3.288	0.511	0.544	0.456	1.67	496
3	Fe	7.414	7.414	4.499	0.607	0.393	1.04	99
4	Fe	7.414	7.414	4.457	0.601	0.399	0.45	18
5	Potash	1.905	2.050	1.089	0.572	0.428	0.45	27

screen and were used with special Kistler 6421 connecting nipples to record the total stress profile inside the granular layer. A Kistler 606A pressure transducer was mounted at port T7 (the shock-tube end wall) without a protective screen and was used to study the shielding effect of the granular layer. Kistler 5007 charge amplifiers were used for all pressure measurements. The recorded data were stored using a data acquisition system Gage-Scope CS 220 with sampling rate at 500 KHz per channel.

Various granular materials were used during these studies, such as PVC (polyvinyl chloride), Al₂O₃, Fe, and potash particles. Characteristic properties of these materials are presented in Table 15.2.1. These properties were obtained as follows. The particle density, ρ_p , was calculated using the measured weight and volume. The mean diameter of the granules, d_p , for materials N1 to N3 was measured using a microscope with an accuracy of ± 0.01 mm. Powders N4 and N5 were grated using sieves with calibrated mesh sizes. The bulk densities, ρ_b , were determined from the overall layer volume and its weight in air. Hereafter, the identifying code number shown in Table 15.2.1 will be used to identify each tested material in the text and figures. Prior to each experiment the test section was lifted off the holding flange at the rear end of the channel. During the material filling, light knocking on the test section wall was applied in order to improve homogeneity of the granular material. As a result, the poured and the bulk density of the material were similar. Special attention was also given to ensure that the granular layer free surface remained flat and normal to the shock tube sidewall. Once a preparation procedure was completed, the granular layer thickness, h , was measured with an accuracy of about ± 1 mm, and the test section with the granular material was bolted at the rear flange of the shock tube (see Fig. 15.2.6a). Note that the thickness of the granular layers in course of these studies was varied up to $L \leq 138 \pm 1$ mm.

Typical pressure traces obtained during experiments with a 138-mm thick layer composed of material N2 (see Table 15.2.1) are presented in Fig. 15.2.7. The pressure trace recorded by transducer G, which was mounted at the shock

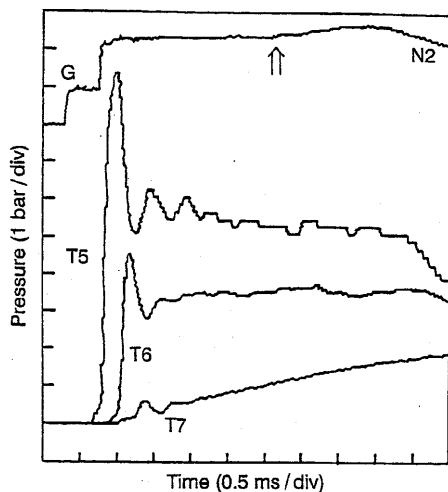


FIGURE 15.2.7 Typical total stress signals as recorded for a 138-mm granular layer at the shock tube presented in Fig. 15.2.6. The arrow indicates the end of the test time period (Ben-Dor *et al.*, 1997).

tube sidewall 80 mm upstream of the granular layer interface, is shown at the top of the figure. This signal shows two pressure jumps, which corresponded with the passage of the incident shock wave and the reflected shock wave, respectively. In order to simplify the analysis of the wave interactions, it was assumed that the shock tube test time terminated when the reflected shock wave collides with the contact surface of the main flow. An arrow in the figure marks this moment. The reflected pressure slightly rose in time at the beginning of the signal and approached the limited value P_5 , which would have been reached had the shock wave been reflected from a bare, rigid end wall. The main reasons for such an unsteady phenomenon at the early time of reflected pressure trace were extensively discussed by Rogg *et al.* (1985) and more recently by Levy *et al.* (1993a) and could be attributed to the initial history of the transmitted wave penetration into the granular layer.

Analysis of the compressive stress signals from transducers T5 to T7 (shown in Fig. 15.2.7) revealed that the stress peaks have nonsteady behavior. Similar observation was obtained in shock tube experiments by Gelfand *et al.* (1989) and Sakakita and Hayashi (1992). The peaks in the stress signal was followed by a quasi-steady period, and after the gas pressure upstream of the bulk started to decrease, the stress signals also decreased. In contrast to this, the stress at the end wall (as recorded by transducer T7) increased gradually in time, while the amplitude of the unsteady peak for this case was small and ill defined.

Although pressure transducers enable indirect recording of stress propagation through the bulk material as a whole, optical visualization and particularly the photoelastic method provide information on the stress history in the vicinity of each contact point across the granular material. Rossmanith and Shukla (1982) were among the first to use this method to visualize unsteady stress pattern inside a lattice structure composed of Homalite 100 disks (12.5 cm thick). When the disks were subjected to a stress, they became temporarily birefringent and resulted in an interference pattern of black and white regions within the circles shown in Fig. 15.2.8a. These fringes, known as isochromatics, represent lines along which the difference of the principal normal stresses is constant. Higher fringe concentrations correspond to higher stress accumulations. The experimental outcome was the record of a time-controlled sequence of 16 discrete instantaneous configurations of a continuous dynamic process. A multiple spark gap camera of the Cranz-Shardin type was triggered at some prescribed delay time after the loading incidence. This high-speed photographic system, illustrated in Fig. 15.2.9, operated with a series of high-intensity, extremely short-duration pulses of light with a rise time of about 0.1 μ s. The framing rate of this recording system was from 20,000 to about 800,000 fps. A pair of field lenses was utilized to control the passage of light through the granular model and to transmit the light to a plane sheet of film resting in the camera. Shukla and Damania (1987) and Shukla (1991) applied this technique to study shock wave attenuation through a single channel as well as one- and two-dimensional assemblies of plastic disks. Electrical-resistance strain gauges, SEA 06-0320W-120, were also used and were mounted at different locations inside the model. The transient and the rising times of the bridge amplifiers were sufficiently small to identify the strain by the arrival of the incident and the reflected pulse at each strain gauge location. The velocities of the incident peak and reflected waves through the disk assembly (shown in Fig. 15.2.8b) were obtained as the ratio of the propagated distance to the time of arrival of the stress wave at the strain gauge. Since the first few disks were compressed more strongly against each other, the ratio of incremental stresses and incremental strains is large and the material appears to be stiffer. Thus, the wave speed is higher in the first few disks and quickly drops from 1240 m/s to 1000 m/s within travel of 4 inches. These data were compared with the photoelastic results and the match between the two was quite good. A special comment should be inserted here about the dynamic loading method used by the authors. Rather than use a shock wave to produce impacts on the lattice, across the whole interface, they applied the local explosion of a small charge (≈ 120 mg) of lead azide (PbN_6). Explosive impact caused strong acceleration of a single top disk, which further impacted the lattice. Hence, the main interest of these studies was focused on the characteristic paths for load transfer from a point source (compactor), and

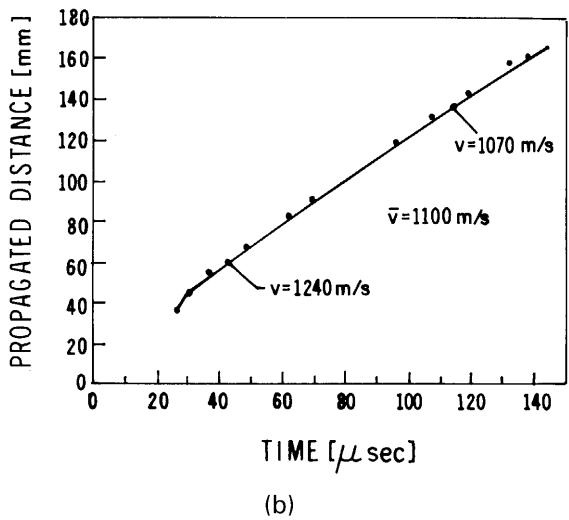
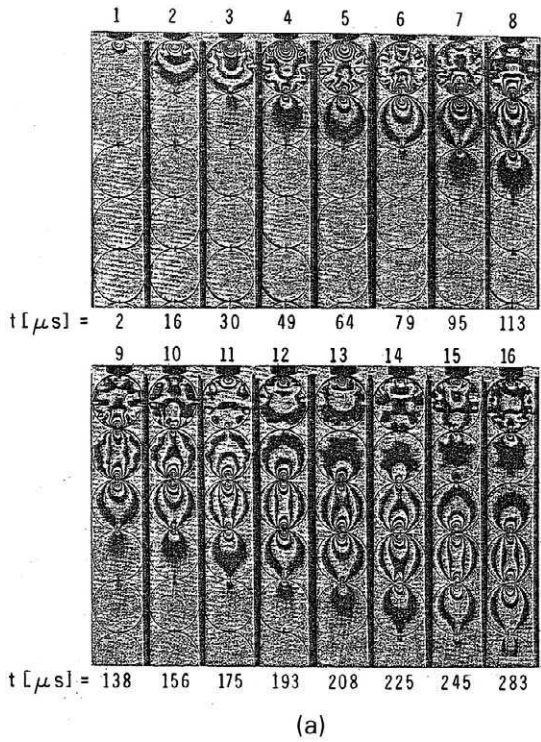


FIGURE 15.2.8 (a) Isochromatic fringe patterns showing dynamic load transfer across contacts in a single chain of plastic disks (Shukla and Damania, 1987). (b) Wave front position as a function of time for the single-chain experiment of Shukla and Damania (1987).

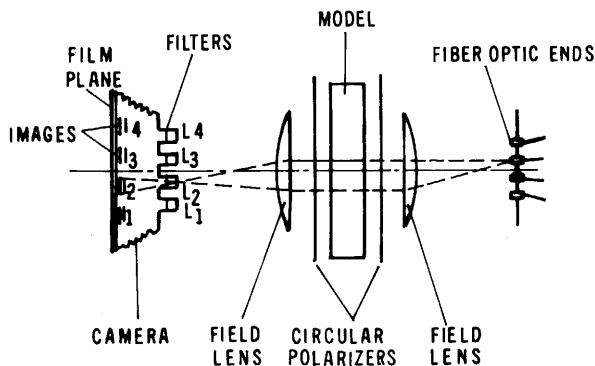


FIGURE 15.2.9 Optical arrangement of a typical Cranz-Schardin multiple-spark high-speed recording system adopted by Rossmanith and Shukla (1982) for photoelastic measurements.

obtaining quantitatively the dynamic contact forces inside the granular assemblies of different geometry. Moreover, in contrast to most shock tube experiments, where filtration effects are of paramount importance in stress formation, in these experiments the latter was entirely excluded. Furthermore, to ensure that combustion gas products did not impede the optics, the combustor was located at the far end of an aluminum punch connected by a half-round bottom with the impacting disk.

15.2.3 TWO-DIMENSIONAL PACKING OF CYLINDERS AND DISKS

15.2.3.1 UNSTEADY FLOW PATTERN

When an incident shock wave impinges head-on upon a granular medium, it results in a reflected and two transmitted (in both the gas and the solid phases) pressure waves. The transmitted wave in the gas phase does not necessarily transform into a shock wave, which propagates inside the pores of the granular layer. In some cases, it appears as a compression wave (e.g., Liakhov and Polyakova, 1972; Mazar *et al.*, 1994). An induced gas flow into the pores of the granular material is followed by the transmitted wave. The induced gas flow tends to increase the pore size and to unpack the granular material, whereas the transmitted wave to the solid phase, tends to compact the bulk material. These two opposite mechanisms interact with each other during the wave propagation and, as a consequence, modify the initial conditions of the granular material. It should be noted that both pressure waves propagate

with different wave velocities since they move in different media. The initial bulk density ρ_b of a granular material can be expressed as a function of the location x_i and the time t_i by

$$\rho_b(x_i, t_i) = v(x_i, t_i) \times \rho_s(x_i, t_i). \quad (15.2.2)$$

Thus, for constant particle density ρ_s , any change in the bulk density ρ_b is due to a change in the bulk relative density, v . When the waves are impacting on a bulk material, the relative density will be changed at the fronts of both transmitted waves, that is, the transmitted wave into the granular phase (the compaction wave) and the transmitted wave into the gas phase. This complex phenomenon results in the formation of a region with lower porosity and is therefore called the compaction wave front. The compaction changes occur primarily at the top of the granular layer and then are transferred down, as the compression forces are being transmitted through the contacts between the granules. Further disruption of the contacts, separation of particles caused by inertia effects, and repositioning follows the transferred contact forces.

It is well established that the effect of the compaction wave on the upstream conditions may be different depending on which impact load (strong or weak shock wave) hits the bulk material interface (Kuo *et al.*, 1980). Strong compression may cause fragmentation of the grains followed by a formation of a plastic flow; impact of a weak shock wave results in particle rearrangement and squeezing inside the large interstitial voids between the granules.

A unique distinctive feature of weak shock wave impact on granular media is that compression forces are propagated directly through the particle contact points and cause nearly the same effect on the bulk skeleton as the drag force when acting on the bulk, because of shock-induced filtration. It should be noted that fundamental coefficients of drag and heat transfer in steady flow thorough packed beds are well known (Kuo and Nydengger, 1978; Jones and Krier, 1983) and are widely correlated to the flow resistance. In contrast to the latter, the unsteady effect that appears when filtration is induced by a shock wave impact is not fully understood (Igra and Takayma, 1992). Rogg *et al.* (1985) conducted experiments of head-on collisions of shock wave with a 2D fixed array of cylinders to observe the main details of this unsteady phenomenon. It should be noted that this type of experiment excluded solid-phase interactions. A series of shadowgraphs describing the shock wave interaction with an array of cylinders is shown in Fig. 15.2.10. In these figures strong unsteady boundary layers, jets, recirculation regions, and shear layers can be observed behind the transmitted shock wave. Dual vortices upstream and downstream of the obstacles and supersonic jets results in a bow shock formation. It should be noted that the multiple wave reflections will also form compression waves, which take place at various locations along the granular layer. Farther upstream, the flow through the cylinder array becomes

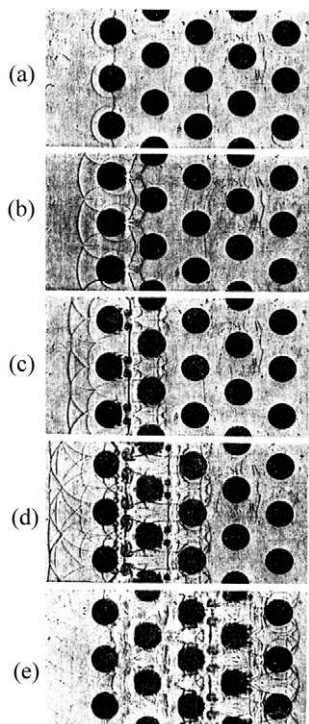


FIGURE 15.2.10 Shadowgraphs of shock wave approaching from the left and impinging on an array of perpendicular cylinders. Time between the pictures is $\approx 30 \mu\text{s}$ (Rogg *et al.*, 1985).

turbulent and the distance between the transmitted wave and the bow shocks increases. Later on, when the flow process becomes dominant, the unsteady phenomena disappear.

Although the unsteady behavior (i.e., vortices, boundary layers, bow shocks and stagnation zones) observed in the flow through the 2D array is important, inside a 3D granular medium it will be less noticeable. Since the packing factor and the void sizes will be much smaller, these disturbances should be weaker and quickly attenuate. Low porosity ($\varepsilon \approx 0.4$) may also lead to choking phenomena. A simple estimation of the choking distance, x_1 , may be done by using the formula derived by Goldshtik (1984) for the choking distance in steady gas flow through a granular bed,

$$x_1 = \frac{1}{3} \frac{\psi d_p}{\varepsilon v k M}, \quad (15.2.3)$$

where $\psi = 0.508 - 0.56 v$ is the hydraulic resistance of the layer, and k and M are the ratio of the specific heats and the local Mach number for the gas phase ahead of the granular layer, respectively. Note that when Equation (15.2.3) is used for low incident shock wave Mach number ($M_s \approx 1.3$) and spherical particles, the choking distance, x_1 , has the same order of magnitude as the diameter of the solid particles. This result shows that the choking phenomenon, as in the case of the compaction wave, occurs at the vicinity of the granular bulk interface. The validity of such a prediction is supported by the fact that strong secondary shocks are clearly visible just upstream of the second row of cylinders (see Fig. 15.2.10b). Since in this case the cylinders are rigid and do not touch each other, the stress wave, which was transmitted to the first row of cylinders, does not continue to propagate through the solid phase. Instead it will propagate only through the gas phase.

15.2.3.2 DYNAMICS OF THE CONTACT STRESS TRANSFER

Shukla and Damania (1987) and Shukla (1991) studied another extreme case of the impact scenarios. In contrast to the experiments of Rogg *et al.* (1985), in these cases close packing of the disks was used. The close packing prevented gas filtration and allowed transmission of stresses through the contact area between the disks. A sequence of isochromatic fringes obtained by Shukla and Damania (1987) with a single chain of disks is shown in Fig. 15.2.8a; the strain values as measured at the contact between the disks are plotted in Fig. 15.2.11. Similarly to the stress velocity shown in Fig. 15.2.8b, the peak strain shown in Fig. 15.2.11 drops rapidly in the first few disks and then decays more gradually. About 20% of the total load was lost, while closing the contact of the first five disks in the chain. This was much higher when compared to 2% losses in peak load for the same distance in a uniform bar composed of the similar material. An interesting aspect of this study was the extension to the case of the two-dimensional pattern of the stress wave propagation, which was simulated experimentally using the hexagonal close-packing arrangement of the disks shown in Fig. 15.2.12. In this case, each disk was in contact with multiple disks in assembly. Since the explosive loading in this case operated at a specific place and was not distributed uniformly, two distinct chains are of interest. The primary chains, such as those 1a and 1b shown in Fig. 15.2.12, emanate from the disk on which the explosive loading takes place. The secondary chains are composed of contacts of other disks with the disks in the primary chain. The normal contact loads in between two neighbor disks are plotted in Fig. 15.2.13. In this figure it can be seen that the peak loads quickly drop significantly from

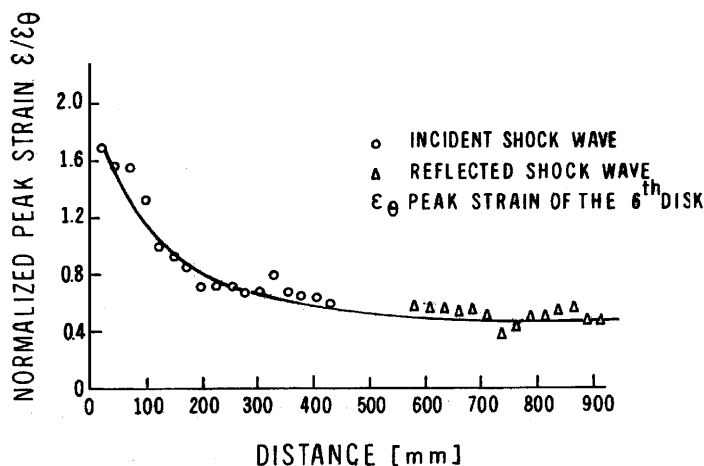


FIGURE 15.2.11 Decay of normalized contact peak strain with distance from the explosive source (Shukla and Damania, 1987).

one contact to another due to additional energy transfer from the primary chain to the disks of the secondary chains. In fact, whereas for the single-chain tests only 20% attenuation of the stress wave was observed, for the primary chain in the hexagonal packing the wave attenuation reached about 70% (for the same distance of five disk diameters).

Shukla (1991) extended this work and assumed that dynamic load transfer and energy losses should depend on the contact angles between the granules.

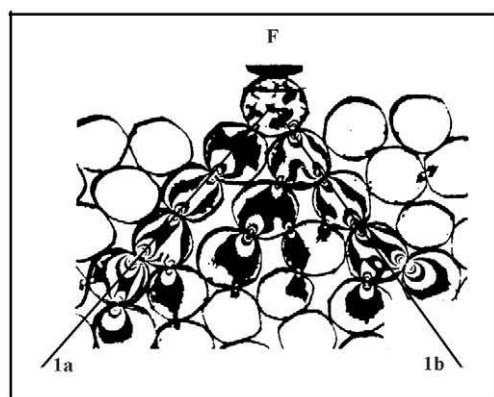


FIGURE 15.2.12 Isochromatic fringes obtained in a hexagonal close-packing arrangement (Shukla, 1991).

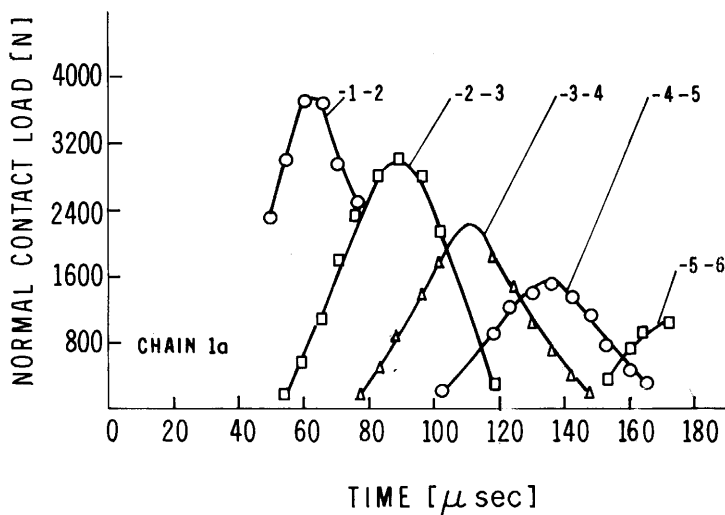


FIGURE 15.2.13 Variation of normal contact load with time along a primary chain (Shukla and Damania, 1987).

To ensure this dependence, the geometry, such as the primary disk chains (shown in Fig. 15.2.14a), was used, and the angles θ_1 and θ_2 between the disk chains were varied between 15° and 90° . The stress waves, which were generated by loading the top disk, traveled in a vertical chain and then entered disk B at point 1. Thus the stress wave disintegrated and was transferred in two chains through contact points 2 and 3. The most interesting aspect of this experiment is shown in Fig. 15.2.14b. It can be seen that when the contact angle increases, the transmitted wavelength of the stress signals increase, while the load transfer decreases. This showed that effectively the lateral load transfer was close to zero. An important question may arise: How can these results be used to predict stress performance in any systematically or randomly arranged granular bulk? For a 2D array of birefringent disks, Shukla (1991) suggested first finding the path of the stress and the energy losses for a single disk in contact with three or four neighbors, and then using superposition of these data with the reset of the ensemble. This experiment clearly identified the need for more experimental and theoretical two-dimensional studies.

15.2.3.3 ROLE OF THE SIDEWALL FRICTION

Angular characteristics of the stress propagation as well as the appearance of stress chains with length larger than the grain size are evident and cannot be

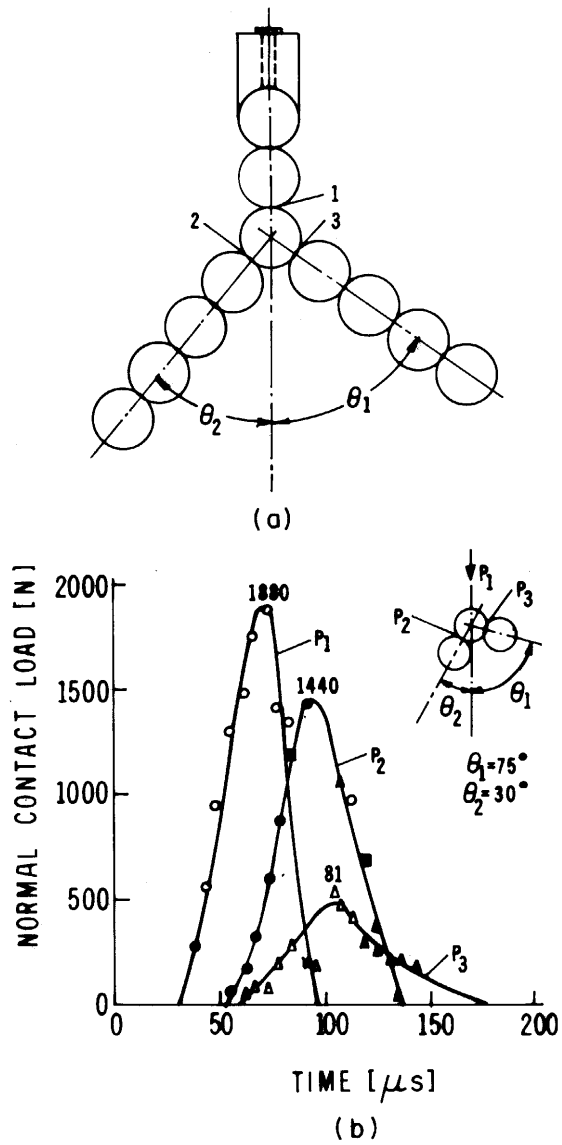


FIGURE 15.2.14 Schematic arrangement of granules (a) and measured dynamic contact loads as a function of time (b) (Shukla, 1991).

obtained with simple average approaches (Herrmann *et al.*, 1997). In order to explain the nonlinear stress behavior correctly, a number of researchers investigated the macro effects caused by the system boundary conditions (Travers *et al.*, 1987, 1988; Ammi *et al.*, 1990). Travers *et al.* (1988) claimed that when an impact causes small deformation, which is typical of the impact of a weak shock wave, only two finite quantities affect the mechanical behavior of the bulk material. They are the geometry of the test section walls, and the overall size of the granular bulk.

For a system that is built starting from a plane wall, the seed and then the end wall impose some geometrical correlations at short distances. Generally, these weak correlations (from a geometrical point of view) may influence the mechanical behavior of the medium at larger distances (e.g., the weak correlations in the transmission of stress through the granular medium). Such a physical amplification and the geometrical perturbations created by the wall are usually observed only up to a distance of a few layers away from the wall (Bideau and Hansen, 1993).

The overall size of the granular bulk becomes of importance when the axial stress causes rearrangement of the granules. Since the movement of the particles gives rise to rotation and squeezing of the grains in the free space, the friction drag force increases and the entire bulk resists further compression (Hill and Kapila, 1996). When particles or disks are interlocked, the resistance at the wall is transmitted throughout the interior, and thus attenuates the downstream transmission of the effective stress. Consequently, the particles inside the bulk material “feel” the sidewall friction on the container vertical walls. When the height of a granular layer increases, the role of the sidewall friction increases. In some cases, such as when the layer height is high enough, the container walls carry out most of the loading and the grains on the bottom of the layer may not know about the steady force that was applied at the top of the layer (Dantu, 1967). This finding is consistent with more recent experimental results published by Travers *et al.* (1988). In this study, a 2D regular array of 4-mm Plexiglas cylinders (number of rows varied from $n = 7$ to $n = 20$) was compressed by a steady force with amplitude of 2000 N, and photoelastic photographs of the stress chains inside the array were taken. The dominant role of the stress chains is of importance during the initial, so-called consolidation phase of compression when deformation of the bulk leads to local displacement, sliding, and rotation of the cylinders (Travers *et al.*, 1988). For these conditions the sidewall friction results in a strong bridging effect, which in turn increases further resistance to packing due to repulsive forces. Appearance of the stress chains shows that solid packing does not allow cylinders to move easily around each other, but instead stress chains are grounded between the top and bottom layers with high local concentrations of solid (Schwarz *et al.*, 1998). Figure 15.2.15 illustrates that the interparticles

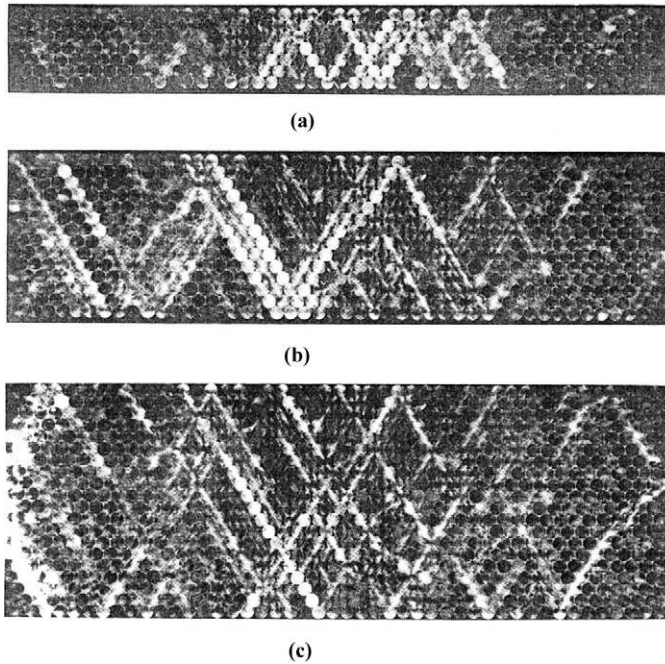


FIGURE 15.2.15 Strongest stresses network for regular packing of Plexiglas cylinders of different heights: (a) $n = 7$, below transition; (b) $n = 14$, transition case; (c) $n = 20$, just above the transition (Travers *et al.*, 1988).

stress networks strongly depend on the length of the granular material. When the packing has fewer than 10 rows (Fig. 15.2.15a), only several isolated stress chains appear to propagate between the upper and the lower edges of the packing. Stresses are mostly transmitted through these chains, which involve only a fraction of all cylinders in the array (Rossmannith and Shukla, 1982; Mueth *et al.*, 1998). When more than 10 rows are present (see Fig. 15.2.15), the system starts to branch out, and a wide network of the stress chains begins to appear. When the number of rows n increases ($n > 20$ –24, Fig. 15.2.15c), the network looks macroscopically homogeneous. In an attempt to explain these results quantitatively, Travers *et al.* (1988) have measured the force F_{Tr} , which was transmitted to the bottom of the sample as a function of the number of the rows n . The results obtained are plotted in Fig. 15.2.16. When $n < 10$, the packing is transparent to force and the whole of the applied force F_a is transferred through the array to the bottom. For $11 < n < 20$, the force at the bottom F_{Tr} drops rapidly, and then starts to change slowly when $n > 20$.

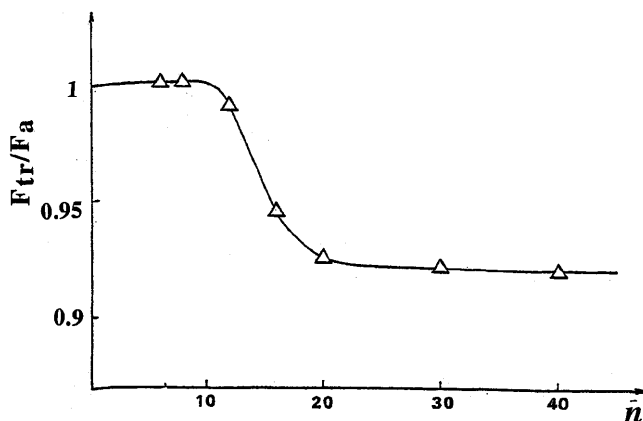


FIGURE 15.2.16 Variations of F_{tr}/F_a for $F_a = 2000$ N with different number of horizontal layers of cylinders n (Travers *et al.*, 1988).

Although the information that can be obtained by the photoelastic method is very effective, it can be applied only for a 2D transparent array of birefringent disks or cylinders. It is clear that for granular materials composed of spherical particles, direct stress measurements have to be used to analyze the stress performance.

15.2.4 THREE-DIMENSIONAL PACKING OF SPHERICAL PARTICLES

15.2.4.1 BEHAVIOR OF THE UNSTEADY END-WALL STRESS PEAK

As already pointed out, when a granular bulk material is impacted by a shock wave, a pressure jump P_5 is registered at the front face of the granular sample and discrete transmitted waves pass through the granular skeleton and through the gas filling the pores. The pressure drop, $\Delta P = P_5 - P$, between the gas pressure, P_5 , and the local gas pressure inside the pores of the bulk material, P , affects the porosity, ε , and even a small variation in ε manifests itself as an unsteady pressure amplification at the rear end of the granular sample. This feature has been extensively studied in investigations that have to a large extent been prompted by the need to find effective protection against blast waves and accidental explosions. Gelfand *et al.* (1975) and Gvosdeva *et al.* (1985) were

probably among the first researchers to observe this effect in experiments with a flexible layer of foam that covered a rigid end wall of the shock tube. Similarly, Gelfand *et al.* (1989) also observed that when a granular layer covered the shock tube end wall, the pressure was significantly larger than if no granular material was present. While most work to date has concentrated on the fact that a high-pressure peak developed, Gelfand *et al.* (1989) were the first to establish that whereas the peak duration is rather short (about 300 μs in the experimental data shown in Fig. 15.2.4), it has a significant mechanical effect on the loaded surface. This effect was demonstrated in a special test case when an incident shock wave with an overpressure of 0.1 MPa impinged on a 0.1-mm thick copper diaphragm covered with a thin layer of powder. The impinging shock wave broke the diaphragm, whereas it did not break it when the diaphragm was not covered with powder.

As for the foams, a comprehensive analysis of the main results obtained in this field was presented by Skews (1995). The common one-dimensional wave diagram model (shown in Fig. 15.1.1a) was used to explain the origin of the unsteady pressure peak. When the incident wave (1–2) strikes the porous material, a reflected wave (2–3) and a transmitted wave (A–B) are formed, resulting in compression of the foam material in region B, and movement of its front face toward the rigid wall. The transmitted wave is then reflected off the end wall and further compresses the foam. The behavior of the foam in region C is strictly dependent on the moment associated with the foam skeleton (solid phase) being transferred to the end wall. When the reflected wave (B–C) reaches the gas/foam interface, it results in a transmitted shock wave (3–4) that propagates out of the foam to the gas, and an expansion wave (C–D) that is reflected back into the foam material. The latter wave will then reflect off the end wall and cause pressure relief at the shock tube end wall. Typical pressure signals obtained from shock tube tests using polyurethane foam with transducers positioned as indicated in Fig. 15.1.1a are shown in Fig. 15.1.1b. Although these pressure traces generally follow the expected pattern, a number of new details might be found if the permeability of the foam is changed.

Experiments by Yasuhara *et al.* (1995, 1996) have clearly confirmed that large porosity (for most open cell foams $\varepsilon \approx 0.98$) allowed the transmitted wave (A–B) to move faster and quickly reach the sample rear face. The leading front BC in the end-wall stress signal (position Z in Fig. 15.1.1b) starts to rise because of stagnation of the foam skeleton at the rigid end wall. The stagnation scenarios can be varied substantially, depending on the foam permeability (small or large). To demonstrate this, the end-wall pressure signals that were obtained in these studies with different foamlike materials are reproduced in Fig. 15.2.17. The material characteristics of these foams are shown in Table 15.2.2. As in similar studies of Gelfand *et al.* (1985) and van Dongen *et al.* (1995, 1996), the pressure transducer for the gas pressure measurement was not in contact with the sample skeleton. The stress values shown in Fig.

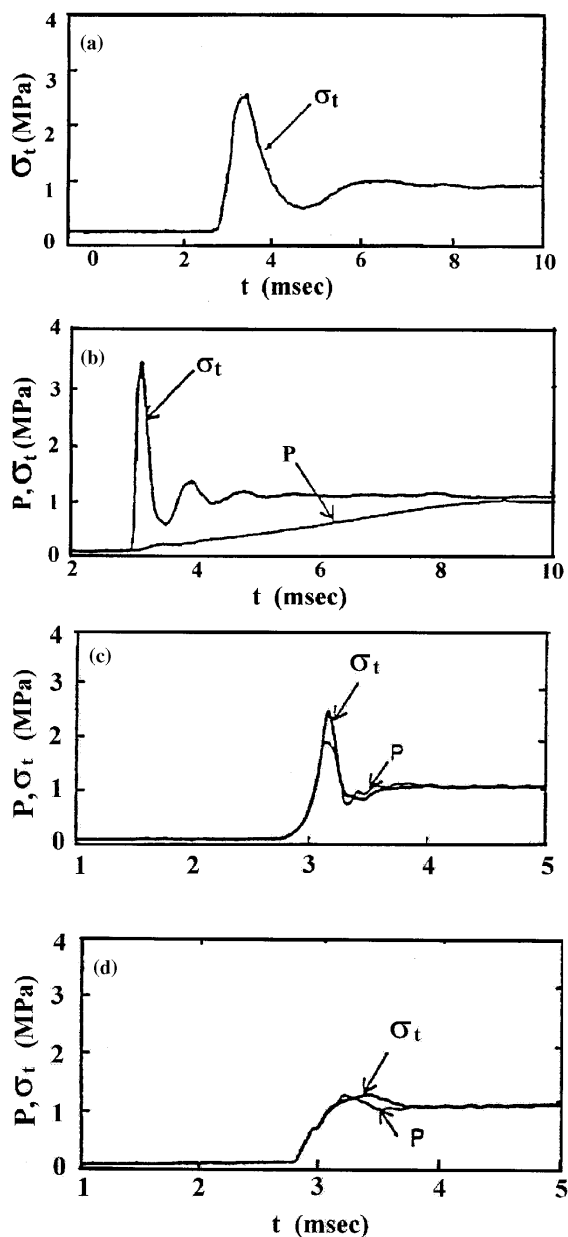


FIGURE 15.2.17 Total stress, σ_t , and gas pressure, P , recorded at the shock tube end wall (Yasuhara *et al.*, 1995, 1996). (a) 30 mm rubber slab, porosity $\varepsilon = 0$ and density $\rho_b = 1.219 \text{ g/cm}^3$; (b) 30 mm foam slab, F1, porosity $\varepsilon = 0.76$ and density $\rho_b = 0.29 \text{ g/cm}^3$; (c) 60 mm foam slab, F2, porosity $\varepsilon = 0.98$ and density $\rho_b = 0.026 \text{ g/cm}^3$; and (d) 60 mm foam slab, F3, porosity $\varepsilon = 0.98$ and density $\rho_b = 0.026 \text{ g/cm}^3$ (larger cell size and wire diameter of the skeleton network compared to F2).

TABLE 15.2.2 Properties of the Foamlike Materials used in Experiments by Yasuhara *et al.* (1995, 1996)

Material	Density (g/cm ³)	Porosity	$x \times y \times z$ (cells/25 mm)
Foam F1	0.2900	0.76	$350 \times 70 \times 70$
Foam F2	0.0263	0.98	$50 \times 50 \times 50$
Foam F3	0.0275	0.98	$13 \times 13 \times 13$
Rubber	1.2190	0.00	—

15.2.17 are the total stress σ_t , or the sum of the stress between particles and the gas pressure, P . It can be seen that the stress profiles of rubber and that of foam F1 samples resemble the stress profiles shown in Fig. 15.2.4 for a granular material and are followed by dumping vibration profiles that eventually approach the pressure P_5 . Since the foam F1 has a light-mobile skeleton (one-fourth that of the rubber) the amplification factor attained for this slab is $\delta_m = 3.3$, whereas for the rubber it is only $\delta_m = 2.6$ (δ_m is the ratio of the peak stress $\sigma_{t_{\max}}$ to pressure P_5). Furthermore, it can also be seen that the foam permeability is of paramount importance for the correlation between the total stress and gas pressure signals. In contrast to the rubber, the foam F1 has small interconnected, open pores, which allow the gas to flow through the foam and presents high friction between the gas and the foam skeleton. Hence, the end-wall pressure, P , in the case with foam F1 increases with time very slowly. The next experimental data, shown in Figs. 15.2.17c,d, were obtained for foams with larger permeability and large pore sizes. In these cases the compaction wave front acts as a leaky piston pushing out the pore gas to the end wall (Skews *et al.* 1993). The gas then stagnates in the vicinity of the end wall and acts as a buffer decreasing the end wall peak stress. This can be seen by the amplification factors for foams F2 and F3, $\delta_m = 1.7$ and $\delta_m = 1.2$, respectively. Moreover, in contrast to the data shown in Fig. 15.2.17b, the gas pressure in Figs. 15.2.17c,d correlates well with the end-wall stress signals. Such correlation should be inherent for all porous materials with light density and large pore size and permeability. It is therefore of interest to stress the different contributions caused by the transmitted and rarefaction waves to an assessment of the end-wall pressure signals shown in these figures. It can be seen (Fig. 15.1.1) that the transmitted wave A–B compresses the foam slab, and the stagnation effects at the end-wall affect the leading front (BC) in the unsteady peak. The backside profile (CD) of the unsteady peak is largely governed by rarefaction waves (C–D) and (D–E), which reduce the pressure to the value that would have been encountered without the foam. Moreover, because of the large flexibility of the foam slab, it can be easily compressed (about 70%).

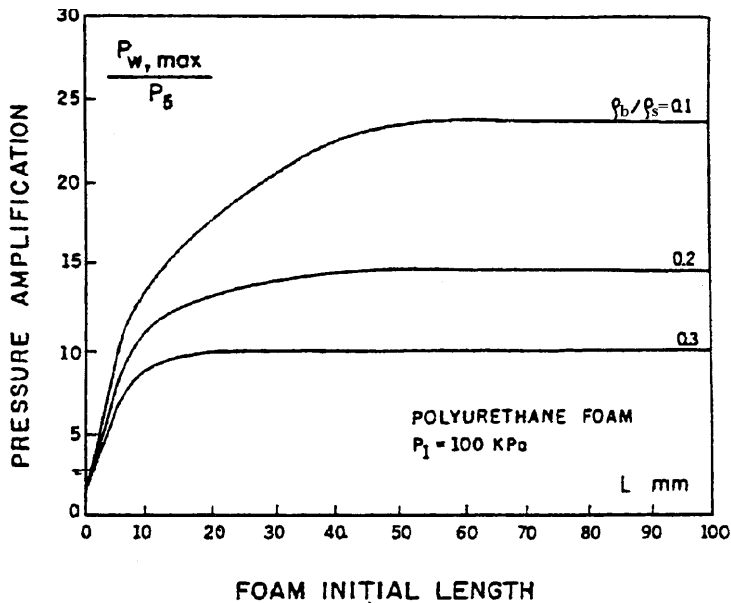


FIGURE 15.2.18 Amplification factor, δ_m , as function of the initial foam length and its relative density (numerical results of Ben-Dor *et al.*, 1994 for polyurethane foam, $P_1 = 100 \text{ kPa}$, and $M_s = 2$).

Hence, the amplitude of the peak and its duration in flexible foam are largely governed by interactions of pressure waves with the sample boundaries. This feature explains the experimental finding of Gvozdeva *et al.* (1985) and Yasuhara *et al.* (1996), which demonstrated further increase in the stress peak with increase in the sample length L . While the numerical results of Ben-Dor *et al.* (1994), shown in Fig. 15.2.18, support this finding, they also showed the following:

1. The amplification factor δ_m increased with L only up to a certain "critical" thickness $L = L'$.
2. The amplification factor δ_m remains essentially constant for $L > L'$.
3. The amplification factor δ_m decreases with increase in the relative density, v .
4. The "critical" length of the sample L' decreases with increase in the relative density, v .

Figure 15.2.19 presents a summary of the results measured by Gelfand *et al.* (1989) for dependence of the granular material peak stress on the sample length, L . The physical properties of the granular material used in these tests

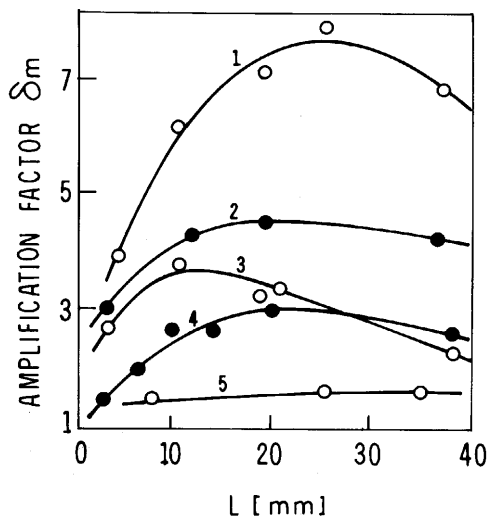


FIGURE 15.2.19 Experimental results of Gelfand *et al.* (1989) for the amplification factor, δ_m , as a function of the initial granular layer length.

are listed in Table 15.2.3. It is worthwhile to demonstrate the similarity and the distinction of the foam and granular material characteristics, which in fact show how much their physical behavior appears alike. Similarity between these two media is apparent from the fact that the amplification factor δ_m in a granular medium also increases with L up to a certain maximum thickness $L = L^*$. Moreover, materials N1 to N4 strictly follow to point 3 and partly to point 4 of the predictions of Ben-Dor *et al.* (1994), which stated that the amplification factor δ_m and “critical” length L' should decrease with increasing relative density, ν .

On the other hand, in contrast to foam, the amplification factor δ_m shown in Fig. 15.2.19 starts decreasing gradually for $L = L^*$. In order to obtain an insight into the problem, one should refer back to the similar logical pattern (based on

TABLE 15.2.3 Properties of the granular materials used in experiments by Gelfand *et al.* (1989)

N	Material	ρ_p (g/cm ³)	ρ_b (g/cm ³)	ν	ε	$f \times 10^7$ (mm ²)	γ (g/cm ³)	d_p (mm)	M_s
1	Plexiglas	1.18	0.34	0.29	0.71	24	0.34	0.01	1.36
2	Polystyrene 1	1.06	0.57	0.49	0.51	310	0.52	0.10	1.36
3	Polystyrene 2	1.06	0.50	0.48	0.52	1400	0.51	0.20	1.36
4	Sand	2.45	1.78	0.73	0.27	250	1.79	0.30	1.36
5	Polyethylene	0.82	0.55	0.67	0.33	90000	0.55	4.50	1.36

the role of the sidewall friction) used previously to explain the dependency of the stress data on L shown in Fig. 15.2.15. Actually, for a short granular sample (small aspect ratio $L/H < 0.2$, where H is a cross-sectional dimension of the test section), the sidewall friction causes negligible effect on the stress performance. Any additional mass (or length L) causes an increase in the peak stress at the end wall due to additional kinetic energy transferred by particles to the end wall. For the bulk material of critical height $L = L^*$, compression forces and forces acting toward the particle movement should be equal to each other. Equilibrium conditions would probably correlate with the inflection point in the plot of Fig. 15.2.19. Beyond the critical height ($L > L^*$), the major portion of the compression force is lost to sidewall friction. If the length L increases further, it will not influence δ_m because the compression force is no longer strong enough to accelerate all granules toward the end wall. The compressive stress is partially supported by the sidewalls. Such conditions should be responsible for strong bridging effects, which in turn cause the homogeneous networks of stress chains that were clearly demonstrated in Fig. 15.2.15c. Hence, the mechanism for restricting the peak stress in granular media differ from those inside foams. Whereas in foams it consists of a simple recovery of the sample caused by an unsteady rarefaction wave, for the granular media it also includes sidewall friction, which acts toward the particle movement and prevents further compression of the granular bulk. As far as is known, such different peak stress behavior in foams and in granular media has not been discussed previously.

Recently, Britan *et al.* (2000) reported on experimental results that also demonstrate the role of particle-wall friction in the stress performance. In their experiments the sidewalls of the steel test section shown in Fig. 15.2.6b were covered by either sandpaper or by smooth glass plates and the end-wall stress and gas pressure were recorded for the different sample lengths L and constant impact conditions. Typical pressure records obtained in these tests from the end-wall transducers T4 and T7 are shown in Fig. 15.2.20. From this figure it can be seen that the sidewall roughness and the height of the bulk material have no practical effect on the final value of the gas pressure and the total stress. It can also be seen that the amplitude of the peak stress changes significantly with L . Namely, the thicker the bulk material is, the smaller the peak stress becomes. It is also apparent that in experiments with rough sidewall the recorded peak of the total stress is significantly smaller than that recorded one for the test section with smooth sidewalls. Thus, the effect of the sidewall friction on the total stress peak is evident.

The same factor is seen to be the major reason for another interesting feature of the granular material, which was discussed previously by Gelfand *et al.* (1989). Pressure signals shown in Fig. 15.2.21 were obtained with a shock wave having a triangular pressure signature and a compression phase



FIGURE 15.2.20 The effect of the sidewall friction on the amplitude, and the profile of the total stress and gas pressure histories as recorded at the shock tube end wall. Vertical scale is 1 bar/div, horizontal scale is 0.1 ms/div (Britan *et al.*, 2000).

duration was of 1.2–1.4 ms. It can be seen that while the overpressure at the granular bulk interface drops to zero because of the finite duration of the shock wave, the end-wall stress still persists and even increases in time. Notably, the end-wall impulse also increases and its value surpasses significantly that in the wave reflected from the granular bulk interface. The net results that were concluded from this test are as follows:

- The sidewall friction and significant cohesive forces may result in irreversible compaction of the granular material.
- The stress condition inside the granular bulk may be preserved and causes residual pressure loading on the shock tube end wall.

Experiments with blastwise shock waves were further extended by Medvedev *et al.* (1996) for two basic ideas. The first one was to observe the effect of

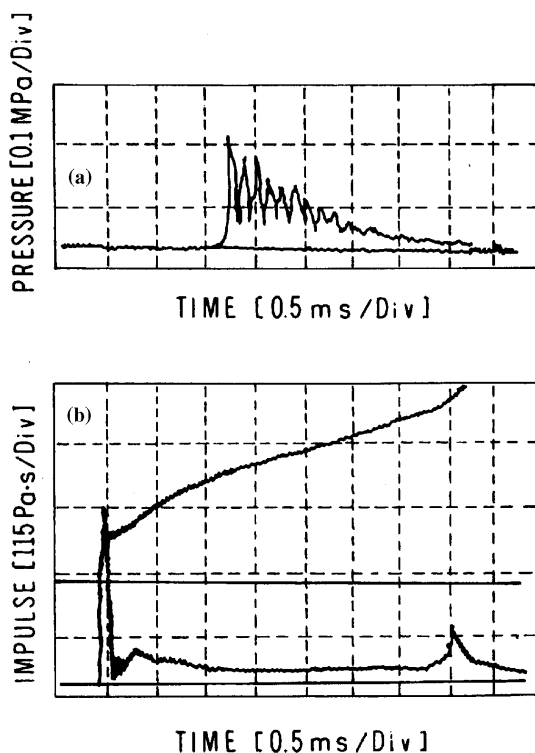


FIGURE 15.2.21 Experimental results of Gelfand *et al.* (1989) for normal incidence of a triangular shape shock wave on a 20-mm granular layer composed of 0.2-mm polystyrene particles. (a) Gas pressure upstream of the bulk interface. (b) The end-wall total stress (bottom trace) and the impulse trace (obtained by electronic integration of the total stress signal), respectively. The time scale is 0.5 ms/div, the impulse scale is 115 Pa-s/div, and the pressure scale is 0.1 MPa/div.

the shock wave duration on the stress profile while keeping the shock wave overpressure at a fixed value. The second idea was to compare the main features of the transmission shock wave loading through a dust deposit with those through a porous layer of compressible foam having the same depth. The authors assumed that during the impact, a column of mass m with a unit cross-sectional area composed of foam would behave similarly to a column of granular material. Hence, a simple equation of motion for a column with mass m was proposed:

$$mx''(t) + cx'(t) + kx = p(t). \quad (15.2.4)$$

Here x is the coordinate, t is time, and k and c are the stiffness and the damping coefficients, consequently. Using such a simplified mechanistic model the

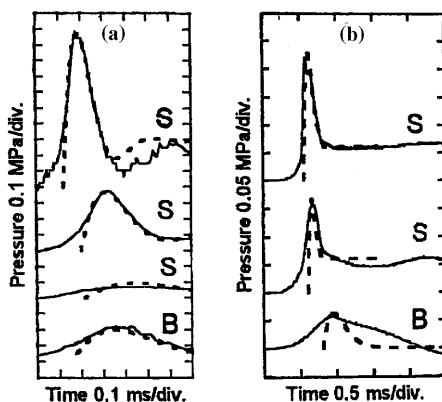


FIGURE 15.2.22 The comparison between recorded (solid curves) and calculated (dotted curves) pressure profiles: (a) polyurethane foam layer; (b) Plexiglas dust bulk material (N1 in Table 15.2.3); S, stepwise loading; B, blastwise loading. The middle record in the right figure was obtained for a layer with 10-mm depth; all the others were obtained for 20-mm layers (Gelfand *et al.*, 1989).

stress behavior shown in Fig. 15.2.22 was simulated. It can be seen that while the end-wall stress profiles for the two materials behave in a similar manner, the peak stress in foam is from 2 to 5 times larger. Of particular interest is the finding that a range of rather short shocks exist for which the porous material protects the structure, whereas for longer shock waves such “protection” becomes destructive.

Although the simple calculations well predict the dynamics of the peak stress in the foam slab and in granular material, the simplified approach was not supported by a physical meaning for the coefficients of k and c . Moreover, since the aspect ratio of the samples used for the experiments was about ≈ 0.5 , this suggests that such a simple theoretical model should probably be valid only for rather short layers when the bridging effect in the granular layer is negligible.

15.2.4.2 BRIDGING EFFECT AND SIZE OF THE PRESSURE TRANSDUCER

After we have discussed the various physical processes that might be responsible for the behavior of the peak stress, the following question should arise: Do the measurements of the stress signals, shown in Figs 15.2.4, 15.2.7, 15.2.18, 15.2.19, and 15.2.22, truly approximate the real stress history inside the 3D granular layer? Since the stress definition is a force per unit area, the

question can also be asked in terms of average force measurement. Thus we should ask: How large should the transducer's diameter, D , be, compared with the average particles diameter, d_p , in order to manifest the measurements as characteristic values of the particulate material as a whole? To answer this question, one can refer to Biarez and Hicher (1994), who stated that the transducer's diameter must be at least 10 times that of the particles. On the other hand, intuition may suggest that the transducer should be as small as possible in order to exclude effects related to the wall boundary conditions, two- or three-dimensional effects inside the granular material. Owing to the complexity of these two opposite requirements, this behavior has not yet been incorporated satisfactorily in shock tube studies.

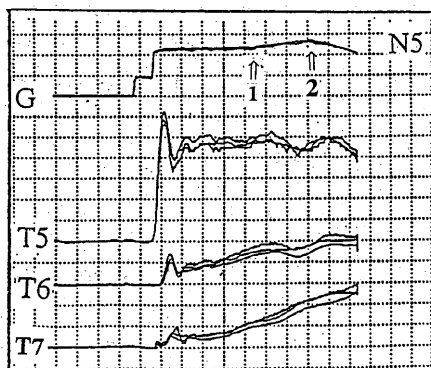
Britan *et al.* (1995) conducted an experimental study that was the first to illustrate what may happen when the foregoing pressure transducer requirements are not met. This study was conducted at the shock tube facility shown in Fig. 15.2.6 and with the granular material N1 (see Table 15.2.1). The results of these tests, shown in Fig. 15.2.23a, demonstrated a significant size effect caused by the transducer on the stress readings. As can be seen, the repeatability of the pressure measurements, by transducer G, 80 mm upstream of the granular layer front, was very good, while the repeatability of the stress peak was very poor. The major reason for large scattering is seen to be related to the relatively small transducer diameter (located at port T5), $D \approx 4.5$ mm, compared with the large particles diameter, $d_p = 3.3$ mm, composing the granular layer. Any variation in the number of particles in contact with the transducer and the orientation of the stress chains can cause unique sensitivity of the gauge output for bridging effects. The presence of this feature is clearly visible during the test time period (restricted by arrow No. 1 at the top of the figure) when amplitudes of the stress ranged from the gas pressure, P_5 , up to the peak value σ_t , which is 10 times larger than the gas pressure, P_5 .

Of particular interest is the finding that after the time marked by the second arrow, all the stress curves tend toward the same amplitude value. Nevertheless, the reasons for this tendency require special comment. The time marked by the second arrow corresponds to the arrival of a strong rarefaction wave, which originated from the driver chamber of the shock tube. This can be seen as a decrease in the pressure signal measured by transducer G. Further on, the rarefaction wave interacts with the front of the granular layer and initiates backward gas filtration through the granular layer. As a consequence, the strong backward filtration relieves the sample. This factor most probably destroys the stress chains across the sample, and later on the stress distribution inside the bulk material became more homogeneous.

The nonuniform stress distribution should have much smaller effect on the pressure reading if the ratio of the transducer diameter to that of the particles is large. To ensure this, one can refer to Fig. 15.2.23b, which demonstrates stress



(a)



(b)

FIGURE 15.2.23 Repeatability of the total stress signals inside a 138-mm granular layer. Vertical scale 1 bar/div, horizontal scale (a) 1 ms/div (material N1), (b) 0.5 ms/div (material N5) (Britan *et al.*, 1995).

signals obtained for the similar conditions while the particles which composed the granular layer have smaller size (marked as N5 in Table 15.2.1). In this case the diameter ratio was $D/d_p \approx 10$. It is now clearly seen that the scattering between the stress signals for all transducers (from T5 to T7) is much smaller ($\approx 15\%$) and that there was no tendency for the scattering to be changed at various distances from the front face of the granular layer. It is somewhat surprising that the stressed state of the particles registered by transducer T5 in Fig. 15.2.23b is well preserved at a level higher than the gas pressure, $P_5 = 2.3$ bar, upstream of the bulk interface. The presence of this feature is clear evidence of the bridging effect, which is also demonstrated in Fig. 15.2.24

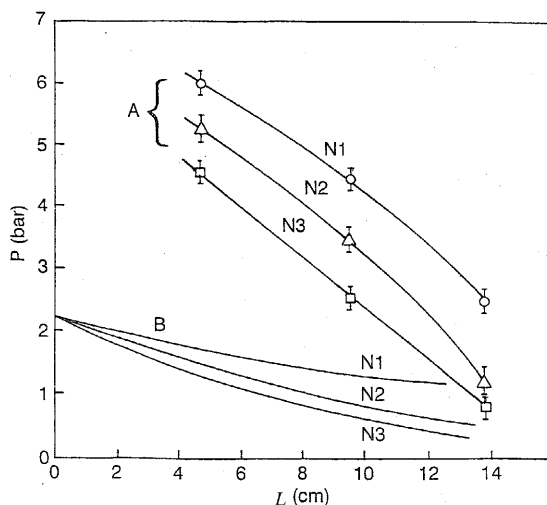


FIGURE 15.2.24 Post-peak compressive stress (A) and gas pressure (B) versus sample length 2.5 ms after the incident shock wave hits the granular layer interface (Ben-Dor *et al.*, 1997).

by comparison of the post-peak compressive stress (A) and gas pressure (B) versus the sample length, for the time moment of 2.5 ms after the incident shock wave hits the granular layer interface. It can clearly be seen that the stress conditions through the granular layer are preserved because of the bridging effect, for all the investigated granular materials (N1 to N3 in Table 15.2.1) and that for a large part of the sample the stress exceeded the pore pressure, P . It is arguable that average stress measured inside the granular layer is influenced by the bridging effect and by the size of the pressure transducer. For small gauges (or large grains), when $D/d_p \approx 1$ this effect damages the reproducibility of the stress data.

15.2.4.3. PACKING DENSITY AND GAS FILTRATION

From a general point of view, the mechanical properties of granular materials are described as density dependent—the denser the packing, the stronger it is, and thus the more transparent to stress propagating through the contacts between the particles. In practice, this description is not accurate, because even a small compaction of the granular layer before the test may affect the peak stress that may be transmitted to the shock tube end wall. The presence of this effect was firstly demonstrated by Gelfand *et al.* (1989) experimentally where a

shock wave impacted a fixed-thickness, $L = 20$ mm, layer composed of powder N1 of Table 15.2.3. The relatively density of the bulk v was increased from 0.29 to 0.41 by using mechanical compression of the bulk before the test. As a consequence, the amplification factor δ_m for the denser bulk material was reduced by 2.5 times. The reasons for this behavior have not yet been explained.

The net effect of the packing density, v , on the stress and the gas pressure behavior was clarified in the experimental study of Britan *et al.* (1999), which was conducted in the vertical shock tube shown in Fig. 15.2.6. In these tests the granular material was not removed and refilled as usually done after each experiment; instead, it was repeatedly loaded by similar shock waves. The 64-mm long granular layer was composed of powder N5 (in Table 15.2.1) and the end-wall transducers T4 and T7, with transducer/particle diameter ratio $D/d_p = 22$, were used for the measurement of the gas pressure and the total stress. The sidewall transducer T3 ($D/d_p = 10$) was complemented at the same cross section by similar transducer T3'. Typical records of these transducers are shown in Fig. 15.2.25. In this figure, remarkable differences in the amplitude and the profile were observed. In addition during the post peak period the growth rate of the stress and the gas pressure signals were quite repetitive from test to test. Close inspection of the first signal rises show a slow rising precursor that occupies a certain part of the peak front. The time intervals between the precursor origin in the traces registered by transducers T3 and T7 decrease with the test number (i.e., the precursor velocity increases). This feature can safely be used to control the packing density v and homogeneous of the granular material Yanagisawa (1983).

Another task of the experimental investigation of Britan *et al.* (1999) was to differentiate the effects caused by the shock wave front from those caused by the shock-induced gas filtration on the stress performances. For this purpose experiments were embarked on a comparative analysis of the results obtained with a so-called "standard" sample and those obtained for the same conditions, whereas the sample was "protected" against filtration by a thin plastic film plugged at the front edge of the sample. Experiments with protected samples (shown in Fig. 15.2.26) demonstrate that the difference between stress signals becomes minimal even after the second test, as was the case with the "standard" sample. The results for the overall test time period are reproduced in Figs. 15.2.27 and 15.2.28 for the protected and the standard samples, respectively. The results showed that the amplification factor of the end-wall peak stress for the protected sample was only $\delta_m = 0.24$, whereas for the standard sample it reached about $\delta_m = 0.7$. Thus, the sensitivity of the peak stress to the filtration effect is evident. Typical compressive stress and gas pressure signals obtained in five subsequent tests with the standard sample are shown in Fig. 15.2.28. From this figure it can be seen that the filtration causes

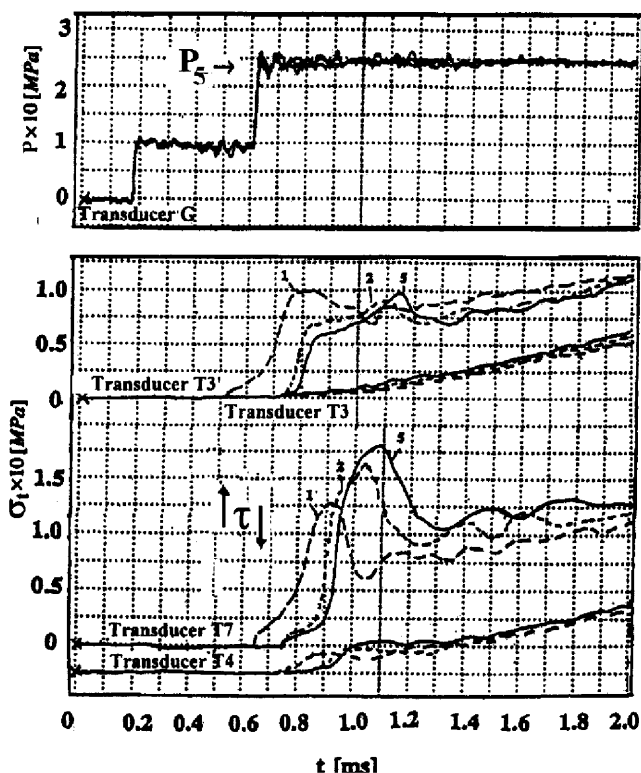


FIGURE 15.2.25 Typical compressive stress and gas pressure signals obtained in five subsequent tests with 64-mm standard granular layer made of material N1 (in Table 15.2.4). The numbers on the curves refer to the serial number of the test (Britan *et al.*, 1999).

monotonic growth of the stress and the gas pressure in the post-peak period. Once the gas pressure, P_5 , ahead of the sample (transducer G) starts to drop because of the arrival of the rarefaction wave, backward filtration starts and relieves the stress. Then a tendency toward equalizing the bulk conditions across the sample is obtained. Note that when gas filtration is excluded (see data in Fig. 15.2.27) the arching effect preserves the stressed conditions between granules after the marked point N2 inside the sample. The authors ascribe the observed features to the different dynamics of microdeformation of the granular layer with and without filtration. While the first several tests cause significant variations in the initial peak of the total stress signals, in the post-peak period these signals do not manifest any dependency on the test number (the maximal discrepancy between the stress curves did not exceed 12%). These results suggest that particle rearrangement appears to be completed even

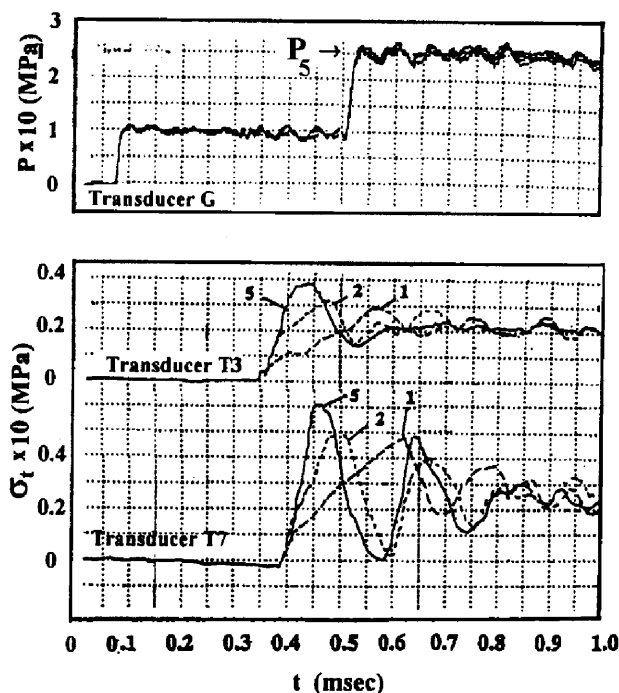


FIGURE 15.2.26 Typical compressive stress signals obtained in five subsequent tests with a protected 64-mm granular layer made of material N1 (Table 15.2.4). The numbers on the curves refer to the serial number of the test (Britan *et al.*, 1999).

during the first unsteady phase of the sample compression, which is coincident with the peak stress formation. Further compression of the sample is weak and causes minimal effect on the stress as well as on the gas pressure in the post-peak period of the signals.

15.2.4.4 EFFECTIVE STRESS BEHAVIOR

Britan *et al.* (1999) have demonstrated that the magnitude and profile of the effective stress σ is also suitable for reconstructing the compression history of the granular material, since it is the parameter responsible for its deformation (Oka, 1996; Lade and De Boer, 1997). While for the standard sample $\sigma = 0$ at the bulk interface, inside the granular layer the effective stress behavior is largely governed by the inflow of gas. On the other hand, for the protected sample (where gas filtration is excluded) the effective stress is maximal at the bulk interface, $\sigma = P_5$, and quickly drops down because of the friction losses.

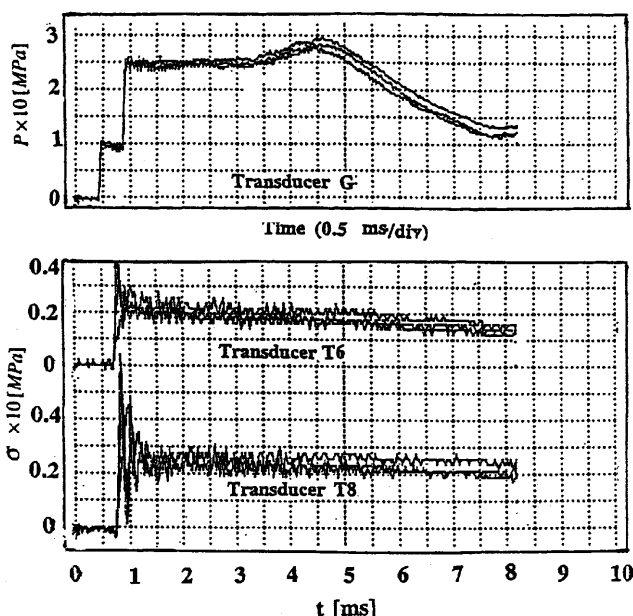


FIGURE 15.2.27 Typical compressive stress signals obtained in five subsequent tests with protected 64-mm granular layer made of material N1 (Table 15.2.4) (Britan *et al.*, 1999).

Gas filtration and friction losses depend on the length of the granular sample, L , and its permeability, f . Both contribute differently to the effective stress; hence, when comparing the data obtained with a standard sample with those for a protected sample, one should clarify the role of gas filtration on the effective stress. In the following several examples, these readings are compared to each other for small and large permeability bulk materials.

15.2.4.4.1 Small Permeability Granular Bulks ($f = 0.00027 \text{ mm}^2$)

The experimental results shown in Fig. 15.2.29 are typical examples of the effective stress profiles as obtained with a film protected small permeability sample (material N5 of Table 15.2.1). In order to elucidate the relative importance of the gas filtration, these signals must be analyzed together with those shown in Fig. 15.2.30 for unprotected samples of the same material. The stress curves in Fig. 15.2.30 present a computerized subtraction of the gas pressure P from the end-wall total stress σ_t , and thus, similar to the data shown in Fig. 15.2.29, comprise effective stress values. One distinctive property of

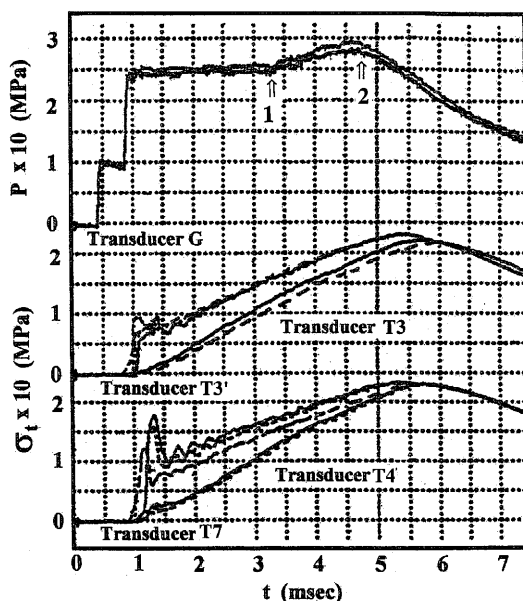


FIGURE 15.2.28 Typical compressive stress and gas pressure signals obtained in five subsequent tests with 64-mm standard granular layer made of material N1 (in Table 15.2.4). The numbers on the curves refer to the serial number of the test (Britan *et al.*, 1999).

these curves is that, whereas in the signals shown in Fig. 15.2.29 the gas filtration effect was excluded, in Fig. 15.2.30 it provided an added source of compressive force (drag force) acting on the particles. Several comments should be made regarding the effective stress histories.

Since the quasi-steady amplitudes of the curves in Fig. 15.2.29 are smaller than those in Fig. 15.2.30, one can conclude that the drag force strongly affects the effective stress values. Moreover, for both cases the effective stress attenuates down the granular layer, and for all curves its value is much smaller than the gas pressure behind the shock wave that was reflected at the granular layer interface (compare its values, which were recorded by transducer G).

The next comment regards the factors that give rise to different profiles of the stress curves shown in these figures. In fact, whereas in Fig. 15.2.29 the amplitudes of the curves in the post-peak period are almost steady during the full test time, in Fig. 15.2.30 they start to decrease dramatically at some moment. The time interval between the first increase in the signal and the onset of the decrease can be calculated if one supposes that the simple wave diagram (shown in Fig. 15.1.1) based on the refraction model considered by Skews *et al.* (1993) is also valid for granular media. According to this model the

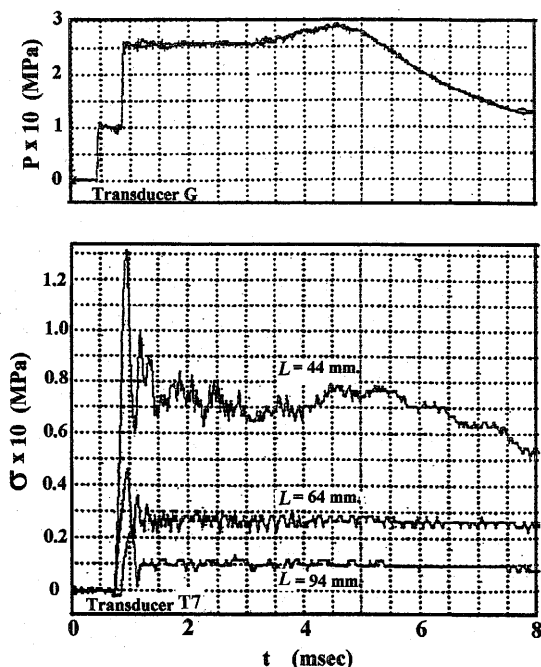


FIGURE 15.2.29 The influence of the layer depth on the effective stress signal. Protected granular layers made of material N1 of Table 15.2.1 (Britan *et al.*, 1999).

first decrease in σ should be caused by the rarefaction wave, which originates inside the granular material after the reflected wave interacts with its interface. Assuming that the velocities of the transmitted (V_g) and compaction (V_s) waves remain constant in the course of their reflection from the end wall, the end wall test time can be estimated to be

$$t_e = \frac{h(3V_s - V_g)}{V_g V_s}, \quad (15.2.5)$$

when the origin time corresponding to t_e is the time of arrival of the compaction wave to the end wall. The values of t_e shown by the arrows in Fig. 15.2.30 were obtained using Eq. (15.2.5) and agree quite well with the onset of the signal decrease, supporting the validity of such an approach.

Since most of the processes involved with particle–particle interaction are frictional in their nature, they must be sensitive to the variation of the granular layer length L . In agreement with this statement the peaks of the amplitudes in the cases showed in Figs. 15.2.29 and 15.2.30 indeed decrease in the course of the compaction wave propagation along the sample. Since the granular layer

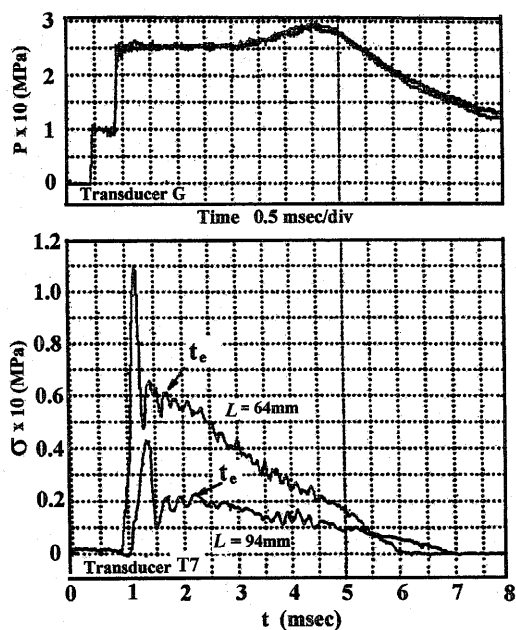


FIGURE 15.2.30 The influence of the layer depth on the effective stress signal. Standard granular layers made of material N1 of Table 15.2.1 (Britan *et al.*, 1999).

permeability increases with the particle diameter d_p , this must be accomplished by an increase in the transmitted wave velocity V_g . On the other hand, increasing V_g decreases t_e , and the rarefaction wave reaches the end wall before the gas–solid interaction is completed. Hence, inside granular materials of large particles the impact energy has not managed to be transmitted completely to the end wall during the test time, and thus the effective stress would be smaller.

15.2.4.4.2 Large Permeability Granular Layers ($f = 0.00099 \text{ mm}^2$)

To illustrate this phenomenon the effective stress profiles as obtained with the standard samples made of material N3 in Table 15.2.1 are shown in Fig. 15.2.31. In spite of the significant difference in the material properties (see Table 15.2.1), comparative analysis of these signals revealed many features in common with those in Figs. 15.2.29 and 15.2.30. The gas filtration through 44-mm and 64-mm granular samples causes a strong rarefaction wave, which limits the amplitude of the unsteady peak and affects the post-peak profile of the effective stress σ curves in Fig. 15.2.31. This feature prevents correct

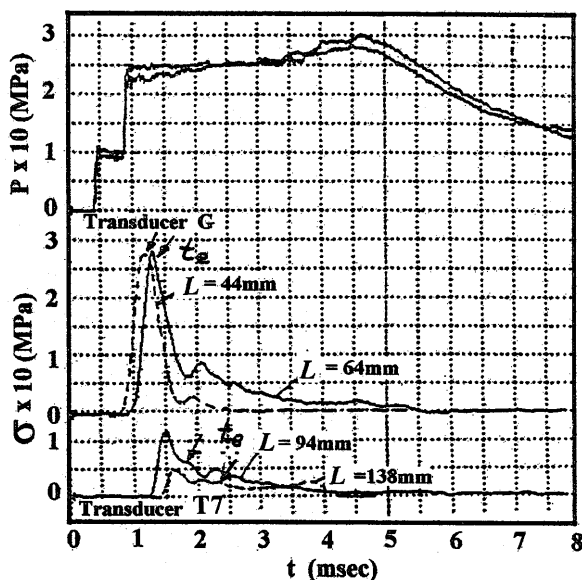


FIGURE 15.2.31 The influence of the layer depth on the effective stress signal. Standard granular layers made of material N3 of Table 15.2.1 (Britan *et al.*, 1999).

comparison of such profiles with the quasi-steady profiles obtained with film-protected samples.

For the longest layer the rarefaction wave reaches the end wall after the unsteady peak formation, and such a peak in the σ curves obtained with the unprotected 94-mm sample is nearly twice as large as that for the protected one. There is no doubt that the gas filtration must be accomplished by strong energy losses, and thus it attenuates with the distance along the sample. Since its contribution to the transmission of the stress through the particles contact would also attenuate with L , so does the effective stress. Consequently, maximal compression would be observed close to the sample interface and would decrease toward its bottom.

15.2.5 DYNAMICS OF THE GRANULAR LAYER COMPRESSION

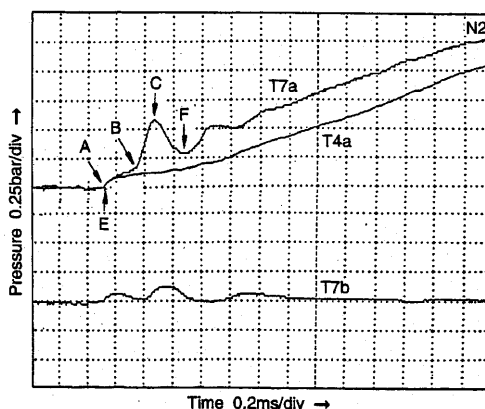
15.2.5.1 WAVE PROCESSES

As discussed previously, when a shock wave hits the granular layer, a reflected wave passes back while a transmitted wave and a shock-induced gas flow

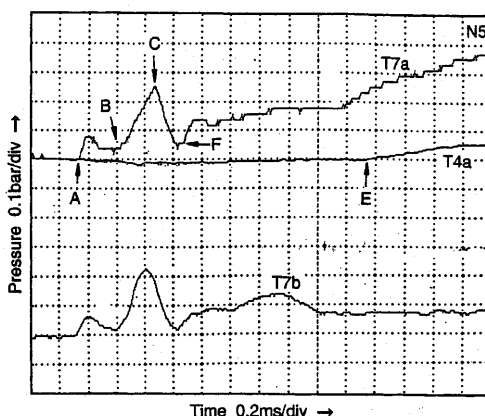
permeate into the pores between the granules, imparting momentum to the solid phase. Thus, two waves (transmitted gas front and compaction wave) hit the shock tube end wall. The stagnation of the granular material is the cause for the peak overpressure, which after several oscillations follows to a quasi-steady level that is usually equal to that obtained by a reflection from rigid end wall. The real flow pattern inside a granular bulk can be reconstructed from a distance–time ($x-t$) diagram, which combines external effects of the gas at the bulk interface with those of the internal gas flow and solid-phase behavior. Britan *et al.* (1997a) reported on a series of such diagrams, which were reconstructed using the pressure measurements conducted upstream and inside the granular layer. Pressure readings obtained in this study for two materials, which differed in their permeability factor, f , are shown in Fig. 15.2.32. In this figure, the points A represent the first increase of the compressive stress signals at the end wall; the points B mark the earlier part of the leading front of the unsteady peak of the compressive stress signals; the points C indicate the time at which the compressive stresses reached their maximum values; the points E indicate the first increase of the gas pressure signals at the end wall; and the points F mark the end of the pressure reduction at the backside of the unsteady peak.

The transmitted waves resolved by transducers T4a and T7a were obtained for relatively large permeability ($f \approx 0.005 \text{ mm}^2$, material N2 in Table 15.2.1) are shown in Fig. 15.2.32a. The points A and E for this case coincide. Since point A indicates the reflection of the transmitted shock wave from the end wall, the recorded signals in the time interval between points A or E and point B have similar profiles, demonstrating a slow pressure rise caused by the gas filtration. The transmitted wave and the gas flow exert a drag force on the particles, which results in an increase of the compressive stress at point B. The time elapsed between the arrival of the transmitted wave at the end wall (at point E) and the compaction wave reflection at point B is determined by particle's inertia. The maximum compressive stress is reached at point C when the lowest sample porosity was achieved. As can be seen, the rates of compressive stress and the gas pressure increase are equal after point F. Hence, it may be concluded that for a certain part of this period the compressive stress performance is determined mostly by the gas filtration.

The recorded signals that were obtained for material with low permeability ($f < 0.0003 \text{ mm}^2$) are shown in Fig. 15.2.32b. The transmitted wave attenuates inside the granular material to such a degree that it cannot be defined by transducer T4a. Thus, point A precedes point E in Fig. 15.2.32b. As can be seen from the effective stress profile, the drag force on the solid particles becomes significant only after point E. Prior to this time, the profile of the unsteady peak in the compressive stress signal (T7a) is nearly the same as for signal T7b obtained when the transmitted wave in gas and filtration were



(a)



(b)

FIGURE 15.2.32 Gas pressure traces recorded by the pressure transducer T4 and compressive stress signals recorded by the pressure transducer T7 at the end wall for the standard (a) and protected (b) samples. The 138-mm granular layers were made of material N5 (Table 15.2.1) (Britan *et al.*, 1997a).

excluded. The peak formation, in this case, is caused mainly by the transmission of the initial pressure drop ΔP through the contact points between the solid particles.

The main differences in the formation of the flow patterns inside materials with high and low permeability are evident from the wave diagrams shown in Figs. 15.2.33 and 15.2.34. The arrival time of the shock wave to the granular

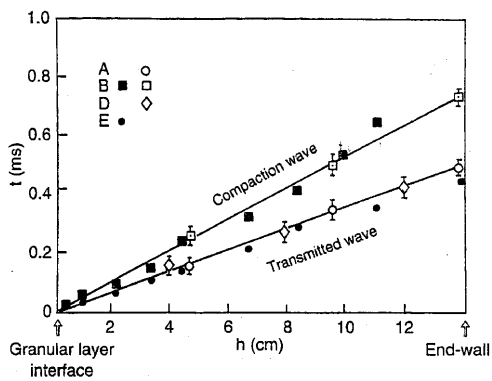


FIGURE 15.2.33 Time-distance diagram obtained for shock wave interaction with a granular layer made of material N2, Table 15.2.1 (Britan *et al.*, 1997a).

layer air interface is indicated as the starting time. The solid line trajectories were plotted following the experimental points denoted by open symbols, as recorded along a 138-mm granular sample. Closed points marked the experimental data that were obtained with a granular layer of variable height L . In addition, points D, appearing in these two figures, denote the arrival time of

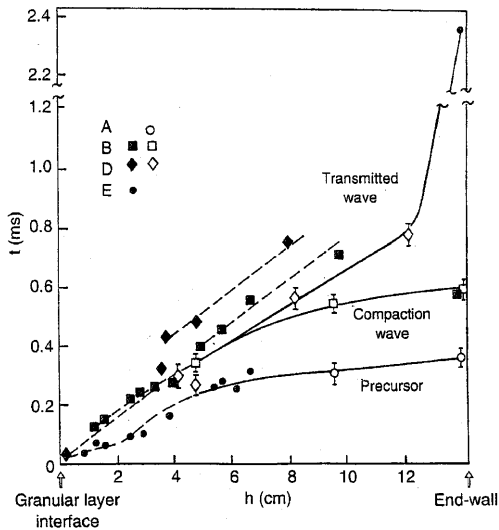


FIGURE 15.2.34 Time-distance diagram obtained for shock wave interaction with a granular layer made of material N5, Table 15.2.1 (Britan *et al.*, 1997a).

the transmitted wave at the location where the pressure transducers T1, T2, and T3 are placed.

It can be clearly seen that the trajectories of the waves shown in Fig. 15.2.33 are straight lines and they all originate at $L = 0$. The transmitted wave raises the pressure in the pore space between the particles and induces gas filtration. After its reflection from the end wall, the flow becomes stagnant in the vicinity of the shock tube end wall and prevents further motion of the particles. The compaction wave velocity was lower than the transmitted wave velocity. As a result, the compaction wave interacted with the reflected transmitted wave before it reached the shock-tube end wall. When the interaction is strong, the arrival time of the compaction wave shown by the dark points B would differ from that shown by the open points. Therefore, close agreement between the results of the two types of experimental data, shown in Fig. 15.2.33, may bring one to an opposite conclusion. Namely, interaction of the compaction wave with the region formed after the reflection of the transmitted wave does not change its trajectory, and therefore the interaction was not strong.

A typical wave diagram as obtained for material with low permeability (N5 in Table 15.2.1) is shown in Fig. 15.2.34. The dashed line trajectories were plotted following the closed symbols. It is clearly seen that contrary to the previous case, the transmitted wave is quickly overtaken by the compaction wave and most of its trajectory is located above the trajectory of the compaction wave. As a result, the compaction wave reflects from the end wall before the transmitted wave, which causes strong attenuation of the transmitted wave in the vicinity of the end wall. This strong attenuation is manifested by the position of the last point E as measured at the end wall by the transducer T4 (see Fig. 15.2.32b).

The first disturbance to be detected, according to Fig. 15.2.34, is the precursor and its trajectory is based on points A, which were obtained previously in the experiments with a 138-mm granular layer using pressure transducers that were in contact with the granular material. Since these pressure transducers recorded disturbances in both the gas and the solid phases, one could not determine from their signals whether the precursor was a gas or a solid disturbance. Experiments done on 70-mm granular layers have clearly showed that the precursor was a gas disturbance because points E, in Fig. 15.2.34, fell on the trajectory of points A shown by the solid line (see points E near $L = 6$ cm). Hence, the following question may arise. Why in the experiments with 138-mm granular layer did the pressure transducer T4 register only the transmitted wave, but not the precursor arrival at the end wall (see point E in Fig. 15.2.34), whereas the transducer T7 registered these two disturbances (see compressive stress profiles T7 in Fig. 15.2.32b). It is reasonable to believe that the main reason for this observation is related to the

effect of the protective screen and the cavity that separates the screen and the pressure transducer T4. The protective screen reduces the amplitude of the precursor, which was already small because of its attenuation while propagating along the layer.

Notably, the precursor origin was not registered by the pressure transducers T1, T2, and T3 even in a shallow layer (for example, $L = 40$ mm). On the other hand, in a shallow layer, upon precursor reflection from the end wall, its pressure signature was amplified and became detectable by the pressure transducer T4. This makes it possible to distinguish between the precursor and the transmitted wave in the experiments. As can be seen in Fig. 15.2.34, the transmitted wave trajectory, near $L = 6$ cm, based on the measurements by transducers T1, T2, and T3 (open points D), appears later than the precursor (points E).

After some distance the precursor moves with the same velocity as the compaction wave until they reflect from the end wall. Whether the compaction wave is the cause of the precursor formation in this material or the transmitted wave, as was the case for material with large permeability, should be ascertained. Close inspection of the data in Fig. 15.2.33 and 15.2.34 enables one to elucidate such phenomena.

The first experimental evidence for the existence of a compaction wave inside the granular layer having large permeability was registered even in the vicinity of the granular layer interface, whereas the time delay between points B and E at $L = 10$ mm in Fig. 15.2.33 is clearly seen. The compaction wave does not accelerate, since its trajectory is a straight line. However, in Fig. 15.2.34 only a small time delay was registered between the origins of the dashed line trajectories for points D and B (see the area near the location $L \approx 15$ mm). This shows that the particles quickly accelerate because of large pressure gradients near the interface, and as a result the compaction and transmitted waves trajectories are close to each other. After a distance of $L \geq 60$ mm, the compaction wave overtakes the transmitted wave and drives the gas ahead of it into the granular layer. Thus, in contrast to the granular layers of large permeability, the origin of the precursor in the material N5, which was also well defined in the compressive stress signal T7 of Fig. 15.2.32b, is not the transmitted wave but the leading front of the gas surge (see points E near $L = 6$ mm in Fig. 15.2.34) that moves ahead of the compaction wave front. At the end wall, the gas surge is stopped, reflects back, increases the gas pressure, and interacts with the compaction wave in the vicinity of the end wall. For the high granular layers, such as $L = 138$ mm, these processes are apparently not so strong, whereas they play a greater role in shallow layers. This is substantiated by the findings shown in Fig. 15.2.34: For both the compaction (points B) and transmitted waves (points D) the dashed and solid line trajectories differ in the range $4 \text{ cm} < L < 10 \text{ cm}$.

15.2.5.2 DYNAMIC YOUNG MODULI

From the results shown in Figs. 15.2.29 to 15.2.31 it may appear that large particles are more productive in the formation of a peak stress than small ones. In practice, such a trend is valid only for some specific conditions illustrated in these figures. Beyond this range (for a wider range of granular layer lengths), such a tendency can be reversed. To demonstrate this, the peak stress data $\sigma_{t\max} = \sigma_{t\max}(L)$ for various granular materials are presented in Figs. 15.2.35 to 15.2.37 for the standard and for the protected samples. The following is clearly seen:

- For each type of granular medium, similarly to the data presented in Fig. 15.2.19, there is an “optimal” layer length L^* that resulted in a maximum in the curve $\sigma_{t\max} = \sigma_{t\max}(L)$.
- The optimal granular layer length L^* depends on both the particle diameter d_p and the particle density ρ_p . This may be noted by comparing two materials consisting of similar particle diameters d_p (Figs. 15.2.35 and 15.2.37), where the maximal peak stress occurs for different values of L^* .
- For all the data obtained with protected samples, the values of $\sigma_{t\max}$ are smaller than those obtained for standard ones. Thus, the effect of gas filtration on the total stress formation is evident.

The data shown in Figs. 15.2.35 to 15.2.37 are very important in constructing the dynamic relation between the average normal stress σ_a and the sample deformation l (Liakhov and Polyakova, 1972). Since the granular material fills the entire cross section of the channel, the particles can move only along the

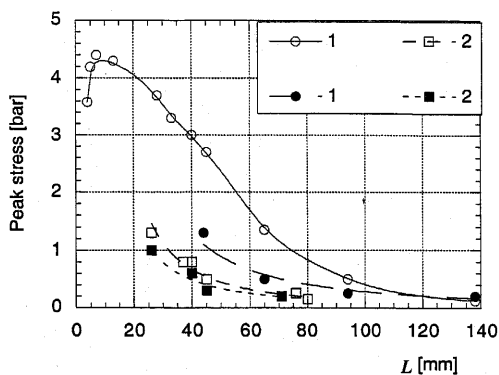


FIGURE 15.2.35 The dependence of the maximum value of the total stress on the length of the sample. Experimental data were obtained at the end wall (1) and at the sidewall (2) of the test section with a standard sample (open symbols) and with a protected sample (closed symbols) of material N1 of Table 15.2.4 (Britan *et al.*, 1999).

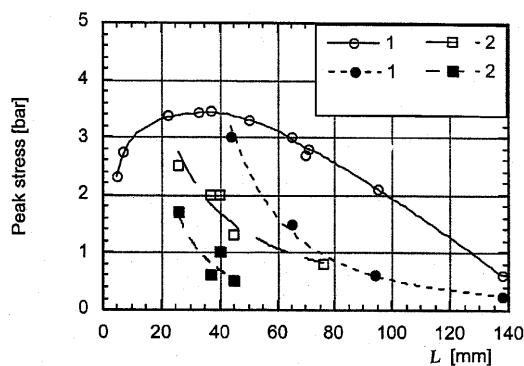


FIGURE 15.2.36 The dependence of the maximum value of the total stress on the length of the sample. Experimental data were obtained at the end wall (1) and at the sidewall (2) of the test section with a standard sample (open symbols) and with a protected sample (closed symbols) of material N2 of Table 15.2.4 (Britan *et al.*, 1999).

test section axis x . Hence, the shock wave impact imposes a uniaxial deformation on the sample. Therefore,

$$l_2 = l_3 = 0 \tag{15.2.6}$$

$$\sigma_2 = \sigma_3 \neq 0, \tag{15.2.7}$$

where l_2, l_3 and σ_2, σ_3 are the lateral (tangential) deformations and stresses, respectively. The average normal stress σ_a is related to the principal stresses $\sigma_1, \sigma_2, \sigma_3$ via the expression

$$\sigma_a = -\frac{1}{3}(\sigma_1 + \sigma_2 + \sigma_3). \tag{15.2.8}$$

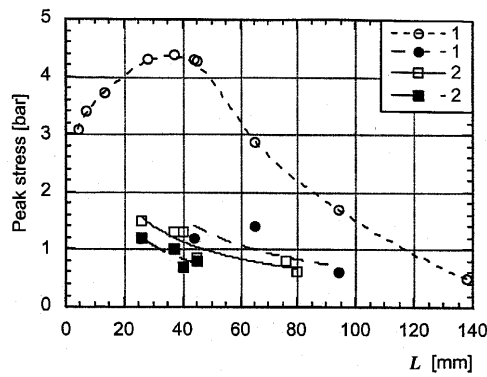


FIGURE 15.2.37 The dependence of the maximum value of the total stress on the length of the sample. Experimental data were obtained at the end wall (1) and at the sidewall (2) of the test section with a standard sample (open symbols) and with a protected sample (closed symbols) of material N3 of Table 15.2.4 (Britan *et al.*, 1999).

Equation (15.2.8) can be written for a symmetry plane motion as

$$\sigma_a = -\frac{1}{3}(\sigma_1 + 2\sigma_2). \quad (15.2.9)$$

For a uniaxial deformation, the sample deformation, l , can be related to the bulk density, ρ_b , by

$$l = \frac{\rho_{b0} - \rho_b}{\rho_b}, \quad (15.2.10)$$

where ρ_{b0} is the initial bulk density of the granular medium. By using the mass and momentum conservation laws at the shock wave front, a simple equation defining the dynamic compression of the granular medium can be obtained:

$$l = -\frac{3\sigma_a}{(1 + 2k_\tau)\rho_0 V_g^2}, \quad (15.2.11)$$

where $k_\tau = \sigma_2/\sigma_1$ is the coefficient of lateral stress. The validity of Eq. (15.2.11) is limited by the assumption that the transmitted pressure wave is a sharp shock wave.

From here onward the term shock wave will also be used to describe a pressure jump (and other quantities). Notably, the profiles of the pressure jump that were obtained in the experiments depend on several factors, namely, the frequency characteristics of the pressure transducer, its manner of installation inside the test section, the type of the granular medium, and the impact shock wave intensity, which can affect the results. In addition, it is not clear how sharp a registered peak should be in order to classify the stress as a shock wave front. The simplest way to address this question is to compare the transmitted wave velocity V_g with the sound speed c_0 for the same conditions inside the granular material. The speed of sound, c_0 , can be calculated from Hooke's law for linearly elastic granular media

$$c_0 = \sqrt{\frac{E_d}{\rho_b}}, \quad (15.2.12)$$

where E_d is a dynamic analog of Young's module of the media (Liakhov and Polyakova, 1972). It can be said that the transmitted wave is a shock wave if $V_g > c_0$ and the peak stress values registered at the sidewall and at the end wall can serve as approximations for σ_1 and σ_2 , respectively. Thus, the experimental data presented in Figs. 15.2.35 to 15.2.37 can be used to obtain a relation between k_τ and σ_a and the granular layer length L . Furthermore, if the length L is excluded, the dynamic equation (15.2.11) is contractible to define the granular layer deformation l as a function of the average normal stress σ_a at the shock wave front. The obtained results are compared in Fig. 15.2.38 with curve N4, which was obtained by Liakhov and Polyakova (1972) during field

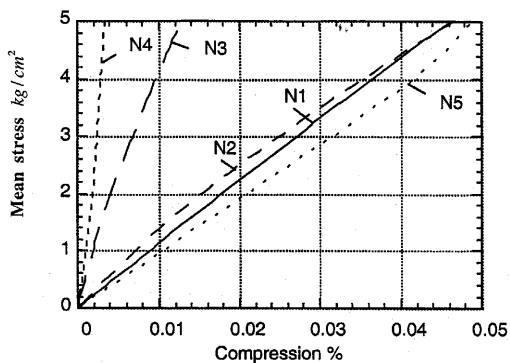


FIGURE 15.2.38 Stress–strain curves for the granular materials obtained by Britan *et al.* (1999). The curve notations refer to the material code of the granular medium as defined in Table 15.2.4.

tests with explosive waves, and with curve N5, which is a result of the shock tube experiments of Liakhov (1968). These data, together with other empirical correlations such as flow resistance and intergranular stress, are usually required for any predictive theory as physical input functions to the computer program (e.g., van Dongen *et al.*, 1996). Moreover, based upon the material characteristics in Table 15.2.4 and criterion (15.2.12), the question whether a shock or a compressive wave exists inside the granular medium may be answered.

It should be noted that although all the studied granular media had nearly the same porosity, $\varepsilon \approx 0.4$, and were subjected to similar stress, their compressions were different by more than a factor of 10. This might be related to the role of the interstitial fluid occupying the granular bulk during its compression. A major part of the compression behavior of materials N4 is concerned with water, which mostly replaced air content. Hence, the clayey soil behaves as an ideal liquid with almost similar normal and lateral stresses ($k_t = 0.9$). The

TABLE 15.2.4 Main Characteristics of the Granular Materials used in Experiments by Britan *et al.* (1999)^a

N	Material	ε	k_t	V_g (m/s)	V_s (m/s)	γ	Water content (%)	E_d (MPa)	c (m/s)
1	Potash	0.428	0.2–0.4	144	236	1.17	—	11.0	97.0
2	Fe 1.04 mm	0.393	0.2	226	170	4.50	—	12.9	53.5
3	Fe 0.45 mm	0.399	0.6	143	175	4.46	—	37.5	91.7
4	Clayey soil	0.011	0.9	—	—	2.01	12–15	100	225.9
5	Sand	0.432	0.3–0.4	80	—	1.50	—	9.5	79.6

^a ε , porosity; k_t , coefficient of lateral stress; V_g , transmitted wave velocity; V_s , compaction wave velocity; γ , skeleton relative density; c , speed of sound.

compressibility of water is close to that of the clayey soil skeleton, and the pore-water pressure produces no effective deformation of the saturated soil (Terzaghi, 1943). Thus, the sound velocity inside the clayey soil and its Young's modulus are maximal for the studied conditions ($E_d = 100$ MPa). The next stiffest sample used in this study was a sample made of material N3 (in Table 15.2.4) with a Young's modulus $E_d = 37.5$ MPa. In contrast to the clayey soil (N4 in Table 15.2.4), the Fe granular sample (N3) was air saturated, as was the case with the other samples used in the experimental study. Notably, Terzaghi's concept of effective stress for this case is meaningless because the compressibility of the air in the pores is higher than that of the granular media skeleton and, as a consequence, the gas pressure strongly affects the sample compression (Oka, 1996). Generally speaking, similar behavior can be expected for any gas-saturated granular layer that is statically loaded with impermeable membrane or, as in our case, during a short-time impact inside the shock tube. For all these conditions the granular medium behaves during compression as a closed system preventing the outflow of air from the bulk (Liakhov and Polyakova, 1972). A lesser value of the coefficient k_τ for these granular materials shows that its behavior must be closer to that of a solid medium whose stiffness is dictated by the skeleton density $\gamma = \rho_s \rho_b / \rho_p$. When γ is large, the granular bulk is densely packed, and thus a stronger force is required to compress it.

The next parameter responsible for the granular sample compression is its tenacity or, in other words, the ratio of mean area of the particles contacts to the mass of the particle. A bulk of spherical particles that are arranged in a uniform array has a limited number of contacts per particle, corresponding to the material porosity. Referring to the data presented in Table 15.2.4, one can see that while the porosities and the skeleton relative densities γ of materials N2 and N3 are close, the particle diameter d_p of material N2 is nearly twice as large as that of material N3. Since the mass of the particle increases with d_p , the tenacity of material N2 is smaller and it could more easily be compressed. On the other hand, the dynamic Young's modulus of material N2 is about $E_d = 12.9$ MPa, which is close enough to that of materials N1 and N5 ($E_d = 11$ and 9.5 MPa, respectively) having similar skeleton relative densities γ .

15.2.6 SHIELDING CHARACTERISTICS OF GRANULAR FILTERS

15.2.6.1 PROBLEM DESCRIPTION

Although granular filters are widely used as protectors against shock and blast waves, to date very little information is available on their performance. Recent

publications in this area were concentrated on the attenuation of shock waves with a decaying pressure profile through the perforated partitions and grids; e.g. see Mori *et al.* (1975), Tong *et al.* (1980), Gelfand *et al.* (1987), and Lind *et al.* (1999). The destructive nature of shock/blast waves depends on the pressure signature of the incident shock as well as on the distance between the various obstacles. This makes the problem rather complex (Baker *et al.*, 1983). Extensive measurements of the post-shock-wave overpressure upstream and downstream of various granular filters for shock waves with steplike pressure profiles were performed by Medvedev *et al.* (1990). The experimental results were compared with calculations, and good agreement was found between experimental and theoretical findings. Similar experiments have been conducted by Engebretsen *et al.* (1996). A summary of physical properties used in the experiments of both Medvedev *et al.* (1990) and Engebretsen *et al.* (1996) is given in Table 15.2.5. From this table it can be seen that both used granular filters in which the length ratio L/d_p and the porosity ε were varied within similar ranges. Furthermore, both used similar incident shock wave Mach numbers. As could be expected, the experimental results obtained by these authors, shown in Fig. 15.2.39, demonstrate a similar tendency in variations of the exit relative pressure behind the transmitted shock wave $\Delta P_{\text{exit}}/P_0$ as a function of filter length (where P_0 is the initial gas pressure inside the shock tube). However, while the results obtained by Medvedev *et al.* (1990) demonstrate strong dependency of the exit relative overpressure on the shock wave Mach number M_s , those of Engebretsen *et al.* (1996), presented in Fig. 15.2.39 by a single dashed line, do not indicate a dependency of $\Delta P_{\text{exit}}/P$ on M_s . In addition, Engebretsen *et al.* (1996) stated that the effect of changing

TABLE 15.2.5 Experimental Conditions in the Shock Tube Studies of Engebretsen *et al.* (1996) [1] and Medvedev *et al.* (1990) [2]

Particle type	Particle size d_p (mm)	Filter porosity ε	Filter length L	Air gap length Δ (mm)	Geometric factor H/d_p	Pressure ratio P_{41} or M_s	Refs.
Plastic spheres	10.00	0.272–0.38	19	2800	12.50	$P_{41} = 5\text{--}20$	[1]
Glass spheres	15.52	0.38–0.41	26	2800	8.05	$P_{41} = 5\text{--}20$	[1]
Polyeth. spheres	3.90	0.38	15	1000	10.26	$M_s = 1.15$, 1.28, 1.47	[2]
Still cylinders	10×12	0.41	16	1000	3.30	$M_s = 1.15$, 1.28, 1.47	[2]
Porcelain spheres	15.8	0.44	10	1000	2.53	$M_s = 1.15$, 1.28, 1.47	[2]
Claydite spheres	21.9	0.50	11	1000	1.82	$M_s = 1.15$, 1.28, 1.47	[2]

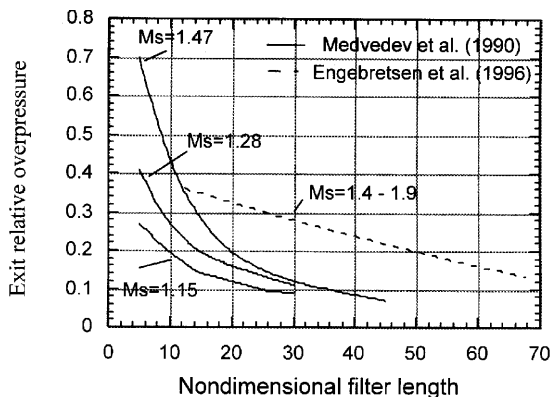


FIGURE 15.2.39 Attenuation of shock waves during their propagation through granular filters. The nondimensional axis used in this figure is the same as used by Medvedev *et al.* (1990). Exit relative overpressure is the ratio of the pressure behind the shock wave transmitted through the granular filter P_{trans} to initial gas pressure P_0 ; the nondimensional filter length is $\Theta = 1.75(1 - \epsilon)L/\epsilon d_p$.

the material density and the size of the granules on the attenuation phenomena is negligibly small. Such a conclusion casts doubt because the particle size is responsible for the granular filter permeability, which has a direct effect on the shock wave attenuation.

Another feature, which most probably should affect the wave attenuation, is the duct and the particle geometry. For cases where the geometry factor $H/d_p < 20$ (where H is the width of the channel cross section), the sidewall friction may strongly affect the flow (Munch-Andersen, 1983). As a result, the one-dimensional presentation of the flow pattern inside a granular filter would be questionable. The air gap length downstream of the filter Δ may also affect the filter performance, depending on how the filter is installed inside the duct, close to or far upstream from the protected surface (Baker *et al.*, 1983). Since the air gap length used by these authors was sufficiently large ($\Delta = 1\text{--}2.8\text{ m}$), one cannot infer any practical information from their results regarding the role of air gap in shock wave attenuation.

Britan *et al.* (2000) conducted experiments that aimed to clarify attenuation performance of various granular filters against shock waves. Experiments were carried out in the vertical shock tube shown in Fig. 15.2.6, with slight modifications concerning installation inside the channel of a rigid grid that used as a granular filter support. A supported grid with an area ratio of 0.31 (ratio between open and total area) was placed inside the test section with an air gap, Δ , from the test section end wall. The length of the air gap Δ can easily be changed from 0 to 228 mm. A summary of the main physical characteristics of the granular materials used for experiments is given in Table 15.2.6.

TABLE 15.2.6 Main Physical Characteristics of the Granular Materials used in Experiments by Britan *et al.* (2000)

Material	Particle diameter d_p (mm)	Particle density ρ_p (g/cm ³)	Filter length L (mm)	Porosity ε
Glass #8	2.4	2.5	8–63	0.38
Glass #18	1.0	2.5	5–63	0.40
Glass #35	0.5	2.5	4–27	0.39
Rimax #8	2.4	4.1	63	0.42
Rimax #18	1.0	4.1	63	0.35
Steel #5	4.4	7.7	4.4–22	0.49
Steel #10	2.0	7.7	12–63	0.39
Steel #14	1.4	7.7	16–46	0.40
Steel #18	1.0	7.7	4–49	0.35
Steel #35	0.5	7.7	6–26	0.40

15.2.6.2 ATTENUATION PERFORMANCE OF GRANULAR MATERIALS

A summary of results obtained by Britan *et al.* (2000) is presented in a nondimensional way in Fig. 15.2.40. It can be clearly seen that the attenuation of the shock wave increases with the filter length. The nondimensional filter length L/d_p is of paramount importance for very short filters. For a short length filter ($L/d_p < 10$), the attenuation coefficient $K_a = P_{trans}/P_{inc}$ is relatively large and it decreases dramatically for longer filters. When $L/d_p > 40$, it approaches a constant value of $K_a \approx 0.05$. This trend is not surprising, since the longer the filter is (or the smaller particles are), the larger is the energy loss, and thus the attenuation of the transmitted shock wave is greater. It should also be noted that numerical prediction employing the simple filtration model described by Britan *et al.* (1997b) predicted the experimental findings well.

Based upon correlation of experiment and theory, it was of interest to compare the present results obtained for K_a with those of Medvedev *et al.* (1990) and Engebretsen *et al.* (1996) that were obtained under similar conditions. Figure 15.2.41 contains a summary of these data. It is apparent that for the very short filters ($L/d_p \leq 20$) good agreement was observed between the present results and the curve fit of Medvedev *et al.* (1990). Note, however, that for longer filters the present experimental results were closer to the curve fit of Engebretsen *et al.* (1996), whereas the data of Medvedev *et al.* (1990) indicate a monotonic decline.

Further insight into the problem may be obtained from analyses of the time duration t_m . This parameter, the so-called “end wall matching time,” is characteristic of the time passed from the moment that the transmitted

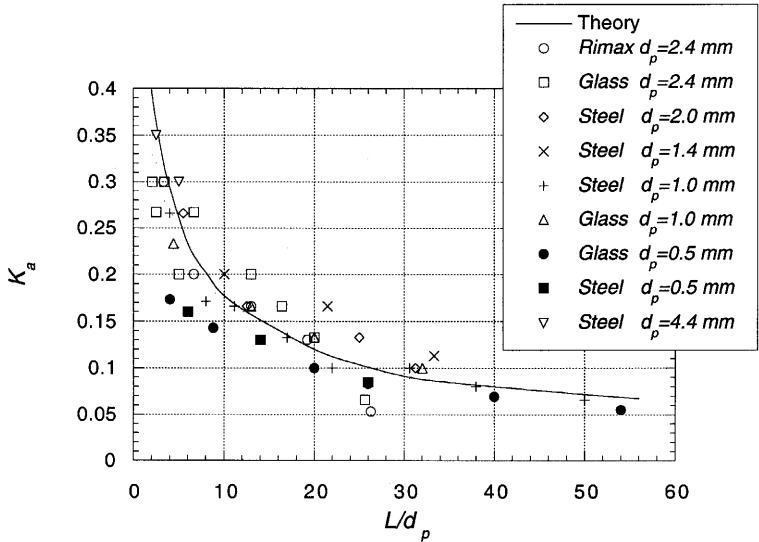


FIGURE 15.2.40 Attenuation coefficients versus nondimensional filter length (Britan *et al.*, 2000).

shock wave reaches the tests section end wall until the moment when the end-wall pressure reaches an equilibrium steady level. The “end-wall matching time” versus the filter nondimensional length for different air gap lengths is shown in Fig. 15.2.42. From the curves and experimental points shown in Fig. 15.2.42, it could be concluded that filters composed of small particles result in

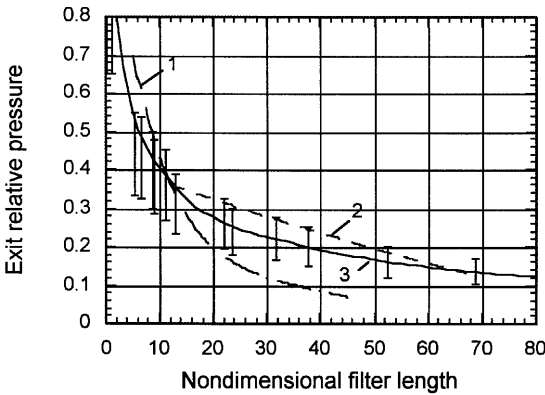


FIGURE 15.2.41 Comparison among experimental results of Medvedev *et al.* (1990) (1), Engebretsen *et al.* (1996) (2), and Britan *et al.* (2000) (3) for incident shock wave Mach number $M_s = 1.47$.

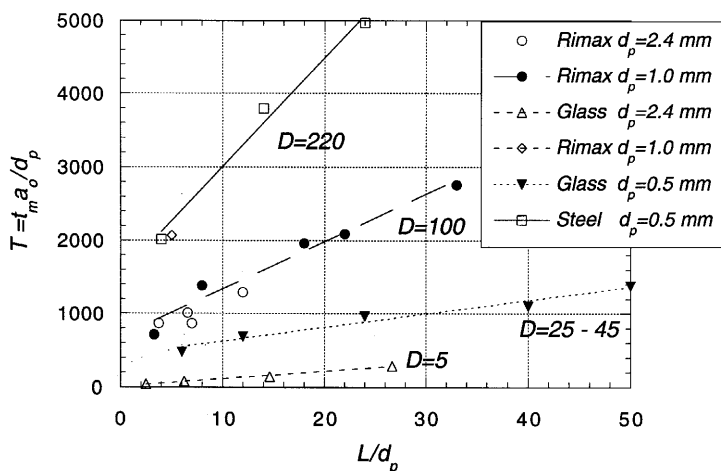


FIGURE 15.2.42 End-wall matching time versus the filter nondimensional length for different air gap lengths Δ (Britan *et al.*, 2000).

a slower pressure buildup between the filler and the shock tube end wall. Similar behavior was presented for the length effect. Namely, the longer the granular filter is (or the longer the distance between the filter and the shock tube end wall), the larger is the “end-wall matching time.” Note that slower pressure buildup would be easier to withstand by the protected surface, and real protective systems should increase the matching time as long as possible. Thus, the particle dimension and both the filter length and length of the air gap are characteristics that cause significant effect on the expected protection produced by the filter. On the other hand, the material composition of the filter (particle density) plays a minor role in increasing the matching time or decreasing the attenuation coefficient K_a .

15.2.7 PHYSICAL MODELS AND SIMULATIONS

During the last decade, unsteady air filtration through granular media induced by shock waves has been modeled and simulated (Sandusky and Liddiard, 1985; Baer and Nunziato, 1986; Baer, 1988; van der Grinten *et al.*, 1988; Powers *et al.*, 1989; Sakakita and Hayashi, 1992; Kutushev and Rudakov, 1993; Levy *et al.*, 1993b; Britan *et al.*, 1997b; and Bdzil *et al.*, 1999). In general, two approaches have been employed by researchers for modeling the flows in a granular medium: the single-phase approach, based on an oversimplified

mixture theory; and the multiphase approach for analyzing transport phenomena in porous media. In the two-phase approach, the fluid(s) filling the pores and the grains of the granular material are considered as two phases, which interact between themselves.

In general, three theoretical approaches can be used for modeling multiphase flow: two-fluid theory, the Eulerian granular approach, and the discrete element method. Both the two-fluid theory and the Eulerian granular theory are based on macroscopic balance equations of mass, momentum, and energy for both the gas and solid phases. It is assumed that both phases occupy any point (x, y, z) of the computational domain, each with its own volume fraction. The solid phase is dealt with as a pseudofluid. The main difference between these theories is that the Eulerian granular method employs the kinetic theory of rare gases to model the granular phase properties, such as pressure, temperature, and viscosity, whereas the two-fluid theory uses macroscopic correlations in order to model similar properties for the solid phase. It should be noted that traditionally, the two-fluid theory was used to model dust flow while the Eulerian granular approach was used to simulate both dense and dilute phase flows. Unlike these theories, the discrete element method is an Eulerian-Lagrangian approach, in which the gas phase is assumed as the continuous phase, which occupies every point in the computational domain, and the solids particles occupy discrete points in the computational domain. As a consequence, mass, momentum, and energy balance equations should be solved for each particle within the computational domain. This method is able to take into account various types of particle-particle and wall-particle interactions from the basic dynamic approach. Hence, there is no need to develop or use macroscopic modeling for the solid phase. As such, this modeling needs a large amount of memory and CPU time in order to solve real problems. As a result, no full-scale problems have yet been solved by using the discrete element method. For example, using the discrete element method, the dynamic response of granular materials to the impact of a spherical projectile was investigated numerically (Tanaka *et al.* 2000). A two-dimensional granular layer composed of nylon spheres, arranged regularly in a rectangular container collided with a steel sphere. The container wall effects on the impact behavior were evident.

It should be noted that the discrete element approach is similar to the other approaches in the limit of solving the Eulerian granular or two-fluid models for n solid phases while n is going to N number of particles.

A detailed description of two-phase modeling was given by Baer and Nunziato (1986). One-dimensional two-phase studies were presented by Baer (1988) and Powers *et al.* (1989). In addition to their numerical simulations (Baer, 1988), Powers *et al.* (1989) also presented simplified analytical models and showed that compaction waves may propagate with a smaller

velocity than the speed of sound. Powers *et al.* (1989) referred to these waves as subsonic compaction waves and showed that they arise from nonideal effects. Furthermore, they showed that the minimal compaction wave velocity is equal to the speed of sound in the solid when the Tait's equation is ideal. From their calculation, Powers *et al.* realized that the change in the density of the grains is only fractions of a percent, and therefore they concluded that the solid phase can be assumed to be incompressible. Similarly to Baer and Nunziato (1986), to account the compressibility effect, they introduced a compaction equation that relates the effective stress to the solid volume fraction.

Bdzil *et al.* (1999) examined the continuum-mixture theory proposed by Baer and Nunziato (1986) with particular attention to the manner in which its constitutive equations were formulated. Connections between the mechanical and the energetic phenomena occurring at the grain scale and their manifestations on the continuum average scale were explored. Bdzil *et al.* (1999) corrected inconsistencies in the equation of state for the granular solid and in the constitutive expression for the interfacial exchange rates.

Sakakita and Hayashi (1992) studied the head-on collision of a planar shock wave with a granular material. They adopted the conservation equations of dust suspension and introduced new terms into the conservation equations to include physical effects associated with granular materials. They took into account the changes in the volume fraction of both the solid and gaseous phases, and solid stress inside the granular material due to particle-particle interactions. Poor agreement was obtained between the numerical and the experimental results of the compressive stress.

Kutushev and Rudakov (1993) proposed a similar model to simulate the pressure signals measured by Gelfand *et al.* (1989) for a 20-mm granular layer. A qualitative agreement was obtained between the numerically predicted and measured compressive stresses at the shock tube end wall. They noted that the pressure profiles inside the granular layer were governed by the gas filtration. This investigation left several questions regarding the use of fitting parameters and the validity of the constitutive equations used in their simulations.

In a later study, Britan *et al.* (1997b) assumed that the skeleton of the granular layer is not compressed during the compaction and therefore the voidage is constant. As a result, the mass and momentum conservation equations of the solid phase were neglected and only the mass, momentum, and energy equation for the gas phase and heat conduction equation for the solid phase were solved. Note that this model did not consider the influence of the solid phase stress, particle rearrangement, and granular layer deformations due to the impact load. In addition, it was assumed that the friction force between the gas and the solid phases could be described by a parabolic law, similarly to the steady state friction force described by the Ergun equations. In

order to obtain an agreement between their numerical predictions and experiments, the coefficients of the Ergun equation were also modified. A good agreement between the experiment and calculations was found for the sidewall gas pressure signals, while good correlation with the end-wall measurements was attained only for an increase rate of gas pressure readings. In addition, the gas phase wave velocities predicted for various materials did not agree well with those obtained experimentally.

Levy (1999) adapted the model of wave propagation in porous materials presented by Levy *et al.* (1996) to simulate wave interaction and propagation with granular materials undergoing small elastic deformation. Macroscopic governing equations of the flow field have been used to investigate the head-on collision of a planar shock with granular medium. The one-dimensional, unsteady version of these equations was solved numerically using a TVD-based numerical code. The validity of using the model, which was developed for porous media, for the shock wave interaction with granular material was examined. A comparison between the predictions of the numerical simulations and the experimental results presented by Ben-Dor *et al.* (1997) showed good agreement. It was found that the prediction of the numerical simulations for the fluid pressure waves velocities is much better than those accepted by Britan *et al.* (1997b). Finally, it was evident that the model that initially was developed for porous material may be used successfully to predict shock wave interaction and propagation with granular materials.

15.2.8 CONCLUSION

This review was aimed toward a better understanding of the dynamics of stress phenomena inside granular materials as well as inside those modeled by random packing of monodisperse disks or cylinders. To date it was thought that the main details of gas flow–skeleton interactions inside granular material are similar in concept to those inside flexible foams. The total stress profiles as measured at the rear end of the foam sample at least resembled those obtained with granular materials. This review first established that such a similarity is apparent and stressed the dominant role of the sidewall friction and arching effect in peak stress formation inside the granular media.

On the other hand, shock-induced gas filtration is also responsible for the total stress performance, and the drag force acting on the granules may increase end-wall peak stress $\sigma_{t\max}$ up to several times. Since the filtration effect is accomplished by energy losses, its contribution to the particle–particle interaction attenuates with distance along the sample, and so does the effective stress.

For each kind of granular medium there is an optimal layer length L^* that results a maximum value of the total stress. Beyond this length two different phenomena are important for the peak stress formation. For shorter layers, $L < L^*$, the peak stress amplitude can be restricted by the rarefaction wave arrival, and for longer layers, $L > L^*$, the peak profile of the total stress is mostly governed by the elastic bulk resistance to the compression due to the arching and particle–wall friction.

Based on the peak stress measurements at the sidewall and at the end wall of the test section, a dynamic stress–strain relation between the average normal stress σ_a and the sample deformation l was constructed. Attempts to define such characteristics have been prompted by the need to design protection against shock wave loading on man-made structures. Comparative analysis of the compression curves clearly shows that for similar stress conditions, air-saturated granular materials can be compressed more than 10 times more than nonsaturated granular materials with water content. In choosing the material type for attenuation purposes, the stiffness or dynamic Young's module E_d for the bulk material must also be compared. Between two materials composed of grains with similar diameter, a bulk material composed of light particles will demonstrate maximal flexibility and as a result is mostly suitable as a shock wave absorber.

The attenuation performance of shock wave absorber (or filter) strongly depends on its geometry. The presence of an air gap between the filter and the protected surface prevents direct contact with particles composing the granular filter. This will eliminate peak pressure/stress on the protected surface. The amplitude of the transmitted shock wave at the filter exit decreases with an increase in the filter length or when the particle diameter decreases. Granular filters followed by an air gap allow an increase in the “matching time.” The “matching time” will become longer when the length of the air gap increases, when the diameter of the particles composing the filter decreases, or when the filter length increases.

Experiments with granular media offer a wide-reaching set of possibilities for studies of nonlinear effects in 3D random systems. The presence of arching, stress localization, chains formation, and strong gas filtration must be considered when analyzing such applications. To the best of our knowledge, among many ways to extend this work, much remains to be done experimentally in terms of coupling between effects inside granular materials and those at the bulk boundaries, and theoretically in terms of introducing the important features of granular materials into the various models. To better understand many questions that still have not been answered in the available literature, optical observations combined with a stress–strain registration inside the granular material are strongly appreciated.

REFERENCES

- Amami, M., Travers, T., Bideau, D., Deligead, Y., Messenger, J. C., Troadec, J. P. and Gervois, A. (1990) Role of angular correlations on the mechanical properties of 2d packings of cylinders. *J. Phys.: Condens. Matter* **2**, 9523–9530.
- Baer, M. R. (1988) Numerical studies of dynamic compaction of inert and energetic granular materials. *Trans. ASME J. Appl. Mech.* **55**, 37–43.
- Baer, M. R., and Nunziato, J. W. (1986) A two-phase mixture theory for the deflagration to detonation transition (DDT) in reactive granular materials. *Int. J. Multiphase Flow* **12**, 861–889.
- Baker, W. E., Koks, P., and Wastain, P. (1983) *Explosion Hazards and Evaluation*. Elsevier, Amsterdam.
- Bideau, D., and Hansen, A. (Eds.) (1993) *Disorder and Granular Media*. Elsevier Science Publ., North-Holland.
- Ben-Dor, G., Mazon, G., Igra, O., Sorek, S., and Onodera, H. (1994) Shock wave interaction with cellular materials. Part II: open cell foams; experimental and numerical results. *Shock Waves* **3**, 167–179.
- Ben-Dor, G., Britan, A., Elperin, T., Igra, O., and Jiang, J. P. (1997) Experimental investigation of the interaction between weak shock waves and granular layers. *Exp. Fluids* **22**, 432–443.
- Bdzil, J. B., Menikoff, R., Son, S. F., Kapila, K., and Stewart, D. S. (1999) Two-phase modeling of deflagration to detonation transition in granular materials: A critical examination of modeling issues. *Phys. Fluids* **11**(2), 378–402.
- Biares, J., and Hicher, P. Y. (1994) *Elementary Mechanics of Soil Behavior*. Balkema, Rotterdam.
- Britan, A., Elperin, T., Igra, O., and Jiang, J. P. (1995) Head-on collision of a planar shock wave with a granular layer, in *Proc. ISCCM Conf.* (ed. S. C. Schmidt and W. C. Tao), Part 2, pp. 971–974, Seattle, WA.
- Britan, A., Ben-Dor, G., Elperin, T., Igra, O., and Jiang, J. P. (1997a) Mechanism of compressive stress formation during weak shock waves impact with granular materials. *Exp. Fluids* **22**, 507–518.
- Britan, A., Ben-Dor, G., Elperin, T., Igra, O., and Jiang, J. P. (1997b) Gas filtration during the impact of weak shock waves on granular layers. *Int. J. Multiphase Flow* **23**, 473–491.
- Britan, A., Ben-Dor, G., Levy, A., and Igra, O. (1999) Shock wave interaction with granular materials. In *Book of Abstracts of 22nd Int. Symp. on Shock Waves, Imperial College, London*.
- Britan, A., Ben-Dor, G., Igra, O., and Shapiro, H. (2000) Shock wave attenuation by granular filters (to be published).
- Carstensen, J. T., Geoffroy, J. M., and Dellamonica, C. (1990) Compression characteristics of binary mixtures. *Powder Technol.* **62**, 119–124.
- Dantu, P. (1967) Etude experimentale d'un milieu purverulent compris entre deux plans verticaux et paralleles. *Ann. Points et Chaussees* **VI**.
- Engelbrechtsen, T., Bakken, J., Hansen, E. W. M., and Lysberg, I. (1996) Shock waves and gas flow through granular materials. In *Proc. Workshop Explosion Effects in Granular Materials, Oslo*, pp. 111–131.
- Gelfand, B. E., Gubin, S. A., Kogarko, S. M., and Popov, O. E. (1975) Investigation of the special characteristics of propagation and reflection of pressure waves in a porous medium. *Sov. J. Appl. Mech. and Tech. Phys.* **6**, 74–77.
- Gelfand, B. E., Medvedev, S. P., Polenov, A. N., and Tsyganov, S. A. (1987) Interaction of non-stationary pressure waves with perforated partitions. *Archivum Combustion* **7**, 215–223.
- Gelfand, B. E., Medvedev, S. P., Borisov, A. A., Polenov, A. N., Frolov, S. M., and Tsyganov, S. A. (1989) Shock loading of stratified dusty system. *Combustion* **9**, 153–165.

- Goldshtik, M. A. (1984) Transfer processes in granular layer. Academy of Sciences of the USSR, Siberian Branch, Institute of Thermophysics, Novosibirsk.
- Gvozdeva, L. G., Faresov, Y. M., and Fokeev, V. P. (1985) Interaction of air shock waves with porous compressible materials. *J. Appl. Mech. and Tech. Phys.* 3, 401–405.
- Herrmann, H. J., Hovi, J. P., and Luding, S. (1997) *Physics of Dry Granular Media*. Kluwer, Dordrecht, The Netherlands.
- Hill, L. G., and Kapila, A. K. (1996) Dynamic compaction of granular materials in a tube with wall fraction, applied to deflagration-to-detonation transition. In *Proc. 20th Int. Symp. Shock Waves, Pasadena, CA*, Vol. 2, pp. 1413–1418. World Scientific.
- Hveding, D. (1985) Air-induced ground pressure waves in granular soil materials. In *Proc. 15th Int. Symp. Shock Waves*, pp. 171–178.
- Igra, O., and Takayma, K. (1993) Shock tube study of the drag coefficient of a sphere in a nonstationary flow. *Proc. R. Soc. London A*442, 231–247.
- Jaeger, H. M., Nagel, S. R., and Behringer, P. (1996) The physics of granular materials. *Physics Today* 4, 32–38.
- Jones, D. P., and Krier, H. (1983) Gas flow resistance measurements through packed beds at high Reynolds numbers. *Trans. Am. Soc. Mech. Engrs.* 105, 168–173.
- Kuo, K. K., and Nydengger, C. C. (1978) Flow resistance measurements and correlation in a packed bed of WC 870 ball propellants. *J. Ballist.* 2, 1–26.
- Kuo, K. K., Yang, V., and Moore, B. B. (1980) *Intergranular stress, particle-wall friction and speed of sound in granular propellant beds*. *J. Ballist.* 4, 697–730.
- Kutushev, A. G., and Rudakov, D. A. (1993) Numerical study of the action of a shock wave on obstacle screened by a layer of porous powder materials. *Comb. Expl. Shock Waves* 5, 25–31.
- Lade, P. V., and De Boer, R. (1997) The concept of effective stress for soil, concrete and rock. *Geotechnique* 7, 61–78.
- Levy, A. (1999) Shock waves propagation in granular materials. *Powder Technol.* 103, 212–219.
- Levy, A., Ben-Dor, G., Skews, B. W., and Sorek, S. (1993a) Head-on collision of normal shock waves with rigid porous materials. *Exp. Fluids* 15, 183–190.
- Levy, A., Ben-Dor, G., Sorek, S., and Bear, J. (1993b) Jump conditions across strong compaction waves in gas saturated rigid porous media. *Shock Waves* 3, 105–111.
- Levy, A., Ben-Dor, G., and Sonek, S. (1996) “Numerical Investigation of the Propagation of Shock Waves in Rigid Porous Materials: Development of the Computer Code and Comparison with Experimentals” *Journal of Fluid Mechanics*, 324, 163–179.
- Liakhov, G. M. (1968) Verification of the soil viscosity. *Sov. J. Appl. Mech. and Tech. Phys.*, 68–71.
- Liakhov, G. M., and Polyakova, N. I. (1972) Waves in solid media and loads on structures. Foreign Techn. Div. Air Force System Command, U.S. Air Force, Wright-Patterson AFB, Ohio.
- Lind, C. A., Cybyk, B. Z., and Boris, J. P. (1999) Attenuation of shocks: High Reynolds number porous flows. In *The 22nd Int. Symp. Shock Waves, Book of Abstracts, London*, p. 272.
- Mazor, G., Ben-Dor, G., Igra, O., and Sorek, S. (1994) Shock wave interaction with cellular materials. Part I: analytical investigation and governing equations. *Shock Waves* 3, 159–165.
- Medvedev, S. P., Frolov, S. M., and Gelfand, B. E. (1990) Shock wave attenuation by granular materials. *Eng. Phys. J. USSR*, 924–928 (in Russian).
- Medvedev, S. P., Polenov, A. N., Khomik, S. V., and Gelfand, B. E. (1996) Experimental verification of the concept of amplification of shock loading by means of compressible covering as applied to the propagation of blast waves over a dust deposit. In *Proc. 20th Int. Symp. Shock Waves, Pasadena, CA*, Vol. 2, pp. 1321–1326. World Scientific.
- Mori, Y., Hijikato, K., and Shimizu, T. (1975) Attenuation of shock wave by multi-orifice. In *Proc. 10th Int. Shock Tube Symp., Kyoto*, pp.400–407.
- Mueth, D. N., Jaeger, H. M., and Nagel, S. R. (1998) Force distribution in a granular medium. *Phys. Rev. E* 57, 3164.

- Munch-Andersen, J. (1983) Scale errors in model silo test. In *Proc 2nd Conf. Design Silos Strength and Flow*, Stanford upon Avon, pp. 230–241.
- Nesterenko, V. F. (1992) *High-Rate Deformation of Heterogeneous Materials*. Nauka, Sib. Div., Novosibirsk.
- Oka, F. (1996) Validity and limits of the effective stress concept in geomechanics. *Mech. Cohesive-Frictional Mat.* 1, 219–234.
- Powers, J. M., Stewart, D. S., and Krier, H. (1989) Analysis of steady compaction wave in porous materials. *ASME J. Appl. Mech.* 56, 15–24.
- Rogg, B., Hermann, D., and Adomeit, G. (1985) Shock-induced flow in regular arrays of cylinders and packed beds. *Int. J. Heat Mass Transfer* 28, 2285–2297.
- Rossmannith, H. P., and Shukla, A. (1982) Photoelastic investigation of dynamic load transfer in granular media. *Acta Mechanica* 42, 211–225.
- Sakakita, H., and Hayashi, A. K. (1992) Study on the interaction between a powder layer and a shock wave. In *Proc. 18th Int. Symp. Space Technology and Science*, pp. 142–146. Kagoshima, Japan.
- Sandusky, H. W., and Liddiard, T. P. (1985) Dynamic compaction of porous beds. NSWC TR 83-256 NAVAL Surface Weapons Center, White Oak, Md.
- Schwarz, O. J., Horie, Y., and Shearer, M. (1998) Discrete element investigation of stress fluctuation in granular flow at high strain rates. *Phys. Rev. E* 57, 2053–2061.
- Shukla, A. (1991) Dynamic photoelastic studies of wave propagation in granular media. *Opt. Lasers Eng.* 14, 165–184.
- Shukla, A., and Damania, C. (1987) Experimental investigation of wave velocity and dynamic contact stresses in an assembly of disks. *Exp. Mechanics* 27, 268–281.
- Skews, B. W. (1995) Shock wave impact on porous material. In *Proc. 19th Int. Symp. Shock Waves*. (eds. R. Brun and I. Z. Dumitrescu) Vol. 3, pp. 12–20, Marseilles.
- Skews, B. W., Atkins, M. D., and Seitz, M. W. (1993) The impact of a shock wave on porous compressible foams. *J. Fluid Mech.* 253, 245–265.
- Tanaka, K., Nishida, M., Kunimochi, T., and Takagi, T. (2000) Numerical and experimental studies for the impact of projectiles on granular materials. In *3rd Israeli Conf. Conveying and Handling of Particulate Solids*, (eds. H. Kalman and A. Levy) Dead Sea, Israel.
- Terzaghi, K. (1943) *Theoretical Soil Mechanics*. John Wiley and Sons, New York, pp. 11–15.
- Tong, K. O., Knight, C. J., and Srivastava, B. N. (1980) Interaction of weak shock waves with screens and honeycombs. *AIAA J.* 18, 1298–1305.
- Travers, T., Ammi, M., Bideau, D., Gervois, A., Messenger, J. C., and Troadec, J. P. (1987) Uniaxial compression of 2d packing of cylinders. Effects of weak disorder. *Europhys. Lett.* 4, 329–332.
- Travers, T., Ammi, M., Bideau, D., Gervois, A., Messenger, J. C., and Troades, J. P. (1988) Mechanical size effects in 2d granular media. *J. Phys. France* 49, 939–948.
- van der Grinten, J. G. M., van Dongen, M. E. H., and van der Kogel, H. (1985) A shock tube technique for studying pore-pressure propagation in dry and water-saturated porous medium. *J. Appl. Phys.* 58(8), 2937–2942.
- van der Grinten, J. G. M., Snickers, R. W. J. M., and van Dongen, M. E. H. (1988) An experimental study of shock induced wave propagation in dry, water saturated and partially saturated porous media. In *Proc. Int. Symp. Modeling Soil–Water–Structure Interactions*, Delft, The Netherlands, 469–478.
- van Dongen, M. E. H., Smeulders, D. M. J., Kitamura, T., and Takayama, K. (1995) On wave phenomena in permeable foam. *Acustica* 81, 63–70.
- van Dongen, M. E. H., Smeets, G. V. R., Hoeijmakers, H. W. M., and Smeulders, D. M. J. (1996) Shock-induced wave phenomena in open-cell permeable and flexible foams. In *Proc. 20th Int. Symp. Shock Waves* (ed. B. Sturtevant, B. E. Sheperd, and H. G. Hornung), Vol. 3, pp. 1363–1368, Pasadena, CA.

- Yanagisawa, E. (1983) Influence of void ratio and stress condition on the dynamic shear modules of granular media. In *Advances in the Mechanics and the Flow of Granular Materials* (ed. M. Shahinpoor), Vol. 2, pp. 946–960. Trans. Tech. Publ., USA.
- Yasuhara, M., Kitagawa, K., Sakashita, S., Tsuzaki, Y., and Watanabe, S. (1995) One-dimensional shock wave interaction with rubber and low-porosity foam. *Shock Waves* 5, 25–32.
- Yasuhara, M., Watanabe, S., Kitagawa, K., Yasue, T., and Mizutani, M. (1996) Experiment on effects of porosity in the interaction of shock wave and foam. *Int. J. JSME, B* 39, 287–293.

Shock Wave Propagation in Multi-Phase Media

15.3 Shock Waves in Inert and Reactive Bubbly Liquids

VALERY K. KEDRINSKII

M. A. Lavrentjev Institute of Hydrodynamics, Novosibirsk, 630090, Russia

15.3.1 Shock Waves in Inert Bubbly Liquids

15.3.1.1 Introduction

15.3.1.2 Shock Wave and Spherical Bubbles

Interaction: cumulative jet formation

15.3.1.3 Plane Shock Waves and Gas Layers

15.3.1.4 Shock Wave Transformation by Bubbly

Layers

15.3.1.5 The Iordansky-Kogarko-van-

Wijngaarten NonEquilibrium Two

Phase Model of a Bubbly Liquid

15.3.1.6 Amplification, Collision and Focusing of

Shock Waves in Bubbly Liquids

15.3.2 Bubbly Detonation Waves in Reactive Bubbly Liquids

15.3.2.1 Introduction

15.3.2.2 Single Bubble Dynamics

15.3.2.3 Reactive Bubble Dynamics with

Chemical Reactions and the Interface

Mass Transfer

15.3.2.4 Shock Waves in Reactive Bubbly Liquids

15.3.2.5 Initiation, Formation, and Collision of

Bubbly Detonation Waves: "Hot Spots"

Mechanism

References

15.3.1 SHOCK WAVES IN INERT BUBBLY LIQUIDS

15.3.1.1 INTRODUCTION

In the 1950s to 1970s a number of experimental studies on the transformation mechanism of shock waves propagating in a liquid containing gas bubbles were performed. Several mathematical models were suggested to investigate analytically and numerically the main features of the interaction of shock waves with bubbly liquids, the most interesting of which arise from the pressure nonequilibrium in the liquid and the gaseous phases, and from the complex nature of the absorption and reradiation of the shock wave energy by the two-phase medium (Kedrinskii, 1968a, 1968b; 1980). These effects are clearly manifested both in the case of short shock waves and in the investigation of long waves with a steep front, provided that one is dealing with a relatively long relaxation process, small initial volume concentrations of gas in the medium, and strongly nonlinear bubble oscillations. Here we interpret short waves as those whose action induces bubble collapse in a time scale on the order of the duration of the positive wave phase.

Fundamentally different phenomena were observed in connection with the propagation of shock waves in mixtures with a high (tens of percents) gas content and with short relaxation times, that is, the pressure in the bubbles became comparable to the average pressure in the liquid phase and their velocity to the average mass velocity of the liquid. These effects were also observed in connection with the interaction of strong shock waves of long duration with gas bubbles, including dissolution of the bubbles. The results of experimental and computational investigations of the wave processes in such mixtures (Campbell and Pitcher, 1958; Lyakhov, 1959; and Parkin *et al.*, 1961) did reveal the just-mentioned features of the wave-medium interaction because they were determined mainly by the equilibrium conditions between two phases for pressure, velocity, and, sometimes, temperature.

It is useful to consider some of these models in view of the possibility of using them for analytical estimations and description of complicated physical processes in bubbly liquids. The adiabatic approximation is used in the *Lyakhov model* (Lyakhov, 1959) for both components of the bubbly liquid provided their interpenetration does not happen:

$$p_g = p_{g0} \left(\frac{\rho_g}{\rho_{g0}} \right)^\gamma, \quad p_l = p_{l0} + \frac{\rho_l c_l^2}{n} \left[\left(\frac{\rho_l}{\rho_{l0}} \right)^n - 1 \right].$$

If ρ_g and α_g , ρ_l and α_l are the density and the volume content of the gas and the liquid components of a mixture, respectively, and the medium

density is determined as $\rho = \alpha_g \rho_g + \alpha_l \rho_l$, the equation of state of a bubbly liquid reads

$$\rho = \frac{\rho_0}{\alpha_g (p/p_0)^{-1/\gamma} + \alpha_l P^{-1/n}}, \quad (15.3.1)$$

where $P = n(p - p_0)/\rho_l c_l^2 + 1$. Using Eq. (15.3.1), the expression for sound velocity in a bubbly liquid is:

$$c^2 = \frac{[\alpha_g (p/p_0)^{-1/\gamma} + \alpha_l P^{-1/n}]^2}{\rho_0 [(\alpha_g/\rho_g c_g^2)(p/p_0)^{-(1+\gamma)/\gamma} + (\alpha_l/\rho_l c_l^2)P^{-(1+n)/n}]}$$

The latter expression can be simplified for an undisturbed medium:

$$c_0^2 = \frac{1}{\rho_0} \left(\frac{\alpha_g}{\rho_g c_g^2} + \frac{\alpha_l}{\rho_l c_l^2} \right)^{-1}.$$

Expressions for the shock wave U_{sh} and the liquid u velocities read

$$\begin{aligned} U_{sh}^2 &= \frac{p - p_0}{\rho_0} \left\{ 1 - \alpha_g \left(\frac{p}{p_0} \right)^{-1/\gamma} - \alpha_l P^{-1/n} \right\}^{-1} \\ u^2 &= \frac{p - p_0}{\rho_0} \left\{ 1 - \alpha_g \left(\frac{p}{p_0} \right)^{-1/\gamma} - \alpha_l P^{-1/n} \right\}. \end{aligned} \quad (15.3.2)$$

The last equations imply that c_0 decays with increasing α_g owing to the sharp increase of the bubbly liquid compressibility $[-(1/v)(\partial v/\partial p)]$ at practically constant density.

In the *Campbell–Pitcher model* (Campbell and Pitcher, 1958), a small parameter μ (the ratio of the gas mass to the liquid mass) is used, the liquid is considered as incompressible, and the gas follows the Boyle law. The medium density ρ is determined as $(1 + \mu)/\rho = \mu/\rho_g + 1/\rho_l$, which yields the following equation of state:

$$\frac{p}{\rho} \left[1 - \frac{\rho}{(1 + \mu)\rho_l} \right] = \text{const.}$$

The sound velocity therewith is defined as

$$c^2 = \frac{p}{\rho} \left[1 - \frac{\rho}{(1 + \mu)\rho_l} \right]^{-1}.$$

Campbell and Pitcher (1958), considered the propagation of stationary shock waves in bubbly liquids and their collisions. The corresponding relations for average ρ , u , p read:

Conservation of mass:

$$\rho_1 u_1 = \rho_2 u_2$$

Conservation of momentum:

$$\rho_1 u_1^2 + p_1 = \rho_2 u_2^2 + p_2$$

Conservation of energy:

$$\frac{p_1}{\rho_1} + \frac{C + \mu C_{vg}}{1 + \mu} T_1 + \frac{u_1^2}{2} = \frac{p_2}{\rho_2} + \frac{C + \mu C_{vg}}{1 + \mu} T_2 + \frac{u_2^2}{2}$$

where C , C_{vg} are the liquid and the gas heat capacities at constant volume. The equation of state takes the form

$$\frac{p_1}{T_1} \left(\frac{1 + \mu}{\rho_1} - \frac{1}{\rho_l} \right) = \frac{p_2}{T_2} \left(\frac{1 + \mu}{\rho_2} - \frac{1}{\rho_l} \right).$$

Neglecting the gaseous phase heat capacity, Campbell and Pitcher (1958) obtained the following relations:

For the temperature jump:

$$\Delta T = \frac{\bar{p}^2 - 1}{2\bar{p}} \frac{\mu B T_1}{mC}$$

For the density jump:

$$\bar{\rho} = \bar{p} \left(1 + \frac{(\bar{p} - 1)\rho_1}{(1 + \mu)\rho_l} \right)^{-1}$$

For the liquid velocity jump:

$$\frac{u_2}{u_1} = \bar{\rho}$$

as well as for entropy:

$$\Delta S = \frac{\mu B}{(1 + \mu)m} \left[\frac{\bar{p}^2 - 1}{2\bar{p}} - \ln \bar{p} \right],$$

where $\bar{\rho} = \rho_2/\rho_1$, $\bar{p} = p_2/p_1$, B is the gas constant, and m is the mean molar gas weight.

Experiments performed in a diaphragm shock tube on the propagation of compression waves in water with small (0.1–0.4 mm) bubbles with a volumetric gas concentration 0.1 and higher verified physical predictions of the model concerning the convergence of compression waves to shock waves and the decrease of rarefaction wave steepness.

Energy estimates based on simple physical considerations about the interaction of compression waves with a bubbly liquid were suggested by Kedrinskii

(1968a). A propagating shock wave dissipates its energy by increasing the internal energy E_g of the gas compressed in the bubbles and the kinetic energy T_l of the surrounding liquid. Assuming uniform size bubbles and that their number density, n , remains constant, we find the following:

The internal energy:

$$E_v = - \int_{k_0}^k p_0 \left(\frac{k_0}{k} \right)^\gamma dk.$$

The kinetic energy:

$$T_v = \frac{3}{2} \rho_l k \left(\frac{dR}{dt} \right)^2,$$

where $k = 4/3\pi R^3 \cdot n$ is the volumetric gas concentration. It can be assumed that the time derivative of the sum of these energies is equal to the power of the external forces, that is,

$$\frac{d}{dt}(T_v + E_v) = \frac{\partial}{\partial x}(pu). \quad (15.3.3)$$

It is well known that the first integral of the bubble oscillation equation expresses the energy balance that can be written for a unit volume of a mixture as

$$E_v + T_v + \int_{k_0}^k p dk = 0, \quad (15.3.4)$$

where the integral is the work in a unit volume performed by the external pressure field in changing the potential energy of the bubbles and can be presented as

$$\int_0^t p \left(\frac{dk}{dt} \right) dt.$$

Using Eq. (15.3.4), Eq. (15.3.3) results in

$$\frac{\partial}{\partial x}(pu) = p \frac{dk}{dt}. \quad (15.3.5)$$

Here p is the average pressure in the mixture. Equation (15.3.5), along with the bubble oscillation equation, the relation $k = n(4/3)\pi R^3$, and the assumption that a liquid velocity may be approximated as $u = p/\rho_0 c_0$, forms a closed set of equations for describing the waves in bubbly liquid. Alternatively, the use of Eq. (15.3.5) in models of a two-phase medium instead of the Rayleigh equation may decrease the order of the governing set of equations.

This approach was used by Kedrinskii (1980) for numerical analysis of propagating and transforming a steplike wave (at $t = 0$, a constant pressure of $p_b = 10$ MPa has been applied at the semiinfinite medium boundary). The computational results of evolving the pressure profile $p(t)$ are shown in Fig. 15.3.1 for two points located at $l = 1.35$ cm (a) and 7.5 cm (c) from the boundary.

Also shown in Fig. 15.3.1 are the dynamics of the volumetric bubble concentration $k(t)$ (b) for a point $l = 7.5$ cm and the distribution of the pressure $p(x)$ (d) in the medium at time $t = 180 \mu\text{s}$. It is easily seen that the suggested model describes quite adequately the characteristic features of the initial stage of the wave transformation during its propagation.

During the 1960s and 1970s more attention was paid to the investigation of propagating waves in bubbly liquids (see Nakoryakov, 1975, 1993; Nigmatullin, 1991, and references therein). Among the published theoretical studies of particular significance are the models developed by Iodansky (1960), Kogarko (1961, 1964), and van Wijngaarden (1968) for bubbly liquids with oscillations of gas bubbles that are described in the Rayleigh equation.

Extensive studies (Nigmatullin, 1991, and Nakoraykov *et al.*, 1993) were performed on the propagation of weak disturbances in bubbly liquids which yield, in particular, the mathematical models based on the Kozteweg-de Vries,

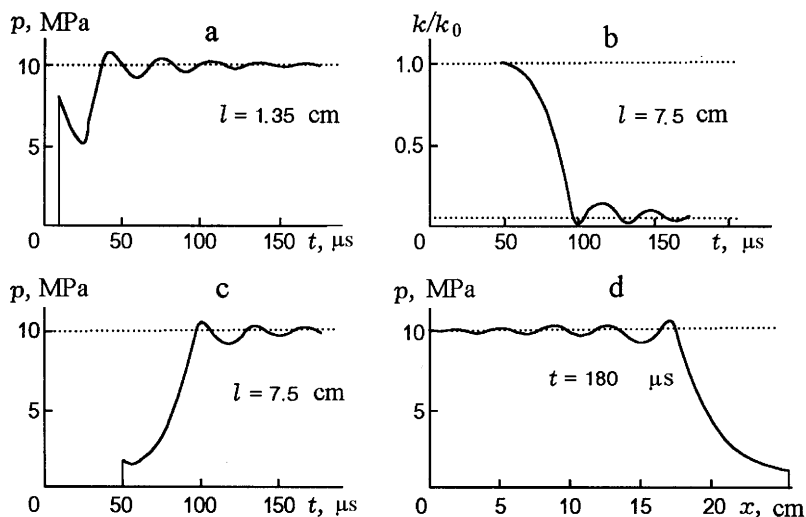


FIGURE 15.3.1 Dynamics of the quasi-stationary shock wave structure at two points spaced at different distances from the boundary (a,c) and the volumetric bubble concentration (b), as well as the pressure distribution in the medium for time $t = 180 \mu\text{s}$ (d).

Boussinesq, and Burgers equations as well as the detailed map of the flow patterns.

Research on stationary wave structures (Nordzij, 1971, and Nordzij and van Wijngaarden, 1974) as well as on attenuating underwater blast loads by bubbly screens (e.g., Kedrinskii, 1968a, 1968b) are typical of the experiments in this field. However, the goal of these studies was rather limited: namely, to determine the dynamics of shock wave amplitudes in their interaction with the screen, the efficiency in attenuating the shock load intensity, and the possibility to control its spectral distribution. In this formulation, however, the only information on energy absorption of a shock wave proves to be inadequate to explain the load behind a bubbly screen, the effective wave amplification, the essential change of its duration, etc.

Experimental studies revealed that the damping is of secondary importance, and the factors of principal significance are the wave transformation mechanism and the reradiation of energy absorbed by the bubbly medium, as well as relaxation, dispersion, and dissipation effects accompanying wave propagation into a bubbly liquid.

All these effects required detailed experimental study of the transformation mechanism of shock waves by a bubbly medium, along with the numerical experiments based on the two-phase mathematical models (Iordansky, 1960; Kogarko, 1961, 1964; and van Wijngaarden, 1968). Clearly the analysis of experimental results should begin with some special features of the dynamics of a single spherical bubble and with the interaction of a gas layer with a shock wave, considering such a structure as a simplified model of a bubbly liquid.

15.3.1.2 SHOCK WAVE AND SPHERICAL BUBBLE INTERACTION: CUMULATIVE JET FORMATION

Analysis of the interaction of a plane wave with a spherical bubble allows one to account for two fundamental aspects of the problem: the gas state in the bubble during its collapse behind the shock front, and the time required for the shock front to traverse the diameter of the bubble.

If the wave length is much greater than the bubble radius and if the collapse time scale of the bubble for fixed wave parameters (amplitude, duration, and postshock pressure decay profile) is much greater than the time for the shock to pass the bubble, then the bubble dynamics can be investigated in a spherically symmetrical setting. It is assumed in this case that the pressure at infinity is specified in correspondence with the wave parameters (Soloukhin, 1961, and Kedrinskii, 1967).

15.3.1.2.1 Dynamics of a Single Bubble: An Experimental Study

A scheme of the experimental setup for the study of the interaction of a shock wave in water with a single gas bubble is shown in Fig. 15.3.2 (Kedrinskii, 1961).

The basic part of the setup is the explosion chamber (EC) comprising a liquid-filled channel of size $50 \times 250 \times 250$ mm. The side walls of the chamber are made of plane-parallel lead glasses 100 mm thick withstanding pulse pressures of the order of 10–15 MPa. At the lower end of the chamber, at the center of the channel, there is a high-voltage discharger shorted with a thin (0.07 mm) manganin wire stabilizing a discharge gap as opposed to a simple electric discharge (Bazhenova and Soloukhin, 1959).

When button 6 is pushed, an activating signal is sent out from a small battery to the input of the pulse transformer IT-2, and the high-voltage (15 kV) signal ionizing the air gap 5 is generated at the output of the transformer. In this case the $110 \mu\text{F}$ capacitor charged up to 0.9 kV discharges to the wire 3, whose explosion results in a shock wave propagation along the channel; the wave amplitude varies over the interval 1–4 MPa, and its duration is within $100 \mu\text{s}$.

The wave is recorded by the pulse pressure gauge made of piezoceramics of barium titanate. An axially polarized piezocell is glued with a special glue to a long zinc rod of the same diameter and the same acoustic resistance, which allows recording of rather long signals. A gas bubble (of size 0.7–2 cm) is blown out of thin rubber (about 0.01 mm thick) and is placed in the channel at a given depth. When the capacitor is discharged, the signal induced by the

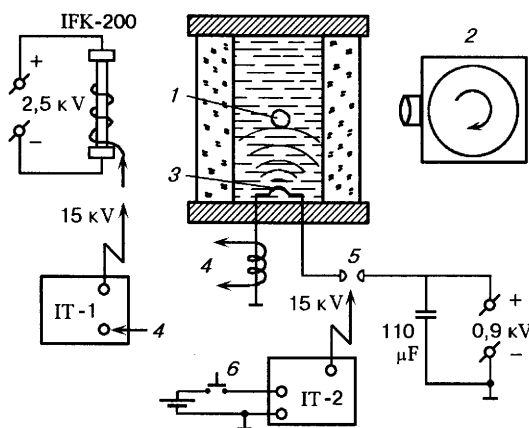


FIGURE 15.3.2 Schematic view of the experimental setup with a single bubble: 1, bubble; 2, photorecorder; 3, wire; 4, Rogovsky's belt; 5, air gap; 6, push button.

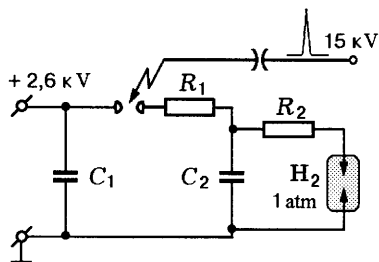


FIGURE 15.3.3 Schematic view of the frequency hydrogen electronic flash tube.

Rogovsky's belt 4 through the transformer IT-2 actuates a flash tube IR-200 by a high-voltage pulse.

The bubble pulsations are recorded within the continuous and frame scanning regimes. In the first case, the bubble dynamics is recorded through a horizontal (flat) slit to a rotary film of a photorecorder 2 at a linear speed up to 100 m/s. In studies of a wave picture in the diagram of Fig. 15.3.2, an optical apparatus IAB-451 is used.

In the latter case, the bubble pulsations are recorded either on SFR or on the same photorecorder 2 within the continuous scanning regime, but with a special scheme for the frame illumination (in Fig. 15.3.3) based on a double discharge.

The scheme involves accumulating $C_1 = 1 \mu\text{F}$ and discharge $C_2 = 0.1 \mu\text{F}$ capacitors, as well as a hydrogen spark discharger. On punching a gap, being a high-voltage switch, the capacitor C_1 is discharged through the resistance $R_1 = 2600 \Omega$ into the capacitor C_2 , across the plates of which the voltage increases to the breakdown value of the discharger placed in a special transparent casing. The latter is sealed, evacuated, and filled with hydrogen ($p = 1 \text{ atm}$). The discharger is made of nichrome wire ($d \approx 1 \text{ mm}$), and the distance between electrodes is about 2 cm. Hydrogen provides a short time of recombination and prevents the existence of an arc. The inductance of the condenser and supply main is on the order of $1\text{--}2 \mu\text{H}$, which provides a discharge duration (and hence an ignition) no longer than $1 \mu\text{s}$ for the resistance $R_2 \approx 1\text{--}2 \Omega$. The ignition frequency reaches 40 kHz. The accuracy of determining the rotation velocity of the photorecorder film is about 1%.

15.3.1.2.2 The Interaction of a Plane Shock Wave with a Spherical Gas Bubble

Oscillations of a single spherical bubble caused by a shock wave (having amplitudes within 1–3 MPa and the positive phase pressure durations of about $100 \mu\text{s}$) are shown in Fig. 15.3.4a,b and in Fig. 15.3.5 (Kedrinskii, 1961).

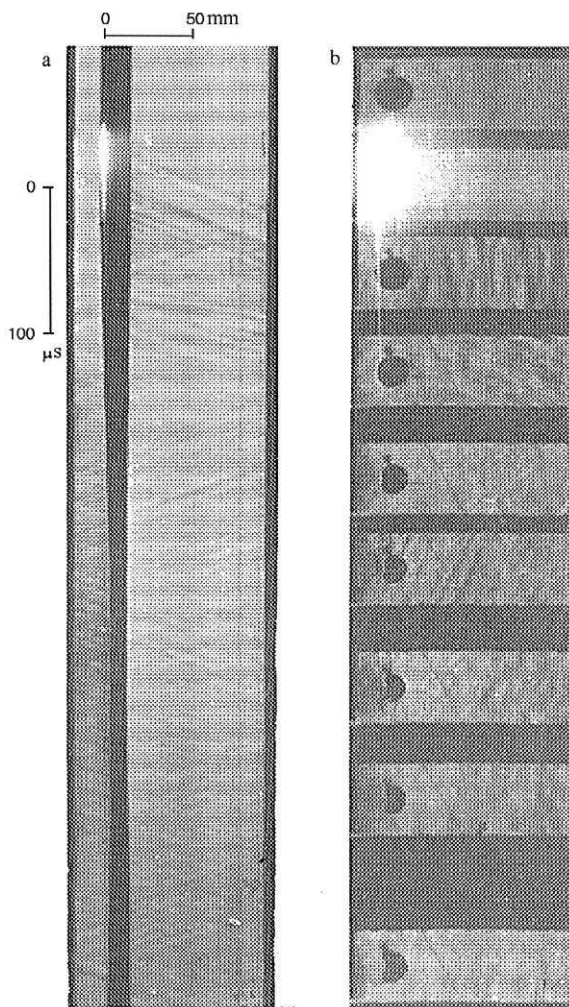


FIGURE 15.3.4 Schlieren continuous (a) and frame (b) scanings of a bubble pulsation by a shock wave.

Figure 15.3.4b shows the shadow frame scanning, obtained with the pulse hydrogen flash, of the bubble collapse by a shock wave propagating from left to right. One can readily see a pronounced asymmetry of the bubble collapse and a somewhat angular form of its end wall in the last frames. The reason for this deformation of the bubble becomes apparent from Fig. 15.3.5 (SFR-gram; the

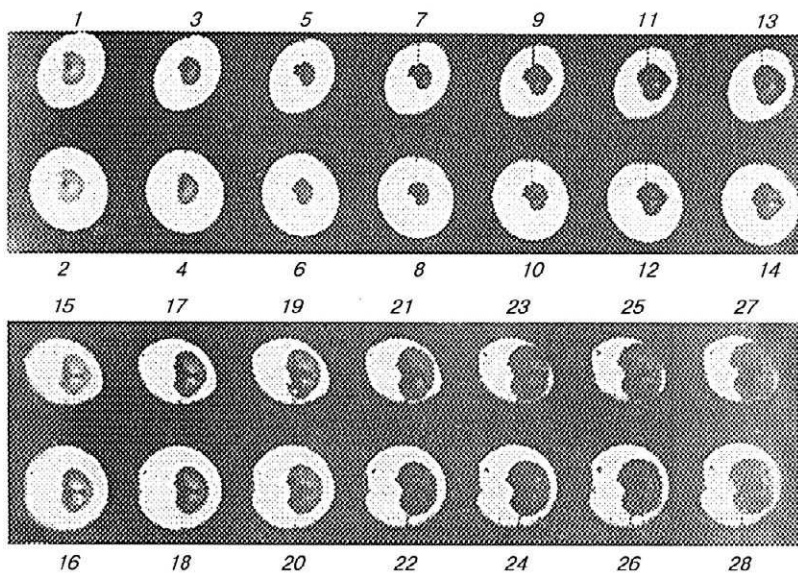


FIGURE 15.3.5 Formation of a cumulative jet in a collapsing bubble by a shock wave.

time interval between the frames is $40\text{ }\mu\text{s}$), on which the development of a cumulative jet flow in the direction of the propagating shock wave inside the bubble is clearly observed (17). As can be seen from this figure the cumulative jet impacts (frames 9–12) at the opposite wall of a bubble. The jet velocity is rather high, which is manifested in the formation of a local bulge at the wall. The jet is clearly observed in the pictures recorded at the stage of a bubble expansion. It is retained for a very long time, but on its breaking a pronounced asymmetry of the bubble shape remains.

As is evident from the analysis of experimental data and the numerical estimations, the cumulative effect develops as a result of a peculiar distribution of initial velocities of the bubble wall arising during the propagation of the plane shock front through it. The front interacts with the bubble wall as a free surface (Kedrinskii, 1961, and Kedrinskii and Soloukhin, 1961) and imparts different initial velocities distributed over the surface as $(2\Delta p/\rho_0 c_0) \cos \alpha$, where α is the angle between the radius at the bubble surface in the contact point with the shock front and the horizontal plane. For this reason, in spite of the uniform distribution of the pressure in the liquid surrounding the bubble, behind the shock wave front (the bubble size is much smaller than a shock wave width), the spherical symmetry of the process is distorted. This in turn causes a collapse with a formation of a small cumulative downwave jet.

Experiments showed that the small jet velocity reaches 30 m/sec and the back wall speed is from 10–15 m/sec (Kedrinskii, 1961). The cumulative effect observed by Kedrinskii (1961), as well as the influence of the distortions of the spherical shape due to, for example, motion of the bubbles relative to the liquid, results in bubble destruction, increases the dissipative losses, and distorts the wave structure reradiated by the bubbly liquid. These effects vanish as the wave front steepens and the pressure amplitude at the front decreases markedly.

15.3.1.2.3 The Effect of Relative Motion

In the presence of an initial translational velocity, the collapse of a bubble in an ideal liquid differs substantially from the case where it is stationary during the pulsations (Voinov and Petrov, 1971). The laws of conservation of energy and momentum in relative motion yield a limiting collapse radius, even in the case of an empty cavity, because of the abrupt increase in the energy of translational motion during the collapse. In the interval of small (relative to the initial) bubble radii, the added mass of the liquid decreases sharply, and the kinetic energies of radial and translational motion are redistributed.

A simple estimate of this effect is readily obtained from the energy conservation law written for the initial and final times when the radial velocity of the bubble wall is equal to zero. It is assumed that the bubble retains its spherical shape. The expressions for the kinetic and potential energies of the liquid are

$$T = 2\pi\rho R^3(\dot{R}^2 + \dot{x}^2/6)$$

and

$$U = p_0 V,$$

respectively, where R is the bubble radius, V is its volume, \dot{R} and \dot{x} are the radial and translational velocities, respectively, and p_0 is the hydrostatic pressure in the liquid.

Since the final value of \dot{x} is related to the minimum cavity radius R_* by the momentum conservation law $V_*\dot{x}_* = V_0\dot{x}_0$ (initial and final values of $\dot{R} = 0$), the condition for determining R_* is

$$p_0 V_0 + \frac{1}{4}\rho V_0 \dot{x}_0^2 = p_0 V_* + \frac{1}{4}\rho V_0^2 \dot{x}_0^2 V_*^{-1},$$

from which one readily obtains

$$\left(\frac{R_*}{R_0}\right)^3 = \frac{1}{4} \frac{\rho \dot{x}_0^2}{p_0}.$$

It is seen that only for $\dot{x}_0 = 0$ is the empty cavity collapse complete ($R_* = 0$).

The effect of translational motion is similarly manifested in the case of interaction of a plane shock wave with an initially stationary bubble. Certainly, the notion of “stationary” is valid here only until the wave front begins to move past the bubble. As a result of this flow, the bubble acquires a certain initial velocity that is determined by the surface distribution function of liquid velocities imparted by the front (Kedrinskii, 1961, and Kedrinskii and Soloukhin, 1961) and wall elasticity.

15.3.1.2.4 The State of the Gas

Estimating the real state of the gas is an important aspect of the investigation of bubble dynamics in a pressure field, both for understanding the shock wave transformation by a bubbly liquid and for the development and numerical study of its mathematical models. In this regard the design of a direct experiment to determine the variation of the state of a gas in an oscillating bubble is of interest. This experiment was performed and described by Kedrinskii (1961) and Soloukhin (1960).

A bubble with walls made of a very thin rubber, filled with a stoichiometric gaseous mixture of $2\text{H}_2 + \text{O}_2$, was placed in water in the path of a shock wave. The bubble pulsations were recorded through a slit by a continuous-scanning streak camera with pulsed illumination and appropriate synchronization (see Fig. 15.3.2). It was expected that during the adiabatic collapse of the bubble behind the shock front the temperature of the mixture inside the bubble would rise to the ignition temperature. In the experiment, the ignition was recorded both according to the spontaneous luminescence of the mixture in the bubble at ignition (the experiment was performed without external illumination in this case) and according to a sudden change in the time variation of the bubble radius (see Fig. 15.3.6), indicating explosive expansion of a bubble.

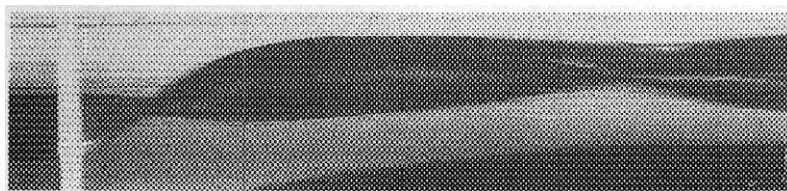


FIGURE 15.3.6 Continuous-scanning streak photograph of bubble oscillations caused by a shock wave.

The dark band at the left center in Fig. 15.3.6 is the initial bubble diameter; the light vertical band is the instant of explosion of the small wire. Two oscillations are shown in Fig. 15.3.6. The moment of explosion is recorded by a sudden deviation of the back bubble wall (see the top of the figure). Notice that owing to the formation a cumulative jet, the front wall in the continuous-scanning photograph would be smoothed all the time. No explosion flash in the mixture was observed at the illuminated background.

Calculation of the temperature as a function of the degree of compression of the bubble was performed assuming adiabatic compression $T_d = T_0(v_0/v_d)^{\gamma-1}$. A comparison of the experimental ignition temperatures of the mixture showed that they are within the limits of the known values for adiabatic heating (Zaitsev and Soloukin, 1958).

Note that in connection with the simulation of spherical cumulation, the explosion of a stoichiometric hydrogen-oxygen mixture may be of interest. Since the detonation product of this mixture is steam, which is cooled and condensed during the expansion of the cavity at the collapse stage, the cavity is practically empty, so its boundary can acquire rather high velocities.

15.3.1.3 Plane Shock Waves and Gas Layers

It is commonly assumed in analyzing the dynamics of a single bubble in a shock-induced flow that its ability to absorb a substantial fraction of the incident shock energy during collapse is insignificant. Thereby it is assumed that the shock-induced flow (or the pressure at infinity) is independent of the bubble dynamics. Although the latter assumption is admissible in the investigation of a single bubble, it is not valid in the analysis of both long and short shock wave interaction with an cluster of bubbles because of the finite amount of energy transferred by the wave during the interaction time and because of the capacity for energy absorption of the bubbly system as a whole.

The work performed by the shock wave on this system (increasing the internal energy of the gas in the bubbles and inducing radial fluid flows around them during their collapse) comprises a considerable fraction of the transferred wave energy even for small volumetric gas concentrations. Clearly, such a bubbly system does not just transmit a part of the wave energy, but also transforms the wave profile. The size of the bubbly region or the volume concentration of the gas in it can be increased to exceed the energy absorption of the medium to a value larger than the energy of the incident shock wave.

Note that a similar effect will be observed for long waves with a constant amplitude behind their fronts, but only over the wave periods corresponding to the collapse time of the bubbles.

In the case of a one-dimensional plane shock wave the simplest model of such a bubbly region can be a finite gas layer (plane cavity) occupying the entire cross section through which the wave front passes.

Let us consider this model and assume that the wave front propagates along the x -axis. Let us locate the gas layer in such a way that at the initial time has the coordinate $x_0(0) = 0$, and the back wall has the coordinate $x_1(0) = h_0$. When a shock wave of amplitude p_* is incident on the layer, its forward wall acquires an initial velocity $v_0 = 2(p_* - p_0)/\rho_0 c_0$ due to the reflection of the wave and begins to move to the right and compresses the gas. The left-propagating rarefaction wave will determine the equation of motion of this wall,

$$\frac{dv}{dt} = -\frac{1}{c_0} \frac{d\Omega}{dt}, \quad (15.3.6)$$

which can be derived on the basis of the conditions of invariance of the function $G = x^0(\omega + u^2/2) = \omega + u^2/2$ along the characteristics propagating to the left with velocity $c_0 - u$ (Kedrinskii, 1980):

$$G_t - (c_0 - u)G_x = 0.$$

Here ω, Ω are the enthalpies, u, v are the mass velocities in the liquid for any point and at the boundary of the layer, respectively. Assuming that the pressure in the gas is described by the expression $p_1 = p_0[h_0/(x_1 - x_0)]^\gamma$, the wave profile has a triangular profile $p(t)$ with a positive phase τ , and the enthalpy can be written as $\Omega = \rho_0^{-1}[p_1 - p(t)]$. We used here the Tait state equation

$$\frac{p + B}{p_0 + B} = \left(\frac{\rho}{\rho_0}\right)^n$$

and assumed that $p_1, p(t)$ are much lesser than B and used the acoustical approximation.

$$\rho_0 c_0 \dot{x}_0 = \rho_0 c_0 v_0 - \left[p_* \frac{t}{\tau} + p_0 \left(\frac{x_1 - x_0}{h_0} \right)^{-\gamma} - p_0 \right]. \quad (15.3.7)$$

As the pressure p_1 in the gas increases, the back wall of the layer will move in the positive x -direction with a velocity \dot{x}_1 and, acting as a piston, will generate a pressure wave that corresponds to the pressure p_1 in the gas:

$$\rho_0 c_0 \dot{x}_1 = p_0 \left(\frac{x_1 - x_0}{h_0} \right)^{-\gamma} - p_0. \quad (15.3.8)$$

Obviously, a pressure gauge placed in the liquid behind the layer will record not a shock wave but an oscillation $p_1(t)$ with a certain maximum amplitude that is determined by the minimum layer thickness h_* obtained from the solution of Eqs. (15.3.7) and (15.3.8), and by a time interval of the order of τ .

The limiting value of the amplitude p_1 can be estimated for the case of a stationary wave where the rate of change of the layer thickness $\dot{h} = \dot{x}_1 - \dot{x}_0$ can be written as

$$-\rho_0 c_0 \dot{h} = 2(p_* - p_0) - 2p_0 \left[\left(\frac{h}{h_0} \right)^{-\gamma} - 1 \right]. \quad (15.3.9)$$

It is clear that the layer will collapse at the time when the velocities of both walls become equal, that is, the condition $\dot{h} = 0$ holds. Equation (15.3.9) shows that at this time the pressure in the gas will become equal to $p_1 = p_*$, $\dot{x}_0 = \dot{x}_1 = (p_* - p_0)/\rho_0 v c_0$, as Eqs. (15.3.7) and (15.3.8) show, and will then remain constant with time. Consequently, a pressure gauge behind the layer will record the same stationary wave, but with a slightly sloping front whose rise time is close to the collapse time for the empty cavity $t_* = \rho_0 c_0 h_0 / 2p_*$ according to Eq. (15.3.9), that is, depends linearly on the layer thickness h_0 .

Let us write the dynamical equation for the layer in variables $x = h/h_0$ and $t_1 = t/\tau$ for short waves:

$$\delta \dot{x} = -\left(1 - \frac{t_1}{2}\right) + \frac{p_0}{p_*} x^{-\gamma}.$$

Here the dimensionless parameter $\delta = \rho_0 c_0 h_0 / 2p_* \tau$ shows the dependence of the maximum pressure amplitude p_1 in the gas on the value h_0 . The condition $\dot{x} = 0$ determines the functional relation $x_*(t_{1*})$. Calculations show that as h_0 increases the maximum of p_1 decreases, shifts toward larger values of t_{1*} , and remains on the curve representing the pressure decay behind the shock front. A characteristic spreading of the signal is observed as well as a delay of the reradiation maximum, which depends only on the layer collapse time.

Note that in the case $\dot{x}_1 = 0$ (the gaseous layer is located at a solid wall), the amplitude of a stationary wave increases by a factor of 2 and the short wave amplitude increases by a factor less than 2. Inertial effects in the dynamics of a bubbly layer at a solid wall and strong compression of the gas in the bubbles can amplify this effect.

The analysis of the behavior of a gaseous layer during its interaction with shock waves provides insight into wave propagation in bubbly liquids. Their mechanisms are quite similar, but a difference can be anticipated in the appearance of strong inertial effects due to spherical symmetry of the bubble and the possibility of transmission through the bubbly medium of a transformed shock pulse. We will start from a detailed analysis of the interaction of shock waves with bubbly layers of finite length.

15.3.1.4 SHOCK WAVE TRANSFORMATION BY AND BUBBLY LAYERS

15.3.1.4.1 Short Shock Waves: Splitting of the Wave into a Precursor and a Wave Packet

We define short waves as waves with a positive pressure phase time approximately equal to the bubble collapse period. In experiments this corresponds to shock waves with an amplitude of the order of $p_{\max} \approx 1$ MPa and a positive phase duration of about $100 \mu\text{s}$ for bubble radii of about 3–4 mm.

The interaction of a shock wave with air bubbles causes their compression increases the internal energy of the gas, and the kinetic energy of the liquid surrounding the bubbles due to their radial oscillations. As a consequence, the intensive energy absorption of an incident shock wave as well as its reradiation by the oscillating bubbly layer are observed as the wave propagates in the bubbly medium. These two processes occur simultaneously, but their maximum effects (transmitted wave after passing through the bubbly layer l and the maximum reradiation of the absorbed energy by the layer) are separated in time (Kedrinskii, 1968a, 1968b).

This time interval depends on the bubble size, and as shown later, it also depends on their concentration in the mixture, the initial parameters of the shock wave, and the layer length. Essentially, this time is determined as a “collective” oscillation time of the bubbly layer.

Figure 15.3.7a shows pressure oscillograms for the initial shock wave ($p_{\max} = 3$ Pa, $\tau_+ = 100 \mu\text{s}$, the second peak is the first explosive cavity pulsation) and the wave transmitted through the bubbly layer with bubble radii of $R = 2$ mm at a volumetric concentration of the gas of $k_0 = 0.004$ and dimensions $12 \times 23 \times 4$ cm (see Fig. 15.3.7b). Experiments were carried out in a container ($1 \times 1 \times 1$ m). Since a point shock wave source was used, the

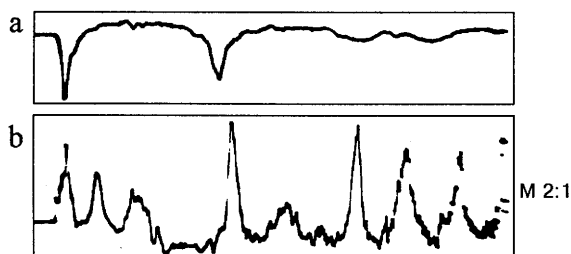


FIGURE 15.3.7 Shock wave transformation by bubbly layer at a concentration of $k_0 = 0.004$: (a) Initial shock wave; (b) wave transmitted through the bubbly layer.

pressure gauge at any location behind the layer recorded a superposition of reradiated waves from different portions of the layer with phase shifts.

It is easily seen that the incident wave pulse transmitted through the bubbly layer splits into three waves. The first wave is the attenuated initial wave, and the second and the third waves are reradiated by the layer. In this case the first reradiated wave is strongly attenuated, and hence the reradiation of the second pulse absorbed by the layer can be recorded. Discrepancy between the second pulsations of the bottom and the top pictures may occur because of the discharge instability and the considerable increase of the amplitude of the second oscillation.

Shock wave transmission through a bubbly layer was studied only in a one-dimensional configuration. Experimental studies were carried out in a vertical hydrodynamic shock tube wherein a shock wave was generated by an exploding wire at its lower end (Fig. 15.3.8).

A stable plane wave shape with steady-state parameters was formed at a certain distance L_* from the exploding wire. Starting with $L > L_*$, pressure gauges 1 and 2 were placed in the test section, to record the profile and parameters of the transmitted and incident waves. A layer of calibrated gas

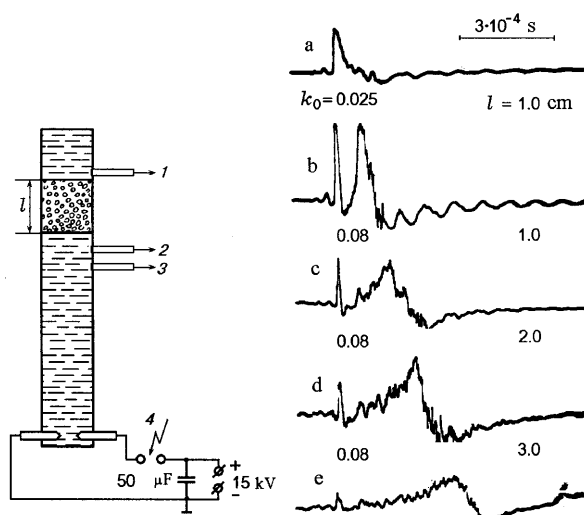


FIGURE 15.3.8 Scheme of the experimental apparatus for generation of shock waves and their transformation in a bubbly layer: 1, 2, pressure sensors; 3, triggering sensor; 4, ionizing high-voltage pulse; (a-e) splitting of a shock wave into a precursor and a general disturbance for different values of k_0 and l .

bubbles made of thin rubber on a special lightweight support that did not disturb the wave was placed between the pressure gauges at a fixed distance from gauge 2.

This method of formation of a two-phase layer, occupying the entire cross section of the tube, facilitated the variation of the gas concentration k_0 and the bubble radius R_0 , monitored its length l , and provided a stable shock wave profile. The upper end of the tube was closed for the investigation of reflection at the wall in the layer. It was equipped with a special wave absorption fitting, permitting the tube to be regarded as infinitely long.

A detailed study of the shock wave interaction with the bubbly layer was carried out for a wide range of parameters: $l = 1\text{--}30$ cm, $k_0 = 0.004\text{--}0.3$, $p_* = 1\text{--}3$ MPa, and $\tau = 50\text{--}100$ μs .

Figure 15.3.8 shows typical pressure records illustrating the initial absorption of a short shock wave by a layer for various values of k_0 and l . A signal amplification scale at the oscillograms with respect to the shock wave incident at the layer (Fig. 15.3.8a) varies from 2.5 to 1. The records b–e clearly demonstrate the effect of splitting of the initial perturbation into two waves (Kedrinskii, 1968a): a shock wave transmitted through the layer ($l = 1$ cm, $k_0 = 0.025$) and the radiation of the narrow bubbly layer. The same effect is observed at a constant bubble concentration ($k_0 = 0.08$) but with a varying length of the layer ($l = 1.2$ and 3 cm) shown in frames c, d, e. Figure 15.3.8 shows that the propagating shock retains its steep front practically until it is completely absorbed, whereas the positive phase is strongly diminished. A linear scale of waves becomes comparable with the bubble's spacing, that is, the medium for this wave cannot be described as a continuum since the wave not only is attenuated but also is scattered by individual bubbles. Wave splitting was subsequently observed many times in experiments, for example, by Nakoryakov *et al.* (1975).

The second wave represents radiation of the wave energy absorbed by the layer. The energy of the incident wave dissipates in the course of the interaction with the gas bubbles and is transformed into the kinetic energy of the radial oscillations and the internal energy of the compressed gas. Eventually all the energy absorbed by the layer in the absence of other types of losses is accumulated in the compressed gas at the moment of completion of the bubble collapse. Thus, the degree of collective bubble compression in the layer for the fixed parameters of a medium and a shock wave will determine the degree of the dissipation of the shock energy and the radiation amplitude, while the inertial effects during the collapse will determine the delay of the inception of the reradiation maximum.

The absorption of the wave energy and its reradiation by the bubbles in the layer are simultaneous and coupled processes whose extremes do not coincide

in time because of the inertial effects during the collapse. The pressure in the collapsing bubbles increases while the pressure in the wave decreases because of the nonstationary effects and dissipation in the layer. At some time these pressures level off, and then the inertia of the liquid causes overcompression of the bubbles. However, the pressure gradient is now directed into the liquid and tends to suppress the velocity rise of the convergent radial flows around the bubbles.

At the instant the velocity of these flows attains a maximum, the pressure in the transmitted wave reaches a minimum value. During the splitting of the short shock wave, the transmitted wave and the reradiation wave, as a rule, are separated by a rarefaction zone. This effect can be explained by the dissipative losses, which for a sufficiently large capacity of the layer reduce the pressure so quickly that it is no longer sufficient to offset the rarefaction occurring in the medium as a result of the convergent radial flows around the bubbles.

Surprisingly, the rarefaction wave is also recorded by the pressure gauge in front of the layer in the case of long shock waves. This intriguing experimental fact is important for understanding shock reflection from a bubbly layer. With an increase in the values of k_0 or l the collapse time of the bubbles in the layer increases while the radial velocity, the degree of compression, and hence the radiation maximum decrease. In this case a value $l = l_k$ is found to exist such that the whole layer acts as a collective bubble, that is, it completely absorbs the shock wave energy (the pressure gauges record only a precursor) and reradiates it as decaying oscillations with their own characteristic frequency.

With a further increase in l the process just described will be repeated, but now for the wave reradiated from the layer l_k : a new value l_{k1} emerges for which the first radiation will be completely absorbed and reradiated, and instead of it the sensor will record only the precursor. The maximum of the second reradiation will be determined by the layer parameters and the first radiation and will be recorded with a time delay relative to its precursor.

The effect of synchronous bubble oscillations in the layer is of fundamental importance since it not only determines the structure of the reradiated compression wave but also reveals the property of the bubbly liquid to form peculiar coherent structures. Note that the requirement of the narrow size distribution of the bubbles to explain the coherence effect is inadequate in this case. Actually, in the experiment described for a 3-cm-long layer, the shock wave is completely absorbed, which indicates the existence of a sharp pressure gradient along the layer that causes a large scatter of the bubbles oscillation parameters in the layer even with the same initial bubble size.

Figure 15.3.9 demonstrates oscillograms recorded during interaction of a shock wave with bubbly layers (up to 30 cm in length) in a wide range of volumetric gas concentration: $k_0 = 0.04, 0.06, 0.08, 0.10$, and 0.15 .

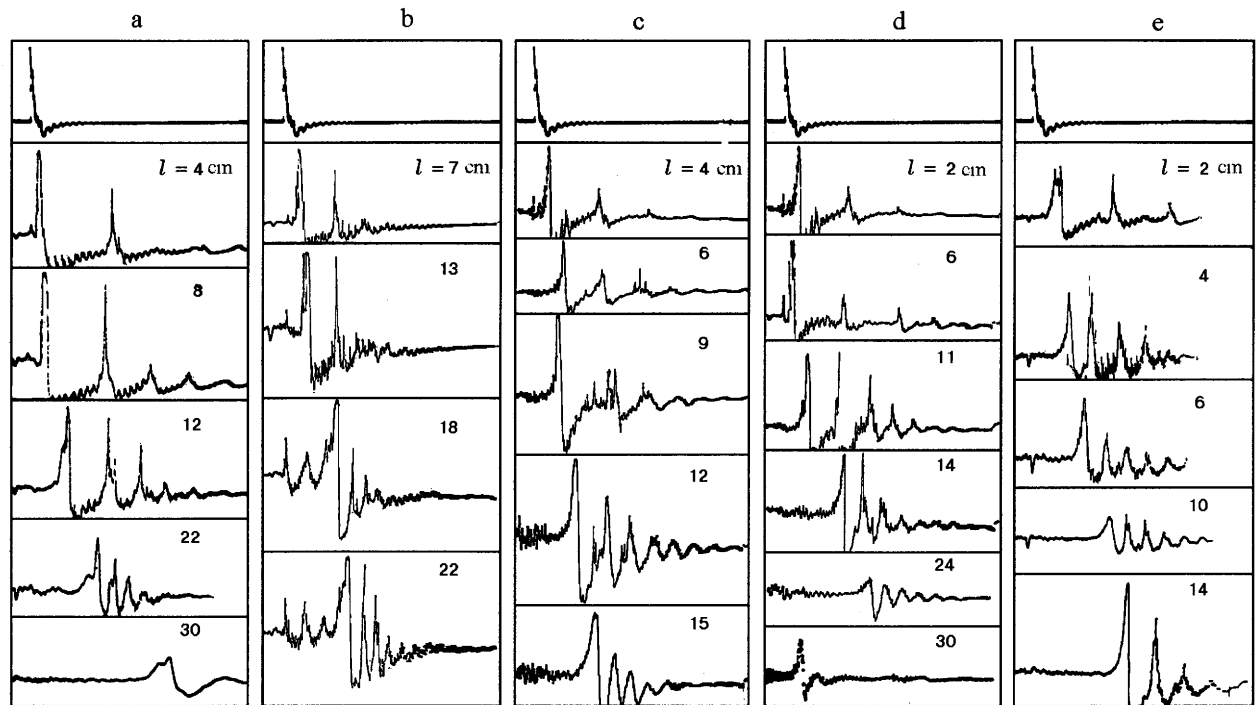


FIGURE 15.3.9 Transformation of a shock wave at various volumetric gas concentrations: (a-e), $k_0 = 0.04, 0.06, 0.08, 0.10$, and 0.15 .

It is easily seen from this figure that as the layer length increases, wave packets with a well-defined periodic structure and decaying amplitude are formed. In spite of the significant difference between the medium parameters in these figures, one can follow the general character of the absorption for an initial wave, the propagation of the consecutive reradiations through the layer, and the formation of a packet. Some features of the wave transformation can be demonstrated with the oscillograms in Fig. 15.3.9b (for which the volumetric gas concentration $k_0 = 0.06$):

1. The wave energy absorption occurs immediately behind the front. Part of the wave is split and its amplitude and duration are reduced, though the front steepness does not change.

2. The split wave retains its position in time, and the reradiated wave maximum shifts to the right in the oscillograms (see the sequence of the oscillograms from top to bottom). In this case the character of the reradiation allows one to conclude that all the bubbles collapse synchronously, that is, the layer behaves as a coherent structure. The experimental data confirm the existence of a series of precursors and indicate the distinct periodic structure of the resultant signal.

3. The length of this coherent layer l_k is limited and is well defined for each concentration and initial parameters of the shock wave. Figure 15.3.10 shows the dependence of the delay times T_{del} of the reradiation maximum for four values of k_0 : 0.04, 0.08, 0.15, and 0.30.

The origin for T_{del} is taken to be the moment of complete absorption of the initial shock wave by the layer. The length of $l_{k,0}(k_0)$ is indicated on the plot as

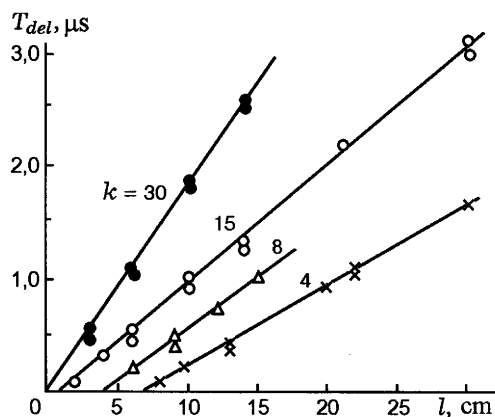


FIGURE 15.3.10 Maximum reradiation delay times T_{del} versus length of the bubbly layer l for various values of k_0 (in percent).

the coordinate at which the function $T_{del}(l)$ intersects the l axis. This approach allows one to analyze the evolution of the resultant signal in the propagation of even a relatively weak reradiated wave with a sloping front and periodic structure. The principal feature of the process of wave transformations by the bubbly layer is distinctly exhibited by the pressure oscillograms (see Fig. 15.3.9): The instant at which the first precursor is recorded corresponds to the propagation velocity c_0 in the pure liquid, the radiation is shifted relative to it, and this shift (see Fig. 15.3.10) grows linearly with the length of the layer.

The increase in the delay time of recording the reradiation maximum is associated with the mechanism of formation and propagation of a so-called long-wave disturbance. The occurrence of the shift is often used to justify the conclusion that the low-frequency component of the signal (reradiation from the layer), unlike its high-frequency part (the precursor), propagates essentially with the equilibrium speed of sound $c_*^2 = \gamma p_0 / \rho_0 k_0$ (Zaitsev and Soloukhin, 1958) typical of a long-wave disturbance in a two-phase medium (Lyakhov, 1959).

The reradiation amplitudes in the experiment are fairly small, the fronts are sloping, and the estimate for c_* seems realistic, at least for high concentrations and large values of l . In this case if the delay time T_{del} is indeed associated with the low propagation velocity of the main part of the resultant signal, the value $\beta = c_*^2 k_0$ is constant ($\gamma p_0 / \rho_0$) for the same gas and the static pressure and does not depend on k_0 . However, in the interval of k_0 shown in Fig. 15.3.10 the value β increases by a factor of 2, casting doubts on the preceding conclusion about the nature of the delay and its connection with the propagation velocity c_* .

The second contradiction arises in the numerical analysis of the process carried out using a two-phase medium model (Iordansky, 1960; Kogarko, 1961, 1964; and van Wijngaarden, 1968) and assuming an incompressible liquid component. In this case $c_0 \rightarrow \infty$ and a wave structure of the *precursor-reradiation* type cannot exit. However, the data of Kedrinskii (1968a) indicate the possibility of the existence of such a structure even in this case. It is likely that the contradiction is embodied in the actual interpretation of the mechanism of the delay T_{del} . As indicated earlier in the example of a plane gaseous layer and in the analysis of the oscillograms (see Fig. 15.3.9), the value T_{del} is determined by the collapse time of the bubbles in the layer or of the layer itself.

Thus, the delay in recording the reradiation maximum is the result of a delay in its generation, rather than the small propagation velocity. In this connection, both the initial shock wave and the disturbances forming the resultant reradiation propagate in the medium with the same velocity c_0 characteristic for the liquid. The total delay time is the superposition of the successive delays of the wave reradiations (see Fig. 15.3.9b) and the width of the front of the resultant reradiation is determined by the time interval from its maximum to the nearest precursor.

4. As a consequence, the reradiation as the wave packets occurs behind the bubbly layer and their structure for different values of k_0 and l is shown in Fig. 15.3.9. Their duration exceeds that of the positive phase of the incident shock wave by an order of magnitude and their frequency ν depends on the layer length l at a fixed value of k_0 .

Analysis of the dependence of the wave packet frequency on the layer length and the gas concentration over a wide range of values of these parameters shows (see Fig. 15.3.11) that $\nu(l)$ for $k_0 = \text{const}$ has a maximum ν_* , which shifts with increasing k_0 towards smaller values of l and decreases. Thus, for $k_0 = 0.04$ one has $\nu_* = 4$ kHz at a distance of $l = 22$ cm, and for $k_0 = 0.23$ the maximum value of the frequency is reduced to $\nu_* = 1.4$ kHz, but now for a layer length $l = 3.5$ cm.

The dynamics of frequency characteristics is essentially the same, and they all have a well-defined maximum for a certain length of the layer l_k . In this case, as observed in the experiment, from this time on, ν_1 becomes equal to the frequency of the pulse sequence of the other pulses ν_n . There occurs a peculiar kind of resonance that manifests itself such that the radiation of the *whole* layer is completely absorbed by the subsequent layer and is radiated at the same frequency (this is typical for a single bubble, particularly with small oscillation amplitudes), which depends on a value k_0 and the layer length beyond a value l_k . For l_k we obtain a well-defined wave packet with its constant frequency and regular decay of amplitudes.

Let us return to Fig. 15.3.9b ($k_0 = 0.06$). If the pressure behind the 14-cm layer is assumed as initial, that is, as the pressure at the boundary for the successive 8 cm, then it is impossible to obtain the oscillograms presented in

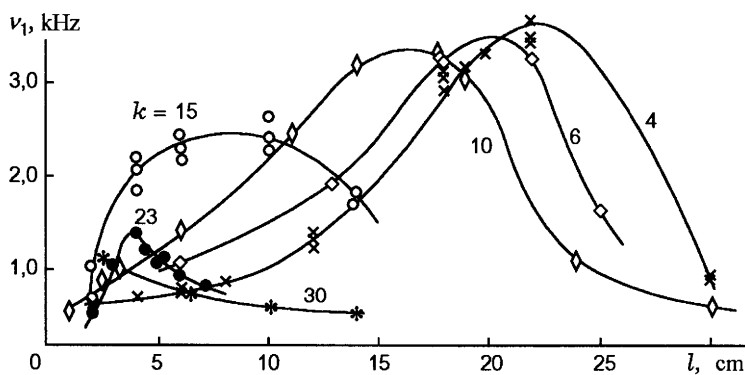


FIGURE 15.3.11 General frequency characteristics of reradiations of a bubbly layer (values of k_0 are given in percent).

the last frame of the figure. The reason is that when additional layers of the medium are involved, the absorbed energy is redistributed near the boundaries between the adjacent layers, which causes damping of the bubbly oscillations and reduces the reradiation frequency. Clearly, the nonlinear character of oscillations retains and affects the shape of reradiated waves.

Generally, studies of shock wave propagation in bubbly liquids are concerned with the damping of a shock wave. However, experiments showed that maximum loads behind the bubbly layer are principally determined by the reradiation by the bubbly medium even for relatively small values of l rather than by the transmitted shock wave.

Plots shown in Figs. 15.3.12 and 15.3.13 (here $\beta = l\sqrt{3k_0/R_0^2}$) confirm the foregoing conclusions. Figure 15.3.12 shows the relative change of the shock wave amplitude during its propagation. Thus, for example, for concentration $k_0 = 0.06$ the initial amplitude is reduced to less than 10% by a layer having a length of $l = 3$ cm. For a more dense bubbly medium this effect is still pronounced. For $k_0 = 0.15$ only a weak trace of the precursor is left on the shock wave transmitted through the 2-cm layer while the maximum of the reradiation amplitude p_1/p_{\max} is about $0.3p_{\max}$ (see Fig. 15.3.13). Besides, the experiments showed that the maximum amplitudes of the reradiation attenuate more slowly than the incident shock wave with increasing the thickness of the bubbly screen.

Inspection of Figs. 15.3.12 and 15.3.13 shows that the principal effect in interacting of a shock wave with a bubbly liquid is the radiation of the medium.

Since the period of oscillations of a single bubble is inversely proportional to the square root of the amplitude of the incident wave, an increase of the amplitude will cause an increase of the oscillation frequency and the sequence

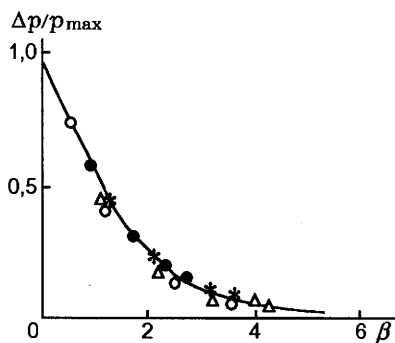


FIGURE 15.3.12 Relative change of the shock wave amplitude during its propagation vs β ; $k_0 = 0.004$ (stars), 0.02 (points), 0.06 (circles), 0.08 (triangles).

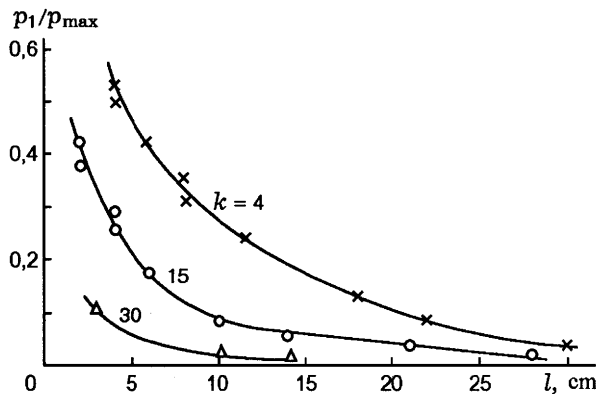


FIGURE 15.3.13 Attenuation of a layer radiation amplitude ($p_1(t)$).

frequencies of waves in the wave packet. Experiments were performed for several gas concentrations, $l = 6$ cm, and for two amplitudes of a shock wave (1 and 2.5 MPa). The results of these experiments, in Table 15.3.1, show that by increasing the pressure one can increase the frequency by several times.

Using the data of Fig. 15.3.9e, variation of the impulse and energy of the wave radiated by the bubbly layer versus its length were calculated.

It turns out that for $k_0 = 0.15$ the relative impulse is essentially constant and the relative energy varies exponentially. In this case the concentration significantly affects the reradiation energy: for $k_0 = 0.04$ and $l = 12$ cm with the same initial shock wave (Fig. 15.3.9) the relative energy of reradiation is about 30% as opposed to 3% for $k_0 = 0.15$ and practically equal relative impulse.

The increase of the incident shock wave amplitude for these pressure ranges does not affect the relative reradiation energy: for $k_0 = 0.05$, $l = 6$ cm and $p_{\max} = 2.5$ MPa, $\bar{E} \approx 75\%$, and the same result is obtained for $p_{\max} = 1$ MPa.

TABLE 15.3.1 Frequencies of Bubble Oscillations (Experiment) for Two Amplitudes of the Incident Shock Wave and for a Fixed Length of the Bubbly Layer, $l = 6$ cm

k_0	0.20	0.15	0.10	0.08	0.06	0.05	0.04	0.025
$\nu_{n,1}$, kHz ($p_m = 1$ MPa)	1.87	2.25	2.9	1.875	1.375	1.1	0.95	0.75
$\nu_{n,2}$, kHz ($p_m = 2.5$ MPa)	2.87	3.125	3.5	3.625	3.75	3.8	3.75	3.5
$\nu_{n,2}/\nu_{n,1}$	1.59	1.39	1.52	1.93	2.73	3.45	3.95	4.67

Kedrinskii (1968a, 1968b) showed that the amplitude p of the transmitted shock wave for various parameters of the bubbly layer varies similarly if the parameter $\beta = \sqrt{3}k_0 l / R_0 = \Omega l / c_*$ is kept constant. Here Ω is the natural frequency of the bubble oscillations. It turns out in this case that the pressure in the shock wave front (p_{\max}) decreases practically instantaneously over the length of the layer l and is consistent with the theoretical function $p_*(\beta)$ obtained using the assumption of an incompressible liquid component. Thus, the wave front passes a bubbly layer having a length of 1 cm in about $7 \mu\text{s}$, irrespectively of the concentration k_0 (see Figs. 15.3.8 and 15.3.9). During this time interval, under the experimental conditions, the bubble radius remains practically constant, the velocity of the radial flows remains close to zero, and the shock wave amplitude (e.g., for $k_0 = 0.08$) decreases by a factor of 2.5.

Physically, this effect is obvious and can be attributed to the attenuation of the pressure in the wave front due to its interaction with the rarefaction waves from the free surfaces of the gas bubbles. It is interesting to analyze the possibility of describing the effect assuming that the initial values of $k(0)$ and $\dot{k}(0)$ remain constant for the time of traversal of the *collective* layer depth by the wave front, which is equivalent to the assumption of infinite velocity of the front propagation. An analysis of the mathematical model of the wave propagation in bubbly media (Kedrinskii, 1980) confirmed the fact that the principal features of the wave transformation are associated with the variation of the function $\partial^2 k / \partial t^2$ which is determined at the initial times by the pressure jump across the front, whereas $k \approx k_0$, $\partial k / \partial t \approx 0$.

15.3.1.4.2 Long Shock Waves: Reflection from a Water-Bubbly Liquid Interface

Experimental studies of long waves in bubbly liquids were performed in a single-diaphragm hydrodynamic shock tube wherein the bubbly layer was located near a solid wall (the lower end of the tube) and a shock wave was induced by rupturing the diaphragm separating the high-pressure (gas) and the low-pressure (liquid with a bubbly layer) sections. In this setup the amplitude of the incident wave propagating in the liquid was equal to the initial gas pressure. However, some difficulties could arise when analyzing pressure in the oscillograms (see frames 1,2,3 in Fig. 15.3.14) because they comprised not only the incident and reflected shock waves from the end of the tube but the rarefaction wave resulting from the reflection of the waves from the free surface of the liquid in the vicinity of the diaphragm. As suggested in Fig. 15.3.14, the lower oscillogram 2 recorded a signal reflected from the bubble boundary (the pressure gauge was located above the boundary), and the upper oscillogram 1 recorded the pressure inside the bubbly layer. The

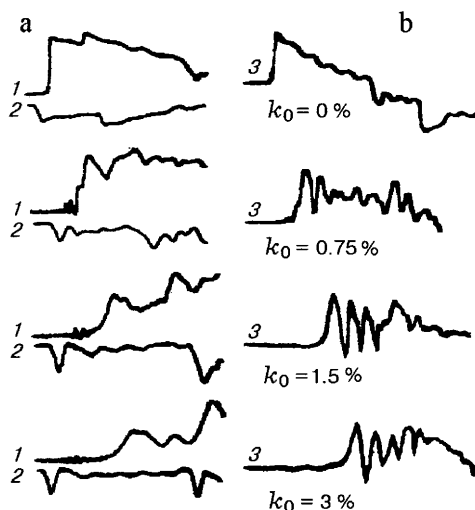


FIGURE 15.3.14 Dynamics of reflection of a shock wave from an interface with a bubbly layer.

scanning length in the oscillograms was 3.6 ms to the left and 1.5 ms to the right.

The study of the propagation of long waves whose positive pressure phase is significantly larger than the bubble collapse time was carried out to elucidate the reflection mechanism of a shock wave from the boundary because the mechanism of the interaction of a long wave with a bubbly medium (see Fig. 15.3.14) is identical to the case of short waves. The experimental study showed that when increasing l with $k_0 = \text{const}$, effects similar to those described earlier were observed. The wave propagation was accompanied by the absorption of the energy at the front, formation of a precursor, and reradiation.

Here the recording of the pressure gauge placed at a distance L ahead of the bubbly liquid boundary (Fig. 15.3.14a,2) was the most interesting. Actually, taking into the account the significant difference in acoustic impedance ρc of the adjacent medium at the location of the gauge, one could expect the occurrence of a rarefaction wave reflected from the front boundary of the bubbly liquid within a time $t_* = 2L/c_0$ needed for the wave front to travel the distance from the gauge to the boundary and back with the velocity c_0 .

Figure 15.3.14 shows that the gauge ahead of the medium indeed recorded the occurrence of the rarefaction wave. However, the time interval required for the appearance of the rarefaction wave differed from the time t_* and was 180 μs instead of 20 μs .

As a consequence, a narrow pressure peak and a rather prolonged low-pressure zone were recorded in the reflected wave. The peak width appeared to be determined by the time required for the fluid particles to gain additional velocity through the bubble collapse. When the latter attained a value of about $\Delta p/\rho_0 c_0$, the reflection was completed. A similar phenomenon did not occur for short waves. This means that in their reflection the contribution of bubbles under relatively weak short waves is small.

15.3.1.5 THE IORDANSKY-KOGARKO-VAN WIJNGAARDEN NONEQUILIBRIUM TWO-PHASE MODEL OF A BUBBLY LIQUID

In the early 1960s, pressure-nonequilibrium two-phase models for the description of wave propagation in a liquid with gas or vapor/gas bubbles were suggested independently by Iordansky (1960), Kogarko (1961), and van Wijngaarden (1968).

They were based on a simple physical model that comprised (a) the conservation laws written for the averaged pressure p , density ρ , and liquid velocity v ; and (b) the state of the two-phase medium described using the Rayleigh equation for the bubble radius R , and the relationships for density ρ , volumetric gas (vapor/gas) concentration k , and R .

The equations of this model are as follows:

$$\begin{aligned} \frac{d\rho}{dt} + \rho \operatorname{div} v &= 0 \\ \frac{dv}{dt} + \frac{1}{\rho} \nabla p &= 0 \\ \rho &= (1 - k_b)\rho_l, \quad k_b = k_0(R/R_0)^3 \\ R \frac{d^2 R}{dt^2} + \frac{3}{2} \left(\frac{dR}{dt} \right)^2 &= \frac{1}{\rho_l} (p_g - p). \end{aligned} \tag{15.3.10}$$

This system has to be supplemented by the equation of state for each component. For the gas in the bubbles, for example, it can be the adiabatic law $pR^{3\gamma} = \text{const}$.

In the acoustic approximation the system of equations (15.3.10) can be reduced to a form that is more convenient for analysis (Kedrinskii, 1968a,

1980, 1968b) by rewriting the Rayleigh equation for the concentration $k = (R/R_0)^3$:

$$\begin{aligned} \Delta p - c_l^{-2} \frac{\partial^2 p}{\partial t^2} &= -\rho_0 k_0 \frac{\partial^2 k}{\partial t^2} \\ \frac{\partial^2 k}{\partial t^2} &= \frac{3k^{1/3}}{\rho_0 R_0^2} (p_0 k^{-\gamma} - p) + \frac{1}{6k} \left(\frac{\partial k}{\partial t} \right)^2. \end{aligned} \quad (15.3.11)$$

Now the medium can be considered as a homogeneous medium with the effective properties described by the foregoing equation of state. This model is applied in the following to describe experiments on wave propagation in bubbly liquids.

15.3.1.5.1 A Precursor

A precursor is the remaining pulse of the incident shock wave that retains the steepness of the front and has an oscillating profile. The wave packet is formed because of reradiation of the layer-absorbed incident wave energy, which was transformed into the kinetic energy of radial bubble oscillations and the internal energy of the compressed gas. The degree of the “collective” bubble compression in a layer for constant parameters of a medium and shock waves determines the dissipation of the shock energy and the reradiation amplitude of the bubbly layer, whereas the inertial character of the bubble collapse determines the delay of the reradiation maximum. The incident wave energy absorption and its reradiation by the bubbles in the layer are coupled and their maxima do not coincide in time.

According to experimental data, one can consider that during the precursor formation the bubbles are radially accelerated, whereas $k \approx 1$, $\dot{k} \approx 0$. Then the Rayleigh equation can be simplified as

$$\frac{\partial^2 k}{\partial t^2} \approx \frac{3}{\rho_0 R_0^2} (p_0 - p),$$

which allows one to transform the first equation of the system of Eqs. (15.3.11) into the Klein–Gordon equation that describes the precursor formation,

$$\Delta p - c_0^{-2} \frac{\partial^2 p}{\partial t^2} = \alpha^2 (p - p_0).$$

In the equation there appears a *similarity parameter*

$$\alpha^2 = 3k_0/R_0^2, \quad (15.3.12)$$

which depends on the bubbly medium structure. The solution of the Klein–Gordon equation reads

$$p(x, c_0 t) - p_0 = \mu(c_0 t - x) - \alpha x \int_0^{c_0 t - x} \mu(\tau) \frac{I_1(\alpha \sqrt{(c_0 t - \tau)^2 - x^2})}{\sqrt{(c_0 t - \tau)^2 - x^2}} d\tau,$$

where $\mu(t)$ is the pressure at the bubbly liquid boundary. A comparison with experimental data (Fig. 15.3.12) shows that a parameter

$$\beta = \alpha \cdot l \quad \text{or} \quad \beta = \sqrt{3k_0} \cdot \frac{l}{R_0}$$

(where l is the bubbly layer length) is a similarity criterion for the attenuation of the shock wave amplitude in the bubbly liquid.

15.3.1.5.2 Dispersion Relationship

In order to estimate a performance of the Iordansky–Kogarko–van Wijngaarden model for small disturbance propagation (Kedrinskii, 1968b), let us consider the dispersion of sound waves, which was studied experimentally by Fox *et al.* (1955) for bubbles with size distributions.

Assume a discrete distribution of the bubble sizes and their concentrations. Then the expression for the effective density reads

$$\rho = \left(\rho_0 + \frac{p - p_0}{c_0^2} \right) (1 + k_b)^{-1},$$

where $k_b = \sum k_j$, $k_j = k_{j0} (R_j/R_{j0})^3$, and the concentration equation in Eqs. (15.3.11) is rewritten for $k_{bj} = (R_j/R_{j0})^3$.

Consider small disturbances of the density and the concentration of bubbles of each size:

$$\rho' = \rho - \rho_0 = \frac{p'}{c_0^2} - \rho_0 k_B, \quad k_j = k_{j0} \left[1 + 3 \left(\frac{R_j}{R_{j0}} - 1 \right) \right].$$

Then Eqs. (15.3.11) in a one-dimensional case read

$$\begin{aligned} c_0^{-2} p_{tt} - p_{xx} - \rho_0 \sum k_{j0} (k_{bj})_{tt} &= 0 \\ k_{bjtt} + \Omega_j^2 k_{bj} &= -\frac{\Omega_j^2}{\gamma p_0} p, \end{aligned} \tag{15.3.13}$$

where $\Omega_j^2 = 3\gamma p_0 / \rho_0 R_{j0}^2$ is the natural frequency of a bubble of j -th kind.

We seek the solution in the form $p = A e^{i(\omega t - mx)}$, $k_{bj} = B_j e^{i(\omega t - mx)}$. Substituting this solution into the linearized system of equations (15.3.13) we arrive at

the expression for a phase sound velocity $c_{ph} = \omega/m$ (here m is the wave number):

$$\frac{c_0^2}{c_{ph}^2} = 1 + \frac{c_0^2}{c_{eq}^2} \sum_{j=1}^N k_{bj0} \frac{1}{1 - (\omega^2/\Omega_j^2)}.$$

Here c_{eq} is the equilibrium sound velocity in the two-phase medium according to Lyakhov (1959).

For $N \rightarrow \infty$ we obtain the following dispersion relationship for the continuous size distribution of the bubbles (see Kedrinskii, 1968a):

$$\frac{1}{c_{ph}^2} = \frac{1}{c_0^2} + \frac{1}{c_{eq}^2} \int_0^\infty \frac{k(R)dR}{1 - (\omega/\Omega)^2}. \quad (15.3.14)$$

In this case,

$$\int_0^\infty k(R)dR = 1, \quad c_{eq}^2 = \frac{\gamma p_0}{\rho_0 k_0(1 - k_0)}, \quad \Omega^2 = \frac{3\gamma p_0}{\rho_0 R^2},$$

where $k(R)$ is the concentration fraction of the bubbles of radius R .

The integral in Eq. (15.3.14) can be transformed as follows:

$$\int_0^\infty \frac{k(R)dR}{1 - (\omega/\Omega)^2} = \frac{1}{2} \left(\int_0^\infty \frac{k(R)dR}{1 - (\omega/a)R} + \int_0^\infty \frac{k(-R_1)d(-R_1)}{1 - (\omega/a)R_1} \right).$$

Since the function $k(R)$ is even,

$$\int_0^\infty \frac{k(R)dR}{1 - (\omega/\Omega)^2} = \frac{1}{2\omega/a} \int_{-\infty}^\infty \frac{k(R)dR}{a/\omega - R}.$$

Now Eq. (15.3.14) can be rewritten as

$$\frac{1}{c_{ph}^2} = \frac{1}{c_0^2} + \frac{1}{c_{eq}^2} \frac{1}{2\omega/a} \int_{-\infty}^\infty \frac{k(R)dR}{a/\omega - R},$$

where $a = \sqrt{3\gamma p_0/\rho_0}$.

The experimental data of Fox *et al.* (1955) on the spectrum of the concentrations of the bubbles can be approximated by the formula

$$k(R) = q \left(\frac{R}{b} \right)^2 \left(1 + \left(\frac{R}{b} \right)^4 \right)^{-1},$$

where b is a scale factor and q is found from the conditions

$$\int_{-\infty}^{\infty} k(R) dR = 2 \int_{-\infty}^{\infty} k(R) dR = qb \int_{-\infty}^{\infty} \frac{z^2 dz}{1+z^4},$$

where $z = R/b$ and therefore $q = 2\sqrt{2}/\pi b$. The integral in the expression for the phase velocity can be written as

$$\begin{aligned} I &= qb^2 \int_{-\infty}^{\infty} \frac{R^2 dR}{(a/\omega - R)(b^4 + R^4)} \\ &= \frac{\sqrt{2}}{2} \pi qb \frac{a (a/\omega)^2 - b^2}{\omega (a/\omega)^4 + b^4}. \end{aligned}$$

Thus, the dispersion relationship for the continuous size distribution of the bubbles reads

$$c_{ph}^{-2} = c_0^{-2} + c_{eq}^{-2} \left[1 - \left(\frac{\omega}{\Omega(b)} \right)^2 \right] \left[1 + \left(\frac{\omega}{\Omega(b)} \right)^4 \right]^{-1}. \quad (15.3.15)$$

Here $\Omega(b)$ is the scale factor that is selected by equating theoretical and experimental values at some point at the curve, such as $c_{ph} = c_0$.

Figure 15.3.15 shows the computational results of the dispersion curve obtained by Eq. (15.3.15) and the experimental data (Fox *et al.*, 1955) for the following conditions: $p_0 = 0.1$ MPa, $\gamma = 1.4$, $k_0 = 0.00025$, 0.0002 and 0.00015 (curves 1–3, respectively).

The calculations were performed using the Iordansky–Kogarko–van Wijngaarden model for the preceding three values of concentration as the average

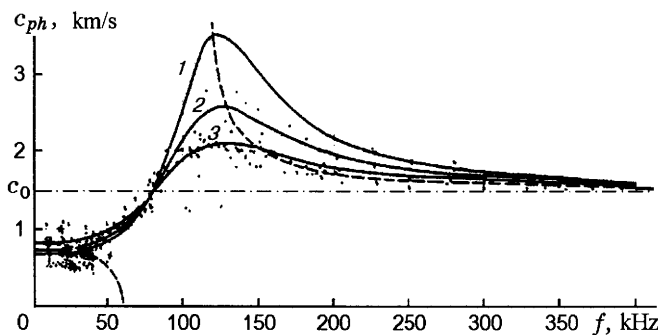


FIGURE 15.3.15 Dispersion curves for various volumetric bubbles concentrations: 1, $k_0 = 2.5 \times 10^{-4}$; 2, 2×10^{-4} ; 3, 1.5×10^{-4} .

for the three continuous size distributions so that the mathematical model could be correlated with the experimental data. The value of $\Omega(b)$ was calculated at the point $c_{ph} = c_0$, which corresponded to the frequency $f = 80$ kHz. The dashed line is the dispersion curve for the bubbles having a size $R = 0.055$ mm, which corresponds to the partial concentration $k_0 = 0.00015$. One can readily see that for $f \rightarrow \infty$ the phase velocity tends to its frozen value which is larger than c_0 , because in this case the bubbles behave as solid particles. It is easy to observe a good agreement between the experimental results and predictions based on the theoretical model. Thus, the experimentally observed *acoustic transparency window* in the resonance frequency region is explained by the existence of the initial spectrum of bubble concentrations, that is, their size dispersion rather than dissipation losses.

15.3.1.5.3 Shock Wave Structure in a Bubbly Medium with Incompressible Liquid Component

Applications of the two-phase model given by Eq. (15.3.11) to the analysis of shock waves in bubbly liquids for determining a precursor (Kedrinskii, 1968a) of the rarefaction waves in a real liquid (Kedrinskii, 1975, and Kedrinskii *et al.*, 1998b) showed that the model allows further simplifications. Some of them are physically well justified. For example, the liquid component compressibility can be neglected compared with that of the gaseous phase, which determines this behavior of the bubbly medium as a whole. Nonlinear terms in the conservation laws for average values can be linearized, but the nonlinear terms in the oscillation equation must be retained.

Other simplifications are less evident and require theoretical justifications. However, if their use yields numerical and analytical estimates that are consistent with the experimental data, then the appropriate approximation may be considered valid. Define a function $\zeta = p - p_0$, a new variable $\eta = r\alpha k^{1/6}$, where $\alpha = \sqrt{3k_0/R_0^2}$, and $k^{1/6} = y^{1/2} = (R/R_0)^{1/2}$.

Then Eqs. (15.3.11) can be transformed as (Kedrinskii, 1968b)

$$\begin{aligned} \frac{d^2\zeta}{d\eta^2} + \frac{v}{\eta} \left(\frac{d\zeta}{d\eta} \right) - \zeta &= 0 \\ \frac{\partial^2 k}{\partial t^2} &= -\frac{3k^{1/3}}{\rho_l R_0^2} \zeta + \frac{1}{6k} \left(\frac{\partial k}{\partial t} \right)^2, \end{aligned} \quad (15.3.16)$$

where $v = 0, 1, 2$ specifies the flow symmetry. The first equation in Eqs. (15.3.16) yields analytical relationships between the average pressure p in the

medium and a volumetric concentration k for plane ($v = 0$), cylindrical ($v = 1$), and spherical ($v = 2$) bubbly clusters:

$$\begin{aligned}\zeta &= Ae^{-\eta} + Be^{\eta} \quad (v = 0) \\ \zeta &= AI_0(\eta) + BK_0(\eta) \quad (v = 1) \\ \zeta &= \eta^{-1/2}[AI_{1/2}(\eta) + BK_{1/2}(\eta)] \quad (v = 2).\end{aligned}\tag{15.3.17}$$

Here I_0 , K_0 , $I_{1/2}$, and $K_{1/2}$ are modified Bessel's functions, and the coefficients A and B are determined from the boundary conditions.

Numerical simulation showed that in bubbly medium with incompressible liquid component the incident wave splits too into a precursor and a reradiated wave packet (Kedrinskii, 1968a), thus confirming that the delay of the pressure maximum reading is associated with a collapse time (see Fig. 15.3.16).

Wave propagation in a bubbly half space is of interest if pressure at the boundary varies with time, since all the disturbances in an incompressible liquid propagate instantaneously. Kedrinskii (1968a) calculated the pressure disturbances for a shock wave incident at the boundary and having a triangular profile with a maximum amplitude of 2 MPa and a 100- μ s-long positive phase pressure (for $k_0 = 0.002$ and $R_0 = 0.4$ cm) for various times (see Fig. 15.3.17). The calculation showed that *a compression wave propagates* in the medium with a variable velocity and that the amplitude decays exponentially with time.

Thus, the Iordansky–Kogarko–van Wijngaarden model allows one to explain the experiment on wave propagation in bubbly liquids.

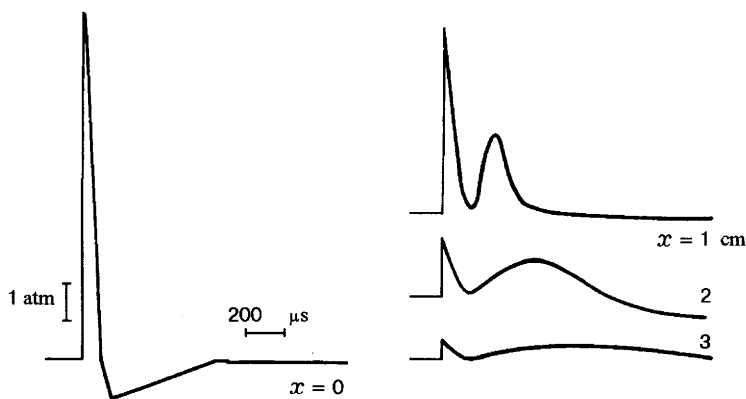


FIGURE 15.3.16 Shock wave transmission through a bubbly medium for $k_0 = 8 \times 10^{-2}$ (a numerical analysis, an incompressible carrying liquid).

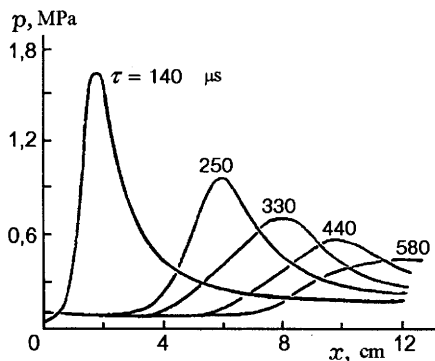


FIGURE 15.3.17 “Moving” compression wave profile in the half space of a bubbly liquid with an incompressible liquid component.

It is useful to summarize the characteristic features of the shock wave propagation in inert bubbly liquids:

- Interaction of a compression wave with a bubbly liquid is characterized by the fact that at a certain length of the layer the total energy of the shock wave, as a result of absorption, is transformed into the energy of the compression waves reradiated by the bubbly medium as a wave packet at a time determined by the bubble collapse time in the layer and dependent on the medium parameters and on the incident shock wave.
- Energy in the formed wave packet accounts for 20–30% of the initial shock wave energy and is concentrated in a narrow radiation spectrum band.

15.3.1.6 AMPLIFICATION, COLLISION, AND FOCUSING OF SHOCK WAVES IN BUBBLY LIQUIDS

Numerous experimental, theoretical, and numerical investigations of the amplification and focusing effects of shock waves in various media have been performed during the past few decades, such as investigations of mechanisms of fracturing kidney stones (lithotripsy) by converging shock waves in a liquid and the initiation of explosions in combustible liquids stored under pressure.

Shock focusing was surveyed by Gronig (1989) and Sturtevant (1993). Experiments and numerical studies of converging cylindrical shock waves in a homogeneous medium were performed by Book *et al.* (1989), Takayama (1989), Watanabe *et al.* (1993), Nagoya *et al.* (1993), Stuka *et al.* (1993), Kuwahara *et*

al. (1991), Isuzukawa and Horiuchi (1993), Fujiwara *et al.* (1993), Demmig *et al.* (1993), Hiroe *et al.* (1993), Itoh *et al.* (1993), and Neemeh (1991). Kedrinskii (1997, 1998) analyzed cavitation effects in the mechanisms of detonation and fracture initiation as well as “acoustic laser”, see also Zavtrac, 1995, 1997.

Experimental data appear to be often insufficient to arrive at some definite conclusions. Therefore, numerical simulation as well as a possibility to evaluate the wave amplification are not only of fundamental but of applied importance as well.

15.3.1.6.1 Shock Wave Amplification by a Cavitation Cluster near a Solid Wall

The possibility to generate high dynamic loads (Kedrinskii, 1968a) on a solid wall by an oscillating cavitation (bubbly) cluster allowed observation of several previously unknown effects. Sudden restoration of the hydrostatic pressure at the boundary of the cavitation cluster, the cumulative character of the bubble collapse, and strong inertial effects result in the generation of a series of pressure pulses at the wall surface (Kedrinskii, 1968a).

These effects were found by numerical calculations of the layer dynamics at a wall performed using the model given by Eqs. (15.3.16). Let us consider the formulation of the problem in more detail. At the solid wall there is a thick layer l of uniform distributed cavitation bubbles with an initial radius R_0 and volume concentration k_0 , formed as a result of pressure decreasing from a hydrostatic pressure p_{hs} to p_0 , by moving the wall away from a liquid. At time $t = 0$ a hydrostatic pressure p_{hs} is restored at the boundary and it is kept constant later on. The pressure at the solid wall is determined by the system of equations

$$\begin{aligned}\zeta &= Ae^{-\eta} + Be^{\eta} \quad (v = 0) \\ \frac{\partial^2 k}{\partial t^2} &= -\frac{3k^{1/3}}{\rho_l R_0^2} \zeta + \frac{1}{6k} \left(\frac{\partial k}{\partial t} \right)^2,\end{aligned}$$

with boundary conditions

$$\begin{aligned}\zeta &= p_{hs} - p_0 k^{-\gamma}, \quad \text{for } x = l \quad \left(\beta = \sqrt{\frac{3k_0}{R_0^2}} l \right) \\ \frac{\partial \zeta}{\partial \eta} &= 0, \quad \text{for } x = 0\end{aligned}$$

The calculations were performed in a wide range of rarefactions in the layer $p_{hs}/p_0 = 300, 200, 100$, and 70 for $\beta = 1, 2, 3$, and 4 . The characteristic pressure profile at the solid wall is shown in Fig. 15.3.18. It is easily seen that

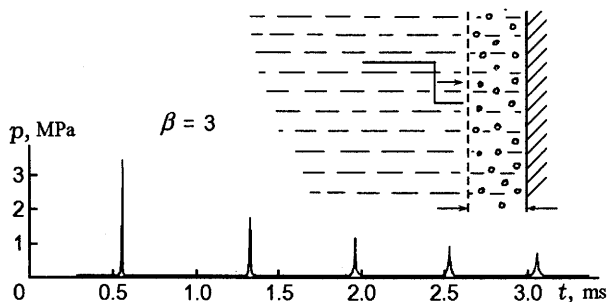


FIGURE 15.3.18 Effect of shock wave amplification during the collapse of the cavitation layer on a solid wall (at $p_{hs}/p_0 = 100$).

in spite of the relatively low pressure jump at the cavitation zone boundary ($p_{hs} = 0.1$ MPa), a series of strong pulses with amplitudes equal to several megapascals arises on the wall. This confirms the conclusions of the previous studies (Kedrinskii, 1968a, 1968b) that the cavitation bubble collapse causes not only the erosion of the surface but also the formation of high pressure pulses produced by a bubbly liquid at the wall.

The analysis of the numerical results showed that enhancement at a wall can be calculated by the formula

$$p \approx 2p_{hs} \frac{\exp(k^{1/6}\beta)}{1 + \exp(2k^{1/6}\beta)} + p_0 k^{-\gamma} \left[\frac{1 - 2\exp(k^{1/6}\beta)}{1 + \exp(2k^{1/6}\beta)} \right]$$

wherein the second term dominates. The pressure maximum at a wall generated by the bubbly cluster appears to comply with the condition $k = k_{\min}$, where k_{\min} can be estimated from

$$k_{\min}^{1/3} \approx 2 \cdot 10^{-2} \beta + \left[1 + (\gamma - 1) \frac{p_{hs}}{p_0} \right]^{1/3(1-\gamma)}.$$

Calculations (see Fig. 15.3.18) showed that for a jump in the amplitude of the hydrostatic pressure by no more than 0.1 MPa over a range of initial pressures in a bubbly layer $p_0 = (0.33-10) \times 10^3$ Pa and in the range the similarity parameter $\beta = 1 \div 6$, the loads on the wall vary from $10p_{hs}$ to $80p_{hs}$ and the maximum is attained at $\beta \approx 3$ for a constant p_0 .

The data shown in Fig. 15.3.18 indicate the existence of an acoustic dissipation in the two-phase medium with an incompressible liquid component, that is, attenuation of the pulse amplitudes is a result of the bubble oscillations in the layer.

15.3.1.6.2 Collision of Stationary Shock Waves

Let us consider the general problem of shock wave interactions (Kedrinskii *et al.*, 1998b).

Assume that the pressure jumps p_b are generated at the time $t = 0$ and kept constant at two opposite boundaries separated by a distance L . For $t > 0$ shock waves are formed in the bubbly liquid, and they split into precursors and main disturbances as the shock waves with oscillating fronts propagate toward one another. The equations describing the formation, propagation, and interaction of the shock waves read as follows:

The conservation laws for average p , ρ , u , in Lagrangian coordinates:

$$\frac{\partial \rho}{\partial t} = -\rho^2 \frac{\partial u}{\partial s}, \quad \frac{\partial u}{\partial t} = -\frac{\partial p}{\partial s}$$

The Rayleigh equation:

$$\frac{\partial \beta}{\partial t} = S, \quad \beta \frac{\partial S}{\partial t} + \frac{3}{2} S^2 = C_1 \frac{T}{\beta^3} - C_2 \frac{S}{\beta} - p$$

The temperature equation:

$$\frac{\partial T}{\partial t} = \delta(\gamma - 1) \text{Nu} \frac{\beta^3(1 - T)}{T} - 3(\gamma - 1) \frac{TS}{\beta} \quad (15.3.18)$$

Parameters and the equation of state of the liquid:

$$p = 1 + \frac{\rho_0 c_0^2}{np_0} \left[\left(\frac{\rho}{1 - k} \right)^n - 1 \right], \quad k = \frac{k_0}{1 - k_0} \rho \beta^3$$

$$\text{Pe} = C_3(\gamma - 1) \frac{\beta |S|}{|1 - T|}, \quad \text{Nu} = \begin{cases} \sqrt{\text{Pe}}, & \text{Pe} > 100 \\ 10, & \text{Pe} \leq 100 \end{cases}$$

$$C_1 = \frac{\rho_{g0} T_0 B}{p_0 M}, \quad C_2 = \frac{4\mu}{R_0 \sqrt{p_0 \rho_0}}, \quad C_3 = \frac{12 R_0 \sqrt{p_0 / \rho_0}}{v}$$

The coefficient δ in the temperature equation is used to account for the heat exchange.

Since the main perturbation velocities are considerably lower than those of the precursors, the latter collides first at the flow symmetry plane, reflect from it, and interact with the main wave packet.

The collision dynamics of the stationary waves will be considered further in some detail in reactive bubbly media. Here we just note that the wave amplitude amplification in the collision arises from the inertial properties of the bubbly liquids and the anomalous value of the bubbly liquid compressi-

bility. Expressions for the speed of the sound in the gas c_g , in the liquid c_{liq} , and in the bubbly medium c_{bubl} read:

$$c_g^2 = \gamma p \frac{1}{\rho_g}, \quad c_{liq}^2 = n(p + B) \frac{1}{\rho_{liq}}, \quad c_{bubl}^2 = \frac{\gamma p}{k_0(1 - k_0)} \frac{1}{\rho_{liq}}.$$

Thus, the equilibrium speed of sound of the bubbly liquid can be much less than that in the gas. For example, at $k + 0 = 0.5$ $c_{bubl}^2 = 4\gamma p / \rho_{liq}$.

The compressibility of the bubbly liquid

$$\varepsilon = -\frac{1}{V} \frac{dV}{dp} = -\frac{k_0}{1 - k_0 \tau_v} \frac{d\tau_v}{dp},$$

where $\tau_v = (R/R_0)^3$, is determined by the volumetric gas concentration.

The data on the amplification during the collision of identical shock waves (e.g., reflection from a solid wall) in a bubbly liquid are shown in Fig. 15.3.19 and in Table 15.3.2 as p_{ref} versus k_0 (an incident wave amplitude 1 MPa, $R_0 = 0.1$ cm). Calculations were carried out for various values of L , sufficient to form the stationary wave structure. The scatter in the data is due to the difference in the interacting phases of the reflected precursors with the main incident wave.

It is clear that the volumetric concentration is crucial in the amplification effect: the increase of k_0 causes a monotone rise of the maximum pressure in the collision plane (at a solid wall) that can be approximated by the following relationship (shown in Fig. 15.3.19 as a dotted line):

$$p_{ref}/p_b \approx 2 + 24.5k_0^{1/4}.$$

The collision of stationary shock waves in a bubbly liquid is essentially transient and requires a certain time interval τ_{col} (in Fig. 15.3.19, it is shown by

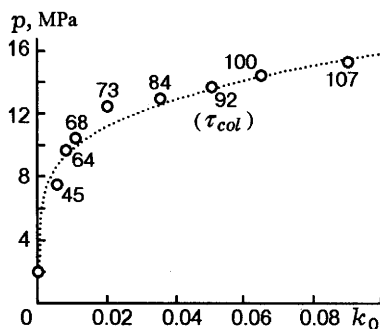


FIGURE 15.3.19 Shock wave amplification after collision: incident wave amplitudes $p_{l,r} = 1$ MPa, a collision time τ_{col} , μ s.

TABLE 15.3.2 Shock Wave Amplification after Collision versus k_0
($p_b = 1$ MPa, $R_0 = 0.1$ cm)

k_0	p_{ref} ($L = 10$ cm)	p_{ref} ($L = 8$ cm)	p_{ref} ($L = 7$ cm)
0	2	—	—
0.005	7.5	—	—
0.0075	9.7	—	—
0.01	10.7	10.5	—
0.02	12.4	13.0	—
0.035	12.8	—	—
0.05	13.7	—	—
0.065	14.4	—	—
0.09	—	—	15.3

numbers in microseconds). The higher the concentration, the longer the process (the rise of the pressure), which appears to be determined by the front steepness of the incident wave.

15.3.1.6.3 Shock Wave Focusing in Inert Bubbly Liquids

Collision effects are expected to be significantly amplified by focusing shock waves. This problem for bubbly media has not been discussed before, although it is clear that the character of the formation of the fine structure of the wave is essentially the same, that is, the formation and focusing of the precursor, and its reflection and interaction with the main incident wave. The system of governing equations describing the cylindrical focusing of waves in a two-phase medium comprises the following equations:

- A system of gas-dynamic equations for average values of p , ρ , u :

$$\begin{aligned}
 \frac{\partial u}{\partial t} &= -\frac{1}{\rho_0} \left(\frac{x(r, t)}{r} \right)^2 \frac{\partial p}{\partial r} \\
 \frac{\partial x}{\partial t} &= u \\
 \frac{1}{\rho} &= \frac{1}{\rho_0} \left(\frac{x(r, t)}{r} \right)^2 \frac{\partial x}{\partial r}
 \end{aligned} \tag{15.3.19}$$

- A system of kinetic equations describing the dynamic state of the medium (including the heat exchange). The latter system of equations is identical to Eqs. (15.3.18).

A numerical method of solving the system was based on the implicit scheme. The gas-dynamic equations were reduced to second-order nonlinear equations for the pressure p , that were solved by an iterative Newton method. The following finite-differences scheme was used:

$$\begin{aligned} & \mathcal{Q}_{i-1/2} \Delta p_{i-1}^{(k)} - \left[\mathcal{Q}_{i-1/2} + \mathcal{Q}_{i+1/2} + \frac{2h^2}{\tau^2} Z_i \frac{1}{\rho_i^{m+1(k)}} \left(\frac{\partial \rho}{\partial p} \right)^{m+1(k)} \right] \Delta p_i^{(k)} \\ & + \mathcal{Q}_{i+1/2} \Delta p_{i+1}^{(k)} + \frac{2h^2}{\tau^2} Z_i \frac{1}{\rho_i^{m+1(k)}} \\ & - \frac{2h}{\tau^2} [x_{i+1/2}^m - x_{i-1/2}^m + \tau(u_{i+1/2}^m - u_{i-1/2}^m)] \\ & + \mathcal{Q}_{i+1/2} (p_{i+1}^{m+1(k)} - p_i^{m+1(k)}) - \mathcal{Q}_{i-1/2} (p_i^{m+1(k)} - p_{i-1}^{m+1(k)}) = 0 \end{aligned}$$

Here, k is the number of the iterations, and $\mathcal{Q}_{i-1/2} = (x_{i-1/2}^m)^2 / \rho_0 r_{i-1/2}^2$, $Z_i = \rho_0 r_i^2 / (x_i^m)^2$. The pressure and the density were calculated as $p_i^{m+1(k+1)} = p_i^{m+1(k)} + \Delta p_i^{(k)}$, $\rho_i^{m+1(k+1)} = \rho(p_i^{m+1(k+1)})$. The iterations were performed until $\max_i |\Delta p_i^{(k)}| < \varepsilon$. The kinetic equations were solved at each time interval $t^m < t < t^{m+1} = t^m + \tau$ by the Runge–Kutta method with a variable time step.

Figure 15.3.20 presents the numerical results for the focusing of a stationary wave in pure liquids. The correlation between the front steepness of the incident wave ($1.5 \mu\text{s}$) and the collision duration is readily seen. By analogy with the reflection, one can expect that when compared to a pure liquid wherein the shock wave amplitude increases by a factor of 20, the focusing in a bubbly liquid will yield the larger effect.

Several convergent one-dimensional cylindrical shock waves were calculated under similar initial and boundary conditions as in the foregoing problem (with a focusing radius $r = 5 \text{ cm}$) using Eqs. (15.3.19) for a bubbly liquid.

Figure 15.3.21 illustrates a part of the focusing range into the axis of a shock wave in the bubbly liquid with $k_0 = 0.02$, $R_0 = 0.2 \text{ cm}$, and $p_b = 1 \text{ MPa}$. The focusing of the precursor (the time interval is $20\text{--}40 \mu\text{s}$) is not shown in Fig. 15.3.21. The reflection of the precursor affects the shape of a main wave reaching a focus at $120 \mu\text{s}$. Note that the wave amplification in the bubbly liquid is by one order of magnitude larger than the amplification in the pure liquid.

Table 15.3.3 demonstrates an interesting effect, namely, that in the range of the concentrations $k_0 = 0.01\text{--}0.03$ the focused wave amplitude increases proportionally to the concentration.

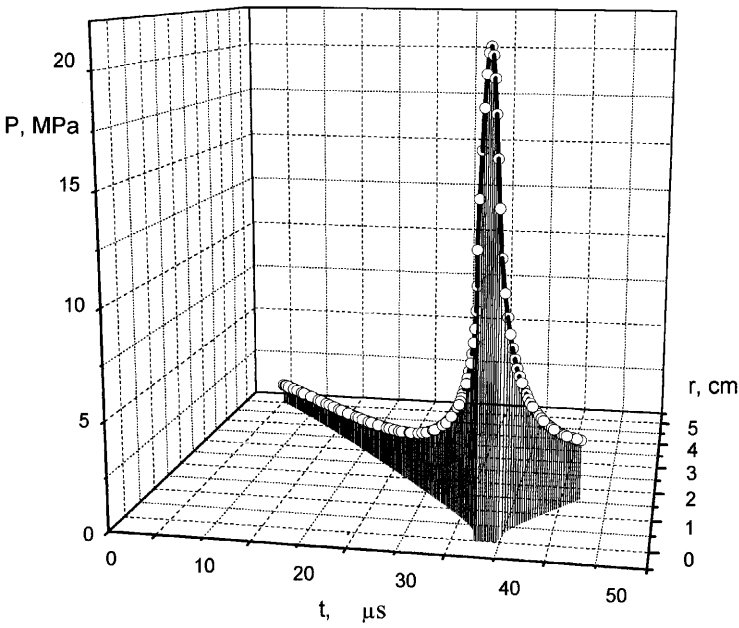


FIGURE 15.3.20 Focusing of a stationary wave in a pure liquid.

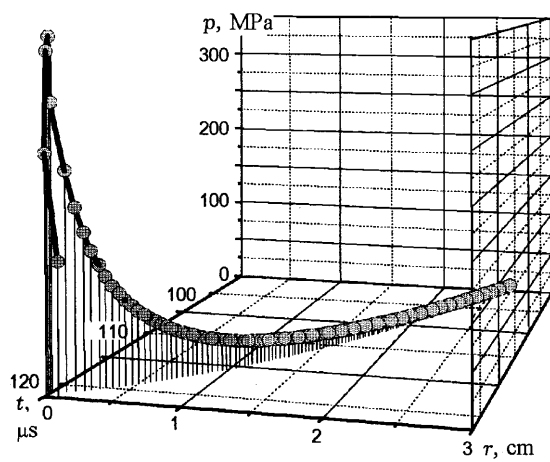


FIGURE 15.3.21 Shock wave amplification by focusing: $k_0 = 0.02$, $R_0 = 0.1 \text{ cm}$, $p_b = 1 \text{ MPa}$, $r = 5 \text{ cm}$.

TABLE 15.3.3 Dependence of the Maximum Focused Pressure p_f on the Volumetric Concentration k_0 ($p_b = 1$ MPa, $R_0 = 0.1$ cm)

k_0	0.0	0.005	0.01	0.02	0.03	0.05	0.07	0.09
p_f , MPa	21.1	69.3	170.0	346.8	509.4	625.0	686.8	827.5

Analysis of the numerical results in a wide range of values of k_0 showed that the pressure $p_{\max}(r)$ at the wave front (at its focusing on the axis) can be approximated by the Lorentz profile

$$p_{\max}(r) = \frac{2ab/\pi}{b^2 + 4(r - c)^2},$$

with parameters for different values of k_0 presented in Table 15.3.4.

A typical example of the dynamics of a shock wave amplitude during focusing is shown in Fig. 15.3.22 for the volume concentration $k_0 = 0.03$. The Lorentz approximation (L) is shown by the dotted line. These examples show that the shock wave amplification occurs mainly in the vicinity of a focus.

TABLE 15.3.4 Parameters of Lorentz Profile versus k_0

k_0	0.01	0.02	0.03	0.05	0.07
a	4192	7191	8565	10069	10242
b	0.795	0.435	0.305	0.194	0.141
c	-0.413	-0.319	-0.245	-0.202	-0.171

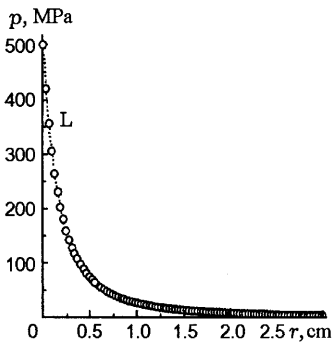


FIGURE 15.3.22 Variation of the shock wave amplitude during focusing: $k_0 = 0.03$, $R_0 = 0.1$ cm, $p_b = 1$ MPa, $r = 5$ cm.

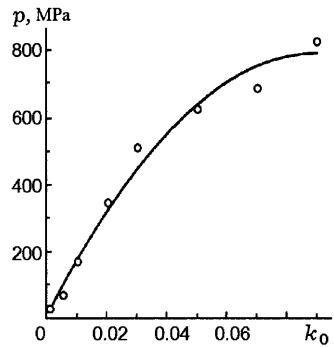


FIGURE 15.3.23 Distribution of the pressure during focusing versus k_0 .

TABLE 15.3.5 Relative Pressure in the Focus versus k_0

k_0	0.0	0.005	0.01	0.02	0.03	0.05	0.07	0.09
\bar{p}_{foc} , MPa	21.1	69.3	170.0	346.8	509.4	625.0	686.8	827.5

Figure 15.3.23 as well as Table 15.3.5 demonstrate the concentration effect on the maximum pressure that is attained by focusing stationary waves in nonreactive bubbly liquids. An oscillating character of the calculated data that is explained by the reflected precursor can be observed. Here we showed also the approximation of this dependence by a second-order polynomial (a solid line)

$$p = p_{foc}/p_{sh} \approx 18.6 + 1718k_0 - 9552k_0^2,$$

describing the results of focusing with a sufficient degree of accuracy.

15.3.2 BUBBLY DETONATION: WAVES IN REACTIVE BUBBLY LIQUIDS

15.3.2.1 INTRODUCTION

Bubbly detonation is known as a quasi-stationary self-sustaining regime for the formation and propagation of the wave packet in reactive bubbly liquid (Sychev and Pinaev, 1986).

Historically, discovery of this phenomenon was delayed by almost a quarter of a century. The investigations started with the study of the single reactive

bubble dynamics (Kedrinskii, 1961), then the detection of a regime of wave “rolling” with a constant velocity during the interaction of a shock wave with a reactive bubble chain (Hasegawa and Fujiwara, 1982), and finally, investigation of wave transformations in reactive bubbly liquids (Sychev and Pinaev, 1986).

Formation of quasi-stationary solitary waves in bubbly detonation depends on the character of the chemical reaction inside a single gas bubble collapsing in the incident shock wave. It is shown that the reaction can proceed in a variety of regimes. Detailed experimental observations of single reactive bubble dynamics are quite involved, and the relevant studies investigate formation and interaction of bubbly detonation waves (Kedrinskii and Mader, 1987; Shagapov and Vakhitova, 1987; Kedrinskii and Zamarayev, 1989; Trotsyuk and Fomin, 1992; and Kedrinskii *et al.*, 1996) and various approaches for determining the detonation velocity (Lyapidevsky, 1990, and Kedrinskii and Mader, 1993). It was assumed a priori that a reactive gaseous mixture in bubbles explodes when a certain compression is attained. The mechanism of the wave amplification in a reactive bubbly liquid was not discussed.

Experiments performed by Barbone *et al.* (1994) confirmed and refined the results concerning special features of a reactive single bubble dynamics. Let us start the analysis of the initiation of a detonation with an adiabatic compression of a gas inside a bubble taking into account the effects that are determined by the liquid inertia.

15.3.2.2 SINGLE BUBBLE DYNAMICS WITH CHEMICAL REACTIONS

15.3.2.2.1 Refracted Wave Function, Todes' Kinetics

The ability of a reactive gaseous mixture inside in a bubble to detonate when it is adiabatically compressed by a shock wave and heated to the ignition temperature was first found and investigated by Kedrinskii (1961).

The first numerical estimations of a reactive bubble dynamics were performed in order to get insight into the initiation of bubbly detonation. One of them led to the detection of the effect, which demonstrated the possibility of initiating a bubble detonation by a quite unexpected scenario. Calculations of the axisymmetric interaction of a strong shock wave with a bubble of oxyacetylene mixture showed that the shock wave refracted by the bubble can initiate a detonation locally inside the bubble in the vicinity of its front wall (Kedrinskii and Mader, 1987); see Fig. 15.3.24. In this case the bubble has no time to acquire the radial velocity, its volume is constant, and a detonation wave inside it has already begun to propagate. Figure 15.3.24 illustrates the pressure (a) and the temperature (b) jumps as well as the density distribution (c): in one-half of the bubble whose boundary coordinates

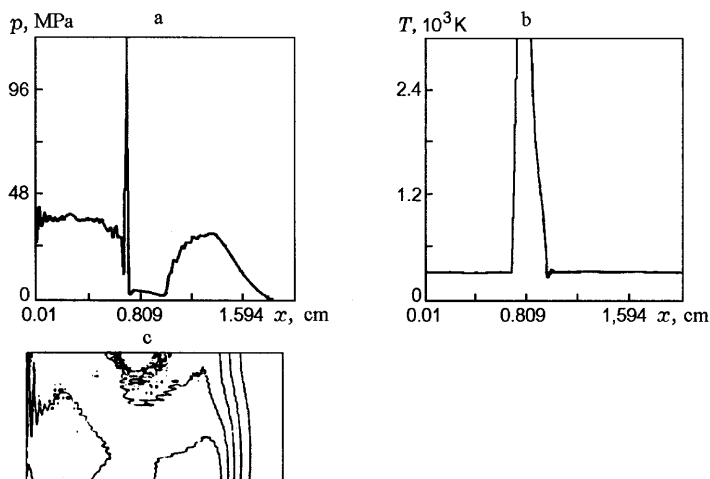


FIGURE 15.3.24 Pressure (a) and temperature (b) distribution in a bubble initiated by a refracted wave; (c) density distribution in the vicinity of a bubble: $t = 10.5 \mu\text{s}$, $p_{sh} = 50 \text{ MPa}$, $R_0 = 2 \text{ mm}$.

correspond with those in Fig. 15.3.24a. Note that the preceding effect is one of the possible ways for realizing the *hot-spots* mechanism.

The second approach is to simplify the physical model assuming adiabatic compression of an explosive mixture in a bubble, the fast chemical reaction, and the instantaneous increase of the internal energy of detonation products (Kedrinskii and Mader, 1987).

The third model employs the Todes bimolecular chemical kinetics proposed in the 1930s and was used by Kedrinskii and Zamarayev (1989) for the analysis of detonation of a single bubble. This model employs the following set of governing equations in dimensionless form ($\beta = R/R_0$):

Rayleigh equation

$$\beta \frac{d^2\beta}{d\tau^2} + \frac{3}{2} \left(\frac{d\beta}{d\tau} \right)^2 = \frac{\bar{T}}{\beta^3} - \bar{p}_\infty - \frac{4}{\beta} \frac{d\beta}{\text{Re} d\tau} \quad (15.3.20)$$

Temperature equation

$$\frac{d\bar{T}}{d\tau} = \eta \frac{d\bar{N}}{d\tau} - \frac{3(\gamma - 1)}{\beta} \bar{T} \frac{d\beta}{d\tau}$$

Kinetics equation

$$\frac{d\bar{N}}{d\tau} = \zeta \beta^{-3} \sqrt{\bar{T}} e^{-\alpha/\bar{T}} (1 - \bar{N})^2,$$

where

$$\tau = t \frac{\sqrt{p_0/\rho_0}}{R_0}, \quad \eta = \frac{Q}{c_m T_0}, \quad \alpha = \frac{E_a}{B T_0},$$

$$\zeta = \frac{AZ\sqrt{T_0}}{V_0} \frac{R_0}{\sqrt{p_0/\rho_0}}, \quad \text{Re} = R_0 \frac{\sqrt{p_0/\rho_0}}{\nu}$$

E_a is the activation energy; B is the gas constant; Q is the reaction heat; c_m is the heat capacity; $N = n/a$, where a is the original concentration of the component, n is the number density of molecules formed during the reaction, $\bar{p}_\infty = p_\infty/p_0$ is the external pressure; $\bar{T} = T/T_0$ is the temperature of the gas mixture; and ν is the kinematic viscosity.

Calculations showed that during interaction of a bubble with a shock wave by adiabatic heating *the reaction in the mixture occurs almost instantaneously at a constant bubble volume*, that is, regular adiabatic explosion at a constant volume. Only the radial acceleration of the collapsing bubble changes abruptly as a result of explosion, namely, the acceleration changes its sign and the velocity sharply decays to zero.

15.3.2.2.2 Generalized Kinetics of Detonation in a Gaseous Phase

It is believed that for excitation of a self-sustaining (multifront) gaseous detonation in a free gaseous volume it is required to release a critical initiation energy E_* . The process has typical spatial scales, such as the unit cell size a (Vasil'ev and Nikolaev, 1978) and the formation radius r_{form} , determining a region outside of which the detonation propagates in the stationary regime.

One of the best approximate models for describing the initiation of a detonation in compliance with the experimental data is a multiple point initiation model. It is based on the assumption that transverse wave collisions at the detonation front initiate multifront detonation. The collision energy E_0 is estimated from the cell model proposed by Vasil'ev and Nikolaev (1978) and is used for evaluating E_* . In the calculations presented below for the mixture $O_2 + H_2$ it is assumed that the induction period τ_i is negligibly small in comparison with the chemical reaction time, and it is determined by the integral equation (White, 1967)

$$\int_{t_*}^{t_* + \tau_i} \frac{dt}{\bar{\tau}} = 1, \quad \bar{\tau} = \frac{A}{c_f^{n_1} c_{Ox}^{n_2}} \exp\left(\frac{E_a}{RT}\right),$$

where t_* is the instant of the self-ignition of the mixture, c_f and c_{Ox} are the fuel and the oxidizer concentrations, respectively, and n_1 and n_2 are the orders of

the reaction. The mixture temperature $T(t)$ in a bubble is determined by an adiabat with different values of the ratio of the specific heats γ before ($\gamma = 1.4$) and after ($\gamma = 1.21$) the chemical reaction.

In a free volume of the gaseous mixture, the initiation energy for a spherical detonation and a unit cell size a are determined using the data of Vasil'ev and Nikolaev (1978). In particular, for the mixture $O_2 + 2H_2$ at $p_0 = 0.1$ MPa and $T_0 = 298$ K ($A = 5.38 \times 10^{-5}$ $\mu\text{s}\cdot\text{mol/L}$, $E_a = 17.15$ kcal/mol), $a = 1.6$ mm and $E_* \approx 6$ J. Clearly, under such conditions the assumption about the multi-point initiation of the reaction of the gas inside a bubble of 1 mm radius is unacceptable. Moreover, in this case the requirements for the correspondence between the characteristics spatial scales is not valid, $R > r_{\text{form}} \gg a$.

However, with increasing pressure p (which occurs in a collapsing bubble), the conditions for initiating the detonation in the bubble improve, with respect to the characteristic spatial scale of the process ($a \approx 1/p$) and also with respect to the critical initiation energy E_* , which decreases as $1/p^2$. Parameters of the main detonation characteristics for the free volume and different initial pressure (appropriate to the pressure p_{ad} of the adiabatic compression of the hydrogen–oxygen mixture) are presented in Table 15.3.6 (Vasil'ev and Nikolaev, 1978, and Vasil'ev *et al.*, 1978).

It is clear that the conditions required for detonation with respect to R/a and E_* can be readily realized in the bubbly liquid interacting with shock waves. Hence, the problem of detonation in a bubbly liquid is reduced to the investigation of the initiation of detonation in a single bubble (Vasil'ev *et al.*, 1998). In this respect self-initiation of the reaction in a mixture due to raising its temperature by external factors (e.g., adiabatic compression by a shock wave) becomes important.

TABLE 15.3.6 Parameters of the Main Detonation Characteristics

R_0/R	P_{ad}	T_{ad}	E	P_{ch}	T_{ch}	P_*	T_d	E_*	ΔE	a	R/a
1	0.1	298.15	4.3×10^{-3}	0.96	3504.1	18.79	3681.6	5.946	0.0	1.594	1
1.4	0.41	478	6.9×10^{-3}	2.57	3694.4	12.09	3888.7	0.2001	0.0026	0.375	3
2	1.827	681	9.9×10^{-3}	8.5	3943.7	8.82	4160.9	0.00651	0.0056	0.0822	9.7
3	9.994	1104	1.6×10^{-2}	30.9	4278.9	5.68	4522	9×10^{-5}	0.0117	0.0126	42.2
4	33.37	1555	2.2×10^{-2}	78.8	4582.1	4.18	4844.4	4.1×10^{-6}	0.0177	0.00324	123
5	85.03	2028	2.9×10^{-2}	164.1	4877.9	3.3	5155	4.4×10^{-7}	0.0247	0.00115	277.2

Note. P_{ad} , T_{ad} and E are the pressure, the temperature, and the internal energy of the mixture corresponding to its adiabatic compression; P_{ch} and T_{ch} are the parameters of detonation products at a constant volume; $P_* = P_d/P_{ad}$ and T_d are the parameters in a detonation wave; ΔE is the increase of the internal energy of the mixture by compressing a bubble. The units are MPa for the pressures, J for energies, and K for temperatures.

Variation of the parameter R/a (see Table 15.3.6) indicates that detonation can be caused in the bubbly liquid by bubble compression.

15.3.2.2.3 Dynamics of Bubbles Filled with a Reactive Gaseous Mixture

The bubble dynamics in the wave field with the constant pressure p_∞ is described by the Rayleigh equation (15.3.20) where acoustic losses are taken into account, that is, the term $-3\gamma\alpha_c\beta^{-3\gamma}(d\beta/d\tau)$ is added to the right-hand side of the equation, where $\alpha_c = c_0^{-1}\sqrt{p_0/\rho_0}$; ρ_0 and c_0 are the initial density and sound velocity in a liquid.

The temperature of a mixture in a bubble at every moment is determined by the equation of state $pV = mRT/\mu$. In this case the change in molar mass caused by the reaction from $\mu_0 = 12$ to $\mu_{ch} = 14.71$ is calculated assuming $m = \text{const}$. The induction period $t = t_*$ can be determined from the condition

$$\bar{E} - 1 = \bar{E}_*$$

where \bar{E}_* and \bar{E} are the ratios of the initiation energy and the internal energy to the initial internal energy of the gaseous mixture. The magnitude of E_* and the temperature of reaction products are calculated with the interpolation formulas derived by analyzing the data presented in Table 15.3.6,

$$E_* = E^0\beta^\delta$$

$$T_{ch} = A_0 + A_1\beta^{-1} + A_2\beta^{-2} + A_3\beta^{-3},$$

where $E^0 = 6.4746\text{J}$, $\delta = 10.2385$, $A_0 = 2925.65947$, $A_1 = 667.16983$, $A_2 = -95.94769$, and $A_3 = 8.1264$.

In this case the induction time τ_i is found by the induction integral and the reaction is initiated at the time $t_{ch} = t_* + \tau_i$ and proceeds instantly.

The problem is simplified by assuming that the mixture temperature rises instantly in a collapsing bubble and that $t_* = 0$ in the induction integral does not change the characteristic times of the explosion. If the reaction is not initiated during the first oscillation the induction integral continues to be calculated for the next oscillation.

Figure 15.3.25a presents the dependence of the bubble-cell ratio (R/a) on the instantaneous relative degree of the bubble compression R_0/R calculated for initial conditions $R = 1.6\text{ mm}$, $a = 1.6\text{ mm}$, $\gamma = 1.4$, and a pressure jump $p_\infty = 10\text{ MPa}$ at infinity in the liquid surrounding the bubble. The moment when the internal energy increase ΔE for the gaseous mixture exceeds the critical initiation energy E_* (Fig. 15.3.25b, a logarithmic scale) is marked by the dotted line.

The increase of R/a and the sharp decrease of E_* as the bubble is compressed indicate that if the detonation at the initial stage does not occur

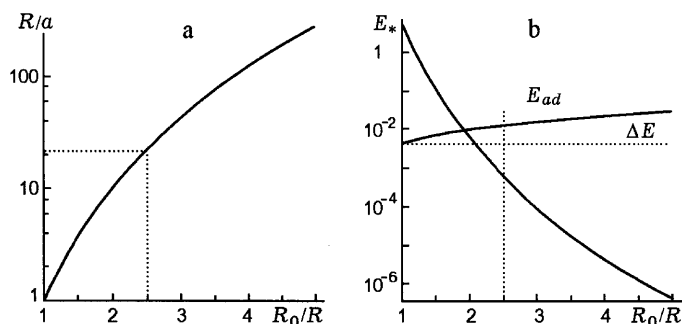


FIGURE 15.3.25 The variation dynamics of the number of the cells (a) and the values of E_* and E_{ad} in a collapsing bubble on its adiabatic compression (b).

during the adiabatic compression of a gas, it occurs later on. Thus, for example, at a certain stage of the compression, the mixture is capable of self-initiating as a result of the increase in the internal energy (ΔE).

The preceding calculation performed with rather high values of p_∞ shows that the pressure jump in the reaction products (p) at the moment of the explosion sharply changes the value of the bubble collapse velocity: the inertia of the liquid surrounding the bubble is appreciable and decelerates the collapse. The gas is compressed up to 920 MPa at $p_{ch} = 44$ MPa and the temperature increases up to 7.3×10^3 K at $T_{ch} = 4.3 \times 10^3$ K (Fig. 15.3.26, $p_\infty = 10$ MPa, $R_0 = 1.6$ mm). This effect determines the most probable mechanism of the wave amplification in settling of a stable regime.

The analysis of the numerical results showed that the acoustic radiation losses in the preceding case decrease the maximum temperature of the overcompressed reaction products by about 10%.

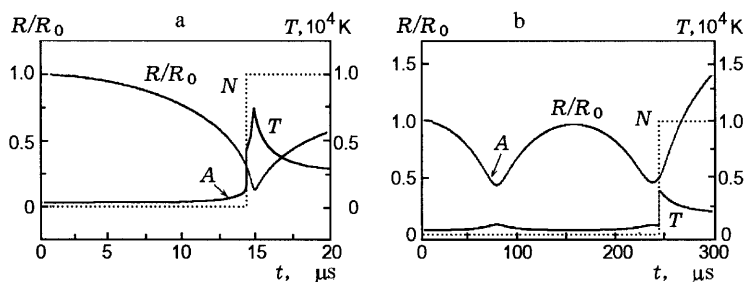


FIGURE 15.3.26 Variation of the mixture temperature T and the relative fraction of reacted molecules N ($t_* = 13.3 \mu s$) during the compression stage (a); a reaction delay to the second oscillation ($t_* = 68.75 \mu s$) (b).

Figure 15.3.26b shows the temporal evolution of various parameters for weak waves with the amplitude $p_{\infty} = 0.52$ MPa. This figure shows that the reaction is initiated at the second oscillation. In this case the gaseous mixture explosion happens in the vicinity of its minimum radius or even in the initial expansion stage. Clearly, the maximum temperature of the reaction products is determined by the energy release in the reaction. The latter can be very important since a weak steplike shock wave with such an amplitude can initiate a self-sustained detonation in a bubbly liquid.

15.3.2.3 REACTIVE BUBBLE DYNAMICS AND THE INTERFACE MASS TRANSFER

Note that already early studies (Bowden and Yoffe, 1958; Andreev, 1958; Johansson, 1958; and Dubovik and Bobolev, 1978) used the *hot-spots* model for detonation initiation in liquids and discussed the significance of microdrops. Microdrops are formed in the bubbles because of their instability during their oscillations behind the shock wave front. This instability results in the formation of microjets and their disintegration into drops.

Alternatively (Pinaev and Sychev, 1986b), the detonation of a bubbly liquid is determined by heat and mass transfer rates that grow with the development of the bubble surface instability, giving rise to microdrops (Dubovik and Bobolev, 1978). Evaporation of microdrops strongly affects the progress of a chemical reaction in the gaseous phase inside the bubbles. Moreover, it is impossible to initiate detonation in a system where the fuel and the oxidizer are in different phases without the interphase heat and mass transfer to form a reactive mixture inside the bubbles (Pinaev and Sychev, 1986a).

Evidently, a model of bubbly detonation has to account for the effects of such bubble dynamics. In the following we consider the influence of the injection time t_{inj} , the initial sizes of microdrops D_0 , and the evaporated liquid mass M_L , both in the case of an instant evaporation of microdrops and in the case of a transient evaporation (Kedrinskii *et al.*, 1999).

15.3.2.3.1 Instant Evaporation of Microdrops

Assume that a gas bubble oscillates in a liquid under the influence of a constant and instantly applied external pressure. Heat and mass transfer are replaced by the instant evaporation of a liquid droplet of mass M_L at time t_{inj} after the beginning of the compression. The bubble dynamics is described by the

Rayleigh equation, assuming that the bubble retains its spherical shape and that the gas inside is perfect:

$$\beta\beta'' + \frac{3}{2}(\beta')^2 = \bar{p} - \bar{p}_\infty.$$

Here the prime denotes derivation with regard to the dimensionless time τ , and \bar{p} is introduced to account for the acoustic radiation losses and the viscous dissipation:

$$\bar{p} = \frac{\rho_g \Re T}{p_0 \mu} - \frac{4\beta'}{\beta \text{Re}} + \frac{1}{c_0} \sqrt{\frac{p_0}{\rho_L}} \left(1 + \frac{\bar{p} - \bar{p}_\infty}{B_1 + \bar{p}_\infty} \right)^{-1/n} \beta \frac{d\bar{p}_g}{d\tau}.$$

Here ρ_g is the gas density, $B_1 = B/p_0$ and n are constants, c_0 is the speed of sound in a liquid, \Re is the universal gas constant, $\text{Re} = (R_0/v_d)\sqrt{p_0\rho_0}$ is the Reynolds number, v_d is the dynamic liquid viscosity, and μ is the molecular weight.

It is assumed that the gas–vapor mixture is nonreactive during the induction time and it is instantaneously transformed to a chemical equilibrium after this time. The induction period t_i is determined from

$$\int_0^{t_i} \frac{dt}{\tau_i} = 1,$$

where $\tau_i = (A_i/\eta) \exp(E_a/\Re T)$, $\eta = \rho\mu^{-1}(v_{\text{H}_2}v_{\text{O}_2})^{-1/2}$, v_{H_2} and v_{O_2} are the mole fractions of H_2 and O_2 , respectively, and A_i and E_a are constants.

Thermodynamic parameters of the mixture are calculated by the kinetics model suggested by Nikolaev and Fomin (1983), Nikolaev and Zak (1988), and Fomin and Trotsyuk (1995). The kinetics model involves the equation for the isentropic process,

$$\frac{dT}{d\rho} = -\frac{U_\mu\mu_\rho - \Re T/\rho\mu}{U_T + U_\mu\mu_T}, \quad \frac{d\rho}{d\tau} = -3\rho_{g0} \frac{\beta'}{\beta^4},$$

which can be rewritten as

$$\frac{dT}{d\tau} = \frac{dT}{d\rho} \frac{d\rho}{d\tau} = \left(-\frac{U_\mu\mu_\rho - \Re T/\rho\mu}{U_T + U_\mu\mu_T} \right) \left(-3\rho_{g0} \frac{\beta'}{\beta^4} \right),$$

and the chemical equilibrium equation

$$\frac{\rho_g}{\mu} \frac{(1 - \mu/\mu_{\max})^2}{\mu/\mu_{\min} - 1} \exp(E_D/\Re T) = \frac{AT^{3/4}}{4K_+} (1 - \exp(-\theta/T))^{3/2}, \quad (15.3.21)$$

where T and U are temperature and the internal gas energy; U_μ , U_T , μ_T and μ_ρ are derivatives with respect to parameters shown in the index; ρ_{g0} is the initial

gas density; and E_D is the mean dissociation energy of the reaction products. The internal gas energy therewith is calculated by

$$U = \left[\frac{3}{4} \left(\frac{\mu}{\mu_a} + 1 \right) + \frac{3}{2} \left(\frac{\mu}{\mu_a} - 1 \right) \frac{\theta/T}{\exp(\theta/T) - 1} \right] \frac{\Re T}{\mu} + E_D \left(\frac{1}{\mu} - \frac{1}{\mu_{\min}} \right)$$

where μ_a , μ_{\min} , and μ_{\max} are the molecular weights in atomic, completely dissociated, and fully recombined conditions, respectively; θ is the effective excitation temperature for the vibrational degrees of freedom; and A and K_+ are the velocity constants of dissociation and recombination of the reaction products. The values of μ_a , μ_{\min} , and μ_{\max} are determined by the gas composition and hence remain constant until $t = t_{inj}$, when they instantaneously assume their new values and remain constant. The new values depend on the chemical composition and on the mass of the evaporated liquid.

The preceding model can be used for hydrogen–oxygen mixtures of arbitrary chemical composition with inert components. It allows one to account for strong changes of the molecular mass, isoentrop exponent, and heat capacities, and for the thermal effect of the chemical reaction, which is caused by recombination and dissociation and by the variation of the fuel–oxidizer ratio in the gaseous phase. For example, the molecular gas mass of the system I [H_2 (gas)– O_2 (liquid)] under cryogenic initial conditions, may be changed by one order of magnitude. After the induction time ($t = t_i$) the gas attains a chemical equilibrium that is continuously affected by the bubble dynamics.

The instantaneous change of the gas parameters was calculated using the chemical equilibrium equation (15.3.6) and the condition $U_1 = U_2$ where U_1 and U_2 are the internal energies of the gas both before and after the change. The bubble radius, the gas density, and the parameters μ_a , μ_{\min} and μ_{\max} do not change at the instant of the abrupt change of the gas parameters. After evaporation of the liquid mass M_L , the gas composition and the thermodynamic parameters are discontinuously changed. Provided that the bubble radius remains constant, the parameters after the discontinuous change are calculated as follows. First, using the law of mass conservation $M_0 + M_L = M_2$, the gas mass M_2 in the bubble and the gas density after the evaporation are calculated. Then the parameters μ_a , μ_{\min} and μ_{\max} are calculated using the procedure suggested by Nikolaev and Fomin (1983), the known value of M_2 , and the initial gas and liquid compositions. The pressure and temperature in a gaseous phase are determined from the equation of state and the conservation of energy $U_1 + U_L = U_2$.

We calculated transient behavior of the bubbles using the foregoing model for two types of mixtures, I and II, composed of [$2H_2 + O_2$ (gas) \rightarrow H_2O (liquid)] with inert dilutant. The calculations were performed with the following initial parameters: $T_0 = 87$ K (in mixture I), $T_0 = 293$ K (in mixture II), the initial gas pressure in the bubble was $p_0 = 1.011 \times 10^5$ Pa, the external

pressure was $p_{\infty} = 100p_0$, $R_0 = 1.6$ mm. All other constants were taken from Trotskyuk and Fomin (1992), Fomin and Trotskyuk (1995), and Grigor'ev and Meilikhov (1991).

Calculations allowed us to verify the validity of the condition concerning the partial pressure of evaporated component which cannot exceed the saturated vapor pressure p_{sat} . The calculation (see Fig. 15.3.27) showed that the dependencies of M_L on the gas parameters differ essentially for mixtures I (a) and II (b). Thus, for example, in mixture I with increasing M_L the average gas temperature in the bubble attains a maximum, whereas in mixture II the increase of M_L causes monotone decrease of the gas temperature in the bubble.

As discussed by Kedrinskii *et al.* (1990), the model based only on pure kinetics of the chemical reactions for the description of the bubbly detonation predicts formation of a solitary wave. In the stationary regime, the predictions of the model concerning the amplitude and the wave propagation velocity agree rather well with the experiments. However, the temperature distribution has an unrealistic long tail in the detonation wave with the amplitude being on the order of that in the initiating wave.

The probable mechanisms of the formation of a real solitary wave without a tail may be associated with the high liquid evaporation rate, which causes a decrease of the temperature and the gas pressure in the tail of a bubbly detonation wave. Figure 15.3.27b shows that the evaporation of a small amount (on the order of the gas mass in the bubble M_0) of liquid reduces the final gas temperature practically to the initial one.

Figure 15.3.28 [where (a) is mixture I and (b) is mixture II] shows temporal variation of gas temperature for various times of the microdrop injection t_{inj} . The calculations showed that the gas parameters (and their values after damping of the oscillations, e.g., T_f) depend strongly on the injection time t_{inj} , if it is close to the moment of the maximum compression of the bubble. Otherwise, this dependence proves to be weak. Note that the low value of T_f for $t_{\text{inj}} \geq 15 \mu\text{s}$ in mixture I is associated with a reduction of gas temperature in the bubble that is caused by the evaporation. This considerably increases the induction period and, combined with acoustic losses in the bubble, causes extinction of the chemical reaction.

The foregoing calculation revealed an unexpected effect of the inert diluter (argon) on the gas temperature fluctuation in the cryogenic mixture I. Introduction of an equal mole fraction of argon into the gaseous phase (hydrogen) with the same ratio M_L/M_0 results in a sudden gas temperature increase due to the increase of M_0 , with a consequent growth of the evaporated oxygen mass M_L . The hydrogen–oxygen ratio in the gaseous phase approaches the stoichiometric one. In addition, the increase of the gaseous argon fraction in a bubble always results in an increase in the final temperature in mixture I and a decrease in the final temperature in mixture II. The pressure and the

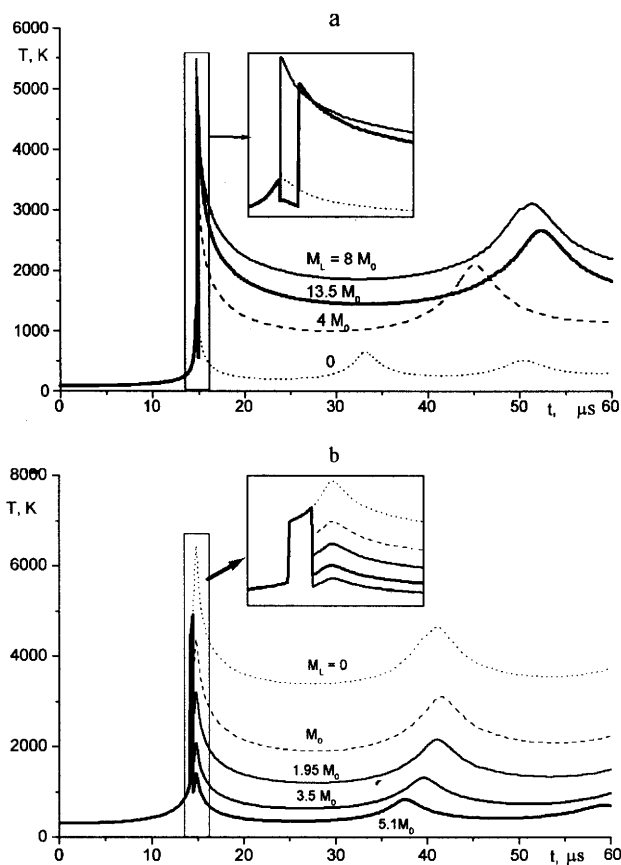


FIGURE 15.3.27 Temperature variation vs time for different M_L . (a) mixture I, $t_{inj} = 14.7 \mu\text{s}$; (b) mixture II, $t_{inj} = 14.5 \mu\text{s}$.

compression degree in the two cases decrease and the temperature at the first oscillation increases.

Figure 15.3.29 shows temporal variation of the ratio of specific heats γ for various M_L for mixture II at $t_{inj} = 14.5 \mu\text{s}$, which shows that the evaporation causes strong variations in the magnitude of $\gamma(t)$. One of the advantages of the suggested approach is that it allows one to account for these variations.

15.3.2.3.2 Continuous Evaporation

In real conditions the microdrops do not evaporate instantly. In order to take this effect into account, let us assume that a number of liquid microdrops with

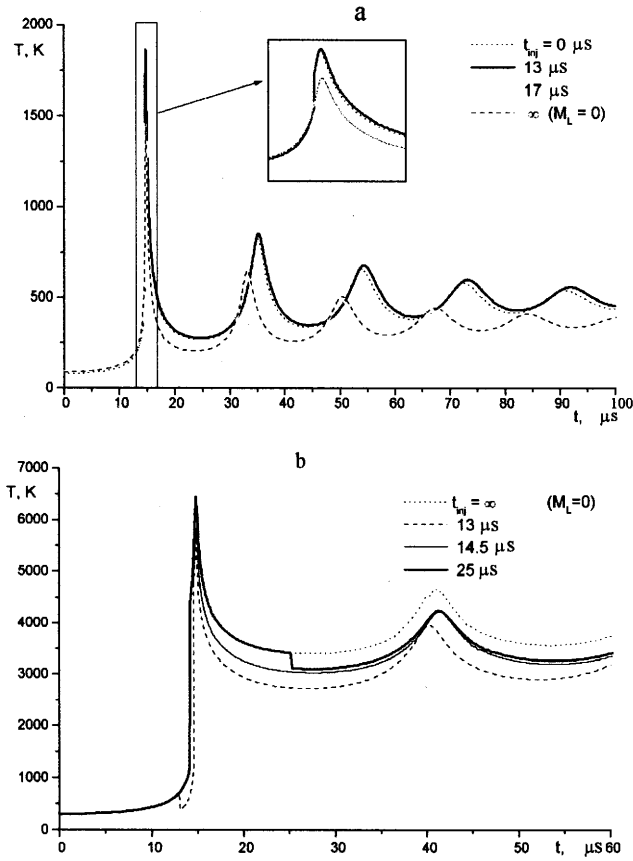


FIGURE 15.3.28 Temperature dynamics vs time for various t_{inj} : (a) mixture I ($M_L/M_0 = 0.4$); (b) mixture II ($M_L/M_0 = 5.1$).

diameter D_0 and the total mass of M_L are formed inside the bubble at time t_{inj} . The continuous evaporation of the microdrops is simulated by the instant evaporation of the mass Δm at each integration step. The latter mass is determined by the actual diameter of the microdrop D (Lambarais and Koms, 1966),

$$\frac{dD}{dt} = -k' \frac{Nu}{4D},$$

where the vaporization coefficient k' is given by

$$k = \frac{8k_g}{\rho_L c_p} \ln \left(\frac{L + c_p \Delta T}{L} \right).$$

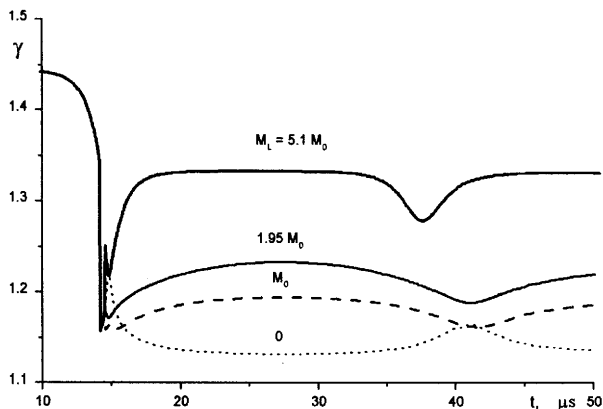


FIGURE 15.3.29 Temporal variation of the specific heat capacities ratio γ (mixture II).

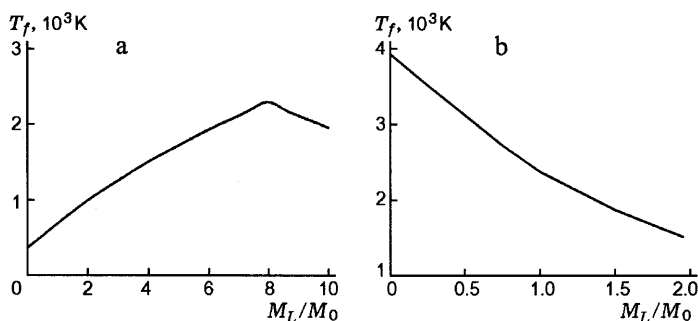
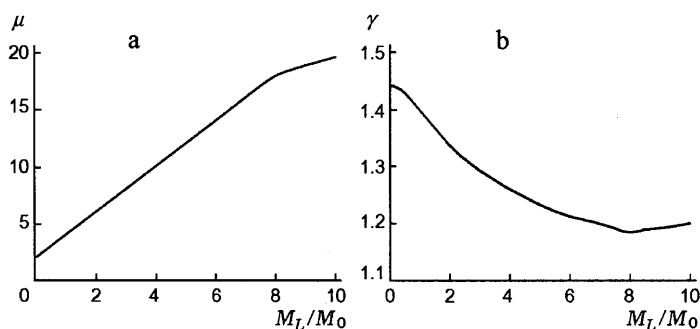
Here k_g is the heat conductivity of the vapor, c_p is the heat capacity at a constant pressure, L is the latent heat of evaporation, ρ_L is the liquid density, $Nu = hD/k_g$ is the Nusselt number, and h is the heat transfer coefficient. If the gas temperature in the bubble becomes less than the initial one, the microdrops do not evaporate ($dD/dt = 0$).

The values of the parameters of the jumps and their time dependencies were calculated using the same method and assumptions as in for the case of instantaneous microdrop evaporation. Calculation of the time dependence of mass of the microdrops (with initial diameters of 1.5 and 15 μm at $t_{inj} = 13 \mu\text{s}$ and $M_L/M_0 = 0.45$) shows that the microdrops with the size of the order of 1 μm evaporate practically instantly (faster than the bubble oscillation period). However, transient evaporation of the rather large microdrops may be important.

Figure 15.3.30 shows the dependence of the final (bubble oscillations were damped) gas temperature T_f on M_L/M_0 for mixture I at $t_{inj} = 14 \mu\text{s}$ and $D_0 = 0.75 \mu\text{m}$ (Fig. 15.3.30a) and for mixture II at $t_{inj} = 14 \mu\text{s}$ and $D_0 = 1 \mu\text{s}$. (Fig. 15.3.30b)

Inspection of Fig. 15.3.30 shows that the mass increase of the injected liquid in mixture II leads to a monotone decrease of the final temperature T_f that causes a weak monotone increase of the final value of μ and γ . In this case the value of μ peaks to μ_{\max} at $M_L/M_0 = 1$ and remains constant. However, for $T_f > T_0$, there are values of parameters t_{inj} and D_0 (e.g., $t_{inj} \approx 15 \mu\text{s}$ and $D_0 \approx 1 \mu\text{m}$) at which the final gas temperature decreases practically to its initial value.

In mixture I the dependencies of T_f , μ , and γ on M_L/M_0 are essentially different. When the ratio M_L/M_0 increases, T_f passes through the maximum

FIGURE 15.330 Dependence of T_f versus M_L/M_0 : (a) mixture I; (b) mixture II.FIGURE 15.331 The dependence of the final values of μ (a) and γ (b) on M_L/M_0 for mixture I: $t_{inj} = 13 \mu\text{s}$, $D_0 = 1 \mu\text{m}$.

(see Fig. 15.330a), which corresponds to the stoichiometric ratio between the fuel and the oxidizer; γ passes through a minimum; and μ increases by several times (see Fig. 15.331).

The dependencies of T_f on the microdrop diameter at fixed values of M_L/M_0 and t_{inj} in mixtures I and II are qualitatively identical. T_f increases monotonically with increasing value of D_0 , tending to the constant values of 800 and 3200 K, respectively. In the absence of evaporation the indicated limits of T_f are equal to 360 and 3900 K, respectively.

15.3.2.4 SHOCK WAVES IN REACTIVE BUBBLY LIQUIDS

15.3.2.4.1 Experimental Study

The propagation of shock waves in a liquid column with a chain of bubbles filled with a reactive gaseous mixture was studied experimentally by Hasegawa

and Fujiwara (1982). The parameters of the shock waves and the bubbles in the chain were selected so that the first bubble that was located on the path of the shock wave consumed the wave energy almost completely and therewith collapsed and attained the mixture ignition temperature. The chemical reaction caused a bubble explosion and a radiation of a secondary shock wave, which interacted with the subsequent bubble similarly to the incident wave. This effect was called a *bubbly detonation*.

Clearly, the propagation velocity of this wave is determined not by the equilibrium velocity in the homogeneous two-phase medium, but by the collapse time of the bubbles in the chain that initiates a detonation in the gaseous mixture.

Experimental studies by Pinaev and Sychev (1986a, 1987) of the shock wave structure in reactive bubbly liquids (the whole cross section of a shock tube was filled with bubbles) revealed the existence of a self-sustained wave propagation as a single wave packet with a propagation velocity D larger than that appropriate to shock waves in nonreactive bubbly liquids with the same volumetric gas concentration.

There is an upper and a lower limit in the volumetric bubble concentration ($>0.5\%$ and $<8\%$) for the initiation of a detonation (Pinaev and Sychev, 1986a). Outside this range a detonation does not occur. Experiments with an acetylene–oxygen mixture $C_2H_2 + 2.5O_2$ showed that for bubbles with a diameter 3–4 mm and with a volumetric concentration $k \approx 6\%$, the detonation has the following parameters: The pressure in the wave packet varies in the range 15 to 40 MPa, the initiation zone length reaches 6–7 cm, the luminescence time is 2–3 μs , the wave duration of the bubbly detonation is 100–200 μs , and its velocity is about 560 m/s.

Pressure oscillograms recorded at different distances from the location of the incident wave penetration into the bubbly medium are shown in Fig.

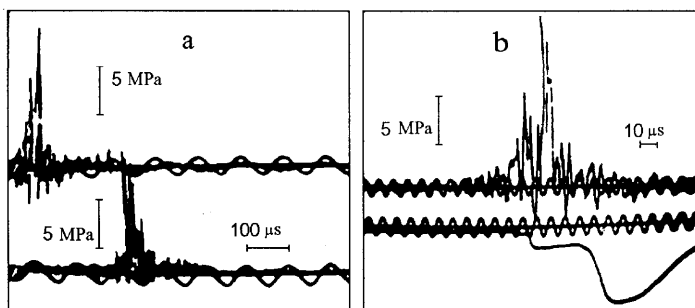


FIGURE 15.3.32 Experimental oscillograms of the bubbly detonation waves (a) and luminescence (b).

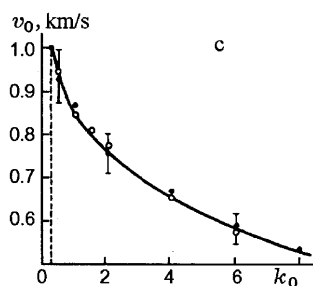


FIGURE 15.3.33 Dependence of the wave velocity on the volume concentration of the bubbly gas.

15.3.32 (the data by Pinaev and Sychev) for mixture volume concentration $k_0 = 0.02$ and bubble diameters $d_0 = 2\text{--}4$ mm. Inspection of Fig. 15.3.32 shows that the bubbly detonation propagates at a velocity of about 760 m/s. The luminescence behind the front of the wave in exploding reactive gas bubbles is recorded at the lower oscillogram (Fig. 15.3.32b).

Figure 15.3.33 shows the attenuation of the wave velocity as a function of k_0 . The lower (in concentration) limit of a detonation occurrence is shown by the dashed line.

Later investigations by Beylich and Gulhan (1989) and Scarinci *et al.* (1991) confirmed the results by Pinaev and Sychev (1986a, 1987).

15.3.2.4.2 Initiation Mechanisms in Liquid Explosives and Combustible Mixtures under Pressure

A comparison of the studies on the detonation of condensed explosives, on explosions in containers with fuel under pressure, and on possible regimes of the bubbly detonation allowed us to conclude that these problems can be analyzed in the framework of one approach (Kedrinskii *et al.*, 1996, 1997; Kedrinskii, 1995, 1997).

Nonuniformity of liquids and cavitation phenomena have a direct relationship to detonation initiation in liquid explosives (models of *hot spots* and *fractional impact*) (Bowden and Yoffe, 1958; Andreev, 1958; Johansson, 1958; Dubovik and Bobolev, 1978; Campbell *et al.*, 1961; Field *et al.*, 1992; and Roberts and Field, 1993). Explosions in volatile and combustible liquids stored under pressure in containers as well as formation of gas–droplet mixtures during disintegration of these liquids by cavitation (e.g., steam explosions, volumetric detonation) (Barbone *et al.*, 1994; Hill and Sturtevant, 1989; and Chaves *et al.*, 1985) have the same physical mechanisms.

We will consider two different aspects of the behavior of liquids with microinhomogeneities under pulse loadings:

1. *Hydrodynamic aspect*, that is, the mechanism of cavitation initiation in a liquid by strong rarefaction waves
2. *Wave aspect*, that is, initiating a bubbly detonation during interaction of shock and rarefaction waves.

Cavitation in volatile and combustible liquids occurs after sudden depressurization of containers and reservoirs and frequently yields catastrophic destruction. These phenomena are also related to steam explosions. These effects were investigated in numerous studies, for example, by Barbone *et al.* (1994), Hill and Sturtevant (1989), and Chaves *et al.* (1985). Two mechanisms (Barbone *et al.*, 1994) in these phenomena are responsible for their destructive action:

- (a) Eruption of compressed liquids in the form of two-phase cavitating jets, their spreading with the formation of a gas-droplet cloud, and the formation of volume detonation charge
- (b) Propagation of a rarefaction wave inside the liquid fuel after the partial depressurization of the container initiates explosive boiling and the pressure inside the container increases by several times.

Kedrinskii (1995, 1997) and Kedrinskii *et al.* (1997) proposed a new mechanism for the generation of high pressures in the compressed volatile and combustible liquids. It was suggested that when the container is filled, a large number of bubbles containing an air-fuel vapor mixture, which can be ignited by adiabatic compression, are formed.

When a container moving at a high velocity experiences a sudden deceleration, for example, as a result of an impact, compression waves in the liquid can initiate a bubbly detonation wave. Conversely, depressurizing the container forms rarefaction waves whose interaction results in, as shown subsequently, some unexpected effects.

The influence of inhomogeneities on the detonation initiation mechanism in liquid explosives was suggested long ago. Thermal mechanism of explosion initiation in liquid HE and identification of small gas bubbles as possible heat sources of explosion (*hot-spots model*) were discussed by Bowden and Yoffe (1958). Andreev (1958) and Johansson (1958) suggested that small particles or gaseous phase of HE in bubbles are the most plausible reason for detonation initiation. Dubovik and Bobolev (1978) studied the mechanism by which drops or vapor in the bubbles affect the formation of *hot-spots*. They estimated

the adiabatic induction period t_i and the critical size d_0 such that a drop will be heated during the bubble collapse:

$$d_0 \leq \pi(\xi_0 \tau_R)^{1/2}, \quad t_i = \frac{c_p B T_*^2}{A Q E_a} \exp(E_a / B T_*).$$

Here T_* is the liquid drop temperature, E_a and A are the activation energy and the pre-exponential coefficient for the monomolecular reaction, Q is the thermal effect of the reaction, B is the universal gas constant, c_p is the specific heat at constant pressure, τ_R is the bubble collapse time, and ξ_0 is the coefficient of thermal conductivity. The last estimate is valid only when T_* is constant over the time t_i .

Also, the fractional impact mechanism was considered whereby the detonation is initiated by a sequence of shock waves. The first wave reflects from the free surface of the liquid and initiates cavitation. Then the second shock wave compresses the bubbles by forming *hot-spots* and initiates a detonation.

Experimental validation that the mechanism of shock initiation is determined by the interaction of the waves with micro inhomogeneities and the formation of *hot spots*, was performed by Campbell *et al.* (1961). The propagating shock wave is amplified until the energy released behind the front is sufficient to initiate detonation.

The interaction of strong shock waves with an amplitude of about 3 GPa with a single cavity and an array of collapsing bubbles in a reactive emulsion was studied by Field *et al.* (1992). They observed light flashes caused by the impact of a cumulative jet at the far wall of the cavity and by collapse of gas petals formed in the process. Roberts and Field (1993) showed that inhomogeneities of diameter 1.5 mm in the sample in the vicinity of the impact point are the sources of the reaction initiation.

The preceding results allow the following conclusions to be drawn:

- The shock sensitivity of the liquid explosives depends on the properties of microinhomogeneities
- A detonation in liquid explosives develops only when these inhomogeneities are formed.

Analysis of the hot-spots model with detonating bubbles leads to the conclusion that the mechanisms that determine the latter phenomena and bubbly detonations are essentially the same. Let us consider some examples of wave processes and wave amplification that can substantiate the validity of this claim.

15.3.2.4.3 Formation and Propagation of Bubbly Detonation Waves: An Instant Energy Release Model

Let us use a pressure-nonequilibrium two-phase model for a reactive bubbly liquid (Kedrinskii and Mader, 1987):

$$\begin{aligned} \frac{d\rho}{dt} + \rho \operatorname{div} v &= 0 \\ \frac{dv}{dt} + \frac{\nabla p}{\rho} &= 0 \\ \rho &= (1 - k)\rho_l, \quad k = k_0(R/R_0)^3 \\ R \frac{d^2 R}{dt^2} + \frac{3}{2} \left(\frac{dR}{dt} \right)^2 &= \rho_l^{-1} (\delta p_g - p). \end{aligned} \quad (15.3.22)$$

Assume that the coefficient δ in the Rayleigh equation equals unity until the gaseous mixture in a bubble is adiabatically compressed to the chemical reaction initiation temperature. In this case of *adiabatic explosion at a constant volume*, the pressure increases to the value determined by the relation

$$p = \rho_*(\gamma_* - 1)Q_{ex},$$

where Q_{ex} is the explosion heat. This expression obtained from the condition that all the energy released in the reaction is transformed into the internal energy of its products, the pressure in the bubble instantly increases to this value, and the adiabatic exponent γ changes instantly to 1.25. Further evolution occurs under the new conditions without modifications in the model. Note that this analysis of the problem without the equation of the chemical kinetics using a simplified model (Kedrinskii, 1968b) is based on the assumption that a liquid in the bubbly medium is incompressible,

$$\begin{aligned} \frac{d^2 \zeta}{d\eta^2} + \frac{v}{\eta} \left(\frac{d\zeta}{d\eta} \right) - \zeta &= 0 \\ \frac{\partial^2 k}{\partial t^2} &= -\frac{3k^{1/3}}{\rho_l R_0^2} (\delta p_g - p) + \frac{1}{6k} \left(\frac{\partial k}{\partial t} \right)^2, \end{aligned} \quad (15.3.23)$$

where $\zeta = -p_g$, $\eta = \alpha y^{1/2}$, $\alpha = \sqrt{3k_0/R_0^2}$, $y = R/R_0$, and $v = 0, 1, 2$, as noted previously, specifies the geometry of the problem.

The first equation in Eqs. (15.3.23) provides an analytical relation between the pressure p in the bubbly liquid and the volumetric gas concentration k . In the one-dimensional case ($v = 0$) this relation becomes

$$\zeta = Ae^{-\eta} + Be^{\eta}.$$

Figure 15.3.34 demonstrates the process of the formation of a bubbly detonation wave calculated by Eqs. (15.3.23) for $k_0 = 0.05$. Here

$y_0 = 5$ MPa, $x_0 = 0.6$ cm, and the spatial pressure distribution $p(x)$ is calculated for $t = 136, 256, 348$, and $400 \mu\text{s}$. Note that at $t \geq 400 \mu\text{s}$ the wave attains a quasi-stationary regime is attained.

Comparison of the parameters and the structure of the bubbly detonation wave (see Fig. 15.3.35) shows that the model performs quite well.

Kedrinskii and Mader (1987, 1993) suggested the following approximate formula to determine the propagation velocity of a bubbly detonation wave:

$$D_{\text{bubl}} \approx \lambda \sqrt{\frac{\rho_* (\gamma^* - 1) Q_{\text{ex}}}{\rho_0 k_0}}. \quad (15.3.24)$$

Here the asterisk denotes detonation products; λ a coefficient calculated from the condition that Eq. (15.3.24) coincides with the experimental data at a certain point (Fig. 15.3.36). In deriving Eq. (15.3.24) we have used the notion

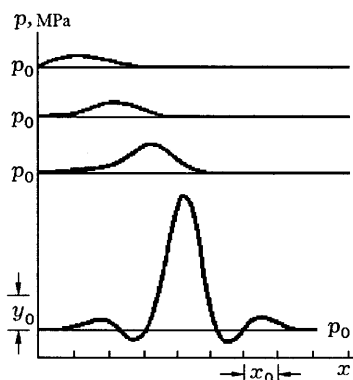


FIGURE 15.3.34 Dynamics of the formation of a bubbly detonation wave.

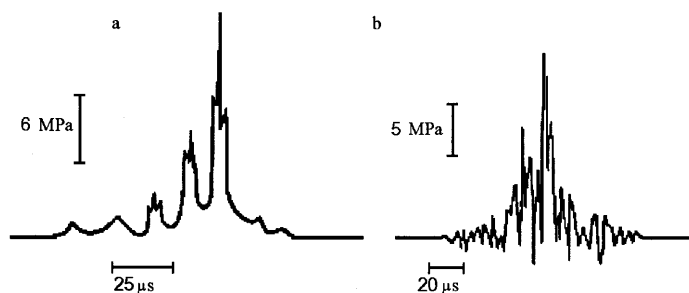


FIGURE 15.3.35 Comparison of calculated (a) and experimental (b) pressure oscillograms for the bubbly detonation wave.

of the *collective collapse time* t_* of a bubble layer with width l introduced by Kedrinskii (1968b):

$$t_* \approx 0.9R_0 \sqrt{\frac{\rho_0}{p_{sh}}} \exp\left(\frac{1}{2} \sqrt{\frac{3k_0}{R_0^2}}\right).$$

The function $D_{bubl}(k_0)$ (see Fig. 15.3.36) is calculated for the mixture $C_2H_2 + 2.5O_2$ and an explosion energy of $Q = 15.2 \text{ MJ/m}^3$ at $\gamma_* = 1.15$, $\lambda^2 \approx 0.16$, and $\rho_* = \rho_{g0}(R_0/R_*)^3$.

Suppose that the reactive bubbly liquid can be considered as a special type of a condensed explosive. Then the wave amplitude p_{bubl} can be estimated from

$$p_{bubl} = \frac{(\rho - \rho_0)\rho_0}{\rho} D_{bubl}^2,$$

where $\rho = \rho_{liq}(1 - k_0 k_*)$ and $\rho_0 = \rho_{liq}(1 - k_0)$, $k_* = R_*/R_0)^3$. Then

$$p_{bubl} = \rho_{liq} k_0 (1 - k_*) D_{bubl}^2.$$

If D_{bubl} is taken from Eq. (15.3.24),

$$p_{bubl} \approx \lambda^2 \rho_* (1 - k_*) (\gamma_* - 1) Q_{ex}.$$

The obtained result is in compliance with the established weak dependence of the detonation wave amplitude on the concentration.

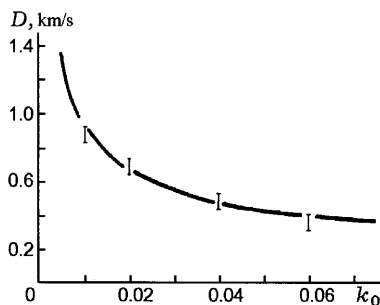


FIGURE 15.3.36 Dependence of a bubbly detonation wave velocity on the gas concentration k_0 .

15.3.2.5 INITIATION, FORMATION, AND COLLISION OF BUBBLY DETONATION WAVES: “HOT-SPOTS” MECHANISM

In Lagrangian coordinates the dimensionless equations (15.3.22), supplemented by the kinetic model of the adiabatic explosion of the reactive gaseous mixture at a constant volume (the bimolecular kinetics; Todes, 1933),

$$\frac{dn}{dt} = A\sqrt{T}e^{-E_a/BT}(a-n)^2$$

reads

$$\begin{aligned} \frac{\partial \rho}{\partial t} &= -\rho^2 \frac{\partial u}{\partial s}, \quad \frac{\partial u}{\partial t} = -\frac{\partial p}{\partial s} \\ \beta \frac{\partial S}{\partial t} + \frac{3}{2} S^2 &= C_1 \frac{T}{\beta^3} - C_2 \frac{S}{\beta} - p, \quad \frac{\partial \beta}{\partial t} = S \\ \frac{\partial T}{\partial t} &= \eta \frac{\partial N}{\partial t} + \delta(\gamma - 1) \text{Nu} \frac{\beta^3(1-T)}{T} - 3(\gamma - 1) \frac{TS}{\beta} \\ \frac{\partial N}{\partial t} &= \zeta \frac{1}{\beta^3} \sqrt{T} e^{-\alpha/T} (1-N)^2 \\ p &= 1 + \frac{\rho_0 c_0^2}{n p_0} \left[\left(\frac{\rho}{1-k} \right)^n - 1 \right], \quad k = \frac{k_0}{1-k_0} \rho \beta^3 \\ \text{Pe} &= C_3(\gamma - 1) \frac{\beta|S|}{|1-T|}, \quad \text{Nu} = \begin{cases} \sqrt{\text{Pe}}, & \text{Pe} > 100 \\ 10, & \text{Pe} \leq 100 \end{cases} \\ C_1 &= \frac{\rho_{g0} T_0 B}{p_0 M}, \quad C_2 = \frac{4\mu}{R_0 \sqrt{p_0} \rho_0}, \quad C_3 = \frac{12R_0 \sqrt{p_0/\rho_0}}{v}. \end{aligned} \tag{15.3.25}$$

Here ρ is the ratio of the density to its initial value, $N = n/a$ is the relative fraction of the reacted components in the gaseous mixture, a is the initial concentration of the components, n is the number density of the molecules formed during reaction, T is the ratio of the temperature of gas mixture to its initial value T_0 , $\beta = R/R_0$, α is the relative activation energy, ζ is a constant depending on the initial parameters and the mixture composition, $\eta = Q/c_m T_0$ is the specific reaction heat, E_a is the activation energy, and B is the gas constant.

The coefficient δ in the temperature equation is used to turn on the heat transfer and to change its rate. The need for such a tuning coefficient is due to the approximate relations used for the Nusselt and Peclet numbers.

Now we present numerical results obtained for a hydrogen–oxygen mixture with the following parameters: $\alpha = 51.5$, $\zeta/R_0 = 2.7 \times 10^9$, $\eta = 70$. Since there is no available information on the initial state of the microinhomogeneities in liquid explosives and flammable liquids, in the calculation we assumed that they are close to those of water.

Figure 15.3.37 shows spatial distribution of the pressure and other parameters in a bubbly detonation wave. Here p is the mean pressure in a bubbly detonation wave, R/R_0 is the relative radius of the bubbles, and S is their radial velocity.

It is known that when a wave propagates through a bubbly liquid it is attenuated because of losses due to the velocity induced in the liquid and the increase of the internal energy of the gas in the bubbles during their compression. If the bubbles are filled with an explosive gaseous mixture, their adiabatic compression will initiate chemical reaction and the release of a large amount of energy. In this case a compression wave will be radiated, and it compensates the energy losses of the incident wave until a self-sustaining regime of wave propagation is attained.

Calculations show that Eqs. (15.3.25) adequately describe the formation and the propagation of a bubbly detonation wave. Its amplitude is unstable for the volume concentration of a gaseous phase $k_0 = 5 \times 10^{-3}$ in agreement with the experimental data, and it varies in the range 80 to 100 MPa.

When analyzing wave propagation, the question arises about the threshold values of the wave amplitude required to initiate a detonation in a reactive bubbly liquid. Figure 15.3.38 partially provides the answer to this question by illustrating a collision effect of weak waves having an amplitude 0.4 MPa. Such waves alone are incapable of initiating the detonation. However after their collision the required conditions may be met. Here the chemical reaction in the gaseous phase is initiated at the collision plane ($t = 361 \mu\text{s}$, see the sharp increase of T) with an amplification of the incident wave (before reaction) up to 2 MPa. The bubbly layer explodes from inside.

In a result of explosion in the vicinity of a collision plane, the mean pressure p increases up to 8 MPa during $2 \mu\text{s}$ and a reflected wave becomes the detonation wave whereby the pressure attains 60 MPa at a distance of 5 cm from the center.

A surprising effect has been found when numerically analyzing rarefaction wave collisions (Kedrinskii *et al.*, 1996). The goal of the calculations was to analyze waves in a container with a flammable liquid after its partial depressurization as well as the pulse loading the liquid explosive with a free boundary. In the latter case the compression wave initiated by the impact interacts with the free surface and is reflected as a rarefaction wave into the sample.

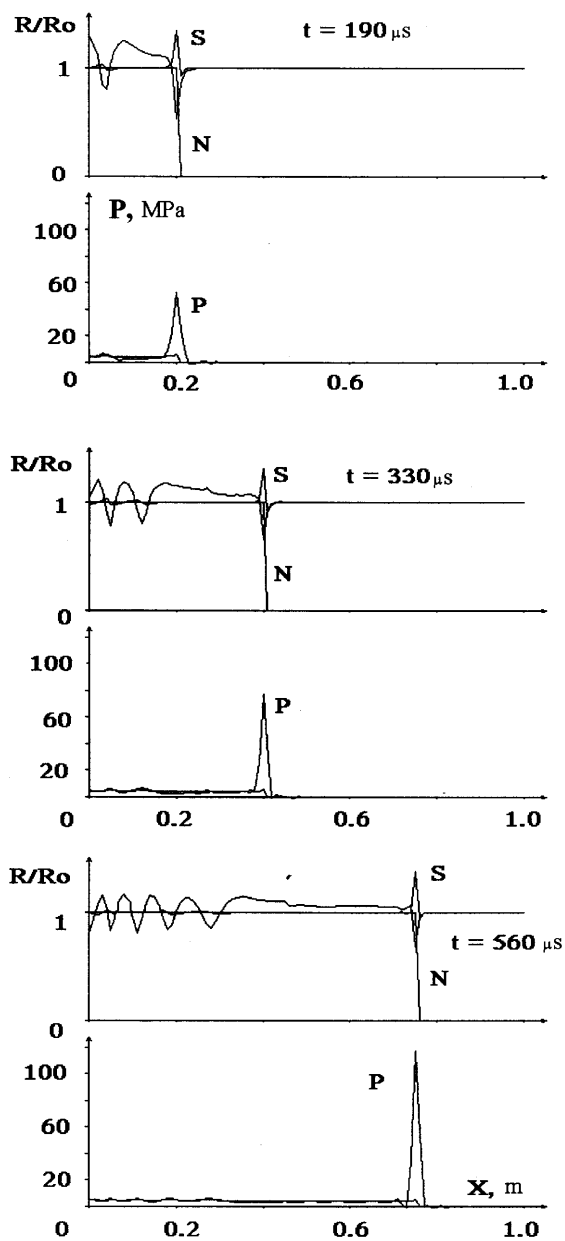


FIGURE 15.3.37 Formation of a bubbly detonation wave.

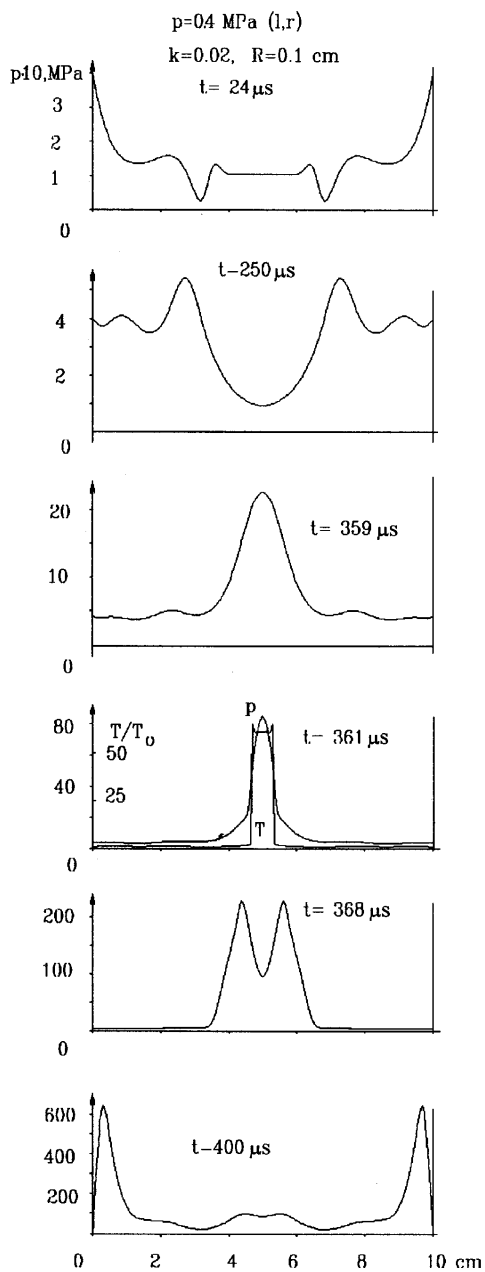


FIGURE 15.3.38 Initiation of explosive process in a reactive media as a result of collision of weak shock waves.

The calculation (Fig. 15.3.39) shows a possibility of bubbly detonation wave initiation at the sample center after the rarefaction wave collision.

This effect can be explained by the transformation of the rarefaction wave when it propagates through a liquid with microinhomogeneities and with the cavitation caused by the wave. Oscillations with a positive phase occur behind the front of the rarefaction wave. After the collision of the waves, they heat the gaseous mixture up to the ignition temperature. Note that the positive phase amplitude of a single rarefaction wave is insufficient for initiating ignition.

According to the calculations, the wave collision (Fig. 15.3.39) happens within 8.5 μs after the onset of the propagation at the center of a 2-cm long sample. The reflected waves therewith become bubbly detonation waves with an amplitude that, at 17.5 μs , reaches almost 40 MPa in the vicinity of the free surface.

The results presented in Figs. 15.3.37, 15.3.38, and 15.3.39 suggest that the collision of the shock waves (and their focusing) deserve special consideration as efficient shock amplification methods.

15.3.2.5.1 Shock Wave Focusing in Reactive Bubbly Liquids

As discussed earlier, the heterogeneous inclusions in liquids play a principal role in initiating explosions (see, e.g., Barbone *et al.*, 1994; Field *et al.*, 1992; Kedrinskii, 1995, 1997; Kedrinskii *et al.*, 1997, 1998a, 1998b).

The reactive bubbly liquid attracts the attention as a probable source of a power acoustic radiation and can be considered as a physical analogy of a pumping in laser systems (Kedrinski *et al.*, 1998b, Zautzak, 1995).

One can attain a high level of shock wave amplitude amplification by focusing them in a reactive bubbly media.

The governing system of equations describing the cylindrical wave focusing comprises two sets of equations:

- Conservation laws for the mean values of p , ρ , u :

$$\begin{aligned}\frac{\partial u}{\partial t} &= -\frac{1}{\rho_0} \left(\frac{x(r, t)}{r} \right)^2 \frac{\partial p}{\partial r} \\ \frac{\partial x}{\partial t} &= u \\ \frac{1}{\rho} &= \frac{1}{\rho_0} \left(\frac{x(r, t)}{r} \right)^2 \frac{\partial x}{\partial r}\end{aligned}\tag{15.3.26}$$

- A set of kinetic equations [see Eq. (15.3.25)] describing the time-dependent equation of state, heat exchange, and chemical reaction kinetics.

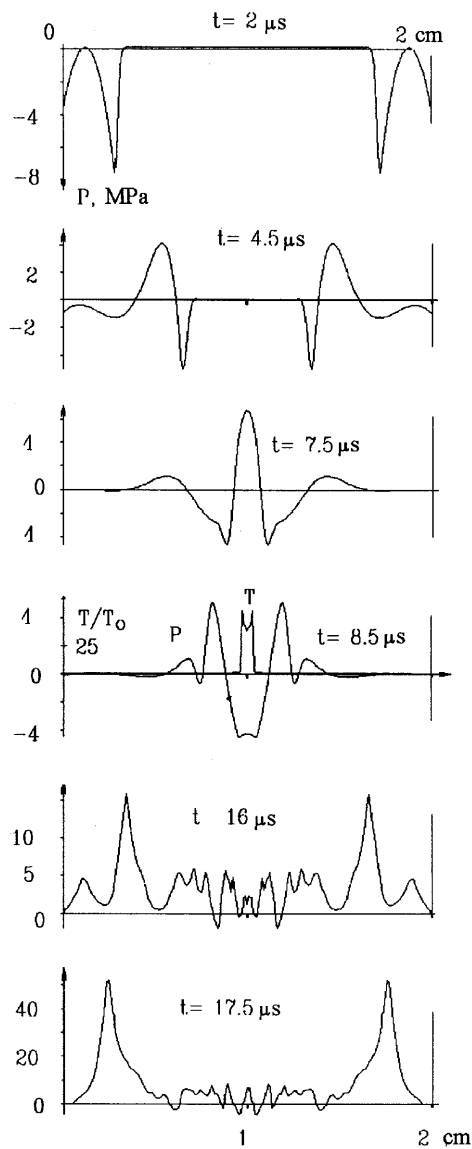


FIGURE 15.3.39 Ignition of chemical reaction in bubbles at the “rarefaction–rarefaction” wave interaction: $k_0 = 10^{-3}$, $R_0 = 0.01$ cm, $d = 2$ cm, $p_{l,r} = 100$ bar, $\tau = 3$ μs.

The formation of the self-sustained wave regime requires a certain time and a distance that depends on k_0 . In the preceding examples the diverging wave amplification was shown to be sufficient to consider the bubbly detonation as an initiation mechanism for explosions in containers with fuel and as a powerful source of a hydroacoustic signal. Note that a bubbly liquid is more interesting as an explosive acoustic source similar to one that was shown in Figs. 15.3.38 and 15.3.39.

Wave focusing in reactive bubbly media enhances the foregoing effects, as is illustrated by the following two examples (in the calculations the same parameters are taken: $\alpha = 51.5$, $\zeta/R_0 = 2.7 \times 10^9$, $\eta = 70$). The first example (Fig. 15.3.40) is the focusing of a short shock wave with an amplitude

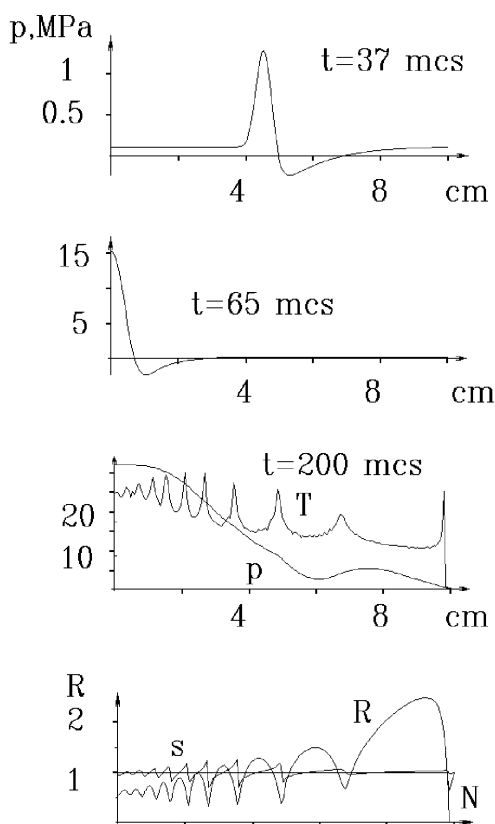


FIGURE 15.3.40 Short shock wave focusing with initiating a detonation in the vicinity of the focus: $k_0 = 10^{-3}$, $R_0 = 0.1 \text{ cm}$, $p_b = 5 \text{ MPa}$.

$p_b = 5$ MPa; the duration of the positive pressure phase is $t_+ = 5 \mu\text{s}$ and that of the negative phase is $t_- = 15 \mu\text{s}$. This profile of the shock wave simulates the wave generated by an underwater explosion. The reactive gaseous phase concentration in the bubbly medium was set to be lower than the critical value, $k_0 = 0.001$. The wave was focused from a distance of $r = 10$ cm.

Calculations showed that at first, the wave attenuated and its amplitude decreased to 1.2 MPa (see Fig. 15.3.40, $t = 37 \mu\text{s}$). In this case the incident wave was found to be incapable of initiating a detonation. In the vicinity of the focus the wave amplitude increased to 15 MPa ($t = 65 \mu\text{s}$), which turned out to be sufficient to compress the bubbles to the ignition temperature, that is, the onset of a chemical reaction. The detonation wave initiated in the focus propagated outward thereafter. The pressure produced by the bubble explosion was greater than 30 MPa (Fig. 15.3.40, $t = 200 \mu\text{s}$) and did not change until the detonation wave reached the external boundary.

If the volumetric concentration of the gaseous phase was increased by one order of magnitude, $k_0 = 10^{-2}$, $R_0 = 0.2$ cm, the situation changed completely. With a lower incident wave amplitude (and the same parameters of its positive and negative phase) focusing allowed initiating the detonation at the boundary at the moment the initiating wave reached the focus line.

Figure 15.3.41 (for $p_b = 3$ MPa and a focusing radius $r = 5$ cm) shows the spatial pressure distribution for different times. It is seen from the figure that at $t = 26 \mu\text{s}$ (with a time delay in the collapsing bubbles until the ignition temperature of the mixture is attained) a bubbly detonation is initiated at the periphery (the temperature jump is shown at the right of Fig. 15.3.41) and the shock wave that causes the detonation reaches the focus at $t = 32 \mu\text{s}$: the wave amplitude increases by a factor of 5. However, the bubble concentration in this example is significantly higher and the focused wave amplitude is too low to initiate detonation at the focus.

The arriving bubbly detonation wave is focused and its amplitude at $t = 60 \mu\text{s}$ (at a distance 2 cm from the axis) attains 40 MPa. The calculations show that the detonation wave amplitude attains a very large value of 10^3 MPa in the vicinity of the axis. Obviously, initiation of such stresses in the container may lead to catastrophic effects.

Note that the high pressures attained during the focusing process are the consequence of the inertial effects in the bubbly oscillations and the over compression of the detonation products. The temperature of the detonation reaches the values of $(1.5-2) \times 10^4$ K, which require a modification of the equation of state [Eq. (15.3.26)].

Nevertheless, the preceding experimental data, models, statements and computational results demonstrate that many physical phenomena arising during pulse loading of liquids can be analyzed using the theory of wave propagation in nonuniform media.

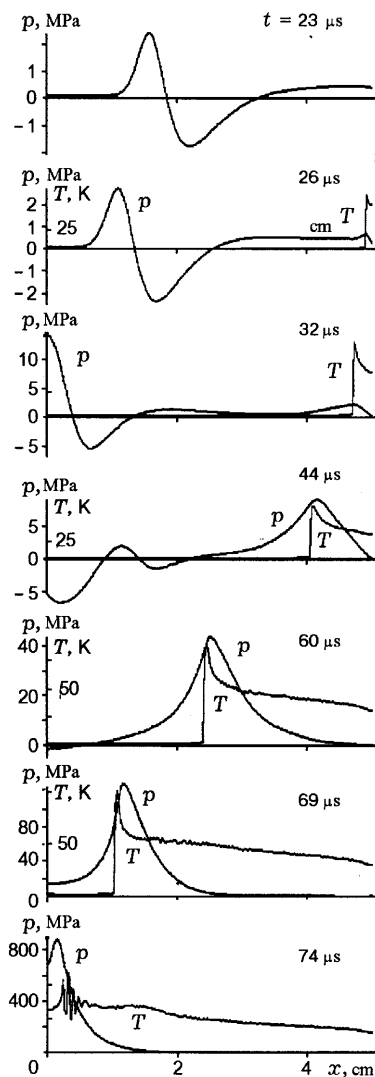


FIGURE 15.3.41 Initiation and focusing of a bubbly detonation wave ($k_0 = 10^{-2}$, $R_0 = 0.1$ cm, $p_b = 3$ MPa).

REFERENCES

- Andreev K. K. 1958 Some consideration on the mechanism of initiation of detonation in explosive. Proc. Roy. Soc. Lond., 246, 257–267.

- Barbone R., Frost D., Makris A., and Nerenberg J. 1994 Explosive boiling of a depressurized volatile liquid, *Proc. IUTAM Symp. Waves in Liquid-Gas and Liquid-Vapor Two-phase Systems*, Kyoto, Japan, Kluwer Acad. Publ., 315–324.
- Bazhenova T. V. and Soloukhin R. I. 1959 Field of pressures, arising in water at electric discharge, In: *Physic Gasdynamics*. Russian Acad. Sci., Energy Inst., Moscow, Russia.
- Beylich A. E. and Gulhan A. 1989 Waves in reactive bubbly liquids, *Proc. IUTAM Symp. Adiabatic Waves in Liquid-Vapour Systems*, Gottingen, Germany, 39–48.
- Book D. and Lohner R. 1989 Quatre foil instability of imploding cylindrical shock. *Proc. Intern. Workshop on Shock Wave Focusing*. K. Takayama (Ed.), Sendai, Japan, 193–206.
- Bowden F. P. and Yoffe A. D. 1958 Fast Reaction in Solid, Butterworths Sci. Publ., London.
- Campbell I. J. and Pitcher A. S. 1958 Shock waves in a liquid containing gas bubbles, *Proc. Roy. Soc. Lond.* A243, 534–545.
- Campbell A. W., Davis W. C., and Travis J. R. 1961 Shock initiation of detonation in liquid explosives, *Phys. Fluids*, 4 (4), 498–510.
- Chaves H., Lang H., Meier G., and Speckmann H. 1985 Flow of Real Fluids, *Lecture Notes in Phys.*, 235, Springer, Berlin.
- Demmig F., Gronig H., Kleine H., and Wallis H. 1993 Experiments and model computation of cylindrical shock waves with time-resolved deformation and fragmentation, *Proc. 19th Intl Symp. on Shock Waves*, Marseille, France, 4, 87–92.
- Dubovik A. V. and Bobolev V. K. 1978 Sensitivity of Liquids to Impact, Nauka, Moscow, Russia.
- Field J. E., Bourne N. K., Palmer S. J., and Walley S. M. 1992 Hot-spot ignition mechanisms for explosives and propellants, *Phil. Trans. Roy. Soc. Lond.*, 339, 269–283.
- Fomin P. A. and Trotsyuk A. V. 1995 Approximate calculation of chemical equilibrium gas isotrope, *Comb., Expl. & Shock Waves*, 31 (4), 59–62.
- Fox F. E., Curley S. R., and Larson G. S. 1955 Phase velocity and absorption measurements in water containing air bubbles, *J. Acoust. Soc. Amer.*, 27 (3), 534–539.
- Fujiwara K., *et al.* 1993 New methods for generating cylindrical imploding shock, *Proc. 19th Intern. Symp. on Shock Waves*. Marseille, France, 4, 81–86.
- Gasenko V. G., Nakoryakov V. Ye., and Schreiber I. R. 1979 The two-wave model of disturbance propagation in liquid with gas bubbles, *J. Appl. Mech. and Techn. Phys*, 20, 119–127.
- Gronig H. 1989 Past, present and future of shock focusing research, *Proc. Intern. Workshop on Shock Wave Focusing*, K. Takayama (Ed.), Sendai, Japan, 1–38.
- Hasegawa T. and Fujiwara T. 1982 Detonation in oxyhydrogen bubbled liquids, *Proc. 19th Int. Symp. Combust.*, Haifa, Israel, 675–683.
- Hill L. and Sturtevant B. 1989 An experimental study of evaporation waves in a superheated liquid, *Proc. IUTAM Symp. Adiabatic Waves in Liquid-Vapor Systems*, G. Meier, P. Thompson (Eds), 25–37.
- Hiroe T., Matsuo H., and Fujiwara K. 1993 A numerical study of explosive-driven cylindrical imploding shocks in solids, *Proc. 19th Int. Symp. Shock Waves*, Marseille, France, 3, 267–272.
- Iordansky S. V. 1960 On motion equations of liquid with gas bubbles, *J. Appl. Mech. & Tech. Phys.*, 1 (3), 102–110.
- Isuzukawa K. and Horiuchi M. 1993 Experimental and numerical studies of blast wave focusing in water, *Proc. 19th Int. Symp. Shock Waves*, Marseille, France, 3, 347–350.
- Itoh S., *et al.* 1993 Converging underwater shock waves for metal processing, *Proc. 19th Int. Symp. Shock Waves*, Marseille, France, 3, 289–294.
- Johansson C. H. 1958 The initiation of liquid explosives by shock and the importance of liquid break-up. *Proc. Roy. Soc. Lond.*, A246, 160–166.
- Kedrinskii V. K. 1961 Collapse of gas cavity in water by a shock wave. *M.Sci. Thesis*. St. Petersburg Polytech. Univ., St. Petersburg, Russia.

- Kedrinskii V. K. 1967 The features of spherical gas bubble dynamics in a liquid, *J. Appl. Mech. & Tech. Phys.*, 8 (3).
- Kedrinskii V. K. 1968a Propagation of disturbances in liquid with gas bubbles, *J. Appl. Mech. & Tech. Phys.*, 9 (4), 29–34.
- Kedrinskii V. K. 1968b Propagation of disturbances in liquid with gas bubbles. Ph.D. thesis. Novosibirsk, Inst. Hydrodynamics, Sib. Div. Russian Academy Sci.
- Kedrinskii V. K. 1975 Dynamics of cavitation zone at underwater explosion nearby free surface, *J. Appl. Mech. & Techn. Phys.*, 16 (5), 68–78.
- Kedrinskii V. K. 1980 Shock waves in a liquid containing gas bubbles, *Combust., Expl. & Shock Waves*, 16 (5), 14–25.
- Kedrinskii V. K. 1995 Bubbly cavitation in intense rarefaction waves and its effects, *Proc. 20th Int. Symp. Shock Waves*. Eds. B. Sturtevant, J. Shepherd, H. Hornung, Springer-Verlag, New York, 1, 107–120.
- Kedrinskii V. K. 1997 The role of cavitation effects in the mechanisms of destruction and explosive processes, *Shock Waves*, 7 (2), 63–76.
- Kedrinskii V. K. and Mader Ch. L. 1987 Accidental detonation in bubbly liquids, *Proc. 16th Int. Symp. Shock Tube & Waves*. H. Gronig (Ed.), 371–376.
- Kedrinskii V. K. and Mader Ch. L. 1993 On the velocity of bubble detonation, *Proc. 13th Int. Symp. Nonlinear Acoustics*, Bergen, Norway, 442–447.
- Kedrinskii V. K. and Soloukhin R. I. 1961 Collapse of gas cavity in water by a shock wave, *J. Appl. Mech. & Tech. Phys.*, 2 (1), 27–29.
- Kedrinskii V. K. and Zamarayev F. N. 1989 Wave amplification in chemically active bubbly media (plenary lecture), *Proc. 17th Int. Symp. Shock Tubes & Waves*, W. Yong (Ed.), 51–62.
- Kedrinskii V. K., Zamarayev F. N., and Mader Ch. 1990 Waves in reactive bubbly media, *J. Appl. Mech. & Tech. Phys.*, 31 (2), 20–26.
- Kedrinskii V. K., Vshivkov V. A., Dudnikova G. I., and Shokin Yu. I. 1996 Shock wave interaction in reactive bubbly media, *Phys.-Dokl.*, 41 (7), 300–303.
- Kedrinskii V. K., Vshivkov V. A., Dudnikova G. I., and Shokin Yu. I. 1997 Cavitation effect role for the mechanisms of fracture and large-scale explosive processes, *J. Comp. Tech.*, 2 (2), 63–77.
- Kedrinskii V. K., Shokin Yu. I., Vshivkov V. A., and Dudnikova G. I. 1998a Shock amplification by bubbly systems with energy release (SABSER), *Proc. 6th Japan–Russian Joint Symp. on Comp. Fluid Dyn.*, Nagoya, Japan, 58–61.
- Kedrinskii V. K., Vshivkov V. A., Dudnikova G. I., and Shokin Yu. I. 1998b Amplification of shock waves at collision and focusing in bubbly media, *Dokl.-Phys.*, 43 (7), 400–403.
- Kedrinskii V. K., Fomin P. A., and Taratuta S. P. 1999 Dynamics of single bubble in liquid in the result of chemical reactions and heat-mass exchange, *J. Appl. Mech. and Tech. Phys.*, 40 (2), 119–127.
- Kogarko B. S. 1961 On a model of cavitating liquid. *Dokl. Akad. Nauk SSSR*, 137 (6), 1331–1333.
- Kogarko B. S. 1964 One-dimensional transient fluid motion and resulting generation and development of cavitation, *Dokl. Akad. Nauk SSSR*, 155 (4), 779–782.
- Kuwahara M., *et al.* 1991 The problems of focused shock waves effect on biological tissues, *Proc. 18th Int. Symp. Shock Waves*, Sendai, Japan, 1, 41–48.
- Lamaraiss S. and Kombs L. 1966 *Detonation and Two-Phase Flow*, Academic Press, New York.
- Lyakhov G. M. 1959 Shock waves in multi-component media, *Izv. Akad. Nauk SSSR, Seriya: Mekh. & Mashinostroyeniye*, 1, 46–49.
- Lyapidevsky V. Yu. 1990 On bubbly detonation velocity, *Combust., Expl. & Shock Waves*, 26 (4), 138–140.
- Nagoya H., Obara T., and Takayama K. 1993 Underwater shock wave propagation and focusing in inhomogeneous media, *Proc. 19th Int. Symp. Shock Waves*, Marseille, France, 3, 439–444.

- Nakoryakov V. Ye., Pokusayev B. G., *et al.* 1975 The experimental investigation of shock waves in liquid with gas bubbles, in: *Wave Processes in Two-Phase Systems*, V. Nakoryakov (Ed.), Novosibirsk, Inst. Thermophysics, Russia.
- Nakoryakov V. E., Pokusaev B. G., and Shreiber I. R. 1993 *Wave Propagation in Gas-Liquid Media*, CRC Press, Boca Raton, FL, 2nd ed.
- Neemeh R. 1991 Propagation and stability of converging cylindrical shocks in narrow cylindrical chamber, *Proc. 18th Int. Symp. Shock Waves*, Sendai, Japan, 1, 273–278.
- Nigmatullin R. I. 1991 *Dynamics of Multiphase Media*, Vols. 1–2, Hemisphere, New York.
- Nikolaev Yu. A. and Fomin P. A. 1983 Approximate kinetic equation for heterogeneous systems of gas-continuous phase, *Combust. Expl. & Shock Waves*, 19 (6), 49–58.
- Nikolaev Yu. A. and Zak D. V. 1988 Correlation between chemical reaction models in gases and second thermodynamics law, *Combust., Expl. & Shock Waves*, 24 (4), 87–90.
- Nordzij L. 1971 Shock waves in bubble-liquid mixtures. *Phys. Comm.*, 3 (1) (Twente Inst. Tech., Enschede, Netherlands).
- Nordzij L. and van Wijngaarden L. 1974 Relaxation effects caused by relative motion on shock waves in gas-bubble/liquid mixture, *J. Fluid Mech.*, 66 (1), 115–145.
- Parkin B. R., Gilmore F. R., and Brode H. L. 1961 Shock waves in bubbly water. Memorandum RM-2795-PR.
- Pinaev A. V. and Sychev A. I. 1986a Discovery and investigation of self-sustaining regimes of detonation of liquid fuel-oxygen bubbly systems, *Sov. Phys.-Dokl.*, 31 (9), 767–769.
- Pinaev A. V. and Sychev A. I. 1986b Structure and properties of detonation in systems of bubbly liquids, *Combust., Expl. & Shock Waves*, 22 (3), 109–118.
- Pinaev A. V. and Sychev A. I. 1987 Influence of physical-chemical gas/liquid properties on the parameters and conditions of detonation wave arising in systems liquid—gas bubbles, *Combust., Expl. & Shock Waves*, 23 (6), 76–84.
- Roberts P. and Field J. 1993 Simulated of fragment attack on cased munition, *Proc. 10th Int. Det. Symp.*, Boston.
- Scarinci T., Bassin X., Lee J., and Frost D. 1991 Propagation of a reactive wave in a bubbly liquid, *Proc. 18th Int. Symp. Shock Waves*, K. Takayama (Ed.), 1, 481–484.
- Shagapov V. S. and Vakhitova N. K. 1987 Waves in reactive bubbly liquid, *Proc. 11th Int. Symp. Nonlinear Acoustics*, Kedrinskii V. K. (Ed.), Novosibirsk, Russia, 56–58.
- Soloukhin R. I. 1960 On bubble mechanism of shock triggered combustion liquids, *Sov. Phys.-Dokl.*, 6 (1), 16–17.
- Soloukhin R. I. 1961 On gas bubble pulsation in incompressible liquid, *Sci. Board Appl. of Expl. Effects. Issue 18*. Novosibirsk, Russia.
- Stuka C., *et al.* 1993 Nonlinear transmission of focused shock waves in nondegassed water, *Proc. 19th Int. Symp. Shock Waves*, Marseille, France, 3, 445–448.
- Sturtevant B. 1993 The physics of shock wave focusing in the context of extracorporeal shock wave lithotripsy, *Proc. 19th Int. Symp. Shock Waves*, Marseille, France, 4, 81–86.
- Sychev A. I. and Pinaev A. V. 1986 Self-sustained detonation in liquids containing the bubbles of a reactive gas, *Appl. Mech. & Tech. Phys.*, 27 (1), 133–138.
- Takayama K. 1989 High pressure generation by shock wave focusing in ellipsoidal cavity, *Proc. Int. Workshop on Shock Wave Focusing*, K. Takayama (Ed.), Sendai, Japan, 1–37.
- Todes O. M. 1933 Adiabatic thermal explosion, *J. Phys. Chem.*, 4 (1), 71–78.
- Trotsyuk A. V. and Fomin P. A. 1992 Bubbly detonation model, *Combust., Expl. & Shock Waves*, 28 (4), 129–136.
- Van Wijngaarden L. 1968 On the equations of motion for mixtures of liquid and gas bubbles, *J. Fluid Mech.*, 33, 465–474.
- Vasil'ev A. A. and Nikolaev Ju. A. 1978 Closed theoretical model of a detonation cell, *Acta Astronautica*, 5, 983–996.

- Vasil'ev A. A., Valishev A. I., Vasil'ev V. A., *et al.* 1978 Detonation wave parameters at high pressures and temperatures, *J. Chem. Phys.*, 16 (9), 113–117.
- Vasil'ev A. A., Kedrinskii V. K., and Taratuta S. P. 1998 Dynamics of single bubble with a reactive gas, *Combust., Expl. & Shock Waves*, 34 (2), 121–124.
- Voinov O. V. and Petrov A. G. 1971 Motion of a variable volume sphere in ideal liquid near a flat surface, *Izv. Akad. Nauk SSSR, Mekh. Zh. & Gaza*, 5, 94–103.
- Watanabe M., Onodera O., and Takayama K. 1993 Shock wave focusing in a vertical annular shock tube, *Proc. 19th Int. Symp. Shock Waves*, Marseille, France, 4, 99–104.
- White D. R. 1967 Density induction times in very lean mixture of D_2 , H_2 , C_2 , C_2H_2 and C_2H_4 with O_2 . *Proc. 11th Int. Symp. Combustion*, Pittsburgh, Academic Press, 147–154.
- Zaitsev S. G. and Soloukhin R. I. 1958 On the problem of ignition of the adiabatically heated gaseous mixture, *Dokl. Akad. Nauk SSSR*, 112 (6).
- Zavtrak S. T. 1995 Generation conditions for an acoustic laser, *Phys. Rev. E.*, 51 (1), 3767–3769.
- Zavtrak S. T. and Volkov I. V. 1997 Sound amplification by stimulated emission of radiation in nonlinear mode, *J. Acoustic Soc. Am.*, 102 (1), 204–206.

This Page Intentionally Left Blank

Shock Wave Propagation in Multi-Phase Media

15.4 Shock Wave Interaction with Liquid Gas Suspensions

MARINUS E. H. VAN DONGEN

Burgers Centre for Fluid Dynamics, Department of Applied Physics, Eindhoven University of Technology, P.O. Box 513, 5600 MB, Eindhoven, The Netherlands

-
- 15.4.1 Introduction
 - 15.4.2 Thermodynamic Properties of a Liquid Gas Suspension
 - 15.4.3 Speeds of Sound
 - 15.4.3.1 Fully Frozen Sound Speed
 - 15.4.3.2 Partly Frozen Sound Speed
 - 15.4.3.3 Equilibrium Sound Speed
 - 15.4.4 Jump Conditions Across a Normal Shock Wave in a Liquid Gas Suspension
 - 15.4.4.1 Approximate Rankine-Hugoniot Relations for Weak Shocks
 - 15.4.4.2 Guha's Exact Analytical Solution for Specified p_1 , T_1 , T_2 and f_g
 - 15.4.5 Transfer of Momentum, Mass, and Energy from Gas to Droplets; Dilute Condensable Component
 - 15.4.5.1 Continuum Regime
 - 15.4.5.2 The Free Molecular Regime
 - 15.4.5.3 The Transition Regime
 - 15.4.6 Estimates of Characteristic Relaxation Times
 - 15.4.6.1 Exchange of Momentum
 - 15.4.6.2 Exchange of Heat
 - 15.4.6.3 Exchange of Mass: Evaporation
 - 15.4.6.4 Comparison of the Characteristic Relaxation Times

- 15.4.7 Shock-Induced Evaporation in the Wet-Bulb Regime
- 15.4.8 Experimental Observations
- 15.4.9 Shock Waves in Wet Steam
- 15.4.10 Fully Dispersed Shock Waves in Wet Steam
- 15.4.11 Conclusions
- References

15.4.1 INTRODUCTION

A shock wave propagating in a mixture of gas, vapor, and droplets shows several interacting relaxation phenomena. In a coordinate system fixed to the shock front, the mixture of carrier gas and droplets enters the shock at supersonic speeds. Whereas the gas and vapor decelerate abruptly when passing the shock front, with a corresponding increase in temperature and pressure, the heavy droplets pass the shock front undisturbed, retaining their initial velocity, temperature, and size. Let us assume that the droplet mass fraction is low, and that the original mixture is in a state of thermodynamic equilibrium, the vapor pressure being equal to its saturated value p_{vs} . The shock compression causes the vapor pressure to increase, so that a super-saturated state exists and some condensation takes place on the still-“cold” droplets. Simultaneously, the droplets are decelerated by the drag force exerted by the carrier gas, and an efficient transfer of heat from gas to droplets occurs. The release of latent heat and the convective heat transfer from gas to droplet both contribute to a rapid increase of droplet temperature. At a certain distance from the shock front the vapor pressure becomes lower than the saturated vapor pressure corresponding to the droplet temperature and the droplets start to evaporate. Then, the heat transferred to the droplet will be partly used to supply the latent heat necessary for evaporation and the increase in droplet temperature will slow down. At the so-called wet-bulb temperature all the heat supplied to the droplets is used for evaporation and the droplet temperature becomes quasi-steady. The remaining part of the condensation process then takes place at wet-bulb conditions. A schematic picture of such a situation is given in Fig. 15.4.1. If the shock strength is sufficient, all droplets will evaporate and the vapor finally ends in a superheated state. Weak shock waves may lead to a post-shock state in which vapor and liquid coexist. If the shock strength is further reduced, then the discontinuous change will disappear and the shock wave becomes fully dispersed.

The structure of shock waves in liquid gas suspensions is related to that in dusty gases, since in both cases transfer of momentum and heat from the carrier gas to the particle cloud occurs. The specific additional effects due to phase

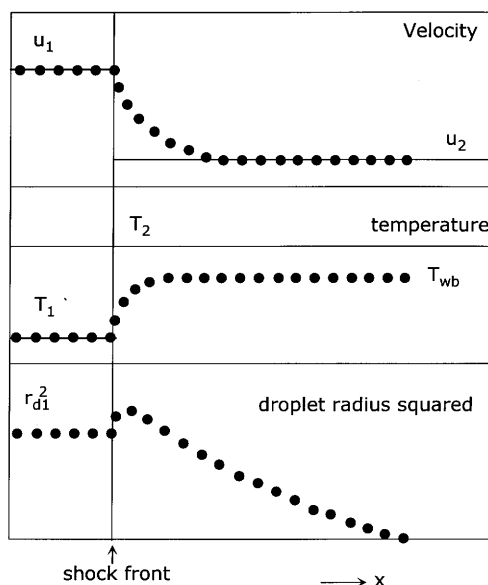


FIGURE 15.4.1 A shock wave and its relaxation zone in a shock fixed reference frame. T_{wb} : wet-bulb temperature.

transition in a cloud of droplets was first investigated by Nayfeh (1966), who studied shock induced ablation of teflon particles. Lu and Chiu (1966) computed the structure of the relaxation zone behind a shock wave in air, water vapor, and water droplets. The characteristic times of the different relaxation phenomena in a pure substance were analysed by Marble (1969). His analysis is based on the assumption that the different relaxation processes do not interfere. Marble's work was extended and improved by Guha and Young (1989), Young and Guha (1991), and Guha (1992), again considering the structure of shock waves in wet steam. In their work a distinction was made between partly dispersed shock waves that move faster than the frozen speed of sound and fully dispersed shock waves that propagate with a speed lower than the frozen speed of sound, but higher than the equilibrium sound speed.

In the analysis of Goossens *et al.* (1988), the convective contribution to heat and mass transfer was taken into account and characteristic relaxation times for the gas-vapor droplet system were introduced. It appears that in a wide range of parameters, velocity and temperature equilibration occurs much faster than droplet evaporation, which opens the possibility for a simplified analysis of the droplet evaporation zone behind a shock wave (Smolders and Van Dongen, 1992; Smolders, 1992). The jump conditions across normal shock waves in wet steam and without an inert carrier gas were extensively studied by

Guha (1992, 1994). Experimental work on the behavior of wet steam passing a shock wave has been reported by Yousif and Bakhtar (1974). The wet steam formed by supercooling of steam passing a Laval nozzle was led through a standing shock wave in the diverging part of the nozzle. Measured and theoretical pressure profiles showed a satisfactory agreement. Hastings and Hodgson (1979) observed a considerable dispersion of the structure of a shock wave propagating in an aqueous fog in a shock tube.

An experimental study of weak shock waves in a fog was published by Goossens *et al.* (1986). They introduced a combination of a shock tube and an expansion wave tube as an effective experimental facility. A mixture of nitrogen gas and water vapor, provided with heterogeneous condensation nuclei, was first expanded by the passage of unsteady expansion waves, resulting in the formation of a well-defined fog. Then, the mixture was subjected to the passage of a shock wave. Their work was later extended and improved by Goossens *et al.* (1988), Smolders (1992), and Smolders and Van Dongen (1992). By combining pressure measurements, time-resolved Mach–Zehnder interferometry, and a wavelength-resolved laser light extinction technique, accurate experimental data were obtained concerning the structure of the relaxation zone. A large set of experimental data was collected concerning the characteristic evaporation time of a droplet after passage of a shock wave as a function of shock strength.

Shock waves in dilute mixtures of carrier gas vapor and droplets can serve as sources of information concerning the physics of droplet evaporation. This was convincingly shown by Roth and co-workers. The conditions were chosen such that the evaporation times were always much larger than the characteristic velocity and temperature relaxation times. Evaporation rates were measured by means of angle-resolved light scattering. Roth and Fischer (1985) studied the effect of Knudsen number on the evaporation rates of DOP and DIDP particles. Timmler and Roth (1989) determined diffusion coefficients for DOP, KBr, and silicol oil PD5 in argon.

Paikert (1990) experimentally studied the evaporation of water and hydrocarbon droplets in air and argon due to the passage of a shock wave reflected from a shock tube end wall. The micron-sized droplets were generated by homogeneous nucleation. The experimental results could be well explained by the droplet-evaporation model of Gyarmathy (1982).

15.4.2 THERMODYNAMIC PROPERTIES OF A LIQUID GAS SUSPENSION

We now consider a mixture of gas (subscript g), vapor (v), and droplets (d). Gas and vapor are considered as calorically perfect components with constant

specific heats. The liquid also has ideal properties; its specific heat c_l is also considered constant. Gas and vapor satisfy the ideal gas law,

$$p_g = \rho_g R_g T \quad (15.4.1)$$

$$p_v = \rho_v R_v T, \quad (15.4.2)$$

with R_g and R_v the specific gas constants of gas and vapor. The densities ρ_g and ρ_v are the actual mixture densities pertaining to a unit volume of mixture. This implies that the volume occupied by the droplets is assumed to be negligible. Also, the droplets are assumed not to contribute to the mixture pressure p :

$$p = p_g + p_v. \quad (15.4.3)$$

An important thermal property is the specific enthalpy h , for which we write

$$h_g = c_{pg} T \quad (15.4.4)$$

$$h_v = c_{pv} T + L_0 \quad (15.4.5)$$

$$h_l = c_l T. \quad (15.4.6)$$

In (15.4.5) we have introduced the formation enthalpy of the vapor L_0 . It is related to the actual latent L by

$$L \equiv h_v - h_l = (c_{pv} - c_l)T + L_0. \quad (15.4.7)$$

This reflects that the assumption of constant specific heats is consistent with a linear dependency of the latent heat on temperature with $(c_{pv} - c_l)$ as its slope. If $\rho_v \ll \rho_l$ the vapor-liquid equilibrium pressure p_{vs} satisfies the Clausius–Clapeyron equation:

$$\frac{T}{p_{vs}} \frac{dp_{vs}}{dT} = \frac{L}{R_v T} = \zeta(T). \quad (15.4.8)$$

We have introduced the dimensionless latent heat $\zeta(T)$ for later use. A combination of (15.4.7) and (15.4.8) leads to the Rankine–Kirchhoff equation for the vapor pressure,

$$p_{vs}(T) = p_{vs}(T_{ref}) \left(\frac{T}{T_{ref}} \right)^{(c_{pv} - c_l)/R_v} \exp \left\{ \frac{L_0}{R_v} \left(\frac{1}{T_{ref}} - \frac{1}{T} \right) \right\}, \quad (15.4.9)$$

where the subscript *ref* refers to an arbitrary reference state. If the liquid phase consists of monodispersed spherical droplets with radius r_d , the equilibrium vapor pressure will be different because of the curvature of the interfaces and the corresponding pressure difference between droplet and vapor,

$$p_{vc}(T, r_d) = p_{vs}(T) \exp Ke(T, r_d), \quad (15.4.10)$$

with the Kelvin number Ke related to the surface tension σ of the liquid:

$$Ke(T, r_d) \equiv \frac{2\sigma}{\rho_l R_v T r_d}. \quad (15.4.11)$$

Since we neglect the liquid volume, the density of the mixture is the sum of the partial densities of the three constituents:

$$\rho = \rho_g + \rho_v + \rho_d \equiv \rho_c + \rho_d. \quad (15.4.12)$$

We have introduced here the density of the continuous phase, gas, and vapor, ρ_c . The droplet density ρ_d is related to the droplet number density n_d , liquid density ρ_l , and average volume $\langle \frac{4}{3}\pi r_d^3 \rangle$ as

$$\rho_d \equiv n_d \rho_l \frac{4}{3} \pi \langle r_d^3 \rangle. \quad (15.4.13)$$

We shall make use of the mass fractions f_i and f'_i of the different constituents i:

$$f_i = \frac{\rho_i}{\rho} \quad (15.4.14)$$

$$f'_i = \frac{\rho_i}{\rho_c}. \quad (15.4.15)$$

It is advantageous to define the following sets of mass-weighted quantities:

$$R' = f'_g R_g + f'_v R_v, \quad c'_p = f'_g c_{pg} + f'_v c_{pv} \quad (15.4.16)$$

and

$$R = f_g R_g + f_v R_v, \quad \bar{c}_p = f_g c_{pg} + f_v c_{pv} + f_d c_l, \quad \bar{\gamma} = \frac{\bar{c}_p}{\bar{c}_p - R}. \quad (15.4.17)$$

Combining Dalton's law (15.4.3) with the ideal gas law (15.4.1), (15.4.2) leads to the mixture equation of state:

$$p = p_g + p_v = \rho_c R' T = \rho R T. \quad (15.4.18)$$

For the mixture enthalpy we write

$$h = f_g h_g + f_v h_v + f_d h_l, \quad (15.4.19)$$

which is the mass averaged sum of the different contributions.

15.4.3 SPEEDS OF SOUND

For the description of shock waves, it is essential to have available the proper expressions for the speeds of sound, since a sound wave can be considered as a degenerate shock wave of infinitesimal strength. As was already pointed out by

Marble (1969), different sound speeds are to be distinguished, depending on the time and length scales involved.

15.4.3.1 FULLY FROZEN SOUND SPEED

For very rapid changes in the state of the mixture, the droplets are not able to participate. Droplet temperature, density, and velocity do not change on this short time scale. In that case the droplet state is frozen and only the changes in the thermodynamic state of the gas and the vapor are relevant. Now let us consider a steady wave front over which gas and vapor undergo an infinitesimal change in velocity du , pressure dp , density $d\rho_c$. The mass fractions f_i' do not change and therefore also c_p' and R' are constant. The fundamental conservation laws of mass, momentum, and energy read in differential form

$$d(\rho_c u) = 0 \quad (15.4.20)$$

$$dp + \rho_c u du = 0 \quad (15.4.21)$$

$$c_p' dT + u du = 0. \quad (15.4.22)$$

It can easily be verified that $c_p' dT$ is the change in enthalpy per unit mass of gas/vapor passing the wave front. Eliminating du from (15.4.20), (15.4.21), and (15.4.22) yields

$$dp = u^2 d\rho_c \quad (15.4.23)$$

$$dp = \rho_c c_p' dT. \quad (15.4.24)$$

With the ideal gas law $p = \rho_c R' T$, the solution for u^2 is easily found. Since the changes are infinitesimal, u equals the fully frozen sound speed a_{ff} ,

$$a_{ff}^2 = u^2 = \frac{dp}{d\rho} = \gamma_{ff} \frac{p}{\rho_c}, \quad (15.4.25)$$

with

$$\gamma_{ff} = \frac{c_p'}{c_p' - R'}. \quad (15.4.26)$$

15.4.3.2 PARTLY FROZEN SOUND SPEED

If the characteristic length scale is sufficiently large, the droplets attain the same temperature and the same velocity as the gas. If no mass exchange takes place between droplets and vapor, the process is called partly frozen and the

corresponding sound speed will be denoted accordingly. In this case the mass fractions of gas, vapor, and droplets, f_i , are constant and the same holds for the mass averaged values \bar{c}_p and R . Energy and momentum conservation can again be combined to give

$$dp = \rho \bar{c}_p dT. \quad (15.4.27)$$

A combination with the ideal gas law in the form $p = \rho RT$ yields

$$a_{pf}^2 = \bar{\gamma} \frac{p}{\rho}, \quad (15.4.28)$$

with

$$\bar{\gamma} = \frac{\bar{c}_p}{\bar{c}_p - R}. \quad (15.4.29)$$

For a one-component two-phase system, such as wet steam, the assumption that droplets and vapor have the same temperature is not appropriate. In that case the correct assumption is that the droplet temperature equals its saturation value corresponding to the vapor pressure. This leads to a different partly frozen sound speed, which is discussed later.

15.4.3.3 EQUILIBRIUM SOUND SPEED

If the mixture attains full thermodynamic equilibrium after passing the wave front, the ratio $dp/d\rho$ yields the square of the equilibrium sound speed a_e^2 . The mass fractions of vapor and droplets do change, since the vapor pressure is always saturated. As a consequence, \bar{c}_p and R also vary across the wavefront. The basic equation to consider is again

$$\rho dh = dp. \quad (15.4.30)$$

Expressing dh in terms of $d\rho$ and dp yields the equilibrium sound speed. Conservation of the condensable component requires that $df_v = -df_d$. Combining this with the definition of h (15.4.19) and eliminating L_0 with (15.4.5) yields

$$dh = \bar{c}_p dT + L df_{vs}. \quad (15.4.31)$$

To evaluate df_{vs} , we use the Clausius–Clapeyron equation (15.4.8) and the vapor equation of state (15.4.2):

$$\frac{df_{vs}}{f_{vs}} = \frac{d\rho_{vs}}{\rho_{vs}} - \frac{d\rho}{\rho} = (\zeta - 1) \frac{dT}{T} - \frac{d\rho}{\rho}. \quad (15.4.32)$$

Dalton's law (15.4.3), combined with (15.4.1) and (15.4.18), and using $R_g f_g / R = 1 - p_{vs} / p$, gives a second expression for dT/T :

$$\left(1 + (\zeta - 1) \frac{p_{vs}}{p}\right) \frac{dT}{T} = \frac{dp}{p} - \left(1 - \frac{p_{vs}}{p}\right) \frac{d\rho}{\rho}. \quad (15.4.33)$$

Using (15.4.32) and (15.4.33) to eliminate df_{vs} and dT from (15.4.30) and (15.4.31) yields for the equilibrium sound speed

$$a_e^2 = \frac{dp}{d\rho} = \gamma_e \frac{p}{\rho}, \quad (15.4.34)$$

with

$$\gamma_e = \bar{\gamma} \frac{1 + \frac{p_{vs}}{p} \left(\frac{\bar{\gamma} - 1}{\bar{\gamma}} \zeta^2 - 1 \right)}{1 + (\bar{\gamma} - 1)(\zeta - 1)^2 \frac{p_{vs}}{p}}; \quad f_d > 0. \quad (15.4.35)$$

It is emphasized that the specific heat ratio $\bar{\gamma}$ in (15.4.35) is the partly frozen value defined in (15.4.29). The equilibrium sound speed, given by (15.4.34) and (15.4.35), is valid for arbitrary mass fractions of the condensible component $f_v + f_d$. So, it also holds for the wet stream, with $f_g = 0$. The expression is in agreement with those of Smolders (1992) and of Guha (1994). It is slightly different from the equilibrium sound speeds introduced by Sislian (1975) and Wegener (1975), who did not account for the temperature dependence of the latent heat.

For water vapor near $T = 295$ K, the numerical value of ζ is approximately 18. If we further consider the case of low vapor and droplet mass fraction, then $\bar{\gamma}$ and a_{pf} are in good approximation the values corresponding to the pure carrier gas. For water in air at atmospheric pressure at 295 K, $p_{vs}/p \simeq 2.6 \times 10^{-2}$ and $\gamma_e/\bar{\gamma} = 0.84$. In that case the equilibrium sound speed is almost 8% lower than the sound speed of air, which is caused by the exchange of latent heat. For any given droplet mass fraction there exists a temperature above which the vapor becomes superheated. At that temperature the equilibrium sound speed jumps to its partly frozen value. This has interesting consequences for the structure of expansion fans in gas-vapor mixtures. If condensation occurs, then the (equilibrium) expansion wave is split into a dry part and a wet part separated by a plateau of constant state as was theoretically and numerically shown by Smolders *et al.* (1989, 1992).

15.4.4 JUMP CONDITIONS ACROSS A NORMAL SHOCK WAVE IN A LIQUID GAS SUSPENSION

Let us consider an equilibrium mixture of gas, vapor, and droplets that passes a shock front. The coordinate frame is fixed to the shock wave, so that a steady flow situation exists. The state far upstream of the shock is denoted with index 1, the state far downstream with index 2. Let us further assume that the shock is sufficiently weak that the post-shock state is also characterized by vapor phase equilibrium, i.e., $f_{d2} > 0$.

The basic laws of conservation of mass, momentum, and energy read

$$\rho_1 u_1 = \rho_2 u_2 \quad (15.4.36)$$

$$p_1 + \rho_1 u_1^2 = p_2 + \rho_2 u_2^2 \quad (15.4.37)$$

$$h_1 + \frac{1}{2} u_1^2 = h_2 + \frac{1}{2} u_2^2. \quad (15.4.38)$$

It is noted that f_g and $f_v + f_d (= 1 - f_g)$ do not change across the shock front. Then it is convenient to rewrite the expression for the enthalpy (15.4.19) as

$$h = (f_g c_{pg} + (1 - f_g) c_{pv}) T - f_d (L_0 - (c_l - c_{pv}) T) + (1 - f_g) L_0. \quad (15.4.39)$$

Defining the constant specific heat \tilde{c}_{pg} as

$$\tilde{c}_{pg} = f_g c_{pg} + (1 - f_g) c_{pv} \quad (15.4.40)$$

and skipping the last constant term of (15.4.39) gives

$$h = \tilde{c}_{pg} T - f_d L(T) = \tilde{c}_{pg} T - (1 - f_v - f_g) L(T). \quad (15.4.41)$$

The vapor mass fraction f_v is directly related to the relative saturated vapor pressure p_{vs}/p :

$$\frac{p_{vs}}{p} = f_v \frac{R_v}{R} = \frac{f_v R_v}{f_g R_g + f_v R_v}. \quad (15.4.42)$$

Equations (15.4.36), (15.4.37), and (15.4.42) in combination with the double set (15.4.9), (15.4.18), and (15.4.43) for the upstream and downstream conditions yields a total of nine equations for the two sets of variables $(\rho, p, T, p_{vs}, u, f_{v1,2})$. Apart from the fixed gas mass fraction f_g , three other variables have to be specified. In most applications this will be the pre-shock state (u_1, p_1, T_1) . In the remainder of this section we will closely follow the treatment by Guha (1994).

15.4.4.1 APPROXIMATE RANKINE–HUGONIOT RELATIONS FOR WEAK SHOCKS

The equilibrium ratio of specific heats, $\bar{\gamma}_e$, is only weakly dependent on temperature and pressure. So, for weak shocks the parameter γ_e is approximately constant. Since for weak shocks the entropy is also constant, we may write with (15.4.30) and (15.4.34)

$$h_2 - h_1 = \int_1^2 \frac{dp}{\rho} = \frac{\bar{\gamma}_e}{\bar{\gamma}_e - 1} \left(\frac{p_2}{\rho_2} - \frac{p_1}{\rho_1} \right), \quad (15.4.43)$$

so that the shock conservation laws become identical to those for a calorically perfect gas. The solution of the shock conservation laws for a perfect gas is given in terms of the shock Mach number Ma_e , based on the upstream equilibrium sound speed a_{e1} :

$$Ma_e = \left(\frac{u_1}{\gamma_e p_1 / \rho_1} \right)^{1/2}. \quad (15.4.44)$$

The solution for the downstream pressure, velocity, and density is

$$\frac{p_2}{p_1} = \frac{2\gamma_e}{\gamma_e + 1} Ma_e^2 - \frac{\gamma_e - 1}{\gamma_e + 1} \quad (15.4.45)$$

$$\frac{u_2}{u_1} = \frac{\rho_1}{\rho_2} = \frac{(\gamma_e - 1)Ma_e^2 + 2}{(\gamma_e + 1)Ma_e^2}. \quad (15.4.46)$$

The approximate solution (15.4.45)–(15.4.46) is valid as well for partly dispersed shock waves as for fully dispersed shock waves. A shock is called partly dispersed when the fully frozen shock Mach number $Ma_{ff} = u_1/a_{ff1} > 1$. It means that a frozen gas-dynamic shock is followed by a relaxation zone toward full thermodynamic equilibrium. For a fully dispersed wave $Ma_{ff} < 1$, but $Ma_e > 1$. In that case the frozen gas-dynamic shock has disappeared and the flow variables gradually change from upstream to downstream conditions.

15.4.4.2 GUHA'S EXACT ANALYTICAL SOLUTION FOR SPECIFIED p_1 , T_1 , T_2 , AND f_g

Guha (1994) describes a procedure to obtain an exact analytical solution of the shock conservation laws. The idea is to use T_1 , p_1 , f_g , and the temperature T_2 as input variables. The upstream thermodynamic state is specified, but the velocity u_1 has to be evaluated. The procedure is as follows. First the saturated vapor pressure p_{v2} is evaluated with (15.4.9). The pressure p_2 is expressed in f_{v2} and p_{v2} with (15.4.42). The downstream density ρ_2 is written in terms of T_2 , P_{v2} and f_{v2} with Eqs. (15.4.2) and (15.4.42). The velocity $u_2 = u_1 \rho_1 / \rho_2$.

The variables u_2 , T_2 , p_{v2} and f_{v2} are substituted in the momentum equation and in the energy equation (15.4.38) using (15.4.41). What remains is a quadratic equation in f_{v2} . The solution is

$$f_{v2} = \frac{B + \sqrt{B^2 + 4AC}}{2A} \quad (15.4.47)$$

$$A = 2L_2 - \left(1 - \frac{p_1}{p_{v2}}\right)R_v T_2 \quad (15.4.48)$$

$$B = 2(1 - f_g) \left(L_2 - \frac{f_{d1} L_1}{1 - f_g} \right) + 2\tilde{c}_p(T_1 - T_2) + f_g R_g T_2 + \frac{p_{v2} - p_1}{\rho_1} \quad (15.4.49)$$

$$C = \frac{f_g R_g p_{v2}}{R_v \rho_1}. \quad (15.4.50)$$

After f_{v2} has been found, p_2 follows from (15.4.42). Also, R_2 can be evaluated and ρ_2 results from $\rho_2 = p_2/R_2 T_2$. The upstream and downstream velocities u_1 , u_2 follow from mass and momentum conservation (15.4.36) and (15.4.37). If, for a given initial state, the shock strength increases, more liquid will be vaporized until the limiting case $f_{d2} = 0$. In that case $f_{v2} = 1 - f_g$ and the solution is easily obtained as indicated previously. If the shock strength

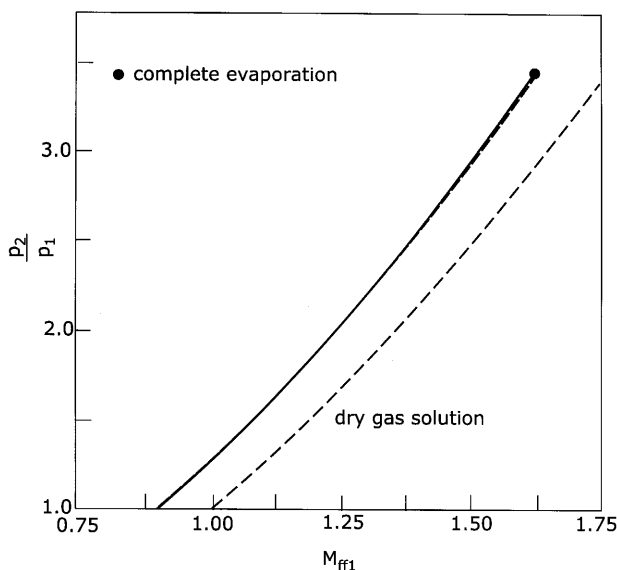


FIGURE 15.4.2 Equilibrium Rankine-Hugoniot relations for a suspension of water droplets in air. Pressure ratio as a function of fully frozen shock Mach number ($p_1 = 1$ bar, $T_1 = 293$ K, $f_g = 0.95$). After Guha (1994).

increases even more, then the vapor is superheated and the liquid–vapor equilibrium is no longer maintained. In Fig. 15.4.2, taken from Guha’s 1994 paper, the Rankine–Hugoniot solution for the pressure ratio is shown as a function of fully frozen shock Mach number: $Ma_{ff} = u_1/a_{ff1}$. Also, the approximate solution is shown, which can hardly be distinguished from the exact solution for the case considered (air/water, $p_1 = 1$ bar, $T = 293$ K, $f_g = 0.95$). The calculation was carried out up to the limiting case in which a complete evaporation of the droplet occurs. It is noted that the frozen Mach number can have a value smaller than unity, which corresponds to the case of a fully dispersed wave. The downstream pressure p_2 for a “wet” shock wave is apparently higher than for a “dry” shock. This pressure increase occurs in the evaporation relaxation zone as discussed later. The evaluation of the Rankine–Hugoniot relations for shocks in which the post-shock vapor state is superheated is quite straightforward, since in that case the post-shock vapor mass fraction simply equals $(1 - f_g)$.

15.4.5 TRANSFER OF MOMENTUM, MASS, AND ENERGY FROM GAS TO DROPLETS; DILUTE CONDENSABLE COMPONENT

In order to evaluate the structure of the relaxation zone, we consider the case of a dilute condensable component, that is, $f_v + f_d \ll 1$. The equilibrium mixture of gas vapor and droplets passes a steady, partly dispersed shock wave that consists of a fully frozen discontinuous wave front followed by a relaxation zone. When passing the discontinuity, the velocity and the thermodynamic state of gas and vapor jump to their “fully frozen” values, while droplet velocity and temperature do not change. Then the droplets are decelerated, heat is transferred to the droplets, and the droplets start to evaporate.

We assume that no droplet breakup takes place. According to Wierzbza (1990), droplets do not disintegrate if the Weber number, $W_e = 2r_d\rho(u - u_d)^2/\sigma$, is smaller than 10. For the analysis of the structure of the post-shock relaxation zone we follow the analysis by Goossens *et al.* (1988), later extended by Smolders (1992) and by Smolders and Van Dongen (1992). Their treatment is based on a physical transport model extensively discussed by Gyarmathy (1982).

A droplet in a hot carrier gas stream of different temperature and velocity will be subjected to a drag force F while there is a heat flux to the droplet surface H and a mass flux M . Part of the heat flowing from gas to droplet, H_{int} , is used to increase the droplet temperature. The major part of H is used to supply the latent heat for evaporation.

We consider the behavior of one single droplet to be determinate for the behavior of a full suspension consisting of many droplets. It is clear that such an approximation has a restricted validity. The average distance between neighboring droplets r_∞ ,

$$r_\infty = \left(\frac{\rho_l}{\rho_d} \langle r_d^3 \rangle \right)^{1/3}, \quad (15.4.51)$$

has to be much larger than the droplet radius. For $r_d = 1 \mu\text{m}$ and $n_d = 10^{12} \text{ m}^{-3}$, the ratio r_∞/r_d is more than 60. According to estimates by Tishkoff (1979) and Gyarmathy (1982), proximity effects will influence the heat and mass transfer rates by about 10% for $r_\infty/r_d \simeq 20$. Also, the drag is affected by the droplet volume fraction. According to Tam (1969), this effect is less than 1% for $r_\infty/r_d \simeq 60$. For the conditions considered here, the assumption of a negligible mutual effect of the droplets is justified, but in general care should be taken. In order to describe the transfer of mass and heat, a quasi-stationary approach is followed. This is again justified for the cases considered here. For a more general discussion the reader is referred to Gyarmathy (1982). Deviations from the quasi-steady drag force are due to added mass ($\frac{1}{2}m_d\rho_c/\rho_l$) and the history effect or the Basset force (Rudinger, 1980; Clift *et al.*, 1978). The ratio of the Basset force and the steady drag is of the order of ρ_c/ρ_l . For water/air at atmospheric conditions $\rho_c/\rho_l \simeq 0.001$, so both unsteady contributions can be neglected.

The conservation laws of mass, momentum, and energy for one single droplet with mass m_d , velocity u_d , and temperature T_d can be formulated as

$$\frac{dm_d}{dt} = \rho_l 4\pi r_d^2 \frac{dr_d}{dt} = M \quad (15.4.52)$$

$$m_d \frac{du_d}{dt} = F \quad (15.4.53)$$

$$m_d c_l \frac{dT_d}{dt} = H + ML(T_d) = H_{int}. \quad (15.4.54)$$

We have adopted the notation d/dt for the total derivative: $d/dt = \partial/\partial t + u_d \partial/\partial x$. In writing (15.4.54) it is implicitly assumed that the droplet temperature is uniform, which is a valid assumption at time scales larger than a characteristic scale $\tau_{int} = r_d^2/(3a_l l)$, with a_l the liquid thermal diffusivity. In the momentum equation (15.4.53) we have made one further assumption, namely that the volume force due to a pressure gradient can be neglected, which is again allowed for $\rho_c/\rho_l \ll 1$. The conservation laws (15.4.52), (15.4.53), and (15.4.54) are related to the driving forces: the differences in velocity, temperature, and vapor pressure. We follow the notation by Gyarmathy (1982), who

introduced Nusselt numbers for mass and heat transfer Nu_M and Nu_H , and also for friction Nu_F (instead of a drag coefficient):

$$M = Nu_M 2\pi r D_m (p_v - p_{vd}) / p_g, \quad (15.4.55)$$

$$F = Nu_F 2\pi r \eta (u - u_d), \quad (15.4.56)$$

$$H = Nu_H 2\pi r_d \lambda (T - T_d). \quad (15.4.57)$$

Here, η and λ are the viscosity and thermal conductivity of the carrier gas, and D_m is a modified diffusion coefficient $D_m = Dp/(R_v T)$, with D the binary diffusion coefficient. The parameters λ , D , η , and D_m have to be evaluated at an intermediate temperature T_m , according to Hubbard *et al.* (1975):

$$T_m = \frac{2T_d + T}{3}. \quad (15.4.58)$$

The vapor pressure at the droplet surface p_{vd} is in equilibrium with the liquid. Therefore, p_{vd} follows from (15.4.10):

$$p_{vd} = p_{ve}(T_d, r_d). \quad (15.4.59)$$

What needs to be done is to specify expressions for the Nusselt numbers, which will depend on the flow situation. The relevant parameters are the relative Reynolds number Re_d and the relative Mach number Ma_d :

$$Re_d = \frac{2r_d |u - u_d|}{v_\infty}, \quad Ma_d = \frac{|u - u_d|}{a_\infty}, \quad (15.4.60)$$

with kinematic viscosity of the gas v_∞ (far from the droplet), and sound speed $a_\infty = (\gamma' R' T)^{1/2}$. The Nusselt number will depend not only on Re_d and Ma_d , but also on the ratio of molecular mean path and droplet diameter, the Knudsen number Kn . We shall first consider the limiting cases of $Kn \rightarrow 0$, the continuum limit, and $Kn \rightarrow \infty$, the free molecular limit.

15.4.5.1 CONTINUUM REGIME

In the continuum regime, correlations due to Ranz and Marshall (1952) are appropriate:

$$Nu_H^c = 2(1 + 0.30 Re_d^{1/2} Pr^{1/3}) \quad (15.4.61)$$

$$Nu_M^c = 2(1 + 0.30 Re_d^{1/2} Sc^{1/3} \pi_g^{1/3}), \quad (15.4.62)$$

with $\pi_g = p_g/p$. The Prandtl and Schmidt numbers, $Pr = \nu/a$ and $Sc = \nu/D$, are evaluated at the intermediate temperature T_m . The values $Nu^c = 2$ for both heat and mass transfer refer to the limiting cases of pure conduction and diffusion. For the drag correlation we neglect the Mach number dependence

(which restricts the range of validity to shock waves of moderate strengths) and we take Neumann's correlation (Gyarmathy, 1982), valid for $Re_d < 800$;

$$Nu_F^c = 3(1 + 0.15Re_d^n), \quad (15.4.63)$$

with $n = 0.687$. For $Re_d \rightarrow 0$, the Stokes drag force is found, $Nu_F^c = 3$.

15.4.5.2 THE FREE MOLECULAR REGIME

For large Knudsen numbers the presence of the droplet does not disturb the surrounding gas. According to Schaaf and Chambré (1961), the free molecular regime starts at $Kn \simeq 7$, in which the Knudsen number is defined as

$$Kn \equiv \frac{l}{2r_d}; \quad l = \frac{2\eta(R'_\infty T_\infty)^{1/2}}{p_\infty}. \quad (15.4.64)$$

The expressions for the free molecular flow regime can be combined with those for the continuum regime. Details are given by Gyarmathy (1982). Somewhat simplified expressions are obtained for $f_v \ll f_g$ and $T_d \simeq T_\infty$:

$$Nu_i^{fm} = \frac{B_i}{Kn}, \quad i = H, M, F, \quad (15.4.65)$$

with

$$B_H = \sqrt{\frac{2}{\pi}} \frac{\gamma_g + 1}{\gamma_g} Pr \alpha_{Hg} \quad (15.4.66)$$

$$B_M = \sqrt{\frac{2}{\pi}} \sqrt{\frac{R_v}{R_g}} \sqrt{Sc} \alpha_{Mv} \quad (15.4.67)$$

$$B_F = \sqrt{\frac{2}{\pi}} \left(\frac{4}{3} + \frac{\pi}{6} \alpha_{Fg} \right). \quad (15.4.68)$$

The parameters B_i depend on the accommodation coefficients α_i . We follow here the viewpoint of Mozurkewich (1986) that their values are close to unity. Using numerical data from Smolders and Van Dongen (1992) for water/nitrogen, typical values at 295 K are $B_H = 0.49$, $B_M = 0.62$ and $B_F = 1.48$.

15.4.5.3 THE TRANSITION REGIME

For intermediate values of the Knudsen number, the collision-free shell surrounding the droplets with a thickness of the order of the molecular mean free path has to be matched with an outer region in which molecular diffusion and heat transfer prevail. On the basis of such a concept, which is

called the flux matching method, several models have been proposed. Examples are the models by Fuchs (1934) and by Young (1993). Gyarmathy proposes the following transition model:

$$Nu = \frac{Nu^c}{1 + KnNu^c/B}. \quad (15.4.69)$$

Davis (1983) compared several theoretical and semiempirical expressions for mass transfer in the transition regime. For mixtures with a vapor component lighter than the carrier gas, he concluded that expression (15.4.69) is reasonable. The model obviously has the correct limiting behavior. Still, the question arises as to what value of the mean free path has to be taken. For heat transfer in a dilute system, the correct molecular mean free path is that of the energy transporting carrier gas molecules. For the diffusion process, the situation is different, since then the interactions between vapor molecules and carrier gas molecules are most relevant. But, we have to realize that the mean free path should be a measure for the random walk distance, that is, the distance over which a molecule loses its original orientation. The mean free path defined in this way is only weakly dependent on the mass ratio of the interacting molecules (Kennard, 1938; Mitchner and Kruger, 1973), so that expression (15.4.64) will be sufficiently accurate for most applications.

15.4.6 ESTIMATES OF CHARACTERISTIC RELAXATION TIMES

Following Goossens *et al.* (1988), we first consider a very dilute suspension of droplets in a carrier gas. In that case the carrier gas acts as a thermodynamic reservoir of momentum and enthalpy. Temperature and velocity of gas and vapor are constant downstream of the shock wave and satisfy the fully frozen shock relations. We shall also assume that the vapor pressure does not vary: $\rho_d \ll \rho_v$. Knudsen effects are ignored and the Kelvin effect is not taken into account. In order to define characteristic relaxation times for momentum, heat, and mass transfer, we shall assume a priori that the vaporization process is much slower than momentum and temperature relaxation. This is verified later. Constant pre-shock and post-shock states will be denoted with subscripts 1 and 2.

15.4.6.1 EXCHANGE OF MOMENTUM

First we follow in time a droplet that passes the frozen shock front with velocity u_{d1} , and that is decelerated according to (15.4.53), (15.4.56), and

(15.4.63). The droplet has a constant mass m_{d1} and radius r_{d1} . The equation of motion then reads

$$m_{d1} \frac{du_d}{dt} = -6\pi r_{d1} \eta_2 (u_d - u_2) (1 + 0.15 Re_d^n), \quad (15.4.70)$$

with $n = 0.687$ and with $Re_d = 2r_{d1}(u_d - u_2)/\nu_2$. Equation (15.4.70) can be solved analytically. The results can be expressed in terms of a time-dependent Reynolds number,

$$t = \frac{2\rho_l r_{d1}^2}{9\eta_2} f(Re_d; Re_{d1}), \quad (15.4.71)$$

with

$$f(Re_d; Re_{d1}) \equiv \ln \frac{Re_{d1}}{Re_d} + \frac{1}{n} \ln \frac{1 + 0.15 Re_d^n}{1 + 0.15 Re_{d1}^n}. \quad (15.4.72)$$

An example of solution (15.4.72) is shown in Fig. 15.4.3. From (15.4.61) and (15.4.62), it follows that the relative contribution of convection to heat and

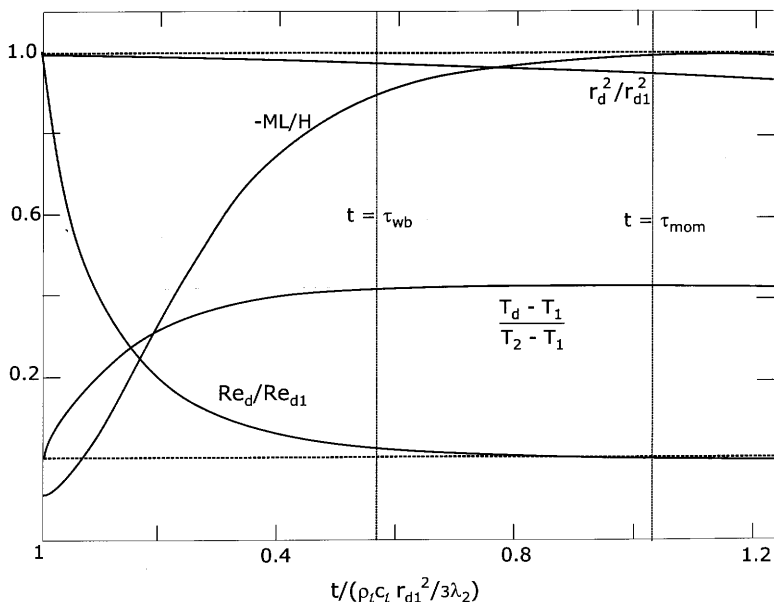


FIGURE 15.4.3 Lagrangian representation of droplet velocity, temperature, and size as a function of time after the passage of a fully frozen shock front. Water/nitrogen. $Ma_{ff} = 1.5$, $p_1 = 60$ kPa, $T = 270$ K, $r_{d1} = 1$ μm , $Re_{d1} = 31.9$, $T_2 = 356$ K. After Goossens *et al.* (1988).

mass transfer becomes less than 0.1 when $Re_d < 0.1$. Therefore, we define the characteristic time for momentum relaxation in the continuum regime as

$$\tau_{mom} \equiv \frac{2}{9} \frac{\rho_l r_{d1}^2}{\eta_2} f(0, 1; Re_{d1}). \quad (15.4.73)$$

The prefactor of (15.4.73) is the momentum relaxation time defined by Marble (1969) and may serve as a first estimate.

15.4.6.2 EXCHANGE OF HEAT

We follow again a droplet after its passage of the fully frozen shock front. The increase in droplet temperature satisfies (15.4.54):

$$m_d c_l \frac{dT_d}{dt} = H + ML. \quad (15.4.74)$$

As indicated before, the droplet temperature can be considered as uniform for $t \gg \tau_{int}$, with the time scale for internal temperature homogenization τ_{int}

$$\tau_{int} \equiv \frac{r_{d1}^2}{3a_{dl}}. \quad (15.4.75)$$

Initially, during a very short time interval, the partial vapor pressure far from the droplet increases, the droplet temperature still being T_1 . In that initial phase, condensation occurs and both H and M are positive, which leads to a fast increase of T_d . As a consequence, the saturated vapor pressure at the droplet surface becomes larger than p_{v2} and the droplets start to vaporize. The mass flow M becomes negative. Combining (15.4.54), (15.4.55) and (15.4.57) leads to the following equation for the droplet temperature:

$$\frac{dT_d}{dt} = \frac{3\lambda_2}{2\rho_l c_l r_d^2} \left[Nu_H (T_2 - T_d) + \frac{D_{m2} L(T_d)}{\lambda_2} Nu_M \frac{[p_{v2} - p_{vs}(T_d)]}{p_{g2}} \right]. \quad (15.4.76)$$

The Nusselt numbers Nu_M and Nu_H are dependent on the relative Reynolds number according to (15.4.61) and (15.4.62). Goossens *et al.* (1986) made the simplifying assumption of neglecting the change in r_d , $r_d \simeq r_{d1}$. Then, the analytical solution (15.4.71), (15.4.72) can be substituted, and (15.4.76) can easily be integrated numerically to give a first-order estimate of $T_d(t)$. An example of this solution is also shown in Fig. 15.4.3, where the ratio $-ML/H$ has also been plotted. In the early phase condensation occurs, $M > 0$. Then, the ratio $-ML/H$ increases and approaches unity, which means that the droplet temperature becomes constant at a value determined by the instantaneous balance of the transfer of latent heat (ML) and of sensible heat H . The droplet

temperature attains its wet-bulb value T_{wb} , which is a solution of the equation $H = -ML$. As a characteristic time for the approach of the wet-bulb state, we adopt the definition that at $t = \tau_{wb}$, the ratio $-ML/H = 0.9$:

$$\tau_{wb} \equiv t(-ML/H = 0.9). \quad (15.4.77)$$

In a formal sense, τ_{wb} can be expressed as

$$\tau_{wb} = \frac{r_{d1}^2 \rho_l c_l}{3\lambda_2} g(Ma_{ff}, Re_{d1}), \quad (15.4.78)$$

in which g has to be evaluated numerically after integration of (15.4.76), using definition (15.4.77).

15.4.6.3 EXCHANGE OF MASS: EVAPORATION

Once the wet-bulb state is established, all heat transferred to the gas is used for evaporation. In view of our assumptions that the vapor pressure p_v , the temperature, and the pressure are constant, the wet-bulb temperature is also constant. It means that for $t > (\tau_{mom}, \tau_{wb})$ the mass transfer is completely governed by diffusion and conduction. Hence, $Nu_M = Nu_H = 2$, and $H = -ML(T_d)$. The mass balance equation (15.4.52) can then be rewritten in the form

$$\frac{dr_d^2}{dt} = -\frac{r_{d1}^2}{\tau_{ev}} \quad (15.4.79)$$

with

$$\tau_{ev} \equiv \frac{r_{d1}^2 \rho_l L(T_{wb})}{2\lambda_2(T_2 - T_{wb})}. \quad (15.4.80)$$

Since τ_{ev} is constant, Eq. (15.4.79) predicts a linear decrease of droplet radius squared. In Fig. 15.4.3, r_d^2/r_{d1}^2 is also depicted. It appears that for the case considered, the assumption of a constant droplet radius during momentum and wet-bulb relaxation was certainly valid. It is noted that the characteristic times (15.4.73), (15.4.75), (15.4.78), and (15.4.80) have been derived on the basis of a continuum approach. For large Knudsen numbers, so for the free molecular flow regime the characteristic relaxation times τ_i^{fm} are related to the continuum regime values τ_i^c by

$$\tau_i^{fm} = \frac{Nu^c}{Nu^{fm}} \tau_i^c = \frac{Kn}{B_i} Nu^c \tau_i^c, \quad (15.4.81)$$

with index i referring to the particular process, and B_i given in (15.4.66)–(15.4.68).

The ratio τ_{ev}/r_{d1}^2 is shown in Fig. 15.4.4a for water droplets in humid nitrogen as a function of the fully frozen shock Mach number. Droplets with a

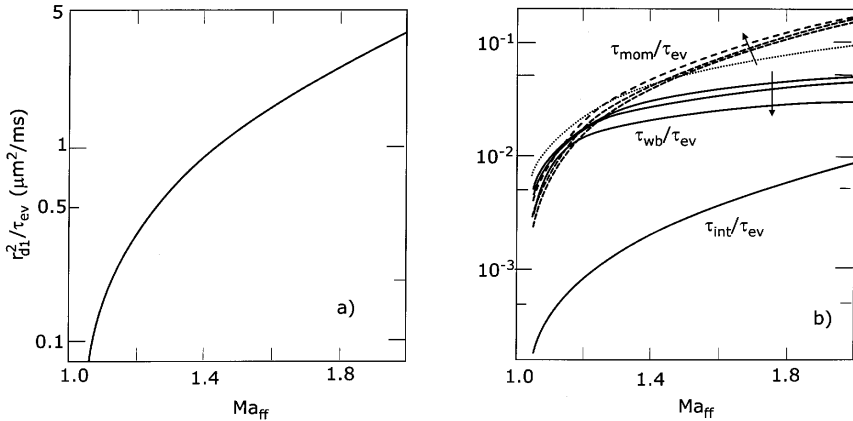


FIGURE 15.4.4 Characteristic relaxation times as function of the fully frozen shock Mach number. Water droplets in humid nitrogen. (a) Rate of evaporation, (b) ratio of characteristic times for internal temperature relaxation (int), momentum transfer (mom), and wet-bulb equilibrium (wb) and for shock induced evaporation (ev). The arrows point to the effect of a change in droplet radius from 0.5 to 1.5 μm . Dashed curve refers to τ_{wb}/τ_{ev} , neglecting the effect of convection to heat and mass transfer. Pre-shock condition: 60 kPa, 270 K. After Goossens *et al.* (1988).

radius of 1 μm have a typical evaporation time of 1 ms for a shock with $Ma_{ff} = 1.6$. It means that the post-shock distance traveled by the droplet before disappearance is $\tau_{ev}u_2 \simeq 25$ cm. Droplet evaporation is a rather slow process. It is noted that the validity of Fig. 15.4.4 is bounded by the stability criterion: $2r_d\rho_2(u_2 - u_{dl})^2/\sigma < 10$. For a droplet with a radius of 1 μm , it means that $Ma_{ff} < 1.86$.

15.4.6.4 COMPARISON OF THE CHARACTERISTIC RELAXATION TIMES

The characteristic times for internal heat diffusion τ_{int} , for momentum relaxation τ_{mom} and for wet-bulb relaxation τ_{wb} are related to the characteristic time for evaporation as

$$\frac{\tau_{int}}{\tau_{ev}} = \frac{2}{3} \frac{c'_p(T_2 - T_{wb})}{L(T_{wb})} \frac{\rho_{c2}}{\rho_l} \frac{a_{t2}}{a_{tl}} \quad (15.4.82)$$

$$\frac{\tau_{wb}}{\tau_{ev}} = \frac{2}{3} \frac{c_l(T_2 - T_{wb})}{L(T_{wb})} g(Ma_{ff}, Re_{dl}) \quad (15.4.83)$$

$$\frac{\tau_{mom}}{\tau_{ev}} = \frac{4}{9} \frac{c'_p(T_2 - T_{wb})}{L(T_{wb})} \frac{a_{t2}}{v_2} f(0.1; Re_{dl}) \quad (15.4.84)$$

with $a_{t2} = \lambda_2/(\rho'_{c2}c'_p)$, and the functions g and f defined in (15.4.72) and (15.4.78).

The time constant ratios (15.4.82)–(15.4.84) are shown in Fig. 15.4.4b as a function of fully frozen shock Mach number for water/nitrogen and a specific pre-shock state. For shock Mach numbers below 1.8, droplet evaporation takes at least 10 times as long as the other relaxation processes, of which momentum relaxation is the second most persistent. Nonuniformities in droplet temperature can be neglected anyhow. The major part of droplet evaporation takes place under wet-bulb conditions. Larger droplets attain wet-bulb equilibrium relatively faster, which is caused by convective contributions. The dashed curve shows the limiting value for τ_{wb}/τ_{ev} if convection is not taken into account.

15.4.7 SHOCK-INDUCED EVAPORATION IN THE WET-BULB REGIME

In the previous section we have shown that the evaporation process is one order of magnitude slower than the processes of velocity and wet-bulb relaxation. This enables us to formulate a simplified model, in which velocity and wet-bulb relaxation are incorporated in the partly frozen shock front. The evaporation of the droplet occurs under wet-bulb conditions. Since we will abandon the assumption that the droplet mass fraction is low, the wet-bulb state may vary with downstream position. Also, the variation of droplet size will be taken into account. The partly frozen post shock state is obtained by means of the standard Rankine–Hugoniot expressions for a calorically perfect gas, similar to (15.4.45) and (15.4.46), but now with specific heat ratio $\bar{\gamma}$ (15.4.29) and partly frozen sound speed a_{pf} (15.4.28). The relevant partly frozen shock Mach number Ma_{pf} is

$$Ma_{pf} = \frac{u_1}{a_{pf1}}. \quad (15.4.85)$$

The shock relations yield the initial values for the post-shock pressure p_2 , density ρ_2 , and velocities $u_2 = u_{d2}$. The gas temperature follows from $T_2 = p_2/\rho_2 R$, with R defined in (15.4.17). The droplet temperature satisfies the implicit wet-bulb relation $H = -ML$, or, with (15.4.55) and (15.4.57),

$$Nu_H \lambda (T - T_d) = -Nu_M D_m L(T_d) (p_v - p_{vd})/p. \quad (15.4.86)$$

The solution of (15.4.86) can formally be written as

$$T_d = T_{wb}(T, p, p_v, r_d). \quad (15.4.87)$$

All variables, T , T_d , p_v , p_{vd} , p , u , and r_d , are functions of the downstream distance, or equivalently of time in a Lagrangian representation.

In a steady reference frame, the flow variables satisfy conservation of mass, momentum, and energy,

$$\rho u = \rho_2 u_2 \quad (15.4.88)$$

$$p + \rho u^2 = p_2 + \rho_2 u_2^2 \quad (15.4.89)$$

$$\frac{1}{2} u^2 + h = \frac{1}{2} u_2^2 + h_2, \quad (15.4.90)$$

with pressure and enthalpy given by (15.4.18) and (15.4.41). Assuming a monodispersed cloud of droplets, the droplet mass fraction is uniquely related to droplet size,

$$f_d = \frac{n_d}{\rho} \frac{4}{3} \pi r_d^3, \quad (15.4.91)$$

since the droplet number density per unit mass of mixture n_d/ρ is constant if droplets do not break up or coalesce. Combining (15.4.52), (15.4.57) with $H = -ML$ gives

$$\frac{dr_d^2}{dt} = u \frac{dr_d^2}{dx} = \frac{Nu_H \lambda}{\rho_l L} (T - T_d). \quad (15.4.92)$$

The rate equation (15.4.92), supplemented with the balance equations as indicated earlier, has been solved numerically for water/nitrogen and a range of initial states by Smolders and Van Dongen (1992). A typical example is shown in Fig. 15.4.5, where pressure, temperature, saturation ratio $S = p_v/p_{vs}$, and droplet surface area are given as a function of Lagrangian time. The time scale has been reduced with τ_{ev} , defined in the previous section. The initial conditions are $p_1 = 0.6$ bar, $T_1 = 270$ K, $f_{d1} = 0.005$, $r_{d1} = 1$ μm , $Ma_{pf} = 1.2$. After the initial jump, gas temperature decreases due to the endothermic phase transition. Droplet temperature slightly increases. At $t/\tau_{ev} \simeq 2$, the droplet completely disappears and the droplet temperature becomes meaningless. A decreasing gas temperature implies an increasing density and a decreasing velocity, so pressure increases. The saturation ratio $S = p_v/p_{vs}(T)$ attains a low value directly after shock compression, after which its value tends to increase. The vapor ends in a superheated state with $S \simeq 0.5$.

It is clear that the evaporation time τ_{ev} defined in (15.4.80) is a very good measure for the initial slope of $r^2(t)$, but it underestimates the real lifetime of a droplet T_{tot} . This was further investigated for different radii and droplet mass fractions and different shock strengths. In Fig. 15.4.6a, the ratio τ_{tot}/τ_{ev} is shown as a function of Ma_{pf} and r_{d1} for the limiting case $f_{d1} \simeq 0$, that is, for constant post-shock velocity and temperature. It is clear that for smaller

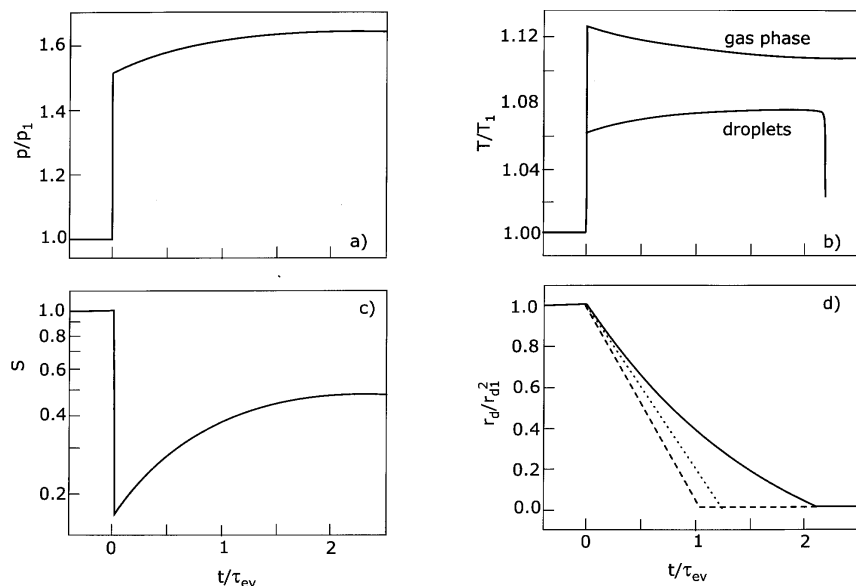


FIGURE 15.4.5 Shock structure in humid nitrogen with water droplets with an initial radius of $1\text{ }\mu\text{m}$. (a–c) Pressure, temperature, saturation ratio, and droplet radius squared as a function of Lagrangian time. (d) Dashed curve, low droplet concentration, no Knudsen effects; dotted curve, tangent according to initial post-shock slope. Initial conditions: 60 kPa, 270 K, $f_{d1} = 0.05$, $Ma_{pf} = 1.2$, $\tau_{ev} = 3.6\text{ ms}$. After Smolders and Van Dongen (1992).

droplets the Knudsen effect become evident. In Fig. 15.4.6b the droplet radius is fixed at $1\text{ }\mu\text{m}$ while f_{d1} is varied. For any f_{d1} , there is a limiting shock Mach number below which droplets only partly evaporate. This limiting Mach number corresponds with the asymptotes indicated.

15.4.8 EXPERIMENTAL OBSERVATIONS

At Eindhoven University of Technology, a combination of an expansion wave tube and a shock tube has been developed in order to study shock wave propagation in a suspension of droplets. The facility shown in Fig. 15.4.7 consists of a central part, the test section, separated by means of diaphragms from a vacuum vessel at one end and a conventional driver section at the other end. After preparation of a mixture of nitrogen, water vapor, and condensation nuclei in the test section, the diaphragm at the vacuum vessel side was ruptured. An orifice O was mounted to control the depth of the expansion wave. As a result of the passage of the expansion wave, the vapor became

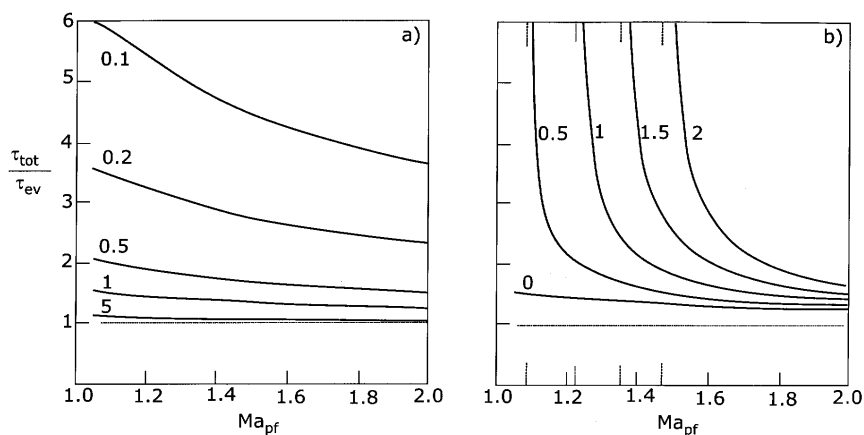


FIGURE 15.4.6 Ratio of total evaporation time and τ_{ev} as defined in the text, as a function of partly frozen shock Mach number. Water droplets in humid nitrogen. Initial conditions: 60 kPa, 270 K, (a) $f_{dl} = 0$, $r_{dl} = 0.1$ – $5 \mu\text{m}$, (b) $f_{dl} = 0$, 0.005, 0.01, 0.015, 0.02, $r_{dl} = 1 \mu\text{m}$. In (b), the limiting Mach numbers corresponding to complete evaporation are indicated. After Smolders and Van Dongen (1992). Shock wave structure in a mixture of gas, vapour and droplets, *Shock Waves* 2: 255–267. With permission from Springer-Verlag.

supersaturated and a cloud of droplets was formed. After reflection of the expansion wave from the closed left end of the test section, the fog became stagnant. Then, the second diaphragm was opened and a shock wave was formed in this stagnant fog.

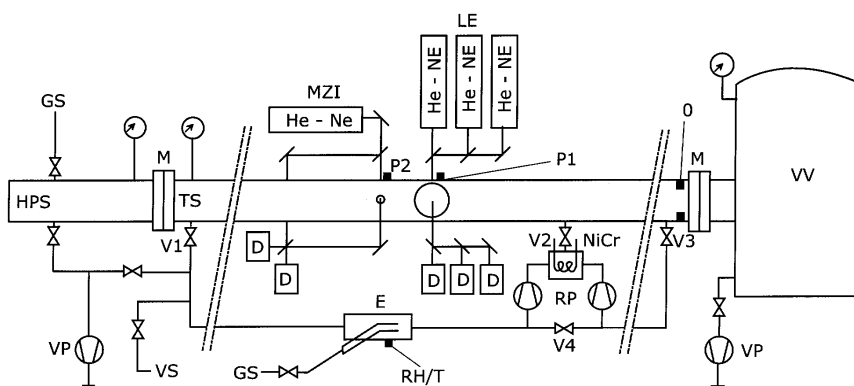


FIGURE 15.4.7 Experimental set-up used by Smolders and Van Dongen (1992). TS, test section; VV, vacuum vessel; HPS, high pressure section; O, orifice; M, membrane; V, valve; VP, vacuum pump; RP, rotary pump; VS, vapor supply; GS, gas supply; E, ejector; NiCr, wire for nuclei production; RH/T, relative humidity and temperature gauge; MZI, Mach-Zehnder interferometer; P, pressure transducer; LE, three-wavelength light extinction setup.

First experimental results were presented by Goossens *et al.* (1986). Later, the experiment was extended and refined by Goossens *et al.* (1988), by Smolders (1992), and by Smolders and Van Dongen (1992). The test section was a nickel-coated steel tube of square cross-section ($100 \times 100 \text{ mm}^2$) with a length of 12.8 m. The vacuum vessel had a volume of 0.4 m^3 . The test section was filled with humid nitrogen.

Then, the mixture was homogenized by means of a recirculation circuit. The water vapor pressure was monitored during the process of filling and recirculation by means of a capacitive gauge (Humicap, HMP 124 B). During recirculation condensation nuclei were added, chromium oxide particles with a diameter of $30 \pm 10 \text{ nm}$, obtained by leading the gas flow around a heated oxidized Ni–Cr wire. Finally, the driver section was pressurized, and the wave experiment was started by electrically heating the wires supporting the polyester diaphragm at the vacuum vessel end of the expansion tube, and by rupturing the second diaphragm after a suitable delay time.

The observation window was situated at a distance of 6.2 m from the HPS diaphragm. The following physical properties were measured: the pressure p by means of a piezoelectric Kistler transducer (coated with epoxy resin), the modal droplet size, the variance in droplet size, and the droplet number density by means of a wavelength-resolved light extinction method (Van Dongen *et al.*, 1994), and the gas density by means of laser interferometry with phase quadrature (Goossens and Van Dongen, 1987). The density jump across a partly frozen shock wave was not measured, but deduced from the pressure jump and the appropriate Rankine–Hugoniot relation. In a previous paper, Goossens *et al.* (1986) did prove experimentally that such a procedure is valid and accurate.

From the measured physical quantities two other important physical variables could be deduced. The temperature was found from $T = p/\rho_c R'$, and the experimental saturation ratio S was obtained by combining the law of conservation of condensable component (water) with the measured liquid concentration $\rho_d = n_d(\frac{4}{3}\pi r_d^3)$. A large number of experimental runs was performed for initial droplet radii around $1 \mu\text{m}$ and partly frozen shock Mach numbers ranging from 1.2 to 2.0.

An example of the experimentally observed shock structure obtained by Smolders and Van Dongen (1992) is shown in Fig. 15.4.8. The pre-shock state is a saturated mixture with a modal droplet radius of $1.59 \mu\text{m}$, a pressure of 58 kPa, and a temperature of 270 K, slightly below the freezing point of water. The droplet number density is $3.0 \times 10^{11} \text{ m}^{-3}$. The experimental time histories of pressure, temperature, saturation ratio $S = p_v/p_{vs}$, and droplet radius squared are compared with the results of the theoretical model based on the wet-bulb approximation. The evaporation process and the associated changes in thermodynamic states are accurately predicted. The saturation

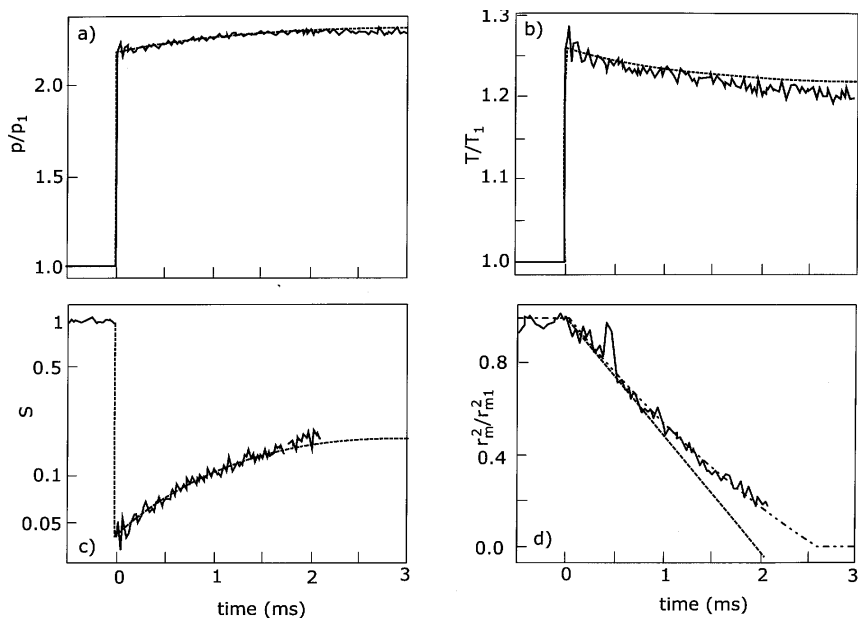


FIGURE 15.4.8 Shock structure in a suspension of water droplets in nitrogen. Experiment and theory, (a) pressure, (b) temperature, (c) saturation ratio, (d) modal droplet radius squared. Conditions: $Ma_{pf} = 1.42$, $r_{d1} = 1.59 \mu\text{m}$, $n_{d1} = 3 \times 10^{11} \text{ m}^{-3}$, $p_1 = 0.58 \text{ bar}$, $T_1 = 270.2 \text{ K}$. From Smolders (1992).

ratio S jumps from an initial value of unity to a very low value of 0.04 due to shock heating. Droplet evaporation leads to an increase of S . In this particular example, all droplets disappear after 2.5 ms, leaving the mixture in an under-saturated state, $S \simeq 0.2$. Also, the decrease in gas temperature due to the endothermic character of droplet evaporation is observed. It should be noted that the time history for an observer in a laboratory reference frame is obviously different from the time history of the physical state of a mass element in a Lagrangian reference frame. The time constant for evaporation τ' in a laboratory reference frame is related to the time constant τ for a droplet while traversing the relaxation time by

$$\tau' \approx (u_{2pf}/u_1)\tau = (\rho_1/\rho_{2pf})\tau. \quad (15.4.93)$$

For all their experimental runs, Smolders and Van Dongen (1992) determined the evaporation time τ' from an estimate of the initial slope dr_d^2/dt , just after shock compression:

$$\tau' = r_{d1}^2 (dr_d^2/dt)_{2,0}^{-1}. \quad (15.4.94)$$

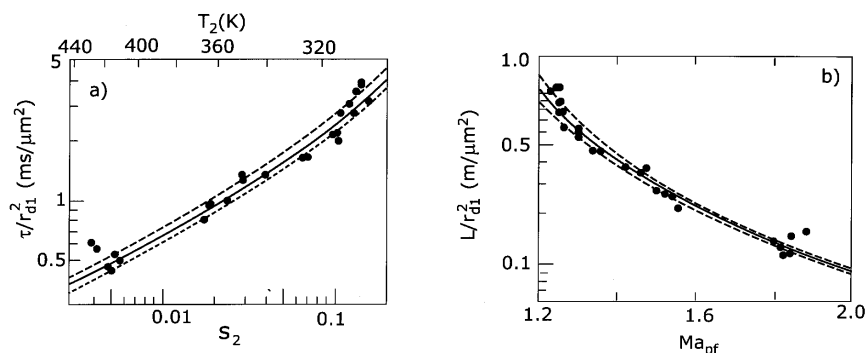


FIGURE 15.4.9 Evaporation times and lengths of relaxation zones for shocks in suspensions of water droplets in nitrogen. Experiment and theory. (a) Lagrangian evaporation times versus post-shock saturation ratio and temperature. (b) Evaporation length versus shock Mach number. Curves correspond with theoretical bounds taking into account the variation in pre-shock conditions. After Smolders and Van Dongen (1992). Shock wave structure in a mixture of gas, vapour and droplets, *Shock Waves* 2: 255–267. With permission from Springer-Verlag.

By combining (15.4.94) with (15.4.93) the results could be expressed in terms of the more universal Lagrangian evaporation time τ . The results are shown in Fig. 15.4.9a. The experimental values of τ/r_{d1}^2 are plotted versus the logarithms of the saturation ratio S_2 , directly after shock compression. As an alternative the same results are shown in Fig. 15.4.9b. Instead of a relaxation time τ , a relaxation length $L = u_1 \tau$ is plotted, now versus the partly frozen shock Mach number. The theoretical curves in Fig. 15.4.9 are based on an average pre-shock state. The dashed lines reflect the small but finite variations in the initial post-shock conditions. It is once more clear that the theoretical model based on the wet-bulb approximation yields an adequate description of the experimental observations.

15.4.9 SHOCK WAVES IN WET STEAM

The shock conservation laws (15.4.47)–(15.4.50) are valid for any mixture of carrier gas, vapor, and droplets and can therefore also be applied to the case of wet steam for which the gas mass fraction $f_d = 0$. Still, there is an important difference between the case of a dilute vapor in a carrier gas and the wet steam case. In the dilute vapor, the appropriate condition at the droplet surface is that the vapor pressure equals its saturation value corresponding to the droplet temperature. In wet steam, however, it is the droplet surface temperature that equals its saturation value corresponding to the vapor pressure.

The structure of shock waves in wet steam has been investigated in great detail by Young and Guha (1991). We follow part of their analysis in a

somewhat simplified form. First, we recall that the expression for the equilibrium sound speed (15.4.34)–(15.4.35) also pertains to the case of wet steam:

$$a_e^2 = \frac{(1 - f_d)R_v T}{1 - \frac{2R_v T}{L} + \frac{\bar{\gamma}}{\bar{\gamma} - 1} \left(\frac{R_v T}{L} \right)^2}. \quad (15.4.95)$$

For $\bar{\gamma}/\bar{\gamma} - 1$ we find with (15.4.17)

$$\frac{\bar{\gamma}}{\bar{\gamma} - 1} = \frac{c_{pv}}{R_v} + \frac{f_d}{1 - f_d} \frac{c_l}{R_v}. \quad (15.4.96)$$

The definition of the partly frozen speed of sound has to be adapted to the situation of pure steam and to the condition that the droplet temperature equals its saturation value $T_s(p)$. Therefore, droplet temperature and vapor pressure are different even in case of frozen mass transfer between droplet and vapor. The derivation of the expression of the wet steam partly frozen sound speed a_{ws} proceeds along the same lines as the derivations of the other sound speeds as given before and is not discussed in detail. The result is

$$a_{ws}^2 = \frac{(1 - f_d)\gamma R_v T}{1 + \frac{f_d}{1 - f_d} \gamma \frac{c_l}{R_v} \left(\frac{R_v T}{L} \right)^2}, \quad (15.4.97)$$

with

$$\gamma = \frac{c_{pv}}{R_v - c_{pv}}. \quad (15.4.98)$$

The proper expressions for the equation of state and for the enthalpy are

$$p = \rho(1 - f_d)R_v T \quad (15.4.99)$$

$$h = (1 - f_d)c_{pv}T + (1 - f_d)L_0 + f_dc_lT_s. \quad (15.4.100)$$

In deriving the equations for the shock structure in wet steam, we assume that there is no velocity slip between droplets and gas, so that n_d/ρ is constant:

$$\frac{df_d}{dt} = \frac{n_d}{\rho} \frac{dm_d}{dt}. \quad (15.4.101)$$

Further, we denote the droplet temperature by T_s to emphasize that this is a saturation temperature. Combining (15.4.101) with mass and energy conservation for a single droplet (15.4.52), (15.4.54) and with the expression for the heat flux (15.4.57), we arrive at

$$L \frac{df_d}{dt} = f_dc_l \frac{dT_s}{dt} + \frac{(1 - f_d)c_{pv}\Delta T}{\tau_{ws}}, \quad (15.4.102)$$

with the superheat $-\Delta T$ defined with

$$\Delta T = T_s - T, \quad (15.4.103)$$

and with a characteristic time τ_{ws} , defined by Young and Guha (1991):

$$\tau_{ws} = \frac{1 - f_d}{f_d} \frac{2c_{pv}r_d^2\rho_l}{3\lambda Nu_H}. \quad (15.4.104)$$

We are now ready to combine the basic conservation laws of mass, momentum, and energy in the shock fixed reference frame (15.4.88)–(15.4.90) with the definitions (15.4.99)–(15.4.104). The conservation laws are used in their differential form, and we write $d/dt \equiv u/dx \equiv uD$, so using the notation $D \equiv d/dx$. The result is

$$\frac{Dp}{p} - \frac{DT}{T} + \frac{Du}{u} + \frac{Df_d}{1 - f_d} = 0 \quad (15.4.105)$$

$$\frac{Dp}{p} + \frac{u^2}{R_v T} \frac{1}{1 - f_d} \frac{Du}{u} = 0 \quad (15.4.106)$$

$$\frac{DT}{T} + \frac{f_d}{1 - f_d} \frac{c_l}{c_{pv}} \frac{DT_s}{T} + \frac{u^2}{c_{pv} T} \frac{1}{1 - f_d} \frac{Du}{u} - \frac{L}{c_{pv} T} \frac{Df_d}{1 - f_d} = 0. \quad (15.4.107)$$

We proceed now as follows. First, we replace the gas temperature T by $T_s - \Delta T$. Further, we use the Clausius–Clapeyron equation (15.4.8):

$$\frac{DT_s}{T_s} = \frac{R_v T}{L} \frac{Dp}{p}. \quad (15.4.108)$$

Finally, we use (15.4.106) to eliminate the pressure in the continuity equation (15.4.105) and the energy equation (15.4.107). We obtain

$$\begin{aligned} & \frac{Du}{u} \left\{ 1 - \frac{u^2}{R_v T} \frac{1}{1 - f_d} \left[1 + \frac{f_d}{1 - f_d} \left(\frac{R_v T}{L} \right)^2 \frac{c_l}{R_v} - \frac{R_v T}{L} \right] \right\} \\ & + \frac{D\Delta T}{T} + \frac{c_{pv} T}{L} \frac{\Delta T}{u\tau_{ws} T} = 0 \end{aligned} \quad (15.4.109)$$

$$\frac{Du}{u} \frac{u^2}{R_v T} \frac{1}{1 - f_d} \left(\frac{R_v T}{L} - \frac{R_v}{c_{pv}} \right) + \frac{D\Delta T}{T} + \frac{\Delta T}{u\tau_{ws} T} = 0. \quad (15.4.110)$$

We have made the approximation that in the prefactors $T_s/T \approx 1$. We take the difference between (15.4.109) and (15.4.110) and we eliminate the last terms of both equations by substitution. This yields two complicated expressions that

can be very much simplified by recognizing the expressions for the sound speeds a_e^2 (15.4.96) and a_{ws}^2 (15.4.97)

$$\frac{Du}{u} \left(1 - \frac{u^2}{a_{ws}^2} \right) - \left(1 - \frac{c_{pv}T}{L} \right) \frac{\Delta T}{u\tau_{ws}T} = 0 \quad (15.4.111)$$

$$\frac{Du}{u} \left(1 - \frac{u^2}{a_e^2} \right) + \left(1 - \frac{c_{pv}T}{L} \right) \frac{D\Delta T}{T} = 0. \quad (15.4.112)$$

It should be noted that Eqs. (15.4.111) and (15.4.112) describe the relaxation zone in wet steam as well for fully dispersed shock waves as for partly dispersed shock waves, provided that the condition is fulfilled that there is no velocity slip between droplets and gas. In the general case, all parameters, such as a_{ws} , a_e , u , τ_{ws} , and T , will vary in the relaxation zone. If the shock wave is very weak, there is no discontinuity and (15.4.111) and (15.4.112) describe the structure of a fully dispersed shock wave.

15.4.10 FULLY DISPERSED SHOCK WAVES IN WET STEAM

The shock wave becomes fully dispersed when $a_e < u < a_{ws}$. Since in a steady shock wave the gas velocity decreases, $Du < 0$, so that according to (15.4.112) $D(\Delta T) < 0$ for $u > a_e$ and $D(\Delta T) > 0$ for $u < a_e$. In the supersonic part of the wave front, the superheat ($-\Delta T$) increases, whereas in the subsonic part the superheat decreases. Far upstream and downstream of the wavefront $\Delta T = 0$, and $-\Delta T$ is maximum for $u = u_e$.

Following Young and Guha (1991), we consider a weak shock wave and assume that parameters such as a_{ws} , a_e , and τ_{ws} can be taken constant. We define a perturbation velocity

$$u = u' + a_e, \quad (15.4.113)$$

since for weak shocks $u'/a_e \ll 1$. Substitution of (15.4.113) into (15.4.112) and retaining terms up to the second order yields

$$\frac{2u'}{a_e^2} Du' = \left(1 - \frac{c_{pv}T}{L} \right) \frac{1}{T} D\Delta T, \quad (15.4.114)$$

which can be integrated to give

$$\frac{u'^2 - u_0'^2}{a_e^2} = \left(1 - \frac{c_{pv}T}{L} \right) \frac{\Delta T}{T}. \quad (15.4.115)$$

It is clear that ΔT vanishes far upstream, with $u' = u'_0$ and far downstream with $u' = -u_0$. The solution (15.4.115) for ΔT can be substituted in (15.4.111), and we obtain

$$\tau_{ws} \frac{du'}{dx} \left[1 - \left(\frac{a_e}{a_{ws}} \right)^2 \left(1 + \frac{2u'}{a_e} \right) \right] = \frac{u'^2 - u_0'^2}{a_e^2}. \quad (15.4.116)$$

Then, dimensionless parameters x^* , u^* and ϕ are introduced:

$$x^* = \left(\frac{a_{ws}}{a_e} \right)^2 \frac{x}{a_e \tau_{ws}} \quad (15.4.117)$$

$$u^* = \frac{u'}{u_0'} \quad (15.4.118)$$

$$\phi = \frac{(a_{ws}/a_e)^2 - 1}{2u_0'/a_e} \quad (15.4.119)$$

$$M_e = 1 + u_0'/a_e. \quad (15.4.120)$$

The upstream Mach number M_e is based on the equilibrium speed of sound and should always exceed unity for a shock wave to exist. Using these definitions, Eq. (15.4.116) is rewritten as

$$(\phi - u^*) \frac{du^*}{dx^*} = \frac{1}{2}(u^{*2} - 1). \quad (15.4.121)$$

The solution is

$$x^* = \ln \left\{ \frac{(1 - u^*)^{(\phi-1)}}{(1 + u^*)^{(\phi+1)}} \right\}, \quad (15.4.122)$$

if we locate the origin at $u^* = 0$.

In Fig. 15.4.10, taken from Young and Guha (1991), the solution is shown for three different values of the upstream Mach number M_e . It is important to note that M_e is the only parameter, and that (15.4.122) is a universal solution, independent of droplet size and wetness parameter f_d . For $M_e = 1.08$ a limiting solution is found. The second derivative d^2u^*/dx^{*2} becomes infinite at the shock front. Stronger shocks become partly dispersed, that is, a discontinuous wave front is followed by the relaxation zone. The real thickness of the shock front corresponds to a range Δx^* of the order of 5. With (15.4.117) we can calculate the corresponding shock thickness Δx . For wet steam with $p = 0.5$ bar and a droplet mass fraction $f_d = 0.1$, Young and Guha (1991) find values for Δx of approximately 100 mm, for droplets with a radius in the range of 0.3–0.4 μm . For more details the reader is referred to the paper by Young and Guha

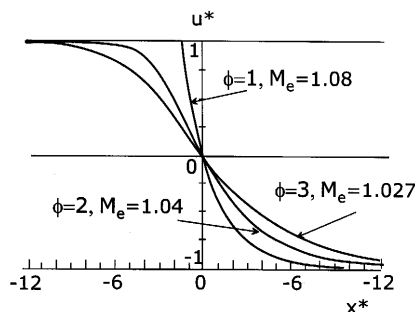


FIGURE 15.4.10 Velocity profiles in a fully dispersed shock wave in wet steam. Preshock condition: $p = 0.5$ bar, $f_d = 0.1$. A shock Mach number 1.08 corresponds with the transition from a fully dispersed to a partly dispersed shock wave. After Young and Guha (1991).

(1991), who also consider the more complicated case of a fully dispersed shock wave with velocity slip.

15.4.11 CONCLUSIONS

A typical property of the description of shock waves in gas liquid suspensions is that the thermodynamics of phase transition and of phase equilibrium comes into play. As a consequence the equilibrium sound speed even in a dilute mixture of water and carrier gas jumps at the point where the droplets fully vaporize and disappear. This jump is even more pronounced for wet steam. Since the ratio of frozen and equilibrium sound speeds for water–gas mixtures and for wet steam is of the order of 1.1, it means that weak compressional waves become fully dispersed shock waves. For wet steam, an analytical description of these fully dispersed waves is possible. It turns out that these fully dispersed waves have a thickness of the order of 10 cm for droplets with a diameter of 1 μm , whereas this thickness is proportional to diameter squared. Partly dispersed shock waves in a dilute mixture of water droplets in a humid carrier gas, such as air or nitrogen, even have a larger thickness, since the evaporation process is delayed by diffusion. In that case, a discontinuous shock front is followed by a relaxation zone. It is shown that this relaxation zone can be subdivided. First, there is a rather rapid equilibration of droplet and gas velocity, while the droplet temperature adopts its quasi-steady wet-bulb value. Then, droplet evaporation takes place on a much longer time and length scale. A theoretical model based on the so-called wet-bulb approximation appears to give an accurate description of shock structure. The model was verified with detailed experimental observations of shock waves in mixtures of water

droplets in humid nitrogen. Profiles of pressure, temperature, saturation ratio, and droplet size show an excellent agreement between theory and experiment. Also, a good agreement is found between predicted and observed droplet evaporation times for a wide range of parameters.

ACKNOWLEDGMENT

The author is indebted to Dr. H. J. Smolders for his important experimental and theoretical contributions to this work.

REFERENCES

- Clift, R., Grace, J. R., and Weber, M. E. (1978) *Bubbles, Drops and Particles*, Academic Press, New York.
- Davis, E. J. (1983) Transport phenomena with single aerosol particles. *Aerosol Sci. Technol.* **2**, 121–144.
- Fuchs, N. A. (1934) Ueber die Verdampfungsgeschwindigkeit kleiner Tröpfchen in einer Gasatmosphäre. *Phys. Z. Sowjet*, 224–243.
- Goossens, H. W. J., Berkelmans, M. C. J. M., and Van Dongen, M. E. H. (1986) Experimental investigation of weak shock waves, propagating in a fog. In: *Proc. 15th ISSWST*, Eds. D. Bershader and R. K. Hanson, Stanford University Press, 721–727.
- Goossens, H. W. J., Cleijne, J. W., Smolders, H. J., and Van Dongen, M. E. H. (1988) Shock wave induced evaporation of water droplets in a gas–droplet mixture. *Exp. Fluids* **6**, 561–568.
- Guha, A. (1992) Structure of partly dispersed normal shock waves in vapour droplet flows. *Phys. Fluids A* **4**, 1566–1578.
- Guha, A. (1992) Jump conditions across normal shock waves in pure vapour–droplet flows. *J. Fluid Mech.* **241**, 349–369.
- Guha, A. (1994) A unified theory of aerodynamic and condensation shock waves in pure vapour–droplet flows. *Phys. Fluids* **6**, 1893–1913.
- Guha, A., and Young, J. B. (1989) Stationary and moving normal shock waves in wet-steam. In: *Adiabatic Waves in Liquid–Vapor Systems*, IUTAM Symposium Göttingen, Eds. G. E. A. Meier, P. A. Thompson, Springer, 159–170.
- Gyarmathy, G. (1982) The spherical droplet in gaseous carrier steams: review and synthesis. In: *Multiphase Science and Technology 1*, Eds. G. F. Hewitt, J. M. Delhay, N. Zuber, McGraw-Hill, 99–279.
- Hastings, D. L., and Hodgson, J. P. (1969) p. 4.
- Hastings, D. L., and Hodgson, J. P. (1979) The formation of an aqueous fog in a shock tube. *J. Phys. D: Appl. Phys.* **12**, 2111–2122.
- Hubbard *et al.* (1975) p. 21.
- Hubbard, G. L., Denny, V. E., and Mills, A. F. (1975) Droplet evaporation: effects of transients and variable properties. *Int. J. Heat Mass Transfer*, **18**, 1003–1008.
- Kennard, E. H. (1938) *Kinetic Theory of Gases*, McGraw-Hill.
- Lu, H. Y., and Chiu, H. H. (1966) Dynamics of gases containing evaporable liquid droplets under a normal shock. *AIAA J* **4**, 1008–1011.

- Marble, F. E. (1969) Some gasdynamic problems in the flow of condensing vapors. *Astronautica Acta* 14, 585–614.
- Mitchner, M., and Kruger, C. H. (1973) *Partially Ionized Gases*, Wiley.
- Mozurkewich (1986) p. 23.
- Mozurkewich, M. (1986) Aerosol growth and the condensation coefficient for water: a review. *Aerosol Sci. Technol.* 5, 223–226.
- Nayfeh, A. H. (1966) Shock wave structure in a gas containing ablating particles. *Phys. Fluids* 9, 2351–2356.
- Paikert, B. (1990) Untersuchung der Kondensation mit Hilfe eines Stoßwellenrohrs. Ph.D. Thesis, University of Essen, Germany.
- Ranz, W. E., and Marshall, W. R. (1952) Evaporation from drops, part I. *Chemical Eng. Prog.* 48, 141–146. II. *Chemical Eng. Prog.* 48, 173–180.
- Roth, P., and Fischer, R. (1985) An experimental shock wave study of aerosol droplet evaporation in the transition regime. *Phys. Fluids* 28, 1665–1672.
- Rudinger, G. (1980) *Fundamentals of Gas-Particle Flow*, Elsevier, Amsterdam.
- Schaaf, S. A., and Chambré, P. L. (1961) *Flow of Rarefied Gases*, Princeton University Press, New Jersey.
- Sislian, J. P. (1975) Condensation of water vapour with or without a carrier gas in a shock tube. UTIAS Report no. 201, University of Toronto, Canada.
- Smolders, H.J. (1992) Non-linear Wave Phenomena in a Gas-Vapour Mixture with Phase Transition. Ph.D. Thesis, Eindhoven University of Technology, The Netherlands.
- Smolders, H. J., and Van Dongen, M. E. H. (1992) Shock wave structure in a mixture of gas, vapor and droplets. *Shock Waves* 2, 255–267.
- Smolders, H. J., Niessen, E. M. J., and Van Dongen, M. E. H. (1989) On the similarity character of an unsteady rarefaction wave in a gas-vapour mixture with condensation. In: *Adiabatic Waves in Liquid-Vapor Systems*, IUTAM Symposium Göttingen, Eds. G. E. A. Meier, P. A. Thompson, Springer, 63–75.
- Smolders, H. J., Niessen, E. M. J., and Van Dongen, M. E. H. (1992) The Random Choice Method applied to non-linear wave propagation in gas-vapour-droplets mixtures. *Comp. Fluids* 21, 63–75.
- Tam, C. K. W. (1969) The drag on a cloud of spherical particles in low Reynolds number flow. *J. Fluid Mech.* 38, 537–546.
- Timmler, J., and Roth, P. (1989) Measurements of high temperature evaporation rates of solid and liquid aerosol particles. *Int. J. Heat Mass Transfer* 32, 1887–1895.
- Tishkoff, J. M. (1979) A model for the effect of droplet interactions on vaporization. *Int. J. Heat Mass Transfer* 22, 1407–1415.
- Van Dongen, M. E. H., Smolders, H. J., Braun, C. J. M., and Snoeijis, C. A. M. (1994) Spectral light extinction to characterize fast fog formation. *Applied Optics* 33, 1980–1988.
- Wegener, P. P. (1975) Nonequilibrium flows with condensation. *Acta Mechanica* 21, 65–91.
- Wierzbna, A. (1990) Deformation and breakup of liquid drops in a gas stream at nearly critical Weber numbers. *Exp. Fluids* 9, 59–64.
- Young, J. (1993) The condensation and evaporation of liquid droplets at arbitrary Knudsen number in the presence of an inert gas. *Int. J. Heat and Mass Transfer* 36, 2941–2956.
- Young, J. B., and Guha, A. (1991) Normal shock wave structure in two-phase vapour-droplet flows. *J. Fluid. Mech.* 228, 243–274.
- Yousif, F. H., and Bakhtar, F. (1974) Behaviour of wet steam after disruption by a shock wave. In: *Multi-Phase Flow Systems*, Vol. II, Inst. Chem. Eng. Symp. Series 38, paper G3.

This Page Intentionally Left Blank

INDEX

A

Acoustic impedance, 186
Acoustic limit, 186–187
Amplification, bubbly liquids and, 703–704
Angle-of-incidence-variation-induced hysteresis
 asymmetric wedges, 101–106
 axisymmetric (conical) wedges, 107
 symmetric wedges, 91–92
Aspect-ratio-variation-induced hysteresis,
 96–97
Asymmetric wedges
 angle-of-incidence-variation-induced
 hysteresis, 101–106
 dual-solution domain, 100
 flow-Mach-number-variation-induced
 hysteresis, 106
 overall configurations, 98–100
Attenuation, granular materials and
 performance of, 656–658
 problems with describing, 653–656
Attenuation law, for spherical waves, 483–488
Atwood numbers, 514–515
AUTODYNE code, 463–464
Axisymmetric (conical) wedges, 106–107
Axisymmetric reflections
 applications, 314–315
 background information, 266–267
 CFD numerical experiments, 298–310
 conclusions, 315–317
 conical Mach reflection results, 280–288
 conical Mach reflection studies, 289–298

 conical Mach reflection theoretical aspects,
 310–313
 curved Mach stems, 278–279
 moving shock waves, 271–274
 postreflection rays, 279–280
 ray-shock theory, 272–274
 shift from regular to Mac reflection in conical
 problems, 312–313
 simple cones in steady supersonic flows,
 267–271
 solution of conical moving shock waves,
 274–280
 solutions for cases without self-similarity,
 279

B

Bernoulli equations, 492, 493, 494, 497, 502
Bessel function, 502
Blast waves
 See also Spherical shock waves
 loading, 562–563
Boundary layer displacement technique, 151
 See also Shock wave/boundary layer
 interactions
Bridging effect, pressure transducer and,
 632–635
Bubbles, 494–500
 experiments of the bubble competition
 process, 532–534
 -merger model and random initial
 conditions, 523–539

Bubbles (*continued*)

- re-shock experiments, 534–539
- three-dimensional effects on late time scaling laws, 528–532
- two-dimensional effects on late time scaling laws, 525–527

Bubbly detonation

- chemical reactions and interface mass transfer, 718–725
- development of, 711–712, 725–727
- evaporation of microdrops, continuous, 722–725
- evaporation of microdrops, instant, 718–722
- focusing and, 737–741
- formation of, 730–732
- generalized kinetics of, 714–716
- hot-spots mechanism, 713, 718, 727–729, 733–741
- initiation of, 727–728
- refracted wave function and Todes' kinetics, 712–714
- single bubble dynamics, 712–718
- waves in reactive bubbly liquids, 725–732

Bubbly liquids, shock waves in inert

- amplification, collision, and focusing, 702–711
- background information, 668–673
- focusing and, 707–711
- gas, state of, 679–680
- Iordansky-Kogarko-van Wijngaarden nonequilibrium two-phase model, 695–702
- plane wave and bubbly layers, 683–695
- plane wave and plane gas layers, 680–682
- plane wave and spherical bubble, 673–680
- relative motion, 678–679
- splitting of narrow waves into precursor and wave packet, 683–693
- wide waves and reflection from bubbly liquid interface, 693–695

Bulk approach, 569–570

C

Campbell-Pitcher model, 669–670

CCW approximation

- channel formula, 356–361
 - focusing and, 400, 401, 404–405
- CFD numerical experiments, 298–310
- comparison of ray-shock theory, 306–310

for conical Mach reflection, 299–306

Channels, shock wave propagation in

- branching channels, 344–348
- Chester-Chisnell-Whitham channel formula, 356–361
- conclusions, 391–392
- curved ducts, 341–343
- data bases, 390–391
- description of, 320–324
- deviations and expansion chambers, 339–341
- flow visualization of, 325–348
- flow visualization, effectiveness of, 348–350
- general Riemann problem, 383–387
- numerical methods, 375–392
- random choice method, 387–390
- Rudinger's method, 352–356
- SHAMRC codes, 377–383
- shock tube, description of, 325
- straight channels with cross-sections, 333–339
- straight ducts, 328–333
- unsteady quasi-one-dimensional flow, 350–352
- Whitham's theory of shock dynamics, 361–366
- Whitham's theory used to analyze propagation through bifurcated ducts, 367–375

Characteristics method, 400–401, 404–405

Chester-Chisnell-Whitham. *See* CCW

approximation

Clausius-Clapeyron equation, 751, 754, 776

Collisions

- See also* Head-on collisions
- bubbly liquids and, 705–707

Compliant limit, 187

Concave cylinders, reflections over, 155–163

Conical Mach reflection

- CFD scheme for, 299–306
- external/expanding flows, 280–284
- internal/converging flows, 285–288
- ray-shock solution for, 274–278
- results from ray-shock theory, 280–288
- theoretical aspects, 310–313
- with and without self-similarity, 278–279

Conical Mach reflection studies

- validation for external cone cases, 289–293
- within conical contractions, 293–298

Conservation equations, 36–37, 403

- of energy, 3
- of mass, 2
- of momentum, 2
- transfer of, from gas to droplets, 759–763
- Constant velocity wave reflections over
 - nonstraight surfaces, 155–170
- Contact discontinuity
 - head-on collision of a rarefaction wave with
 - a, 19–20
 - head-on collision of a shock wave with a,
 - 15–19
- Contact stress transfer, 617–619
- Continuity conditions, 185–186
- Continuum-mixture theory, 660
- Continuum regime, 761–762
- Convex cylinders, reflections over, 163–167

D

- Dalton's law, 752, 755
- Density ratio dependence, 498–500
- Detachment criterion, 76–79
- Detachment points, 194
- Dimensionality dependence, 501–502
- Direct Simulation Monte Carlo (DSMC)
 - technique, 92, 253
- Discontinuities
 - pseudo-steady flows and non-infinitely thin
 - contact, 153–154
 - pseudo-steady flows and nonstraight,
 - 148–149
 - steady flows and nonstraight, 115
- Discrete element method, 659
- Double-Mach reflection (DMR), 68
 - analytical formulation of, 126–131
 - pseudo-steady flow, 126–132
 - subtypes of, 131–132
- Downstream-pressure-variation-induced
 - hysteresis, 107–108
- Dual-solution domain, 81–82
 - asymmetric wedges, 100
 - stability of RR in, 91

E

- Effective stress behavior, 638–643
- Electrohydraulic lithotrippers, 421–426
- Electromagnetic lithotrippers, 426–427
- Electronic measuring of spherical waves,
 - 466–468
- Equilibrium equation, chemical, 719

- Eulerian granular approach, 659
- Extracorporeal shock wave application
 - (EWSA), 430
- Extracorporeal shock wave lithotripsy (ESWL),
 - 415–429
 - development of, 415–416
 - electrohydraulic lithotrippers, 421–426
 - electromagnetic lithotrippers, 426–427
 - goal of, 421
 - microexplosive lithotrippers, 429
 - piezoelectric lithotrippers, 428–429
 - pressure pulses, 417–418
 - shock wave propagation and interaction with
 - matter, 418–421
- Extracorporeal shock wave therapy (ESWT),
 - 430

F

- Fermat's principle, 201
- Finite difference (FD) codes, 376
- Finite element (FE) codes, 376
- Flow deflection process, 119–120
- Flow-Mach-number-variation-induced
 - hysteresis
 - asymmetric wedges, 106
 - axisymmetric (conical) wedges, 106–107
 - symmetric wedges, 91, 92–96
- Focusing
 - background information, 397–403
 - basic equations, 403
 - blast waves, 408–412
 - bubbly liquids and, 707–711, 737–741
 - CCW approximation, 400, 401, 404–405
 - characteristics method, 400–401, 404–405
 - logarithmic spiral-shaped contraction, 398
 - numerical simulations, 402
 - random choice Method, 401
 - shock tube experiment, 407–408
 - similarity method, 402, 405–407
 - tear drop insertion, 398
- Food preservation applications, 434–436
- Forchheimer equation, 550
- Free field experiments, 601
- Free molecular regime, 762
- Friedlander equation, 449

G

- Gas filtration, packing density and,
 - 635–638

Generalized Riemann problem (GRP) solver, 2, 26–35, 383–387

Granular media, weak shock wave interaction with

- applications and research, 598–599
- attenuation, problems with describing, 653–656
- attenuation performance of, 656–658

Granular media (*continued*)

- conclusions, 661–662
- contact stress transfer, 617–619
- dynamic Young moduli, 649–653
- effective stress behavior, 638–643
- experimental methods and materials, 600–614
- free field experiments, 601
- gas dynamic theory, 604
- layer compression, 643–653
- packing density and gas filtration, 635–638
- physical models and simulations, 658–661
- pressure transducer and bridging effect, 632–635
- shock tube experiments, 601, 603–604, 607
- sidewall friction, 619–623
- three-dimensional packing of spherical particles, 623–643
- two-dimensional packing of cylinders and disks, 614–623
- unsteady end-wall stress peak, 623–632
- unsteady flow pattern, 614–617
- wave movement and processes, 643–648

Guha's solution, 757–759

H

Hartree's method, 401

Head-on collisions

- between shock and rarefaction waves, 9–15
- between two shock waves, 3–9
- of planar shock waves with a nonrigid wall, 35–62
- of a rarefaction wave with a contact discontinuity, 19–20
- of a shock wave with a contact discontinuity, 15–19

Height-of-burst curves, 473–477

Hopkinson effect, 421

Hot-spots mechanism, 713, 718, 727–729, 733–741

Hypersonic interactions, consequences of, 230

heat transfer, 232–234

real gas effects, 234–235

wall temperature effects, 231–232

Hypersonic interactions, modeling of, 258–259

Hysteresis phenomenon, 82–83, 88–90

- angle-of-incidence-variation-induced, 91–92, 101–106, 107
- aspect-ratio-variation-induced, 96–97
- asymmetric wedges, 98–106
- axisymmetric (conical) wedges, 106–107
- downstream-pressure-variation-induced, 107–108
- flow-Mach-number-variation-induced, 91, 92–96, 106, 107
- symmetric wedges, 91–98
- three-dimensional effects, 97–98
- wedge-angle-variation-induced, 91–92
- wind tunnel construction and, 97

I

Incident-reflecting shock, 220–222

Incident shock wave (I.S.W.), 58

Inertial Confinement Fusion (ICF), 490

Instability

- applications, 490
- background information, 490–491
- experimental studies, 506–523
- random initial conditions, 523–539
- Rayleigh-Taylor, 491–502, 506–508
- Richtmyer-Meshkov, 503–506, 508–523

Inverse Mach reflection, 68, 75, 158–159, 160–163

Iordansky-Kogarko-van Wijngaarden nonequilibrium two-phase model

- development of, 695–696
- dispersion relationship, 697–700
- precursor, 696–697
- wave structure in bubbly incompressible liquid, 700–702

Irregular reflections (IR), 68

- dual-solution domain, 81–82
- regular reflection \leftrightarrow hysteresis phenomenon, 82–83
- regular reflection \leftrightarrow transition criteria, 75–81

J

Jump conditions, 3–4, 765–759

K

Kinetics equation, 713–714
 Klein-Gordon equation, 696–697
 Knudsen number, 750, 761, 762, 766

L

Lagrangian approach/coordinates, 36, 38, 463, 570, 733
 Laplace equations, 492, 502
 Layzer model, 497–498, 529
 Length scale criterion, 80–81, 144–145
 Liquid gas suspensions, interaction of waves with
 background information, 748–750
 conclusions, 779–780
 continuum regime 761–762
 experimental observations, 770–774
 free molecular regime, 762
 Guha's solution, 757–759
 heat, exchange of, 765–766
 jump conditions, 756–759
 mass, exchange of, 766–767
 momentum, exchange of, 763–765
 Rankine-Hugoniot relations, 757
 relaxation times, estimating, 763–768
 shock-induced evaporation in wet-bulb regime, 768–770
 speed of sound, equilibrium, 754–755
 speed of sound, fully frozen, 753
 speed of sound, partly frozen, 753–754
 thermodynamic properties of, 750–752
 transfer of momentum, mass, and energy, 759–763
 transition regime, 762–763
 waves in wet steam, 774–779
 Linear analysis, 491–494
 Linear Electric Motor (LEM), use of, 511, 528
 Logarithmic spiral-shaped contraction, 398
 Lyakhov model, 668

M

Mach, Ernst, 68
 Mach number
 experiments with high Mach numbers, 519–523
 experiments with low Mach numbers, 511–514

experiments with moderate Mach numbers, 518–519
 flow-Mach-number-variation-induced hysteresis, 91, 92–96
 wide-angle-variation-induced hysteresis, 91–92

Mach reflections (MR), 68

See also Conical Mach reflections; Pseudo-steady flows; Steady flows

analytical approaches for describing, 69–83
 analytical prediction of, 108–115
 curved Mach stems, 278–279
 direct, 68, 75
 double, 68, 126–132
 inverse, 68, 75, 158–159, 160–163
 ray-shock calculations for conical, 275
 shock polars, 74–75
 simple, 310, 314
 single, 68, 122–123
 spherical waves and, 471–472
 stationary, 68, 75, 158
 three-shock theory, 71–72
 transitional, 68, 123–125

Mach reflection \leftrightarrow regular reflection transition, 156–159

Macroscopic governing equations, 575–579

Mechanical equilibrium criterions, 79

Medicine, shock wave applications in
 extracorporeal shock wave lithotripsy (ESWL), 415–429
 in oncology and gene therapy, 432–434
 in ophthalmology, 431–432
 in orthopedics, 429–431
 thrombus ablation, 436–437

Microexplosive lithotripters, 429

Minimum time principle, 201–202

Monotonicity of interaction curves, 29–30

Moving shock waves, 271–274
 solution of conical, 274–280

Multiphase approach, 571–575

N

Navier-Stokes equations, 211, 252–253

Newton-Raphson scheme, 28, 32

Nonconstant velocity wave reflections over straight surfaces, 171

Nonlinear stages

 analysis of early, 494–496
 analysis of late, 497–498

Nonsteady effects, 148
 Nusselt numbers, 761, 765

O

Oblique shock impedance, 190–191
 Oblique shock wave reflections, 68
 analytical approaches for describing regular and Mach, 69–83
 conservation equations, 69
 detachment criterion, 76–79
 dual-solution domain, 81–82
 historical background, 68–69
 length scale criterion, 80–81
 regular reflection \leftrightarrow irregular reflection
 hysteresis phenomenon, 82–83
 regular reflection \leftrightarrow irregular reflection
 transition criteria, 75–81
 shock polars, 72–75
 sonic criterion, 79–80
 steady, 83–118
 three-shock theory, 71–72
 two-shock theory, 70
 von Neumann criterion, 79
 Oncology and gene therapy, 432–434
 One-dimensional refraction. *See* Refraction, one-dimensional
 One-dimensional wave interactions
 background information and research, 1–3
 conclusions, 63–64
 generalized Riemann problem (GRP) solver, 2, 26–35
 head-on collision between shock and rarefaction waves, 9–15
 head-on collision between two shock waves, 3–9
 head-on collision of planar shock waves with a nonrigid wall, 35–62
 head-on collision of rarefaction waves with a contact discontinuity, 19–20
 head-on collision of shock waves with a contact discontinuity, 15–19
 shock waves overtaken by rarefaction waves, 22–24
 shock waves overtaking another one, 20–22
 shock waves overtaking rarefaction waves, 24–26
 with flexible foam, 584–588
 with rigid porous material, 588–584
 Ophthalmology, 431–432
 Orthopedics, 429–431

P

Packing density and gas filtration, 635–638
 Padé approximation, 504
 Partial differential equations (PDEs), 376
 Passive measuring of spherical waves, 470–471
 Perturbation theory, third-order, 495
 Phacoemulsification and aspiration, 431–432
 Photogrammetric measuring of spherical waves, 468–470
 Piezoelectric lithotripters, 428–429
 Piston-path method, 465, 470
 Plane waves
 bubbly layers and, 683–695
 plane gas layers and, 680–682
 spherical bubble and, 673–680
 Poisson ratio, 38
 Polyvinylidene fluoride (PVDF), 417–418
 Porous media, shock wave propagation in
 background information, 546
 blast wave loading, 562–563
 case studies, 579–592
 flexible skeletons, systems with, 551–560
 general description of, 546–548
 macroscopic governing equations, 575–579
 multidimensional studies, 563–569
 multiphase approach, 571–575
 nature of porous foams, 548–551
 one-dimensional interaction with flexible foam, 584–588
 one-dimensional interaction with rigid material, 580–584
 regular reflection from rigid porous surface, 588–592
 rigid skeletons, systems with, 560–562
 single phase approach, 569–591
 theory and modeling, 569–575
 Power reflection and transmission, 185
 Prandtl-Meyer expansion, 111, 191
 Prandtl number, 761
 Pressure coefficients, 184
 Pressure-deflection shock polar, 72
 Pressure release condition, 187
 Pressure transducer and bridging effect, 632–635
 Principle of acoustic reciprocity, 187
 Pseudo-gas approach, 570–571
 Pseudo-steady flows
 diffraction process, 119–120
 domains of different types of reflections, 146–147
 double-Mach reflection, 126–132

- modification of two- and three-shock theories, 147–154
 - reflection phenomena, 120
 - regular reflection, 121–122
 - single-Mach reflection, 122–123
 - transitional-Mach reflection, 123–125
 - transition criteria, 144–146
 - triple point trajectory angles, 135–144
 - von Neumann reflection, 132–134
- R**
- Radius-time plane, 443–445
 - Ramp-induced interaction, 223–225
 - Random choice method (RCM), 387–390, 401, 484
 - Random initial conditions, 523–525
 - experiments of the bubble competition process, 532–534
 - re-shock experiments, 534–539
 - three-dimensional effects on late time scaling laws, 528–532
 - two-dimensional effects on late time scaling laws, 525–527
 - Rankine-Hugoniot shock equations, 3, 193, 215, 325, 513, 768
 - spherical waves and, 444–445, 460–461, 462, 466
 - weak shocks and, 757
 - Rankine-Kirchhoff equation, 751
 - Rarefaction waves
 - shock waves overtaken by, 22–24
 - shock waves overtaking, 24–26
 - Rarefaction waves, head-on collisions
 - between a shock wave and a, 9–15
 - of, with a contact discontinuity, 19–20
 - Rayleigh equation, 713, 719
 - Rayleigh-Taylor (RT) instability
 - density ratio dependence, 498–500
 - dimensionality dependence, 501–502
 - experimental studies, 506–508
 - linear analysis, 491–494
 - nonlinear stages, analysis of early, 494–496
 - nonlinear stages, analysis of late, 497–498
 - random initial conditions, 523–539
 - spike behavior, 500–501
 - Ray-shock theory, 272–274
 - calculations in conical Mach reflection, 275
 - CFD results, 306–310
 - equations for generalized, 276–278
 - results from, 280–288
 - summary of, 274–275
 - Real gas effects
 - pseudo-steady flows and, 149–150
 - on shock wave-boundary layer interactions, 234–235
 - steady flows and, 118
 - Reflecting surfaces, 151
 - nonsolid, 153
 - perforated, 152
 - porous, 152–153
 - rough, 152
 - slitted, 152
 - Reflection of waves
 - See also* Oblique shock wave reflections; Pseudo-steady flows; Steady flows; Unsteady flows; *under type of*
 - irregular (IR), 68
 - Mach (MR), 68
 - regular (RR), 68
 - von Neumann (vNR), 68, 76, 79
 - Reflection point, 68
 - Refracted wave function, bubbly detonation and, 712–714
 - Refraction
 - minimum time principle, 201–202
 - research on, 182
 - solution of fast-slow, 197–198
 - solution of slow-fast, 198–200
 - transmitted versus receiving, 182
 - Refraction, one-dimensional
 - continuity conditions at interface, 185–186
 - limits, 186–187
 - reflection and transmission coefficients, 184–185
 - solution of, 187–188
 - wave impedance, 184
 - wave systems, 183
 - Refraction, two-dimensional
 - refraction law, 191–192
 - relative refractive index, 193
 - shock polar, 193–197
 - wave impedance, 190–191
 - wave systems, 188–190
 - Refraction law, 191–192
 - Regular reflection \leftrightarrow irregular reflection
 - hysteresis phenomenon, 82–83
 - Regular reflection \leftrightarrow irregular reflection
 - transition criteria, 75–81
 - steady flows, 87–88
 - Regular reflection \leftrightarrow Mach reflection, 165–167, 170

- Regular reflections (RR), 68
 - See also Steady flows
 - analytical approaches for describing, 69–83
 - from rigid porous surface, 588–592
 - pseudo-steady flow, 121–122
 - shock polars, 73–74
 - spherical waves and, 471–472
 - stability of, in dual-solution domain, 91
 - transitional, 159–163
 - two-shock theory, 70
 - Relative motion, 678–679
 - Relative refractive index, 193
 - Relaxation times, estimating
 - comparison of, 767–768
 - exchange of heat, 765–766
 - exchange of mass, 766–767
 - exchange of momentum, 763–765
 - Representative elementary volume (REV)
 - concepts, 572
 - Re-shock experiments, 534–539
 - Reynolds averaged Navier-Stokes (RANS)
 - equations, 253
 - Reynolds-Favre averaged Navier-Stokes (RANS) equations, 256
 - Reynolds number, 209, 214, 764, 765
 - Richtmyer-Meshkov (RM) instability
 - Atwood numbers, 514–515
 - description of, 503–506
 - double-diaphragm shock tube, use of, 508–511
 - experimental studies, 508–523
 - experiments with high Mach numbers, 519–523
 - experiments with low Mach numbers, 511–514
 - experiments with moderate Mach numbers, 518–519
 - Linear Electric Motor (LEM), use of, 511, 528
 - random initial conditions, 523–539
 - single-mode, 511
 - three-dimensional, 516–518
 - Riemann problem, 2
 - Rigid limit, 187
 - Rudinger's method, 352–356
 - Runge-Kutta method, 406
 - three-dimensional effects on late time scaling laws, 528–532
 - two-dimensional effects on late time scaling laws, 525–527
 - Schmidt number, 761
 - Self-similarity, 154, 279, 311–312
 - SHAMRC (second-order hydrodynamic automatic mesh refinement code), 377–383
 - SHARC code, 463–464
 - Shock intensity, 185
 - Shock polars, 72–75
 - presentation of a von Neumann reflection, 134
 - refraction and, 193–197
 - Shock tube
 - description of, 325
 - experiment, 407–408
 - re-shock experiments, 534–539
 - Shock wave/boundary layer interactions
 - boundary layer response, 216–219
 - conclusions, 260–261
 - control actions, examination of, 247–252
 - control mechanisms, 245–247
 - effects of, 206–207
 - hypersonic interactions, 230–235
 - incident-reflecting shock, 220–222
 - interaction modeling, problems of, 252–259
 - interactions with boundary layer separation, 216–230
 - interactions without boundary layer separation, 211–216
 - normal shock interaction, 225–230
 - numerical accuracy, 253–256
 - outer inviscid flow structure, 220–230
 - physical modeling, 256–259
 - ramp-induced interaction, 223–225
 - structure of boundary layer, 211–213
 - three-dimensional effects, 237–245
 - transitional interactions, 235–236
 - types of interactions, 208–211
 - unsteady phenomena, 236–237
 - upstream influence length, 213–214
 - Shock wave diffraction process, 119–120
 - Shock waves
 - overtaken by rarefaction waves, 22–24
 - overtaking others, 20–22
 - overtaking rarefaction waves, 24–26
 - Shock waves, head-on collisions
 - between rarefaction waves and, 9–15
- S**
- Scaling laws, 455–460

- between two, 3–9
 - of, with a contact discontinuity, 15–19
 - of planar, with a nonrigid wall, 35–62
 - Sidewall friction, 619–623
 - Similarity method, 402, 405–407
 - Single-Mach reflection (SMR), 68
 - pseudo-steady flow, 121–122
 - Single phase approach, 569–591
 - Sonic criterion, 79–80
 - Spallation damage, 421
 - Speed of sound
 - equilibrium, 754–755
 - fully frozen, 753
 - partly frozen, 753–754
 - Spherical bubbles, plane waves and, 673–680
 - Spherical particles, three-dimensional packing
 - of, 623–643
 - Spherical shock waves
 - analytical solutions, 460–462
 - compendium of physical properties, 451–455
 - electronic measuring of, 466–468
 - experimental measurement techniques, 466–471
 - focusing, 408–412
 - formation of, 442–443
 - front properties, 445–447
 - general attenuation law for, 483–488
 - numerical modeling, 462–465
 - numerical reconstruction, 465
 - passive measuring of, 470–471
 - photogrammetric measuring of, 468–470
 - physical properties of expanding, 443–455
 - piston-path method, 465, 470
 - radius-time plane, 443–445
 - scaling laws, 455–460
 - shape of, 447–451
 - smoke tracers, use of, 465
 - Spherical shock wave reflections
 - height-of-burst curves, 473–477
 - over straight and nonstraight surfaces, 171–174
 - regular and Mach reflections, 471–472
 - Spike, defined, 494
 - Spike behavior, 500–501
 - Stanton number, 232
 - Stationary Mach reflection, 68, 75, 158
 - Steady flows
 - analytical prediction of Mach reflection wave configurations, 108–115
 - categories of reflections, 83–88
 - hysteresis phenomena, 88–108
 - modification of two- and three-shock theories, 115–118
 - reflection of curved incident waves from curved surfaces, 85
 - reflection of curved incident waves from straight surfaces, 83–84
 - reflection of straight incident waves from curved surfaces, 85
 - reflection of straight incident waves from straight surfaces, 86
 - types of reflections, 86–87
 - Strong shock solution, 73
 - Symmetric wedges
 - aspect-ratio-variation-induced hysteresis, 96–97
 - flow-Mach-number-variation-induced hysteresis, 91, 92–96
 - wide-angle-variation-induced hysteresis, 91–92
- T**
- Taylor-Sakurai theory, 460–462
 - Tear drop insertion, 398
 - Temperature equation, 713
 - Thermal conduction effects
 - pseudo-steady flows and, 153
 - steady flows and, 118
 - Thermodynamic properties, of liquid gas suspension, 750–752
 - Three-dimensional packing of spherical particles, 623–643
 - Three-dimensional shock wave-boundary layer interactions, 237–245
 - Three-shock theory, 71–72, 76
 - modification of, 115–118, 147–154
 - Thrombus ablation, 436–437
 - Todes' kinetics, 712–714
 - Total internal reflection, 187
 - Total reflection, 187
 - Transitional-Mach reflection (TMR), 68
 - analytical formulation of, 125
 - pseudo-steady flow, 123–125
 - Transitional regular reflection (TRR), 159–163
 - Transition criteria
 - detachment, 76–79
 - length scale, 80–81, 144–145
 - pseudo-steady flow, 144–146
 - sonic, 79–80

Transition criteria (*continued*)

von Neumann, 79

Transition regime, 762–763

Transmitted compression wave (T.C.W.), 58

Triple-deck theory, 211

Triple point trajectory angles

comparison of first and second, 143–144

first, 135–137

first, for small wedge angles, 137–139

at glancing incidence, 139

second, 140–143

Turbulent mixing zone (TMZ), 538–539

TVD approach, 299

Two-dimensional packing of cylinders and disks, 614–623

Two-dimensional refraction. *See* Refraction, two-dimensional

Two-dimensional wave interactions. *See*

Oblique shock wave reflections

Two-facet wedges, reflections over, 168–170

Two-fluid theory, 659–660

Two-shock theory, 70

modification of, 115–118, 147–154

U

Underwater shock waves, 415

Unsteady end-wall stress peak, 623–632

Unsteady flows

constant velocity wave reflections over

nonstraight surfaces, 155–170

nonconstant velocity wave reflections over

straight surfaces, 171

reflections over concave cylinders, 155–163

spherical wave reflections over straight and

nonstraight surfaces, 171–174

Unsteady quasi-one-dimensional flow, 350–352

Upstream influence length, 213–214

V

Viscous effects

pseudo-steady flows and, 150–151

steady flows and, 115–118

von Neumann criterion, 79

von Neumann Mach reflection (NMR), 310–311

von Neumann paradox, 132

von Neumann reflections (vNR), 68, 76, 79

effects in conical reflections, 310–311

pseudo-steady flow, 132–134

shock polar presentation of, 134

W

Wave impedance

oblique shock, 190–191

one-dimensional refraction, 184

two-dimensional refraction, 190–191

Weak shock solution, 73

triple point trajectory for, 163

Weak shock wave interaction. *See* Granular

media, weak shock wave interaction with

Wedge-angle-variation-induced hysteresis

asymmetric wedges, 101–106

symmetric wedges, 91–92

Wet-bulb regime, shock-induced evaporation

in, 768–770

Wet steam, waves in, 774–779

Whitham channel formula, 356–361

Whitham theory of shock dynamics, 361–366

used to analyze wave propagation through

bifurcated ducts, 367–375

Y

Young moduli, granular media and, 649–653